NASA/TP—2019–220459

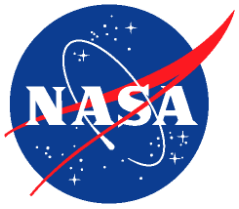

A Summary of NASA Rotary Wing Research: Circa 2008–2018

Gloria K. Yamauchi, Editor
Ames Research Center
Moffett Field, California

December 2019

NASA STI Program ... in Profile

Since its founding, NASA has been dedicated to the advancement of aeronautics and space science. The NASA scientific and technical information (STI) program plays a key part in helping NASA maintain this important role.

The NASA STI program operates under the auspices of the Agency Chief Information Officer. It collects, organizes, provides for archiving, and disseminates NASA's STI. The NASA STI program provides access to the NTRS Registered and its public interface, the NASA Technical Reports Server, thus providing one of the largest collections of aeronautical and space science STI in the world. Results are published in both non-NASA channels and by NASA in the NASA STI Report Series, which includes the following report types:

- TECHNICAL PUBLICATION. Reports of completed research or a major significant phase of research that present the results of NASA Programs and include extensive data or theoretical analysis. Includes compilations of significant scientific and technical data and information deemed to be of continuing reference value. NASA counterpart of peer-reviewed formal professional papers but has less stringent limitations on manuscript length and extent of graphic presentations.

- TECHNICAL MEMORANDUM. Scientific and technical findings that are preliminary or of specialized interest, e.g., quick release reports, working papers, and bibliographies that contain minimal annotation. Does not contain extensive analysis.

- CONTRACTOR REPORT. Scientific and technical findings by NASA-sponsored contractors and grantees.

- CONFERENCE PUBLICATION. Collected papers from scientific and technical conferences, symposia, seminars, or other meetings sponsored or co-sponsored by NASA.

- SPECIAL PUBLICATION. Scientific, technical, or historical information from NASA programs, projects, and missions, often concerned with subjects having substantial public interest.

- TECHNICAL TRANSLATION. English-language translations of foreign scientific and technical material pertinent to NASA's mission.

Specialized services also include organizing and publishing research results, distributing specialized research announcements and feeds, providing information desk and personal search support, and enabling data exchange services.

For more information about the NASA STI program, see the following:

- Access the NASA STI program home page at http://www.sti.nasa.gov

- E-mail your question to help@sti.nasa.gov

- Phone the NASA STI Information Desk at 757-864-9658

- Write to:
  NASA STI Information Desk
  Mail Stop 148
  NASA Langley Research Center
  Hampton, VA 23681-2199

NASA/TP—2019–220459

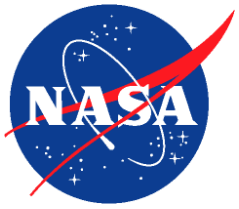

A Summary of NASA Rotary Wing Research: Circa 2008–2018

Gloria K. Yamauchi, Editor
Ames Research Center
Moffett Field, California

National Aeronautics and
Space Administration

Ames Research Center
Moffett Field, CA 94035-1000

December 2019

Available from:

NASA STI Support Services
Mail Stop 148
NASA Langley Research Center
Hampton, VA 23681-2199
757-864-9658

National Technical Information Service
5301 Shawnee Road
Alexandria, VA 22312
webmail@ntis.gov
703-605-6000

This report is also available in electronic form at
http://ntrs.nasa.gov

PREFACE

The purpose of this report is to provide a summary of NASA rotary wing research from 2008–2018. The report is divided into 12 chapters and each chapter was written by one or more authors. The author(s) of each chapter was given a list of references and copies of each reference. In general, papers were binned into subcategories and then summarized in chronological order. Using this approach, the reader can follow the evolution of research in a particular technical area. The window of 2008–2018 for capturing publications is approximate, hence the "Circa" in the report title. For example, if a major research activity just preceded 2008 or concluded shortly after 2018, the publications related to that activity outside of the 10-year window were included to present a more complete representation of the work. Therefore, some chapters cite references before 2008 and/or after 2018.

The summaries are based largely on just the abstract, introduction, and conclusion of each publication. In his seminal American Helicopter Society Alexander Nikolsky Honorary Lecture in 2010—*Milestones in Rotorcraft Aeromechanics*—Wayne Johnson reminded us "…… we should take care to compose good introductions for our papers and reports. Remember that we are writing for the historical record." After sifting through hundreds of papers for this report, the authors and I heartily agree with his prudent advice.

Many thanks are extended to the authors of the chapters: Brian Allan, Athena Chan, Paula Dempsey, Paul Giel, Karen Jackson, Wayne Johnson, Lee Kohlman, Richard Kreeger, Winnie Kuang, David Lewicki, Carlos Malpica, Mike Marcolini, Chris Silva, Chris Snyder, and Larry Young. They did their best to provide a concise and accurate summary of each paper. Choice of figures in each chapter was at the discretion of these authors, with occasional input by the Editor. Gathering, sorting, and summarizing hundreds of papers was more work than expected, stretching the 1-year project into 2 years. Despite what we thought was a careful accounting of the papers published between roughly 2008 and 2018, omissions of papers may have occurred—I offer my apologies in advance for these unintended omissions.

I am grateful to the following people for their contributions in reviewing chapters, finding papers, and/or checking the sources of the figures: Martin Annett, Doug Boyd, Susan Gorton, Luther Jenkins, Susan Johnson, Tim Krantz, Beth Lee-Rausch, Tom Norman, Norm Schaeffler, Noah Schiller, Linda Taylor, Li Wang, and Bill Warmbrodt. Also, the library staff at NASA Glenn Research Center did a great job in collecting the bulk of the papers we requested for this report.

Since late 2005, NASA rotary wing/vertical takeoff and landing (VTOL) research has been performed under various project names, but the one constant has been the steadfast leadership of Susan Gorton. The research summarized in this document was performed under Susan's watch, which continues at the time of this publication. Her advocacy of rotary wing/VTOL research to internal and external stakeholders, her ability to navigate through budget challenges, and most importantly, her ability to motivate and lead researchers across multiple NASA Centers to work as a team, has enabled 14 years (and counting) of highly productive research for the Nation. Susan, her leadership team, and the researchers conducting rotary wing/VTOL work are an exceptional group of people; working with them these many years has been a privilege for me.

Finally, I am very grateful to Catherine Dow of Dow Technical Services for her amazing professionalism, patience, and optimism in preparing this report for publication.

Gloria K. Yamauchi, Editor
NASA Ames Research Center
December 2019

TABLE OF CONTENTS

Introduction 1

Chapter 1. Acoustics

Introduction 3
External Noise Sources 3
Noise Modeling 4
Noise Reduction and/or Control 10
Interior Noise Sources 17
Interior Noise Modeling 17
Interior Noise Control 20
Noise Propagation, Modeling, Optimized Flight Paths, and Auralization 25
Noise Propagation 25
Noise Modeling 30
Design of Optimized Flight Paths 36
Auralization 39
Alternative Vehicle Concepts 43
Electric Propulsion 43
Open Rotors 47
Additional Research 47
References 47

Chapter 2. Aeromechanics

Introduction 55
Testing and Simulations of the UH-60A Rotor 58
Individual Blade Control Wind Tunnel Test 58
UH-60A Airloads Wind Tunnel Test 59
Rotor Loads Correlation and Stall 62
High Advance Ratio 64
Compounds, Lift-Offset Rotors, and Coaxial Rotors 65
Structural Loads Modeling and Prediction 68
Three-Dimensional (3D) Rotor Structural Dynamic Analysis 68
Structural Loads Prediction 71
HART Blade Structural Properties 71
Adjoint Capability for Comprehensive Analysis 73
Flow Control 74
Fuselage Drag and Downwash Reduction 74
Dynamic Stall Mitigation 79
Active Flap and Active Twist Rotors 81
Active Flap Rotors 81
Other Active Flap Rotors 87
Active Twist Rotors 89

Chapter 2. Aeromechanics (cont.)

Tiltrotors 91
JVX 92
Tiltrotor Aeroelasticity....95
Large Heavy Lift Tiltrotors....96
Operational Issues....102
Tiltrotor Modeling 103
General Aeromechanics....109
References....110

Chapter 3. Computational Fluid Dynamics (External Flow)

Introduction....121
Advanced CFD Development....121
Adaptive Mesh Refinement (AMR)....121
Higher-Order Schemes....124
Overset Methods for Unstructured Mesh....124
Multigrid Methods 125
Turbulence Modeling....126
Flow Visualization....126
Computational Structural Dynamics....127
Additional Research....128
CFD Applications and Validations 130
UH-60A Airloads Simulations....130
Slowed Rotor 145
Active Aerodynamic Load Reduction on a Rotorcraft Fuselage 146
Active Twist Rotor....149
HART-II....150
Hover Validation....151
Coaxial Rotor....154
Novel CFD Applications....155
Rotor Design Optimization Using Adjoint-Based Approach in FUN3D 157
References....162

Chapter 4. Experimental Methods

Introduction....169
Particle Image Velocimetry 169
Pressure Sensitive Paint....176
Blade Deformation Measurement Techniques....178
Background Oriented Schlieren....181
Infrared Thermography....183
Sensor Development and Novel Applications 186
References....188

Chapter 5. Flight Dynamics and Control

Conceptual Design and Simulation....193
Vehicle Modeling....198
Flight Control Design....198
Active Rotor Control....199
Modeling....199
On-Blade Control....200
Individual Blade Control (IBC)....200
Continuous Trailing-Edge Flaps....202
Large Rotorcraft....203
Pilot-Vehicle Interface....206
Active Inceptors....206
Rotational Throttle Interface....207
Control Augmentation for Degraded Visual Environments....208
Handling Qualities Requirements....209
Stability Margins for Large Rotorcraft....209
Hover and Low-Speed Response Types for Large Rotorcraft....210
Open-Loop Onset Point Criteria....211
Modeling of Pilot Control Behavior....213
Flexible Dynamic Systems....217
References....217

Chapter 6. Drive Systems

Introduction....221
Multispeed Drive Systems....221
Multispeed Drive Dynamic Analysis....226
Gear Windage....226
Advanced Hybrid Composite Components....228
Drive System Component Life....231
Advanced Drive System Components....237
High-Speed Gearing....247
Lubrication....250
Health Monitoring and Condition-Based Maintenance....253
Gas Foil Bearings....273
Nickel-Titanium Alloys for Rolling Element Bearing Applications....284
References....285

Chapter 7. Engines

Introduction....299
Engine/Drive System Studies....300
Variable Speed Power Turbine (VSPT)....301
High Efficiency Centrifugal Compressor (HECC)....316
Modeling and Simulation (MODSIM): Compressor Flow Modeling and Experiments....321
Modeling and Simulation (MODSIM): Engine Health Assessment....322
Modeling and Simulation (MODSIM): Wave Rotor....323

Chapter 7. Engines (cont.)

Modeling and Simulation (MODSIM): PyCycle—Future Engine Modeling Code 324
References 325

Chapter 8. Crashworthiness

Introduction 331
WASP Skid Gear Testing and Simulation 333
Experimental Program 333
Analytical Modeling 335
Important Findings and Significance 338
Full-Scale Crash Test and Simulation of an MD-500 Helicopter With and Without an External Deployable Energy Absorber (DEA) 339
Important Findings and Significance 347
ATD Impulsive Loading and Simulation 347
Important Findings and Significance 358
Model Calibration Using Uncertainty Propagation and Parameter Sensitivity 359
Important Findings and Significance 363
Development and Evaluation of Two Composite Energy Absorbers 365
Description of the Energy Absorbers 365
Coupon Level 367
Element/Component Level 368
Full-Scale Level 371
Important Findings and Significance 379
Bird Strike Simulation 380
Important Findings and Significance 380
Modeling and Simulation of the ATR42-300, a Commuter Airplane 381
Experimental Program 381
Model Development 383
Test-Analysis Comparisons 384
Important Findings and Significance 389
Drop Testing and Simulation of Two F28 Fuselage Sections 389
Experimental Testing 390
Model Development 392
Test-Analysis Comparisons 394
Important Findings and Significance 402
Survivable Affordable Repairable Airframe Program (SARAP) 402
Important Findings and Significance 409
Full-Spectrum Crashworthiness 410
Important Findings and Significance 411
Recommendations for Future Rotorcraft Crashworthiness Research 412
Facilities and Equipment for Conducting Aircraft Crash Testing 412
Updated Aircraft Crash Certification Requirements 412
Crash Modeling and Simulation Techniques 413
Structural Design for Improved Aircraft Crashworthiness 413
Conclusions 414
References 415

Chapter 9. Icing

Introduction....425
Background....425
Rotorcraft Icing Computational Tool Development....426
Cartesian Methods....428
Unstructured Methods....428
Hybrid Methods....429
Computational Models....429
Validation Experiments in the Icing Research Tunnel....430
Heated Tail Rotor Experiments....430
Oscillating Airfoil Experiments....431
Experimental Method Development....431
Development of 3D Scanning Techniques....432
Scaling Techniques for Rotorcraft....433
Ice Adhesion Measurement....434
Ice Adhesion and Shedding Prediction....436
Shedding Prediction....436
Ice Adhesion Modeling....437
Ice Protection Systems (IPSs) for Rotorcraft....438
Summary....439
References....441

Chapter 10. Structures and Materials

Introduction....447
Erosion-Resistant Thermal Barrier Coatings....448
Ceramic Materials and Composites....449
Durability and Damage Tolerance....451
Cabin Noise Reduction....456
Smart Materials....458
Concluding Remarks....459
References....459

Chapter 11. Conceptual Design and System Analysis

Introduction....463
NASA Design and Analysis for Rotorcraft (NDARC)....464
Civil Tiltrotors (CTRs)....467
Propulsion Architectures for the LCTR/LCTR2....469
Operational Concepts for a Fleet of Civil Tiltrotors....472
Civil Tiltrotor Aerodynamics....474
Conceptual Design Tool Chain Development....475
Task 1: Developed Conceptual Design-Level Tools or Surrogates....478
Task 2: Developed Appropriate Metrics for Handling Qualities, Acoustics, and Emissions....479
Task 3: Integrated Tools Within OpenMDAO Using a Modular Approach....480

Chapter 11. Conceptual Design and System Analysis (cont.)

Task 4: Demonstrated Process by Generating Designs of Low-Noise, Low-Emission VTOL Aircraft 481
Lessons Learned From the TC 484
Small UAS (sUAS) Research 485
Performance of Multi-Rotor Vehicles 486
Acoustics 488
High-Fidelity Simulations 492
Urban Air Mobility (UAM) 494
UAM Concept Vehicles 494
Electric/Hybrid-Electric Propulsion Studies 496
UAM System Studies 497
Concepts for Public Service 499
References 500

Chapter 12. Mars Helicopter

Introduction 509
Testing in the JPL Space Simulator 512
Supplemental Testing and Analysis in a Mars Environment 519
Testing in the Planetary Aeolian Laboratory (PAL) 519
Rotor Aerodynamic Analysis 523
References 525

A SUMMARY OF NASA ROTARY WING RESEARCH: CIRCA 2008–2018

Gloria K. Yamauchi, Editor

NASA Ames Research Center

INTRODUCTION

The general public may not know that the first "A" in NASA stands for Aeronautics. If they do know, they will very likely be surprised that in addition to airplanes, the "A" includes research in helicopters, tiltrotors, and other vehicles adorned with rotors. There is, arguably, no subsonic air vehicle more difficult to accurately analyze than a vehicle with lift-producing rotors. No wonder that NASA has conducted rotary wing research since the days of the NACA and has partnered, since 1965, with the U.S. Army in order to overcome some of the most challenging obstacles to understanding the behavior of these vehicles.

Since 2006, NASA rotary wing research has been performed under several different project names [Gorton et al., 2015]: Subsonic Rotary Wing (SRW) (2006–2012), Rotary Wing (RW) (2012–2014), and Revolutionary Vertical Lift Technology (RVLT) (2014–present). In 2009, the SRW Project published a report that assessed the status of NASA rotorcraft research; in particular, the predictive capability of NASA rotorcraft tools was addressed for a number of technical disciplines. A brief history of NASA rotorcraft research through 2009 was also provided [Yamauchi and Young, 2009]. Gorton et al. [2015] describes the system studies during 2009–2011 that informed the SRW/RW/RVLT project investment prioritization and organization. The authors also provided the status of research in the RW Project in engines, drive systems, aeromechanics, and impact dynamics as related to structural dynamics of vertical lift vehicles.

Since 2009, the focus of research has shifted from large civil VTOL transports, to environmentally clean aircraft, to electrified VTOL aircraft for the urban air mobility (UAM) market. The changing focus of rotorcraft research has been a reflection of the evolving strategic direction of the NASA Aeronautics Research Mission Directorate (ARMD). By 2014, the project had been renamed the Revolutionary Vertical Lift Technology Project. In response to the 2014 NASA Strategic Plan, ARMD developed six Strategic Thrusts. Strategic Thrust 3B was defined as the "Ultra-Efficient Commercial Vehicles—Vertical Lift Aircraft." Hochstetler et al. [2017] uses Thrust 3B as an example for developing metrics usable by ARMD to measure the effectiveness of each of the Strategic Thrusts. The authors provide near-, mid-, and long-term outcomes for Thrust 3B with corresponding benefits and capabilities. The importance of VTOL research, especially with the rapidly expanding UAM market, eventually resulted in a new Strategic Thrust (to begin in 2020): Thrust 4—Safe, Quiet, and Affordable Vertical Lift Air Vehicles.

The underlying rotary wing analysis tools used by NASA are still applicable to traditional rotorcraft and have been expanded in capability to accommodate the growing number of VTOL configurations designed for UAM. The top-level goal of the RVLT Project remains unchanged since 2006: Develop and validate tools, technologies and concepts to overcome key barriers for vertical lift vehicles. In 2019, NASA rotary wing/VTOL research has never been more important for supporting new aircraft and advancements in technology.

A decade is a reasonable interval to pause and take stock of progress and accomplishments. In 10 years, digital technology has propelled progress in computational efficiency by orders of magnitude and expanded capabilities in measurement techniques. The purpose of this report is to provide a compilation of the NASA rotary wing research from ~2008 to ~2018. Brief summaries of publications from NASA, NASA-funded, and NASA-supported research are provided in 12 chapters: Acoustics, Aeromechanics, Computational Fluid Dynamics (External Flow), Experimental Methods, Flight Dynamics and Control, Drive Systems, Engines, Crashworthiness, Icing, Structures and Materials, Conceptual Design and System Analysis, and Mars Helicopter.

We hope this report serves as a useful reference for future NASA vertical lift researchers.

REFERENCES

Gorton, S. A., López, I., and Theodore, C. R., "NASA Technology for Next Generation Vertical Lift Vehicles," AIAA paper 2015-0949, AIAA SciTech Forum, 56th AIAA/ASCE/ AHS/ASC Structures, Structural Dynamics, and Materials Conference, Kissimmee, FL, Jan. 5-9, 2015. DOI: 10.2514/6.2015-0949

Hochstetler, R. D., Salvano, D., and Gorton, S. A., "Metrics for NASA Aeronautics Research Mission Directorate (ARMD) Strategic Thrust 3B Vertical Lift Strategic Direction," AIAA paper 2017-3341, Aviation Forum, 17th Annual Technology, Integration, and Operations Conference, Denver, CO, June 5-9, 2017.

Yamauchi, G. K., and Young, L. A, "A Status of NASA Rotorcraft Research," NASA/TP–2009-215369, Sept. 2009.

CHAPTER 1. ACOUSTICS

Michael A. Marcolini[1]

INTRODUCTION

Noise has historically been, and continues to be, a significant issue for rotorcraft, and exterior noise has proven to be a barrier issue for civil operations in many communities. Noise also adversely affects some military operations, since acoustic detection is one of the primary means of rotorcraft detection and identification. In addition, the noise inside the vehicle is also a frequent issue, as most acoustic treatments can add significant weight to the vehicle, adversely impacting performance. Since the compilation of the status report on NASA Rotorcraft Research by Yamauchi and Young [2009], which contains a very thorough explanation of all the various rotorcraft noise sources and historical research in the area, NASA has continued to invest heavily in rotorcraft acoustic research. Much of the work has focused on improving noise modeling capabilities, as well as acquiring the requisite high-fidelity databases necessary for validating these new models, while additional efforts have emphasized noise reduction technologies. Just as in Yamauchi and Young [2009], the bulk of the NASA Rotorcraft Project's acoustic investments have focused on both conventional helicopters and tiltrotors, and logically divide into three main categories: external noise sources; interior noise sources; and noise propagation, modeling, optimized flight paths, and auralization. Research in each of these categories is addressed in a separate section of this chapter. However, some of the more recent research has delved into nontraditional rotorcraft, such as quad-copters and tiltwing personal air vehicles with distributed electric propulsion (DEP), etc., or simply does not fit into one of the above three categories. These efforts are collectively described in a fourth section, titled "Alternative Vehicle Concepts." Publications describing tangential work to the four categories are listed at the end of the chapter under "Additional Research."

EXTERNAL NOISE SOURCES

The easiest way to reduce rotorcraft noise is to simply design them to be quieter. However, this is not nearly as easy as it sounds. First, while great strides have been made in rotorcraft noise prediction over the last 40+ years, noise modeling is still not an exact science. Modeling techniques include analytical techniques, full computational fluid dynamics/computational structural dynamics (CFD/CSD), comprehensive analyses, and empirical and/or semi-empirical approaches, as well as alternative experimental techniques. All of these are addressed here in separate subsections. After discussing the various modeling work supported by the NASA Rotorcraft Project over the past decade, the remainder of this section addresses all of the external noise reduction efforts. While the bulk of these efforts are grouped as some form of active noise control (ANC), passive alternatives are described as well.

[1] Marcolini Consulting, LLC, 4506 West Benoit Trail, Blacksburg, VA 24060-0000.

Noise Modeling

Analytical: Lee et al. [2007] addressed the issue of noise scattering from surfaces. While not directly related to the modeling of the rotor noise itself, prior work had shown that both noise level and directivity can be significantly impacted by the presence of bodies, primarily the vehicle fuselage. A critical input required to compute this effect is the acoustic pressure gradient on the surface of the body. The authors developed two analytical models of this gradient, both of which were implemented in the noise prediction code PSU-WOPWOP. The first formulation ("G1") was derived by taking the gradient of Farassat's Formulation 1A. This approach required taking numerical time derivatives of the acoustic integrals and was found to be relatively sensitive to the numerical algorithm used. The second formulation ("G1A") performed the differentiation analytically by taking the derivatives inside the integrals. While this approach is more complicated analytically, it was more computationally efficient, and the authors suspect it was more robust as well. Both of these predictions were validated using numerical calculations for two different model rotors, with very good agreement for both stationary and moving observers. Both the G1 and G1A formulations are also implemented in the NASA ANOPP2 code, along with an additional formulation known as G0. In the G0 formulation, none of the time derivatives have been taken inside the integrals.

Farassat and Casper [2012] showed that a slight change to Farassat's original Formulation 1 produced a new analytical solution that was applicable to the prediction of rotor broadband noise, although they did require a comprehensive simulation of the turbulence in order to implement the approach. They felt that this methodology could also be applied to airframe noise prediction as well and referred to it as Formulation 2B of Farassat. Of note is that in this methodology the authors derived the acoustic velocity potential for both the thickness and loading noise terms of the Ffowcs Williams-Hawkings (FW-H) equation. This capability could be used to provide a high-fidelity boundary condition to the Fast Scattering Code (FSC). ANOPP2 includes implementation of Formulation 2B. Though it is available for use, because of the extensive data requirements discussed above, extensive exercise of this implementation has not be performed to date.

Lopes [2015, 2017] applied a compact assumption to the monopole term of several of Farassat's formulations. For situations such as high-aspect-ratio rotor blades, a compact form of the solution can be derived that is a function of the blade cross-sectional area. This greatly speeds up the resulting computation, since the calculation is now a line integral instead of a surface integral. He applied this approach to two example cases—a short span wing with a constant airfoil cross section evaluated at three different speeds and a rotor at two different advance ratios. Both the acoustic time histories and power spectral densities for the compact solution compared very favorably with the predictions from the non-compact calculations (see Fig. 1.1). He also examined the effect of rotor blade shape on the higher frequency portion of the power spectral density and found that the aspect ratio of the airfoil had a significant impact on the accuracy of the calculation using the compact form. The compact form required far less than one percent of the computation time required for the non-compact solution, making it a much more viable candidate for including noise predictions early in the design phase.

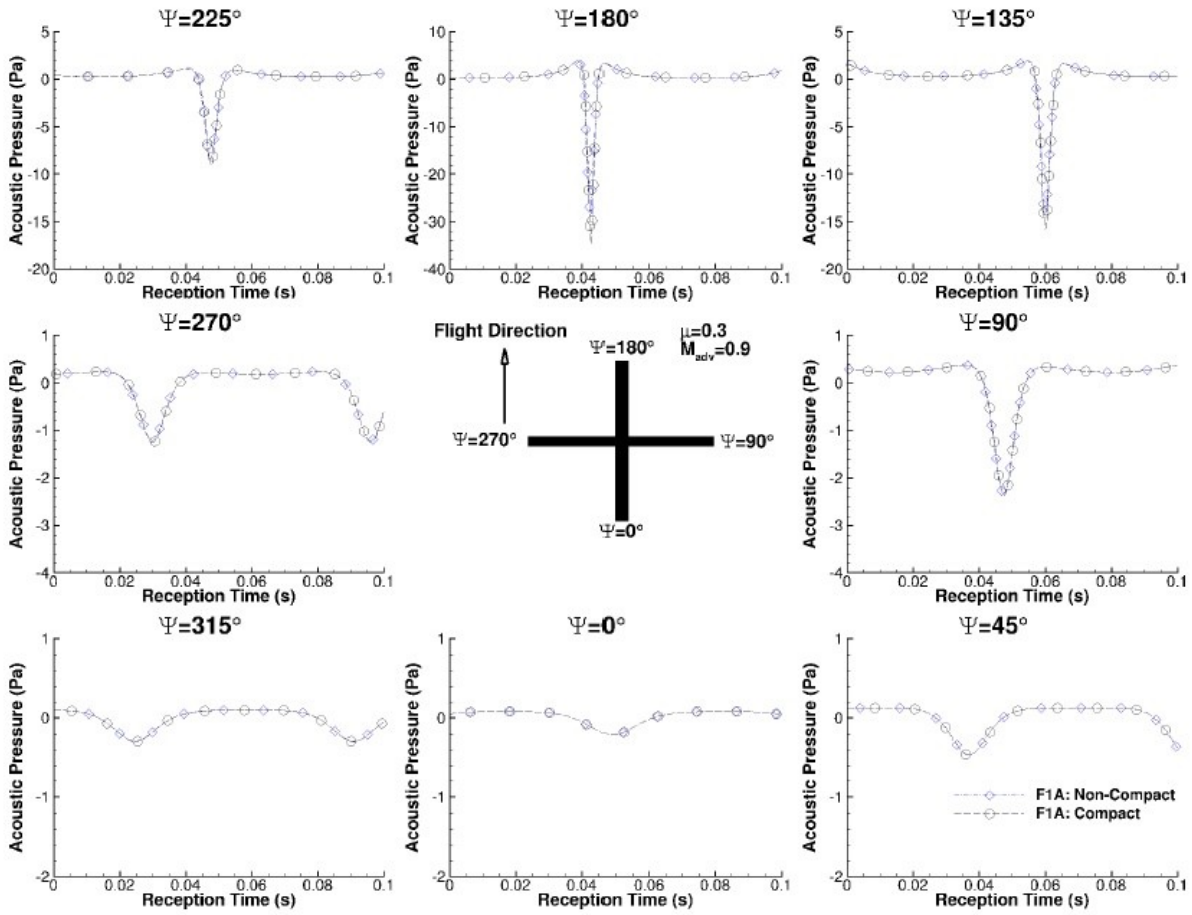

Figure 1.1. Acoustic pressure time history predicted by non-compact and compact forms of Formulation 1 and 1A at in-plane observer positions. Advance ratio of 0.3 and advancing tip Mach number of 0.9. (Fig. 9 of Lopes [2015].)

Lopes et al. [2017a] examined the ability to include acoustic objective functions in an adjoint-based multidisciplinary design optimization, which required defining the sensitivity of the acoustic metrics being used. Adjoint methods are attractive because they significantly reduce the computation time required to achieve an optimized design. They examined both frequency-integrated metrics such as overall sound pressure level (OASPL) and time- and frequency-integrated metrics such as effective perceived noise level (EPNL). The analytical sensitivities of these metrics were derived and validated by comparing the results to those obtained using complex differentiation and finite differencing. They provided an example test case using a monopole whose strength was a function of height and calculated the noise-minimal footprint.

Lopes et al. [2017b] examined the impact of neglecting the quadrupole term in integral forms of the permeable surface formulation of the FW-H equation. Neglecting the quadrupole term in such solutions produces inaccuracies referred to as spurious signals. The authors examined how such signals are generated, developed methods to identify them, and provided examples that demonstrated their presence. They also provided a potential approach for the removal of these signals based on the equivalent source method (ESM) and the sensitivity of Formulation 1A.

Comprehensive: Barbely (now Schatzman) et al. [2010] examined low-frequency acoustic reflections in wind tunnel measurements on the full-scale Boeing SMART rotor, which was tested in the U.S. Air Force National Full-Scale Aerodynamics Complex (NFAC) 40- by 80-Foot Wind Tunnel (see Fig. 1.2). They employed a reflection analysis based on the method of images to evaluate the effect of these reflections on the measured acoustic time histories and the pairing of the comprehensive analysis tool CAMRAD II and PSU-WOPWOP for their free-field acoustic predictions. They compared both free-field and reflection-corrected predictions to the experimental results, showing that the effect of reflections could be quite significant, especially below 100 Hz.

Boyd et al. [2017] developed and examined a fast noise prediction technique that they paired with CAMRAD II, and then compared their predictions with measured results from flight testing of a Eurocopter AS350 SD1 helicopter. Their noise prediction approach used Farassat's Formulation 1A as installed in ANOPP2 for the harmonic noise, while broadband noise was computed using Pegg's method. Figure 1.3 shows that only considering the main rotor produced results that significantly underpredicted many of the noise metrics computed, thus it is critical to include the tail rotor in the prediction of integrated noise metrics.

CFD/CSD: Boyd [2009a] examined a rotorcraft noise prediction capability that utilized a first-principles combination of computational fluid dynamics (CFD) and computational structural dynamics (CSD). He developed new interface codes in order to loosely couple these two analytical tools (OVERFLOW2 for the CFD and CAMRAD II for the CSD) that implement the methods from Potsdam, et al. [2006]. Elastic blade motion was included in the CFD analysis. This coupled solution was then fed into a noise prediction tool that computed the harmonic rotor noise using a solution to the FW-H equation (PSU-WOPWOP). He then applied this combined prediction technique to a number of cases from the Higher Harmonic Aeroacoustic Rotor Test II (HART-II) experiment conducted some years before in the German-Dutch Wind Tunnel Large Low-Speed Facility (DNW-LLF). The author used the complete experimental configuration (not just the rotor, but also the model fuselage and sting mount) in the CFD/CSD calculations. He showed very good agreement between his calculations and the experimental results for the blade loading at the 0.87R location, the qualitative wake geometry via flow visualization, and the mid–sound pressure level (SPL) acoustics at the measured microphone locations (see Fig. 1.4).

Meanwhile, Koushik and Schmitz [2008] first developed a new experimental technique to simulate blade vortex interaction (BVI) noise under controlled conditions. The new technique, called Blade-Controlled Disturbance-Interaction (B-CD-I), consisted of generating vertical gusts in an anechoically treated hover chamber. These gusts were then intersected by a single rotor blade, in this case the Operational Loads Survey (OLS) rotor blade. One advantage of this approach is that the authors could control the gusts to emulate various types of BVIs via the ability to rotate the alignment of the gust generator with respect to the rotor. Hotwire measurements were used to identify the optimum blade passage location, while far-field microphone measurements were used to acquire the necessary acoustic data to validate the approach.

a) SMART Rotor Testing in NFAC

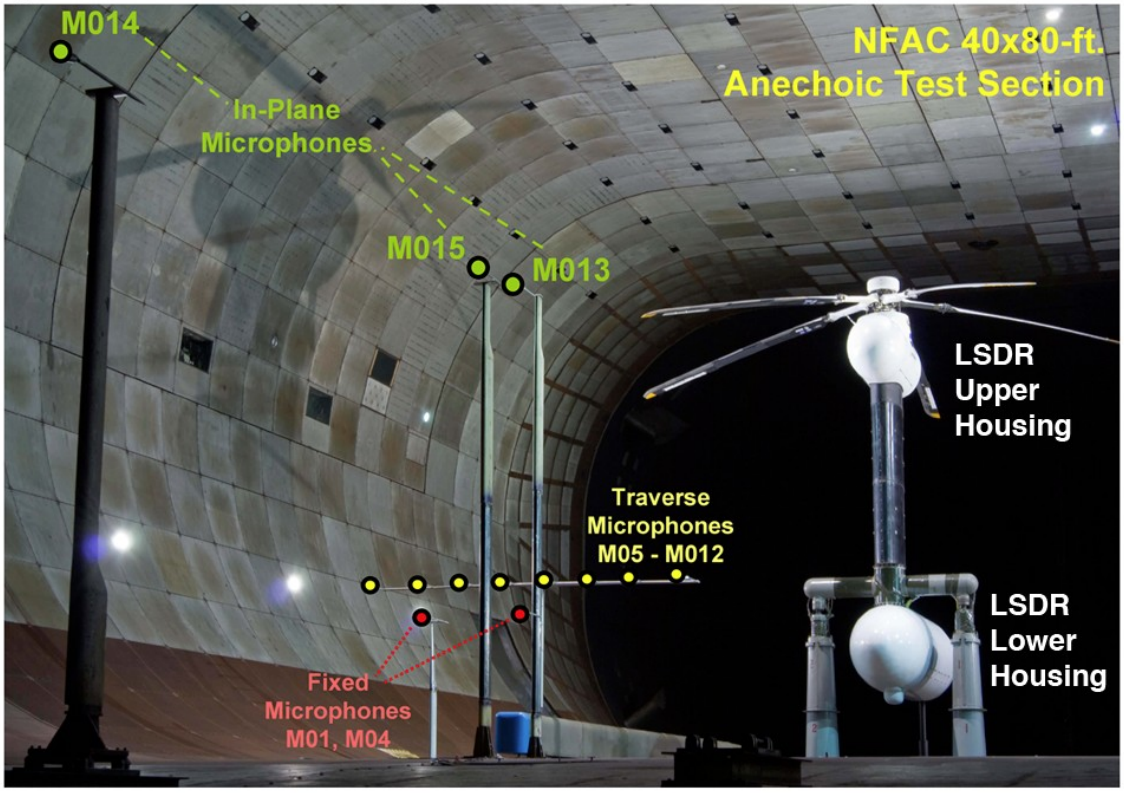

b) Microphone Layout (Top View)

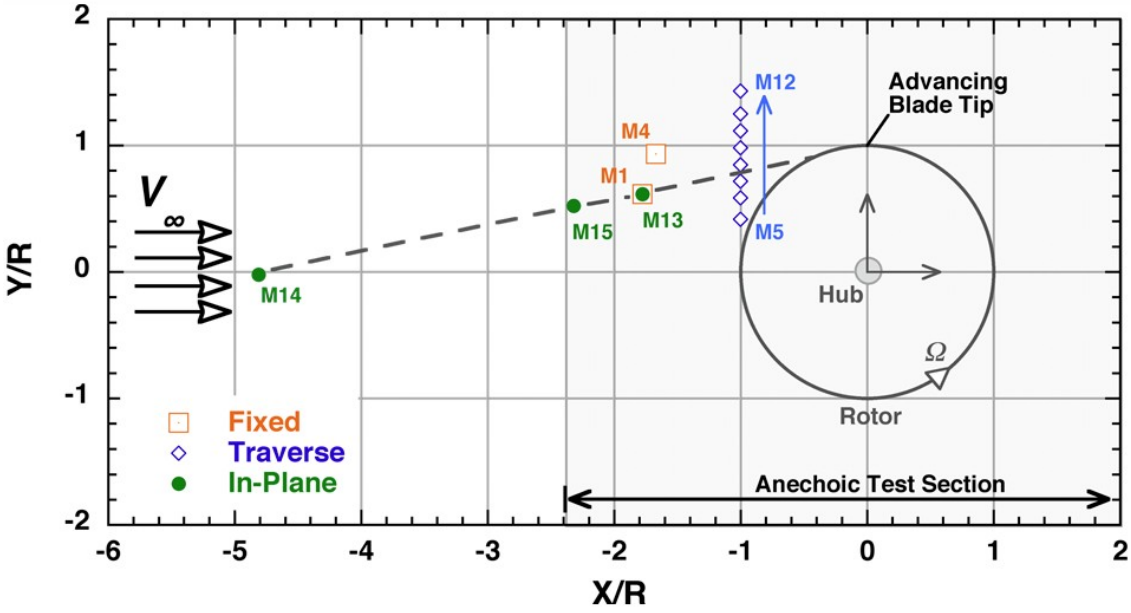

Figure 1.2. Boeing SMART Rotor testing in NFAC 40- by 80-Foot Wind Tunnel (Fig. 3 of Barbely et al. [2010]).

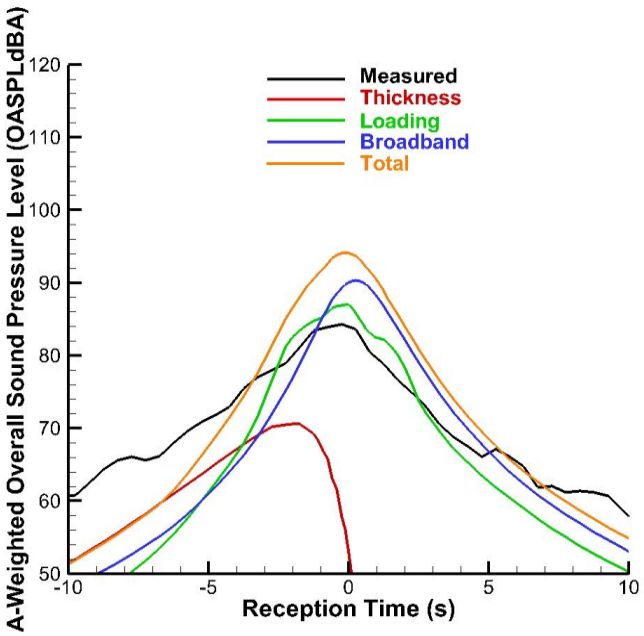

a) Level flight: Measured and predicted A-weighted OASPL [dBA]. This prediction includes the main rotor only (Fig. 8 of Boyd et al. [2017]).

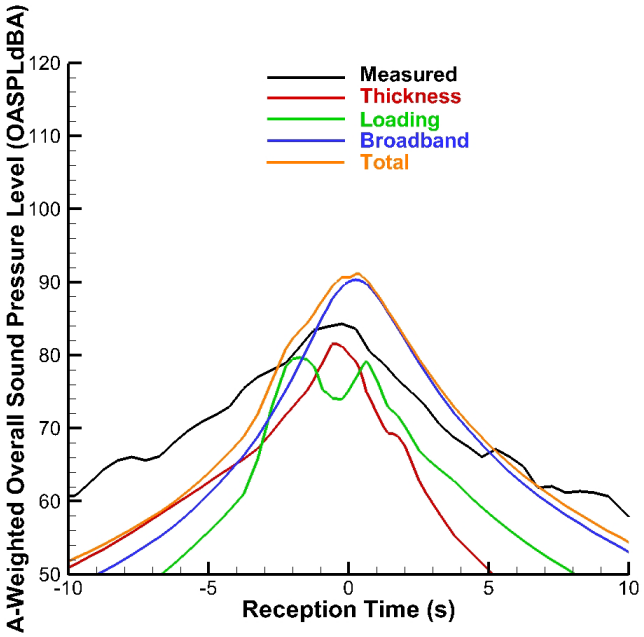

b) Level flight: Measured and predicted A-weighted OASPL [dBA]. This prediction includes both the main rotor and tail rotor (Fig. 9 of Boyd et al. [2017]).

Figure 1.3. Comparison of measured and predicted noise for the AS350 SD1 helicopter.

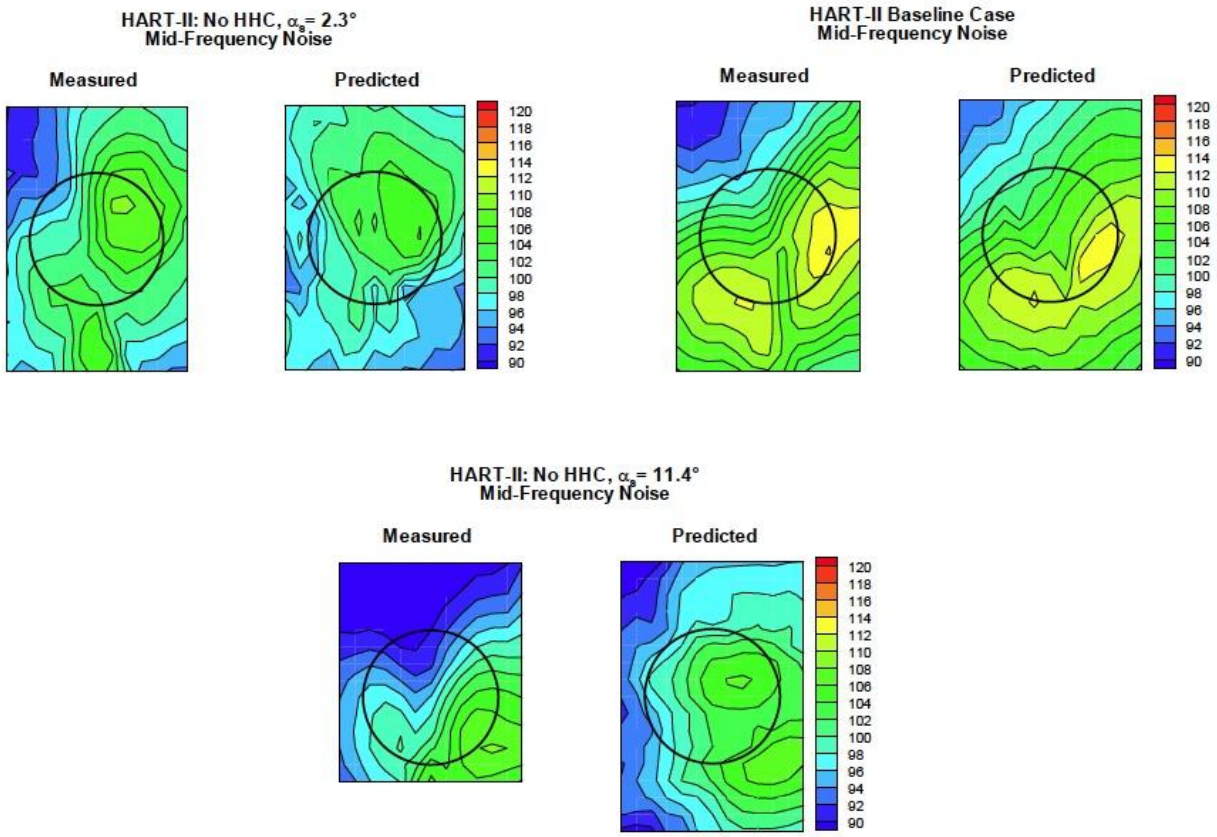

Figure 1.4. Measured and predicted mid-frequency noise for a range of shaft tilt angles (Fig. 11 of Boyd [2009a]).

Koushik et al. [2009] then compared these measurements to CFD-based acoustic computations, using the Transonic Unsteady Rotor Navier Stokes (TURNS) code for the aerodynamics, coupled with the University of Maryland Acoustic Code (UMAC), another codification of Farassat's Formulation 1A, for the acoustic predictions. Experimental/predicted results compared quite favorably for conditions emulating BVIs; the results were not so favorable, however, when nominally in-plane results were examined, as the computed results significantly underpredicted those measured during the experiment.

Sim et al. [2010] used CFD to predict the low-frequency noise from a helicopter main rotor. While the authors termed this a "direct CFD" approach, it was actually a loose coupling of OVERFLOW for the CFD and CAMRAD II for the CSD, using a coupling on a per-revolution basis. The authors compared their predictions to measured results from both wind tunnel and flight test measurements of an MD-902 helicopter at several different operating conditions. Results indicate their success at predicting low-frequency noise due to thickness and steady loading noise. They were not as successful at predicting mid-frequency BVI noise, however, with discrepancies of up to 20 dB, which they attributed to CFD modeling and grid limitations.

Noise Reduction and/or Control

The research described here is a combination of application of computational methods such as described above, or purely experimental examinations, or a combination of the two. Many of the efforts included here are directed at reduction of BVI noise, which is often the dominant main rotor noise source during approach conditions; the vehicle is typically operating at fairly low altitudes in closer proximity to the surrounding population, and also at fairly low speeds so that the duration of that noise exposure is significantly longer. Also, while BVI reduction approaches using techniques such as trim changes in flight vehicles were investigated, the preponderance of these efforts involve ANC, either on-blade or within the rotor control system. BVI noise is extremely well suited to such control, since fairly small changes in either the wake structure, or its orientation with respect to trailing blades, can produce dramatic changes in the noise signature. However, some of the efforts described here do address other noise sources, including the first one below.

Sim [2008] developed an approach to reducing in-plane, low-frequency main rotor noise utilizing on-blade active controls to change the aerodynamic forces on the advancing side of the rotor. This produced a noise pulse designed to cancel the typical strong rotor-thickness-noise negative pulse. He then applied this technique theoretically to the Boeing SMART rotor, which was equipped with an active trailing edge flap. As is often found with such noise cancellation approaches, the technique worked locally, but not globally. He calculated reductions of up to 5.5 dB at a single forward location nominally in the rotor plane, using a 2/rev flap control with a flap motion of 2 degrees, with only about a 2-percent increase in rotor power required. Efforts with a 5/rev flap control were less effective. He believed that an active flap was not the ideal approach for reducing in-plane noise, since it tends to generate more out-of-plane noise elsewhere. He proposed that a drag-only control effector may reduce in-plane noise more effectively.

Next, Sim et al. [2009, 2014] expanded upon Sim's previous work, demonstrating up to 6 dB reduction in the first six harmonics of the blade passage frequency in-plane during level-flight operating conditions, resulting in predicted aural detection distance reductions of up to 18 percent but also showing large increases in vibratory loads due to increased hub shear forces. They also showed performance penalties on the order of 3 percent. Figure 1.5 shows measured and predicted reductions in low-frequency SPL.

Later, Sim et al. [2012] expanded upon their examination of the efficacy of nonharmonic active flap motion for BVI noise reduction, using the full-scale Aviation Applied Technology Directorate (AATD)/Sikorsky/United Technologies Research Center (UTRC) active flap demonstration rotor that was tested in the NFAC 40- by 80-Foot Wind Tunnel (see Fig. 1.6). They evaluated three different flap motions—4/rev harmonic, localized nonharmonic, and motions derived via closed-loop control. All three approaches demonstrated similar effectiveness in reducing near in-plane noise. The localized nonharmonic flap motion incurred a performance penalty of no more than 2 percent but also induced higher hub vibration levels.

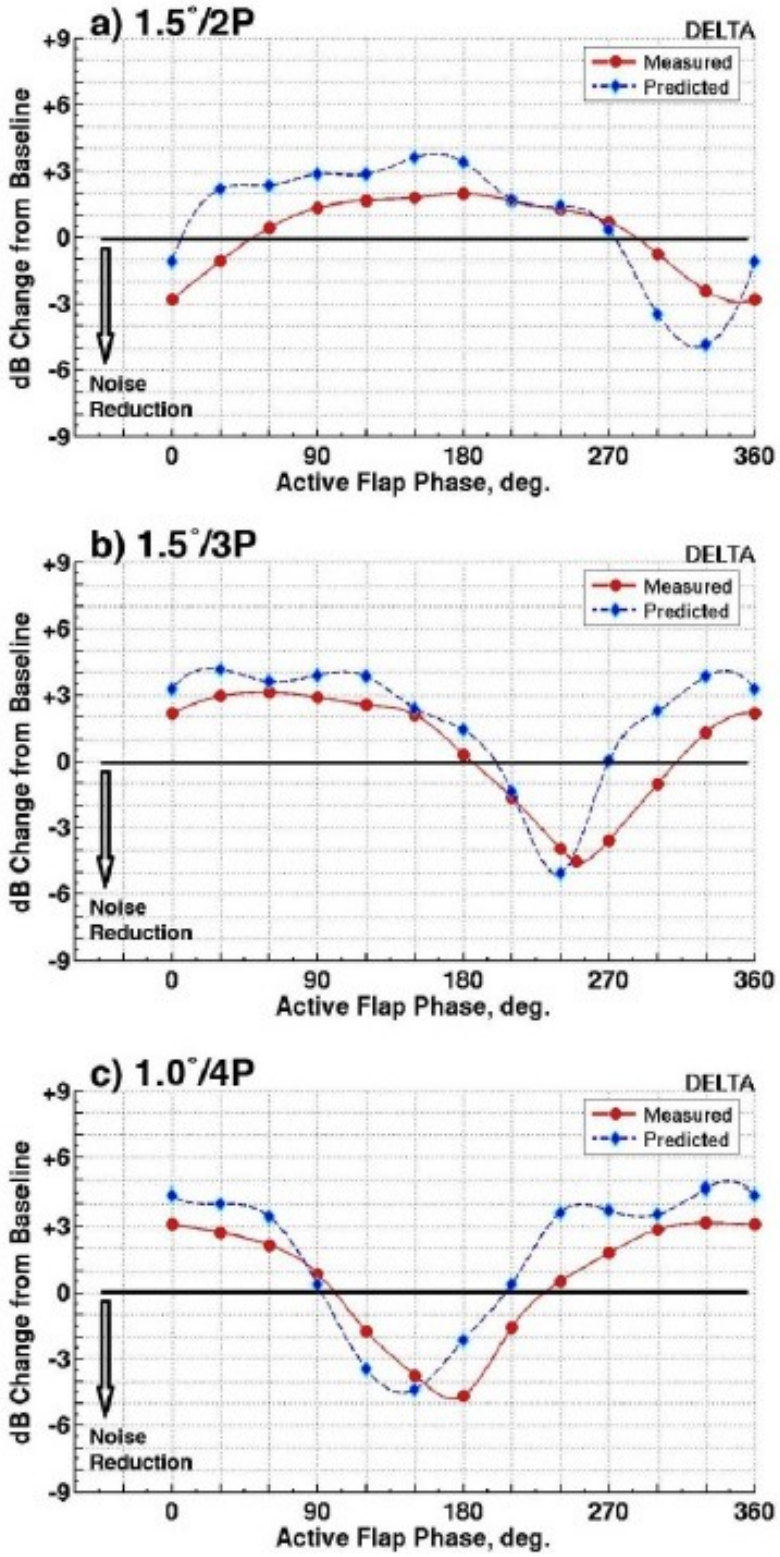

Figure 1.5. SMART rotor—changes in low-frequency SPL (from baseline) at microphone M13 as a function of active flap phase input: a) 1.5° and 2/rev, b) 1.5° and 3/rev, c) 1.0° and 4/rev. (Fig. 9 of Sim et al. [2009].)

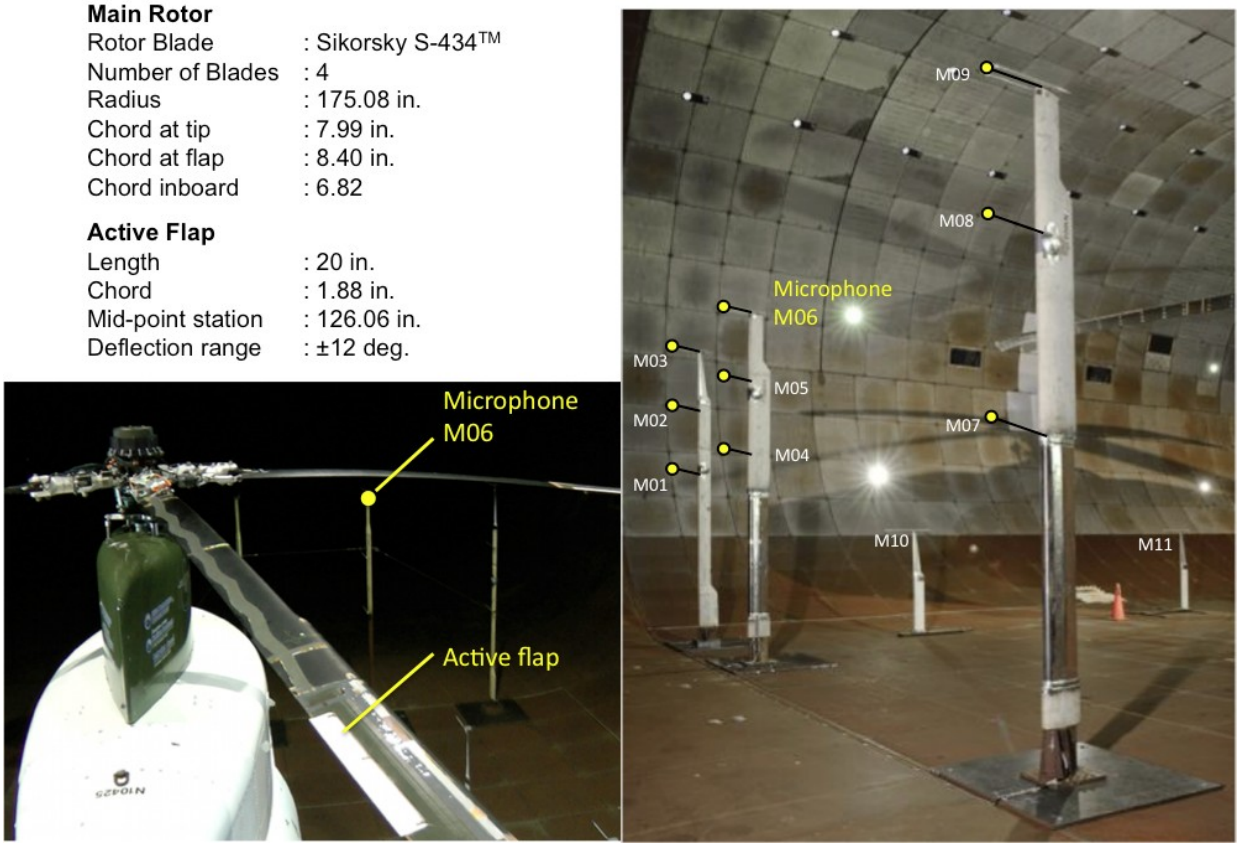

Figure 1.6. Sikorsky active flap demonstration rotor in NFAC 40- by 80-Foot Wind Tunnel (Fig. 1 of Sim et al. [2012]).

Gopalan and Schmitz [2008a] developed an analytical approach for predicting near in-plane low- to mid-frequency harmonic noise in hover using an approximate solution to the FW-H equation. They showed that these approximations worked well up to moderate hover tip Mach numbers (in the 0.85 range for a 9-percent-thick airfoil), so delocalization was not an issue. They examined thickness and loading noise as a function of multiple rotor design parameters in both the time and frequency domains, and developed unsteady on-blade point controllers, both force and volume, to reduce thickness noise at an in-plane location. They found that higher frequency controllers require much lower control levels, but only work over a very small region near the target observer, while low-frequency controllers work over a much larger region but need much larger control inputs as well. Later, Gopalan and Schmitz [2008b] used this same approach to assess the relative benefits of lower (1/rev to 3/rev) versus higher (4/rev and above) on-blade force controllers in reducing in-plane thickness noise, with conclusions very much in agreement with previous assessments. They did show that single harmonic control could reduce peak thickness noise levels by up to 12 dB.

JanakiRam et al. [2009] examined the ability of an active-flap rotor to reduce BVI noise for a full-scale MD 900 helicopter rotor also tested in the NFAC 40- by 80-Foot Wind Tunnel. All five rotor blades contained identical flaps with a span of 18 percent radius, covering the last 25 percent of the blade chord, and centered at 83 percent radius, with the flaps driven by piezoelectric actuators. They presented results for three different descent conditions where BVI noise was expected to dominate the acoustic signature. For each condition, the baseline (0-degree flap deflection) cases were examined using closed-loop flap control, while the BVI reduction cases, using anywhere from 2/rev to 5/rev actuation frequencies, were examined using open-loop control. They were able to achieve BVI noise reductions from 2 to 7 dB using the active flap control. However, predictions made using CAMRAD II/PSU-WOPWOP did not agree well with the active flap cases, although they did show reasonably good agreement with the BVI noise generated from the baseline cases. They also noted that hub loads did increase for the active flap test cases. Figure 1.7 shows the reduced acoustic pressure and higher harmonic spectral levels with flap actuation resulting in a 7.1-dB reduction in BVISPL relative to the baseline. However, the reduction in noise was accompanied by large vibratory hub loads relative to those for the baseline rotor.

.

Along with flaps, another on-blade active noise and vibration control approach is the use of active twist control via embedded actuation devices. Boyd [2009b] used the same prediction method on the same configuration as used in Boyd [2009a], but applied active twist instead of higher harmonic control (HHC). Two active twist amplitudes were examined. It was found that active twist could produce quantitatively similar BVI noise to that of the HHC when the resultant elastic twists were similar. However, the higher-amplitude active twist amplitudes dramatically increased the rotor profile power, thus reducing rotor performance (indicated by significantly lower lift/drag (L/D) ratio of the rotor).

Fogarty et al. [2010] conducted a computational study examining the potential for BVI noise reduction using this approach, studying the Apache Active Twist Rotor, which had 36 Macro Fiber Composite (MFC) actuators embedded in each rotor blade to achieve active twist control, via a combination of CAMRAD II and PSU-WOPWOP. They examined actuation frequencies from 2/rev to 5/rev, phase angles around all 360 degrees, and tip-twist amplitudes from 0.5 to 4 degrees for a single low-speed mild descent condition, predicting the noise on a plane 1.1 diameters below the rotor. They found BVI noise reductions of up to 11 dB using 1.25 degrees of tip twist, with negligible effect on 4/rev hub shear for this four-bladed vehicle. Next, Fogarty et al. [2011] studied the effects of nonharmonic active-twist control on the same rotor, using the same modeling approach. They varied the azimuthal location where the twist actuation was initiated, the duration of the actuation, and its amplitude. Evaluating the same test condition and measurement plane as before, the authors found reductions of up to 10 dB in BVI noise using a starting azimuthal location for actuation of 90 degrees, a duration of actuation of 90 degrees, and an amplitude of 1.5 ft-lb. In follow-on work, Fogarty et al. [2012a, 2012b] compared and contrasted two different approaches for predicting BVI noise on the active twist rotor. The first was a combined CFD/CSD technique coupling OVERFLOW2 and CAMRAD II, and the second exclusively used the CAMRAD II free-wake model, while still using PSU-WOPWOP for the acoustic calculations. They showed that the coupled CFD/CSD computations produced trends that agreed well with the measured wind tunnel acoustic data, while the free-wake-alone predictions were not as successful (see Fig. 1.8).

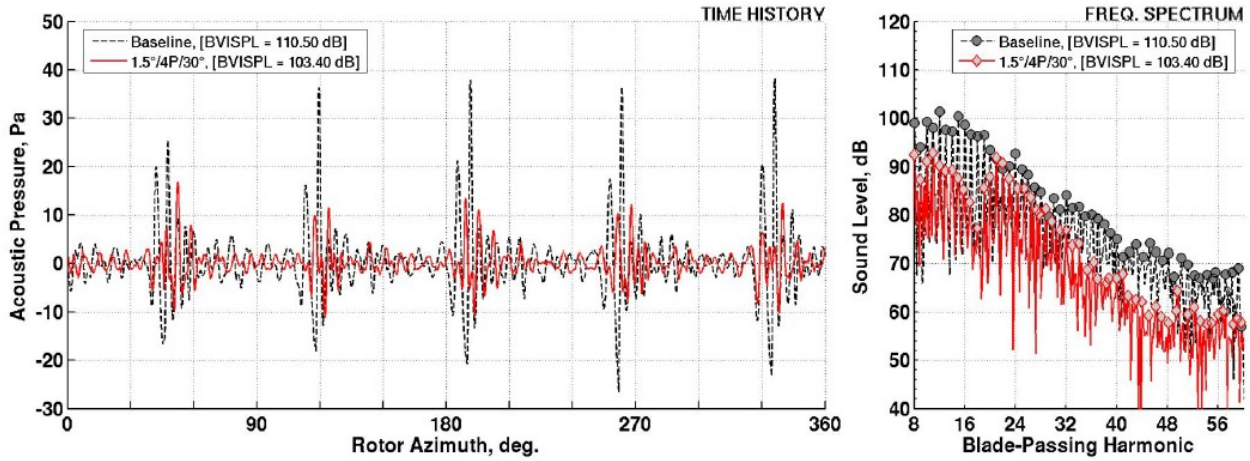

Figure 1.7. Acoustic pressure time histories and spectral data for SMART rotor baseline and with active flap actuation (1.5°/4P/30°) for Test Case 1 (advance ratio = 0.150, rotor shaft angle = 4.0°) at microphone M07 (traverse station: –120, –0.59 R). (Fig. 10 of JanakiRam et al. [2009]).

As mentioned previously, along with the various active rotor control approaches described above, the use of trim control for rotor noise reduction was also investigated. Malpica et al. [2016] conducted a parametric analysis of the impact of both fuselage drag and pitching moment on BVI noise generated by a Sikorsky S-70/UH-60 helicopter during descent, applying the concept of X-force posed by Schmitz et al. [2007] for BVI noise control. Like many others discussed previously, the authors used CAMRAD II to compute the vehicle trim, wake geometry, and integrated blade airloads, and PSU-WOPWOP for the acoustics. The authors showed BVI noise reductions in excess of 6 dB using a combination of fuselage drag and pitching moment. Later, Malpica [2017] examined the effects of lateral and longitudinal rotor trim flapping angle changes (i.e. tip-path-plane tilt) on an isolated 26-foot-diameter proprotor that is quite similar to that of the AW609 tiltrotor operating in helicopter mode. He investigated three tip-path-plane angles of –9, 0, and 6 degrees, all at 80 knots airspeed, and found that by changing the cyclic trim he could produce significant changes to both the low-frequency and BVI noise, in terms of both amplitude and directivity, with up to 3 dB reduction in low-frequency noise, as shown in Figure 1.9.

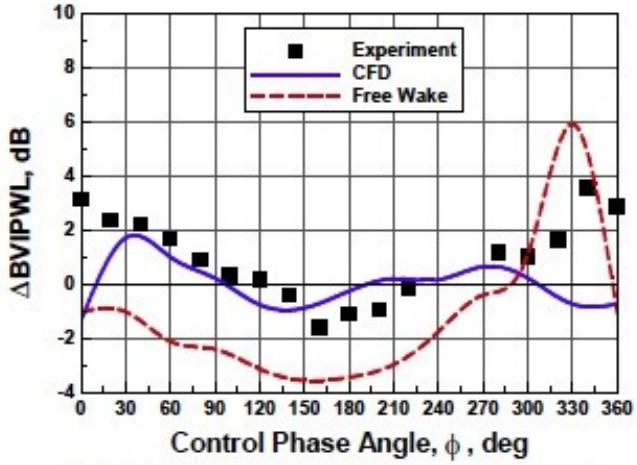

(a) ΔBVIPWL as a function of control phase angle.

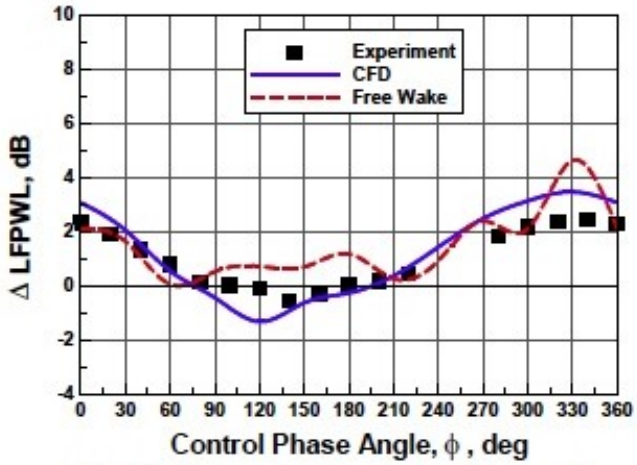

(b) ΔLFPWL as a function of control phase angle.

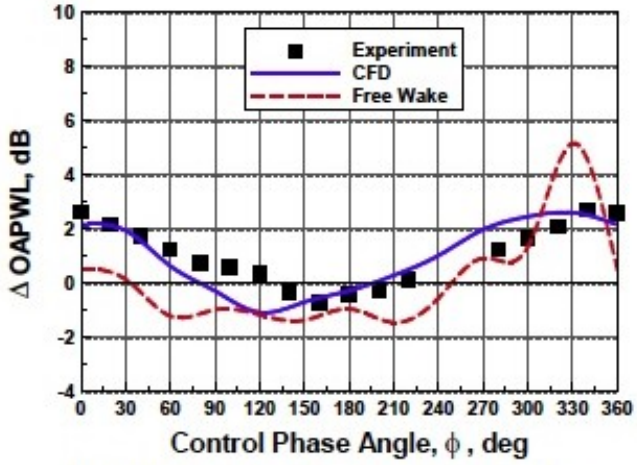

(c) ΔOAPWL as a function of control phase angle.

Figure 1.8. Incremental metrics for 3/rev, 1000V actuation, advance ratio = 0.14, shaft angle = 8.0°. Experimental results from the Active Twist Rotor installed in the NASA Langley Transonic Dynamics Tunnel (Fig. 12 of Fogarty et al. [2012a]).

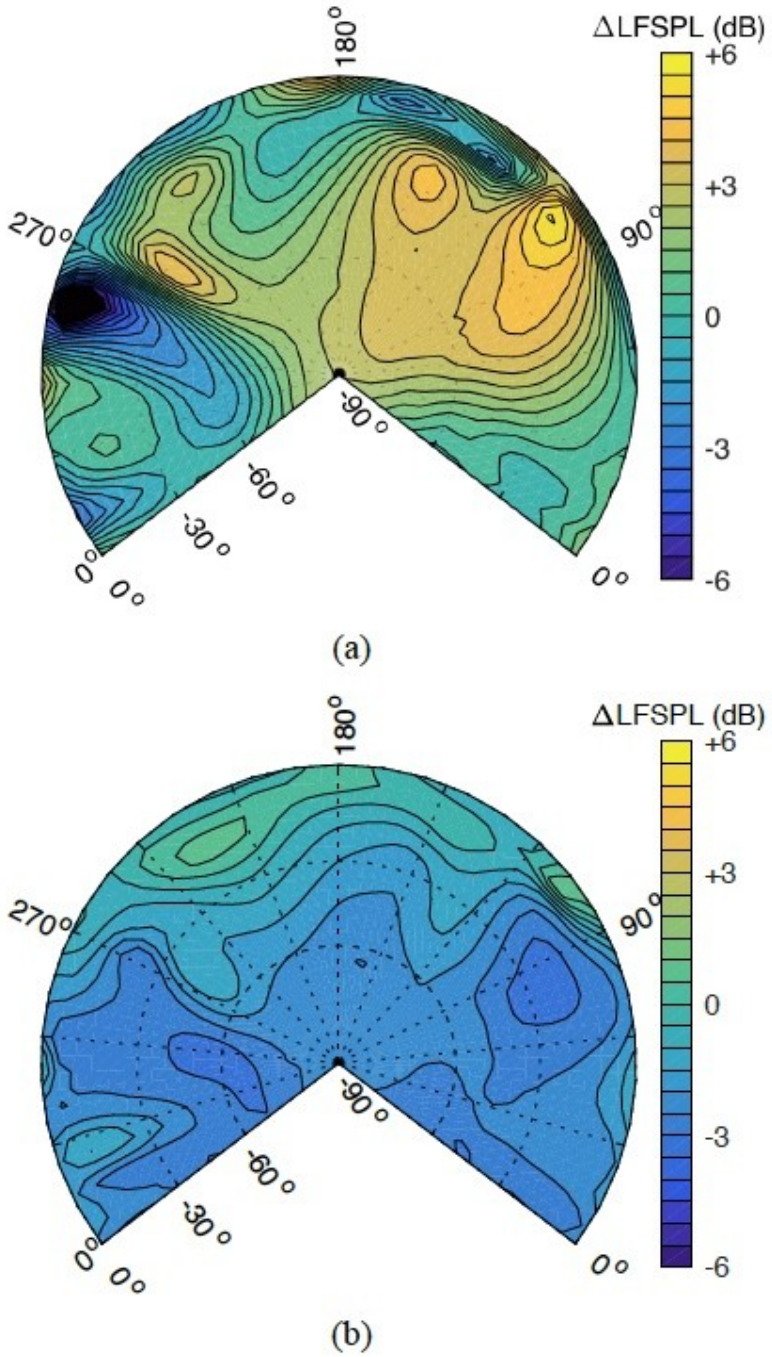

Figure 1.9. Calculated ΔLFSPL (change in low-frequency SPL) contours for rotor tip-path-plane angle = –9°: (a) lateral flapping = –4°, and (b) lateral flapping = 4°. Rotor is an isolated proprotor, similar to the AW609 (Fig. 12 of Malpica [2017]).

INTERIOR NOISE SOURCES

While noise radiation into the surrounding community is justifiably the primary concern in rotorcraft acoustics, for those passengers, pilots, and anyone else who rides inside such vehicles, the noise inside the aircraft is also a primary concern. As such, a portion of the Subsonic Rotary Wing (SRW) project's acoustic investments are directed at this concern. Within this section, the research logically divides into two major categories—noise modeling and noise control. In the former, the research for conventional helicopters is then separated from that of large civil tiltrotors, because the technical differences are so substantial. For noise control, the research obviously divided into passive and active control techniques. As such, research into each of these four categories is described separately.

Interior Noise Modeling

For conventional helicopters, the primary interior noise source is the transmission bolted directly to the roof of the vehicle, often just feet (if that) away from passengers' heads. Along with the noise, excessive vibration can also produce a significant adverse impact on passenger ride quality. In fact, this vibration can actually excite the windows in the fuselage, causing them to radiate sound into the cabin as well. Because of this, the ability to accurately model the vibroacoustic response of structures such as panels and cylinders to external stimuli such as the aforementioned transmissions is critical to rotorcraft interior noise and vibration control. Cabell et al. [2008] acquired vibroacoustic response data on two different structures, a panel and a cylinder, to facilitate research into modeling of such structures. The former was a 1.22-meter-square stiffened aluminum panel designed to simulate a representative commercial aircraft sidewall section, while the latter was an enclosed, stiffened aluminum cylinder, nominally 3.66 meters in length and 1.22 meters in diameter, designed to represent a small aircraft fuselage. Excitation inputs included both single and multiple shakers, as well as a diffuse acoustic field. Vibroacoustic response measurements included drive point impedance, point acceleration, laser vibrometer velocity scans, and two-microphone acoustic intensity probe scans. These data were made available to the larger research community for their own modeling and validation efforts. The authors also described plans for a third test article—a composite fuselage of similar length and 1.68-meter diameter. Later data from this third test article were used by Grosveld et al. [2011] to validate both Statistical Energy Analysis (SEA) and Energy Finite Element Analysis (EFEA) predictions. SEA has been in use for many years and is typically used at frequencies where the modal density and the modal overlap are high, while EFEA requires derivation of the governing differential equations in terms of energy density variables and then utilizes a finite element approach to solve them. The SEA method predicted SPLs inside the composite cylinder that were higher than those for the EFEA-computed levels in 1/3-octave bands below 250 Hz, while they were lower at the higher-frequency bands.

Hambric et al. [2010] developed and demonstrated a computational technique designed to model both the sound and vibration transmitted through a helicopter transmission, with emphasis on emulating the effects of rolling element and journal bearings. They used Penn State's Computational Hydroacoustic Modeling Programs (CHAMP) approach, which is based on component mode synthesis (CMS). The authors compared their technique with data acquired using the NASA Glenn Research Center (GRC) test gearbox with three different bearing

configurations—one used traditional ball and roller bearings, and the other two used journal and wave bearings. The sound radiated by the gearbox was computed using a boundary element (BE) acoustic model. The authors found that using journal bearings reduced the second harmonic of the gear meshing tones but did not impact the noise from the fundamental tones.

Allen and Schiller [2016] examined the vibroacoustic characteristics of two structures—one had a corrugated-core sandwich design and the other had a honeycomb-core design. The structures were being considered for use in a launch vehicle fairing but could also be applied to a helicopter roof panel. The corrugated-core sandwich concept was attractive because it can contain resonant noise control systems with minimal impact to both the mass and volume. Modal information, wavelength dispersion, and damping were obtained for each of the two test panels using vibrometer measurements and subsequent analyses. Both numerical and analytical modeling techniques were later applied in order to assess not only the assumed material properties, but also to examine underlying structural dynamic aspects of each panel. The finite element approach used here accurately modeled the low-frequency (<500 Hz) structural dynamic behavior of the honeycomb-core sandwich panel in both warp and ribbon directions and also the corrugated-core sandwich panel in the axial direction. However, the modeled dynamics of the corrugated-core sandwich panel in the cross-corrugation direction showed discrepancies with the measured results of above 10 percent. The authors postulated that this was most likely due to the stiffening effects of excess adhesive at the core-to-facesheet bond regions, which was an artifact of the test article fabrication and was not modeled.

Bean et al. [2016] developed a full gradient solution to adaptive hybrid control, focusing on the adaptation mechanisms available in such controllers. The great majority of these controllers update two filters individually according to the filtered-reference least mean squares (FxLMS) algorithm. However, the FxLMS algorithm cannot accommodate a feedback loop in the gradient calculation because it was designed for feedforward control. The authors derived a weight vector gradient that properly handles a feedback loop by using a single weight vector that is updated, as opposed to the two individual ones used in the FxLMS algorithm. They assumed an internal model structure for the feedback loop, and they provide some simulations to demonstrate the efficacy of their approach.

The interior noise issues associated with tiltrotor aircraft can be much different than those for conventional helicopters. While structure-borne noise may still be an issue, it is less so for a tiltrotor, because the transmissions are located out at the end of the wings. Meanwhile, in cruise (a.k.a “airplane mode”), aeroacoustic issues tend to be the dominant interior noise concerns. These can be any combination of thickness and loading noise generated from the blades, which pass very near the fuselage in this configuration, as well as the turbulent boundary layer (TBL) formed along the fuselage during this higher-speed flight condition, similar to the issue for conventional takeoff and landing (CTOL) aircraft. In a series of papers, Grosveld et al. [2013], Grosveld and Cabell [2011], and Grosveld [2013] attempt to predict the interior noise levels likely to be seen in a future Large Civil Tiltrotor (LCTR2), which, as described elsewhere in this report but briefly described here for completeness of this chapter, served as a notional vehicle in the SRW project. The stated design goal was to enable transportation of 90 passengers 1800 km at a speed of 550 km/hr. This would result in a blade-passage frequency for a four-bladed rotor as low as 6.9 Hz during cruise conditions. The resulting low-frequency acoustic excitation,

coupled with the very high likelihood that the fuselage would be constructed from composite materials, may make it very difficult to achieve acceptable interior noise levels. The authors performed initial assessments of the anticipated interior noise environment in the LCTR2 cabin, utilizing a combination of semi-empirical, analytical, and statistical energy analysis methods. Since it was impossible to validate their predictions on an actual LCTR2 because that vehicle does not actually exist, the authors also applied their approach to both the XV-15 tiltrotor and Bombardier Q400 turobprop aircraft, both of which had measured interior noise data available. Initial results indicated that the predicted noise levels inside the LCTR2 may not be acceptable to passengers. However, after further refining their model and assumptions, the authors predicted lower interior noise levels. Predicted levels above the 63-Hz 1/3-octave band were less than levels measured inside a Q400 turboprop aircraft. Tonal noise associated with the tiltrotor blades was predicted to be below the measured Q400 noise associated with the propellers, except for the LCTR2 predictions at the 6.75-Hz blade passage frequency and its first harmonic at 13.5 Hz. While those frequencies are inaudible (< 20 Hz) they may still have adverse impacts on both passengers and crew. Figure 1.10 shows the measured SPL in the front of the Q400 cabin compared with the predicted SPL for the LCTR2 cabin.

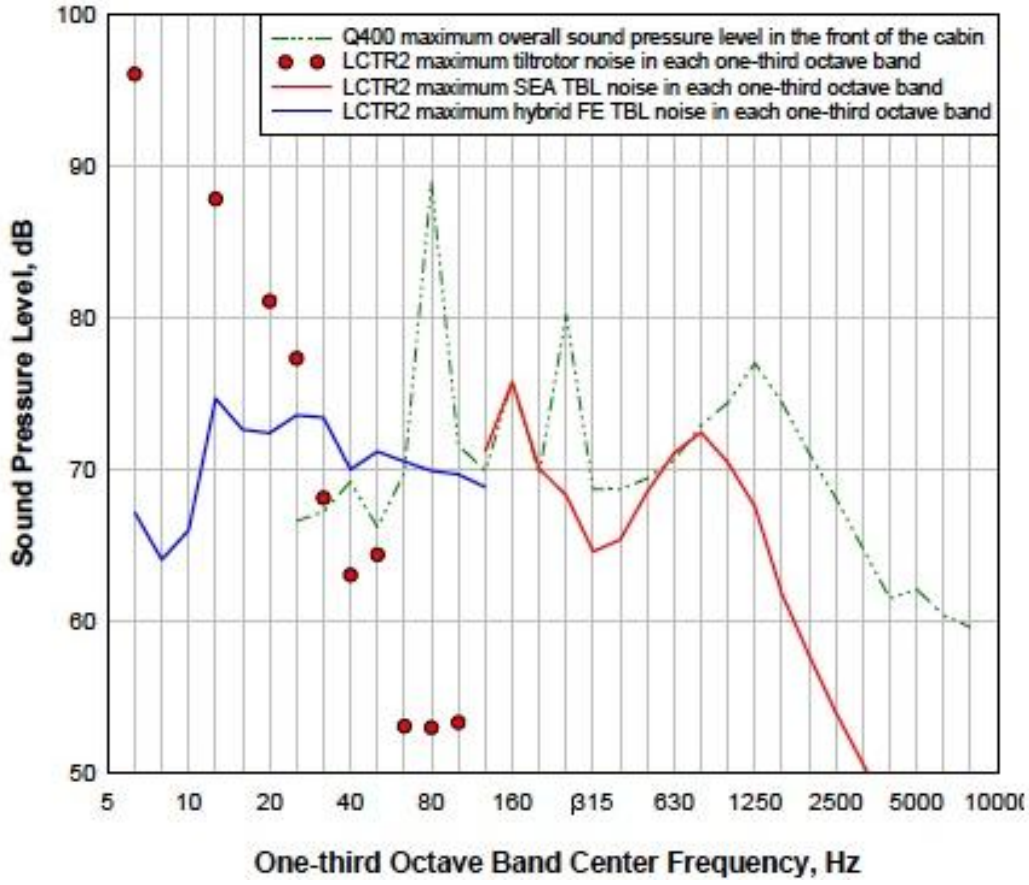

Figure 1.10. Maximum 1/3-octave-band LCTR-2 cabin SPLs for the tiltrotor noise excitation, and hybrid FE/SEA and SEA predicted TBL excitation compared with the highest measured overall level at a location in the forward cabin of the Q400. (Fig. 20 of Grosveld et al. [2013].)

Interior Noise Control

While it is important to be able to model/predict the rotorcraft noise environment inside the fuselage, it is at least equally important to determine ways to mitigate that noise as efficiently as possible, minimizing the likely adverse impacts on vehicle performance because of items such as increased cost and/or complexity, increased weight penalties, etc. Interior noise mitigation strategies typically fall into one of two categories: either passive control or active control, with said control being applied to either the source itself or its transmission path. Scheidler and Asnani [2016] conducted a literature review of both source and path control, and then divided their assessment into both mature and emerging technologies, focusing on vibration control technologies near the source. Figure 1.11 summarizes their findings.

Passive: In general, a fuselage is constructed of thin plates attached to a stiff beam. The beams transfer high-frequency energy to the panels, causing the panels to vibrate and radiate noise into the cabin. Reducing this structural-borne noise in a helicopter cabin typically translates into added weight to the vehicle because damping treatment is used to cover large noise-radiating surfaces. Schiller et al. [2012] offer a thin-plate design that focuses flexural (bending) wave energy to a small region, which can then be treated. The design uses a smoothly varying cross-sectional thickness to focus the waves. Simulations indicate the combination of focusing and targeted local damping treatment has the potential to significantly dissipate flexural wave energy, offering a potential savings in weight compared to traditional noise damping treatments.

		Technology	Approx. freq., Hz	IL, dB	TRL	Mass/ Size	Retrofit	Vary freq.	Key challenge
Broad-band	S	Passive gear isolation	>500	3-7	3-6				temperature limits
		Bearing shunt damper	>100	7-18	4				design integration
		Periodic shaft	500-4k	0-40	4				shaft length
	P	Elastomeric hard mount	>250	0-60	4-?				reliability
		Periodic fluid mount	500-3k	30-81	5				system-level data
Narrow-band	S	High CR spur gear	500-4k	2	9				n/a
		Superfinished gear	500-4k	4-7	8				n/a
		Helical gear	500-4k	2-17	9				added thrust load
		Magnetic gear	500-1.6k	?	4				specific torque
		Active gear	<1k	7.5	3-4				complex, force required
		Active transverse shaft	<4k	2-28	4				size, force required
		Active bearing	<1k	0-45	4				size, force required
	P	Active strut	200-2.5k	11-20	7-?				reliability
		Active at mounting points	200-1.5k	8-18	7-?				force required
		Variable stiffness mount	<1k	?	3				unproven performance

Figure 1.11. Characteristics of the reviewed technologies; green/red shading denote positive/ negative attributes (Table 3 of Scheidler and Asnani [2016]).

Schiller et al. [2013] performed a numerical simulation of the acoustic attenuation when sound passes through a structure comprised of a lightweight panel layered with bagged gas, so as to examine the effects of the gas on transmission loss (TL). As part of the study, both the speed of sound of the gas and its density were varied independently to evaluate the effects of each, and the authors found that reducing the speed of sound in the gas produced the most dramatic improvements in low-frequency attenuation. They showed that using a 2-inch-thick layer of gas with the same density as air but with a 25-percent lower speed of sound increased the TL by 8 dB at 1 kHz.

Later, both Allen et al. [2014] and Schiller et al. [2014] investigated the effect of structurally integrated resonators on the TL of a sandwich panel that had facesheets over a corrugated core, which created long aligned chambers that ran parallel to the facesheets. With the inclusion of ports in the facesheets, these chambers can act as low-frequency acoustic resonators, where they can simultaneously serve as both part of the load-bearing capability of the structure and also help attenuate the noise. Allen et al. [2014] tested 2- and 4-inch-thick, 4- by 8-foot panels, constructed so that each panel was comprised of three subpanels aligned side by side. Testing was conducted at the Riverback Acoustical Laboratories, where both 1- and 2-inch inlet diameters were evaluated. Results were mixed, possibly because of room effects in the test chamber. Meanwhile, Schiller et al. [2014] developed an analytical model of a panel containing such structures, and also conducted numerical simulations (see Fig. 1.12). They showed that these acoustic resonators could greatly increase the TL of the panel in the vicinity of their natural resonant frequency, demonstrating benefits of up to 22 dB around 104 Hz, with no increase in either weight or volume with respect to the baseline structure. Such devices are particularly efficient because they

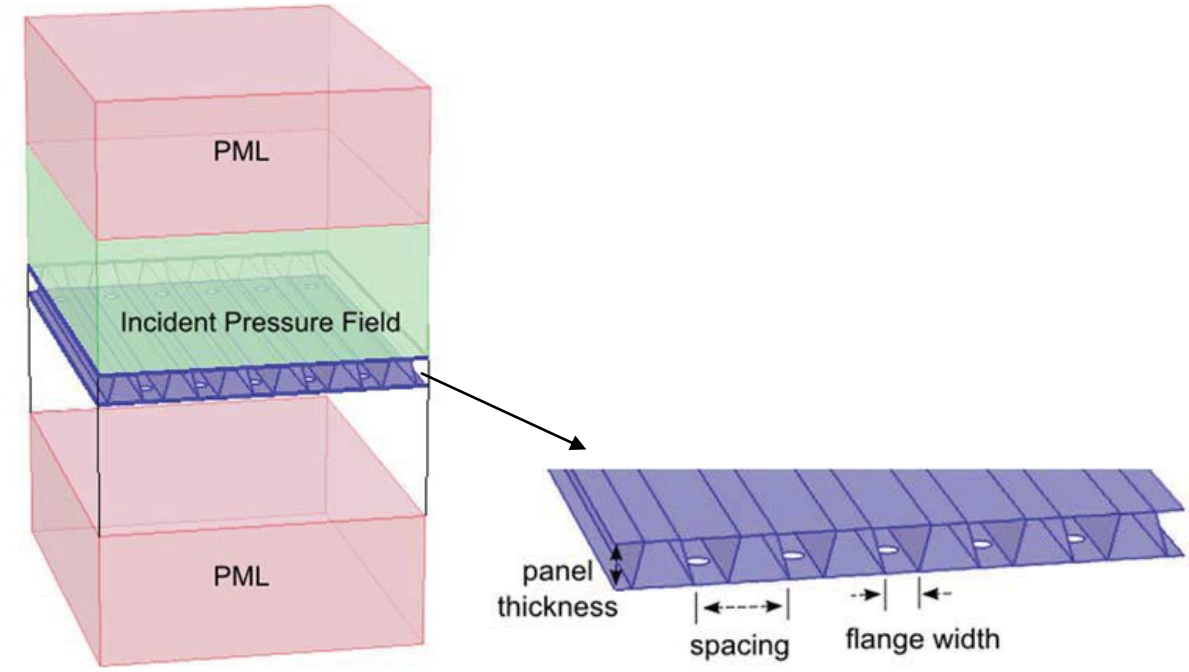

a) Acoustic and structural domains in the numerical model.

b) panel cross section.

Figure 1.12. Numerical model (Figs. 3 and 4 of Schiller et al. [2014]).

radiate sound out-of-phase with the structure, resulting in destructive interference, producing a significant reduction in the transmitted sound power into the interior of the structure. Finally, the authors concluded that the performance of such resonators is ultimately dependent on their total volume. Thus, this volume should be increased to the maximum extent possible without producing any adverse impacts.

Beck et al. [2015] designed a dual-resonance acoustic liner for engine noise reduction, with the dual-resonance approach coming from the simultaneous use of both a traditional honeycomb liner covered with a perforated plate (referred to as a "POHC—perforate over honeycomb") and a Helmholtz resonator acoustic metamaterial, which adds a second, low-frequency resonance to the liner system. In conducting an assessment of the impedance characteristics of this concept, the authors found that the normal incidence absorption coefficient of their concept was 10 times that of the traditional honeycomb liner at the design frequency of the Helmholtz resonator, and it increased absorption at all frequencies below 1 kHz, while retaining the higher-frequency performance of a traditional liner. Figure 1.13 presents measured and predicted absorption coefficients for the POHC and dual-resonance liners.

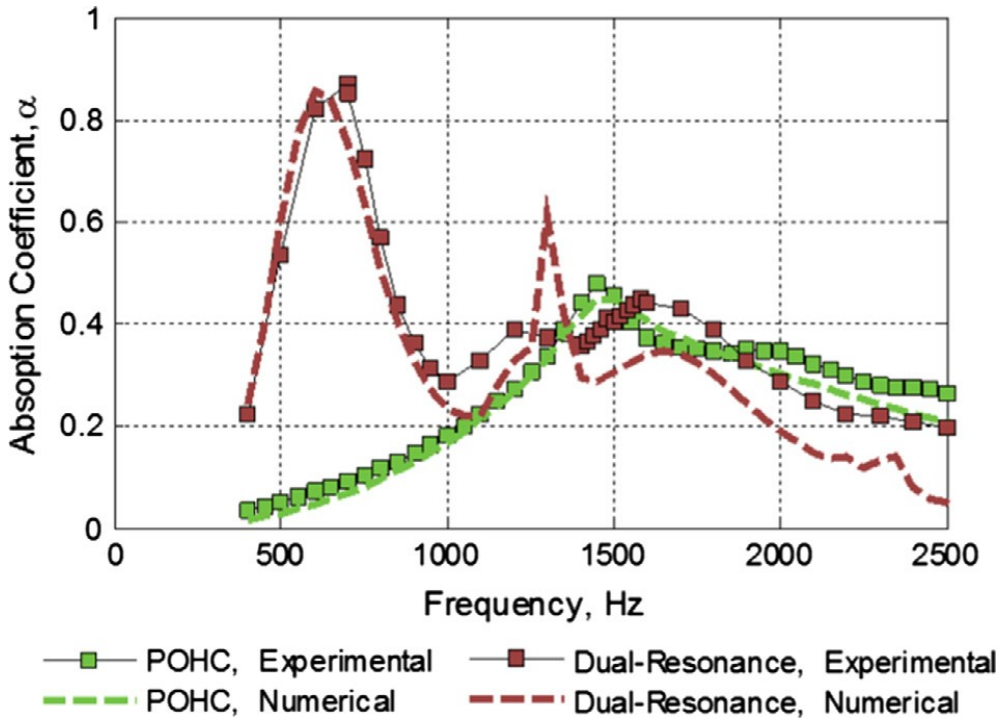

Figure 1.13.Comparison of absorption coefficient, α, between the POHC liner and the dual-resonance liner for a 120-dB SPL (Fig. 12 of Beck et al. [2015]).

Later, Hambric et al. [2015a, 2015b] redesigned a rotorcraft roof sandwich panel in order to maximize TL for frequencies between 1 and 4 kHz, so as to minimize the adverse impact that the transmission noise has on voice audibility. The original panel comprised a single honeycomb panel, while the redesigned panel split the cross section into two thinner panels separated by an air gap. This design was intended to reduce the panel resonant frequency from near 700 Hz to below 500 Hz, in order to increase TL in the 1–4 kHz range, while simultaneously maintaining structural integrity for both normal operations and loading because of maintenance. Experimental results showed the new panel produced from 6 to 11 dB of acoustic TL improvement and 6 to 15 dB of structure-borne sound reduction at typical rotorcraft transmission frequencies. Their analytical TL model agreed quite well with the experimental data.

More recently, Schiller and Allen [2017] examined the absorption potential of a combination of acoustic resonators and porous foam. While acoustic resonators have been shown to be effective at controlling lower frequencies (as discussed above), porous foam provides both broadband noise control and some measure of thermal insulation. The authors compared both measured and predicted acoustic absorption for flat panels containing acoustic resonators, foam treatment alone, and a combination of the two. As before, they found that acoustic resonators increase the low-frequency absorption in those bands for which they were designed, while the addition of the foam not only increased high-frequency absorption, but also improved low-frequency performance as opposed to resonators alone (see Fig. 1.14).

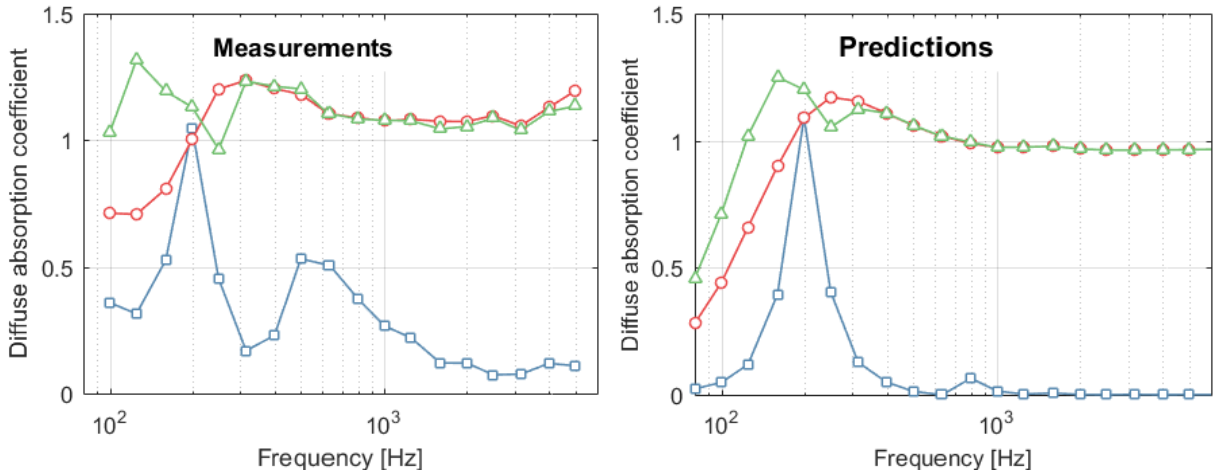

Figure 1.14. Diffuse absorption coefficient measurements (left figure) compared with predictions (right figure). Three configurations are compared: resonator array tuned for 200 Hz (□), foam with an air gap over inactive resonators (o), and foam with an air gap over the 200-Hz resonator array (Δ).(Fig. 5 of Schiller and Allen [2017].)

Active: While passive approaches to reducing interior noise are desirable if possible (i.e. if they work without a performance penalty), sometimes ANC approaches are required. Schiller et al. [2010] investigated the viability of applying active damping utilizing distributed anisotropic actuators. They distributed decentralized control units around the perimeter of a window. Each of these units comprised a triangularly shaped piezoelectric actuator, a miniature accelerometer, and analog electronics. Such systems had previously been shown to increase damping up to approximately 1 kHz. The authors used these new anisotropic actuators, made up of piezoelectric material between interdigitated electrodes, in an attempt to increase this bandwidth. They tested this approach on a Plexiglas® panel intended to emulate a helicopter window. While they did see increased damping at low frequencies, high-frequency performance was not improved. They believed this was due to the flexible boundary conditions on the test apparatus. In spite of this issue, they still measured reductions in the spatially averaged velocity of the panel by up to 11 dB at individual resonance peaks, with an integrated reduction of 3 dB through 550 Hz. In follow-on work, Schiller et al. [2011] successfully demonstrated significantly improved high-frequency response using a revised version of these actuators. These new diamond-shaped actuators were constructed using macro-fiber composite material to create a system that is not sensitive to the boundary conditions. They deployed using five of these new actuators around the perimeter of the window to obtain up to 10 dB reductions in resonance peaks of the spatially averaged velocity, along with a 2.4-dB integrated reduction between 500 and 3,000 Hz.

Later, Cabell et al. [2013] expanded upon this approach, applying 12 of these actuators to a 1.2-meter-square interior trim panel in a helicopter cabin mockup located at ONERA's Centre de Toulouse, with the purpose of achieving broadband active vibration control. Four accelerometers, one mounted at each vertex of the diamond-shaped actuator, were utilized to achieve sensor-actuator pairs that were effective over a wide range of frequencies, allowing for efficient, low-power control. Initial results on an acrylic window were encouraging, but results were significantly less so (<0.5 dB from 1–3 kHz) when the actuators were applied to a composite trim panel, since the feedback gains had to be reduced for stability purposes. The authors believed this was most likely due to some of the material properties of the trim panel, and they conducted a finite element study whose results seemed to concur.

Mendoza et al. [2014] developed an active vibration control approach entitled Minimum Actuation Power (MAP) to reduce helicopter interior noise from multiple gear meshing frequencies. MAP minimized the total input power into a structure by examining and controlling the input power of the controlling sources without requiring knowledge of the details of the excitation sources and works by minimizing the total input power from the excitation and controlling sources. They successfully demonstrated MAP on a realistic rotorcraft interior structure, measuring an average global vibration reduction of a single frequency of up to 15–20 dB using a single secondary actuator, and an average of 8–10 dB reduction at up to three frequencies using the same configuration. Simulations were also conducted that demonstrate the potential interior noise reduction using MAP to be, on average, 13.8 dB.

Going in a different direction, Bean et al. [2017] investigated the feasibility of implementing ANC in an aircraft headrest instead of attempting to quiet the entire interior of the vehicle. While passengers have used ANC headphones for many years, they are not allowed in some instances, especially where safety might be an issue, whereas an ANC system imbedded in the headrest

could simply create a "quiet zone" in the vicinity of the passenger's head. The authors quantified the potential benefit of such a system and examined the use of both virtual error sensors (i.e. virtual sensors located at the passenger's ears) as well as remote microphones to estimate the acoustic pressure around said passenger. They constructed a finite element model of the ANC headrest, and then examined its performance with respect to primary fields of both a diffuse and plane wave nature. Since this was a numerical model, multiple placements and quantities of both speakers and microphones could easily be examined, so that the relative efficacy of using virtual sensors versus physical microphones could be quantified. They found that the addition of a third speaker in the ANC system improved both the overall attenuation of the system and broadened the "quiet zone." They also found that using the virtual sensors allowed them to shift the region of maximum benefit from the vicinity of the control microphones more towards the passenger's ears.

NOISE PROPAGATION, MODELING, OPTIMIZED FLIGHT PATHS, AND AURALIZATION

While rotorcraft noise reduction is ideally implemented during the vehicle design phase, noise is often not the driving force behind design decisions, often trumped by other critical design parameters such as performance, vibration, etc. As such, it is important to have the ability to both model the noise generated by existing rotorcraft, and design (to the maximum extent possible) optimized flight paths that minimize the noise impact of these vehicles to the surrounding communities during normal operations. NASA has invested heavily in not only the modeling itself, but also the acquisition of the extensive databases required to validate these models. Yamauchi and Young [2009] documented both the technical background and NASA's historical investments in this area; this section addresses progress to date since publication of that report. This research logically divides into four primary areas with respect to conventional rotorcraft: noise modeling, propagation, and design of low-noise rotorcraft operating procedures—all of which are continuations of prior work described by Yamauchi and Young—but with the addition of auralization studies, which enable the study of the psychoacoustic effects of rotor noise on citizens. Obviously, many of the references cited here overlap between these areas, so each reference will be "binned" into the category that predominates in that report.

Noise Propagation

Once the rotorcraft sources are modeled, it is then necessary to propagate those sources to the ground. Predominant impacts on acoustic propagation include, but are not limited to, temperature, wind (both speed and direction), atmospheric pressure, altitude, and terrain. Because modeling of the entire atmosphere between the vehicle and the ground would be prohibitively computationally intensive, not to mention virtually impossible to validate, the acoustic propagation is most typically modeled as rays. Heath et al. [2008] conducted a validation of the Ray Tracing Program (RTP) using helicopter noise data acquired at Eglin Air Force Base in 2007 using a Mil MI-8 helicopter. RTP included refractive propagation effects due to wind and temperature, which enabled it to explain large variations in the data observed during the flight test. Four flyover test cases were used for the validation, all of which were level flight conditions at 150 knots and 300 feet altitude. The difference was that two flights were conducted at two different headings 80 degrees apart on one day, and then those same two were repeated

the next day. The different conditions resulted in significantly different refraction effects among the four test cases. Comparing data to prediction at a single microphone location situated at the far east end of the test range, the two cases from the first day, for which the measurements indicate definite shadow and multi-path regions resulting from refraction, show very good agreement between measured and predicted SPL losses out to approximately 15,000 feet from the helicopter. Meanwhile, Case 3 from the second day only shows good agreement to about 10,000 feet, while Case 4 shows significant lack of agreement between theory and measurement. In Case 3, it is likely that the shadow region becomes overpowered by a multi-path region just beyond 10,000 feet, while the authors could only speculate regarding the significant discrepancies in Case 4.

Schmitz et al. [2007] acquired simultaneous noise measurements in flight and on the ground using a Bell 206B helicopter. The University of Maryland converted a crop-dusting spray boom into a microphone array; the array was attached to the helicopter, forward of the main rotor. A NASA-developed Portable Programmable Guidance Display (PPGD) for precision pursuit guidance was installed in the helicopter to assist the pilot performing required maneuvers. Using the PPGD, the pilot was able to perform tasks accurately and efficiently with minimum control movement. Figure 1.15 shows a schematic of the PPGD. The authors showed, experimentally, that microphones close to the helicopter can be used to estimate the specific noise sources that radiate to the far field, provided the microphones are correctly positioned relative to the noise source. For steady turning flights, directivity patterns were developed and related to the turning performance of the helicopter. The data from this test were key in developing noise models discussed later in this chapter.

Greenwood and Sim [2013] examined the effects of crosswind flight on rotor harmonic noise radiation. Here, the effects of crosswinds on main rotor harmonic noise radiation were assessed using a model of the Bell 430 helicopter. Crosswinds were found to have a significant effect on BVI noise radiation when the helicopter was trimmed with the fuselage oriented along the inertial flight path, while there was negligible difference in the amplitude of the BVI noise when the pilot oriented the fuselage along the aerodynamic velocity vector, i.e. “crabbing” to avoid sideslip. They conclude that the pilot’s choice of trim can have a significant effect on BVI noise

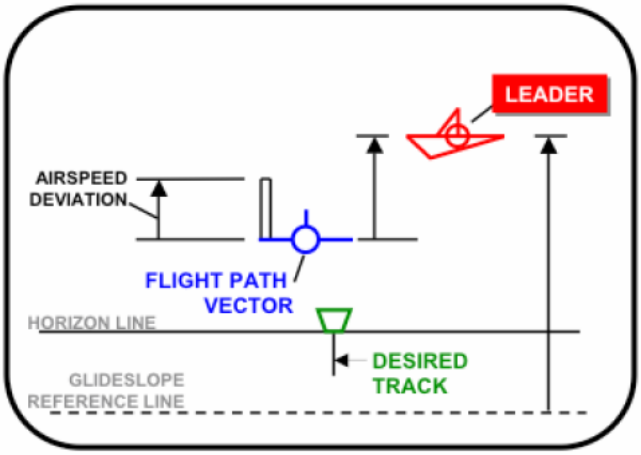

Figure 1.15. The NASA-developed PPGD in a Pursuit Guidance Mode (Fig. 7 of Schmitz et al. [2007]).

generation, which also means that the pilot, at lower descent angles, could utilize this effect to reduce BVI noise generation. Still, this effect is lower than the impact of headwinds on BVI noise. Meanwhile, for lower harmonic noise sources at higher flight speeds, the directivity of radiated noise was somewhat changed by the crosswind, while having negligible impact on the overall amplitude. The model predictions agree well with flight test data for the Bell 430 helicopter captured under various wind conditions. The authors suggest that flight paths for future acoustic flight testing should be aligned across the prevailing wind direction, as opposed to encountering either headwinds or tailwinds, so as to minimize the effects of winds on noise measurements for those instances when testing in no- to low-wind conditions cannot be achieved. Figure 1.16 shows predicted contours for various wind directions.

Watts et al. [2016] characterized the impact of altitude on helicopter noise. They conducted a flight test campaign performed at three different test sites whose altitudes ranged from sea level to 7,000 feet. Data were acquired for both a Eurocopter AS350 and a Sikorsky EH-60L, which had been modified to make it as close to a standard UH-60L as possible. They investigated the effects of altitude and gross weight variation on noise generation, while also establishing the statistical variability in acoustic flight testing of helicopters, as well as characterizing the effects of transient maneuvers on radiated noise for a medium-lift utility helicopter. They showed that changes in ambient conditions due to changes in altitude above sea level can result in significant changes in the radiated noise of helicopters when the flight conditions are defined in the dimensional terms typically employed by operators and mission planners (see Fig. 1.17). As theoretically predicted, thickness noise increases with decreasing air density and temperature, with changes as great as 5.4 dB over the 7,000-foot-altitude variation observed. Significant changes in BVI noise due to altitude variation were also observed. In general, BVI noise levels decreased with increasing altitude, although the authors surmise this was probably dependent on the specific indicated airspeed (IAS) and flight path angle selected to define the flight condition. In summary, significant changes in acoustic amplitudes were observed when the helicopter was operated at constant IAS and gross weight at the three sites. However, acoustic amplitudes were found to scale with ambient pressure when flight conditions were defined in terms of the nondimensional parameters, such as the weight coefficient and effective hover tip Mach number. In a companion paper using the same data sets for the AS350, Greenwood et al. [2016] examined the effects of ambient atmospheric conditions, air temperature, and density, on rotor harmonic noise radiation. Significant changes in the thickness, loading, and BVI noise levels and radiation directions were observed across the three test sites. The noise was found to scale with ambient pressure when the helicopter's operating condition was defined in nondimensional terms. While the effective tip Mach number is typically identified as the primary governing parameter for thickness noise, the nondimensional weight coefficient also impacts lower harmonic loading noise levels, which impact the overall low-frequency noise both in and out of plane. Strategies for maintaining the same nondimensional rotor operating condition under different ambient conditions were developed using an analytical model of a single main rotor helicopter trim and confirmed using a CAMRAD II model of the helicopter. The ability of the Fundamental Rotorcraft Acoustics Modeling from Experiments (FRAME) technique, which is discussed in detail in the following section, to generalize noise measurements made under one set of ambient conditions to make accurate noise predictions under other ambient conditions, was also validated (see Fig. 1.18).

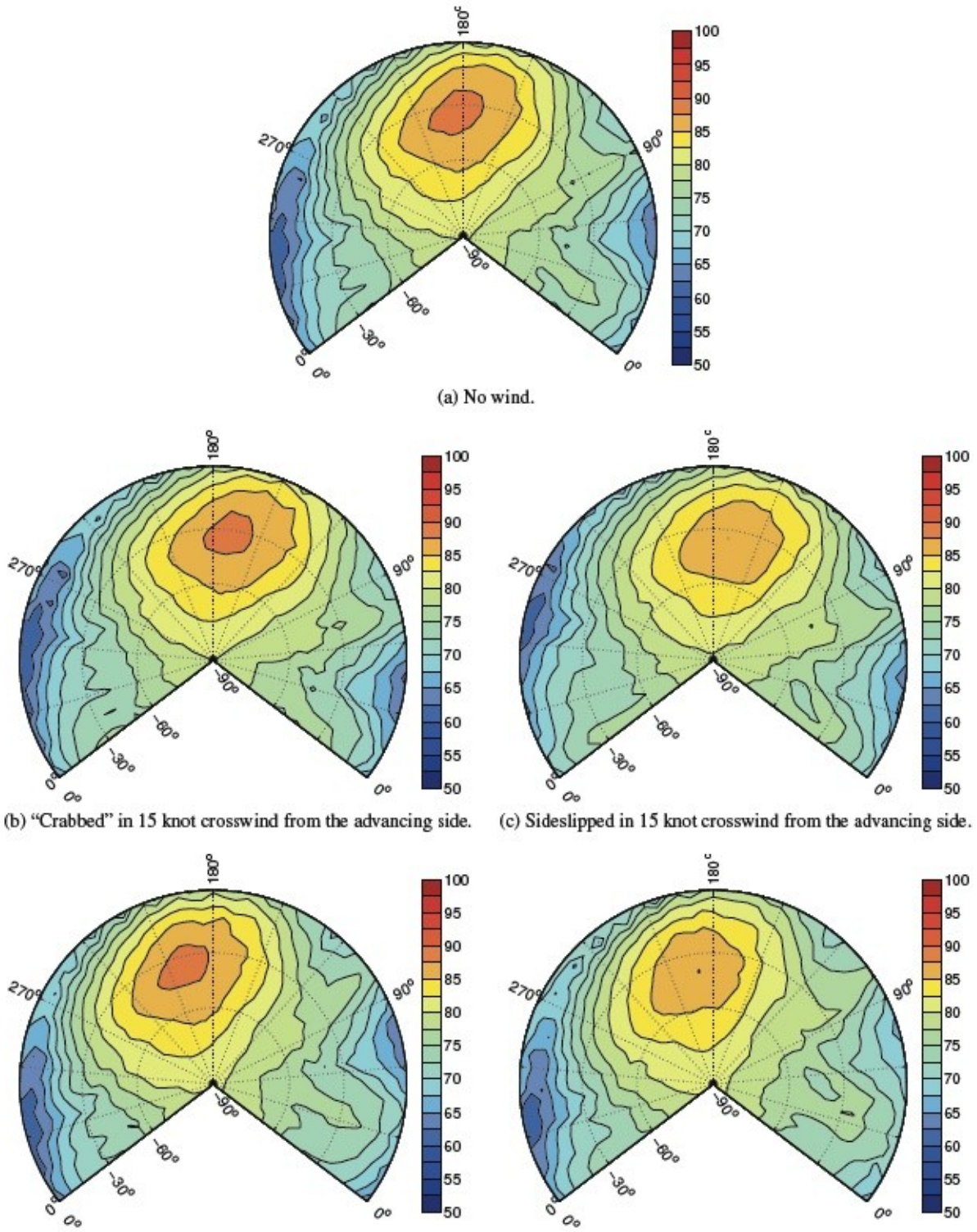

(a) No wind.

(b) "Crabbed" in 15 knot crosswind from the advancing side.

(c) Sideslipped in 15 knot crosswind from the advancing side.

(d) "Crabbed" in 15 knot crosswind from the retreating side.

(e) Sideslipped in 15 knot crosswind from the retreating side.

Figure 1.16. Predicted BVI noise hemispheres for a Bell 430 helicopter: 50 KIAS, –7.5° flight path angle, contours of dB BVISPL (Fig. 11 of Greenwood and Sim [2013]).

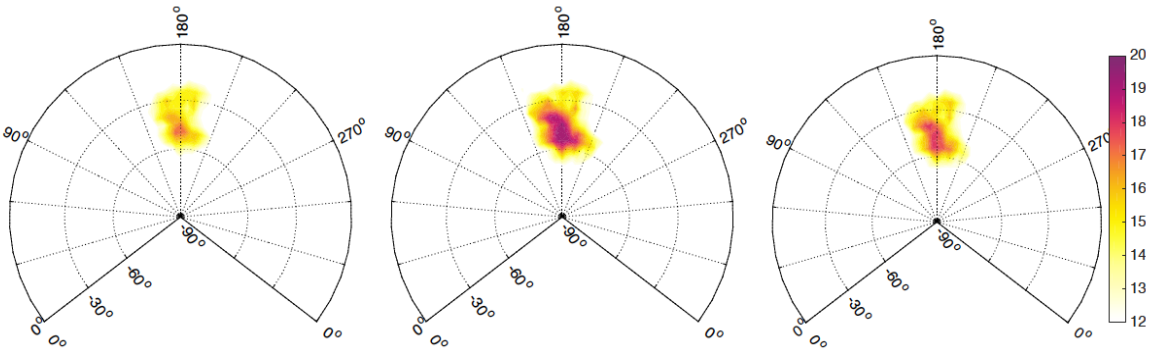

(a) Salton Sea, 0 ft (b) Amedee, 4000 ft (c) Sweetwater, 7000 ft

Figure 1.17. BVI peak-to-peak variations with location for AS350 SD1, 80 KIAS descent condition (V5) in normalized pascals (Fig. 21 of Watts et al. [2016]).

.

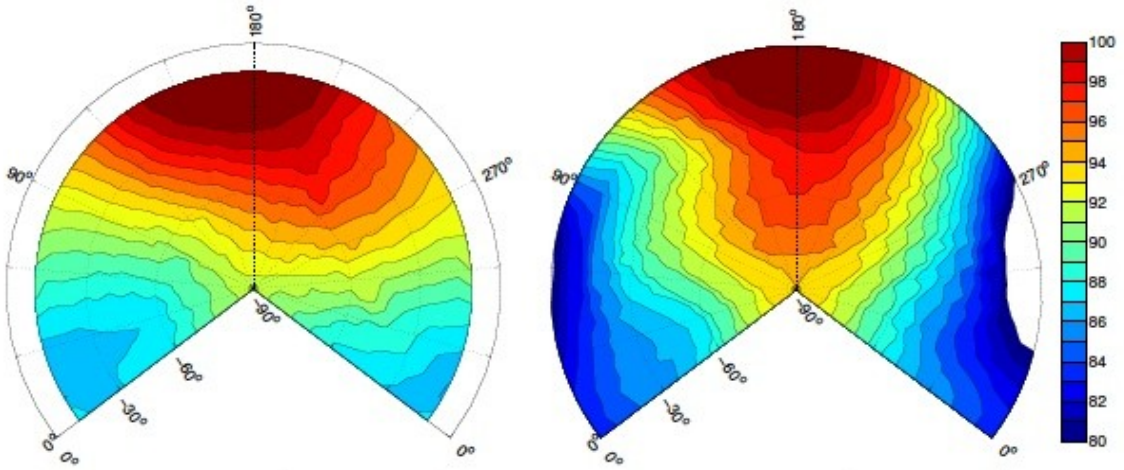

(a) RNM/ART hemisphere, Sea Level, dB OASPL. (b) FRAME hemisphere, Sea Level, dB OASPL.

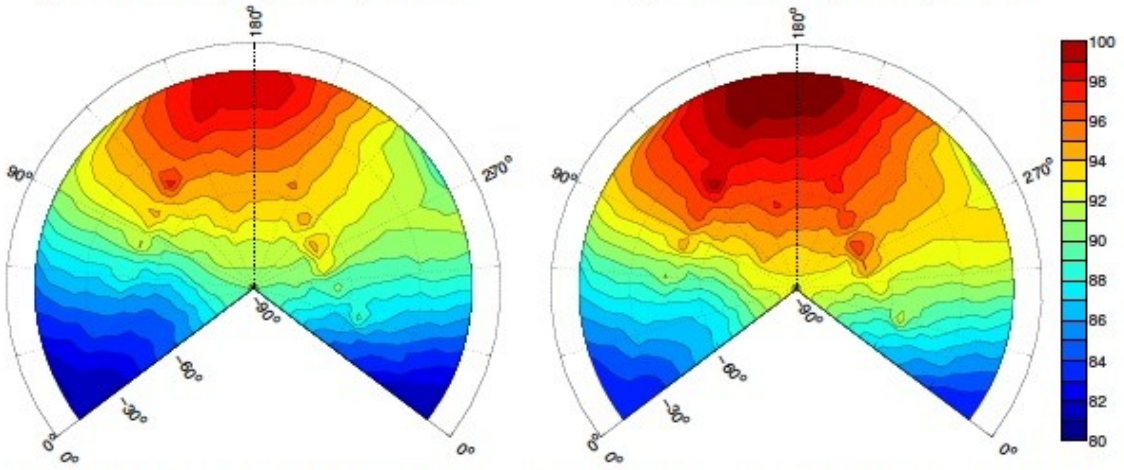

(c) RNM/ART hemisphere, 7000 ft MSL, dB OASPL. (d) RNM/ART hemisphere, 7000 ft MSL re. Sea Level, dB OASPL.

Figure 1.18. Measured, predicted, and scaled noise hemispheres for nondimensionally defined level flight calibration condition, effective hover tip Mach number = 0.791, main rotor weight coeffcient = 0.0038 (Fig. 6 of Greenwood et al. [2016]).

Noise Modeling

Rotorcraft noise modeling efforts can range from completely theoretical to semi-empirical, and even totally empirical. They can also involve either modeling the full vehicle or modeling the different noise sources separately (most often the main rotor and tail rotor). The latter efforts are much more difficult to validate using flight data, as the recorded acoustic measurements obviously contain all noise sources, so more sophisticated data processing is required to attempt to isolate the measured noise from a single source. In this section both the modeling efforts themselves and the related acquisition of flight validation data are examined.

Greenwood and Schmitz [2010] developed a physics-based parameter identification method for rotor harmonic noise sources using an acoustic inverse simulation technique, which enables the user to identify individual rotor harmonic noise sources. Those individual sources can then be characterized in terms of their individual nondimensional governing parameters, and the method is applicable to both wind tunnel and ground-based noise measurements of two-bladed rotors. While their approach could be applied to all rotor harmonic noise sources, the focus of their study was on main rotor BVI noise. They successfully applied their method to both wind tunnel measurements of a 1/7th-scale OLS rotor and ground-based measurements of a Bell 206B3 helicopter. This approach eventually resulted in the development of the FRAME modeling tool [Greenwood, 2011] (see Fig. 1.19). FRAME employed the parameter identification methodology described above to adapt analytical models of the rotor noise sources to fit measured acoustic data captured over a wide range of steady-state operating conditions, while transient conditions such as maneuvers are treated as dynamic deviations from these steady-state conditions. Using this approach, a semi-empirical model for a specific helicopter can be produced that allows the user to predict the main rotor BVI noise radiation of a maneuvering helicopter.

Next, Greenwood and Schmitz [2011] applied the FRAME methodology to examine the impact of ambient noise on rotor harmonic noise, using the measured noise from a Bell 206B3 helicopter operating at multiple altitudes. The authors found significant variation in BVI noise with altitude depending on whether the pilot was operating using IAS or true airspeed (TAS) (see Fig. 1.20). Typically, pilots fly using IAS regardless of altitude, which means that the TAS increases with altitude, producing simultaneously an increase in advance ratio and a decrease in speed of sound. This caused dramatic changes in BVI noise of up to 7 dB for every 10,000 feet of altitude change, while if TAS was used, BVI noise levels and directivity remained fairly constant. The authors also found significant increases in thickness noise (up to 8 dB per 10,000 feet) when flying IAS, but less than 1 dB if TAS was used. The authors pointed out the importance of considering altitude when evaluating possible helicopter noise-minimal operations.

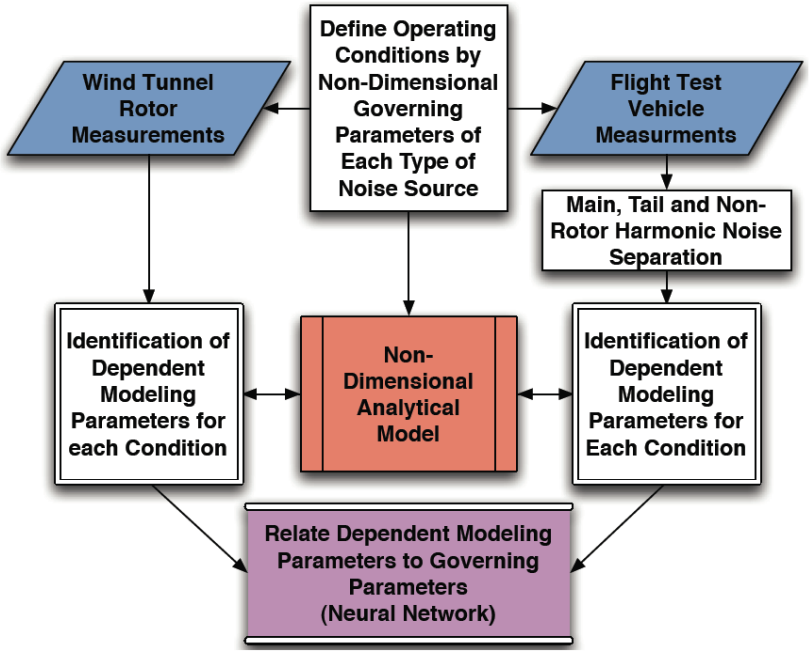

Figure 1.19. A flowchart describing the FRAME method for developing rotorcraft source noise models (Fig. 3 of Greenwood and Schmitz [2011]).

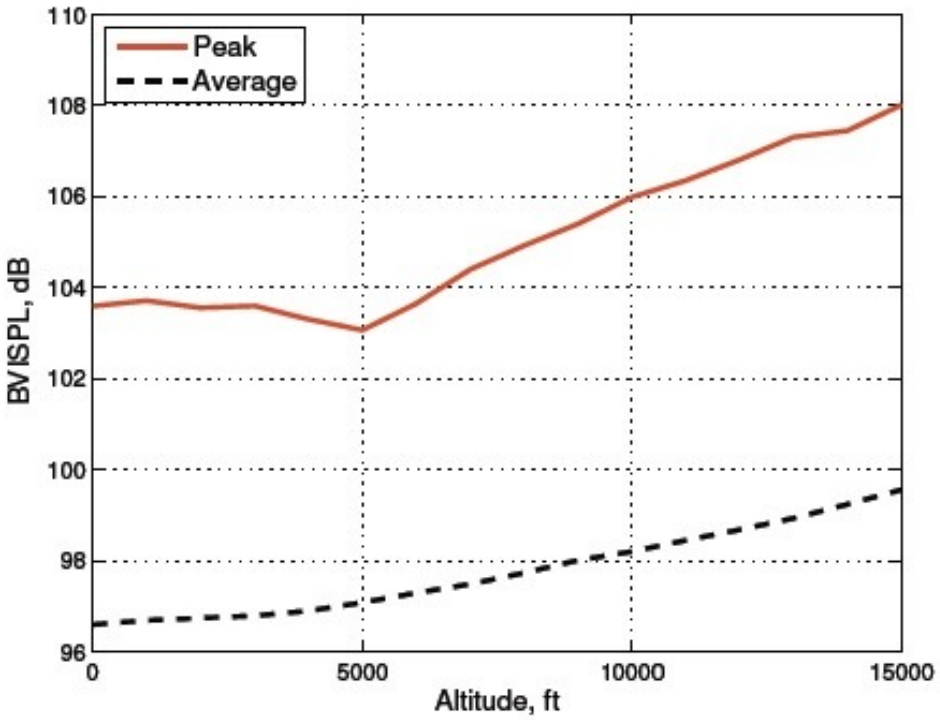

Figure 1.20. Variation of BVISPL values with ISA altitude conditions for 60 kts IAS, –6° descent flight (Fig. 18 of Greenwood and Schmitz [2011].)

In a continuation of expanding the capability of FRAME, Greenwood et al. [2012, 2015a] developed a new semi-empirical model for BVI noise during maneuvering flight; the new model was named FRAME-D. The FRAME-D BVI noise model is an extension of the steady-state BVI noise model used in a previous version of FRAME. FRAME-D uses quasi-steady assumptions throughout the prescribed maneuvers (pure pitch and roll transients). Comparison of FRAME-D calculations with the maneuvering flight data of a Bell 206B helicopter show that many of the noise radiation details are captured. FRAME-D can be run in real time to predict transient maneuver noise and is suitable for use in an acoustic mission-planning tool.

As mentioned previously, accurate validation, either for the full vehicle or the individual rotor noise sources, is critical to the above modeling efforts. Using the data from the Bell 206B acquired by Schmitz et al. [2007], Sargent et al. [2008, 2010] processed and analyzed the data in the time domain via a theoretical tail rotor 1/rev signal, to obtain tail rotor acoustic time histories for both forward and descending flight. This technique provided insight into both the directivity and noise mechanisms associated with the periodic harmonic noise generated by a Bell 206B tail rotor. Comparisons between linear harmonic noise theory and the time-averaged experimental data showed good agreement (see Fig. 1.21) and indicate that the noise from the 206B tail rotor was dominated by thickness noise near the tip-path-plane of the tail rotor and by loading noise at the out-of-plane microphone positions, as should be expected. The measured data also provided trends associated with the OASPL with respect to both forward velocity and descent angle. They also showed significant variance about the tail rotor harmonic noise, and postulated that other sources of aperiodic tail rotor harmonic noise may be both present and important.

Greenwood and Schmitz [2014] developed an innovative method of separating main and tail rotor noise using ground-based acoustic measurements. They utilized time-domain de-Dopplerization to transform the acoustic pressure time-history data collected from a fixed array of ground-based microphones to the equivalent time-history signals that would presumably be seen by an array of virtual in-flight microphones traveling with the helicopter. Those now-stationary signals were then periodically averaged with each of the main and tail rotor blade passages, which were inferred from the acoustic signals using wavelet analysis. This approach suppresses noise that is not periodic with the respective rotor, allowing for the separation of main and tail rotor pressure time histories. The averaged measurements were then interpolated across the range of directivity angles to generate separate acoustic hemispheres for the main and tail rotor noise sources. This approach enables a more direct comparison of ground-based noise measurements of rotorcraft with theoretical predictions and wind tunnel measurements of isolated rotors as opposed to comparing with full vehicle measurements. They applied their approach to ground-based microphone measurements of a Bell 206B3 helicopter, showing the strong directivity characteristics of harmonic noise radiation from both the main and tail rotors of that vehicle.

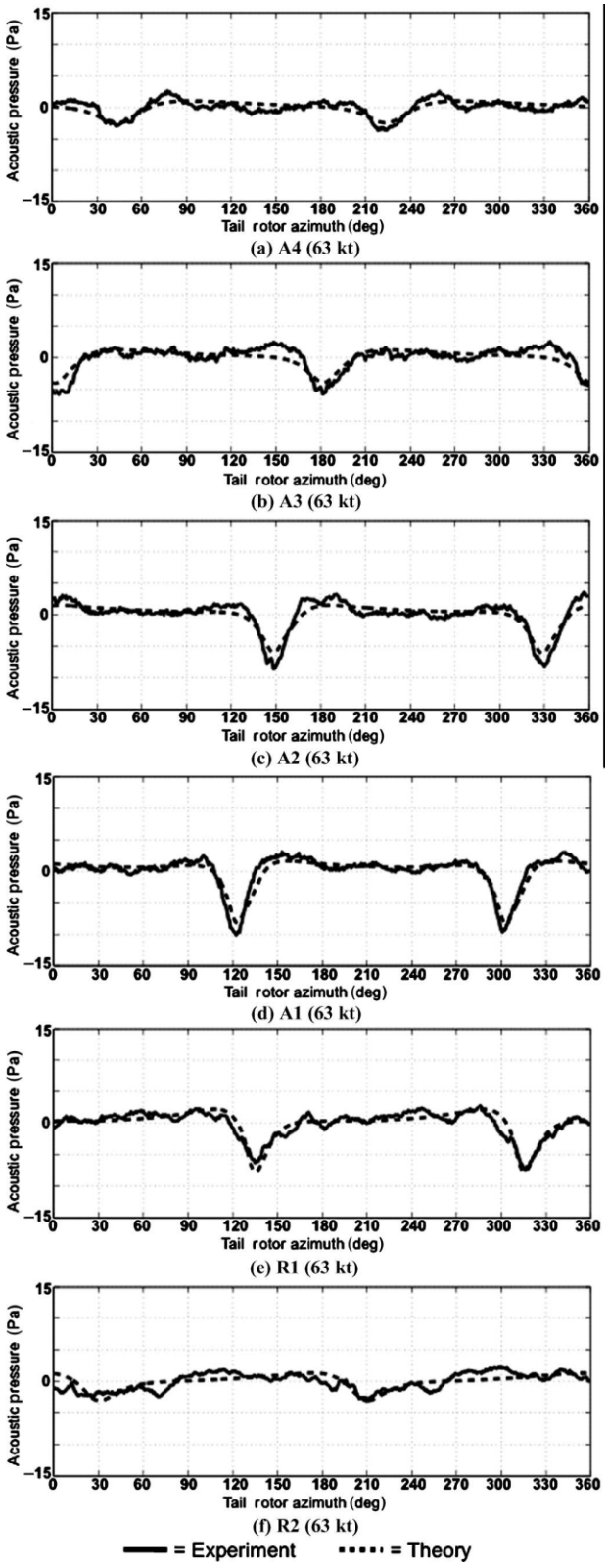

Figure 1.21. Comparison of linear harmonic noise theory and experiment (Fig. 16 of Sargent et al. [2008]).

Later, Stephenson and Greenwood [2015] examined the effects of vehicle weight and TAS versus IAS on BVI noise during steady descending flight. They analyzed BVI noise measurements from an AS350 B helicopter operated at 7,000 feet above sea level, as was described above in the discussion of Watts et al. [2016]. BVI noise from four 6-degree-descent conditions were investigated with descents flown at 80 knots true and indicated airspeed, as well as 4,400- and 3,915-pound gross take-off weights. BVI noise was extracted from the acquired acoustic signals by way of a previously developed time-frequency analysis technique explored by Stephenson in his dissertation. The BVI extraction technique provides a better localization of BVI noise, when compared to the standard Fourier transform integration method. The authors found that large changes in BVI noise amplitude occurred because of changes in vehicle gross weight. These changes were far too large to be solely due to changes in the vortex strength caused by varying vehicle weight. They postulated that changes to the vehicle weight must modify the tip-path-plane angle of attack, as well as induced inflow, which then produces large variations in BVI noise. Defining flight conditions by TAS, rather than IAS, provided more consistent BVI noise signals (see Figs. 1.22 and 1.23).

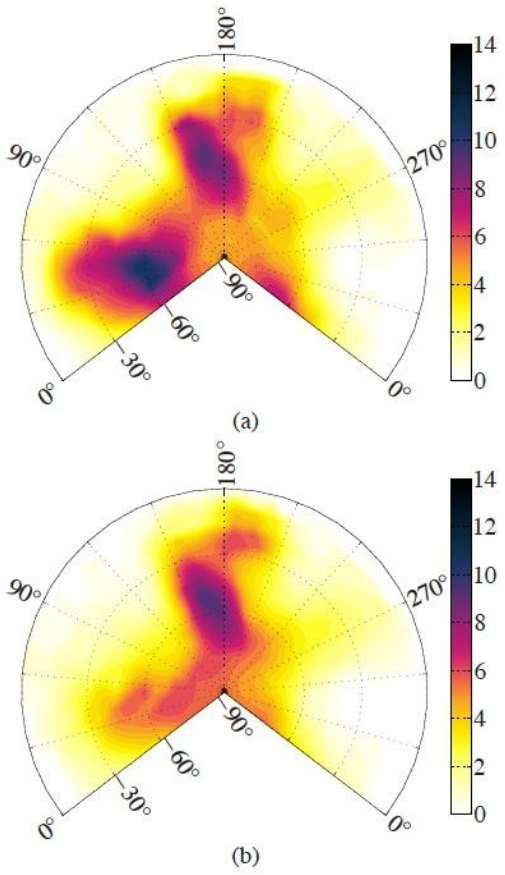

Figure 1.22. Extracted BVI peak-to-peak pressure amplitudes [Pa] for (a) 4400 lb and (b) 3915 lb, 80 KIAS test condition. (Fig. 6 of Stephenson and Greenwood [2015].)

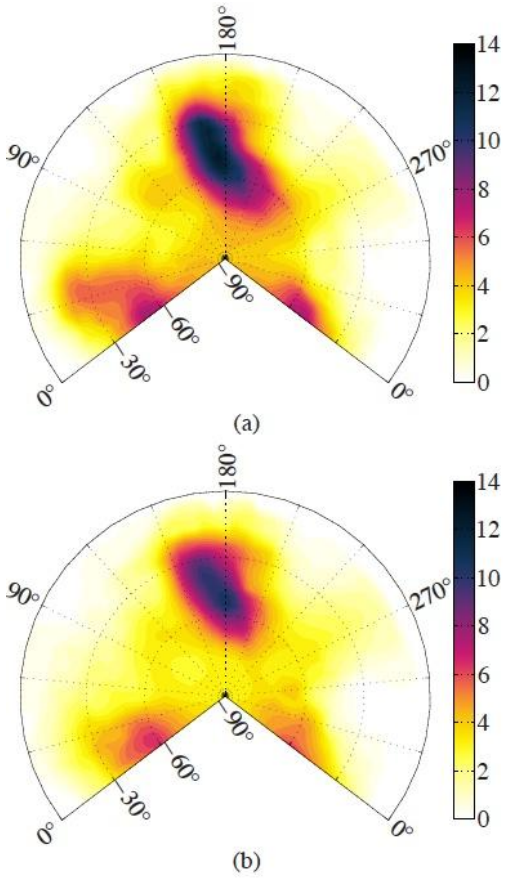

Figure 1.23. Extracted BVI peak-to-peak pressure amplitudes [Pa] for (a) 4400 lb and (b) 3915 lb, 80 KTAS test condition. (Fig. 7 of Stephenson and Greenwood [2015].)

Acquiring validation-quality ground-based acoustic data is difficult when the rotorcraft is operating at constant operating conditions, and it is significantly more difficult under nonsteady conditions such as maneuvering flight. Not only are the vehicle conditions much more difficult to repeat, but the directivity of the noise is constantly changing, often very quickly. Watts et al. [2012, 2014] conducted a cooperative flight test by NASA, Bell Helicopter, and the U.S. Army in order to both characterize the steady-state acoustics and measure the maneuver noise of a Bell 430 helicopter. The test, which occurred during June/July of 2011 at Eglin Air Force Base, Florida, acquired data from a total of 410 test conditions over 10 test days, and compiled an extensive database of dynamic maneuver measurements. Three different microphone layouts with up to 31 microphones in each configuration were used to acquire the acoustic data. Aircraft data included Differential Global Positioning System (DGPS), and aircraft state and rotor state information. The authors showed that maneuvers do lead to significant increases in noise, as has been known for many years. They found that maneuvers that involve using cyclic control inputs to change the pitch of the rotor tip-path-plane angle result in a particularly large increase in noise (see Fig. 1.24), while the noise due to collective inputs did not produce much change in noise. They postulate that primarily using collective inputs and minimizing rapid cyclic inputs when changing altitude will result in a lower-noise technique for this vehicle.

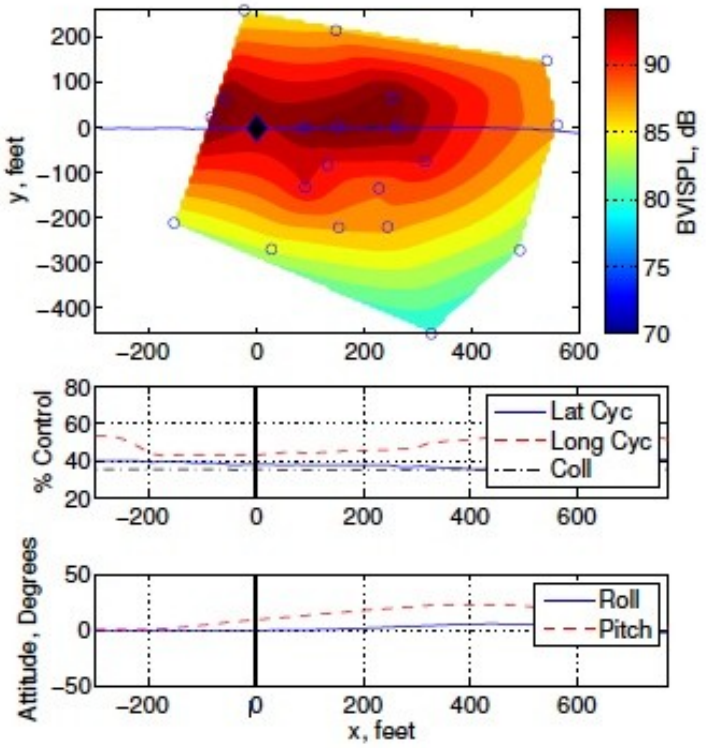

Figure 1.24. Fast cyclic pull-up initiated from 80 kts level flight (Fig. 25 of Watts et al. [2012]).

Greenwood et al. [2015b] developed a new model for estimating the noise radiation during maneuvering flight. The authors applied the Quasi-Static Acoustic Mapping (Q-SAM) method developed at the University of Maryland to a database of acoustic spheres generated using Greenwood's FRAME technique. A realistic flight trajectory is generated from a limited set of waypoints and is used to calculate the quasi-static operating condition and corresponding acoustic sphere for the vehicle throughout a maneuver. A database of pre-computed acoustic spheres can then be used to quickly predict the acoustic impact of proposed helicopter operations for mission planning. The new model, FRAME-QS, was applied to near-horizon noise measurements acquired by Watts et al. [2014] for the Bell 430. For the conditions of transient pitch-up and roll maneuvers, the authors showed good agreement between the measured data and the FRAME-QS model.

Design of Optimized Flight Paths

The purpose of this section is to enable the design of quieter flight procedures, with the penultimate goal of providing real-time "noise in the cockpit" information that would allow pilots to operate their vehicles in the quietest way possible. However, it is not sufficient to just be quiet. In order to be practical, these procedures must be quiet, safe, AND easy to fly, so that a test pilot is not required to perform the operations; a typical pilot can safely and easily utilize this guidance. This subsection describes the efforts of the NASA Rotorcraft Project in this area over the past decade.

Padula et al. [2009] successfully demonstrated the efficacy of utilizing an optimization procedure for identifying quiet rotorcraft approach trajectories. The procedure employed a multi-objective genetic algorithm (MOGA) in order to reduce noise and create approach paths that will be acceptable to both pilots and passengers. The concept is demonstrated by application to two different helicopters—the Bell CH-146 and the McDonnell Douglas MD-900. The CH-146 optimization effort used measured noise hemispheres, while the MD-900 effort used predicted noise hemispheres. The optimized paths were compared with one another and to a standard 6-degree-approach path. The two demonstration cases validated the optimization procedure but highlighted the need for improved noise prediction techniques and for additional rotorcraft acoustic data sets (hence all of the efforts described in the two previous subsections). The optimized approaches compared favorably with the Helicopter Association International (HAI) Fly Neighborly recommendations and were consistent with previous low-noise flight test results. They were also validated by repeating the MOGA procedure with 300 and then 1,000 objective function evaluations, with similar results. Additionally, they were validated by using a Latin hypercube design of experiments (DOE) methodology to generate alternate approach paths. This DOE study showed that the MOGA functioned correctly, and also suggested that by intentionally reducing noise at five individual locations, the MOGA was also reducing total noise in the area represented by the noise footprint.

In a series of efforts in the early 2010s, Morris [2011] and Morris et al. [2012a, 2012b, 2013] coupled rotorcraft noise modeling procedures with an automated optimization approach to facilitate the design of new low-noise-approach trajectories. They applied a constraint-based optimization model and a local search, paired with a robust noise simulator, to design optimized

noise-minimal approaches. Their technique allowed them to incorporate constraints representing the knowledge provided by pilots and other technical experts. They later noted the limitations of their approach, such as using an artificial grid model of the environment that neglects any considerations other than noise and comfort; using a simple dynamic control model that only considered the effects of reducing velocity and/or altitude and neglected all other effects; and using an incomplete search method that did not conduct a full search over the entire space of solutions. Their use of search techniques, originally developed for artificial intelligence purposes, coupled with simulation and field tests, allowed them to design low-noise flight profiles that could then be tested in either simulation or through field tests (or preferably both). They concluded by investigating the use of simulation based on predictive physical models, combined with the A* path planning algorithm, for their low-noise-approach designs.

Later, Greenwood [2017a] used his FRAME-QS model described previously to evaluate the community noise impact of practical variations on several helicopter flight procedures typical of normal operations. He studied, both individually and in combination, such operations as turns, "quick-stops," approaches, and climbs on an AS350 SD1 helicopter. Even fairly small variations in flight procedures were shown to cause significant changes to Sound Exposure Levels (SELs) over a wide area. He developed guidelines for pilots to provide effective strategies for reducing the adverse impacts of rotorcraft noise on the surrounding community. He also performed optimization studies of flight trajectories to identify low-noise optimal flight procedures and then quantify the magnitude of community noise reductions that can be obtained through tailored helicopter flight procedures. Physically realizable optimal turns and approaches were identified that achieved global noise reductions of as much as 10 dBA SEL.

Next, Greenwood [2017b] developed an approach that could actually lead to providing pilots with the "noise in the cockpit" awareness of how much noise they were radiating to the surrounding community, which has been an ultimate goal of the NASA rotorcraft acoustics community for decades. Again, building upon the FRAME-QS capability, he constructed an acoustic model of the AS350 helicopter, fabricating a series of acoustic hemispheres over a wide range of the vehicle's operating conditions. He then used an off-the-shelf flight simulator model of the SA-342 Gazelle, which is quite similar to the AS350, to provide inputs of position, velocity, acceleration, and orientation to his model, using these inputs to determine which noise hemisphere is most appropriate at that particular flight condition. He then used that particular noise sphere, coupled with straight ray propagation, to generate the contours of noise on the ground. He also noted that significant cockpit/human factors research will likely be required before that penultimate "noise in the cockpit" goal is eventually realized.

Meanwhile, Watts [2017] described the flight acoustic testing capabilities at NASA Langley via the Mobile Acoustic Facility, which is used to acquire acoustic data from up to 36 wireless microphones mounted on ground boards (see Fig. 1.25). The Wireless Acoustic Measurement System (WAMS) negates the need to string microphone cables across long distances, which greatly mitigates the potential adverse impact of such things as weather and "natural fauna." WAMS also digitizes the data directly at the microphone, so there are no risks associated with attempting to transmit low-level acoustic analog signals through very long cables. Weather and

some vehicle tracking and state data are also captured in this system. This capability is completely self-contained, with quiet generators to provide power, although it can also operate using 220-V AC power if available, and was utilized to acquire the acoustic data used in some of the semi-empirical modeling described previously. He highlighted two example tests—a joint NASA/Army/Bell Helicopter maneuver acoustic test conducted in 2011 with the Bell 430 and an altitude variation flight test of an AS350 SD1, described previously. Example results were provided.

Finally, Greenwood [2018] used machine learning techniques on the vast quantity of helicopter noise data acquired by NASA Langley over the past 10+ years (10 helicopters and over 1,500 flight conditions). To accomplish this, he first had to come up with a means to quantify the total noise exposure that a vehicle radiated to the ground for a given operating condition, allowing that condition to be classified as either noisy or not noisy. Next, he nondimensionalized all of the operating conditions, put the data for all vehicles into one large database, and then applied multiple machine learning tools on a subset of that data to "train" the models to identify noisy flight conditions. He validated the models with data that were excluded from the initial training set and found that the models could identify noisy regions of the flight regime for multiple helicopters (see Fig. 1.26).

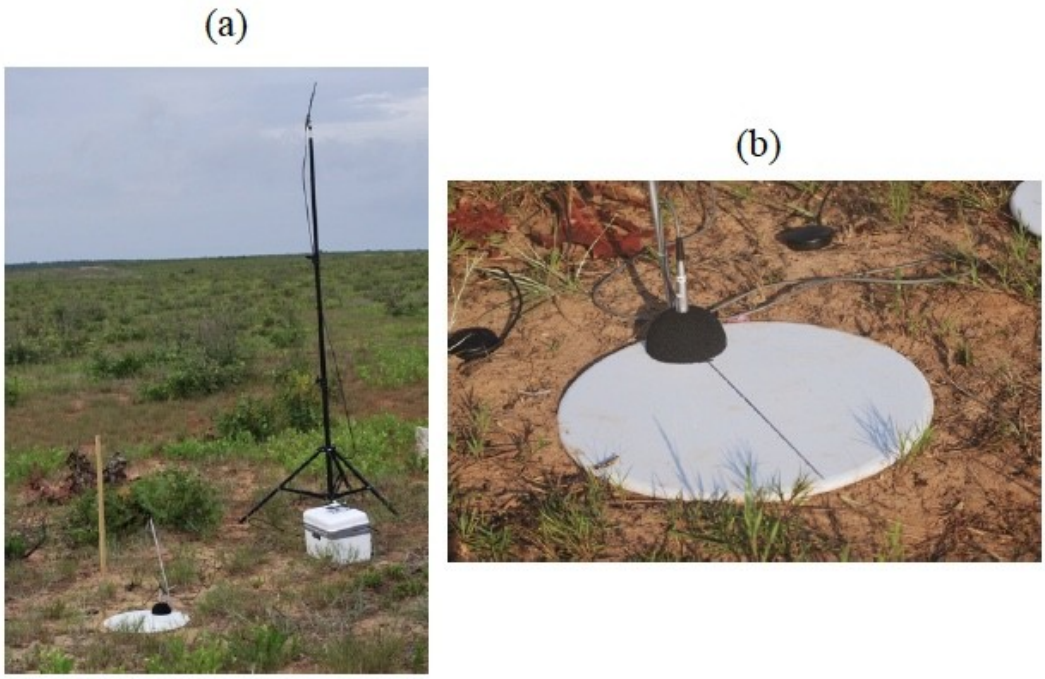

Figure 1.25. (a) WAMS system deployed, and (b) B&K 4189 inverted over ground board (Fig. 2 of Watts [2017]).

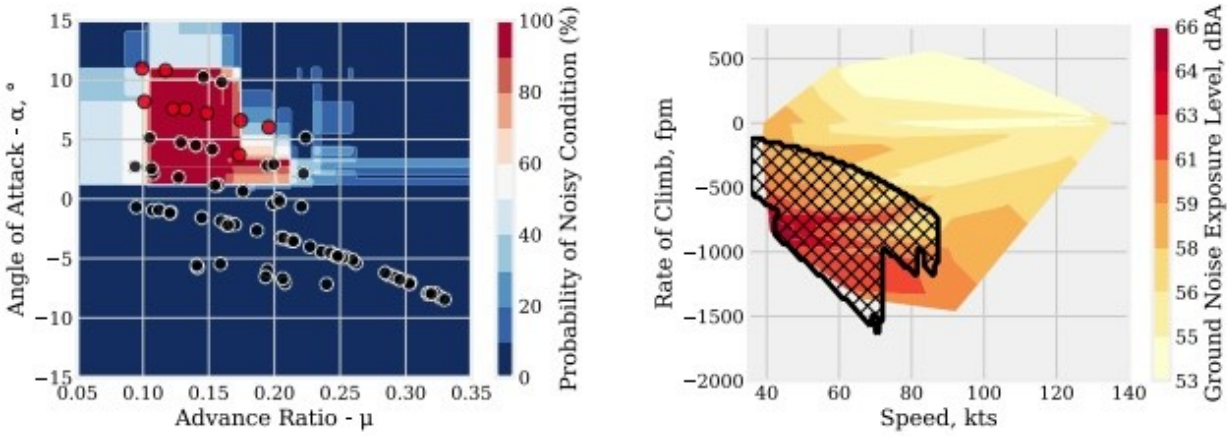

a) Estimated probability of a noisy rotor operating condition. Measured flight conditions are marked with circles: black circles were identified as quiet and red circles as noisy. Wright coefficient = 0.006, hover tip Mach = 0.61, number of main rotor blades = 5.

b) Predicted noisy region (hashed) plotted over ground noise exposure level contours derived from measured data.

Figure 1.26. Output of the Random Forest (RF) model compared to measured data for the MD-902 as tested at Eglin AFB (Fig. 9 of Greenwood [2018]).

Auralization

An important aspect of completely understanding the adverse impacts of rotor noise on the surrounding community is the psychoacoustic/subjective response of such noise on humans. This is true not just for rotor noise, but for all flight vehicles. To study this issue, many years ago NASA Langley constructed an Exterior Effects Room (EER), a 39-seat theater/auditorium that enabled researchers to play either actual or synthesized audio recordings of aircraft, while test subjects provided their opinions as to the relative annoyance of each sound. Previous rotorcraft studies using the EER required installation of additional speakers to accurately emulate the low-frequency noise generated by rotorcraft. During the past decade, NASA has invested significant funds into refurbishing the EER to facilitate rotorcraft studies within the existing facility. A summary of those efforts is described below, as well as other subjective response studies that were conducted elsewhere.

Faller et al. [2010a] describe the efforts to upgrade the EER to transition from only monaural studies to a facility that could accurately simulate a full three-dimensional (3D) audio and visual experience. The room, shown in Figure 1.27, was upgraded to include a 27.4 3D audio system, coupled with video simulation, to better emulate a realistic rotorcraft flyover. The authors documented the acoustic calibration of the improved EER, accounting for not only the relative gains in each speaker during the emulated flyover but also the requisite time delay between speakers required for whichever flight path direction is being simulated, and the myriad positions of the various speakers as they were installed in this large, irregularly shaped room. They identified issues associated with the computational requirements needed for the long-equalization finite impulse response (FIR) filters required for the subwoofers and suggested potential future research solutions. Next, Faller et al. [2010b] addressed this issue by developing reduced-length surrogate IIR filters as replacements for the originally used FIR filters, which allowed for use in

real-time operations. Rizzi and Christian [2015] built upon this approach to better enable subjective response testing for rotorcraft noise under controlled laboratory conditions, using these improvements in source noise synthesis, propagation modeling, and reproduction. They used individual blade passage time histories from both the main and tail rotors, which could be either obtained from acoustic predictions or from the inverse propagation of ground-based measurements from actual flight testing. For this particular study, the authors used synthesized noise from a Eurocopter AS350 helicopter (also known as the AStar) to demonstrate the efficacy of their approach. Later, Rizzi et al. [2017a] evaluated the capability to quantifiably examine both the audibility and localization of rotorcraft noise in a controlled laboratory environment, again using synthesized noise from the AStar. They showed the ability to resolve audibility differences due to variations in ground impedance, propagation modeling techniques, and directionality. They also suggested that they should be able to assess the effects of unsteadiness in the received acoustic waveform using this approach.

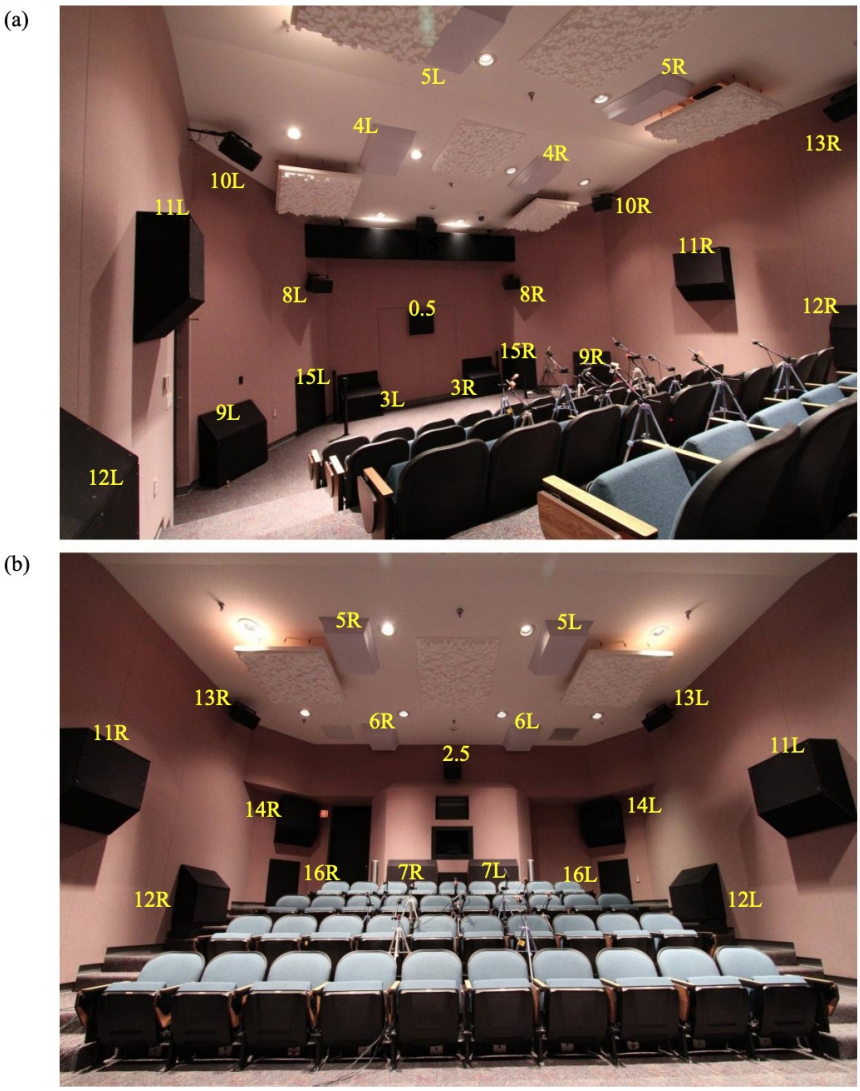

Figure 1.27. Front (a) and rear (b) views of the EER showing the mounted satellite and subwoofer speaker locations (Fig. 1 of Faller II, et al. [2013]).

In follow-on work, Pera et al. [2018] expanded their efforts so as to allow a range of emission angles in their auralization simulation, still using the AStar flight data as a base for their technique. Their approach used a source noise definition process that yielded both periodic and aperiodic (i.e. modulation) components for a series of emission angles, although only the periodic components were used in this study. The authors did note differences between the synthesized and measured flight data (see Fig. 1.28) and described possible techniques for improving the synthesis.

Shortly afterwards, Krishnamurthy et al. [2018] took the auralization methodology a step further by incorporating optimized noise computations from a baseline AS350 helicopter in lieu of incorporating measured data in the NASA Auralization Framework described above. They used CAMRAD II for the rotor design calculations and the AeroAcoustic Rotor Noise (AARON) capability in ANOPP2 for the acoustic predictions, which is another implementation of Farassat's Formulation 1A. This is a huge step in the development of a "design for noise" capability, since most of the aeromechanic input required as input to these noise predictions is also required to assess the new vehicle's performance capability as well, and often uses the same analytical tools. This means that designers can easily take multiple potential vehicle designs and then have human observers actually hear what each one would sound like, without ever building a single piece of hardware. Another capability enhancement is the incorporation of spherical phase interpolation in the auralization instead of linear, which eliminated some of the artifacts seen in the prior work in this area. The authors used two different optimization schemes in the rotor design phase—one using EPNL and the other using A-weighted SEL. Since the noise predictions were produced in the time domain, they proved to be more effective than the measured 1/3-octave noise spectra used previously. They also examined the efficacy of using increased resolution of the source noise modeling in this approach, but question the cost of significant increases in computational time.

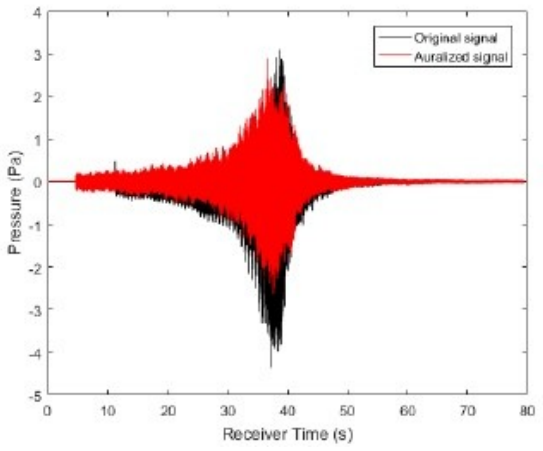

a) Comparison of ground recording with auralized signal (Fig. 23 of Pera et al. [2018]).

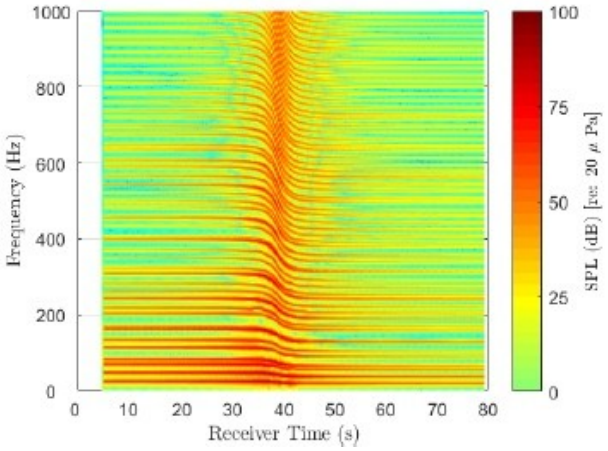

b) Spectrogram of auralized signal (Fig. 24 of Pera et al. [2018]).

Figure 1.28. Auralization of AS350 sound measurement.

Allen et al. [2012] attempted to improve the realistic quality of synthesized noise sources by introducing rapid fluctuations in the inlet-radiated tones generated from an engine fan (see Fig. 1.29). The authors used data from the existing engine turbofan data set acquired in 2005 during joint NASA/Honeywell Aerospace tests, the Engine Validation of Noise and Emissions Reduction Technology (EVNERT) experiment. They isolated tonal noise radiated from the engine inlet due to the fan, and then added short-term fluctuations to those tones to improve the realism of the synthesized acoustic signal. They also expanded the methodology to allow examination of engine conditions that were not tested, which also permits variations in either power setting or emission angle (see Fig. 1.30). They were also able to simulate fluctuations in broadband noise seen in the experimental data using their approach, although including the broadband noise reduced the realism of the synthesized signals.

Arntzen et al. [2012] examined the effects of noise propagation through a nonstandard atmosphere, modeling these effects via a ray-tracing algorithm allowing multiple propagation paths from the source to the observer. Since (obviously) the sound from each path is produced at a different emission angle, the synthesis of these sounds must be handled independently, and then combined at the prescribed observer location, accounting for time delay, acoustic spreading, and both ground and atmospheric absorption. These results are then implemented at a single observer location in a simulated flyover. The multipath results were shown to be of particular importance when the source was much further from the observer, while when the source is very close to the receiver, the straight-path analysis dominates. However, the multipath results do not appear to have a significant effect on typical acoustic metrics.

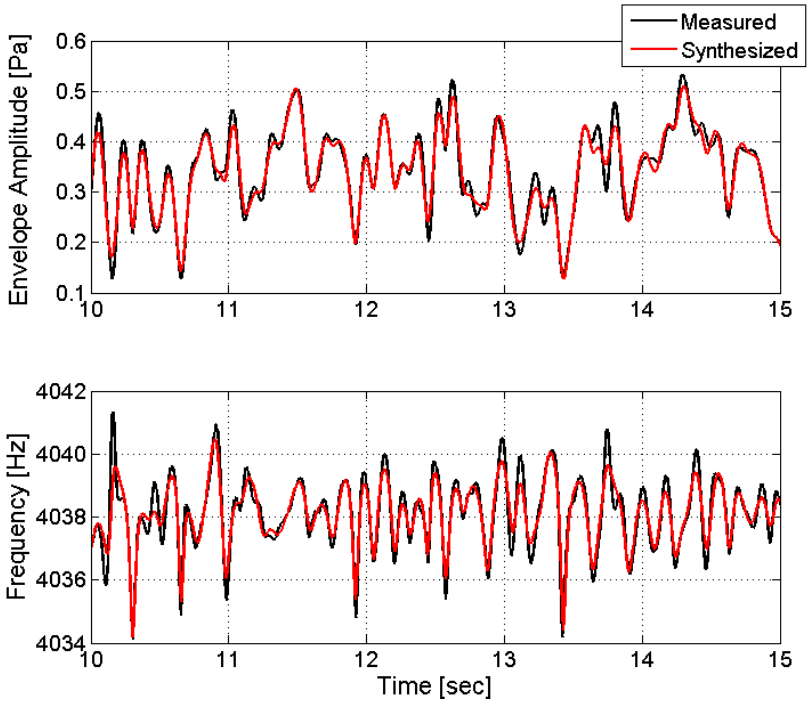

Figure 1.29. Comparison of measured and directly synthesized time histories for amplitude and frequency of the 2BPF tone at 48% engine power and 75° emission angle (Fig. 14 of Allen et al. [2012]).

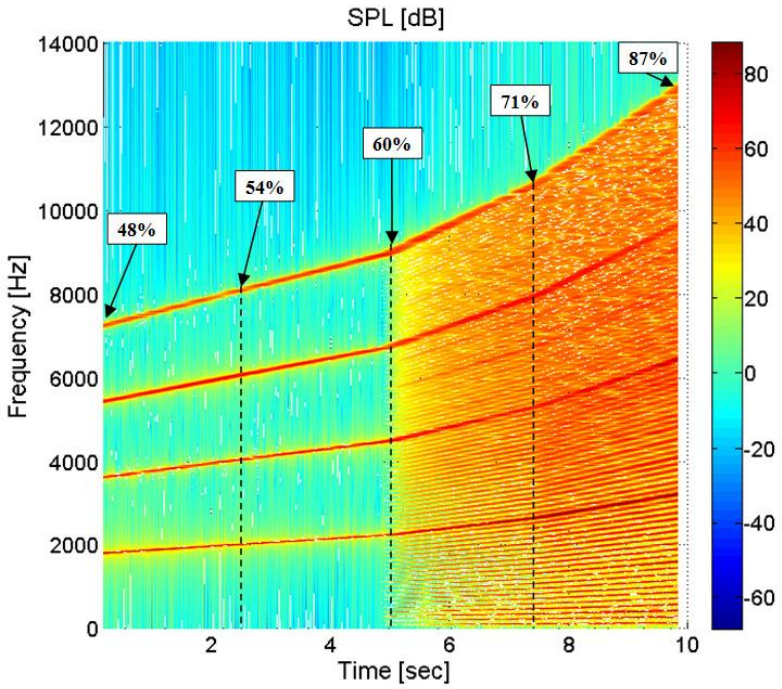

Figure 1.30. Synthesized engine spool-up at 45° emission angle using time-variant mean values and fluctuations based on interpolated model parameters. Percentages indicate engine power settings (Fig. 15 of Allen et al. [2012]).

ALTERNATIVE VEHICLE CONCEPTS

This section is devoted to nontraditional vertical flight vehicles (i.e. anything that does not look or operate like either a conventional helicopter or a tiltrotor). While many of these papers could easily be combined in some of the technical sections discussed earlier in this chapter, the author chose to group them all together in this section, since in many cases the technical problems encountered in modeling or even measuring the acoustic signatures of these vehicles are so inherently different than those for traditional rotorcraft.

Electric Propulsion

Huff and Henderson [2018] and Henderson et al. [2018], in a pair of companion papers, examined the electric motor noise from small quadcopters. Huff and Henderson [2018] address acoustic measurements performed in the Acoustic Testing Laboratory (ATL) at the NASA GRC, while the latter examined the source characteristics of such motors, also via use of the ATL. In the first paper, noise produced by the electric motors—when the rotors were both loaded and unloaded, for both installed and uninstalled configurations, using both sinewave and conventional controllers—was measured and computed. Three motors that are often used in small commercial quadcopters were each evaluated over multiple speeds: the 3DR 2830 (850 kV), DJI 2212 (920 kV), and DJI 2312 (960 kV), with each one tested using three different controllers—the DJI E300, 3DR, and DJI 420S. The E300 and 3DR controllers use square wave inputs to control the speed, while the 420S uses a sine wave. Both free-field acoustic

measurements and a phased array were used in the acquisition of the acoustic data. The authors found that, as might be expected, the predominant noise source from the motor was due to the tones, although they did measure some significant broadband noise on certain motors. They also showed that motor noise is highest in a direction orthogonal to the motor axis, and that attaching the proprotor produced rotor shaft tones, as well as the expected BPF tones, including the higher frequency harmonics. In addition, they identified some increase in the broadband noise as well. The inclusion of the proprotor also produced increases in the motor tone noise by 5 to 15 dB. In Henderson et al. [2018], which focused on electrical measurements and their relationship to the resulting noise and vibration, vibration measurements showed mode 2 vibration frequencies from 4,400 to 5,100 Hz for the static motor; rotation slightly altered the resonance frequencies. The highest acoustic levels were found to be a function of choice of motor, controller, and rotor speed. They found that installing the motors in a typical quadcopter increased the acoustic radiation near the mode 1 azimuthal frequency, as well as over a range of frequencies between 2,000 and 4,000 Hz (see Fig. 1.31).

An advanced aircraft concept that NASA and others have been researching over the past several years is tiltwing aircraft with distributed electric propulsion (DEP). DEP concepts often implement a high-lift system with a large number of low-tip-speed propellers mounted upstream of the wing leading edge for lift augmentation during low-flight-speed operations, enabling extreme short takeoff and landing (E-STOL) maneuvers. Once the vehicle establishes sufficient forward airspeed, the inboard propellers fold up to reduce drag, and the vehicle operates much like a conventional twin-engine propeller-driven aircraft. One such concept evaluated by NASA was the Leading Edge Asynchronous Propellers Technology (LEAPTech) conceptual vehicle, which is a critical technology for the NASA X-57 flight demonstrator. Rizzi et al. [2017b] conducted a psychoacoustic test of the LEAPTech concept, utilizing the XROTOR design tool to evaluate a number of different high-lift propeller designs, coupled with the Propeller Analysis System (PAS) in ANOPP and PSU-WOPWOP for the acoustic predictions. The noise prediction process is shown in Figure 1.32. Time varying effects were also included in the model. Both the number of propellers and their operating speeds were varied during this assessment, as well as the number of blades on each propeller. The authors found that annoyance varies with the number of propellers and with the inclusion of time varying effects but that RPM variation between propellers was not a significant factor. They also developed an annoyance model using loudness, roughness, and tonality as predictors.

Meanwhile, one of the original conceptual vehicles in this class is the Greased Lightning GL-10, a 55-pound tiltwing unmanned aerial vehicle (UAV) equipped with a series of 10 proprotors driven by electric motors that enable vertical takeoff and landing (VTOL), E-STOL, and CTOL operation. For such vehicles to be operated within a typical community, either as a UAV or a personal air vehicle, noise is anticipated to be a barrier issue. Pascioni and Rizzi [2018] developed noise predictions for both the thickness and steady loading noise of a GL-10 proprotor using the PAS in ANOPP. The predictions were made for a single proprotor and then combined to estimate the noise at a far-field observer. Given this approach, the authors could examine the effect of relative phase control (i.e. where the blades are in different azimuthal positions relative to one another) on the noise seen by a typical observer and found that, for a subset of observers, the noise could be reduced by as much as 20 dB using this approach (see Fig. 1.33).

In related work, Galles et al. [2018] examined the potential to reduce the noise from such vehicles by incorporating feedback control into the flight system. Again, the GL-10 was used as the vehicle within their modeling. The authors developed an acoustic model based on the approach of Gutin, and incorporated feedback into the flight control system to adjust the flight speed until the prescribed noise level was achieved. Only flight speed as adjusted—no change in the vehicle's flight path was considered. They typically were able to achieve the desired noise metric within 7–10 seconds after implementing the control logic, thus demonstrating the feasibility of this approach. The authors also found that the GL-10 consumed less energy when the noise abatement control logic was used.

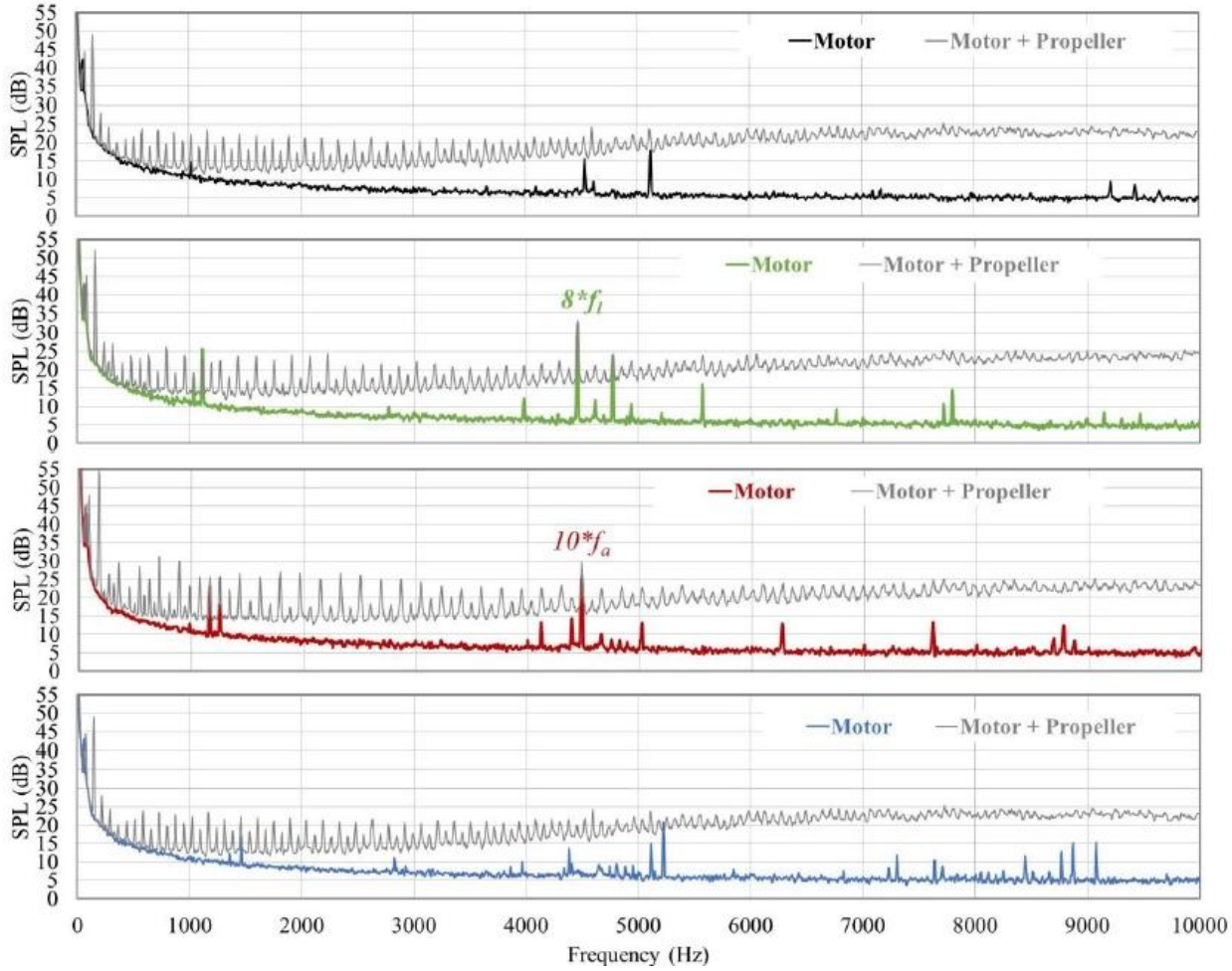

Figure 1.31. The acoustic data acquired for the DJI 2212 motor and motor loaded with a propeller. The data were acquired with the sine wave controller and are for motor speeds equal to 4,380 RPM (top), 4,773 RPM (row 2), 5,370 RPM (row 3), and 6,260 RPM (bottom). Harmonics of the fundamental line frequency, *fl*, and the unexpected additional frequency, *fa*, are marked for reference. (Fig. 22 of Henderson et al. [2018].)

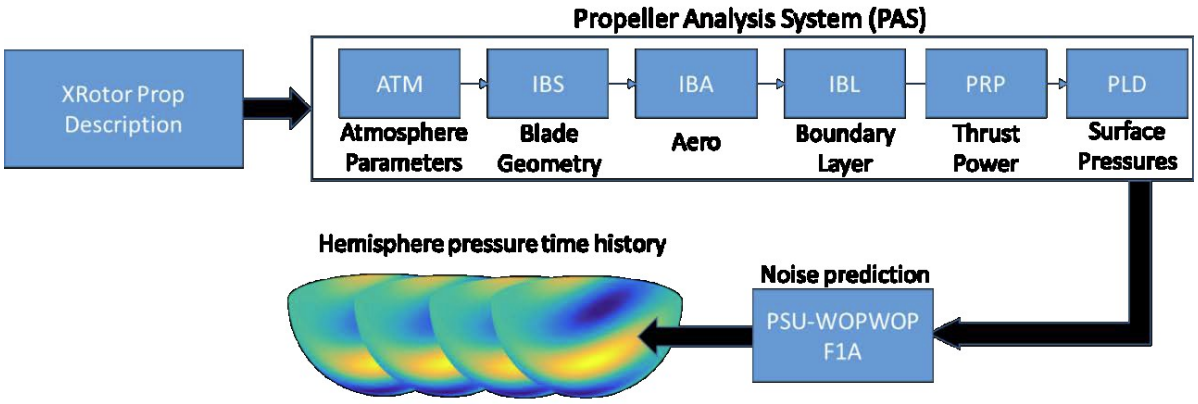

Figure 1.32. Propeller noise prediction process (Fig. 3 of Rizzi et al. [2017b]).

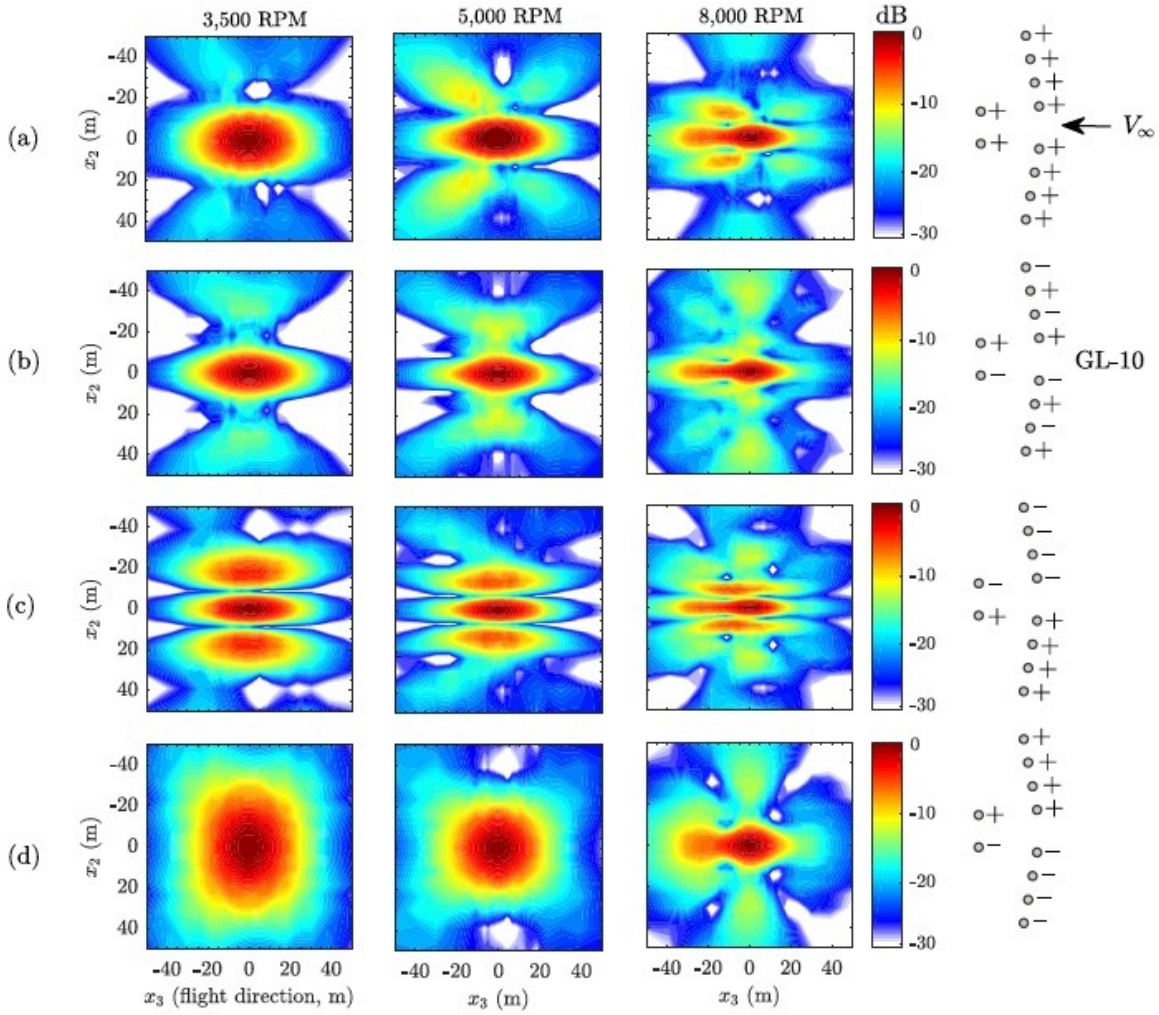

Figure 1.33. Predicted noise contours displaying the effect of RPM and rotation direction for the GL-10. Contours are normalized by the maximum level per case. Rotation direction of each GL-10 propeller is shown on the right side of the figure for cases (a)–(d). (Fig. 9 of Pascioni and Rizzi [2018].)

Open Rotors

Open rotors have been examined for many years. Their ability to decrease fuel burn is well-known, but noise is definitely a barrier issue before they will ever be incorporated into commercial vehicles. They typically come in two different categories—either a single rotor system or a pair of contra-rotating blade sets. Zawodny et al. [2015] examined the effects of both in-flow and geometry on the broadband noise generated by the latter configuration. They used the historical F31/A31rotor configuration as a baseline, but conducted a simplified two-dimensional blade analysis, replacing the actual blade geometries with cambered National Advisory Committee for Aeronautics (NACA) four-digit airfoil profiles. They calculated both broadband rotor wake interaction (BRWI) noise and broadband rotor trailing edge (BRTE) noise. The focus of the work was to develop simplified noise models that do not require CFD calculations, which is highly desirable during the rotor design process, although they did compare their inflow calculations with CFD results. The authors' predicted noise levels for both takeoff and approach flight conditions agreed favorably with measurements previously made in the NASA GRC 9- by 15-Foot Low Speed Wind Tunnel (LSWT).

Later, Nark et al. [2016] paired CFD for the rotor aerodynamics and an FW-H solver for the noise predictions, also examining the F31/A31 contra-rotating blade set to facilitate comparison with the same previously measured data. They used both structured (OVERFLOW 2) and unstructured (FUN3D) CFD codes in the aerodynamic analysis. For the noise predictions, both PSU-WOPWOP and the F1A module of ANOPP2 were used. Comparisons with the experimental results were again favorable.

ADDITIONAL RESEARCH

Tinetti et al. [2007] examined the viability of using the Fast Scattering Code (FSC) to predict noise radiating from a duct. The effects of duct curvature, acoustic treatment, and uniform background flow were all considered. FSC uses an equivalent source method (ESM) to solve an exterior Helmholtz equation boundary value problem (BVP). Comparisons for a constant cross-section rectangular duct were made with both an analytical solution and experimental data acquired in the Curved Duct Test Rig (CDTR) at NASA Langley, with favorable results showing that the FSC was able to successfully predict the modal properties inside the duct, including properly modeling the effects of liners, with excellent correlation with the measured results.

REFERENCES

Allen, M. P., Rizzi, S. A., Burdisso, R., and Okcu, S., "Analysis and Synthesis of Tonal Aircraft Noise Sources," Paper AIAA-2012-2078, 18th AIAA/CEAS Aeroacoustics Conference, Colorado Springs, CO, June 2012.

Allen, A. R. and Schiller, N. H., "Vibroacoustic Characterization of Corrugated-core and Honeycomb-core Sandwich Panels," NASA/TM–2016-219347, Nov. 2016.

Allen, A., Schiller, N., Zalewski, B., and Rosenthal, B., "Transmission Loss and Absorption of Corrugated Core Sandwich Panels with Embedded Resonators," Noise-Con 2014, Ft. Lauderdale, FL, Sept. 2014.

Arntzen, M., Rizzi, S. A., Visser, H. G., and Simons, D. G., "A Framework for Simulation of Aircraft Flyover Noise Through a Non-standard Atmosphere," Paper AIAA-2012-2079, 18th AIAA/CEAS Aeroacoustics Conference, Colorado Springs, CO, June 2012.

Barbely, N. L., Sim, B. W., Kitaplioglu, C., and Goulding, P., "A Study of Acoustic Reflections in Full-Scale Rotor Low Frequency Noise Measurements Acquired in Wind Tunnels," American Helicopter Society Aeromechanics Specialists' Conference, San Francisco, CA, Jan. 20-22, 2010.

Bean, J., Schiller, N., and Fuller, C., "Full Gradient Solution to Adaptive Hybrid Control," Acoustical Society of America, Honolulu, HI, Nov. 28-Dec. 2, 2016.

Bean, J., Schiller, N., and Fuller, C., "Numerical Modeling of an Active Headrest," Inter-Noise 2017, Hong Kong, Aug. 27-30, 2017.

Beck, B., Schiller, N., and Jones, M., "Impedance Assessment of Dual-Resonance Acoustic Liner," *Journal of Applied Acoustics*, vol. 93, June 2015, p. 522.

Boyd, Jr., D. D., "HART-II Acoustic Predictions using a Coupled CFD/CSD Method," 65th Annual Forum of the American Helicopter Society, Grapevine, TX, May 27-29, 2009a.

Boyd, Jr., D. D., "Initial Aerodynamic and Acoustic Study of an Active Twist Rotor using a Loosely Coupled CFD/CSD Method," 35th European Rotorcraft Forum, Hamburg, Germany, Sept. 22-25, 2009b.

Boyd, Jr., D. D., Greenwood, E., Watts, M. E., and Lopes, L.V., "Examination of a Rotorcraft Noise Prediction Method and Comparison to Flight Test Data," NASA/TM–2017-219370, Jan. 2017.

Cabell, R., Klos, J., Buehrle, R., and Schiller, N., "Vibroacoustic Response Data of Stiffened Panels and Cylinders," Proceedings of Noise-Con 2008: The National Conference and Exposition on Noise Control Engineering, Dearborn, MI, July 28-30, 2008.

Cabell, R., Schiller, N., and Simon, F., "Application of a Broadband Active Vibration Control System to a Helicopter Trim Panel," Noise-Con 2013, Denver, CO, Aug. 26-28, 2013.

Faller II, K. J., Rizzi, S. A., Klos, J., Chapin, W. L., Surucu, F., and Aumann, A. R., "Acoustic Calibration of the Exterior Effects Room at the NASA Langley Research Center," 159th Meeting of the Acoustical Society of America and Noise-Con 2010, Baltimore, MD, April 19-23, 2010a. See also Proceedings of Meetings on Acoustics (POMA) is an online open-access journal published by the Acoustical Society of America (ASA).

Faller II, K. J., Rizzi, S. A., Schiller, N., Cabell, R., Klos, J., Chapin, W. L., and Aumann, A. R., "Acoustic Performance of an Installed Real-Time Three-Dimensional Audio System," 160th Acoustical Society of America Meeting, Cancun, Mexico, Nov. 2010b.

Faller II, K. J., Rizzi, S. A., and Aumann, A. R., "Acoustic Performance of a Real-Time Three-Dimensional Sound-Reproduction System," NASA/TM–2013-218004, June 2013.

Farrassat, F. and Casper, J., "Broadband Noise Prediction When Turbulence Simulation is Available - Derivation of Formulation 2B and its Statistical Analysis," *Journal of Sound and Vibration*, vol. 331, no. 10, p. 2203-2208, May 2012. DOI:10.1016/ j.jsv.2011.07.044

Fogarty, D., Wilbur, M., and Sekula, M., "A Computational Study of BVI Noise Reduction Using Active Twist Control," 66th Annual Forum of the American Helicopter Society, Phoenix, AZ, May 10-12, 2010.

Fogarty, D., Wilbur, M., and Sekula, M., "The Effect of Non-Harmonic Active Twist Actuation on BVI Noise," 67th Annual Forum of the American Helicopter Society, Virginia Beach, VA, May 3-5, 2011.

Fogarty, D., Wilbur, M., Sekula, M., and Boyd, Jr., D. D., "Prediction of BVI Noise for an Active Twist Rotor Using a Loosely Coupled CFD/CSD Method and Comparison to Experimental Data," 68th Annual Forum of the American Helicopter Society, Ft. Worth, TX, May 1-3, 2012a.

Fogarty, D., Wilbur, M., Sekula, M., and Boyd, Jr., D. D., "CFD/CSD Investigation of BVI Noise Reduction Using Harmonic Active-Twist Control," Paper 075, 38th European Rotorcraft Forum, Amsterdam, The Netherlands, Sept. 4-7, 2012b.

Galles, M. B., Schiller, N. H., Ackerman, K. A., and Newman, B., "Feedback Control of Flight Speed to Reduce Unmanned Aerial System Noise," AIAA Aviation Forum, 2018 AIAA/CEAS Aeroacoustics Conference, Atlanta, GA, June 2018, DOI: 10.2514/6.2018-2950. See also corrections documented in DOI: 10.2514/6.2018-2950.c1

Gopalan, G. and Schmitz, F., "Understanding Far-Field Near In-Plane High Speed Harmonic Helicopter Rotor Noise in Hover: Governing Parameters and Active acoustic Control Possibilities," AHS Specialist's Conference on Aeromechanics, San Francisco, CA, Jan. 2008a.

Gopalan, G., and Schmitz, F. H., "Far-Field Near-In-Plane Harmonic Main Rotor Helicopter Impulsive Noise Reduction Possibilities," 64th Annual Forum of the American Helicopter Society, Montreal, Canada, April 29-May 1, 2008b.

Greenwood, E. and Schmitz, F., "A Parameter Identification Method for Helicopter Noise Source Identification and Physics-Based Semi-Empirical Modeling," 66th Annual Forum of the American Helicopter Society, Phoenix, AZ, May 10-12, 2010.

Greenwood, E., "Fundamental Rotorcraft Acoustic Modeling from Experiments (FRAME)," Ph.D. thesis, University of Maryland, Jan. 2011.

Greenwood, E. and Schmitz, F., "The Effects of Ambient Conditions on Helicopter Rotor Source Noise Modeling," 67th Annual Forum of the American Helicopter Society, Virginia Beach, VA, May 3-5, 2011.

Greenwood, E., Schmitz, F., and Sickenburger, R., "A Semi-Empirical Noise Modeling Method for Helicopter Maneuvering Flight Operations," 68th Annual Forum of the American Helicopter Society, Ft. Worth, TX, May 1-3, 2012.

Greenwood, E. and Sim, B., "The Effects of Crosswind Flight on Rotor Harmonic Noise Radiation," 69th Annual Forum of the American Helicopter Society, Phoenix, AZ, May 21-23, 2013.

Greenwood, E. and Schmitz, F. H., "Separation of Main and Tail Rotor Noise Sources from Ground-Based Acoustic Measurements using Time-Domain De-Dopplerization," *Journal of Aircraft,* vol. 51, no. 2, Feb 2014.

Greenwood, E., Schmitz, F. H., and Sickenberger, R. D., "A Semi-Empirical Noise Modeling Method for Helicopter Maneuvering Flight Operations," *Journal of the American Helicopter Society,* vol. 60, no. 2, April 2015a, pp. 1-13, https://doi.org/10.4050/JAHS.60.022007

Greenwood, E., Rau, R., May, B., and Hobbs, C. A., "Maneuvering Flight Noise Model for Helicopter Mission Planning," 71st Annual Forum of the American Helicopter Society, Virginia, Beach, VA, May 2015b.

Greenwood, E., Sim, B. W., and Boyd, Jr., D. D., "The Effects of Ambient Conditions on Helicopter Harmonic Noise Radiation: Theory and Experiment," 72nd Annual Forum & Technology Display of the American Helicopter Society, May 2016.

Greenwood, E., "Helicopter Flight Procedures for Community Noise," 73rd Annual Forum & Technology Display of the American Helicopter Society, Fort Worth, TX, May 9-11, 2017a.

Greenwood, E., "Real Time Helicopter Noise Modeling for Pilot Community Noise Awareness," Noise-Con 2017, Grand Rapids, MI, June 12-14, 2017b.

Greenwood, E., "Estimating Helicopter Noise Abatement information with Machine Learning," 74th Annual Forum of the American Helicopter Society, Phoenix, AZ, May 14–17, 2018.

Grosveld, F. W., "Large Civil Tiltrotor (LCTR2) Interior Noise Predictions Due to Turbulent Boundary Layer Excitation," NASA/CR–2013-218005, 2013.

Grosveld, F. W. and Cabell, R. H., "Preliminary Assessment of the Interior Noise Environment in the Large Civil Tiltrotor (LCTR2)," Aircraft Interior Noise session at Noise-Con 2011, Portland, OR.

Grosveld, F. W., Cabell, R. H., and Boyd, Jr., D. D., "Interior Noise Predictions in the Preliminary Design of the Large Civil Tiltrotor (LCTR2)," 69th Annual Forum of the American Helicopter Society, Phoenix, AZ, May 21-23, 2013.

Grosveld, F., Schiller, N., and Cabell, R, "Statistical Energy Analysis (SEA) and Energy Finite Element Analysis (EFEA) Predictions for a Floor-Equipped Composite Cylinder," NASA/TM–2011-217171, NASA Langley Research Center, Hampton VA. Aug. 2011.

Hambric, S. A., Hanford, A. D., Shepherd, M. R., Campbell, R. L., and Smith, E. C., "Rotorcraft Transmission Noise Path Model, Including Distributed Fluid Film Bearing Impedance Modeling," NASA/CR–2010-216812.

Hambric, S., Shepherd, M., Koudela, K., Wess, D., Snyder, R., May, C., Kendrick, P., Lee, E., and Cai, L-W., "Acoustically Tailored Composite Rotorcraft Fuselage Panels," NASA/CR–2015-218769, July 2015a.

Hambric, S., Shepherd, M., and Schiller, N., "Measurements of the Air-borne and Structure-borne Sound Power Transmission Through a Quiet Honeycomb Core Sandwich Panel for a Rotorcraft Roof," Inter-Noise 2015, San Francisco, CA, Aug. 9-12, 2015b.

Heath, S. L., McAninch, G. L., Smith, C. D., and Conner, D. A., "Validation of Ray Tracing Code Refraction Effects," Paper AIAA 2008-2994, 14th AIAA/CEAS Aeroacoustics Conference (29th AIAA Aeroacoustics Conference), Vancouver, Canada, May 6-9, 2008.

Henderson, B. S., Huff, D. L., Cluts, J. D. and Ruggeri, C. R., "Electric Motor Noise for Small Quadcopters: Part II Source Characteristics and Predictions," AIAA Aviation Forum, 2018 AIAA/CEAS Aeroacoustics Conference, Atlanta, GA, June 2018, DOI: 10.2514/6.2018-2953

Huff, D. L. and Henderson, B. S., "Electric Motor Noise for Small Quadcopters: Part I Acoustic Measurements," AIAA Aviation Forum, 2018 AIAA/CEAS Aeroacoustics Conference, Atlanta, GA, June 2018, DOI: 10.2514/6.2018-2952

JanakiRam, R. D., Sim, B. W., Kitaplioglu, C., and Straub, F. K., "Blade-Vortex Interaction Noise Characteristics of a Full-Scale Active Flap Rotor," 65th Annual Forum of the American Helicopter Society, Grapevine, TX, May 27-29, 2009.

Koushik, S., Gopalan, G., and Schmitz, F. H., "Measurements and XFD-Based Acoustic Computations of Experimentally Simulated Blade Vortex Interaction (BVI) Noise, 65th Annual Forum of the American Helicopter Society, Grapevine, TX, May 27-29, 2009.

Koushik, S. and Schmitz, F. H., "A New Experimental Approach to Study Helicopter Blade-Vortex Interaction Noise," Paper AIAA-2008-3070, 14th AIAA/CEAS Aeroacoustics Conference (29th AIAA Aeroacoustics Conference), Vancouver, British Columbia, May 5-7, 2008.

Krishnamurthy, S., Rizzi, S. A., Boyd, Jr., D. D., and Aumann, A. R., "Auralization of Rotorcraft Periodic Flyover Noise from Design Predictions," 74th Annual Forum & Technology Display of the Vertical Flight Society, Phoenix, AZ, May 14-17, 2018.

Lee, S., Brentner, K. S., and Farassat, F., "Analytic Formulation and Implementation of the Gradient of the Acoustic Pressure for Rotor Noise," Presented at the 13th AIAA/CEAS Aeroacoustics Conference, May 21- 23, 2007, Rome, Italy.

Lopes, L. V., "Compact Assumption Applied to the Monopole Term of Farassat's Formulations," 21st AIAA/CEAS Aeroacoustics Conference, Dallas, TX, June 22-26, 2015. See also Lopes, L. V., "Compact Assumption Applied to the Monopole Term of Farassat's Formulations," *Journal of Aircraft*, vol. 54, no. 5, Sept.–Oct. 2017.

Lopes, L. V., Boyd, Jr., D. D, Nark, D. M., and Wiedemann, K. E., "Identification of Spurious Signals from Permeable Ffowcs Williams and Hawkings Surfaces," 73rd Annual Forum & Technology Display of the American Helicopter Society, Fort Worth, TX, May 9-11, 2017a.

Lopes, L. V., Venkat, R. I., and Born, J. C., "Robust Acoustic Objective Functions and Sensitivities in Adjoint-Based Design Optimizations," Paper AIAA 2017-1673. AIAA SciTech Forum, 55th Aerospace Sciences Meeting, Grapevine, TX, Jan. 9-13, 2017b, DOI: 10.2514/6.2017-1673

Malpica, C., "Parametric Investigation on the Use of Lateral and Longitudinal Rotor Trim Flapping for Tiltrotor Noise Reduction," 73rd Annual Forum & Technology Display of the American Helicopter Society, Fort Worth, TX, May 9-11, 2017.

Malpica, C. A., Greenwood, E., and Sim, B.W., "Helicopter Non-Unique Trim Strategies for Blade-Vortex Interaction (BVI) Noise Reduction," American Helicopter Society Technical Meeting on Aeromechanics Design for Vertical Lift, San Francisco, CA, Jan. 20-22, 2016.

Mendoza, J., Chevva, K., Sun, F., Blanc, A., and Kim, S.B., "Active Vibration Control for Helicopter Interior Noise Reduction Using Power Minimization," NASA/CR–2014-218147, Jan. 2014.

Morris, R., "Designing Noise-Minimal Rotorcraft Trajectories," Association for the Advancement of Artificial Intelligence, International Workshops on Planning and Scheduling for Space (IWPSS), Darmstadt, Germany, June 2011.

Morris, R., Venable, K. B., and Lindsey, J., "Automated Design of Noise-Minimal, Safe Rotorcraft Trajectories," 68th Annual Forum of the American Helicopter Society, Ft. Worth, TX, May 1-3, 2012a.

Morris, R., Venable, K. B., Pegoraro, M., and Lindsey, J., "Local Search for Designing Noise-Minimal Rotorcraft Approach Trajectories," 26th Association for the Advancement of Artificial Intelligence (AAAI) Conference on Artificial Intelligence, Toronto, Ontario, Canada, July 22-26, 2012b.

Morris, R., Johnson, M., Venable, K. B., Lindsey, J., "A Path Planning Approach to Noise-Minimal Rotorcraft Landing Trajectories," International Workshop on Planning and Scheduling for Space, March 25-26, 2013, Ames Research Center, Moffett Field, CA.

Nark, D. M., Jones, W. T., Boyd, Jr., D. D., and Zawodny, N. S., "Isolated Open Rotor Noise Prediction Assessment Using the F31A31 Historical Blade Set," 54th AIAA Aerospace Sciences Meeting, San Diego, CA, Jan. 4-8, 2016, DOI: 10.2514/6.2016-1271

Padula, S. L., Burley, C. L., Boyd, Jr., D. D., and Marcolini, M. A., "Design of Quiet Rotorcraft Approach Trajectories," NASA/TM–2009-215771, July 2009.

Pascioni, K. A. and Rizzi, S. A., "Tonal Noise Prediction of a Distributed Propulsion Unmanned Aerial Vehicle," AIAA Aviation Forum, 2018 AIAA/CEAS Aeroacoustics Conference, Atlanta, GA, June 2018, DOI: 10.2514/6.2018-2951

Pera, N., Rizzi, S., Krishnamurthy, S., Fuller, C. and Christian, A., "A Recording-Based Method for Auralization of Rotorcraft Flyover Noise," AIAA SciTech Forum, Kissimmee, FL, Jan. 2018, DOI: 10.2514/6.2018-0267

Potsdam, M., Yeo, H., and Johnson, W., "Rotor Airloads Prediction Using Loose Aerodynamic/Structural Coupling," *Journal of Aircraft,* vol. 43, no. 3, May-June 2006.

Rizzi, S. A. and Christian, A., "A method for simulation of rotorcraft fly-in noise for human response studies," *InterNoise 2015*, San Francisco, CA, 2015.

Rizzi, S. A, Christian, A. W., and Rafaelof, M., "A Laboratory Method for Assessing Audibility of Rotorcraft Fly-In Noise," 73rd Annual Forum & Technology Display of the American Helicopter Society, Fort Worth, TX, May 9-11, 2017a. See also JAHS 64 (2019), for the equivalent journal article.

Rizzi, S., Palumbo, D., Rathsam, J., Christian, A., and Rafaelof, M., "Annoyance to Noise Produced by a Distributed Electric Propulsion High-lift System," AIAA Aviation Forum, 21st AIAA/CEAS Aeroacoustics Conference, Denver, CO, June 5-9, 2017b, DOI: 10.2514/6.2017-4050

Sargent, C., Schmitz, F. H., and Sim, B. W-C, "In-flight Array Measurements of Tail Rotor Harmonic Noise," 64th Annual Forum of the American Helicopter Society, Montreal, Canada, April 29-May 1, 2008.

Sargent, D. C., Schmitz, F. H., and Sim, B. W., "In-flight Array Measurements of Tail Rotor Harmonic Noise," *Journal of the American Helicopter Society*, vol. 55, no. 1, 2010, pp. 12006, doi.org/10.4050/JAHS.55.012006

Scheidler, J. J. and Asnani, V. M., "A Review of Noise and Vibration Control Technologies for Rotorcraft Transmissions," 45th International Congress and Exposition on Noise Control Engineering, Hamburg, Germany, Aug. 21-24, 2016.

Schiller, N., Cabell, R., Quinones, J., and Wier, N. "Active Damping Using Distributed Anisotropic Actuators," 2010 ASME International Mechanical Engineering. Vancouver, Canada, Nov. 12-18, 2010. See also U.S. Patent No. 7,893,602, issued to Noah Schiller and Ran Cabell for the triangular patch actuator.

Schiller, N. H., Perey, D. F., and Cabell, R. H., "Development of a Practical Broadband Active Vibration Control System," Paper IMECE2011-62533, ASME 2011 International Mechanical Engineering Congress & Exposition, IMECE2011, Denver, CO, Nov. 11-17, 2011.

Schiller, N. H., Lin, S-C. S., Cabell, R. H., and Huang, T. J., "Design of a Variable Thickness Plate to Focus Bending Waves," Internoise 2012ASME NCAD Meeting, New York, NY, Aug. 19-22, 2012.

Schiller, N., Beck, B., and Slagle, A., "Numerical Study of Sound Transmission Through a Thin Partition Lined with Slow Acoustic Treatment," Noise-Con 2013, Denver, CO, Aug. 26-28, 2013.

Schiller, N. H., Allen, A. R., Zalewski, B. F., and Beck, B. S., "Sound Transmission Loss Through a Corrugated-Core Sandwich Panel with Integrated Acoustic Resonators," ASME 2014 International Mechanical Engineering Congress & Exposition, IMECE2014, Montreal, Quebec, Nov. 14-20, 2014.

Schiller, N. and Allen, A., "Absorption Characteristics of Acoustic Resonators Combined with Porous Foam," Noise-Con 2017, Grand Rapids, MI, June 12-14, 2017.

Schmitz, F. H., Greenwood, E., Sickenberger, R. D., Gopalan, G., Sim, B., W.-C., Conner, D., Moralez, E., and Decker, W.A.: "Measurement and Characterization of Helicopter Noise in Steady-State and Maneuvering Flight," AHS 63rd Annual Forum & Technology Display, Virginia Beach, VA, May 1-3, 2007.

Sim, B., "Suppressing In-plane, Low-Frequency Helicopter Harmonic Noise with Active Controls," AHS Specialist's Conference on Aeromechanics, San Francisco, CA, Jan. 2008.

Sim, B. W., JanakiRam, R. D., Barbely, N. L., and Solis, E., "Reduced In-Plane Low Frequency Helicopter Noise Using an Active Flap Rotor," 65th Annual Forum of the American Helicopter Society, Grapevine, TX, May 27-29, 2009.

Sim, B. W., JanakiRam, R. D., and Lau, B. H. "Reduced In-Plane, Low-Frequency Noise of an Active Flap Rotor," *Journal of the American Helicopter Society*, vol. 59, no. 2, April 2014. DOI: 10.4050/JAHS.59.022002-1-17

Sim, B. W., Potsdam, M., Conner, D., and Watts, M. E., "Direct CFD Predictions of Low Frequency Sounds Generated by Helicopter Main Rotors," 66th Annual Forum of the American Helicopter Society, Phoenix, AZ, May 10-12, 2010.

Sim, B., Potsdam, M., Kitaplioglu, C., LeMasurier, P., Lorber, P., and Andrews, J., "Localized, Non-Harmonic Active Flap Motions for Low Frequency In-Place Rotor Noise Reduction," 68th Annual Forum of the American Helicopter Society, Ft. Worth, TX, May 1-3, 2012.

Stephenson, J. and Greenwood, E., "Effects of Vehicle Weight and True versus Indicated Airspeed on BIV Noise during Steady Descending Flight," 71st Annual Forum of the American Helicopter Society, Virginia, Beach, VA, May 2015.

Tinetti, A. F., Dunn, M. H., and Farassat, F., "Curved Duct Noise Prediction Using the Fast Scattering Code," Paper AIAA-2007-3528, 13th AIAA/CEAS Aeroacoustics Conference, Rome, Italy, May 2007.

Watts, M., "Rotorcraft Acoustic Flight Testing for Community Noise Reduction," Noise-Con 2017, Grand Rapids, MI, June 12-14, 2017.

Watts, M., Greenwood, E., Snider, R., and Baden, J., "Maneuver Acoustic Flight Test of the Bell 430 Helicopter," 68th Annual Forum of the American Helicopter Society, Ft. Worth, TX, May 1-3, 2012.

Watts, M., Greenwood, E., Smith, C., Snider, R., and Conner, D., "Maneuver Acoustic Flight Test of the Bell 430 Helicopter Data Report," NASA/TM–2014-218266, May 2014.

Watts, M. E., Greenwood, E., and Stephenson, J. H., "Measurement and Characterization of Helicopter Noise at Different Altitudes," 72nd Annual Forum & Technology Display of the American Helicopter Society, May 2016.

Yamauchi, G. K. and Young, L. A, "A Status of NASA Rotorcraft Research," NASA/TP–2009-215369, Sept. 2009.

Zawodny, N. S., Nark, D. M., and Boyd, Jr., D. D., "Assessment of Geometry and In-Flow Effects on Contra-Rotating Open Rotor Broadband Noise Predictions," AIAA SciTech Forum, 53rd Aerospace Sciences Meeting, 2015, Kissimmee, FL, Jan. 5-9, 2015, DOI: 10.2514/6.2015-0741

CHAPTER 2. AEROMECHANICS

Michael A. Marcolini,[1] Wayne Johnson,[2] and Gloria K. Yamauchi[2]

INTRODUCTION

In 2010, Wayne Johnson was selected to give the American Helicopter Society Alexander A. Nikolsky Honorary Lecture. The title of the lecture was "*Milestones in Rotorcraft Aeromechanics*" [Johnson, 2011a, 2011b]. In his lecture, the author proposed the following definition for Aeromechanics:

The branch of aeronautical engineering and science dealing with equilibrium, motion, and control of elastic rotorcraft in air.

The definition encompasses much of what an engineer requires to analyze a rotary wing vehicle: performance, loads, vibration, stability, flight dynamics, and acoustics. Except for acoustics (see Chapter 1) and flight dynamics (see Chapter 5), the other topics included in Johnson's definition are included in this chapter.

As shown in Figure 2.1, the author provides his choice of 19 milestones in the evolving area of aeromechanics.

Interestingly, there are no milestones listed in the 15-year window between the last milestone in 1994 and the 2010 lecture, because "a perspective of some years is needed to judge an event to be a critical achievement or a turning point, so we can see what made a difference." The UH-60A and HART airloads tests—the last milestone listed in Figure 2.1—continue to serve as benchmark data sets for analysis validation. Just after the 2010 lecture, testing of the UH-60A Airloads rotor in the National Full-Scale Aerodynamics Complex (NFAC) 40- by 80-Foot Wind Tunnel was completed, resulting in many publications summarized in this chapter and others in this report.

This chapter, like most chapters in this report, has a corresponding chapter in the 2009 NASA report that described the status of NASA rotorcraft research [Yamauchi and Young, 2009]. While preparing the Aeromechanics chapter of the 2009 report, Bousman and Norman [2008, 2010] used a simple statistical approach to assess the accuracy of analytical predictions. The authors focused on the prediction accuracy of comprehensive analyses, CFD, and CFD coupled with a computational structural analysis, CSD. Their statistical approach consisted of plotting the predicted result as the dependent variable and the measured result as the independent variable. The linear regression of these variables was then computed; the slope of the regression line was considered a measure of accuracy. For example, a slope of 1 represents perfect agreement between predictions and measurements, greater than 1 implies overprediction, and less than 1 implies underprediction. The standard error of estimate of the linear regression is a measure of

[1] Marcolini Consulting, LLC, 4506 West Benoit Trail, Blacksburg, VA 24060-0000.
[2] NASA Ames Research Center, Moffett Field, CA, 94035-1000.

the scatter. This approach is applicable to a broad range of problems and can be used to assess the hierarchy of predictive accuracy.

The analyses used for simulations described in this chapter are not high-fidelity computational fluid dynamics (CFD) methods. Descriptions of the CFD methods used by the NASA rotary wing projects and the application of the methods are contained in Chapter 3 of this document. This chapter (Chapter 2) focuses on the class of methods known as "comprehensive analyses."

Johnson [2012, 2013] offers a definition of a rotorcraft comprehensive analysis—a digital program that calculates aeromechanical behavior of rotorcraft. Comprehensive implies a single tool performing all computations, for all operating conditions, for all rotorcraft configurations. Because the tool is necessarily multi-disciplinary, the internal models must be of similar technology level. The tool must be efficient, expandable, and compatible with different computing platforms. The author reviews the development of the comprehensive analysis that began with the availability of digital computers in the mid-1960s. Figure 2.2 shows the major analyses and their developers through 2010.

1926	The beginning	Glauert
1943	Ground resonance	Coleman
1952	Aeromechanics book	Gessow and Myers
1956	Hover wake geometry	Gray
1957	Unsteady aerodynamics	Loewy
1958	Beams	Houbolt and Brooks
1960	Digital computer	IBM
1962	Rotor airloads tests	H-34
1962	Airloads and wakes	Miller, Piziali
1972	Lateral flapping	Harris
1972	Multiblade coordinates	Coleman, Hohenemser
1974	Beams	Hodges and Dowell
1974	Comprehensive analysis	C81
1981	Dynamic inflow	Pitt and Peters
1981	Rotor aerodynamic state	Bousman
1981	Hover airloads	Caradonna and Tung
1982	Computational fluid dynamics	Caradonna, Tung, and Desopper
1984	CFD/CSD loose coupling	Johnson
1994	Rotor airloads tests	UH-60A, HART

Figure 2.1. Milestones in rotorcraft aeromechanics (Table 1 of Johnson [2011a]).

A number of the analyses shown in Figure 2.2 have been loosely coupled with CFD analyses. Loose coupling, one of the milestones in Figure 2.1, is the interface between CFD and computational structural dynamics (CSD). The comprehensive analysis provides the CSD or the structural dynamic motion of the blades, as well as the trim of the aircraft. Loose coupling infers that information between the CFD and CSD analyses is exchanged for the entire revolution of periodic loads or motion, whereas information is exchanged every time step for tight coupling. In Chapter 3, accurate high-fidelity forward-flight simulations are shown to require CFD/CSD coupling.

Some of the work highlighted in this chapter used the RotCFD tool, which is neither a comprehensive analysis nor a high-fidelity CFD tool, but rather a hybrid analysis developed with the needs of the everyday engineer in mind. RotCFD was developed by Sukra Helitek, Inc. primarily through NASA Small Business Innovative Research (SBIR) funding and other government contracts. The tool attempts to connect the areas of conceptual design and CFD through an integrated environment specific to rotorcraft. As described in Rajagopalan et al. [2012], RotCFD includes the following key modules integrated in one environment: geometry, semi-automated grid generation, a flow-solver, rotor, and flow visualization and analysis. Two options are available for the rotor model: discrete blade model and a disk model. Both models represent the rotor blades using momentum sources and look-up tables for the airfoil performance at each blade radial station. Guntupalli et al. [2016] describes recent capabilities added to RotCFD including aircraft trim (though presently not general enough for all vehicle configurations).

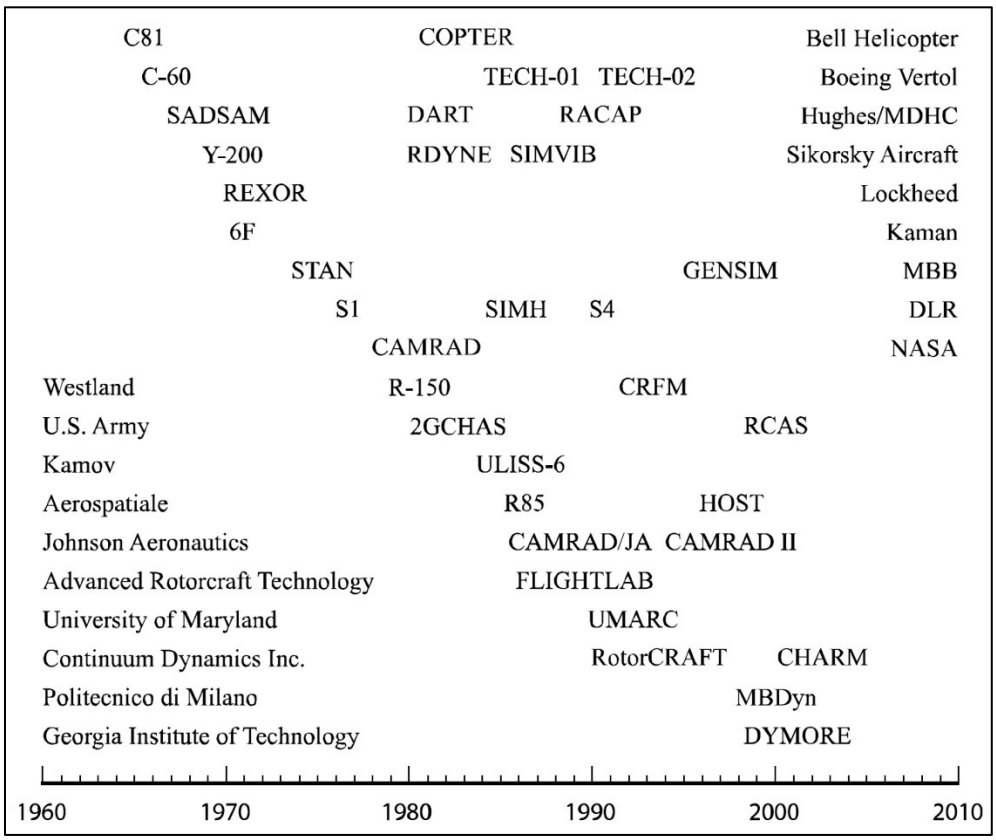

Figure 2.2. Comprehensive analyses (Fig.1 of Johnson [2012]).

This chapter includes a wide range of topics including comparisons with the extensive set of wind tunnel data collected during the UH-60A Airloads rotor test in the NFAC; analysis of compounds, lift-offset rotors, and coaxial rotors; structural loads modeling and prediction; flow control; rotors with active flaps and twist; and tiltrotors. The chapter concludes with topics that fall in the general aeromechanics category.

TESTING AND SIMULATIONS OF THE UH-60A ROTOR

Individual Blade Control Wind Tunnel Test

Norman et al. [2009] described a full-scale wind tunnel test of a UH-60A rotor in the National Full-Scale Aerodynamics Complex 40- by 80-Foot Wind Tunnel. The test was conducted to evaluate the potential of Individual Blade Control (IBC) to improve performance; to reduce vibration, loads, and noise; to affect flight control characteristics; and to perform reconfiguration and in-flight tuning tasks. This test was the culmination of a long-term collaborative wind tunnel test program between NASA, U.S. Army, Sikorsky Aircraft Corporation, and ZF Luftfahrttechnik GmbH (ZFL) to demonstrate the benefits of IBC for a UH-60A rotor. The test results demonstrated rotor power reductions (up to 5 percent), multi-parameter hub load reductions, multi-frequency pitch link load reductions, and in-plane noise reductions. Additional results indicated the benefits of IBC for in-flight tuning and showed minimal coupling of IBC with UH-60A rotor flight dynamics. Figure 2.3 shows the effect of power reduction using IBC.

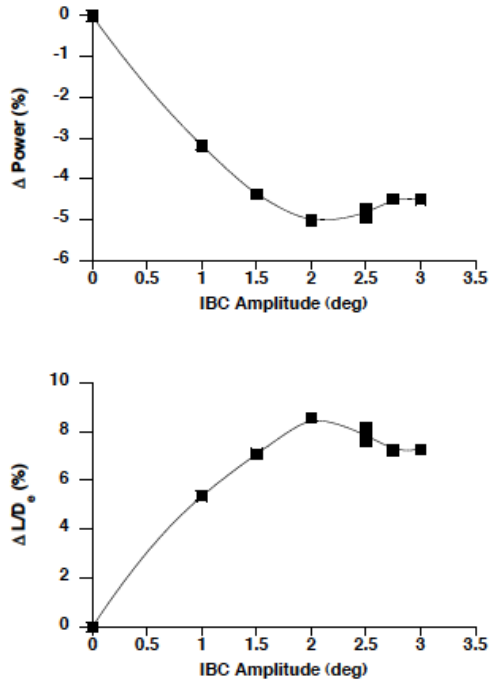

Figure 2.3. Power reduction and L/De improvement for 2/rev manual IBC amplitude sweep (at 225° phase) with trim controller active, CL/σ = 0.077, μ = 0.40, and αs = –8.6° (Fig. 9 of Norman et al. [2009]).

Yeo et al. [2010, 2011] compared data from the UH-60A IBC test with calculations obtained using the comprehensive helicopter analysis CAMRAD II and a coupled CAMRAD II/ OVERFLOW 2 analysis. Measured data showed a 5.1-percent rotor power reduction (8.6 percent rotor lift-to-effective-drag ratio increase) using 2/rev IBC actuation with a 2.0-degree amplitude at $\mu = 0.4$. At the optimum IBC phase for rotor performance, IBC actuator force (pitch link force) decreased, and neither flap nor chord bending moments changed significantly. CAMRAD II predicted the rotor power variations with the IBC phase reasonably well at $\mu = 0.35$. However, the correlation degrades at $\mu = 0.4$. Coupled CAMRAD II/OVERFLOW 2 showed excellent correlation with the measured rotor power variations with the IBC phase at both $\mu = 0.35$ and $\mu = 0.4$. Maximum reduction of IBC actuator force was better predicted with CAMRAD II, but general trends were better captured with the coupled analysis. The correlation of vibratory hub loads was generally poor by both methods, although the coupled analysis somewhat captured general trends.

UH-60A Airloads Wind Tunnel Test

Flight testing of the UH-60A Airloads rotor in 1993 [Kufeld et al., 1994; and Bousman and Kufeld, 2005] resulted in a unique and extensive database for many level flight and transient maneuver conditions. The key data from this test were the rotor airloads (section normal force, pitching moment, and chord force) integrated from chordwise pressure arrays located at nine radial stations. These data, in combination with other measured parameters (structural loads, control positions, and rotor shaft moments), have helped to provide physical insights into specific flight regimes, including high-speed flight.

To provide an expanded database for validation of these predictive tools, NASA and the U.S. Army completed a full-scale wind tunnel test of the UH-60A Airloads rotor in May 2010. The rotor was the same one tested during the landmark 1993 NASA/Army UH-60A Airloads flight test and included a highly pressure-instrumented blade to measure rotor airloads. The test, described in Norman et al. [2011], was conducted in the NFAC 40- by 80-Foot Wind Tunnel and was designed to produce unique data not available from the flight test. This included data from a number of new measurements, such as rotor balance forces and moments, oscillatory hub loads, blade displacements and deformations, and rotor wake measurements using large-field Particle Image Velocimetry (PIV) and Retro-reflective Background Oriented Schlieren (RBOS). The test matrix also included data acquired at conditions outside the conventional flight envelope, such as at high-speed, high-thrust, and slowed-rotor conditions. The UH-60A Airloads rotor is shown in Figure 2.4 installed in the NFAC. Figure 2.5 shows the installation of the PIV system.

The primary wind tunnel test data were acquired during speed sweeps at 1-g simulated flight conditions, up to advance ratios of $\mu = 0.4$, and during parametric thrust sweeps (up to and including stall) at various combinations of shaft angles and forward speeds. Data were also acquired at matching conditions from previous full-scale flight tests and small-scale wind tunnel tests to assess rotor and wind tunnel scaling issues. Finally, data were acquired while performing unique slowed-rotor simulations at reduced RPM (40 percent and 65 percent), up to advance ratios of $\mu = 1.0$.

Norman et al. [2011] included detailed descriptions of the hardware, instrumentation, and data acquisition and reduction systems. In addition, the data validation process, the test objectives and approach, and some sample results were presented. These new data provide an excellent resource for validating new and emerging predictive tools.

Prior to the full-scale wind tunnel test of the UH-60A Airloads rotor, a shake test was completed on the LRTA (Fig. 2.6). The goal of the shake test, described in Russell [2014, 2015], was to characterize the oscillatory response of the test rig and provide a dynamic calibration of the balance to accurately measure vibratory hub loads. The paper provided a summary of the shake test results, including balance, shaft bending gauge, and accelerometer measurements. Sensitivity to hub mass and angle of attack were investigated during the shake test. Hub mass was found to have an important impact on the vibratory forces and moments measured at the balance, especially near the UH-60A 4/rev frequency. Comparisons were made between the accelerometer data and an existing finite-element model, showing agreement on mode shapes, but not on natural frequencies. The results of a simple dynamic calibration were presented, showing the effects of changes in hub mass. The results showed that the shake test data can be used to correct in-plane loads measurements up to 10 Hz and normal loads up to 30 Hz.

Figure 2.4. UH-60A Airloads rotor installed on the Large Rotor Test Apparatus (LRTA) in the NFAC 40- by 80-Foot Wind Tunnel (Fig. 1 of Norman et al. [2011]).

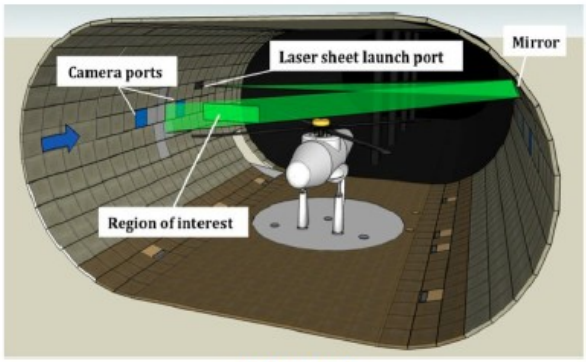

a) Schematic

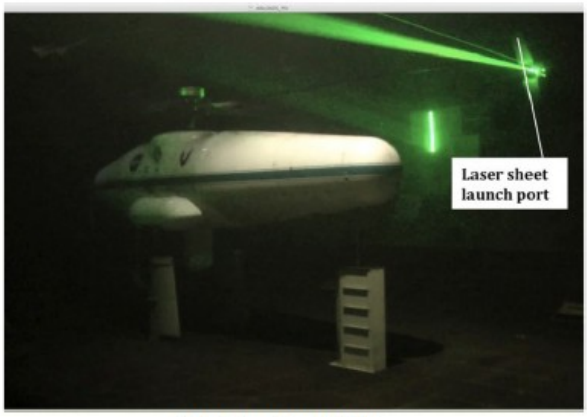

b) Actual installation

Figure 2.5. Test section schematic and photo showing PIV installation during the UH-60A Airloads test in the NFAC 40- by 80-Foot Wind Tunnel (Fig. 12 of Norman et al. [2011]).

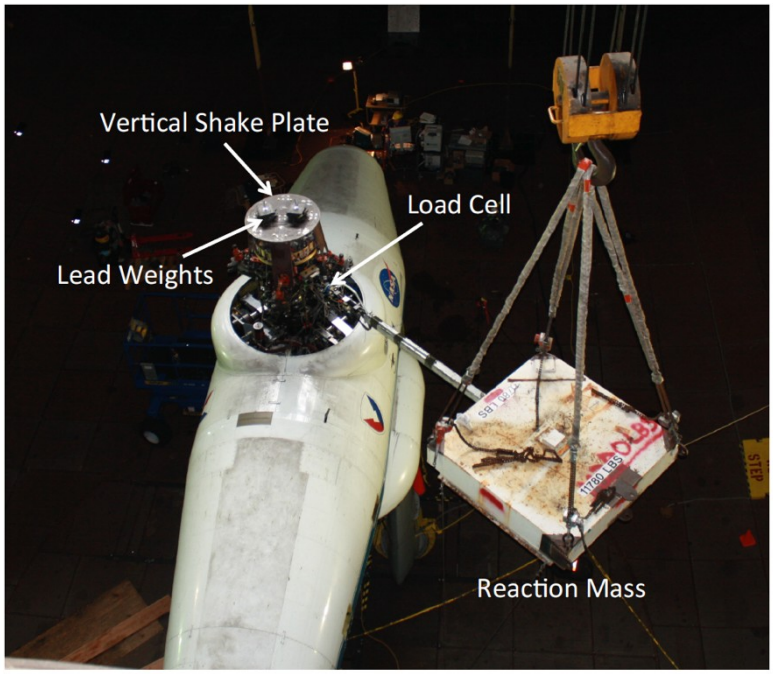

Figure 2.6. LRTA shake test installation (Fig. 3 of Russell [2015]).

Figure 2.7. UH-60A rotor tests: full-scale wind tunnel (NFAC), flight, and small-scale wind tunnel (DNW) (Figs. 1–3 of Norman et al. [2012]).

Norman et al. [2012] compared data obtained during the full-scale UH-60A Airloads wind tunnel test with measurements from the full-scale UH-60A Airloads flight test and the UH-60A small-scale test in the German-Dutch Wind Tunnel (DNW) (Fig. 2.7). Rotor power, airloads (section normal force and moment), and structural loads were examined and compared to help understand the effects of the wind tunnel and model scale on the measured data. The measured power matched well with both flight and small-scale results, suggesting that the procedures and trim targets used to match the rotor conditions were fundamentally sound. For the flight test comparisons, rotor airloads were generally well simulated in the wind tunnel, although there were noticeable differences in the waveforms at the outboard radial stations that cannot be explained by bad measurements or integration errors. Rotor structural loads were also well simulated with the exception of chord bending moments. Further investigation is necessary to determine the exact cause of these differences. For the DNW test comparisons, the rotor airloads and structural loads showed significant differences in waveform, especially for 3/rev torsion loads. These results were consistent with those found during earlier DNW/flight test comparisons and provided additional verification that the different blade modal properties of the DNW model had a significant effect on blade response and ultimately, blade airloads.

Rotor Loads Correlation and Stall

Yeo and Romander [2012, 2013] compared wind tunnel measurements of the rotor trim, blade airloads, and structural loads of a full-scale UH-60A Black Hawk main rotor with calculations obtained using the comprehensive rotorcraft analysis CAMRAD II and a coupled CAMRAD II/OVERFLOW 2 analysis. A speed sweep at constant lift up to an advance ratio of 0.4 and a thrust sweep at constant speed into deep stall were investigated. The coupled analysis showed significant improvement over comprehensive analysis. Normal force phase was better captured and pitching moment magnitudes were better predicted including the magnitude and phase of the two stall events in the fourth quadrant at the deeply stalled condition. Structural loads were, in general, improved with the coupled analysis, but the magnitude of chord bending moment was still significantly underpredicted. As there were three modes around 4 and 5/rev frequencies, the structural responses to the 5/rev airloads due to dynamic stall were magnified and thus care must be taken in the analysis of the deeply stalled condition.

In Marpu et al. [2013], the authors studied a subset of the U.S. Army/NASA wind tunnel tests of a full-scale UH-60A Black Hawk rotor system using a Hybrid Navier–Stokes Free-Wake CFD

methodology, coupled with a multi-body dynamics analysis code. A speed sweep at constant lift for advance ratios ranging between 0.15 and 0.37 and a thrust sweep at constant advance ratio ranging from no stall to deep stall conditions were investigated. Results were presented for sectional airloads, structural loads, and integrated forces and moments at the hub. There was reasonable agreement between measured and predicted performance indicators such as thrust and power for the parametric speed and the thrust sweeps, while the propulsive force was overpredicted. The lift-to-equivalent-drag ratio was slightly underpredicted for both parametric sweep conditions. The predicted trim settings were consistent with measurements.

Yeo et al. [2016] investigated the NASA/Army UH-60A Airloads Program flight test and full-scale UH-60A Airloads wind tunnel test data in order to better understand and predict the chord bending moments, one of the unresolved issues in the UH-60A rotor loads prediction. Coupled Helios/RCAS analysis was performed and the calculated rotor loads were compared with the test data. RCAS-alone analysis was also performed by applying measured airloads from the tests as prescribed external loads. Effects of the lag damper model were examined by calculating lag damper loads using a nonlinear lag damper model or by applying measured lag damper loads as prescribed external loads. Both airloads and damper loads were important for the accurate prediction of chord bending moments. The calculated chord bending moments with the prescribed measured airloads and measured damper loads showed the best correlation with the wind tunnel test data. In particular, the 4 and 5/rev harmonic correlation was excellent. The effects of drive train dynamics and hub impedance on the chord bending moments appeared to be very small for the wind tunnel test. Those effects may still be important for the flight test vehicle.

Abhishek et al. [2011] conducted a computational investigation to isolate the physics governing the aerodynamics and structural dynamics of a UH-60A rotor in an unsteady maneuvering flight. They proposed a hypothesis for the mechanism of advancing blade stall observed during pull-up maneuvers. The advancing blade stall observed during Counter 11029 pull-up maneuver of the 1994 flight test was in addition to the two conventional dynamic stall events observed on the retreating side of the blade. Both lifting-line as well as CFD analyses predicted all three stall cycles with calculated deformations. The advancing blade transonic stall, observed from revolution 12 onward, was a twist stall triggered by 5/rev elastic twist deformation that increased the angle of attack beyond the static stall limit, resulting in shock-induced flow separation culminating in stall. The 5/rev elastic twist was triggered by the two retreating-blade stalls from the previous revolution, which were separated by 1/5th rev. The accurate prediction of both stall cycles on the retreating blade holds the key to prediction of advancing blade stall. In the analysis, advancing blade stall was triggered by a correct combination of control angles and 5/rev elastic twist.

Yeo and Johnson [2015] investigated maximum rotor lift capability, using the wind tunnel test data of McHugh (modified 1/10-scale CH-47B rotor) and a full-scale UH-60A rotor. Rotor performance calculations with the comprehensive rotorcraft analysis CAMRAD II were compared with the wind tunnel test data. The analysis of the McHugh rotor with the Reynolds-number-corrected airfoil table showed good correlation with the measurements for $\mu = 0.1$ to 0.5 and was able to predict the maximum rotor lift reasonably well, especially at $0.2 \leq \mu \leq 0.4$. The analysis was also able to predict the maximum lift of the full-scale UH-60A rotor within about 3.5 percent at $\mu = 0.24$ and 0.3. Calculations with dynamic stall models, in general, showed only

a small influence on rotor performance and were not necessary to predict maximum lift. Airfoils had an important role in defining the maximum lift capability of the rotor. The VR-12 airfoil, which has stall characteristics superior to the baseline V23010 airfoil, substantially improved the maximum lift capability of the McHugh rotor, showing the potential to improve the behavior of a rotor by improving the airfoil's static stall characteristics.

High Advance Ratio

As described in Norman et al. [2011], high-advance-ratio conditions were achieved by reducing the RPM of the UH-60A Airloads rotor. Datta et al. [2011, 2013] provided a detailed analysis of the measurements acquired for test conditions up to an advance ratio of 1.0. A comprehensive set of measurements that included performance, blade loads, hub loads, and pressures/airloads made this data set unique. The measurements revealed new and rich aeromechanical phenomena that were special to this exotic regime. These included reverse chord dynamic stall, retreating side impulse in pitch-link load, large inboard-outboard elastic twist differential, supersonic flow at low subsonic advancing tip Mach numbers, diminishing rotor forces yet dramatic build-up of blade loads, and dramatic blade loads yet benign levels of vibratory hub loads. The objective of the research was the fundamental understanding of these unique aeromechanical phenomena, with the intention of providing useful knowledge for the design of high-speed, high-efficiency, slowed-RPM rotors of the future and a challenging database for advanced analyses validation.

Kottapalli [2012] compared measured data from the slowed-rotor testing of the UH-60A Airloads Rotor with CAMRAD II calculations. The emphasis was to correlate overall trends. This analytical effort considered advance ratios from 0.3 to 1.0, with the rotor rotational speed at 40 percent NR. The rotor performance parameters considered were the thrust coefficient, power coefficient, L/De, torque, and H-force. The blade loads considered were the half peak-to-peak, mid-span and outboard torsion, flatwise and chordwise moments, and the pitch-link load. For advance ratios ≤ 0.7, the overall trends for the performance and loads (excluding the pitch-link load) could be captured. The correlation gradually deteriorated as the advance ratio increased. There is considerable scope for improvement in the prediction of the blade loads. Considering the modeling complexity associated with the unconventional operating condition under consideration, the current predictive ability to capture overall trends is encouraging.

Bowen-Davies and Chopra [2013] compared wind tunnel measurements of the performance, airloads and blade loads of the UH-60A Black Hawk rotor operating at 40 percent RPM and advance rations between 0.3 and 0.6, using the comprehensive analysis UMARC. The capability of UMARC to predict the physics of the high-advance-ratio rotor was evaluated. The sensitivity of rotor thrust to collective was well predicted, but with an offset in collective. Attention was brought to the importance of modeling the drag in the root cut-out region to achieve good correlations to the rotor lift and power performance. The blade sectional normal force was well predicted in magnitude and phase, except for a region to the rear of the rotor disk. Pitching moments were poorly correlated. The important characteristics of the free-wake model were assessed in terms of its impact on the sectional normal force. Flap bending moment peak-to-peak loads were underpredicted with some phase error. The high-frequency 11/rev content in the torsional measurements was well captured by the analysis and shown to correspond to the excitation of the first torsional mode.

COMPOUNDS, LIFT-OFFSET ROTORS, AND COAXIAL ROTORS

The slowed-rotor compound rotorcraft configuration promises to increase the cruise speed relative to a conventional helicopter, without compromising the basic efficiency of the edgewise moving rotor. A helicopter rotor in forward flight encounters limits to the lift and propulsive force capability, caused by stalling of the rotor in the asymmetric aerodynamic environment of high-speed flight. Adding a wing to the aircraft reduces the rotor lift requirement and adding a propeller eliminates the propulsive force requirement, resulting in the compound helicopter configuration. High tip speed is desirable to minimize the blade area needed to hover, so in high-speed forward flight it is necessary to reduce the tip speed in order to avoid significant compressibility effects on the advancing blade tips. The CarterCopter Technology Demonstrator (CCTD) was a slowed-rotor compound designed to operating at very high advance ratios, exceeding $\mu = 1$. At high advance ratio, the dynamic behavior of the rotor might limit the utility of the slowed-rotor concept. Floros and Johnson [2007] investigated the stability and control of rotors at the high advance ratio applicable to a slowed-rotor compound helicopter. Stability of teetering, articulated, and gimbaled hub types was considered. The teetering rotor was found to be the most stable hub type, showing no instabilities up to an advance ratio of 3 and a Lock number of 18. The articulated rotor was unstable above an advance ratio of about 2.2 but could be stabilized to higher speed with δ_3. The gimbaled rotor was unstable above advance ratios of about 2 and was not stabilized by δ_3.

Floros and Johnson [2009] examined the calculated performance of a slowed-rotor compound aircraft, particularly at high flight speeds. The performance of slowed-rotor compound aircraft was calculated using the comprehensive analysis CAMRAD II. Correlation of calculated and measured performance was presented for a NASA Langley high-advance-ratio wind tunnel test to establish the capability to model rotors in such flight conditions. CAMRAD II with a rigid wake model was able to capture performance trends of high-speed rotors to at least an advance ratio of 1.45. The calculated performance of an isolated rotor and a wing and rotor combination were examined, based on a rotor similar to that used on the CCTD. Rotor and wing power were found to be primarily from profile drag, except at low speed where the wing was near stall. Increased altitude off-loaded lift from the rotor to the wing, reducing total power required. The optimum collective for a high-speed autorotating rotor was that which produced a small amount of positive thrust on the rotor.

Yeo and Johnson [2009] conducted a design and aeromechanics investigation for a 100,000-pound compound helicopter with a single main rotor, which would cruise at 250 knots (Fig. 2.8). Performance, stability, and control analyses were conducted with the comprehensive rotorcraft analysis CAMRAD II. Wind tunnel test measurements of the performance of the H-34 and UH-1D rotors at high advance ratio were compared with calculations to assess the accuracy of the analysis for the design of a high-speed helicopter. An assessment of various design parameters (disk loading, blade loading, wing loading) on the performance of the compound helicopter was conducted. Lower wing loading (larger wing area) and higher blade loading (smaller blade chord) increased aircraft lift-to-drag ratio. The optimum lift sharing between the rotor and wing was the rotor carrying 8–9 percent of the gross weight. The optimum aircraft lift-to-drag ratio for the baseline design occurred with a small, positive shaft power to the rotors.

Figure 2.8. Compound helicopter (Fig. 1 of Yeo and Johnson [2009]).

Following a small-scale hover test of a coaxial rotor at the U.S. Army Aeroflightdynamics Directorate, Lim et al. [2007, 2009] used the comprehensive analysis CAMRAD II to investigate correlation of several coaxial helicopter rotors. This work started from previous correlation with the Harrington rotors and the XH-59A aircraft. The free-wake analysis was crucial to calculating hover performance for these coaxial rotors (Fig. 2.9). McAlister's rotor, which was roughly a 1/6-scale XV-15 rotor, operated at relatively low Reynolds numbers (36–180K), so the airfoil code MSES was used to generate airfoil tables for this operating range. The rotor spacing effect on hover performance was minimal in a coaxial rotor for rotor spacing larger than 20 percent of the rotor diameter. The lower rotor in-ground effect (IGE) thrust increased quickly by 26 percent as the rotor ground height decreased from the position of 80 percent rotor diameter to 10 percent, while the corresponding IGE power increased by 17 percent. These thrust and power trends were well predicted.

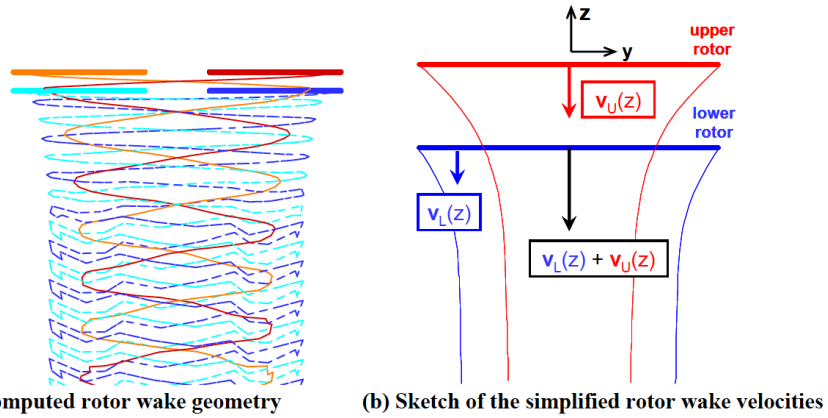

Figure 2.9. Computed free-wake tip vortex geometry for the Harrington coaxial rotor (Fig. 1 of Lim et al. [2009]).

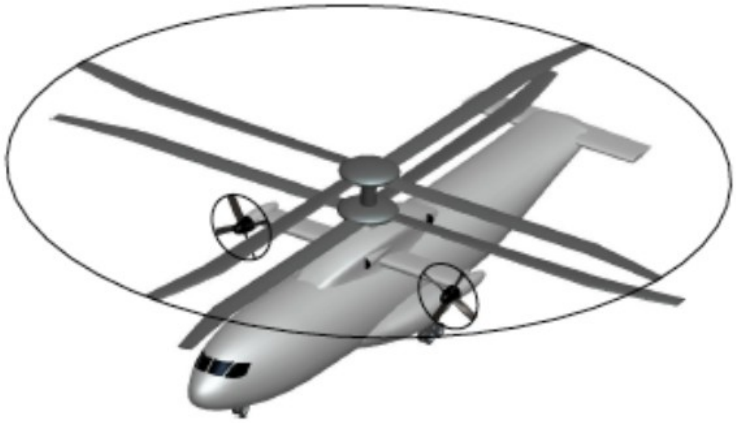

Figure 2.10. Coaxial lift-offset helicopter (Fig. 1 of Johnson [2009]).

A lift-offset rotor, or advancing blade concept, is a hingeless rotor that can attain good efficiency at high speed, by operating with more lift on the advancing side than on the retreating side of the rotor disk. The influence of lift offset on the performance of several rotorcraft configurations was explored by Johnson [2008]. Figure 2.10 shows the baseline coaxial, lift-offset rotorcraft. Lift offset of about 0.25 was effective in reducing the rotor-induced power and minimizing the rotor-profile power. The aerodynamic modeling requirements for performance calculations were evaluated, including rotor wake and drag models for the high-speed-flight condition. Figure 2.11 shows the rotor wake models for 250 knots, consisting of trailed vorticity of two rotors and a wing. The design cruise condition was at a high advance ratio, so free-wake geometry was not required. The influence of configuration on the performance of rotorcraft with lift-offset rotors was explored, considering tandem and side-by-side rotorcraft as well as wing-rotor lift share. Hover performance was dominated by the variation of disk loading with twin rotor separation and rotor radius (disk loading based on projected total rotor area). Cruise performance was insensitive to longitudinal separation of the rotors, so the coaxial and tandem configurations had nearly the same power required and lift-to-drag ratio. Lateral separation of the rotors increased the effective span of the lifting system, so the side-by-side configuration had about a 10-percent improvement in performance for separations greater than 0.5 diameter (assuming fixed fuselage and hub drag). The compound helicopter had total aircraft power comparable to the lift-offset rotor. In order to compare lift-offset rotors and compound helicopters in terms of total aircraft metrics, it is necessary to consider component weights as well as performance.

A key parameter in sizing an aircraft design is the maximum blade loading (C_T/σ) capability of a rotor or rotor system. The blade loading is basically proportional to the mean lift coefficient, averaged over the blade span and azimuth. Stall of the blade produces a fundamental limit on the maximum C_T/σ of a rotor, and because of the asymmetric loading distribution in edgewise forward flight (producing high angle of attack on the retreating side), this limit decreases with rotor advance ratio. If a rotor carries a significant roll moment in forward flight, i.e. a lift offset, the retreating-side angle of attack is reduced for a given total rotor lift. Yeo and Johnson [2013, 2014] investigated the maximum blade loading capability of a coaxial lift-offset rotor, using a rotorcraft configuration designed in the context of short-haul, medium-size civil and military

missions. For the rotor performance calculations, the collective pitch angle was progressively increased up to and through stall with the shaft angle set to zero. There was good agreement between the analysis and McHugh's rotor test data, which showed the validity of the analysis tool and approach. The calculated maximum lift capability of the coaxial rotor increased as lift offset increased and extended well beyond the McHugh lift boundary as the lift potential of the advancing blades was fully realized. Airfoils, taper, and twist were important in defining the maximum lift capability of the lift-offset rotors.

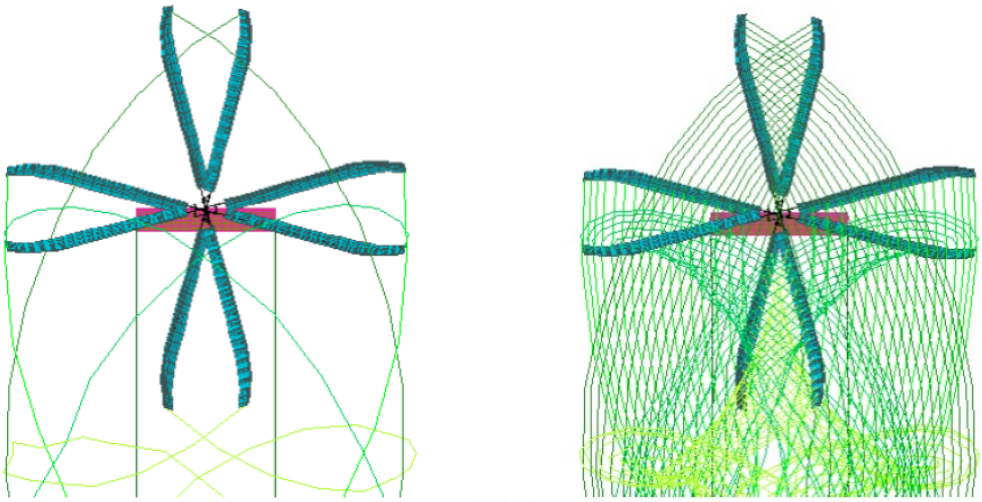

b) Free wake geometry, rolled-up model. d) Free wake geometry, multiple-trailer model.

Figure 2.11. Wake geometry of coaxial rotors and wing (Figs. 27b and 27d of Johnson [2008]).

STRUCTURAL LOADS MODELING AND PREDICTION

Three-Dimensional (3D) Rotor Structural Dynamic Analysis

When rotor aerodynamic behavior is calculated using high-fidelity, 3D aerodynamic models (CFD, typically Reynolds-average Navier–Stokes), common practice is to deal with blade motion and aircraft trim by coupling with a rotorcraft comprehensive analysis. Three-dimensional structural analyses are applied to rotor components, including hubs, linkages, pitch cases, and blade root structures. For a complete high-fidelity analysis of rotors, it is necessary to couple 3D aerodynamic and 3D structural models of the full system.

Datta and Johnson [2009, 2010, 2011] developed a dual-primal iterative substructuring method, that is parallel and scalable, for the solution of a 3D finite element dynamic analysis of helicopter rotor blades. The finite element analysis was developed using isoparametric hexahedral brick elements. Particular emphasis is placed on the formulation of the inertial terms that are unique to rotary wing structures. The scalability of the solution procedure was studied using two prototype problems—one for steady hover (symmetric) and one for transient forward flight (non-symmetric)—both carried out on up to 48 processors. In both hover and forward flight, a linear speed-up was observed with the number of processors, up to the point of substructure optimality. Substructure optimality and the range of linear speed-up were shown to depend both on the

problem size as well as a corner-based global coarse problem selection. An increase in problem size extended the linear speed-up range up to the new substructure optimality. A superior coarse problem selection extended the optimality to a higher number of processors. The method also scaled with respect to problem size. The key conclusion is that a 3D finite element analysis of a rotor can be carried out in a fully parallel and scalable manner. The careful selection of substructure corner nodes, which are used to construct the global coarse problem, is the key to extending linear speed-up to as high a processor number as possible, thus minimizing the solution time for a given problem size.

Datta and Johnson [2014] coupled a full 3D finite-element multibody structural dynamic solver to a 3D Reynolds-averaged Navier–Stokes solver for the prediction of integrated aeromechanical stresses and strains on a rotor blade in forward flight. The objective was to lay the foundations of all major pieces of an integrated 3D rotor dynamic analysis—from model construction to aeromechanical solution to stress/strain calculation (Fig. 2.12). The primary focus was on the aeromechanical solution. Two types of 3D CFD/CSD interfaces are constructed for this purpose with an emphasis on resolving errors from geometry mismatch so that initial-stage approximate structural geometries can also be effectively analyzed. A 3D structural model was constructed as an approximation to a UH-60A-like fully articulated rotor. The aerodynamic model is identical to the UH-60A rotor. For preliminary validation, measurements from a UH-60A high-speed flight were used where CFD coupling was essential to capture the advancing side tip transonic effects. The key conclusion was that an integrated aeromechanical analysis was indeed possible with 3D structural dynamics but required a careful description of its geometry and discretization of its parts.

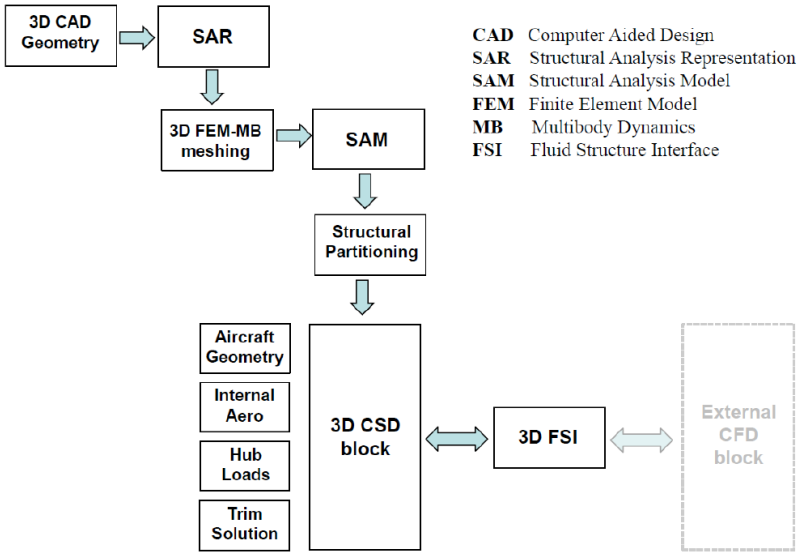

Figure 2.12. Integrated 3D workflow (Fig. 1 of Datta and Johnson [2014]).

Staruk et al. [2015] describe the development of a 3D structural analysis model of the NASA Tilt Rotor Aeroacoustic Model (TRAM) proprotor. The model includes 3D computer-aided design (CAD) geometry of the rotor, finite element meshes of flexible parts, multibody joint definitions, composite material modeling, and assembly into an integrated model suitable for dynamic analysis. Preliminary analysis was carried out on a single processor using a novel, high-fidelity, 3D rotor CSD solver. The solver used a multibody formulation and treated flexible components with full 3D finite element analysis. The process for creating the proprotor model, from CAD geometry through discretization of flexible parts into hexahedral meshes and definition of joints, was discussed. Additionally, the use of an effective modulus method to homogenize the constitutive properties of laminated composites was presented. Static analysis of the rotor flexbeam revealed accurate modeling of its bending stiffness. Mass properties for the rotor were also well captured, suggesting the CAD geometry is well defined. Some rotor frequencies were well matched, but others created problems, likely due to a lack of information on the original properties of the materials used in the rotor. It was demonstrated that the rotor model was capable of predicting the kinematics of complex root end flexures, bearings, and attachments with multiple load paths from first principles.

Staruk et al. [2017] presented aerodynamic and structural loads predictions for a 3D rotor structural analysis model of the TRAM gimballed proprotor in edgewise flight. The aeromechanics analysis was performed using X3D, a next-generation 3D finite-element-based rotor structural dynamics solver. Predictions using three aerodynamic models were presented: linear inflow lifting-line, free-wake lifting-line, and RANS CFD using the Helios solver. Rotor frequencies were examined for a gimbaled three-bladed model of the TRAM rotor and compared to one-bladed models with fixed- and free-flapping root hinges. The rotor was also modeled using a free-flap hinge at the hub with a single blade, the motion of which was suppressed at integer multiples of the Nb per rev, where Nb is the number of blades. This was accomplished by introducing harmonics of the joint rotation angle as additional trim variables. Rotor frequencies were examined for a three-bladed gimbaled rotor model and were found to combine the modes of both free-flap hinge and fixed-flap hinge (cantilevered) one-bladed rotor models, similar to the behavior of a teetering rotor, justifying the gimbal modeling methodology. Gimbal flapping was examined for a proprotor in edgewise flight: successful suppression of steady and 3/rev flapping indicated the gimbal model was performing as intended. The 6/rev and higher harmonics were negligible to begin with for this case and were left uncontrolled, but the same method could also be applied to suppress them if required. Airloads and blade loads were examined with a free-flap-hinge blade with the gimbal model, revealing an increase in 3/rev sectional normal aerodynamic force on the blade but a decrease in 3/rev flap and lag bending moment when the gimbal was added. Three-dimensional axial stress distribution at the blade root was examined, revealing only minor differences between the two hub rotor models, primarily in the flexbeam.

Structural Loads Prediction

Yeo and Johnson [2008] investigated the blade flap and chord bending and torsion moments for five rotors operating at transition and high speed: H-34 in flight and wind tunnel, SA 330 (research Puma), SA 349/2, UH-60A full-scale, and BO-105 model (HART I) (Fig. 2.13). The measured data from flight and wind tunnel tests were compared with calculations obtained using the comprehensive analysis CAMRAD II. The calculations were made using two free-wake models: rolled-up and multiple-trailer with consolidation models. At transition speed, there was fair to good agreement for the flap and chord bending moments between the test data and analysis for the H-34, research Puma, and SA 349/2. Torsion moment correlation, in general, was fair to good for all the rotors investigated. Better flap bending and torsion moment correlation was obtained for the UH-60A and BO-105 rotors by using the multiple-trailer with consolidation wake model. In the high-speed condition, the analysis showed generally better correlation in magnitude than in phase for the flap bending and torsion moments. However, a significant underprediction of chord bending moment was observed for the research Puma and UH-60A. The poor correlation of the chord bending moment for the UH-60A appeared to be caused by both the airloads model (at all radial locations) and the lag damper model (mostly at inboard locations).

HART Blade Structural Properties

Jung et al. [2012] describe the structural properties of the Higher Harmonic Aeroacoustic Rotor Test (HART I) blades. The properties were measured using the original set of blades tested in the wind tunnel in 1994. A comprehensive rotor dynamics analysis was performed to address the effect of the measured blade properties on airloads, blade motions, and structural loads of the rotor. The measurements included bending and torsion stiffness, geometric offsets, and mass and inertia properties of the blade. The measured properties were correlated against the estimated values obtained initially from the blade manufacturer. The previously estimated blade properties showed consistently higher stiffness, up to 30 percent for the flap bending in the blade inboard root section. The measured offset between the center of gravity and the elastic axis was larger by about 5 percent chord length, as compared with the estimated value. The comprehensive rotor dynamics analysis was carried out using the measured blade property set for the HART I rotor with and without higher harmonic control (HHC) pitch inputs. A significant improvement of blade motions and structural loads predictions was obtained with the measured blade properties.

Using the HART II International Workshop Data, a number of comprehensive analyses, including several shown in Figure 2.2, were used to predict the wake physics of the HART rotor [van de Wall et al., 2012] for a descent operating condition with and without HHC. The descent condition creates blade vortex interactions (BVIs), resulting in a complex flow environment. The workshop included international participants using their respective analyses to simulate the complex test conditions. The NASA/U.S. Army team used CAMRAD II to closely match the measured BVI airloads, but accurately capturing the blade bending moments was challenging. Regarding the predicted noise footprint beneath the rotor, the calculations closely matched the measured peak level but the predicted directivities were inconsistent. The correlation assessments from the other workshop participants are provided in van der Wall et al. [2012].

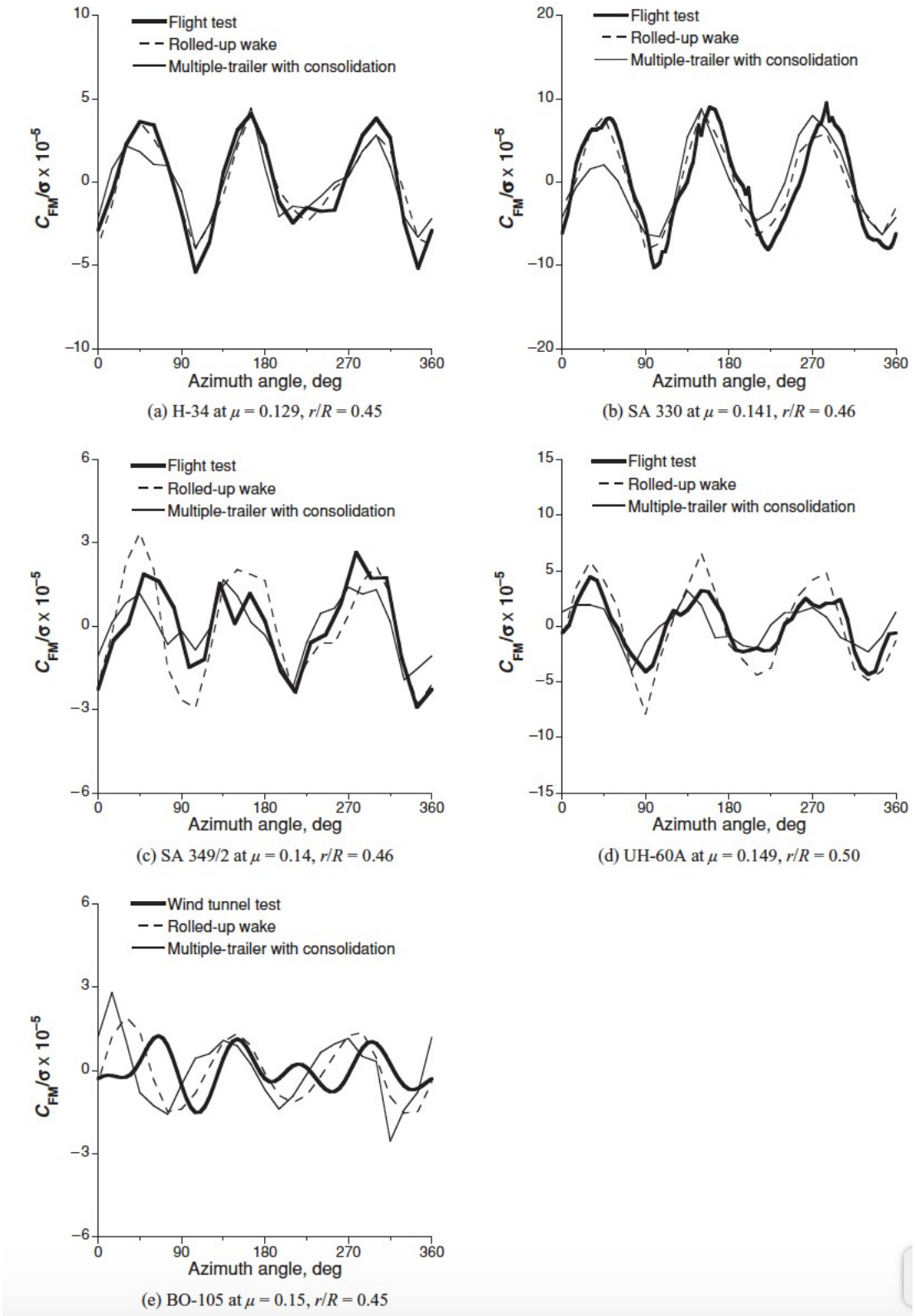

Figure 2.13. Calculated and measured blade vibratory flap bending moment at low speed near r/R = 0.5 for five rotors (Fig. 16 of Yeo and Johnson [2008]).

Adjoint Capability for Comprehensive Analysis

In late 2016, the Revolutionary Vertical Lift Technology (RVLT) Project began a concerted effort—defined as a Technical Challenge—to demonstrate design and flight operation methods for reducing the impact of vertical takeoff and landing (VTOL) aircraft noise. The 4-year effort included three technical approaches—flight operations, rotor/vehicle design, and human factors research—and was aimed at significantly reducing the noise generated by rotary wing vehicle flight. The flight operations and human response research are described in Chapter 1, Acoustics, of this report. To address the rotor/vehicle design, RVLT funded a 3-year (October 2015–October 2018) ambitious contract to develop a discrete adjoint capability for a rotorcraft comprehensive analysis. The work was led by the National Institute of Aerospace (NIA) in collaboration with the Georgia Institute of Technology and the University of Maryland. The objective was to develop a practical high-fidelity, gradient-based, multidisciplinary sensitivity analysis tool for rotorcraft aeromechanics simulations. The tool coupled state-of-the-art discipline solvers: DYMORE, a rotorcraft comprehensive analysis (CA); FUN3D, a NASA sensitivity-enabled CFD solver; and TACS, a scalable, sensitivity-enabled finite-element structural solver.

To accomplish the contract objective, tasks were divided among the team members. The NIA, working closely with the NASA FUN3D experts, developed DYMORE/FUN3D interfaces and corresponding adjoint formulations and sensitivity analysis capabilities in the DYMORE/FUN3D toolset [Nielsen and Diskin, 2017; and Wang et al., 2017]. The NIA also developed and demonstrated a framework for multidisciplinary rotorcraft design optimization [Wang et al., 2018, 2019a, 2019b, 2019c].

Georgia Tech was responsible for developing unsteady rotor capabilities in TACS and interfaces for TACS/FUN3D [Boopathy and Kennedy, 2017, 2019; Jacobson et al., 2018; Kennedy and Boopathy, 2016; and Kiviaho et al., 2017, 2018].

The University of Maryland had a 1-year task to develop a framework of motion formalism in DYMORE, enhance the computational capabilities of DYMORE, and develop adjoint-based formulation for sensitivity analysis in DYMORE [Bauchau and Sonneville, 2017; Callejo and Bauchau, 2017, 2018; Callejo et al., 2017a, 2017b, 2018; Han and Bauchau, 2017; Sonneville and Bauchau, 2017a, 2017b, 2017c, 2018a, 2018b, 2018c; and Sonneville et al., 2016a, 2016b, 2017a, 2017b, 2018, 2018d].

The team used established CAMRAD II/FUN3D rotorcraft simulations to verify the numerical accuracy, and the HART II wind tunnel and UH-60A fight test data to validate their tool set. In addition to achieving significantly improved computational efficiency [Wang et al., 2019b], the team successfully demonstrated constrained single and multipoint rotorcraft design optimization [Wang et al., 2018, 2019a, 2019b, 2019c] to improve rotor performance while maintaining required flight conditions. Figure 2.14 shows convergence of the rotor power (Fig. 2.14a) and rotorcraft figure of merit (FM) (Fig. 2.14b) for a DYMORE/FUN3D multipoint optimization of the UH-60A rotor in high-speed forward and hover flight. A reduction of 3.91 percent in the rotor power for the forward-flight condition and an increase of 1.03 percent in the rotorcraft FM

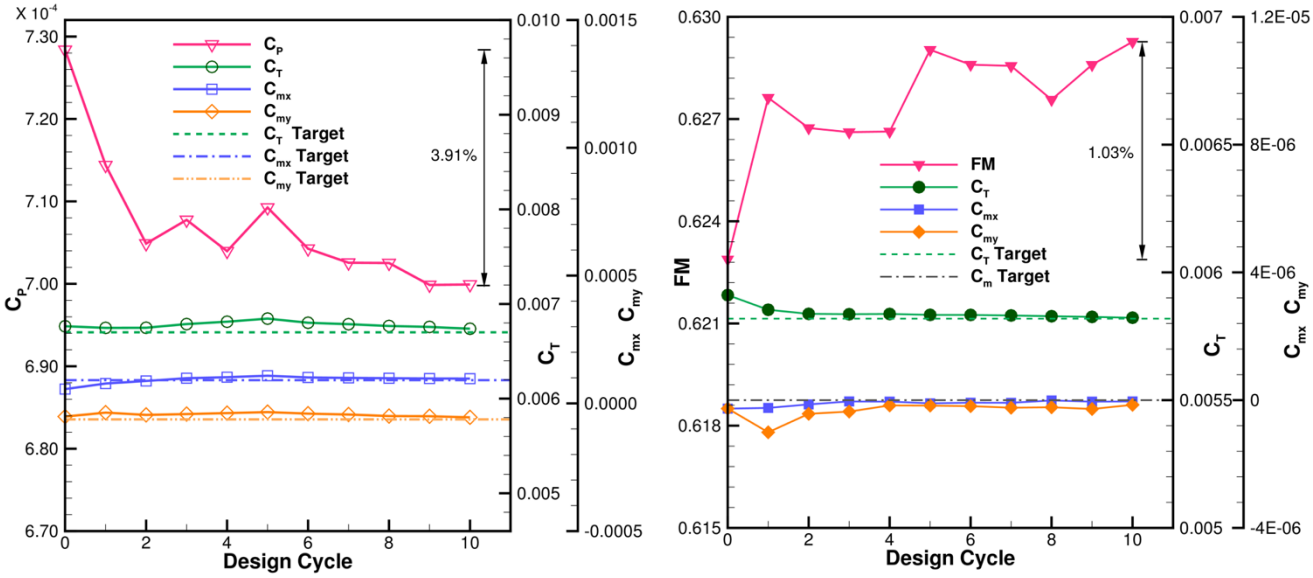

a) High-speed forward flight (C8534). b) Hover flight (C9605).

Figure 2.14. Multipoint UH-60A rotor design optimization using DYMORE/FUN3D toolset (Fig. 9 of Wang et al. [2019a]).

for the hover-flight condition have been simultaneously achieved after 10 design cycles. All design constraints, including rotor thrust and rolling and pitching moments, have been maintained. The team completed the contract on schedule and within budget.

FLOW CONTROL

Motivated by promising investigations into the application of active flow control (AFC) within the fixed-wing community, two principal applications of AFC to rotary wing vehicles were examined. These two were utilizing AFC for fuselage drag and downwash reduction, and then to mitigate the effects of dynamic stall on the retreating side of helicopter blades. A summary of NASA-supported research in each of these two areas is described below.

Fuselage Drag and Downwash Reduction

Parasite drag, the drag produced by non-lifting portions of a helicopter such as the fuselage and that typically increases significantly with cruise speed, is a long-known problem in the research community, and some researchers began investigating the efficacy of utilizing AFC techniques in an attempt to ameliorate this issue. In a combined NASA/Office National d'Etudes et de Recherches Aérospatiales (ONERA) effort, Schaeffler et al. [2010] examined the effects of AFC on fuselage drag reduction via a combined CFD and experimental approach, using a generic fuselage model, the ROBIN (ROtor Body INteraction)-mod7. The experiments were conducted in the 2- by 3-Foot Boundary Layer Channel Wind Tunnel at NASA Langley, a closed-circuit tunnel with a maximum speed of ~45 m/sec, while the CFD computations were performed at both NASA and ONERA, using different compressible Reynolds-averaged Navier–Stokes

(RANS) flow solvers and multiple turbulence models. NASA used OVERFLOW and ONERA used elsA (French acronym for "Ensemble Logiciel de Simulation en Aérodynamique"). CFD computations were performed for both the isolated fuselage and the fuselage installed in the wind tunnel, with the latter showing very good agreement with the experimental results, matching the zero angle-of-attack case (see Fig. 2.15) and underpredicting by 3 percent for the –5-degree case, while the former showed a positive shift in centerline pressure. For both configurations, the ONERA and NASA CFD results were in close agreement, finding that the flow separation location was minimally impacted by the inclusion of the installation effects. For the flow control simulations, eight slots were placed around the separation lines, and the authors calculated 35 percent fuselage drag reduction using steady blowing and 26 percent reduction using unsteady zero-net-mass flow control. The steady-blowing computations also showed a delayed flow separation on the rear ramp of the fuselage.

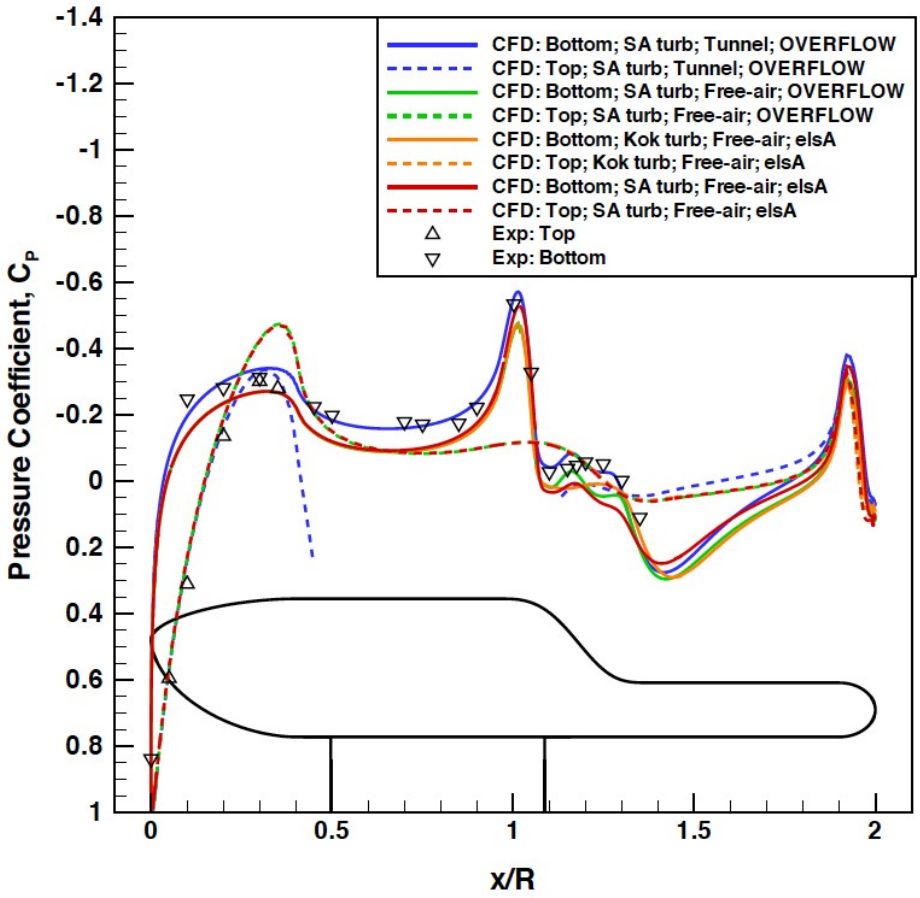

Figure 2.15. Comparison of the centerline surface C_P values from the baseline CFD simulations and the experiment for 0° angle of attack for a free-stream Mach number of 0.1 (Fig. 5 of Schaeffler et al. [2010]).

A logical follow-on to the above work was to examine AFC potential at a larger scale and include the effects of the presence of a rotor above the fuselage. Schaeffler et al. [2014] conducted a larger-scale experiment on the ROBIN-mod7 fuselage in the NASA Langley 14- by 22-Foot Subsonic Tunnel. This powered model, with a nominal 10-foot-long fuselage and 11-foot-diameter rotor, was notionally 1/3-scale when compared to a typical medium civil helicopter; the rotor and fuselage had separate balances so the forces and moments on each could be measured independently, and PIV measurements were also made downstream of the fuselage ramp. Extensive CFD computations using OVERFLOW, with the rotor dynamics being simulated via a loose coupling with CAMRAD II, were conducted pre-test and reported by Allan and Schaeffler [2011] (see Chapter 3). As in the small-scale unpowered testing, there were eight AFC actuators aligned in a U-shaped pattern on the aft ramp near the flow separation location for the baseline (no AFC) condition. The slot arrangement and the model as installed in the Langley 14- by 22-Foot Subsonic Tunnel are shown in Figure 2.16.

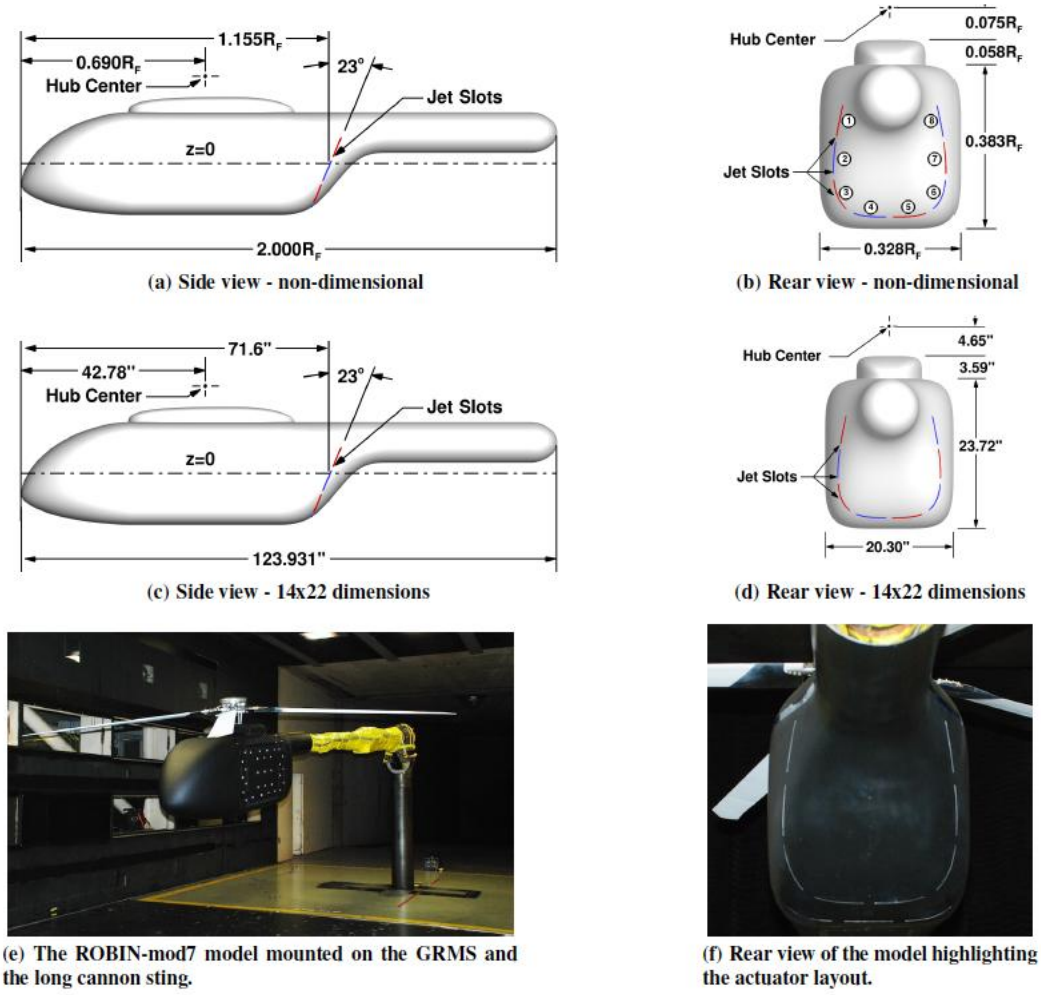

Figure 2.16. The ROBIN-mod7 fuselage: dimensions and as a model installed in the Langley 14- by 22-Foot Subsonic Tunnel (Fig. 1 of Schaeffler et al. [2016]).

Both steady blowing and zero-net-mass-flow blowing (also known as synthetic jets) were used to generate the requisite flow changes, using the same set of flow control slots. The efficacy of both actuation techniques was evaluated for a variety of advance ratios, thrust coefficients, and angles of attack, and both techniques were found to generate significant reductions in both drag and download. However, only the steady blowing had sufficient control authority to successfully implement AFC at higher advance ratios (up to 0.35), measuring drag reductions of 33 percent and download reductions of 58 percent. The synthetic jets were only successful up to an advance ratio of 0.225 because of a lack of control authority, but they did measure reductions of 22 percent for drag and 43 percent for download at that setting. Comparisons of the larger-scale experimental results with CFD computations using OVERFLOW, with the rotor dynamics being simulated via a loose coupling with CAMRAD II, are reported in Allan et al. [2015] (see Chapter 3 herein) and Schaeffler et al. [2016].

Meanwhile, Lienard et al. [2015] expanded upon the earlier NASA/ONERA collaborations, with ONERA performing two experiments using their ASF2, another generic fuselage, tested in the ONERA L1 wind tunnel in Lille, France. The L1 is an open-return wind tunnel with a 2.4-m-diameter circular test section and a maximum velocity of 75 m/s. Again, NASA used OVERFLOW for their CFD calculations while ONERA used elsA. The elsA computations were time-accurate while the OVERFLOW results were steady-state, but both showed good agreement with the experimental results, including PIV measurements. They measured average drag reductions of 15–20 percent when AFC was used in the experiment, again with up to eight actuators. For nose-down angles of attack, the highest drag reductions were found using four side slots for control, while for nose-up angles, the four bottom slots were more effective. While the CFD results captured the major trends in the flows, neither was able to accurately predict fuselage forces nor active flow effects quantitatively.

In related work, Martin et al. [2014] also conducted two larger-scale experiments on the ROBIN-mod7 fuselage in the NASA Langley 14- by 22-Foot Subsonic Tunnel. The first test entry was unpowered (i.e. fuselage only), while the second one was a powered test with an 11-foot rotor operated above the fuselage model, and the influence of AFC on the fuselage was examined utilizing fluidic oscillators as the AFC device. Fluidic oscillators were an attractive device to try, because an assessment of their effectiveness complemented research on other AFC devices (including those described immediately above), they have no moving parts, and they are proven to be robust as literally millions of them are in use in automobile windshield washers. The experimental results for the initial test provided primarily fuselage force/moment information, while the test with the rotor included PIV measurements in the fuselage wake as well. Drag reductions above 20 percent were measured for the testing with the rotor using this AFC technique, with no negative impact, and in some cases even having a positive impact, on the download in forward flight. The PIV results showed that this optimum actuator configuration, which reduced both drag and download simultaneously, seemed to be generating what the authors termed a “fluidic boat-tail fairing” as opposed to attaching the flow to the aft ramp surface. This was a significant finding, as it permitted a change in focus for separated flows from reattaching boundary layers to altering the overall wake flow. Figure 2.17 shows the effect on the streamwise velocity of the AFC as captured by the PIV measurements.

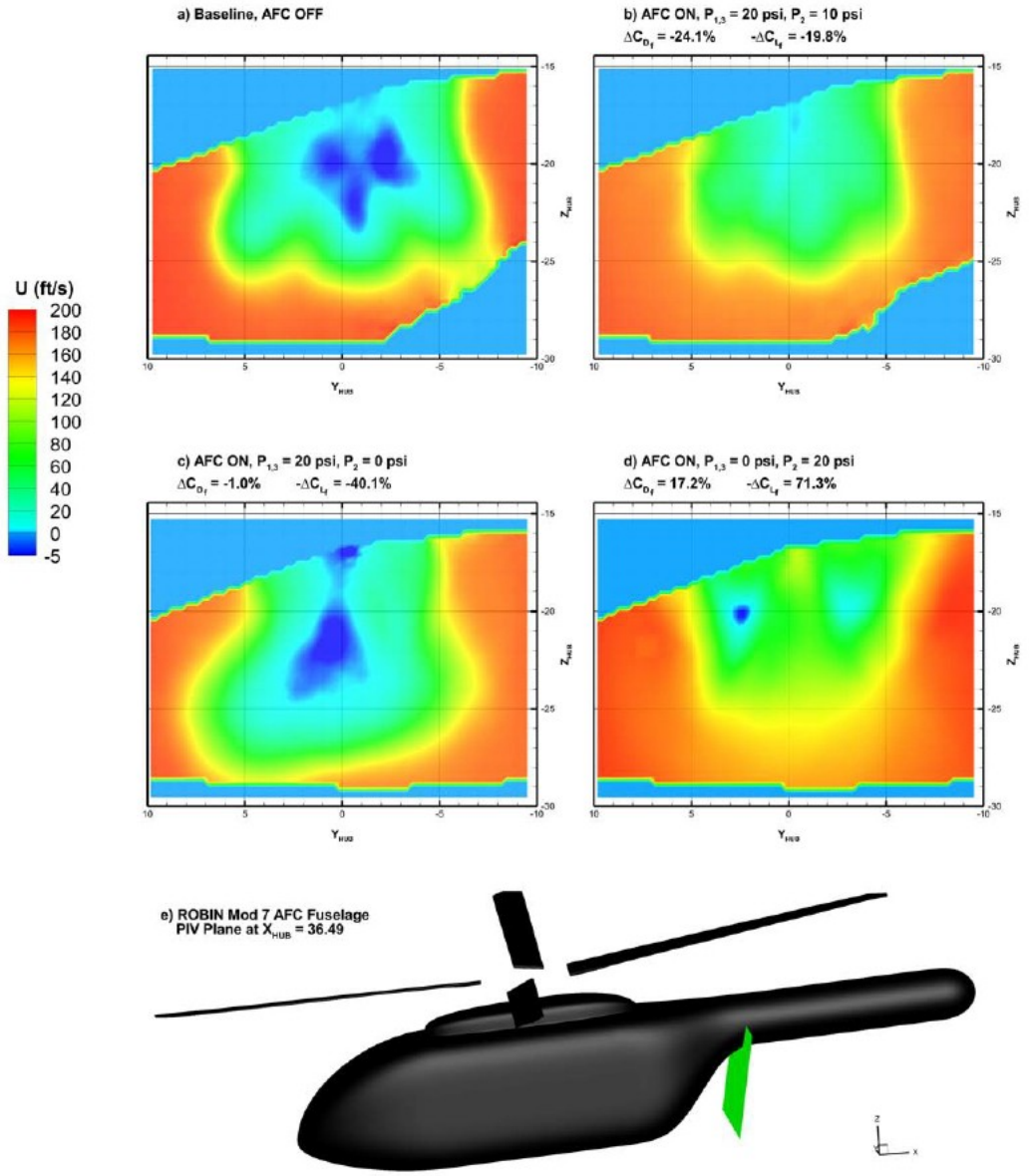

Figure 2.17. PIV results for α = –3:58°, advance ratio = 0:30, and CT/σ = 0:08. Contours of streamwise component of velocity (Fig. 24 of Martin et al. [2014]).

Dynamic Stall Mitigation

Active flow control can be applied to the fuselage parasite drag problem and also be used to address dynamic stall issues often found on the retreating side of the rotor, especially at higher cruise speeds. Narducci et al. [2014] investigated the potential for sweeping jet actuators (SJAs) to actively control the flow around an oscillating wing, with potential application to the dynamic stall problem. The original plan involved both experimental and CFD results, with the experiments to be performed on a VR-7 airfoil (the airfoil currently in use on the CH-47 Chinook helicopter) in the Oran W. Nicks Low Speed Wind Tunnel at Texas A&M University, with the test section reduced from 7x10 feet to 6x5 feet to achieve the desired Mach number of 0.5. Both two-dimensional (2D) and three-dimensional (3D) CFD computations were performed using OVERFLOW for both static and dynamic conditions. Regrettably, budgetary constraints forced cancellation of the experimental portion of the program, so only CFD results were obtained. Detached eddy simulation with the Spalart–Allmaras turbulence model in the boundary layer was used to model the jet interactional aerodynamics for the AFC conditions.

Another AFC approach to consider in an attempt to address retreating-blade stall (RBS) issues involves the use of combustion-powered actuation (COMPACT). In a multi-year effort, NASA funded a team comprising United Technologies Research Center, Georgia Institute of Technology, and Sikorsky Aircraft to explore the feasibility of COMPACT. Matalanis et al. [2014] examined the potential for such actuation to improve RBS concerns on a VR-12 airfoil using a combination of high-speed CFD and low-speed wind tunnel experiments. CFL3D with the Spalart–Allmaras turbulence model was used for the computations at Mach numbers ranging from 0.3 to 0.5, while the experiments were performed in a low-speed wind tunnel at Georgia Tech, acquiring both pressure tap and PIV data on a 0.381-meter airfoil section. Actuation configurations examined both experimentally and computationally included variations in both actuator slot chordwise location and angle, as well as actuator pulse amplitude, frequency, and timing. The CFL3D results indicated cycle-averaged lift increases of 4 to 8 percent at Mach numbers of 0.3 and 0.4 using COMPACT, with decreases in cycle-averaged drag as well, and that actuators mounted in tangential slots were more effective than those installed normal to the airfoil surface. However, the authors also found that this actuation approach was much less effective at $M = 0.5$. The low-speed wind tunnel experiments only examined static stall but indicated that the actuator locations that the computational results showed to be quite effective at $M = 0.3$ and 0.4 were also effective at $M < 0.1$. The experiments also agreed with the CFD with respect to tangential versus normal slot alignment.

This same research group next expanded upon their computational analyses for both 2D and 3D studies, again using CFL3D and examining Mach numbers from 0.3 to 0.5, only this time with a particular emphasis on optimizing actuator position and alignment [Jee et al., 2015]. Chordwise position, slot angle, and slot thickness were all optimized via the 2D calculations, confirming that a tangential alignment was better, and also that the $x/c = 0.1$ position examined in the previous study was also better than the $x/c = 0.15$ location examined here. They also found that doubling the slot thickness produced over 50 percent improvement in cycle-averaged lift. However, the authors found that the 3D results showed much poorer performance than those found in the 2D calculations. This appeared to be due to the uncontrolled flow through the gaps

between the actuator locations. They found that skewing the actuator slots at angles of up to 30–40 degrees helped to ameliorate this issue, but they also needed to taper the dividers between slots in the flow direction, producing what they described as a "vanishing-gap slot." This helped to further close the difference between computed 2D and 3D performance.

A logical follow-on to the above work was to extend the experimental results for the COMPACT actuators installed on a pitching airfoil to higher speeds. Matalanis et al. [2016a] conducted experiments at Mach numbers ranging from 0.2 to 0.5 on the same scale 15-inch (which is 0.381 m) VR-12 airfoil in the Icing Research Tunnel (IRT) at NASA Glenn. The airfoil was mounted vertically and covered the entire height of the 6- by 9-foot test section (except for the obviously necessary small clearance gaps required at the floor and ceiling), and both static and dynamic stall were examined. The COMPACT actuators were mounted roughly in the middle of the blade, covering 31 percent of the span, and were examined in two different configurations—a single row located at 0.1 x/c, and a dual configuration where a second row was added at 0.17 x/c. A baseline configuration with no actuators installed was also tested. Data were acquired using 24 Kulite dynamic pressure sensors and 30 ESP pressure taps, and PIV measurements were also obtained. The authors found static post-stall improvements in lift at Mach numbers from 0.2 to 0.4 and that, for dynamic testing, the COMPACT actuators only had to be in use over 1/3 of the pitch cycle. While the single row of actuators was effective, they found that either continuous or alternating application of both rows was even more effective. PIV results indicated very similar flow behavior at M = 0.4 as seen earlier in the low-speed testing described above. Figure 2.18 captures the effects of pulse frequency and number of pulses on the mean lift coefficient for M = 0.3. An excellent review of all of the work described in the above three papers is contained in a highly detailed NASA Contractor Report by Matalanis et al. [2016b].

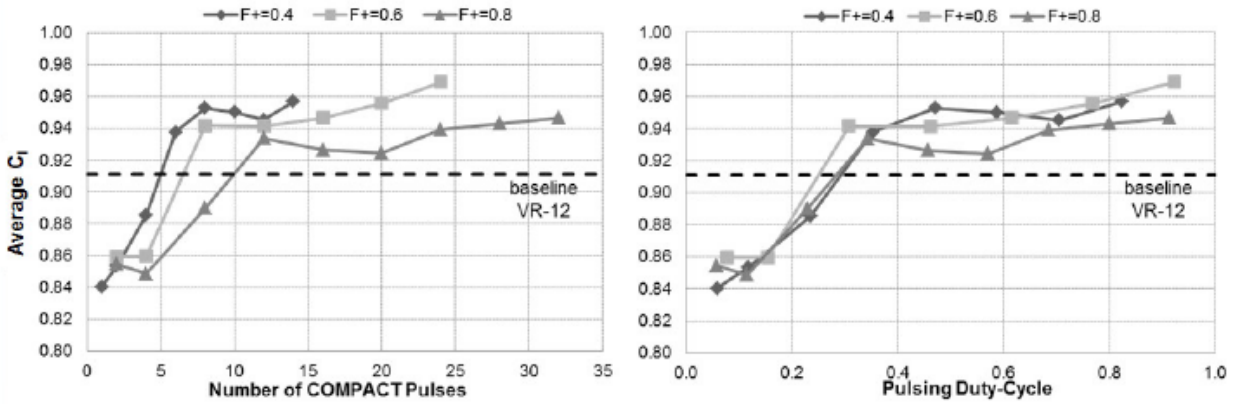

Figure 2.18. The effect of number of pulses and nondimensional pulse frequency (F+) on average lift coefficient for Mach = 0.3, mean airfoil angle of attack = 10°, amplitude of airfoil angle of attack = 10°, and reduced frequency = 0.07. (Fig. 215 of Matalanis et al. [2016b]).

ACTIVE FLAP AND ACTIVE TWIST ROTORS

Along with the various actuator-based AFC techniques (steady blowing, etc.) described in the previous section, on-blade active control uses various means of electro-mechanical actuation to deflect either the entire rotor blade or a blade section. Whole-blade deflection typically involves an embedded series of actuators that actively twists the blade as needed, while the most-investigated methodology for actuating a subsection of the blade usually involves some sort of active flap mechanism, with the flap located on the outboard portion of each rotor blade at the trailing edge portion of the chord. The preponderance of NASA-supported research over the last decade or so involves the latter technique and is summarized next.

Active Flap Rotors

While hub-based active control approaches such as higher harmonic control (HHC)/individual blade control (IBC) may be easier to implement, especially on fully-articulated rotors, on-blade controls via things such as trailing edge flaps provide more localized control. This enables the user to more closely tailor the controller motion to meet the desired goal, be it for noise and/or vibration reduction or performance improvement. Extensive work has been performed on active trailing edge flaps over the past decade, and the aeromechanics portion of that work is summarized in this subsection.

Swashplateless rotors

Falls et al. [2008] conducted performance predictions of a modified version of a UH-60, in both hover and forward flight, that did not have a swashplate and where integrated trailing edge flaps (as opposed to servo-flaps) were the primary means of rotor control, and then compared their results to a UH-60A baseline. The principal focus of their research was on the drag produced by the trailing edge flaps, since while integrated flaps produce less parasitic drag then servo-flaps, they do require significantly more flap deflection to obtain the same measure of control authority. The authors coupled 2D CFD calculations using TURNS (to generate the airfoil tables for the new rotor) with the University of Maryland Advanced Rotorcraft Code (UMARC) to perform the rotor analysis. Both free wake and dynamic stall are included in the rotor analyses. In hover, the authors predicted a slight improvement in FM for the swashplateless rotor with flaps over the baseline UH-60A at lower thrust levels, but at thrust levels beyond the maximum FM, the power required for the new rotor increased dramatically. In forward flight, they showed the power required for the swashplateless rotor was 21 percent greater than that of the baseline at an advance ratio of 0.15, with the differences between the two rotors diverging further at lower advance ratios. Between advance ratios of 0.22 and 0.30, the power required was within 5 percent for the two rotors, but above that the results again began to diverge to the detriment of the swashplateless rotor.

Next, Copp and Chopra [2008] followed up the analytical study described above with an experimental study. They designed a 5.5-foot-diameter rotor that matched the M = 0.65 tip speed of the UH-60A and was both swashplateless and contained an integrated trailing edge flap actuated by means of a piezoelectric bender. The rotor was untwisted with a rectangular planform and used a National Advisory Committee for Aeronautics (NACA) 0012 airfoil section throughout the blade. The tip speed matched the UH-60A rotor, which necessitated operating at 2,400 RPM. To achieve the full control authority desired, flap deflections of ±5.5 degrees were

required. However, during initial hover testing, flap deflection degraded rapidly with increasing RPM, measuring less than 2 degrees at only 1,500 RPM. While initially suspecting friction where the flap attached to the blade as the culprit, the authors found that the increased propeller moment, caused by the torsional inertia of the flap about its hinge, was the root cause. Although only tested in a vacuum chamber at the time of this writing, a redesigned rotor with a more powerful actuator showed much more promise towards achieving their research goal.

Later, Sekula and Wilbur [2011, 2012] analyzed the potential benefits of a swashplateless rotor that had two trailing edge flaps (TEFs)—one to control cyclic and one to control collective (see Fig. 2.19). They performed a parametric study of multiple design variables on the required TEF deflection, utilizing a CAMRAD II model of a utility-class helicopter with rigid rectangular blades trimmed for steady level flight. The authors performed gradient-based optimizations, first on a single-TEF rotor system and then later on the two-TEF rotor, to determine the minimum flap deflection required. They found that a two-flap configuration, where the outer flap controlled cyclic and the inner one controlled collective, was more effective than a single-flap system, and it also had a negligible effect on power required. Other key findings include showing that a torsionally soft rotor (frequencies around 1.3 to 1.4/rev) minimized flap deflection, as did increasing the flap span and having a flap chord of 20 to 26 percent of the overall blade chord.

Next, Thornburgh et al. [2014] expanded upon the research described in the previous paragraph by examining the efficacy of continuous, as opposed to discretely actuated, hinged trailing edge flaps, which they term CTEFs here, as a means of primary rotor control. They again evaluated a utility-class helicopter, only this time they analyzed the impact of using an optimized bimorph with embedded Macro-Fiber Composite (MFC) actuators to create two hingeless flaps in the blade. They retained the idea of the inner flap (which spans from 70 to 82.5 percent of the blade radius) to control collective, while the outer flap (which spans from 82.5 percent to the blade tip) controls cyclic. The authors used a number of computational tools to generate the airfoil tables for the CTEF blade sections (XFOIL, TURNS, OVERFLOW, and FUN3D), while CAMRAD II was again used for the overall rotor comprehensive analysis. Along with examining whether the CTEF concept could operate functionally, including effectively transferring aerodynamic loads to the blade spar, they also evaluated the impact of blade root pitch index (RPI), finding that its primary effect was on collective control; cyclic control was relatively insensitive to the choice of RPI. While the CTEF concept is promising for primary rotor control, the use of RPI, either in addition to or in lieu of CTEF, offers promise for primary rotor control as well.

SMART rotor

The Defense Advanced Research Projects Agency (DARPA), NASA, and Boeing, along with numerous other collaborators, conducted a test of the Boeing Smart Material Actuated Rotor Technology (SMART) active flap rotor, a full-scale MD-900 helicopter rotor with trailing edge flaps that spanned from 0.74 to 0.92 R, and used piezoelectric actuation installed on each blade. The test was conducted in the anechoic test section of the NFAC 40- by 80-Foot Wind Tunnel and, along with demonstrating the concept in full-scale, the experimental database was used to validate numerous analytical tools. Straub et al. [2009, 2018] presented an overview summary of the 11-week test program, where the SMART rotor was examined at forward-flight speeds up to 155 knots, although at those highest speeds, the flap could not be actuated, so only baseline (i.e. no flap deflection) data were acquired. This was the first full-scale test of such a concept, and

along with successfully demonstrating its viability over more than 60 hours of wind-on testing in both open- and closed-loop control modes, the ability of the active flap rotor to reduce noise and vibration was also quantified at full-scale, validating prior smaller-scale experiments. Reductions of 3–6 dB in BVI noise and up to 6 dB in in-plane noise were measured, as were 80 percent reductions in vibratory hub loads, and the test team was able to control the trailing edger flap to within nominally 0.1 degree of the commanded value. Rotor performance was also examined, although the benefits of the active flap on high-speed performance were too small to be noted. Figure 2.20 shows the installation of the model and microphones in the wind tunnel. Figure 2.21 shows the effect of flap frequency and amplitude on the noise measured at Microphone 13 (M13).

In a companion paper, Kottapalli and Straub [2009] used the SMART rotor data to assess their ability to predict the loads for this active trailing edge flap rotor using CAMRAD II. They compared their predictions with the experimental results for two high-speed (advance ratio of 0.3) forward-flight conditions—a baseline (no flap deflection) case and a 5/rev, 2-degree flap deflection case, and found reasonable agreement with the experimental results, although the frequency of the torsion moment was underpredicted. The impact of the flaps is also well predicted, although there is a slight overprediction in the 105- and 120-degree azimuthal locations. The authors also found that the actual flexbeam torsion stiffness may be four to six times that of the baseline value they used in this study.

In still another related paper, Hall et al. [2009] focused on the vibration reduction potential of the SMART active flap rotor. They showed that the active flap rotor could successfully reduce vibratory loads, in particular, the normal force loads. When the active flaps were actuated, using a continuous-time HHC algorithm reduced the normal force loads, due to the first five harmonics of the rotor, by up to 95 percent in both cruise and descending flight operating conditions, with a total reduction (including broadband loads) of over 84 percent. To a lesser degree they also found successful reductions in both vibratory roll and pitch moments. As found above, the authors also were able to control the active flap movement accurately, with total movement errors within 0.2 degrees RMS.

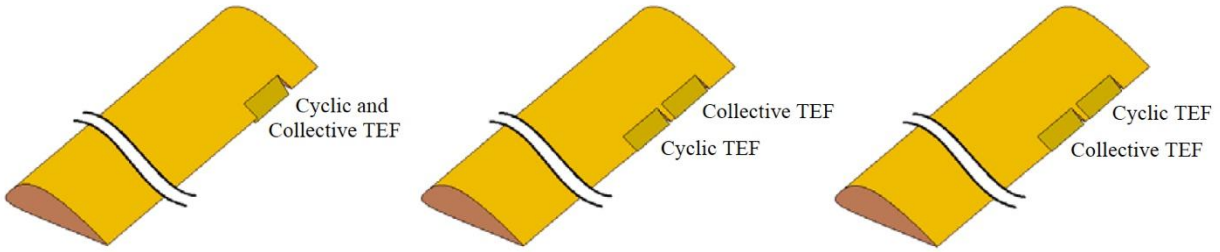

(a) Single-TEF control system for cyclic and collective control.

(b) Two-TEF control system: outboard flap collective control, inboard flap cyclic control.

(c) Two-TEF control system: outboard flap cyclic control, inboard flap collective control.

Figure 2.19. Single- and two-TEF swashplateless rotor, flap function distribution (Fig. 1 of Sekula and Wilbur [2011]).

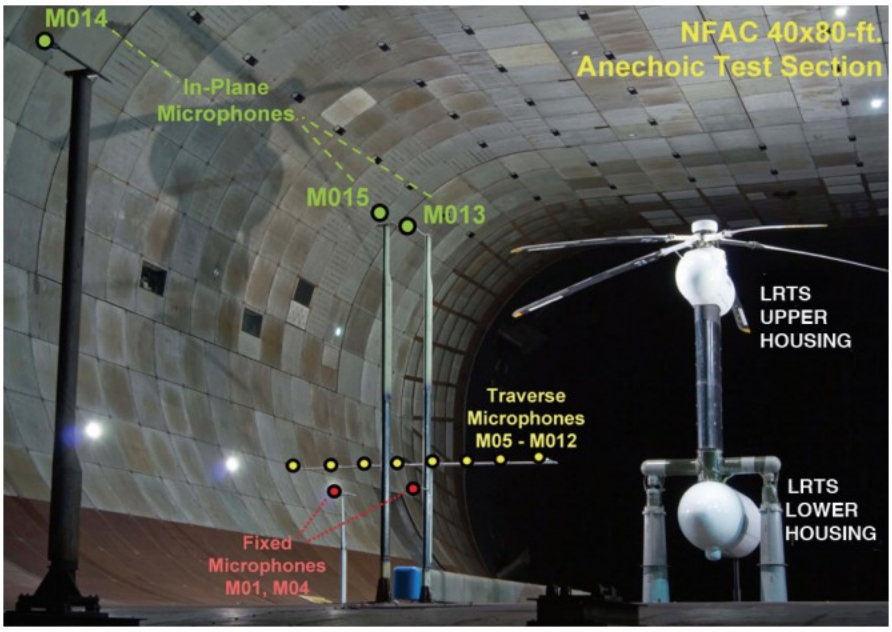

a) SMART rotor installed in the test section of the NFAC 40- by 80-Foot Wind Tunnel (Fig. 2 of Lau et al. [2010]).

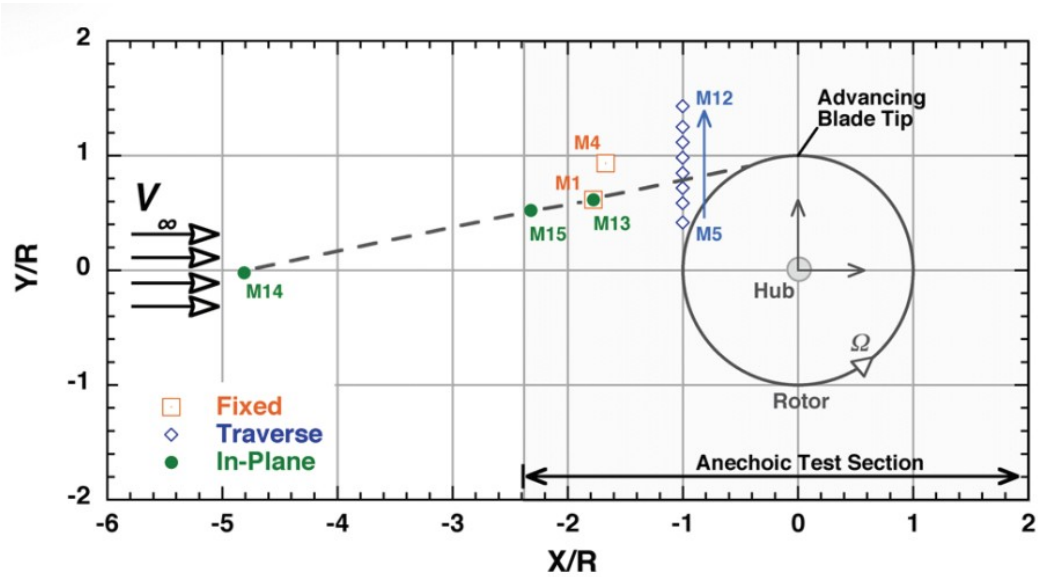

b) Top view of the test setup of the microphone layout with rotor hub at uncorrected shaft angle = 0º (Fig. 3 of Lau et al. [2010])

Figure 2.20. SMART rotor wind tunnel installation and microphone placement.

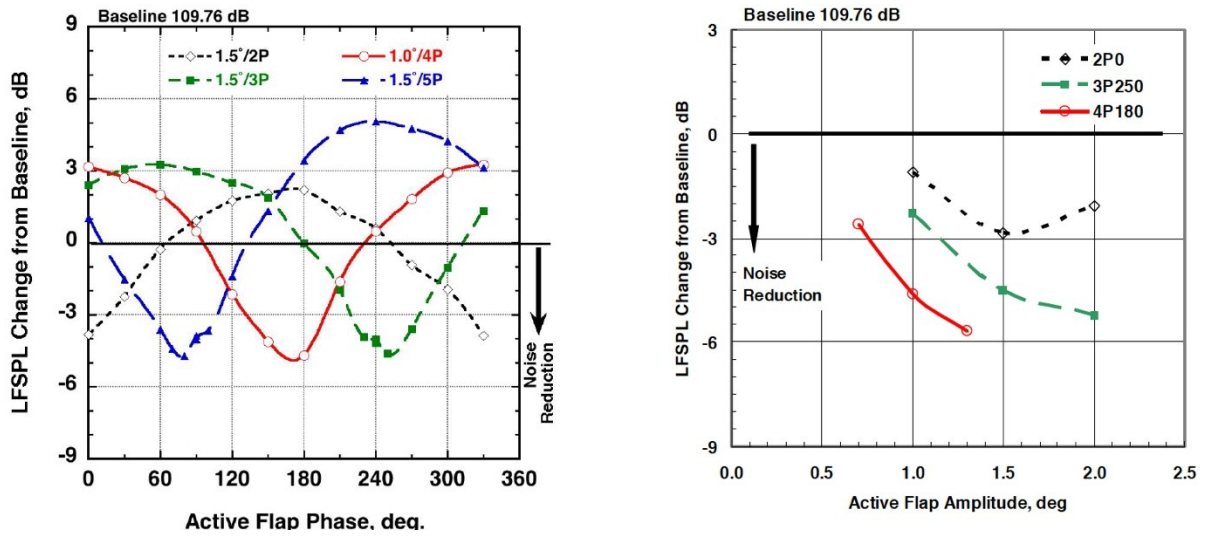

a) Effect of active flap excitation frequency and phase.

b) Effect of active flap excitation frequency and amplitude for "best" phase.

Figure 2.21. Effect of active flap excitation frequency on low-frequency sound pressure level (LFSPL) at microphone M13; advance ratio = 0.3, shaft angle = –9.1° (Fig. 11 of Straub et al. [2009]).

In a final report to DARPA, Lau et al. [2010] provided a significantly more detailed overview and assessment of the test than could possibly be contained in the Straub et al. [2009] conference paper summarized at the beginning of this subsection. They found the repeatability of test conditions to be adequate and chose the test points from five different operating conditions that they recommended to be used for follow-on code validation efforts (some of which are described immediately below). They also found means to remove extraneous noise sources from the actual rotor data via postprocessing. The report contains a large number of data quality plots (Figure 2.22 is just one example). Figure 2.22 shows the repeatability of the rotor performance measurements for the baseline (flap not actuated) case. The standard deviations, calculated from 64 revolutions of data at each azimuth, are compared with the averaged revolution and a revolution synthesized from the integer harmonics.

Later, in a pair of studies, Kottapalli [2010, 2011] expanded upon his initial studies with Straub (described above) and examined predicted versus measured rotor loads due to the active flap for the SMART rotor for both open- and closed-loop control using CAMRAD II. In the 2010 study, he evaluated one open-loop and three closed-loop high-speed cases along with one low-speed closed-loop condition, updating the HH-06 pitching moment airfoil tables from the previous study as well as increasing the flap hinge stiffness. In general, Kottapalli found the correlation between measured and predicted rotor loads to be "fair," although he did note that it was poor for bending. Figure 2.23 compares the measured and predicted torsion moments, plotted using the approach used by Bousman and Norman [2008, 2010] to assess prediction accuracy.

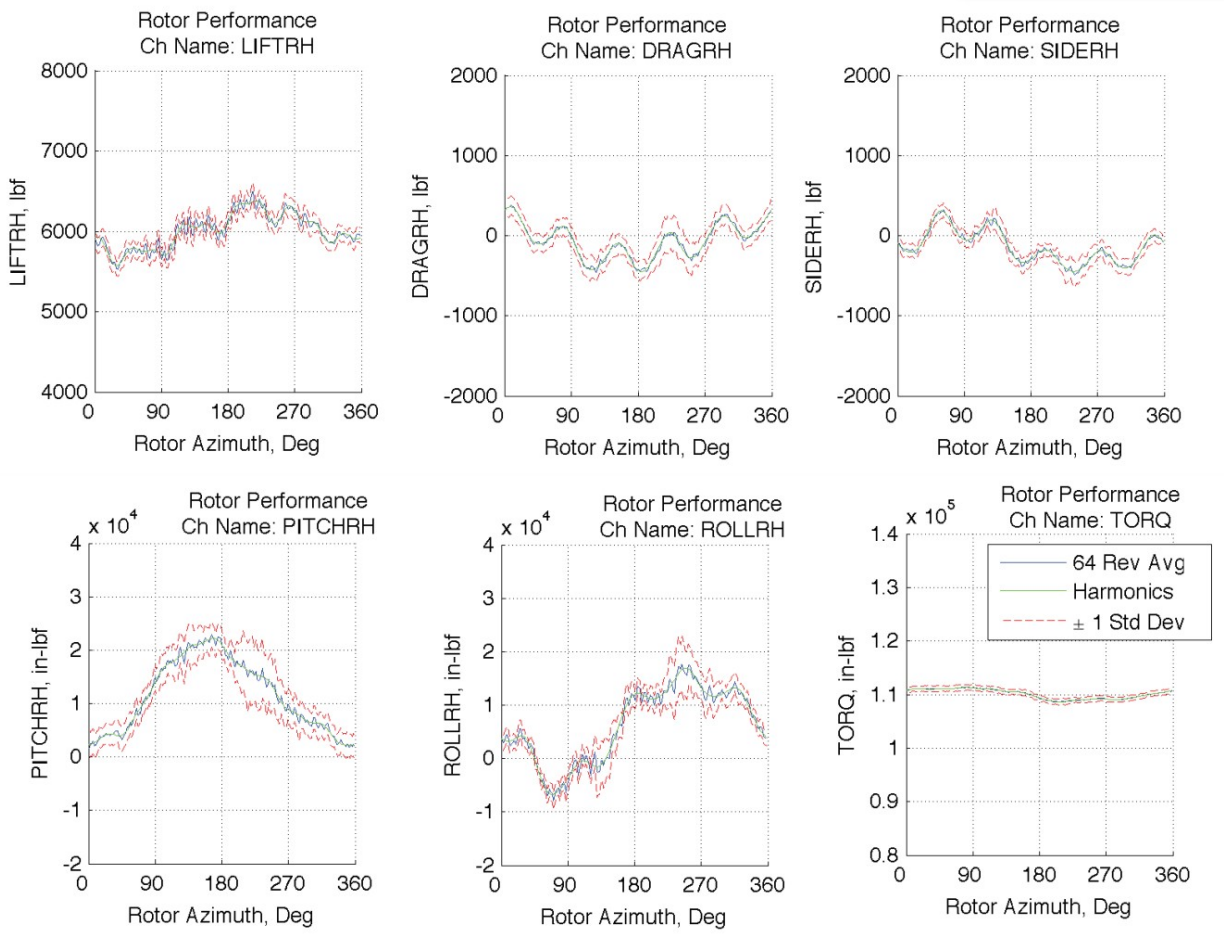

Figure 2.22. Standard deviation of rotor performance measurements (Fig. C14 of Lau et al. [2010]).

In the 2011 paper, Kottapalli utilized updated flexbeam properties provided by Boeing Mesa to improve his calculations, as well as increasing the number of blade modes to better model the active flap dynamics, again using CAMRAD II. He also added an assessment of the multiple-trailer wake model to the rolled-up wake model he had used previously, which produced a small improvement in the correlation with the measured loads. He focused on three high-speed (advance ratio of $\mu = 0.3$) cases—one open-loop and two closed-loop conditions. Kottapalli found that the effect of updating the flexbeam properties produced a negligible impact on his predictions, while increasing the number of blade modes produced a factor of four increase in the flap hinge stiffness, as opposed to the factor of three found previously. The correlation of both the inboard loads and the loads from the free-flap case were found to be "reasonable," as were those for the 2-degree flap case actuated at 5/rev.

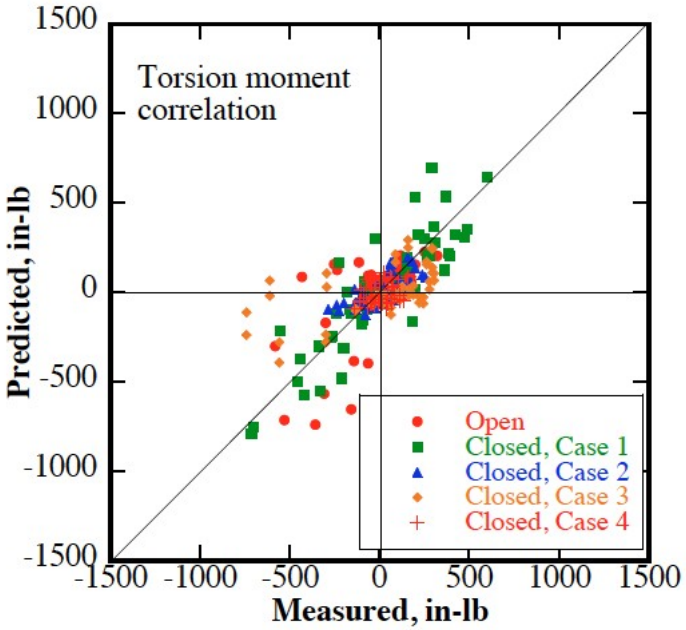

Figure 2.23. Comparison of measured and predicted torsion moments for open-loop control and four cases of closed-loop control of the SMART rotor active flap (Fig. 7a of Kottapalli [2010]).

Later, Kottapalli and Leyland [2014] performed an analytical study to minimize the hub loads on the SMART rotor utilizing an alternative optimization strategy that involved nonlinear programming. The actual algorithm they used was Sequential Quadratic Programming (SQP), which is contained in the NLPQLP (a Fortran subroutine) system. The authors then incorporated this into NLP10x10, a tool specifically designed to minimize hub loads on an active flap rotor. They evaluated this new approach against two other optimization techniques—a linear unconstrained method and the nonlinear General Reduced Gradient (GRG) approach, which does contain constraints. The authors reviewed the theory behind NLP10x10 in detail, verified it was functioning properly, and then applied the tool to the SMART rotor, successfully demonstrating the code's ability to reduce hub loads.

The extensive data reports compiled by Lau et al. [2010], Straub et al. [2015], and Kottapalli et al. [2016] should be consulted by anyone interested in this full-scale active flap database.

Other Active Flap Rotors

To complement all of the active flap rotor research described both above and below in the remainder of this subsection, Min et al. [2008, 2009] examined the potential of a deployable Gurney flap, primarily to reduce vibratory loads in forward flight and the descent rate needed to maintain autorotation. The authors implemented a hybrid CFD/CSD approach utilizing the Generic Numerical Compressible Airflow Solver (GENCAS) RANS solver for the former and DYMORE for the latter, applying this approach to a model-scale BO-105 rotor. Three different 2/rev deployment schedules for the Gurney flap were compared to the baseline (no flap) condition, with the flaps deployed over the entire rotor span. They found that the Gurney flap did

have the potential to reduce vibratory loads on the rotor if deployed at the proper schedule, with negligible impact on power required. In descent, the Gurney flap decreased the descent rate required to maintain autorotation, with the most improvement again dependent on the proper deployment (Fig. 2.24). Here the deployment was fixed but needed to be at lower angles with respect to the chord line for optimum performance.

		Baseline	30 deg. GF	45 deg. GF
C_T		3.6×10^{-03}	3.6×10^{-03}	3.8×10^{-03}
Descent Rate	α_s [deg.]	28.9	17.5	25.0
	$V_\infty \sin(\alpha_s)/\Omega R$	0.0735	0.0457	0.0642

Figure 2.24. Effect of Gurney flap on the vertical descent rate needed to sustain autorotation (zero torque) (Table II of Min et al. [2008]).

Meanwhile, Chandrasekhara et al. [2008] investigated the use of a small Gurney flap to help control the compressible dynamic stall of a VR-12 airfoil equipped with a variable droop leading edge (VDLE). They examined three different Gurney height flaps, all of which were mounted at the trailing edge of the airfoil. To assess the effectiveness of the various flaps, the authors measured the unsteady pressures on the airfoil over a wide range of test conditions. They found that a Gurney flap whose height was 1 percent of the airfoil chord (the smallest of the three tested) eliminated the dynamic stall, producing large increases in lift while also reducing both drag and moment coefficients, although they caution that their drag measurements need to be supplemented with a more detailed set of measurements.

Later, Saito et al. [2010] presented an overview of the Novel Intelligent JAXA Active Rotor (NINJA Rotor) program, which was a cooperative effort between JAXA and NASA, with ultimate plans to test this pressure-instrumented, active-flap rotor in the test section of the NFAC 40- by 80-Foot Wind Tunnel at NASA Ames. This four-bladed rotor had a radius of 5.8 meters, a nominal chord of 0.4 meters, and a design tip speed of 200 m/sec. Along with the overview of the entire NINJA Rotor program, the authors also presented a series of preliminary pretest predictions. Ultimately, because of dwindling resources, the joint program ended before the wind tunnel test was executed.

With SBIR funding, McKillip and Quackenbush [2012] investigated a full-span on-blade camber control system that could conceivably be retrofitted onto existing rotor blades without requiring a complete redesign of the hub, flight controls, etc. They used a single Shape Memory Alloy (SMA)-actuated tab on each blade that covered nearly the entire blade span to effectively achieve full-span camber control. While the use of multiple tabs would have provided a greater level of control authority, the authors intentionally kept their design as simple as possible, since they felt that increased complexity was a major reason why all of the different active control systems had never "bought their way" onto a production rotorcraft. Along with the analysis they performed using the CHARM model, they also produced an initial design that they then tested, which demonstrated improved performance in both hover (Fig. 2.25) and forward flight, as well as reduced noise and vibration.

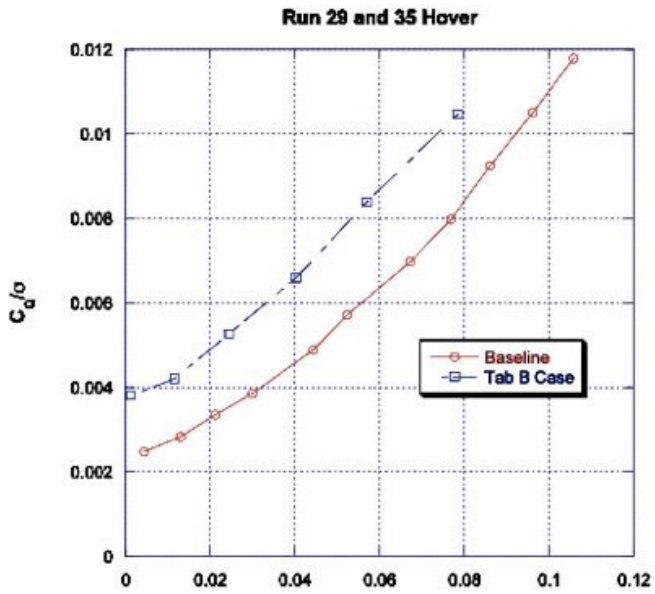

Figure 2.25. Comparison of measured hover performance for the untabbed baseline rotor at 600 RPM compared to the Tab B distribution case (Fig. 25 of McKillip and Quackenbush [2012]).

Active Twist Rotors

Instead of electro-mechanically actuating a trailing edge flap, an alternative means of active rotor control involves imbedding actuators inside the blades to actively twist the rotors. This actuation can either be just at the tip or across a much longer portion of the rotor planform.

Sekula and Wilbur [2014] performed an analytical study using CAMRAD II to determine the optimum blade tip planform for a model-scale active twist rotor (ATR). The baseline ATR design was one previously tested in the Transonic Dynamics Tunnel (TDT) at NASA Langley; it had a 4.685-foot radius, rectangular tip shape, and a hover tip Mach number of 0.628 when operated in the heavy-gas environment often used in the TDT, which reduces the speed of sound by nominally half. Their optimization was a two-step process, first utilizing a genetic algorithm with a response surface metamodel to get close to an overall optimum solution, then using that result as a starting point in a gradient-based optimization approach that used CAMRAD II as the rotor modeling technique. When the authors optimized the new rotor for performance (which they defined as minimum rotor power required), they found that they could achieve a 5-percent improvement over the baseline, but at a cost of reducing the vibration control authority of the ATR by 75 percent. However, when they optimized the rotor design to maximize the blade twist response, they achieved a 50-percent increase in vibration control authority with a negligible impact on performance. Finally, when the authors attempted to do a combined optimization, they successfully achieved a 3.4-percent increase in performance when compared to their baseline, with virtually no impact on vibration control authority. Figure 2.26 shows the geometry of the optimized blade planforms.

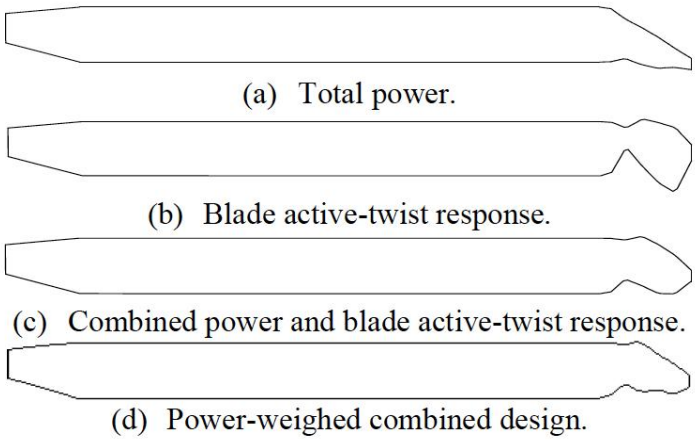

Figure 2.26. Optimized blade planforms (Fig. 4 of Sekula and Wilbur [2014]).

While the previous authors focused on performance enhancement and vibration reduction, Lim et al. [2014] took the ATR concept a step further, including potential for noise reduction in their assessment of the Smart-Twisting Active Rotor (STAR). The STAR was a 40-percent scale-model Bo105 rotor, and the actual rotor design included embedded MFC actuators to produce the active twist, which was evaluated using up to 5/rev active twist harmonic control inputs. The STAR program is an international collaboration, still intact as of this publication, with participation from the U.S. Army and the NASA RVLT Project from the United States; German DLR, French ONERA, and Dutch DNW from Europe; and Konkuk University and Korea Aerospace Research Institute (KARI) from Korea, and Japan Aerospace Exploration Agency (JAXA) from Japan as the Asian partners. As one might assume given the list of participating partners, a number of different analytical tools were employed, including CAMRAD II, S4, HOST, rFlow3D, and *elsA*. Obviously, given the wide range of fidelities represented by these codes, some disagreement was found, although overall the differences were often small. The effects of the various control inputs examined were evaluated over a range of flight conditions, including hover, descent, forward flight, and also slowed rotor conditions that allowed assessment at very high advance ratios. The authors computed benefits of the ATR in hover to be a 1- to 2-percent improvement in FM relative to the baseline Bo-105 rotor, while in descent a reduction in BVI noise of 2–5 dB was predicted. While the performance benefits at high speed were quite small (<1 percent), vibration reductions of nearly 50 percent were computed. ATR benefits for the slowed rotor conditions were negligible at best. Figure 2.27 shows the computed change in FM by the various STAR partners. After Lim et al. [2014] was published, the University of Glasgow joined the STAR team. The STAR test is currently scheduled for the German-Dutch Wind Tunnel Large Low-Speed Facility (DNW-LLF) in 2021.

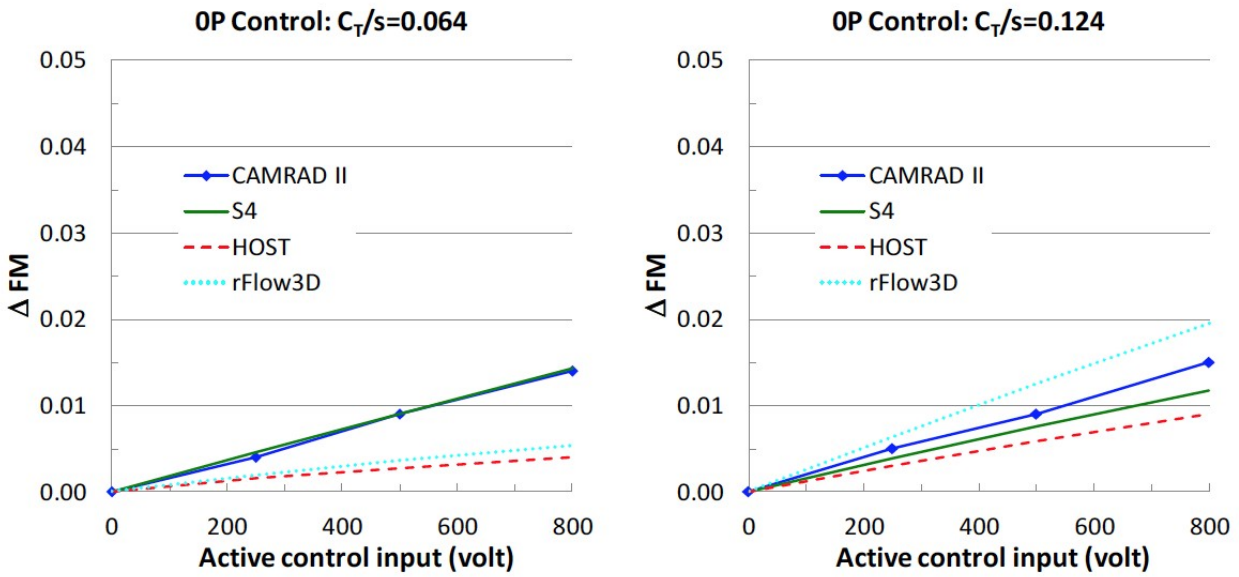

Figure 2.27. Change in FM in hover with the 0 per rev active twist up to 80 percent (800 V) input at CT/σ = 0.064 and 0.124 (Fig. 7 of Lim et al. [2014]).

Tiltrotors

While the ability to take off and land vertically is critical to many civil and military missions, the traditional helicopter design has inherent disadvantages with respect to both speed and range during cruise. As a result of the desire to design a vehicle that takes off and lands vertically while simultaneously operating nearly as efficiently as a conventional airplane during cruise, the concept for tiltrotors was first envisioned. The Bell XV-3, a joint Air Force/Army program, performed the first ever complete conversion from takeoff to horizontal flight and back for a tiltrotor aircraft in 1958 (https://www.nationalmuseum.af.mil/Visit/Museum-Exhibits/Fact-Sheets/Display/Article/195785/bell-helicopter-textron-xv-3/). Later, the NASA/Army/Bell XV-15 tiltrotor aircraft expanded upon the unique capabilities of such vehicles, logging one of the longer life spans of any experimental aircraft, with over 700 hours of testing from 1979–2003 (https://airandspace.si.edu/collection-objects/bell-xv-15-trra-tilt-rotor-research-aircraft-ship-2), and leading the way to the V-22, the first ever tiltrotor vehicle in production.

Franklin D. Harris (formerly of Bell and Boeing), probed the literature for propeller performance data and, with the aid of student interns from NASA Ames, collected the information in two very useful reports that should serve as excellent resources for future tiltrotor/tiltwing designers. Harris and Dominguez [2017] reexamined the hover performance of the XC-142A, a tiltwing aircraft of slightly less gross weight than the V-22, and built and tested in the 1960s by both the Department of Defense (DoD) and NASA (see https://www.nationalmuseum.af.mil/Visit/Museum-Exhibits/Fact-Sheets/Display/Article/195770/chance-voughtltv-xc-142a/ for additional details on the vehicle). Working with a group of interns, the authors digitized the hover data contained in two reports published in 1970 containing results from testing performed by Wright-Patterson Air Force Base personnel; this testing was done at Point Mugu, California, on two different propellers—the baseline 2FE16A3-4A propeller, and the redesigned 2FF16A1-4A, both

of which were 15.625 feet in diameter. A comparison of the hover performance of the two propellers showed significant performance improvement in the redesigned propeller. They next reexamined the comparisons of isolated propeller hover performance versus that of the full vehicle, identifying a discrepancy of approximately 175 pounds, or the nominal weight of one soldier (of the 32 this vehicle was designed to transport). The authors use the information to point out inadequacies in using isolated propeller performance to predict on-vehicle performance, a deficiency that they believe still exists today.

Harris [2017] also compiled a hover database from previous testing of eight proprotors and two propellers (the following list is from page 1 of Harris [2017]):

1. XV-15 Metal Blade Proprotor, NASA OARF and WADC Test (Mtip = 0.60 to 0.73).
2. XV-15 Advanced Technology Blade (ATB) Proprotor, NASA OARF Test (Mtip = 0.60 to 0.74).
3. 0.658-Scale JVX Proprotor, NASA OARF Test (Mtip = 0.35 to 0.73).
4. XC-142A Initial Propeller (2FE), WADC Test (Mtip = 0.725 to 1.0) Data Set #6.
5. XC-142A Final Propeller (2FF), WADC Test (Mtip = 0.725 to 1.0) Data Set #23.
6. 0.15-Scale JVX Three-Bladed Proprotor, Bell Test (Mtip = 0.35 to 0.73).
7. 0.15-Scale JVX Four-Bladed Proprotor, Bell Test (Mtip = 0.35 to 0.73).
8. 0.2364-Scale Boeing Vertol Model 160 (Twist of –40.9 deg) WADC Test (Mtip = 0.51 to 0.87).
9. 0.2364-Scale Boeing Vertol Model 160 (Twist of –36.0 deg) WADC Test (Mtip = 0.51 to 0.87).
10. 0.2364-Scale Boeing Vertol Model 160 (Twist of –29.0 deg) WADC Test (Mtip = 0.51 to 0.87).

Detailed appendices are provided for each of the above tests, describing the blade geometry and providing a summary background, tabulated experimental data, and a number of performance plots to facilitate comparison with new and/or improved analytical techniques as they are developed. Harris also provided a comparison of the first five configurations listed above (Fig. 2.28), an analysis of the impact of a three- versus four-bladed proprotor (items 6 and 7 above), the influence of blade twist (items 8–10 above), and an assessment of scaling effects (items 3 and 6 above).

JVX

The V-22 program began with the Joint-service Vertical take-off/landing Experimental (JVX) aircraft program in 1981, led by the U.S. Army. Many of the models used for aerodynamic testing continued to be used for research purposes for many years afterwards. Acree [2008a] used several different CAMRAD II models to predict both hover and airplane-mode (high-speed forward flight) performance, and he compared those results with both 0.658-scale JVX data acquired at the Outdoor Aerodynamic Research Facility (OARF) and the NFAC at NASA Ames, and later, TiltRotor Aeroacoustic Model (TRAM—a 0.25-scale V-22 rotor) data acquired in the DNW-LLF. He showed that a free-wake model with a single tip vortex matched the hover data well at high thrust, but a multiple-trailer model was needed for accuracy at low thrust, albeit at a

significant impact on efficiency. Lower-resolution wake models were much less effective. For airplane mode, all of the models evaluated agreed at least reasonably well with the measured data. Figure 2.29 shows correlations for several wake models in hover and airplane-mode flight. He closed by recommending, when conducting proprotor design studies, the conventional rolled-up free-wake model for hover evaluation, and a differential-momentum model for airplane mode. A much more extensive presentation of these analyses, including details such as data tables for the numerical results, was then published in Acree [2009].

Acree [2008b] then extended those analyses to examine both analysis and optimization of JVX proprotor performance, with intended application to optimized proprotor design. He again used CAMRAD II as his analysis engine, with varying levels of analysis fidelity, evaluating changes in blade twist distribution (Fig. 2.30), solidity, taper, sweep, and droop. The purpose of the research was to identify the minimum level of analytical methodology required to provide sufficient accuracy for proprotor aerodynamic design optimization. He found that a rolled-up free wake with 3D stall delay was the minimum fidelity required for adequate hover performance assessment, and also identified limitations with his modeling approaches with respect to any design that causes significant changes in tip vortex formation. An extended version of these results is presented in a NASA report by Acree [2008c].

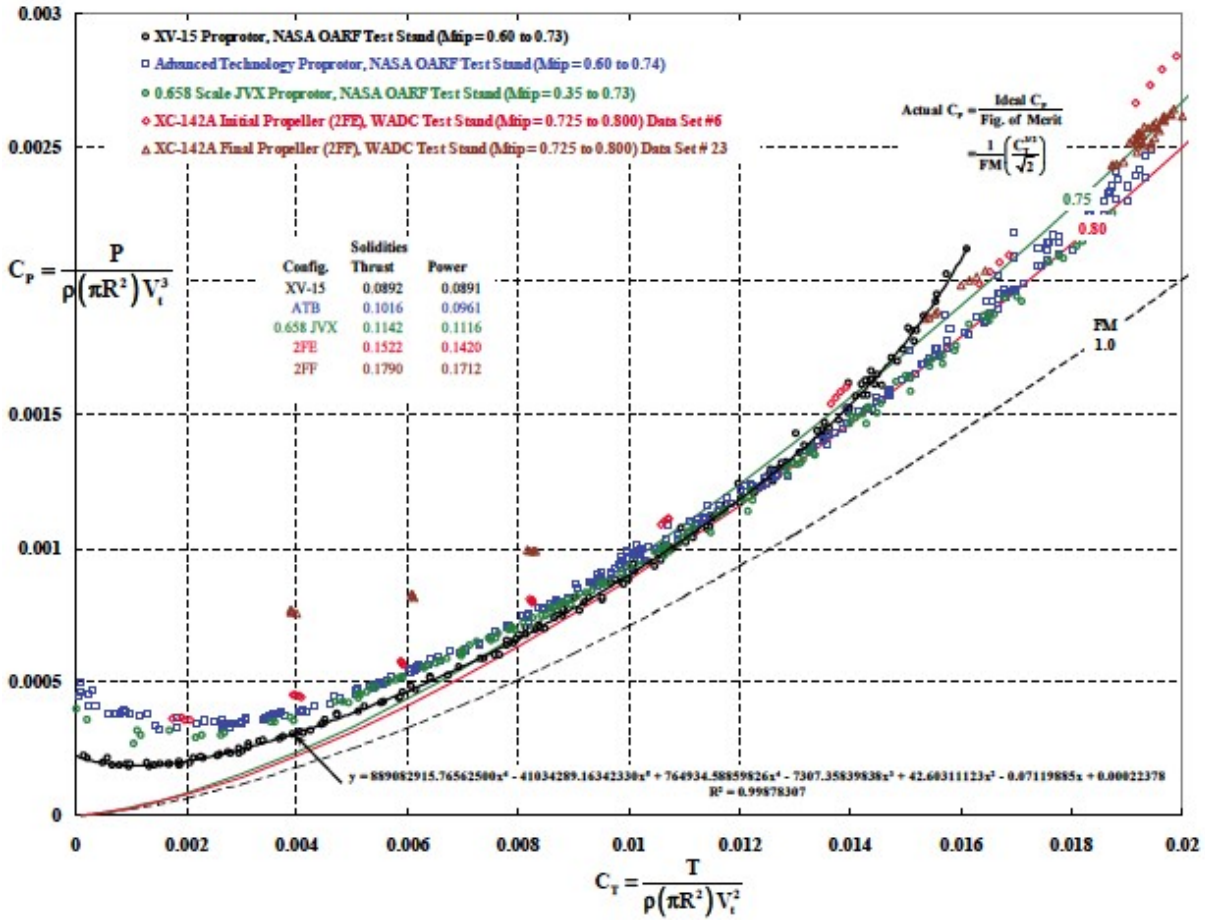

Figure 2.28. The thrust coefficient required to obtain optimum performance increases as solidity increases (Fig. 13 of Harris [2017]).

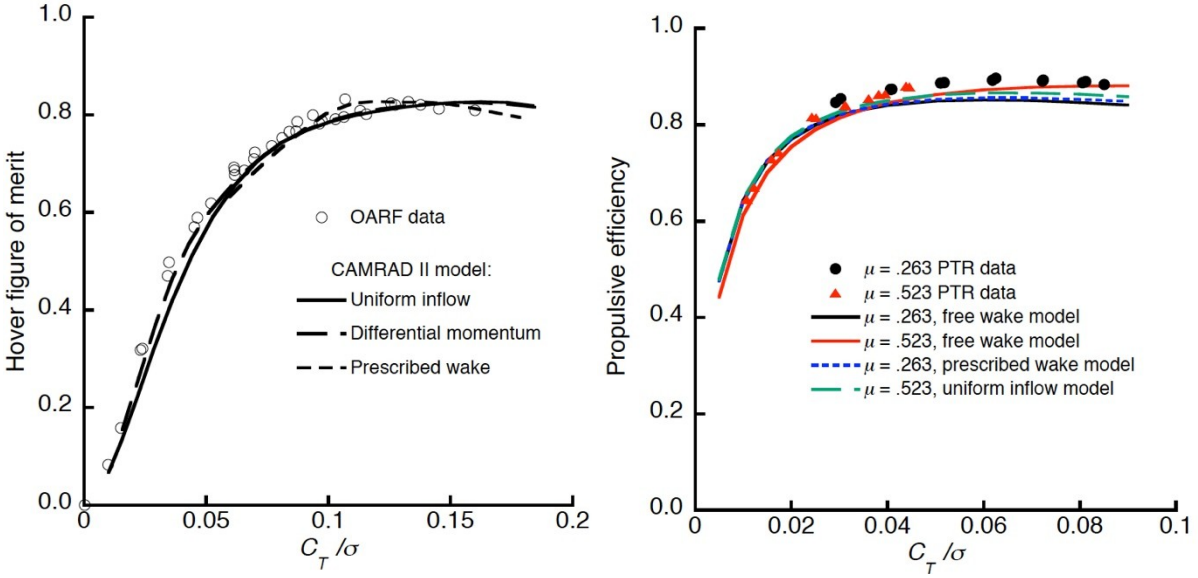

a) CAMRAD II hover predictions of JVX FM for three simplified aerodynamic models (Fig. 11 of Acree [2008a]).

b) Predictions of JVX propulsive efficiency made with three different aerodynamic models compared with test data (Fig. 17 of Acree [2008a].

Figure 2.29. JVX performance predictions for hover and airplane mode.

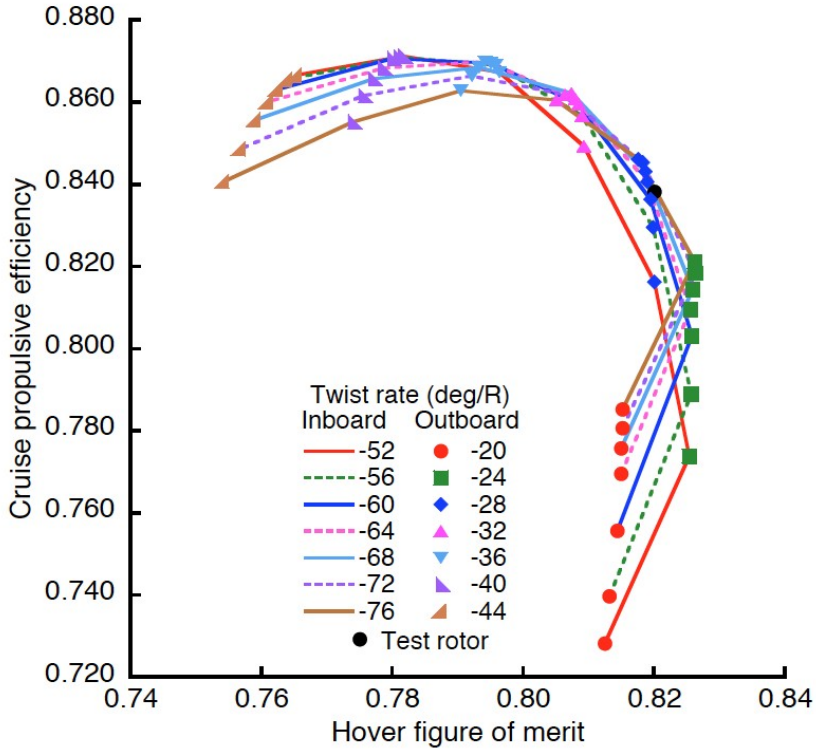

Figure 2.30. Bilinear twist optimization for the JVX rotor with a mixed inflow model (Fig. 23 of Acree [2008b]).

Acree [2016] conducted a very extensive analysis of the 0.656-scale-model JVX experimental results, with a particular emphasis on issues that could adversely impact experimental results. These included hub spinner tares, torque/thrust measurement interactions, and tunnel blockage effects. Primary recommendations for future experimentalists include the importance of including calibration data for all transducers as part of the resulting database, documentation of all data reduction equations, provisions for uncertainty and other statistical analyses, and the importance of pretest predictions as part of the test planning process.

Tiltrotor Aeroelasticity

One of the major aeroelastic issues associated with tiltrotors is whirl flutter stability, which would be exacerbated if proprotors were to become less stiff than they have traditionally been.

Zhang and Smith [2014] conducted an analytical parametric study of both wing extensions and winglets on whirl flutter speed. They used a quasi-steady aerodynamic model combined with a finite element structural model, applied to a three-bladed gimballed rotor based on the analytical model of the aforementioned XV-15, only with the wing torsion stiffness reduced by 50 percent to simulate a thinner wing. They developed an elastic winglet model that they used to evaluate various winglet geometric angles, as well as investigating the effects of composite tailoring of both wing extensions and winglets. The authors showed that wing tip devices can produce significant effects on both wing beam bending and torsion mode damping, but not on wing chord mode. By structurally tailoring both the main wing and wing extension, increases in whirl flutter speed between 75 and 150 knots from the baseline system were predicted.

Next, Costa et al. [2015] built upon this work, designing, building, and testing a series of three semispan tiltrotor wind tunnel models in the Penn State low-speed wind tunnel. The primary purpose of these experiments was to provide a relatively low cost means of validating the analytical models described above. The wind tunnel models were designed to have as low of a flutter speed as possible, so as to test up to that point within the operational capabilities of the tunnel. Different numbers of configurations were examined for each of the three models, labeled Gen-1, Gen-2, and Gen-3. The first two were unable to exhibit whirl flutter without the addition of extra mass to the wing trailing edge, but two configurations of the Gen-3 model did successfully demonstrate whirl flutter at 95 and 105 ft/sec. The authors showed very good agreement between the analytical and experimental results.

Yeo et al. [2017, 2018] conducted an analytical study of whirl flutter using both CAMRAD II and RCAS. The authors began with a very simple model of a generic three-bladed gimballed rotor, and then gradually added design variables one-by-one to improve the model. The effects of a great many tiltrotor design variables on whirl flutter speed were examined. Among the most significant results, they found that blade pitch-flap coupling has a significant influence on proprotor aeroelasticity, with increased positive coupling having a negative effect on stability, and that rotor lag mode has a significant effect on wing beam mode damping. In fact, reducing the yoke chord stiffness produced such significant decreases in damping that the system was unstable over the entire speed range examined. Perhaps most importantly, however, the authors found that CAMRAD II and RCAS showed very good agreement with each other, as shown in Figure 2.31.

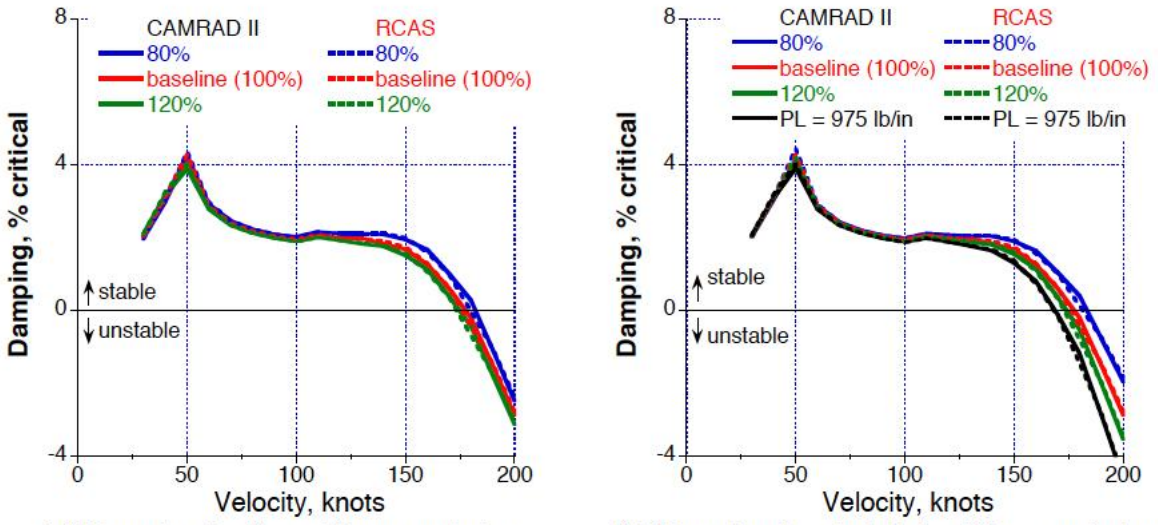

(a) Damping for flap stiffness variation. (b) Damping for pitch link stiffness variation.

Figure 2.31. Damping of wing beam mode with yoke flap stiffness and pitch link stiffness variation (Yeo et al. [2017]).

Large Heavy Lift Tiltrotors

Over the past decade, one of the major focus areas of the NASA rotorcraft effort has been potential designs for a large, heavy-lift tiltrotor, typically referred to initially as the LCTR, and then after design changes, as the LCTR2. In fact, many of the JVX studies described above were conducted with this focus in mind. The initial LCTR concept (also referred to as LCTR1) was designed to carry 120 passengers for 1200 nm, with performance of 350 knots at 30,000 feet altitude at a gross weight of 124,000 pounds, while the LCTR2 was designed to carry 90 passengers at 300 knots over at least a 1,000-nm range.

Acree [2010] examined both rotor performance and aeroelastic stability for the initial LCTR design. This concept had a low wing (as opposed to the high wing for both the XV-15 and V-22), hingeless rotors, and an extremely low cruise tip speed of 350 ft/sec. The U.S. Army Aeroflightdynamics Directorate's design code, RC, was used for the vehicle sizing, CAMRAD II was used for the performance, loads, and stability calculations, and a NASTRAN model was used for the airframe. He included new airfoil designs for both the rotors and wing, compared them to current airfoils, and conducted a design optimization across multiple design parameters, with particular emphasis on twist, taper, and precone. The new airfoils were intended to provide improved cruise performance, which he demonstrated, and the optimization calculations resulted in a design with a hover FM of 0.79 and a propulsive efficiency of 0.83.

Yeo and Johnson [2007] examined the aerodynamic interference effects on tiltrotor performance for two different tiltrotor concepts—a traditional design with a single wing and two rotors, and a quad tiltrotor, with two wings and four rotors. The basic size of the conventional tiltrotor was determined using RC, with the performance computed via CAMRAD II. The quad tiltrotor was developed based on that sizing, using the same gross weight (146,600 pounds), disk loading (15 lb/ft^2), airframe size, and even rotor tip speeds in both helicopter (750 ft/sec) and propeller (625 ft/sec) modes. The authors conducted a parametric study to assess the relative impact of various design parameters on the performance of the two designs. Aerodynamic effects were found to enhance the vehicle lift-to-drag ratio for the conventional tiltrotor design, while adversely impacting that of the quad tiltrotor, primarily due to interference effects from the forward to aft rotors and wings. They also found that, of all the design variables evaluated, lowering rotor tip speed produced the largest improvement in lift-to-drag ratio.

Johnson et al. [2007] examined the aerodynamic performance of rotorcraft designed for heavy lift and high-speed cruise, in a joint investigation between NASA and the U.S. Army at Ames Research Center. The NASA Heavy Lift Rotorcraft Systems Investigation examined in depth several rotorcraft configurations for large civil transport, designed to meet the technology goals of the NASA aeronautics program. Further explorations were conducted of the performance of tiltrotor, compound helicopter, and lift-offset rotor configurations, for both military and civil missions. Figure 2.32 shows the wake geometry of conventional and quad tiltrotors. The performance metric is total power, in terms of equivalent aircraft lift-to-drag ratio, where L/D = WV/P for cruise, and FM for hover. These investigations have shown that heavy-lift, high-speed, long-range rotorcraft can be designed that are economically competitive and operationally effective, with the potential for substantial impact on both civil and military air transportation systems.

Next, Acree and Johnson [2008] examined the aeroelastic stability of the LCTR2, focusing on whirl flutter stability in cruise. The extremely large size of the LCTR2 (nominally three times the gross weight of the V-22) requires significantly different wings and rotors than prior art, with the potential for major differences in aeroelastic behavior than seen previously. By this point, the rotor tip speeds for the conventional LCTR2 conceptual design had been reduced to the extremely low values of 650 ft/sec in hover and 400 ft/sec in cruise. Again, the impacts of multiple design parameters were assessed using CAMRAD II. The authors found that the first rotor lag mode, coupled with the wing torsion motion, was the critical mode for stability, while rotor flapwise stiffness was the most sensitive of the parameters evaluated. However, they identified several other parameters, in particular wing flapwise, chordwise, and torsional stiffness, along with rotor pitch-link, lag, and torsional stiffness, that showed significant nonlinear effects on whirl flutter stability. They then made extensive recommendations as to future LCTR2 research.

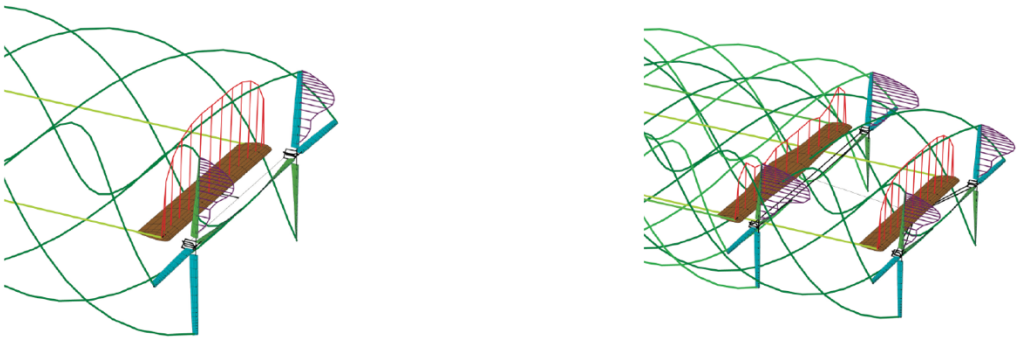

Figure 2.32. Wake geometry of conventional tiltrotor and quad tiltrotor (Figs. 21 (left) and 22 (right) of Johnson et al. [2007]).

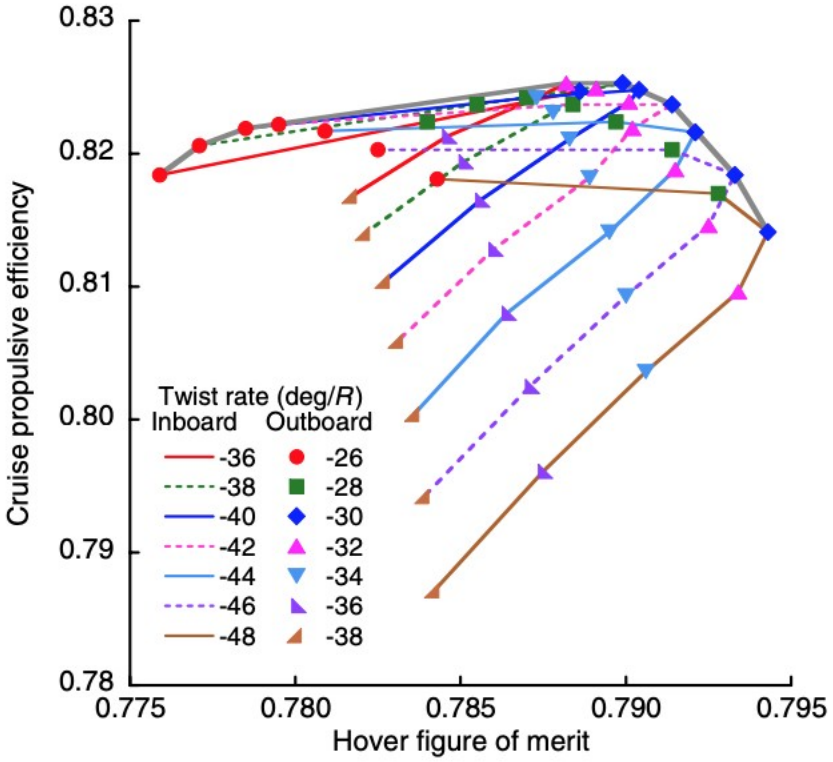

Figure 2.33. Large Civil Tiltrotor (LCTR2)—example twist optimization map for nominal tip speed, solidity = 0.150 (Fig. 7 of Acree et al. [2008b]).

Around the same time, Acree et al. [2008a, 2008b] conducted a performance optimization and analysis of the LCTR2 concept, which had a low wing (as opposed to the high wing for both the XV-15 and V-22), hingeless rotors, and an extremely low cruise tip speed of 350 ft/sec (hover tip speed of 650 ft/sec). The aerodynamic performance optimization for twist (Fig. 2.33), taper, and solidity included rotor/wing interference effects, while performance during turns and hover/cruise tradeoffs at varying tip speeds were also assessed. As above, RC was used for the vehicle design, with CAMRAD II used for the aerodynamic analysis. The rotor/wing interference effects were found to produce slight improvements in cruise efficiency, while the optimum cruise tip speed was somewhat higher than expected. The authors attributed the latter to likely being due to slight changes in torque and blade load distribution. They also found that reducing root airfoil thickness significantly improved cruise performance.

In related work, Yeo et al. [2008] examined blade loading criteria for such heavy life tiltrotors as the LCTR2 and the Army's High Efficiency Tiltrotor (HETR). Similar to the previous papers discussed above, RC was used for the aircraft sizing, while CAMRAD II was used for all hover, cruise, and turn performance calculations. The authors selected a 45-degree banked turn at 80 knots to determine the key blade loading criterion during a continuous maneuver. Three different criteria were examined: available aircraft power, stall boundary as determined by slope of aircraft power, and stall boundary as determined by rotor profile power. They found that it is possible to meet available power criteria, while still having a significant increase in rotor profile power, which very likely indicates a stalled rotor condition. Thus, there would be a very high potential that the vehicle's maneuver capability might be limited. This was addressed by slightly increasing the rotor solidity (by 2.3 percent) to meet the maneuver design criterion. Both vehicle designs were then updated using the new solidity, which slightly degraded the vehicle performance for each. For the LCTR2, this resulted in a slight decrease in mission range, while for the HETR, mission range was fixed, so a slight increase in gross weight was required instead. Figure 2.34 shows the updates to both the LCTR2 and HETR designs.

Theodore et al. [2014] presented results from a joint NASA/Army test of two, nominally 6 percent airframe models, the NASA LCTR (Fig. 2.35) and the Army's HETR, in the U.S. Army 7- by 10-Foot Wind Tunnel at NASA Ames. Along with force and moment measurements on these unpowered models, flow visualization via tufts, infrared thermography, and oil flow data were also acquired in order to examine such flow phenomena as trajectories, boundary layer transition, and separation. These results were intended for validation of the predictions of conceptual design performance and CFD tools, as well as for the development of flight simulation models. While data were acquired in both airplane and helicopter modes for both models, the authors emphasized results in airplane mode at 200 knots. Multiple wing tips and nacelle configurations were evaluated, as well as a wing-only case. They found that the nacelles increased lift when compared to the wing-alone case, and that wing extensions outboard of the nacelles produced a notable increase in lift-to-drag ratio, while somewhat surprisingly simultaneously reducing drag. This was particularly seen in the region of maximum L/D (nominally +2 degrees)—see Figure 2.36. The authors speculated that this drag decrease was likely due to aerodynamic interactions between the nacelle and the wing extension.

	HETR		LCTR2	
	baseline	update	baseline	update
Design gross weight (lb)	142,800	146,480	107,500	107,100
Op. Wt. empty (lb)	89,131	92,180	67,300	67,630
Rotor diameter (ft)	75.0	75.9	65.0	65.0
Disk loading W/A (lb/ft^2)	16.16	16.19	16.20	16.14
Rotor solidity (thrust weighted)	0.110	0.118	0.130	0.133
C_W/σ (thrust weighted)	0.154	0.144	0.154	0.151
Rotor weight (lb)	10,844	13,370	8,756	8,891
Hover FM	0.783	0.778	0.787	0.783
Cruise η	0.873	0.851	0.870	0.837
Cruise L/D$_e$	10.3	10.1	10.1	9.4
Mission range (nm)	500	500	1,246	1,102

Figure 2.34. LCTR2 and HETR design updates (Table 2 of Yeo et al. [2008]).

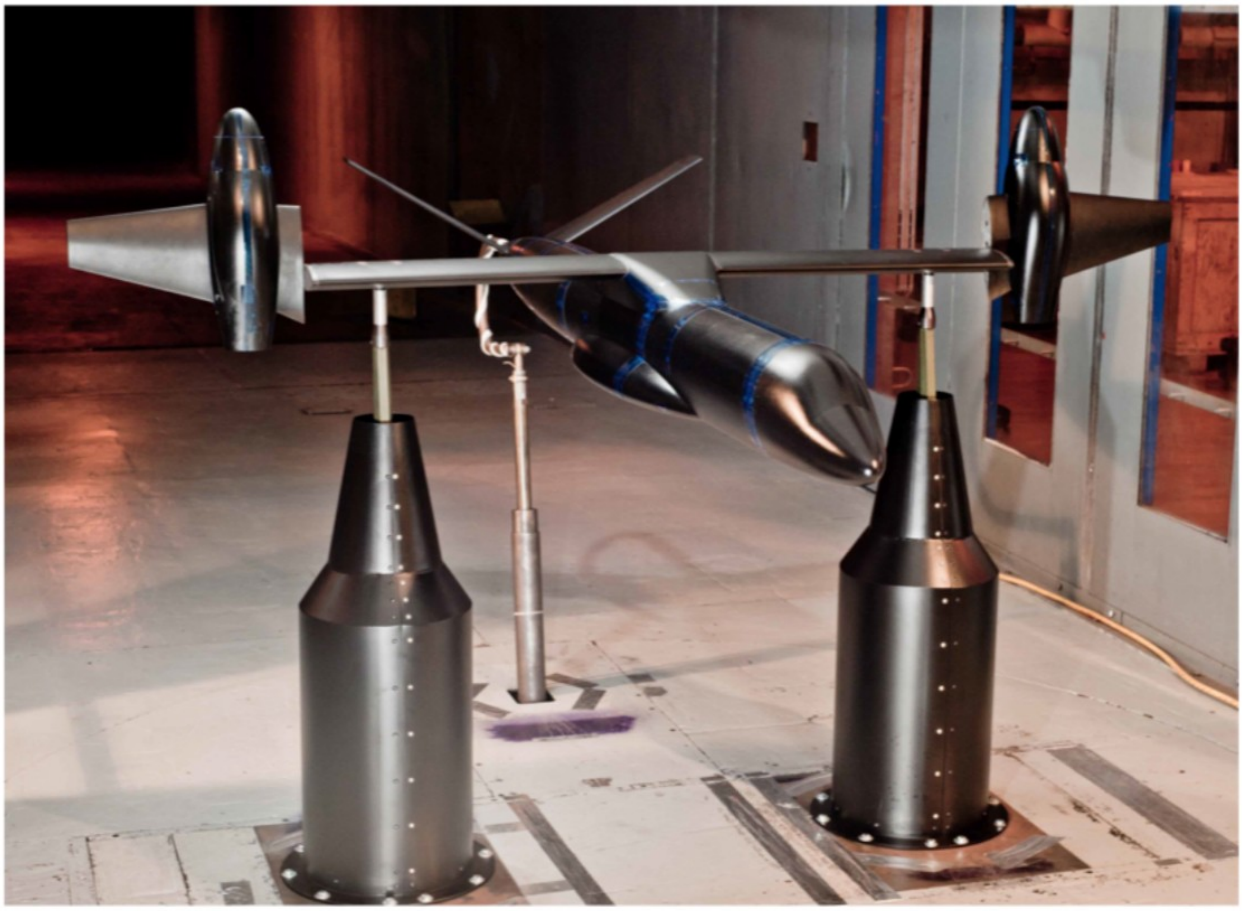

Figure 2.35. LCTR model in helicopter mode. The strut and fairing configurations shown were used for low-speed testing (Fig. 2 of Theodore et al. [2014]).

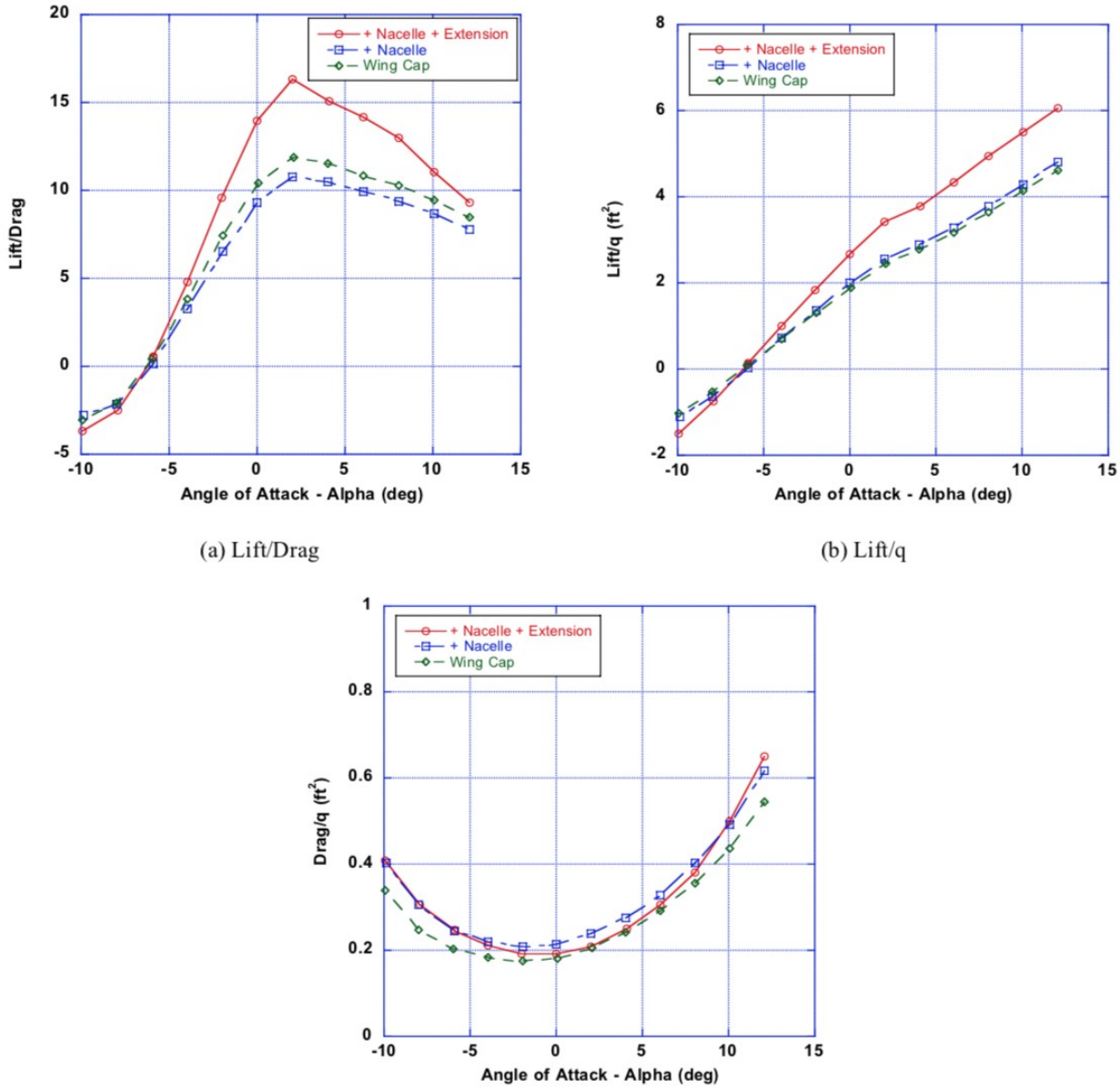

Figure 2.36. Effect of wing-tip configuration on LCTR airframe model aerodynamic loads for slideslip angle = 0°, V = ~168 kt, and Re = 1.2 x10^6 (Fig. 10 of Theodore et al. [2014]).

Operational Issues

For an eventual civil LCTR2 vehicle to be viable commercially, and to significantly offload traffic at the many major airports already operating at or near capacity, the vehicle must be able to safely operate in urban areas, with vertiports located at places such as the rooftops of tall buildings, parking garages, etc., or even perhaps at a vertiport collocated with an existing airport by use of simultaneous, non-interfering (SNI) operations. Obviously, in many cases there will likely be other, perhaps taller, buildings, nearby. Young et al. [2013] used RotCFD, a hybrid CFD tool specifically developed for conceptual designs, to examine rotor wake interactions of tiltrotors in the vicinity of such ground infrastructure, as shown in Figure 2.37. The authors initially validated the use of RotCFD for this purpose by comparing outcomes to V-22 downwash experiments, with encouraging results in comparing rotor thrust and power. They then gradually developed more detailed models of the region around the vehicle, starting with large flat plates and ending up with a notional vertiport terminal building. They also performed an initial simulation of a potential interaction between an LCTR and a small General Aviation (GA) aircraft.

Later, Young [2015] expanded upon the above work by performing validation studies of RotCFD's ability to predict tiltrotor operations in urban vertiports using data acquired in the early 2000s in the U.S. Army 7- by 10-Foot Wind Tunnel on a nominal 1/48-scale wind tunnel model. In-ground-effect results showed good agreement between the two if rotor thrust was accurately matched, while the results for the building/tiltrotor interaction comparison were not nearly as good, with some trends not even moving in the same direction. Young speculates on potential reasons for the disagreement, including use of a fully-turbulent CFD model, discrepancies between the model and RotCFD geometries, gridding resolution between the vehicle and the building, and biases due to the predicted building wake.

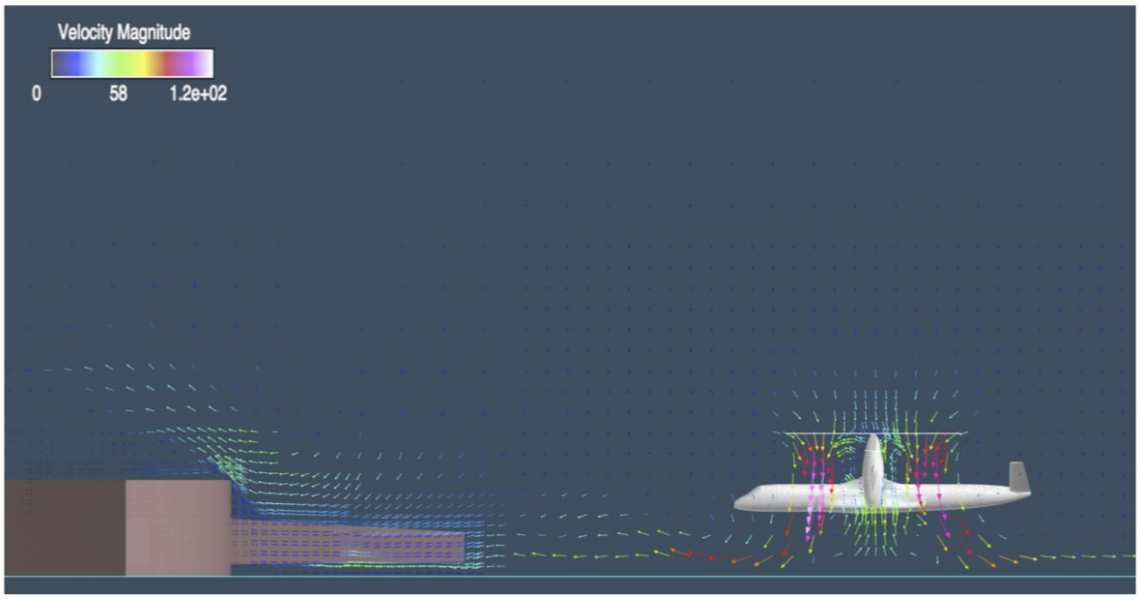

Figure 2.37. LCTR2 operating at a height-to-rotor radius ratio of 1.39 (Fig. 20a of Young et al. [2013]).

Tiltrotor Modeling

Koning et al. [2016] used RotCFD to predict the performance of an isolated XV-15 tiltrotor in multiple operational states and validated the results via comparison with previously acquired experimental data. Comparisons with hover data from the OARF using a stall-delay model were quite favorable except at the highest thrust levels, while those using the tip-loss model were significantly less so (see Fig. 2.38). In tiltrotor mode (nacelle angles from 15 to 75 degrees), the authors found that RotCFD results agreed quite well with measured results from the NFAC, while the airplane-mode results typically underpredicted the proprotor performance, but at a level comparable to that found from CAMRAD II predictions. Overall, they felt that RotCFD was an adequate tool to examine wind tunnel wall effects on isolated rotor performance, which led to the next study.

Koning [2016] used RotCFD to examine wind tunnel interference effects, working with an XV-15 isolated rotor model in the NFAC. He simulated hover, tilt, and airplane modes; the latter two were compared to previously existing wind tunnel and theoretical data, showing reasonably good correlation with both, while the hover comparisons were made using data from the OARF. For the hover data, Koning found that the tip loss model overcorrected, likely due to the tip vortex or pressure equalization over the blade tip, whereas the wind tunnel comparison in both tilt and airplane modes showed very good agreement. He then simulated wall interference effects in both NFAC test sections for both an isolated rotor and one mounted on the Tiltrotor Test Rig (TTR). He used a "quasi linear trim" to enable comparison of power as a unique variable, finding differences of –7 to 0 percent between free-field and wind tunnel conditions in the NFAC 80- by 120-foot test section and –1.6 to 4.8 percent in the 40- by 80-foot test section.

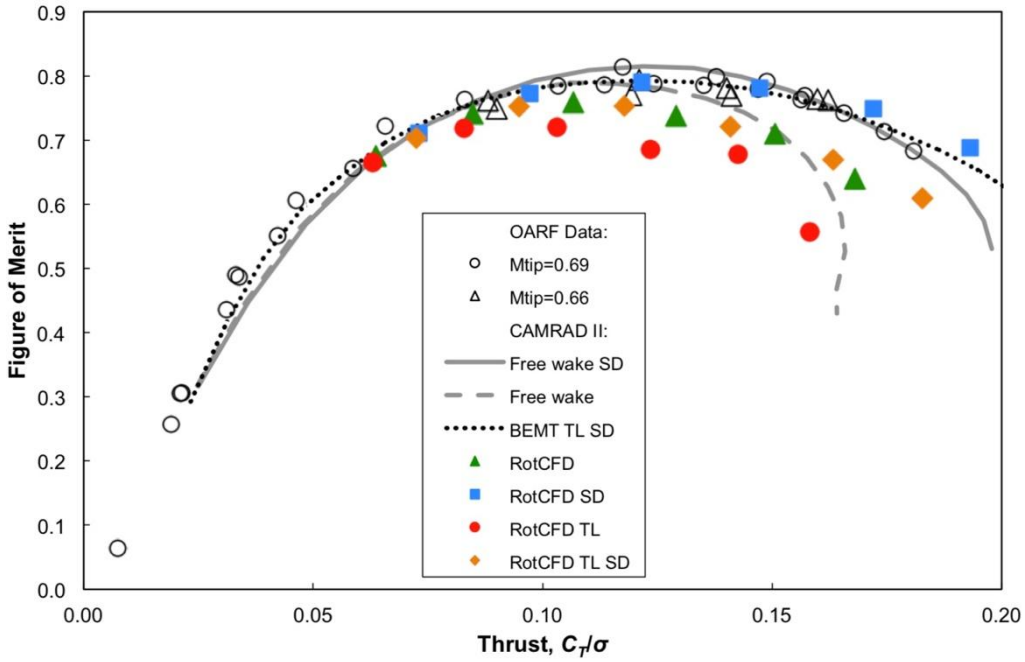

Figure 2.38. RotCFD and CAMRAD II results compared with measured XV-15 isolated rotor hover FM as a function of thrust (Fig. 5 of Koning et al. [2016]). BEMT = blade element momentum theory, TL = tip loss, and SD = stall delay.

Tiltrotor Test Rig (TTR)

Acree and Sheikman [2018] describe the TTR, a national capability designed and developed as a joint NASA/Army/Air Force proprotor test system. The TTR was designed for the NFAC in order to provide unprecedented capability to examine combinations of rotor size (26 feet diameter) and speed (up to 300 knots), which will be critical for validation of the variety of design and analysis tools, both those in use today and enhanced tools developed in the future. The authors describe the rotating and nonrotating TTR instrumentation, summarize the multi-year TTR development activities, and list the test objectives of the check-out test. Figure 2.39 shows the TTR installed in the wind tunnel. Figure 2.40 lists the attributes of the TTR and the rotor system.

A critical part of the development of any new rotor test rig is determining the frequency response of the system, most typically measured via either shake or impact testing. Russell and Acree [2018] reviewed the shake testing conducted for the TTR, describing the test procedure and results from that testing, with comparisons to a finite element analysis using NASTRAN. They showed frequency response functions for a number of different test configurations, as well as images of both the predicted and measured key mode shapes. Random shaking, swept sine shaking, and hammer impact were all used to attempt to excite those key modes. Comparing the impact and shake test results, the authors found generally good agreement between the two test techniques, indicating that impact testing is a reasonable alternative to shake testing. However,

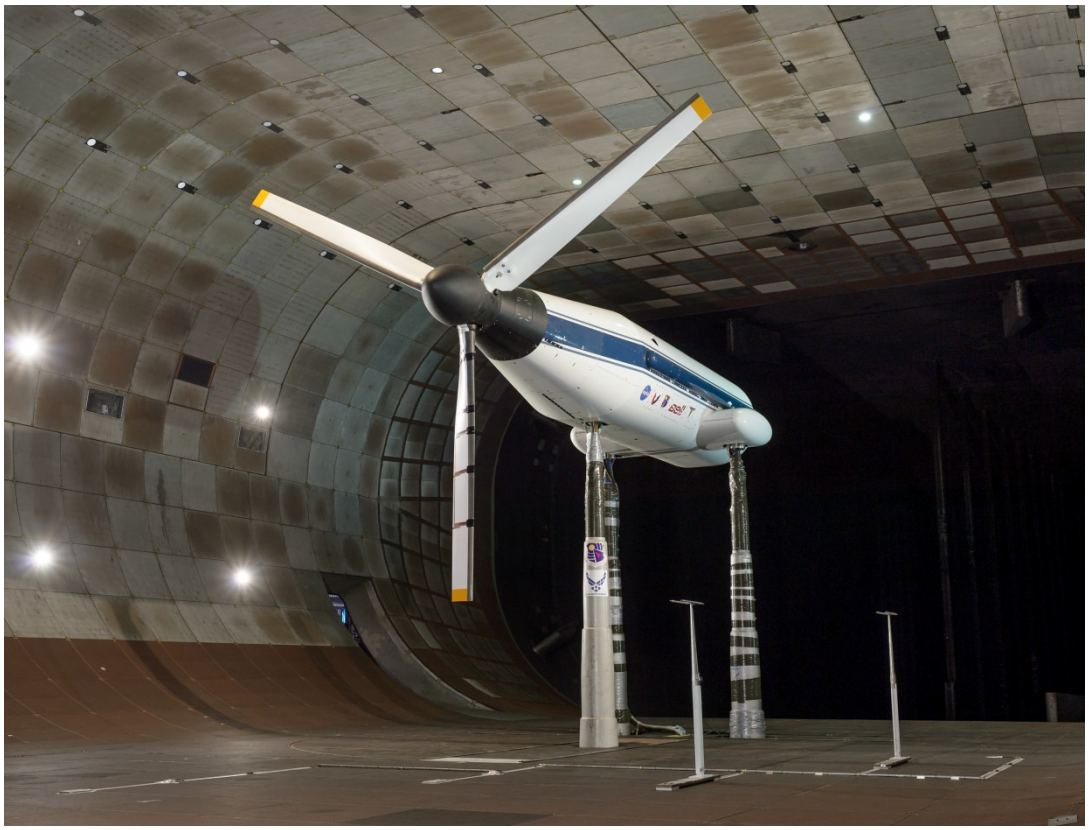

Figure 2.39. TTR in the test section of the NFAC 40- by 80-Foot Wind Tunnel, oriented in airplane mode (0° yaw) (Fig. 1 of Acree and Sheikman [2018]).

they did caution that there were notable differences in the modal damping results between the two approaches. Very little difference was found between swept sine and random shaking, except at low off-peak frequencies. While mode shapes were well predicted with the NASTRAN analysis, the predicted frequencies did not agree nearly as well with the test results. The authors further recommend that, if either the rotor or testing configuration is changed, impact test results should be verified with at least a brief random shake test. Figure 2.41a shows the setup for lateral shaking at the hub, with a close-up of the hub area shown in Figure 2.41b.

Length, including spinner	435 in
Width, main nacelle only	85 in
Width, including pylons	140 in
Depth, main nacelle only	67 in
Weight, including rotor	60,800 lb
Rotor hub position:	
fwd of balance center	88 in
height above floor (40x80)	234 in
Power, max design	6,000 hp
Power, max qualified (30 min)	5,500 hp
Power, continuous (2 hr)	5,000 hp
Rotor shaft speed, max	629.5 rpm
Max airspeed, 0-deg yaw	300 knots (305 lb/ft^2)*
Max airspeed, 90-deg yaw	180 knots (110 lb/ft^2)*

*40x80 limit=262 lb/ft^2, 80x120 limit=33 lb/ft^2

a) TTR dimensions and design capabilities (Table 1 of Acree and Shiekman [2018]).

Number of blades	3
Diameter	26.0 ft
Disc area (per rotor)	530.9 ft^2
Solidity (thrust weighted)	0.0908
Blade chord (thrust weighted)	14.83 in
Blade area (per rotor)	48.2 ft^2
Blade twist (non-linear)	47.5 deg
Blade planform	linear taper
Blade tip shape	square
100% rotor speed (helicopter mode)	569 rpm
Tip speed	775 ft/sec
84% rotor speed (airplane mode)	478 rpm
Tip speed	651 ft/sec
Collective range*	61.5 deg
Gimbal limit (flapping stop)	±11 deg
Precone	2.75 deg
Undersling	0.36 in
Delta-3	−15 deg
Direction of rotation (looking aft)*	CCW

*As installed on TTR.

b) TTR rotor characteristics (Table 3 of Acree and Shiekman [2018]).

Figure 2.40. Characteristics of the TTR.

a) Lateral shaking at the hub—90° yaw (helicopter mode) (Fig. 3 of Russell and Acree [2018]).

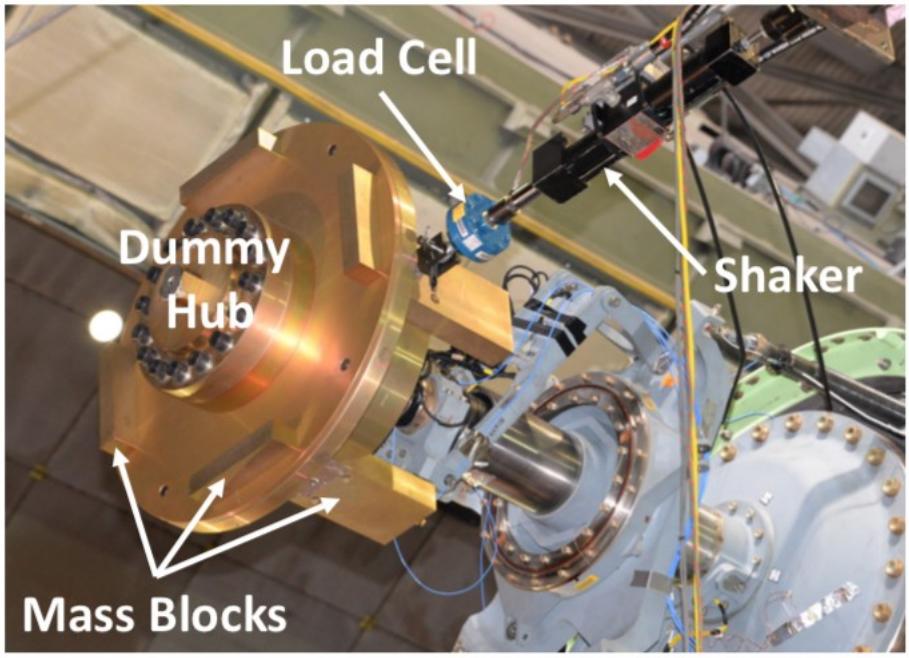

b) Hardware close-up—lateral shaking at the hub (Fig. 7 of Russell and Acree [2018]).

Figure 2.41. TTR shake-test setup in the test section of the NFAC 40- by 80-Foot Wind Tunnel.

Kottapalli and Acree [2018] used CAMRAD II to provide pre-test predictions of the performance, loads, and whirl flutter stability of the isolated research proprotor (based on the AW609 rotor), to be tested on the TTR in the NFAC 40- by 80-Foot Wind Tunnel. Performance and loads were predicted for hover, helicopter mode, conversion, and cruise (i.e. airplane mode), using flexible blades and hub, but with no fixed system flexibility. For the stability calculations,

the fixed system dynamics were determined based on the shake test of the TTR. Initially, the authors performed a "sanity check" by comparing their results to previous JVX predictions, since the two proprotors are very similar. These pre-test predictions were used to guide the development of the test matrix to ensure the test would be conducted safely. Their predictions showed that there would likely be some limitations on the test matrix because of performance and loads, but that the proprotor/TTR combination should be quite stable within the test envelope. Figure 2.42 shows two similar predictions of the helicopter stability envelope, one based on rap test data and one based on shake test data.

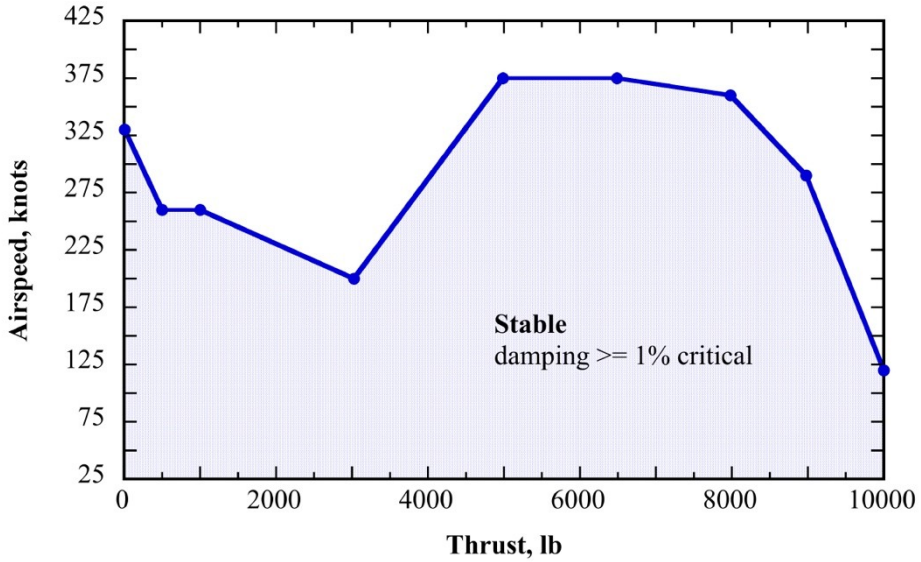

a) 1 percent damping stability envelope, 90° yaw, 569 RPM—rap test modal data. (Fig. 11a of Kottapalli and Acree [2018]).

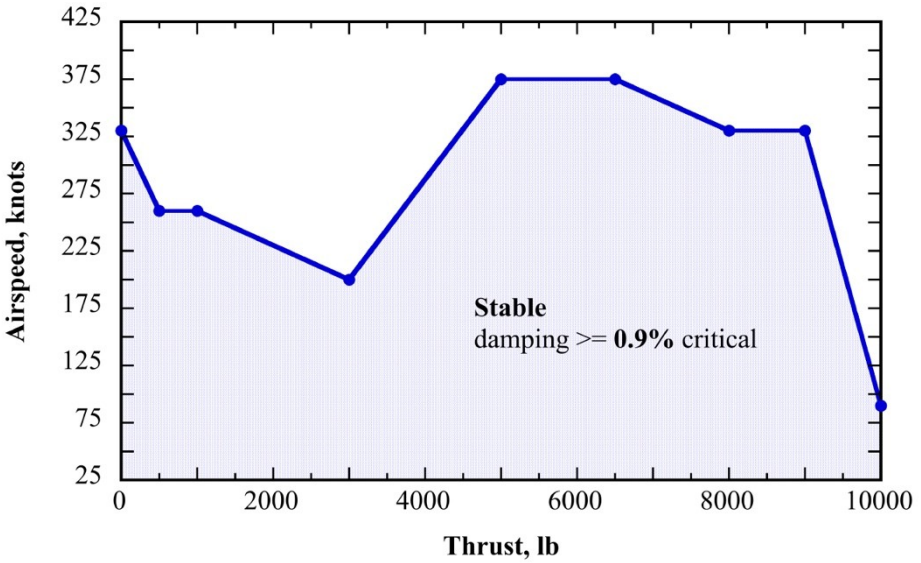

b) 0.9 percent damping stability envelope, 90° yaw, 569 RPM—shake test modal data (Fig. 11c of Kottapalli and Acree [2018]).

Figure 2.42. Predicted TTR/proprotor stability envelope in helicopter mode.

The TTR test was eventually completed in November 2018, after a delay of nearly 12 months because of issues with the NFAC fan drive system.

Test accomplishments included:

- Acquired hover/vertical-climb data in several NFAC configurations.
- Performed airplane-mode thrust sweeps up to 264 knots.
- Acquired extensive airplane-mode data at two tip speeds.
- Performed thrust sweeps over most of the rotor conversion envelope.
- Acquired acoustics reference data at all test points.
- Acquired a total of 3314 data points—more than enough to evaluate TTR test capabilities and limitations.
- Identified areas requiring upgrades/modifications (e.g., control system).

Acree et al. [2019] provides a summary of the test and provides examples of the most significant data (Fig. 2.43, for example). This new test rig is now available for proprotor performance measurements at unprecedented power, speed, and accuracy.

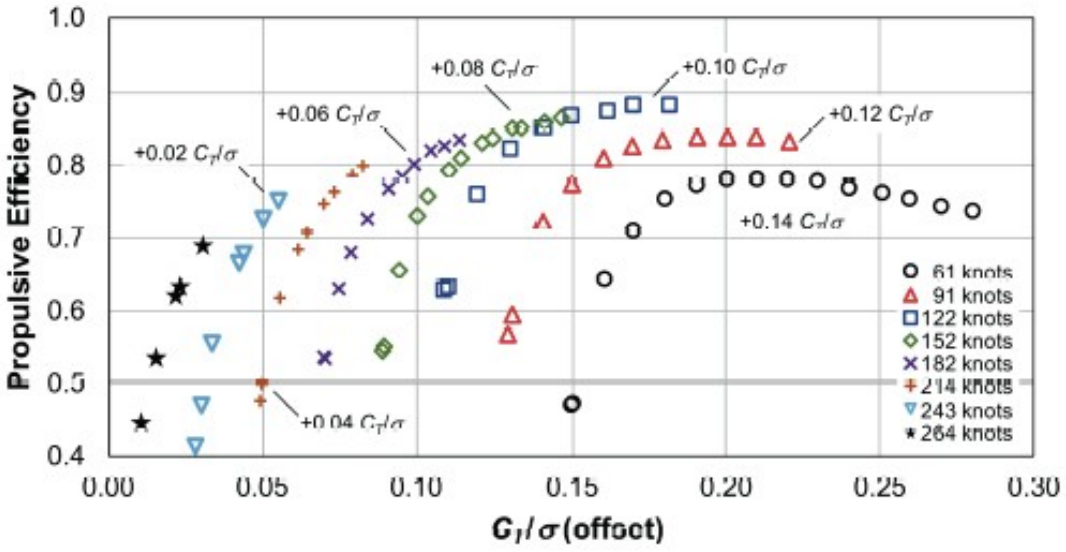

Figure 2.43. TTR/699 propulsive efficiency at Mtip = 0.583. Each speed is offset by CT/σ = 0.02 (Fig. 33 of Acree et al. [2019]).

GENERAL AEROMECHANICS

A series of papers focused on analytical models of vortices and vortex filaments was published by Young during 2007–2008.

The effect of initial vorticity distribution on axisymmetric vortex breakdown and reconnection was studied by Young [2007a] for laminar flow. Breakdown and reconnection were related to phenomena such as blade-vortex interaction (BVI) or other vortex-body interactions. The author reduced the Helmholz equation to the unsteady heat equation, enabling analytical solutions to a diverse set of vortex breakdown flow structures.

Young [2007b] next developed a new analytical model for a family of vortices such as those typically found in the wakes of vehicles that employ either rotors or propellers for their propulsive force. These prescribed, laminar vortices can be either single- or dual-core and can be either columnar or filaments undergoing reconnection and breakdown. The columnar results are exact solutions of the Helmholtz equations, while the others are only approximate solutions, but are 3D and should provide overall insight into such complex flows. The result of the model is both the vorticity and velocities for each member of the group of vortices. He also examined Reynolds number effects on vortex reconnection utilizing turbulent effective viscosity to simulate mean turbulent flow and found that they had little effect on the overall flow behavior. Young proposed that this model could be extended to model AFC techniques that seek to modify the principal vortical flow via either a periodic or pulsed control approach.

Continuing the work of Young [2007a, 2007b], Young [2008a] describes a new analytic model of the flow behavior resulting from pulsed or periodic disruption to line vortices. Three different forms of disruption were studied: spatial cuts or breaks, embedded inner core negative vorticity, and/or sinusoidal varying circulation. The feasibility of a fourth disruption—destabilization—was also explored. The author discusses the relevance of the results with respect to active and passive control of vortical structures. Modeling a turbulent line vortex was the next focus for Young [2008b]. The derived turbulent vortex model was a hybrid stochastic/deterministic solution. The preliminary analysis represented a significant departure from previous work in the literature, according to the author, and provided a proposed analytical framework that addressed poorly understood aspects of turbulent vortex behavior. For example, novel results from the work included the modeling of vortex transition from laminar to turbulent flow states and the modeling of a relaminarization process for turbulent vortices.

Quackenbush and Wachspress [2008] also studied rotor performance at high advance ratios. The objective of their research was to enhance modeling capabilities for extreme advance ratios to support future advanced VTOL configurations. The first phase of their research included a three-pronged approach: 1) model testing of a 52-inch-diameter, three-bladed rotor in the Glenn L. Martin Wind Tunnel at the University of Maryland up to an advance ratio of 1.7; 2) development of initial enhancements of yawed flow corrections and new lifting-surface models for CHARM, a comprehensive analysis developed by the authors at Continuum Dynamics, Inc.; and 3) eventual identification and demonstration of high-fidelity CFD methods. The wind tunnel data revealed key aspects of rotor behavior in this challenging flight regime and contributed valuable validation data.

For nearly 7 years, Frank Harris worked on a three-volume book, *Introduction to Autogyros, Helicopters, and Other V/STOL Aircraft*. The book was published as a NASA Special Publication and funded by the RVLT Project and the U. S. Army. Each volume is a tome—written in the first person in Frank's inimitable style—and packed with information, references (nearly 1,600 in all three volumes), and appendices.

In *Volume I: Overview and Autogyros* [Harris, 2011] (567 pages), Harris provided a brief overview of the development of the helicopter. He identified four major milestones in this development: successful demonstration of the autogyro by Juan de la Cierva, demonstration of a practical helicopter by E. H. Henrich Focke, demonstration of the Model VS-300 single main rotor helicopter by Igor Sikorsky, and the influential First Convertible Aircraft Congress meeting in 1949 (which generated an intense search for VTOL aircraft). The majority of Volume I was devoted to the Autogyro.

In *Volume II: Helicopters* [Harris, 2012] (946 pages), the author addressed eight topics related to helicopter shortcomings (and why the problems are difficult to solve): engines, weight, performance, vibration, noise, purchase price, operating costs, and safety record. Harris provided suggestions to overcome these shortcomings in the conclusion section of this volume.

Volume III: Other V/STOL Aircraft [Harris, 2015] (796 pages) focused primarily on rotary wing performance at high advance ratios and low-speed fixed-wing performance. Harris also examined 100 V/STOL aircraft and selected 16 as examples of what has been accomplished over nine decades.

A fitting end to this chapter on aeromechanics is the tribute to Professor René H. Miller written by three of his former students: Peretz Friedmann, Wayne Johnson, and Michael Scully (see Friedmann et al. [2011, 2012]). The authors review the life and career of one of the most influential pioneers in rotary wing aeromechanics. Professor Miller was also a visionary whose dream was the development of a tilt-wing/tilt-rotor-based, short-haul air transportation system.

REFERENCES

Abhishek, A., Ananthan, S., Baeder, J., and Chopra, I., "Prediction and Fundamental Understanding of Stall Loads in UH-60A Pull-Up Maneuver," *Journal of the American Helicopter Society*, vol. 56, no. 4, JAHS.56.042005-1 to -14, Oct. 2011.

Acree, C. W., Jr., "Calculation of JVX Proprotor Performance and Comparisons with Hover and High-Speed Test Data," AHS Specialists' Conference on Aeromechanics, San Francisco, CA, Jan. 23-25, 2008a.

Acree, C. W., Jr., "Modeling Requirements for Analysis and Optimization of JVX Proprotor Performance," 64th Annual Forum of the American Helicopter Society, Montreal, Canada, April 29-May 1, 2008b.

Acree, C. W., Jr., "Modeling Requirements for Analysis and Optimization of JVX Proprotor Performance," NASA/TM–2008-214581, May 2008c.

Acree, C. W., Jr., "JVX Proprotor Performance Calculations and Comparisons with Hover and Airplane-Mode Test Data," NASA/TM–2009-215380, April 2009.

Acree, C. W., Jr., "Impact of Aerodynamics and Structures Technology on Heavy Lift Tiltrotors," *Journal of the American Helicopter Society*, vol. 55, no. 1, 2010.

Acree, C. W., Jr., "Assessment of JVX Proprotor Performance Data in Hover and Airplane-Mode Flight Conditions," NASA/TM–2016-219070, Feb. 2016.

Acree, C. W., Jr., and Johnson, W., "Aeroelastic Stability of the LCTR2 Civil Tiltrotor," American Helicopter Society Next Generation Vertical Lift Technologies Specialists' Meeting, Dallas, TX, Oct. 15-17, 2008.

Acree, C. W., Jr., and Sheikman, A.L., "Development and Initial Testing of the Tiltrotor Test Rig," 74th Annual Forum of the American Helicopter Society, Phoenix, AZ, May 2018.

Acree, C. W., Jr., Sheikman, A. L., and Norman, T. R., "High-Speed Wind Tunnel Tests of a Full-Scale Proprotor on the Tiltrotor Test Rig," 75th Vertical Flight Society Annual Forum & Technology Display, Philadelphia, PA, May 13-16, 2019.

Acree, C. W., Jr., Yeo, H., and Sinsay, J., "Performance Optimization of the NASA Large Civil Tiltrotor," NASA/TM–2008-215359, June 2008a.

Acree, C. W., Jr., Yeo, H., and Sinsay, J., "Performance Optimization of the NASA Large Civil Tiltrotor," International Powered Lift Conference, London, UK, July 22-24, 2008b.

Allan, B. G., and Schaeffler, N. W., "Numerical Investigation of Rotorcraft Fuselage Drag Reduction using Active Flow Control," 67th Annual Forum of the American Helicopter Society, Virginia Beach, VA, May 2011.

Allan, B. G., Schaeffler, N. W., Jenkins, L. N., Yao, C. S., Wong, O. D., and Tanner, P. E., "Active Aerodynamic Load Reduction on a Rotorcraft Fuselage with Rotor Effects - A CFD Validation Effort," 71st Forum of the American Helicopter Society, Virginia Beach, VA, May 2015.

Bauchau, O. A., and Sonneville, V., "Parallel Implementation of Flexible Multibody Dynamics Simulation Based on the Motion Formalism," IUTAM Symposium on Intelligent Multibody Systems–Dynamics, Control, Simulation, Sozopol, Bulgaria, Sept. 2017.

Boopathy, K., and Kennedy, G. J., "Adjoint-Based Derivative Evaluation Methods for Flexible Multibody Systems With Rotorcraft Applications," AIAA Paper 2017-1671, AIAA SciTech Forum, 55th Aerospace Sciences Meeting, Grapevine, TX, Jan. 9-13, 2017, DOI: 10.2514/6.2017-1671

Boopathy, K., and Kennedy, G. J., "Parallel Finite Element Framework for Rotorcraft Multibody Dynamics and Discrete Adjoint Sensitivities" *AIAA Journal*, vol. 57, no. 8, Aug. 2019, DOI: 10.2514/1J056585

Bousman, W. G., and Kufeld, R. M., "UH-60A Airloads Catalog," NASA/TM–2005-212827, 2005.

Bousman, W. G., and Norman, T., "Assessment of Predictive Capability of Aeromechanic Methods," American Helicopter Society Specialists' Conference on Aeromechanics, San Francisco, CA, Jan. 23-25, 2008.

Bousman, W. G., and Norman, T., "Assessment of Predictive Capability of Aeromechanic Methods," *Journal of the American Helicopter Society*, vol. 55, 012001, 2010, DOI: 10.4050/JAHS.55.012001

Bowen-Davies, G., and Chopra, I., "Investigation of the UH-60A Slowed Rotor Wind Tunnel Tests using UMARC," AHS 69th Annual Forum, Phoenix, AZ, May 21-23, 2013.

Callejo, O., and Bauchau, O. A., "Adjoint Sensitivity Analysis of Three-Dimensional Beam Formulation," ECCOMAS Thematic Conference on Multibody Dynamics, Prague, Czech Republic, June 19-22, 2017a.

Callejo, A., and Bauchau, O. A., "Efficient Design Optimization of Beam Cross-sections for Multibody Dynamics," Fifth Joint International Conference on Multibody System Dynamics, Lisbon, Portugal, June 2018.

Callejo, A., Bauchau, O. A., Diskin, B., and Wang, L., "Sensitivity Analysis of Beam Cross-Section Stiffness Using Adjoint Method," ASME 2017 IDETC, paper no. 67846, 2017.

Callejo, A., Sonneville, V., and Bauchau, O. A., "Discrete Adjoint Method for the Sensitivity Analysis of Flexible Multibody Systems." *Journal of Computational and Nonlinear Dynamics*, advanced on-line publication Aug. 15, 2018, doi:10.1115/1.4041237

Chandrasekhara, M .S., Martin, P. B., and Tung, C., "Comprehensive Dynamic Stall Performance of a Variable Droop Leading Edge Airfoil with a Gurney Flap," *Journal of the American Helicopter Society*, vol. 53, no. 1, Jan 2008, pp 18-25.

Copp, P., and Chopra, I., "Continued Development of a Mach Scale Swashplateless Rotor with Integrated Trailing Edge Flaps," 64th Annual Forum of the American Helicopter Society, Montreal, Canada, April 29-May 1, 2008.

Costa, G., Kambampati, S., Johnson, S., and Smith, E., "Design, Fabrication, Test and Evaluation of Small-Scale Tiltrotor Whirl Flutter Wind Tunnel Models," 71st Annual Forum of the American Helicopter Society, Virginia, Beach, VA, May 2015.

Datta, A., and Johnson, W., "Three-Dimensional Finite Element Formulation and Scalable Domain Decomposition for High Fidelity Rotor Dynamics Analysis," 65th Annual Forum of the American Helicopter Society, Grapevine, TX, May 27-29, 2009.

Datta, A., and Johnson, W., "Large-Scale Domain Decomposition for a Scalable, Three-Dimensional Brick Finite Element Based Rotor Dynamic Analysis," AHS Aeromechanics Specialists' Conference, San Francisco, CA, Jan. 20-22, 2010.

Datta, A., and Johnson, W. "Three-Dimensional Finite Element Formulation and Scalable Domain Decomposition for High Fidelity Rotor Dynamic Analysis," *Journal of the American Helicopter Society*, vol. 56, no. 2, April 2011.

Datta, A., and Johnson, W. "Integrated Aeromechanics with Three-Dimensional Solid-Multibody Structures," American Helicopter Society 70th Annual Forum, Montreal, Canada, May 2014.

Datta, A., Yeo, H., and Norman, T., "Experimental Investigation and Fundamental Understanding of a Slow UH-60A Rotor at High Advance Ratios," Proceedings of the 67th Annual Forum of the American Helicopter Society, Virginia Beach, VA, May 3-5, 2011.

Datta, A., Yeo, H., and Norman, T. R., "Experimental Investigation and Fundamental Understanding of a Full-Scale Slowed Rotor at High Advance Ratios," *Journal of the American Helicopter Society*, vol. 58, no. 2, April 2013.

Falls, J., Datta, A., and Chopra, I., "Performance Analysis of Trailing-Edge Flaps in Helicopter Primary Control," AHS Specialists' Conference on Aeromechanics, San Francisco, CA, Jan. 23-25, 2008.

Floros, M. W., and Johnson, W. "Stability and Control Analysis of the Slowed-Rotor Compound Helicopter Configuration," *Journal of the American Helicopter Society*, vol. 52, no. 3, July 2007.

Floros, M. W., and Johnson, W. "Performance Analysis of the Slowed-Rotor Compound Helicopter Configuration," *Journal of the American Helicopter Society*, vol. 54, no. 2, April 2009.

Friedmann, P. P., Johnson. W., and Scully, M. P., "A Tribute to Professor René H. Miller: A Pioneer in Aeromechanics and Rotary Wing Flight Transportation," 67th Annual Forum of the American Helicopter Society, Virginia Beach, VA, May 3-5, 2011.

Friedmann, P. P., Johnson. W., and Scully, M. P., "A Tribute to Professor René H. Miller: A Pioneer in Aeromechanics and Rotary Wing Flight Transportation," *Journal of the American Helicopter Society*, vol. 57, no. 4, Oct. 2012, DOI: 10.4050/JAHS.57.042004

Guntupalli, K., Novak, L. A., and Rajagopalan, R. G., "RotCFD: An Integrated Design Environment for Rotorcraft," American Helicopter Society Specialists' Conference on Aeromechanics Design for Vertical Lift, San Francisco, CA, Jan. 20-22, 2016.

Hall, S., Straub, F., Anand, V., and Lau, B., "Active Flap Control of the SMART Rotor for Vibration Reduction," 65th Annual Forum of the American Helicopter Society, Grapevine, TX, May 27-29, 2009.

Han, S., and Bauchau, O. A., "High-fidelity, 3D Stress Prediction for Composite Rotor Blades," 73rd Annual Forum of the American Helicopter Society International Annual Forum & Technology Display, Fort Worth, TX, May 9–11, 2017.

Harris, F. D., "Introduction to Autogyros, Helicopters, and Other V/STOL Aircraft. Volume I: Overview and Autogyros," NASA/SP–2015-215959, Vol. I, May 2011.

Harris, F. D., "Introduction to Autogyros, Helicopters, and Other V/STOL Aircraft. Volume II: Helicopters," NASA/SP–2015-215959, Vol. II, Oct. 2012.

Harris, F. D., "Introduction to Autogyros, Helicopters, and Other V/STOL Aircraft. Volume III: Other V/STOL Aircraft," NASA/SP–2015-215959, Vol. III, Nov. 2015.

Harris, F. D., "A Reexamination of the Hover Performance of the XC-142A Tiltwing (Including the U.S. Air Force Propeller Static Performance Test Data Bank)," NASA/CR–2017-219485, March 2017.

Harris, F. D., and Dominguez, M., "Hover Performance of Isolated Proprotors and Propellers—Experimental Data," NASA/CR–2017-219486, April 2017.

Jacobson, K., Kiviaho, J. F., Smith, M. J., and Kennedy, G. J., "An Aeroelastic Coupling Framework for Time-accurate Analysis and Optimization," AIAA paper 2018-0100, 2018,

AIAA/ASCE/AHS/ASC Structures, Structural Dynamics, and Materials Conference, AIAA SciTech Forum, Kissimmee, FL, Jan. 8-12, 2018, doi:10.2514/6.2018-0100.

Jee, K., Matalanis, C., Min, B-Y, Bowles, P., Wake, B., Crittenden, T., and Glezer, A., "Computations of Dynamic Stall Control with Combustion Powered Actuation," AHS 71st Annual Forum, Virginia, Beach, VA, May 2015.

Johnson, W., "Influence of Lift Offset on Rotorcraft Performance," Presented at the AHS Specialists' Conference on Aeromechanics, San Francisco, CA, Jan. 23-25, 2008.

Johnson, W., "Influence of Lift Offset on Rotorcraft Performance," NASA/TP–2009-215404, Nov. 2009.

Johnson, W., "Milestones in Rotorcraft Aeromechanics," NASA/TP–2011-215971, May 2011a.

Johnson, W., "Milestones in Rotorcraft Aeromechanics," *Journal of the American Helicopter Society,* vol. 55, no. 3, July 2011b, DOI: 10.4050/JAHS.56.031001

Johnson, W., "A History of Rotorcraft Comprehensive Analyses," NASA/TP–20121-216012, April 2012.

Johnson, W., "A History of Rotorcraft Comprehensive Analyses," 69th Annual Forum of the American Helicopter Society, Phoenix, AZ, May 21-23, 2013

Johnson, W., Yeo, H., and Acree, C. W., Jr., "Performance of Advanced Heavy-Lift, High-Speed Rotorcraft Configurations," AHS International Forum on Rotorcraft Multidisciplinary Technology, Seoul, Korea, Oct. 15-17, 2007.

Jung, S., Lau, B. H., Johnson, W. and Lim, J., "Evaluation of Rotor Structural and Aerodynamic Loads Using Measured Blade Properties," 38th European Rotorcraft Forum, Amsterdam, The Netherlands, Sept. 2012.

Kennedy, G. J. and Boopathy, K., "A Scalable Adjoint Method for Coupled Flexible Multibody Dynamics," AIAA paper 2016-1907, AIAA SciTech Forum, 57th AIAA/ASCE/AHS/ASC Structures, Structural Dynamics, and Materials Conference, San Diego, CA, Jan. 4-8, 2016, DOI: 10.2514/6.2016-1907

Kiviaho, J. F., Jacobson, K., Smith, M. J., and Kennedy, G. J., "A Robust and Flexible Coupling Framework for Aeroelastic Analysis and Optimization," AIAA paper 2017-4144, 18th AIAA/ISSMO Multidisciplinary Analysis and Optimization Conference, AIAA Aviation Forum, Denver, CO, June 5-9, 2017, DOI:10.2514/6.2017-4144

Kiviaho, J. F., Jacobson, K., Smith, M. J., and Kennedy, G. J., "Application of a Time-Accurate Aeroelastic Coupling Framework to Flutter-Constrained Design Optimization," AIAA paper 2018-2932, AIAA Aviation Forum, 2018 Multidisciplinary Analysis and Optimization Conference Atlanta, GA, June 25-29, 2018, DOI: 10.2514/6.2018-2932

Koning, W. J. F., "Wind Tunnel Interference Effects on Tiltrotor Testing Using Computational Fluid Dynamics," NASA/CR–2016-219086, March 2016.

Koning, W. J. F., Acree, C. W., Jr., and Rajagopalan, G., "XV-15 Tilt Rotor Performance Validation Using Computational Fluid Dynamics," AHS Technical Meeting on Aeromechanics Design for Vertical Lift, San Francisco, CA, Jan. 20-22, 2016.

Kottapalli, S., "Low-Speed and High-Speed Correlation of SMART Active Flap Rotor Loads," AHS Aeromechanics Specialists' Conference, San Francisco, CA, Jan. 20-22, 2010.

Kottapalli, S., "Enhanced Correlation of SMART Active Flap Rotor Loads," 52nd AIAA/ASME/ASCE/AHS/ASC Structures, Structural Dynamics, and Materials Conference, Denver, CO, April 4-7, 2011.

Kottapalli, S., "Performance and Loads Correlation of a UH-60A Slowed Rotor at High Advance Ratios," 2012 AHS Future Vertical Lift Aircraft Design Conference, San Francisco, CA, Jan. 2012.

Kottapalli, S., and Acree, Jr., C. W., "Analytical Performance, Loads, and Aeroelastic Stability of a Full-Scale Isolated Proprotor," AHS International Technical Conference on Aeromechanics Design for Transformative Vertical Flight; San Francisco, CA, Jan. 16-19, 2018.

Kottapalli, S., Hagerty, B., and Salazar, D., "Boeing SMART Rotor Full-Scale Wind Tunnel Test Data Report," NASA/TM–2016-216048, Jan. 2016.

Kottapalli, S., and Leyland, J., "Application of Sequential Quadratic Programming to Minimize SMART Active Flap Rotor Hub Loads," Fifth Decennial AHS Aeromechanics Specialists' Conference, San Francisco, CA, Jan. 2014.

Kottapalli, S., and Straub, F., "Correlation of SMART Active Flap Rotor Loads," 65th Annual Forum of the American Helicopter Society, Grapevine, TX, May 27-29, 2009.

Kufeld, R. M., Balough, D. L., Cross, J. L., Studebaker, K. F., Jennison, C. D., and Bousman, W. G., "Flight Testing of the UH-60A Airloads Aircraft," 50th Annual Forum of the American Helicopter Society, Washington D.C., May 1994.

Lau, B. H., Obriecht, N., Gasow, T., Hagerty, B., Cheng, K. C., and Sim, B. W., "Boeing-SMART Rotor Wind Tunnel Test Data Report for DARPA Helicopter Quieting Program (HQP) Phase 1B," NASA/TM–2010-216404, Sept. 2010.

Lienard, C., Allan, B. G., Le Pape, A., and Schaeffler, N. W., "Comparing Numerical and Experimental Results for Drag Reduction by Active Flow Control Applied to a Generic Rotorcraft Fuselage," 71st Annual Forum of the American Helicopter Society, Virginia, Beach, VA, May 2015.

Lim, J. W., McAlister, K. W., and Johnson, W., "Hover Performance Correlation for Full-Scale and Model-Scale Coaxial Rotor Systems," AHS 63rd Annual Forum & Technology Display of the American Helicopter Society, Virginia Beach, VA, May 1-3, 2007.

Lim, J.W., McAlister, K. W., and Johnson, W., "Hover Performance Correlation for Full-Scale and Model-Scale Coaxial Rotors," *Journal of the American Helicopter Society*, vol. 54, no. 3, July 2009.

Lim, J. W., Boyd, Jr., D. D., Hoffman, F., van der Wall, B. G., Kim, D-H, Jung, S. N., Young, H. Y., Tanabe, Y., Bailly, J., Lienard, C., and Delrieux, Y., "Aeromechanical Evaluation of the Smart-Twisting Active Rotor," 40th European Rotorcraft Forum, Southampton, U.K., Sept. 2014.

Marpu, R. P.; Sankar, L. N.; Norman, T. R.; Egolf, T. A.; and Makinen, S., "Analysis of the UH-60A Rotor Loads Using Wind Tunnel Data." AIAA Paper No. 2013-0635, Jan. 2013.

Martin, P., Overmeyer, A., Tanner, P., Wilson, J., and Jenkins, L., "Helicopter Fuselage Active Flow Control in the Presence of a Rotor," 70th Annual Forum of the American Helicopter Society, Montreal, Canada, May 2014.

Matalanis, C. G., Bowles, P. O., Jee, S., Min, B. Y., Kuczek, A. E., Croteau, P. F., Wake, B. E., Crittenden, T., Glezer, A., and Lorber, P. F., "Dynamic Stall Suppression Using Combustion-Powered Actuation (COMPACT)," NASA/CR–2016-219336, Sept. 2016b.

Matalanis, C., Bowles, P., Lorber, P., Crittenden, T., Glezer, A., Schaeffler, N., Min, B.Y., Jee, S., Kuczek, A. E., and Wake, B., "High-Speed Experiments on Combustion-Powered Actuation for Dynamic Stall Suppression," 72nd Annual Forum of the American Helicopter Society, May 2016a.

Matalanis, C., Min, B-Y., Bowles, P., Jee, S., Wake B., Crittenden, T., Woo, G., and Glezer, A., "Combustion-Powered Actuation for Dynamic Stall Suppression—Simulations and Low-Mach Experiments," AHS 70th Annual Forum, Montreal, Canada, May 2014.

McKillip, R., Jr., and Quackenbush, T., "The Flight Adaptive Blade for Optimum Rotor Response (FABFORR) Concept," 2012 AHS Future Vertical Lift Aircraft Design Conference, San Francisco, Jan. 2012.

Min, B-Y, Sankar, L. N., Rajmohan, N., and Prasad, J. V. R, "Computational Investigation of the Effects of Gurney Flap on the Forward Flight Characteristics of Helicopter Rotors," AIAA Guidance, Navigation, and Control Conference, Honolulu, HI, Aug. 18-21, 2008.

Min, B. Y., Sankar, L., Rajmohan, N., and Prasad, J.V.R., "Computational Investigation of the Effects of Gurney Flap on the Forward Flight Characteristics of Helicopter Rotors," *Journal of Aircraft*, vol. 46, no. 6, Nov.-Dec. 2009, pp. 1957-1964.

Narducci, R., Bowersox, R., Bussom, R. McVeigh, M., Raghu, S., and White, E., "Investigation of Active Flow Control to Improve Aerodynamic Performance of Oscillating Wings," NASA/CR–2014-218146, Jan. 2014.

Nielsen, E. J. and Diskin, B. "Adjoint-Based Sensitivity Analysis of Unsteady and Chaotic Flows in FUN3D," SIAM Computational Science and Engineering-2017, Atlanta, GA, March 1, 2017.

Norman, T. R., Theodore, C., Shinoda, P., Fuerst, D., Arnold, U.T.P., Makinen, S., Lorber, P., and O'Neill, J., "Full-Scale Wind Tunnel Test of a UH-60 Individual Blade Control System for Performance Improvement and Vibration, Loads, and Noise Control," 65th Annual Forum of the American Helicopter Society, Grapevine, TX, May 2009.

Norman, T. R., Peterson, R. L., Shinoda, P., and Datta, A., "Full-Scale Wind Tunnel Test of the UH-60A Airloads Rotor," 67th Annual Forum of the American Helicopter Society, Virginia Beach, VA, May 3-5, 2011.

Norman, T., Peterson, R., Maier, T., and Yeo, H., "Evaluation of Wind Tunnel and Scaling Effects with the UH-60A Airloads Rotor," AHS 68th Annual Forum of the American Helicopter Society, Ft. Worth, TX, May 1-3, 2012.

Quackenbush, T. R. and Wachspress, D. A., "Measurement and Analysis of High Advance Ratio Rotor Performance," 64th Annual Forum of the American Helicopter Society, Montréal, Canada, April 29–May 1, 2008.

Rajagopalan, R. G., Baskaran, V., Hollingsworth, A., Lestari, A., Garrick, D., Solis, E., and Hagerty, B., "RotCFD - A Tool for Aerodynamic Interference of Rotors: Validation and Capabilities," American Helicopter Society Future Vertical Lift Aircraft Design Conference, San Francisco, CA, Jan. 18-20, 2012.

Russell, C., "Shake Test Results and Dynamic Calibration Efforts for the Large Rotor Test Apparatus," Fifth Decennial AHS Aeromechanics Specialists' Conference, San Francisco, CA, Jan. 2014.

Russell, C., "Shake Test Results and Dynamic Characterization of the Large Rotor Test Apparatus in the NFAC 40- by 80-Foot Wind Tunnel," NASA/TM–2015-218877, Sept. 2015.

Russell, C. R., and Acree, Jr., C. W., "Modal Test and Analysis of the NASA Tiltrotor Test Rig," AHS International Technical Conference on Aeromechanics Design for Transformative Vertical Flight, San Francisco, CA, Jan. 16-19, 2018.

Saito, S., Kobiki, N., Tanabe, Y., Johnson, W., Yamauchi, G., and Young, L., "Overview of the Novel Intelligent JAXA Active Rotor Program," HeliJapan 2010 Conference, Omiya, Japan, Nov. 1-3, 2010.

Schaeffler, N. W., Allan, B. G., Lienard, C., and Le Pape, A., "Progress Towards Fuselage Drag Reduction via Active Flow Control: A Combined CFD and Experimental Effort," Presented at the 36th European Rotorcraft Forum (ERF), Paris, France, Sept. 7-9, 2010.

Schaeffler, N. W., Allan, B, G., Wong, O. D., and Tanner, P. E., "Experimental Investigation of Active Aerodynamic Load Reduction on a Rotorcraft Fuselage with Rotor Effects," 7th AIAA Flow Control Conference, Atlanta, GA, June 16-20, 2014.

Schaeffler, N., Allan, B., Jenkins, L., Yao, C. S., Bartram, S., Mace, W. D., Wong, O., and Tanner, P., "Mechanisms of Active Aerodynamic Load Reduction on a Rotorcraft Fuselage with Rotor Effects," AHS Technical Meeting on Aeromechanics Design for Vertical Lift, San Francisco, CA, Jan. 20-22, 2016.

Sekula, M., and Wilbur, M., "Analysis of a Multi-Flap Control System for a Swashplateless Rotor," 67th Annual Forum of the American Helicopter Society, Virginia Beach, VA, May 3-5, 2011.

Sekula, M. K., and Wilbur, M. L., "Analysis of a Multiflap Control System for a Swashplateless Rotor," *Journal of the American Helicopter Society*, vol. 57, no. 3, 2012, DOI: 10.4050/JAHS.57.032006

Sekula, M., and Wilbur, M., "Optimization of an Active Twist Rotor Blade Planform for Improved Active Response and Forward Flight Performance," Fifth Decennial AHS Aeromechanics Specialists' Conference, San Francisco, CA, Jan. 2014.

Sonneville, V., and Bauchau, O. A., "Efficient Numerical Simulation of Helicopter Rotor Dynamics Based on a Parallel Domain Decomposition Local Frame Motion Formalism," AHS Forum 73, May 2017a.

Sonneville, V., and Bauchau, O. A., "Parallel Implementation of Comprehensive Rotor Dynamics Simulation Based on the Motion Formalism." AHS Forum 73, May 2017b.

Sonneville, V., and Bauchau, O. A., "Parallel Implementation of Flexible Multibody Dynamics Simulation Based on the Motion Formalism," ECCOMAS Thematic Conference on Multibody Dynamics, June 2017c.

Sonneville, V., and Bauchau, O. A., "Parallel Implementation of Comprehensive Rotor Dynamics Simulation Based on the Motion Formalism," AHS Specialists' Conference on Aeromechanics Design for Transformative Vertical Flight, Jan. 2018a.

Sonneville, V., and Bauchau, O. A., "The Motion Formalism for Flexible Multibody Systems," AIAA paper 2018-0182, 2018b.

Sonneville, V., and Bauchau, O. A., "Comparison of Motion Representations for Efficient Numerical Simulation of Flexible Multibody Systems." 5th Joint International Conference on Multibody System Dynamics, Lisbon, Portugal, June 2018c.

Sonneville, V., Brüls, O., and Bauchau, O.A., "On the Compatibility Equations in Geometrically Exact Beam Finite Element," ASME 2016 IDETC, paper no. 59954, 2016a

Sonneville, V., Brüls, O., and Bauchau, O. A., "A Lie Group Approach for the Formulation of Beam and Shell Refined Theories used in Flexible Multibody Systems." 4th Joint International Conference on Multibody System Dynamics, Montreal, Canada, May 2016b.

Sonneville, V., Brüls, O., and Bauchau, O. A., "Interpolation Schemes for Geometrically Exact Beams: A Motion Approach," ECCOMAS Thematic Conference on Multibody Dynamics, June 2017a.

Sonneville, V., Brüls, O., and Bauchau, O. A., "Interpolation Schemes for Geometrically Exact Beams: a Motion Approach," *International Journal for Numerical Methods in Engineering*, vol. 112, no. 9, pp. 1129-1153, Nov. 2017b.

Sonneville, V., Bauchau, O. A., and Sinotte, T. "Modal reduction of Fatigue Sensitive Components for Comprehensive Rotorcraft Dynamics Simulation." AHS Forum 74, May 2018.

Staruk, W., Weiner, E., and Chopra, I., "CAD-Based 3-D Structural Dynamic Modeling of the Tilt Rotor Aeroacoustic Model (TRAM) Proprotor," 71st Annual Forum of the American Helicopter Society, Virginia, Beach, VA, May 2015.

Staruk, W., Chopra, I., and Datta, A., "Loads Prediction for a Gimbaled Tiltrotor in Conversion Flight Using CAS-Based 3-D Structural Analysis Models," 73rd Annual Forum of the American Helicopter Society International, Fort Worth, TX, May 9-11, 2017.

Straub, F., Anand, V., and Birchette, T., "SMART Rotor Wind Tunnel Test Report," NASA/CR–2015-219075, July 2015.

Straub, F., Anand, V., Birchette, T., and Lau, B., "Wind Tunnel Test of the SMART Active Flap Rotor," AHS 65th Annual Forum, Grapevine, TX, May 27-29, 2009.

Straub, F. K., Anand, V. R., Birchette, T., and Lau, B. H., "Wind Tunnel Test of the SMART Active Flap Rotor," *Journal of the American Helicopter Society*, vol. 63, no. 1, Jan. 2018, pp. 1-16(16), doi.org/10.4050/JAHS.63.012002

Theodore, C., Willink, G., Russell, C., Amy, A. and Pete, A., "Wind Tunnel Testing of a 6%-Scale Large Civil Tilt-Rotor Model in Airplane and Helicopter Modes," 5th Decennial AHS Aeromechanics Specialists' Conference, San Francisco, CA, Jan. 2014.

Thornburgh, R., Kreshock, A., Wilbur, M., Sekula, M., and Shen, J., "Continuous Trailing-Edge Flaps for Primary Flight Control of a Helicopter Main Rotor," AHS 70th Annual Forum, Montreal, Canada, May 2014.

van der Wall, B. G., Lim, J. W., Smith, M. J., Jung, S. N., Bailly, J., Baeder, J. D., and Boyd, D. D., Jr., "An Assessment of Comprehensive Code Prediction State-of-the-Art Using the HART II International Workshop Data," 68th Annual Forum & Technology Display of the American Helicopter Society, Ft. Worth, TX, May 1-3, 2012.

Wang, L., Diskin, B., Biedron, R. T., Nielsen, E. J., and Bauchau, O. A., "Sensitivity Analysis of Multidisciplinary Rotorcraft Simulations," AIAA paper 2017-1670, AIAA SciTech 2017, 55th Aerospace Sciences Meeting, Grapevine, TX, Jan. 9-13, 2017.

Wang, L., Diskin, B., Biedron, R. T., Nielsen, E. J, Sonneville, V., and Bauchau, O. A., "High-Fidelity Multidisciplinary Design Optimization Methodology with Application to Rotor Blades," AHS Specialists' Conference on Aeromechanics Design for Transformative Vertical Flight, San Francisco, CA, Jan. 2018.

Wang, L., Diskin, B., Biedron, R. T., Nielsen, E. J., Sonneville, Valentin, Bauchau, O. A., High-Fidelity Multidisciplinary Sensitivity Analysis Framework for Multipoint Rotorcraft Optimization, AIAA 2019-1699, AIAA SciTech 2019, Jan. 2019a.

Wang, L., Diskin, B., Biedron, R. T., Nielsen, E. J, Sonneville, V., and Bauchau, O. A., "High-Fidelity Multidisciplinary Design Optimization Methodology with Application to Rotor Blades," *Journal of the American Helicopter Society*, Vol. 64, No. 3, 032002, July 2019b, DOI: 10.4050/JAHS.64.032002.

Wang, L., Diskin, B., Biedron, R. T., Nielsen, E. J., and Bauchau, O. A., "High-Fidelity Multidisciplinary Sensitivity Analysis and Design Optimization for Rotorcraft Applications", *AIAA Journal*, vol. 57, no. 8, Aug. 2019c, DOI: 10.2514/1.J056587

Yeo, H., Bosworth, J., Acree, C. W., and Kreshock, A. R., "Comparison of CAMRAD II and RCAS Predictions of Tiltrotor Aeroelastic Stability," AHS 73rd Annual Forum, Fort Worth, TX, May 9-11, 2017; also *Journal of the American Helicopter Society*, vol. 63, April 2018, DOI: 10.4050/JAHS.63.022001

Yeo, H., and Johnson, W., "Performance and Design Investigation of Heavy Lift Tiltrotor with Aerodynamic Interference Effects," AHS 63rd Annual Forum, Virginia Beach, Virginia, May 1-3, 2007.

Yeo, H., and Johnson, W., "Prediction of Rotor Structural Loads with Comprehensive Analysis," *Journal of the American Helicopter Society*, vol. 53, no. 2, April 2008, pp. 193-209.

Yeo, H., and Johnson, W., "Optimum Design of a Compound Helicopter," *Journal of Aircraft*, vol. 46. no. 4, July-Aug. 2009.

Yeo, H., and Johnson, W., "Investigation of Maximum Blade Loading Capability of Lift-Offset Rotors," AHS 69th Annual Forum, Phoenix, AZ, May 21-23, 2013.

Yeo, H., and Johnson, W., "Investigation of Maximum Blade Loading Capability of Lift-Offset Rotors," *Journal of the American Helicopter Society*, vol. 59, no. 1, Jan. 2014 012005.

Yeo, H., and Johnson, W., "Prediction of Maximum Lift Capability of Helicopter Rotors," *Journal of Aircraft*, vol. 52, no. 1, Jan.-Feb. 2015, DOI: 10.2514/1.C032693

Yeo, H., Potsdam, M., and Norman, T. R., "Investigation of UH-60A Rotor Structural Loads Between Flight and Wind Tunnel Tests," American Helicopter Society International's 72nd Annual Forum & Technology Display, May 2016.

Yeo, H., and Romander, E. A., "Loads Correlation of a Full-Scale UH-60A Airloads Rotor in a Wind Tunnel," AHS 68th Annual Forum and Technology Display, Ft. Worth, TX, May 1-3, 2012,

Yeo, H., and Romander, E. A., "Loads Correlation of a Full-Scale UH-60A Airloads Rotor in a Wind Tunnel," *Journal of the American Helicopter Society*, vol. 58, no. 2, April 2013.

Yeo, H., Romander, E., and Norman, T., "Investigation of Rotor Performance and Loads of a UH-60A with Individual Blade Control," Presented at the 66th Annual Forum of the American Helicopter Society, Phoenix, AZ, May 10-12, 2010.

Yeo, H., Romander, E., and Norman, T., "Investigation of Rotor Performance and Loads of a UH-60A Individual Blade Control System," *Journal of the American Helicopter Society*, vol. 56, no. 4, JAHS.56.042006-1 to -18, Oct. 2011.

Yeo, H., Sinsay, J., and Acree, C. W., Jr., "Blade Loading Criteria for Heavy Lift Tiltrotor Design," AHS Southwest Region Technical Specialists' Meeting, Dallas, TX, Oct. 15-17, 2008.

Young, L., "Influence of Initial Vorticity Distribution on Axisymmetric Vortex Breakdown and Reconnection," 45th AIAA Aerospace Sciences Meeting and Exhibit, Reno, NV, Jan. 8-11, 2007a.

Young, L., "A Family of Vortices to Study Axisymmetric Vortex Breakdown and Reconnection," 25th AIAA Applied Aerodynamics Conference, Miami, FL, June 25-28, 2007b.

Young, L., "Vortex Filament Evolution Subject to Pulsed/Periodic Disruption," 46th AIAA Aerospace Sciences Meeting and Exhibit, Reno, NV, Jan. 7-10, 2008a.

Young, L., "Modeling of a Turbulent Line Vortex," 5th AIAA Theoretical Fluid Mechanics Conference, Seattle, WA, June 23-26, 2008b.

Young, L., "Simulated Tiltrotor Aircraft Operation in Close Proximity to a Building in Wind and Ground-Effect Conditions," AIAA Aviation 2015 Conference Dallas, TX, June 22-26, 2015.

Young, L., Yamauchi, G., and Rajagopalan, G., "Simulated Rotor Wake Interactions Resulting from Civil Tiltrotor Aircraft Operations Near Vertiport Terminals," 51st AIAA Aerospace Science Meeting, Grapevine, TX, Jan. 2013.

Zhang, J., and Smith, E. C., "Parametric Studies of Wing Extensions and Winglets on Whirl Flutter Stability," 5th Decennial AHS Aeromechanics Specialists' Conference, San Francisco, CA, Jan. 2014.

CHAPTER 3. COMPUTATIONAL FLUID DYNAMICS (EXTERNAL FLOW)

Brian G. Allan[1] and Gloria K. Yamauchi[2]

INTRODUCTION

Over the years rotorcraft have become increasingly more sophisticated with higher operational requirements resulting in the need for increased modeling accuracy and understanding. Areas where improved accuracy is especially needed include the prediction of rotorcraft aeromechanics and acoustics. From 2008–2018, NASA outlined a strategy to address the need for increased rotorcraft aerodynamic modeling accuracy by improving the capability of its high-fidelity computational fluid dynamics (CFD) codes. These improvements included mesh adaption for both off-body and on-body flow fields, higher-order numerical schemes with lower numerical dissipation, higher-order time schemes, improved turbulence modeling, development of boundary layer transition modeling, and general code performance improvements to reduce computational cost. As additional capabilities were added to the high-fidelity CFD codes, comparisons and validations were made against various wind tunnel experiments demonstrating their improved predictive capabilities. During 2016–2018, a rotor-blade multidisciplinary design optimization capability was developed and demonstrated using a high-fidelity unstructured CFD code and an adjoint-based optimization method. The improvements to the NASA CFD codes and validation activities are summarized in this chapter.

ADVANCED CFD DEVELOPMENT

This section highlights the improvements in capabilities made to NASA-developed high-fidelity CFD codes for increased accuracy and performance of rotorcraft simulations from 2008–2018. Most significant improvements have been in the areas of dynamic adaptive mesh refinement (AMR) and higher-order numerical methods. Combined, these two improved capabilities have significantly increased the fidelity of rotorcraft simulations resulting in increased aerodynamic accuracy.

Adaptive Mesh Refinement (AMR)

The state-of-the-art (SOA) survey for vertical lift technologies [Yamauchi and Young, 2009] recommended the development of AMR to allow for accurate simulation of the rotorcraft-wake system. One of the main barriers to capturing the rotor wakes has been the required grid resolution needed to accurately capture the vortical wake structures emanating from the rotor tips. This can be accomplished by using a very fine mesh over the entire rotor wake region, however this is typically prohibitively expensive. An alternative to uniform mesh refinement is to use dynamic mesh adaption and refine only the regions of the wake that require mesh

[1] NASA Langley Research Center, 1A East Reid St., Hampton, VA 23681-2199.
[2] NASA Ames Research Center, Moffett Field, CA 94035-1000.

refinement. The difficulty lies in how to best identify the regions that require adaption with the goal of achieving results similar to those obtained using uniform mesh refinement of the rotor wake.

The main focus of AMR for NASA vertical lift research over the last 10 years was to add dynamic mesh adaption capability to the structured Navier–Stokes flow solver, OVERFLOW2, initially for off-body mesh and then subsequently for near-body mesh. The mesh adaption approach was to develop a solution-adaptive capability using the existing chimera zonal grid framework in OVERFLOW2. While this is less rigorous than an adjoint-based approach as used in the unstructured Navier–Stokes flow solver, FUN3D [Park, 2011], the solution-based approach is much simpler to implement with a lower computational cost and is more conducive to dynamic mesh adaption for unsteady flow needed for rotor wakes.

Initial development of a solution-adaptive capability was performed by Holst and Pulliam [2009, 2010] for off-body Cartesian meshes where the mesh is divided into a series of uniform sub-regions. Each sub-region is evaluated for mesh refinement based on a sensor value of flow gradients such as a vortex core. The sub-regions matching the refinement criteria are uniformly refined. This research by Holst and Pulliam [2009, 2010] demonstrated that this dynamic local mesh refinement approach uses approximately five times less computational resources than a uniformly refined mesh. This work also demonstrated a significant improvement in the prediction of the vortex-core growth with wake age as compared to experiment, however, the vortex-core size for the CFD simulations were still larger than observed in the experiment. Calculations of the hover performance figure of merit (FM) matching a Tilt Rotor Aeroacoustics Model (TRAM) experiment showed improved prediction of FM from 0.73, about 6 percent below the experimental value of 0.75, to an FM of 0.75 for two levels of mesh refinement (~4 percent difference), and to an FM of 0.77 for three levels of refinement (~1.3 percent difference).

The mesh adaption work by Holst and Pulliam [2009, 2010] was followed by an improved off-body solution adaption capability implemented in OVERFLOW2 by Buning and Pulliam [2011]. This new capability was based on the original work done by Meakin [1995] and provides for the automatic creation of multiple levels of finer Cartesian off-body meshes. The adaption capability was also coupled with load-balancing and an in-memory solution interpolation procedure, providing good performance for time-accurate simulations on parallel computer platforms. The work by Buning and Pulliam [2011] used a simple error estimation derived from the flow solution. The error estimation was calculated by the undivided second-difference of the primary flow variables of density, momentum, and stagnation energy per unit volume. This error estimation was shown by Buning and Pulliam [2011] to be effective for identifying both shock waves and vortices.

The new off-body AMR capability developed and implemented by Buning and Pulliam [2011] in OVERFLOW2 was used by Chaderjian and Buning [2011] to perform time-dependent CFD simulations of the highly resolved rotor wake of the TRAM rotor in hover. Figure 3.1 shows the highly resolved rotor wake using a two-level dynamic AMR grid system for the TRAM in hover. This work showed that the rotor performance in terms of the FM was more a function of the near-body rotor mesh resolution than the off-body rotor wake mesh. From this work Chaderjian

and Buning [2011] showed that using a Detached Eddy Simulation (DES) turbulence model, as opposed to a Reynolds-averaged Navier–Stokes (RANS) model, was crucial to accurately predicting the rotor FM. In addition to AMR, Chaderjian and Buning [2011] also used high-order spatial differencing developed by Pulliam [2011] to reduce numerical dissipation of rotor blade tip vortices and other wake flow structures. Chaderjian [2012b] followed this work by using AMR on an isolated UH-60A rotor in forward flight and demonstrating good agreement of the time-varying normal force and pitching moments with flight test data. He also showed good agreement of the vortex-core growth for the V22 (TRAM) hover case to experimental measurements.

Near-body mesh adaption capability was added to OVERFLOW2 by Buning and Pulliam [2016]. Near-body mesh adaption is a much more difficult problem to solve than off-body adaption because the off-body grids are Cartesian and straightforward to refine. Near-body grids are typically curvilinear since they are fitted to curved body surfaces and also include highly refined near-wall regions to resolve the boundary layers. The near-body mesh adaption capability in OVERFLOW was evaluated for a UH-60A rotor in forward flight by Chaderjian [2018]. Maintaining algorithm stability proved very difficult with the near-body adaption. This was mostly due to the Courant–Friedrichs–Lewy numbers becoming too high as the near-body grids were refined using an isotropic approach (grid is refined in all three dimensions). Using a non-isotropic approach would allow for refinement in the spanwise direction without increasing the

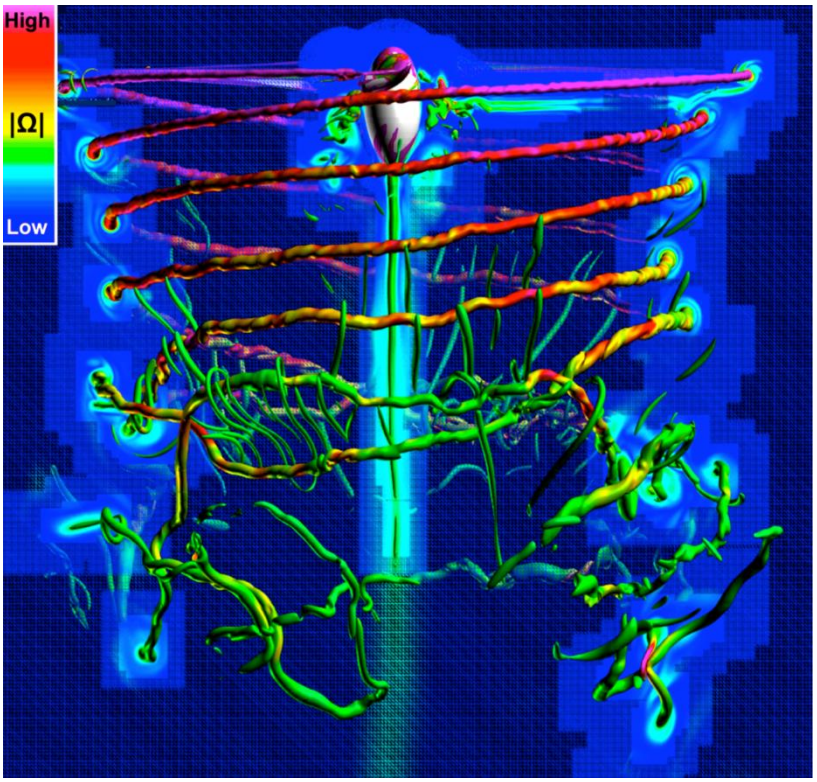

Figure 3.1. OVERFLOW two-level dynamic AMR grid system for the TRAM in hover with Mtip = 0.625, θ = 14°, and Re = 2.1 million. Vorticity magnitude sensor function (Fig. 6 of Chaderjian and Buning [2011]).

viscous clustering normal to the wall and should be considered for future work on improving near-body adaption. Chaderjian [2018] found that turning off the near-body adaption near the surface improved the algorithm stability and also significantly helped reduce the total number of grid points. Overall, the near-body adaption resulted in little change in the blade sectional airloads for up to two levels of adaption. OVERFLOW2 now has a near-body adaption capability, however further developmental and application work can be performed to improve its robustness and usability.

Higher-Order Schemes

Another area of research identified by the SOA survey for vertical lift technologies was the development and implementation of high-order spatial-differencing schemes, as well as higher-order time-stepping schemes including fully implicit multistage and compact schemes for OVERFLOW2. These improvements are required to help improve the performance and airloads accuracy for rotorcraft flows, as well as capturing the vortex wake system that includes wake-wake and blade-wake interactions for acoustics applications [Yamauchi and Young, 2009].

Two fifth-order spatial-weighted essentially non-oscillatory numerical schemes for the convective terms were added to OVERFLOW2 by Nichols et al. [2008]. These new schemes had much lower numerical dissipation/dispersion than the traditional third-order spatial monotone upstream-centered schemes. The reduced numerical dissipation allowed vortices to be propagated for much longer distances and was quickly adopted and demonstrated for rotor simulations by Boyd [2009].

Third- and fifth-order finite difference schemes for the convective terms of the Navier–Stokes equations were developed by Pulliam [2011] and implemented into OVERFLOW2. The third-order scheme uses a fourth-order central difference with third-order artificial dissipation, and the fifth-order scheme uses a sixth-order central difference with a fifth-order artificial dissipation. Pulliam [2011] showed how these new high-order schemes were able to improve the accuracy of a rotor wake using less grid resolution than lower-order schemes by comparing the vortex-core growth rate for the third- and fifth-order schemes for varying mesh sizes. The fifth-order-scheme results shown in Figure 3.2 have good agreement to the experimental results for 380 million grid points, whereas the third-order scheme would need 3 billion grid points, using uniform grid refinement, to achieve the same vortex growth rate.

Overset Methods for Unstructured Mesh

An unstructured overset mesh capability was added to FUN3D by Biedron and Thomas [2009] extending the mesh motion capabilities. Previously, FUN3D only allowed rigid mesh motion of the entire domain, which limited the range of applications [Biedron and Thomas, 2009]. Rotorcraft applications are particularly challenging for mesh motion since the rotor blades undergo large rotational and pitch motions, as well as aeroelastic deformations. These large rotor motions in the presence of a fuselage without overset grids would require remeshing, which is not only costly but also not easily compatible with the backward-time integration schemes.

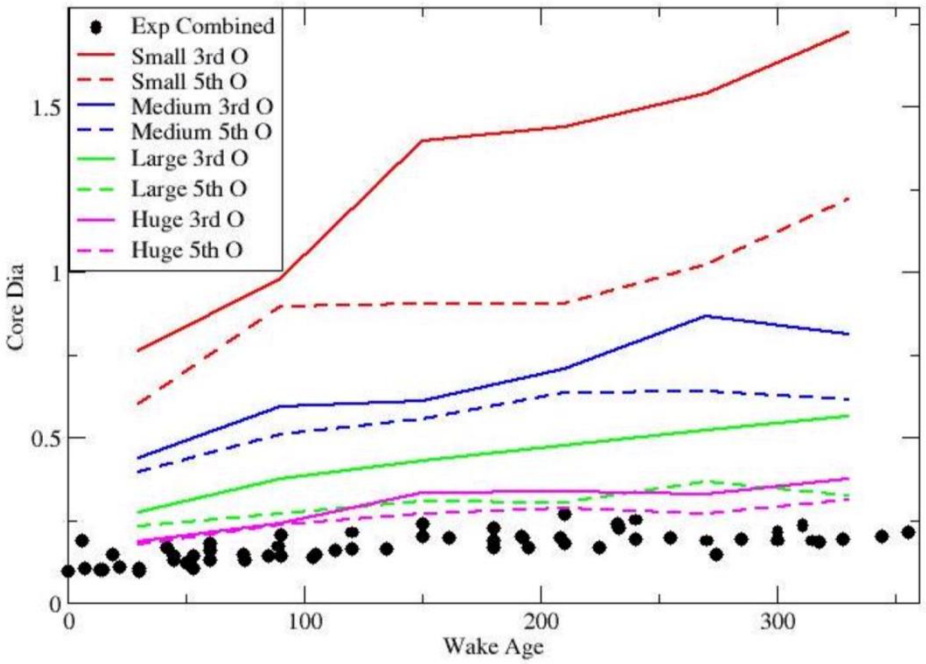

Figure 3.2. Growth rate of vortex core with wake age for third- and fifth-order schemes for the baseline small (13.7 million), medium (58.4 million), large (379.8 million), and huge (3.087 billion) grids (Fig. 9 of Pulliam [2011]).

The overset unstructured mesh methodology has a set of overlapping meshes that require the computation of the domain connectivity information to establish how the overset meshes exchange information between each other. In order to maintain the parallel scalability, the computation of the overset domain connectivity needs to also be parallel and have sufficient scalability when using a large number of computer nodes in order to keep the entire flow solver scalable. Noack et al. [2009] developed a new code called Suggar++. It was developed from scratch using C++ and had the same general capability as an existing overset mesh assembly code called SUGGAR, but it was more efficient and had improved serial and parallel execution performance because of efficient hole cutting and grid partitioning methods.

Multigrid Methods

To improve the efficiency of a three-dimensional (3D) unsteady compressible Navier–Stokes flow solver, research on improving multigrid methods was performed by Diskin et al. [2007] and Liao et al. [2008]. They were able to demonstrate “textbook” multigrid efficiency, which is the optimal efficiency of a multigrid method, for the unsteady subsonic compressible Navier–Stokes equations in three dimensions, for an implicit discretization that was second-order accurate in time and space. The multigrid method was shown to have optimal efficiency at high Reynolds numbers and for large time steps. The application was for a domain with periodic boundary conditions, with future work for more general inflow, outflow, and no-slip boundary conditions.

Turbulence Modeling

The influence of turbulence modeling on the vortical wake of rotorcraft simulations was conducted by Potsdam and Pulliam [2008]. They showed that some turbulence model formulations, like the Spalart–Allmaras model, were observed to produce too much turbulent eddy viscosity if the production was based on the vorticity field of a vortex-dominated rotor wake. As a result of excessive turbulent eddy viscosity in the rotor wake, and its subsequent convection and diffusion, the wall-bounded viscous flow was modified. To remedy this, the turbulence model production source terms were turned off in the rotor wake, demonstrating an improvement in the solution accuracy for hover and forward flight.

A computational study on the parameters affecting Large Eddy Simulations (LES) for bluff body flows was investigated by Mankbadi and Georgiadis [2014]. This investigation examined the numerical sensitivities of the mesh size, time step, and sample frequency, as well as the extent of the spanwise domain on the prediction of the flow over a square cylinder. This study showed that an insufficient spanwise extent results in an overprediction of the streamwise and transverse turbulent intensities. This research was followed by a comparison between high- and low-order methods for LES simulations of a compressible shear layer [Mankbadi et al., 2015]. This investigation showed that the low- and high-order methods had similar results on a fine mesh but that the high-order method could achieve the same results on a coarse mesh.

Flow Visualization

Unsteady-flow visualization is required to understand complex flow fields, especially because of the large amounts of data from rotorcraft CFD simulations [Yamauchi and Young, 2009]. Of particular interest is the tracking of rotor tip vortices and their properties like vortex-core size and cross-flow velocity profiles. Kao and Chaderjian [2010] developed an automated approach that extracts vortex-core trajectories as well as cross-flow velocity profiles from a CFD solution. This was an improvement over a previous vortex-core detection algorithm that extracted noncontinuous vortex-core line segments. The approach was improved by Kao [2011] to generate contiguous vortex-core line segments that can span multiple grid zones. This work was then followed up by improvements of the vortex-core properties for a UH-60A application [Kao et al., 2015] and vortex-core growth rate for an isolated V22 TRAM rotor in hover [Kao et al., 2018]. Figure 3.3 shows the blade tip vortices tracked from a fine-grid CFD case.

Kao et al. [2013] also explored other flow visualization techniques that examined clipping of iso-surfaces to reduce the visual clutter of traditional iso-surfaces, and a flow texture mapping technique to provide an efficient way to depict flow patterns on cutting planes and aerodynamic surfaces. Figure 3.4 shows a comparison between a traditional streamline flow visualization, where the streamlines are restricted to the blade surface, and the texture map technique. The textured map technique has the advantage of not being dependent on the seed location (as in the streamline visualization) thus helping to quickly identify flow features of interest.

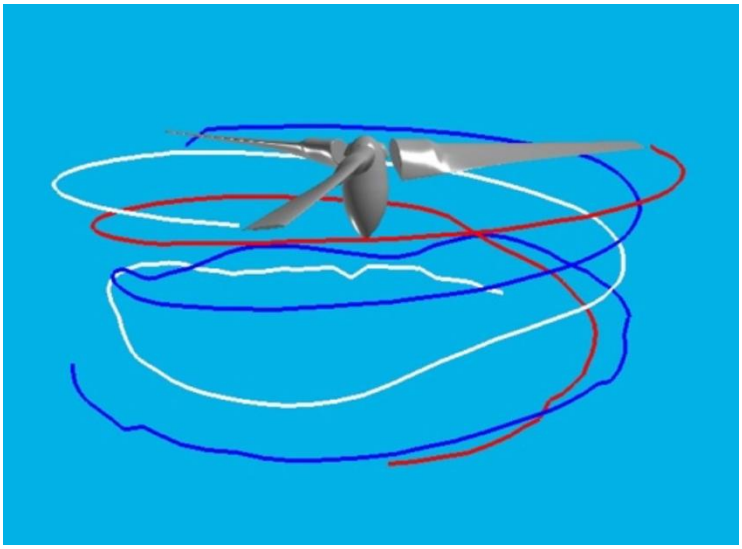

Figure 3.3. Blade tip vortices tracked from three blades using a fine-grid CFD case (Fig. 17 of Kao et al. [2018]).

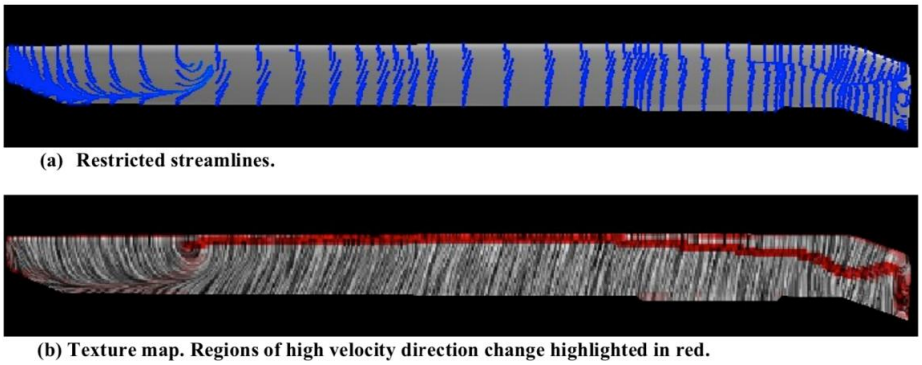

Figure 3.4. Comparison of upper surface flow patterns using two different approaches at 90° azimuth (Fig. 9 of Kao et al. [2013]).

Computational Structural Dynamics

Work was done by Guruswamy [2008, 2009, 2010] to couple a beam-finite-element-based structure solver with a Navier–Stokes flow solver, OVERFLOW, for time-accurate, tight coupling for rotor blade simulations. Calculations for a nonrotating blade, rotating rigid blade, and rotating elastic blade were made and compared to experiments. Overall the dynamic aeroelastic responses compared well in both magnitude and phase to the experimental data. In 2012, Guruswamy [2012a] used the above tight-coupling approach to predict and compare results to the HART-II wind tunnel data. Figure 3.5 shows the time-accurate tight-coupling sectional normal force results comparted to the HART-II wind tunnel data for $\mu = 0.14$, a shaft angle of 4 degrees, and a blade rotation of 1,020 RPM. The rotor blade collective and cyclic inputs from the experiment were used in the coupled simulation.

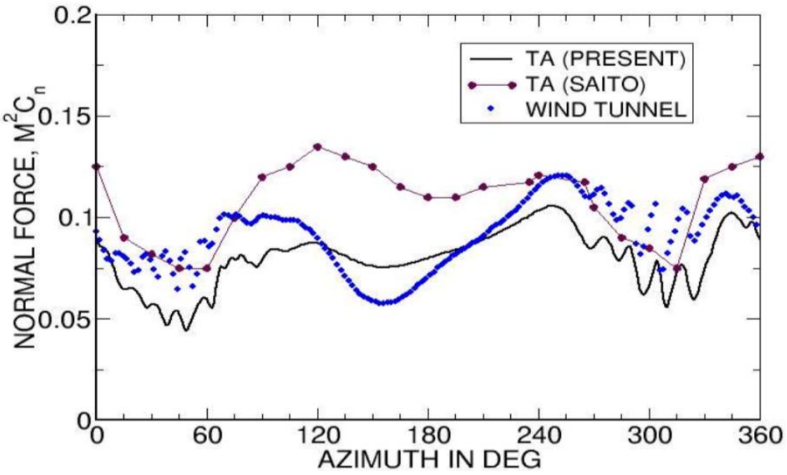

Figure 3.5. Comparison of sectional normal forces at 87% radial station for the HART-II for μ = 0.14, 4° shaft angle, and 1,020 RPM blade rotation (Fig. 7 of Guruswamy [2012a]).

Guruswamy [2012b] performed a procedure to compute the bending-torsion flutter boundaries for a rotating blade using unsteady aerodynamic data from a time-accurate Navier–Stokes flow solution. The flutter speeds were computed by solving the eigenvalues equations that determine the system damping to identify the flutter point. The approach was compared to nonrotating blade experimental data. A flutter analysis was performed for a typical rotating blade case to demonstrate the approach.

Additional Research

A multi-code Python-based infrastructure that uses different gridding paradigms was demonstrated by Wissink et al. [2008]. The main advantage of this approach is to couple well-established, documented CFD codes that capture near-wall viscous turbulent flows together with structured cartesian grids away from the wall that have automatic grid generation with high-order numerical accuracy and time-dependent automatic mesh refinement. The focus of this research is the design of the infrastructure and mechanisms needed to turn existing standalone codes into modules that may be used in the infrastructure. The infrastructure was demonstrated using an unstructured near-body solver, NSU3D, with a structured off-body solver, SAMRAI, on an isolated V-22 rotor case [Wissink et al., 2008].

Jain et al., [2016] reported on a collaborative effort between the U.S. Army Aeroflightdynamics Directorate (AFDD) and NASA to integrate FUN3D as a near-body unstructured grid solver into the Helicopter Overset Simulation (Helios) tool, a high-fidelity computational framework for rotorcraft modeling supported by the U.S. Department of Defense High Performance Computing Modernization Program (HPCMP) Office and the U.S. Army. To demonstrate the integration of FUN3D into Helios, the following cases were tested: an isolated TRAM rotor in hover for performance and airloads; an isolated UH-60A rotor in high-speed forward flight for airloads and CFD/computational structural dynamics (CSD) coupling; the HART-II rotor-fuselage for blade-

vortex interaction (BVI) load, wake predictions, and combined rotor-fuselage modeling; dual counter-rotating UH-60A rotors for airloads; and a tandem rotor H-47 full aircraft for multiple near-body solvers, CFD/CSD coupling, and free-flight trim.

A hybrid CFD approach for rotorcraft simulations was developed by Anusonti-Inthra and Floros [2008] where a RANS flow solver was fully coupled with a Particle-based Vorticity Transport Method (PVTM). The approach divides the flow field into two regions, near-body and off-body, and uses an appropriate flow solver according to the dominate flow physics of that region. The near-body flow contains the solid surfaces, is dominated by boundary layer and viscous effects, and is best solved by a compressible RANS solver. The off-body regions are dominated by vortices shed by the aerodynamic surfaces. The off-body region is challenging to accurately solve using a RANS flow solver and requires sufficient mesh resolution to accurately predict, resulting in significant computer resources. Alternatively, a PVTM requires much less computer resources and maintains the vortex core without the numerical dissipation typically seen using RANS methods. This study looked at coupling the RANS and PVTM flow solvers and evaluated the approach by comparison to experimental data of a wing tip vortex. Figure 3.6 shows a vortex-core swirl velocity comparison of the RANS and coupled RANS/PVTM methods to the experimental data six chord lengths downstream from the wing tip. This comparison demonstrates how the RANS approach dissipated the vortex core with a lower peak velocity as measured in the experiment. The coupled RANS/PVTM approach shows significant improvement but still underpredicts the peak velocities measured in the experiment.

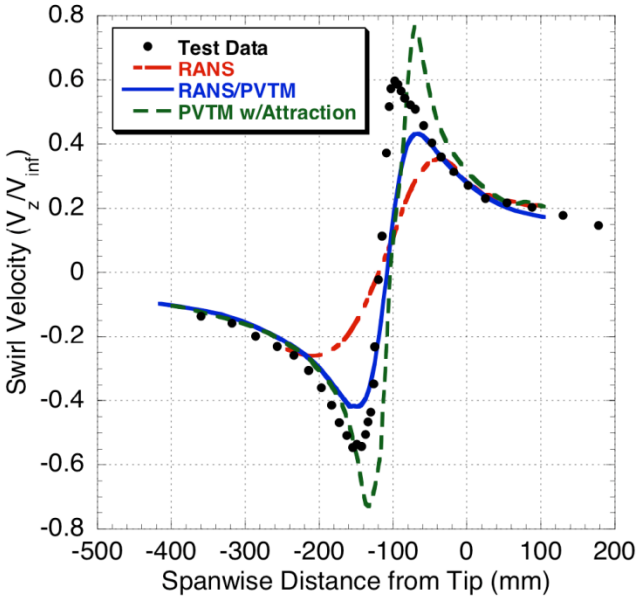

Figure 3.6. Swirl velocity profile in tip vortex six chords behind trailing edge (Fig. 14 of Anusonti-Inthra and Floros [2008]).

The quantification of errors in a CFD simulation was investigated by Derlaga et al. [2017]. The authors looked at using the linearized Error Transport Equations (ETE), combined with a truncation error estimate, to help quantify the source of errors in a simulation. The ETE was implemented using a complex-step method to provide an exact linearization requiring minimal modifications to the CFD source code. These linearized ETE functional error estimates were compared to a more rigorous adjoint-based method by Derlaga et al. [2017] to check for equivalency. The ETE method has several advantages over an adjoint-based method. First, it costs much less than an adjoint-based approach (at the cost of one single solution compared to one solution per functional error needed by the adjoint method). Second, the ETE allows for visualization of the local error estimates allowing the user to better judge the accuracy of the computational solution. The ETE method was implemented in FUN3D and evaluated on three American Institute of Aeronautics and Astronautics (AIAA) Prediction Workshop cases—drag prediction, high lift, and sonic boom. These cases showed that the discretization error estimates from the ETE method compared well to the adjoint approach, and that they were underestimated or overestimated in regions with under-resolved flow features or strong nonlinearities. Since the ETE solution alone does not provide direct guidance on mesh adaption, a complementary ETE and adjoint error estimate method is identified as critical in order to estimate, understand the impact of, and reduce discretization error to meet the goals of CFD Vision 2030.

CFD APPLICATIONS AND VALIDATIONS

This section highlights the application of high-fidelity CFD to compare against experimental databases such as the V-22 tiltrotor, UH-60A flight and airloads wind tunnel tests in the National Full-scale Aerodynamics Complex (NFAC), and the HART-II test. The objective is to exercise the high-fidelity CFD codes for various aeromechanics applications for prediction of rotor performance, airloads, acoustics, rotor wakes, etc., demonstrating their predictive capabilities and limitations.

UH-60A Airloads Simulations

The UH-60A flight test [Kufeld et al., 1994] and the UH-60A Airloads wind tunnel test in the NFAC 40- by 80-Foot Wind Tunnel in 2010 [Norman et al., 2011] generated a wealth of high-quality full-scale data that continues to represent “truth” data for many correlation studies using different analyses. The forum for sharing selected data from both tests was the UH-60 Airloads Workshop sponsored by the National Rotorcraft Technology Center, NASA, and the U.S. Army. The workshop was held twice per year, beginning in the summer of 2001 and ending in the summer of 2018, and was attended by government, industry, and academia. Through this community effort, discrepancies in both data and analyses were identified and corrected, moving the SOA in CFD forward. In particular, the data were extensively used to validate results from two of NASA’s workhorse CFD analyses, OVERFLOW2 and FUN3D. Comparisons of the data with comprehensive analysis are summarized in the UH-60 Airloads section of Chapter 2, Aeromechanics.

Simulation efforts that compare results with the flight test data are presented next, followed by validation efforts using the full-scale wind tunnel data.

Correlation with flight test data

In anticipation of the 2010 benchmark wind tunnel test of the UH-60A Airloads rotor [Norman et al. 2011], Chang et al. [2010] investigated the effects of wind tunnel walls on an isolated UH-60A rotor. The loosely-coupled CFD and CSD analyses, OVERFLOW2 and CAMRAD II, respectively, were used to simulate the UH-60A rotor in free flight and in the NFAC 40- by 80-Foot Wind Tunnel. Three flight conditions were chosen for the comparison: C8534—high speed with advancing blade negative lift, C8513—low speed with BVI, and C9017—high thrust with dynamic stall. The flight conditions and their identifiers are from the UH-60A Airloads flight test in the 1990s. A simplified model of the wind tunnel was represented as a straight duct of approximately 20 rotor radii with a cross-section geometry matching the NFAC 40- by 80-Foot Wind Tunnel. Overall results, generated using coarse grids, showed that applying the coupled CFD/CSD approach to the wind tunnel environment was generally successful. Wind-tunnel-interference effects on blade airloads, and rotor thrust and power, were relatively minor for the three test cases, with the possible exception of the high-thrust case (C9017), though convergence issues prevented a definitive conclusion.

Biedron and Lee-Rausch [2011] compared results from FUN3D, loosely coupled with CAMRAD II, with data (Counters 8534 and 9020) from the UH-60A flight test. Counters 8534 and 9020 represent the high-speed and high-thrust conditions, respectively. Simulations were performed both with and without the fuselage (see Fig. 3.7).

Computed results for the high-speed case did not show any sensitivity to the CFD inputs but were affected by inclusion of the aircraft fuselage (see Fig. 3.8). Comparisons between computed and measured unsteady loads were significantly better than the mean loads comparisons. The computed mean loads were not noticeably affected by varying the computational parameters. The authors noted that their findings for Counter 8534 were similar to previously published results using a structured grid. Computed results for Counter 9020 showed sensitivity to one of the two dynamic stall events on the retreating side. In summary, the CFD modeling parameters (mesh size, turbulence model, and time step) produced only small changes in the computed results.

An interesting comparison between FUN3D and the structured solver OVERFLOW was conducted by Ahmad and Biedron [2011], with both codes simulating UH-60A flight Counters 9017 (high thrust) and 8513 (low speed). The same scheme was used by both codes to loosely couple with CAMRAD II to account for rotor trim and blade elastic deformation. For Counter 9017, discrepancies between the forces and moments calculated by the two codes were observed near the stall location, especially for the chord forces (see Fig. 3.9). The stall location, however, was captured by both analyses. The calculations from the two codes agreed well for the low-speed conditions of Counter 8513.

Ahmad and Chaderjian [2011] conducted a study of dual-time-stepping accuracy using OVERFLOW and CAMRAD II by simulating the conditions of Counters 8513 (low speed) and 8534 (high speed). The authors found that larger time steps with enough dual-time sub-iterations

for convergence tended to result in less computational work while maintaining time accuracy. If the time step is too large, however, the dual-time process may diverge with an increased number of sub-iterations. A time step must be chosen that resolves all frequencies of interest while maintaining less than one Level 1 Cartesian grid cell of travel by the rotor tip. As for comparisons between computed and measured airloads, the computed normal force and pitching moment coefficients (Fig. 3.10) were in good agreement with the data from both flight Counters, achieving a factor of two improvement in the SOA prediction accuracy. The authors attribute the improvement to using fifth-order spatial differences rather than third-order spatial differences.

Following their work on dual time-stepping accuracy, Chaderjian and Ahmad [2012] used OVERFLOW coupled with CAMRAD II to compute highly resolved vortex wakes by exercising AMR and DES. Their work focused on simulating hover and the conditions of Counter 8534 (high speed) for forward flight. All OVERFLOW calculation simulations used second-order dual-time accuracy, fifth-order central differencing, Cartesian AMR in the rotor wake, and the Spalart–Allmaras DES hybrid turbulence model. The AMR/DES simulation produced vortical worms for forward flight and hover conditions, similar to previous results obtained for the TRAM rotor in hover [Chaderjian and Buning, 2011]. AMR proved to be an efficient means to capture a rotor wake without a priori knowledge of the wake geometry. Figure 3.11 shows the computed flow field for two levels of AMR.

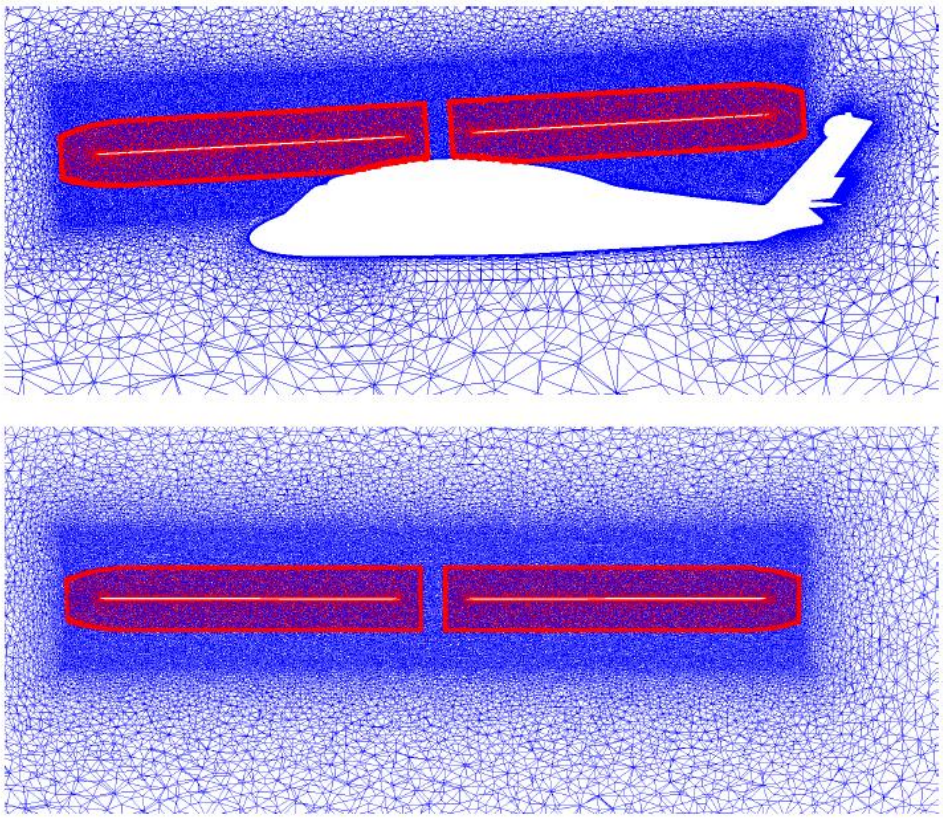

Figure 3.7. Slice through the baseline volume grid systems, with and without fuselage (19 million and 18 million grid points, respectively) (Fig. 3 of Biedron and Lee-Rausch [2011]).

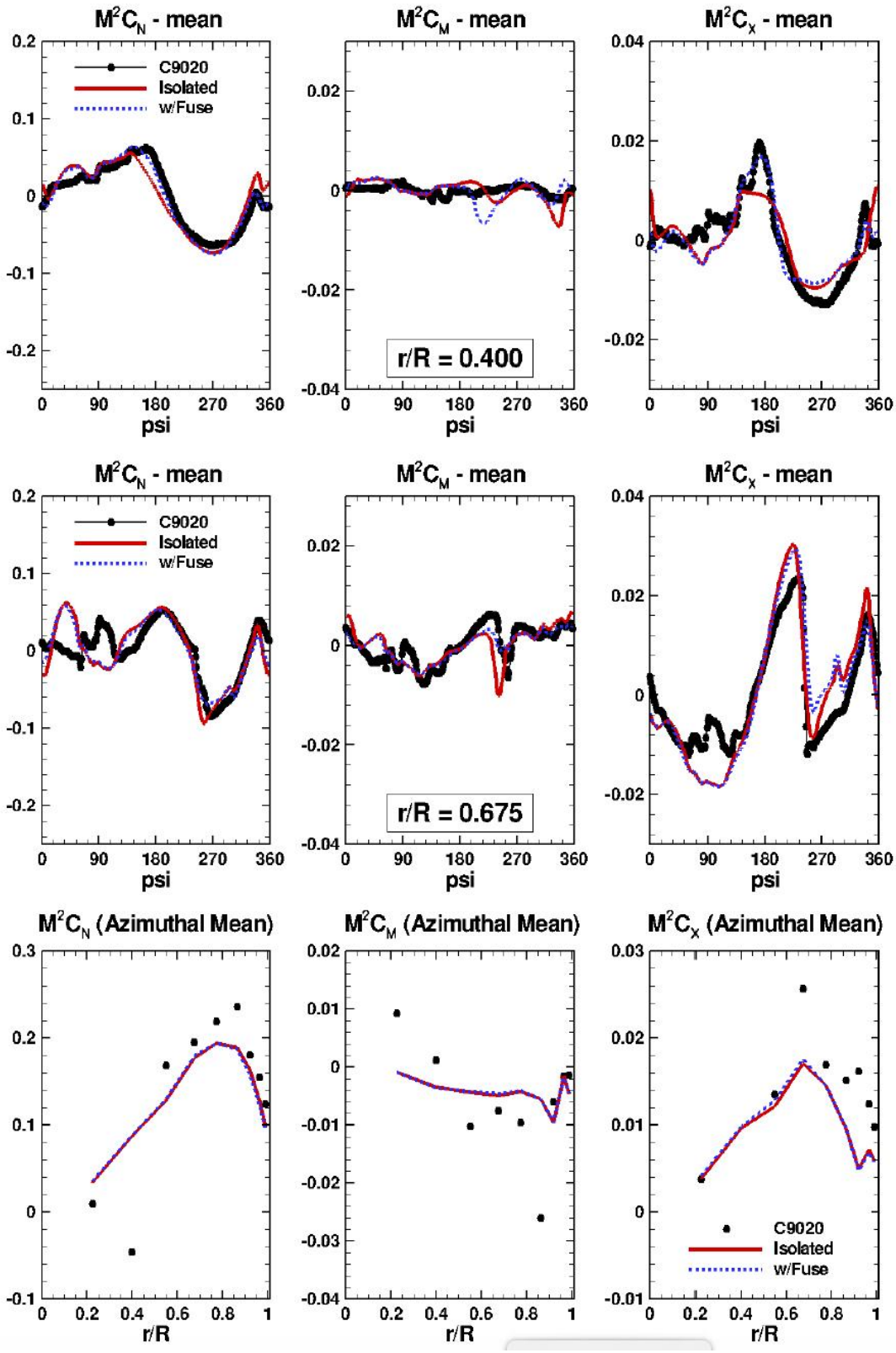

Figure 3.8. Effect of fuselage on computed airloads at r/R = 0.400 and r/R = 0.675, together with azimuthal averages, for Counter 9020 (Fig. 16 of Biedron and Lee-Rausch [2011]).

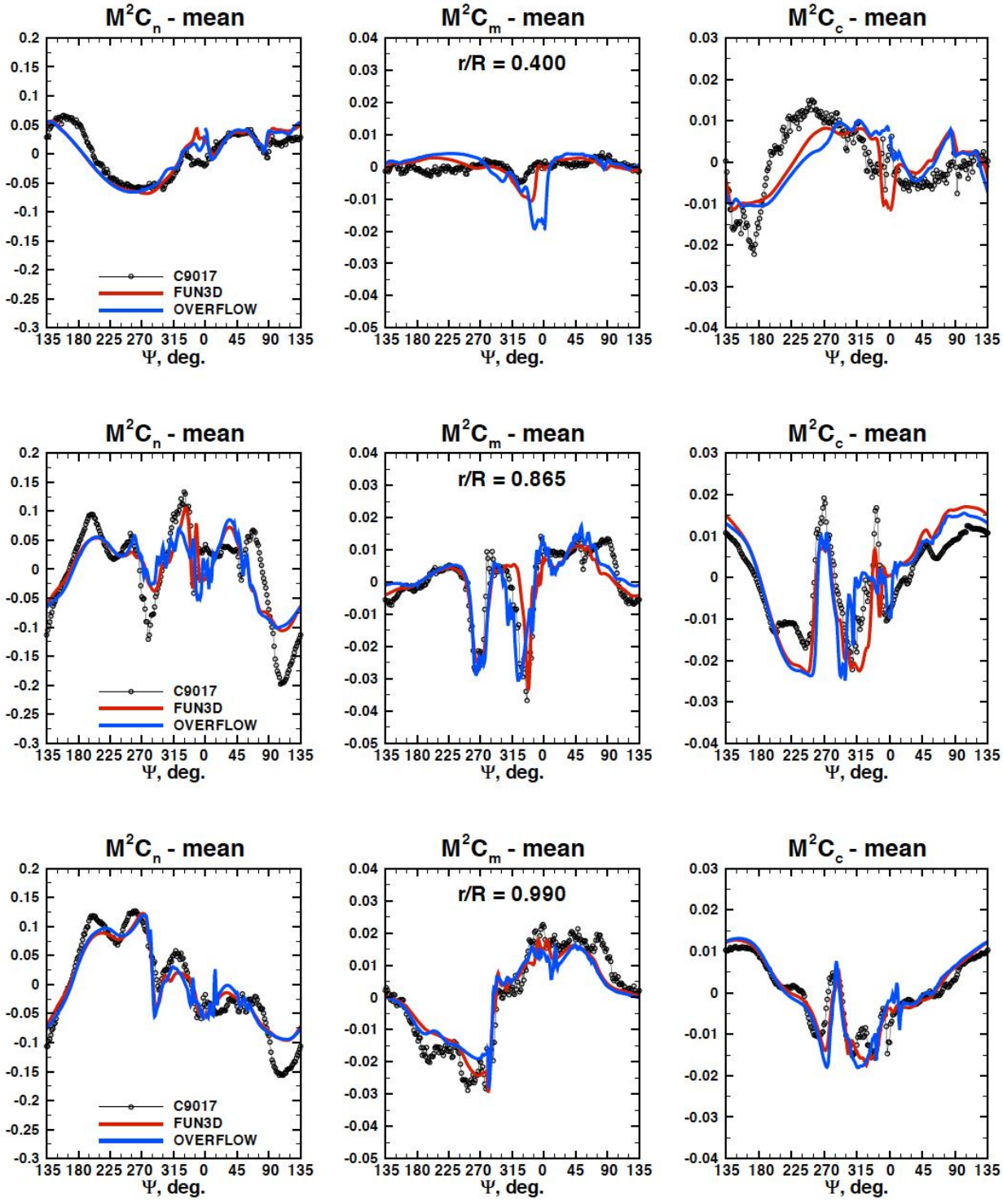

Figure 3.9. Comparison of computed and measured sectional airloads at r/R = 0.400, r/R = 0.865, and r/R = 0.990, for Counter 9017 (Fig. 8 of Ahmad and Biedron [2011]).

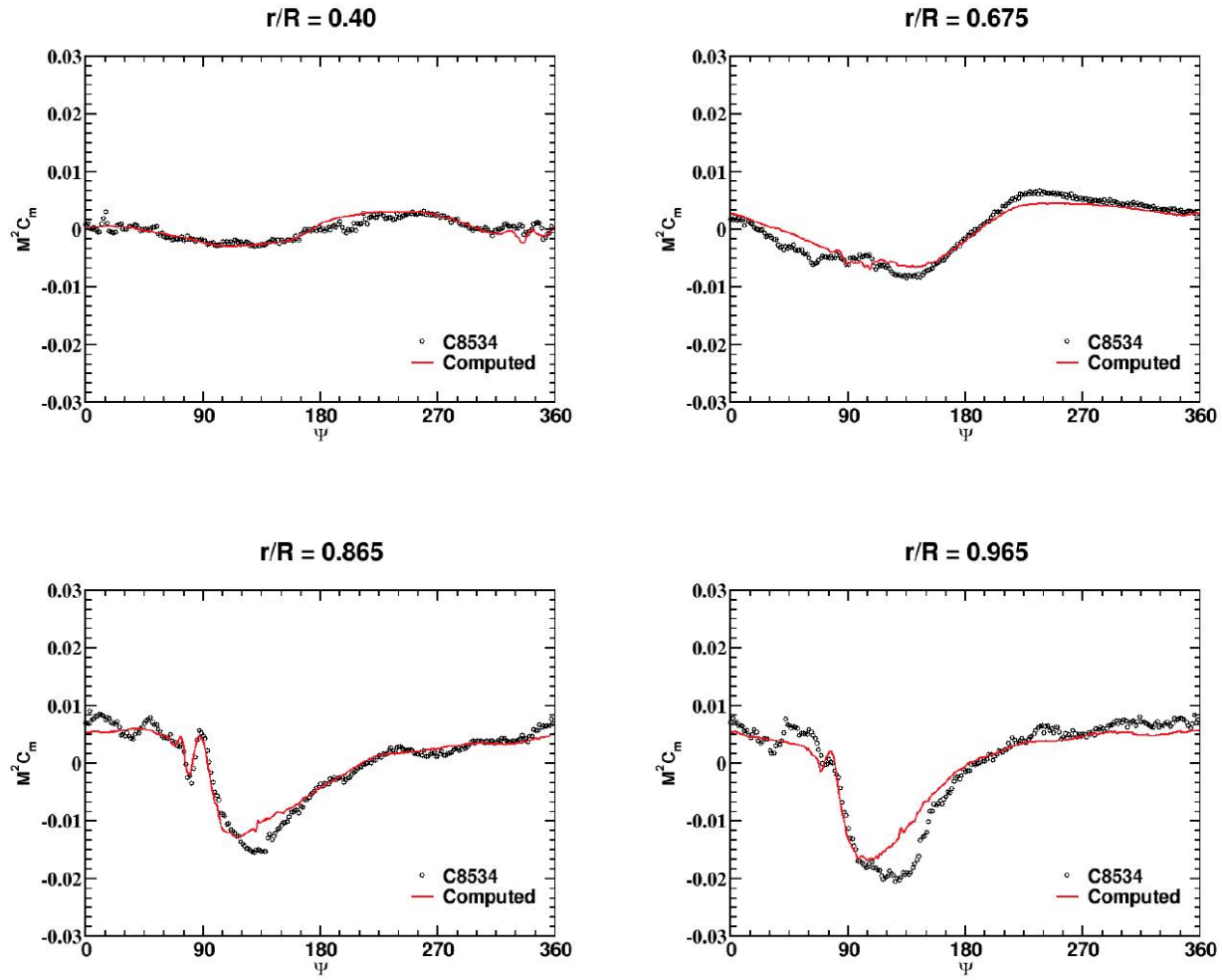

Figure 3.10. Pitching moment coefficient variation with azimuth angle at various radial stations. High-speed case, flight Counter 8534, M_∞ = 0.236, and μ = 0.37 (Fig. 7 of Ahmad and Chaderjian [2011]).

Biedron and Lee-Rausch [2012] further examined the discrepancies between the unsteady airloads calculations and the UH-60A flight data from Counters 8534 and 9017. The authors noted that the correlation results from Biedron and Lee-Rausch [2011] were similar to those obtained by different organizations using different CFD and CSD codes simulating the same UH-60A flight conditions. The differences in sectional airloads between the various simulations were considerably smaller than the difference between the simulations and flight measurements. The authors examined whether the difference in the surface pressure integration method used for the measured data and the computed data contributed to the discrepancies in sectional airloads. In addition to the native integration method used by FUN3D to compute sectional airloads, the airloads were also computed using the same software (identified as TRCPCL) used to process the flight data pressures at chord locations coinciding with functional pressure taps on the flight blade. Using a consistent integration method enabled the authors to directly compare the

simulated and measured unsteady blade pressures. The comparison showed that the relatively sparse number of pressure taps used for the TRCPCL integration code did not contribute significantly to previously observed discrepancies between flight and computation for sectional normal force and pitching moment. However, the sectional chord force showed a significant effect from the integration method, particularly on the advancing side of the rotor disk, as shown in Figure 3.12.

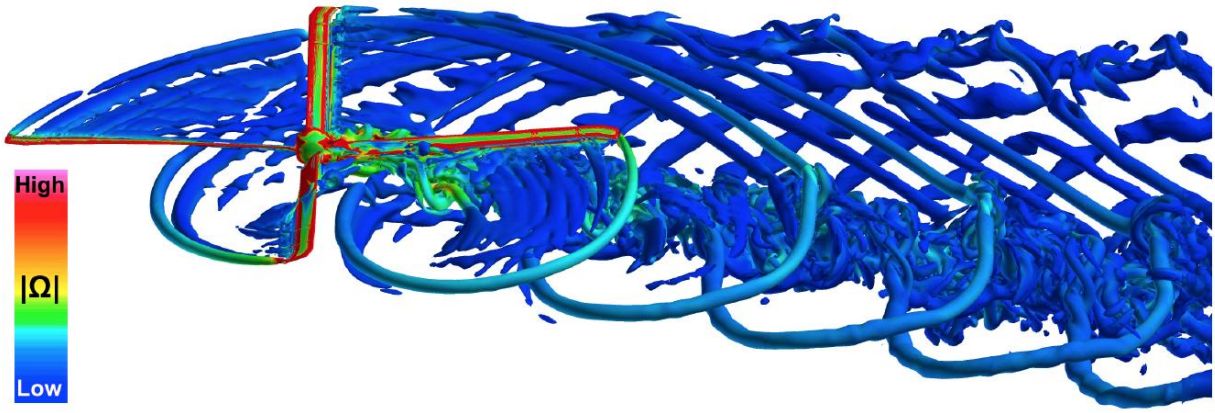

a) Baseline AMR0 vortex wake: Δ = 10% c_{tip}, 960 grids, 61 million grid points (Fig. 16 of Chaderjian and Ahmad [2012].

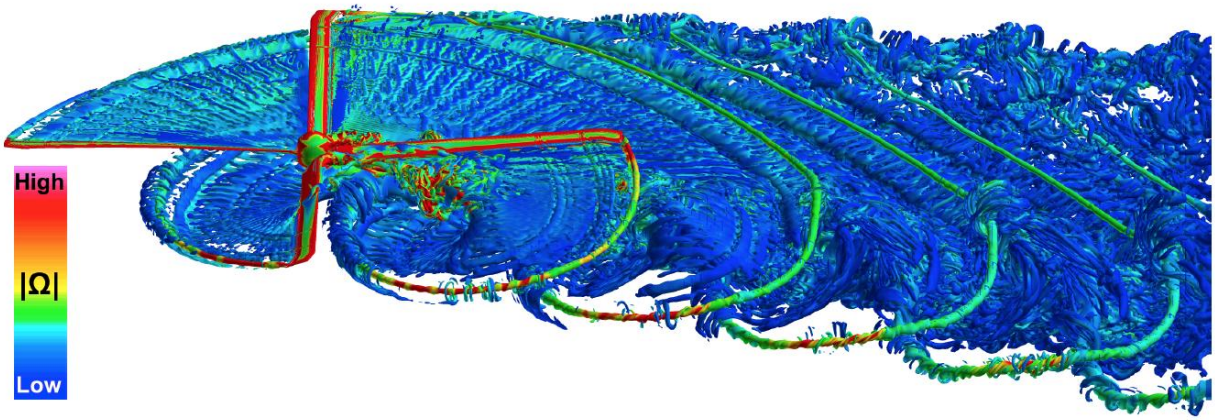

b) AMR2 vortex wake: Δ = 10%, 5%, and 2.5% c_{tip}, 18,500 grids, 754 million grid points (Fig. 17 of Chaderjian and Ahmad [2012].

Figure 3.11. Flow field for Counter 8534—vortices rendered with the Q-criterion.

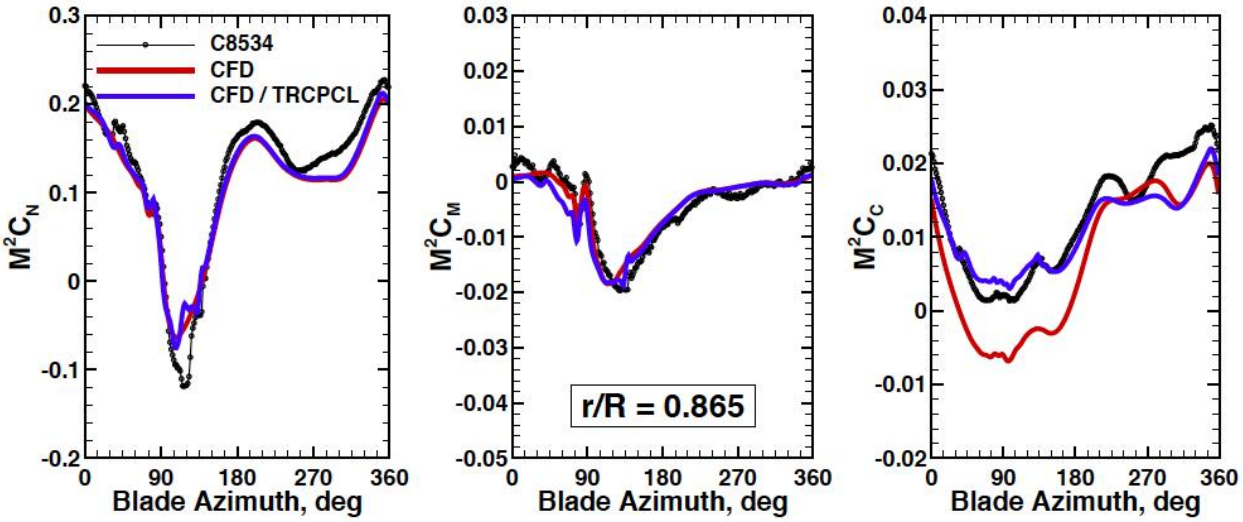

Figure 3.12. Comparison of computed (FUN3D) and measured airloads at r/R = 0.865 for Counter 8534. Flight data and CFD/TRCPCL use identical integration of pressure and neglect skin friction (Fig. 5 of Biedron and Lee-Rausch [2012]).

Chaderjian [2017] continued exploring the application of AMR for Counters 8513 (low speed, with BVI) and 9017 (dynamic stall). Specifically, the author examined the effects of wake grid resolution on the predicted blade airloads when the vortex wake interacted with the rotor blades. Time-dependent flow visualization of the complex flow field enabled improved understanding of the numerical and physical mechanisms involved with 3D dynamic stall. In particular, BVI was found to trigger dynamic stall (Fig. 3.13).

Correlation with wind tunnel data

Romander et al. [2011] compared wind tunnel measurements with predictions from the loosely coupled combination of OVERFLOW2 and CAMRAD II. The primary calculations modeled the rotor in free air with a corrected rotor-shaft angle based on the Prandtl–Glauert wall correction (some results were also shown for a rotor with simulated wind tunnel walls). A speed sweep at constant lift up to an advance ratio of 0.4, and a thrust sweep at constant speed into deep stall, were simulated and compared with measurements. The authors noted a discrepancy between OVERFLOW2 and CAMRAD II in the thrust trim, with CAMRAD II matching experimental thrust targets and OVERFLOW2 showing a 2- to 2.5-percent overprediction of thrust. Despite this discrepancy, the OVERFLOW2 trim targets were used since OVERFLOW2 provided the better representation of the blade aerodynamics compared to CAMRAD II. Comparisons between predicted and measured integrated performance, such as power and propulsive force, were reasonable with some significant differences noted. Figures 3.14 (μ = 0.4, CT/σ = 0.093) and 3.15 (μ = 0.3, CT/σ = 0.1255) show comparisons of computed and measured sectional airloads for the extremes of the speed sweep and thrust sweep, respectively. The authors concluded that the sectional airloads correlation was good in overall trends for normal force and pitching moment, with the pitching moment mean value often differing from the measured value. Predicted chord force was frequently subject to shifts in mean values and an overprediction of

drag on the advancing side. The locations of major aerodynamic phenomena were predicted accurately, though the magnitude of individual events was often missed.

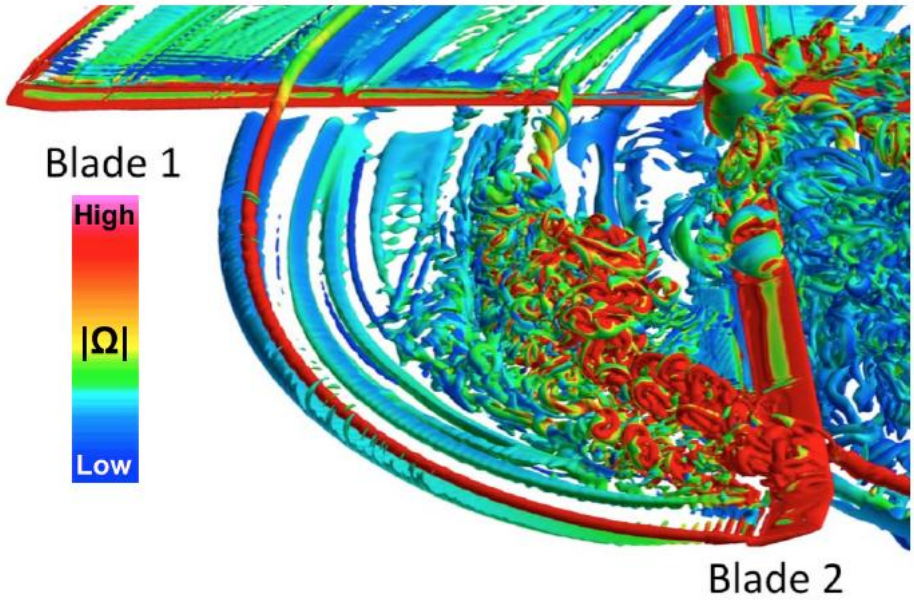

a) Blade 1 at ψ=180°.

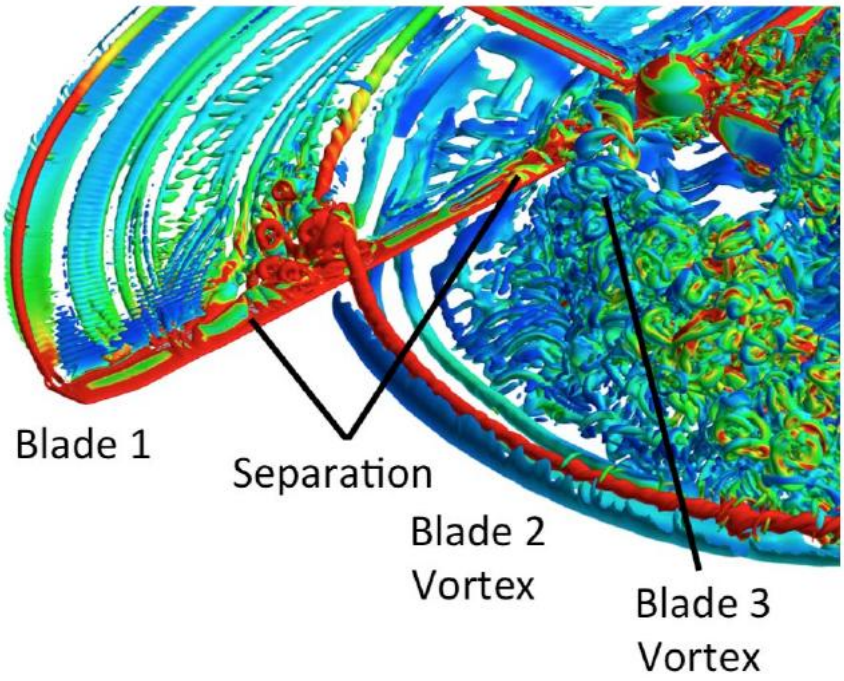

b) Blade 1 at ψ=225°.

Figure 3.13. Close-up view of vortex-induced dynamic stall, ΔS = 2.5% c_{tip}. Q-criterion iso-surface (Fig. 26 of Chaderjian [2017]).

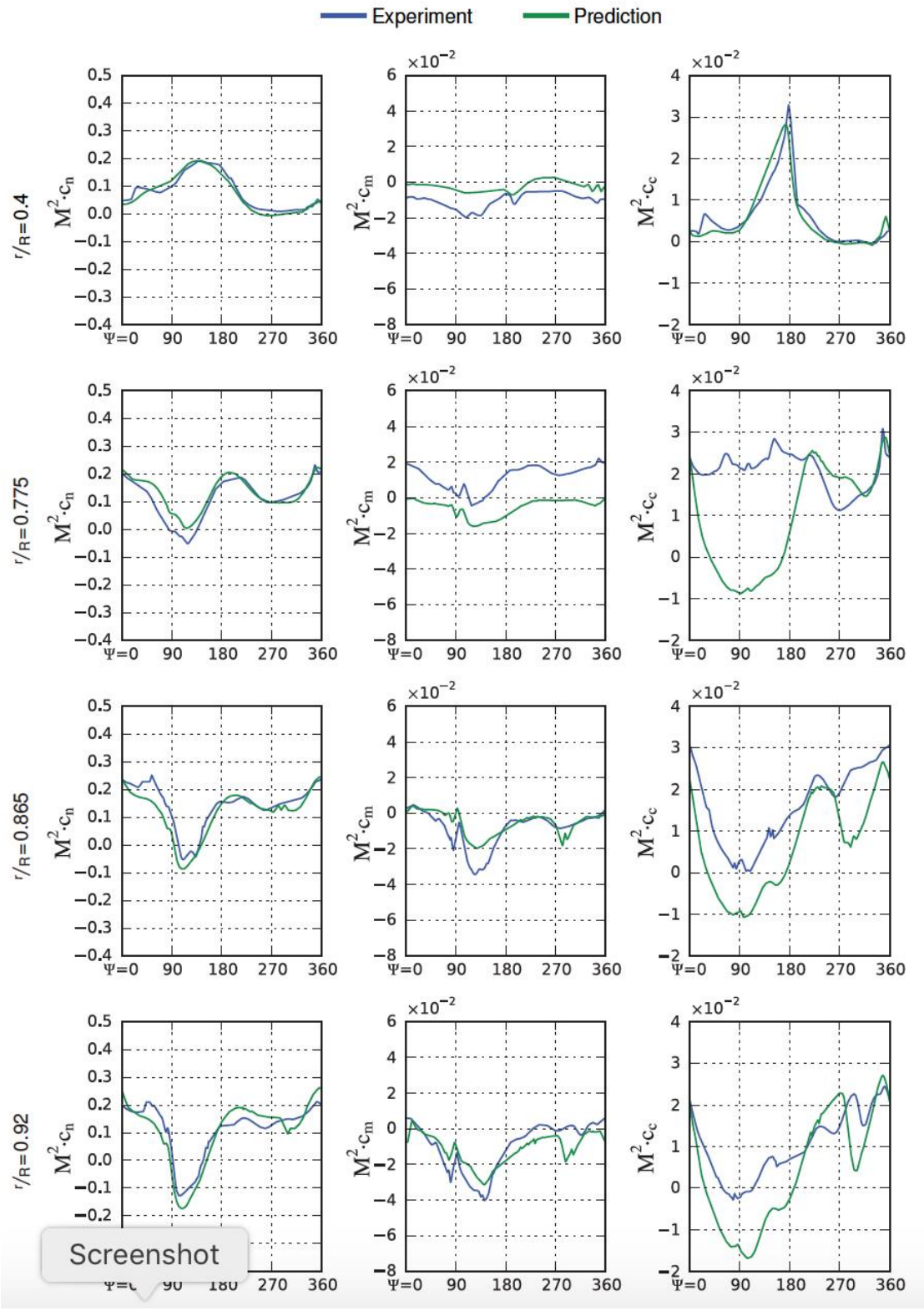

Figure 3.14. UH60A rotor blade sectional airloads at μ = 0.4, CT/σ = 0.093 (Fig. 11 of Romander et al. [2011]).

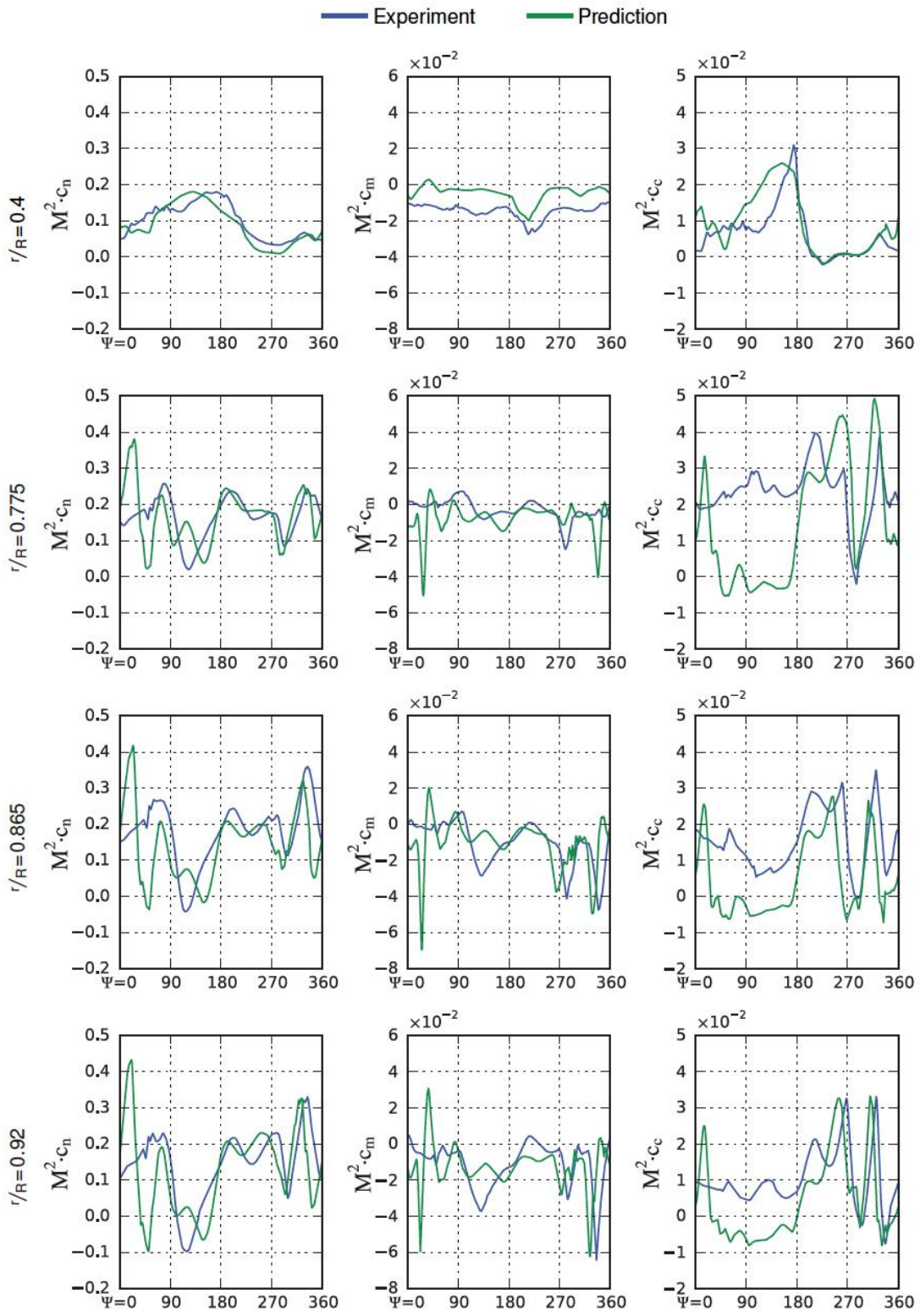

Figure 3.15. UH-60A rotor blade sectional airloads, $\mu = 0.3$, $C_T/\sigma = 0.1255$ (Fig. 16 of Romander et al. [2011]).

Lee-Rausch and Biedron [2013] used FUN3D, a RANS solver for unstructured grids, to compute rotor performance and airloads for the UH-60A rotor. The UH-60A rotor, Large Rotor Test Apparatus (LRTA), and the wind tunnel walls were simulated. Figure 3.16 shows the FUN3D grid for the rotor and the LRTA.

The authors examined the influence of the LRTA, wind tunnel walls, and rotor trim tab deflections on the rotor performance and airloads; FUN3D/CAMRAD II computations focused on a speed sweep at constant lift up to an advance ratio of 0.40. Calculations were compared with rotor trim loads and trim control angles, rotor performance loads, rotor sectional loads, and blade pressures. For the speed sweep conditions, measured and computed solidity weighted propulsive force and power coefficient compared well. Rotor performance and sectional airloads were not sensitive to the inclusion of the wind tunnel walls, while the sensitivity of the rotor performance and sectional airloads to the LRTA/hub increased with advance ratio. Including the LRTA slightly improved the correlation of rotor propulsive force, however, at an advance ratio of 0.37, comparisons of rotor power and sectional airloads showed noticeable differences (see Fig. 3.17).

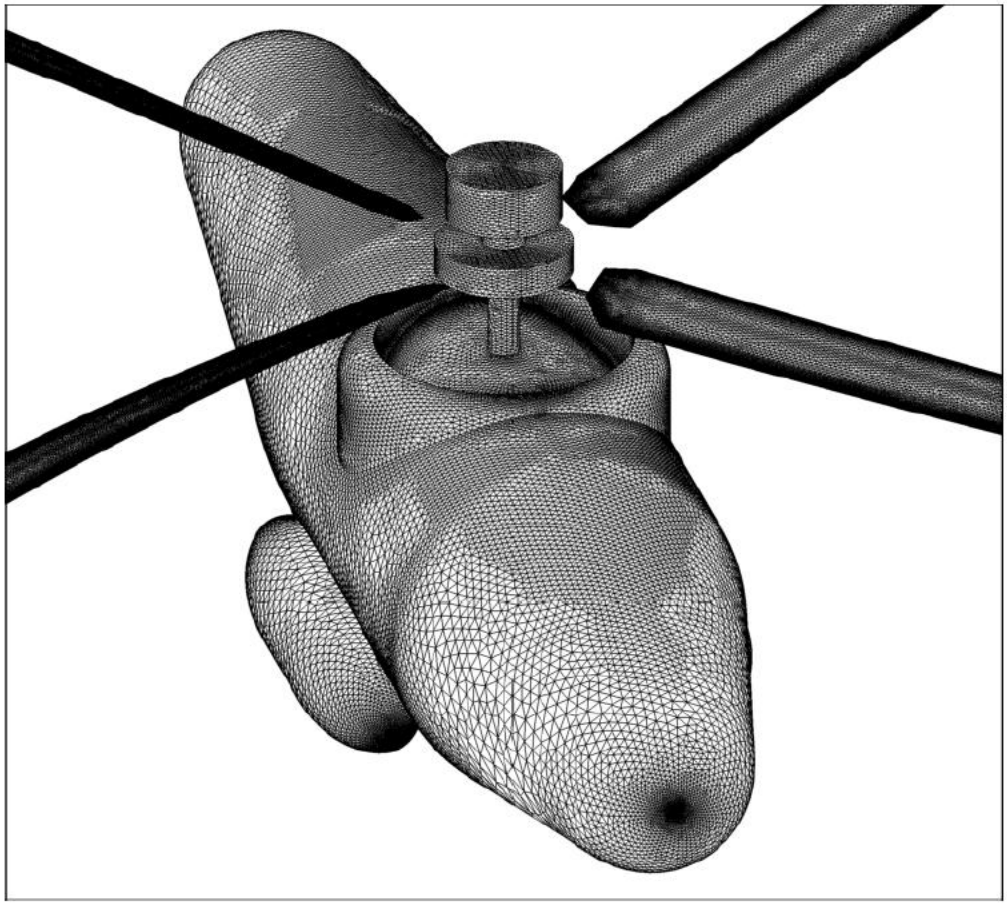

Figure 3.16. CFD model of the UH-60A Airloads rotor on the LRTA (Fig. 3 of Lee-Rausch and Biedron [2013]).

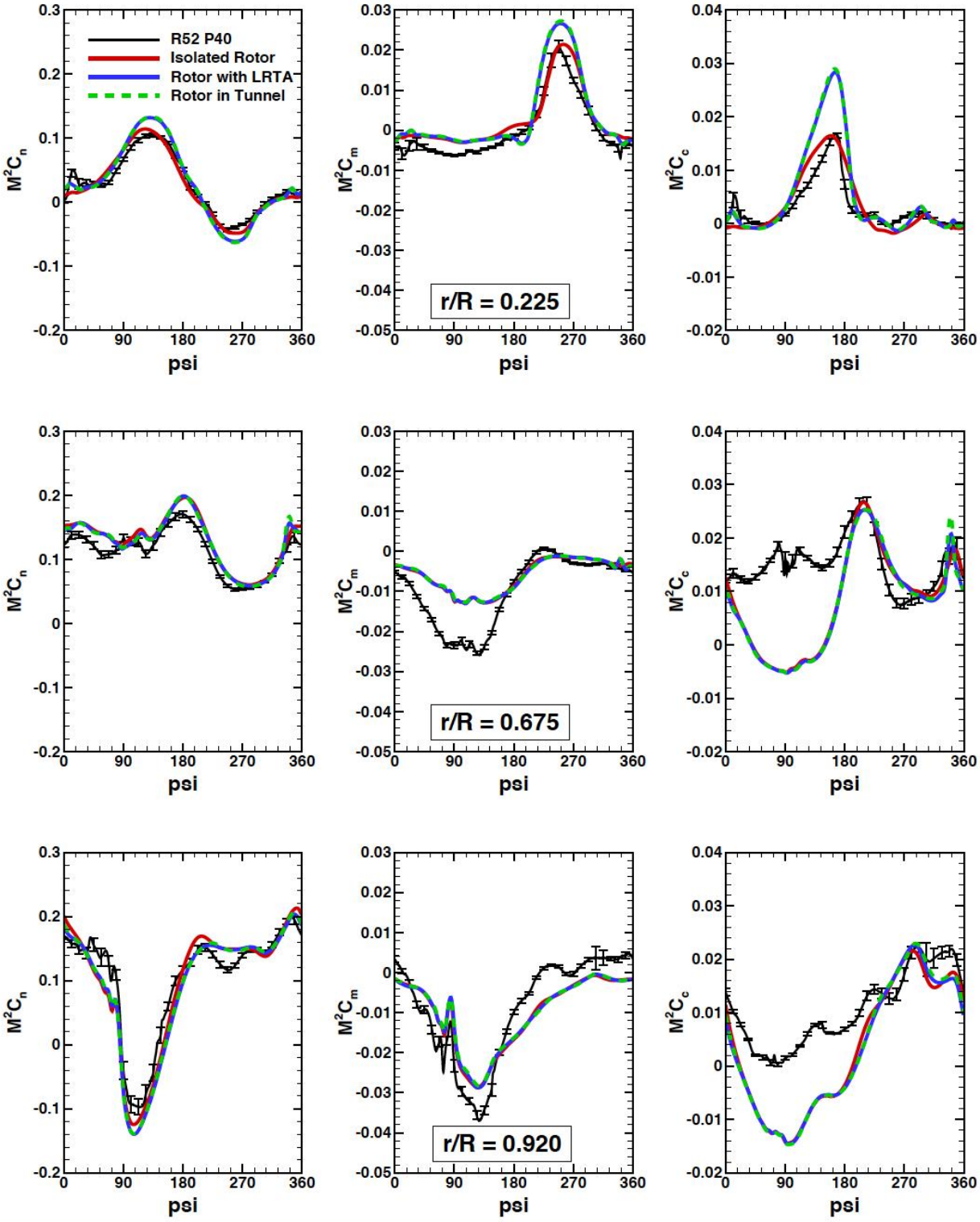

Figure 3.17. Sectional forces and pitching moment for μ = 0.37 (Fig. 20 of Lee-Rausch and Biedron [2013]).

Using OVERFLOW coupled with CAMRAD II, Ahmad et al. [2013] simulated conditions from the wind tunnel test for which particle image velocimetry (PIV) measurements were acquired. The PIV measurements were acquired in a cross-flow plane located at a 90-degree rotor azimuth position; details about the PIV data are described in Chapter 4, Experimental Methods. Qualitative and quantitative comparisons of the computed and measured flow field revealed key features of the complex rotor wake that were captured by the simulation (Fig. 3.18). Although the simulation captures the measured BVI events represented in the blade section airloads, the grid resolution was not adequate for predicting vortex properties, however, the computed vortex property trends agree with the measured trends.

One of the objectives of the UH-60A wind tunnel test was to simultaneously measure the deformation of each of the four rotor blades for the majority of the conditions tested. The deformation measurements based on photogrammetry (called the blade displacement (BD) system) are described in Chapter 4, Experimental Methods. Romander et al. [2014] used OVERFLOW2 loosely coupled with CAMRAD II to compute blade pitch, flap, and lag angle, and compared the calculations with the BD measurements and another independent measurement system from blade-motion hardware (BMH). Similar to Romander et al. [2011], only the rotor and a representative hub were modeled by OVERFLOW2; the wind tunnel walls and LRTA were not included. Four test conditions, representing edges of the test envelope, were chosen for the comparison study: a low-speed case featuring multiple BVIs, a high-speed case, a high-thrust case with the rotor deeply stalled, and a slowed-rotor case at high advance ratio. In general, comparisons between measurement and simulation were very good, with maximum deviations on the order of a few degrees. Collective and cyclic pitch magnitudes tended to be overpredicted by the analyses, while flap-angle calculations were typically within 1 degree of both BD and BMH measurements (see Fig. 3.19). Shifts in lag-angle mean value between the BD and BMH measurements and the analysis highlighted areas to explore in the analysis and also cast doubt on the BD mean lag-angle value.

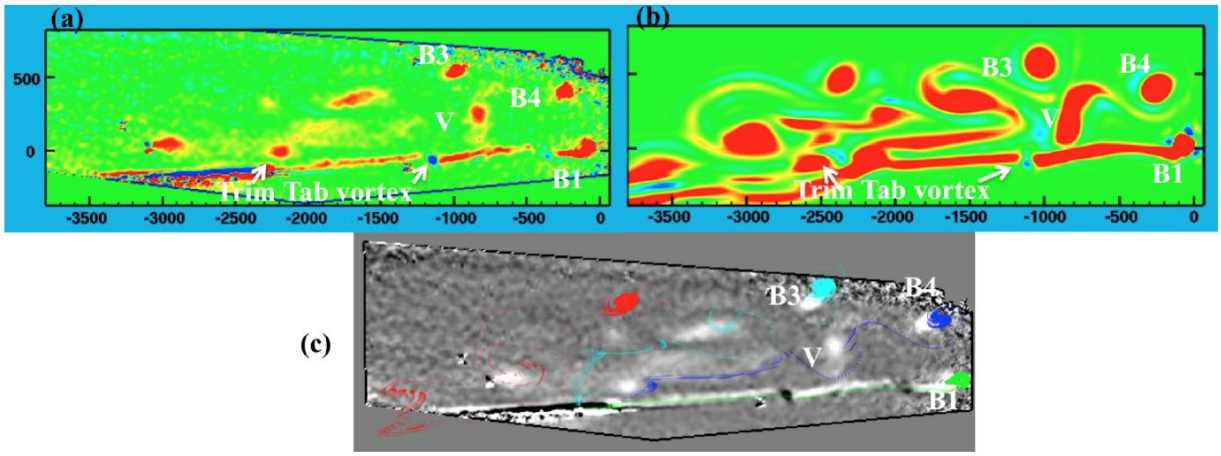

Figure 3.18. Vorticity fields generated by Blade 1 at Δψ1 = 5o: (a) Expt: Run 73, (b) computed, and (c) computed particle trace overlays on grey-scale experimental vorticity field as shown in (a). (Fig. 11 of Ahmad et al. [2013].)

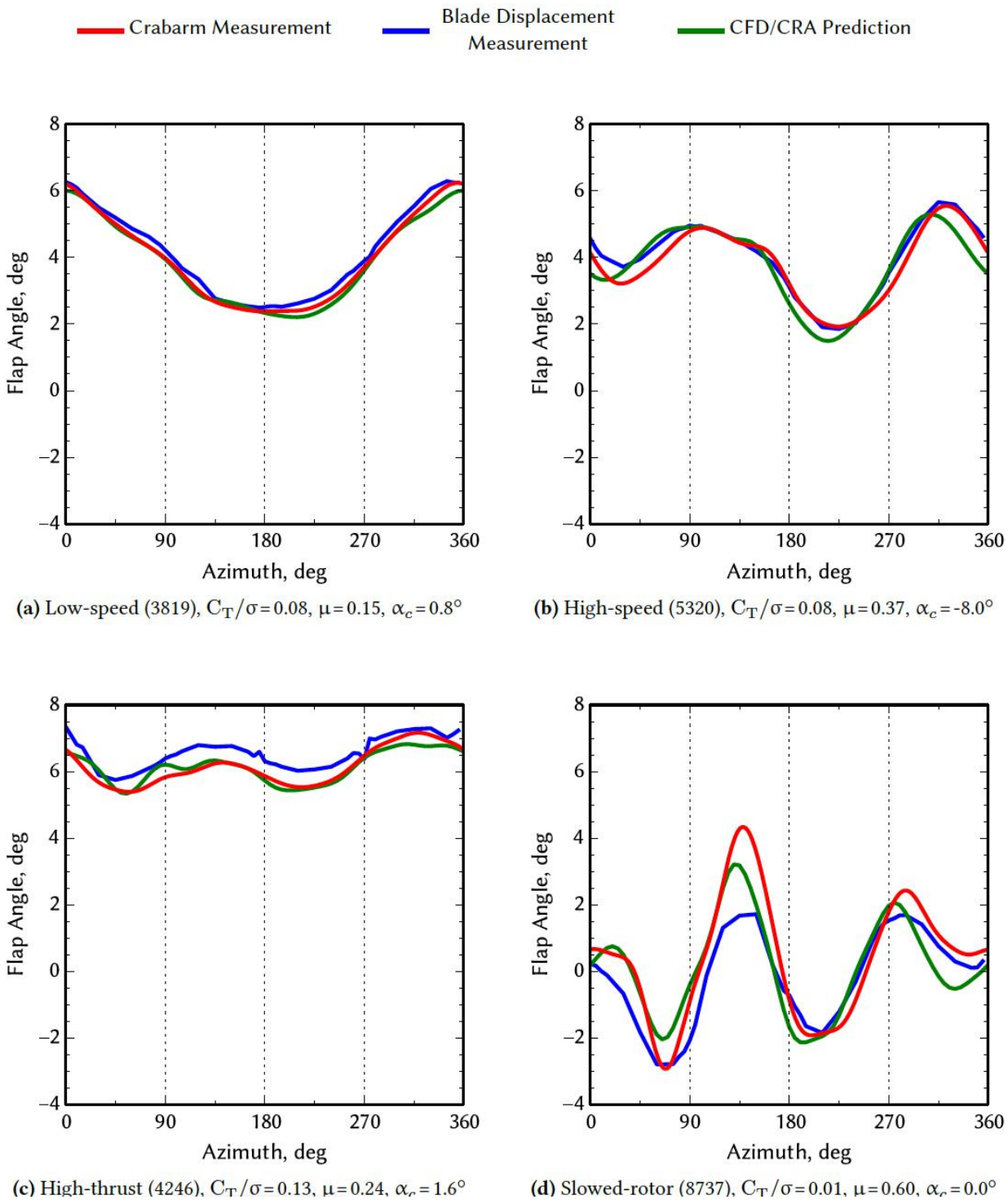

Figure 3.19. Flap motion comparison at selected test conditions (Fig. 8 of Romander et al. [2014]).

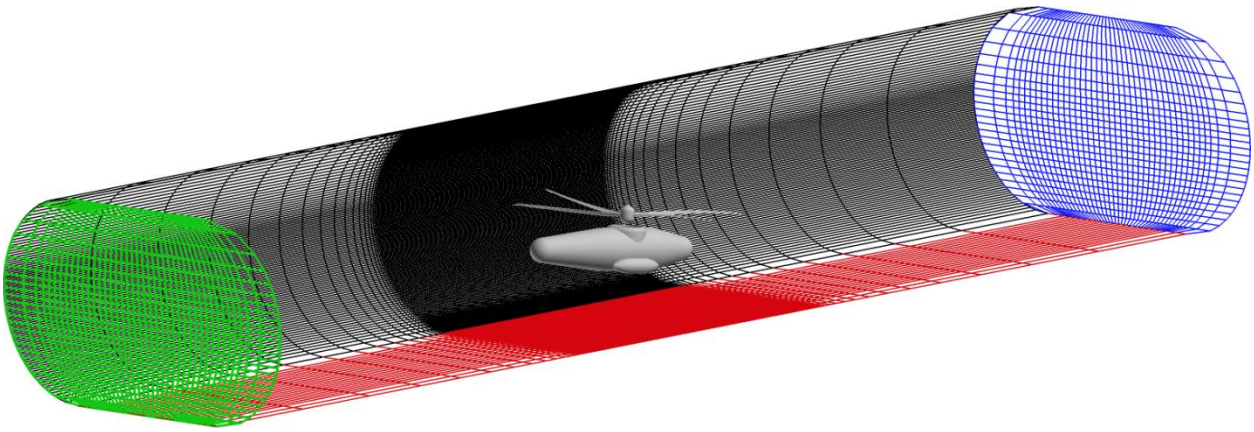

Figure 3.20. Off-body grid set illustrating full wind tunnel grid (level 1 and 2 grids not shown and some points removed for clarity) (Fig. 4 of Chang et al. [2013]).

Following the 2010 UH-60A Airloads wind tunnel test, Chang et al. [2013] revisited the topic of wall effects on the UH-60A rotor, this time including the LRTA test stand (see Fig. 3.20) and using the data from the test [Norman et al., 2011] to validate results.

OVERFLOW2/CAMRAD II (loosely coupled) predictions for the full-scale UH-60A rotor inside the NFAC 40- by 80-Foot Wind Tunnel were compared with measured wind tunnel data for a speed sweep at constant lift, a thrust sweep at constant speed, and an investigation of a single matched flight test condition. To separate installation effects, three configurations were considered: rotor only; rotor and wind tunnel; and rotor, LRTA, and wind tunnel.

The rotor airloads and rotor performance were reasonably well predicted. Including the LRTA and wind tunnel in the simulation appeared to have only limited benefits at low speeds when compared to rotor-only calculations with simple angle-of-attack corrections. At advance ratios greater than 0.37, wind tunnel modeling becomes important, and the presence of the LRTA in the simulation becomes increasingly important as the advance ratio increases. Simulating the LRTA and wind tunnel at high thrust had a noticeable effect on the predicted airloads; wind tunnel modeling becomes important for $CT/\sigma > 0.11$, and LRTA modeling becomes increasingly important for $CT/\sigma > 0.09$.

Slowed Rotor

Time-accurate numerical simulations were performed using the RANS flow solver OVERFLOW for a heavy-lift slowed-rotor compound helicopter configuration tested in the NASA Langley 14- by 22-Foot Subsonic Tunnel [Allan et al., 2009]. The primary purpose of these simulations is to provide support for the development of a large field of view PIV flow measurement technique. These simulations provide a better understanding of the rotor and body wake flows and help to define PIV measurement locations as well as requirements for validation of flow solver codes.

The large field PIV system can measure the 3D velocity flow field in a 0.914-m by 1.83-m plane. PIV measurements were performed upstream and downstream of the vertical tail section and were compared to simulation results. The simulations are also used to better understand the tunnel wall and body/rotor support effects by comparing simulations with and without tunnel floor/ceiling walls and supports. Comparisons were also made to the experimental force and moment data for the body and rotor. Figure 3.21 shows the slowed rotor configuration of the tunnel as modeled by CFD depicting the surface overset meshes. The fuselage was supported by a cylindrical post and the rotor by a separate Isolated Rotor Test System (IRTS). From the CFD investigation it was shown that the wake from IRTS had a significant effect on the rotor airloads since CFD could be run with and without IRTS. Figure 3.22 compares the CFD wake predictions to the large field of view PIV just downstream of the vertical tail on the vehicle. This comparison shows that CFD was able to capture the main rotor wake vortices and well as vortices from the wing and horizontal tail. CFD was also able to identify the source of the vortices and wakes measured by the PIV.

Active Aerodynamic Load Reduction on a Rotorcraft Fuselage

Typically, the design of a rotorcraft fuselage has a greater emphasis on its function rather than aerodynamic efficiency. An example is the design choice of an aft-facing ramp on some rotorcraft, used for easily loading and unloading equipment, that contributes to significant drag at cruise because of the massive flow separation on the rear of the fuselage. In a joint collaboration between NASA, the U.S. Army, and ONERA, different active flow control approaches were explored using CFD on a generic rotorcraft fuselage designed by NASA, in collaboration with the U.S. Army, and a fuselage designed by ONERA. The goal of the joint effort was to design an active flow control strategy to reduce fuselage drag, and then build and test the flow control design and compare the experimental results to the CFD predictions. The experimental efforts are summarized in the Flow Control section of Chapter 2, Aeromechanics. The CFD investigation of the active flow control strategy was presented by Schaeffler et al. [2010] for an isolated fuselage with no rotor effects with promising results for steady and unsteady zero-net-mass blowing. Using the lesson learned from Schaeffler et al. [2010], a CFD study of the active flow control in rotor effect was performed by Allan and Schaeffler [2011, 2015] before and after a 1/3-scale wind tunnel experiment in the NASA Langley 14- by 22-Foot Subsonic Tunnel with the fuselage and a rotor. Overall, CFD was able to predict the trends of the flow control in reducing the drag and fuselage download, however CFD was not able to match the experimental fuselage forces. It was speculated that a more sophisticated turbulence modeling approach like DES or LES may be needed in order to better match the experiment because of the bluff body flow separation on the fuselage ramp region. Figures 3.23 and 3.24 show comparisons of CFD using the Spalart–Allmaras (SA) and Shear Stress Transport (SST) turbulence models to PIV wake measurements. These comparisons show that CFD was able to capture the separated wake flow features for the baseline and the active flow control case.

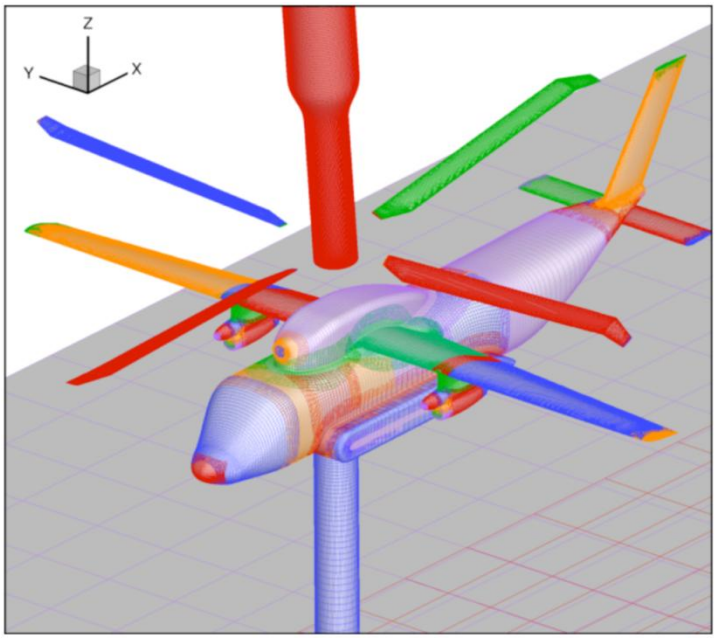

Figure 3.21. Surface grids on rotorcraft vehicle, model support post, wind tunnel floor, and IRTS (Fig. 1 of Allan et al. [2009]).

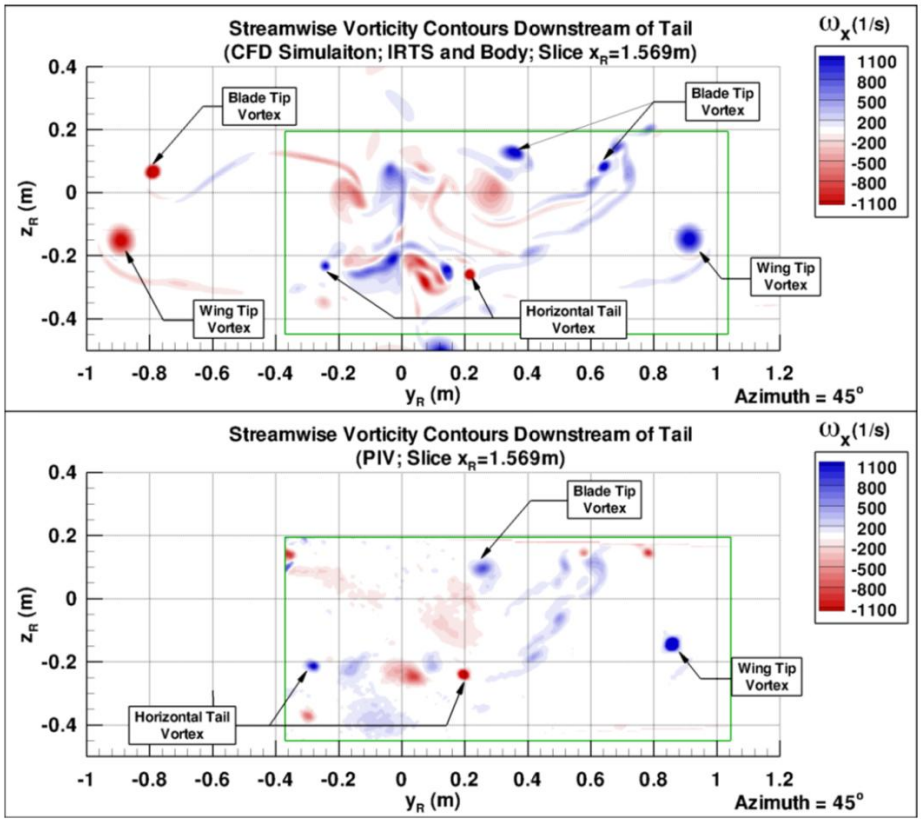

Figure 3.22. Comparison of the wind tunnel PIV measurements in the wake of the rotor and body downstream of the tail to the numerical simulation results modeling the body support post and IRTS (Fig. 11a of Allan et al. [2009]).

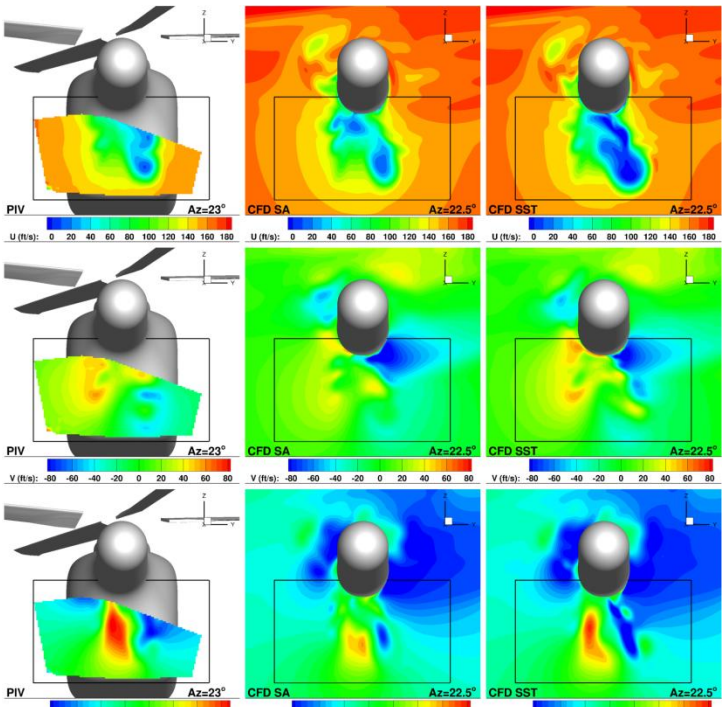

Figure 3.23. Comparison of CFD and PIV data for the baseline. AoA = −6°, μ = 0.25, and CT/σ = 0.075 (Fig. 25 of Allan et al. [2015]).

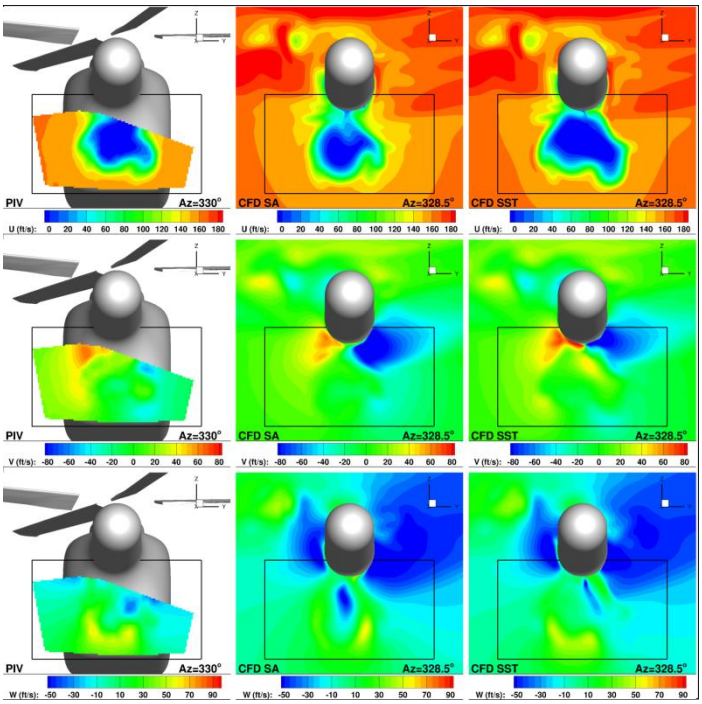

Figure 3.24. Comparison of CFD and PIV data for the AFC jet, VR = 2.6 using full U-configuration. AoA = −6°, μ = 0.25, and CT/σ = 0.075 (Fig. 26 of Allan et al. [2015]).

Active Twist Rotor

An unsteady RANS analysis loosely coupled with a comprehensive rotorcraft code was performed for a second-generation active-twist rotor [Massey et al., 2013, 2015]. The high-fidelity Navier–Stokes results for three configurations—an isolated rotor, a rotor with fuselage, and a rotor with fuselage mounted in a wind tunnel—are compared to lifting line theory–based comprehensive rotorcraft code calculations and wind tunnel data. Results indicate that CFD/CSD predictions of flapwise bending moments are in good agreement with wind tunnel measurements for configurations with a fuselage, and that modeling the wind tunnel environment does not significantly change the predictions. Figure 3.25 shows the iso-surfaces of the Q-criterion along with the unstructured surface mesh for the rotor with fuselage mounted in the wind tunnel. Actuated rotor results for the rotor-with-fuselage configuration are also validated for predictions of vibratory blade loads and fixed-system vibratory loads. Varying levels of agreement with wind tunnel measurements are observed for blade vibratory loads, depending on the load component (flap, lag, or torsion) and the harmonic being examined. Predicted trends in fixed-system vibratory loads are in good agreement with wind tunnel measurements.

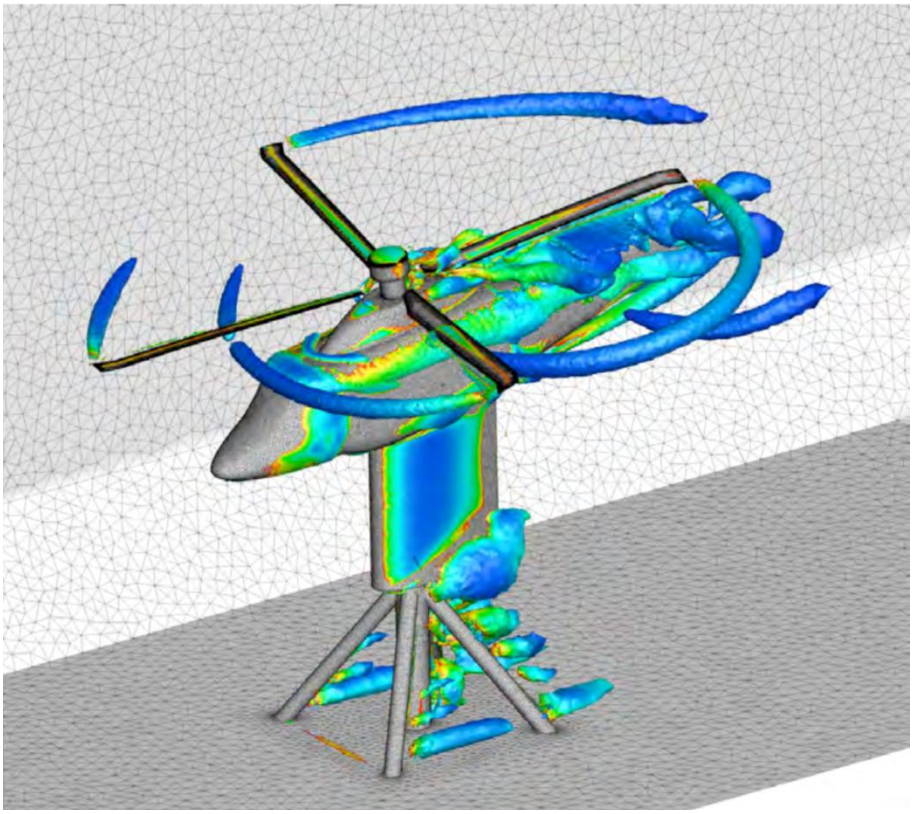

Figure 3.25. Surface meshes and iso-surfaces of Q = 0.00005 colored by vorticity magnitude for the active-twist rotor and fuselage configuration in the Transonic Dynamics Tunnel (TDT) for μ = 0.33 (Fig. 3c of Massey et al. [2015]).

HART-II

The Higher harmonic control Aeroacoustics Rotor Test II (HART-II) is an extensive rotor experimental data set developed through an international collaboration between the German Aerospace Center (DLR), the German-Dutch Wind Tunnels (DNW), the French Office National D'Etudes et de Recherches Aerospatiales (ONERA), NASA Langley Research Center, and the U.S. Army Aeroflightdynamics Directorate (AFDD) research organizations. The test used an aeroelastically scaled model of the BO-105 main rotor that was tested at DNW [Biedron et al., 2008]. Measured data for the HART-II includes detailed acoustic, aerodynamic, rotor wake, blade deformation, and rotor airloads data on a pressure instrumented blade.

A validation of rotor airloads using a Navier–Stokes solver for unstructured grids, FUN3D, coupled with a rotorcraft CSD code, was performed by Biedron et al. [2008]. This validation effort used the HART-II data modeling the rotor and fuselage as shown in Figure 3.26. This study compared rotor airloads and structural deformations for three different HART-II operating conditions: baseline, minimum noise, and minimum vibration. Overall, the study showed good agreement between the CFD and experimental airloads and blade deflections. This study showed that a mesh resolution of approximately 10 percent of the tip chord or finer was needed in order to see any BVI effects.

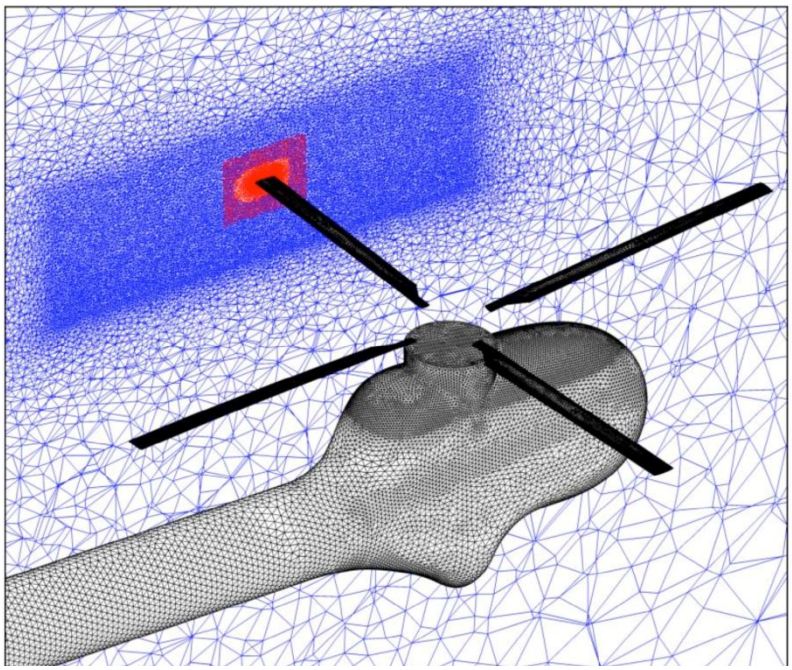

Figure 3.26. HART-II overset unstructured grids (Fig. 3 of Biedron et al. [2008]).

A summary of a HART-II international workshop, which had many international participants using several different CFD and CSD codes, is given by Smith et al. [2012, 2013]. The study found that for rotor operating conditions that had interaction between the blades and trailing tip vortices, higher-order numerical schemes in both spatial discretization and time-advancing algorithms are crucial for improved predictions. It was also shown that off-body grid resolution, grid refinement techniques, time step size, and sub-iterations were important contributors to the solution accuracy. The research also found that different RANS turbulence models did not have a significant impact on the solution accuracy. The workshop results also showed that the BVI events on the advancing rotor disk were influenced by the fuselage while events on the retreating side were not.

Hover Validation

One of the unique capabilities of a rotorcraft is hover, which has been a challenging problem for CFD to predict. Specifically, the challenge lies in the ability of CFD to predict the hover performance known as the figure of merit (FM). The FM represents the ratio of the ideal torque from momentum theory to the actual torque required to spin the rotor. Simulations of an isolated tiltrotor were performed by Lee-Rausch and Biedron [2009] using an unstructured overset-grid RANS solver, FUN3D. The simulations were validated against experimental data from the TRAM rotor constructed and tested for tiltrotor aeromechanics research. Because of the rigid nature of the TRAM blades, it is not necessary to model the aeroelastic blade effects in the CFD simulations. This eliminates any uncertainty in the hover performance predictions that may be introduced by modeling the blade structural dynamics. The hover performance from this study is shown in Figure 3.27 where there is a 3-percent error on the FM at high thrust and a 6-percent error at lower thrust. Considering that a 0.5-percent error in FM is nearly equivalent to one passenger on a small- to medium-size helicopter, NASA began research to further investigate prediction of hover accuracy by developing higher-order numerical spatial schemes and dynamic AMR.

As a follow-up to the work by Lee-Rausch and Biedron [2009], Chaderjian and Buning [2011] performed an extensive computational study on the prediction of hover performance using newly implemented higher-order spatial schemes and dynamic mesh adaption in the structured overset grid RANS flow solver, OVERFLOW. Figure 3.28 shows the highly refined rotor wake of a hover flow solution by Chaderjian and Buning [2011] using mesh adaption and a high-order spatial scheme. One of the major findings of this study was that near-body rotor-blade grid resolution and spatial accuracy of the numerical algorithm were more important to predicting the FM than the grid resolution in the rotor wake. Previous studies had incorrectly speculated that poor wake resolution was responsible for underpredicting the FM. A second finding was that using a DES was crucial to accurately predicting the FM as shown in Figure 3.29. The DES model resulted in a more realistic turbulent length scale in the rotor wake as compared to a RANS model, which uses the distance to the nearest body, significantly reducing the turbulent eddy viscosity in the rotor wake. Lastly, the research by Chaderjian and Buning [2011] identified small vortical worms that were prevalent in the rotor wake. These vertical worm-like structures are hypothesized to be the result of the entrainment of the vortex wake shear layer from the blades into the rotor tip vortices, as shown in Figure 3.30, where the worms are formed during a process of vortex stretching.

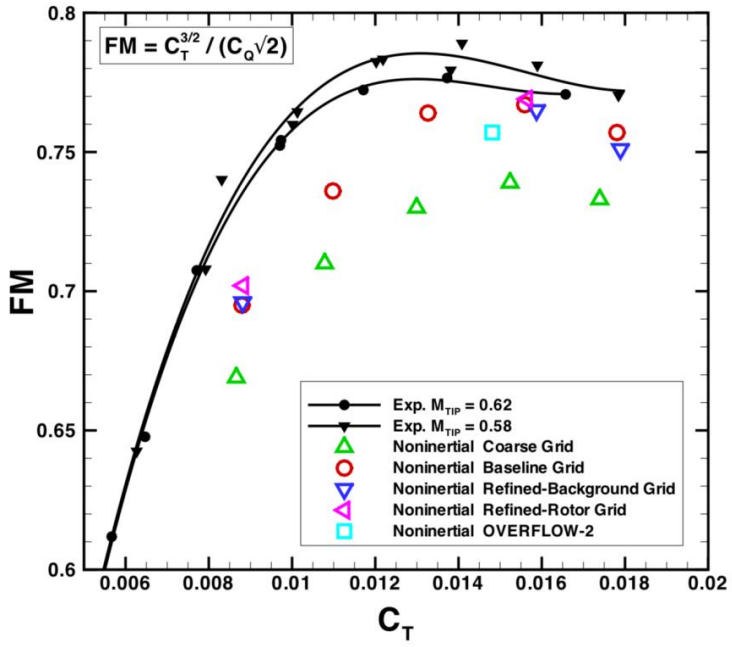

Figure 3.27. Isolated TRAM rotor hover performance in terms of FM vs. thrust coefficient (Fig. 6 of Lee-Rausch and Biedron [2009]).

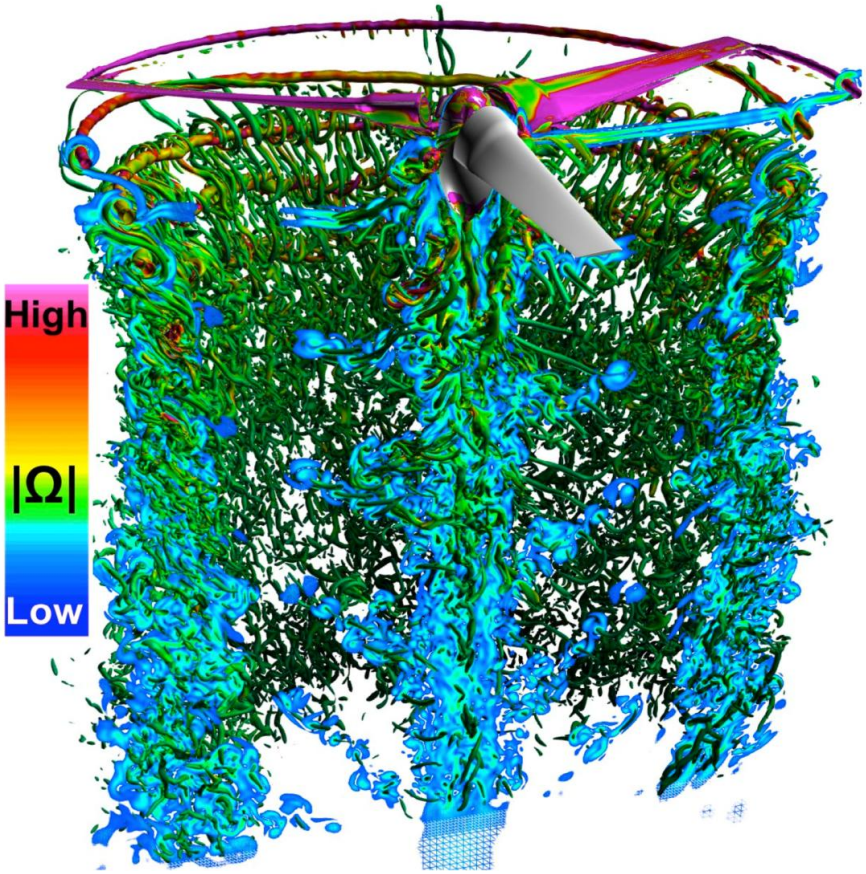

Figure 3.28. Cut-away view of vortex wake. Mtip = 0.625, θ = 10°, and Re = 2.1 million (Fig. 29 of Chaderjian and Buning [2011]).

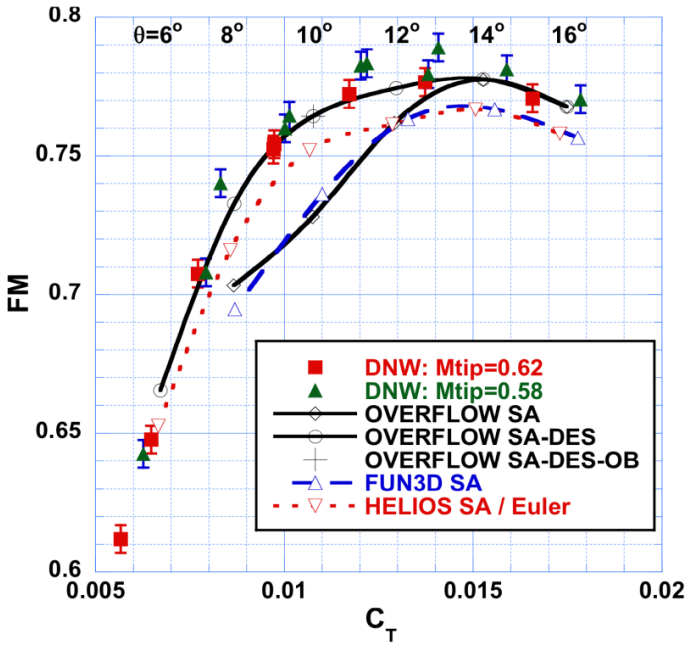

Figure 3.29. FM variation with C_T for the TRAM rotor in hover. Mtip = 0.625 and Re = 2.1 million (Fig. 13 of Chaderjian and Buning [2011]).

A CFD comparison to an XV-15 rotor hover experiment made by Yoon et al. [2014, 2015] looked at the effects of turbulence models in the off-body grids, including the evaluation of using a laminar off-body approach. This research showed that the laminar off-body approach resulted in similar FM predictions as the DES model, and that the RANS model underpredicted the FM as was previously reported by Chaderjian and Buning [2011]. This research also showed that the FM was sensitive to far-field boundaries less than 15 rotor radii away.

The success of improving hover performance predictions using high-fidelity CFD methods has resulted in a need to improve FM predictions within a few tenths of a percent of error. Unfortunately, the current hover experimental data lacks this type of measurement accuracy for FM. Also, there is a need to have an experimental data set that uses recently developed experimental measurement techniques like blade deformation and laminar-to-turbulent boundary-layer transition on the blades. In planning for a new hover test using these advanced measurement techniques, Chaderjian and Ahmad [2015] examined the effects of two different test facilities on hover performance by performing a CFD investigation. This CFD investigation included the Rotor Test Cell (RTC) at NASA Langley and the NFAC at NASA Ames. The conclusion was that the RTC had significant wall effects on hover performance and FM, and that the NFAC facility would be the best facility to minimize wall effects.

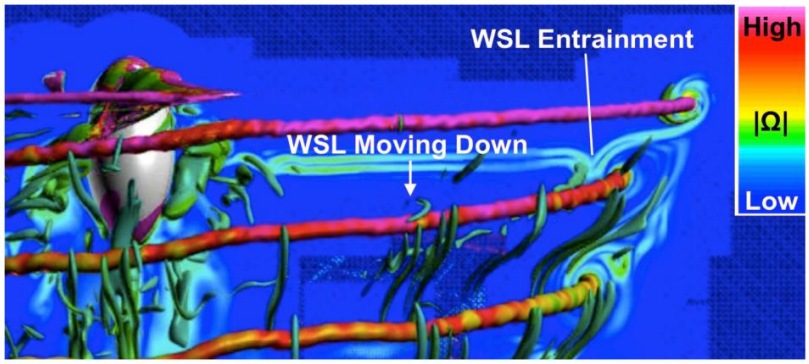

a) Wake shear-layer entrainment.

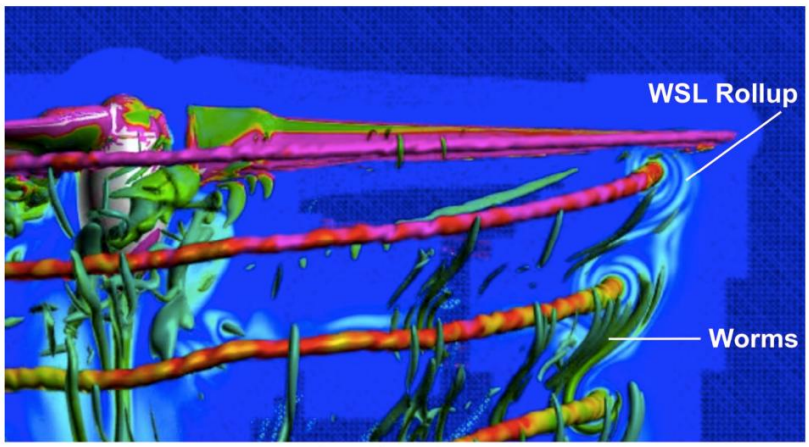

b) Worms and wake shear-layer rollup.

Figure 3.30. Two frames from a CFD-generated movie. Mtip = 0.625, θ = 14°, and Re = 2.1 million (Fig. 24 of Chaderjian and Buning [2011]).

Coaxial Rotor

An investigation by Barbely et al. [2016] on the flow physics of a coaxial rotor was made for a future study on coaxial rotor acoustics. This study used RotCFD with the RotUNS unstructured flow solver and a discrete unsteady actuator disk model for 3D simulations of the coaxial rotors, and the OVERFLOW flow solver for 2D airfoil crossing. The 2D airfoil crossing investigation was continued by Schatzman et al. [2017] using OVERFLOW with improved airfoil wake resolution using mesh adaption. The outcome of this research was a better understanding of the complex nature of the aerodynamic impulses generated by blade-blade interactions with implications for aeroelastic loads and aeroacoustics sources.

Yoon et al. [2016] performed a high-fidelity simulation of the interactional aerodynamics of a coaxial rotor by looking at the effects of rotor spacing and a fuselage in hover on rotor thrust. Figure 3.31 shows three different rotor separation distances and the highly resolved rotor wakes and their interaction.

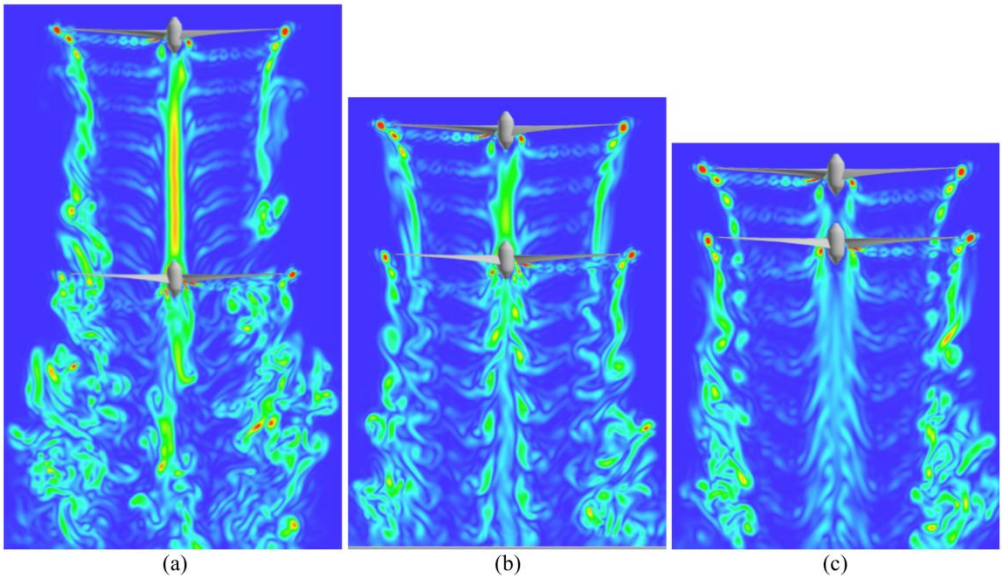

Figure 3.31. Vorticity magnitude for coaxial rotors in hover: (a) inter-rotor spacing = 1.0D, (b) inter-rotor spacing = 0.5D, and (c) inter-rotor spacing = 0.25D. XV-15 rotors, M_{tip} = 0.69, Re_{Ctip} = 4.9 million, and $\theta = 10°$ (Fig. 2 of Yoon et al. [2016]).

Novel CFD Applications

A unique investigation by Hill et al. [2008] was made on validating the use of high-fidelity CFD modeling to predict gearbox windage power losses. This power loss is associated with the rotational deceleration torques on spinning gears by aerodynamic forces within the air-oil atmosphere in the gearbox. The windage losses are a source of significant heating and fuel consumption in rotorcraft vehicles. It has been shown that geometric modifications to control the air flow path, such as shrouding and baffle configurations, can significantly reduce windage losses and lubricating oil consumption. However, design of such modifications is typically done by trial and error, where hardware and testing become expensive and time consuming. Having a validated numerical simulation capability can have a significant impact on lowering the cost and reducing the design cycle time for improved gearboxe designs that have lower gear windage losses. In this research Hill et al. [2008] used NPHASE-PSU, an unstructured multiphase flow solver with overset mesh capability. Figure 3.32 shows the surface mesh with a hybrid mesh topology with a structured hexahedral cell for the gear teeth to the outer boundary and an unstructured prism cell for the region above the gear. Comparisons of the power loss between the experiment and CFD results are presented in Figure 3.33 showing good agreement for four different gears.

An investigation into the use of CFD for the prediction of airfoil data in reverse-flow and significant cross-flow effects was made by Smith et al. [2009]. The motivation for this research was to explore and expand the understanding of the aerodynamic phenomena that rotor blades encounter at high-speed, high-advance-ratio flight; specifically, the large regions over the rotor disk where rotor blades experience reverse- and cross-flow effects that cannot be simply neglected in a design and analysis for efficient rotors at high advance ratios. The authors also

wanted to see if there was the potential to use CFD to generate data that captures the physics of airfoil/rotor blade behavior in these reverse- and cross-flow regions so that it could be used in situations where wind tunnel testing might not be feasible. This investigation showed that 3D simulations using LES-based turbulence models were necessary to capture the physics at and above stall where the RANS methods would overpredict or underpredict the integrated loads and moments near the stall location.

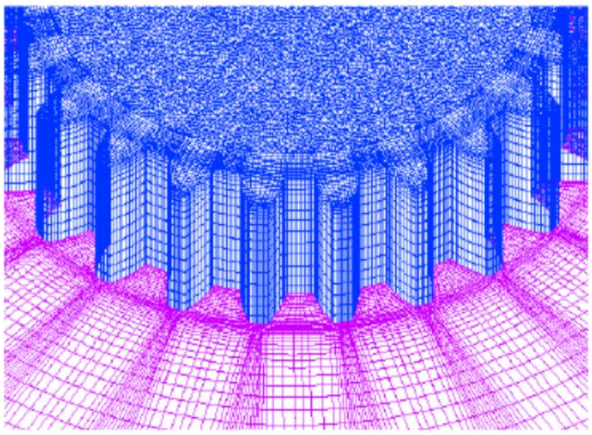

Figure 3.32. Mesh topology for Gear 4 (Fig. 10 of Hill et al. [2008]).

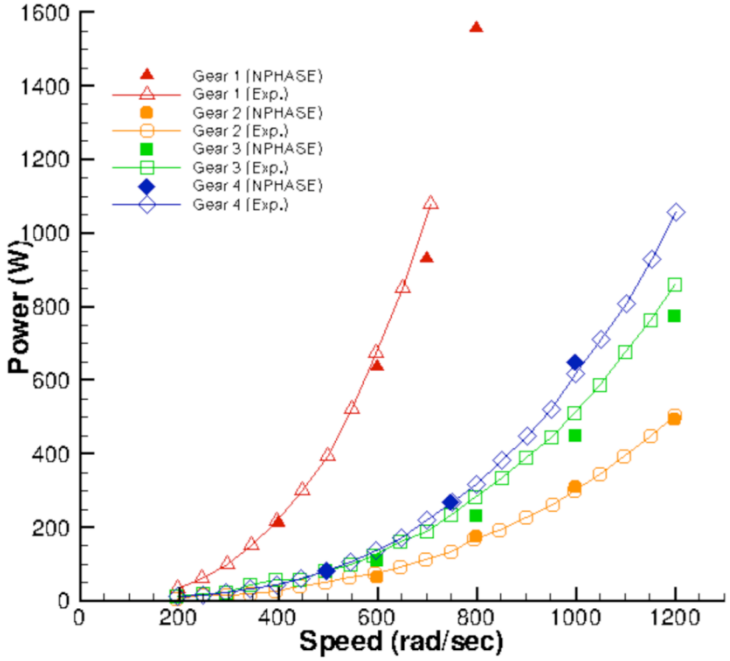

Figure 3.33. Comparisons between the experimental results and the NPHASE-PSU analysis (Fig. 12 of Hill et al. [2008]).

A computational investigation on a dynamically variable droop leading edge on a rotor blade was made by Bain et al. [2008] for a suppression of dynamic stall. To perform the analysis, modifications were made to the NASA Navier–Stokes flow solver, OVERFLOW, to allow for the deforming mesh capability. The simulations were also loosely coupled with the rotorcraft comprehensive code, DYMORE. The variable-droop leading edge was compared to a baseline UH-60A case (Counter 9017: high thrust with dynamic stall) that had two dynamic stall cycles. The high-fidelity CFD simulation predictions showed a 2.9-percent improvement in rotor efficiency, a reduced torque of 3.3 percent, and an 8-percent reduction in the 4/rev component of the vertical force.

A Large Eddy Simulations (LES) of a novel flow control device using Combustion Powered Actuation (COMPACT) was performed by Srinivasan et al. [2008] to better understand the flow physics and assess the efficiency of the device. This simulation includes a combustion model to capture the combustion physics inside the actuator. The authors observed that a strong swirl driven by the radial injection of the reactants resulted in combustion occurring primarily in the near-wall region and not in the core of the device. Their findings suggest that the orientation of the injectors probably has an important consequence on the quality of the mixing because of the influence of the walls.

ROTOR DESIGN OPTIMIZATION USING ADJOINT-BASED APPROACH IN FUN3D

One of the challenges in design optimization using CFD is obtaining sensitivity information for the flow field at a reasonable cost [Nielsen et al., 2009a]. Conventional finite difference methods become cost prohibitive for optimizations with an increasing number of design variables since the computational cost scales linearly with the number of design variables. The use of complex variables improves limitations of step-size over conventional finite difference methods but still becomes cost prohibitive as the number of design variables increases. Adjoint methods can overcome this prohibitive cost by solving an adjoint set of equations that provide the aerodynamic sensitivities needed for gradient-based-design optimization [Nielsen et al., 2009a]. The cost of the adjoint method is nearly equivalent to solving the analysis problem and is independent of the number of design variables. The challenges in using an adjoint method are its rigorous mathematical formulation and implementation into an adjoint solver. Rotorcraft applications are even more challenging for adjoint methods because of inherent unsteady flow and the moving rotor blades with elastic deformation.

In 2009 Nielsen et al. developed and implemented a discrete adjoint-based methodology for optimization of unsteady flows governed by the 3D RANS equations on dynamic unstructured grids in FUN3D [Nielsen et al., 2009a]. This methodology accounts for mesh motion on both rigid and deforming bodies and was successfully applied to a tiltrotor based on the TRAM model in a pitch-up maneuver from hover to forward flight. The objective function for the optimization was to maximize the rotor thrust coefficient over a pitch-up maneuver. There were a total of 44 design variables describing the thickness and camber at different locations along the blade, in addition to the collective control. Using the same blade design variables, Nielsen et al. [2009b, 2010] performed an adjoint-based optimization for the TRAM rotor in hover using a non-inertial reference frame for both single- and multi-point design optimizations. The multi-point optimization had an objective defined at a collective of 14 degrees, while the functions defined at

10 and 12 degrees collective served as constraints with a minimum FM of 0.71 and 0.72, respectively. Figure 3.34 shows the improvement of the FM blade design that meets these constraints during the design cycles. Figure 3.35 shows five different blade sections with the baseline airfoil shape and the optimized geometry using the explicit constraints strategy, as well as the results from two other optimization strategies.

The adjoint-based optimization for unsteady turbulent flow was then extended to dynamic overset unstructured grids in FUN3D by Nielsen et al. [2012, 2013]. The overset grids enable the analysis of vehicles experiencing large relative motions of vehicle components, such as a rotating rotor and a fuselage. This work includes three test cases: a wind turbine, a biologically inspired flapping wing, and a UH-60A helicopter. Figure 3.36 shows the surface mesh for the UH-60A used in the optimization with a single overset component grid for each rotor, and one for the fuselage with over 54 million tetrahedral elements. The rotor geometry was optimized at a forward flight condition with the advance ratio of 0.37 at 0 degrees angle-of-attack. The design variables consisted of 64 shape parameters describing the rotor blades with 32 variables for thickness and 32 for camber, as well as 3 additional design variables for the collective and cycle rotor controls. The objective of the optimization was to maximize the lift while satisfying the constraints on the lateral and longitudinal moments such that the vehicle results in a trimmed flight condition.

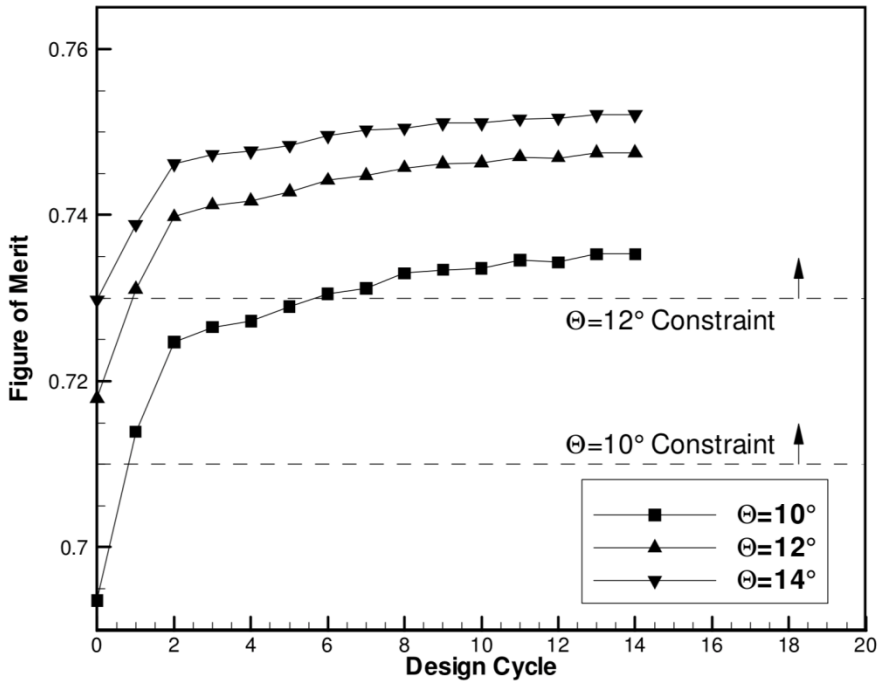

Figure 3.34. FM histories for multi-point optimization based on the explicitly constrained approach. Arrows indicate feasible side of constraints (Fig. 10 of Nielsen et al. [2009b]).

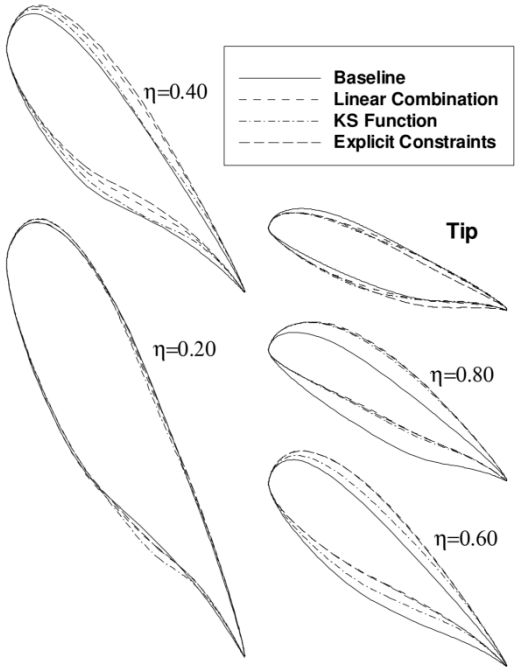

Figure 3.35. Blade cross sections at various radial stations before and after multi-point optimization using the three different strategies considered. The vertical scale has been exaggerated and all blades have been rotated to the Θ = 14° collective setting for comparison (Fig. 11 of Nielsen et al. [2009b]).

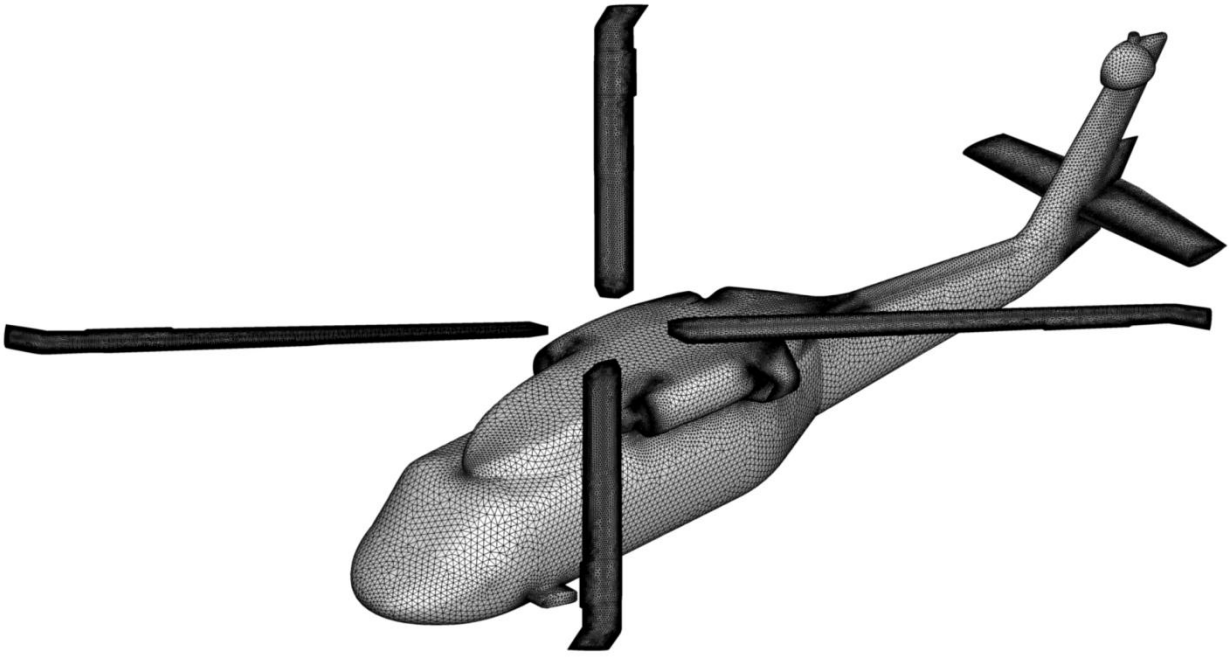

Figure 3.36. Surface mesh for UH-60A configuration (Fig. 14 of Nielsen et al. [2012]).

A more rigorous design optimization was performed by Jones et al. [2014] using an adjoint-based method for an isolated tiltrotor that considers optimizing the performance of the rotor at multiple design points. In this research, the optimization simultaneously maximized the rotor FM in hover and the propulsive efficiency in airplane-mode of the TRAM tiltrotor shown in Figure 3.37. This investigation used a non-inertial reference frame demonstrated by Nielsen et al. [2009b, 2010] for a rotor configuration where the problem could be cast as a steady-state problem. Note that casting the problem in a non-inertial reference frame is valid for isolated rotors in hover and where the free-stream velocity is aligned to the axis of rotation, and greatly simplifies the adjoint calculation and reduces the cost as compared to an unsteady adjoint analysis. Figure 3.38 shows the 21 geometric design variables used in the optimization that included thickness, camber, twist, and taper along the blade. The objective function was a linear combination of the objective for hover and cruise with a constant weighting factor, α, applied to the corresponding objective function. Four different optimizations were performed in this study. The first just looked at camber and thickness, the second included blade twist, and the third included blade taper, with all three optimizations having a 2:1 (α_{hover}:α_{cruise}) composite objective function weighting with the emphasis on hover performance versus cruise. The fourth optimization included camber, thickness, twist, and taper with a 1:2 composite objective function weighting with the emphasis on optimizing for cruise. Figure 3.39 shows the convergence of the composite objective function along with the FM, rotor cruise thrust coefficient, C_T, for hover and cruise, and propulsive efficiency, η, versus design cycle for the 2:1 weighted composite objective function using camber, thickness, twist, and taper. This optimization shows a 1.89-percent increase in the hover FM with a 4.23-percent increase in the cruise performance over the baseline case. The optimized airfoil shapes are shown in Figure 3.40 with modest changes from the baseline along most of the blade and an additional upsweep to the trailing edge at the rotor tip.

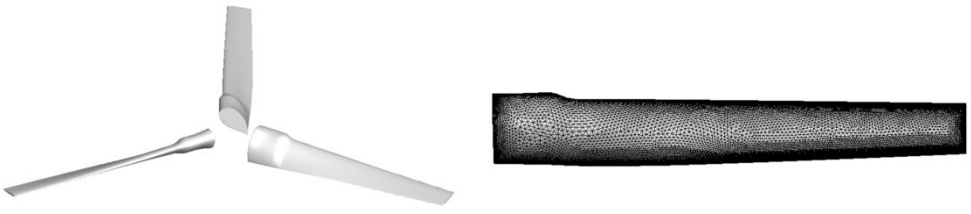

(a) Rotor surface geometry (b) Typical blade surface mesh used for design computations

Figure 3.37. TRAM used in adjoint-based design optimization (Fig. 1 of Jones et al. [2014]).

A multidisciplinary sensitivity analysis framework for a rotorcraft computation using a tightly coupled high-fidelity flow solver and a comprehensive analysis was performed by Wang et al. [2017]. The unstructured Navier–Stokes solver FUN3D was used to compute the adjoint-based sensitives arising from the unsteady turbulent flow and unstructured dynamic overset mesh, while a complex variable approach was used for the structural sensitivities in the comprehensive code, DYMORE. Results show that the blade sectional airload derivatives computed by the adjoint-based and complex-variable methods are in good agreement. Sensitivities of the lift-and-drag functions obtained by complex-variable FUN3D/DYMORE simulations are compared with sensitivities computed by the multidisciplinary sensitivity analysis, which couples an adjoint-based flow and grid sensitivities of FUN3D and FUN3D/DYMORE interfaces with the complex-variable sensitivities of DYMORE structural responses [Wang et al., 2017].

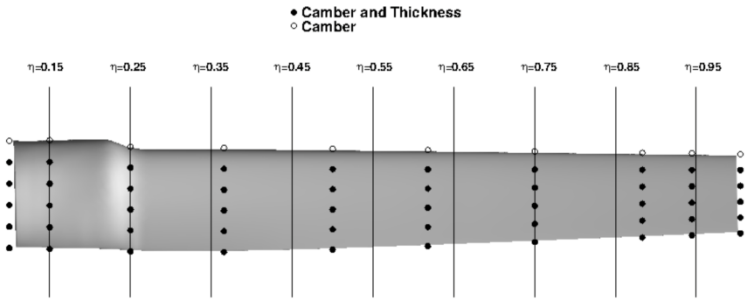

Figure 3.38. Design variables and radial blade locations (Fig. 2 of Jones et al. [2014]).

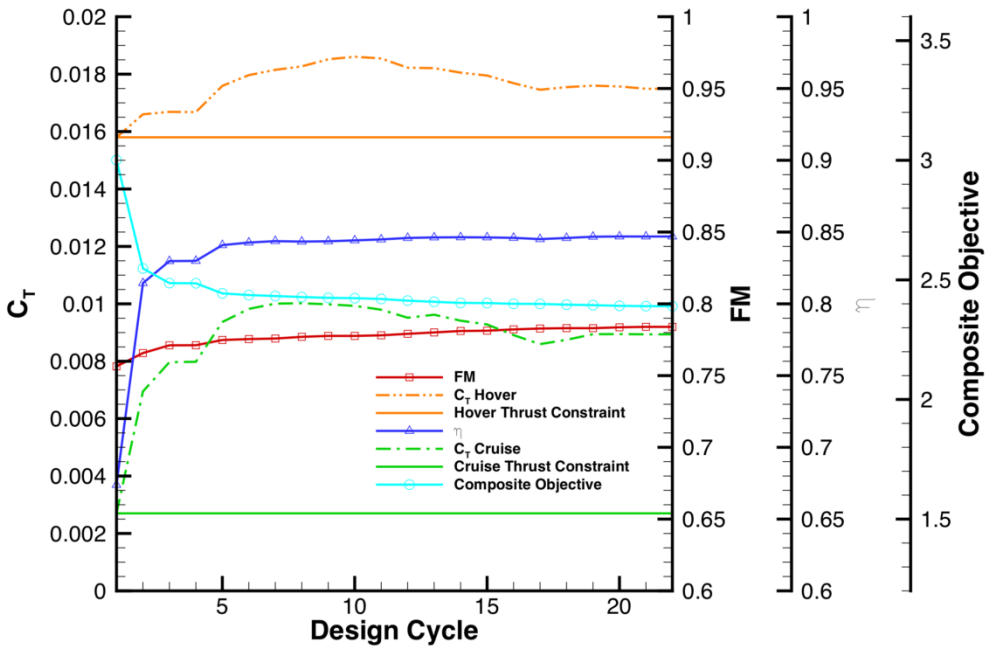

Figure 3.39. Convergence of the composite objective function with a 2:1 (α_{hover}:α_{cruise}) weighting, FM, C_T, and propulsive efficiency, η, versus design cycle (Fig. 9 of Jones et al. [2014]).

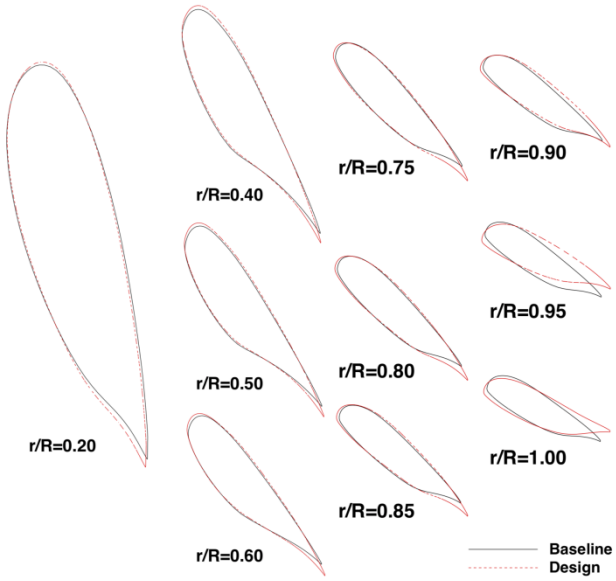

Figure 3.40. Optimized and baseline airfoil shapes along the blade for the composite objective function with a 2:1 (α_{hover}:α_{cruise}) weighting (Fig. 5 of Jones et al. [2014]).

REFERENCES

Allan, B. G, Jenkins, L., Yao, C., Bartram, S., Hallisey, J., Harris, J., Noonan, K., Wong, O., Jones, H., Malovrh, B., Reis, D., and Mace, D., "A Navier–Stokes Simulation of a Heavy Lift Slowed-Rotor Compound Helicopter Configuration," American Helicopter Society 65th Annual Forum, Grapevine, TX, May 27-29, 2009.

Allan, B. G., and Schaeffler, N. W., "Numerical Investigation of Rotorcraft Fuselage Drag Reduction using Active Flow Control," American Helicopter Society 67th Annual Forum, Virginia, VA, May 2011.

Allan, B. G., Schaeffler, N. W., Jenkins, L. N., Yao, C. S., Wong, O. D., and Tanner, P. E., "Active Aerodynamic Load Reduction on a Rotorcraft Fuselage with Rotor Effects - A CFD Validation Effort," 71st Annual Forum of the American Helicopter Society, Virginia Beach, VA, May 2015.

Ahmad, J. U., and Biedron, R. T., "Code-to-Code Comparison of CFD/CSD Simulation for a Helicopter Rotor in Forward Flight," 29th AIAA Applied Aerodynamics Conference in Honolulu, HI, June 27-30, 2011.

Ahmad, J. U., and Chaderjian, N. M., "High-Order Accurate CFD/CSD Simulation of the UH60 Rotor in Forward Flight," 29th AIAA Applied Aerodynamics Conference in Honolulu, HI, June 27-30, 2011.

Ahmad, J. U., Kao, D., Yamauchi, G., and Wadcock, A., "Comparison of Computed and Measured Vortex Evolution for a UH-60A Rotor in Forward Flight," 31st AIAA Applied Aerodynamics Conference, San Diego, CA, June 24-27, 2013.

Anusonti-Inthra, P., and Floros, M., “Coupled CFD and Particle Vortex Transport Method: Wing Performance and Wake Validations,” Paper AIAA-2008-4177, 38th AIAA Fluid Dynamics Conference and Exhibit, Seattle, WA, June 23-38, 2008.

Bain, J., Sankar, L., Prasad, J., Bauchau, O., Peters, D., and He, C., “Computational Modeling of Variable Droop Leading Edge in Forward Flight,” Paper AIAA-2008-3872, 4th AIAA Flow Control Conference Seattle, Washington, June 23–26, 2008.

Barbely, N. L., Komerath, N. M., and Novak, L. A., “A Study of Coaxial Rotor Performance and Flow Field Characteristics,” American Helicopter Society Technical Meeting on Aeromechanics Design for Vertical Lift, San Francisco, CA, Jan. 20-22, 2016.

Biedron, R., and Lee-Rausch, E., “Rotor Airloads Prediction Using Unstructured Meshes and Loose CFD/CSD Coupling,” Paper AIAA-2008-7341, 26th AIAA Applied Aerodynamics Conference, Honolulu, HI, Aug. 18-21, 2008.

Biedron, R., and Thomas, J., “Recent Enhancements to the FUN3D Solver for Moving-Mesh Applications,” Paper AIAA-2009-1360, 47th AIAA Aerospace Sciences Meeting, Orlando, FL, Jan. 5-8, 2009.

Biedron, R. T., and Lee-Rausch, E. M., “Computation of UH-60A Airloads using CFD/CSD Coupling on Unstructured Meshes,” 67th Annual Forum and Technology Display of the American Helicopter Society, Virginia Beach, VA, May 3-5, 2011.

Biedron, R. T., and Lee-Rausch, E. M., “An Examination of Unsteady Airloads on a UH-60A Rotor: Computation versus Measurement,” 68th Annual Forum and Technology Display of the American Helicopter Society, Ft. Worth, TX, May 1-3, 2012.

Boyd, Jr., D. D., “HART-II Acoustic Predictions using a coupled CFD/CSD Method,” American Helicopter Society 65th Annual Forum, Grapevine, TX, May 27-29, 2009.

Buning, P. G., and Pulliam, T. H., “Cartesian Off-Body Grid Adaption for Viscous Time-Accurate Flow Simulation,” Paper AIAA 2011-3693, 29th AIAA Applied Aerodynamics Conference in Honolulu, HI, June 27-30, 2011.

Buning, P. G., and Pulliam, T. H., “Near-Body Grid Adaption for Overset Grids,” Paper AIAA-2016-3326, AIAA Aviation 2016, Washington, DC, June 13-17, 2016.

Chaderjian, N. M., and Buning, P. G., “High Resolution Navier–Stokes Simulation of Rotor Wakes,” AHS 67th Annual Forum, Virginia Beach, VA, May 3-5, 2011.

Chaderjian, N. M., and Ahmad, J., “Detached Eddy Simulation of the UH-60A Rotor Wake Using Adaptive Mesh Refinement,” 68th Annual Forum and Technology Display of the American Helicopter Society, Ft. Worth, TX, May 1-3, 2012.

Chaderjian, N. M., “Advances in Rotor Performance and Turbulent Wake Simulation using DES and Adaptive Mesh Refinement,” Paper ICCFD7-3693, 7th International Conference on Computational Fluid Dynamics (ICCFD7), Kohala Coast, HI, July 9-13, 2012b.

Chaderjian, N. M., and Ahmad, J. U., “Navier–Stokes Assessment of Test Facility Effects on Hover Performance,” American Helicopter Society 71st Annual Forum, Virginia Beach, VA, May 5-7, 2015.

Chaderjian, N. M., "Navier‐Stokes Simulation of UH-60A Rotor/Wake Interaction Using Adaptive Mesh Refinement," AHS International 73rd Annual Forum, Fort Worth, TX, May 9-11, 2017.

Chaderjian, N. M., "Numerical Simulation of Dynamic Stall Using Near-Body Adaptive Mesh Refinement," Paper ICCFD10-102, 10th International Conference on Computational Fluid Dynamics (ICCFD10), Barcelona, Spain, July 9-13, 2018.

Chang, I.-C., Romander, E. A., Potsdam, M., and Yeo, H., "Airloads Air-loads Predication of a UH-60A Rotor Inside the 40-by 80-Foot Wind Tunnel," American Helicopter Society Aeromechanics Specialists' Conference, San Francisco, CA, Jan. 20-22, 2010.

Chang, I.-C., Norman, T., and Romander, E., "Airloads Correlation of the UH-60A Rotor Inside the 40-by 80-Foot Wind Tunnel," Paper No. AIAA-2013-0636, 51st AIAA Aerospace Sciences Meeting, Grapevine, TX, Jan. 7-10, 2013.

Derlaga, J. M., Park, M. A., and Rallabhandi, S. K., "Application of Exactly Linearized Error Transport Equations to AIAA CFD Prediction Workshops," Paper AIAA-2017-0076, 55th AIAA Aerospace Sciences Meeting, Grapevine, TX, Jan. 9-13, 2017.

Diskin, B., Liao, W., and Luo, L.-S., "Textbook-Efficiency Multigrid Solver for Three-Dimensional Unsteady Compressible Navier–Stokes Equations," Paper AIAA-2007-4328, 18th AIAA Computational Fluid Dynamics Conference, Miami, FL, June 2007.

Guruswamy, G. P., "A Modular Approach to Euler/Navier–Stokes-Based Aeroelasticity of Helicopter Rotor Blades," Paper AIAA-2008-2179, 49th AIAA/ASME/ASCE/AHS/ ASC Structures, Structural Dynamics, and Materials Conference, Schaumburg, IL, April 7-10, 2008.

Guruswamy, G. P., "CFD- and CSD-based Aeroelastic Computations of Helicopter Rotor Blades using a Modular Approach," Paper AIAA-2009-4199, 39th AIAA Fluid Dynamics Conference, San Antonio, TX, June 22-25, 2009.

Guruswamy, G. P., "Computational-Fluid-Dynamics- and Computational-Structural- Dynamics-Based Time-Accurate Aeroelasticity of Helicopter Rotor Blades," *AIAA Journal of Aircraft*, vol. 47, no. 3, May-June 2010, pp. 858-863.

Guruswamy, G. P., "Fluid/Structure Interaction Modeling of Helicopters Using Navier Stokes Equations," Paper AIAA 2012-4789, AIAA Modeling and Simulation Technologies Conference, Minneapolis, MN, Aug. 13-16, 2012a.

Guruswamy, G. P., "Large Scale Aeroelastic Data for Design of Rotating Blades using Navier–Stokes Equations," Paper AIAA-2012-5629, 12th AIAA Aviation Technology, Integration, and Operations (ATIO) Conference and 14th AIAA/ISSM, Indianapolis, IN, Sept. 17-19, 2012b.

Hill, M., Kunz, R., Noack, R., Long, L., Morris, P., and Handschuh, R., "Application and Validation of Unstructured Overset CFD Technology for Rotorcraft Gearbox Windage Aerodynamics Simulation," 64th American Helicopter Society Annual Forum, Montreal, Canada, April 29-May 1, 2008.

Holst, T. L., and Pulliam, T. H., "Overset Solution Adaptive Grid Approach Applied to Hovering Rotorcraft Flows," Paper AIAA-2009-3519, 27th AIAA Applied Aerodynamics Conference, San Antonio, TX, June 22-25, 2009.

Holst, T. L., and Pulliam, T. H., "Optimization of Overset Solution Adaptive Grids for Hovering Rotorcraft," American Helicopter Society Aeromechanics Specialists' Conference, San Francisco, CA, Jan. 20-22, 2010.

Jain, R., Biedron, R., William, J., Lee-Rausch, E., "Modularization and Validation of NASA FUN3D as a HPCMP CREATETM-AV Helios Near-body Solver," Paper AIAA-2016-1298, The 54th AIAA Aerospace Sciences Meeting, San Diego, CA, Jan. 4-8, 2016.

Jones, W. T., Nielsen, E. J., Lee-Rausch, E. M., and Acree, C. W., "Multi-point Adjoint-Based Design of Tilt-Rotors in a Noninertial Reference Frame," Paper AIAA-2014-0290, AIAA SciTech, National Harbor, MD, Jan. 13-17, 2014.

Kao, D. L., and Chaderjian, N. M., "Automatic Tip Vortex Core Profiling for Numerical Flow Simulations of Rotorcraft," Paper AIAA-2010-4752, 40th AIAA Fluid Dynamics Conference in Chicago, IL, June 28 to July 1, 2010.

Kao, D. L., "Automated Vortex Core Analysis for Multi-Zone Numerical Flow Simulations," Paper AIAA-2011-3679, 20th AIAA Computational Fluid Dynamics Conference, Honolulu, HI, June 27-30, 2011.

Kao, D. L., Ahmad, J. U., Holst, T. L., and Allan B. G., "Visualization and Analysis of Vortex Features in Helicopter Rotor Wakes," Paper AIAA-2013-1162, 51st AIAA Aerospace Sciences Meeting, Grapevine, TX, Jan. 7-10, 2013.

Kao, D. L., Ahmad, J. U., and Holst, T. L., "Visualization and Quantification of Rotor Tip Vortices in Helicopter Flows," Paper AIAA-2015-1369, AIAA 53rd AIAA Aerospace Sciences Meeting, Kissimmee, FL, Jan. 5-9, 2015.

Kao, D. L., Smith, K. L., and Liu Z., "Tracking Blade Tip Vortices for Numerical Flow Simulations of Hovering Rotorcraft," Paper AIAA-2018-1175, AIAA 2018 Aerospace Sciences Meeting, Kissimmee, FL, Jan. 8-12, 2018

Kufeld, R. M., Balough, D. L., Cross, J. L., Studebaker, K. F., Jennison, C. D., and Bousman, W. G., "Flight Testing of the UH-60A Airloads Aircraft," American Helicopter Society 50th Annual Forum, Washington D.C., May 1994.

Lee-Rausch, E. M., and Biedron, R. T., "Simulation of an Isolated Tiltrotor in Hover with an Unstructured Overset-Grid RANS Solver," American Helicopter Society 65th Annual Forum, Grapevine, TX, May 27-29, 2009.

Lee-Rausch, E. M., and Biedron, R. T. "Fun3D Airload Predictions for the Full-Scale UH-60A Airloads Rotor in a Wind Tunnel," American Helicopter Society 69th Annual Forum, Phoenix, AZ, May 21-23, 2013.

Liao, W., Diskin, B., Peng, Y., and Luo, L.-S., "Textbook-Efficiency Multigrid Solver for Three-Dimensional Unsteady Compressible Navier–Stokes Equations," *Journal of Computational Physics*, July 2008, vol. 227, no. 15, pp. 7160–7177.

Massey, S. J., Kreshock A. R., and Sekula, M. K., "Coupled CFD/CSD Analysis of Rotor Blade Structural Loads with Experimental Validation," Paper AIAA-2013-3157, 31st AIAA Applied Aerodynamics Conference, San Diego, CA, June 24-27, 2013.

Massey, S. J., Kreshock A. R., and Sekula, M. K., "pled CFD/CSD Analysis of an Active-Twist Rotor in a Wind Tunnel with Experimental Validation," American Helicopter Society 71st Annual Forum, Virginia, Beach, VA, May 2015.

Mankbadi, M. R., and Georgiadis, N. J., "An Examination of Parameters Affecting Large Eddy Simulations of Flow Past a Square Cylinder," Paper AIAA-2014-2089, AIAA Aviation 2014 Conference Atlanta, GA, June 16-20, 2014.

Mankbadi, M., Georgiadis, N., and DeBonis, J., "Comparison of High-Order and Low-Order Methods for Large-Eddy Simulation of a Compressible Shear Layer," Paper AIAA-2015-2939, AIAA Aviation 2015 Conference Dallas, TX, June 22-26, 2015.

Meakin, R. L., "An Efficient Means of Adaptive Refinement Within Systems of Overset Grids," Paper AIAA-1995-1722, 12th Computational Fluid Dynamics Conference, San Diego, CA, June 19-22, 1995.

Nichols, R. H., Tramel, R. W., and Buning, P. G., "Evaluation of Two High-Order Weighted Essentially Nonoscillatory Schemes," *AIAA Journal*, vol. 46, no. 12, Dec. 2008, pp. 3090-3102.

Nielsen, E. J., Diskin, B., and Yamaleev, N. K., "Discrete Adjoint-Based Design Optimization of Unsteady Turbulent Flows on Dynamic Unstructured Grids," Paper AIAA-2009-3802, 27th AIAA Applied Aerodynamics Conference, San Antonio, TX, June 22-25, 2009a.

Nielsen, E. J., Lee-Rausch, E. M., and Jones, W. T., "Adjoint-Based Design of Rotors Using the Navier–Stokes Equations in a Noninertial Reference Frame," American Helicopter Society 65th Annual Forum, Grapevine, TX, May 27-29, 2009b.

Nielsen, E. J., Lee-Rausch, E. M., and Jones, W. T., "Adjoint-Based Design of Rotors in a Noninertial Reference Frame," Journal of Aircraft, vol. 47, no. 2, 2010, pp. 638–646, DOI: 10.2514/1.46044

Nielsen, E. J., and Diskin, B., "Discrete Adjoint-Based Design for Unsteady Turbulent Flows on Dynamic Overset Unstructured Grids," Paper AIAA-2012-0554, 50th AIAA Aerospace Sciences Meeting including the New Horizons Forum and Aerospace Exposition, Nashville, TN, Jan. 9-12, 2012.

Nielsen, E. J., and Diskin, B., "Discrete Adjoint-Based Design for Unsteady Turbulent Flows on Dynamic Overset Unstructured Grids," *AIAA Journal*, June 2013, vol. 51, no. 6, pp. 1355-1373. DOI:10.2514/1.J051859

Noack, R., Boger, D., Kunz, R., and Carrica, P., "Suggar++: An Improved General Overset Grid Assembly Capability," Paper AIAA-2009-3992, 19th AIAA Computational Fluid Dynamics, San Antonio, TX, June 22-25, 2009.

Norman, T. R., Peterson, R. L., Shinoda, P., and Datta, A., "Full-Scale Wind Tunnel Test of the UH-60A Airloads Rotor," Proceedings of the 67th Annual Forum of the American Helicopter Society, Virginia Beach, VA, May 3-5, 2011.

Park, M. A., “Low Boom Configuration Analysis with FUN3D Adjoint Simulation Framework,” Paper AIAA-2011-3337, 29th AIAA Applied Aerodynamics Conference, Honolulu, HI, June 27-30, 2011.

Pulliam, T., “High Order Accurate Finite-Difference Methods: as seen in OVERFLOW,” Paper AIAA-2011-3693, 29th AIAA Applied Aerodynamics Conference in Honolulu, HI, June 27-30, 2011.

Potsdam, M., and Pulliam, T., “Turbulence Modeling Treatment for Rotorcraft Wakes,” American Helicopter Society Specialist’s Conference on Aeromechanics, San Francisco, CA, Jan. 23-25, 2008.

Romander, E., Norman, T., and Chang, I-C, “Correlating CFD Simulation with Wind Tunnel Test for the Full-Scale UH-60A Airloads Rotor,” 67th Annual Forum and Technology Display of the American Helicopter Society, Virginia Beach, VA, May 3-5, 2011.

Romander, E., Meyn, L., Norman, T., Barrows, D., and Burner, A., “Blade Motion Correlation for the Full-Scale UH-60A Airloads Rotor, “Fifth Decennial AHS Aeromechanics Specialists’ Conference, San Francisco, CA, Jan. 22–24, 2014.

Schaeffler, N. W., Allan, B. G., Lienard, C., and Le Pape, A., “Progress Towards Fuselage Drag Reduction via Active Flow Control: A Combined CFD and Experimental Effort,” 36th European Rotorcraft Forum Paper 064, Paris, France, Sept. 2010.

Schatzman, N., Komerath, N. M., and Romander, E., “Time-Varying Loads of Co-Axial Rotor Blade Crossings,” 2017 SAE AeroTech Congress & Exhibition, Fort Worth, TX, Sept. 26-28, 2017.

Smith, M. J., Lim, J. W., van der Wall, B. G., Baeder, J. D., Biedron, J. T., Boyd, Jr., D. D., Jayaraman, B., Jung, S. N., and Min, B.-Y., “The HART II International Workshop: An Assessment of the State of the Art in CFD/CSD Prediction,” *CEAS Aeronautical Journal,* vol. 4, no. 4, Dec. 2013.

Smith, M.; Min, B. Y.; Lim, J.; van der Wall, B.; Baeder, J.; Biedron, R.; Boyd, D.; Jayaraman, B.; and Jung, S., “An Assessment of CFD/CSD Prediction State-of-the-Art Using the HARTII International Workshop Data,” American Helicopter Society 68th Annual Forum and Technology Display, Ft. Worth, TX, May 1-3, 2012.

Smith, M. J., Koukol, B. C. G., Quackenbush, T., and Wachspress, D., “Reverse- and Cross-Flow Aerodynamics for High-Advance-Ratio Flight,” 35th European Rotorcraft Forum, Hamburg, Germany, Sept. 22-25, 2009.

Srinivasan, S., Girgis, B., and Menon, S., “Large-Eddy Simulation of a Combustion Powered Actuator,” Paper AIAA-2008-4680, AIAA/ASME/SAE Joint Propulsion Conference & Exhibit, Hartford, CT, July 21-23, 2008.

Wang, L., Diskin, B., Biedron, R., Nielsen, E., and Bauchau, O., “Sensitivity Analysis of Multidisciplinary Rotorcraft Simulations,” Paper AIAA-2017-1670, AIAA SciTech 2017, Grapevine, TX, Jan. 9-13, 2017.

Wissink, A. M., Sitaraman, J., Sankaran, V., Mavriplis, D. J., Pulliam, T. H., “A Multi-Code Python-Based Infrastructure for Overset CFD with Adaptive Cartesian Grids,” Paper AIAA-2008-0927, AIAA 46th Aerospace Sciences Meeting, Reno, NV, Jan. 7-10, 2008.

Yamauchi, G. K., and Young, L. A, "A Status of NASA Rotorcraft Research," NASA/TP–2009-215369, Sept. 2009.

Yoon, S., Pulliam, T. H., and Chaderjian, N. M., "Simulations of XV-15 Rotor Flows in Hover Using OVERFLOW," Fifth Decennial American Helicopter Society Aeromechanics Specialists' Conference, San Francisco, CA, Jan. 2014.

Yoon, S., Chaderjian, N. M., Pulliam, T. H., and Holst, T. L., "Effect of Turbulence Modeling on Hovering Rotor Flows," Paper AIAA-2015-2766, 45th Fluid Dynamics Conference, Dallas, TX, June 22-26, 2015.

Yoon, S., Lee, H. C., and Pulliam, T. H., "Computational Study of Flow Interactions in Coaxial Rotors," AHS Technical Meeting on Aeromechanics Design for Vertical Lift, San Francisco, CA, Jan. 20-22, 2016.

CHAPTER 4. EXPERIMENTAL METHODS

Gloria K. Yamauchi[1]

INTRODUCTION

Advances in camera and computer technology since 2007 have translated into huge gains in the quality and quantity of rotorcraft flow-field measurements and measurements on rotating surfaces. With the high throughput of images and improvement in image-processing techniques, new understanding has been achieved in the last decade, with optical techniques applied to large and small-scale models in wind tunnels and in flight.

A catalyst for pushing the boundaries of multiple optical techniques, in terms of scale, for NASA rotorcraft applications was the wind tunnel test of a full-scale, pressure-instrumented UH-60A Airloads rotor. The test was executed in the National Full-Scale Aerodynamics Complex (NFAC) 40- by 80-Foot Wind Tunnel (40x80) and was completed in 2010. The NFAC test represented the capstone of a series of UH-60 tests that included a small-scale wind tunnel test and a flight test campaign. The UH-60 tests were enabled by the strong partnership between the U.S. Army and NASA. Norman et al. [2011] provide an overview of the NFAC test. The ambitious test program had many objectives, including the measurements of blade deformation, rotor flow field, and rotor wake geometry. The primary test objectives were to provide a benchmark data set for analyses validation. Though the UH-60A test was the largest model tested in terms of scale since 2007, a number of small-scale wind tunnel tests in the NASA Langley 14- by 22-Foot Subsonic Tunnel (14x22), the U.S. Army 7- by 10-Foot Wind Tunnel (7x10) at NASA Ames Research Center, and hover test facilities contributed to the growing database that continues to serve as truth data for analyses.

The progress of five key measurement techniques applied to rotorcraft testing at/by NASA since the publication of Yamauchi and Young [2009] is reviewed in this chapter: Particle image velocimetry (PIV), pressure sensitive paint (PSP), background oriented schlieren (BOS), blade deformation (BD) using photogrammetry, and infrared thermography (IRT). In addition, a review of several component technologies using optical and nonoptical approaches is also provided.

PARTICLE IMAGE VELOCIMETRY

Jenkins et al. [2009] completed a test campaign in the NASA Langley 14x22 that focused on rotor wake diagnostic techniques in forward flight. The model consisted of a fuselage with a 6-foot wing and a four-bladed, 2.94-foot-radius rotor (see Fig. 4.1). A large field-of-view PIV (LFPIV) system, shown in Figure 4.2, was developed and used for the first time in the 14x22; the PIV measurements were augmented by data from multi-hole probes and a laser Doppler velocimetry (LDV) system. The PIV region of interest (ROI) was as large as 5 feet wide by

[1] NASA Ames Research Center.

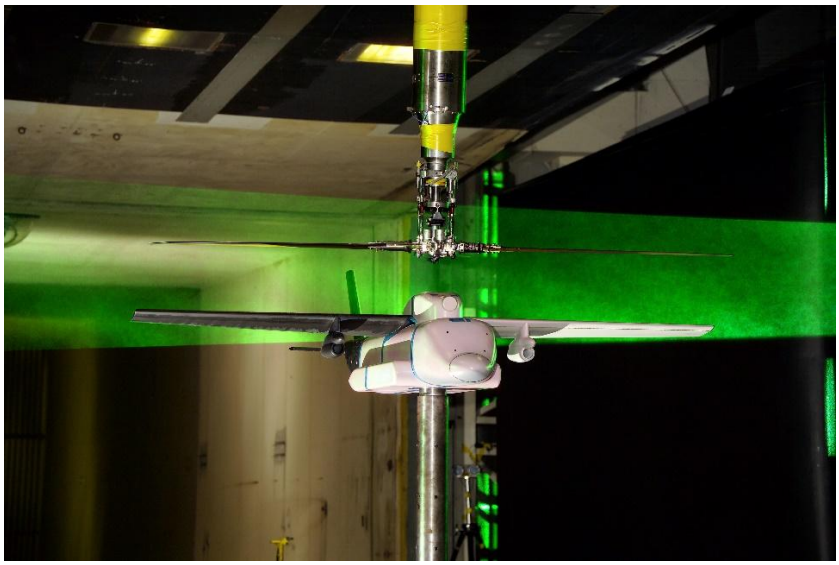

Figure 4.1. Slowed rotor model installed in the Langley 14x22 with laser light sheet used for PIV measurements.

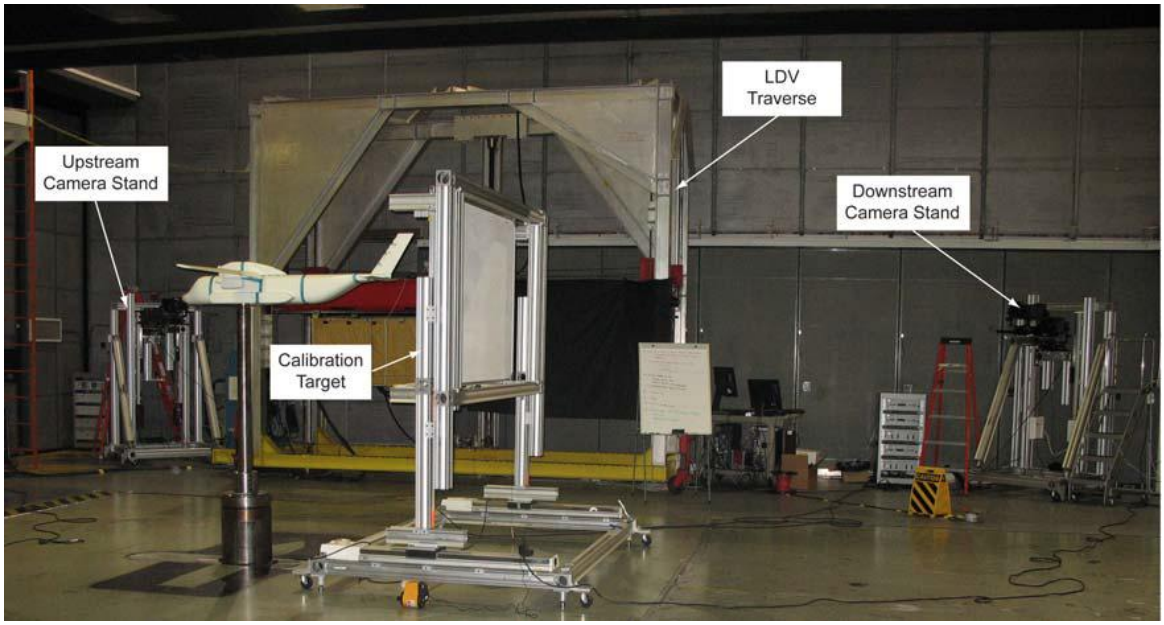

Figure 4.2. Slowed-rotor compound helicopter model (body alone) with PIV cameras, LDV system, and calibration target in the Langley 14x22 with the walls raised. (Note: cameras and LDV system are behind the shear layer, outside the airstream.) (Fig. 3 of Jenkins et al. [2009].)

3 feet high, sufficient to capture a large portion of the wake from the fuselage, wing, and rotor (advancing side). The measurements were synchronized with the rotor to capture the wake at specific azimuthal positions. This was made possible by a Rotor Azimuthal Synchronization Program (RASP) designed by Fleming [2008], which triggered the PIV system using 1/rev and 1024/rev signals from an encoder on the rotor shaft. The data from the probes and LDV were consistent with the LFPIV system. This first and successful use of PIV in the 14x22 for rotor applications provided the foundation for an efficient and accurate means for flow measurements in this facility. The efficiency of the PIV system was later improved by traversing the laser and camera together, eliminating the need for recalibrating cameras for every ROI location. Following the 14x22 entry, Jenkins et al. [2009] applied PIV to an ongoing hover experiment [Wong et al., 2010] in the Rotor Test Cell (RTC). A generic fuselage with a four-bladed, 5.5417-foot-radius rotor was installed in the RTC (see Fig. 4.3). The focus of PIV measurements in the RTC was to characterize the rotor tip vortex. Valuable lessons learned from the forward flight and hover tests were identified, as described in Jenkins et al. [2009] and incorporated into future applications of the PIV system at Langley Research Center. This updated version of the PIV system was applied to a generic fuselage that was tested with a four-bladed, 5.5417-foot-radius rotor in forward flight. Two versions of the fuselage rear ramp were tested, each equipped with their own unique active flow control actuators with the goal of reducing the effect of rotor download and drag on the fuselage. Martin et al. [2014] were able to capture the effectiveness of fluidic actuators to create a virtual (fluidic) boat-tail fairing directly behind the rear ramp of the fuselage. Schaeffler et al. [2014, 2016] were able to capture the effect of steady blowing and zero-net-mass-flux blowing on the flow near the fuselage for various rotor conditions. The PIV measurements obtained for both of these configurations enabled a deeper understanding of the flow physics of these complex aerodynamic environments. Overmeyer et al. [2015] used the acquired data from the first entry of this generic fuselage and rotor as a case study for applying a design of experiments (DOE) approach to powered rotor wind tunnel testing. Most rotor tests involve a multi-dimensional array of parameters to be tested—the DOE approach can greatly reduce the matrix by developing surface response models.

As an alternative to using mechanically driven actuators to control separated flows, Rajendar et al. [2008] explored the properties of a combustion-powered actuation (COMPACT) device. Using PIV, the authors characterized the internal flow properties of a small-scale combustion-powered fluidic actuator over a range of combustion chamber geometries and gas mixture flow conditions. The work was an initial step before installing COMPACT devices in airfoils and eventually on a rotor blade. In a 5-year study funded by NASA, PIV was used to explore the effectiveness of using the COMPACT approach to suppress dynamic stall on a pitching airfoil. Although this study was performed on a nonrotating model, the test was conducted on a modern rotor blade airfoil (spanning floor to ceiling) at speeds up to 0.5 Mach number with a corresponding chord Reynolds number of 4.7×10^6. Matalanis et al. [2016, 2017] describe the experiment executed in the NASA Glenn Icing Research Tunnel (IRT). Two rows of actuators were installed near the leading edge of the airfoil over a limited section of the airfoil span. A PIV camera was mounted directly above the model in the test section ceiling in order to image the flow field (see Fig. 4.4). The flow fields measured by PIV were instrumental to understanding how the controlled flow was affecting the pressure over the dynamic stall cycle. Though the COMPACT system proved effective in mitigating stall, the measured adverse effect on airfoil drag may have been caused by the limited region of actuation that precluded a two-dimensional

(2D) representation of the flow. Finally, like most flow control concepts for rotor blades that are demonstrated in the nonrotating system on airfoils, implementing the concept on a rotating blade is exceptionally difficult.

Unlike the 14x22 or the IRT, the NFAC 40x80 wind tunnel has very limited optical access, constraining the location and size of the ROI, the location of the laser and sheet-forming optics, and the PIV cameras. Wadcock et al. [2011] provides a detailed description of the PIV system and installation for the UH-60A test in the 40x80. An ROI approximately 13 feet wide and 4 feet high was located at approximately 90 degrees rotor azimuth, covering the outer 50 percent of the UH-60A blade radius, in a stationary cross-flow plane. The laser and camera systems were synchronized with the rotor 1/rev so that the PIV images were acquired for different rotor blade azimuths. Figure 4.5 illustrates the key installation components. The size of the test section and height of the ROI (approximately 20 feet above the test section floor) presented major technical challenges, including the alignment of the laser sheet with the ROI, alignment of the camera calibration target, and seeding. In addition, implementing safety protocols for controlling access to the test section during laser operation proved to be very challenging for the size and configuration of the NFAC 40x80. After several years of planning and preparation, PIV data were acquired in about 5 days in 2010 for a range of rotor shaft angles, advance ratios, and thrust coefficients. Procedures for PIV data processing and results for the primary rotor conditions are documented in Yamauchi et al. [2012]. Figure 4.6 shows the out-of-plane velocity field and vorticity field of the UH-60A rotor.

Figure 4.3. PIV laser beam path and light sheet location in the RTC
(Fig. 5 of Wong et al. [2010]).

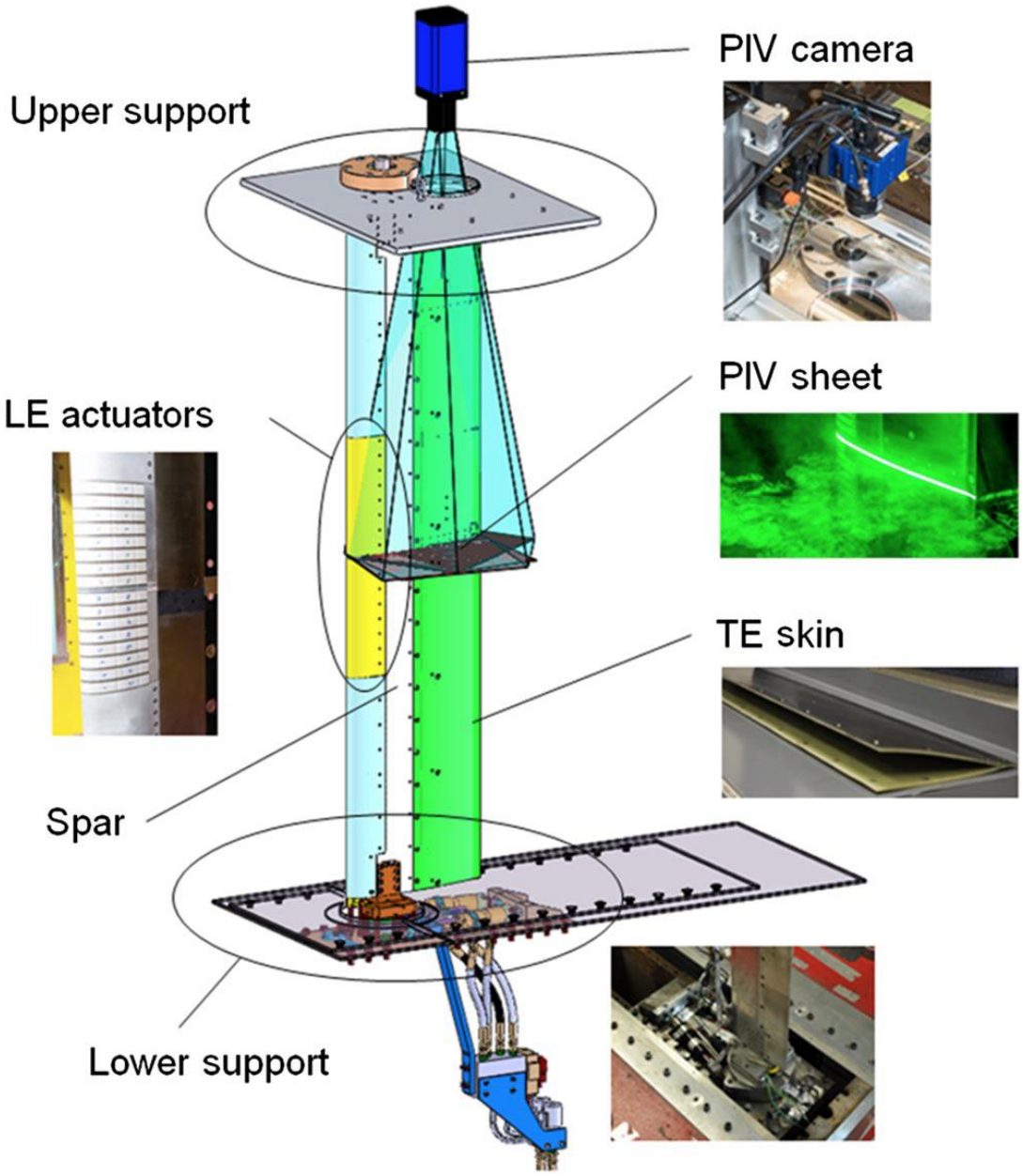

Figure 4.4. Overall CAD-rendering and photographs showing various components of the test article (Fig. 1 of Matalanis et al. [2017]).

The U.S. Army and NASA have partnered to study rotor downwash and outwash using PIV since 2007. The interaction of rotor wakes with the ground continues to be a challenging phenomenon to analyze and characterize experimentally because of the large distances (5–10 rotor diameters in multiple directions from the rotor's center) that must be simulated. In general, the downwash and outwash from a rotor hovering above the ground adversely affects nearby ground personnel and structures—an issue for military and civil operations. Tanner et al. [2015], using the same model and rotor used by Schaeffler et al. [2014], acquired downwash and

outwash measurements in the RTC. The model and rotor were suspended over a ground plane, and outwash velocities were measured using a rake of probes and PIV (at one rotor azimuth location). The fuselage (with the rotor system) was sting-mounted; the presence of the fuselage and sting were the likely reason that the outwash velocity profiles varied with rotor azimuth (and why the probe data differed from the PIV data). Ramasamy et al. [2015, 2017] delved into the flow mechanisms contributing to tandem-rotor outwash. Using approximately 1/56th-scale CH-57 rotors, Ramasamy acquired PIV data for a range of hover configurations that included both isolated and tandem-rotor configurations, in- and out-of-ground effect, and with/without a generic fuselage. PIV measurements were also acquired for jets of different sizes. The size of the rotors permitted flow-field measurements out to four rotor diameters, acquired in the U.S. Army 7- by 10-Foot Wind Tunnel (7x10) and hover chamber at NASA Ames. Three PIV cameras, each viewing an ROI of about 1.5 feet wide, were required to capture the outwash out to four rotor diameters. The correlation of outwash velocity results—nondimensional outwash velocity profile, peak mean outwash velocity, and the wall jet width—between the tandem-rotor configuration and full-scale CH-57 anemometer data (acquired by the U.S. Navy) were quite good.

Since 2007, the use of PIV in rotorcraft applications has increased tremendously. PIV data-reduction software has advanced in concert with advances in camera technology, such that PIV is now a mainstream tool for rotor flow-field research in government labs and universities. Raffel et al. [2012a] describe remaining challenges (e.g., particle voids, spatial averaging) in the application of PIV to helicopter aerodynamics and offer some insight into future trends. In particular, the use of PIV efficiently combined with other flow techniques will promote increased understanding. Raffel et al. [2017] provide a review of PIV applied to helicopter aerodynamics since 1992.

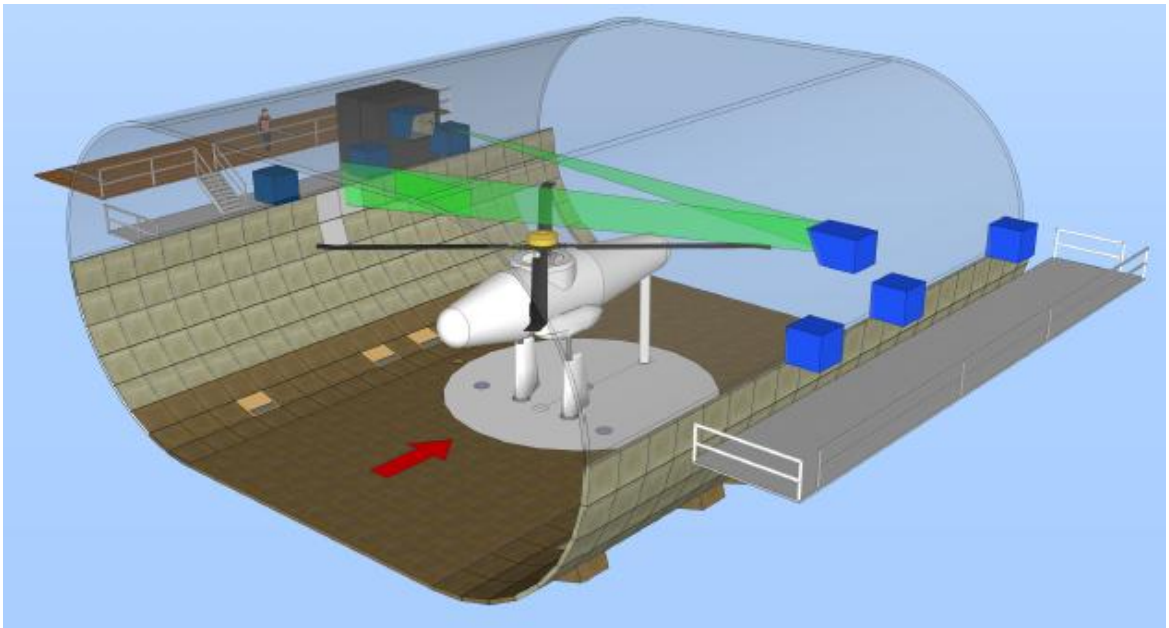

Figure 4.5. Laser launch window and NFAC facility camera ports
(Fig. 5 of Wadcock et al. [2011]).

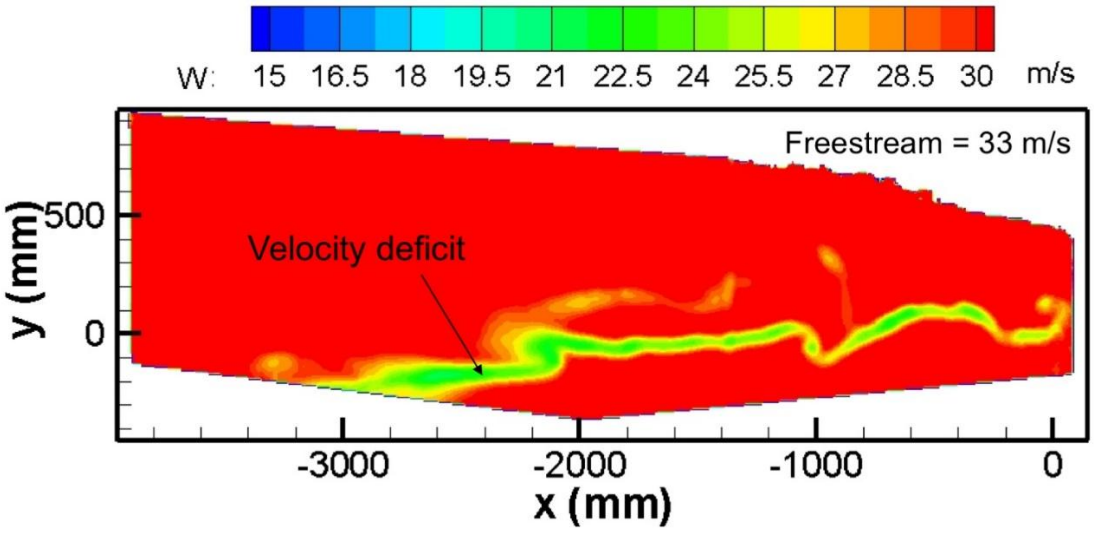

a) Out-of-plane velocity field.

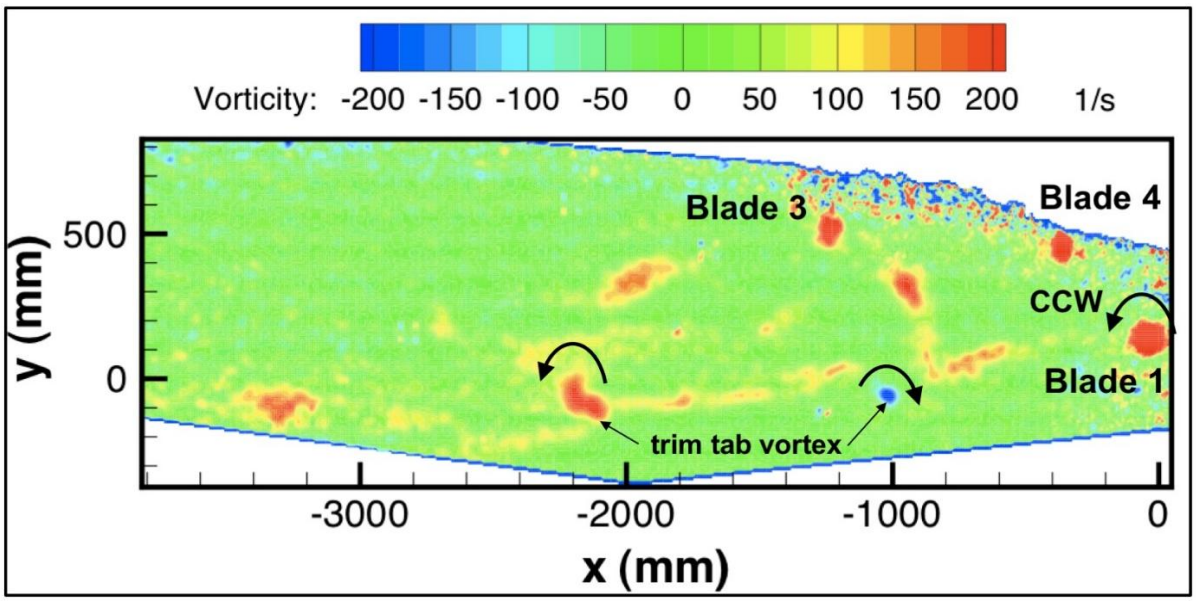

b) Vorticity.

Figure 4.6. UH-60A full-scale rotor flow field, measured at 90° rotor azimuth angle for rotor thrust coefficient-to-solidity ratio = 0.080, advance ratio = 0.150, uncorrected rotor shaft angle = 0°, and tip Mach number = 0.6. View is looking upstream. Yamauchi et al. [2012].

PRESSURE SENSITIVE PAINT

Since approximately 2007, significant advancements in applying pressure sensitive paint (PSP) to rotor blades have been achieved. Like other optical techniques, the progression of faster and higher-resolution digital cameras has contributed to the advancements in PSP image acquisition.

Watkins et al. [2007] executed a proof-of-concept experiment in the Langley RTC using a five-bladed rotor (the PSP blades) mounted on the U.S. Army 2-meter test stand (2MRTS). The rotor was operated in hover only. The aim was to measure global surface pressures using two PSP techniques: intensity- and lifetime-based approaches. The intensity-based approach suffered from poor registration between the at-rest and rotating images, while the lifetime-based approach proved to be necessary for these elastically deforming blades. A number of lessons regarding illumination, cameras, and calibration were gleaned from this experiment.

Wong et al. [2010] implemented the lessons learned from Watkins et al. [2007] in a follow-on hover experiment using the lifetime-based approach. A new four-bladed rotor was acquired for this experiment; two of the four blades had pressure transducers installed near the blade tip to serve as truth data for validating the PSP results. A higher-resolution charge coupled device (CCD) camera (2048x2048 pixels, 14-bit resolution compared to 1392x1024 pixels, 12-bit resolution in the 2007 experiment) and optimized lighting improved the PSP image quality. The rotor was installed on the Generic Rotor Model System (GRMS) with a generic fuselage in the RTC. In addition to the PSP measurements, wake measurements were acquired using PIV. Data from the pressure transducers were compared with the PSP data for three rotor thrust conditions at blade radial stations of 93 and 99 percent. In general, the PSP measurements, though noisy, agreed with the transducer data. These promising results laid the foundation for applying PSP to a rotor in forward flight.

A new approach for exciting paint [Watkins et al., 2011] was demonstrated in both hover [Wong et al., 2012] and forward flight [Watkins et al., 2011, 2012; Wong et al., 2012]. The rotor and test stand described in Wong et al. [2010] were installed in the RTC and then, with some minor modifications, in the Langley 14x22. The work by Watkins, Wong, and their teams during 2011–2012 is the first application of PSP, by NASA, to a rotor in forward flight. Two of the four rotor blades were painted with a porous polymer PSP capable of frequency responses of approximately 20 kHz. A laser-based data acquisition was designed and used to acquire data from a single blade at a maximum of four azimuth locations. Instead of exciting the paint using a light-emitting diode (LED) system as in previous experiments, Watkins et al. [2011, 2012] and Wong et al. [2012] took advantage of PIV laser and camera technology to improve the image acquisition efficiency. Using an Nd:YAG laser typically used for PIV, the laser was instead used to excite the paint with one laser pulse, and PIV cameras were used to acquire all image data in one rotor rotation. Data were acquired for several advance ratios and rotor thrusts. The problem of image blur was somewhat remedied using a point spread function (PSF) approach to deconvolve the blur. Agreement between the PSP data and the pressure transducers at the 99-percent radial station were within 10 percent. This groundbreaking experiment identified additional technical challenges for further pursuit, including image blur, resolution of the PSP images around the leading and trailing edges of the blade, and temperature effects. Thus far, the hover and forward flight tests have focused on acquiring PSP image data near the blade tip.

The next 14x22 test (using the same rotor, fuselage, and test stand used in the previous forward flight experiment) focused on expanding the image area from just the blade tip region to the entire upper surface of the blades. Also, building on the results from their previous tests, Watkins et al. [2014, 2015] used two approaches to tackle the temperature effects: 1) one of the four rotor blades was painted with temperature sensitive paint (TSP), and 2) TSP was applied to a small area of a blade painted with PSP to get an estimate of the blade temperature. For a rotor blade in forward flight, there are large temperature gradients from blade root to tip and azimuthally, so developing a temperature-correction scheme is challenging. Watkins et al. concluded that calculating the adiabatic recovery temperature was the best method of temperature correction (verified by the blade coated with TSP) (see Fig 4.7), though further work that enables TSP to operate in conjunction with PSP is necessary. Image blur continued to be another major challenge for the PSP technique.

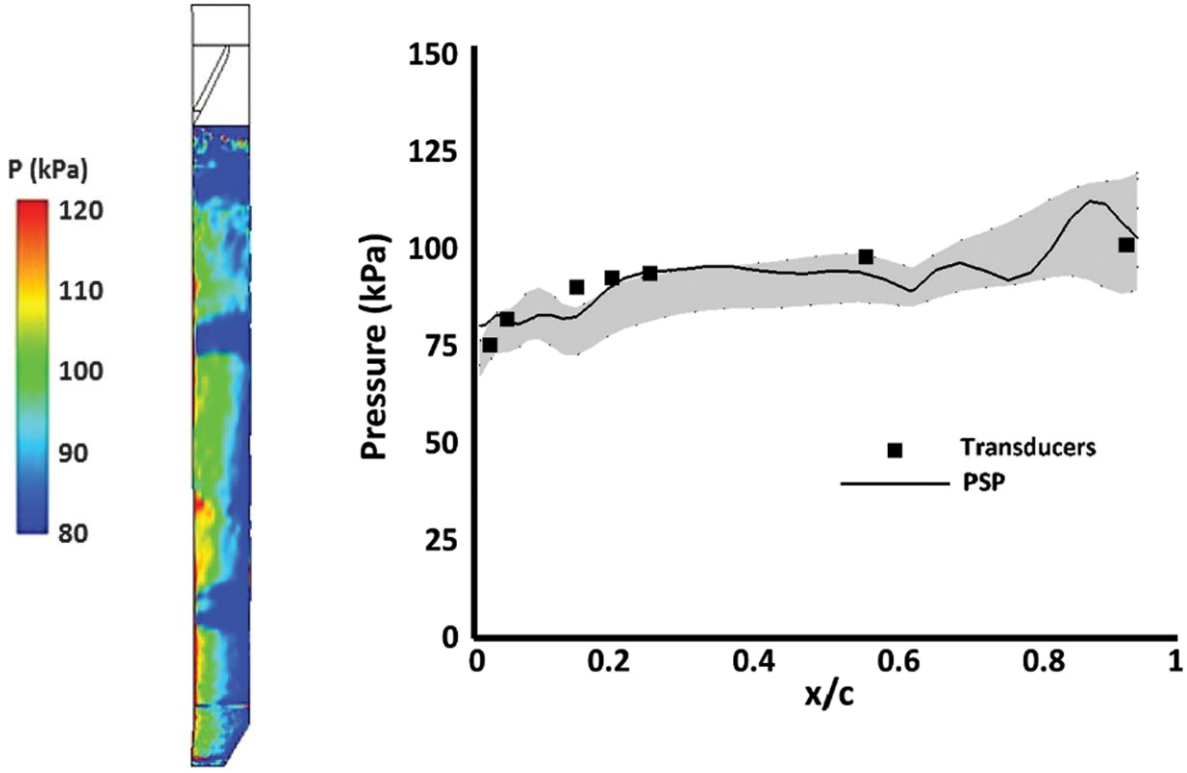

a) PSP results mapped to the rotor blade and corrected for adiabatic wall temperature.

b) PSP results compared to transducer measurements.

Figure 4.7. PSP results obtained in forward flight, $C_T/\sigma = 0.080$, Mu = 0.30, alpha_shaft = 0°, $M_{tip} = 0.6$ (Figs. 11 and 12 of Watkins, et al. [2015]).

In work supported by NASA Small Business Innovation Research (SBIR) funding, Ali et al. [2016] used fast-response PSP to measure the acoustic pressure field in a rectangular cavity. The authors used a high-speed camera to record a continuous time record of the pressure fluctuations in the cavity and then used dynamic mode decomposition (DMD) to extract the spatial modes of the pressure field. Proper orthogonal decomposition (POD) was also applied to the data. Both the DMD and POD results were compared with the phase-averaged results. The DMD technique was better than POD for suppressing noise in parts of the spectrum; DMD was also more effective at separating spectral energy when multiple acoustic excitation frequencies were present.

BLADE DEFORMATION MEASUREMENT TECHNIQUES

Along with measured blade airloads, the measured elastic deformation of a rotor blade is key to validating the results of high-fidelity computational fluid dynamics (CFD) and computational structural dynamics (CSD) analyses. In particular, coupled CFD-CSD simulations use measured out-of-plane, in-plane, and torsional blade deformation (BD) as supporting information when calculating blade structural loads. Since 2007, NASA has focused on two approaches for measuring the displacement of an elastic rotor blade under aerodynamic load: projection Moire interferometry (PMI) and photogrammetry. Leveraging the hovering rotor setup in the RTC by Wong et al. [2010], Sekula [2012] used PMI to measure the flap deflections of all four rotor blades. PMI is a noncontact technique that uses line patterns projected onto the surface of interest—in this case, the surfaces of the rotor blades. Interference fringes caused by the line patterns, together with the knowledge of absolute distance from the camera to the subject blade (via blade targets and photogrammetry), were employed to determine the out-of-plane flap angle of each blade (see Fig. 4.8). The PMI-derived flap angle compared well with the measured root flap angle for a rotor height of 0.55 rotor diameters above the ground plane. Several lessons learned from this effort are shared in Sekula [2012].

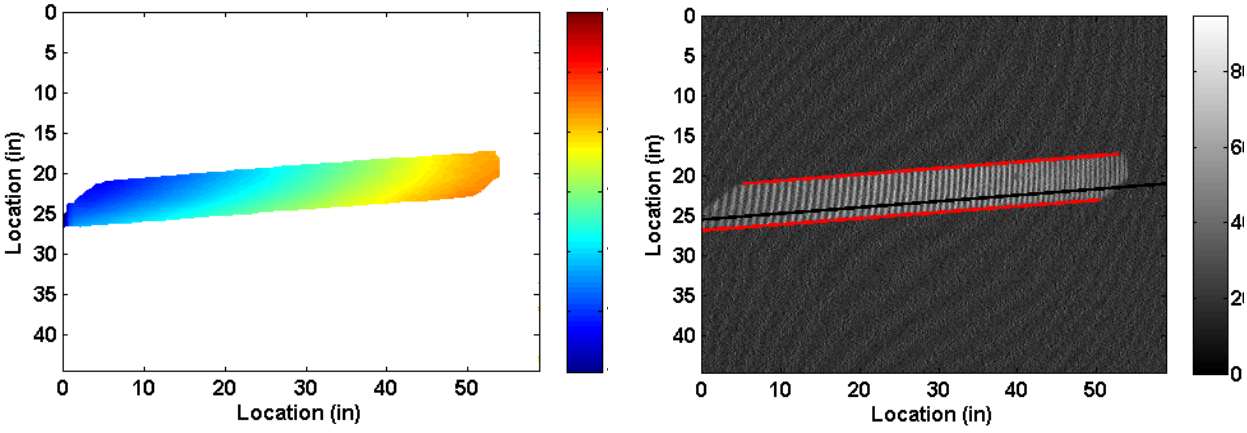

(a) Height above the ground plane (in.). (b) Moire pattern on individual blade.

Figure 4.8. Sample height above the ground and raw PMI image (Fig. 15 of Sekula [2012]).

For the UH-60A test in the NFAC, photogrammetry was deemed the appropriate technique given the desired accuracies (0.1 degree accuracy for instantaneous measurement of blade twist at each target radial station) and goal to measure the deformation of all four blades simultaneously. Similar to preparations for PIV measurements, the UH-60A BD measurements required several years of preparation leading up to the test. In 2008, preliminary BD measurements were acquired on one blade of the Boeing/Defense Advanced Research Projects Agency (DARPA) SMART rotor that was tested in the 40x80 [Straub et al., 2009, 2018]. Building on the lessons learned from the SMART test, another opportunity was leveraged in 2009 when a UH-60 rotor configured with individual blade control (IBC) was tested in the 40x80. Taking advantage of this test opportunity, BD measurements were acquired in two of the four quadrants of the rotor for several advance ratios and rotor thrust coefficients [see Olson et al., 2010]. Each quadrant required two cameras—each with a strobe mounted in a floor cavity of the tunnel—to capture the motion of the entire blade. Reflective targets were applied to the lower surface of two of the four blades. Transforming the stereo images into elastic blade deformations in the desired reference frame required three independent camera calibrations. The external camera calibration necessitated the installation of 84 6-inch-diameter reflective targets on the ceiling of the 40x80. With the experience gained from the SMART and IBC UH-60 tests, the BD installation was expanded to include all four quadrants of the rotor disk for the 2010 UH-60A Airloads test. Reflective targets (48 per blade) were installed on the lower surface of the remaining two blades. Figure 4.9 provides a schematic of the final installation. As described in Barrows et al. [2011], BD measurements were acquired for all four blades throughout the test envelope, including advance ratios of 0.15 to 1.0, rotor thrust coefficient-to-solidity ratios of 0.01 to 0.13, and rotor shaft angles of –10 to 8 degrees. Processing the volume of data was a huge endeavor. Inconsistent target contrast, lens calibrations/corrections, and bias errors required careful inspection of thousands of images [Abrego et al., 2012]. Abrego et al. [2016] provides a summary of the final reduced data set, together with comparisons with CFD/CSD predictions. A capstone to this effort is presented in the two-volume report by Meyn et al. [2017]. In Volume I of their report, the authors describe the UH-60A BD measurement methodology, system development, and data analysis techniques including necessary corrections to account for blade elasticity. Sample results are included in Volume I; selected data are provided in Volume II.

Since the UH-60A test, the V-STARS photogrammetry system (manufactured by Geodetic Systems, Inc.), which was used to locate the targets fixed to the 40x80 ceiling and targets on the PIV calibration plate, has been used whenever the precise location of an object is required. For example, Solis and Meyn [2016] used photogrammetric measurements to determine the location and orientation of applied forces during a complex, multi-component, rotor balance calibration. A total of 2800 retro-reflective targets and 120 coded targets were used to measure deflections during the balance calibration (see Fig. 4.10). The system can also be used to determine the outer mold line of complex geometries, though for geometries with sharp edges such as rotor blades the photogrammetry measurements are augmented or replaced by three-dimensional (3D) laser-scanning results.

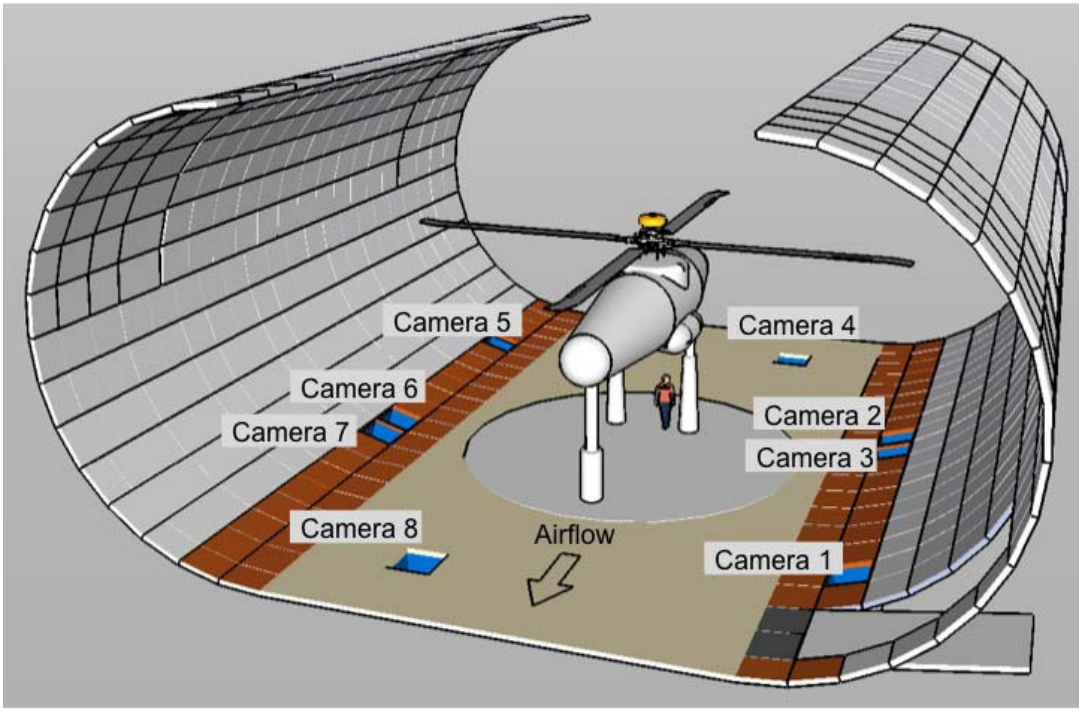

Figure 4.9. Schematic of camera layout for BD measurements over four quadrants in the NFAC 40- by 80-Foot Wind Tunnel (Fig. 2 of Barrows [2011]).

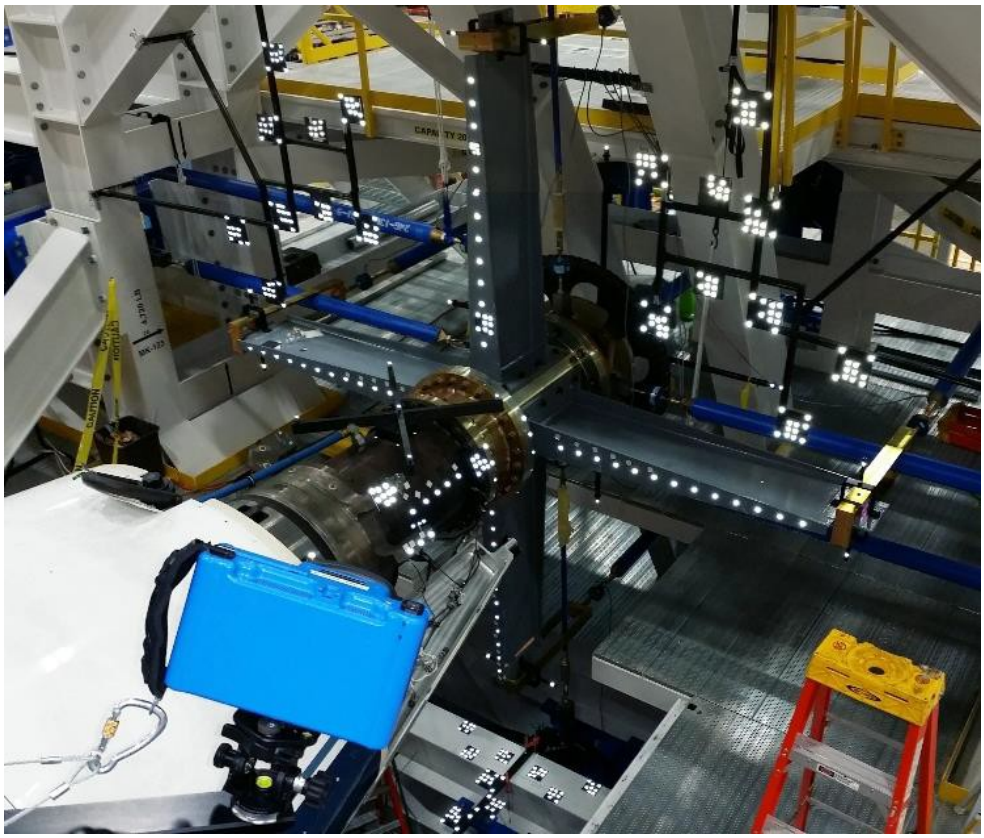

Figure 4.10. Retro-reflective targets installed on deflection hardware and calibration body (Fig. 16 of Solis and Meyn [2016]).

BACKGROUND ORIENTED SCHLIEREN

The long-term collaboration between the German Aerospace Center (DLR) and NASA that has focused on optical techniques for rotorcraft applications is responsible for several innovative advances that NASA has leveraged. The background oriented schlieren (BOS) technique is one such innovation. BOS, developed by the DLR, was implemented in the 40x80 for the UH-60A Airloads test. Like the UH-60A PIV and BD researchers, Heineck et al. [2010] leveraged the UH-60 IBC test in the NFAC in 2009 to develop a prototype BOS system to capture rotor tip vortex filament images. Several 4- by 4-foot panels, covered with retro-reflective material and splattered with a random pattern of black paint spots, were fastened to the sidewall of the 40x80 test section. The panel positions were selected to accommodate an ROI that encompassed the outer two-thirds of the blade, 4 feet below and 8 feet above the blade tip. The intent was to provide vortex filament locations that would augment the tip vortex locations captured by the single PIV plane. The BOS system required two cameras, each accompanied by LED ring lights; one camera was placed in a light port in the ceiling of the tunnel test section, and the other camera was placed in a facility camera port in the sidewall of the test section. Overall, the BOS system proved successful at acquiring usable images over the large distances in the 40x80 test section. Raffel et al. [2012b, 2014a] continued refining the BOS technique on full-scale rotors via flight tests. For flight tests, a natural background was required in lieu of an artificially prepared speckled background. For example, grass, with high contrast and high spatial frequency, meets the requirement for a natural background. Raffel et al. [2014a] developed a data reduction process that did not require a reference image. The innovation of reference-free BOS using natural backgrounds (eventually termed AIR-BOS) is very useful for imaging rotor wakes in flight; the technique has since been applied to imaging shocks on supersonic aircraft.

In 2010, BOS measurements were acquired during the UH-60A Airloads test [Schairer et al., 2013]. Despite lower signal-to-noise ratio in the speckle-displacement distribution of the ceiling camera, the spatial positions of vortex filaments near the tip of the advancing blade were successfully measured. BOS was used to visualize the vortex filaments. Figure. 4.11 shows instantaneous speckle-displacement distributions measured by the sidewall and ceiling cameras at three rotor azimuth angles. The authors describe the origin of the primary features captured in the flow field. Using custom photogrammetry software, the authors computed the filament positions, as shown in Figure 4.12. Filament visibility improved with increasing rotor thrust and vortices from all four blades were seen. More vortices were typically seen from the sidewall camera compared to the ceiling camera, which had a more complex optical path.

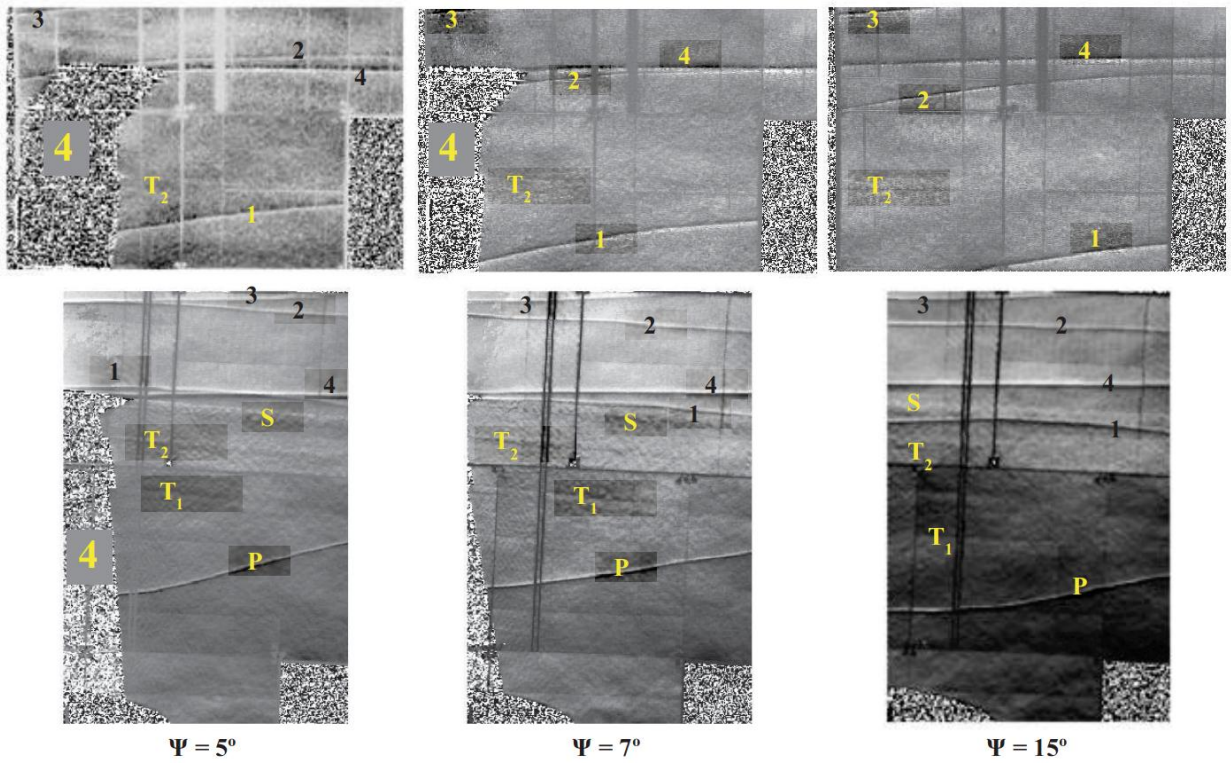

Figure 4.11. Speckle-displacement distributions for ceiling (top) and sidewall (bottom) cameras at three azimuth angles. Blade 4 is in the region of interest (Case 1: α = 0°, μ = 0.15, C_T/σ = 0.12). Callouts: 1, 2, 3, 4 = blade number; T1 = inboard trim tab; T2 = outboard trim tab; S = disturbance; and P = prominent vortex (Fig. 11 of Schairer et al. [2013]).

.

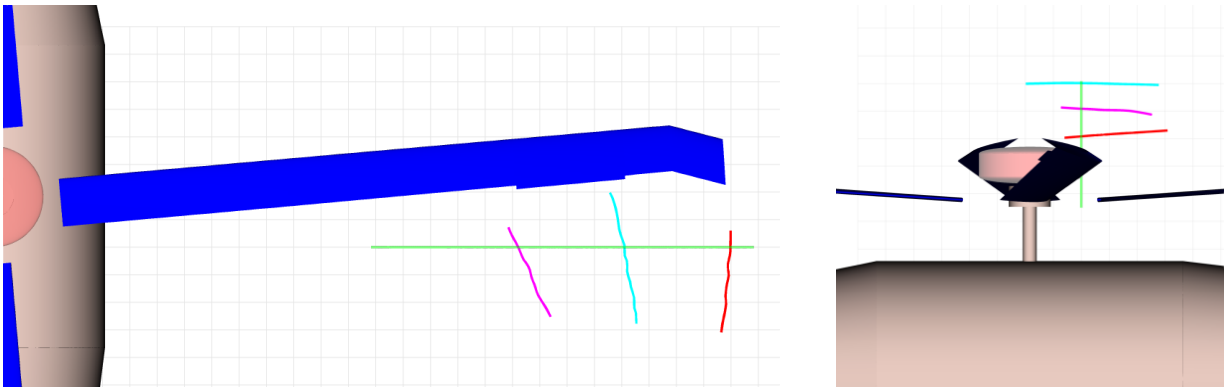

a) Top view b) Side view

Figure 4.12. Position of vortex filaments captured using RBOS relative to the PIV measurement plane (ψ = 5º, α = 0º, μ = 0.15, C_T/σ = 0.12) (Fig 12. of Schairer, et al. [2013]).

INFRARED THERMOGRAPHY

For CFD practitioners, *predicting* boundary layer transition on a rotor blade rather than *modeling* transition is still an unachieved goal. For experimentalists, measuring transition using relatively unobtrusive techniques has finally become a reality in the past several years. As mentioned in the beginning of this chapter, camera technology has advanced tremendously since 2007. NASA invested in a succession of FLIR Systems cameras since 2007, which has enabled boundary layer transition measurements on rotor blades in hover and forward flight. Once again, collaboration with the DLR proved very fruitful in two key areas: image de-rotation and differential infrared thermography (DIT).

For PSP, TSP, and boundary layer transition techniques applied to rotating blades, camera exposure times on the order of milliseconds cause image blur. As mentioned in the section on PSP, a point spread function (PSF) can be used to de-blur the image post-test. Raffel and Heineck [2014b] devised a rotating mirror system to de-rotate an image and eliminate blur prior to recording the image. The rotating mirror system has since been incorporated into PSP and flow transition installations for rotorcraft applications. Heineck et al. [2014] successfully incorporated the rotating mirror in a test of a four-bladed, 1.67-foot-radius rotor in hover at the DLR. This test was followed by Heineck et al. [2016] using the rotating mirror in a simultaneous, multi-technique hover test in the U.S. Army Hover Chamber at Ames. The measurements included thermal imaging (with the mirror incorporated in the installation), retro-reflective BOS, BD using photogrammetry, and an exploratory attempt at tomographic PIV. The two-bladed rotor had a diameter of 5.94 feet and was positioned about 10 feet above the ground. From the experience of the UH-60A wind tunnel test, simultaneous measurements are optimum for test efficiency, but with optical techniques, camera and illumination requirements are typically incompatible between techniques. As described in Heineck et al. [2016], transition measurements, BD, and vortex filament location were simultaneously measured successfully. In addition, the photogrammetric calibration from the BD measurement system was used to map the thermal image data to the blade surface grid, thus accurately locating flow transition along the length of the blade.

Overmeyer and Martin [2017] tested a three-bladed, 11.08-foot-diameter rotor in hover during the summer of 2016. The goal of the test was to investigate the effect of boundary layer transition on hover performance. The blades were the same PSP blades tested by Wong et al. [2010] except one of the blades was treated with a paintable heater. Two FLIR Systems TM SC6701 strained-layer superlattice (SLS) cameras were used to acquire simultaneous images of the upper and lower surface of the treated blade. Trip dots were applied near the leading edge of the upper and lower surface of the treated blade for fixed-transition test conditions. Transition locations on upper/lower blade surfaces were acquired for rotor thrust coefficient-to-solidity ratios of 0.03 to approximately 0.10 (see Fig. 4.13).

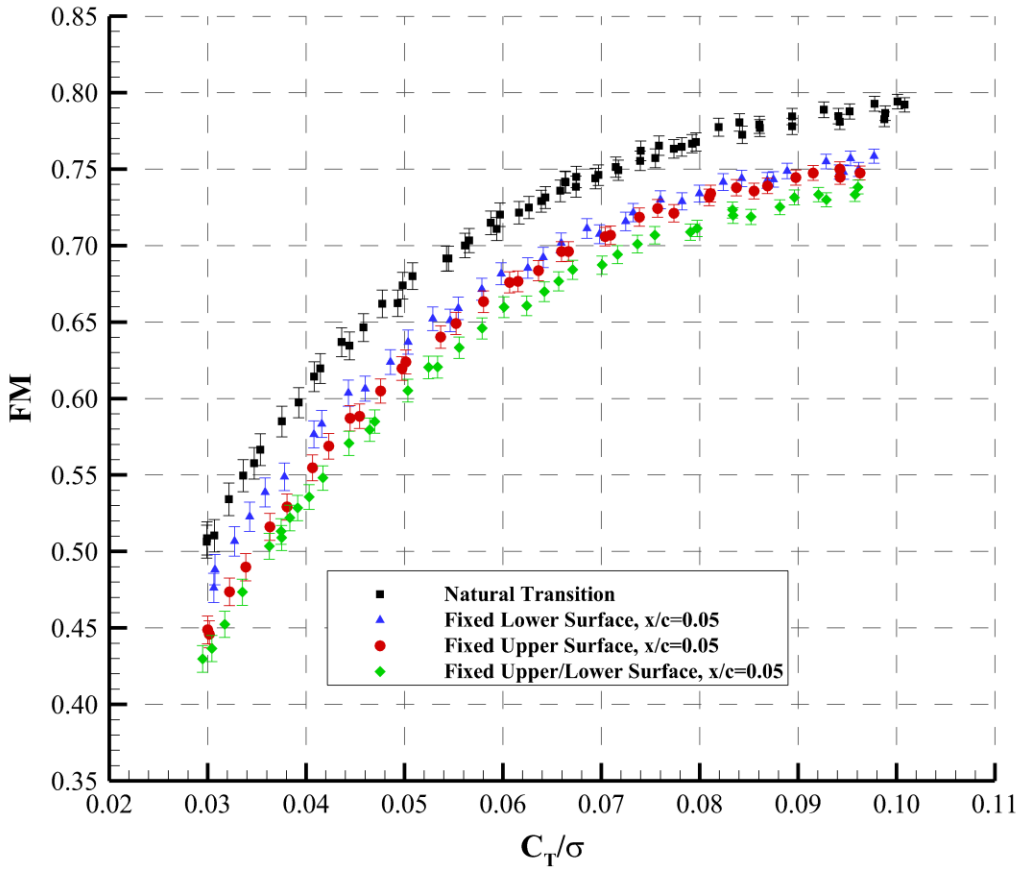

Figure 4.13. Measured hover performance for the PSP blade (Fig. 9 of Overmeyer and Martin [2017]).

The next major advancement was to measure transition on a rotor blade in forward flight; the test was conducted by the U.S. Army in collaboration with NASA and the DLR. Using a newly acquired FLIR Systems X6900sc SLS camera procured by NASA, Overmeyer et al. [2018] tested the same three-bladed rotor in the Langley 14x22 during the summer of 2017. Infrared (IR) thermography images were acquired on the lower surface of the rotor blade for a range of test conditions: advance ratios of 0.10 to 0.38, rotor thrust coefficient-to-solidity ratio of 0.04 to 0.12, and rotor shaft angles of –6 to 0 degrees. The blade was painted black to improve the emissivity of the surface. The authors concluded that the DIT method is capable of measuring the unsteady thermal blade response of a rotor in forward flight. Figure 4.14 shows images for low- and high-thrust cases at a fixed advance ratio. Figure 4.15 shows the approximate transition location over the lower surface of the rotor disk for an advance ratio of 0.30 and a rotor thrust coefficient-to-solidity ratio of 0.08. Additional data is required to identify conclusive transition locations. Still, this experiment, together with the data from the companion hover test of 2016, signifies a huge step forward in measurement capability and understanding of transition behavior. In a companion paper to Overmeyer et al. [2018], Heineck et al. [2018] provides additional details on the imaging installation in the 14x22 tunnel and presents sample images processed using two approaches of the differential infrared thermography technique.

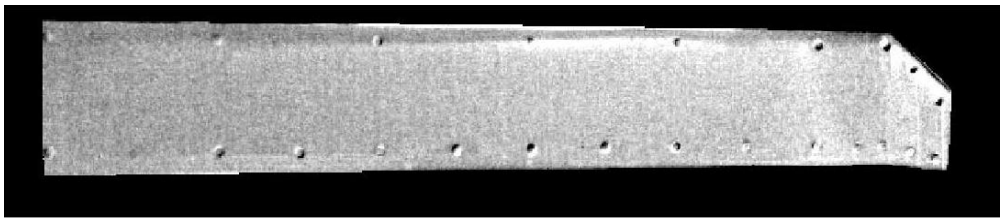

a) DIT image lower surface, μ = 0.30, C_T/σ =0.04.

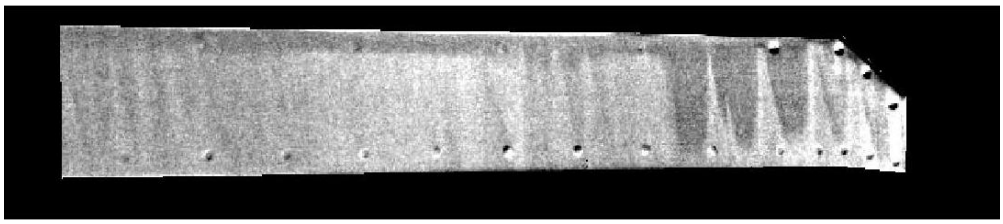

b) DIT image lower surface, μ = 0.30, C_T/σ =0.12.

Figure 4.14. Images showing transition locations on the blade lower surface at ψ = 90° and two different rotor thrust coefficient-to-solidity ratios (Figs. 11 and 13 of Overmeyer et al. [2018]).

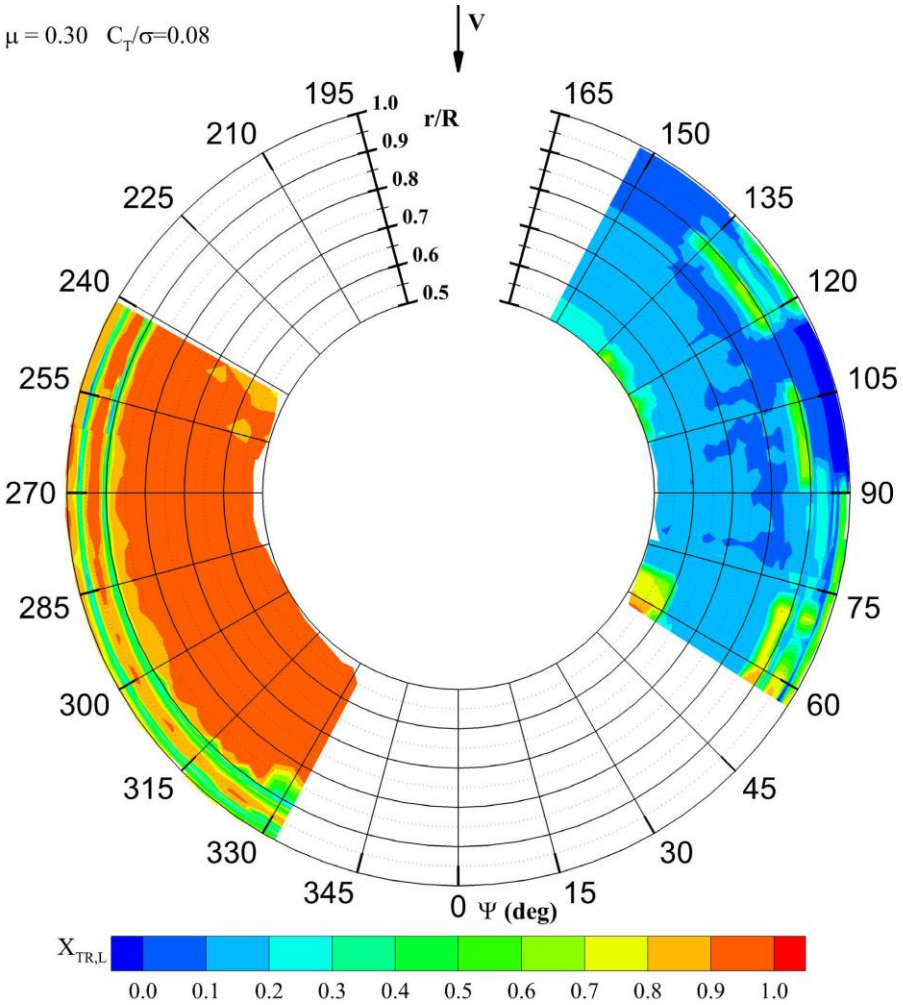

Figure 4.15. Measured transition versus radius and azimuthal position: μ = 0.30, C_T/σ = 0.08 (Fig. 14 of Overmeyer, et al. [2018]).

SENSOR DEVELOPMENT AND NOVEL APPLICATIONS

Although wind tunnel and flight test campaigns offer the opportunity to demonstrate measurement techniques at higher Technology Readiness Levels (TRLs), laboratory experiments are necessary for demonstrating techniques at a less-complex, and typically less costly, component level.

For rotorcraft flight tests, one of the difficult but critical parameters to deduce, let alone measure, is the rotor tip path plane (TPP) angle. Typically, the TTP angle in flight is computed using estimates for the aircraft drag, flight path angle, and rotor flapping. In 2006, supported by NASA funding, Sickenberger and Schmitz [2007] developed and installed a prototype system for measuring the TPP angle on a Bell 206B helicopter. The optics-based system (two cameras, each fitted with a laser) was successfully deployed and a number of needed improvements were identified. Sickenberger and Schmitz [2008] improved the prototype by expanding the system (that is, incorporating more cameras) to track both longitudinal and lateral components of the TPP and developing a faster blade-tip-tracking algorithm that adapted to changing background ambient light. In 2008, the improved system was flown on a Bell 206B (two-bladed teetering main rotor) and a Hughes 500E (five-bladed main rotor). The issues identified in the 2006 flight test were overcome with the improved system.

Vibration control, whether in an aircraft cabin or on rotating machinery, is necessary to reduce fatigue and damage to parts and passengers. Approaches to vibration control vary according to application. Beck and Schiller [2013] explored two forms of active vibration control using a Plexiglas® panel as a test structure. An active damping (velocity feedback) approach, using accelerometers as sensors and a piezoelectric actuator, was compared with a negative capacitance shunt damping approach. The latter approach used a single piezoelectric patch as both sensor and actuator. The active damping approach performed significantly better than the negative shunt damping but at a cost of about three times the power required and with added complexity. As with any system, the trade-offs between performance and cost must be considered per application. Asnani et al. [2016] compared piezoelectric and magnetorestrictive shunt dampers as a means to control vibration energy caused by rotating machinery. A novel mechanism called a vibration ring is under development. The ring converts unwanted vibration into electrical energy that provides a damping effect on the driveline of the helicopter (or other machinery with rotating parts); the converted energy can be used to power other devices. Follow-on work included Scheidler et al. [2016a, 2016b] where an electrically controllable magnetorestrictive spring capable of dynamic stiffness tuning was designed, manufactured, and tested. Linear models of electrically shunted magnetorestrictive transducers were later developed and validated in Scheidler and Asnani [2017].

Kohlman et al. [2012] attempted to use digital image correlation (DIC) to evaluate deformation of composite rotating drive system components. At the time, however, limitations on camera resolution, image blur, and lighting issues prevented satisfactory results. Improvements to the DIC system, documented in Kohlman et al. [2013a, 2013b], achieved the desired results. The main improvement was the introduction of a high-intensity LED array, which reduced image blur and noise levels to a level expected from nonrotating imaging.

Though planar measurement techniques such as PIV have become the preferred approach for flow-field interrogation, there is still a role for point-measurement systems. Meyers et al. [2012] repurposed and upgraded a long-focal-length laser velocimeter (from the early 1980s) to improve usability, reliability, and serviceability. The original system was developed for the Langley 14- by 22-Foot Subsonic Wind Tunnel. Using fiber optics, the upgraded system allowed most of the optics and the laser to be located outside of the wind tunnel test section. The signal processors were replaced with current instrumentation and software.

Okojie et al. [2007] studied high-temperature (up to 500°C) pressure sensors aimed at combustion engine environments. The long-term reliability of single crystal silicon carbide (SiC) piezoresistive pressure sensors was evaluated and failure analysis performed to identify two possible sensor failure mechanisms. The authors pursued a different sensor packaging as a result of their findings and Okojie [2009] filed a patent for "MEMS Direct Chip Attach Packaging Methodologies and Apparatuses for Harsh Environments."

A novel application of an old flow visualization technique was effectively used by Wadcock et al. [2008] to visualize the helicopter downwash flow of a full-scale UH-60 Black Hawk. The purpose of the experiment was to obtain understanding of the aerodynamic conditions contributing to brownout. The authors applied 1-foot-long tufts in a 60- by 60-foot grid on the ground and captured the movement of the tufts (using video and single photographs) as the helicopter hovered at discrete distances above the ground. Tufts of 6.5 inch length were applied

Figure 4.16. UH-60 airframe tufts in hover at 5-ft wheel height (IGE). Overlay of three instantaneous airframe images (Fig. 5(d) of Wadcock et al. [2008]).

to parts of the helicopter fuselage as well. Figure 4.16 shows three images, overlaid, of the tuft grid on the port side of the fuselage when the wheels of the helicopter were 5 feet above ground. Unlike the images out-of-ground effect, many of the tufts in Figure 4.16 are pointing upward. Using the tuft images and CFD flow-field results, the authors suggest that airframe geometry contributes to the more severe brownout experience of the Black Hawk compared to the EH-101 helicopter.

REFERENCES

Abrego, A., Olson, L., Romander, E., Barrows, D., and Burner, A., "Blade Displacement Measurement Technique Applied to a Full-Scale Rotor Test," 68th Annual Forum and Technology Display of the American Helicopter Society, Ft. Worth, TX, May 1-3, 2012.

Abrego, A.I., Meyn, L., Burner, A. W., and Barrows, D. A., "Summary of Full-Scale Blade Displacement Measurements of the UH-60A Airloads Rotor," American Helicopter Society Specialists' Conference on Aeromechanics Design for Vertical Lift, San Francisco, CA, Jan. 20-22, 2016.

Ali, M., Pandey, A., and Gregory, J., "Dynamic Mode Decomposition of Fast Pressure Sensitive Paint Data," *Sensors*, 16, 862; June 2016, DOI:10.3390/s16060862

Asnani, V., Deng, Z., Scheidler, J., and, Dapino, M., "Experimental comparison of piezoelectric and magnetostrictive shunt dampers," 2016 SPIE Smart Structures/NDE conference, Las Vegas, NV, March 20-24, 2016.

Barrows, D. A., Burner, A. W., Abrego, A. I., and Olson, L., "Blade Displacement Measurements of the Full-Scale UH-60A Airloads Rotor," Paper AIAA-2011-3655, AIAA 29th Applied Aerodynamics Conference, Honolulu, HI, June 27-30, 2011, DOI: 10.2514/ 6.2011-3655.

Beck, B., and Schiller, N., "Experimental Comparison of Two Active Vibration Control Approaches: Velocity Feedback and Negative Capacitance Shunt Damping," Noise-Con 2013, Denver CO, Aug. 26-28, 2013.

Fleming, G. A., "RASP: Rotor Azimuth Synchronization Program (RASP) User's Guide, Version 1.3," NASA Langley Research Center, Feb. 6, 2008.

Heineck, J., Kushner, L., Schairer, E., and Walker, L., "Retroreflective Background Oriented Schlieren (RBOS) as applied to Full-scale UH-60 Blade Tip Vortices," American Helicopter Society Aeromechanics Specialists' Conference, San Francisco, CA, Jan. 20-22, 2010.

Heineck, J. T., Schairer, E., and Raffel, M., "Boundary Layer Transition Detection on a Rotor Blade Using Rotating Mirror Thermography," Fifth Decennial American Helicopter Society Aeromechanics Specialists' Conference, San Francisco, CA, Jan. 2014.

Heineck, J. T., Schairer, E.T., Roozeboom, N., and Ramasamy, M., "Simultaneous Boundary-Layer Transition, Tip Vortex, and Blade Deformation Measurements of a Rotor in Hover," American Helicopter Society Specialists' Conference on Aeromechanics Design for Vertical Lift, San Francisco, CA, Jan. 20-22, 2016.

Heineck, J., Overmeyer, A, Klein, C., and Raffel, M., "Boundary Layer Transition Visualizations on a Helicopter Blade in Forward Flight Using Thermography," International Symposium for Flow Visualization, Zurich, Switzerland, June 2018.

Jenkins, L., Yao, C. S., Bartram, S., Harris, J., Allan, B., Wong, O., and Mace, D., "Development of a Large Field of View PIV System for Rotorcraft Testing in the 14x22 Subsonic Wind Tunnel," 65th Annual Forum and Technology Display of the American Helicopter Society, Grapevine, TX, May 27-29, 2009.

Kohlman, L., Ruggeri, C., Roberts, G., Handschuh, R., Roth, D., and Martin, R., "Full-field Deformation Measurement Techniques for a Rotating Composite Shaft," 68th Annual Forum and Technology Display of the American Helicopter Society, Ft. Worth, TX, May 1-3, 2012.

Kohlman, L., Ruggeri, C., Roberts, G., and Handschuh, R., "Improvements in High Speed, High Resolution Dynamic Digital Image Correlation for Experimental Evaluation of Composite Drive System Components," 69th Annual Forum and Technology Display of the American Helicopter Society, Phoenix, AZ, May 21-23, 2013a.

Kohlman, L. W., Ruggeri, C. R., Roberts, G. D., and Handschuh, R. F., "Improvements in High Speed, High Resolution Dynamic Digital Image Correlation for Experimental Evaluation of Composite Drive System Components," NASA/TM–2013-216537, July 2013b.

Martin, P. B., Overmeyer, A. D., Tanner, P. E., Wilson, J. S., and Jenkins, L. N., "Helicopter Fuselage Active Flow Control in the Presence of a Rotor," American Helicopter Society 70th Annual Forum, Paper 335, Montreal, Quebec, Canada, 2014.

Matalanis, C., Bowles, P., Lorber, P., Crittenden, T., Glezer, A., Schaeffler, N., Min, B-Y., Jee, S., Kuczek, A., Lorber, and Wake, B., "High-Speed Experiments on Combustion-Powered Actuation for Dynamic Stall Suppression," 72nd Annual Forum of the American Helicopter Society, West Palm Beach, FL, May 17-19, 2016.

Matalanis, C. G., Bowles, P. O., Min, B-Y, Jee, S., Kuczek, A. E., Lorber, P. F., Crittenden, T., Glezer, A., and Schaeffler, N. W., "High-Speed Experiments on Combustion-Powered Actuation for Dynamic Stall Suppression," *AIAA Journal*, vol. 55, no. 9, Sept. 2017, DOI: 10.2514/1.J055700

Meyers, J. F., Lee, J. W., Cavone, A. A., and Fletcher, M. T., "The Modernization of a Long-Focal Length Fringe-Type Laser Velocimeter," 16th International Symposium on Applications of Laser Techniques to Fluid Mechanics, Lisbon, Portugal, July 9-12, 2012.

Meyn, L., Abrego, A., Barrows, D., and Burner, A., "Blade Displacement Measurements During the NFAC UH-60A Airloads Test Volume I–Methodology, System Development, and Data Analysis Techniques," NASA/TM–2017-219094, Aug. 2017.

Meyn, L., Abrego, A., Barrows, D., Burner, A., "Blade Displacement Measurements During the NFAC UH-60A Airloads Test Volume II–Selected Data and Plots," NASA/TM–2017-219094, Aug. 2017.

Norman, T. R., Shinoda, P. M., Peterson, R. L. and Datta, A., "Full-Scale Wind Tunnel Test of the UH-60A Airloads Rotor," American Helicopter Society 67th Annual Forum, Virginia Beach, VA, May 2011.

Okojie, R. S., Nguyen, P., Nguyen, V., Savrun, E., Lukco, D., Buehler, J., and McCue, T., "Failure Mechanisms in MEMS Based Silicon Carbide High Temperature Pressure Sensors," IEEE 45th Annual International Reliability Physics Symposium, Phoenix, AZ, 2007.

Okojie, R. S.: Patent Awarded for Chip Packaging: U.S. Patent # 7,518,234, entitled "MEMS DIRECT CHIP ATTACH PACKAGING METHODOLOGIES AND APPARATUSES FOR HARSH ENVIRONMENTS," April 14, 2009.

Olson, L., Abrego, A., Barrows, D., and Burner, A., "Blade Deflection Measurements of a Full-Scale UH-60A Rotor System," American Helicopter Society Aeromechanics Specialists' Conference, San Francisco, CA, Jan. 20-22, 2010.

Overmeyer, A., Tanner, P., Martin, P., and Commo, S., "Case Studies for the Statistical Design of Experiments Applied to Powered Rotor Wind Tunnel Tests," AIAA Aviation 2015 Conference Dallas, TX, June 22-26, 2015.

Overmeyer, A. D. and Martin, P. B. "Measured Boundary Layer Transition and Rotor Hover Performance at Model Scale," Paper AIAA-2017-1872, 55th AIAA Aerospace Sciences Meeting, SciTech Forum, Grapevine, TX, Jan. 9-13, 2017.

Overmeyer, A., Heineck, J., and Klein, C., "Unsteady Boundary Layer Transition Measurements of a Rotor in Forward Flight," 74th Annual Forum and Technology Display of the American Helicopter Society, Phoenix, AZ, May 2018.

Raffel, M., Kindler, K., Mulleners, K., and Heineck, J. T., "Particle Image Velocimetry in Helicopter Aerodynamics: Developments, Challenges and Trends," 68th Annual Forum and Technology Display of the American Helicopter Society, Ft. Worth, TX, May 1-3, 2012a.

Raffel, M., Schairer, E., Heineck, J. T., Leopold, F., and Kindler, K., "Background Oriented Schlieren Techniques for Helicopter Related Large-Scale and Flight Testing," Paper 161, European Rotorcraft Forum 2012, Amsterdam Sept. 4-7, 2012b.

Raffel, M., Heineck, J. T., Schairer, E., Leopold, F., and Kindler, K., "Background-Oriented Schlieren Imaging for Full-Scale and In-Flight Testing," *Journal of the American Helicopter Society*, vol. 59, no. 1, Jan. 2014a.

Raffel, M. and Heineck, J. T., "Mirror-Based Image De-rotation for Aerodynamic Rotor Measurements," *AIAA Journal*, vol. 52, no. 6, June 2014b, DOI: 10.2514/1.J052836

Raffel, M., Bauknecht, A., Ramasamy, M., Yamauchi, G., Heineck, J., and Jenkins, L., "Contributions of Particle Image Velocimetry to Helicopter Aerodynamics," *AIAA Journal*, May 2017, DOI: 10.2514/1.J055571

Rajendar, A., Crittenden, T. M., and Glezer, A., "Characterization of the Internal Flow Dynamics of Combustion Powered Actuators," Paper AIAA-2008-3760, 4th Flow Control Conference, Seattle, WA, June 23-26, 2008, DOI: 10.2514/6.2008-3760

Ramasamy, M., Potsdam, M., and Yamauchi, G. K., "Measurements to Understand the Flow Mechanisms Contributing to Tandem-Rotor Outwash," 71st Annual Forum and Technology Display of the American Helicopter Society, Virginia Beach, VA, May 21–23, 2015.

Ramasamy, M. and Yamauchi, G. K., "Using Model-Scale Tandem-Rotor Measurements in Ground Effect to Understand Full-Scale CH-47D Outwash," *Journal of the American Helicopter Society,* vol. 62, no. 1, Jan. 2017, pp. 1-14, https://doi.org/10.4050/JAHS.62.012004

Schaeffler, N. W., Allan, B. G., Wong, O. D., and Tanner, P. E., "Experimental Investigation of Active Aerodynamic Load Reduction on a Rotorcraft Fuselage with Rotor Effects," Paper AIAA-2014-2561, 32nd AIAA Applied Aerodynamics Conference, Atlanta, GA, June 16-20, 2014, DOI: 10.2514/6.2014-2561

Schaeffler, N. W., Allan, B. G., Jenkins, L. N., Yao, C. S., Bartram, S. M., Mace, W. D., Wong, O. D., and Tanner, P. E., "Mechanisms of Active Aerodynamic Load Reduction on a Rotorcraft Fuselage with Rotor Effects," AHS Technical Meeting on Aeromechanics Design for Vertical Lift, San Francisco, CA, Jan., 2016.

Schairer, E., Heineck, J. T., and Kushner, L., "Measurement of Tip Vortices from a Full-Scale UH-60A Rotor by Retro-Reflective Background Oriented Schlieren and Stereo Photogrammetry," 69th Annual Forum and Technology Display of the American Helicopter Society, Phoenix, AZ, May 21-23, 2013.

Scheidler, J., Asnani, V., and Dapino, M., "Vibration Control Via Stiffness Switching of Magnetostrictive Transducers," 2016 SPIE Smart Structures/NDE conference, Las Vegas, NV, March 20-24, 2016a.

Scheidler, J., Asnani, V., and Dapino, M., "Dynamically Tuned Magnetostrictive Spring with Electrically Controlled Stiffness," *Smart Materials and Structures*, vol. 25, no. 3, 2016b.

Scheidler, J. and Asnani, V., "Validated Linear Dynamic Model of Electrically-Shunted Magnetostrictive Transducers with Application to Structural Vibration Control," *Smart Materials and Structures*, vol. 26, no. 035057, 2017.

Sekula, M., "The Development and Hover Test Application of a Projection Moire Interferometry Blade Displacement Measurement System," 68th Annual Forum and Technology Display of the American Helicopter Society, Ft. Worth, TX, May 1-3, 2012.

Sickenberger, R. D., and Schmitz, F. H., "Longitudinal Tip-Path-Plane Measurement Using an Optics-Based System," 63rd Annual Forum and Technology Display of the American Helicopter Society, Virginia Beach, VA, May 2007.

Sickenberger, R. and Schmitz, F., "An Optics-Based Tip-Path Plane Tracking System for Rotorcraft Applications," Paper AIAA-2008-7315, AIAA Guidance, Navigation, and Control Conference, Honolulu, HI, Aug. 18-21, 2008, DOI: 10.2514/6.2008-7315

Solis, E., and Meyn, L., "Photogrammetric Deflection Measurements for the Tiltrotor Test Rig (TTR) Multi-Component Rotor Balance Calibration," American Helicopter Society Specialists' Conference on Aeromechanics Design for Vertical Lift, San Francisco, CA, Jan. 20-22, 2016.

Straub, F. K., Anand, V. R., Birchette, T. S., and Lau, B. H., "Wind Tunnel Test of the SMART Active Flap Rotor," 65th Annual Forum and Technology Display of the American Helicopter Society, Grapevine, TX, May 27-29, 2009. See also *Journal of the American Helicopter Society*, vol. 63, no.1, Jan. 2018, DOI: 10.4050/JAHS.63.012002

Tanner, P., Overmeyer, A., Jenkins, L., Yao, C-S., and Bartram, S., "Experimental Investigation of Rotorcraft Outwash in Ground Effect," 71st Annual Forum and Technology Display of the American Helicopter Society, Virginia, Beach, VA, May 2015.

Wadcock, A. J., Ewing, L. A., Solis, E., Potsdam, M., and Rajagopalan, G., "Rotorcraft Downwash Flow Field Study to Understand the Aerodynamics of Helicopter Brownout," American Helicopter Society Southwest Region Technical Specialists' Meeting, "Technologies for the Next Generation of Vertical Lift Aircraft," Dallas-Fort Worth, TX, Oct. 2008.

Wadcock, A. J., Yamauchi, G. K., Solis, E., and Pete, A. E., "PIV Measurements in the Wake of a Full-Scale Rotor in Forward Flight," Paper AIAA-2011-3370, AIAA Applied Aerodynamics Conference, Honolulu, HI, June 27-30, 2011, DOI: 10.2514/6.2011-3370

Watkins, A. N., Leighty, B. D., Lipford, W. E., Wong, O. D., Oglesby, D. M., and Ingram J. L., "Development of a Pressure Sensitive Paint System for Measuring Global Surface Pressures on Rotorcraft Blades," International Congress on Instrumentation in Aerospace Simulation Facilities (ICIASF), Pacific Grove, CA, July 10-14, 2007.

Watkins, A. N., Leighty, B. D., Lipford, W. E., Wong, O. D., Goodman, K. Z., Crafton, J., Forlines, A., Goss, L. P., Gregory, J. W., and Juliano, T. J., "Deployment of a Pressure Sensitive Paint System for Measuring Global Surface Pressures on Rotorcraft Blades in Simulated Forward Flight Preliminary PSP Results from Test 581 in the 14- x 22-Foot Subsonic Tunnel," NASA/TM–2011-217316, Dec. 2011.

Watkins, A. N., Leighty, B. D., Lipford, W. E., Wong, O. D., Goodman, K. Z., Crafton, J., Forlines, A., Goss, L. P., Gregory, J. W., and Juliano, T. J., "Deployment of a Pressure Sensitive Paint System for Measuring Global Surface Pressures on Rotorcraft Blades in Simulated Forward Flight," AIAA Paper 2012-2756, 28th Aerodynamic Measurement Technology, Ground Testing, and Flight Testing Conference (AIAA), New Orleans, LA, June 2012.

Watkins, A. N., Leighty, B. D., Lipford, W. E., Goodman, K. Z., Crafton, J., and Gregory, J. W., "Applying Pressure Sensitive Paint Technology to Rotor Blades," NASA/TM–2014-218259.

Watkins, A. N., Leighty, B. D., Lipford, W. E., Goodman, K. Z., Crafton, J., and Gregory, J. W., "Measuring Surface Pressures on Rotor Blades Using Pressure Sensitive Paint," *AIAA Journal*, Posted online 10/6/2015, DOI:10.2514/1.J054191

Wong, O., Noonan, K., Watkins, A., Jenkins, L., and Yao, C. S., "Non-Intrusive Measurements of a Four-Bladed Rotor in Hover--A First Look," American Helicopter Society Aeromechanics Specialists' Conference, San Francisco, CA, Jan. 20-22, 2010.

Wong, O., Watkins, N., Goodman, K., Crafton, J., Forlines, A., Goss, L., Gregory, J., and Juliano, T., "Blade Tip Pressure Measurements using Pressure Sensitive Paint," 68th Annual Forum and Technology Display of the American Helicopter Society, Ft. Worth, TX, May 1-3, 2012.

Yamauchi, G. K. and Young, L. A., Editors, "A Status of NASA Rotorcraft Research," NASA/TP–2009-215639, Sept. 2009.

Yamauchi, G., Wadcock, A., Johnson, W., and Ramasamy, M., "Wind Tunnel Measurements of Full-Scale UH-60A Rotor Tip Vortices," 68th Annual Forum and Technology Display of the American Helicopter Society, Ft. Worth, TX, May 1-3, 2012.

CHAPTER 5. FLIGHT DYNAMICS AND CONTROL

Winnie Kuang[1] and Carlos A. Malpica[2]

CONCEPTUAL DESIGN AND SIMULATION

Typically, it is not until flight tests that handling qualities problems are uncovered, and corrective measures determined, which can make vehicle development time-consuming and expensive. Advancements in rotorcraft research have propelled the need to abandon the traditional approach of addressing handling qualities at later stages of development. Considering handling qualities early on in development provides an opportunity to address critical handling qualities factors on a design while the design can still be changed, and to provide margins in the design to accommodate unforeseen handling qualities problems that may occur in later development stages. Thus, subsequent analysis will be more meaningful and tractable.

The NASA Design and Analysis of Rotorcraft (NDARC) software (see Johnson [2015]), which is primarily used in the conceptual design stage, comprises analysis, synthesis, and optimization processes. NDARC is used to dimension vehicles and determine the best configuration that will optimize operational capabilities and performance, while providing information on the trends and relative benefits of certain configurations. NDARC's low-fidelity modeling can be used for rapid calculations and flight performance analysis of an aircraft, addressing variables such as payload, range, and maximum speed. However, NDARC currently does not consider handling qualities in the design optimization process.

Recent developments in rotorcraft conceptual design trend towards incorporating stability, control, and handling qualities analysis in the early design trade-space. There are challenges with incorporating handling qualities into conceptual design: the lack of adequate modeling to represent the flight dynamics and controls in most of the conceptual design tools currently used, and the uncertainty of incorporating handling qualities in the design at the conceptual stage.

Lawrence [2014] developed a preliminary framework for conducting flight dynamics and control analysis in the conceptual stage. Figure 5.1 shows the proposed methodology for integrating handling qualities into the NDARC-based conceptual design stage; NDARC's output results will then be used to generate flight dynamics models appropriate for handling qualities analysis.

Adding a certain amount of stability augmentation to bare-airframe models in the conceptual design phase is important because of the inherent instability of the models. There are two main requirements to implement a control law for handling qualities models used for conceptual design: 1) the control law architecture needs to be generic enough to be used for a variety of vehicle configurations and sizes with different stability and control characteristics, and 2) the process of gain selection should meet a form of stability or handling qualities target criteria.

[1] Science and Technology Corporation, 21 Enterprise Parkway, Suite 150, Hampton, VA 23666.
[2] NASA Ames Research Center, Moffett Field, CA 94035-1000.

Figure 5.2 depicts a simple approach based on model-following control-law architecture used in conjunction with the root locus control-feedback gain selection algorithm.

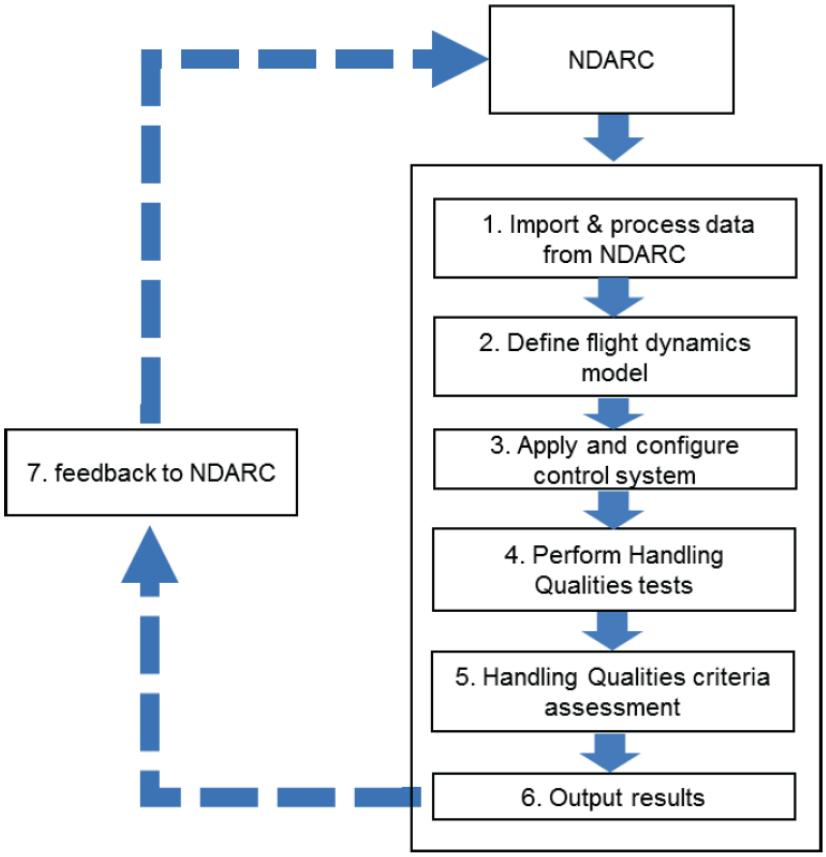

Figure 5.1. Proposed methodology for incorporating handling qualities into an NDARC-based conceptual design process (Fig. 1 of Lawrence [2014]).

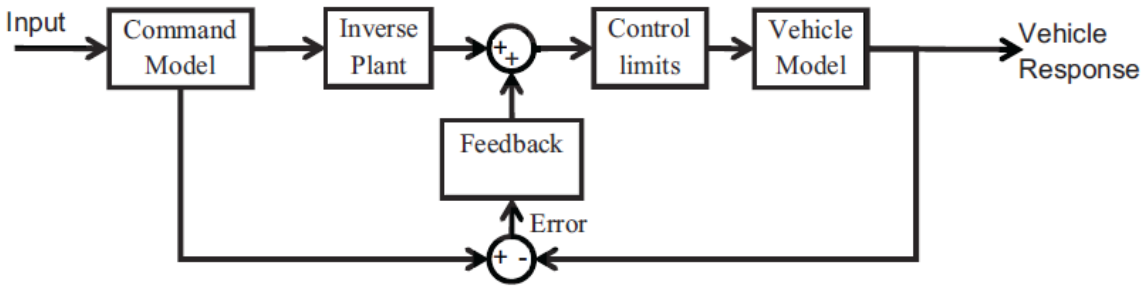

Figure 5.2. Model-following control-law architecture (Fig. 3 of Lawrence [2014]).

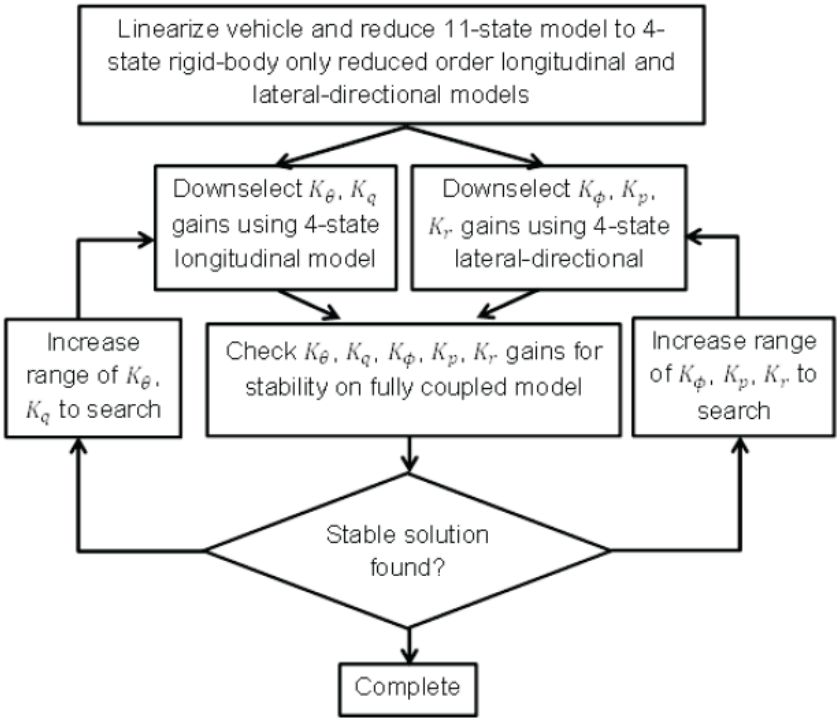

Figure 5.3. Flowchart depicting the feedback gain selection process (Fig. 4 of Lawrence [2014]).

Figure 5.3 illustrates the process of selecting feedback gain employed in this preliminary framework analysis. This approach of selecting gains is based on root locus design methodology. The second stage in the flowchart uses predetermined arrays of gains to calculate eigenvalues for the reduced-order closed-loop systems for combinations of gains. Eigenvalues chosen for gain sets met the following criteria: 1) contain no unstable modes, 2) be of any oscillatory modes above a certain frequency (very low frequency modes were ignored), and 3) be within a certain percentage of a target damping ratio, which in the study had a value of 0.707 [Lawrence, 2014].

A handling qualities assessment was completed after the vehicle model was generated, and the control system defined and configured. Through this, the study concluded that current Aeronautical Design Standard-33 (ADS-33) handling qualities boundaries may not be applicable to flight dynamics models that are currently derived from conceptual design data. Changes to boundaries were proposed to compensate for simplifications made on modeling, increased fidelity, and representation of higher fidelity effects by using equivalent delays.

With the preliminary conceptual design framework proposed and verified, more studies were conducted on implementing this framework to a more comprehensive toolset. This toolset, Simplified Flight Dynamics for Conceptual Design (SIMPLI-FLYD), is a collaborative NASA and U.S. Army development that uses tools including NDARC, MATLAB/Simulink©, Control Designer's Unified Interface (CONDUIT), and X-Plane. SIMPLI-FLYD is used to model and analyze rotorcraft configurations, set up stability and control augmentation systems, and incorporate the combined flight dynamics and control models in X-Plane simulation. Thus, SIMPLI-FLYD can be used for pilot-in-the-loop, real-time simulations of conceptual designs.

The SIMPLI-FLYD architecture for integrating stability and control analysis into the conceptual design stage is shown in Figure 5.4. In the future context of incorporating handling qualities into the conceptual design stage, the process might also include a variety of other analyses in a multidisciplinary design and optimization (MDAO) environment to assess and make changes to the design. The main outputs of the conceptual stage will be stability and control handling qualities parameters, and a compatible X-Plane real-time simulation model vehicle.

A goal of the development of SIMPLI-FLYD is to be able to model arbitrary rotorcraft configurations with different combinations of aircraft components (e.g., rotors, wings, aerodynamic surfaces, fuselage, and auxiliary propulsion). Figure 5.5 is a schematic illustrating how the flight dynamic models are created. Geometric, aerodynamic, and configuration data about the vehicle, and a sweep of trim flight conditions data from NDARC are imported. These imported data are processed with user input to configure the number of model states and controls, and the types of aircraft components. The flight dynamic calculations then use these processed data to calculate linear stability and control derivatives for each component. The total vehicle linear models are then computed through summation of state-space matrix terms from various components. Simplifications are imposed on specified analysis point models to reduce the complexity of the initial implementation of the control law gain optimization performed with CONDUIT. These simplifications mainly consist of the decoupling of the off-axis responses and an order-reduction retaining only the 6-degrees-of-freedon (6-DoF) attitude dynamics.

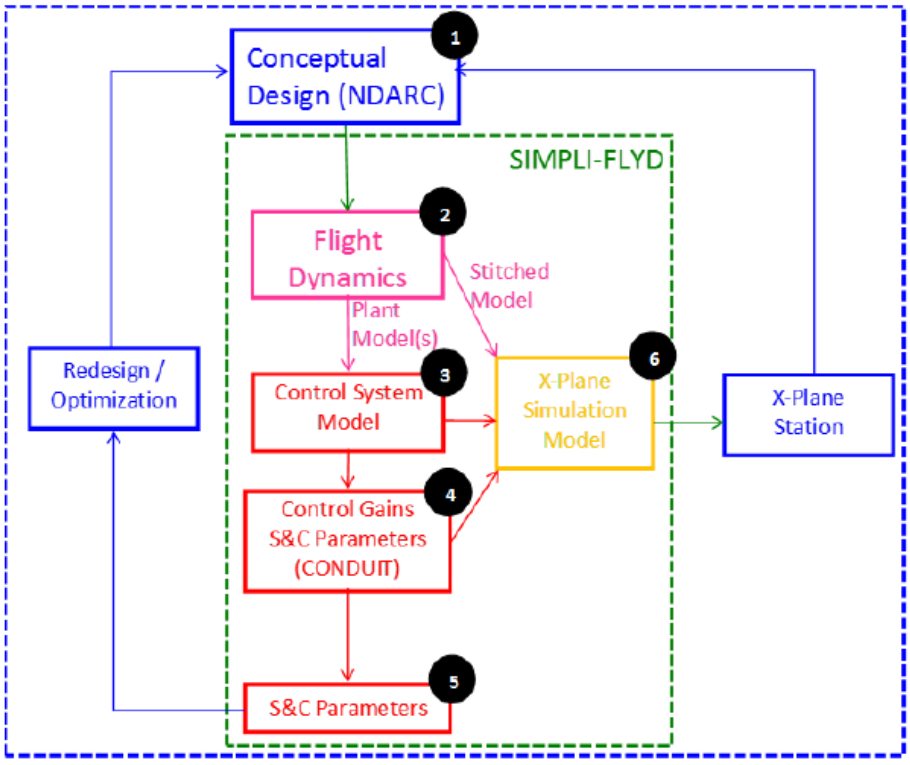

Figure 5.4. SIMPLI-FLYD architecture consisting of stability and control analysis within the conceptual design stage (Fig. 1 of Lawrence et al. [2016]).

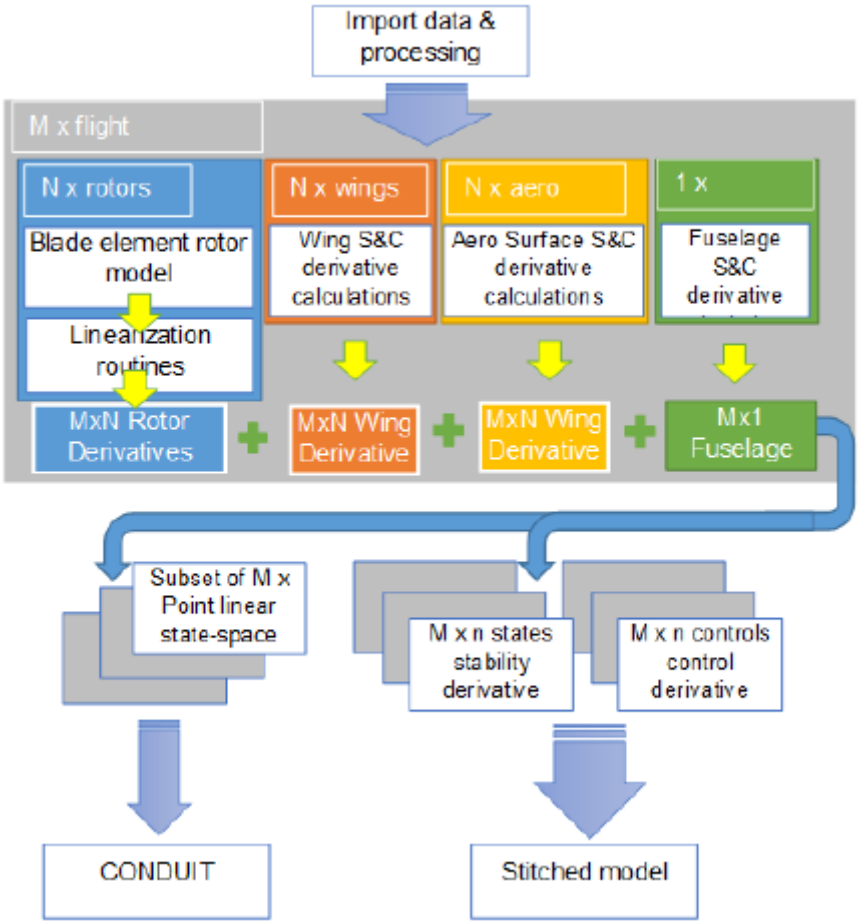

Figure 5.5. Schematic showing creation of flight dynamic models (Fig. 2 of Lawrence et al. [2016]).

An added feature of the SIMPLI-FLYD toolset is the ability to facilitate piloted real-time simulation of the vehicle. This is done through the X-Plane real-time simulation shown in Figure 5.6, which consists of the MATLAB/Simulink-based "stitched model" or Linear Parameter Varying (LPV) model, and a control system that involves gain-scheduled versions of the control laws that were optimized in the CONDUIT analysis stage. The objective of this simulation is to add an intuition of how flight dynamics and control characteristics behave when flown pilot-in-the-loop. Although this simulation is not meant for rigorous handling qualities analysis, it provides an opportunity to inspect design tradeoffs in flight dynamics characteristics when used in operational scenarios.

NDARC was subsequently used to generate flight dynamics models for handling qualities analysis. Through the study, and by using a robust handling-qualities-centric control law optimization procedure formulated in CONDUIT, the NDARC output data was verified to provide adequate information to define a basic rotorcraft flight dynamics model; the model may, however, need a definition of vehicle moment of inertia characteristics if this was not defined by NDARC [Lawrence et al., 2016].

Figure 5.6. X-Plane fixed-base simulator station (Fig. 19 of Lawrence et al. [2016]).

VEHICLE MODELING

Linear Parameter Varying (LPV) methods are a class of nonlinear systems that can be modeled as parameterized linear systems whose parameters change with their state. In the context of aircraft vehicle modeling, LPV methods consist of numerical interpolation methods where multiple linear state-space models are "stitched" together through their component trim states, and stability and control derivatives, which are lookup-table functions of flight condition and configuration. The LPV modeling approach can reproduce trim characteristics such as input gradients and attitude changes in the flight envelope. Moreover, this modeling approach can act as the datum point from which perturbation linear dynamics are referenced, and it avoids some of the complexities and computational demands involved in nonlinear real-time models. Parametrization of the nonlinear dynamics into the LPV form also facilitates the design of gain-scheduled linear controllers over a wide performance envelope. For these reasons, the technique has been widely used in flight dynamics and control research over the last decade. The quasi-Linear Parameter Varying (qLPV) model is a variation of LPV where the "quasi" term refers to the system having the possibility of not being strictly linear [Lawrence, 2010].

Research in developing mathematical models for rotorcraft-load combinations during maneuvers was also conducted. Sridharan and Celi [2013] developed a mathematical model of a helicopter towing a fully submerged body, which was fitted with pitching hydrofoils to maintain a user-specified depth in water. Vertical offset of the cable attachment point on the load, tail fin placement, and main fin area were key parameters that influenced cable forces. The impact of pitching fins for steady forward and turning flight was also studied; collective pitch achieved depth control in forward and turning flight. The speed and turn rate range, correlated to depth control, decreased as separation increased between the target and the trim depth of the passive load. A flight maneuver that was shaped like a "teardrop" was considered; this maneuver allowed the swashplate and tail rotor control inputs to be obtained.

FLIGHT CONTROL DESIGN

Flight control design for rotorcraft comes with challenges because of cross-coupling effects, higher-order dynamics, and the inherent instability of flight dynamics. Flying a rotorcraft

involves multiple state information sources, hence flight control techniques were developed to address this.

The LPV control technique is a reliable alternative to the standard gain-scheduling technique for multivariable systems. Gain scheduling involves designing controllers for dynamic systems over a wide performance envelope. In this sense, gain scheduling obtains a global controller based on interpolation of a family of locally linearized controllers. However, the gain-scheduling technique only guarantees stability or performance at the design points. The LPV control technique is advantageous because it offers the same benefits as the gain-scheduling technique while also ensuring local stability and performance.

Hess [2010a, 2011a] applied the pseudosliding mode control (pseudo-SMC) technique to design a multi-axis flight control system for a UH-60A in a hover flight condition. Rotor dynamics that were not modeled were successfully grouped together with actuator dynamics as "parasitic" elements in the sliding mode approach. The "pseudo" indicates that the actual SMC will eventually be replaced by designs with control boundary layers, thus eliminating switching behavior. In general, SMC was stable and had a robust performance. A design step methodology, which was similar to that used in fixed-wing and ducted-fan unmanned aerial vehicles, was implemented for designing this rotorcraft control. Simulation experiments confirmed that this approach was robust despite significant variations in control system, vehicle, and sensors. Even so, the control system was sensitive to sensor noise, and the performance was dependent on actuator characteristics such as rate limits.

ACTIVE ROTOR CONTROL

Many flight-controller designs for helicopters present a challenge in achieving a suitable controller bandwidth while maintaining rotor stability, rotor vibratory loads, and the like. Traditional swashplate controls (i.e., collective, longitudinal cyclic, and lateral cyclic) provide a limited number of controls to address flight and rotor control issues. Active rotor control, such as individual blade control (IBC) and on-blade control (OBC) concepts, allows more room in the control design space to address flight and rotor control issues by adjusting control input signals to desired blade responses. Developments in active rotor control offer many potential benefits; innovative controllers can be developed to lessen the compressibility effects and reverse flow effects on blades, transient effects with rotor speed variation, coupling between body and rotor in large-sized helicopters, etc. Despite these potential benefits, the impact of implementing active rotor control concepts needs to be considered before these concepts can be fully implemented. Areas of development include cost reduction of implementation, improved reliability and ease of manufacture of active control devices, and elimination of safety concerns about the use of active rotor controls.

Modeling

The process for obtaining Linear Time Invariant (LTI) models of nonlinear systems about a period equilibrium by using the harmonic domain representation of Linear Time Periodic (LTP) model states is well established. Such LTI models can be used as a basis of handling qualities analysis or evaluation for small amplitude maneuvers. These models include the required

coupling between rotor and body dynamic interactions in controller development. Therefore, these models can be used to develop integrated controllers to simultaneously address rotor control and flight control while exploring the effects of IBC and OBC concepts.

Prasad et al. [2009] developed a computationally efficient method for deriving the LTI model. This was done by simultaneously extracting the LTP model from a nonlinear model about a specific equilibrium condition using perturbation methods, and using harmonic decomposition on the LTP model to arrive at the LTI model of a specified order. The method was tested on a helicopter model and verified with response comparisons in both time and frequency domains.

On-Blade Control

This development in a computationally efficient method for extracting LTI models from nonlinear models was applied to OBC concepts. Olcer et al. [2010] developed an artificial Neural Network (NNET) from computational fluid dynamics (CFD) for an approach to reduced-order modeling of the aerodynamic effects of an on-blade trailing-edge flap (TEF) actuator. TEFs typically require high-fidelity aerodynamic analysis (e.g., changes in angle of attack, TEF deflection, and deflection rates), which are usually acquired by coupling CFD methods. However, this is a computationally expensive approach that might pose difficulties in controller development and handling qualities assessment. The method requires three steps: 1) creating a CFD database for a chosen OBC concept, 2) training the NNET, in addition to the existing baseline air loads model, to achieve the required level of fidelity for the CFD database, and 3) integrating the developed NNET of the chosen OBC concept into a nonlinear helicopter model. In the study, the fidelity of the extracted LTI models was validated by comparing with FLIGHTLAB results (Fig. 5.7). The computed error index of 0.0135 shown in Figure 5.7 showed good fidelity of the extracted LTI model, and the feasibility of using the model in integrated flight control and rotor control studies. Future steps for this study involve applying the reduced-order modeling approach to other types of on-blade actuation (e.g., leading edge slats, micro trailing-edge flaps, etc.).

Individual Blade Control (IBC)

Theodore and Tischler [2010] developed a rotor trim controller for a test in the National Full-Scale Aerodynamic Complex (NFAC) 40- by 80-Foot Wind Tunnel to evaluate the impact of IBC on the performance, vibration, noise, and loads of a UH-60A rotor. Figure 5.8 depicts a simplified representation of three different controls for the rotor blade pitch angles: the “Manual Trim Inputs” block refers to the rotor operator inputs through the primary control console; the “Rotor Trim Controller” block refers to the trim control commands through the dynamic control console; and “IBC Actuator Commands” control pitch angle perturbations in the rotating frame to the individual blades. This trim control system was developed specifically for use during the IBC wind tunnel test, and enabled ease of setting and repeating the rotor trim states compared to the rotor operator setting the trim condition manually. Moreover, the developed trim control system was able to maintain desired trim condition, despite changes in IBC actuation in open- and closed-loop IBC modes and long-period transients in wind tunnel flow. Figure 5.9 shows that without trim control (fixed swashplate), the rotor hub forces and moments experience large variations over the range of IBC phase. With trim control, the forces and moments are

maintained at the target values. The capabilities of the developed trim control system allowed for ease of testing different IBC inputs without requiring the rotor operator to re-trim the rotor.

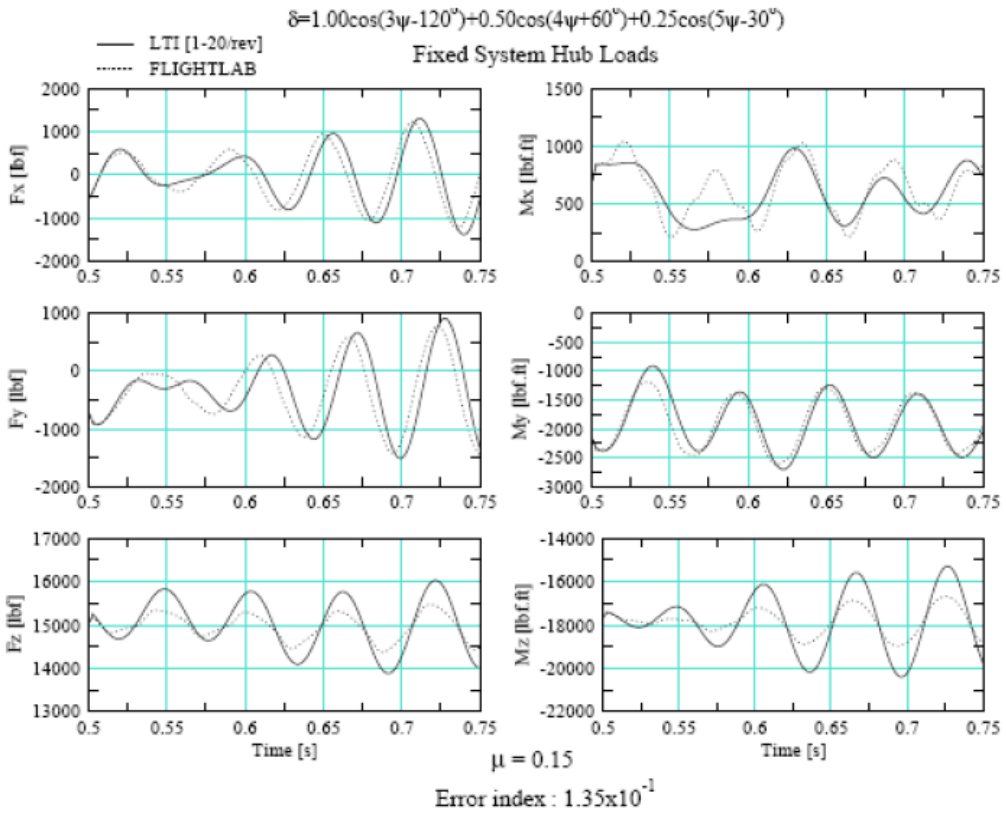

Figure 5.7. Predicted fixed system hub load variations to combination of 3, 4, and 5/rev TEF input (Fig. 6b of Olcer et al. [2010]).

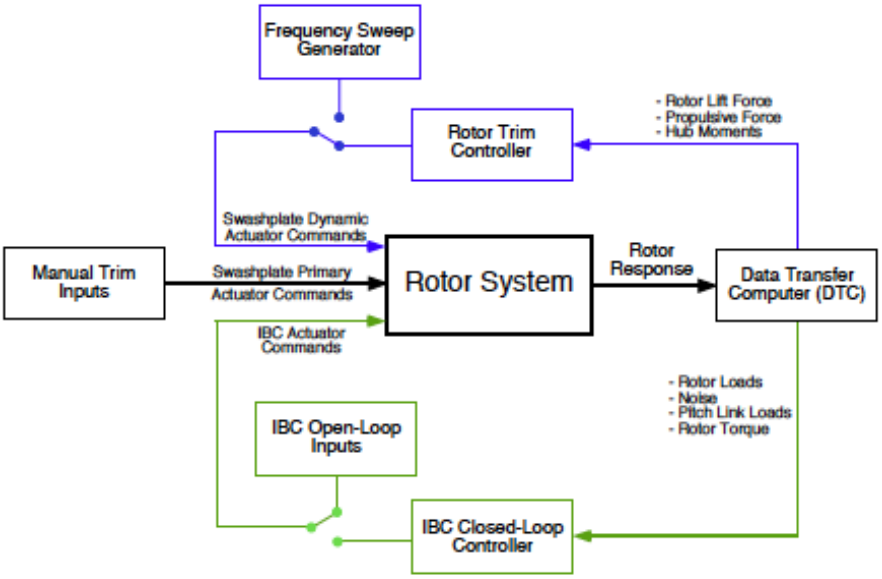

Figure 5.8. Simplified block diagram of three rotor-blade-pitch-control systems (Fig. 4 of Theodore and Tischler [2010]).

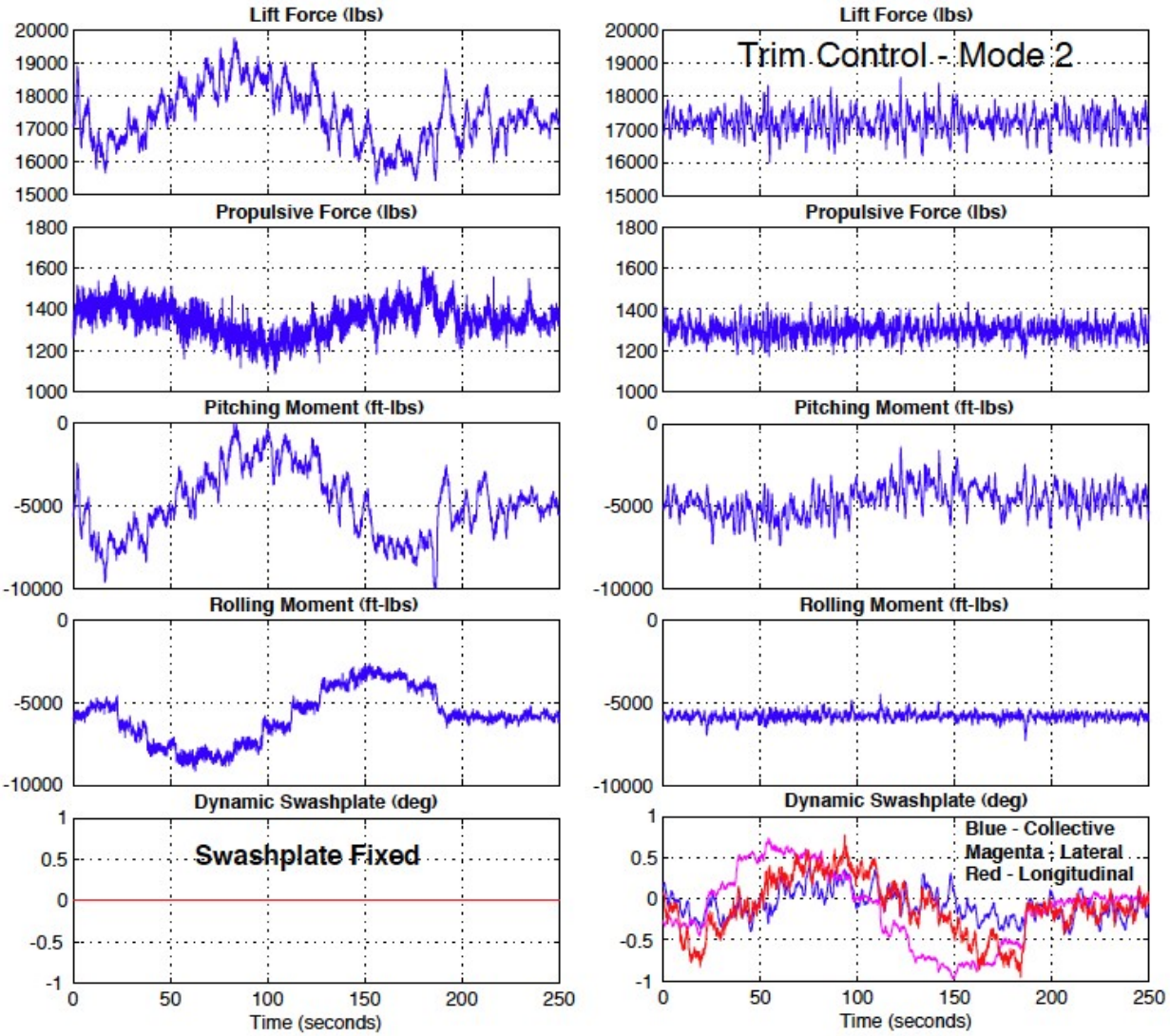

Figure 5.9. Time histories during 2/rev (1° amplitude) IBC phase sweeps with no trim control (left) and trim control active in mode 2 (right). Advance ratio = 0.35, CL/σ = 0.077 (Fig. 14 of Theodore and Tischler [2010]).

Continuous Trailing-Edge Flaps

Thornburgh et al. [2014] studied the use of continuous trailing-edge flaps (CTEFs) for primary flight control of a helicopter main rotor. The CTEF design involves embedded active materials in the airfoil section to change the trailing-edge section to influence effects in lift and pitching moments. In this way, the CTEF approach does not involve mechanical linkages and flap hinges in the rotating system, which minimizes drag and allows sufficient control authority. Their study made use of an optimized bimorph design with Macro-Fiber Composite actuators, a coupled structure, and CFD analysis to study the behavior of an airfoil with CTEFs. Furthermore, the effect of blade root pitch index (RPI) on CTEF control authority was also examined. The results from this study determined that using CTEFs for flight control was promising; however, a more

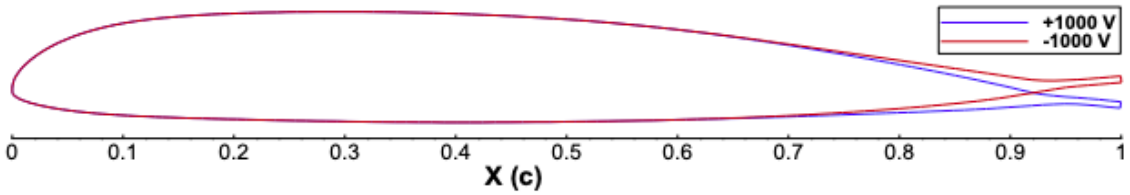

Figure 5.10. Deformed airfoil shape of the developed CTEF design at Mach 0.65 (Fig. 2 of Thornburgh et al. [2014]).

suitable option would possibly be to use blade RPI control instead of, or in addition to, collective CTEF control for primary flight control. Figure 5.10 shows the airfoil with the CTEF deflected in two different positions: downward deflection at +1,000 V = –0.135 inch, and upward deflection at –1,000 V = 0.0996 inch.

LARGE ROTORCRAFT

Large, heavy lift rotorcraft have shown promise in becoming the future vertical lift civil transport vehicles. Large advanced tiltrotors, in particular, have consistently shown better performance than other rotorcraft configurations in meeting the proposed civil mission of operating short-haul regional routes that involve carrying approximately 90 passengers over a range of at least 1,000 nautical miles at a cruise speed of 300 knots.

There has been significant research at NASA in this area to further understand and investigate large rotorcraft. Development of large rotorcraft comes with unique challenges because of the complexities and instabilities inherent in the flight vehicle, such as larger mass and inertias resulting in low-bandwidth response and larger distance from center of mass to the cockpit. There are also challenges in the operational environment because large rotorcraft often have poor visibility at low altitudes. As new technologies, including vehicle design and operation trends, emerge, the need for the flight dynamics and control discipline, and the respective tools, techniques, and technologies to advance as well, becomes more apparent.

There are two main focuses of rotorcraft research at NASA related to large rotorcraft: 1) to develop a sustaining vision for vertical lift vehicles, specifically for use in future passenger transportation, and 2) to improve the performance, efficiency, safety, noise, and emissions of current rotary wing vehicles. Hence, NASA has focused on investigating the flight control and handling qualities challenges of large rotary wing vehicles and the effect of control system augmentation on handling qualities for current civilian helicopters to improve vehicle safety. A comprehensive overview can be found in Malpica et al. [2015].

NASA has chosen the Large Civil Tiltrotor (LCTR) concept design as having the most potential in meeting technology goals that are related to a civil mission of operating short-haul regional routes, and in impacting the air transportation system [Theodore et al., 2014a]. Moreover, having a vertical lift aircraft at one or both ends of a 300- to 600-nautical-mile mission increases airport capacity.

The second generation of the Large Civil Tiltrotor (LCTR2) was designed to be equivalent in size to regional jets and turboprops. The LCTR2 can carry approximated 90 passengers, at a cruise speed of 300 knots over a range of at least 1,000 nautical miles. This configuration weighs close to 100,000 pounds with a 107-foot wingspan and has two tilting nacelles with 65-foot-diameter rotors, as shown in Figure 5.11.

A series of experiments were conducted at the Vertical Motion Simulator (VMS) at NASA Ames Research Center to study the impact of vehicle size on flight control requirements and pilot handling qualities. The long distance from the center of mass to the cockpit produced a pitch and heave motion at the cockpit from attitude changes, and abrupt side-force from yaw. For high-bandwidth control system configurations there were also undesirable impulsive load factors at the pilot station, and an unpredictable aircraft response as a result of large pilot offsets from the center of mass. Furthermore, proprioceptive and visual cueing at such large offsets were compromised because of the coupling of pitch and heave motions of the cockpit.

Initial research on the hover flight dynamics, control, and handling qualities characteristics for large civil transport rotorcraft configurations used single-point stability derivative state-space models, which were generated using CAMRAD II (Comprehensive Analytical Model of Rotorcraft Aeromechanics and Dynamics), an established comprehensive analysis described in Johnson [1994]. This linear model was then reduced in order, the longitudinal and lateral dynamics decoupled, and then augmented with a model-following control system.

The qLPV modeling approach was chosen to expand on the baseline models for larger rotorcraft because the approach provides a wider flight envelope (up to 60 knots for hover and low-speed flight, and nacelle angles between 60 and 95 degrees) to fully represent the dynamics (including full inter-axes coupling) in the ADS-33 handling qualities maneuvers. Moreover, the qLPV approach also provides nacelle tilt degree of freedom. Thus, the nacelles can be used in a closed-loop controller. This property was utilized in conjunction with lateral cyclic inputs to achieve Translational Rate Control (TRC) in the longitudinal and lateral axes with minimal attitude changes [Lawrence, 2010]. Figure 5.12 shows the LCTR2 qLPV model system architecture.

Multiple studies were done with the qLPV modeling approach successfully integrated into the NASA VMS, with several inceptor configurations implemented, to determine resulting flight dynamics and handling qualities of large rotorcraft with specified control laws implemented.

Figure 5.13 shows the qLPV model integrated into the model-following structure for longitudinal TRC. This control system architecture involves two functions: a feedback path for the desired and measured response, and a command and inverse plant model that is used to translate stick inputs to idealized responses for swashplate control. In this configuration, the swashplate actuators were modeled to have rate limiting, while the nacelle actuators were modeled as second-order systems with angular and rate limiting. The nacelle actuator natural frequency was selected to be high (8 rad/s) to ensure sufficient control bandwidth. The objective of this approach was to illustrate the art of the possible, assuming the actuators could respond with required bandwidth. An engineering analysis to assess whether these requirements could realistically be met was not conducted, however.

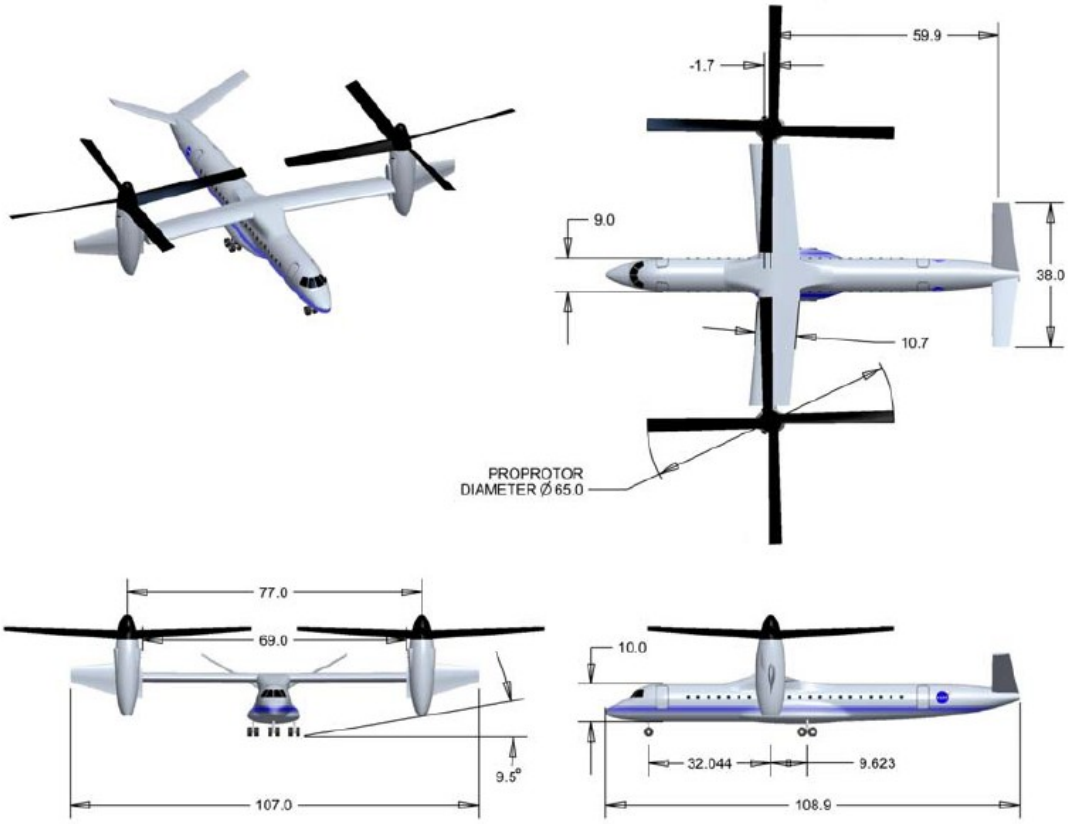

Figure 5.11. The NASA LCTR2 (dimensions are in feet) [Lawrence, 2010].

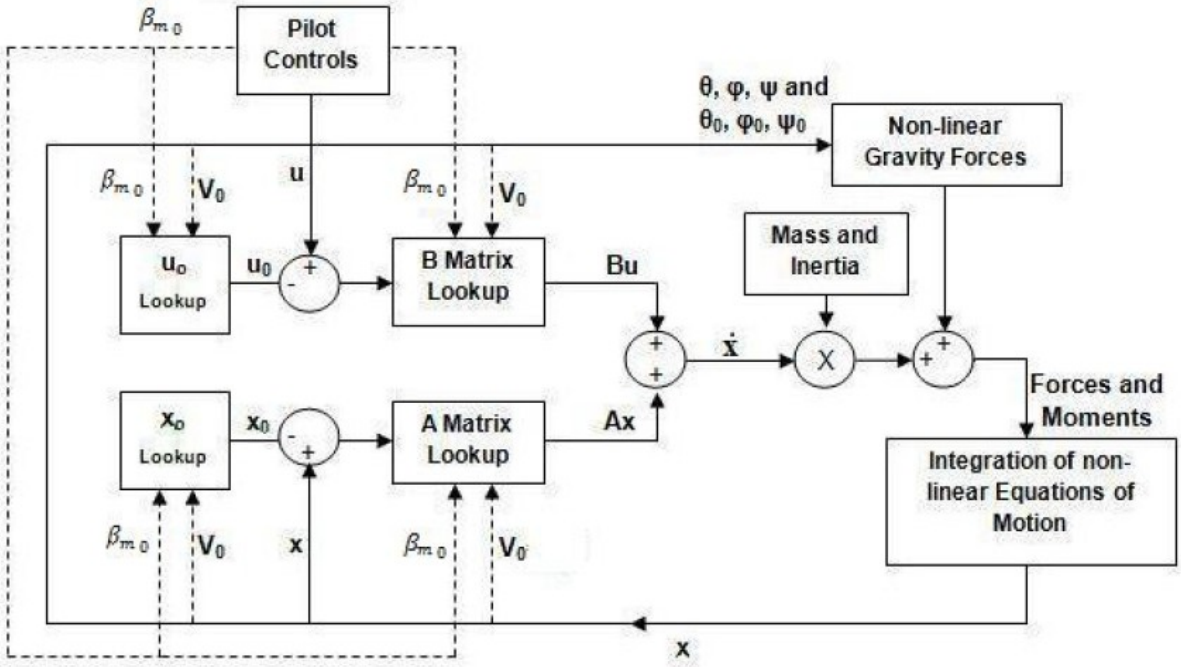

Figure 5.12. LCTR2 qLPV model system architecture (Fig. 2 of Lawrence et al. [2010]).

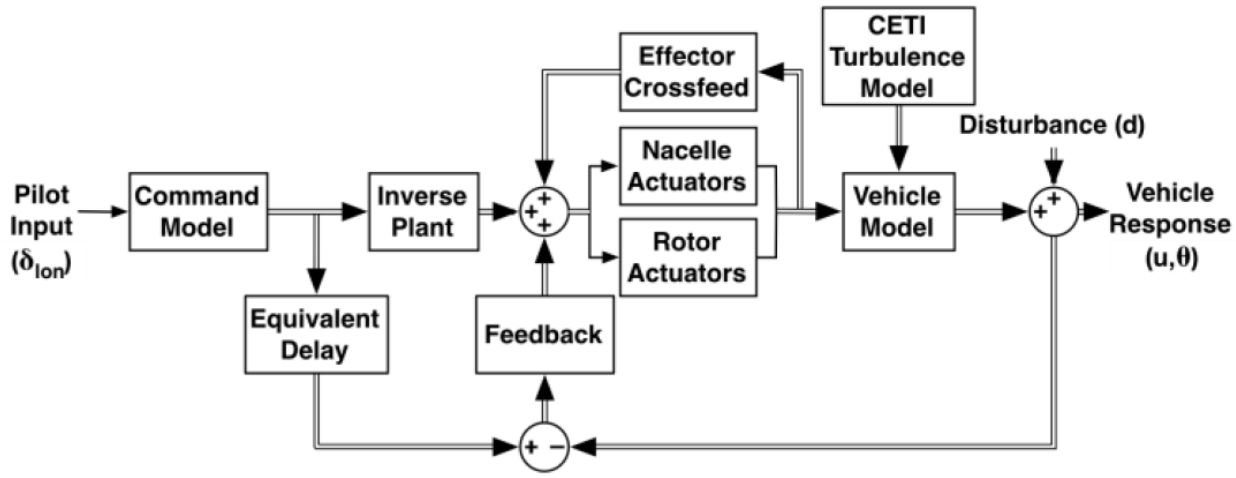

Figure 5.13. Model-following architecture for longitudinal TRC (Fig. 1 of Malpica et al. [2012]).

PILOT-VEHICLE INTERFACE

Active Inceptors

There is an increasing interest in providing better haptic cueing or force-feel system characteristics to rotorcraft pilots. In the past, the force-feel system characteristics of the control inceptors of most helicopters were determined by the mechanical component's characteristics in the control system (e.g., mass, spring, friction, dampener). Now, with the advent of fly-by-wire control systems and active inceptors, the force-feel characteristics are programmable based on the closed-loop response of the active inceptor. Equivalent inertia, force/displacement gradient, damping, breakout force, and detent shape are all configurable parameters in the inceptor control laws. This opens a new design space to explore.

Studies have been conducted to determine the impact of active inceptor force-feel characteristics on handling qualities. Through this effort, low damping of the inceptor was shown to possibly degrade handling qualities, and pilots have expressed dislike of the low damping, low natural frequency of the inceptor for the Hover Mission Task Element (MTE). Furthermore, the theoretical handling qualities level boundaries were shown to be inappropriate for the Hover MTE.

Lusardi et al. [2012] confirmed that cyclic force-feel characteristics have a significant impact on rotorcraft handling qualities. High-precision tasks such as Hover MTE were preferred to be performed with Attitude Command over Rate Command in good visual environment with a center stick. The pilot's perception of the aircraft ride quality was also impacted by the damping of the center stick cyclic inceptor. The current ADS-33 Level 1 bandwidth requirements from force inputs were not enough to ensure Level 1 handling qualities. Hence, bandwidth requirements should be revisited, considering force as an input. Malpica and Lusardi [2013]

confirmed that theoretical handling qualities boundaries were not appropriate for Hover MTE where vestibular cueing was significant. Low damping of the inceptor was also potentially linked to handling qualities degradation.

Rotational Throttle Interface

The development of tiltrotors has motivated development of control interfaces that are better suited to all reconfiguration phases. Comparison studies were conducted to assess the performance of the conventional Thrust Control Lever (TCL)—see Figure 5.14—and the Rotational Throttle Interface (RTI) in the NASA Ames Vertical Motion Simulator (VMS). Figure 5.15 shows the TCL in one of the cabs of the VMS. The RTI was developed with the intention of increasing pilot awareness of the vehicle's configuration state, particularly the nacelle angle. In this regard, the RTI was designed to adjust its orientation based on the angle of the tiltrotor's nacelles. Studies have found three predominant effects about the RTI: 1) an unanticipated binding of the RTI system on the throttle axis, which makes it difficult to precisely control the throttle and make fine power adjustments along the throttle axis; 2) confusion about which way to move the RTI during transition modes; and 3) difficulty in distinguishing small angle differences during RTI transitions, which makes determining the exact nacelle position difficult. Still, despite these reported effects, the development of the RTI remains crucial to developing a suitable inceptor that maps nacelle position congruently without requiring the pilot to remove his/her hand [Rozovski and Theodore, 2011].

Figure 5.14. NASA Ames Thrust Control Lever (TCL) (Fig. 5 of Rozovski and Theodore [2011]).

Figure 5.15. NASA Ames VMS Transport Cab with TCL (Fig. 7 of Rozovski and Theodore [2011]).

Control Augmentation for Degraded Visual Environments

The impact of control system augmentation on handling qualities was also studied in Good Visual Environment (GVE) and Degraded Visual Environment (DVE). Poor handling qualities were attributed to poor pilot situational awareness, and spatial disorientation. Research in this area has focused on three aspects: 1) improving sensors for detecting the surrounding environment of the rotorcraft in DVE conditions; 2) improving visual aids (e.g., heads-up and heads-down displays); and 3) improving flight controls through advanced control modes. Four control system concepts were studied with an OH-58D vehicle model and control systems such as the Rate Command (RC) system, short-term Attitude Command/Attitude Hold (st-ACAH), Modernized Control Laws (MCLAWS), and Modernized Control Laws with Position Hold (MCLAWS + PH). Results from the study have shown that the Handling Qualities Ratings (HQRs) for Hover MTE were consistent with those from the OH-58D flight test for RC and st-ACAH control systems. The st-ACAH control system was shown to improve handling qualities for all the examined MTEs, particularly those with a high task bandwidth (ADS-33 Hover MTE). The MCLAWS with an Attitude Command/Attitude Hold (ACAH) response type produced Level 1 handling qualities for all MEs examined in GVE, and borderline Level 1 handling qualities for MTEs in DVE. Adding Position Hold to the MCLAWS only slightly improved the average HQR. It was also noted that a 10-percent-authority Stability Control Augmentation System (SCAS) was enough to achieve an ACAH response type with MCLAWS control system up to a transition speed of 40 knots. The Emergency Medical Services (EMS) approach MTE had similar handling qualities results as the Hover MTE and improved with increased augmentation, with borderline Level 1 handling qualities achieved with MCLAWS in DVE. Saturation of the partial authority actuators did not contribute to the resulting handling qualities for this study. The study confirmed that in night vision goggles (NVGs), flight time and proficiency were significant because NVGs were not adequate to improve handling qualities without good training [Theodore et al., 2014a, 2014b]. Figure 5.16 shows the helmet-mounted NVG.

Figure 5.16. Night vision goggles (NVGs) mounted to pilot's helmet (Fig. 9 of Theodore et al. [2014b]).

HANDLING QUALITIES REQUIREMENTS

The ADS-33 Handling Qualities Requirements for Military Rotorcraft specification provides a framework that can be used to precisely quantify handling qualities and provide guidelines for good design. Quantitative requirements, which are significant as a guide, are minimum values of metrics that are correlated with response to piloted stick inputs. These include bandwidth and phase delay, short-term response damping, and attitude quickness. SAE AS94900 presents industry "best practice" technical concepts and approaches for the general performance, design, development, and quality assurance requirements for the flight control-related functions of the Vehicle Management System (VMS). It is also applicable to military rotorcraft, and supersedes or incorporates parts of various standards including MIL-F-9490D, MIL-F-83300, and even ADS-33. While these standards are not required by civil airworthiness certification authorities, they encompass fundamental guidelines to rotorcraft flight control design, and the development of advanced rotorcraft technologies and larger configurations require the standards to be updated. This is the focus of the studies that are discussed in this section.

Stability Margins for Large Rotorcraft

Blanken and Decker [2009] evaluated four aircraft configurations: a utility-class helicopter, a medium-lift helicopter with and without an external slung load, and an LCTR through simulation and experimental testing (see Fig. 5.17). It was concluded that higher disturbance rejection bandwidth (DRB) and lower phase margins were more suitable for larger aircraft. Low-phase-margin cases (i.e., 20–23 degrees) were rated as pilot-induced-oscillation (PIO) prone, led to

Aircraft	Weight (lbs)	Rotor Diameter (ft)
H-60	16,000	53.6
H-53	46,000	79
H-53 with slung load	46,000+29,500 (ext load)	79
LCTR	120,000	65 (x2)

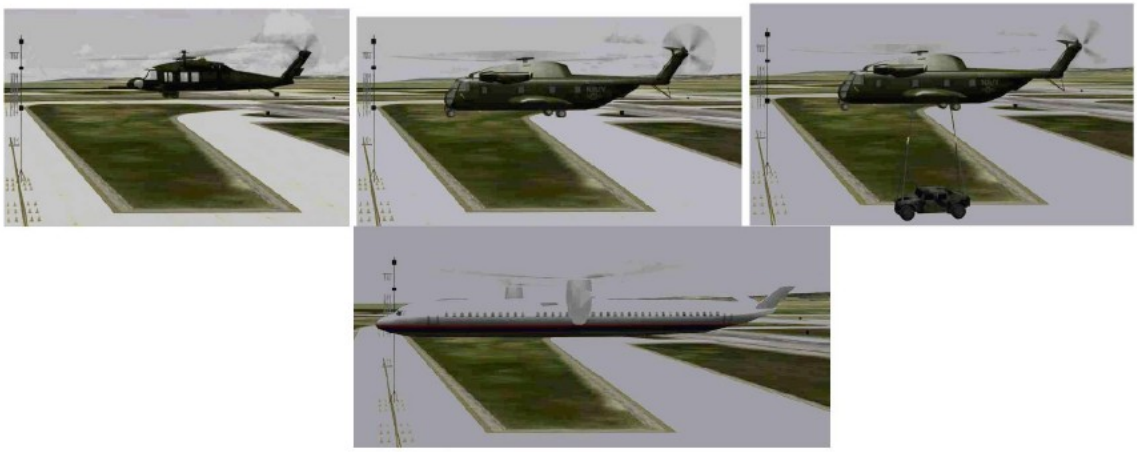

Figure 5.17. Characteristics of the four aircraft tested (Table 1 and Fig. 7 of Blanken et al. [2009]).

objectionable oscillations, resulted in low disturbance-response damping ratios, and had an indication of an incipient handling qualities cliff. The study also noted that pilot comments on the disturbance response of the aircraft aligned with the DRB guidelines in the ADS-33 Test Guide, and that the ADS-33 midterm-response-to-control damping ratio metrics can be applied to the disturbance-response damping ratio. For the utility-class helicopter, disturbance-response damping ratios less than 0.2 with low-phase-margin cases resulted in highly objectionable oscillations. For medium-lift helicopters, lateral axis disturbance-response damping ratios below 0.3–0.35 resulted in worse or objectionable oscillations. This study concluded that stability-phase margin requirements for the LCTR, specifically, could be relaxed to a 38-degree phase margin design point. Pilots' preference included a higher DRB/lower stability margin configuration (roughly 30 degrees). At reduced-margin starting points, however, degradations from uncertainty and wear become even more significant and should be avoided.

Hover and Low-Speed Response Types for Large Rotorcraft

Preliminary testing of the LCTR yaw bandwidth indicated that the current Level 1 boundary needs to be relaxed to accommodate a large pilot-offset from the center of mass. Blanken and Decker [2009] also concluded that lateral and longitudinal position tolerances for ADS-33 Hover MTE should be increased to be more suitable for the vehicle size. The Lateral Reposition MTE standards were satisfactory for a vehicle of this size, and hence remained unchanged.

A thorough examination of short-term response requirements for large rotorcraft was conducted by Malpica et al. [2010]. Pilot station location was explicitly evaluated in this study by comparing the handling qualities of rotorcraft with identical dynamics but varying the simulated location of the pilot. Overall, handling qualities were found to be significantly degraded for pilot stations on the order of 30 feet and higher. Low bandwidths resulted in difficulties with control, and slow aircraft response, which lead to excessive pilot workload. The challenges were exacerbated by the increased pilot station offset from the center of mass, with Level 1 handling qualities in pitch and roll not being attainable based on the Hover MTE. An increased likelihood of PIO triggered by actuator rate limiting, and the resulting handling qualities degradation, were observed to impose a fundamental upper bound on acceptable bandwidths for all axes. A broad range of acceptable yaw bandwidths were identified based on a proposed Heading Capture MTE, however. As a side note, it was observed that if the bandwidth requirements were reduced from 2.0–2.5 rad/s, the structural and rotor design requirements should also be alleviated.

Considering the difficulties posed by the geometries of large rotorcraft, the TRC with minimal attitude response was favorably preferred over ACAH response types. The TRC law was developed by using nacelle angle deflections as longitudinal velocity control, and lateral cyclic as lateral control in hover and low-speed maneuvering. With the TRC law, translational maneuvers were possible with minimal pitch and roll attitude responses because attitude control loops were engaged in parallel with the TRC, and trim attitudes were maintained. Moreover, using this TRC law would avoid the large unsatisfactory accelerations resulting from using ACAH.

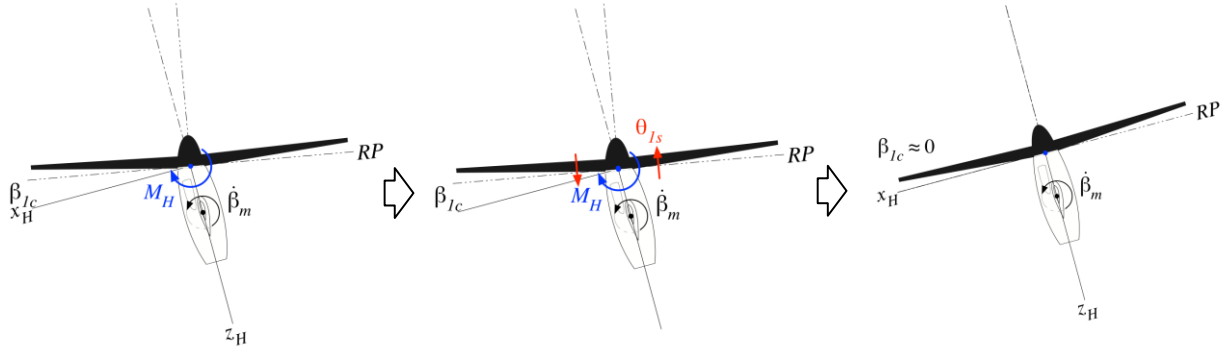

Nacelle rotates and rotor tip-path plane lags behind hub plane.

Crossfeed inputs longitudinal cyclic proportional to nacelle rate.

Tip-path plane maintained close to perpendicular to shaft axis; flap does not lag behind nacelle or induce pitching.

Figure 5.18. Crossfeed mechanism minimizing nacelle-rate-induced flap and pitch (Fig. 86 of Malpica et al. [2015]).

TRC enabled Level 1 handling qualities in Hover and Lateral Reposition MTEs [Lawrence et al., 2011] for the LCTR2 configuration, despite turbulent conditions, by installing necessary nacelle actuator bandwidth and quickening the TRC response through rotor cyclic inputs with a reduced nacelle bandwidth. To guarantee satisfactory performance of the closed-loop control system, the nacelle actuators needed to provide enough response bandwidth (>4 rad/s), or employ a longitudinal cyclic control to augment low-bandwidth nacelle actuation [Malpica et al., 2012]. However, high-bandwidth nacelle actuators introduced the risk of non-minimum phase pitch response from rotor flap-back dynamics. Consequently, this resulted in a pitch that was opposite to what was commanded by the cyclic inceptor input. This also resulted in PIOs and degraded handling qualities. To effectively counteract this, the nacelle conversion rate signal was crossfed to the longitudinal cyclic control. This method is shown in Figure 5.18 and is essentially keeping the rotor disc plane perpendicular to the nacelle/shaft axis [Lawrence et al., 2011]. Minimizing the pitch attitude changes also helped with the undesirable pitch and heave motion, and perception issues. Another issue with using nacelles for longitudinal velocity control occurred when the pilot inputted high Root Mean Square inputs—there was a noticeable rate limiting that increased the effective delay. Hence, the input amplitude was kept low to prevent negative control characteristics. Higher response bandwidth was confirmed to result in negative ride qualities [Malpica et al., 2011; and Theodore et al., 2014a].

Open-Loop Onset Point Criteria

The Open-Loop Onset Point (OLOP) design criteria were not a focus of research but were used consistently throughout the control system design methodology as a means of addressing the PIO likelihood of a design. Category II PIOs are associated with the nonlinear effects of rate and position limiting, which can be very dangerous and have been a factor in most recent PIO-related accidents. With linear analysis methods, the effects of position and rate limiting are ignored. Thus, it is possible to push the linear design of the system beyond the actual capability of the aircraft. The OLOP criteria attempt to predict the onset point of a nonlinearity that may trigger a

subsequent PIO. In practice the OLOP criteria were used to determine the maximum command model bandwidth for RC and ACAH control laws. Therefore, OLOP criteria effectively mark the upper limit on acceptable bandwidths. These criteria were found to agree fairly well with piloted experimental evaluations.

The OLOP design criteria were used to predict the impact of nacelle rate limiting on handling qualities of TRC implementations of the LCTR2. Figure 5.19 shows the impact of pilot input amplitude and crossfeed on the OLOP requirements. The center stick maximum displacement range was ±5 inches, which allowed handling qualities impact on piloted input frequency and amplitude to be examined. Figure 5.20 illustrates the effect of selected nacelle rate limits on the OLOP phase and amplitude requirements, with the assumption of a 1-inch-maximum amplitude control input.

More studies were pursued to determine the feasibility of using additional longitudinal cyclic control to augment low-bandwidth nacelle actuation. Malpica et al. [2012] proposed and validated a frequency-domain handling quality that characterized TRC responses in terms of bandwidth and phase delay. In this study, the longitudinal phase delay indicated that the Level 1 boundary is around 0.4–0.5 seconds.

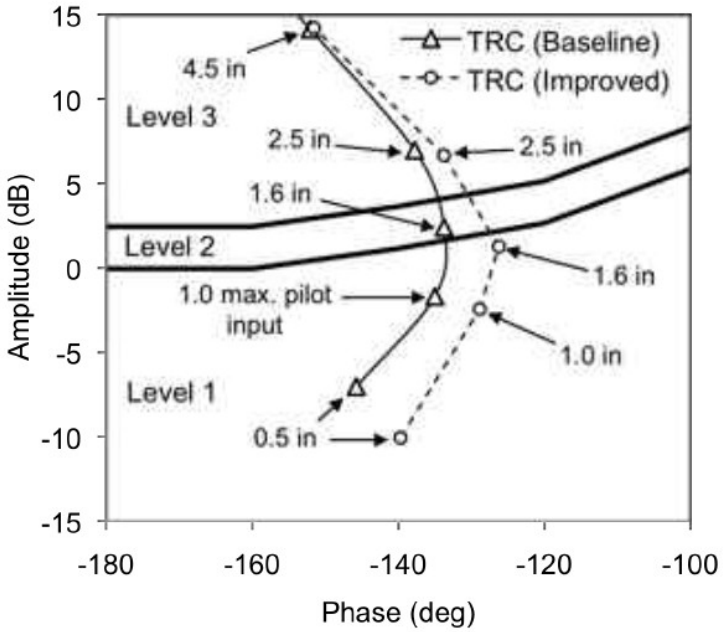

Figure 5.19. OLOP specifications for the baseline and the improved TRC configurations (15 ft/s/in. control sensitivity and ±7.5-deg/s rate limits) (Fig. 5 of Malpica et al. [2011]).

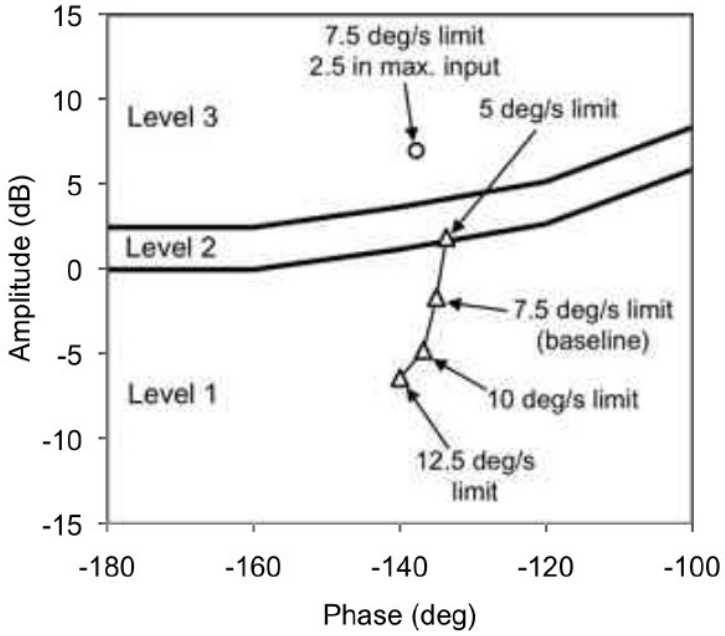

Figure 5.20. OLOP specifications for varying nacelle rate limits (15 ft/s/in. sensitivity, 1.0-in.-max pilot input) (Fig. 6 of Malpica et al. [2011]).

MODELING OF PILOT CONTROL BEHAVIOR

Adaptive and reconfigurable flight control systems have recently been of interest because of the focus of modern rotorcraft technology developments (e.g., on-blade control, in-blade control, variable speed rotor) on minimizing noise and maximizing performance for operation in urban environments. These types of control systems are prevalent in many aircraft control tasks, as pilots need to adapt their control techniques in response to aircraft dynamics that change over time. Examples of adaptive and reconfigurable flight include the manual control of rotorcraft with variable speed rotors, tilt-rotor aircraft during hover and forward flight transitions, and other aircraft with reconfigurable flight control systems. Much of past research was devoted to pilot control behavior and control tasks with constant dynamics. Thus, there has been a focus on understanding the impact of time-varying vehicle dynamics and the pilot's response, developing a model for human pilot adaption, and applying this model to control tasks in which time-varying control system dynamics occur.

Wavelet transforms have been developed and implemented to characterize pilot behavior when time-varying pilot-vehicle system dynamics are present. Wavelet transforms offer an advantage over Fourier transforms, which were traditionally used for estimating frequency response. Wavelet transforms allow transient analysis, whereas Fourier transforms are an average response for a time frame. Figures 5.21 and 5.22 show the difference between the two transforms.

The wavelet-based scalograms were developed using a scalogram filter bank. Wavelet transform scalograms can provide more information than a windowed Fourier transform plot. Transient analysis is enabled by using different frame sizes for the wavelet transform; the windowed Fourier transform is an average response for that frame. The authors illustrate this point using an example of a windowed Fourier transform and wavelet transform of a simple time series input consisting of two sinusoids of equal amplitude and duration. The resulting wavelet scalogram (Fig. 5.23) shows peaks in power and the time the sinusoids occurred. This characteristic makes wavelets a powerful tool in detecting changes in time-varying systems. The results of Figure 5.23 are shown in Figure 5.24 as a two-dimensional plot of power versus frequency—note that the power (area under the curve) at the two frequencies is the same. If the conditions used for estimation are not ideal, a smoothing technique must be used. The variance of the estimate should be determined, with the estimate with the lower variance using a smoothed estimate of the cross-spectral density divided by a smoothed estimate of the input power spectra density.

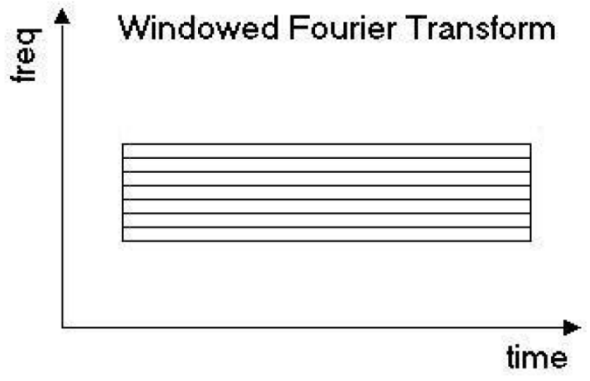

Figure 5.21. Fourier transform: constant time window with frequency (Fig. 1a of Klyde et al. [2010]).

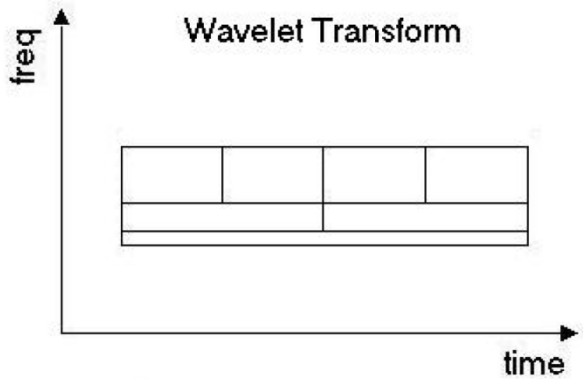

Figure 5.22. Wavelet transform: decreased time window with frequency (Fig. 1b of Klyde et al. [2010]).

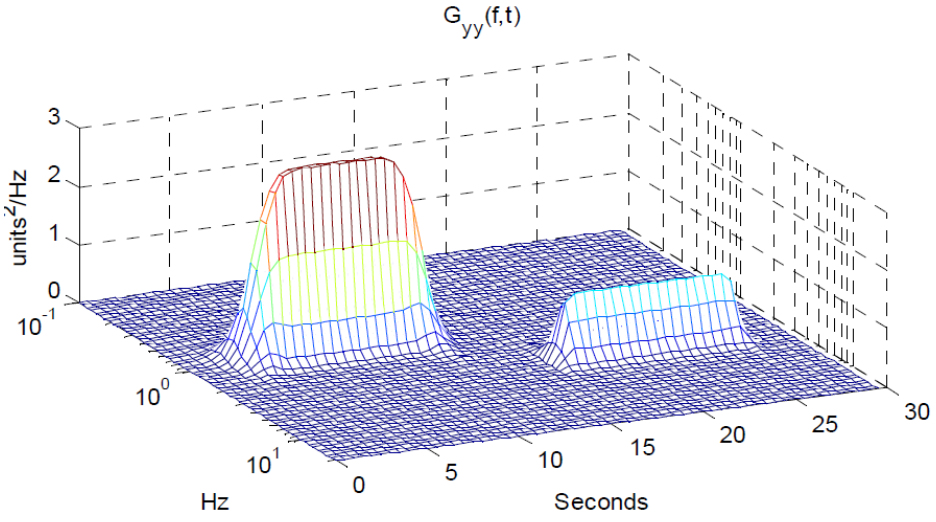

Figure 5.23. Wavelet transform auto-spectrum scalogram (Fig. 3c of Klyde et al. [2010]).

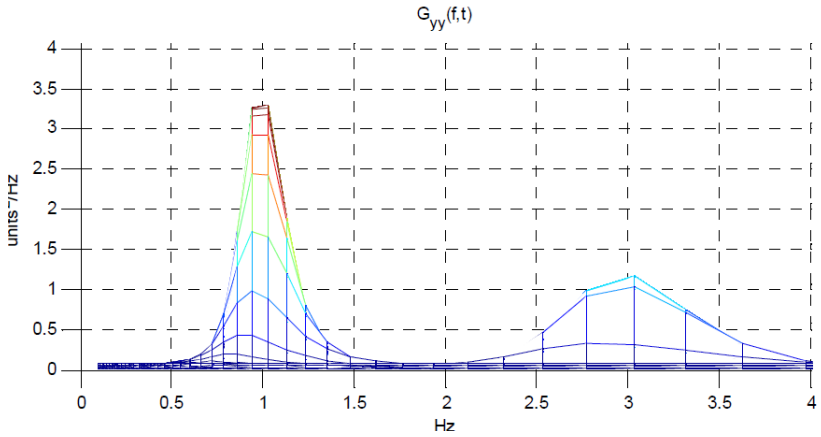

Figure 5.24. Scalogram (linear frequency scale) (Fig. 4 of Klyde et al. [2010]).

Previous research has correlated pilot sensitivity to added dynamics as a function of the basic dynamics (i.e. bandwidth properties) of the vehicle. This means that low bandwidth (due to low roll damping) attenuates the effects of the added dynamics, as compared to high bandwidth. Nicoll and Mitchell [2009] investigated the effects of added dynamics on rotorcraft control and the thresholds for detecting added dynamics. To assess the allowable error envelopes, the added dynamics were categorized into three sets: 1) those not noticed by the pilots, 2) those noticed without any effect on tasks performance, and 3) those noticed with effect on task performance. They reported a significant preliminary study on what limits will be established on permissible levels of time-varying added dynamics. Moreover, their paper confirmed that the methods pursued for evaluation were effective, the pilots could detect changes in added dynamics, and that the changes could be measured using wavelet transform.

Developments in fly-by-wire control architectures have motivated interest in identifying time-varying pilot control behavior in multi-axis control tasks. Understanding time-varying pilot control behavior can potentially provide a rational basis for pilot control actions and be used in conjunction with vehicle dynamics in forming predictions or in explaining the behavior of pilot-vehicle systems. Previous developments have focused on pilot control behavior in single-axis control tasks, however most pilot control tasks involve simultaneous control inputs from multiple axes. Zaal and Sweet [2011] proposed a Maximum Likelihood Estimation (MLE) method to determine the parameters of a pilot model with time-dependent sigmoid functions and characterized time-varying human control behavior. The estimation method was analyzed experimentally with flight tests involving time-varying aircraft dynamics and supported with analysis of pilot's adaptation in different axes of control to the time-varying aircraft dynamics. The proposed MLE method is far more efficient than previous efforts, such as the time-windowing MLE method, however, not necessarily more accurate. The study showed that the growth factor of the sigmoid functions had the lowest estimation accuracy because the sigmoid function was inherently unbounded for higher values. Furthermore, the study also showed that time-varying control behavior in both the roll and pitch axes was greatly affected by the axis with the time-varying aircraft dynamics and the growth factor. Cross-coupling was found to exist in pilot control behavior between two axes. Despite identical aircraft dynamics and forcing

functions, pilot performance was higher and control activity was lower in pitch compared to roll. This was also reflected in significantly different pilot control behavior in both axes.

Hess [2009a] expounded on various aspects of modeling human pilot behavior in rotorcraft flight control. Hess and Marchesi [2009] developed and implemented a pursuit tracking model of a human pilot adapting to sudden changes in vehicle dynamics. A key feature of this adaptive model is simplicity. By only varying two gain parameters in each control loop, pilot adaption to time-varying vehicle dynamics can be accommodated. This simplified pursuit control model was then integrated into a model of an adaptive human pilot, with a limiter at the pilot's inceptor output to address amplitude limitations of the device. Adaptive logic for the pilot model was presented, based on the following four criteria:

1. Only signals that can be easily sensed by humans are used.
2. Logic driving adaptation needs to be simple.
3. Post-adapted pilot models should follow the dictates of the crossover model of the human pilot.
4. Adaptation times should be relatively short and consistent with experiments.

The study verified the proposed model's applicability in realistic, multi-axis, multi-loop flight control tasks when separate pilot model structures in each axis subject to pilot control were employed. Moreover, the proposed model's sequential loop closures suggest that pilot model adaptation may be limited to two innermost loops for any axis of control in multi-axis tasks. Nonetheless, the model provided a control-theoretic framework that can be used to study pilot control behavior in situations with sudden, unpredictable changes in vehicle dynamics [Hess, 2009b, 2009c].

Hess [2010b] developed a human pilot model that included the effects of biodynamic interference. Six requirements were stressed so that the model structure was suitable for rotorcraft applications: 1) the model control of the rotorcraft should be similar to that of a human pilot in multi-axis flight tasks; 2) the principal sensory cues available to the rotorcraft pilot (e.g., visual, proprioceptive, and vestibular) should be used; 3) the inclusion of biodynamic inputs should be allowed; 4) an approximate inclusion of the effects of task interference should be allowed; 5) reasonable predictions of task performance and handling qualities levels should be offered; and 6) tractability should be reasonable in applications.

The human pilot can create dynamics that are correlated with the crossover model of the human during controlled element transitions. The estimation algorithm was applied for time-varying pilot identification with success in both single- and multi-loop tasks, which allowed the optimization of regressor parameters. Moreover, a brief study was conducted with a Model Reference Adaptive Control System, which verified the use of this system for improving pilot/vehicle performance in the presence of a large time delay. The study showed that instabilities could possibly occur while pilots interact with an adaptive flight control system [Hess, 2011b].

Flexible Dynamic Systems

Plants with flexible structure dynamics, such as rotorcraft and wind turbines, have non-minimum phase modes that compromise the ability of adaptive controllers to achieve stability. In these systems, employing adaptive control techniques can be useful to alleviate problems introduced by these troublesome modal systems. Residual Mode Filters (RMFs) have been used to augment the adaptive controller to compensate for problems introduced by the modal subsystems. This allows the system to satisfy the stability requirements for the adaptive controller so that there is a guaranteed convergence and bounded gains. Balas and Frost have examined and verified this method to show that the RMF can restore stability in an otherwise unstable adaptively controlled system. This finding was useful because the adaptive controller design was not modified; only the RMF and disturbance estimator were added to the original adaptive controller. Additional research was conducted to address the leakage of the disturbance into the troublesome modal systems. Further reading into the theory of this work can be found in Balas and Frost [2010a, 2010b, 2011a, 2011b], Frost and Balas [2011], and Frost et al. [2011].

REFERENCES

Balas, M. J. and Frost, S., "Adaptive Control of Linear Modal Systems using Residual Mode Filters with Application to Flexible Structures," American Control Conference, San Francisco, CA, June 29, 2011a.

Balas, M. J. and Frost, S. A., "Adaptive Control of Flexible Structures Using Residual Mode Filters," 49th IEEE Conference on Decision and Control, Atlanta, GA, Dec. 15-17, 2010a.

Balas, M. J. and Frost, S. A., "Adaptive Control of Non-minimum Phase Modal Systems Using Residual Mode Filters: Part I & Part II," submitted Council of European Aerospace Societies 1st European Aerospace Guidance, Navigation and Control Conference, Munich, Germany, April 13-15, 2011b.

Balas, M. J. and Frost, S. A., "Augmented Adaptive Control of Flexible Structures Using Residual Mode Filters," ASME 2010 Conference on Smart Materials, Adaptive Structures and Intelligent Systems, SMASIS2010-3624, Philadelphia, PA, 28 Sept.-1 Oct. 2010b.

Blanken, C. L., Lusardi, J. A., Iveler, C. M., Tischler, M. B., Decker, W. A., Malpica, C. A., Höfinger, M. T., Berger, T., and Tucker, G. E. "An Investigation of Rotorcraft Stability-Phase Margin Requirements in Hover," 65th AHS Forum, Grapevine, TX, May 27-29, 2009.

Frost, S. A. and Balas, M. J., "Adaptive Control Using Residual Mode Filters Applied to Wind Turbines," submitted AIAA Infotech at Aerospace Conference, St. Louis, MO, March 29-31, 2011.

Frost, S. A., Balas, M. J., and Wright, A. D., "Generator Speed Regulation in the Presence of Structural Modes through Adaptive Control Using Residual Mode Filters," *IFAC Mechatronics Journal*, 2011.

Hess, R. and Marchesi, F., "Modeling the Human Pilot Controlling a Vehicle with Time-Varying Dynamics," 65th AHS Forum, Grapevine, TX, May 27-29, 2009.

Hess, R., "Analytical Assessment of Performance, Handling Qualities, and Added Dynamics in Rotorcraft Flight Control," IEEE: SMC-A, Jan. 2009a.

Hess, R., "Candidate Structure for Modeling Pilot Control Behavior with Sudden Changes in Vehicle Dynamics," AIAA Atmospheric Flight Mechanics Conference and Exhibit, Chicago, IL, Aug. 10-13, 2009b.

Hess, R., "Modeling Pilot Control Behavior with Sudden Changes in Vehicle Dynamics," *AIAA Journal of Aircraft,* vol. 46. no. 5, Sept.-Oct. 2009c, pp. 1584-1593.

Hess, R., "A Framework for Robust Rotorcraft Flight Control Design," AHS Aeromechanics Specialists' Conference, San Francisco, CA, Jan. 20-22, 2010a.

Hess, R., "Modeling Biodynamic Interference in Helicopter Piloting Tasks," AHS Aeromechanics Specialists' Conference, San Francisco, CA, Jan. 20-22, 2010b.

Hess, R., "A Framework for Robust Rotorcraft Flight Control Design," *Journal of the American Helicopter Society*, 2011a.

Hess, R., "A Preliminary Study of Human Pilot Dynamics in the Control of Time-Varying Systems," AIAA MST Conference, Portland, OR, Aug 8-11, 2011b.

Johnson, W., "Technology Drivers in the Development of CAMRAD II," American Helicopter Society Aeromechanics Specialists' Meeting, San Francisco, CA, Jan. 1994.

Johnson, W., "NDARC. NASA Design and Analysis of Rotorcraft," NASA/TP–2015-218751, April 2015.

Klyde, D. H., Schulze, P. C., Liang, C. Y., and Thompson, P. M., "Use of Wavelet Scalograms to Characterize Rotorcraft Pilot-Vehicle System Interactions," American Helicopter Society 66th Annual Forum, Phoenix, AZ, May 11-13, 2010.

Lawrence, B., "Incorporating Handling Qualities Analysis into Rotorcraft Conceptual Design," AHS Handling Qualities Specialists' Meeting, Huntsville, AL, Feb. 2014.

Lawrence, B., Malpica, C. A., and Theodore, C. R., "The Development of a Large Civil Tiltrotor Simulation for Hover and Low-speed Handling Qualities Investigations," 2010 European Rotorcraft Forum, Paris, France, Sept. 7-9, 2010.

Lawrence, B., Malpica, C., Theodore, C., Decker, W., and Lindsey, J., "Flight Dynamics Aspects of a Large Civil Tiltrotor Simulation using Translational Rate Command," Proceedings of the 67th Annual Forum of the American Helicopter Society, Virginia Beach, VA, May 3-5, 2011.

Lawrence, B., Berger, T., Tischler, M. B., Theodore, C., Tobias, E. L., Elmore, J., and Gallaher, A., "Integrating Flight Dynamics and Control Analysis and Simulation in Rotorcraft Conceptual Design," 72nd Annual Forum of the American Helicopter Society, West Palm Beach, FL, May 17-19, 2016.

Lusardi, J., Blanken, C., Ott, C., Malpica, C., and von Gruenhagen, W., "In-Flight Evaluation of Active Inceptor Force-Feel Characteristics and Handling Qualities," AHS 68th Annual Forum and Technology Display, Ft. Worth, TX, May 1-3, 2012.

Malpica, C. A., Decker, W. A., Theodore, C. R., Blanken, C. L., and Berger, T., "An Investigation of Large Tilt-Rotor Short-Term Attitude Response Handling Qualities Requirements in Hover," Presented at the 66th Annual Forum of the American Helicopter Society, Phoenix, May 10-12, 2010.

Malpica, C. and Lusardi, J., "Analysis of Handling Qualities for Active Inceptor Force-Feel Characteristics," AHS 69th Annual Forum, Phoenix, AZ, May 21-23, 2013.

Malpica, C., Decker, W., Theodore, C., Lindsey, J., Lawrence, B., and Blanken, C., "An Investigation of Large Tiltrotor Hover and Low Speed Handling Qualities," Proceedings of the 67th Annual Forum of the American Helicopter Society, Virginia Beach, VA, May 3-5, 2011.

Malpica, C., Theodore, C., Lawrence, B., and Blanken, C., "Handling Qualities of Large Rotorcraft in Hover and Low Speed," NASA/TP-2015-216656, March 2015.

Malpica, C., Theodore, C., Lawrence, B., Lindsey, J., and Blanken, C., "Handling Qualities of a Large Civil Tiltrotor in Hover using Translational Rate Command," AHS 68th Annual Forum and Technology Display, Ft. Worth, TX, May 1-3, 2012.

Nicoll, T. K. and Mitchell, D. G., "Effects of Time-Varying Rotorcraft Dynamics on Pilot Control," American Helicopter Society 66th Annual Forum, Phoenix, AZ, May 11-13, 2010.

Olcer, F. E., Prasad, J. V. R., Sankar, L. N., Bain, J., Zhao, J., and He, C., "Development and Evaluation of Reduced Order Models of On-Blade Control for Integrated Flight and Rotor Control," AHS 66th Annual forum, May 2010.

Prasad, J. V. R., Olcer, F. E., Sankar, L. N., and He, C., "Linear Time Invariant (LTI) Models for Integrated Flight and Rotor Control," 35th European Rotorcraft Forum, Hamburg, Germany, Sept. 22-25, 2009.

Rozovski, D. and Theodore, C., "Evaluation of the Rotational Throttle Interface for Converting Aircraft Utilizing the NASA Ames Vertical Motion Simulator," Proceedings of the 67th Annual Forum of the American Helicopter Society, Virginia Beach, VA, May 3-5, 2011.

Sridharan, A. and Celi, R., "Flight Dynamics and Control of a Rotorcraft Towing a Submerged Load," AHS 69th Annual Forum, Phoenix, AZ, May 21-23, 2013.

Theodore, C. and Tischler, M., "Development and Operation of an Automatic Rotor Trim Control System for the UH-60 Individual Blade Control Wind Tunnel Test," AHS Aeromechanics Specialists' Conference, San Francisco, CA, Jan. 20-22, 2010.

Theodore, C. R., Malpica, C., and Lawrence, B., "Rotorcraft Flight Dynamics and Controls Research at NASA," 3rd Asian Australian Rotorcraft Forum, Melbourne, Australia, Dec. 18-19, 2014a.

Theodore, C., Malpica, C., Lawrence, B., Blanken, C., Tischler, M., Lindsey, J., and Berger, T., "Effect of Control System Augmentation on Handling Qualities and Task Performance in Good and Degraded Visual Environments," American Helicopter Society 70th Annual Forum and Technology Display, Montreal, Canada, May 2014b.

Thornburgh, R., Kreshock, A., Wilbur, M., Sekula, M., and Shen, J., "Continuous Trailing-Edge Flaps for Primary Flight Control of a Helicopter Main Rotor," American Helicopter Society 70th Annual Forum and Technology Display, Montreal, Canada, May 2014.

Zaal, P. and Sweet, B., "Identification of Time-Varying Pilot Control Behavior in Multi-Axis Control Tasks," AIAA Modeling and Simulation Technologies Conference, Portland, OR, Aug 8-11, 2011.

CHAPTER 6. DRIVE SYSTEMS

David G. Lewicki[1] and Paula J. Dempsey[2]

INTRODUCTION

The propulsion system of a vertical lift vehicle includes the engines, drive system, and supporting subsystems required for lift and forward thrust. The range and payload flight characteristics depend on the efficiency and power density of the propulsion system driven by its weight, engine fuel efficiency, and operational characteristics. Advanced propulsion technologies can reduce vehicle noise, fuel burn, and operating costs while increasing speed, payload, and range for the next generation of vertical lift vehicles.

A status of NASA rotorcraft research, published over 10 years ago [Yamauchi and Young, 2009], noted that within the propulsion system of U.S. helicopters, drive systems are single reduction ratios and engines operate at constant output power speed, resulting in a constant-speed rotor. The ability to vary rotor speed for varying missions and flight regimes is one method to improve the speed and efficiency of vertical lift vehicles. A variable speed rotor can also overcome additional barriers that include reduced noise via lower rpm rotor, increase of maximum forward-flight speed, increased payload and range, reduced fuel burn, and lower operating costs. One approach to change the rotor speed is by using a variable speed power turbine (VSPT), but the reduction currently causes significant losses in engine efficiency. Another approach is to use a two-speed drive system, but there is a high weight and efficiency penalty with current technology. Both of these approaches were pursued vigorously within NASA in the past decade with substantial progress achieved, as described in part of this chapter and the companion chapter, Engines.

The overall focus of this chapter is on advancements made, through NASA research efforts from circa 2007 to 2018, overcoming key barriers in the drive systems of vertical lift vehicles. Topics covered in this chapter include: multispeed drive systems and dynamic systems modeling, gear windage, advanced hybrid composite components, drive system component life, advanced drive system components, high-speed gearing, lubrication, health monitoring and condition-based maintenance (CBM), gas foil bearings, and nickel-titanium alloys for bearing applications.

MULTISPEED DRIVE SYSTEMS

Propulsion systems of current manned vertical lift vehicles are optimized for operation such that the rotors operate over a narrow range of rotating speed regardless of whether the vehicle's flight condition is vertical takeoff and landing, hover, or forward cruise. However, certain missions and markets benefit greatly if the rotor speed can be adjusted over a wide range of speed to match demands of different missions and flight regimes. Key barriers addressed by the wide range of rotor speed include noise reduced via lower rpm rotor, increase of maximum forward-flight

[1] DGL Technical Engineering Services, LLC, 37782 Hatteras Way, Avon, OH 44011.
[2] NASA Glenn Research Center, 21000 Brookpark Road, Cleveland, OH 44135.

speed, increased payload and range, reduced fuel burn, and lower operating costs. One viable approach is to make use of a two-speed-ratio drive system such that the engine can continue to operate over a narrow speed range, whereby engine performance is optimal, while adjusting the rotor speed as needed using the two-speed drive system. Motivated by such needs and by the results of several system studies, a Technical Challenge within the NASA Revolutionary Vertical Lift Technology (RVLT) Project was established to develop and demonstrate required technologies and designs for achieving a 50-percent reduction in rotor rpm via a two-speed drive system that incurs less than 2 percent power loss and maintains current power-to-weight ratios [Krantz et al., 2018].

Over the past 10-year period, two-speed-ratio drive systems with a 50-percent reduction in main rotor speed for forward flight, while maintaining full engine speed, were developed and demonstrated. An initial study was completed that investigated possible drive system arrangements to accommodate up to the 50-percent speed change [Stevens et al., 2008a, 2008b, 2009]. In this study, inline discrete two-speed configurations, dual-input planetary differential configurations, and variable-speed multi-shaft split-power configurations were investigated, evaluated, and ranked. Results identified the most promising gear-based drives to be designed and fabricated for future testing. Two inline discrete two-speed configuration concepts were identified: 1) the patented offset compound gear (OCG) design [Stevens et al., 2010], and 2) the dual-star idler (DSI) planetary design. They were selected to be developed because of their simplicity and high degree of reliability.

Test articles were then developed of the two gear train concepts [Stevens et al., 2015]. In addition, two clutch types were developed. One was a dry clutch based on high-performance automotive components. The other was a wet clutch based loosely on friction/steel drive elements of a traditional automotive automatic transmission design. The test articles were modular in design, capable of testing two interchangeable gear train designs and two clutch designs. The groundbreaking approach also included development of a new facility to test scaled two-speed transmissions. The OCG transmission (Fig. 6.1) and the DSI planetary transmission (Fig. 6.2) were tested in the NASA Glenn Research Center (GRC) Variable-Speed Transmission Test Facility [Lewicki et al., 2015]. The Variable-Speed Transmission Test Facility, shown in Figure 6.3, utilizes two identical alternating-current (AC) variable-speed motors. These motors can be used as a driver or a regenerative load. This multispeed facility is capable of a maximum power level of 149 kW and an input/output speed of 15,000 rpm. Both the OCG and DSI configurations successfully performed speed shifts at full-rated 15,000-rpm input speed. The transient shifting behavior of the OCG and DSI configurations were very similar. For these tests, the dry clutch configuration was used for both transmissions. It was deduced that the shift clutch had more of an effect on shifting dynamics than the reduction gearing configuration itself.

Further investigations were completed [Stevens et al., 2018] into the power loss associated with a rotating feed-through design feature of the test setup. This feature was used to transfer lubrication and a hydraulic control signal from the static reference frame to a rotating reference frame in the NASA GRC two-speed transmission tests conducted in the Variable-Speed Transmission Test Facility. Results were used in an overall power loss assessment for a scaled

conceptual 1,000-hp inline concentric two-speed transmission to support a NASA RVLT Technical Challenge, demonstrating 50 percent speed change with less than 2 percent power loss while maintaining current power-to-weight ratios.

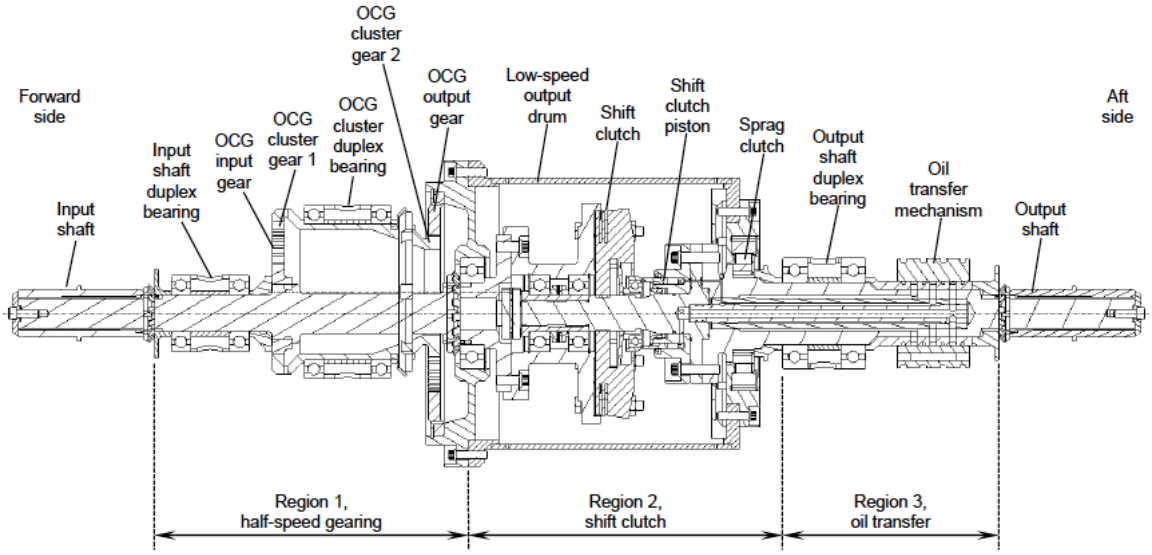

(a) Cross-sectional view.

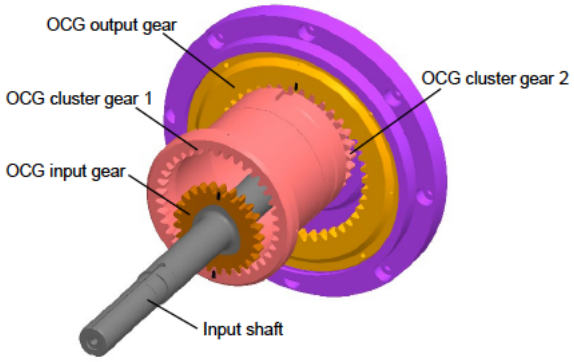

(b) 3D view of OCG gearing (region 1).

Figure 6.1. Offset compound gear (OCG) transmission configuration (Fig. 5 of Lewicki and Stevens [2015]).

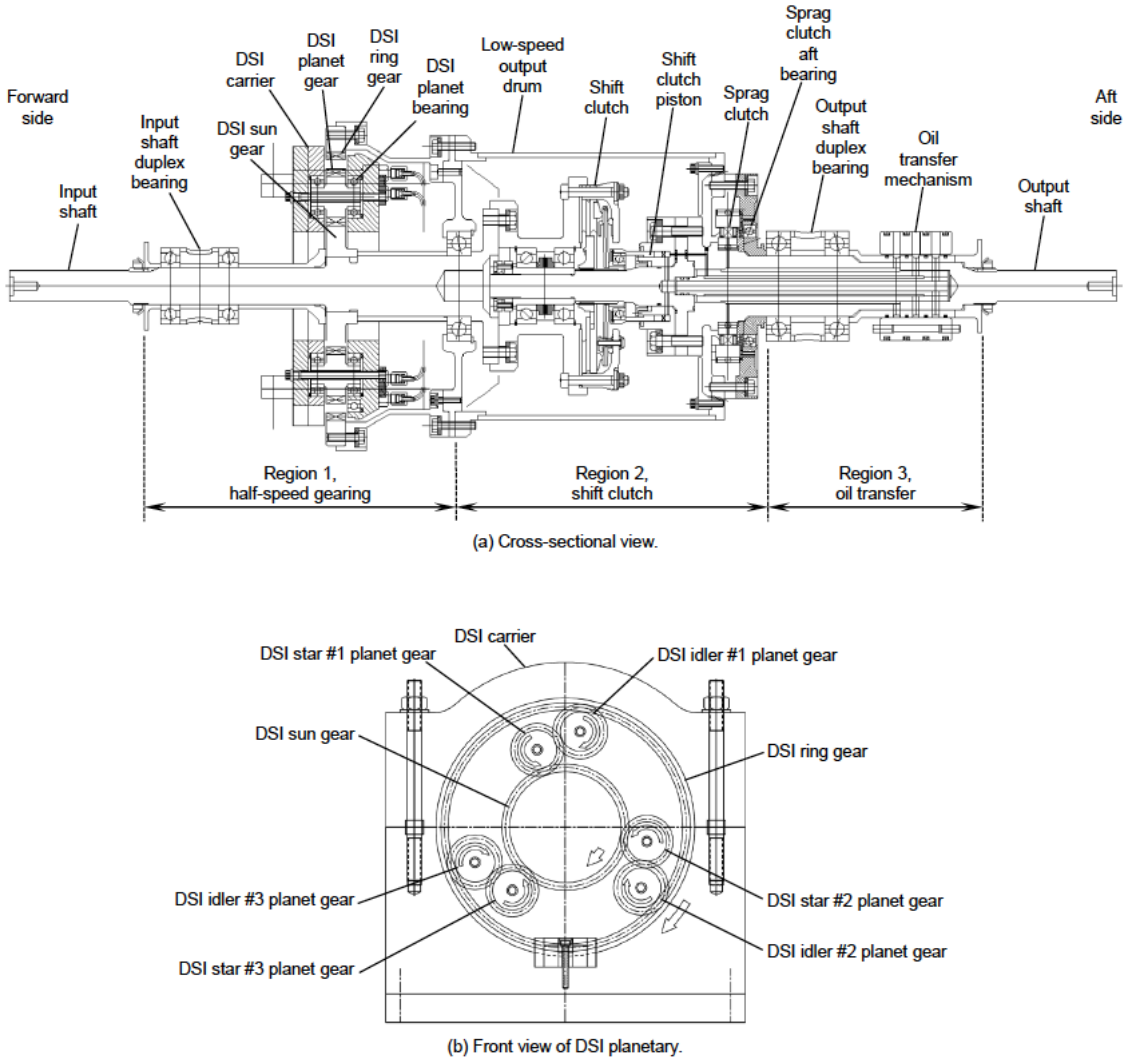

Figure 6.2. Dual star-idler (DSI) planetary transmission configuration (Fig. 8 of Lewicki and Stevens [2015]).

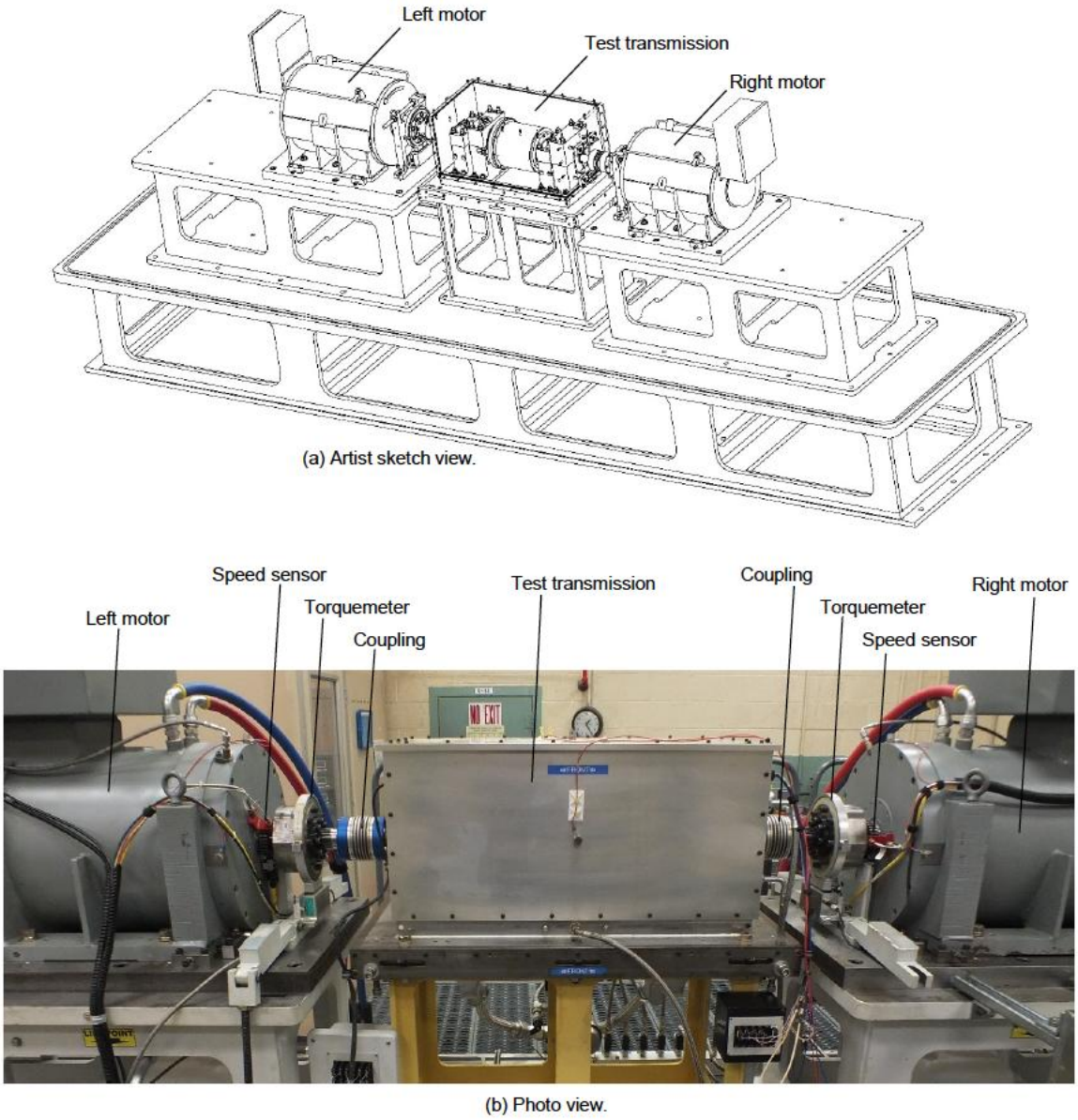

Figure 6.3. NASA GRC Variable-Speed Transmission Test Facility (Fig. 1 of Lewicki and Stevens [2015]).

MULTISPEED DRIVE DYNAMIC ANALYSIS

In addition to the development of multispeed drives and corresponding technologies, dynamic modeling of multispeed rotorcraft drive systems was also performed. An initial study was performed to validate a gearbox dynamic model of a NASA-developed two-speed gearbox for a lunar space application [Lewicki et al., 2010a, 2013]. A six-degrees-of-freedom model of the gearbox was created to predict gearbox performance during shifting, then experimental tests were performed for model validation, comparing measured speeds and torques to model predictions during shifting profiles. Results found that the model matched the experiment data, validating dynamic simulation methodologies.

Other foundational dynamic modeling work was performed demonstrating the importance of nonlinear mesh phase interactions in multi-gearbox drive systems [DeSmidt, 2010a]. Further investigations, using a variable-speed rotorcraft propulsion system modeling tool developed under NASA funding, were performed on the Second-Generation Large Civil Tiltrotor (LCTR-2) concept vehicle in forward-flight airplane mode [DeSmidt et al., 2011, 2012, 2013]. Analysis was performed using a sequential shifting control strategy for the transient shifting response under variable-speed operation of a two-speed transmission for cruise conditions. Although sequential shifting control provided smooth rotor speed changes, transient shocks were produced by the engine during engagement and disengagement from their freewheeling clutches. This produced engine compressor surges that exceeded their limits. It was also found that this effect could be minimized by optimizing the dual-clutch transmission shift rate.

GEAR WINDAGE

Power losses due to interactions between the air-oil atmosphere and rotating gears in a gearbox are referred to as gear windage. These power losses cause increased heating and fuel consumption in the power train. Windage research was performed to experimentally validate NASA investments in gear windage computational tools based on computational fluid dynamics (CFD). This research included modeling, testing capabilities, and power loss prediction. These efforts enable the development of methods to evaluate and reduce the power loss of high-speed gearing due to windage in advanced power-train designs.

An unstructured overset moving mesh CFD method was developed, validated, and applied to spinning gear systems with emphasis on predicting windage losses [Hill et al., 2008]. Several spur gears and a disc, spinning in air at rotation rates up to 1,200 1/s were studied. It was observed that the CFD simulations returned good agreement with measured windage power loss, as determined by the deceleration of the gears due to torques exerted by viscous and pressure forces on the gear surfaces. The CFD method developed for gear windage aerodynamics was expanded to predict windage losses with validation studies performed using three-dimensional (3D) spur gears in free space and to configurations with and without shrouding using available published experimental data [Hill et al., 2009, 2010, 2011]. Validation studies showed good agreement with the data. This preliminary work provided a better understanding of the physics of windage losses and means to reduce these losses through shrouding and gear-tooth designs.

A new test facility, the Gear Windage Test Facility at NASA GRC, was then developed to further investigate design parameters that contribute to gear windage as well as methods to reduce windage through new designs [Handschuh et al., 2010, 2011a]. Tests could be performed with varying speeds, with and without shrouding, and with and without lubricant. Data generated can be used for model validation. The test facility, shown in Figure 6.4, has a 112-kW (150-hp) DC drive motor connected to a 5.7:1 speed-up gearbox. Based on dimensions of the test specimen, the pitch-line velocity of the gear can be as high as 280 m/s (~55,000 ft/min).

The gear windage CFD method was then further developed to validate numerical and modeling approaches, and to develop and evaluate new methods for minimizing windage losses [Hill and Kunz, 2012; Kuntz, 2014]. Several CFD modeling techniques were implemented to achieve these goals that included absolute and relative frame CFD simulation, overset gridding, multiphase flow analysis, and sub-layer resolved turbulence modeling. Comparisons made with experimental data collected in the Gear Windage Test Facility showed good agreement.

Additional parametric tests were also performed in the Gear Windage Test Facility, with and without shrouding, at varying oil inlet temperatures. Results indicated shrouding effectiveness above 15,000 ft/min pitch-line velocity when oil flow and temperatures were considered [Delgado and Hurrell, 2017a, 2017b, 2018]. From these tests, design guidelines were developed for shroud designs for pitch-line velocities higher than 10,000 ft/min. These included recirculation avoidance of the air/oil mixture in the meshing region, provision of a method for the fluid to exit axially in spur gear mesh, and provision of a method for the lubricant to rapidly cool and exit mesh.

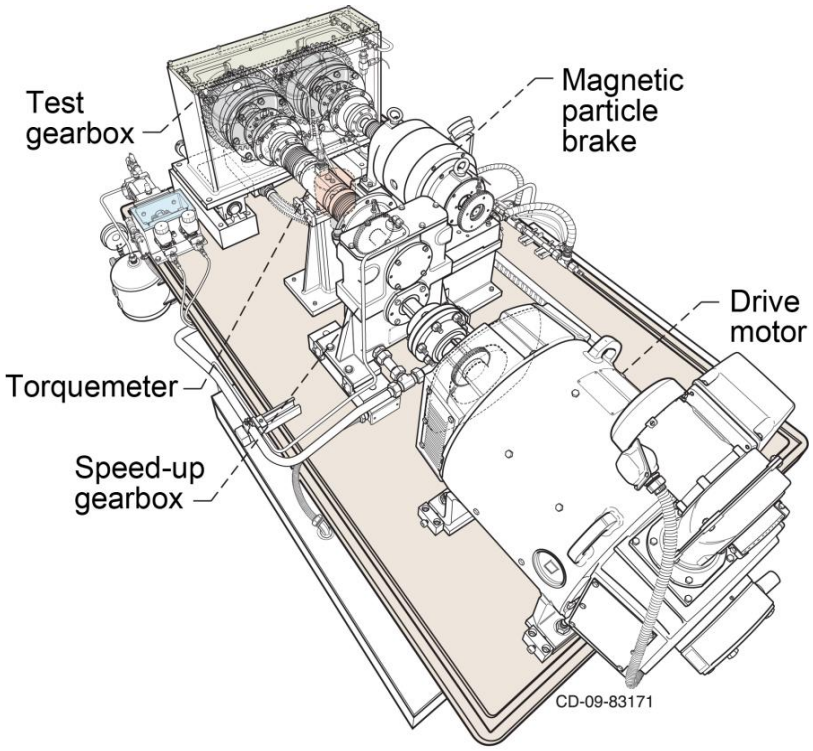

Figure 6.4. Overview sketch of the NASA GRC Gear Windage Rig (Fig. 1 of Handschuh and Hurrell [2011a]).

ADVANCED HYBRID COMPOSITE COMPONENTS

The drive system within a helicopter is a substantial part of the vehicle's dry weight. Because of the low density and high strength of composite materials, the use of composites to replace steel rotorcraft transmission components can significantly reduce its weight. Technologies were developed and demonstrated to enable the use of composite materials and composite/metal hybrid structures in vertical lift vehicle drive systems. The research focused primarily on hybrid gears, including integration of hybrid gears with other structures within the drive system such as shafts, couplings, bearings, and splines.

Research was performed at NASA GRC on composite gears to identify the issues that need to be addressed to enable this technology for rotorcraft drive systems [Handschuh et al., 2012a, 2012b; Roberts et al., 2013]. Composite spur gears were first fabricated by replacing the central web, between the gear teeth and a metallic hub of a spur gear, with carbon composite as shown in Figure 6.5. The hybrid gears were operated over 300 million cycles at 10,000 rpm and 553 in-lb torque with no degradation. They were also 20 percent lighter than the all-steel gears without optimization of the components.

Additional free vibration and dynamic operational tests were performed, comparing all-steel gears to hybrid gears, in the NASA GRC Spur Gear Fatigue Test Facility [Handschuh et al., 2014]. Hybrid gears showed no signs of degradation after being fatigue tested to one billion stress cycles at representative loads and speeds. Results found the natural frequency of the hybrid gear to be 800 Hz lower than the steel test gear of the same size and dimension. It was also found that the level of vibration was sensitive to load and rotational speed.

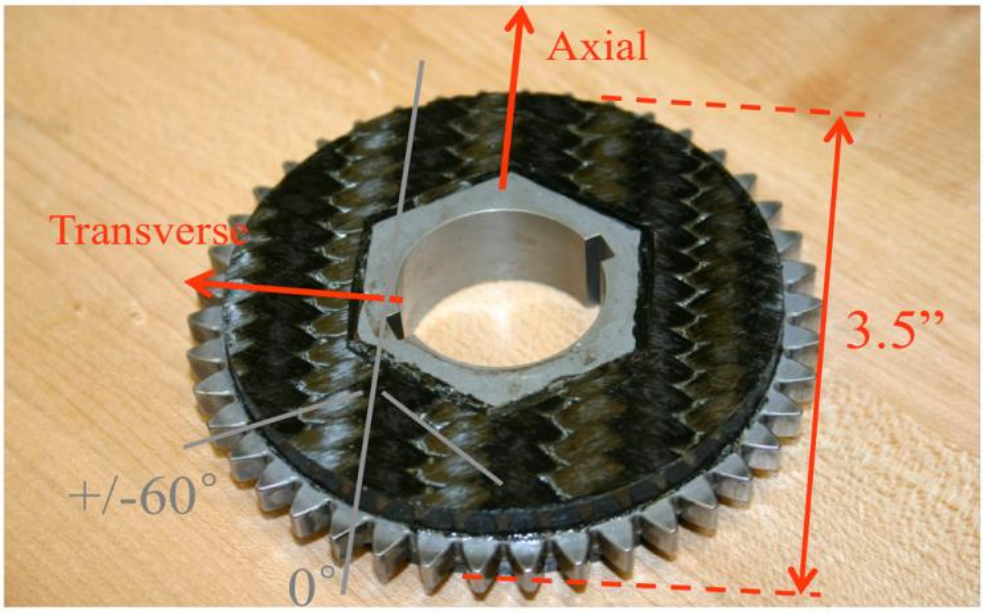

Figure 6.5. Hybrid gear (Fig. 2 of Handschuh et al. [2012a]).

The research then transitioned to testing of a full-scale hybrid bull gear with a baseline (steel) web configuration and a hybrid (steel-composite) configuration in the NASA GRC High-Speed Helical Gear Rig [LaBerge et al., 2016]. The hybrid gear is shown in Figure 6.6 and the High-Speed Helical Gear Rig is shown in Figure 6.7. For the hybrid gear web configurations, the structural material between the shaft interfaces was replaced with a lightweight carbon fiber composite, while using the same gear rim. Vibration, orbit, and temperature data measured during testing were similar between the hybrid and steel configurations. NASA-patented lightweight driveline hybrid composite components were developed to replace all-steel components. The weight benefit of the new lightweight hybrid component technologies has significant benefits to the vertical lift community and extends to other aviation vehicles, new emerging markets, and the automotive industry.

Studies were also executed evaluating hybrid gear performance under loss-of-lubrication conditions in the NASA GRC Contact Fatigue Test Facility [LaBerge et al., 2017]. Experiments were performed, using small-scale 3.5-in. (8.9-cm) pitch diameter gears, comparing hybrid gears to steel gears. Results found limitations to the use of a hexagonal interlock pattern between the steel and composite. However, there were positive results in that the presence of polymer in the gear during an oil-out event has potential to increase time to failure.

In addition to hybrid gear concepts with a constant composite thickness, a new variable thickness hybrid composite gear was designed, manufactured, and tested in static torsion tests and operationally in the NASA GRC High-Speed Helical Gear Rig [LaBerge et al., 2018]. This new design, shown in Figure 6.8, greatly exceeded previous design performance with a torque capacity of more than 240,000 in-lb (27,100 N-m) and was feasible up to 5,000 hp (3,730 kW).

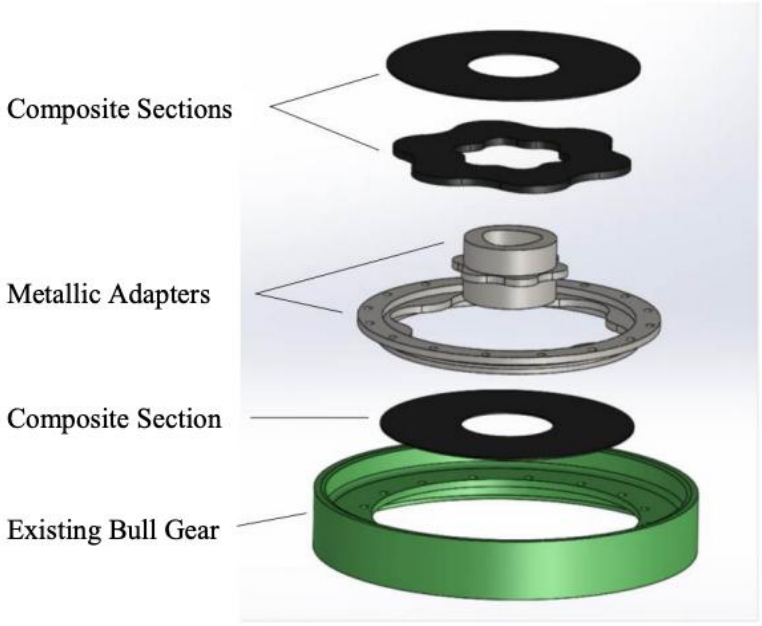

Figure 6.6. Exploded view of hybrid bull gear design (Fig. 2 of LaBerge et al. [2016]).

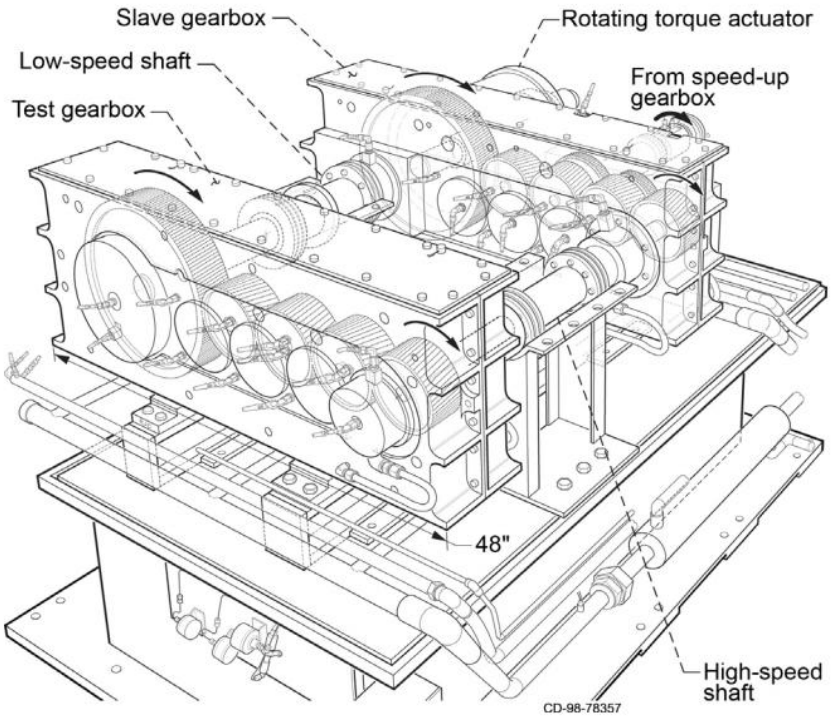

Figure 6.7. NASA GRC High-Speed Helical Gear Rig (Fig. 1 of LaBerge et al. [2016]).

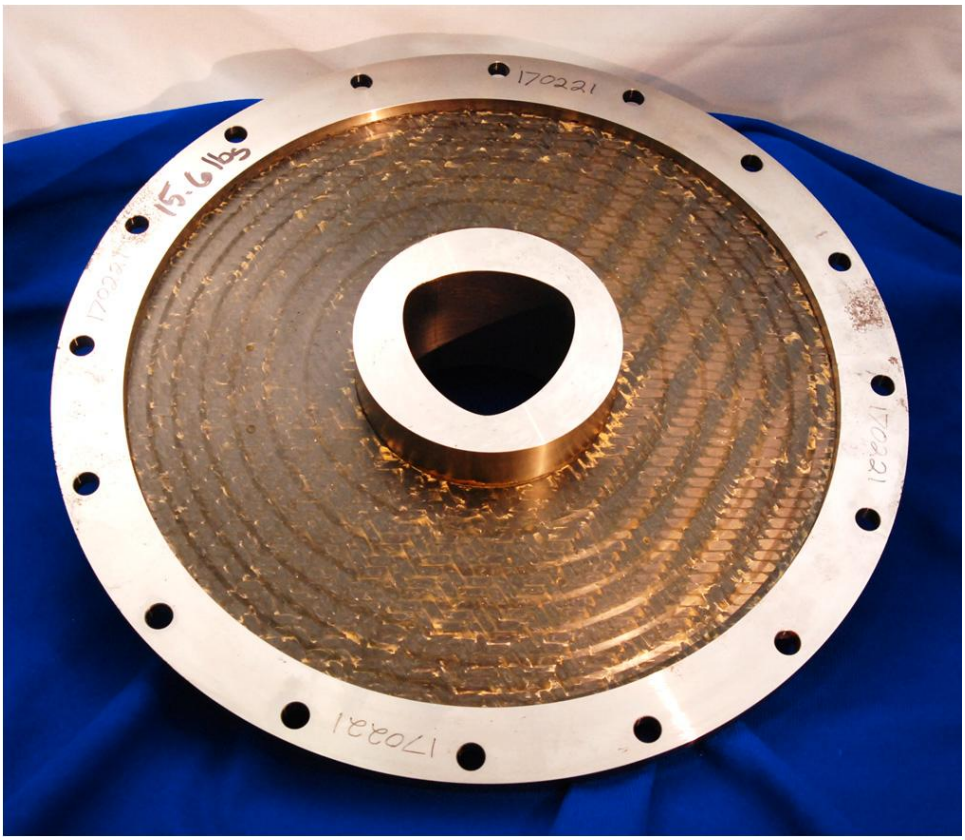

Figure 6.8. Variable thickness hybrid gear web (Fig. 2 of LaBerge et al. [2018]).

DRIVE SYSTEM COMPONENT LIFE

For aircraft mechanical power trains, design requirements such as low weight and high power capacity need to be balanced with long life, high reliability, and low maintenance costs. The primary components of these power trains are combinations of rolling-element bearings, gears, and shafting. Accurate prediction of the lives of these components is necessary to establish reliability, predict replacement rates, set up maintenance and replacement schedules, and ascertain warranty limits. Two computational models to determine the fatigue life and reliability of a commercial turboprop gearbox were compared with each other and with field data [Zaretsky et al., 2007a, 2007b]. The field data suggested that the life of the gearbox was underpredicted by a factor of 7. The component failure distribution of the gearbox from the Monte Carlo simulation was nearly identical to that using the strict-series system reliability analysis, proving the compatibility of these methods.

The effect of hoop stresses on cylindrical roller bearing fatigue life was determined for various classes of inner ring interference fit [Oswald et al., 2008]. Calculations were performed for up to 7 interference fit classes for each of 10 bearing sizes. The hoop stresses were superimposed on the Hertzian principal stresses created by the applied radial load to calculate roller bearing fatigue life. Results are presented as tables and charts of life factors for bearings with light, moderate, and heavy loads. Interference fits ranging from extremely light to extremely heavy and bearing accuracy class are also presented. The effect of hoop stresses on the rolling-element fatigue life of angular-contact and deep-groove ball bearings was determined for common inner-ring interference fits [Oswald et al., 2010a]. The analysis was applied to over 1,150 bearing configurations and load cases. Results are presented as tables and charts of life factors for angular-contact and deep-groove ball bearings with light, normal, and heavy loads, and interference fits ranging from extremely light to extremely heavy.

The effect of internal clearance on radially loaded deep-groove ball and cylindrical roller bearing load distribution and fatigue life was determined for four clearance groups defined in the bearing standards [Oswald et al., 2010b, 2012a, 2012b]. The analysis was extended to negative clearance (interference) conditions to produce a curve of life factor versus internal clearance. Relationships were found between bearing life and internal clearance as a function of ball or roller diameter, adjusted for load. Results are presented as life factors for radially loaded bearings independent of bearing size or applied load. In addition, a modified Stribeck Equation is presented that relates the maximum rolling-element load to internal bearing clearance.

The power density of a gearbox is an important consideration for many applications and is especially important for gearboxes used in rotorcraft. The gearbox power density is limited by the ability of the gear teeth to transmit power for the required number of cycles without pitting or spalling on the tooth face (pitting fatigue), or fatigue in the root-fillet region (bending fatigue). Significant research has been performed at the NASA GRC over the past 10 years to evaluate advancements in new material alloys, new steel processing techniques, and improved modeling techniques to improve the performance, durability, and reliability of aircraft gear systems.

In certain gear applications, the level of loading applied to the gear mesh members can be large enough to cause a great deal of the gear's life to be used in a short number of cycles. Published

experimental data for the fatigue of case-carburized gears for loads sufficient to fail the gear in the range of hundreds to several thousand cycles is sparse. An investigation of the low-cycle bending fatigue of spur gears made from AISI 9310 gear steel was completed [Handschuh et al., 2007a, 2007b, 2008]. Tests were conducted on spur gears in a fatigue test machine using a dedicated gear test fixture for single-tooth bending fatigue. Stress-cycle test results of gear-tooth crack initiation are shown in Figure 6.9. In follow-on work, the bending-fatigue capacity of a high-temperature, nickel-based alloy, typically used for turbine disks in gas turbine engines, and two tool steel materials with high vanadium content, were compared to that of a typical aerospace alloy, AISI 9310 [Handschuh and Burke, 2012c]. All four materials performed similarly for the room temperature tests at four load levels. At higher temperature, the nickel-based alloy appeared to perform better at the higher bending stress conditions.

A new class of ultra-high-strength (UHS) alloy steels has been evaluated by analysis and laboratory testing [Shen et al., 2011a, 2011b]. The steels included Ferrium C61 and C64, secondary hardening steels that were offered for significant improvements in both core (gear-shaft) and case (gear-tooth) properties that require higher performance in strength and toughness. Single-tooth bending-fatigue test data of UHS Ferrium C61 and C64 alloys are presented in comparison with historical test data of conventional gear steels (9310 and Pyrowear 53). Statistical analysis of test data for the four gear steels indicated that the UHS grades exhibit increases in fatigue strength in the low cycle fatigue regime. However, because of considerable scatter in the UHS test data, the anticipated overall benefits of the UHS grades in bending fatigue have not been fully demonstrated.

The rotorcraft community's shift toward condition-based maintenance (CBM) strategy seeks to extend the useful life of gears and bearings in order to increase the overall affordability of aircraft. Fatigue failures, including gear-tooth bending fatigue, take on considerable importance as the number of cycles increases. To help meet these needs, a new high-speed test capability for determining the high-cycle bending-fatigue characteristics of gear teeth has been developed at the NASA GRC [Stringer et al., 2011]. A photograph of the new facility is shown in Figure 6.10. Initial experiments were performed in the new facility using an AISI 9310 steel spur gear specimen to establish baseline data.

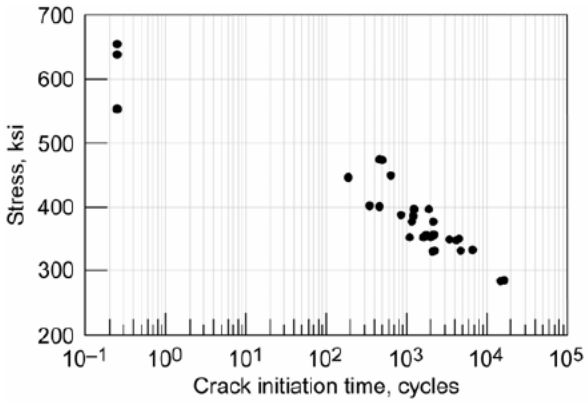

Figure 6.9. Single-tooth bending data (Fig. 8 of Handschuh at al. [2007a]).

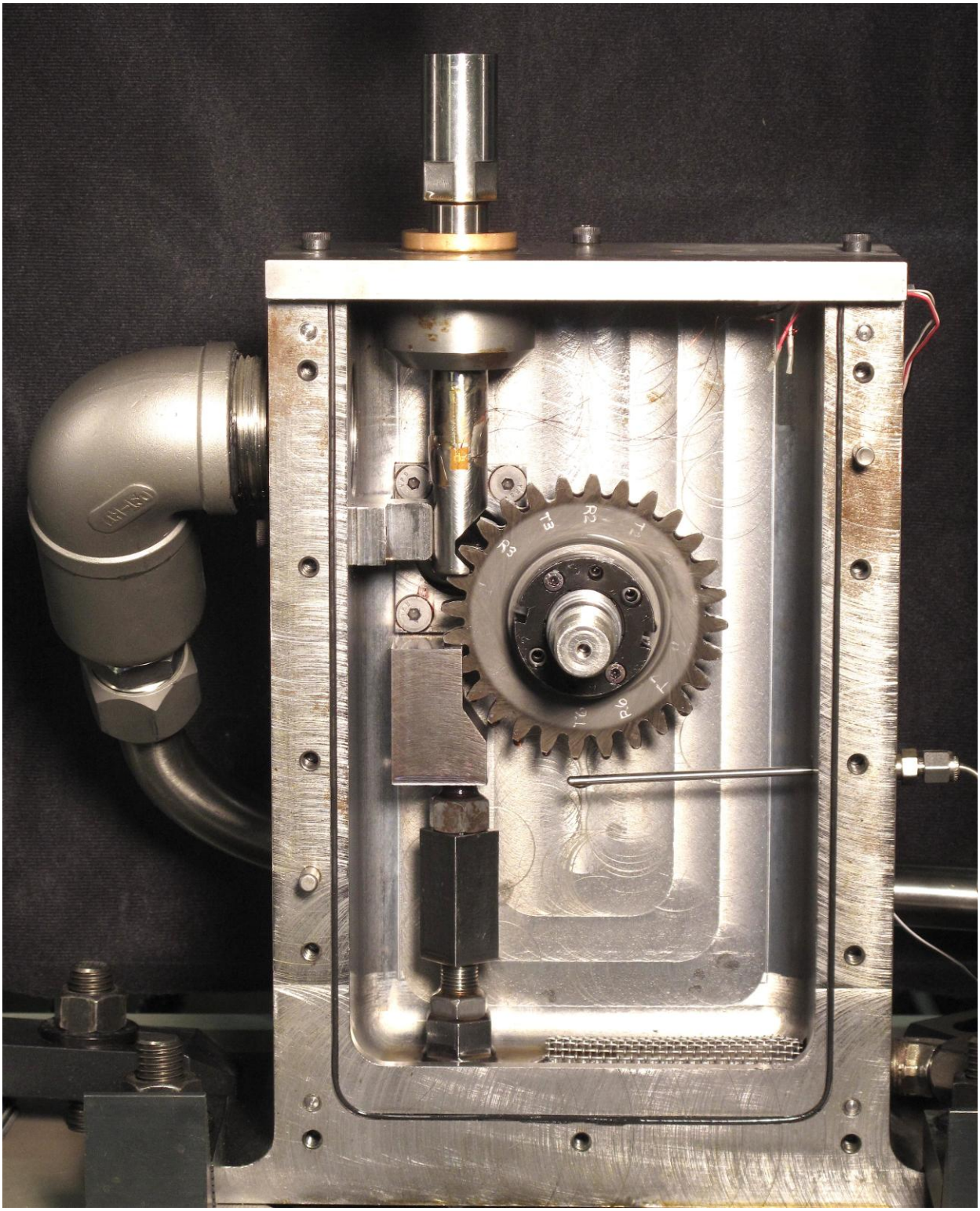

Figure 6.10. NASA GRC Single-Gear-Tooth Bending Test Facility (Fig. 1 of Stringer et al. [2011]).

To further understand gear-tooth bending fatigue, a study on fatigue-induced seeded cracks in spur gears was performed [Nenadic et al., 2011a, 2011b]. Cracks were initiated using a fatigue tester to simulate overload conditions. The fatigue-induced cracks were then propagated on the dynamometer-based fixture to create well-documented, statistically significant data for monitoring cracks from inception to failure (Fig. 6.11). Crack propagation analysis tools (FRANC2D) and finite element analysis (FEA) (ANSYS simulation software) were used for gear-tooth crack prediction analysis and compared to the experiments. In further work, capabilities to predict contact and bending-fatigue damage and life of spiral-bevel gears were developed [Vijayakar, 2016]. Customized contact analysis in the gear-tooth meshing region was merged with conventional FEA to estimate tooth contact and tooth bending stresses (Fig. 6.12).

The fatigue performance of gears made from a relatively new steel alloy, Ferrium® C69, was investigated [Krantz and Tufts, 2007a, 2007b, 2008]. The Ferrium C69 alloy was selected and processed to achieve a higher surface hardness compared to production gears. The performance of the C69 gears was compared to the performance of gears made from two alloys currently used for aviation gearing, AISI 9310 (AMS 6265) and Pyrowear 53 (AMS 6308B). Gear-tooth surface fatigue tests were performed in the NASA GRC gear fatigue test apparatus (Fig. 6.13). The new alloy exhibited significantly better performance in surface fatigue testing, demonstrating the value of the improved properties in the case layer. However, the alloy exhibited lesser performance in single-tooth bending-fatigue testing because of lower fracture toughness characteristics. In another study, test gears made from SAE AMS 6308D steel alloy specification and additional company-specific proprietary material specifications were tested [Krantz et al., 2017]. Bending-fatigue, pitting, and scuffing test procedures and results are documented.

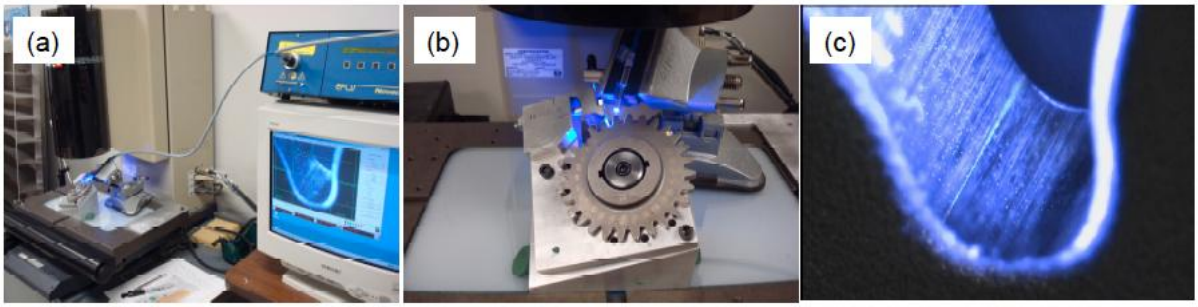

(a) Imaging system. (b) Custom gear fixture. (c) Imaged tooth.

Figure 6.11. Nondestructive method for crack verification (Fig. 8 of Nenadic et al. [2011b]).

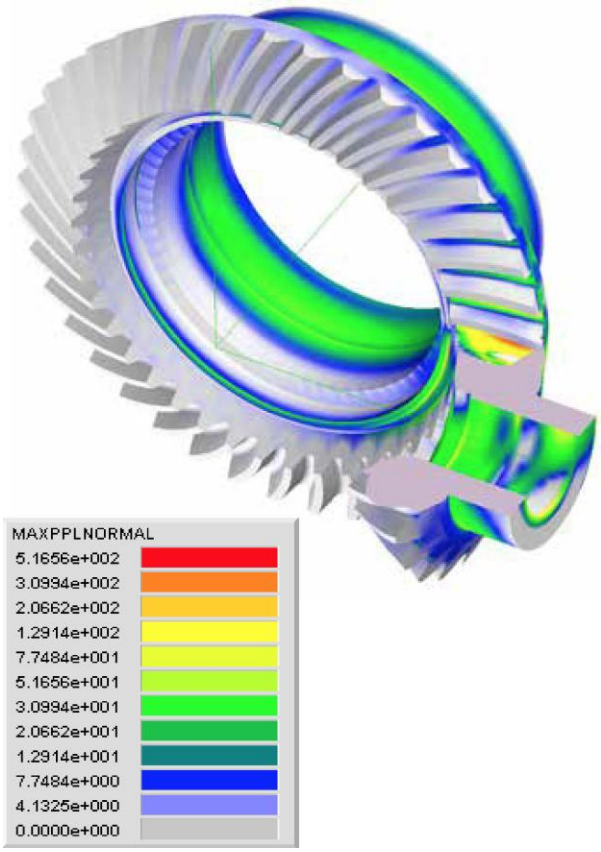

Figure 6.12. Distribution of the maximum principal normal stress in the Transmission 3D Finite Element model, in MPa at 6000 in-lb of gear torque (Fig. 3 of Vijayakar [2016]).

Gear and bearing performance is strongly influenced by the lubrication condition and the topography of the contacting surfaces. The lubrication condition and surface topography have a strong influence on friction, scoring and scuffing, wear, micro-pitting, and surface fatigue of gears and bearings. Gear surface fatigue lives for a wide range of specific film values (defined as the ratio of lubricant film thickness to the composite surface roughness) were studied using tests done with common rigs, speeds, lubricant temperatures, and test procedures [Krantz, 2014]. This study included previously reported data, results of an additional 50 tests, and detailed information from laboratory notes and tested gears. The observed trends were found to be in good agreement with data and recommended practice for gears and bearings (Fig. 6.14).

Lastly, expertise from rotorcraft gear research was used to support the NASA space shuttle activities. The Space Shuttle orbiter body flap actuator was presented as a case study to determine estimates of the tooth fillet and root stresses of a very heavily loaded pinion-ring gear mesh [Krantz and Handschuh, 2015]. The analysis used was a multi-body contact analysis approach employing finite element methods. The results were compared to the stresses as calculated using a high point of single-tooth contact analysis method.

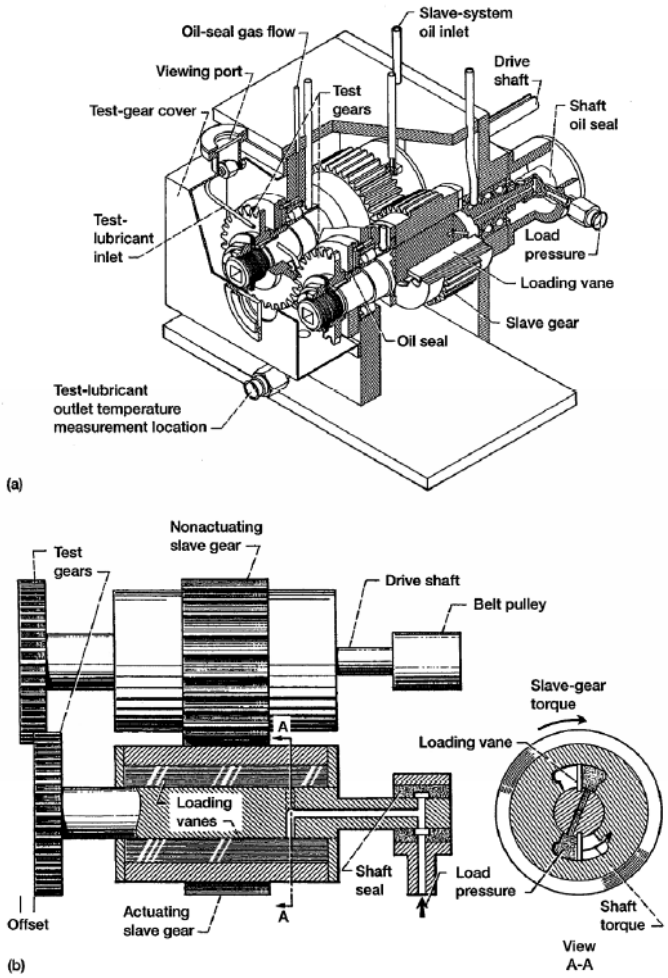

Figure 6.13. NASA GRC gear fatigue test apparatus, (a) cutaway view, (b) schematic view (Fig. 4 of Krantz and Tufts [2007a]).

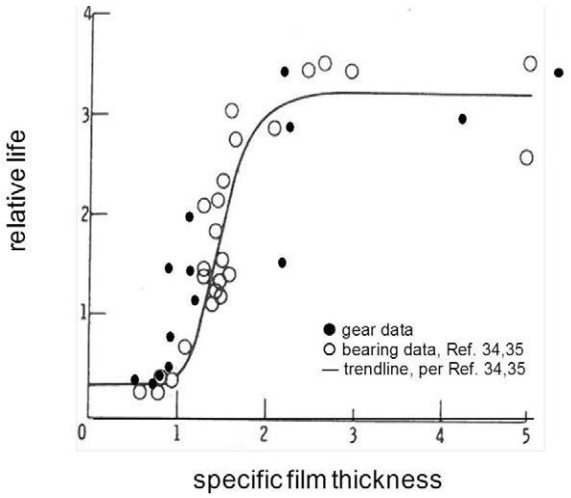

Figure 6.14. Compilation of the bearing life data of Skurka [1970] and Anderson [1970] for cylindrical and tapered roller bearings (open symbols) and the gear life data of this study (solid symbols) (Fig. 10 of Krantz [2014]).

ADVANCED DRIVE SYSTEM COMPONENTS

Modern rotorcraft drive system components operate at high speeds, high loads, and high temperatures, and require state-of-the-art design and materials. Drive research at NASA GRC continues to investigate improvements in components to increase power capacity, reduce weight, reduce noise and vibration, and increase life. One example of this is the use of face gears in helicopter transmissions, which have been identified to significantly reduce weight in a modern military attack helicopter. Experimental fatigue tests were performed to determine the surface durability life of a face gear in mesh with a tapered spur involute pinion [Lewicki et al., 2007a]. The gears were carburized and ground, shot peened and vibro-honed, and made from VIM-VAR Pyrowear 53 steel per AMS 6308 (Fig. 6.15). The gears were tested in the NASA GRC Spiral-Bevel-Gear/Face-Gear Test Facility (Fig. 6.16). From the tests, the surface pitting fatigue allowable stress was determined to validate the design guidelines used in the power train development.

Face gear technology was further developed into a high-power-density gear set that splits torque evenly and quietly along two load paths to demonstrate the power density characteristics of a split-torque face gear concept [Heath et al., 2009]. Full-scale system testing was conducted to verify the endurance of a concept demonstrator transmission. System tests validated that the endurance configuration transmission successfully met the 200-hour test plan. ABAQUS nonlinear contact analysis tools were developed and refined to attain cost-effective solution convergence for multi-mesh FEA face gear models. The capability to design and precision-grind low-angle face gears was validated, allowing future use of this new gear type. The technologies were transitioned to the U.S. Army Apache Block III Program.

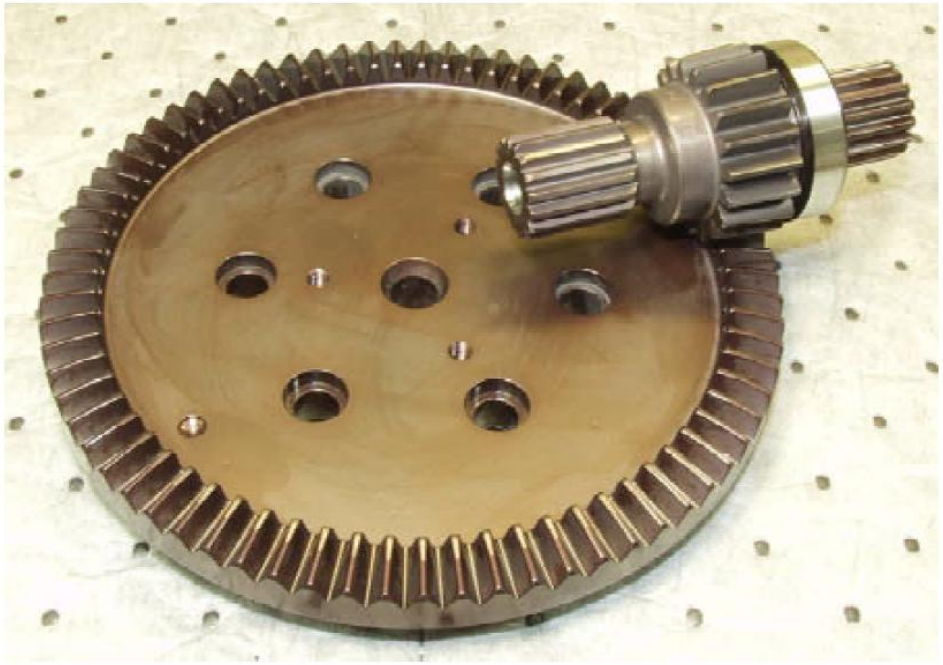

Figure 6.15. Test gear (Fig. 2 of Lewicki et al. [2007a]).

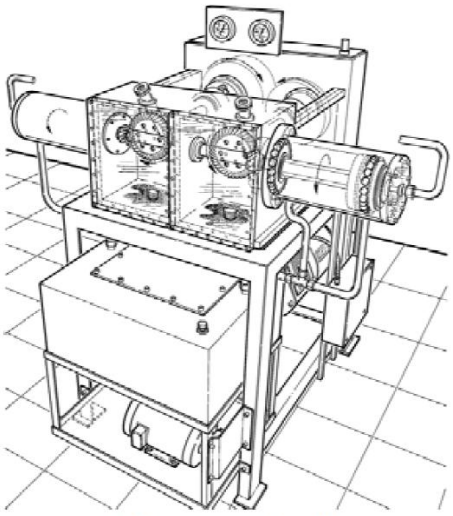

a) Overview of facility.

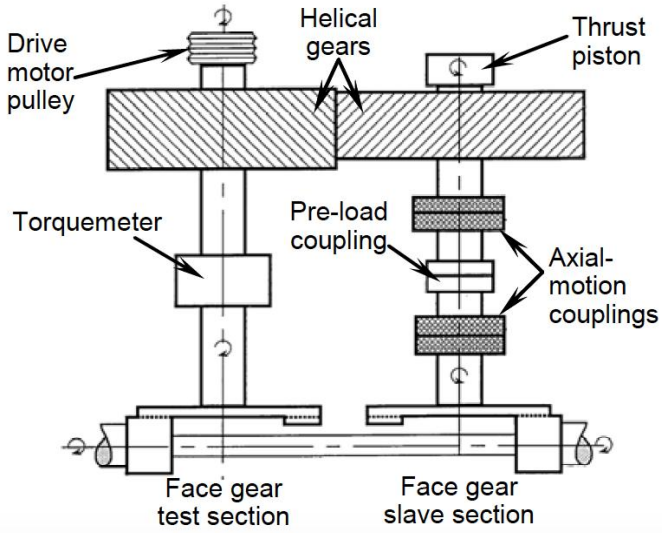

b) Schematic view.

Figure 6.16. NASA GRC Spiral-Bevel-Gear/Face-Gear Test Facility (Fig. 1 of Lewicki et al. [2007a]).

Follow-on studies were performed to evaluate helical face gears for improved power density [Heath et al., 2011]. Here, extensive work was performed to develop helical-face-gear grinding manufacturing equipment (Fig. 6.17), as well as gear-tooth pattern-development tests and improved FEA tools. Figure 6.18 tabulates the test conditions and preliminary results of four sets of helical tapered pinions and helical face gears. The initial tests (sets 1 and 2) were run at 2,300 rpm and 6000 lb-in face-gear speed and torque. Moderate tooth wear and no fatigue failures were observed after 8.2 million face-gear cycles were completed. Sets 3 and 4 were next installed on the right side and run at 2,200 rpm to reduce vibrations. The load was increased to 7200 lb-in face-gear torque, resulting in pinion tooth pitting fatigue failures. However, the surface durability life of helical face gears and isotropic super-finished face gears did not perform as well as expected based on experimental fatigue tests performed at NASA GRC [Lewicki and Heath, 2016].

Figure 6.17. MKII™ face-gear grinding machine (Fig. 6 of Heath et al. [2011]).

Table II. Preliminary Test Results.

Set	Gear Speed (rpm)	Gear Torque (lb-in)	Gear Cycles	Side	Results
1	2200, 2300	6000, 7200	46.1	Left	Suspended, moderate wear
2	2200, 2300	6000, 7200	20.9	Right	Suspended, moderate wear
3	2200	7200	7.7	Right	Pitted/fractured pinion tooth
4	2200	7200	17.5	Right	Pitted pinion tooth

Figure 6.18. Preliminary test results of four sets of helical tapered pinions and helical face gears (Table II of Heath et al. [2011]).

Various studies have been performed for drive system components to analyze, evaluate, and reduce noise and vibration of rotorcraft transmission systems. Studies to evaluate low-noise Formate spiral-bevel gears were performed [Lewicki et al., 2007b, 2007c] on the OH-58D helicopter main-rotor transmission (Fig. 6.19) in the NASA GRC 500-hp Helicopter Transmission Test Stand (Fig. 6.20). The Formate process reduces the time and cost needed for manufacture of spiral-bevel gears. Results showed a decrease in noise with the Formate spiral-bevel design compared to the baseline OH-58D design but not as much reduction as previously tested low-noise designs. The Formate spiral-bevel design gave the same benefit in reduced vibration compared to the baseline OH-58D design and as that of the previously tested low-noise designs. The spiral-bevel pinion tooth fillet stresses for the Formate design showed a significant decrease compared to the baseline OH-58D design, and an even greater decrease than previously tested high-strength and low-noise designs.

In a further study on noise and vibration, a literature survey evaluation of properties for the types of bearings used in helicopter gearboxes was performed [Fleming, 2007a, 2007b]. The vibration-transmitting properties of bearings are of paramount importance to reduce gearbox vibration transfer, and thus, helicopter cabin noise. A novel analytical model was described to enable easy calculation of vibration transfer through different bearings based on bearing stiffness and damping. In another study, a literature survey of vibration control technologies that serve to attenuate helicopter gearbox vibration near the source was performed [Scheidler and Asnani, 2016]. The scope considered vibration control treatments and modifications of the gears, driveline, housing structures, and the strut connections to the airframe. Literature findings are summarized, and persistent and unresolved issues are identified. An emphasis is placed on components and systems that have been demonstrated in flight vehicles. Then, a discussion is presented of emerging technologies that have the potential to make significant advancements over the state of the art.

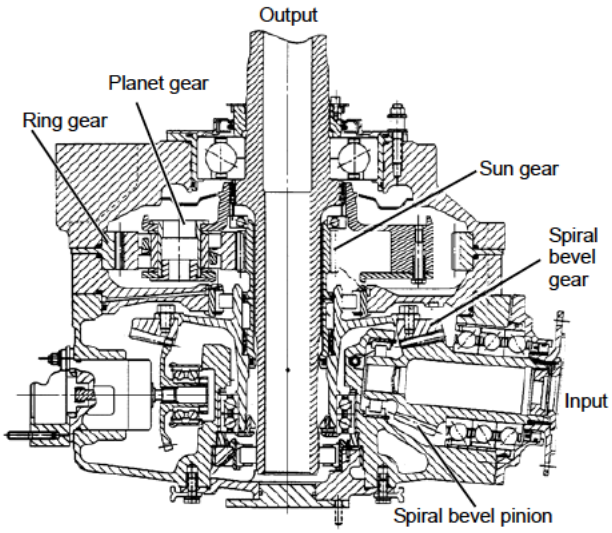

Figure 6.19. OH-58D helicopter main-rotor transmission (Fig. 1 of Lewicki et al. [2007c]).

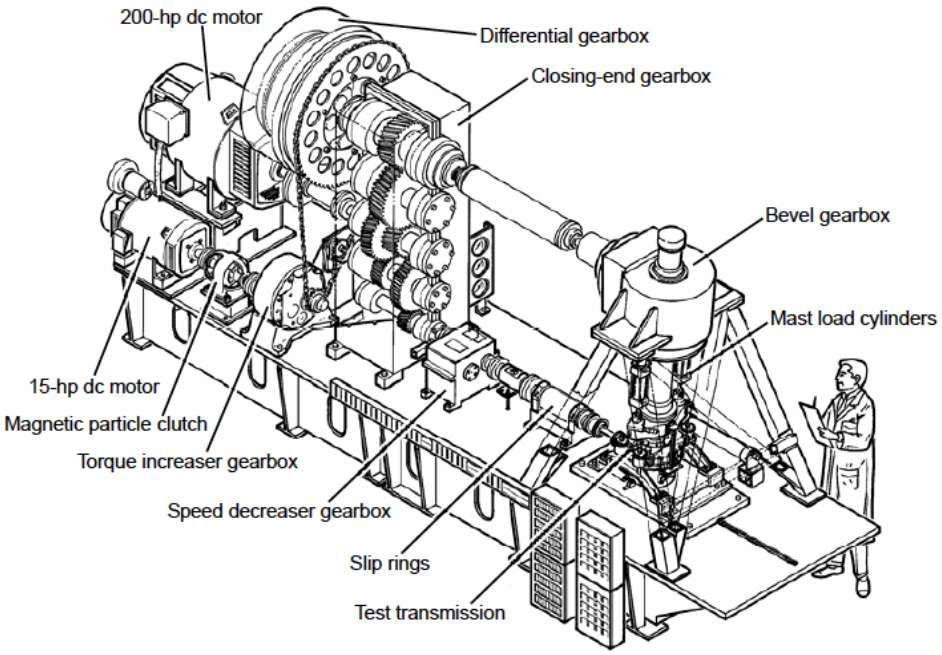

Figure 6.20. NASA GRC 500-hp Helicopter Transmission Test Facility (Fig. 2 of Lewicki et al. [2007c]).

As previously mentioned, composite materials have the potential to reduce the weight of rotating drive system components as well as to alter structural vibration. The use of a graphite/epoxy composite shaft with dynamically tailored extension-twist coupling and a viscoelastic material core aimed at suppressing the gear-mesh-induced instabilities was analyzed [DeSmidt and Zhao, 2010b]. Through structural tailoring of the shaft ply angles and core thickness, coupled gear-shaft modal interactions can be enhanced resulting in the introduction of significant damping into gear mesh mode vibrations and increased stability margin (Fig. 6.21). For a given level of extension-twist coupling there is an optimal core thickness that maximizes the modal energy exchange where the highly damped core becomes dynamically linked with the gear mesh mode increasing the stability margin by roughly a factor of two. However, these composite components are more complex to design and evaluate than static structural components, in part because of limited ability to acquire deformation and failure initiation data during dynamic tests. In another study, improvements in digital image correlation methods were made, allowing deformation measurements to be made during rotating component tests with resolution comparable to that which can be achieved in static tests [Kohlman et al., 2013a, 2013b]. The high-intensity synchronous pulsed light-emitting diode (LED) illumination method was successful in reducing the noise during image capture on rotating composite components for digital image correlation measurement (Fig. 6.22).

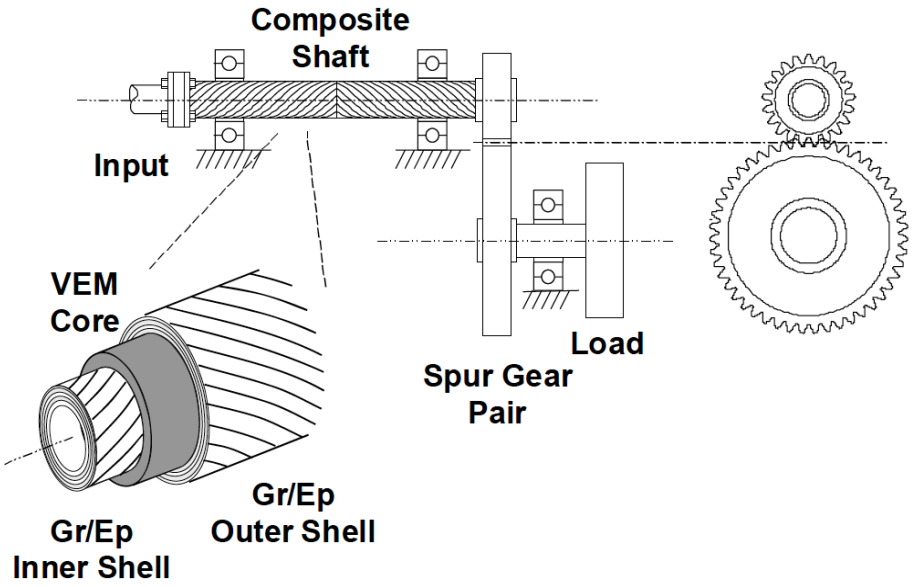

Figure 6.21. Spur gear/composite shaft system (Fig. 1 of DeSmidt and Zhao [2010b]).

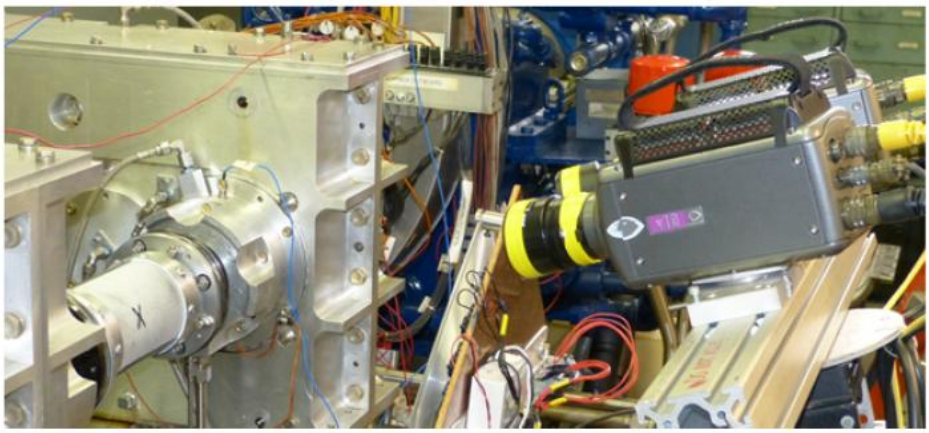

Figure 6.22. Image of the cameras (right), LED array (middle), and shaft (left) (Fig. 2 of Kohlman et al. [2013b]).

To further reduce noise and vibration, a magnetostrictive vibration ring was proposed, which generates electrical energy and dampens vibration when installed in a machine driveline [Deng et al., 2015]. The work focused on optimizing the magnetostrictive elements (Fig. 6.23), which are either Terfenol-D or Galfenol. A parametric study considering loss factor and average electrical output power was conducted using a two-dimensional (2D) axisymmetric finite element model. A prototype vibration ring was designed and tested [Scheidler et al., 2015]. For this prototype, the stiffness was indirectly varied by controlling the excitation current, as opposed to direct variation through control of the magnetic field.

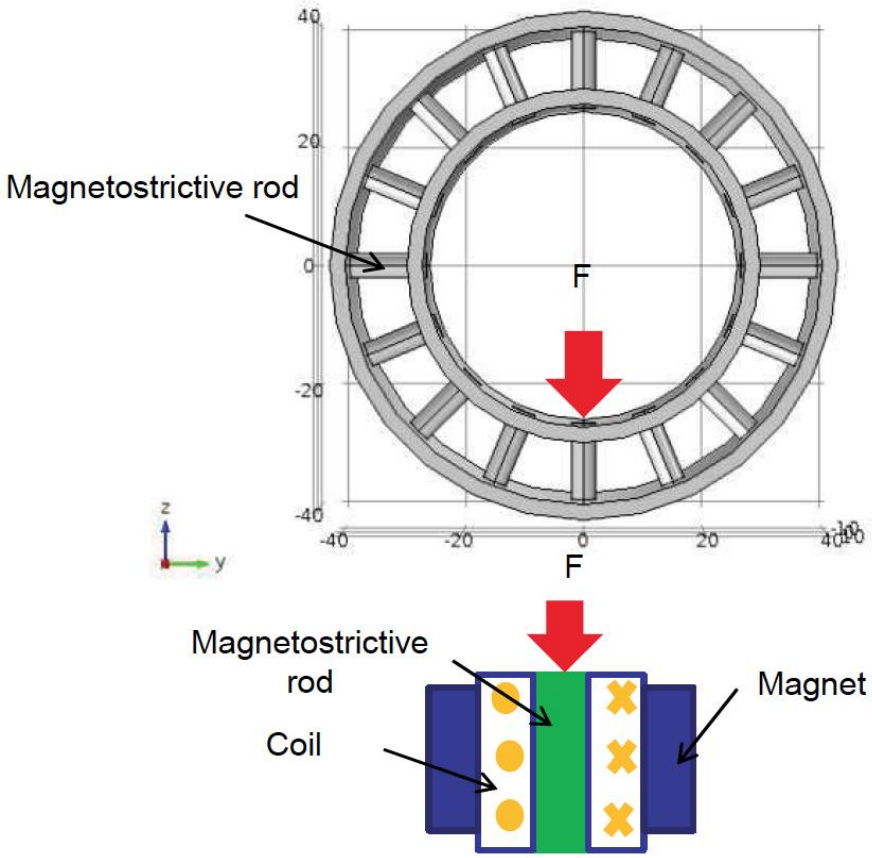

Figure 6.23. Compression spoke design of a magnetostrictive vibration ring. Terfenol-D has a tensile strength of about 28 MPa, thus it must be operated in compression. The Terfenol-D rod is press fit between the two rings. Galfenol can be threaded into the rings, since it has a tensile strength of about 500 MPa and good resistance to torsion and impact. (Fig. 2 of Deng et al. [2015].)

Another method to reduce noise and vibration is the use of a fluid film wave journal bearing to dampen structural gear mesh vibration. To help fluid film wave bearings overcome marginal lubrication at start and stop or oil-off operations, various physical vapor deposition (PVD) coatings were investigated by testing them in a real bearing environment [Dimofte and Krantz, 2008a]. Tests were performed using the NASA GRC Fluid Film Bearing Test Rig (Fig. 6.24) to impose typical operating conditions for aerospace bearings and gears in order to evaluate the PVD coatings' properties for aerospace-transmission applications. Results of the tests for various types of PVD coatings are discussed and compared to the performance of uncoated bearings and gears. A discussion about the consistency of the coating performance is also presented. Additional investigations at the NASA GRC on PVD coatings were performed [Dimofte et al., 2008b]. Diamond Like Carbon (DLC) and Titanium Carbide (TiC) coatings were tested. Preliminary analyses of the coatings were performed before testing, as well as post analyses. The oil-off test revealed the coating performance was better than other tests. The coatings were also investigated at the Laboratory for Machine Tools and Manufacturing Engineering of the Aristotele University of Thessaloniki, Greece, using an innovative indentation technique. The indentation investigations revealed differences in the thickness and adhesion of the coating that could explain the differences in bearing performance during the tests at NASA GRC.

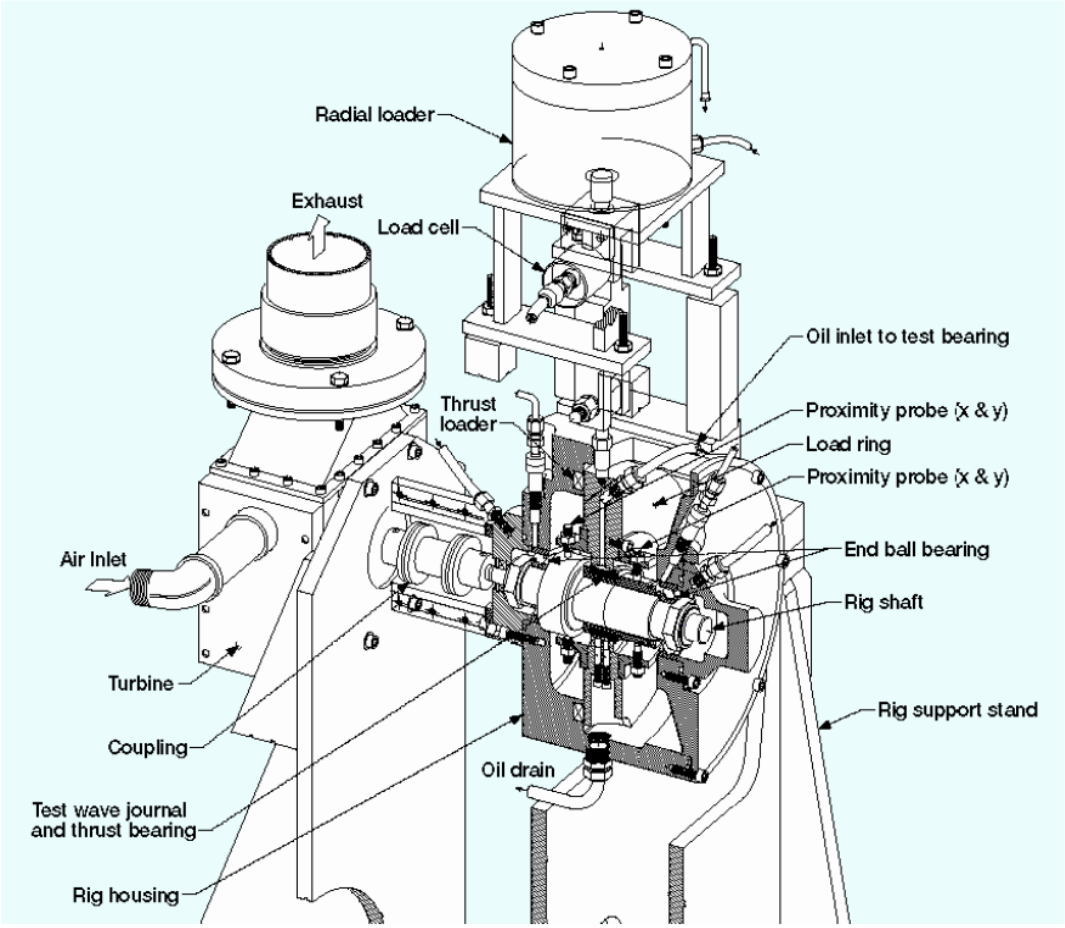

Figure 6.24. NASA GRC Fluid Film Bearing Test Rig, cutaway view (Fig. 1 of Dimofte and Krantz [2008a]).

Experiments were conducted in the NASA GRC Gear Noise Rig to investigate the gear mesh noise and vibration transmission of the fluid film wave bearings compared to rolling-element bearings [Dimofte et al., 2011]. Vibration and noise measurements were recorded at 20 different speeds from 2,000 to 5,800 rpm and three different torques. Tests were performed with the gears supported by both baseline rolling-element bearings and fluid film wave bearings. Results show that for lower-speed operating conditions, the fluid film wave bearings can reduce the gear mesh vibration and noise compared to rolling-element bearings (Fig. 6.25).

Further research in magnetics looked at magnetic gearing as an alternative to mechanical gearing, where torque is transferred through magnetic force as opposed to contact force [Asnani et al., 2018]. The technology has the potential to be used in aircraft applications, without the lubrication, noise, and maintenance issues that can exist with mechanical gearing. Initial design and prototype development work of a magnetic gear (Fig. 6.26) was done at NASA GRC to create a foundational understanding of the technology and the factors that influence its specific torque. The specific torque achieved through design optimization was found to be less than that of high-torque mechanical aircraft transmissions, but may be comparable to that of lower-torque mechanical transmissions for electrified vertical takeoff and landing (VTOL) aircraft.

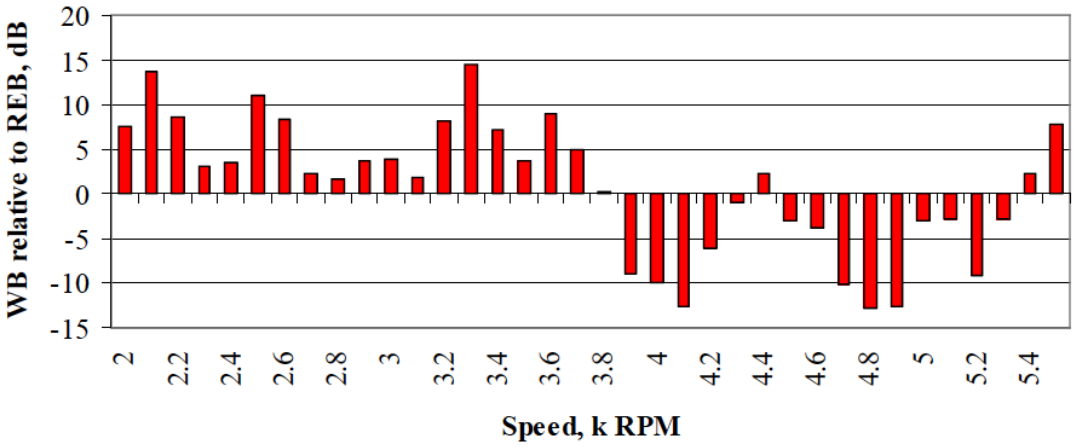

Figure 6.25. Vibration reduction (WB-REB) in vertical direction from accelerometers located at bearing no. 2, 34 N-m torque (Fig. 8 of Dimofte et al. [2011]).

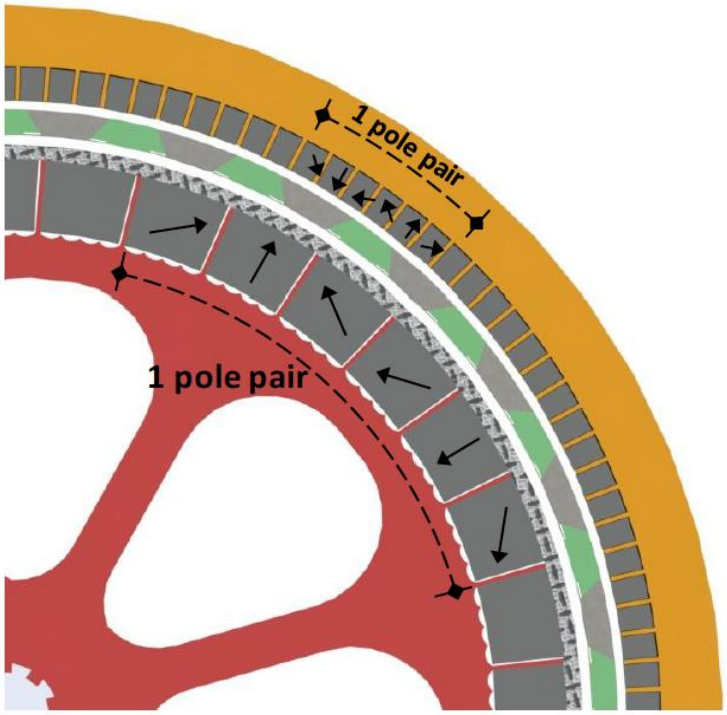

Figure 6.26. Magnetic configuration of PT-2 (Fig. 10 of Asnani et al. [2018]).

In addition to advanced drive system components, advanced transmission configurations were investigated. A new rotorcraft transmission design called the pericyclic configuration was proposed [Cameron et al., 2018]. The pericyclic drive is composed of an input shaft that drives the pericyclic motion converter (PMC) body through the PMC bearings, meshes with the reaction control member gear, and drives the output gear and shaft (Fig. 6.27). The pericyclic transmission provides exceedingly high reduction ratios in a single stage that would normally require multiple gear stages. This could lead to lighter transmissions with fewer components, increased reliability, efficiency, speed, and decreased maintenance costs. A comprehensive look at dynamic loads generated by nutating bodies was performed. Methods to address these dynamic loads, via application of counterbalances and deviation from conventional pericyclic transmission designs, were utilized to negate the dynamic moment of concern.

Lastly, improved dynamic modeling of planetary gears was performed [Guo and Parker, 2009, 2010]. Tooth wedging occurs when a gear tooth comes into contact on the drive-side and back-side simultaneously. Tooth wedging can cause premature bearing failures because of increased loads on the gear teeth. This work studied the nonlinear tooth wedging behavior and its correlation with planet-bearing forces by analyzing the dynamic response of an example planetary gear based on a real application of a wind turbine gear train. A 2D lumped-parameter model was extended to include tooth separation, back-side contact, tooth wedging, and bearing clearances. The simulation results show significant impact of tooth wedging on planet-bearing forces for a wide range of operating speeds.

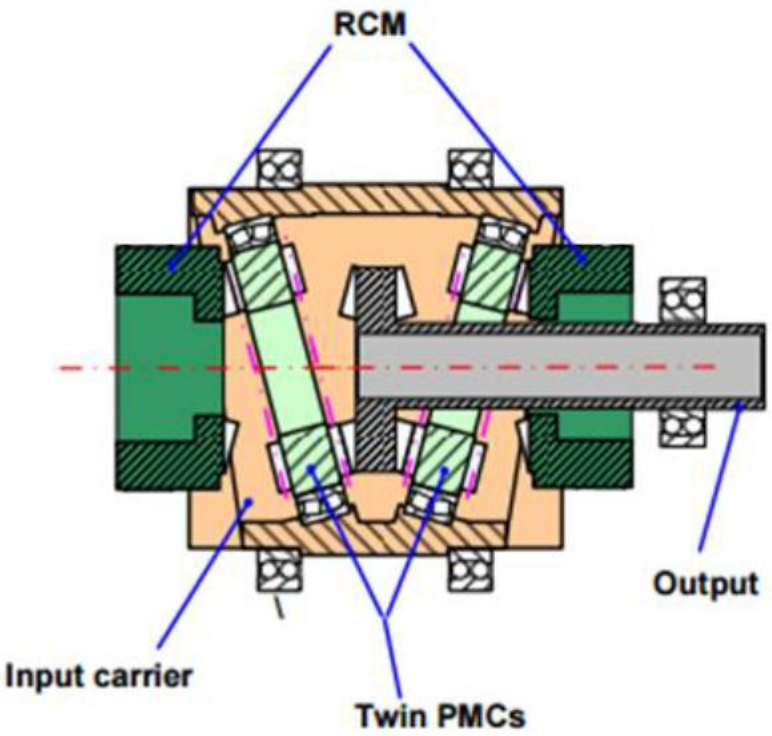

Figure 6.27. Dual PMC pericyclic transmission with external input carrier driving PMC gears (Fig. 1 of Cameron et al. [2018]).

HIGH-SPEED GEARING

High-speed, heavily loaded, and lightweight gearing components are found in propulsion systems for rotorcraft. The high pitch-line velocity that is part of these systems makes the thermal aspects of the gear system design very important. Also, certain applications, such as tiltrotors, have additional thermal problems as the idler gears in these systems receive two meshing cycles (on opposite sides of the gear teeth) per revolution. Therefore, weight-optimized aerospace drive system components can have difficulty when operation includes primary lubrication system failure. An experimental effort using the NASA GRC High-Speed Helical Gear Train Test Facility was conducted on an aerospace-quality helical gear train to investigate the thermal behavior of the gear system [Handschuh et al., 2007c]. In-depth temperature measurements were made across the face width and at the axial end of the gear mesh. The majority of the tests were conducted at extremely high pitch-line velocity; the results indicated that superfinishing (Fig. 6.28) offered no improvement in performance because of the high lubricant film thickness generated at these test conditions.

The tests were then expended to a double helical gear design [Handschuh et al., 2009]. Double helical gear trains that outwardly pump the air-lubricant mixture axially produced the highest performance when compared to other tested conditions that included inward-pumping double helical gears and single helical gear trains (ground and superfinished). The double helical, outward-pumping shrouded arrangement was also the best when lubricant pressure was reduced, providing the lowest temperature increase at nearly all conditions.

Figure 6.28. Close-up of superfinished gear (Fig. 9 of Handschuh et al. [2007c]).

Further studies compared four different design configurations, including the current aircraft design, the current design with isotropic superfinished gear surfaces, a double helical design (inward and outward pumping), and an increased pitch (finer teeth), increased helix angle design [Handschuh et al., 2013a, 2013b]. High-speed-gearing benefits resulted from the use of shrouding when the pitch-line velocity exceeded 15,000 ft/min for which windage losses dominated those from other sources (gear meshing and bearing losses) (Fig. 6.29). Gear design characteristics impacted the drive system power losses where the fine pitch gear design had the least power loss and lowest temperature increase of the lubricant across the gearbox. Also, lubricant jet pressure and flow affected the power loss and temperature change from the inlet to exit of the gearbox. Lower flow resulted in less power required but an increase in temperature across the gearbox.

Analytical modeling of the thermal and fluid dynamics of high-speed gearing has also been performed [Yu et al., 2013]. A multi-scale computational model has been developed for application to the micro- and macro-scale thermo-fluid-dynamics in high-speed gear systems. At the micro-space/time-scale, a model of gear mesh lubrication film transport and heating is presented based on elastohydrodynamic lubrication (EHL) tribology and mesh kinematics. At the macro-space/time-scale, CFD tools are used to resolve the time-dependent conduction and convection (windage) processes within the gears and gearbox. Scale-spanning averaging procedures were developed for coupling the instantaneous meshing and macro-scale physics. Also, the model demonstrated a physically realistic equilibrium under EHL operation (Figs. 6.30 and 6.31).

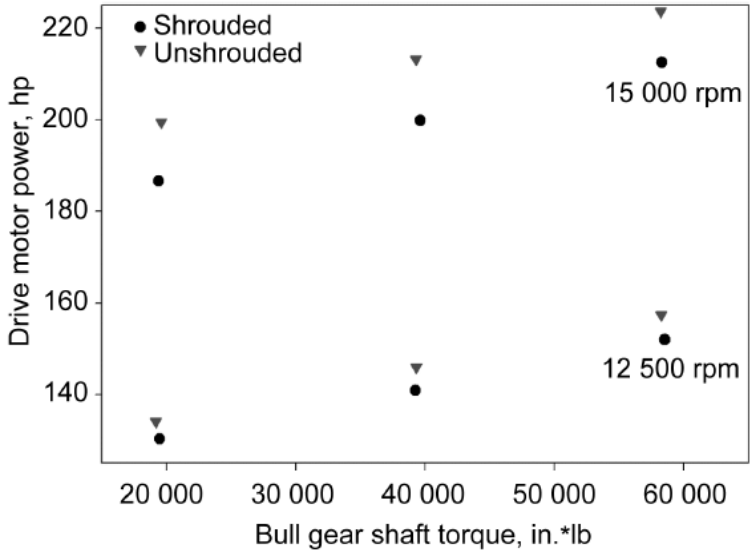

Figure 6.29. Effect of shrouding on drive motor power. Double helical gears, outward pumping, 200°F oil inlet temperature (Fig. 12 of Handschuh et al. [2013b]).

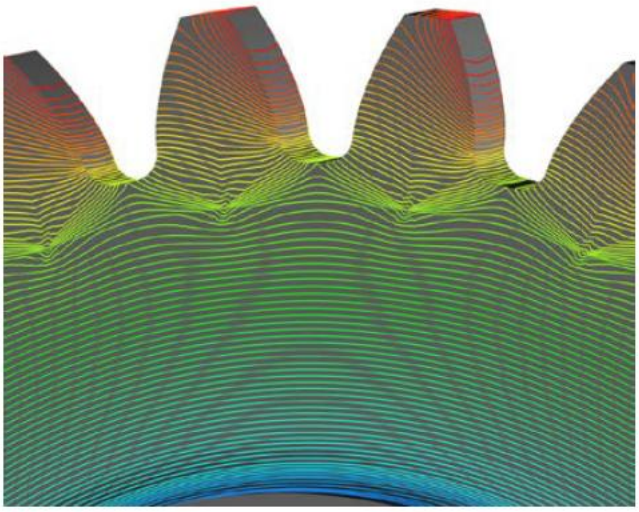

Figure 6.30. Contours of steady temperature distribution (Fig. 20 of Yu et al. [2013]).

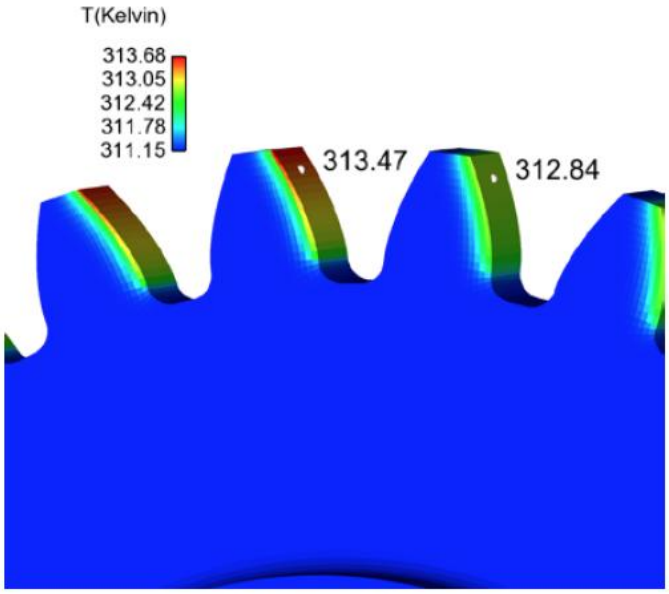

Figure 6.31. Temperature at mesh after 10 revolutions (Fig. 21 of Yu et al. [2013]).

LUBRICATION

Advances in the development of future rotorcraft drive systems will depend on successful high-temperature lubrication for the bearings and gears. In addition, the drive system used in rotorcraft applications has to pass a 30-minute loss-of-lubrication test prior to aircraft certification, meaning that the drive system must continue to operate for 30 minutes with the primary lubrication system inoperative. Current state-of-the-art organic liquid lubricants rapidly degrade at temperatures above 300°C, thus, another form of lubrication is necessary. Vapor or mist phase reaction lubrication is a unique, alternative technology for high-temperature lubrication. The majority of past studies have employed a liquid phosphate ester that was vaporized or misted, and delivered to bearings or gears where the phosphate ester reacted with the metal surfaces generating a solid lubricious film. This method resulted in acceptable operating temperatures suggesting some good lubrication properties, but the continuous reaction between the phosphate ester and the iron surfaces led to wear rates unacceptable for gas turbine engine or aircraft gearbox applications. In a NASA study, an alternative nonphosphate liquid was used to mist phase lubricate a spur gearbox rig operating at 10,000 rpm under highly loaded conditions [Morales et al., 2007a, 2007b]. After 21 million shaft revolutions of operation the gears exhibited only minor wear (Fig. 6.32).

To further address these needs, an experimental program to determine the loss-of-lubrication characteristics of spur gears in an aerospace simulation test facility has been completed [Handschuh et al., 2011b, 2011c]. The system consisted of a shrouded spur gear pair with a lubricating jet and provisions for emergency lubrication systems (Fig. 6.33). The lubricant, delivery method, gear design, and gear material were all parameters altered during testing. From the results, tests without any emergency lubrication system in a shrouded gearbox led to failure within several minutes (Fig. 6.34). Gear material and gear backlash may have some benefit in increasing loss-of-lubrication behavior, but this would need further verification through additional testing. Grease injection was demonstrated to be a viable emergency lubrication system, but it requires greater evolution to determine if it can be used in an aerospace environment.

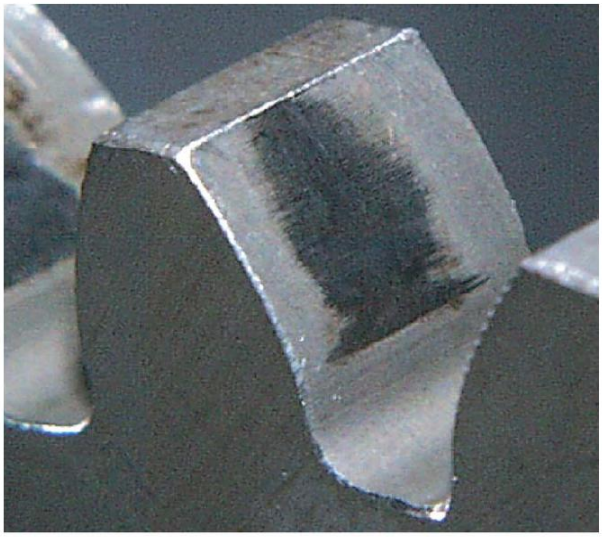

Figure 6.32. Typical condition of gear-tooth surface after 7.6 million shaft revolutions at test speed and load (Fig. 7 of Morales et al. [2007b]).

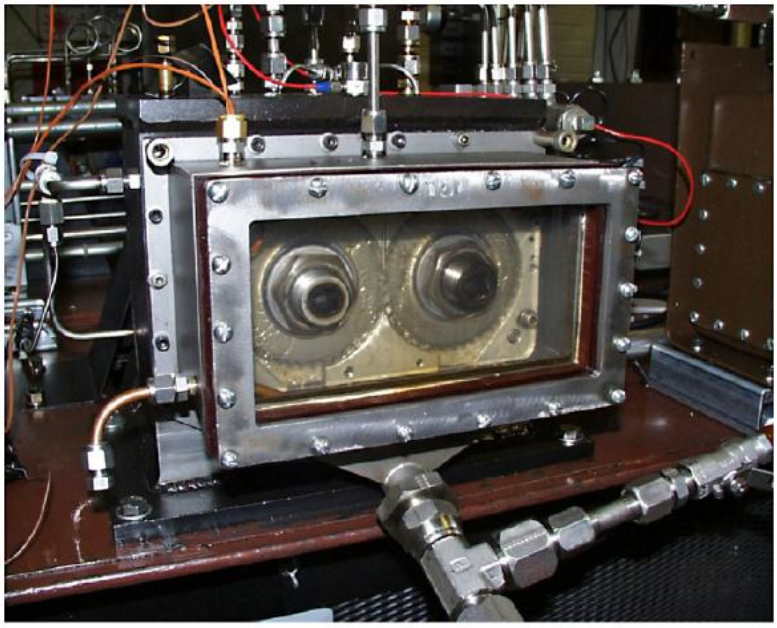

Figure 6.33. Current test gearbox arrangement using shrouds and improved lubricant drainage (Fig. 4 of Handschuh et al. [2011c]).

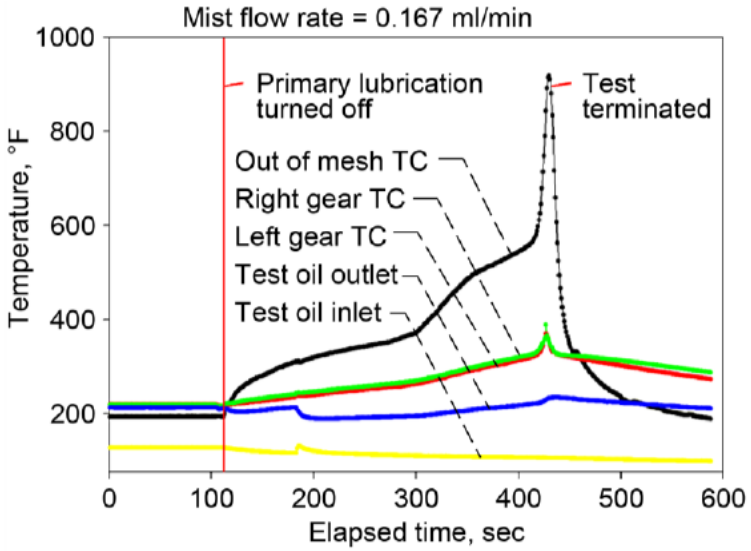

Figure 6.34. Loss of lubrication data from test that failed after 6 minutes (Fig. 7 of Handschuh et al. [2011c]).

Further studies were performed to gain additional loss-of-lubrication understanding for gears [Handschuh, 2015]. The results showed that a 40-percent increase of torque resulted in a decrease in average loss-of-lubrication operation time by 75 percent. Operation in loss-of-lubrication mode at lower torque produced an elevated steady-state temperature condition. During the higher torque tests, the temperature continued to increase until failure of the teeth. A high-speed, full-field, infrared thermal imaging system was utilized in the unshrouded and instrumented gear test. The results attained agreed with that found using thermocouples (Fig. 6.35).

The preceding experiments also led to the development of a comprehensive gearbox aero-thermodynamics and tribology simulation tool, applicable to both well-lubricated and loss-of-lubrication operation [McIntyre and Kunz, 2017]. The simulation employs a multi-scale approach. Included are meshing tribology, convection heat transfer within the system and to the environment, high-frequency thermodynamic effects induced by the gear meshing frequency, and the long-time response of the overall gearbox temperature to a net imbalance of heat generation and transfer to the environment. These factors are simulated separately and coupled with one another iteratively through appropriate boundary and initial conditions. Figure 6.36 shows flow streamlines colored by temperature for a simulation of the simplified gearbox geometry.

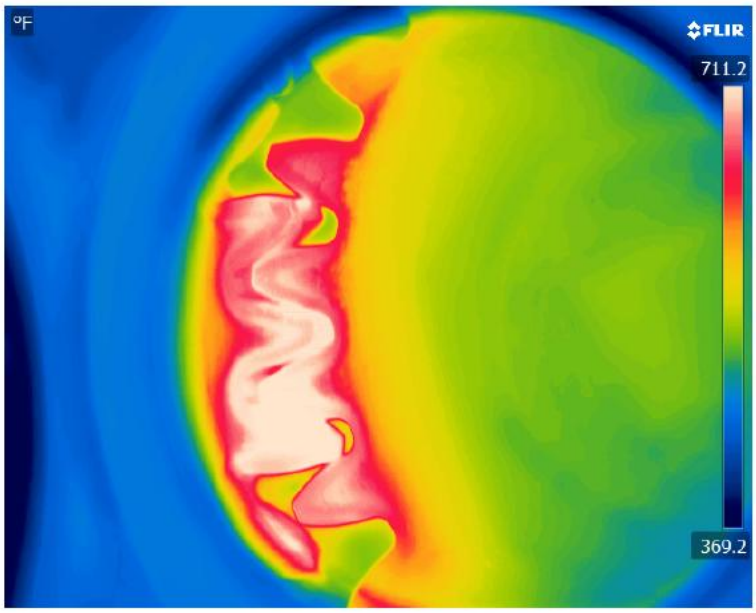

Figure 6.35. Thermal image of unshrouded gear nearer to test completion (10,000 rpm, 59.3 N-m (525 in-lb)). (Fig. 23 of Handschuh [2015].)

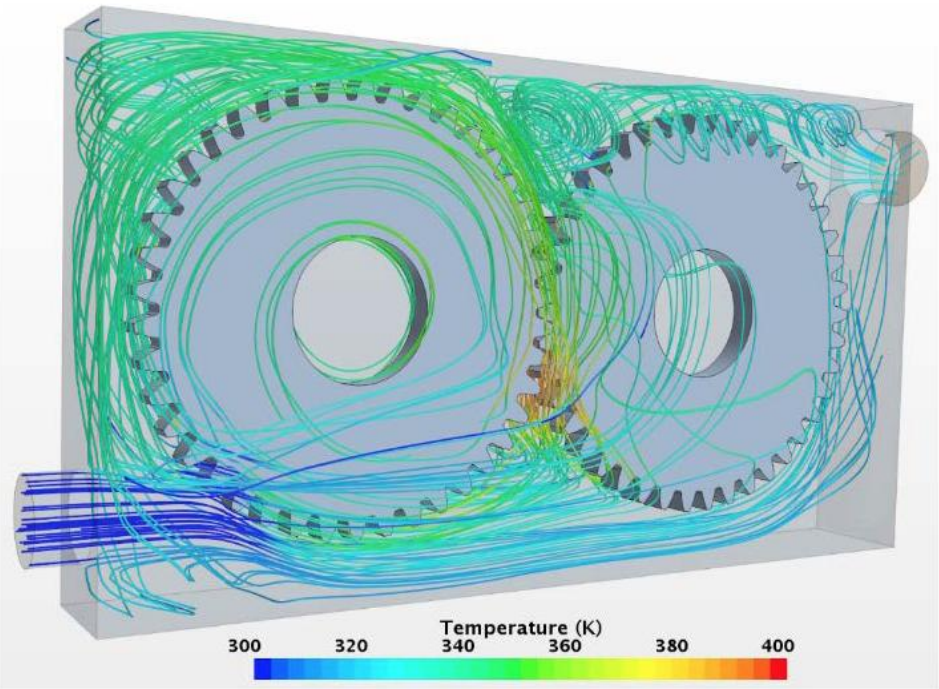

Figure 6.36. Flow streamlines colored by temperature (Fig. 21 of McIntyre and Kunz [2017]).

HEALTH MONITORING AND CONDITION-BASED MAINTENANCE

Rotorcraft drive system integrity is important to safety because rotorcraft depend on the power train for propulsion, lift, and flight maneuvering. Drive system health monitoring has the potential for both economic and safety benefits. If component usage is more severe than the design life of a component, health monitoring can provide safety benefits. If component health has degraded because of anomalies caused by harsh operational environments, limited maintenance, assembly errors, or manufacturing faults, health monitoring can also provide safety benefits. If component usage is less severe, and no anomalies are detected by the monitoring systems, the service life (time between component replacement or overhauls) of components may be extended. This is known as condition-based maintenance (CBM). In order to identify anomalies/faults that occur in the field within a specific component, the health monitoring system must demonstrate a high level of reliability to detect anomalies/faults with minimal false alarms.

Identification of the health of the gears in rotorcraft drive systems is crucial. Because of the expertise in rotorcraft drive systems as well as available test facilities, NASA GRC has performed extensive research in gear health and diagnostics over the past 10 years. An initial overview of guidelines used by the Federal Aviation Administration (FAA) in the U.S. and Civil Aviation Authority in the U.K. in developing and certifying health monitoring systems for gear systems was performed [Dempsey et al., 2007a]. Techniques used to process vibration data to calculate condition indicators (CIs) in commercial systems and different methods used to set

thresholds to detect damage were studied. Also, an initial assessment of a method to set thresholds applied to flight and test rig data was presented. Gear CI FM4 distribution values on a healthy OH-58 helicopter and a healthy OH-58 transmission test stand were similar. Distributions between healthy and damaged gears on the test rig showed significant differences.

A study was performed to evaluate fault detection effectiveness as applied to gear-tooth pitting fatigue damage [Lewicki et al., 2009, 2010b]. Vibration and oil-debris monitoring (ODM) data were gathered from 24 sets of spur pinion and face gears run during a previous endurance evaluation study. Three common gear health CIs (RMS, FM4, and NA4) were deduced from the time-averaged vibration data and used with the ODM to evaluate their performance for gear fault detection. The NA4 parameter was a very good CI for the detection of gear-tooth surface pitting failures (Fig. 6.37).

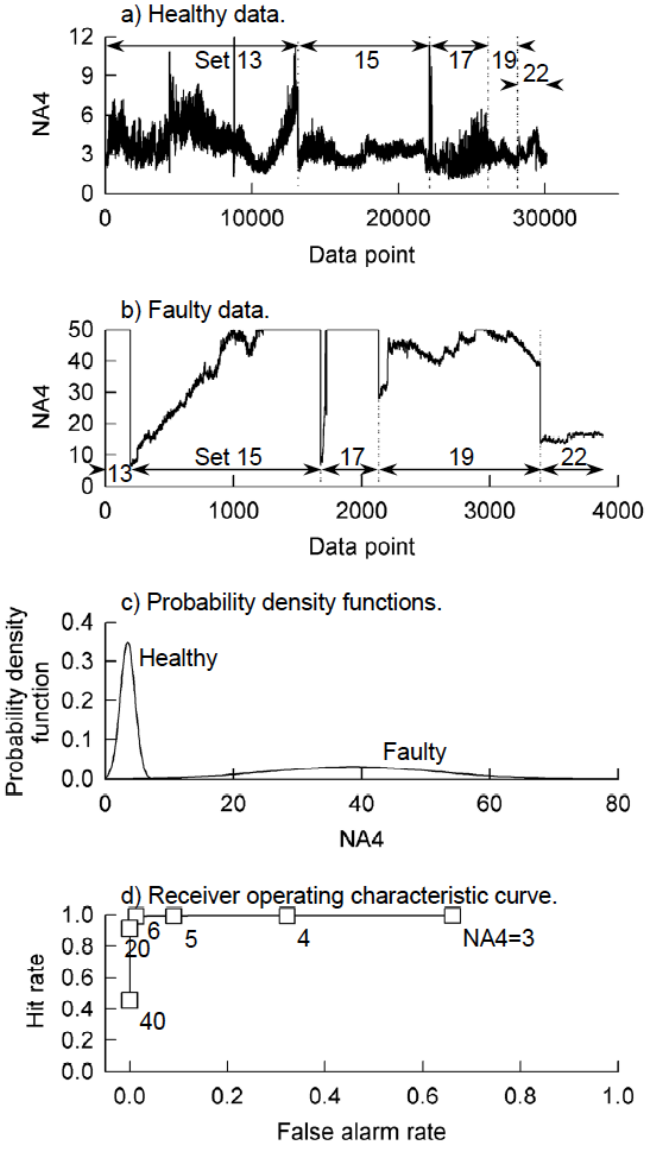

Figure 6.37. Summary results for NA4 CIs for macro-pitting, single/few teeth failures (Fig. 11 of Lewicki et al. [2009]).

Based on extensive experience in gear diagnostics, NASA GRC collaborated with the U.S. Army in identifying the most effective gear CIs for fleet use based on both a theoretical foundation and field data [Antolick et al., 2010]. Results of more than 5 years of health monitoring for gear faults of Army helicopters equipped with health and usage monitoring systems (HUMS) are presented. More than 10 examples of gear faults indicated by gear CIs have been compiled and each reviewed for accuracy. False alarm indications and performance data from test rigs and seeded-fault tests are also presented. Three algorithms have proven reliable on most spiral-bevel-gear damage cases examined: Sideband Index, Sideband Level Factor, and DA1. These algorithms, however, warrant further research and enhancements.

Previous studies showed it was very difficult to establish thresholds or limits for gear-vibration-based CIs that distinctly show when a gear is in need of maintenance. Further, no single CI was sensitive to every failure mode of a gear. This suggested that any CBM system for gears should have some form of sensor fusion. Gear CI thresholds based on statistics and some small probability of false alarm were investigated [Bechhoefer et al., 2011]. Three statistical models were developed to define a gear health indicator (HI) as a function of CI: order statistics (max of n CIs), sum of CIs, and normalized energy. These models were developed for CIs with Gaussian or Rayleigh (skewed) distributions. Finally, these functions, used to generate HIs, were tested on gear test stand data and their performance evaluated as compared to the end state of the gear. Results show the HIs performed well detecting pitting damage to gears (Fig. 6.38). A follow-on integrated approach for gear health prognostics was performed using particle filters [He et al., 2012]. The presented method effectively addressed the issues in applying particle filters to gear health prognostics by integrating several new components into a particle filter. These were data-mining-based techniques to effectively define the degradation state transition and measurement functions using a one-dimensional health index obtained by whitening transform, and an unbiased one-step-ahead remaining useful life (RUL) estimator updated with measurement errors. The feasibility of the presented prognostics method was validated using data from a spiral-bevel-gear case study.

Further investigation using data fusion explored the application of wind turbine drivetrain gears [Dempsey and Sheng, 2011a]. Vibration-based health-monitoring techniques, oil debris analysis techniques, and wind turbine operational parameters, combined using data fusion, provided improved detection and decision-making capabilities as compared to that provided by individual diagnostic tools (Fig. 6.39). Data were collected from healthy and damaged gearboxes, both tested on the National Renewable Energy Laboratory (NREL) dynamometer test stand. Vibration and oil debris data were collected along with torque and speed data. Results indicate that the vibration-based CI Sideband Index can be used to indicate damage to the gear teeth of the high-speed-shaft gear set. Quantifying the strengths, weaknesses, and constraints of each measurement technology currently used to monitor wind turbine health, and then capitalizing on these strengths via data fusion, is the key to the development of future health-monitoring systems.

An overview of 2011 time frame rotorcraft health monitoring technologies for detecting anomalies in dynamic mechanical systems is presented in Dempsey and Zakrajsek [2011b]. Standard practices in acquiring and processing vibration data are discussed, lessons learned from systems currently installed on rotorcraft are summarized, and future challenges to developing more advanced rotorcraft health monitoring systems are outlined.

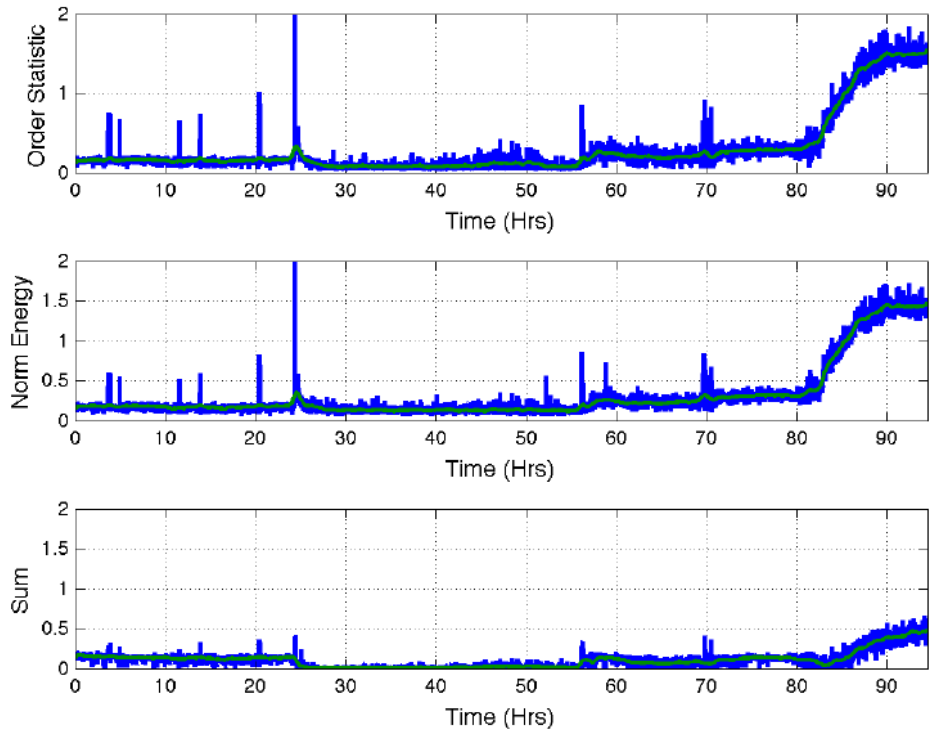

Figure 6.38. Test BV2_10_15_01EX4 (Fig. 2 of Bechhoefer et al. [2011]).

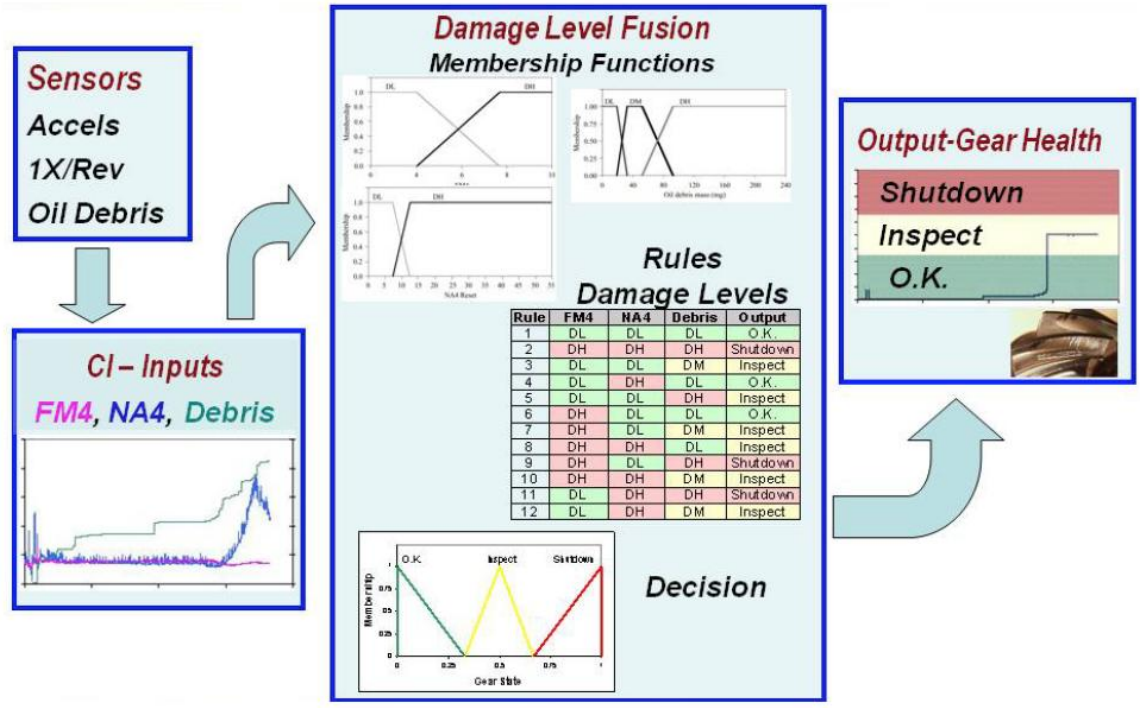

Figure 6.39. Fusion applied to rotorcraft spiral-bevel gears (Fig. 11 of Dempsey and Sheng [2011a]).

Just considering oil analysis for gear health, a study was performed comparing the performance of an inductance in-line oil debris sensor and a magnetic plug oil debris sensor when detecting transmission component health in the same system under the same operating conditions [Dempsey et al., 2012]. Both sensors were installed in series in the NASA GRC Spiral Bevel Gear Fatigue Rig during tests performed on five gear sets when different levels of damage occurred on the gear teeth. Results of this analysis found that both the inductance in-line oil debris sensor and the magnetic plug oil debris sensor have benefits and limitations when detecting gearbox component damage (Fig. 6.40). The inductance-type oil debris sensor provides a good indication of damage progression for slow-progressing fatigue failures that generate particles less than the sensor's upper limit defined by sensor type and signal saturation of the electronics. The magnetic chip detector is a simple low-cost sensor that provides a good indication of gear failure modes that generate debris particle sizes that exceed the particle size upper limit on the inductance-type oil debris sensor and bin size.

Further work on the Sideband Index CI to detect contact fatigue damage on spiral-bevel gears was investigated [Dempsey, 2013a]. Tests were performed in the NASA GRC Spiral Bevel Gear Fatigue Rig on eight prototype gear sets during four damage progression tests. Vibration data were measured at varying torques, while varying modes and levels of tooth damage were observed. For these tests, individual, average, and maximum Sideband Indexes responded differently for each test, torques, damage levels, damage modes, and component. The performance of CI RMS was also evaluated for its ability to detect spiral-bevel gear-tooth damage. RMS values trended with damage progression when torque was maintained but did not trend well with damage progression at varying torque levels.

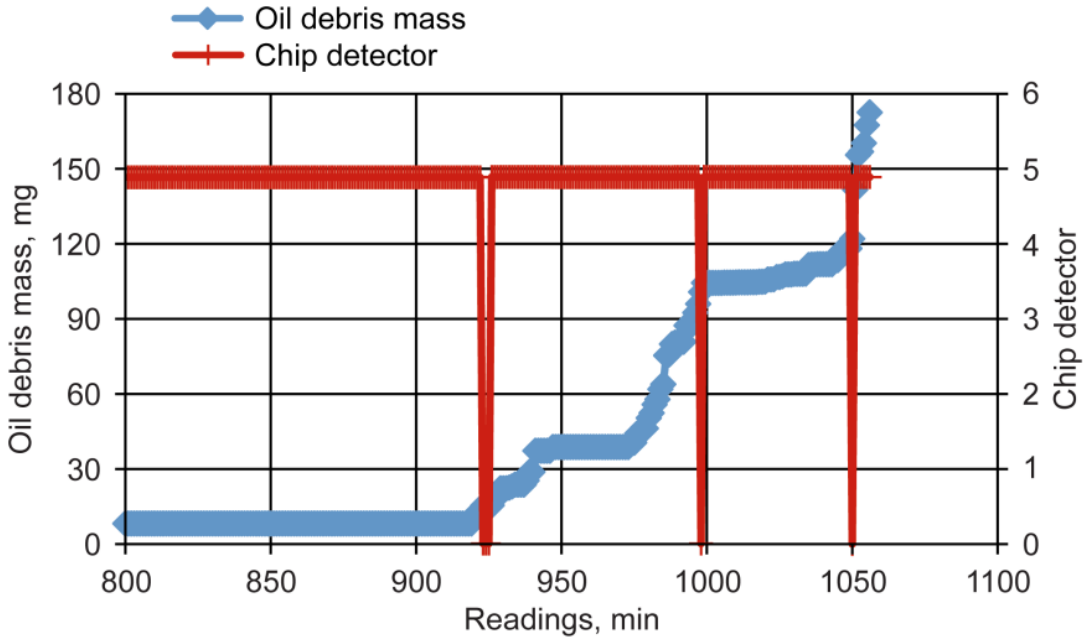

Figure 6.40. Sensor data for Test 5 (Fig. 10 of Dempsey et al. [2012]).

The benefit of combining usage operational parameters with gear fault CIs was studied for the potential to improve the performance and reliability of both systems to indicate progression of damage and remaining time in operation [Dempsey et al., 2013b, 2013c]. Three gear sets were tested in the NASA GRC Spiral Bevel Gear Fatigue Rig. Damage was initiated and progressed on the gear and pinion teeth. Damage progression was measured by debris generation and documented with inspection photos at varying torque values (Fig. 6.41). A contact fatigue analysis was applied to the gear design indicating the effect of temperature, load, and reliability on gear life. Results of this study illustrated the benefits of combining HUMS data and actual usage data to indicate progression of damage for spiral-bevel gears. Decreasing both temperature and load can increase the fatigue life of the components.

In further collaboration with the U.S. Army, gear CI performance validation methods that combined in-service faulted spiral-bevel-gears data from helicopters in the field with seeded-fault tests on spiral-bevel gears were studied [Dempsey and Brandon, 2013d, 2013e]. For this approach, existing in-service HUMS flight data from naturally occurring faults were used to define the requirements for spiral-bevel-gear seeded-fault tests. Gear CI data from AH-64 helicopter nose gearboxes were used. The tested gears were designed with comparable material, heat treatments, and tooth contact loads as the helicopter gears. Using spiral-bevel gears as an example, the hybrid approach was mapped to standards for using seeded-fault tests for HUMS validation presented in the U.S. Army Aeronautical Design Standard Handbook for CBM. Further details of the AH-64 nose gearbox analysis are given in Delgado et al. [2013a, 2013b]. Ten nose gearbox data sets underwent two specific analyses. A mean CI-level analysis was performed where CI performance was based on a “batting average” measured before and after part replacement. Two specific CIs, Diagnostic Algorithm 1 and Sideband Index, were found to perform well for the data sets studied. A CI versus gear-wear analysis was also performed, where gear-wear photographs and descriptions from Army tear-down analyses were categorized based on ANSI/AGMA 1010-E95 standards.

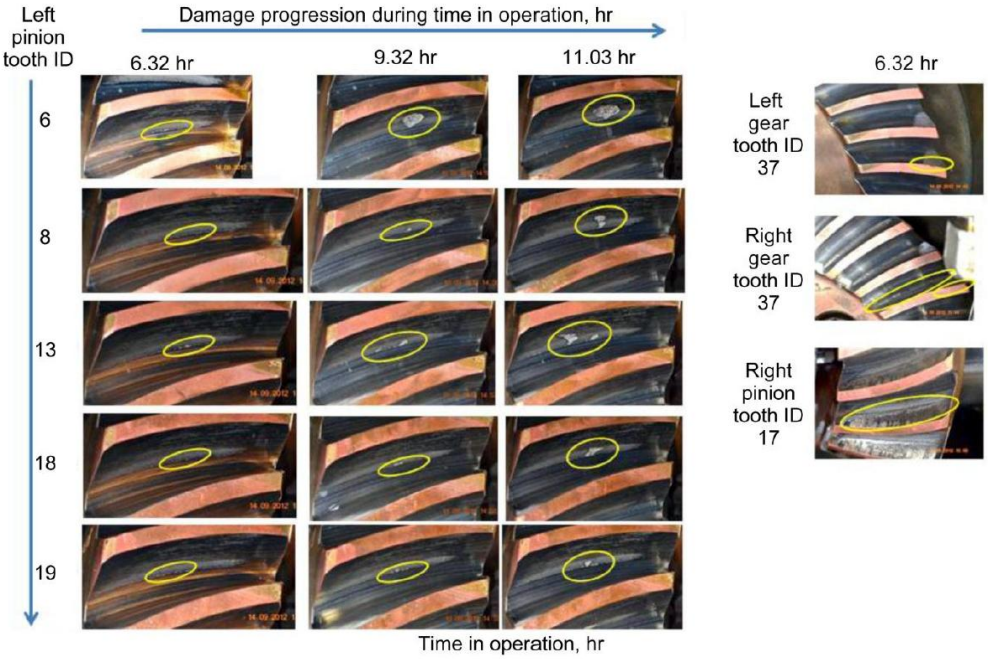

Figure 6.41. Damage conditions on teeth during Test 1 (Fig. 5 of Dempsey et al. [2013b]).

In other studies, the effect of the structural vibration transfer path on gearbox vibration and gear health indication was investigated. Vibration transfer paths are characterized by frequency response functions derived from the input/output relationship between applied force and dynamic response through a structure as a function of frequency. With an objective to investigate the differences in transfer paths, transfer path measurements were recorded under similar conditions in the left- and right-nose gearboxes of an AH-64 helicopter and in an isolated left-nose gearbox in a test fixture at NASA GRC [Islam et al., 2013, 2014]. The test fixture enabled the application of measured torques, common during an actual operation. An impact hammer as well as commercial and laboratory piezoelectric shakers were used in conjunction with two types of commercially available accelerometers to collect the vibration response under various test conditions. The frequency response functions measured under comparable conditions of both systems were found to be consistent. Gear vibration transfer path dynamics appeared to be somewhat dependent on the presence of oil, and the transfer path dynamics were notably different if the force input was on the internal ring gear rather than on the external gearbox case. Transfer path measurements taken on the test rig to assess the utility of static vibration transfer paths in determining dynamic gear CI performance provided some insight into gear CI performance [Dempsey et al., 2013f]. Although some useful information can be gleaned from static transfer path measurements, the system structure (such as the test rig or helicopter gearboxes) did not significantly affect the vibration response of an accelerometer to the dynamic gear mesh signatures. It was more important to understand the dynamic characteristics unique to each system to be used for CI development that affect individual gear CI response for a healthy and damaged tooth.

In further work regarding data fusion, a software tool was developed to fuse the data generated from three individual data acquisitions systems and damage progression photos during spiral-bevel-gear damage progression tests in the NASA GRC Spiral Bevel Gear Fatigue Test Rig [Dempsey et al., 2014a]. The response of gear CIs RMS, FM4, and average Sideband Indexes were compared to gear-tooth damage progression, gearbox oil temperatures, and applied torque. The tool enabled comparison of CI performance for different damage modes. CI data were also correlated with the operational conditions that the gear sets were exposed to during damage initiation and progression (Fig. 6.42). Results found sensitivities of some CIs to damage modes, levels of damage, and environmental conditions that must be taken into consideration when developing reliable gear health monitoring tools.

In addition to advancement of existing gear health CIs, new methods for fault detection were being investigated. A new method called the transient impulse response–based method (TIRM) was introduced for gear condition monitoring [Chen et al., 2014]. TIRM is based on the characteristic features of the transient impulse response: 1) the impulse response is carried by an invariant system natural frequency called the carrier frequency, and 2) the magnitude of impulse response is proportional to the meshing force impulse. TIRM was applied to four gear vibration data sets from the NASA GRC Spiral Bevel Gear Fatigue Test Rig. TIRM was competitive with other prevalent CIs in providing effective detection of the gear damage severity, and offered superior performance in locating the damage source in the gear/pinion pairs (Fig. 6.43).

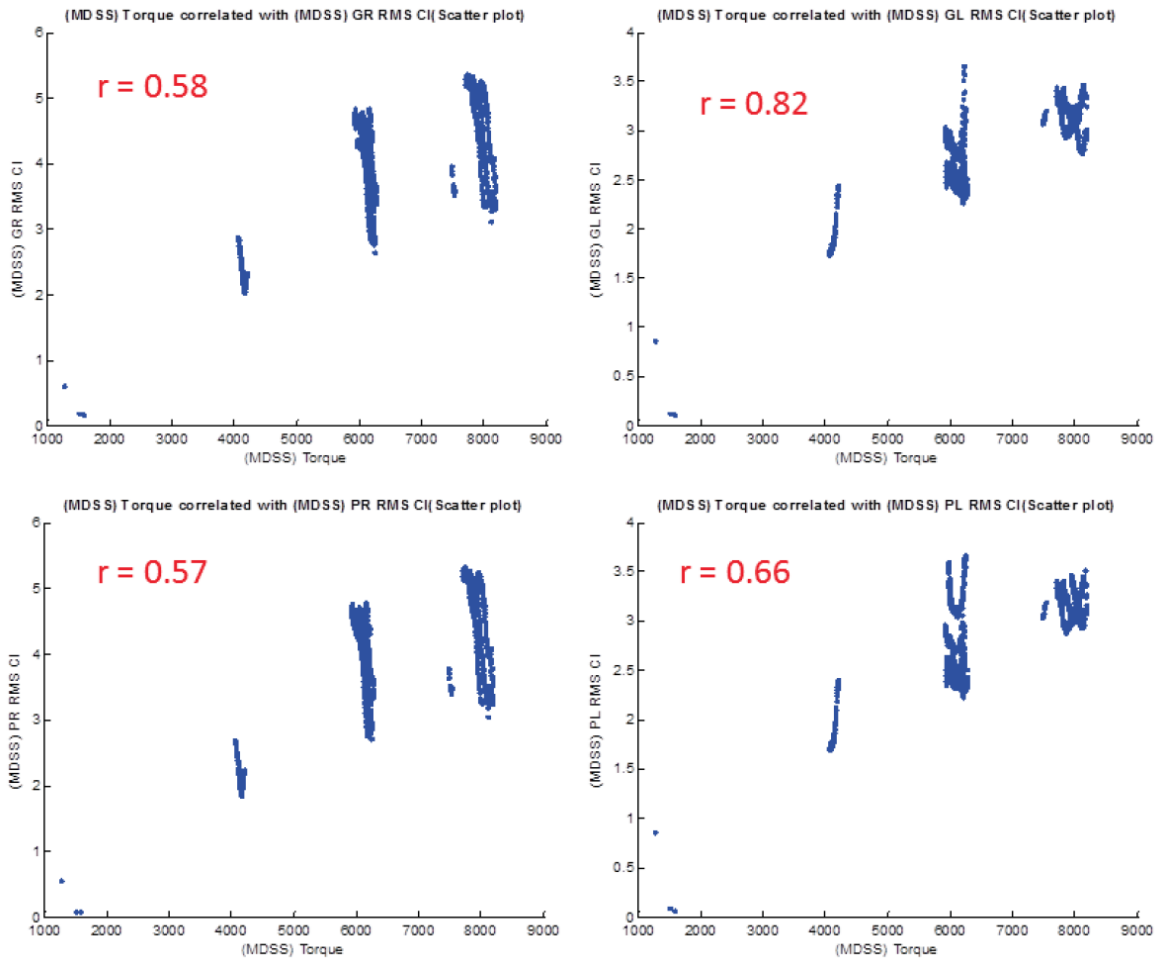

Figure 6.42. Correlation between RMS and torques (Fig. 20 of Dempsey et al. [2014a]).

In another study, a new prognostic estimation technique for an online gear health management system was proposed and demonstrated with spiral-bevel-gear run-to-failure test data [Yoon et al., 2014]. Unlike conventional particle-filter-based prognostic estimation methods, the prognostic technique presented in this work was a hybrid of the unscented Kalman filter and particle filter. It was designed to improve the processing efficiency while the state estimation accuracy was maintained. The unscented Kalman filter was used to obtain the "best estimate" of the states of a degrading nonlinear component. The particle filter one-step-ahead prediction technique was employed to obtain the RUL of the component. The prognostic estimator was demonstrated with satisfactory results using the data obtained from the NASA GRC Spiral Bevel Gear Fatigue Test Rig (Fig. 6.44). Lastly, a study was performed for ranking gear health CIs and developing algorithms that fuse multiple gear CIs into a single health index [Siegel et al., 2014]. Again, data from the NASA Spiral Bevel Test Facility were used. Three different variable ranking methods based on the Fisher criterion, the area under the receiver operating characteristic curve, and the monotonic criteria were weighted together to rank and select the best performing CIs. A principal component-based HI provided the most consistent health trend when compared with the distribution overlap and auto-associative neural network methods (Fig. 6.45).

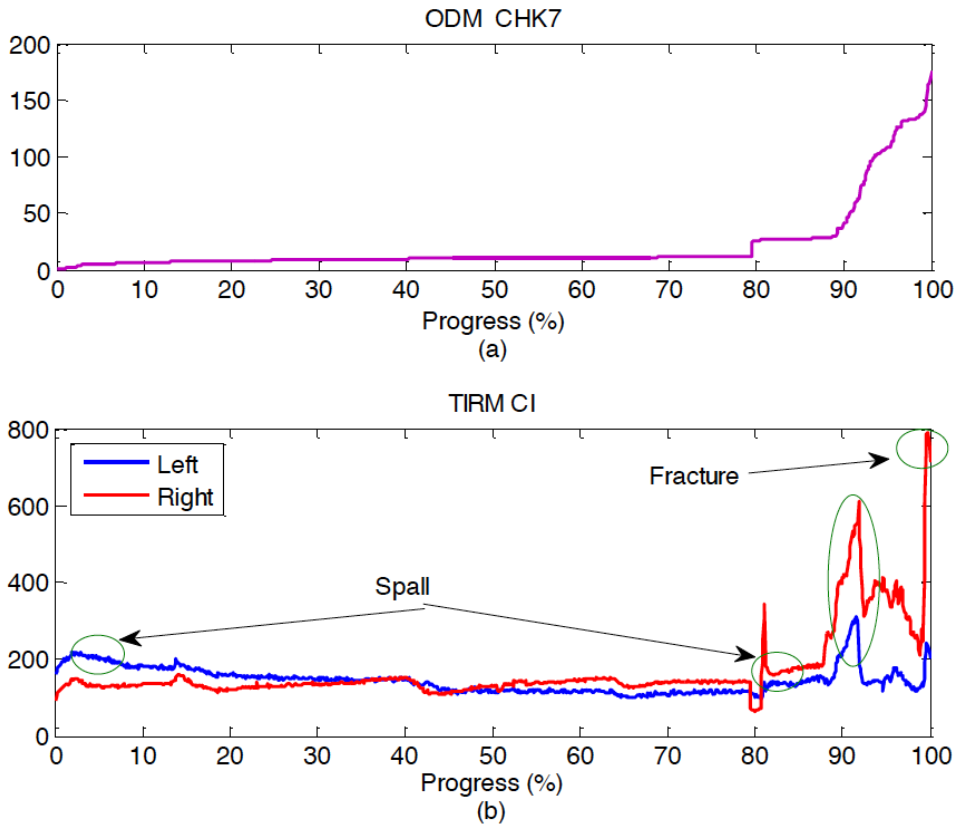

Figure 6.43. (a) ODM history, and (b) TIRM CI of two accelerometers (Fig. 10 of Chen et al. [2014]).

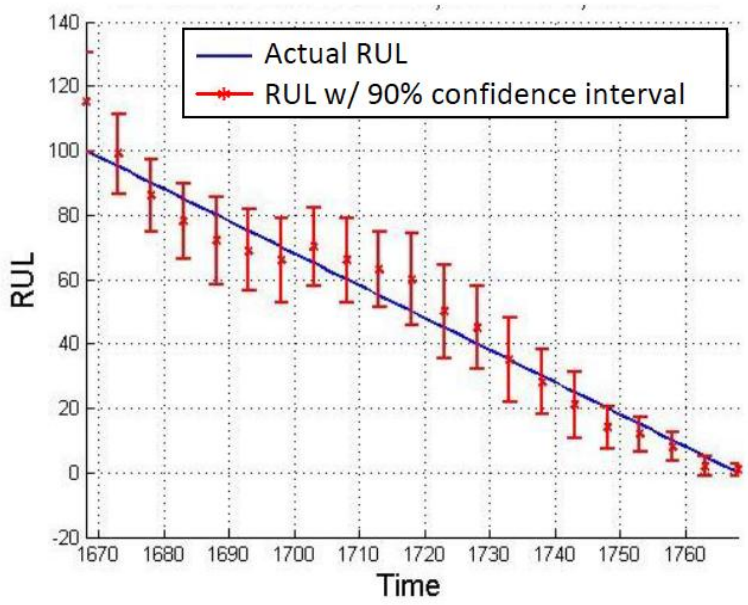

Figure 6.44. RUL estimation result for spiral-bevel gear application (Fig. 10 of Yoon et al. [2014]).

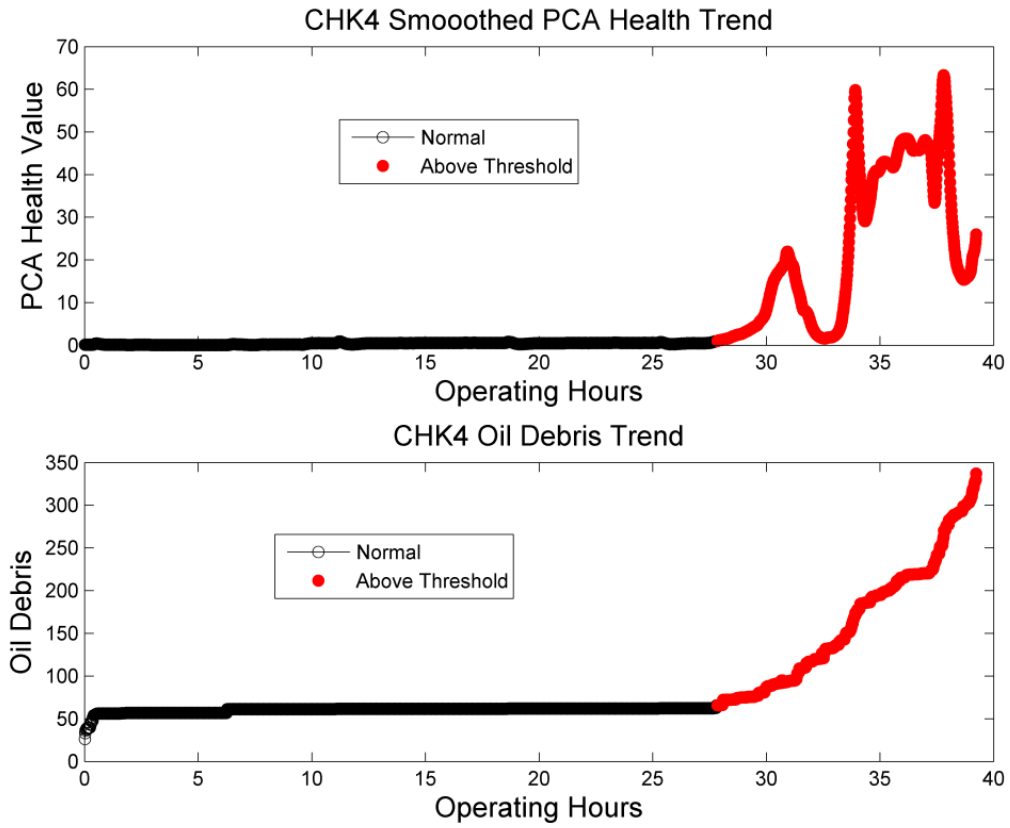

Figure 6.45. Trends of health indicator, based on principal component analysis (PCA), and measured oil debris mass as a function of operating hours of spiral bevel gears (Fig. 18 of Siegel et al. [2014]).

Based on their extensive experience in gear diagnostics, NASA GRC entered a Space Act Agreement with the FAA to support validation and demonstration of rotorcraft health and usage monitoring systems for maintenance credits via FAA Advisory Circular AC-29-2C, Airworthiness Approval of Rotorcraft HUMS. The overarching goal of the work was to determine a method to validate CIs in a laboratory that better represent their response to faults in the field. A series of final reports were generated to document the findings. In the first report, results of spiral-bevel-gear rig endurance tests were presented [Dempsey, 2014b]. Various gear health CIs were used to identify gear-tooth failures. Results of rig testing found that CIs FM4, SI1, and SI3 could be used to detect macro pitting on two or more gear teeth as long it is detected before damage progresses to other components or other failure modes are generated. In the second report, analysis of gear CI data collected on a U.S. Army fleet helicopter with spiral-bevel-gear damage was presented [Dempsey et al., 2014c]. The purpose of the data analysis was to use existing in-service helicopter HUMS flight data from faulted spiral-bevel gears as a case study to better understand the differences between HUMS data response in a helicopter and a component test rig. In the third report, results from the rig and helicopter data analysis were compared for differences and similarities in CI response [Dempsey, 2015]. System factors that affect CI response that included system structural design were outlined and discussed. A process flowchart was also provided that outlined the steps required for rig test CI validation. CI performance metrics of detection rates, false alarm rates, and accuracy were also calculated for the rig data using simple thresholds.

Also, detection of spiral-bevel-gear damage modes using oil debris particle distributions was performed [Dempsey and Handschuh, 2016]. Damage prognostic tests were performed in the NASA GRC Spiral Bevel Gear Fatigue Test Rig. During testing, debris generated were measured with an inductance-type oil debris sensor, while different classes, modes, and degrees of damage occurred on the gear teeth. Debris particle counts, along with approximate size and mass, were measured by the oil debris sensor. Tooth damage was documented with photographs.

Recent research in gear diagnostics considered data-mining and machine-learning techniques. Considering data mining, CI performance was assessed with traditional methods and data-mining methods that included clustering and a decision tree model [McCaslin et al., 2016]. Tests were performed in the NASA GRC Spiral Bevel Gear Fatigue Test Rig from damage initiation to progression on the gear and/or pinion teeth. Six gear sets were tested with varying levels of tooth damage, and vibration-based gear CIs, amount of debris generated, and oil temperatures were measured, and damage progression was documented with photographs. The state of the gear tooth was quantified with a numerical continuous damage factor. The CIs and operational parameters that were good predictors of health state found from the data-mining investigation aligned with those observed during testing, with minimal knowledge of the system. Considering machine learning, techniques to explore the inherent structure of data from rotorcraft gear tests, to determine relationships between features and damage states, and to build a system for predicting gear health for future rotorcraft transmission applications were investigated [Cody and Dempsey, 2017]. Two techniques were used: 1) hidden Markov models were used to create a binary classifier for identifying scuffing transitions, and 2) recurrent neural networks were used to leverage long-distance relationships in predicting discrete damage states. When combined in a workflow, where the binary classifier acted as a filter for the fatigue monitor, the system was able to demonstrate accuracy in damage state prediction and scuffing identification (Fig. 6.46). However, the time-dependent nature of the data restricted this project to collecting and analyzing data from the model selection process.

The previously mentioned work in gear diagnostics primarily dealt with gear-tooth pitting or tooth-cracking failure modes. Gear-tooth wear-detection algorithms were considered in Delgado [2015]. Testing performed at NASA GRC have shown correlations between specific CIs and specific types of gear wear. To speed up the detection and analysis of gear teeth, an image detection program based on the Viola–Jones algorithm was trained to automatically detect spiral-bevel gear-wear pitting. The detector was tested using a training set of gear-wear pictures and a blind set of gear-wear pictures. The detector accuracy for the training set was 75 percent while the accuracy for the blind set was 15 percent. Further improvements on the accuracy of the detector are required but preliminary results have shown its ability to automatically detect gear-tooth wear.

Similar to gears, bearings of the rotorcraft drive system are critical components for safety, reliability, and cost. As with gears, bearing health monitoring has the potential for both economic and safety benefits. A diagnostic tool was developed for detecting fatigue damage to tapered roller bearings [Dempsey et al., 2007b]. This diagnostic tool was developed and evaluated experimentally by collecting oil debris data from failure progression tests. Tests were performed on one healthy bearing and three pre-damaged bearings, and an in-line inductance-type oil debris sensor was monitored and recorded for the occurrence of debris generated during failure of the

bearing. Results indicated that accumulated oil debris mass was a good predictor of damage on tapered roller bearings. The use of a fuzzy logic model to enable an easily interpreted diagnostic metric was proposed and demonstrated.

In collaboration with the U.S. Army Research Laboratory, a series of seeded-fault experiments were conducted to evaluate the characteristics of degraded AH-64 Apache helicopter forward hanger bearings, which support the tail rotor drive shaft [Dykas et al., 2009a]. These bearings were one of a handful of maintenance-intensive components originally identified for CBM proof of principle. Several fault modes were simulated in the test specimens including salt water corrosion, sand contamination, and trench flaws on the races (Fig. 6.47). The vibration characteristics of the faulted bearings were then recorded in a component-level bearing test stand, and analyzed to corroborate or modify current fault detection methodology in the aircraft. For the bearings with substantial amounts of damage or removed material, the vibration response showed increase content in a portion of the spectrum not monitored by the CIs currently in use at the time. Impact experiments suggest this was a result of the bearing vibration exciting the hanger assembly's natural frequencies.

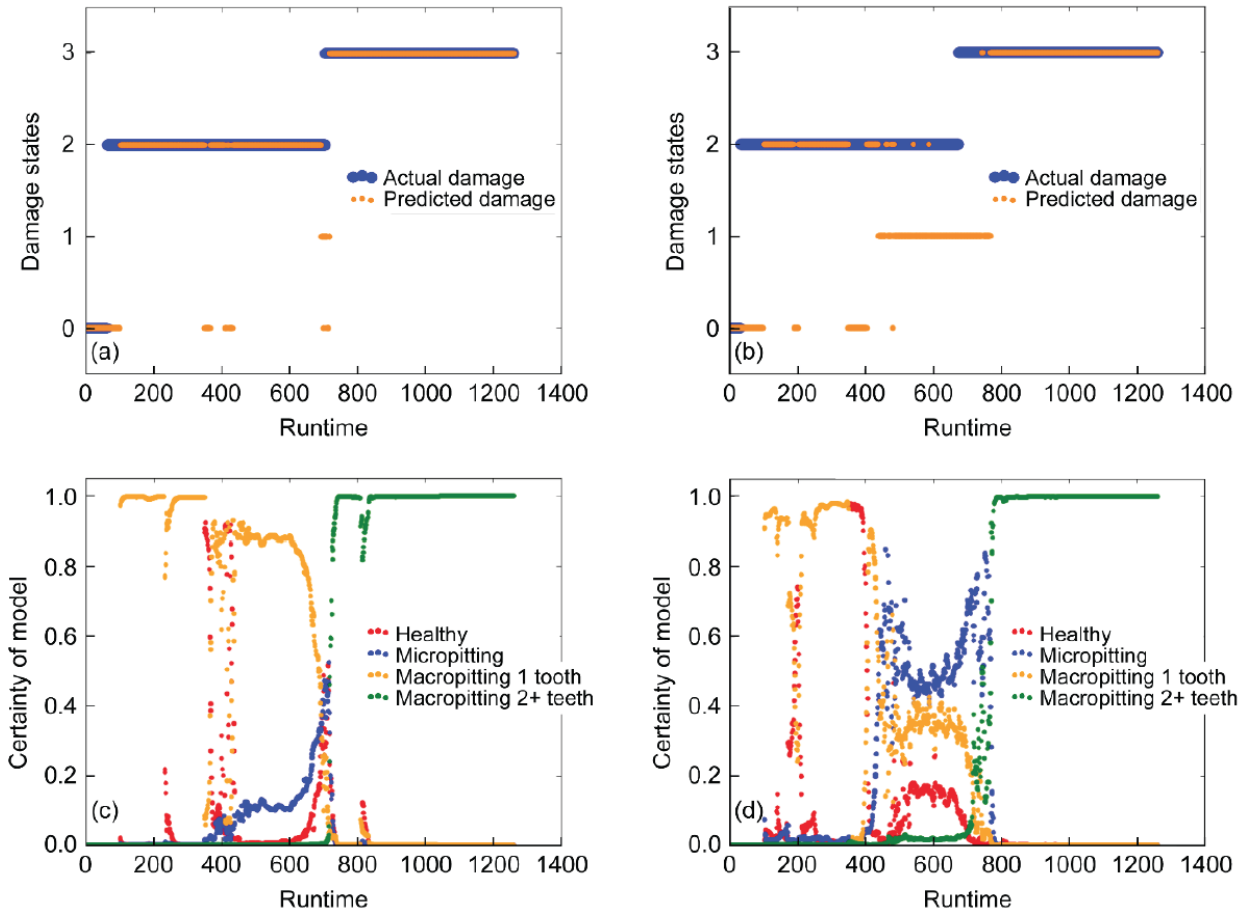

Figure 6.46. Monitor system output. (a) Predicted and actual current damage states for the fatigue data set, (b) predicted and actual future damage states for the fatigue data set, (c) certainty of model in current damage state prediction over time, and (d) certainty of model in future damage prediction over time. (Fig. 8 of Cody and Dempsey [2017].)

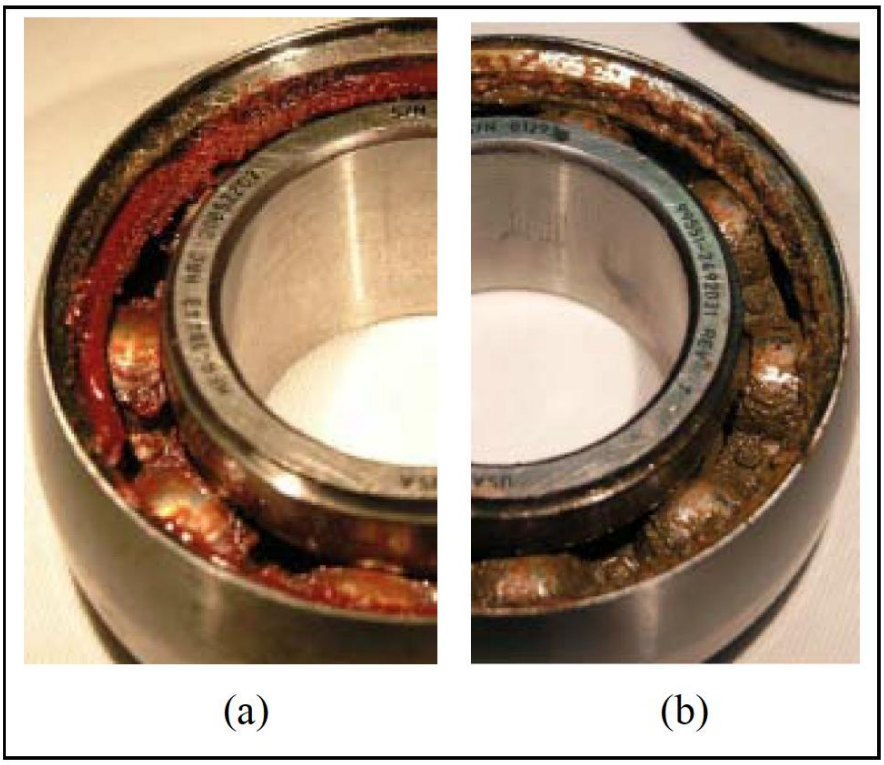

Figure 6.47. Photographs of characteristic grease appearance for each attempted method to corrode the bearing: (a) salt water mixed into grease; (b) reduced grease, salt water injected directly into bearing (Fig. 8 of Dykas et al. [2009a]).

In collaboration with the U.S. Army Aviation Engineering Directorate, research was performed to correlate bearing RUL predictions with helicopter health usage monitoring CIs to identify the damage state of a transmission component [Dempsey et al., 2010a]. CIs were monitored and recorded on the UH-60M (Black Hawk helicopter) tail gearbox output shaft thrust bearings, which had been removed from the helicopter and installed in a bearing spall propagation test rig. CIs monitoring the tail gearbox output shaft thrust bearings in UH-60M helicopters were also recorded from an on-board HUMS. The spall-propagation data collected in the test rig was used to generate CIs for bearing fault detection. A damage progression model was also developed from this data using fuzzy logic techniques (Fig. 6.48). Results indicated that data fusion analysis techniques could be used to map the CI response to the damage levels.

Further studies on the UH-60M tail gearbox output shaft thrust bearings were performed using oil debris monitoring [Dempsey et al., 2011c]. Again, the objective was to determine if a diagnostic tool for detecting fatigue damage of helicopter tapered roller bearings could be used to determine RUL. The diagnostic tool was developed and evaluated experimentally by collecting oil debris data during spall progression tests on four bearings. During each test, data from an in-line inductance-type oil debris sensor was monitored and recorded for the occurrence of pitting damage. Results from the four bearings tested indicated that measuring the debris generated when a bearing outer race begins to spall could be used to indicate bearing damage progression and remaining bearing life (Fig. 6.49).

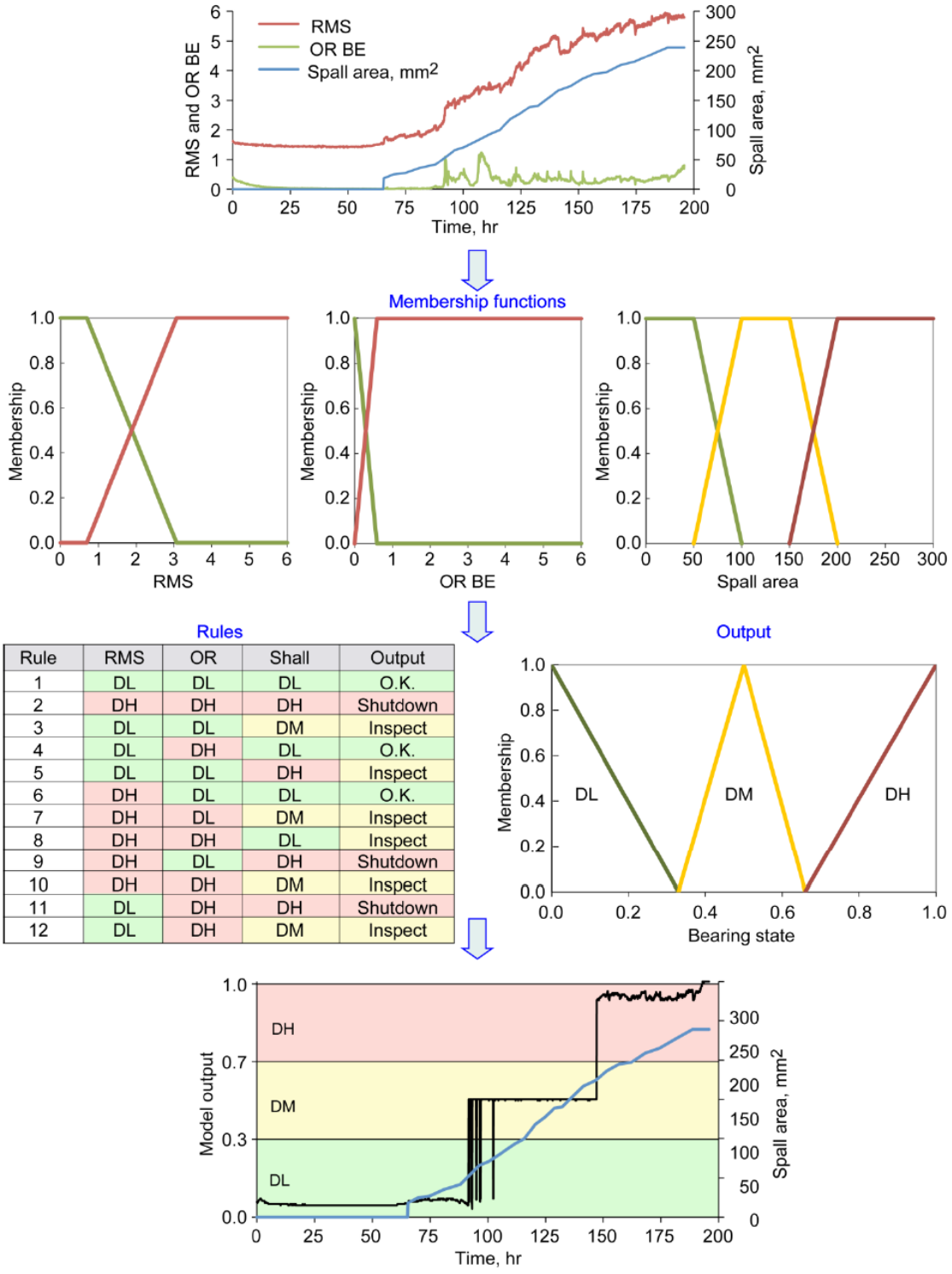

Rule	RMS	OR	Shall	Output
1	DL	DL	DL	O.K.
2	DH	DH	DH	Shutdown
3	DL	DL	DM	Inspect
4	DL	DH	DL	O.K.
5	DL	DL	DH	Inspect
6	DH	DL	DL	O.K.
7	DH	DL	DM	Inspect
8	DH	DH	DL	Inspect
9	DH	DL	DH	Shutdown
10	DH	DH	DM	Inspect
11	DL	DH	DH	Shutdown
12	DL	DH	DM	Inspect

Figure 6.48. Data fusion example (Fig. 12 of Dempsey et al. [2010a]).

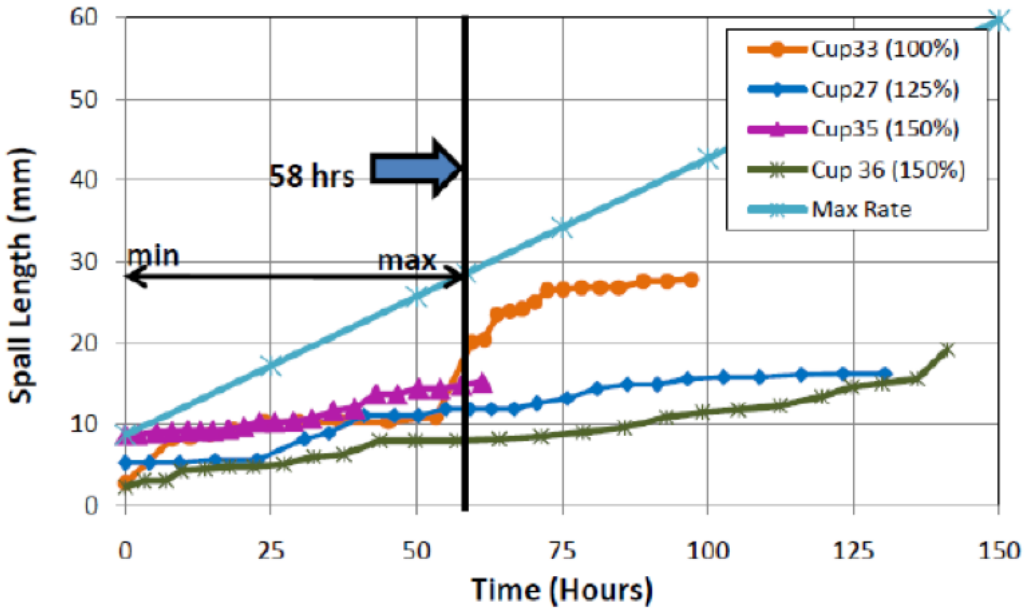

Figure 6.49. Illustration of RUL per detection limits of ODM (Fig. 11 of Dempsey et al. [2011c]).

In further studies with the Army, additional comparison of the performance of HUMS CIs for detecting a bearing fault in a test stand or on a helicopter were performed [Dempsey et al., 2010b]. This study compared data from two sources: 1) CI data collected from accelerometers installed on two UH-60 Black Hawk helicopters when oil cooler bearing faults occurred, along with data from helicopters with no bearing faults, and 2) CI data that was collected from 10 cooler bearings, healthy and faulted, that were removed from fielded helicopters and installed in a test stand. A method using Receiver Operating Characteristic (ROC) curves to compare CI performance was demonstrated (Fig. 6.50). Results indicated that the bearing energy CI responded differently for the helicopter and the test stand.

Additional results using ROC curves are given in Dempsey et al. [2008, 2009]. In addition to the UH-60 oil cooler bearings results, studies were done on the UH-60 main gearbox bevel gear, UH-60 tail gearbox output gear, AH-64A nose gearbox bearing, AH-64D hanger bearing, and AH-64D test stand hanger bearing. Results of the analysis indicated that ROC curves could be used to assess the performance of commercial HUMS CIs. For this assessment, four CI data sets are required: 1) a healthy helicopter component, 2) a faulted helicopter component, 3) a healthy test stand component, and 4) a faulted test stand component. The ROC curves can determine the probability of detection and false alarms based on a CI threshold. The ROC curves can be incorporated into HIs that provide decision-making tools for the end user on component health.

Many bearings in rotorcraft drive systems, such as in tail rotor shaft support, are sealed grease-lubricated bearings. Grease degradation can lead to early failure of the bearing and drive system. Accelerated life testing of grease-lubricated bearings from helicopter drivetrains was conducted to evaluate the mechanism of degraded lubrication for a given aviation grease [Dykas et al., 2010a]. Chemical analysis of samples taken at regular intervals during testing confirmed

generally accepted degradation processes whereby additives were depleted exposing the base oil to degradation and evaporation (Fig. 6.51).

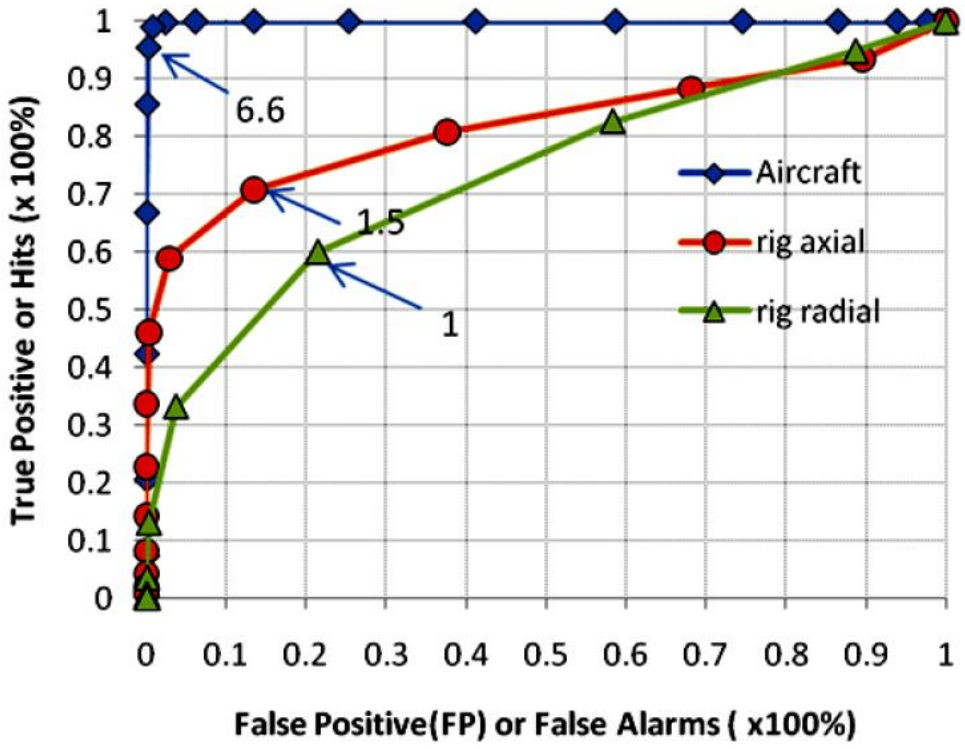

Figure 6.50. ROC curves for UH-60 and test stand bearing energy data (Fig. 12 of Dempsey et al. [2010b]).

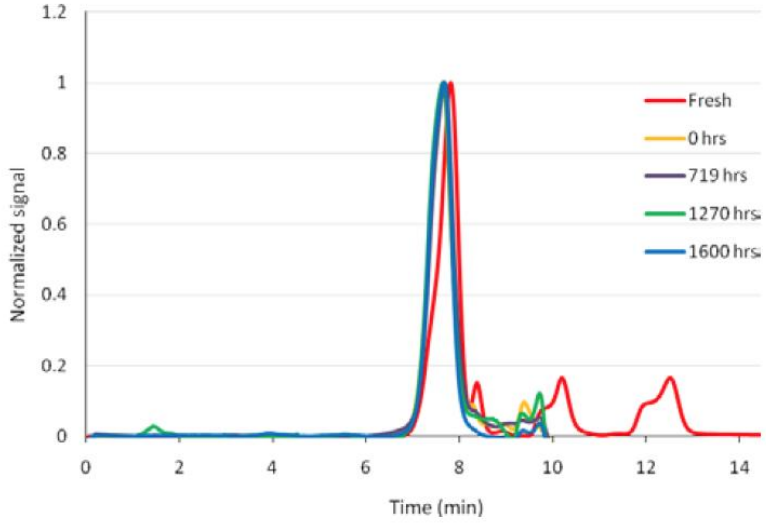

Figure 6.51. Results from Size Exclusion Chromatography (SEC) analysis of grease samples after various exposure times (Fig. 3 of Dykas et al. [2010a]).

Further studies on grease degradation were performed in accelerated testing of UH-60 viscous bearings supporting the tail rotor drive shaft [Dykas et al., 2015]. Over the course of approximately 5,800 hours of aging tests at elevated temperature, four bearings were declared to have failed and were removed and inspected. Slight increases in bearing temperature, as well as increases in RMS vibration and torque, generally accompanied the onset of failure. However, sensor placement, measurement accuracy, and the simultaneous operation of 10 identical bearings made it difficult to reach strong conclusions on the implications for diagnostic monitoring by those sensor types. The mechanism of grease degradation seen in this bearing in a simulation environment was more likely one of lubricant depletion and not mechanical or chemical breakdown of the base oil or thickener. As a lightly loaded bearing, it may be possible for various methods of diagnostic monitoring to provide robust detection without significant risk of catastrophic failure.

Planetary, or epicyclic, transmission configurations are used on many rotorcraft in the final stage of main-rotor drive systems. Planetary systems provide an efficient and compact method to reduce speed and have been used successfully for years in aerospace and automotive applications. Planetary systems, however, exhibit unique challenges relating to gear and bearing fault detection. First, multiple planets are contained in such systems. Since these planets all operate at the same speeds and loads, healthy components could potentially mask the vibration signatures of faulty components. Second, the planet gears exhibit epicyclic motion about a sun gear. Thus, the location of a faulty component, such as a planet tooth defect, changes position in time. This could provide a challenge for fixed-position accelerometers (usually mounted on the transmission housing) that measure the vibration signals that monitor component health.

A few studies were completed at NASA GRC in planetary gearbox fault detection. In the first, vibration data from the OH-58C planetary system were collected on a healthy transmission as well as one with various seeded-fault components (see Table 6.1) [Lewicki et al., 2011]. Planetary fault detection algorithms were used with the collected data to evaluate fault detection effectiveness. Planet gear-tooth cracks and spalls were detectable using the vibration separation techniques (Fig. 6.52). Sun gear-tooth cracks were not discernibly detectable from the vibration separation process. Sun gear-tooth spall defects were detectable. Ring gear-tooth cracks were only clearly detectable by accelerometers located near the crack location or directly across from the crack. Enveloping provided an effective method for planet-bearing inner- and outer-race spalling fault detection.

In a second study, a unique fiber-optic strain sensor array was used in conjunction with the OH-58C planetary tests mentioned above [Kiddy et al., 2011]. Fiber-optic strain sensors represent an appealing alternative to accelerometers. Their small size and multiplexibility allows for potentially greater sensing resolution and accuracy, as well as redundancy, when employed as an array of sensors. The work presented focused on the detection of gear damage in the planetary stage of a helicopter transmission using a fiber-optic strain sensor band. The sensor band included an array of 13 strain sensors, and was mounted on the ring gear of the transmission (Fig. 6.53). Damage detection was performed on the high-frequency component of the strain signal using CIs previously developed for accelerometer-based measurements. Using these indicators, the fiber-optic strain measurements were capable of detecting several types of damage including planet gear cracks and spalls. However, the technique showed limitation in detecting

other damage cases such as damaged sun gears and bearing race pitting. Overall, the strain-based sensors appeared to achieve results similar to conventional accelerometers with respect to damage detection using existing CIs.

Table 6.1. List of Tests Performed (Table 1 of Lewicki et al. [2011]).

TEST	DESCRIPTION	TEST COMPONENT PHOTO
1	Baseline test, all healthy components.	
2	Planet gear tooth crack, 25% depth, opened when in mesh with sun gear.	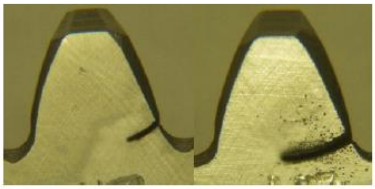
3	Planet gear tooth crack, 25% depth, opened when in mesh with ring gear.	
4	Planet gear tooth crack, 50% depth, opened when in mesh with sun gear.	
5	Planet gear tooth crack, 50% depth, opened when in mesh with ring gear.	
6	Planet gear tooth spall at pitch line, in mesh with sun gear.	
7	Planet gear tooth spall at pitch line, in mesh with ring gear.	
8	Sun gear tooth crack, 25% depth.	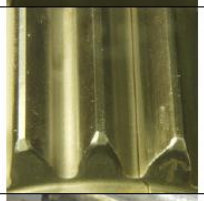
9	Sun gear tooth spall at pitch line.	
10	Ring gear tooth crack, 25% depth.	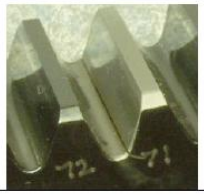
11	Ring gear tooth crack, 50% depth.	
12	Planet bearing outer-race defect.	
13	Planet bearing inner-race defect.	
14	Demo test 1, Planet gear tooth crack, 50% depth, opened when in mesh with sun gear.	
15	Demo test 2, Baseline test, all healthy components.	

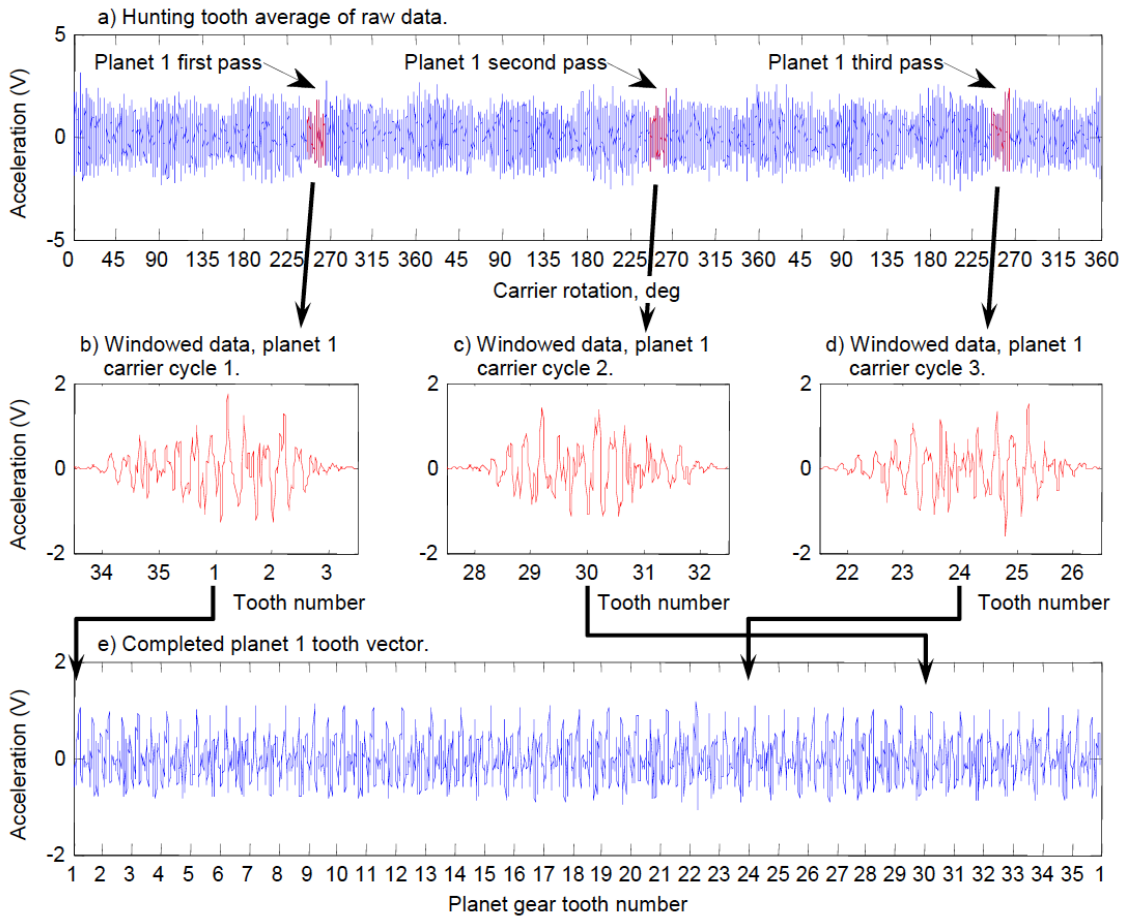

Figure 6.52. Planet gear-tooth vibration separation fault detection technique (Fig. 6 of Lewicki et al. [2011]).

Lastly, additional seeded-fault experiments were conducted on the planetary stage of an OH-58C helicopter transmission [Hood et al., 2013]. Two vibration-based methods were used that isolate the dynamics of the sun gear from that of the planet gears, bearings, input spiral-bevel stage, and other components in and around the gearbox. Three damaged sun gears, two spalled and one cracked, were tested. For the first method, a nonsequential vibration separation algorithm was developed and the resulting signals analyzed. The second method used only the time synchronously averaged data, but took advantage of the signal/source mapping required for vibration separation. Both algorithms were successful in identifying the spall damage. Sun gear damage was confirmed by the presence of sun mesh groups. The sun tooth crack condition was inconclusive.

Much of the previously described work in gear, bearing, and rotorcraft drive system diagnostics was compiled by the U.S. Army Aviation Engineering Directorate for proposed extensions to time/cycle-based overhaul intervals of legacy U.S. Army aircraft. Details of this process are given in Rickmeyer and Dempsey [2011]. The authors explain the process in which legacy rotorcraft, drive systems, and engines are initially assigned Time Between Overhauls (TBOs) as

a result of qualification specifications, testing, tear down analyses, and customer maintenance requirements. The discussion then addresses Army recommended processes to extend original rotorcraft drive system/engine TBOs in accordance with Aeronautical Design Standards while considering the applicable platform maintenance program. A review of beneficial relationships between CBM initiatives and field data to facilitate TBO extension approvals is also included. Subsequently, current pursuits of on-condition maintenance paths for propulsion drive/engine systems through the use of vibratory CBM are described.

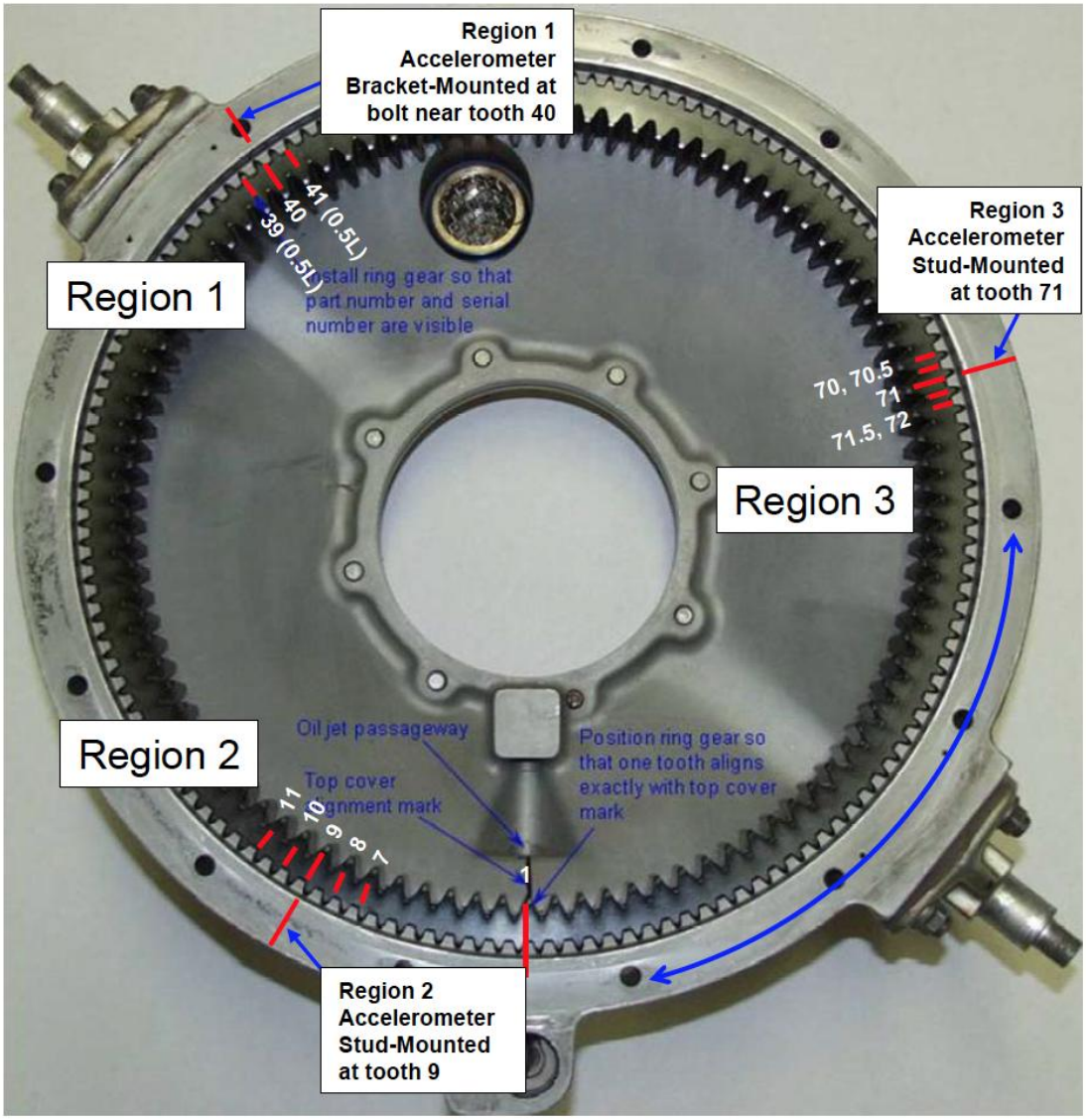

Figure 6.53. Final fiber-optic sensor and accelerometer locations (Fig. 6 of Kiddy et al. [2011]).

GAS FOIL BEARINGS

The NASA GRC has been performing research in gas foil bearing technology for a number of years. Gas foil bearing technology was first developed to support high-speed rotating shaft systems that could not operate using conventional oil-lubricated bearings or rigid-geometry gas bearings because of contamination, speed, or thermal stability requirements. Specifically for rotorcraft, gas foil bearings are being investigated for use in an oil-free gas turbine engine. Oil-free engines have significant weight reduction potential, as well as reduced logistics and maintenance costs. In addition, current lubricants can be tailored for drive systems and gearing in cases where a common lubricant is used for the engine and the gearboxes.

In an early paper, the literature for publicly available information related to early gas foil bearing design and fabrication, as well as a description of a project to reproduce and characterize first-generation (Generation I) and second-generation (Generation II) journal foil bearings, are presented [DellaCorte et al., 2007a]. The bearings were designed, fabricated, and tested to demonstrate the processes needed to develop bearings for new turbomachinery applications (Fig. 6.54). A novel tooling system is described to enable, with a modest financial investment, the convenient production of a wide range of foil bearing design geometries. The performance of these Generation I and II bearings was compared to state-of-the-art, commercially available Generation III bearings.

In another early study, an optimized rotorcraft propulsion system incorporating a foil-air-bearing-supported oil-free engine coupled to a high-power-density gearbox using high-viscosity gear oil is explored [DellaCorte and Bruckner (2007b, 2007c]. In this paper, the state-of-the-art for highly loaded gears is reviewed in the context of a lubricant-optimized helicopter gearbox. Recently developed gas foil bearing load capacity and power loss models are presented that greatly aid evaluation efforts for an oil-free helicopter engine. In addition to reviewing the key technologies and systems needed for such an optimized helicopter propulsion system, this paper considered the remaining technical challenges to be addressed before such a system can be implemented in future rotorcraft.

As a follow-on activity, a conceptual rotorcraft engine was analyzed to determine the feasibility of a foil-bearing-supported core using a combination of rotordynamic analyses and a load capacity model [Howard et al., 2007, 2008a]. A correlated baseline model of an existing rotorcraft engine was analyzed in two configurations to determine if foil bearing technology could possibly be used based upon loads and dynamic considerations. The initial study indicated that the concept was plausible from the standpoint of an oil-free gas generator section. The radial load capacity of foil journal bearings was adequate for the rotorcraft engine size class. The critical speeds could be designed to be outside of the operating speed range. Further, both oil-free core configurations were predicted to be stable throughout the operating speed range.

In addition, thermal management techniques for gas foil bearings were investigated [Radil et al., 2006, 2007]. Tests were performed to evaluate three different methods of utilizing air to provide thermal management control for compliant journal foil air bearings. The first method utilized direct impingement of air on the inner surface of a hollow test journal during operation. The second, less indirect method achieved heat removal by blowing air inside the test journal to simulate air flowing axially through a hollow, rotating shaft. The third method emulated the most

common approach to removing heat by forcing air axially through the bearing's support structure. Tests were performed in a high-temperature, high-speed, Journal Foil Bearing Test Rig at NASA GRC (Fig. 6.55). The tests indicated that all three methods provided thermal management but at different levels of effectiveness.

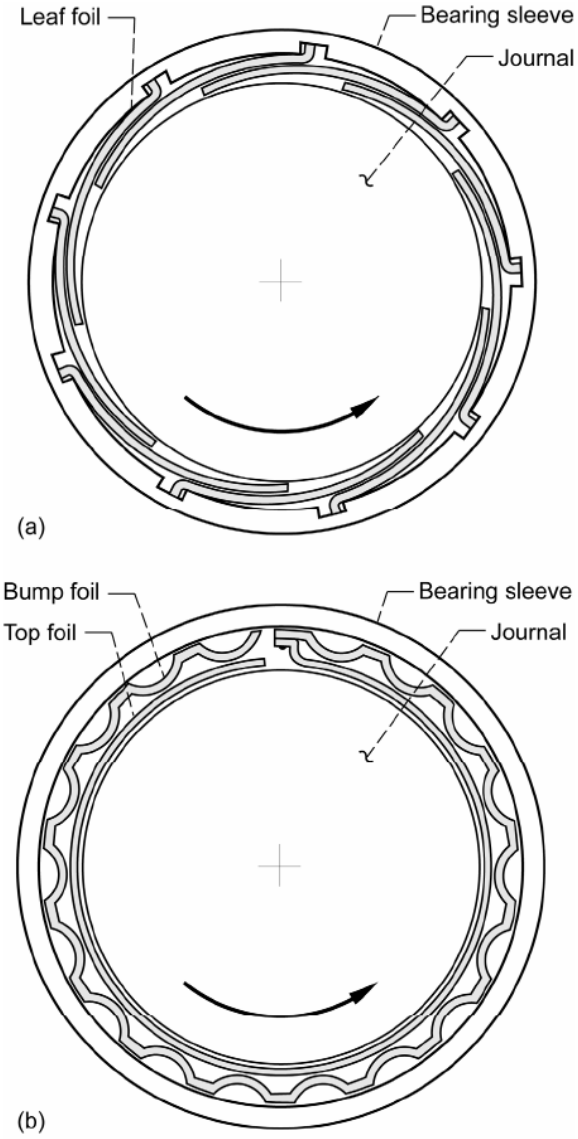

Figure 6.54. Schematic example of first-generation foil bearings with axially and circumferentially uniform elastic support elements: (a) leaf-type foil bearing,(b) bump-type foil bearing. (Fig. 2 of DellaCorte et al. [2007a].)

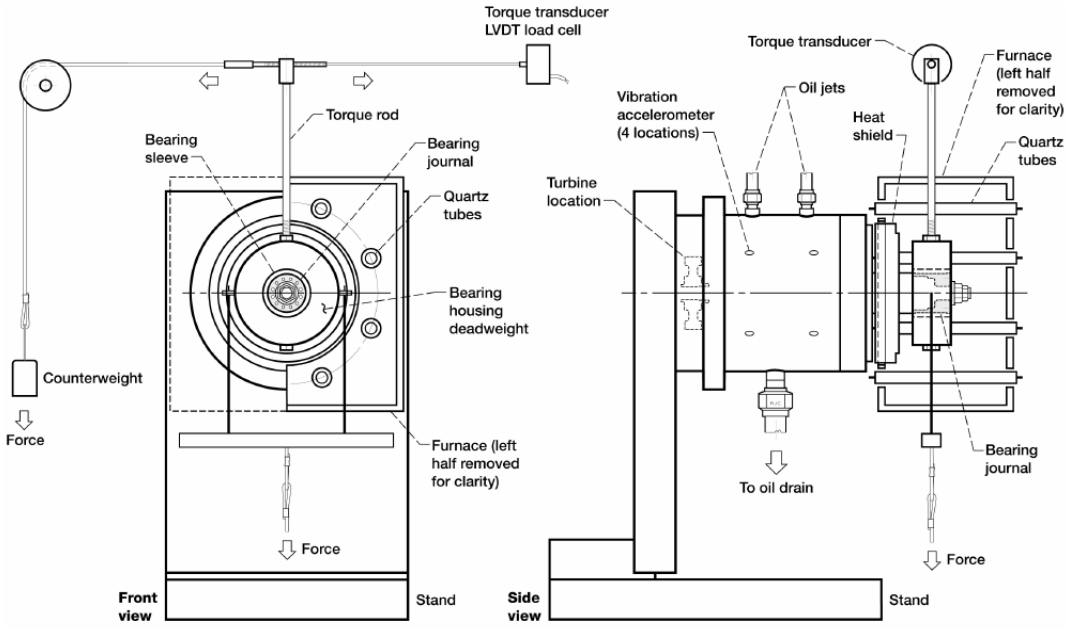

Figure 6.55. High-temperature, high-speed Journal Foil Bearing Test Rig at NASA GRC (Fig. 5 of Radil et al. [2006]).

In further rotordynamic work, studies were performed describing an Extended Kalman Filter (EKF) designed to identify stiffness and damping properties of two identical journal bearings from measurements of the shaft motion in a rotor-bearing system [Miller and Howard, 2008]. The EKF successfully identified the rotordynamic bearing properties in numerical experiments when the shaft motion was excited by impact and imbalance, but it failed when the shaft motion was excited solely by imbalance. The filter performance was influenced more significantly by the initial values of the bearing parameters and error covariance matrix. Estimates for the direct damping and direct and cross-coupled stiffness values were considerably better than estimates for the cross-coupled damping values. The paper also discussed the inadequacy of orbit comparison as a means to assess the quality of bearing parameter estimates from the EKF.

Misalignment and unbalance effects on a gas-foil-bearing supported rotor have been studied [Howard, 2008b]. The Rotordynamic Simulator Test Rig at NASA GRC was used to conduct misalignment tests on two 50.8-mm-diameter (2.00-in.-diameter) journal gas foil bearings (Fig. 6.56). The ability of bearings to handle high degrees of misalignment were verified. Successful operation was achieved with misalignments of 20, 6, and 2 times the acceptable level for angular contact ball, cylindrical roller, and radial ball bearings, respectively. The effect of unbalance on the operation of a simulated rotor was also presented. Results implied that increased unbalance forces resulted in higher bearing stiffness. Based upon these tests, with high tolerance to misalignment and ability to sustain large unbalance levels, gas foil bearings represented an excellent enabling technology for long-life, oil-free turbomachinery power conversion systems. Additional results for misalignment in gas foil bearings is given in Howard [2008c, 2008d]. The experimental results indicated that gas foil bearings were quite tolerant of high levels of misalignment, at least an order of magnitude higher than angular contact ball bearings, the technology they most often replace. However, because of other system

requirements such as a desire to keep bearing power loss and wear low, and compressor and turbine tip clearance requirements, allowable misalignment limits for a given machine are likely to be much lower than what the foil bearings could handle. It was found that the necessity of special design practices, such as flexible, self-aligning bearing mounts, was not likely to be required. In addition, while the full implications are yet to be discovered, gas-foil-bearing misalignment appeared to have an influence on system rotordynamics in terms of bearing force coefficients and the onset of subsynchronous vibrations.

An experimental test program was conducted to determine the performance of highly loaded current-generation gas foil bearings at alternate pressures and temperatures [Bruckner and Puleo, 2008a, 2008b]. Two facilities were used in the test program, the ambient-pressure rig and the high-pressure rig. Results showed an increase in load capacity with increased ambient pressure and a reduction in load capacity with increased ambient temperature (Figs. 6.57 and 6.58). Knowledge of foil bearing performance at operating conditions found within potential machine applications will reduce program development risk of future foil-bearing-supported turbomachines.

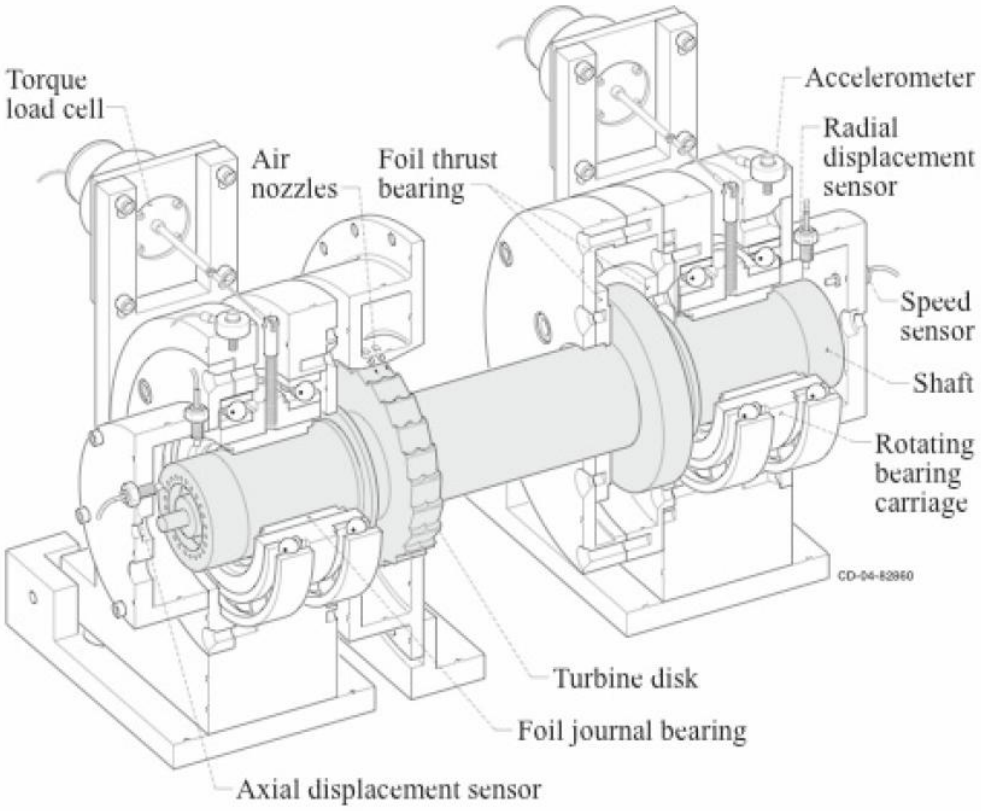

Figure 6.56. Cutaway view of the Rotordynamic Simulator Test Rig at NASA GRC (Fig. 2 of Howard [2008b]).

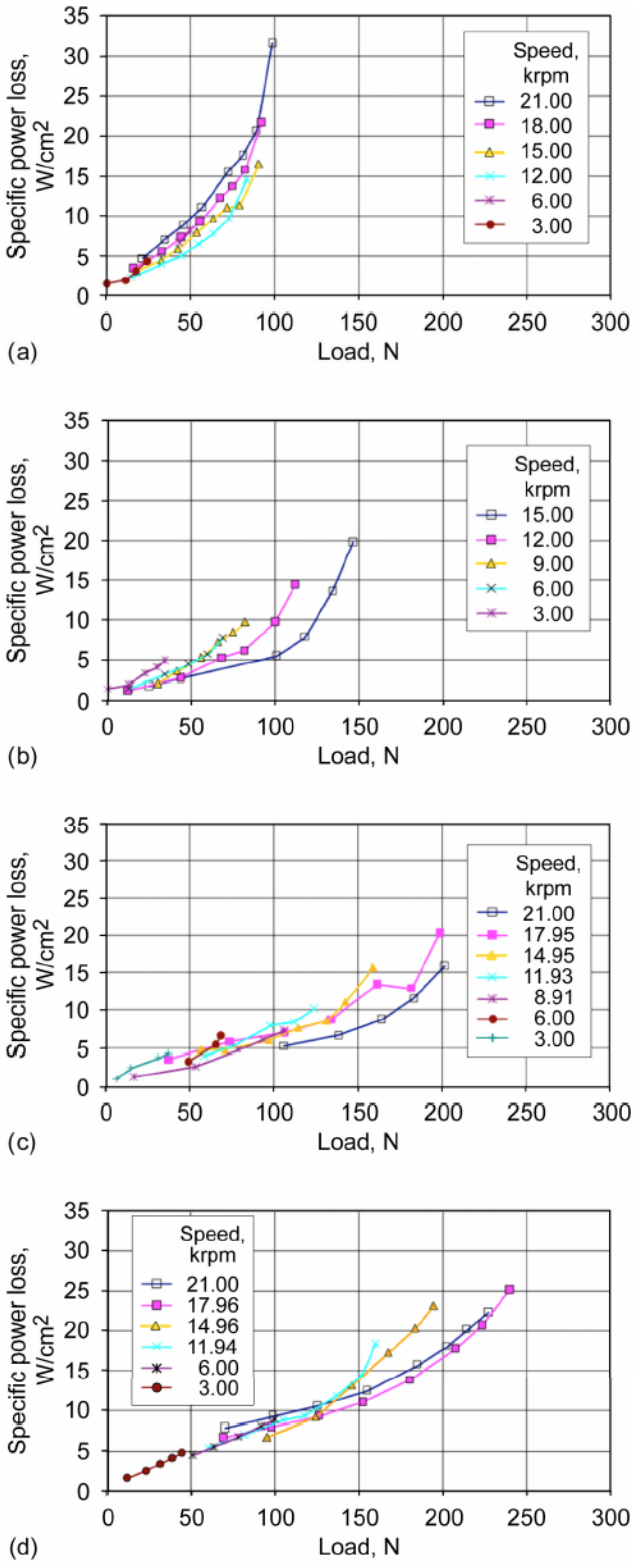

Figure 6.57. Foil bearing performance in air at ambient temperature and various pressures: (a) 0.1 atm, (b) 0.7 atm, (c) 1.5 atm, and (d) 2.5 atm. (Fig. 7 of Bruckner and Puleo [2008a].)

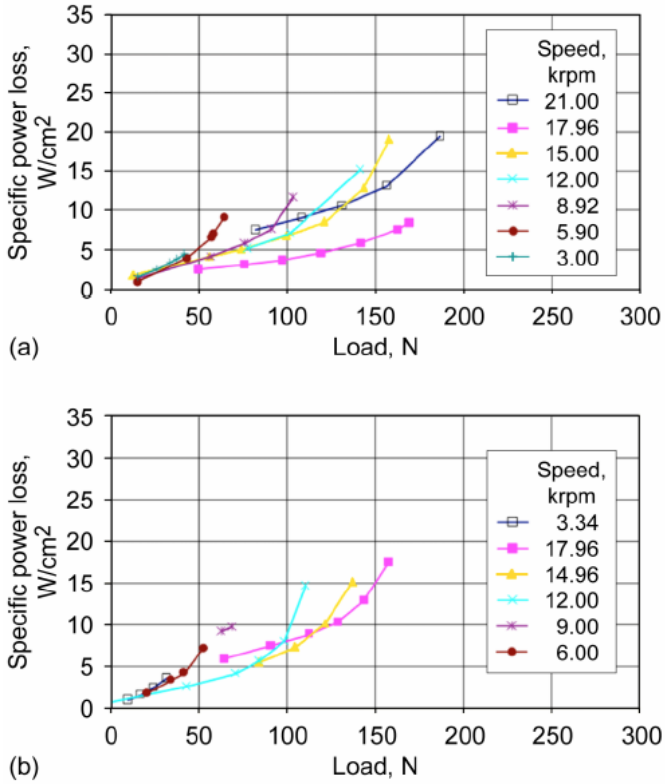

Figure 6.58. 1.0 atmosphere ambient pressure foil bearing performance in air at two temperatures: (a) 200°C, and (b) 400°C. (Fig. 8 of Bruckner and Puleo [2008a].)

A methodology for the design and construction of simple foil thrust bearings intended for parametric performance testing and low marginal costs is presented in Dykas et al. [2008a, 2008b, 2009b, 2010b]. Features drawn from a review of the open literature are discussed as they relate to bearing performance. The design of fixtures and tooling required to fabricate foil thrust bearings is presented, using conventional machining processes where possible. A prototype bearing with dimensions drawn from the literature is constructed, with all fabrication steps described (Fig. 6.59). A load-deflection curve for the bearing is presented to illustrate structural stiffness characteristics. Start-stop cycles were performed on the bearing at a temperature of 425°C to demonstrate early-life wear patterns. A test of bearing load capacity demonstrated useful performance when compared with data obtained from the open literature. To further develop foil thrust bearings, a new test rig was designed to evaluate the start-stop cyclic durability of high-temperature solid-lubricant coatings applied to foil thrust bearing systems [Dykas and Tellier, 2008c]. This test rig allowed the characterization of low-speed thrust bearing performance, augmenting existing high-speed test capabilities. The NASA GRC Low-Speed Thrust Bearing Test Rig was designed to test foil thrust bearings at speeds up to 21,000 rpm and temperatures up to 540°C (1,000°F), with variable thrust loads (Fig. 6.60).

Figure 6.59. Prototype bearing with one top foil removed (Fig. 11 of Dykas et al. [2008a]).

Continued work was performed in applying gas foil bearings in a helicopter engine [Howard et al., 2009]. This work describes an effort to demonstrate gas foil journal bearing use in the hot section of a full-scale helicopter engine core. Rotordynamic feasibility, bearing sizing, and load capability were assessed. In previous engine studies, the foil bearing was used in both the front and rear locations. In this study, the front rolling-element bearing was retained so that the geometry of the rotor was constrained to fit in the existing architecture. The results of the rotordynamic analysis indicated that the combined ball bearing/foil bearing configuration was feasible. The stability analysis indicated that all three modes below the maximum speed of the rotor were stable up to and including 50,000 rpm, which represented a 10-percent-overspeed condition. All indications from experimental tests showed that the foil bearing should perform well in the hot-section of a T700 rotorcraft propulsion engine.

To effectively apply compliant gas foil bearings to increasingly larger and more challenging turbomachinery, a comprehensive method that compares a foil bearing's capabilities with the application's operating requirements was needed. Extensive laboratory and field experience suggests foil bearing failure is generally due to thermal stress brought on by excessive viscous power loss. An investigation was completed in which a performance map, featuring a 3D contour plot that illustrates the expected power loss in a foil bearing as a function of applied load and shaft speed, was produced (Fig. 6.61) [Radil and DellaCorte, 2009]. Using this performance map, bearing capabilities can be examined at the anticipated system operating conditions, and safety margins between an operating point and incipient bearing failure can be ascertained.

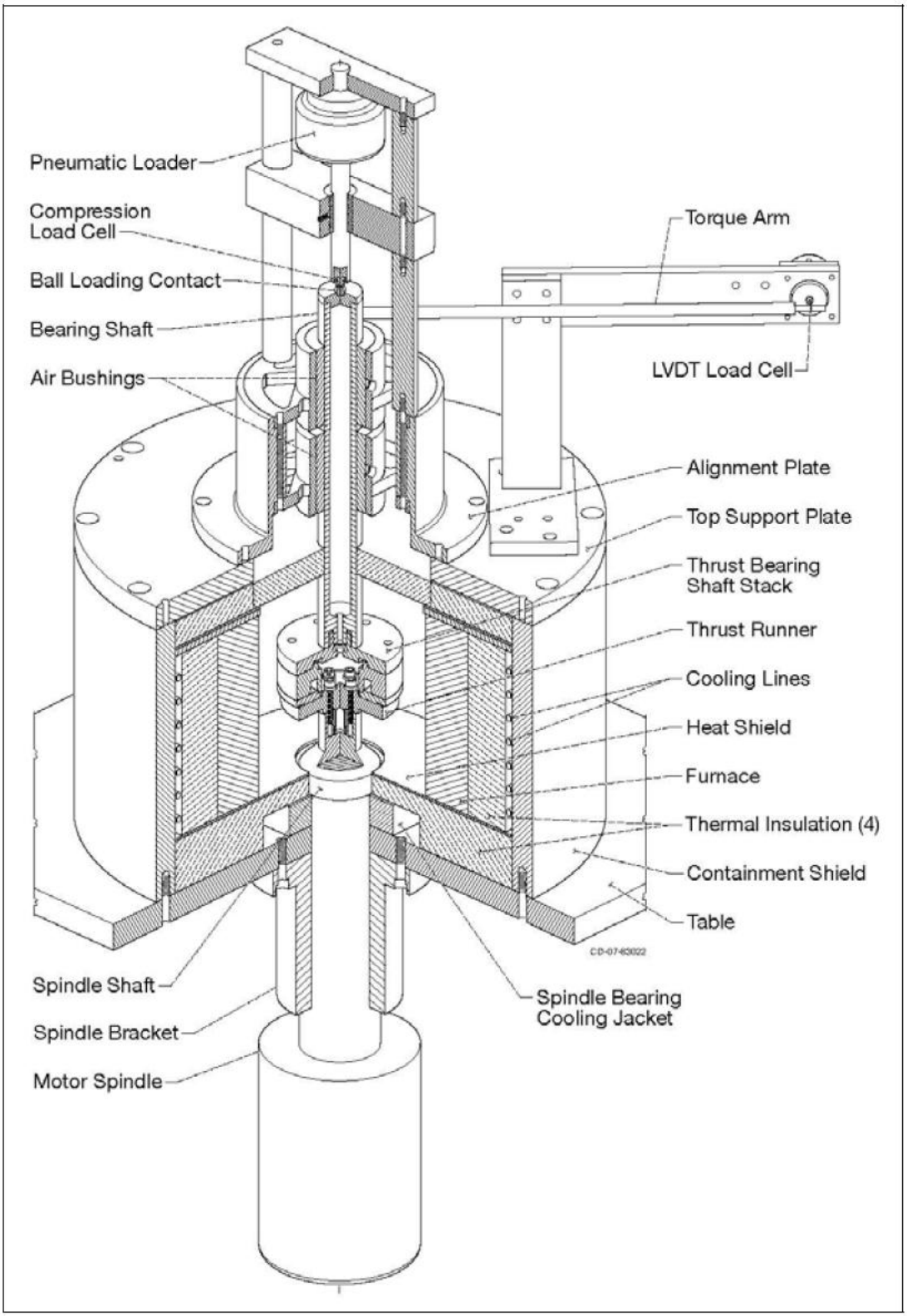

Figure 6.60. Section view of the NASA GRC Low-Speed Thrust Bearing Rig as assembled (Fig. 7 of Dykas et al. [2008c]).

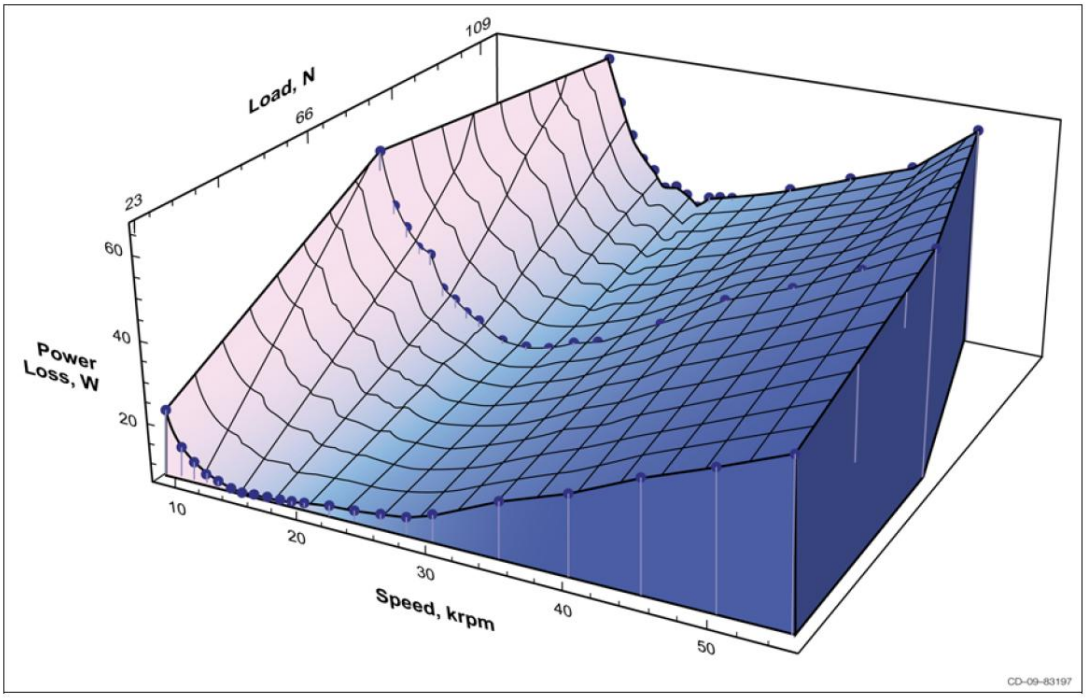

Figure 6.61. A 3D performance map for the 35-mm-diameter foil bearing generated from three load curves (Fig. 5 of Radil and DellaCorte [2009]).

It was found that thermal management is fundamental to the application of gas foil bearings for turboshaft supports in rotorcraft propulsion systems. A study was completed for a thermal energy transport model in a rotor/foil bearing system operating at high temperature with typical inner and/or outer cooling flows [Andres and Kim, 2009]. Predicted film temperatures agreed with published test data, demonstrating the effectiveness of an outer cooling stream to remove heat and to control the operating temperature (Fig. 6.62). The analysis showed paths of thermal energy by conduction and convection to assist in the design and troubleshooting of gas foil bearings (GFB)–rotor systems operating hot. Bearing temperatures and shaft motions measurements were obtained in a test rotor, electrically heated to 132°C.

In addition, a novel thermal management technique for radial foil air bearings was demonstrated [Radil and Batcho, 2010]. The technique was based on injecting air directly into the internal circulating fluid film to reduce bulk temperatures and axial thermal gradients. Tests were performed on a single top foil, Generation III, radial foil bearing instrumented with thermocouples to monitor internal temperatures (Fig. 6.63). The tests were conducted at room temperature with bearing operating speeds from 20,000 to 50,000 rpm while supporting a 222N load. Test results suggested that the air injection approach was a viable thermal management technique capable of controlling bulk temperatures and axial thermal gradients in radial foil air bearings.

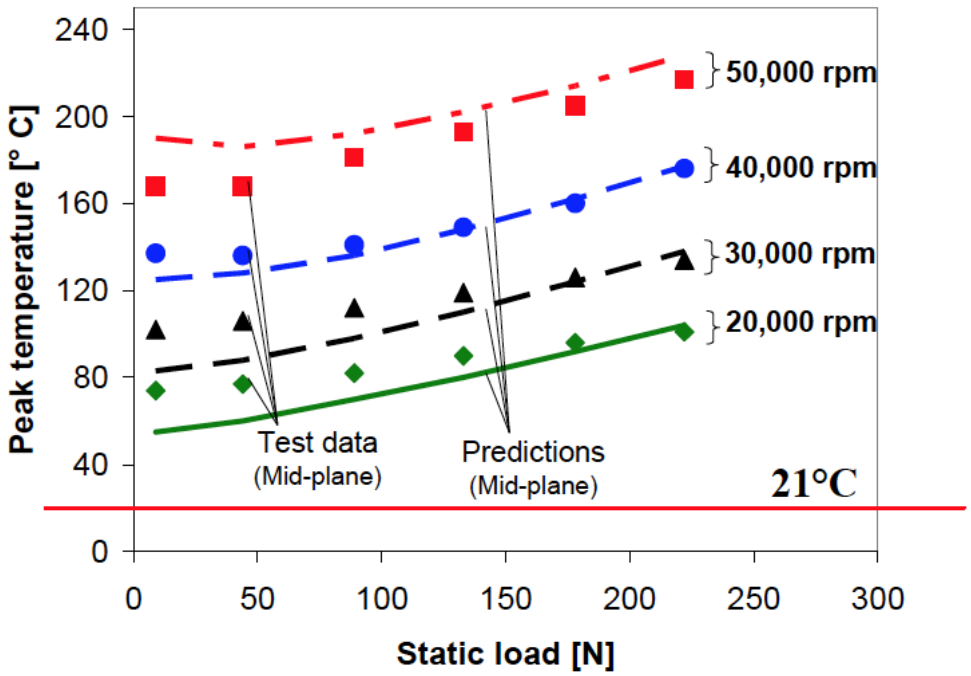

Figure 6.62. Predicted peak film temperature versus static load for increasing rotor speeds. Supply air temperatures at 21°C. Comparison to measurements in Radil, K. C. and Zeszotek, M., 2004, "An Experimental Investigation into the Temperature Profile of a Compliant Foil Air Bearing," STLE Tribol. Trans., 47 (4), pp. 470-479. (Fig. 3 of Andres and Kim [2009].)

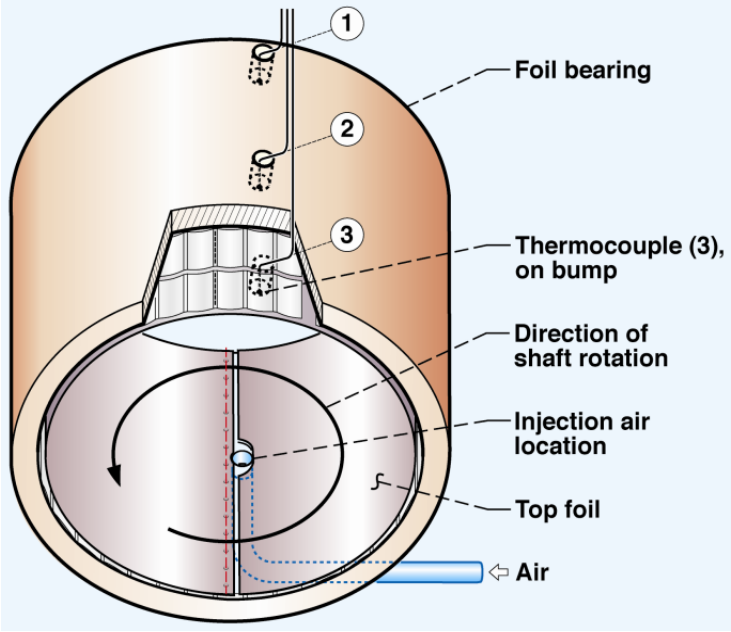

Figure 6.63. Test bearing schematic showing locations of thermocouples and inlet hole for air injection (Fig. 1 of Radil and Batcho [2010]).

Journal wear is an issue in gas foil bearings, especially for startup and stop conditions as well as high-temperature applications (such as rotorcraft engines). A new solid lubricant coating, NASA PS400, has been developed for high-temperature tribological applications. PS400 differs from previous coatings in that it relies on the matrix material, nickel-aluminum-molybdenum, to enhance oxidative and dimensional stability. Detail of PS400's formulation and baseline tribological performance is reported in DellaCorte and Edmonds [2009a]. Pin-on-disk friction and wear tests were performed and showed improvements to previous coatings. To explore the limits of compositional tailoring for improved tribological performance, several PS400 coatings were doped with additional solid lubricants (graphite, MoS2, and BN) and tribologically tested [DellaCorte et al., 2010b, 2010c]. The test results clearly showed that, compared to previous PS300 coatings, PS400 achieves a smoother surface finish via a reduced lubricant content. Coatings prepared with higher than the baseline level of lubricants exhibited higher final surface roughness than the earlier generation PS300 coatings.

Interest in the use of gas foil bearings in high-speed turbomachinery has been increasing in recent years, although the pace has been slow. One of the contributing factors to the slow growth has been a lack of analysis tools, benchmarked to measurements, to predict gas foil bearing behavior in rotating machinery. To address this shortcoming, NASA GRC has supported the development of analytical tools to predict gas foil bearing performance. One of the codes, XLGFBTH©, has the capability to predict rotordynamic coefficients, power loss, film thickness, structural deformation, and more [Howard and Andres, 2010a, 2011]. A simulated case study to compare rotordynamic analysis using output from the code to actual rotor response as measured in the test rig was presented. The resulting comparison showed that the rotordynamic coefficients calculated using XLGFBTH represented the dynamics of the system reasonably well, especially as they pertained to predicting critical speeds (Fig. 6.64).

A four-step integration methodology used in the development of several oil-free turbomachines was presented in Howard et al. [2010b, 2010c]. For the first step (preliminary feasibility and design layout), determination if a proposed application is plausible from the standpoint of bearing performance and system rotordynamics is proposed. In step two (component level testing), the bearings chosen in step one are fabricated and subjected to a battery of tests to verify their capability to perform as needed in the system. Step three is a rotordynamic simulation intended to ensure that the system designed in steps one and two performs as expected. The last step is full-scale demonstration. A simulated turbocompressor example is given to illustrate the methodology. Proper application of the methods presented should enable successful design of oil-free turbomachinery. Lastly, the technological history, primary physics, engineering practicalities, and existing experimental and experiential database for scaling foil bearings are reviewed, and the major remaining technical challenges are identified [DellaCorte and Bruckner, 2010a, 2011a].

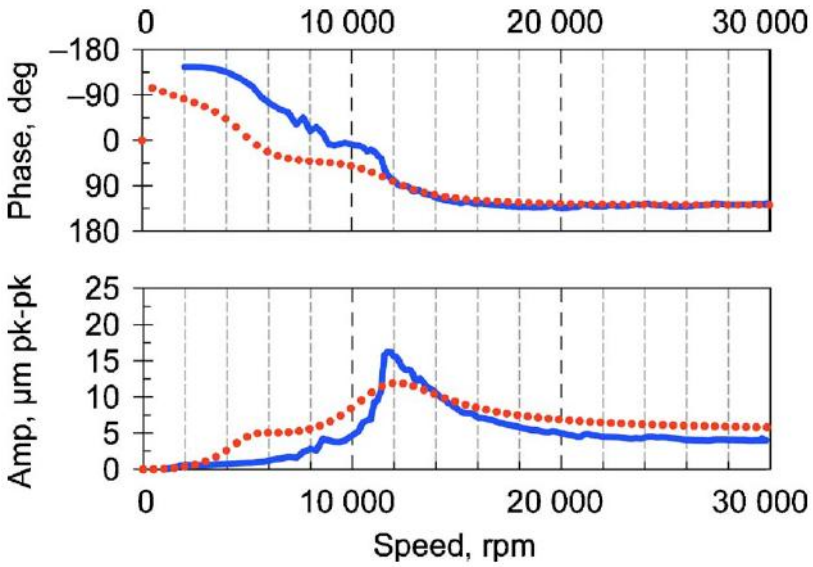

Figure 6.64. Bode plots: measured (solid) and predicted (dotted) amplitude and phase of rotor unbalance response at left bearing, vertical direction, using revised unbalance vectors in the rotordynamic model (Fig. 15 of Howard and Andres [2010a]).

NICKEL-TITANIUM ALLOYS FOR ROLLING ELEMENT BEARING APPLICATIONS

In rotorcraft, engine bearings, rotor mechanisms, and drive systems are examples where improved corrosion resistance is a benefit. Flight and water vehicles exposed to marine environments are also prone to corrosion-related failures despite the widespread use of lubricants with corrosion inhibitors. In select applications involving electric machines and sensitive instrumentation, good electrical conductivity and nonmagnetic properties can also be highly desirable. Unfortunately, no currently deployed material possesses all of these properties. Research has identified NITINOL 60 as a promising candidate material for bearing and mechanical component applications [DellaCorte et al., 2009b]. NITINOL 60, when appropriately processed and fabricated, is dimensionally stable, hard, wear resistant, nongalling, and tribochemically benign in the presence of liquid lubricants.

In follow-on work, the superelastic alloy, 60NiTi, was considered for rolling-element bearing applications [DellaCorte et al., 2011b, 2011c, 2012a]. A series of Rockwell and Brinell hardness, compressive strength, fatigue, and tribology tests were conducted and reported (Fig. 6.65). The combination of high hardness, moderate elastic modulus, large recoverable strain, low density, and intrinsic corrosion immunity provided a path to bearings largely impervious to shock load damage. In addition, the preliminary design and manufacture of ball bearings made from 60NiTi were considered for a highly corrosive, lightly loaded, low-speed bearing application found inside the International Space Station's water recycling system [DellaCorte and Wozniak, 2012b, 2012c]. The reduced elastic modulus, compared to steel, may impact highly loaded bearing internal geometry, but for the distillation assembly bearing application being considered, a direct 60NiTi replacement was reasonable. Lastly, the static load capacity of 60NiTi was measured by

conducting indentation experiments in which 12.7-mm-diameter balls made from the ceramic Si_3N_4 were pressed into highly polished, hardened 60NiTi flat plates [DellaCorte et al., 2012d, 2012e]. Hertz stress calculations were used to estimate contact stress. The results showed that the 60NiTi surface could withstand approximately 3,400 kN load before significant denting occurred. This load capacity is approximately twice that of high-performance bearing steels, suggesting that the potential exists to make highly resilient bearings and components from such materials.

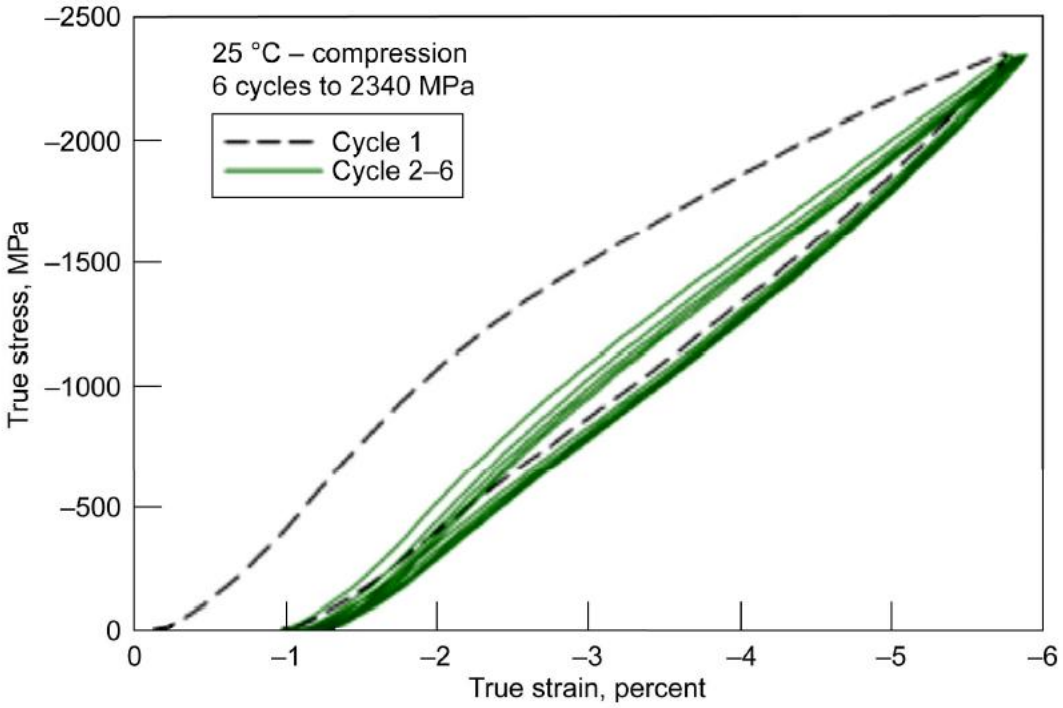

Figure 6.65. Compression behavior of hot-rolled plus hardened 60NiTi. Note: The maximum stress level is limited by test fixtures, not the specimen (Fig. 6 of DellaCorte et al. [2011b]).

REFERENCES

Anderson, W. J., "Elastohydrodynamic Lubrication Theory as a Design Parameter for Rolling Element Bearings," ASME 70-DE-19, ASME Design Engineering Conference and Show, 1970.

Andres, L. S., and Kim, T. H., "Thermohydrodynamic Model Predictions and Performance Measurements of Bump-type Foil Bearing for Oil-Free Turboshaft Engines in Rotorcraft Propulsion Systems," 65th American Helicopter Society Annual Forum, Grapevine, TX, May 27-29, 2009.

Antolick, L. J., Branning, J. S., Wade, D. R., and Dempsey, P. J., "Evaluation of Gear Condition Indicator Performances on Rotorcraft Fleet," 66th American Helicopter Society Annual Forum, Phoenix, AZ, May 11-13, 2010.

Asnani, V., Scheidler, J., and Tallerico, T., "Magnetic Gearing Research at NASA," 74th American Helicopter Society Annual Forum, Phoenix, AZ, May 14-17, 2018.

Bechhoefer, E., He, D., and Dempsey, P. J., "Gear Health Threshold Setting Based on a Probability of False Alarm," 2011 Annual Conference of the Prognostics and Health Management Society, Montreal, Canada, September 25-29, 2011.

Bruckner, R. J., and Puleo, B. J., "Compliant Foil Journal Bearing Performance at Alternate Pressures and Temperatures," Turbo Expo 2008 Gas Turbine Technical Congress and Exposition, Berlin, Germany, June 9-13, 2008a.

Bruckner, R. J., and Puleo, B. J., "Compliant Foil Journal Bearing Performance at Alternate Pressures and Temperatures," NASA/TM-2008-215219, May 2008b.

Cameron, Z. A., Smith, E. C., DeSmidt, H., and Bill, R. C., "Design Space Exploration of Pericyclic Transmission with Counterbalance and Bearing Load Analysis," 74th American Helicopter Society Annual Forum, Phoenix, AZ, May 14-17, 2018.

Chen, Y., Chaudhry, Z., and Dempsey, P. J., "A Novel Gear Condition Monitoring Method Based on Transient Impulse Response," 70th American Helicopter Society Annual Forum, Montreal, Canada, May 20-22, 2014.

Cody, T., and Dempsey, P. J., "Application of Machine Learning to Rotorcraft Health Monitoring," NASA/TM-2017-219408, Jan. 2017.

Delgado, I. R., Dempsey, P. J., Antolick, L. J., and Wade, D. R., "Continued Evaluation of Gear Condition Indicator Performance on Rotorcraft Fleet," Airworthiness, Condition Based Maintenance (CBM), and Health and Usage Monitoring (HUMS), Huntsville, AL, Feb. 11-13, 2013a.

Delgado, I. R., Dempsey, P. J., Antolick, L. J., and Wade, D. R., "Continued Evaluation of Gear Condition Indicator Performance on Rotorcraft Fleet," NASA/TM-2013-217876, June 2013b.

Delgado, I. R., "Gear Tooth Wear Detection Algorithm," NASA/TM-2015-218830, July 2015.

Delgado, I. R., and Hurrell, M. J., "Experimental Investigation of Shrouding on Meshed Spur Gear Windage Power Loss," 73rd American Helicopter Society Annual Forum, Fort Worth, TX, May 9-11, 2017a.

Delgado, I. R., and Hurrell, M. J., "Baseline Experimental Results on the Effect of Oil Temperature on Shrouded Meshed Spur Gear Windage Power Loss," ASME IDETC/CIE 2017, Cleveland, OH, Aug. 6-9, 2017b.

Delgado, I. R., and Hurrell, M. J., "The Jetting Phenomena in Meshed Spur Gears," 74th American Helicopter Society Annual Forum, Phoenix AZ, May 14-17, 2018.

DellaCorte, C., Radil, K. C., Bruchner, R. J., and Howard, S. A., "Design, Fabrication and Performance of Open Source Generation I and II Compliant Hydrodynamic Gas Foil Bearings," NASA/TM-2007-214691, April 2007a.

DellaCorte, C., and Bruckner, R. J., "Oil-Free Rotor Support Technologies for an Optimized Helicopter Propulsion System," 18th International Society for Air Breathing Engines (ISABE) Conference, Beijing, China, Sept. 2-7, 2007b.

DellaCorte, C., and Bruckner, R. J., "Oil-Free Rotor Support Technologies for an Optimized Helicopter Propulsion System," NASA/TM-2007-214845, June 2007c.

DellaCorte, C., and Edmonds, B. J., "NASA PS400: A New High Temperature Solid Lubricant Coating for High Temperature Wear Applications," NASA/TM-2009-215678, Aug. 2009a.

DellaCorte, C., Pepper, S. V., Noebe, R., Hull, D. R., and Glennon, G., "Intermetallic Nickel-Titanium Alloys for Oil Lubricated Bearing Applications," NASA/TM-2009-215646, March 2009b.

DellaCorte, C., and Bruckner, R. J., "Remaining Technical Challenges and Future Plans for Oil-Free Turbomachinery," Turbo Expo 2010 Gas Turbine Technical Congress and Exposition, Glasgow, Scotland, June 14-18, 2010a.

DellaCorte, C, Stanford, M. K., Thomas, F., and Edmonds, B. J., "The Effect of Composition on the Surface Finish of PS400: A New High Temperature Solid Lubricant Coating," 65th Society of Tribologists and Lubrication Engineers Annual Meeting and Exhibition, Las Vegas, NV, May 16-20, 2010b.

DellaCorte, C, Stanford, M. K., Thomas, F., and Edmonds, B. J., "The Effect of Composition on the Surface Finish of PS400: A New High Temperature Solid Lubricant Coating," NASA/TM-2010-216774, Sept. 2010c.

DellaCorte, C., and Bruckner, R. J., "Remaining Technical Challenges and Future Plans for Oil-Free Turbomachinery," *Journal of Engineering for Gas Turbines and Power*, vol. 133, no. 4, pp. 042502-042502-7, April 2011a.

DellaCorte, C., Noebe, R. D., Stanford, M. K., and Padula, S. A., "Resilient and Corrosion-Proof Rolling Element Bearings Made From Superelastic Ni-Ti Alloys for Aerospace Mechanism Applications," 2011 ASTM Symposium on Rolling Element Bearings, Anaheim, CA, April 13-15, 2011b.

DellaCorte, C., Noebe, R. D., Stanford, M. K., and Padula, S. A., "Resilient and Corrosion-Proof Rolling Element Bearings Made From Superelastic Ni-Ti Alloys for Aerospace Mechanism Applications," NASA TM-2011-217105, Aug. 2011c.

DellaCorte, C., Noebe, R. D., Stanford, M. K., and Padula, S. A., "Resilient and Corrosion-Proof Rolling Element Bearings Made From Superelastic Ni-Ti Alloys for Aerospace Mechanism Applications," STP 1542: Rolling Element Bearings, Takeuchi, Y., and Mandler, W., ed., pp. 143-166, 2012a.

DellaCorte, C., and Wozniak, W. A., "Design and Manufacturing Considerations for Shockproof and Corrosion-Immune Superelastic Nickel-Titanium Bearings for a Space Station Application," 41st Aerospace Mechanisms Symposium, Pasadena, CA, May 16-18, 2012b.

DellaCorte, C., and Wozniak, W. A., "Design and Manufacturing Considerations for Shockproof and Corrosion-Immune Superelastic Nickel-Titanium Bearings for a Space Station Application," NASA/TM-2012-216015, May 2012c.

DellaCorte, C., Moore, L. E., and Clifton, J. S., "Static Indentation Load Capacity of the Superelastic 60NiTi for Rolling Element Bearings," 2012 Society of Tribologists and Lubrication Engineers Annual Meeting and Exhibition, St. Louis, MI, May 6-10, 2012d.

DellaCorte, C., Moore, L. E., and Clifton, J. S., "Static Indentation Load Capacity of the Superelastic 60NiTi for Rolling Element Bearings," NASA/TM-2012-216016, May 2012e.

Dempsey, P. J., Lewicki, D. G., and Le, D. D., "Investigation of Current Methods to Identify Helicopter Gear Health," 2007 IEEE Aerospace Conference, IEEEAC paper 1079, Big Sky, MT, March 3-10, 2007a.

Dempsey, P. J., Krieder, G., and Fichter, T., "Investigation of Tapered Roller Bearing Damage Detection Using Oil Debris Analysis," Power Transmission Engineering, pp. 20-29, Feb. 2007b.

Dempsey, P.J., Keller, J.A., and Wade D.R., "Signal Detection Theory Applied to Helicopter Transmission Diagnostic Thresholds," NASA/TM-2008-215262, AMRDEC PAO Control Number FN 3597, July 2008.

Dempsey, P. J., Keller, J. A., and Wade D. R., "Signal Detection Theory Applied to Helicopter Transmission Diagnostic Thresholds," 65th American Helicopter Society Forum, Grapevine, TX, May 27-29, 2009.

Dempsey, P. J., Bolander, N., Haynes, C., Branning, J., and Wade D. R., "Correlate Life Predictions and Condition Indicators in Helicopter Tail Gearbox Bearings," 66th American Helicopter Society Annual Forum, Phoenix, AZ, May 10-12, 2010a.

Dempsey, P. J., Branning, J., Wade, D. R., and Bolander, N., "Comparison of Test Stand and Helicopter Oil Cooler Bearing Condition Indicators," 66th American Helicopter Society Annual Forum, Phoenix, AZ, May 11-13, 2010b.

Dempsey, P. J., and Sheng, S., "Investigation of Data Fusion Applied to Health Monitoring of Wind Turbine Drive Train Components," 2011 American Wind Energy Association (AWEA) Wind Power Conference, Anaheim, CA, May 22-25, 2011a.

Dempsey, P. J., and Zakrajsek, J. J., "Rotorcraft Health Management," Chapter 37 of System Health Management with Aerospace Applications, Johnson, S.B. et al. ed., pp. 577-587, May 2011b.

Dempsey, P. J., Bolander, N., Haynes, C., and Toms, A. M., "Investigation of Bearing Fatigue Damage Life Prediction Using Oil Debris Monitoring," NASA/TM-2011-217117, Nov. 2011c.

Dempsey, P. J, Tuck, R., and Showalter, S., "Comparison of an Inductance in-Line Oil Debris Sensor and Magnetic Plug Oil Debris Sensor," 68th American Helicopter Society Annual Forum, Ft. Worth, TX, May 1-3, 2012.

Dempsey, P. J., "Investigation of Sideband Index Response to Prototype Gear Tooth Damage," NASA/TM-2013-216610, Nov. 2013a.

Dempsey, P. J., Handschuh, R. F., and Delgado, I. R., "Integrating Condition Indicators and Usage Parameters for Improved Spiral Bevel Gear Health Monitoring," 69th American Helicopter Society Annual Forum, Phoenix, AZ, May 21-23, 2013b.

Dempsey, P. J., Handschuh, R. F., and Delgado, I. R., "Integrating Condition Indicators and Usage Parameters for Improved Spiral Bevel Gear Health Monitoring," NASA/TM-2013-217896, June 2013c.

Dempsey, P. J., and Brandon, E. B., "Validation of Helicopter Gear Condition Indicators Using Seeded Fault Tests," Joint 2013 Machinery Failure Prevention Technology and 59th International Instrumentation Symposium, Cleveland, OH, May 13-17, 2013d.

Dempsey, P. J., and Brandon, E. B., "Validation of Helicopter Gear Condition Indicators Using Seeded Fault Tests," NASA/TM-2013-217872, April 2013e.

Dempsey, P. J., Islam, A. A., Feldman, J., and Larsen, C., "Investigation of Gearbox Vibration Transmission Paths on Gear Condition Indicator Performance," NASA/TM-2013-216617, December 2013f.

Dempsey, P. J., Antolick, L. J., Branning, J. S., and Thomas, J., "Data Fusion Tool for Spiral Bevel Gear Condition Indicator Data," 2014 Machinery Failure Prevention Technology Conference, Virginia Beach, VA, May 20-22, 2014a.

Dempsey, P. J., "Investigation of Spiral Bevel Gear Condition Indicator Validation via AC–29–2C Using Damage Progression Tests," NASA/TM-2014-218384, Oct. 2014b.

Dempsey, P. J., Wade, D. R., Antolick, L. J., and Thomas, J., "Investigation of Spiral Bevel Gear Condition Indicator Validation Via AC–29–2C Using Fielded Rotorcraft HUMS Data," NASA/TM-2014-218406, Nov. 2014c.

Dempsey, P. J., "Investigation of Spiral Bevel Gear Condition Indicator Validation via AC–29–2C Combining Test Rig Damage Progression Data With Fielded Rotorcraft Data," NASA/TM-2014-218478, Jan. 2015.

Dempsey, P. J., and Handschuh, R. F., "Detection of Spiral Bevel Gear Damage Modes Using Oil Debris Particle Distributions," *International Journal of COMADEM*, vol. 19, no. 4, Oct. 2016.

Deng, Z., Asnani, V. M., and Dapino, M. J., "Magnetostrictive Vibration Damper and Energy Harvester for Rotating Machinery," Proceedings of SPIE Smart Structures, vol. 9433, Paper No. 94330C, Mar. 2015.

DeSmidt, H. A., "Analysis of a Dual Gearbox/Shaft System with Nonlinear Dynamic Mesh Phase Interactions," 51st AIAA/ASME/ASCE/AHS/ASC Structures, Dynamics, and Materials Conference, Orlando, FL, April 12-15, 2010a.

DeSmidt, H. A., and Zhao, J., "Extension-Twist Coupled Graphite/Epoxy Composite Driveshafts for Gear-Mesh Vibration Suppression," 66th American Helicopter Society Annual Forum, Phoenix, AZ, May 11-13, 2010b.

DeSmidt, H. A, Wang, K. W., Smith, E. C., and Lewicki, D. G., "Variable-Speed Simulation of a Dual-Clutch Gearbox Tiltrotor Driveline," 67th American Helicopter Society Annual Forum, Virginia Beach, VA, May 3-5, 2011.

DeSmidt, H. A, Wang, K. W., Smith, E. C., and Lewicki, D. G., "Variable-Speed Simulation of a Dual-Clutch Gearbox Tiltrotor Driveline," NASA/TM-2012-217212, Jan. 2012.

DeSmidt, H. A., Smith, E. C., Bill, R. C., and Wang, K. W., "Comprehensive Modeling and Analysis of Rotorcraft Variable Speed Propulsion System with Coupled Engine/Transmission/Rotor Dynamics," NASA/CR-2013-216502, May 2013.

Dimofte, F., and Krantz, T. L., "Tests of Bearings and Gears With PVD Coatings for Aerospace Transmissions; Results and Problems," The Coatings Meeting, Kassándra, Greece, Oct 1-3, 2008a.

Dimofte, F., Ene, N. M., Handschuh, R. F., Krantz, T. L., Bouzakis, K. D., Asimakopoulos, A., and Batsiolas, M., "Current Results of Testing PVD Coatings for Wave Bearings for Use in Aerospace-Transmissions," The Coatings Meeting, Kassándra, Greece, Oct 1-3, 2008b.

Dimofte, F., Ene, N. M., and Oswald, F. B., "An Investigation of the Wave Bearing Attenuation Effects on Vibration and Noise Generated by a Gearbox Compared to the Rolling Element Bearings," 67th American Helicopter Society Annual Forum, Virginia Beach, VA, May 3-5, 2011.

Dykas, B. D., Bruckner, R. J., DellaCorte, C., Edmonds, B., and Prahl, J., "Design, Fabrication, and Performance of Foil Gas Thrust Bearings for Microturbomachinery Applications," Turbo Expo 2008 Gas Turbine Technical Congress and Exposition, Berlin, Germany, June 9-13, 2008a.

Dykas, B. D., Bruckner, R. J., DellaCorte, C., Edmonds, B., and Prahl, J., "Design, Fabrication, and Performance of Foil Gas Thrust Bearings for Microturbomachinery Applications," NASA/TM-2008-215062, Jan. 2008b.

Dykas, B. D., and Tellier, D. W., "A Foil Thrust Bearing Rig for Evaluation of High Temperature Performance and Durability," Army Research Laboratory, ARL-MR-0692, April 2008c.

Dykas, B. D., Krantz, T. L., Decker, H. ., and Lewicki, D. G., "Experimental Determination of AH-64 Apache Tailshaft Hangar Bearing Vibration Characteristics with Seeded Faults," 65th American Helicopter Society Forum, Grapevine, TX, May 27-29, 2009a.

Dykas, B. D., Bruckner, R. J., DellaCorte, C., Edmonds, B., and Prahl, J., "Design, Fabrication, and Performance of Foil Gas Thrust Bearings for Microturbomachinery Applications," *Journal of Engineering for Gas Turbines and Power*, vol. 131, no. 1, pp. 012301-012301-8, Jan. 2009b.

Dykas, B. D., Krantz, T. L., Berger, G., Street, K., and Morales, W., "Grease Degradation in Critical Helicopter Drivetrain Bearings," STLE/ASME International Joint Tribology Conference, San Francisco, CA, Oct. 17-21, 2010a.

Dykas, B. D., DellaCorte, C., and Edmonds, B., "Foil Gas Thrust Bearing for High-Speed Turbomachinery," NASA Tech Briefs Magazine, vol. 34, no. 4, pp. 19-20, April 2010b.

Dykas, B. D., Hood, A., Krantz, T. L., and Klemmer, M., "Accelerated Testing of UH-60 Viscous Bearings for Degraded Grease Fault," AIAC16 16th Australian International Aerospace Congress, Melbourne, Australia, Feb. 23-24 2015.

Fleming, D. P., "Vibration Transmission Through Bearings With Application to Gearboxes," 4th Biennial International Symposium on Stability Control of Rotating Machinery (ISCORMA–4), Alberta, Canada, Aug. 27–31, 2007a.

Fleming, D. P., "Vibration Transmission Through Bearings With Application to Gearboxes," NASA/TM-2007-214954, July 2007b.

Guo, Y., and Parker, R. G., "Dynamic Modeling and Analysis of A Planetary Gear Involving Tooth Wedging and Bearing Clearance Nonlinearity," 2009 ASME International Design Engineering Technical Conferences, San Diego, CA, Aug. 30-Sept. 2, 2009.

Guo, Y., and Parker, R. G., "Dynamic Modeling and Analysis of a Spur Planetary Gear Involving Tooth Wedging and Bearing Clearance Nonlinearity," *European Journal of Mechanics A/Solids*, vol. 29, no. 6, pp. 1022-1033, 2010.

Handschuh, R. F., Krantz, T. L., Lerch, B. A., and Burke, C. S., "Investigation of Low-Cycle Bending Fatigue of AISI 9310 Steel Spur Gears," 10th ASME International Power Transmission and Gearing Conference, Las Vegas, NV, Sept. 4-7, 2007a.

Handschuh, R. F., Krantz, T. L., Lerch, B. A., and Burke, C. S., "Investigation of Low-Cycle Bending Fatigue of AISI 9310 Steel Spur Gears," NASA/TM-2007-214914, July 2007b.

Handschuh, R. F., Kilmain, C., and Ehinger, R., "Operational Condition and Superfinishing Effect on High-Speed Helical Gearing System Performance," 63rd American Helicopter Society Annual Forum, Virginia Beach, VA, May 1-3, 2007c; also NASA/TM–2007-214696, June 2007c.

Handschuh, R. F., Krantz, T. L., Lerch, B. A., and Burke, C. S., "Low Cycle Bending Fatigue of AISI 9310 Steel Spur Gears," Gear Solutions Magazine, pp. 18-25, Jan. 2008.

Handschuh, R. F., Ehinger, R., Sinusas, E., and Kilmain, C., "Double Helical Gear Performance in High Speed Helical Gear Trains," 65th American Helicopter Society Annual Forum, Grapevine, TX, May 27-29, 2009.

Handschuh, R. F, and Hurrell, M. J., "Initial Experiments of High-Speed Drive System Windage Losses," International Conference on Gears, Munich, Germany, Oct. 4-6, 2010.

Handschuh, R. F, and Hurrell, M. J., "Initial Experiments of High-Speed Drive System Windage Losses," NASA/TM-2011-216925, Nov. 2011a.

Handschuh, R. F., Polly, J., and Morales, W., "Gear Mesh Loss-of-Lubrication Experiments and Analytical Simulation," 67th American Helicopter Society Annual Forum, Virginia Beach, VA, May 3-5, 2011b.

Handschuh, R. F., Polly, J., and Morales, W., "Gear Mesh Loss-of-Lubrication Experiments and Analytical Simulation," NASA/TM-2011-217106, Nov. 2011c.

Handschuh, R. F., Roberts, G. D., Sinnamon, R. R., Stringer, D. B., Dykas, B. D., and Kohlman, L.W., "Hybrid Gear Preliminary Results - Application of Composites to Dynamic Mechanical Components," 68th American Helicopter Society Annual Forum, Ft. Worth, TX, May 1-3, 2012a.

Handschuh, R. F., Roberts, G. D., Sinnamon, R. R., Stringer, D. B., Dykas, B. D., and Kohlman, L. W., "Hybrid Gear Preliminary Results - Application of Composites to Dynamic Mechanical Components," NASA/TM-2012-217630, July 2012b.

Handschuh, R. F., and Burke, C., "Simulated Single Tooth Bending of High Temperature Alloys," NASA/TM-2012-217805, Dec. 2012c.

Handschuh, R. F., Kilmain, C., Ehinger, R., and Sinusas, E., "Gear Design Effects on the Performance of High Speed Helical Gear Trains as Used in Aerospace Drive Systems," 69th American Helicopter Society Annual Forum, Phoenix, AZ, May 21-23, 2013a.

Handschuh, R. F., Kilmain, C., Ehinger, R., and Sinusas, E., "Gear Design Effects on the Performance of High Speed Helical Gear Trains as Used in Aerospace Drive Systems," NASA/TM-217897, June 2013b.

Handschuh, R. F., LaBerge, K. E., DeLuca, S., and Pelagalli, R., "Vibration and Operational Characteristics of a Composite-Steel (Hybrid) Gear," NASA/TM-2014-216646, ARL-TR-6973, June 2014.

Handschuh, R. F., "Thermal Behavior of Aerospace Spur Gears in Norman and Loss-of-Lubrication Conditions," 71st American Helicopter Society Annual Forum, Virginia, Beach, VA, May 5-7, 2015.

He, D., Bechhoefer, E., Dempsey P., and Ma, J., "An Integrated Approach for Gear Health Prognostics," 68th American Helicopter Society Annual Forum, Ft. Worth, TX, May 1-3, 2012.

Heath, G. F., Slaughter, S. C., Morris, M. T., Fetty, J., Lewicki, D. G., and Fisher, D. J., "Face Gear Development Under the Rotorcraft Drive System for the 21st Century Program," 65th American Helicopter Society Annual Forum, Grapevine, TX, May 27-29, 2009.

Heath, G. F., Slaughter, S. C., Fisher, D. J., Lewicki, D. G., and Fetty, J., "Helical Face Gear Development Under the Enhanced Rotorcraft Drive System Program," 67th American Helicopter Society Annual Forum, Virginia Beach, VA, May 3-5, 2011.

Hill, M. J., Kunz, R. F., Noack, R. W., Long, L. N., and Handschuh, R. F., "Application and Validation of Unstructured Overset CFD Technology for Rotorcraft Gearbox Windage Aerodynamics Simulation," 64th American Helicopter Society Annual Forum, Montreal, Canada, April 29-May 1, 2008.

Hill, M. J., Kunz, R. F, Noack, R. W., Long, L. N., Morris, P. J., and Handschuh, R. F., "CFD Technology for Rotorcraft Gearbox Windage Aerodynamics Simulation," Gear Technology, *The Journal of Gear Manufacturing*, pp. 48-55, Aug. 2009.

Hill, M. J., Kunz, R. F, Medvitz, R. B., Handschuh, R. F., Long, L. N., and Noack, R. W., "CFD Analysis of Gear Windage Losses: Validation and Parametric Aerodynamic Studies," 66th American Helicopter Society Annual Forum, Phoenix, AZ, May 10-12, 2010.

Hill, M. J., Kunz, R. F, Medvitz, R. B., Handschuh, R. F., Long, L. N., Noack, R. W., and Morris, P. J., "CFD Analysis of Gear Windage Losses: Validation and Parametric Aerodynamic Studies," *Journal of Fluids Engineering*, vol. 133, no. 3, pp. 031103-031103-10, March 2011.

Hill, M. J., and Kunz, R. F., "A Computational Investigation of Gear Windage," NASA/CR-2012-217807, Dec. 2012.

Hood, A., LaBerge, K. E., Lewicki, D. G., and Pines, D., "Vibration Based Sun Gear Damage Detection," 2013 ASME Power Transmission and Gearing Conference, Portland, OR, Aug. 4-7, 2013.

Howard, S. A., Bruckner, R. J., DellaCorte, C., and Radil, K. C., "Preliminary Analysis for an Optimized Oil-Free Rotorcraft Engine Concept," 63rd American Helicopter Society Annual Forum, Virginia Beach, VA, May 1-3, 2007.

Howard, S. A., Bruckner, R. J., DellaCorte, C., and Radil, K. C., "Preliminary Analysis for an Optimized Oil-Free Rotorcraft Engine Concept," NASA/TM-2008-215064, March 2008a.

Howard, S. A., "Gas Foil Bearing Misalignment and Unbalance Effects," NASA/TM-2008-215176, May 2008b.

Howard, S. A., "Misalignment in Gas Foil Journal Bearings: An Experimental Study," Turbo Expo 2008 Gas Turbine Technical Congress and Exposition, Berlin, Germany, June 9-13, 2008c.

Howard, S. A., "Misalignment in Gas Foil Journal Bearings: An Experimental Study," NASA/TM-2008-215223, May 2008d.

Howard, S. A., Bruckner R. J., and Radil, K. C., "Advancements Toward Oil-Free Rotorcraft Propulsion," 65th American Helicopter Society Annual Forum, Grapevine, TX, May 27-29, 2009.

Howard, S. A., and Andres, L. S., "A New Analysis Tool Assessment for Rotordynamic Modeling of Gas Foil Bearings," Turbo Expo 2010 Gas Turbine Technical Congress and Exposition, Glasgow, Scotland, June 14-18, 2010a.

Howard, S. A., DellaCorte, C., and Bruckner, R. J., "Integration Methodology for Oil-Free Shaft Support Systems: Four Steps to Success," 8th International Conference on Rotor Dynamics, International Federation for the Promotion of Mechanism and Machine Science (IFToMM), Seoul, Korea, Sept. 12-15, 2010b.

Howard, S. A., DellaCorte, C., and Bruckner, R. J., "Integration Methodology for Oil-Free Shaft Support Systems: Four Steps to Success," NASA/TM-2010-216827, Nov. 2010c.

Howard, S. A., and Andres, L. S., "A New Analysis Tool Assessment for Rotordynamic Modeling of Gas Foil Bearings," *Journal of Engineering for Gas Turbines and Power*, vol. 133, no. 2, pp. 022505-022505-9, Feb. 2011.

Islam, A. A., Dempsey, P. J., Feldman, J., and Larsen, C., "Characterization and Comparison of Vibration Transfer Paths in a Helicopter Gearbox and a Fixture Mounted Gearbox," NASA/TM-2013-216586, Sept. 2013.

Islam, A. A., Dempsey, P. J., Feldman, J., and Larsen, C., "Characterization and Comparison of Vibration Transfer Paths in a Helicopter Gearbox and a Fixture Mounted Gearbox," SPIE: Smart Structures/NDE Conference, San Diego, CA, March 9-13, 2014.

Kiddy, J. S., Samuel, P. D., Lewicki, D. G., LaBerge, K. E., Ehinger, R. T., and Fetty, J., "Fiber Optic Strain Sensor for Planetary Gear Diagnostics," 67th American Helicopter Society Annual Forum, Virginia Beach, VA, May 3-5, 2011.

Kohlman, L. W., Ruggeri, C. R., Roberts, G. D., and Handschuh, R. F., "Improvements in High Speed, High Resolution Dynamic Digital Image Correlation for Experimental Evaluation of Composite Drive System Components," 69th American Helicopter Society Annual Forum, Phoenix, AZ, May 21-23, 2013a.

Kohlman, L. W., Ruggeri, C. R., Roberts, G. D., and Handschuh, R. F., "Improvements in High Speed, High Resolution Dynamic Digital Image Correlation for Experimental Evaluation of Composite Drive System Components," NASA/TM-2013-216537, July 2013b.

Krantz, T. L., and Tufts, B., "Pitting and Bending Fatigue Evaluations of a New Case-Carburized Gear Steel," 2007 ASME International Design Engineering Technical Conferences, Las Vegas, NV, Sept. 4-7, 2007a.

Krantz, T. L., and Tufts, B., "Pitting and Bending Fatigue Evaluations of a New Case-Carburized Gear Steel," NASA/TM-2007-215009, ARL-TR-4123, Dec. 2007b.

Krantz, T. L., and Tufts, B., "Pitting and Bending Fatigue Evaluations of a New Case-Carburized Gear Steel," Gear Technology, *The Journal of Gear Manufacturing*, pp. 52-57, March/April 2008.

Krantz, T. L., "On the Correlation of Specific Film Thickness and Gear Pitting Life," AGMA 2014 Fall Technical Meeting, Washington D.C., Oct. 2014.

Krantz, T. L., and Handschuh, R. F., "Gear Tooth Root Stresses of a Very Heavily Loaded Gear Pair - Case Study: Orbiter Body Flap Actuator Pinion and Ring Gear," 2015 ASME International Design Engineering Technical Conferences, Boston, MA, Aug. 2-5, 2015.

Krantz, T. L., Anderson, C., Shareef, I., and Fetty, J., "Testing Aerospace Gears for Bending Fatigue, Pitting, and Scuffing," 2017 ASME International Design Engineering Technical Conferences, Cleveland, OH, Aug. 6-9, 2017.

Krantz, T. L., Handschuh, R. F., and Roberts, G. D., "Results of NASA Technical Challenge to Demonstrate Two-Speed Drive for Vertical Lift," 74th American Helicopter Society Annual Forum, Phoenix, AZ, May 14-17, 2018.

Kunz, R. F., "High Fidelity CFD Analysis and Validation of Rotorcraft Gearbox Aerodynamics under Operational and Oil-Out Conditions," NASA/CR-2014-216651, July 2014.

LaBerge, K. E., Handschuh, R. F., Roberts, G. D., and Thorp, S. A., "Performance Investigation of a Full-Scale Hybrid Composite Bull Gear," 72nd American Helicopter Society Annual Forum, West Palm Beach, FL, May 17-19, 2016.

LaBerge, K. E., Berkebile, S. P., Handschuh, R. F., and Roberts, G. D., "Hybrid Gear Performance Under Loss-of-Lubrication Conditions," 73rd American Helicopter Society Annual Forum, Fort Worth, TX, May 9-11, 2017.

LaBerge, K. E., Johnston, J. P., Handschuh, R. F., and Roberts, G. D., "Evaluation of a Variable Thickness Hybrid Composite Bull Gear," 74th American Helicopter Society Annual Forum, Phoenix, AZ, May 14-17, 2018.

Lewicki, D. G., Heath, G. F., Filler, R. R., Slaughter S. C., and Fetty, J., "RDS-21 Face-Gear Surface Durability Tests," 63rd American Helicopter Society Annual Forum, Virginia Beach, VA, May 1-3, 2007a.

Lewicki, D. G., Woods, R. L., Litvin, F. L., and Fuentes, A., "Evaluation of a Low-Noise Formate Spiral-Bevel Gear Set," 10th International Power Transmission and Gearing Conference, Las Vegas, NV, Sept. 4-7, 2007b.

Lewicki, D. G., Woods, R. L., Litvin, F. L., and Fuentes, A., "Evaluation of a Low-Noise Formate Spiral-Bevel Gear Set," NASA/TM-2007-215032, Dec. 2007c.

Lewicki, D. G., Dempsey, P. J., Heath, G. F., and Shanthakumaran, P., "Gear Fault Detection Effectiveness as Applied to Tooth Surface Pitting Fatigue Damage," 65th American Helicopter Society Forum, Grapevine, TX, May 27-29, 2009.

Lewicki, D. G, DeSmidt, H. A., Smith, E. C., and Bauman, S. W., "Two-Speed Gearbox Dynamic Simulation Predictions and Test Validation," 66th American Helicopter Society Annual Forum, Phoenix, AZ, May 10-12, 2010a.

Lewicki, D. G., Dempsey, P. J., Heath, G. F., and Shanthakumaran, P., "Gear Fault Detection Effectiveness As Applied to Tooth Surface Pitting Fatigue Damage," Gear Technology, *The Journal of Gear Manufacturing*, pp. 48-59, Nov./Dec. 2010b.

Lewicki, D. G., LaBerge, K. E, Ehinger, R. T., and Fetty, J., "Planetary Gearbox Fault Detection Using Vibration Separation Techniques," 67th American Helicopter Society Annual Forum, Virginia Beach, VA, May 3-5, 2011.

Lewicki, D. G, DeSmidt, H. A., Smith, E. C., and Bauman, S. W., "Dynamics of a Dual-Clutch Gearbox System: Analysis and Experimental Validation," *Journal of the American Helicopter Society*, vol. 58, no. 1, pp. 17-28, Jan. 2013.

Lewicki, D. G., and Stevens, M. A., "Testing of Two-Speed Transmission Configurations for Use in Rotorcraft," NASA/TM-2015-218816, June 2015.

Lewicki, D. G., and Heath, G. F., "Advanced Face Gear Surface Durability Evaluations," NASA/TM-2016-218943, March 2016.

McCaslin, R., Bayoumi, A., and Dempsey, P. J., "Investigation Of Condition Indicators, Operational Conditions And Gear Health State Using Data Mining Techniques," 2016 Machinery Failure Prevention Technology Conference, Dayton, OH, May 24-26, 2016.

McIntyre, S., and Kunz, R., "Advances and Applications in Comprehensive Gearbox Aero-Thermodynamics and Tribology Simulation," 73rd American Helicopter Society Annual Forum, Fort Worth, TX, May 9-11, 2017.

Miller, B. A, and Howard, S. A., "Identifying Bearing Rotordynamic Coefficients Using an Extended Kaman Filter," NASA/TM-2008-215298, Aug. 2008.

Morales, W., Handschuh, R. F., and Krantz, T. L., "Feasibility Study of Vapor-Mist Phase Reaction Lubrication Using a Thioether Liquid," 62nd Society of Tribologists and Lubrication Engineers Annual Meeting and Exhibition, Philadelphia, PA, May 6–10, 2007a.

Morales, W., Handschuh, R. F., and Krantz, T. L., "Feasibility Study of Vapor-Mist Phase Reaction Lubrication Using a Thioether Liquid," NASA/TM-2007-215035, Dec. 2007b.

Nenadic, N. G., Wodenscheck, J. A., Thurston, M. G., and Lewicki, D. G., "Seeding Cracks Using a Fatigue Tester for Accelerated Gear Tooth Breaking," SEM IMAC XXIX: A Conference and Exposition on Structural Dynamics, Jacksonville, FL, Jan. 31-Feb. 3, 2011a.

Nenadic, N. G., Wodenscheck, J. A., Thurston, M. G., and Lewicki, D. G., "Seeding Cracks Using a Fatigue Tester for Accelerated Gear Tooth Breaking," NASA/TM-2011-216983, Feb. 2011b.

Oswald, F. B., Zaretsky, E. V., and Poplawski, J. V., "Interference Fit Life Factors for Roller Bearings," 63rd STLE Annual Meeting and Exhibition, Cleveland, OH, May 18-22, 2008.

Oswald, F. B., Zaretsky, E. V., and Poplawski, J. V., "Interference-Fit Life Factor for Ball Bearings," NASA/TM-2010-216913, Nov. 2010a.

Oswald, F. B., Zaretsky, E. V., and Poplawski, J. V., "Effect of Internal Clearance on Load Distribution and Life of Radially Loaded Ball and Roller Bearings," 65th STLE Annual Meeting and Exhibition, Las Vegas, NV, May 16-20, 2010b.

Oswald, F. B., Zaretsky, E. V., and Poplawski, J. V., "Effect of Internal Clearance on Load Distribution and Life of Radially Loaded Ball and Roller Bearings," NASA/TM-2012-217115, April 2012a.

Oswald, F. B., Zaretsky, E. V., and Poplawski, J. V., "Effect of Internal Clearance on Load Distribution and Life of Radially Loaded Ball and Roller Bearings," Tribology Transactions, vol. 55, no. 2, pp. 245-265, March 2012b.

Radil, K. C., DellaCorte, C., and Zeszotek, M., "Thermal Management Techniques for Oil-Free Turbomachinery Systems," NASA/TM-2006-214358, Oct. 2006.

Radil, K. C., DellaCorte, C., and Zeszotek, M., "Thermal Management Techniques for Oil-Free Turbomachinery Systems," Tribology Transactions, vol. 50, no. 3, pp. 319-327, 2007.

Radil, K. C., and DellaCorte, C., "A Three-Dimensional Foil Bearing Performance Map Applied to Oil-Free Turbomachinery," Army Research Laboratory, ARL-TR-4473, April 2009.

Radil, K. C, and Batcho, Z., "A Novel Thermal Management Approach for Radial Foil Air Bearings," Army Research Laboratory, ARL-MR-0749, July 2010.

Rickmeyer, T., and Dempsey, P. J., "Processes & Considerations in Extensions to Time Between Overhauls and Paths to On-Condition for US Army Rotorcraft Propulsion Systems," 67th American Helicopter Society Annual Forum, Virginia Beach, VA, May 3-5, 2011.

Roberts, G. D., Kohlman, L. W., Ruggeri, C. R., Handschuh, R. F., and Thorp, S. A., "A Hybrid Composite/Metal Gear Concept for Rotorcraft Drive Systems," Composites World Carbon Fiber 2013, Knoxville, TN, Dec. 9-12, 2013.

Scheidler, J. J, Asnani, V. M., and Dapino, M. J., "Design and Testing of a Dynamically-Tuned Magnetostrictive Spring with Electrically-Controlled Stiffness," Proceedings of SPIE Smart Structures, Vol. 9433, Paper No. 94330F, March 2015.

Scheidler, J. J, and Asnani, V. M., "A Review of Noise and Vibration Control Technologies for Rotorcraft Transmissions," Inter-Noise 2016, Hamburg, Germany, Aug. 21-24, 2016.

Shen, T., Krantz, T. L., and Sebastian, J., "Advanced Gear Alloys for Ultra High Strength Applications," 67th American Helicopter Society Annual Forum, Virginia Beach, VA, May 3-5, 2011a.

Shen, T., Krantz, T. L., and Sebastian, J., "Advanced Gear Alloys for Ultra High Strength Applications," NASA/TM-2011-217121, Nov. 2011b.

Siegel, D., Lee, J., and Dempsey, P. J., "Investigation And Evaluation Of Condition Indicators, Variable Selection, And Health Indication Methods And Algorithms For Rotorcraft Gear Components," 2014 Machinery Failure Prevention Technology Conference, Virginia Beach, VA, May 20-22, 2014.

Skurka, J. C., "Elastohydrodynamic Lubrication of Roller Bearings." *Journal of Lubrication Technology*, 92.2 (1970): pp. 281-288.

Stevens, M. A., Handschuh, R. F., and Lewicki, D. G., "Concepts for Variable/Multi-Speed Rotorcraft Drive System," 64th American Helicopter Society Annual Forum, Montreal, Canada, April 29-May 1, 2008a.

Stevens, M. A., Handschuh, R. F., and Lewicki, D. G., "Concepts for Variable/Multi-Speed Rotorcraft Drive System," NASA/TM-2008-215276, Sept. 2008b.

Stevens, M. A., Handschuh, R. F., and Lewicki, D. G., "Variable/MultiSpeed Rotorcraft Drive System Concepts," NASA/TM-2009-215456, ARL-TR-4758, March 2009.

Stevens, M. A., Handschuh, R. F., and Lewicki, D. G., "Offset Compound Gear Drive," NASA Tech Briefs Magazine, Vol. 34, No. 5, pp. 49-50, May 2010.

Stevens, M. A., Lewicki, D. G., and Handschuh, R. F., "Concepts for Multi-Speed Rotorcraft Drive System - Status of Design and Testing at NASA GRC," 71st American Helicopter Society Annual Forum, Virginia Beach, VA, May 5-7, 2015.

Stevens, M. A., Valco, M. J., and LaBerge, K. E., "Two-Speed Rotorcraft Research Transmission Power-Loss Associated with the Lubrication and Hydraulic Rotating-Feed-Through Design Feature," 74th American Helicopter Society Annual Forum, Phoenix, AZ, May 14-17, 2018.

Stringer, D. B., Dykas, B. D., LaBerge, K. E., Zakrajsek, A. J., and Handschuh, R. F., "A New High-Speed, High-Cycle, Gear-Tooth Bending Fatigue Test Capability," 67th American Helicopter Society Annual Forum, Virginia Beach, VA, May 3-5, 2011.

Vijayakar, S., "Contact and Bending Durability Calculation for Spiral-Bevel Gears," NASA/CR-2016-219112, June 2016.

Yamauchi, G. K. and Young, L. A, "A Status of NASA Rotorcraft Research," NASA TP-2009-215369, Sept. 2009.

Yoon, J., He, D., and Dempsey, P. J., "An Efficient Prognostic Estimator," 2014 Machinery Failure Prevention Technology Conference, Virginia Beach, VA, May 20-22, 2014.

Yu, Q., McIntyre, S., Kunz, R., Saribay, Z., and Bill, R., "A Multi-Scale Computational Framework for Modeling the Thermo-Fluid-Dynamics of High Speed Gearbox Systems," 69th American Helicopter Society Annual Forum, Phoenix, AZ, May 21-23, 2013.

Zaretsky, E. V., Lewicki, D. G., Savage, M., and Vlcek, B. L., "Determination of Turboprop Reduction Gearbox System Fatigue Life and Reliability," Tribology Transactions, Society of Tribologists and Lubrication Engineers, vol. 50, no. 4, pp. 507-516, Oct. 2007a.

Zaretsky, E. V., Lewicki, D. G., Savage, M., and Vlcek, B. L., "Determination of Turboprop Reduction Gearbox System Fatigue Life and Reliability," NASA/TM-2007-215019, Nov. 2007b.

CHAPTER 7. ENGINES

Christopher A. Snyder[1] and Paul W. Giel[2]

INTRODUCTION

The overarching goals of the NASA Revolutionary Vertical Lift Technology (RVLT) project are to enable the next generation of vertical lift vehicles with aggressive goals for efficiency, noise, and emissions, to expand current capabilities and to develop new commercial markets. Significant improvements to the propulsion system of the vehicle—drive systems and engines—are key to accomplishing these goals. Chapter 6 summarized NASA research in advanced drive systems for VTOL aircraft circa 2008–2018. NASA engine research for rotary wing vehicles during this same time period is summarized here. The research revolved around the gas turbine (Brayton cycle), which is the dominant engine for conventional rotorcraft. Many years of research and development by government, industry, and university groups have made gas turbines reliable and compact, with a high power-to-weight ratio, and reasonably efficient. Combining the gas turbine engine with a high-energy-density (predominantly hydrocarbon) fuel often results in the most mission-capable, lowest takeoff-gross-weight vehicle.

This chapter begins by reviewing system studies of propulsion architectures that NASA sponsored or conducted. Assessing potential engine and drive system technologies can reveal the individual or combinations of technologies that will yield optimum benefits. Results from the studies provided justification for establishing two Technical Challenges (TCs)—one focused on a Two-Speed Transmission (described in Chapter 6, Drive Systems) and the other on a Variable Speed Power Turbine (VSPT). The TCs were executed over a 5-year period by the RVLT project. The VSPT TC was executed during 2012–2017 with a goal to demonstrate a VSPT with 50 percent improvement in efficient operational capability. This aggressive goal was achieved by partnering with industry and the U.S. Army. The VSPT research is described following the systems studies' section. After the summary of the VSPT work, research in High Efficiency Centrifugal Compressors (HECCs) is described. Modeling and simulation (MODSIM) efforts for the critical compression system are summarized next. These MODSIM efforts help to relate hardware tests and detailed modeling so that basic phenomena such as the source and propagation of fluid flow instabilities are better understood. Mitigating these instabilities improves compressor and overall engine performance, stability, and reliability. Progress in assessing engine health is described next. Monitoring engine performance using Health Usage and Monitoring Systems (HUMS) data can help assess engine capability for continued operations or signal potential maintenance needs based on performance metrics, as opposed to arbitrary schedules. This chapter is completed with summaries of research in wave rotor performance and a description of PyCycle. Wave rotors can potentially be used as a topping cycle on gas turbine engines, which can improve gas turbine performance. PyCycle is an engine modeling code that uses gradient-based optimization techniques to design an optimized engine.

[1] NASA Glenn Research Center, 21000 Brookpark Road, Cleveland, OH 44135.
[2] Vantage Partners, LLC, 3000 Aerospace Pkwy, Brook Park, OH 44142.

ENGINE/DRIVE SYSTEM STUDIES

After the Large Civil Tiltrotor (LCTR) vehicle and mission were developed to help focus overall research directions [Acree et al., 2008], engine studies were commenced to define potential engine systems that could meet assumed engine performance levels. The preliminary vehicle and mission studies also assumed an almost 50 percent reduction in rotor speed from takeoff/hover to cruise conditions to maintain high levels of rotor performance over the entire mission. This speed reduction was enabled by a two-speed gearbox. Snyder and Thurman [2009, 2010a] defined initial gas turbine engine characteristics that could potentially meet the power and aggressive fuel-efficiency goals. The notional engine would be operating at more stringent temperatures and pressures than present engines in that particular power class, but not as stringent as those in modern, large engines. The authors noted that the rotor speed reduction from hover to cruise could also potentially be achieved with a single-speed gearbox if the power turbine could maintain sufficient power and efficiency at the significantly reduced rpm at cruise conditions.

The initial gas turbine engine was conceptualized with one or two independent shafts for the gas generator core; each core engine would have an additional shaft for the free power turbine. With the two-speed gearbox, both engine concepts met all power requirements from the preliminary vehicle studies. However, with a single-speed gearbox, the single-shaft core engine did not meet cruise power levels at the required 50 percent rpm reduction. From a compressor design aspect, the two-shaft core design appeared more feasible. Preliminary assessment of the compressor design suggested that using all axial stages would result in impractically small exit blade heights, even with assumptions of near-term advanced technologies. Therefore, the authors proposed a two-shaft core with an axial-centrifugal compressor design and a free power turbine as the reference gas turbine engine. Power turbine flow and power requirements were developed to help assess the viability of a single-speed-gearbox drive system with all speed variation achieved in the power turbine (aptly named the Variable Speed Power Turbine—VSPT).

Subsequently, Snyder and Thurman [2010b, 2010c] updated engine component performance assumptions, performed subsequent engine design optimization, and then assessed the inclusion of various advanced engine component technologies on engine size, weight, fuel efficiency, and the subsequent benefit on vehicle design gross weight and fuel burn. Since the vehicle fuel weight is significantly larger (5×) than the gas turbine engine weight, advanced technologies that improved engine fuel efficiency yielded greater benefits than those from engine weight reduction. The largest benefits (12 percent reduction in takeoff gross weight (TOGW), 39 percent reduction in fuel burn) resulted from advanced, high-temperature turbine materials that could eliminate parasitic flows for turbine cooling, but were deemed fairly high risk. A similar overall engine and vehicle benefit could be achieved from the synergistic inclusion of modest improvements in all the other engine technologies reviewed, and this approach seemed more technically feasible.

A final engine technology assessment based on the second-generation LCTR (LCTR2) vehicle and mission was performed and reported in Snyder [2014]. Relevant small engine technology efforts were discussed and used to update engine technology assumptions for current (operating) levels and two levels of future, advanced technology engines. Significant benefits for vehicle TOGW, fuel burn, and reduction in oxides of nitrogen emissions resulted from the development and inclusion of advanced engine technologies.

Regarding engine-drive-system design for optimum vehicle performance, Snyder [2014] explored using a gas turbine engine with VSPT technology coupled with a single-speed gearbox versus an engine using more conventional power turbine technology with a two-speed gearbox to achieve rotor rpm reduction for cruise efficiency. Similar but mixed results were noted between government in-house and industry-contracted studies. Industry reported 0.5 percent reduced TOGW and 5 percent lower fuel burn advantage for the conventional turbine, two-speed-gearbox combination. Government in-house studies noted 0.5 percent TOGW benefit and 2.6 percent fuel burn for the VSPT, single-speed-gearbox combination. Snyder [2014] also reported that "Both results are strongly dependent on the technology assumptions for efficiency and weight for the VSPT and gearbox technologies." Assuming current engine technology and more conventional turbine technology would require a two-speed gearbox, optimum vehicle (TOGW and fuel burn) was achieved at minimum rotor cruise rpm (almost 50 percent speed reduction). Advanced engines using fixed-geometry VSPT technology weighed almost the same as the traditional turbine technology designs. Therefore, with advanced engines the optimum vehicle would use the engine with VSPT and a single-speed gearbox (resulting in the lightest engine/drive system combination). Optimum vehicle TOGW and fuel burn was a compromise between improved rotor versus reduced VSPT performance as rotor cruise rpm decreased. The reduction in rotor rpm from takeoff/hover to cruise was 30 to 40 percent for the optimum vehicle, compared to a 50-percent reduction for other engine gearbox combinations.

VARIABLE SPEED POWER TURBINE (VSPT)

Advanced future rotary wing vehicles of all classes and sizes will require wider rotor speed variation capability and improved operational efficiency under varying conditions. Currently, the variation of rotor rotational speed is about 15 percent, achieved primarily through a reduction in turbine engine speed, which degrades engine efficiency. Various engine system studies referenced above reported on the potential viability of a VSPT to efficiently meet the propulsion requirements of the notional LCTR and other future rotary wing vehicle configurations. Beginning in fiscal year 2009, a research focus was initiated within RVLT to assess the range of practicality of a VSPT. While the initial motivation for VSPT research focused on the notional LCTR configuration, the need for variable speed turbines grew across many civil and military applications. This includes the expanding role of turbines to produce varying levels of electrical power across flight regimes while also producing propulsive thrust.

The VSPT research needs were identified and outlined by Welch [2010], and a conceptual design was described and the necessary elements of a VSPT research plan were laid out. The plan included studies of the aerodynamics associated with large incidence angles, highly loaded turbine blades, and low Reynolds number flows at altitude. The technical incidence angle challenges originated from the requirements of the LCTR main rotors to operate over a wide speed range—100 percent speed at takeoff to 54 percent speed at cruise—which leads to vane and blade incidence angles of 60 degrees or more. The highly loaded turbine blade challenges originated from engine studies that showed the need for nearly constant enthalpy extraction from takeoff to cruise, leading to turbine work factors at the 54-percent cruise condition being approximately 3.5 times higher than at the 100-percent takeoff condition. The low Reynolds number challenges result from operation at 28,000-foot-altitude cruise. To address these challenges, the following research steps were laid out for the VSPT subproject:

- VSPT Requirements Definition and Conceptual Design
- Detailed Design of Incidence-Tolerant Blading
- Flow Transition Sub-Model Assessment and Implementation
- Transonic Cascade Testing of Two-Dimensional (2D) Blade Sections
- Rotordynamics Assessment
- VSPT Component Experiment

These steps were accomplished through a number of in-house NASA efforts and through a number of contracted efforts, culminating with two VSPT component test contracts issued jointly with the U.S. Army Aviation Applied Technology Directorate.

As a first step, Welch [2011] conducted the conceptual design of a VSPT at the meanline level, leading to a four-stage turbine with a design point at the 54-percent cruise operating speed. The design of 2D airfoil sections and the resulting three-dimensional (3D) vane and blade geometries were documented. A computational fluid dynamics (CFD) assessment of the aerodynamic performance of a VSPT for the LCTR application was then described. Three-dimensional Reynolds Averaged Navier-Stokes (RANS) computations were used to assess the design and off-design performance of an embedded 1.5-stage portion of the VSPT; Rotor 1, Stator 2, and Rotor 2. The 3D CFD results yielded the same efficiency-versus-speed trends that were predicted by the meanline analyses, supporting the design choice to execute the turbine design at the 54-percent cruise operating speed. The agreement of the analyses was despite the strongly 3D flow features that were observed in the CFD solutions. For example, a tornado-like vortex, shown in Figure 7.1, was observed near the pressure surface cove separation region of Rotor 2. The agreement between the 3D RANS computations and the meanline analysis corroborated the incidence correlation of the meanline code and supported the conceptual design approach that established the design speed at the 54-percent cruise operating speed point, selected to minimize overall mission fuel burn.

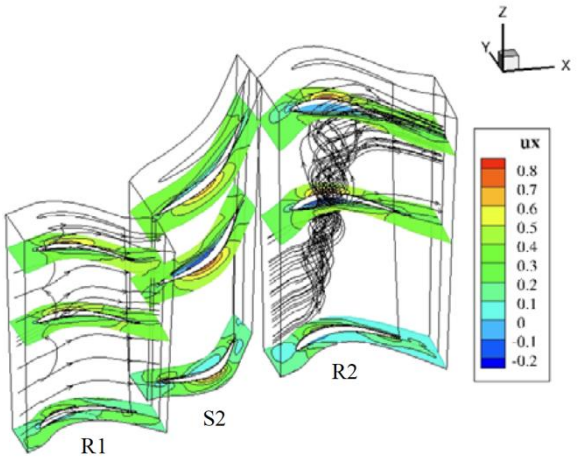

Figure 7.1. Computed contours of axial velocity and streamlines in Rotors 1 and 2 at the 100-percent-speed off-design takeoff point (Fig. 16 of Welch [2011]).

In preparation for the turbine design tool needs that were anticipated, efforts were undertaken to develop and improve preliminary design tools for axial flow turbines. Chen [2009a] evaluated a pair of intermediate level-of-fidelity computer codes, TD2-2 (design), and AXOD (off-design). TD2-2 employs a streamline curvature method for design, while AXOD performs a flow analysis with an equal radius-height domain decomposition strategy. Both methods resolve only the flows in the annulus region while modeling the impact introduced by the blade rows. Two validation cases for existing high-efficiency turbines were analyzed at design and off-design conditions; one was a two-stage cooled high-pressure turbine and the other was a five-stage uncooled low-pressure turbine. The results were consistent with the performance predicted using the actual turbine designs, and both compared favorably to the experimental data reported.

Using the validated design and off-design codes, TD2-2 and AXOD, Chen [2009b] performed preliminary turbine analyses applicable to the LCTR. The first set of analyses examined the aerodynamic feasibility of a variable pitch turbine. The results indicated that significant efficiency improvements could be realized if the practical complications associated with actively resetting the turbine vane and blade cambers could be overcome. The second set of analyses considered the One Engine Inoperative (OEI) condition. Calculations were performed for two contingency methods: throttle push and steam injection. The results indicated that 30 to 45 percent additional power, relative to the nominal takeoff power, could be extracted from the remaining operative engine by either of the two methods.

The capability of the turbine off-design code, AXOD, was extended to include configurations with an outlet guide vane as described by Chen [2011]. The updated code was validated by comparison to experimental data from separate 4-1/2-stage and 3-1/2-stage highly loaded fan-drive turbine tests.

A more detailed follow-on analysis of an embedded 1.5-stage portion of the notional VSPT for the LCTR application was performed by Welch (2012). The design and off-design performance levels were assessed using RANS analyses with mixing plane and sector-periodic, unsteady RANS analyses. The intent of the effort was to assess the impact of unsteadiness of blade-row interactions on the time-mean flow, and specifically, to identify potential departure from the predicted trend of efficiency with shaft-speed change of meanline and 3D RANS/mixing-plane analyses used for design. The trend of efficiency with changing VSPT shaft speed from the URANS simulation, from 54 percent (28,000 feet, cruise) to 100 percent (2,000 feet, takeoff), was found to agree with the corresponding trends from the two RANS/mixing plane codes and meanline codes used for turbine design. This key finding gives confidence to turbine designers in their selection of optimum turbine design speed for minimizing mission fuel burn.

The research plan laid out by Welch [2010] recognized the importance of design considerations beyond just the aerodynamic performance of VSPTs. Ford et al. [2012a] identified key technological challenges and gaps associated with the LCTR application of a VSPT. They proposed component-level aerodynamic research and technology development plans to address the challenges. Noting that the large speed variation made rotordynamics another potential obstacle, they performed the conceptual design of a VSPT with sufficient definition to perform a rotordynamics analysis. To address the rotordynamics concerns, Howard [2012] performed a preliminary feasibility study for a conceptual engine sized for the LCTR. The analysis considered critical speed placement in the operating speed envelope, stability analysis up to the maximum anticipated operating speed, and potential unbalance response amplitudes to determine that a VSPT is likely to be challenging, but not impossible to achieve in a tiltrotor propulsion engine.

The aerodynamic challenges associated with the large-incidence-angle variations of a VSPT, combined with the 28,000-foot-cruise requirement, exacerbated the need for CFD analyses to accurately predict the location and effects of laminar-to-turbulent flow transition on the turbine vanes and blades. Aerodynamic losses depend critically on flow separation, to which blades are particularly susceptible at off-design flow angles. Separation, in turn, depends critically on the local state of the boundary layer; laminar, transitional, or turbulent. In recognition of this, Ameri [2012] considered several turbulence models that offered an improved transition prediction capability. The three-equation model of Walters and Leylek [2004] was implemented in the Glenn-HT CFD code. Two-dimensional heat transfer predictions of flat plate flow, and 2D and 3D heat transfer predictions on a turbine blade, were performed. Surface heat transfer, a strong indicator of flow transition, was analyzed. The location of transition was successfully predicted on the suction side, and the transition modeling on the pressure side was reasonable. A loss bucket—loss levels versus incidence angle—was predicted for comparison to anticipated experimental data that was being acquired at NASA Glenn Research Center (GRC) (see Fig. 7.2).

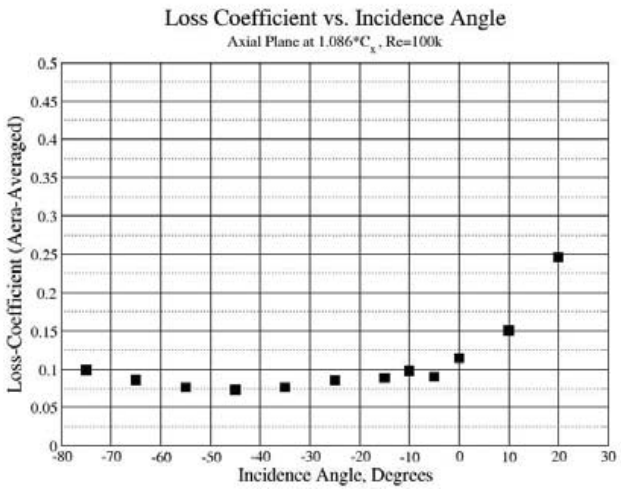

Figure 7.2. Computed loss bucket calculated from integrated wakes (Fig. 18 of Ameri [2012]).

NASA issued several contracts to gas turbine engine manufacturers in order to incorporate industry insight into the VSPT development program. In a study performed by Williams International, LLC, a VSPT design was executed for the LCTR using overall fuel burn for a notional mission as the figure of merit. The results of the Williams International study were reported by Suchezky and Cruzen [2012]. A methodical, multiple design-point process was used to arrive at a flow path that was fundamentally speed insensitive. Three- and four-stage VSPTs were examined, with the latter emerging from the flow path study as having the best potential to minimize fuel burn. Various designs were analyzed and traded against each other with a turbine meanline code and CFD calculations being used to corroborate the results. Figure 7.3 shows a meridional view of the four-stage VSPT, along with details of the third-stage CFD analysis. CFD consistently showed better negative incidence tolerance (high speed) than the one-dimensional (1D) meanline loss systems, suggesting that moving the design point selection to a lower speed than the 1D prediction may be prudent. In order to verify this and other design alternatives, a cost-effective plan was delineated to design, fabricate, instrument, and experimentally test a VSPT component. The design methodology and technology investigated in this study can provide benefits to other systems beyond the LCTR. Any system that can benefit from improved off-design performance, whether turbofan, turboshaft, or turboprop, may be able to take advantage of the proposed approach to avoid the complexity and cost associated with traditionally variable geometry approaches.

A parallel study was performed by Rolls-Royce North American Technologies, Inc. (aka Liberty Works) to apply their experience with VSPT technology developed for the V-22 Osprey, as well as to apply a proprietary blade design/optimization system to address the problem of a 50-percent variation in power turbine speed and Reynolds numbers between sea level and 35,000 feet. The results of the study were reported by Ford et al. [2012b]. In the study, meanline analyses were used to analyze three- and four-stage VSPTs to meet the specified engine requirements. After considering stage efficiency potential versus work factor (e.g., a Smith Chart analysis;

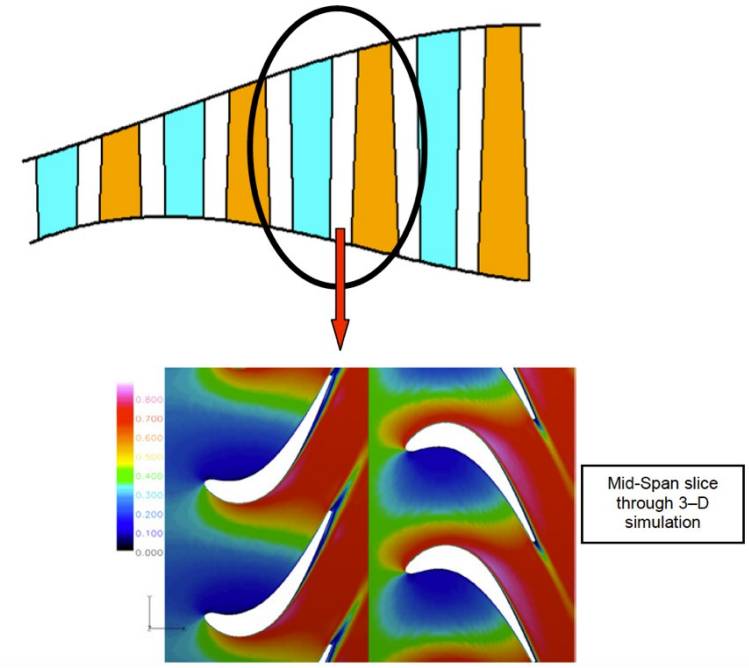

Figure 7.3. Third-stage extracted from full simulation to investigate off-design performance (Fig. 2.18 of Suchezky and Cruzen [2012]).

Smith [1965]), which restricts the level of acceptable stage work factor, a four-stage turbine was selected. A detailed 3D blade aero design/optimization was concentrated on the second rotor of the selected four-stage meanline design. Rotor 2 was selected as a representative embedded blade row, both in terms of overall flow turning (96 degrees at cruise and 53 degrees at takeoff) and incidence range (42 degrees) requirements between cruise and takeoff. The midspan section, which was optimized to minimize loss at the cruise condition (i = 5.8 degrees) and achieve required incidence range at acceptable loss levels, was chosen for a subsequent series of cascade tests at NASA GRC. Along with the cascade tests, a cost-effective plan to design, fabricate, instrument, and test a multistage, rotating VSPT component was also delineated.

The experimental and computational VSPT research efforts at NASA GRC were summarized in an interim report by Welch et al. [2012]. Initial steps toward experimental testing of incidence tolerant blading in a transonic linear cascade were described, and progress towards the development/improvement of a simulation capability for multistage turbines with low-Reynolds-number transitional flow was summarized. Preliminary rotordynamics analyses indicated that concept engines with 50 percent VSPT shaft-speed range were viable. Assessments of potential paths toward VSPT component-level testing were summarized.

To further assess the ability of CFD to simulate VSPT-relevant flows, unsteady computations of a 1-1/2-stage large-scale rotating turbine were reported by To [2012]. The unsteady CFD calculations were performed with the TURBO code running in multistage single passage (phase lag) mode. The United Technologies Research Center (UTRC) 1-1/2-stage Large Scale Rotating

Turbine was selected as the candidate engine configuration for this computational effort because of the completeness and availability of the data. Time-averaged midspan pressure coefficients for each blade were compared to the test data. Time-averaged flow speed, flow angle, and static pressure at the midspan blade exit plane were computed and compared with the data. The comparisons show that the CFD results were only in qualitative agreement with the test data and indicate that the poor mesh quality might be the cause for the discrepancies (an inherent drawback for turbine blades gridded with an H-mesh). Improvements were recommended for future research in this area.

The LCTR conceptual design was developed as part of the NASA Heavy Lift Rotorcraft Systems Investigation in order to establish a consistent basis for evaluating the benefits of advanced technology for large tiltrotors. As the conceptual studies proceeded, the conceptual LCTR evolved into the second-generation LCTR2. The LCTR2 design goal was to carry 90 passengers for 1,000 nautical miles at 300 knots, with vertical takeoff and landing capability. Snyder and Acree [2012] examined the impact of the vehicle change on its propulsion system, particularly on the VSPT. They performed a preliminary assessment of VSPT technology on LCTR2 sizing, while maintaining the same advanced technology engine core. Six concepts were studied: one with a single-speed engine and a multi-speed (shifting) gearbox; and five VSPT concepts, comprising a matrix of either three or four turbine stages, fixed or variable guide vanes, and a minimum weight, two-stage, fixed-geometry VSPT. The study concluded that, based on study assumptions, fixed-geometry VSPT concept options performed better than their variable-geometry counterparts. However, the outcome for some optimum configurations was so unexpected as to recommend a deeper look at the underlying technology assumptions.

As a first step towards the experimental assessment of incidence effects brought about by the variable-speed requirements, the NASA GRC Transonic Turbine Blade Cascade Test Facility was modified to accommodate the large negative incidence variation as described by McVetta et al. [2012]. As shown in Figure 7.4, the cascade blades are mounted on a large-diameter disc, which can be rotated to change the inlet incidence. The original configuration allowed a 45-degree variation in inlet flow angles ranging from 33.8 to 78.6 degrees as measured from the blade's axial direction. The facility modifications allowed for the cascade to be rotated to inlet flow angles as low as –17 degrees, although only at distinct angles because of the discrete upper inlet board extensions needed for the lower inlet flow angles. The facility modifications also included replacement of the facility exhaust duct and structural members within the exhaust section to provide better periodicity at the new, lower inlet flow angles. The facility modifications were validated using a GE Energy Efficient Engine (EEE) tip section blade so the results could be compared to previously acquired data. The facility's ability to independently vary Reynolds number and Mach number were capitalized on in order to examine a factor of eight variation in Reynolds number as shown in the operating envelope of Figure 7.5. Detailed exit total pressures, flow angles, and blade-loading data acquired over a wide range of Reynolds numbers, Mach numbers, and incidence angles showed good repeatability, periodicity, and consistency with scaling laws. A key finding of the study was the strong correlation of blade-row loss levels with Zweifel coefficient, along with the finding that the correlation breaks down at the extreme negative incidence. The loss levels correlated consistently with incidence angle and Reynolds number, and the loss bucket narrowed (incidence-tolerance diminished) at lower Reynolds numbers.

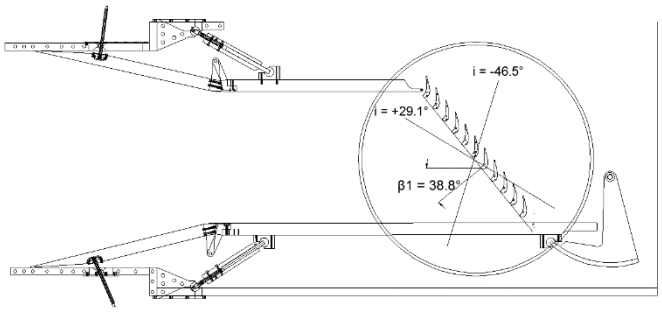

Figure 7.4. Cascade layout with GE EEE blades at β_1 = 38.8° (i = 9.1°) (Fig. 1 of McVetta et al. [2012]).

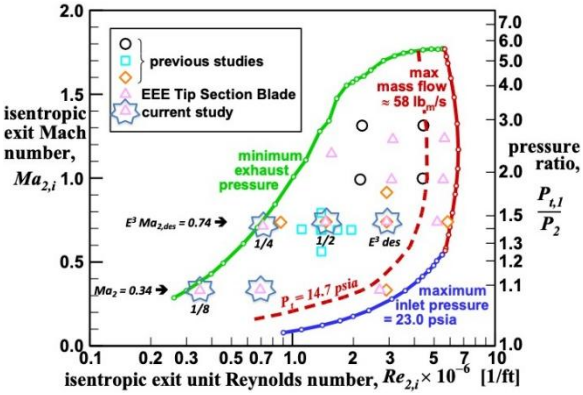

Figure 7.5. Operating envelope of NASA's Transonic Turbine Blade Cascade Test Facility (Fig. 2 of McVetta et al. [2012]).

With the Transonic Turbine Blade Cascade Test Facility modified and validated, assessment of the incidence-tolerant 2D blade section designed under the Rolls-Royce North America (N.A.) contract described above was undertaken. The results of the experimental study are presented by McVetta et al. [2013]. Steady-state data were obtained for 10 incidence angles ranging from 15.8 to −51.0 degrees. At each angle, data were acquired at five flow conditions with the exit Reynolds number (based on axial chord) varying over an order-of-magnitude from 2.12×10^5 to 2.12×10^6. Data were obtained at the design exit Mach number of 0.72 and at a reduced exit Mach number of 0.35 as required to achieve the lowest Reynolds number. Midspan total pressure and exit flow angle data were acquired using a five-hole pitch/yaw probe surveyed on a plane located 7.0 percent axial chord downstream of the blade trailing edge plane, spanning three blade passages. Blade loading data were also acquired. Data from this study were acquired at low inlet turbulence intensity levels in order to admit transitional flow appropriate to altitude conditions. The inlet turbulence level was estimated to range from 0.25 to 0.40 percent. The midspan total pressure survey data were integrated to generate the loss buckets shown in Figure 7.6. These data were then scaled by Reynolds number; interestingly, the strongest collapse of the overall bucket was obtained by scaling with $Re^{-0.5}$, indicative of a significant influence of laminar flow on the midspan loss levels as shown in Figure 7.7.

The cascade measurements provided an incidence-tolerant blade data set against which analysis tools could be validated and improved. Ameri et al. [2013] used these data to assess the ability of the three-equation RANS turbulence model to calculate transitional flow over a wide incidence range. The measured pressure distributions and integrated spanwise total pressure losses and flow angles for two incidence angles corresponding to cruise (i = 5.8 degrees) and takeoff (i = −36.7 degrees) were used for this study. For the higher loading condition of cruise and the negative incidence condition of takeoff, overall agreement with data may be considered satisfactory but areas of needed improvement are also indicated. In particular, some blade-loading discrepancies were noted near the trailing portion of the suction surface, perhaps suggesting persistent laminar flow and laminar separation in that region that were not reproduced.

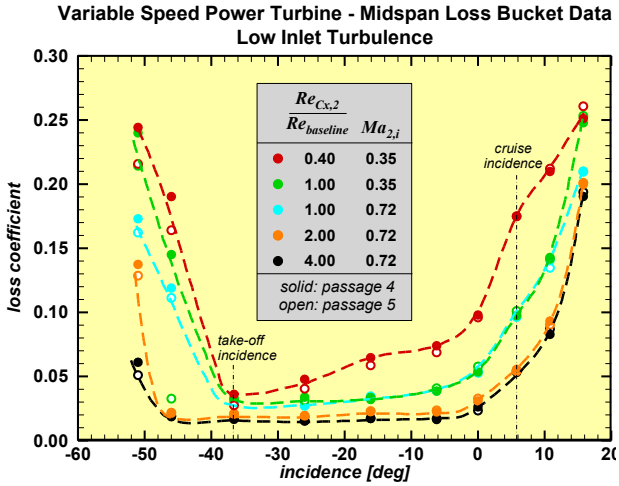

Figure 7.6. Midspan loss vs. incidence—low *Tu* (Fig. 18 of McVetta et al. [2013]).

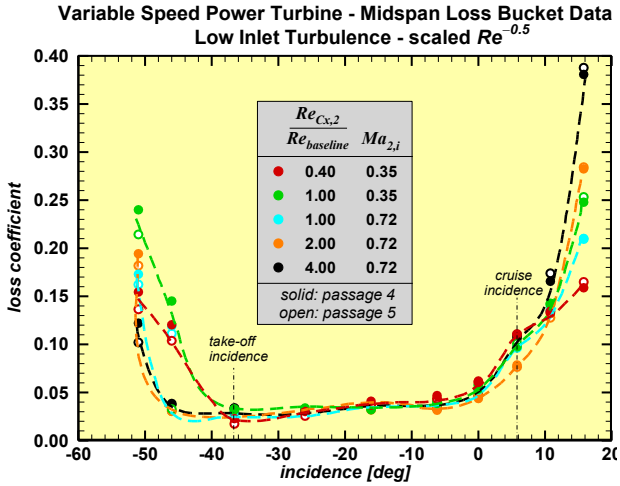

Figure 7.7. $Re^{-0.5}$ scaled midspan loss vs. incidence—low *Tu* (Fig. 19 of McVetta et al. [2013]).

While low-inlet-turbulence intensity served to emulate the transitional flow conditions associated with low Reynolds numbers, Flegel et al. [2014] added an inlet turbulence grid to extend the transonic cascade measurements to higher VSPT-relevant turbulence levels. The inlet turbulence levels ranged from 8 to 15 percent for this study. Comparisons of blade-loading diagrams at low- and high-*Tu* conditions showed that the flow at the high-*Tu* conditions remained attached on both the suction surface and the pressure surface at all incidence, Reynolds number, and Mach number conditions. These results were in strong contrast to the blade loading at low *Tu,* which exhibited separation, transition, and reattachment on both suction and pressure sides of the blade, depending on incidence angle. The pressure side cove separation, a key feature in the data at low *Tu* for all flow conditions, was not evident in the high-*Tu* data. The lack of flow separation was also evident in the downstream wake profiles, which were integrated to generate the loss buckets shown in Figure 7.8. For these high-*Tu* data, a strong collapse was achieved with scaling by $Re^{-0.1}$, indicating that the midspan losses were dominantly influenced by turbulent flow. The high-*Tu*-scaled loss buckets are shown in Figure 7.9.

A companion study to the cascade aerodynamic measurements was performed to carefully document the inlet turbulence quantities. As reported by Thurman et al. [2014], constant temperature hotwire anemometry data were acquired to determine the inlet mean and turbulence quantities for the low- and high-inlet-turbulence conditions. The data were acquired for the GE EEE blade and VSPT blade conditions at various Reynolds numbers and spanwise locations. Turbulence data included intensity, integral length scale, dissipation length scale, power spectra, and turbulence decay. Turbulence decay was determined from measurements that were acquired a given streamwise distance apart. Those data are particularly useful to specify both the turbulence kinetic energy, *k*, and the length scale or dissipation rate at the inlet boundary when using turbulence models in CFD.

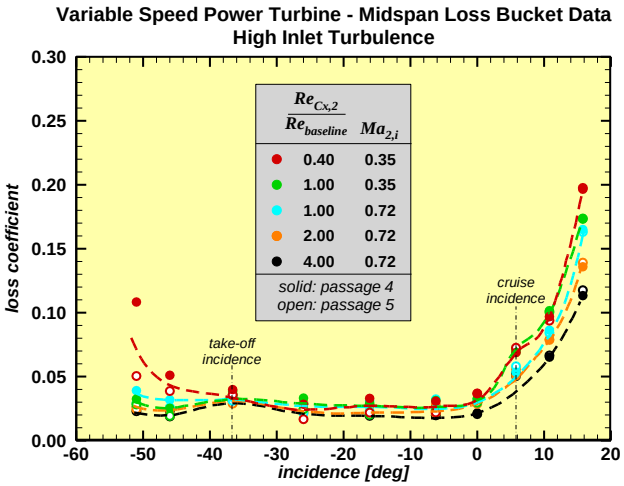

Figure 7.8. Midspan loss vs. incidence—high *Tu* (Fig. 21b of Flegel et al. [2014]).

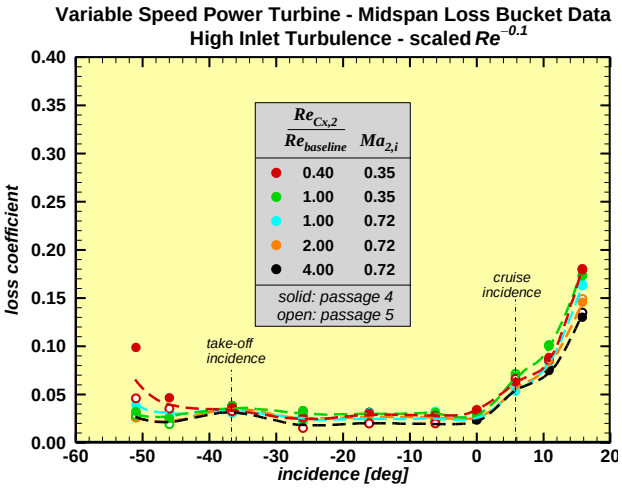

Figure 7.9. $Re^{-0.1}$ scaled midspan loss vs. incidence—high *Tu* (Fig. 22b of Flegel et al. [2014]).

The CFD studies were expanded to include the high-inlet-turbulence data as reported by Ameri et al. [2014]. Comparisons with experimental data were made for blade loading, total-pressure loss, and exit flow angles under conditions of high- and low-turbulence intensity for a single Reynolds number. Analyses were performed with the three-equation turbulence models of Walters and Leylek [2004] and Walters and Cokljat [2008]. Ameri et al. [2014] concluded that at the low-freestream-turbulence conditions, the Walters-Cokljat model is better suited to prediction of VSPT flows, while for high-freestream conditions, the two models generate similar predications that were generally satisfactory.

Heat transfer is typically not a critical technology in power turbines, but surface heat transfer rate distributions can serve as an excellent indicator of the local state of the boundary layer; laminar, transitional, or turbulent. Because of the strong dependence of aerodynamic losses on the boundary-layer state, studies were undertaken at the University of North Dakota (UND) and North Dakota State University under a NASA EPSCoR CAN Award to measure and predict vane and blade surface heat transfer. Stahl et al. [2014] reported on vane heat transfer measurements obtained in a small-scale linear cascade facility that has the ability to run at near-vacuum conditions, achieving the very low Reynolds numbers characteristic of VSPT altitude conditions. At the same time, the facility runs in the transonic flow range, achieving engine-realistic pressure ratios and Mach numbers. Their data showed the influence of Mach number, Reynolds number, and turbulence level on transition and heat transfer augmentation and are expected to be useful in grounding heat transfer predictive methods applicable to VSPTs.

A subsequent study by the same research group similarly measured the blade loading and surface heat transfer distributions but on a scaled version of the same incidence tolerant blade that was designed by Rolls-Royce N.A. and tested in the NASA GRC Transonic Turbine Blade Cascade Test Facility. As reported by Moualeu et al. [2014], the North Dakota facility was modified with a series of discrete inlet nozzles that were designed to accommodate the widely varying incidence range. Data were acquired at eight separate incidence angles ranging from 5.8 to –51.2

degrees. At each angle, data were acquired at four Reynolds numbers ranging from 50,000 to 568,000 based on true chord and exit conditions (see Fig. 7.10). Conditions were also run matching some selected NASA conditions. The blade-loading data show changes in loading, the movement of the stagnation line, and regions of separation with changing incidence angle and Reynolds number. The heat transfer data show areas of laminar flow, regions of transition, locations of separation, as well as information on flow reattachment.

The traditional turbine design process focuses on designing at a single operating point. The VSPT concept does not fit well into that design process because the wide range of operating conditions results in large incidence angles when far away from the design point. Hendricks et al. [2014] recognized this and explored the design of a VSPT using multi-point design optimization techniques based on a meanline analysis. They applied the techniques to NASA's new meanline tool, the Object-Oriented Turbomachinery Analysis Code (OTAC). Their results show that an improved design can be achieved with several distinct features compared to the initial design. First, the overall performance was improved by having a positive incidence on all blade rows at the low-speed-cruise condition. Additionally, trends for the work split between stages, reaction, and flow coefficient of the preliminary optimum design differed from those of the initial VSPT design. The multi-point design optimization also pointed out some deficiencies in the semi-empirical loss models, highlighting the need to incorporate higher fidelity analyses into the design process to account for more subtle flow phenomenon.

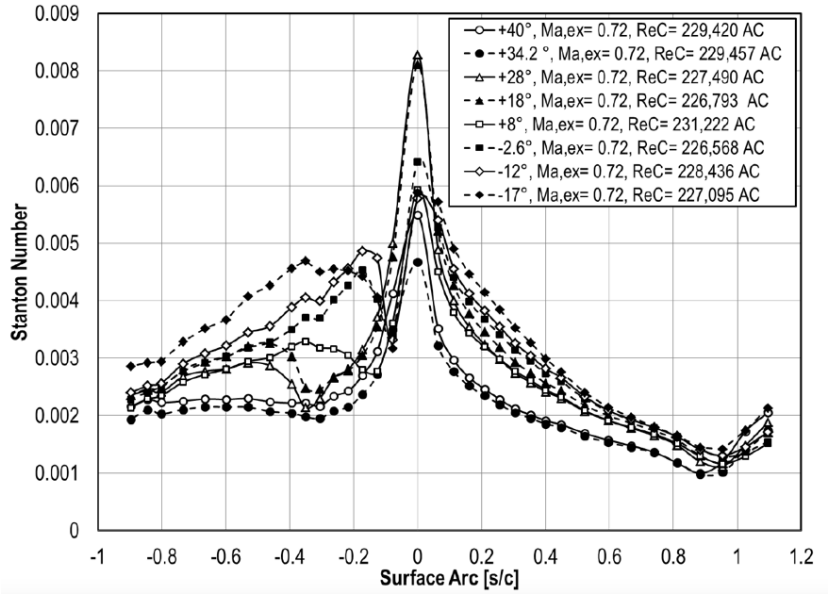

Figure 7.10. Surface Stanton number distributions for an exit chord Reynolds number of 228,000; high turbulence comparing incidence angle effects (Fig. 20 of Moualeu et al. [2014]).

While RANS and URANS calculations have been proven to provide accurate predictions for certain flows, more advanced methods such as Large Eddy Simulation (LES) provide the promise of more universal validity. Working towards the development of LES methods for practical and relevant flows, Mankbadi and Georgiadis [2014] examined parameters that affect the accuracy of numerical large eddy simulation (NLES) calculations with no sub-grid modeling for the geometrically simple flow past a square cylinder. The turbulent flow around a square cylinder features a variety of complex flow phenomena such as highly unsteady vortical structures, reverse flow in the near wall region, and wake turbulence. Sensitivities to time stepping were minimized and sampling frequency sensitivities were not present. While increasing the spanwise depth and resolution can be costly, this practice was found to be necessary to eliminate the artificial turbulent energy exchange. In doing so, the mean and turbulent statistics computed from the NLES were found to be in good agreement with experimental data.

Additional CFD comparisons were reported by Booth and Flegel [2015] using the commercial software packages, Pointwise and CFD++, for the grid generation and RANS and URANS computations. Comparisons were made at cruise and takeoff conditions. The CFD results were compared to blade loading and downstream probe survey data. For the positive incidence cruise condition, negligible differences were noted between the RANS and URANS calculations. However, for the negative incidence takeoff condition, significant differences between RANS and URANS calculations suggested that the flow is unsteady. The URANS solutions agreed appreciably better with the experimental data. Overall, the CFD++ code showed fair to good results as compared to the experiment for the VSPT blade. The combined k-ε turbulence model and algebraic transition model produced the closest overall agreement with the experiment, although the authors suggested that further model comparisons should be made in the future as the code develops more capability.

The VSPT blade data sets from two independent facilities at NASA GRC and UND were compared and contrasted as described by Flegel et al. [2015]. As described above, the NASA facility has the ability to test over a high range of Reynolds numbers while the UND facility complemented the data set by testing at lower Reynolds numbers at the design exit Mach number, and by acquiring blade heat transfer measurements aimed at quantifying transitional flow behavior. Comparisons of the aerodynamic data sets were made for three “match point” conditions. The blade-loading data at the match point conditions show good agreement between the facilities. This comprehensive data set provides insight to the transitional flow behavior across a large incidence range. The data sets continue to be used to advance the understanding of the aerodynamic challenges associated with operating turbines efficiently over a wide shaft-speed range.

Experimental work at the NASA GRC Transonic Turbine Blade Cascade Facility continued with the measurement of endwall heat transfer rates as reported by Thurman et al. [2018]. Infrared thermography was used to determine the endwall heat transfer distribution. Changes in the local heat transfer rates with Reynolds number were used to identify the laminar, turbulent, and transitional flow regimes, as well as to determine regions of flow separation. A Nusselt-Reynolds

number correlation of the form $Nu \propto Re^B$ provided insight to identify the flow regimes. When comparing the ratios of data from two cases, the value of the exponent B helped identify the local flow regime, with values of B near 0.5 indicating laminar flow and values near 0.8 indicating turbulent flow. Results from an example case are shown in Figure 7.11.

The culmination of the VSPT research plan was to assess the performance of turbines with improved incidence tolerance and operating speed ranges through a component test. NASA and the U.S. Army Aviation Applied Technology Directorate teamed to award two cost-share contracts to U.S. engine manufacturers to design, fabricate, instrument, and test turbines under the Army's Advanced Variable Speed Power Turbine (AVSPOT) technology development program. The objective of the AVSPOT technology is to develop and validate turbine aerodynamics for variable-speed operation with high efficiency across a wide speed range. Current state-of-the-art power turbines operate in the 95- to 105-percent speed range, operating to a fixed 100 percent speed for normal operation. For certain next-generation aircraft configurations, future power turbine designs will need to be robust enough to allow for optimized power turbine speed in the range of 55–100 percent. A robust power turbine design, capable of operation over this range at high-efficiency levels, will provide a versatile power system design compatible with future rotorcraft concepts for NASA and U.S. Army Future Vertical Lift/Joint Multi Role development. The contracts were awarded to GE Aviation and Pratt & Whitney (P&W). Both engine companies used either NASA's or a subcontractor's high-speed linear cascade data to help design incidence-tolerant airfoils, then designed multi-stage power turbines for test validation. GE's test article and its installation in the Notre Dame Turbomachinery Lab (NDTL) is shown in Figure 7.12. The results of the GE tests will be published in 2019/2020. Seleski et al. [2016] reported on P&W's results. The P&W AVSPOT three-stage component rig is shown in Figure 7.13. Their key success was summarized by the power turbine efficiency-versus-speed chart shown in Figure 7.14. Figure 7.14 shows that the AVSPOT program efficiency goals were exceeded at the 55- and 100-percent speed points, demonstrating that the strong efficiency lapse at low speed has been successfully minimized.

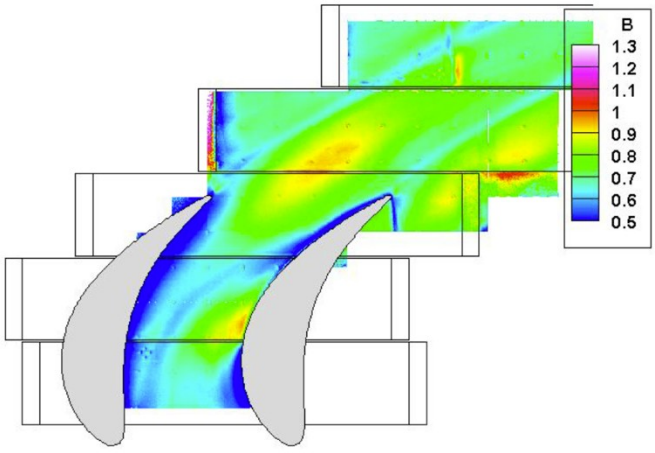

Figure 7.11. Sample endwall heat transfer exponent (Fig. 9c of Thurman et al. [2018]).

a. GE AVSPOT component rig assembly (Fig. 13a of Suder et al. [2018]).

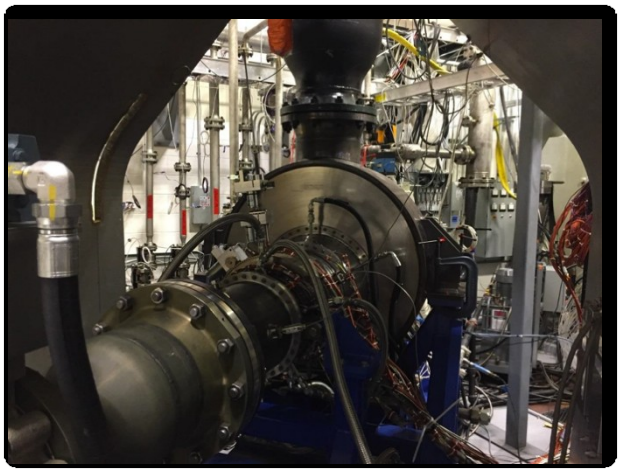

b. GE rig installed in NDTL test facility (Fig. 13b of Suder et al. [2018]).

Figure 7.12. GE Aviation AVSPOT component test rig.

Figure 7.13. P&W component rig installed in the P&W Continuous Flow Turbine Facility (Fig. 11 of Suder et al. [2018]).

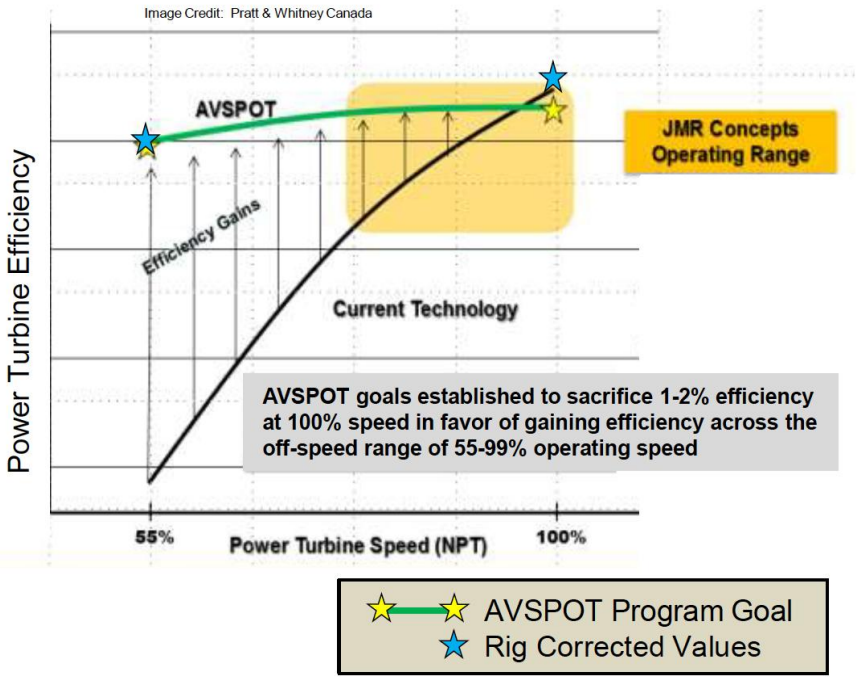

Figure 7.14. P&W AVSPOT rig-based engine performance results (Fig. 4 of Seleski et al. [2016]).

The VSPT research concluded with the successful completion of the RVLT TC, "Variable Speed Power Turbine Demonstration." As described by Suder et al. [2018], the Technical Challenge was to demonstrate a variable-speed power turbine with 50 percent improvement in efficient operational capability. The performance requirements were to achieve Maximum Rated Power (MRP) sea-level static hover at 100 percent speed with 92 percent efficiency and to achieve Maximum Continuous Power (MCP) at 25,000 feet altitude, 0.5M at 55 percent speed with 90 percent efficiency. The exit criteria included VSPT system demonstration to Technology Readiness Level (TRL) 4 with performance measurement and comparison to analysis. The TC was completed on schedule and on budget. The VSPT started at TRL 2 and ended at TRL 5, exceeding the successful exit criteria of TRL 4. The success of this VSPT design and demonstration has led to a funded Army DoD 6.3 Alternative Concept Engine (ACE) program to build and demonstrate an engine with a VSPT. An ACE development contract was awarded to the Advanced Turbine Engine Company (ATEC). Upon successful completion of the ACE 6.3 effort, VSPT technology will achieve TRL 6 and be adequately matured for incorporation into a potential future Engineering and Manufacturing Development (EMD) effort that would complete the technology maturation process of this technology and allow for potential fielding in future rotorcraft. Subsequently, the U.S. Army selected the GE Aviation T901-GE-900 engine for the EMD phase of the Improved Turbine Engine Program (ITEP). Going forward, the turbine variable-speed capability and airfoil incidence tolerance technology is being further exploited for hybrid-electric aircraft propulsion systems with gas turbines providing thrust and significant electrical power generation for propulsion in order to incorporate distributed propulsion and/or boundary-layer ingestion technologies.

HIGH EFFICIENCY CENTRIFUGAL COMPRESSOR (HECC)

Advances in gas turbine engines, and specifically compressor technology, can help enable the next generation of advanced rotary wing vehicles. Work supported under the Gas Generator subproject, and more specifically the High Efficiency Centrifugal Compressor (HECC) task within the RVLT project, is reported here. Welch et al. [2009] and Welch [2012] discuss how stringent vehicle and engine performance requirements result in gas turbine engines with low-compressor-exit corrected flows. An optimum gas turbine using a high-efficiency centrifugal aft stage is an enabling technology to meet compressor and overall engine efficiency goals. The authors also provide an overview of ongoing compressor research at NASA GRC, such as relevant compressor hardware development and testing in NASA's Small Engine Component Test Facility (Fig. 7.15). The high-quality data gathered in that facility can be used to improve design and analysis tools. The Centrifugal Compressor, 3× scale (CC3) and HECC test hardware are discussed later in this section. Stall control efforts are also discussed, ranging from component work and accompanying computer modeling up to engine-level hardware testing on the T700 engine.

To supplement the higher-ordered compressor analyses, a mean-line analysis method and an associated program to estimate key aerodynamic parameters of single and multistage axial and centrifugal compressors were developed and reported in Veres [2009a, 2009b]. A strength of the method was the ability to quickly develop data to guide the engine design process. This program was used to conceptually design and screen options for the compressor section of the LCTR engine [Veres, 2009c, 2009d; Veres and Thurman, 2010]. These efforts confirmed the choice of an aft centrifugal stage (versus multiple axial stages) for the LCTR engine to meet weight, volume, and manufacturability constraints. Additionally, relevant flow conditions were developed that could be used to guide ancillary research efforts (such as compressor hardware test conditions or material property requirements).

As part of the NASA Research Announcement (NRA) for HECC, United Technologies Research Center (UTRC) performed "the design of a high efficiency, compact centrifugal stage scaled for use as a measurement test bed that is representative of a state-of-the-art compressor stage in rotorcraft engine" [Lurie et al. 2011]. The design for this new test article evolved from the CC3 test article (shown in Figure 7.16), a well-studied existing centrifugal compressor. The CC3 is a 3× scale of a state-of-the art, small centrifugal compressor. The 3× scaling allows incorporation of significant, meaningful instrumentation to gather high-quality flow and performance data while staying close to the desired small scale and manufacturing limits with small size. To develop the advanced HECC design, a CFD-based process was performed after additional constraints were included to narrow-down the potential design space. The UTRC advanced HECC design was predicted to have improved efficiency compared to the original HECC design; in addition, the maximum stage diameter of the UTRC design was 23 percent less than the original design (see Fig. 7.17). An outline of the rig instrumentation layout development was also included "to answer fundamental research and design confirmation questions." This work was reported during HECC fabrication and before initial test entry.

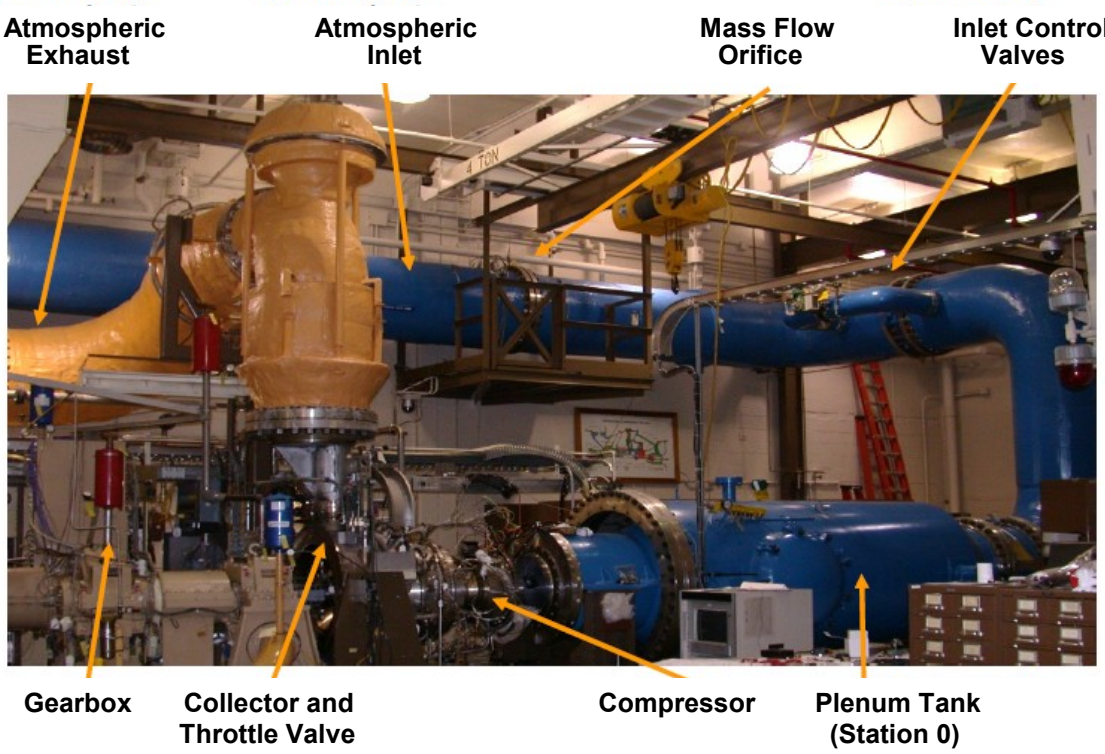

Figure 7.15. Small Engine Component Test Facility (GRC CE-18) (Fig. 2 of Braunscheidel et al. [2014]).

Figure 7.16. CC3 impeller and vaned diffuser hardware (Fig. 1 of Kulkarni et al. [2013a]).

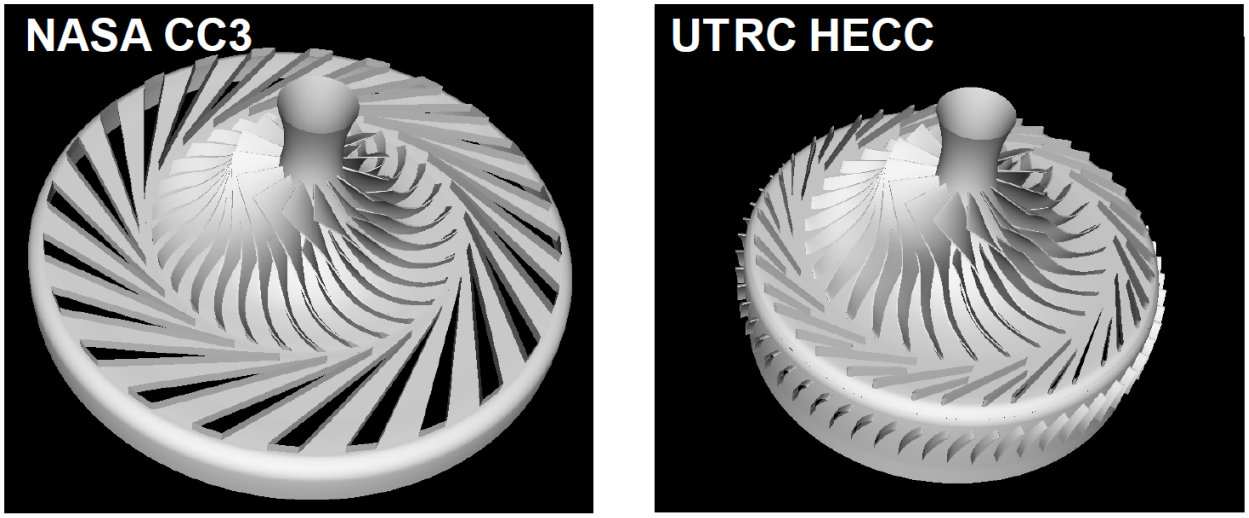

Figure 7.17. Original (left) and redesigned (right) stage (Fig. 46 of Medic et al. [2014]).

Significant modeling efforts were performed to test the applicability of existing tools and explore new approaches to take advantage of the test data being developed. In preparation for simulations based on the HECC hardware tests, computational studies were performed using the CC3 centrifugal impeller in its vaneless diffuser configuration [Kulkarni et al., 2013a, 2013b]. The studies were part of an effort to understand potential causes of RANS CFD mis-prediction in these types of geometries. The TURBO code was run using the default CMOTT k-ε turbulence model with a baseline and refined grid and Wilcox's k-ω turbulence model with the refined grid. All three models compared favorably with data from the inlet to the impeller trailing edge. Downstream of the impeller trailing edge, the *k-ω* turbulence model better matched test data as shown in Figure 7.18. This effort highlighted the potentially large impact of turbulence model choice on predicted performance.

Actual performance of the HECC hardware fell short of pre-test predictions. Braunscheidel et al. [2014, 2015] provides an initial reporting for some of the performance data, such as shown in Figure 7.19, and also includes some discussion about potential reasons for the performance shortfalls. Preliminary data analyses suggest that impeller diffuser interaction issues that did not show up in the HECC design modeling are the most likely cause of the performance shortfalls. This report also includes a good summary of the overall effort as well as additional references to help guide those interested in further analyses of the HECC data.

A significantly more complete reporting of the NRA effort concerning HECC is provided in the UTRC contractor report [Medic et al., 2014]. This report is comprehensive in its detail about the HECC hardware geometry, test performance, and root-cause analyses to help identify possible causes for the discrepancies between pre-test analyses and actual hardware performance. Recommendations for additional tests to help verify possible causes for various performance shortfalls identified are also included. Although the test article did not achieve design performance, this reporting does satisfy the goals of developing an advanced centrifugal

compressor design, testing such design, and reporting extensive databases detailing rig geometry and performance. This effort produced data that is rich with future potential for advancing the state of the art in centrifugal compressor modeling and future hardware.

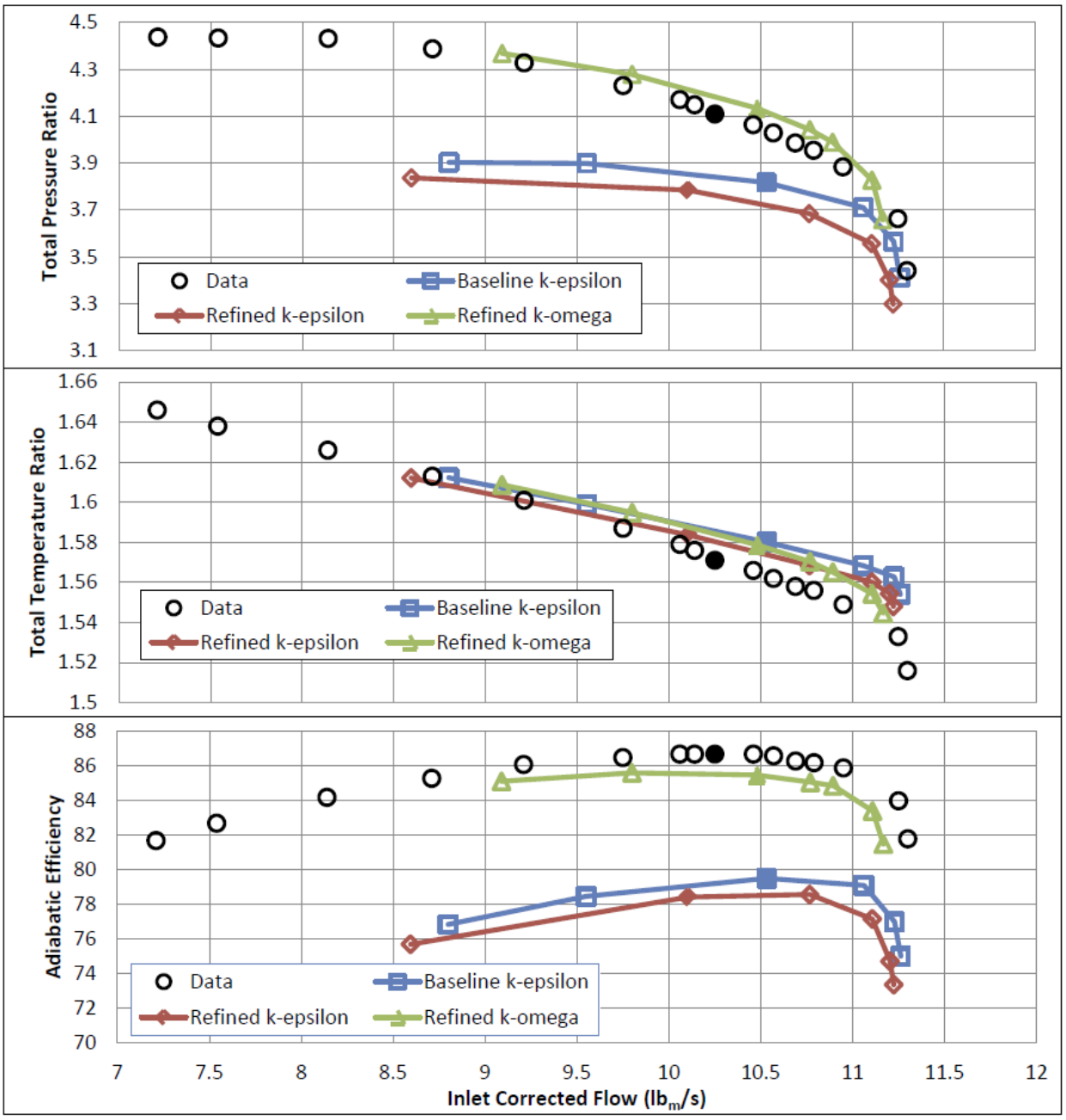

Figure 7.18. Total pressure ratio, total temperature ratio, and adiabatic efficiency of CC3 vaneless diffuser configuration at design speed. Note: the computed speedlines were not run to stall. (Fig. 8 of Kulkarni et al. [2013a].)

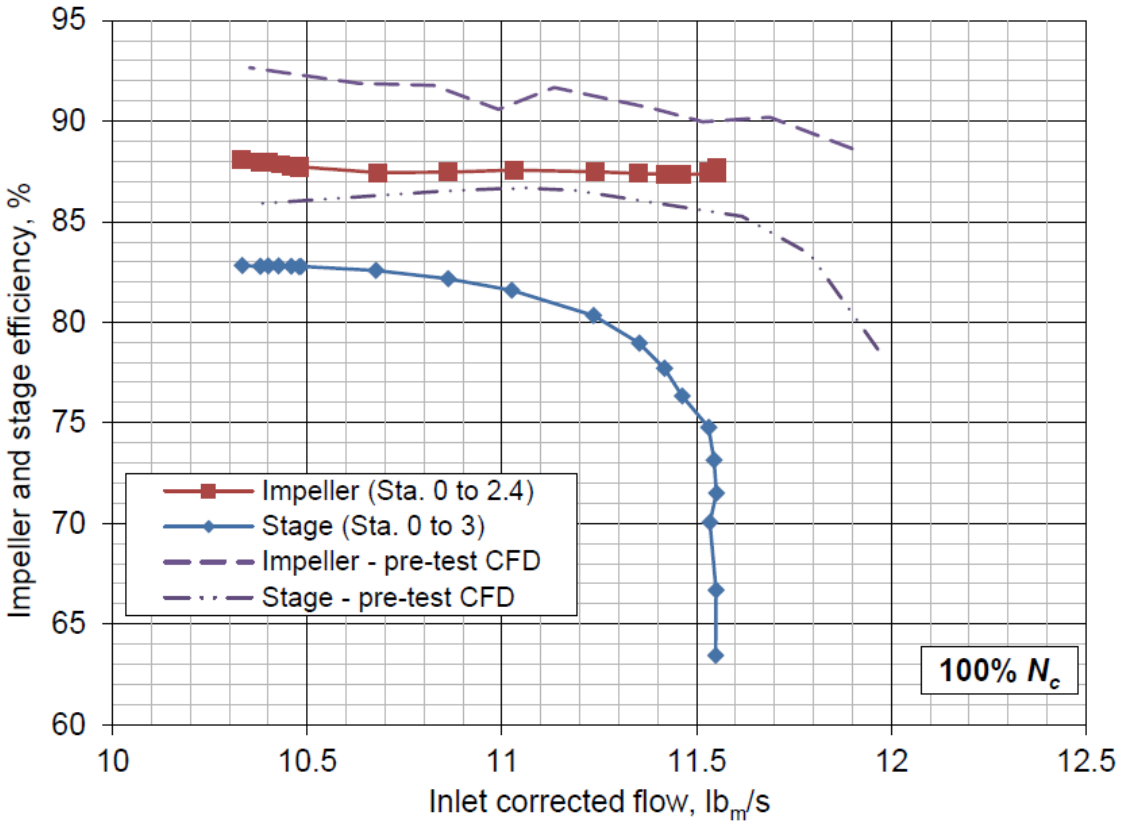

Figure 7.19. Comparison of impeller and stage adiabatic efficiency at 100 percent corrected rpm as a function of inlet corrected flow from measurements at suppressed inlet conditions and pre-test CFD computed at standard day conditions (i.e., not corrected for suppressed inlet). (Fig. 13 of Braunscheidel et al. [2014].)

Kulkarni and Beach [2017] is the final NASA-reported effort on HECC within this decadal reference frame and discusses modeling of HECC using TURBO. TURBO is a time-accurate, 3D multistage analysis code, developed at Mississippi State University under NASA sponsorship. TURBO has been a workhorse compressor analysis code at NASA. This work reported the results of various additions and modifications to better analyze centrifugal compressors and compare results with the design-intent CFD results from Code Leo. Peripheral tools for developing the initial converged flow field for TURBO, as well as interpolating, integrating, and averaging TURBO results using ParaView are reported.

MODELING AND SIMULATION (MODSIM): COMPRESSOR FLOW MODELING AND EXPERIMENTS

Advanced and efficient gas turbine engines are often limited by compressor performance and that component's stable operating range. Significant compressor and overall engine benefits can be realized from improved understanding of the causes of compressor instabilities that limit their useful operating range and performance. Chen et al. [2008] used the TURBO code to model and explore the initiation of these instabilities. The advent of high-performance/parallel computing has made computational exploration of the precursor flow behavior possible in the correct computational regime (time dependent, 3D, and multi-stage analyses). Simulation work was also validated with extensive experimental results from the NASA compressor Stage 35 facility. Simulation results provided evidence that such codes and their analyses have sufficient fidelity to predict compressor flow and pressure ratio characteristics (Fig. 7.20) and the onset of flow instabilities and their subsequent growth into fully developed rotating stall.

Subsequent simulation results reported in Herrick et al. [2009] showed that TURBO was very effective at matching speedline characteristics for the compressor during nominal operation and as choke conditions were approached (see Figs. 7.21 and 7.22).

Chen et al. [2009] showed that the TURBO code could also be effective for modeling steady tip injection as a stall control technique. Simulations included modeling the initiation of flow instabilities potentially leading to spikes, which can also be viewed as embryonic stall cells and local flow breakdowns. Steady tip injection can help prevent the formation of these spikes or help sweep them downstream and out of the compressor flow passages before they can develop into full stall regions and cause compressor surge or stall.

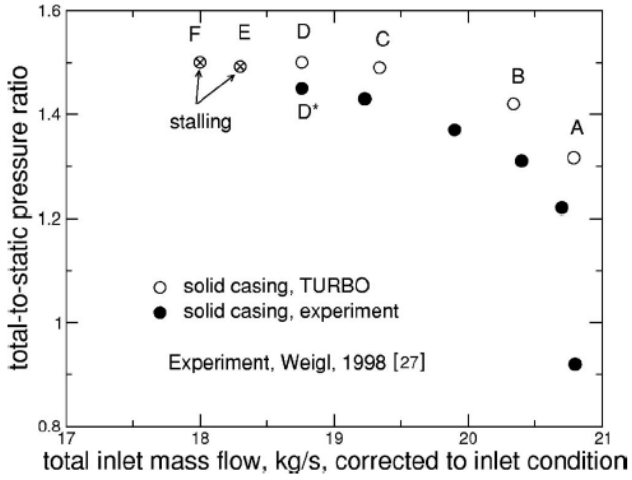

Figure 7.20. Stage 35 computed and measured speedlines, design speed (Fig. 5 of Chen et al. [2008]).

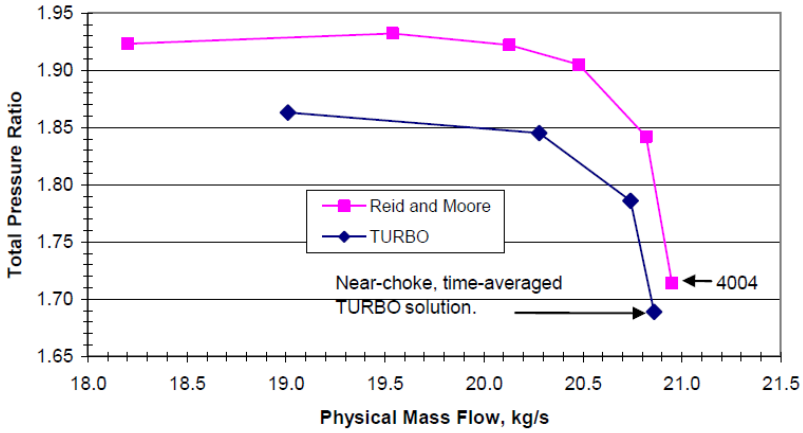

Figure 7.21. Stage 35 total pressure ratio speedline (Fig. 10 of Herrick et al. [2009]).

Parameter	Experiment Point 4004	TURBO Near-Choke	Experiment Uncertainty (%)	TURBO Deviation (%)
Stage Total Pressure Ratio	1.714	1.689	1.9	1.5
Stage Total Temperature Ratio	1.198	1.193	0.46	0.42
Stage Adiabatic Efficiency	0.841	0.837	0.99	0.48
Mass Flow, kg/s	20.95	20.86	1.4	0.4

Figure 7.22. Stage 35 aerothermodynamic performance approaching choke (Table 4 of Herrick et al. [2009]).

MODELING AND SIMULATION (MODSIM): ENGINE HEALTH ASSESSMENT

As engines degrade, performance margins are reduced that impact safe and normal vehicle operations. A real-time, onboard, automated health assessment code could inform operators of engine state to help them make informed decisions regarding engine condition. Litt and Simon [2007] reports study efforts using data from sand ingestion tests performed on a T700-GE-401 turboshaft engine (see Fig. 7.23) to develop algorithms of compressor efficiency and therefore, engine degradation. The algorithm was applied to real-time Health Usage and Monitoring Systems (HUMS) data from a T700-GE-701C to track compressor efficiency. Although applied to a different engine model, results were very encouraging. The health assessment tool produced very consistent and repeatable results. The algorithm was also easy to implement.

Subsequent work was reported in Simon and Litt [2008]. Presently, a manual procedure called a Maximum Power Check (MPC) is performed on U.S. Army Blackhawk helicopters on a periodic basis. The MPC establishes an Engine Torque Factor (ETF), which is used to indicate available power. An automated approach would enable continuous, real-time assessment of available power and engine health, especially if using data already collected within the helicopter HUMS. The automated approach was applied to data from the HUMS data sets from UH-60L aircraft and

compared to manually calculated ETFs. Results from this work indicate that the automated approach typically underestimates ETF values determined from the manual calculation. Additional development and validation is required to mature the automated approach before becoming suitable for actual implementation.

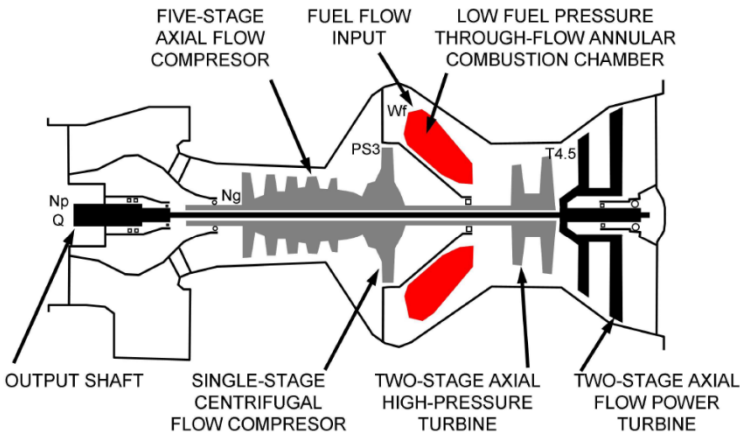

Figure 7.23. Cross section of a T700 turboshaft engine showing the rotating components and sensor locations (Fig. 1 of Litt and Simon [2007]).

MODELING AND SIMULATION (MODSIM): WAVE ROTOR

As stated by Paxson et al. [2007]: "Wave rotors have been under investigation at the NASA GRC and other organizations for a number of years. Although many potential applications for these devices exist, the primary focus at NASA has been in their use as topping cycles for gas turbine engines." Figure 7.24 shows a schematic of a wave rotor. A time-accurate, 1D, CFD-based simulation code has been developed specifically for wave rotors. For code assessment and validation, design, fabrication and then performance and operability testing of a laboratory-scale, four-port wave rotor were performed. Many aspects of the rig design were determined from the simulation code. Rig performance was compared to predictions from the simulation code at both on- and off-design conditions. Overall, the match between the code and rig was good. At operating points where there were disparities, the assumption of larger-than-expected internal leakage rates successfully realigned code predictions and laboratory measurements. Possible mechanisms for such leakage rates were also discussed but could not be confirmed.

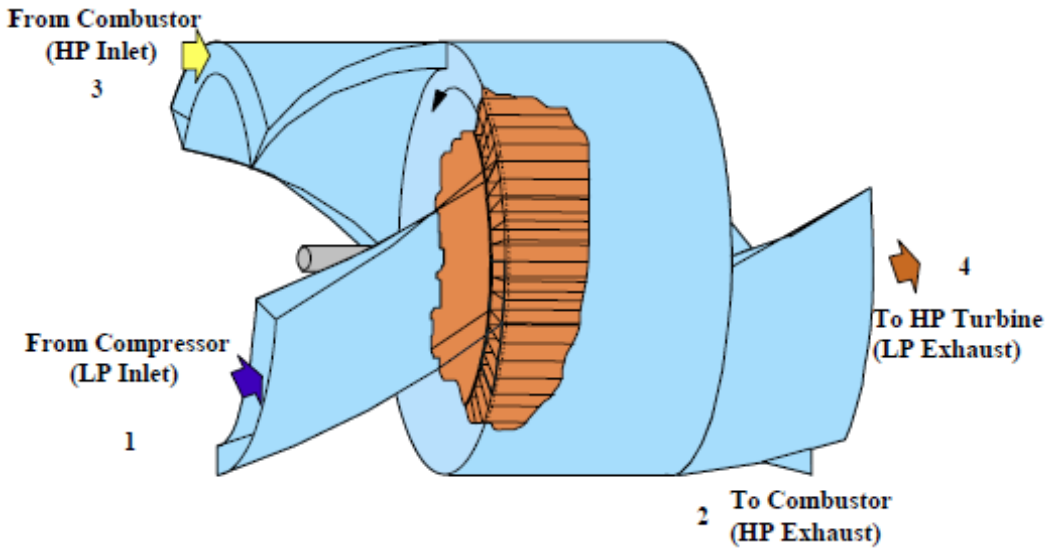

Figure 7.24. Four-port, through-flow wave rotor schematic (Fig. 1 of Paxson et al. [2007]).

MODELING AND SIMULATION (MODSIM): PYCYCLE—FUTURE ENGINE MODELING CODE

Analysis codes continue to be developed and enhanced to use less empiricism and more fundamental physics and thermodynamic relationships. Efforts are also underway to link these codes into multi-disciplinary analysis and optimization (MDAO) environments to explore new design and operational possibilities for systems, vehicles, and missions, as well as to capture the interactions among the various systems and subsystems. These analysis codes often use gradient-based methods and finite-difference approximations for finding an optimum solution. However, such methods scale poorly as the number of design variables increase, as well as being sensitive to the step size used. One propulsion analysis code to explore methods to potentially circumvent these limits is PyCycle [Hearn et al., 2016], which can provide analytic derivatives for an efficient use of gradient-based optimization methods. PyCycle was used to compare the optimization of a high-bypass turbofan engine versus NASA's state-of-the-art propulsion analysis code, the Numerical Propulsion System Simulation (NPSS)—see Claus et al. [1991] and Jones [2007]. NPSS uses finite-difference approximations during gradient-based optimizations. For the example turbofan engine optimization, PyCycle obtained essentially the same optimized engine solution using three to eight times less run time and requiring five to eight times less model executions. Such calculation efficiency is highly desirable to potentially enable more ambitious optimization problems in the future.

REFERENCES

Acree, C. W., Yeo, H., and Sinsay, J. D., "Performance Optimization of the NASA Large Civil Tiltrotor," International Powered Lift Conference, London, UK, July 2008, NASA/TM–2008-215359, June 2008.

Ameri, Ali A., "Use of Transition Modeling to Enable the Computation of Losses for Variable-Speed Power Turbine," Paper no. GT2012-69591, Proc. of the ASME Turbo Expo, Copenhagen, Denmark, June 11-15, 2012; also NASA/CR–2012-217435.

Ameri, Ali A., Giel, Paul W., and McVetta, Ashlie B., "Validation of a CFD Methodology for Variable Speed Power Turbine Relevant Conditions," Paper no. GT2013-95030, Proc. of ASME Turbo Expo, San Antonio, TX, June 3-7, 2013.

Ameri, Ali A., Giel, Paul W., and Flegel, Ashlie B., "Simulation of VSPT Experimental Cascade under High and Low Free-Stream Turbulence Conditions," AIAA Paper 2014-3935, 50th AIAA/ASME/SAE/ASEE Joint Propulsion Conference, Cleveland, OH, July 28-30, 2014; see also NASA/TM–2015-218457.

Booth, David T., and Flegel, Ashlie B., "Comparison of Computational and Experimental Results for a Variable-speed Power-turbine Blade Operating with Low Inlet Turbulence Levels," AIAA Paper 2015-3928, 51st AIAA/SAE/ASEE Joint Propulsion Conference, Orlando, FL, July 27-29, 2015.

Braunscheidel, E. P., Welch, G. E., Skoch, G. J., Medic, G., and Sharma, O. P., "Aerodynamic Performance of a Compact, High Work-Factor Centrifugal Compressor at the Stage and Subcomponent Level," AIAA Paper 2014-3632, 50th AIAA Joint Propulsion Conference, Cleveland, OH, July 28-30, 2014; see also NASA/TM–2015-218455.

Chen, J-P, Hathaway, M. D., and Herrick, G. P., "Prestall Behavior of a Transonic Axial Compressor Stage via Time-Accurate Numerical Simulation," *ASME Journal of Turbomachinery*, vol. 130, Oct. 2008.

Chen, Shu-cheng S., "Preliminary Axial Flow Turbine Design and Off-Design Performance Analysis Methods for Rotary Wing Aircraft Engines; I-Validation," NASA/TM–2009-215651/PART 1, May 2009a.

Chen, Shu-cheng S., "Preliminary Axial Flow Turbine Design and Off-Design Performance Analysis Methods for Rotary Wing Aircraft Engines; II-Applications," NASA/TM–2009-215651/PART 2, May 2009b.

Chen, J-P, Johnson, B., Hathaway, M. D., and Webster, R. S., "Flow Characteristics of Tip Injection on Compressor Rotating Spike via Time-Accurate Simulation," *Journal of Propulsion and Power*, vol. 25, no. 3, May–June 2009.

Chen, Shu-cheng S., "Capability Extension to the Turbine Off-Design Computer Program AXOD With Applications to the Highly Loaded Fan-Drive Turbines," NASA/TM–2011-217129, July 2011.

Claus, R. W., Evans, A. L., Lytle, J. K., and Nichols, L. D., 1991, "Numerical Propulsion System Simulation," Computing Systems in Engineering, vol. 2, no. 4, pp. 357–364.

Flegel, A. B., Giel, P. W., and Welch, G. E., "Aerodynamic Effects of High Turbulence Intensity on a Variable-Speed Power-Turbine Blade with Large Incidence and Reynolds Number Variations," AIAA Paper 2014-3933, 50th AIAA/ASME/SAE/ASEE Joint Propulsion Conference, Cleveland, OH, July 28-30, 2014; see also NASA/TM–2014-218137.

Flegel, A. B., Welch, G. E., Giel, P. W., Ames, F. E., and Long, J. A., "Complementary Aerodynamic Performance Datasets for Variable Speed Power Turbine Blade Section from Two Independent Transonic Turbine Cascades," Paper no. ISABE2015-20163, 22nd International Symposium on Air Breathing Engines, Phoenix, AZ, Oct. 25-30, 2015.

Ford, A., Turner, E., Bloxham, M., Gegg, S., King, B., Harris, C., Bell, M., and Eames, D., "Variable-Speed Power-Turbine Component Research Plan," NASA/CR–2012-217423, 2012a.

Ford, A., Bloxham, M., Turner, E., Clemens, E., and Gegg, S., "Design Optimization of Incidence-Tolerant Blading Relevant to Large Civil Tilt-Rotor Power Turbine Applications," NASA/CR–2012-217016, 2012b.

Hearn, T., Hendricks, E., Chin, J., Gray, J., and Moore, K., "Optimization of Turbine Engine Cycle Analysis with Analytic Derivatives," AIAA Aviation 2016, Washington, D. C., June 13-17, 2016.

Hendricks, Eric S., Jones, S. M., and Gray, J. S., "Design Optimization of a Variable-Speed Power-Turbine," AIAA Paper 2014-3445, 50th AIAA/ASME/SAE/ASEE Joint Propulsion Conference, Cleveland, OH, July 28-30, 2014.

Herrick, G. P., Hathaway, M. D., and Chen, J-P., "Unsteady Full Annulus Simulations of a Transonic Axial Compressor Stage," AIAA Paper 2009-1059. 47th AIAA Aerospace Sciences Meeting including The New Horizons Forum and Aerospace Exposition, Orlando, FL, Jan. 5-8, 2009.

Howard, S. A., "Rotordynamic Feasibility of a Conceptual Variable-Speed Power Turbine Propulsion System for Large Civil Tilt-Rotor Applications," 68th Annual Forum of the American Helicopter Society, Fort Worth, TX, May 1-3, 2012; see also NASA/TM–2012-217134, July 2012.

Jones, S. M., "An Introduction to Thermodynamic Performance Analysis of Aircraft Gas Turbine Engine Cycles Using the Numerical Propulsion System Simulation Code," NASA/TM–2007-214690, March 2007.

Kulkarni, S., Beach, T. A., and Skoch, G. J., "Computational Study of the CC3 Impeller and Vaneless Diffuser Experiment," AIAA Paper 2013-3631, 49th AIAA Joint Propulsion Conference and Exhibit, San Jose, CA, July 14-17, 2013a; see also NASA/TM–2013-216566, Sept. 2013b.

Kulkarni, S., and Beach, T. A., "Progress of High Efficiency Centrifugal Compressor Simulations Using TURBO," NASA/TM–2017-219418, March 2017.

Litt, J. S., and Simon, D. L., "Toward a Real-Time Measurement-Based System for Estimation of Helicopter Engine Degradation Due to Compressor Erosion," American Helicopter Society 63rd Annual Forum, Virginia Beach, VA, May 1-3, 2007.

Lurie, E. A., Van Slooten, P. R., Medic, G., Mulugeta, J. M., Holley, B. M., Feng, J., Sharma, O., and Ni, R., "Design of a High Efficiency Compact Centrifugal Compressor for Rotorcraft Applications," American Helicopter Society 67th Annual Forum, Virginia Beach, VA, May 3-5, 2011.

Mankbadi, M. R., and Georgiadis, N. J., "An Examination of Parameters Affecting Large Eddy Simulations of Flow Past a Square Cylinder," AIAA Paper 2014-2089, 44th AIAA Fluid Dynamics Conference, Atlanta, GA, June, 16-20, 2014.

McVetta, A. B., Giel, P. W., and Welch, G. E., 2012, "Aerodynamic Investigation of Incidence Angle Effects in a Large-Scale Transonic Turbine Cascade," AIAA Paper 2012-3879, 48th AIAA/ASME/SAE/ASEE Joint Propulsion Conference, Atlanta, GA, July 30-Aug. 1, 2012; see also NASA/TM–2013-218070/REV1.

McVetta, A. B., Giel, P. W., and Welch, G. E., "Aerodynamic Measurements of a Variable-Speed Power-Turbine Blade Section in a Transonic Turbine Cascade at Low Inlet Turbulence," Paper no. GT2013-94695, Proc. of ASME Turbo Expo, San Antonio, TX, June 3-7, 2013.

Medic, G., Sharma, O. P., Jongwook, J., Hardin, L. W., McCormick, D. C., Cousins, W. T., Lurie, E. A., Shabbir, A., Holley, B. M., and Van Slooten, P. R., "High Efficiency Centrifugal Compressor for Rotorcraft Applications," NASA/CR–2014-218114/REV1.

Moualeu, L. P. G., Long, J. A., Stahl, K., Ames, F. E., and Suzen, Y. B., "Midline Heat Transfer and Pressure Measurements on an Incident Tolerant Blade Section for a Variable Speed Power Turbine at Low to Moderate Reynolds Numbers in a Transonic Turbine Cascade," AIAA Paper 2014-3936, 50th AIAA/ASME/SAE/ASEE Joint Propulsion Conference, Cleveland, OH, July 28-30, 2014.

Paxson, D. E., Wilson, J., and Welch, G. E., "Comparison Between Simulated and Experimentally Measured Performance of a Four Port Wave Rotor," 43rd AIAA/ASME/SAE/ASEE Joint Propulsion Conference & Exhibit, Cincinnati, OH, July 8-11, 2007.

Seleski, R., Hu, J., Grover, E., Liles, J., Pyra, D., Ghai, A., and Aggarwala, A., "Advanced Variable Speed Power Turbine (AVSPOT)," Paper no. RDECOM TR 16-D-19, U.S. Army Research, Development and Engineering Command, 2016.

Simon, D. L., and Litt, J. S., "Automated Power Assessment for Helicopter Turboshaft Engines," 64th Annual Forum and Technology Display (AHS Forum 64), Montreal, Canada, April 29–May 1, 2008.

Smith, S. F., "A Simple Correlation of Turbine Efficiency," *Journal of the Royal Aeronautical Society*, vol. 69, 1965, pp. 467-470.

Snyder, C. A. and Thurman, D. R., "Gas Turbine Characteristics for a Large Civil Tilt-Rotor (LCTR)," AHS International, 65th Annual Forum & Technology Display, Grapevine, TX, May 27-29, 2009; see also NASA/TM–2010-216089, Feb. 2010a.

Snyder, C. A., and Thurman, D. R., "Effects of Gas Turbine Component Performance on Engine and Rotary Wing Vehicle Size and Performance," AHS 66th Annual Forum Proceedings, Phoenix, AZ, May 2010b; see also NASA/TM–2010-216907, Nov. 2010c.

Snyder, C., and Acree, Jr., C. W., "Preliminary Assessment of Variable Speed Power Turbine Technology on Tiltrotor Size and Performance," Paper no. 295, 68th Annual Forum of the American Helicopter Society, Ft. Worth, TX, May 1-3, 2012.

Snyder, C. A., "Exploring Advanced Technology Gas Turbine Engine Design and Performance for the Large Civil Tiltrotor (LCTR)," AIAA Propulsion and Energy Forum, 50th AIAA/ASME/SAE/ASEE Joint Propulsion Conference, Cleveland, OH, July 2014.

Stahl, K. A., Moualeu, L. P. G., Long, J. A., Ames, F. E., and Suzen, Y. B., "Heat Transfer Measurements in a Compressible Flow Vane Cascade Showing the Influence of Reynolds Number, Mach Number, and Turbulence Level on Transition and Augmentation of Laminar Heat Transfer by Free-Stream Turbulence," AIAA Paper 2014-3938, 50th AIAA/ASME/SAE/ASEE Joint Propulsion Conference, Cleveland, OH, July 28-30, 2014.

Suchezky, M., and Cruzen, G. S., "Variable-Speed Power-Turbine for the Large Civil Tilt Rotor," NASA/CR–2012-217424, Feb. 2012.

Suder, K. L., Durbin, K, S., Giel, P., Poinsatte, P., Thurman, D. R., and Ameri, A. A, "Variable Speed Turbine Technology Development and Demonstration," Paper no. AHS-2018-1354, 74th Annual Forum of the American Helicopter Society, Phoenix, AZ, May 14-17, 2018.

Thurman, D., Flegel, A., and Giel, P., "Inlet Turbulence and Length Scale Measurements in a Large Scale Transonic Turbine Cascade," AIAA Paper 2014-3934, 50th AIAA/ASME/ SAE/ASEE Joint Propulsion Conference, Cleveland, OH, July 28-30, 2014.

Thurman, D., Poinsatte, P., Giel, P., and Lucci, B., "Heat Transfer Measurements on the Endwall of a Variable Speed Power Turbine Blade Cascade," Paper no. AHS-2018-0202, 74h Annual Forum of the American Helicopter Society, Phoenix, AZ, May 14-17, 2018; see also NASA/TM–2018-220033, Dec. 2018.

To, W-M., "Unsteady Aero Computation of a 1-1/2 Stage Large Scale Rotating Turbine," NASA/CR–2012-217438, May 2012.

Veres, J. P., "Axial and Centrifugal Compressor Mean Line Flow Analysis Method," Paper no. AIAA-2009-1641, 47th Aerospace Sciences Meeting, Orlando, FL, Jan. 5-8, 2009a; see also NASA/TM–2009-215585, Nov. 2009b.

Veres, J. P., "Compressor Study to Meet Large Civil Tilt Rotor Engine Requirements," American Helicopter Society 65th Annual Forum, Grapevine, TX, May 27-29, 2009c; see also NASA/TM–2009-21564, Aug. 2009d.

Veres, J. P., and Thurman, D. P., "Conceptual Design of a Two Spool Compressor for the NASA Large Civil Tilt Rotor Engine," American Helicopter Society 66th Annual Forum, Phoenix, AZ, May 11-13, 2010.

Walters, D. K., and Leylek, J. H., "A New Model for Boundary Layer Transition Using a Single-Point RANS Approach," *ASME Journal of Turbomachinery*, vol. 126, no. 1, 2004, p. 193.

Walters, D. K., and Cokljat, D., "A Three-Equation Eddy-Viscosity Model for Reynolds-Averaged Navier-Stokes Simulation of Transitional Flows," *ASME Journal of Turbomachinery*, vol. 130, 2008, pp. 121401-01 to 121401-13.

Welch, G. E., Hathaway, M. D., Skoch, G., J., and Snyder, C. A., "Rotary-Wing Relevant Compressor Aero Research and Technology Development Activities at Glenn Research Center," Paper no. ARL-TR-4757, American Helicopter Society 65th Annual Forum, Grapevine, TX, May 27-29, 2009; see also NASA/TM–2012-217280, March 2012.

Welch, G. E., "Assessment of Aerodynamic Challenges of a Variable-Speed Power Turbine for Large Civil Tilt-Rotor Application," 66th Annual Forum of the American Helicopter Society, Phoenix, AZ, May 10-12, 2010; see also NASA/TM–2010-216758, Aug. 2010.

Welch, G. E., "Computational Assessment of the Aerodynamic Performance of a Variable-Speed Power Turbine for Large Civil Tilt- Rotor Applications," 67th Annual Forum of the American Helicopter Society, Virginia Beach, VA, May 3-5, 2011; see also NASA/TM–2011-217124, Nov. 2011.

Welch, G. E., "Computational Study of the Impact of Unsteadiness on the Aerodynamic Performance of a Variable-Speed Power Turbine," AIAA Paper 2012-0937, 50th AIAA Aerospace Sciences Meeting, Nashville, TN, Jan. 9-12, 2012; see also NASA/TM–2012-217425, April 2012.

Welch, G. E., McVetta, A. B., Stevens, M. A., Howard, S. A., Giel, P. W., Ameri, A. A., To, W., Skoch, G. J., and Thurman, D. R., "Variable-Speed Power-Turbine Research at Glenn Research Center," 2012, 68th Annual Forum of the American Helicopter Society, Fort Worth, TX, May 1-3, 2012; see also NASA/TM–2012-217605, July 2012.

CHAPTER 8. CRASHWORTHINESS

Karen E. Jackson[1]

INTRODUCTION

Crashworthiness is defined as the ability of a vehicle to protect its occupants (crew and passengers) from injury in the event of a crash impact. NASA Langley Research Center has a long history of supporting crashworthiness research, dating from the General Aviation Crash Research Program of the late 1960s and 1970s. Research has recently focused on rotorcraft crashworthiness. The rationale for incorporating crashworthy design features into rotorcraft is to minimize the number of fatalities and serious injuries experienced by the crew and passengers and to reduce the amount of structural damage to the airframe and payload during a severe, but survivable, crash. Crashworthy design of rotorcraft requires a systems approach in which various subcomponents work together to absorb and dissipate the kinetic energy of impact [Hurley and Vandenburg (2002)]. The crashworthy helicopter is capable of: (1) limiting the loads and decelerations that are transferred to the occupants to humanly tolerable or non-injurious levels, usually through crushable landing gear, energy-absorbing subfloors, and load-limiting seats, (2) providing a livable volume for the occupant by preventing collapse of fuselage frames and other structural components used to support the overhead rotor and transmission mass, (3) providing a secure tiedown for the occupant through seats, restraint systems, seat tracks, and floor attachments, (4) eliminating head-strike potential through the use of pretensioned restraint systems and cockpit airbags, and (5) minimizing post-crash fire hazards and ensuring emergency egress. The crashworthy helicopter must perform all of these functions while experiencing transitory, multidirectional decelerations associated with impact onto different terrains.

Figure 8.1 depicts the systems approach to crashworthiness, as applied to rotorcraft [Burrows (1992)]. As illustrated in this figure, the landing and/or skid gear is designed to crush and limit loads, which are then transmitted to the airframe. Within the airframe, the subfloor is designed to crush and absorb additional energy, while the seat strokes. In this manner, the occupant is slowed down using a controlled management of crash energy. The restraints are intended to hold the occupant securely in the seat and the seat attachments are designed to keep the seat attached to the floor, thus preventing the occupant from becoming a projectile within the cabin. Finally, the cabin must be designed to be sufficiently stiff and strong to prevent the overhead rotor/transmission mass from collapsing the airframe and intruding into the occupiable space.

The current research program at NASA Langley Research Center in rotorcraft crashworthiness is focused in several areas including the application of state-of-the-art explicit transient dynamic crash simulation tools for predicting the impact response of helicopters, seats, and occupants; the demonstration of advanced visualization technology using three-dimensional (3D) photogrammetry [Littell (2010)]; the development of novel composite energy-absorbing

[1] National Institute of Aerospace, 100 Exploration Way, Hampton, VA 23666.

concepts for airframe retrofit; and experimental testing using the Landing and Impact Research (LandIR) facility as well as two drop towers and laboratory equipment to generate test data for model validation and energy-absorbing concept evaluation. This chapter documents results of the past 10 years (2009–2018) of rotorcraft crashworthiness research, including: (1) impact testing and simulation of a redesigned skid gear for the HX-2 Wasp helicopter, (2) full-scale crash testing of an MD-500 helicopter with and without an external Deployable Energy Absorber (DEA), (3) impulsive loading and simulation of Anthropomorphic Test Devices (ATDs), (4) model calibration using uncertainty propagation and parameter sensitivity, (5) development and evaluation of two composite energy-absorbing subfloor concepts, eventually leading to full-scale crash testing of a CH-46E helicopter, with and without retrofit of the subfloor concepts, and (6) bird strike simulations. In addition, the results of three projects that were conducted as customer-funded cooperative research studies, two with the Federal Aviation Administration (FAA) and one with the U.S. Army Aviation Applied Technology Directorate (AATD)/Sikorsky Aircraft Corporation, are discussed. The first project involved modeling and simulation of a vertical drop test of a commuter-aircraft, the ATR42-300, which was drop tested at the FAA Technical Center. The second project involved testing and simulation of two F28 fuselage sections, a forward section and a wing-box section. The fuselage sections were tested at NASA Langley's LandIR facility. The third customer project was a vertical drop test of a prototype composite fuselage section, developed by Sikorsky under the Survivable Affordable Repairable Airframe Program (SARAP). Finally, NASA participated in the development of a new crashworthiness criteria, called the Full Spectrum Crashworthiness (FSC) criteria. Each section of the chapter ends with a statement of important findings and the significance of the work. Finally, the paper closes with recommendations for the future of crash research.

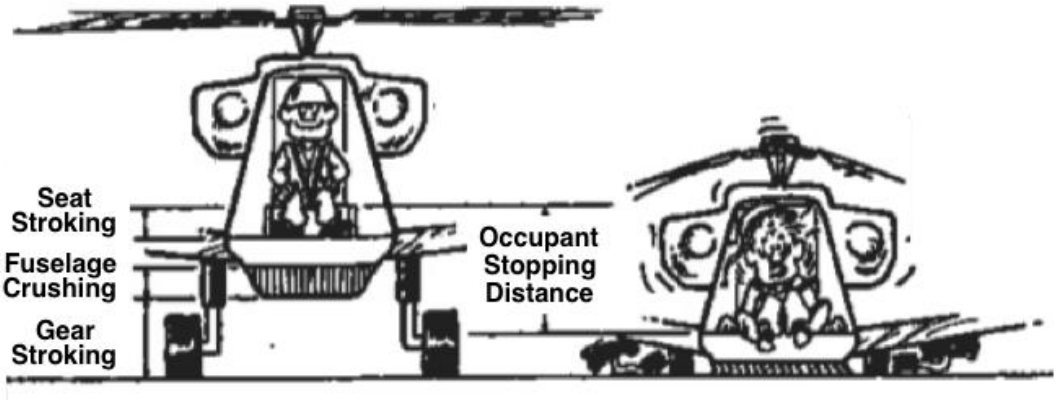

Figure 8.1. Helicopter crash schematic [Fig. 1 of Burrows, 1992].

WASP SKID GEAR TESTING AND SIMULATION

In 2007, HeloWerks, Inc. of Hampton, Virginia, approached NASA to conduct a test evaluation program on a skid gear redesign for their HX-2 WASP, which is a 1,000-pound kit-built two-seat helicopter fabricated using monocoque composite sandwich construction. The helicopter is 19 feet long, 9 feet high, and 7 feet wide at the skids, as shown in Figure 8.2. During a flight demonstration of the prototype aircraft, the pilot inadvertently shut off the engine during hovering flight resulting in a crash. As a result, the pilot experienced severe back injuries. The flight demonstration aircraft was outfitted with a composite skid gear that was designed for energy absorption. However, during the actual crash, the skid gear snapped and failed, absorbing very little crash energy. This accident led HeloWerks engineers to redesign the helicopter's skid gear and to approach NASA to conduct a test evaluation program to meet the Federal Aviation Regulation (FAR) crash energy absorption requirements for FAA certification.

LS-DYNA is a commercial, nonlinear, explicit transient dynamic finite element code marketed by Livermore Software Technology Corporation (LSTC). LS-DYNA simulations of the HeloWerks redesigned skid gear provided an opportunity for NASA to evaluate current occupant modeling capabilities within LS-DYNA [Hallquist (2006, Mar. 2006, and Aug. 2006)] using vertical impact test data from a fairly simple test article. To pursue this mutually beneficial program, a cooperative Space Act Agreement (SAA) was developed between HeloWerks, Inc. and NASA Langley Research Center [SAA (2006)]. HeloWerks designed and fabricated several test articles, and NASA instrumented the test articles, performed the vertical drop tests, and shared all test information with HeloWerks.

Figure 8.2. Photograph of the HX-2 WASP helicopter with original skid gear [Fig. 1 of Fuchs and Jackson, 2011].

Experimental Program

An 8.4-ft/s impact test of the final skid gear design was selected to evaluate the human occupant response models in LS-DYNA. The gear was redesigned based on the work reported in Tho et al. (2003). The redesigned gear was fabricated using aluminum circular cross-section tubes; the tubes were reinforced at the crossbeam attachments using 4130 steel sleeves and at the intersection with the skid beams using saddles to prevent premature collapse and local buckling of the gear. The fully instrumented test article, shown in Figure 8.3, weighed 1,064 pounds, including 320 pounds of ballast and 450 pounds for the two 95th-percentile Hybrid III male ATDs. The test article consisted of the redesigned skid gear mounted beneath a steel plate, a seating platform attached to the upper surface of the steel plate, and two 95th-percentile Hybrid

III male ATDs seated on the platform and secured using a four-point restraint system. Ballast weights were mounted to the test article to ensure the correct position of the center of gravity (CG).

An opening was cut into the seat platform to allow space for seat foam filler, as shown in Figure 8.4. The foam filler space under ATD-1 was filled with several layers of Styrofoam, as shown in Figures 8.4(a) and 8.4(b). Under ATD-2, three blocks of polyisocyanurate foam were used, as shown in Figures 8.4(c) and 8.4(d), with two blocks facing forward and one intersecting block positioned laterally.

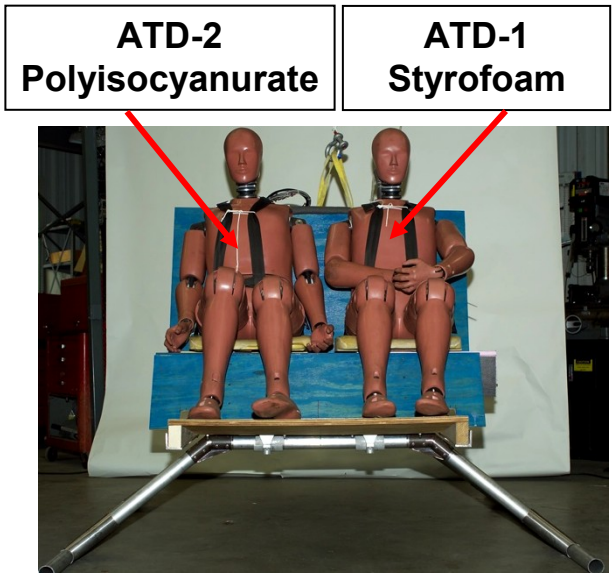

Figure 8.3. Front view of test article with ATD naming convention [Fig. 2 of Fuchs and Jackson, 2011].

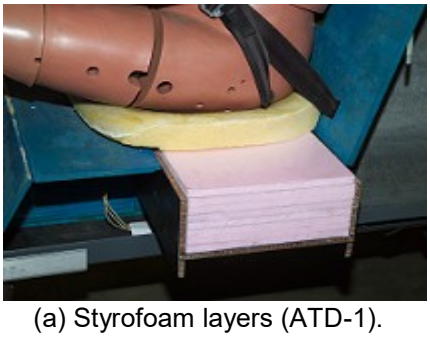

(a) Styrofoam layers (ATD-1).

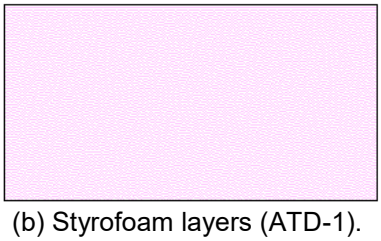

(b) Styrofoam layers (ATD-1).

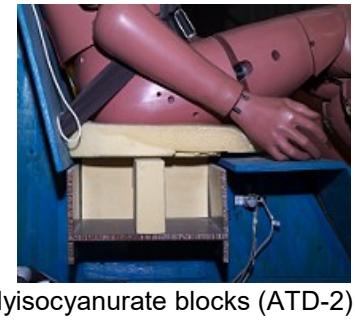

(c) Polyisocyanurate blocks (ATD-2).

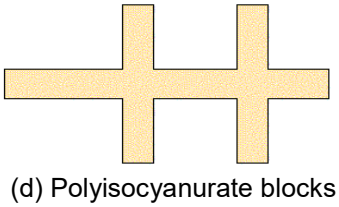

(d) Polyisocyanurate blocks (ATD-2).

Figure 8.4. Styrofoam and polyisocyanurate foam fillers [Fig. 4 of Fuchs and Jackson, 2011].

The test article and two 95th-percentile ATDs were instrumented with a total of 26 accelerometers and 2 lumbar load cells. Test data were collected at 50,000 samples per second using a digital data acquisition system (DAS). The vertical drop test was performed by attaching lifting cables to the test article, raising the test article through its CG, and then releasing the test article to impact a smooth concrete surface at 8.4 ft/s. Post-test measurements of permanent deformation show that the measured spread of the skid gear was 4.4 inches. No permanent deformation of either the Styrofoam stack or the polyisocyanurate foam blocks was visible post-test.

The peak magnitudes of the acceleration responses range from 6 to 9 g. The acceleration responses of the head have the lowest magnitude (6 g) and the pelvic acceleration responses have the highest magnitude (9 g). Some minor differences are seen between the ATD-1 and ATD-2 acceleration responses for the head and chest, however both curves have similar magnitudes. ATD-2 exhibits a higher peak acceleration of 9 g in the pelvis, than seen for ATD-1 (8 g).

Analytical Modeling

A finite element model (FEM) of the final skid gear design including ATD occupants was developed using the commercial nonlinear explicit transient dynamic code, LS-DYNA [Hallquist (2006, Mar. 2006, and Aug. 2006)]. The complete LS-DYNA FEM of the modified skid gear is shown in Figure 8.5. The structural model consists of 52 parts; 12,564 nodes; and 15,511 elements including 11,908 Belytschko-Tsay quadrilateral shell elements, 2,275 hexagonal solid elements, 925 beam elements, 371 seatbelt elements, and 32 lumped mass elements. Material properties were defined for the various parts including *MAT_PLASTIC_ KINEMATIC for 4130-steel, 6061-T6 and 2024-T6 aluminum shell elements used to represent the skid gear test platform, and *MAT_ELASTIC for the plywood and beam elements. The seat foam fillers were represented using solid elements that were assigned a material model in LS-DYNA called *MAT_CRUSHABLE_FOAM. Material characterization testing was performed to evaluate the behavior of the two seat foams, Styrofoam and polyisocyanurate. The test data were used as input to the material models.

The skid gear was modeled using circular cross-section beam elements of varying thickness. Concentrated masses were used in the model to represent the ballast weights. Two Hybrid III 95th-percentile male occupants were inserted into the structural model using the *COMPONENT_HYBRIDIII command. These models represent the human body using rigid links, surrounded by ellipsoids, with kinematic joints that mimic the motion of the human body. Once added, the two occupants were positioned using LS-PrePost, a pre- and post-processing software for LS-DYNA. Beam seatbelt elements were used to represent seatbelts in the test article to constrain the motion of the occupant models.

Contact surfaces were defined to represent contact between the skid gear and the impact surface, between the occupants and the seatbelts, and between the occupants and the seating platform. The impact surface was modeled as a nonrigid surface and given properties of 4130 steel. The contact friction between the skid gear and impact surface was defined as 0.1. The model was executed in LS-DYNA version 971 on a Linux workstation computer with a single processor. A simulation time of 0.2 seconds required 8 hours and 50 minutes of central processing unit (CPU) time.

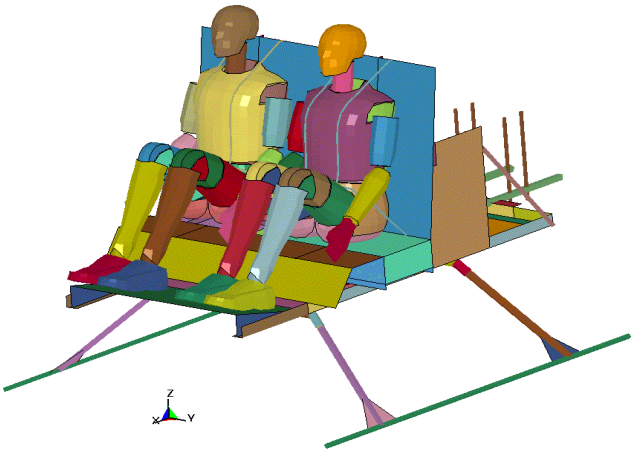

Figure 8.5. LS-DYNA model of the skid gear with occupants [Fig. 14 of Fuchs and Jackson, 2011].

Comparisons of the filtered vertical acceleration responses of the pelvis and chest of the two ATD occupants with LS-DYNA analytical predictions are shown in Figures 8.6 and 8.7, respectively. Both the experimental and analytical results were filtered with an SAE J211/1 equivalent low-pass filter with a cut-off frequency of 60 Hz [SAE (1995)]. For the original model, the peak accelerations correlate within an average of 7.4 percent for both ATD-1 and ATD-2 pelvis and chest comparisons. The time durations of the pulses match well but are slightly too short in the analysis data for both pelvic responses. The predicted curves match better for ATD-1 than for ATD-2. There is a strong secondary pulse shown in the analysis data for both ATD-1 and ATD-2 with an average overprediction of 92.5 percent. Note that in both ATD-1 and ATD-2 chest comparisons the analysis shows a slight onset rate delay as compared to the test response.

Examining the model further, the energy results indicate that there is a sharp increase in the internal energy at the same time that the strong secondary pulse is seen in the ATD-2 chest response. There is also an associated increase in the hourglass energy at that time that can be traced down to the energy associated with the polyisocyanurate material on which ATD-2 is seated. Also, a secondary hourglass energy spike is observed in the polyisocyanurate foam. Hourglass energy is used in the model to prevent nonphysical element deformations, and a *HOURGLASS_CONTROL type 6 was defined for the polyisocyanurate foam. In general, an hourglass energy of 10 percent or less of the total energy is desirable in a model, and sharp increases in hourglass energy can signify additional nonphysical energy additions and unwanted deformation shapes of elements.

Hourglass energy for foam materials is often related to the material representation and mesh size. In standard compression testing, the increase in bulk modulus of the foam once the cells have tightly compacted is not typically captured. Testing the same material in quasi-static loading would not provide the correlation with the dynamic data or capture the dynamic hardening effects. The material test data ends at just over 70 percent strain. Using this material curve alone will produce nonphysical results in LS-DYNA. To allow the compaction of the elements to propagate from the top element of the foam down through the foam without producing negative volume elements in the FEM, it is necessary to include the “tail” in the material response to represent the large bulk modulus stiffening of the foam. When the original results showed that

the hourglass energy from the foam was observed to impart large, nonphysical accelerations into ATD-2, the tail of the curve was modified to have a smoother response.

The simulation was repeated utilizing the modified polyisocyanurate material load curve. The results of this simple change on ATD-1 and ATD-2 responses are shown in Figures 8.8 and 8.9, respectively. In addition, the results of the modified model show a much-improved internal and hourglass energy response. All qualitative correlations are improved for both ATD-1 and ATD-2, except that the peak acceleration for ATD-2 is now underpredicted by the analysis. The initial peak magnitudes correlate within an average of 15 percent, and the secondary peak acceleration magnitudes correlate within an average of 38.4 percent. The large secondary response previously seen in the ATD-2 chest has been reduced, and in general the ATD-2 analysis curves now more closely match the shape of the test acceleration curves. In addition, ATD-1 also saw benefits by modifying the polyisocyanurate foam response. Additional information regarding this project can be found in Fuchs and Jackson (2008 and 2011) and Jackson and Fuchs (2007).

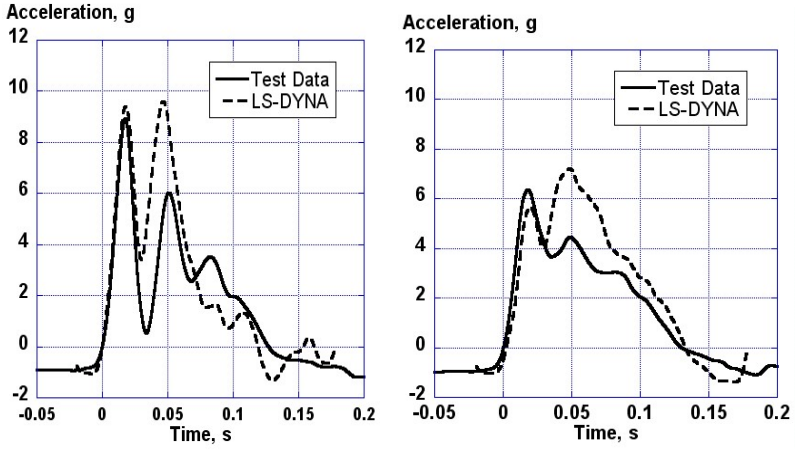

(a) Pelvis responses. (b) Chest responses.

Figure 8.6. ATD-1 (Styrofoam) test data versus updated LS-DYNA results [Fig. 16 of Fuchs and Jackson, 2011].

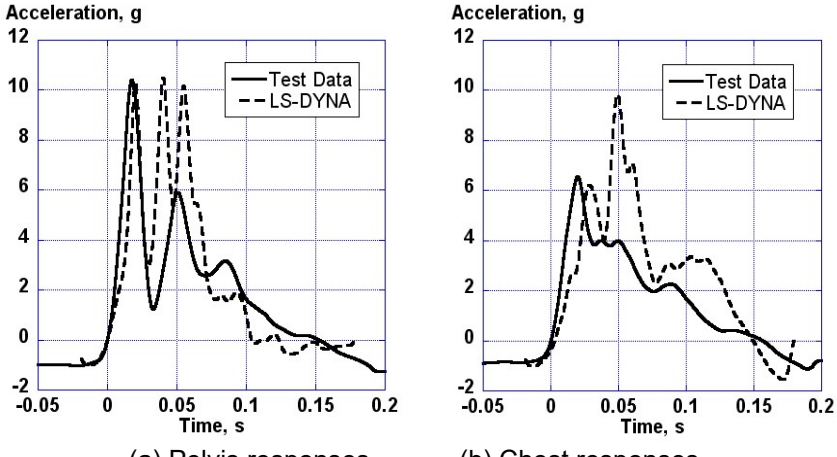

(a) Pelvis responses. (b) Chest responses.

Figure 8.7. ATD-2 (polyisocyanurate) test data versus updated LS-DYNA results [Fig. 17 of Fuchs and Jackson, 2011].

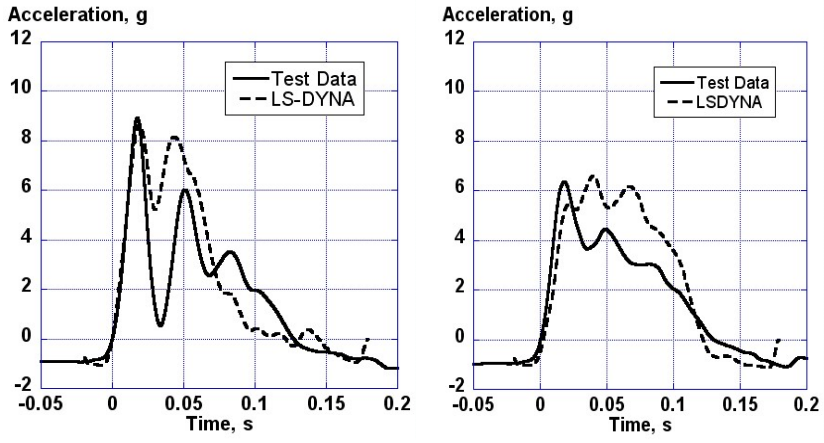

(a) Pelvis responses. (b) Chest responses.

Figure 8.8. ATD-1 test data versus updated LS-DYNA results for the 8.4-ft/s test [Fig. 21 of Fuchs and Jackson, 2011].

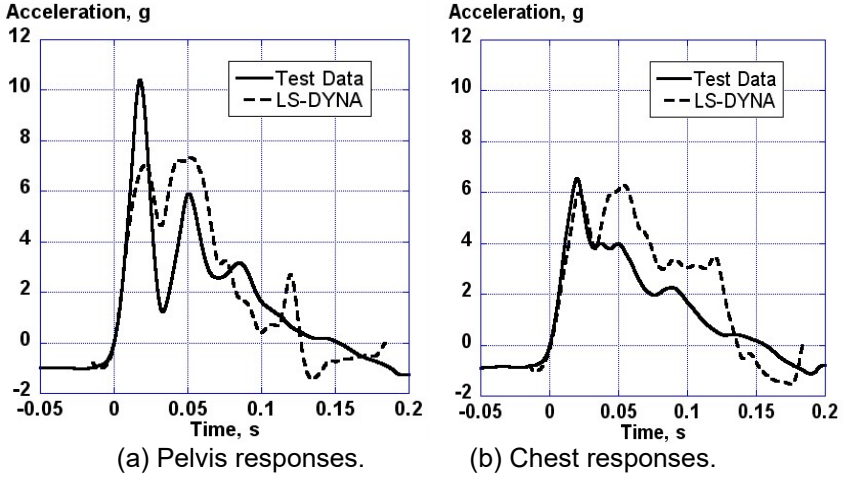

(a) Pelvis responses. (b) Chest responses.

Figure 8.9. ATD-2 test data versus updated LS-DYNA results for the 8.4-ft/s test [Fig. 22 of Fuchs and Jackson, 2011].

Important Findings and Significance

An 8.4-ft/s vertical drop test was performed on the final skid gear redesign provided by HeloWerks, Inc. The redesigned skid gear was intended as a replacement for an existing composite design that did not perform well during an actual crash event of the WASP prototype helicopter. Two 95th-percentile Hybrid III male ATDs were seated on the test platform and secured using a four-point restraint system. The vertical drop test was used to obtain ATD test data for correlation with the built-in LS-DYNA occupant models.

Major conclusions from this research project are: (1) The built-in *COMPONENT_HYBRIDIII occupant models available in LS-DYNA predicted peak responses within 15 percent. Based on these preliminary findings, the LS-DYNA occupant models may be used in aerospace simulation applications to determine occupant body motion response. (2) Changes to the foam material properties substantially improved the overall simulation results. (3) Yvonne Fuchs won the 2008 Robert L. Lichten Award for this work; it is given by the Vertical Flight Society (VFS) to provide an incentive to VFS members, who have not previously presented the results of their work at a technical forum, to begin presenting their work at local and regional VFS meetings.

FULL-SCALE CRASH TEST AND SIMULATION OF AN MD-500 HELICOPTER WITH AND WITHOUT AN EXTERNAL DEPLOYABLE ENERGY ABSORBER (DEA)

In March 2010, a full-scale crash test of an MD-500 helicopter was performed at NASA Langley's Landing and Impact Research (LandIR) facility. The purpose of the test was twofold: to evaluate the performance of an external Deployable Energy Absorber (DEA) [Kellas (2006), Jackson (2010), Jackson et al. (2010, 2011, and 2012), Kellas and Jackson (2010), Polanco (2010), and Polanco et al. (2009)] and to assess the ability of LS-DYNA to predict the impact responses of the DEA, the airframe, and the seated ATDs, based on an integrated finite element model (FEM). This LS-DYNA FEM was one of the first system-integrated models developed and executed at NASA. Measured impact conditions were 25.6 ft/s vertical and 38.8 ft/s horizontal with a –5.7-degree pitch, 7.0-degree roll, and 9.3-degree yaw attitude at impact. Although this impact condition is severe, it is still considered survivable. Details regarding the test and simulation can be found in Kellas et al. (2010), Littell et al. (2010), Fasanella et al. (2014), Annett and Polanco (2010), Annett (2010), Littell (2011), and Annett et al. (Nov. 2012). A photograph of the test article is shown in Figure 8.10.

The MD-500 helicopter is designed to seat four occupants, two crew and two passengers. The total weight of the test article, including the DEA, was 2,940 pounds. Four instrumented ATDs were used to represent two crew and two passengers. The pilot in the front left crew position was a 50th-percentile Hybrid III male ATD. The copilot in the front right crew position was a 50th-percentile Hybrid II male ATD, and the rear passenger on the left side was a 50th-percentile Hybrid II male ATD. The Hybrid II and III ATDs weighed 170 pounds each. For the right rear passenger, a specialized Human Surrogate Torso Model (HSTM) developed by the Johns Hopkins University-Applied Physics Laboratory (JHU-APL) was used [Roberts et al. (2005, 2007) and Annett et al. (2010)]. The biofidelic HSTM contained detailed representations of thoracic organs, skeletal structure, and soft tissue that is mated to the pelvis and legs of a 50th-percentile Hybrid III male ATD. The HSTM/Hybrid III ATD weighed 170 pounds. Note that the HSTM/Hybrid III was included in these tests specifically to study the possibility of aortic rupture [Annett et al. (2010)].

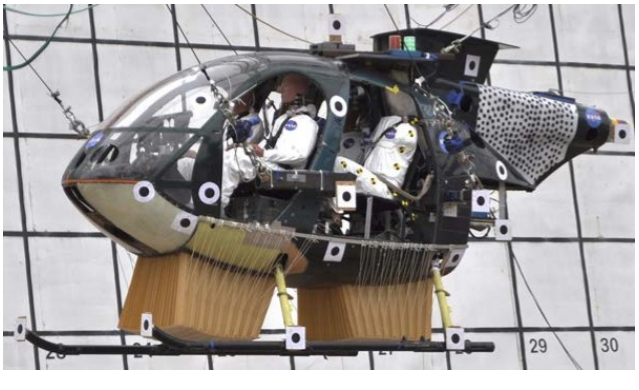

Figure 8.10. Photo of the MD-500 helicopter retrofitted with DEAs [Fig. 2(b) of Annett et al., Nov. 2012].

The fuselage and skid gear were instrumented with a combination of strain gages and accelerometers. ATD instrumentation included head, chest, and pelvic accelerometers, lumbar load cells, restraint load cells, and pressure gages. A total of 160 channels of data were collected at a sampling rate of 10,000 Hz. Measurements of vehicle kinematics were recorded using 2-dimensional (2D) and 3-dimensional (3D) large field photogrammetry.

A critical component evaluated in the impact test was the externally mounted DEA, which was conceived and patented by Dr. Sotiris Kellas of NASA Langley [Kellas (2006)]. The DEA is constructed of Kevlar-129 fabric and consists of multiple hexagonal cells. Two DEA blocks, spanning the fuselage belly surface, were secured to the fuselage outer skin with parachute cord. The flexible honeycomb design allows the DEA to be stowed flat, external to the fuselage belly, and to be deployed into the hexagonal configuration during an emergency. In this way, the DEA concept is similar to external airbags, providing extra energy absorption to the airframe when needed. In the deployed configuration, the DEA is loaded along the normal axes of the cells causing them to permanently deform under load and absorb energy. When loaded, the cell walls fold to form a controlled accordion-like pattern. The DEA concept was evaluated, prior to the MD-500 crash test, by testing and simulation of components, as well as retrofit of a composite fuselage section that was tested under multi-terrain impact conditions [Jackson et al. (2014a), Kellas and Jackson (Oct. 2010), and Jackson and Fuchs (2008)].

Two crew seats and a single passenger bench seat were installed in the airframe. The seats are standard military issue, constructed of aluminum frames with nylon mesh fabric stretched over the frames. The seat geometry was reconstructed using 3D photogrammetric techniques. Finite element models of the 50th-percentile Hybrid III male were used to represent the Hybrid II and III ATDs. These models contained a combination of rigid and deformable elements for body parts. Using the LS–DYNA preprocessor, the ATD models are easily imported and positioned within the helicopter model. The Livermore Software Technology Corporation (LSTC) occupant model contained 4,295 elements and is shown in Figure 8.11(a).

A reduced human torso model was constructed and adapted from the JHU-APL detailed Human Torso Finite Element Model (HTFEM) [Roberts et al. (2005 and 2007)]. This model includes organs and soft tissue components made from solid silicone elements; the sternum, ribcage, vertebrae, and scapula are modeled with fiberglass beam and shell elements. The reduced HTFEM, depicted in Figure 8.11(b), was attached to the LSTC Hybrid III pelvis and legs, and the total model contained 8,034 elements. The pilot and copilot models are restrained with four-point harnesses, and the passenger model and reduced HTFEM are restrained with three-point harnesses.

The system-integrated MD-500 FEM with the DEA is shown in Figure 8.12. This model contains approximately 400,000 elements in total, with 266,000 elements representing the DEA. For a simulation time of 0.2 seconds, the system-integrated MD-500 model run time was approximately 24 hours, with execution on a Linux-based workstation computer with eight processors running LS-DYNA version 971 Symmetric Multi-Processing (SMP) [Hallquist (2006, Mar. 2006, and Aug. 2006)].

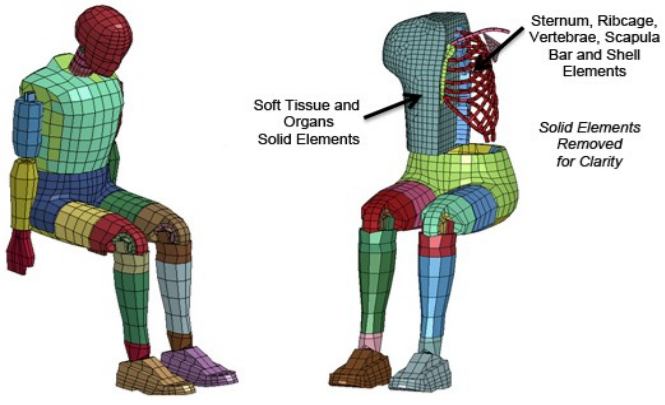

(a) LSTC Hybrid III model. (b) HTFEM/Hybrid III dummy model.

Figure 8.11. Dummy FEM depictions [Fig. 16 of Annett et al., Nov. 2012].

The impact orientation and deformation at peak acceleration are shown in Figure 8.13 for the test and analysis. Qualitatively, the global deformation pattern of the DEA model was similar to the deformation observed from the high-speed video, which included folding on the right side and crushing on the left side, relative to the passenger's view. In the simulation, dimpling of the skin occurred in the region above the rear DEA, whereas post-test inspection of the test article revealed no damage. During the test, the DEA exhibited folding, crushing, and sliding along the belly, which was attributed to the presence of roll attitude and shear loading. This behavior was only partly captured by the shell-based DEA model.

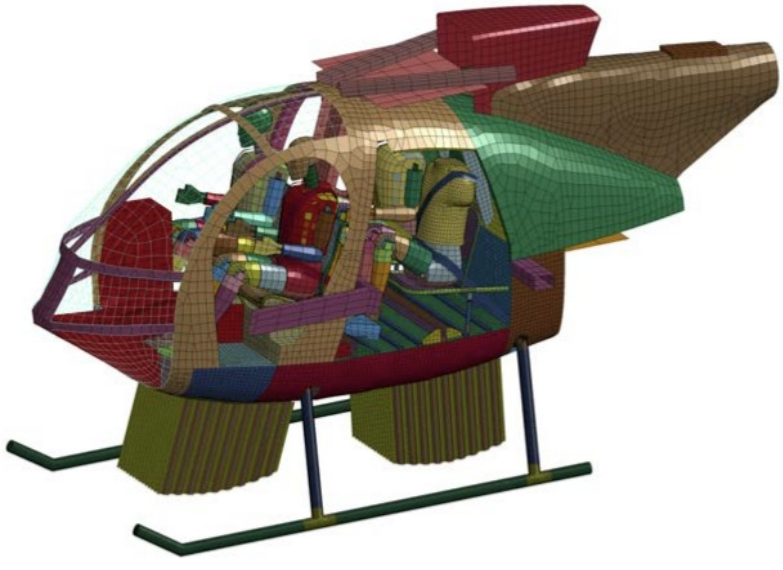

Figure 8.12. MD-500 system-integrated FEM [Fig. 17 of Annett et al., Nov. 2012].

(a) MD-500 prior to initial impact. (b) MD-500 at peak acceleration.

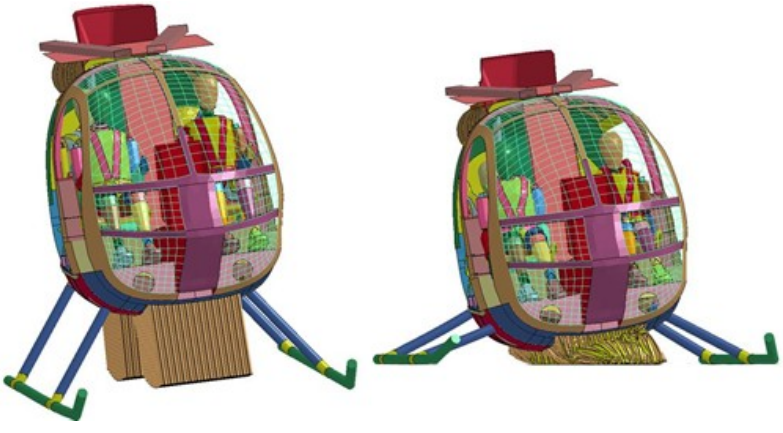

(a) Model prior to impact. (b) Model at peak acceleration.

Figure 8.13. Test-analysis depictions at a time just prior to impact and at peak acceleration [Fig. 18 of Annett et al., Nov. 2012].

Despite minor qualitative differences between local deformation patterns, reasonable agreement is obtained between the simulation and the overall response of the test article. At time = 0.0 s, the skid gear initially impacts the concrete surface. At time = 0.03 s, the DEA begins to attenuate energy. As expected from previous testing of the DEA, vertical accelerations of the airframe are effectively trapezoidal in shape. In this manner, the DEA performs as a load-limiting shock absorber, regulating the loads between 10 and 15 g and expanding the deceleration pulse duration through crushing and folding.

Test and analysis acceleration responses are plotted in Figure 8.14(a), and changes in vertical velocity are plotted in Figure 8.14(b) at the centerline of the floor beneath the passenger seats. At this location, the model does a good job of predicting the initial peak acceleration and the pulse duration. The test response shows a second peak acceleration at approximately 0.0125 s, which occurs earlier in time for the predicted response. The velocity change responses are similar initially. At 0.065 s, the two curves begin to deviate slightly, with the simulation removing velocity more quickly than the test. However, by the end of the pulse the two curves are in close agreement once again.

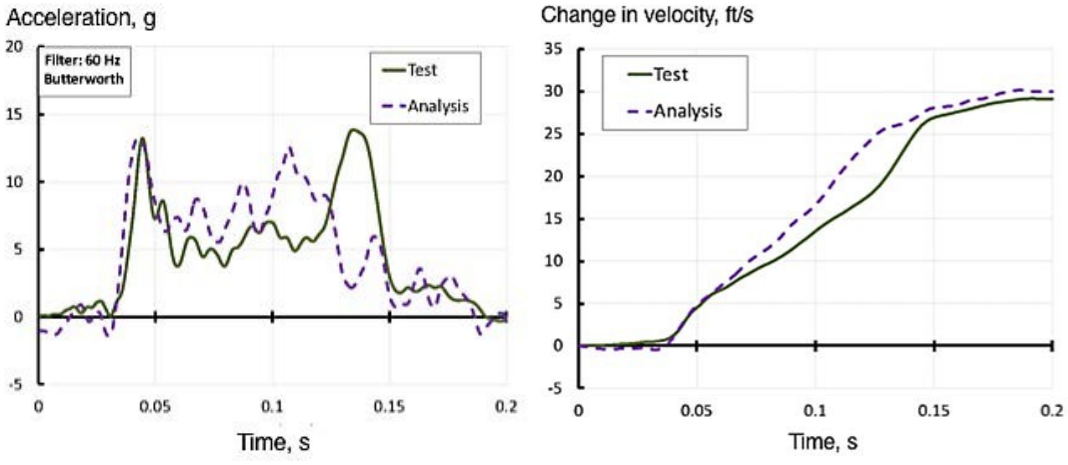

(a) Acceleration responses. (b) Velocity responses.

Figure 8.14. Comparison of test and analysis; centerline of the floor beneath the passenger seats [Figs. 21 and 22 of Annett et al., Nov. 2012].

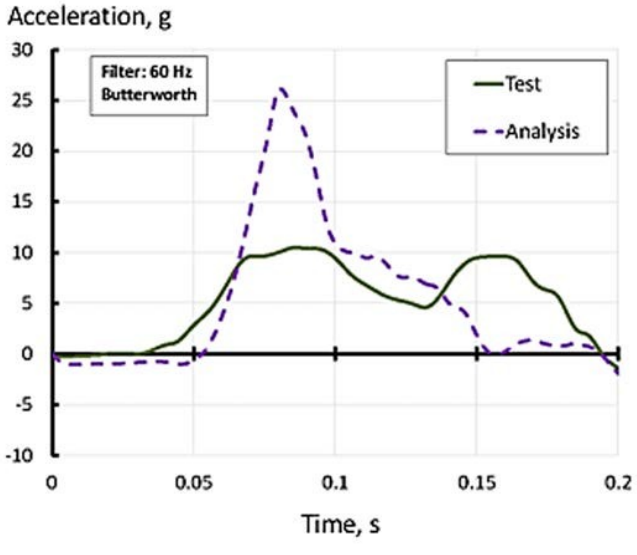

Figure 8.15. Comparison of test and analysis; pilot pelvic vertical acceleration [Fig. 23 of Annett et al., Nov. 2012].

The predicted and experimental pilot pelvic vertical acceleration responses are shown in Figure 8.15. The peak acceleration from the analysis is over twice the magnitude of the test response and the pulse shape is also noticeably different. These results provided the first indication that the ATD models, which were developed originally for automotive crash simulations, were not calibrated for the dominant vertical loading environments experienced in a rotorcraft crash.

A second full-scale crash test of the MD-500 helicopter was performed at the NASA Langley LandIR facility using the same airframe hardware that was previously tested with the DEA [Annett (2011), Annett et al. (2012), and Littell (2011)]. The rationale for conducting this second test was threefold: (1) To generate data to validate finite element computer modeling efforts,

(2) to study the crashworthy features typically associated with a representative small helicopter, and (3) to compare responses obtained with the helicopter in a baseline configuration to data collected from a previously conducted MD-500 crash test, which included the DEA blocks. The MD-500 helicopter was inspected following the first crash test with the DEA and minor damage was found. Consequently, repairs were necessary to prepare the MD-500 helicopter for the test.

The second MD-500 crash test was a replicate of the original test with the DEA, having a similar loading configuration and similar impact conditions. The impact surface was concrete. The MD-500 test article weighed 2,906 pounds. It was instrumented to collect strain, acceleration, load and ATD occupant response data. The layout of the ATD occupants and seats was the same as used in the previous test.

A sequence of high-speed photographs is shown in Figure 8.16, including a side view and a front view for three discrete time steps during the impact event. The measured impact conditions for this test were: 39.1 ft/s forward velocity, 24.1 ft/s vertical velocity, 0.6 ft/s lateral velocity, –6.2 degree pitch, 1.9 degree roll, and 2.1 degree yaw. Post-test damage to the airframe included external skin damage. The skin rippling seen on the right side near the right front skid gear attachment indicates that the movement of the gear during impact has caused some of the internal structure on the subfloor to buckle.

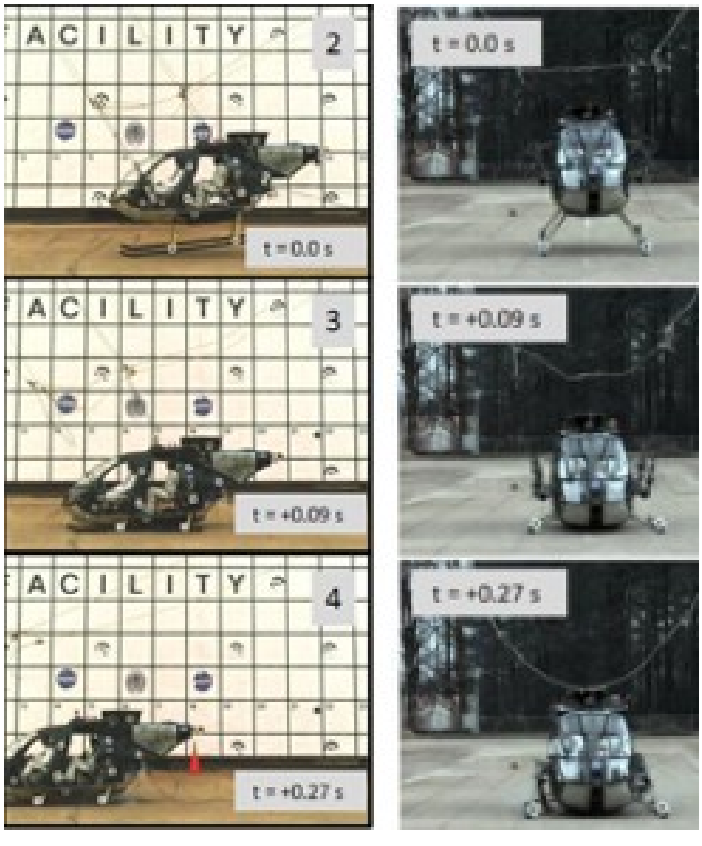

(a) Side view. (b) Front view.

Figure 8.16. Impact sequence of the full-scale crash test of the MD-500 without DEA [Figs. 6 and 24 of Annett et al., Nov. 2012].

Following the removal of the MD-500 helicopter post-test, the seats and occupants were removed to examine the floor and subfloor. Much of the subfloor and bottom skin was severely deformed, indicating that these regions absorbed the majority of the impact energy. The center keel beam was severely dented in multiple places from the nose to the rear bulkhead, while the frames extending from the keel beam to the outer structure were bent and buckled in multiple places. Similar damage was observed on the pilot-side subfloor. Severe deformations were observed on the keel beam underneath the rear occupants. In many locations, the keel beam had buckled and cracked, leaving little or no structural integrity. Much of the upper portion of the airframe was intact post-test suggesting that the impact loads were absorbed by deformation and failure of the subfloor structure. It should be noted that none of these damage mechanisms were observed on the MD-500 airframe with the DEA following its crash test.

Plots of measured floor and rotor ballast vertical acceleration time histories are shown in Figure 8.17. Figure 8.17(a) shows a distinct large spike at approximately 0.075 seconds after impact, which is attributed to the belly of the airframe impacting the concrete surface. The peak value for the right accelerometer was 56.7 g, while the peak value for the left accelerometer was 45.9 g. The approximate 10-g difference was attributed to the right side impacting the ground first. The second, smaller spike at 0.1 second is part of the larger initial contact, and is probably due to the inertia of the ATD occupants impacting the seats slightly after the initial belly contact. After the initial spikes, the acceleration traces show no more distinct characteristics.

Figure 8.17(b) shows two acceleration traces that contrast the results plotted in Figure 8.17(a); one from the rear floor and one from near the top rotor ballast location. All acceleration traces were filtered with a 4-pole low-pass Butterworth filter with a cutoff frequency of 60 Hz. The curves in Figure 8.17(b) exhibit two peaks for both the rear floor and the top ballast response locations. The shape and relative peak values of the two curves show that the pulse widths are much longer in the rear and at the top of the helicopter. While the duration of the large front acceleration pulse was approximately 10 ms, the rear and top accelerations had durations closer to 40 ms. The longer duration was attributed to the subfloor deformation and crushing, and thus absorbing much of the initial impact load and lengthening the pulse width. The rear floor showed a higher peak at 46.3 g while the top ballast showed a lower peak of 37.4 g, demonstrating the dissipation of approximately 10 g by the airframe between the floor and the roof of the cabin.

It is useful to compare the floor-level acceleration responses shown in Figure 8.17 for the MD-500 crash test without the DEA with similar acceleration responses, shown in Figure 8.14, for the MD-500 crash test with the DEA. Acceleration magnitudes are significantly reduced with the DEA, i.e. less than 15 g compared with 45 to 55 g, which is a reduction of 30 to 40 g. Reduced floor-level accelerations translate into reduced loading transmitted to the seats and occupants, thus improving the chance for occupant survivability.

Additional comparisons of the two crash tests are shown in Figure 8.18, which provides comparison plots of lumbar load time histories for the pilot and copilot for each test. The pilot and copilot responses in the MD-500 crash test without the DEA exceeded the 1,500-pound lumbar injury criteria established by the FAA. In contrast, the crew responses for the crash test of the MD-500 with DEA were substantially lower. For the crash test without the DEA, both occupants were subjected to a load pulse with a (filtered) maximum peak of approximately 1,900 pounds. The effect of the DEA was to attenuate that pulse by 67 and 60 percent for the pilot and copilot, respectively. The difference in the load attenuation can be attributed to several factors

including differences in the ATDs (Hybrid III for pilot, Hybrid II for copilot), the foam block under the copilot's seat and, most importantly, the difference in the impact orientation between the two tests with the first test having greater roll and yaw attitude at impact. Additional comparisons of the two crash tests are provided in Annett (2011) and Littell (June 2011).

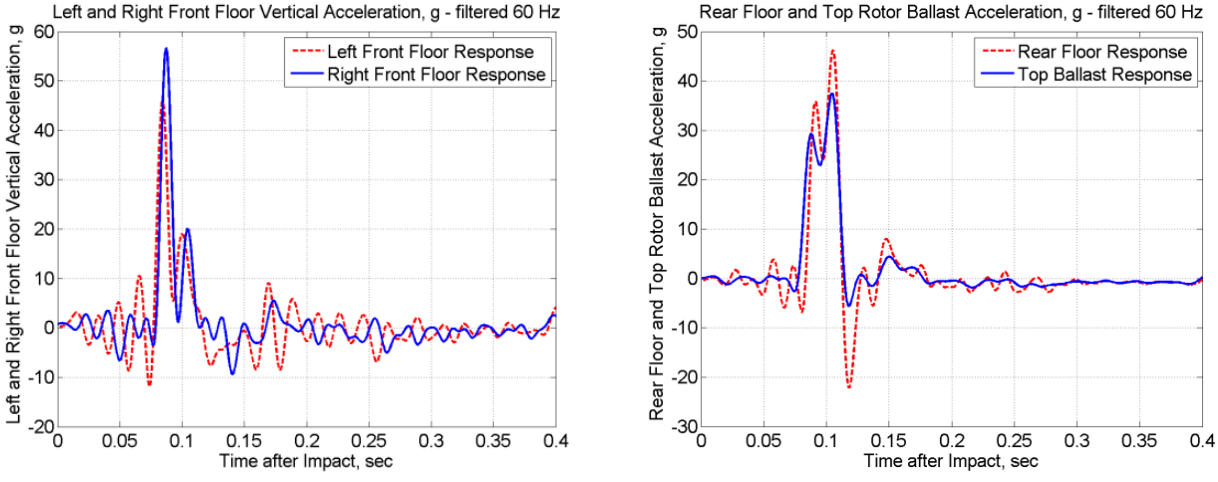

(a) Left and right front floor vertical acceleration. (b) Rear floor and top ballast vertical acceleration.

Figure 8.17. Measured acceleration time histories from the MD-500 crash test without DEA [Figs. 12 and 13 of Littell, 2011].

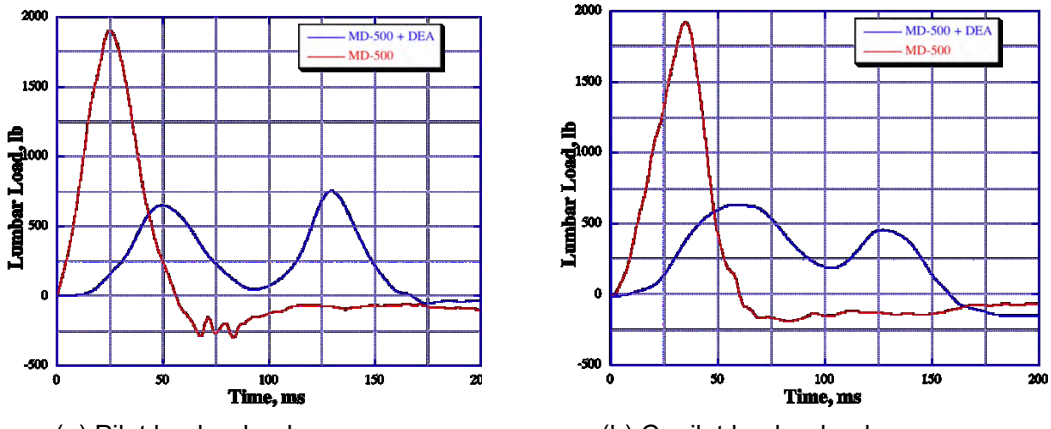

(a) Pilot lumbar load responses. (b) Copilot lumbar load responses.

Figure 8.18. Measured lumbar loads of the pilot and copilot in the MD-500 crash tests with and without DEA [Figs. 14 and 15 of Kellas et al., 2010].

The MD-500 crash test and simulation effort described herein actually spawned some follow-on work. The first follow-on project relates to the inadequacy of LSTC downloadable ATD FEMs. As noted previously, these models were calibrated for automotive crashes where loading to the occupant is primarily normal to the spine, whereas loading in aircraft/rotorcraft crashes is primarily parallel to the spine. As a result of the poor performance of the Hybrid III dummy model, an experimental program was conducted in which 14 vertical drop tests were performed using the Hybrid III 50th-percentile ATD, Hybrid II 50th-percentile ATD, and later the Test Device for Human Occupant Restraint (THOR) 50th-percentile dummy [Shaw et al. (2002)]. In the second follow-on project, a more computationally rigorous approach was applied to calibrate the MD-500 model without DEA. These two follow-on studies are highlighted in the next sections of this chapter.

Important Findings and Significance

There are several important findings as a result of this work. The two MD-500 helicopter crash tests were the first to demonstrate the capabilities of the DEA as an effective and efficient crash load attenuator. As a result, the DEA is being considered as an energy-absorbing concept for the NASA Mars Sample Return mission. The system-integrated FEM was one of the first models to include all relevant parts including the airframe, skid gear, seats, ATDs, restraints, and ballast. The poor performance of the LSTC downloadable ATD model has led to follow-on research, as described in the next section. Finally, this work spawned a second follow-on project related to model calibration and uncertainty propagation, which is also highlighted later in this chapter.

ATD IMPULSIVE LOADING AND SIMULATION

The aerospace industry relies heavily on the development of automotive dummies and injury criteria originally developed for automotive use. However, the aerospace industry must address injuries associated with vertical loading conditions (i.e. an aircraft crash scenario) individually or in combination with horizontal loading conditions, which are largely ignored in the automotive world. Thus, the aerospace industry must develop its own specialized guidelines. One example is from the FAA. Federal Aviation Regulation (FAR) 27.562 Subpart C “Emergency Landing Conditions” [Code of Federal Regulations (1989)] has generated guidelines on occupant injury, which establish a 1,500-pound limit on vertical lumbar loading from a “...170-pound [50th-percentile] ATD.” However, the choice of the ATD is not specified. It is common for researchers in the aerospace fields to use a Hybrid III ATD modified to include the straight lumbar spine originally used on the Hybrid II ATD, as documented in Gowdy (1999). The straight spine is used in the aerospace industry because it is commonly believed to better replicate the occupant’s seated posture than a Hybrid III ATD with a curved spine. The differences between the Hybrid II, Hybrid III with curved spine, and Hybrid III with straight spine are not well understood.

Researchers at NASA Langley have conducted full-scale crash tests and simulations of aircraft involving ATD occupants [Jackson et al. (2002), Jones and Carden (1995), and Fasanella and Jackson (2002)] using variations of the Hybrid III and Hybrid II. Elsewhere, researchers have used the various ATDs in aircraft loading conditions to establish limits for lumbar loading with regard to military seats [Rappaport et al. (1997)], to evaluate seat performance [Hu et al. (2009)], and to evaluate injury due to ejection seat loading [Salzar et al. (2009)]. Researchers at Wright Patterson Air Force Base commonly test dummies in their Vertical Decelerator Tower [Buhrman (1991) and Perry et al. (2000)], which simulates ejection seat loading and evaluates the effect of

variables such as helmets and seating posture. NASA is also examining the feasibility of including ATDs in the Orion spacecraft [Lawrence et al. (2008)] testing and simulations. The performance and accuracy of these ATDs are critical when evaluating probable risks of injury for crew during an aircraft crash or spacecraft landing.

To address these concerns, a research program was undertaken at NASA Langley to examine vertical loading responses using three common configurations of ATDs [Polanco and Littell (2011)]. A Hybrid III with a straight spine, a Hybrid III with a curved spine, and a Hybrid II ATD were tested under vertical loading conditions to evaluate their responses and to generate data for correlation with predictions from two occupant simulation models. In addition, a later study examined the THOR 50th-percentile dummy [Putnam et al. (2013 and 2015), and Shaw et al. (2002)]. Along with the test series, an evaluation of commercially available ATD FEMs is presented.

All tests were conducted using a 14-foot vertical drop tower at NASA Langley. For each test configuration, the ATD was seated on a rigid aluminum platform, which was connected directly to the drop tower rails. The desired input pulse was generated by impacting the platform against layers of either weak paper honeycomb (nominal crush strength of 30 psi) or strong paper honeycomb (nominal crush strength of 50 psi). The average impact velocity was 17.3 ft/s for tests conducted with the strong paper honeycomb and 16.6 ft/s for tests conducted with the weak paper honeycomb. Figure 8.19(a) shows the test setup.

During the test series, each ATD was instrumented with six accelerometers; two in the head, chest, and pelvis measuring vertical and forward accelerations, and a lumbar load cell, measuring vertical lumbar loads only. Lateral responses were assumed to be minor, therefore no data were collected in the lateral direction. The platform was instrumented with two accelerometers measuring vertical acceleration. Data were sampled at 10 kHz and collected on a National Instruments NI-DAQ DAS using LabView software. As shown in Figure 8.19(b), targets for 3D photogrammetry were also placed on each ATD at specific locations to compare position measurements pre- and post-test, along with transient motion that occurred during the impact. Among the entire set, targets were placed at both the head and chest center-of-gravity (CG) locations. Other targets were placed to measure angular and relative motion between various components of the ATD, while some were placed and used for positioning in computer model development. Targets were also placed on the platform to check for flexure during impact. Care was taken to place the targets in similar spots between the different ATD configurations.

Each test was filmed with two high-speed cameras at 1,000 frames per second (fps). All photogrammetry, high-speed video, and acceleration data were time synchronized with an IRIG-B master clock. There were no restraints as part of the test setup so the ATD was free to move throughout the impact. Safety straps were loosely placed around the neck and waist to restrain the ATD within the platform. The final test setup is shown in Figure 8.19(b) with the straps, photogrammetry targets, and coordinate system highlighted.

The THOR data generated from the 16.6-ft/s test is compared to the previously generated data obtained from similar tests with the Hybrid series of ATDs, also performed at 16.6 ft/s onto weak honeycomb. The head and pelvis vertical accelerations are first compared in Figure 8.20. The general shape and peak values for each of the ATDs are approximately the same. Each ATD displays a generalized plateau-shaped acceleration pulse with sinusoidal peaks and valleys

attributed to crushing of individual layers of the stacked paper honeycomb. The major difference between the curves is that the onset rate of the THOR lags the onset rate of the Hybrid ATDs. The THOR maximum value is 11.4 g at 30 ms after impact, whereas the generalized Hybrid maximums are between 8 and 10 g, and occur between 12 and 20 ms after impact. The tail end of the plateau region after the 100-ms mark agrees well between the THOR and Hybrid III ATDs. The pelvis acceleration responses, plotted in Figure 8.20(b), show similar trends. The onset rate for the THOR response lags the Hybrid ATD responses, however the peak acceleration values are nearly the same.

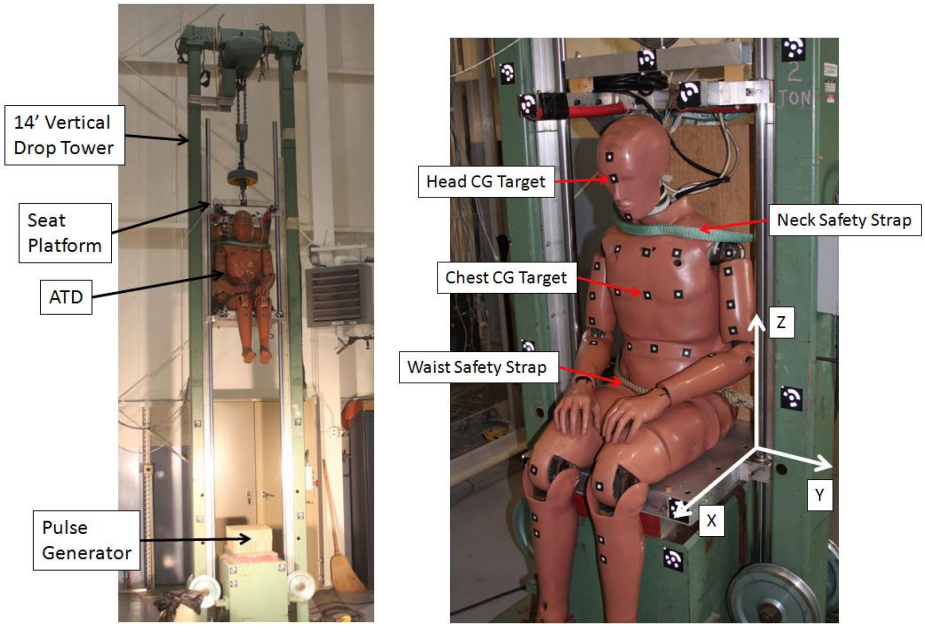

(a) 14-ft drop tower. (b) ATD positioning and coordinate system.

Figure 8.19. Drop tower and ATD setup [Figs. 1 and 2 of Polanco and Littell, 2011].

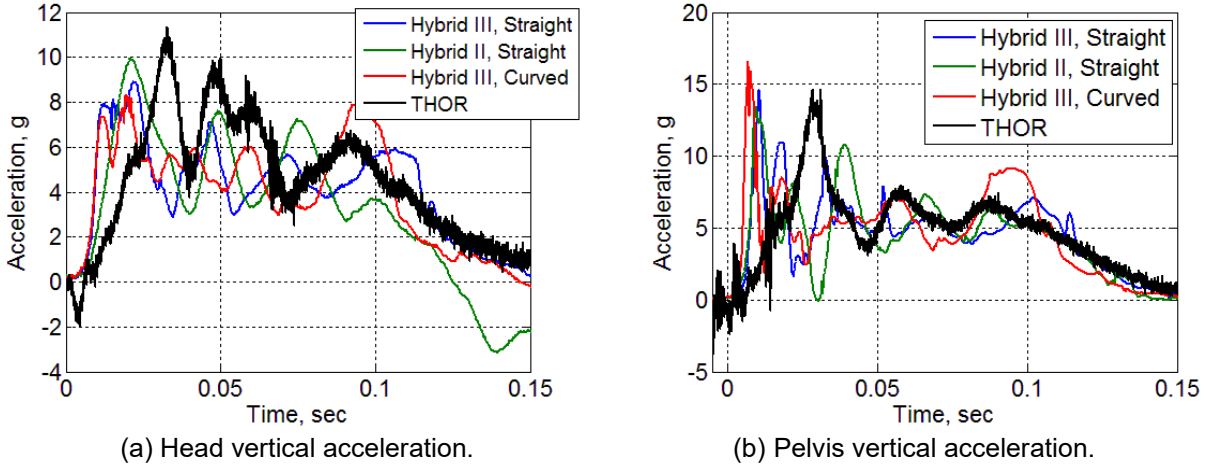

(a) Head vertical acceleration. (b) Pelvis vertical acceleration.

Figure 8.20. Comparison of THOR and Hybrid ATD responses for the 16-ft/s vertical velocity condition [Figs. 15 and 16 of Littell and Annett, 2013].

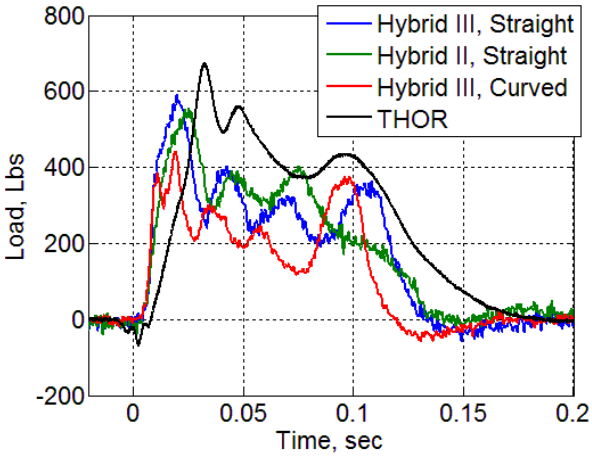

Figure 8.21. Comparison of lumbar loads for the Hybrid and THOR ATDs [Fig. 17 of Littell and Annett, 2013].

Finally, lumbar load responses are examined and plotted in Figure 8.21. The lumbar load response curves parallel the trends of the pelvic accelerations, showing a plateau-shaped response following an initial peak. However, unlike the pelvic accelerations, which exhibit almost identical response durations, the total duration of the loading is between 100 and 150 ms for the Hybrid ATDs and approaches 200 ms for the THOR. The THOR has a maximum lumbar load of 673 pounds, which occurs at 37 ms after impact. The next highest load occurs in the Hybrid III with a straight spine configuration. The maximum load is 591 pounds and occurs 20 ms after impact. All ATDs having the straight spine configuration are at, or slightly above, the 600-pound maximum load mark, whereas the maximum load for the Hybrid III with curved spine configuration is slightly above 400 pounds. Some of the scatter in the data could be due to ATD test positioning, however the majority of the difference can be attributed to the orientation of each ATD's load cell with respect to the vertical axis. Three of the ATDs tested—the Hybrid II, the Hybrid III in a straight spine configuration, and the THOR—all have straight spinal columns with the load cell positioned parallel to the vertical direction. The Hybrid III with a curved spine configuration, however, contains a load cell with a measurement axis positioned 22 degrees off-axis from the vertical direction. Therefore, it is expected that the loads measured from the curved spine load cell would be lower than those measured from the straight spine.

Two different FEMs of the Hybrid III 50th-percentile ATD were evaluated in the vertical loading regime using LS-DYNA, and analytical predictions were compared with test data. One model was developed by First Technology Safety Systems (FTSS) [FTSS (2008)] and the other by LSTC. Both models used the curved spine (automotive) configuration only. The FTSS Hybrid III model contained 100,822 nodes, 23,399 rigid elements, and 95,173 deformable elements. The FTSS model is shown in Figure 8.22, along with the LSTC rigid model.

One specific area of interest is the lumbar pelvic region on both models, because of the vertical nature of the loading. The FTSS lumbar pelvic region contains null shells for contact, pelvis skin represented using a viscoelastic material model, and pelvis foam assigned a strain-rate-dependent material property for low-density foam. The pelvis skin was modeled using a constant-stress solid element formulation, while the pelvis foam utilized a tetrahedral element formulation with one integration point through the element thickness. Contact was defined in the FTSS model

using a global-based contact algorithm to account for all body parts contacting one another. The LSTC Rigid-FE model of the Hybrid III ATD contains 7,444 nodes, 2,453 rigid elements, and 1,842 deformable elements. Unlike the FTSS model, the LSTC model only has the pelvis foam modeled, using hexagonal elements with one integration point through the thickness. The pelvis foam utilizes an isotropic material property for low-density foams with a rate-independent stress-strain curve defined.

Both models were set up such that impact conditions closely matched those of the test. Acceleration time histories were applied on the seat platform bottom spread out over a cross-sectional area equal to the honeycomb dimensions from the tests. For each model, six cases were executed, where the acceleration time-history input was based on the test condition (Hybrid II or Hybrid III, curved or straight lumbar spine, strong or weak paper honeycomb). Each input acceleration time history was filtered using a low-pass 4-pole Butterworth filter with a 1,000-Hz cutoff frequency. In each case, the ATD models were positioned according to photogrammetry angular measurements, which included head, chest, and limbs.

Response data taken from the FTSS and LSTC models were compared with test data, as shown in Figures 8.23–8.26. Overall, the FTSS acceleration and lumbar load responses match the trends seen in the test data regardless of the input acceleration type used for different ATD and lumbar spine configurations. The correlation level between the LSTC model results and test data in all impact cases is extremely low. One obvious trend seen in the model is that an initial spike appears immediately after impact in the lumbar, chest, and head regions. Secondary peaks not present in the test data occur in the acceleration time histories because of uneven initial distribution of impact loads acting upon the pelvis, and pelvis rotation occurring afterwards as a result of slouching in the occupant. Between the initial spike and when the second highest peak occurs (25 ms for strong paper honeycomb and 40 ms for weak paper honeycomb), the pelvis adjusts position where load is distributed on all pelvic foam segments contacting the seat. For purposes of comparing equal ATD and spinal configurations between physical and numerical entities, responses for a Hybrid III with a curved spine configuration are shown. As shown in

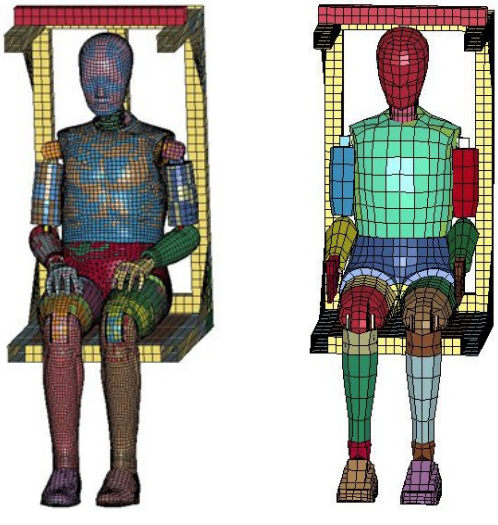

Figure 8.22. FTSS model (left) and the LSTC rigid model (right) [Figs. 11 and 12 of Polanco and Littell, 2011].

Figure 8.23, for both strong and weak paper honeycomb, the vertical head acceleration in the FTSS model matches the initial peak magnitude seen in the test responses before dropping, then rebounding because of increased load transfer into the head. A time lag between peak accelerations in the FTSS model and test data is present in all cases analyzed. The peak acceleration in the LSTC analysis is three times higher than that of the test using a strong paper honeycomb pulse, and twice as high as that of the test using a weak paper honeycomb pulse.

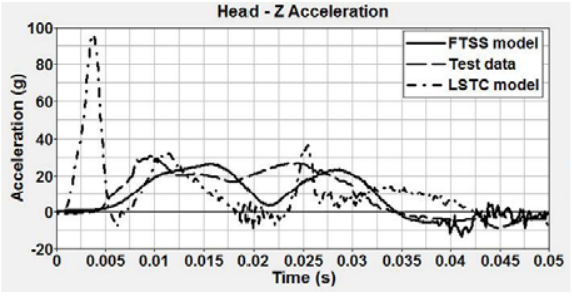

(a) Strong paper honeycomb.

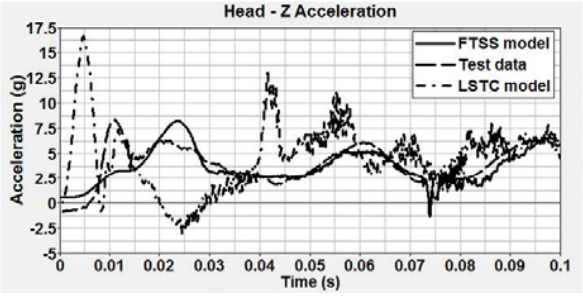

(b) Weak paper honeycomb.

Figure 8.23. Head acceleration responses for curved spinal configuration in test and analysis [Figs. 14(a) and (b) of Polanco and Littell, 2011].

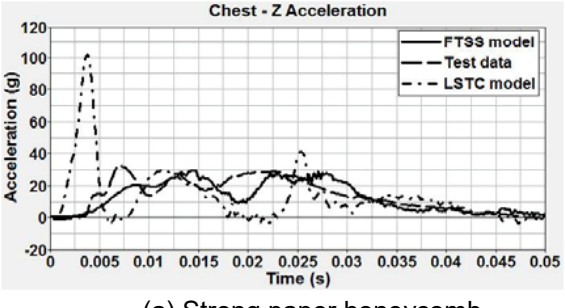

(a) Strong paper honeycomb.

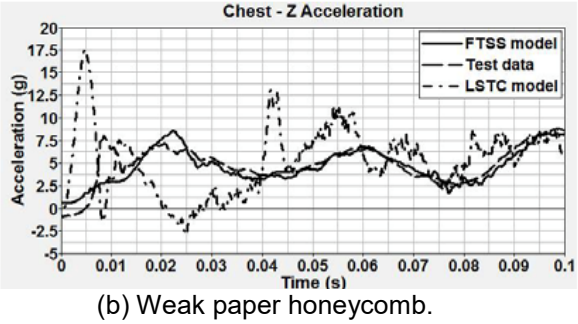

(b) Weak paper honeycomb.

Figure 8.24. Chest acceleration responses test/analysis comparison for curved spine configuration [Figs. 15(a) and (b) of Polanco and Littell, 2011].

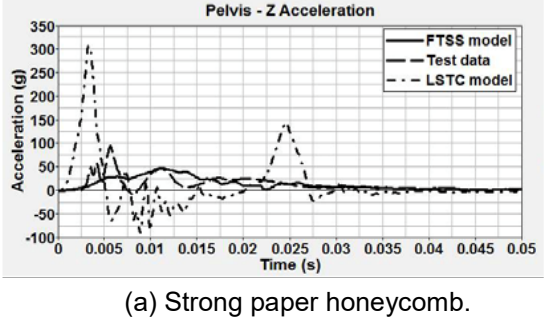

(a) Strong paper honeycomb.

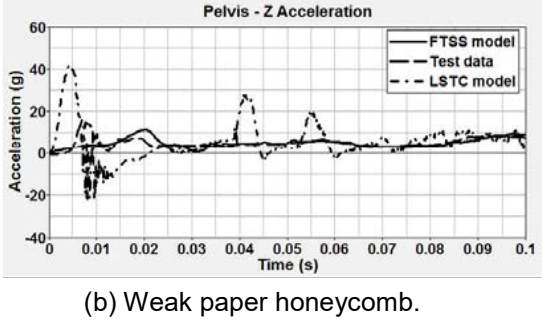

(b) Weak paper honeycomb.

Figure 8.25. Pelvis acceleration response test/analysis comparisons for curved spine configuration [Figs. 16(a) and (b) of Polanco and Littell, 2011].

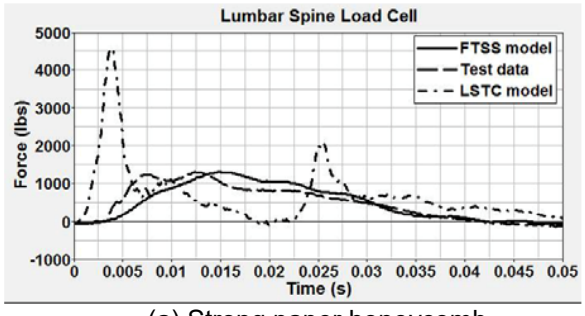

(a) Strong paper honeycomb.

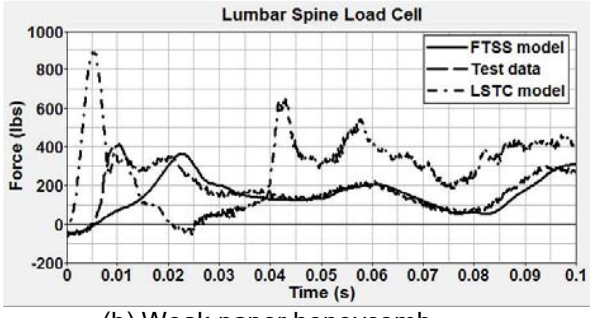

(b) Weak paper honeycomb.

Figure 8.26. Lumbar spine load response test/analysis comparisons for curved spine configurations [Figs. 17(a) and (b) of Polanco and Littell, 2011].

The vertical chest acceleration time histories in the FTSS and LSTC models exhibit similar trends as those seen in the head response, as shown in Figure 8.24. In the FTSS model, the acceleration magnitudes match the test response before a slight drop in magnitude and rise before the curve drops again. This slight drop and rise comes from the load starting to pick up as it makes its way from the pelvis into the chest. When the weak paper honeycomb is used, the post-impact curve matches the test data very well. The LSTC model, however, shows an initial spike that overpredicts the test response by a factor of three compared with that seen in the chest using strong paper honeycomb, and about twice that seen using a weak paper honeycomb pulse.

The pelvis and lumbar spine responses, shown in Figures 8.25 and 8.26 respectively, for the FTSS model agree very well with test data, particularly the post-impact trends and magnitudes. A slight underprediction in vertical pelvis acceleration occurs when strong paper honeycomb is used. In the LSTC model, the vertical accelerations are overpredicted by three times the values seen in the test data. The lumbar loads are overpredicted by three times the test values using a strong paper honeycomb input, while the loads are overpredicted by twice those seen in the test data using a weak paper honeycomb pulse.

The study was extended to evaluate the current THOR FEM [Putnam et al. (2013 and 2015)] in comparison to both kinematic and loading response of the physical THOR tested at NASA Langley. One of the two test conditions for the THOR (16.6-ft/s impact onto weak honeycomb) matched the velocity conditions used to impart impulsive vertical loading into the Hybrid II and Hybrid III ATDs. A photograph of the test setup and the THOR model are shown in Figure 8.27. Comparisons of test/analysis vertical head acceleration responses and lumbar load responses are shown in Figure 8.28. In general, excellent agreement is obtained. Additional information can be found in Littell and Annett (2013).

In 2017, an extension to the prior study was performed at NASA Langley in which a series of vertical drop tests was conducted on three sizes of ATDs for the evaluation of their vertical loading response [Littell and Annett (2018)]. The three sizes of ATDs represented a 5th-percentile female, a 50th-percentile male, and a 95th-percentile male. There were two variations of the 50th-percentile male as defined in 49 CFR 25 Part 572: a Hybrid II and an FAA Hybrid III. Tests were conducted using a drop tower located at NASA Langley's LandIR facility. The ATDs were seated on 14 CFR § 25.562 certified seats, in either a triple (window, middle, and aisle) or a double (window and aisle) seat configuration, with seat leg spacing replicating a Fokker F28 MK-1000 aircraft. The seat and ATDs were attached to a drop plate on the tower,

which was lifted to a height of 14 feet, as depicted in Figure 8.29. Note that the seats were removed from an in-service Boeing 737-800 aircraft in the fall of 2016.

The ATD/seat/platform system was dropped onto stacked layers of crushable honeycomb to achieve three input deceleration pulses. Pulse shape 1 was a plateau-shaped pulse with an average peak acceleration of 8 g and pulse duration of 0.14 s. Pulse shape 2 was triangular shaped, achieving a peak acceleration of 14 g at a rise time of 0.08 s. The third pulse was intended to replicate the pulse shape from the seat certification test of a transport category rotorcraft in 14 CFR § 29.562 [FAR (1989)]. This pulse shape was triangular in nature, achieving a peak acceleration of 35 g at a rise time of 0.035 s. The objectives of the test were to compare and contrast different input loading environments and their effects on the ATD response, to compare and contrast the different sized ATDs, to compare and contrast different builds of ATDs (i.e. Hybrid II versus FAA Hybrid III), and to further understand the capabilities and limitations for ATD computational models. Table 8.1 shows the test matrix, which was developed to vary the configuration of the ATDs, seats, and input acceleration pulses in order to study sizing variability, pulse variability, and seat location variability. Shortened notation is used, as follows: FAA H3 50 is the FAA Hybrid III 50th-percentile ATD; H3 5 is the Hybrid III 5th-percentile ATD, etc.

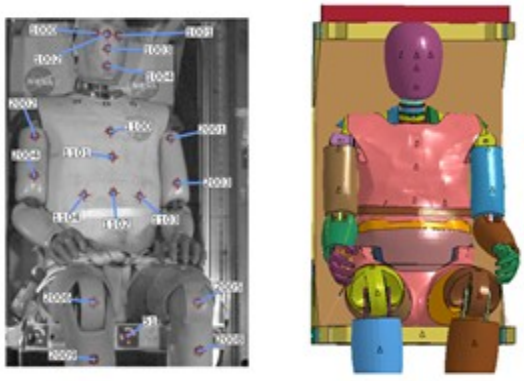

(a) Test photograph. (b) Model.

Figure 8.27. Comparison between pre-test conditions of experiment (a) and model (b) [Fig. 1 of Putnam et al., 2015].

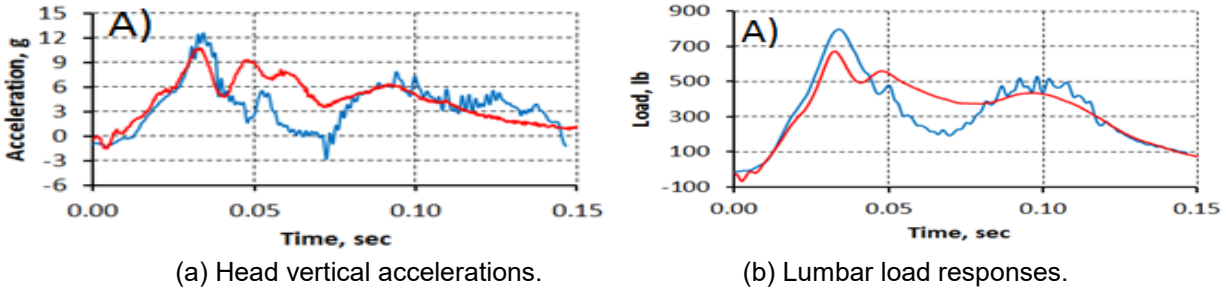

(a) Head vertical accelerations. (b) Lumbar load responses.

Figure 8.28. Comparisons of test/analysis head vertical acceleration and lumbar load responses. Blue curves represent simulation, and test responses are shown in red [Figs. 3(a) and 11(a) of Putnam et al., 2015].

(a) Three- and two-seat configuration. (b) Drop test setup.

Figure 8.29. Photographs of the ATD/seat test configuration [Figs. 2 and 3 of Littell and Annett, 2018].

The first comparison of results was loading environment. Plots of Hybrid III 50th-percentile ATD lumbar load, pelvic vertical accelerations, and head vertical accelerations were generated for pulse shape 1, 2, and 3. Pulse shape 3 created the highest magnitude response, by far. For example, the lumbar load measured for the Hybrid III 50th percentile was 2,784 pounds for pulse shape 3; however, it was 1,257 and 1,044 pounds, respectively, for pulse shape 1 and 2. Similar trends were obtained for the Hybrid III 5th-percentile ATD and the Hybrid III 95th-percentile ATD, as documented in Littell and Annett (2018).

The type of ATD was investigated next because both the Hybrid II and FAA Hybrid III ATDs are used in FAA seat certification testing—often interchangeably—for the examination of occupant loads and injury. The tests were conducted using the double seat since seat supports and positions of the seat legs were generally the same for both the window and aisle seats in that configuration. Tests 12, 16, and 20, were used for the comparisons. Each test represented one of the three pulse shapes. The setup for these tests had the H2 50 seated in the aisle seat and the FAA H3 50 seated in the window seat. The lumbar loading and head vertical acceleration results are shown in Figure 8.30. The plots show six curves each. The red curves represent the results from pulse shape 1 (Test 12), the blue curves represent the results from pulse shape 2 (Test 16), and the black curves represent the results for pulse shape 3 (Test 20). The H2 50 is plotted as a dotted line, and the FAA H3 50 is plotted as a solid line.

Table 8.1. Test Matrix.

Test No.	Pulse Shape No.	Window	Middle	Aisle	Impact Velocity (ft/s)
		Triple-Seat Configuration			
1	1	FAA H3 50	H2 50	H2 50*	29.1
2	1	H3 5	H3 95	FAA H3 50	28.9
3	1	H2 50	FAA H3 50	H3 5	28.9
4	1	H2 50	H2 50*	FAA H3 50	28.8
6	2	H3 5	H3 95	FAA H3 50	28.9
8	2	FAA H3 50	H2 50	H2 50*	28.9
9	2	FAA H3 50	H2 50	H2 50*	28.9
10	3	FAA H3 50	H2 50	H2 50*	28.8
11	3	H3 5	H3 95	FAA H3 50	28.7
		Double-Seat Configuration			
12	1	FAA H3 50		H2 50	29.0
14	1	H3 5		H3 95	28.7
16	2	FAA H3 50		H2 50	28.6
17	2	H3 5		H3 95	28.6
20	3	FAA H3 50		H2 50	28.6
21	3	H3 5		H3 95	28.8
*Not instrumented.					

For the lumbar loads, the ATD responses generally matched well for all three pulse shapes. The H2 50 ATD peak load value was higher than the FAA H3 50 for pulse shape 2, but lower for pulse shapes 1 and 3, though the actual values are not significantly different. For pulse shape 2, if this test had been an actual certification test, both ATDs would be below the 1,500-pound limit, as specified in 14 CFR § 25.562 (c)(2). The head acceleration results showed higher magnitudes for the H2 ATD for all three pulse shapes. The durations and shapes were similar between ATDs for each of the pulse shapes, with the exception of a small but noticeable second peak, which occurred in the FAA H3 for test 20, at 0.049 seconds after impact. The ATDs also showed a second spike in acceleration at 0.117 seconds after impact. A second spike was produced when ATD heads contacted each other during rebound, post-impact. Note that additional comparisons were made, as documented in Littell and Annett (2018), including comparisons of ATD size and ATD responses between the seat/platform tests and the F28 forward section drop test.

As a final aspect of the project, comparisons were made with computer simulations. The double- and triple-seat models were previously developed for the full-scale drop test efforts and available for use in the component level analyses. A complete description of the efforts to develop the seat models is described in Littell and Annett (2018). The ATD model used for the simulations was an automotive Hybrid III model known as the "LSTC Detailed Finite Element Model (FEM)" [Guha (2014)], developed by LSTC and mainly used in automotive applications. A major difference between the ATD model and the ATDs used in the tests was in the lumbar spine region. The automotive ATD used a curved spine, whereas the ATDs used in the tests were dictated by 14 CFR § 25.562 and configured with a straight spine. These differences in lumbar region caused both minor positioning differences between the simulation model and actual ATD,

and differences in the location and orientation of the measured lumbar load cells. It is because of these differences that the lumbar loads were unable to be compared directly. Instead, the vertical acceleration in the pelvis was used as the metric for comparison since it was the best way to measure the pulse transmission from the seat/impact plate into the ATD. Two component-level tests were used in the comparison efforts. The first was Test 4, in which H2 50 ATDs were mounted in the window and middle seats, while the FAA H3 50 was seated in the overhung aisle seat. Because of computing constraints, only the aisle FAA H3 50 ATD model was included in the simulation. The H2 50 ATDs were represented using a 170-pound rigid torso and pelvis mass surrogate. These two ATDs were not evaluated using simulation comparisons. Figure 8.31 shows the test-to-simulation comparison images, taken at a time of maximum FAA H3 50th sink into the seat.

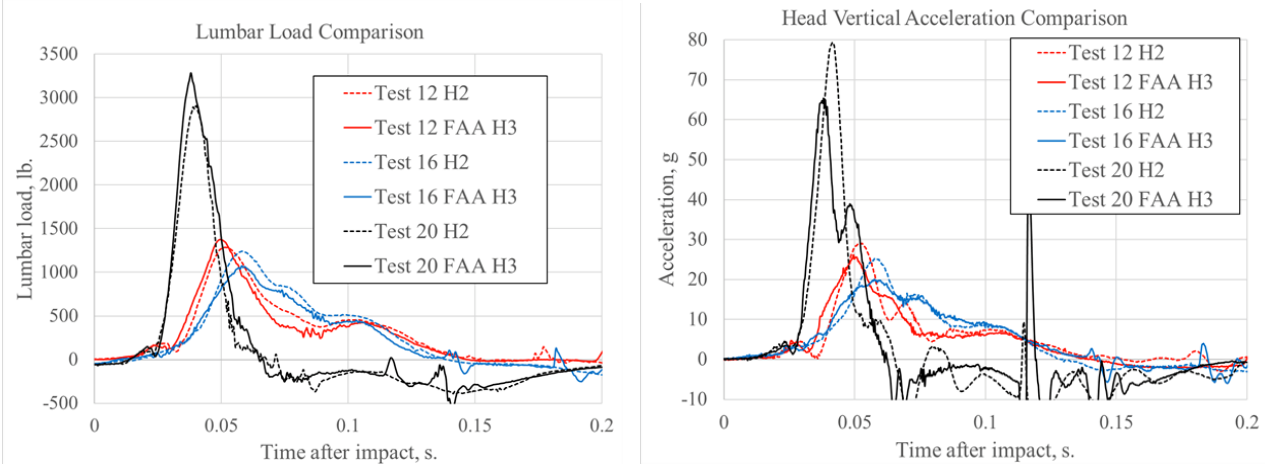

Figure 8.30. ATD comparison results. Lumbar vertical load (left), head vertical acceleration (right) [Fig. 8 of Littell and Annett, 2018].

Figure 8.31. Test 4 (left) and simulation (right) at maximum ATD sink [Fig. 16 of Littell and Annett, 2018].

The general motion for the ATD between the test and analysis showed good agreement. The ATD sank into the seat and tilted slightly to its right. The agreement for the seat was not as good. The previously measured maximum vertical deformation measured at the aisle-side armrest in the seat-pan support tube was 1.95 inches for the test and 2.3 inches for the analysis. Additionally, the seat model did not include a headrest component, which would account for differences in mass properties of the seat back. Further investigations into the performance of the seat were not preformed.

Figure 8.32 shows the data plotted for the pelvic acceleration on the FAA H3 50 between the test and simulation. The seat deformation differences were reflected in the ATD pelvic response. The peak acceleration experienced in the test was 21.0 g, which occurred at 0.055 seconds after impact, while the maximum acceleration experienced in the simulation was 17.7 g, which occurred at 0.093 seconds after impact. The response shapes generally agree for times outside of these two peak occurrences, specifically before the first 0.050 seconds and after 0.100 seconds. For the first 0.050 seconds, the test and simulation results agree both in trends and in magnitude. They begin to deviate afterward, and then trend back toward each other after the 0.100-second mark. For both the test and simulation curves, all significant acceleration occurred before the first 0.200 seconds of the impact.

Important Findings and Significance

This follow-on project has reconfirmed the adage that "you get what you pay for." Both the FTSS and the THOR dummy models cost money for a yearly lease, whereas the LSTC downloadable dummy model is free. Both the FTSS and the THOR models did a superior job of predicting the dummy vertical impulsive loading responses. Some modifications were made to the LSTC dummy model in an attempt to improve its performance. However, these changes need to be implemented by LSTC so that they can be made available to all LS-DYNA users. This project may be the first ever to isolate vertical impact loading into ATDs, which represents typical loading during aircraft/rotorcraft crashes.

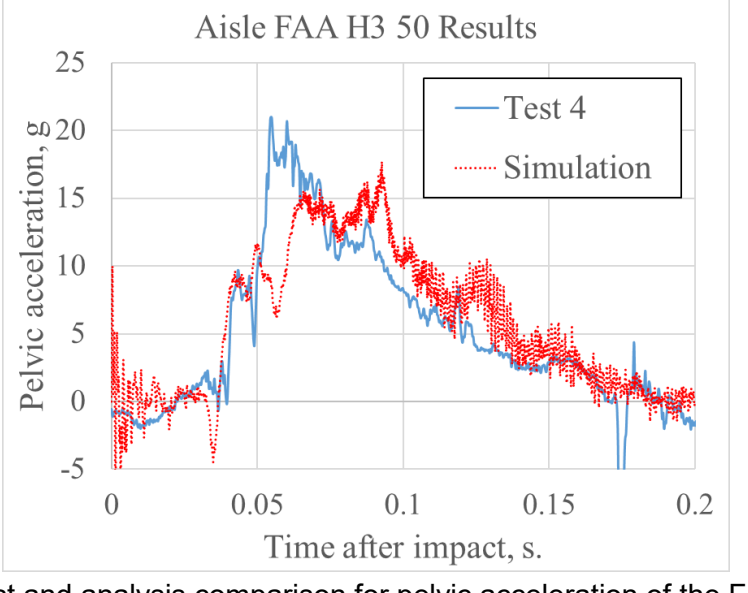

Figure 8.32. Test and analysis comparison for pelvic acceleration of the FAA H3 50 ATD [Fig. 17 of Littell and Annett, 2018].

Several findings were made based on the extension project in which vertical drop tests were conducted for a range of ATDs under various vertical loading environments. The drop test article consisted of a triangular platform to which either double or triple seats were attached using standard seat tracks. When examining pulse shape variations, there were minimal differences in the responses between pulse shape 1 and 2. However, pulse shape 3 provided much higher magnitude responses. Test data was also generated using nonstandard dummies, the Hybrid III 5th- and 95th-percentile, in addition to the Hybrid II and the FAA Hybrid III 50th-percentile ATDs. No catastrophic seat failures were observed during the test program, however some seats exhibited plastic deformation.

MODEL CALIBRATION USING UNCERTAINTY PROPAGATION AND PARAMETER SENSITIVITY

As discussed previously, two full-scale crash tests of an MD-500 helicopter were conducted at NASA Langley's LandIR facility in support of NASA's Subsonic Rotary Wing Crashworthiness Project. The first crash test was conducted to evaluate the performance of an externally mounted composite Deployable Energy Absorber (DEA) under combined impact conditions. In the second crash test, the energy absorber was removed to establish baseline loads that are regarded as severe, but survivable. Accelerations and kinematic data collected from the crash tests were compared to a system-integrated finite element model (FEM) of the test article. Results from 19 accelerometers placed throughout the airframe were compared to FEM responses. The model, which was developed for the purpose of predicting acceleration responses from the first crash test, was inadequate when evaluating more severe conditions seen in the second crash test. A newly developed model calibration approach that includes uncertainty estimation, parameter sensitivity, impact shape orthogonality, and numerical optimization was used to calibrate model results for the second full-scale crash test [Horta et al. (2010 and 2011) and Annett et al. (2012)]. This combination of heuristic and quantitative methods was used to identify modeling deficiencies, evaluate parameter importance, and propose required model changes.

Since the DEA significantly attenuated the impact response during the first crash test, this experimental data may not have been sufficient to validate the analytical model for the subsequent, more severe impact test. The airframe model acceleration responses were low and generally in the linear elastic range. The DEA acted as an isolator, accurately imparting loads into the airframe while obscuring deficiencies in the airframe model. These deficiencies became apparent when severe loads and highly nonlinear responses were introduced for the second full-scale test. There are multiple modes of failure in the test without the DEA, which may or may not need to be represented by the FEM. The previous assertion of a "validated" model based on the crash test with the DEA was questioned. To determine whether more physical detail is required in the model or modification of existing parameters was sufficient to accurately capture responses, a comprehensive model calibration was performed.

The calibration approach adopted for comparison with the second test uses uncertainty propagation and quantification to assess model adequacy. The first step in this approach is parameter selection, which relies heavily on the analyst's knowledge and familiarity with the model and the assumptions used in its development. After an initial parameter set is selected, uncertainty models to prescribe parameter variations are defined with the aid of empirical data or engineering judgment. With an initial parameter set and an uncertainty model at hand, parameter importance is assessed using uncertainty propagation. Parameter values are created using the

Halton deterministic sampling technique [Halton (1960)]. Time-history results are processed to compute the velocity and acceleration metrics, and to assess variability and rank parameters. Adequacy of the parameter set is judged based on the probability of being able to reconcile test with analysis.

Uncertainty propagation is conducted to evaluate uncertainty bounds and to gage the ability of the model to explain the observed behavior. The statistics of the 2-norm of a response vector between test and analysis are compared. An important benefit of using this metric is that it provides for a direct measure of multidimensional closeness of two models, with closeness quantified at each time step. Because parameters are uncertain, statistical measures of the metric need to be used to conduct assessments. With limited information about parameter uncertainty, a uniform distribution function, which is the least informative distribution function, is the most appropriate choice to represent parameter uncertainty.

Analysis of variance (ANOVA) is used for parameter sensitivity. In classical ANOVA studies, data is collected from multiple experiments while varying all parameters and also while varying one parameter at a time. These results are then used to quantify the output response variance due to variations of a particular parameter, as compared to the total output variance when varying all the parameters simultaneously. The ratio of these two variance contributions is a direct measure of the parameter importance. Sobol et al. [2007] and others [Mullershon and Liebsher (2008), Homma and Saltelli (1996), and Sudret (2008)] began using variance-based methods. To compute sensitivity using these variance-based methods, one must be able to compute many response predictions as parameters are varied. For this effort, after a suitable set of LS-DYNA solutions are obtained, response surface surrogates are used to estimate additional solutions. The Extended Radial Basis Functions (ERBF) response surface method, as described by Mullur and Messac (2005 and 2006), is used to estimate time-history responses, as opposed to just extreme values.

The use of norms, although convenient, tends to hide the spatial relationships that exist between responses at different locations in the model. In order to study this spatial multidimensional dependency explicitly, a different metric must be established. Work by Anderson et al. (1998) and Horta et al. (2003) proposed the application of singular value decomposition derived basis vectors, or impact shapes. With this approach, time histories from analysis or experiments can be decomposed using singular value decomposition. Note that details of the model calibration procedure are documented in Horta et al. (2011) and are not repeated herein.

If the model can be reconciled based on both time and spatial calibration metrics, a parameter set is computed that minimizes the squared sum of the prediction error using the Constrained Optimization Response Surface (CORS) optimization scheme of Regis and Shoemaker (2005). Specifically, the algorithm starts by looking for parameter values away from the initial set of LS-DYNA solutions, then slowly steps closer to known solutions by solving a series of locally constrained optimization problems. This optimization process will produce a global optimum if enough steps are taken. The user controls the number of steps and therefore the accuracy and computational expense in conducting the optimization. In cases where the predictive capability of the surrogate model is poor, CORS adds solutions in needed areas. Because parameter uncertainty is not used explicitly in the optimization, this approach is considered to be deterministic.

For the purposes of this calibration effort, 19 sensor locations, containing either triaxial or uniaxial accelerometers and totaling 23 channels, were used. At the outset of performing calibration runs, the velocity 2-norm of the sensor set was used as a comparison metric. Velocity metrics were used because high-frequency responses of structures evident in acceleration time histories become naturally filtered once integrated to velocity. Direct comparison between test and analysis velocities is only achievable by integrating the test accelerometer time histories. The integrated test curves are shifted to match to the localized initial velocities that are directly output in the respective local coordinate systems from the analysis. For many of the accelerometers, integration of the signal revealed drifting and inconsistent changes in velocity. The contribution of drift was unique from sensor to sensor and was difficult to detrend. The accelerometers in the calibration sensor set could be successfully integrated and therefore retained.

Altogether, seven different calibration cycles were performed with different parameter sets and varying ranges for each parameter. For the first several calibration cycles, initial conditions were chosen as parameters to vary based on the supposition that there was variability in computing the initial velocities and attitudes from photogrammetry. However, impact conditions such as vertical and horizontal velocities and pitch angle had the highest contribution to the total response variance, which tended to overshadow the importance of structural parameter values. The photogrammetry results were reexamined, and initial conditions permanently fixed.

As calibration cycles were performed, it was also evident that solely using velocity as the comparison metric had a disadvantage. Integration removes critical low- to mid-frequency modes and responses that could be important in identifying shifting load paths as the airframe plastically deforms. Both acceleration and velocity 2-norms were used to determine whether the parameter sets, and their range of values, were appropriately chosen. Because of run-time stability issues, the ATD models were removed from the airframe model and their masses were evenly distributed onto the seat frames and floor. The calibration model is shown in Figure 8.33(a), and the calibration sensor locations are shown in Figure 8.33(b).

Figure 8.33. Calibration model [Fig. 17 of Annett et al., 2012].

Parameter selection for the calibration study addresses two essential aspects of the model, stiffness and plasticity. Most of the critical airframe components in the load path are modeled with shell elements with effective stiffness properties. Seemingly, the thickness of components could be directly measured from the test article. However, the presence of rivets, doublers, and small stiffeners, which could not be included in the model without sacrificing computational efficiency, would stiffen the test article. Conversely, cutouts and holes would reduce the stiffness. The term "effective" accounts for the omission of these features. To change the effective in-plane and bending stiffness, either the modulus of elasticity or the thickness defined in the shell property can be modified. For this study, the thickness was modified for four structural components: belly thickness, keel beam thickness, seat box thickness, and seat box bulkhead thickness. The airframe is a combination of different alloys of thin sheet or cast aluminum. A fifth parameter, the initial yield stress, was chosen specifically for parts in the floor and subfloor region where extensive damage occurs.

To illustrate the value of computing the calibration metric, the acceleration and velocity 2-norms are plotted in Figure 8.34 for a set of 60 LS-DYNA runs, with five parameters chosen. All acceleration data are low-pass filtered to SAE Channel Filter Class (CFC) 60. The test acceleration 2-norms fall outside the bounds provided by the analysis. The velocity 2-norm also indicates that test responses fall outside analytical bounds, but the discrepancy is not as prominent.

Calibration runs were conducted with the keel beam thickness increased to a range of 0.10 to 0.15 inches. A total of 60 LS-DYNA runs were performed using the newly defined keel beam parameter range, combined with four other parameters previously defined. Uncertainty bound results for acceleration indicate that the increase in keel beam thickness shifted the peak acceleration response to align better with the test results. Results plotted in Figure 8.35 indicate that, based on acceleration and velocity 2-norm, there is a high likelihood that a set of parameters within the range established will reconcile to the test response.

The calibrated set of values for the airframe model without the DEA is shown in Table 8.2. Of the five parameters, three remained close to the nominal value (belly thickness, keel beam thickness, and seat box thickness), while the seat box bulkhead thickness approached the upper bound, and the yield stress approached the lower bound.

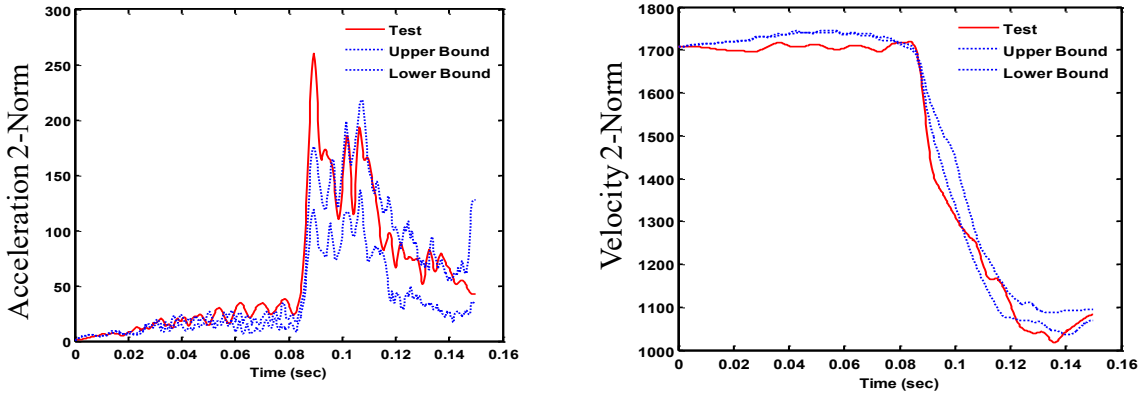

Figure 8.34. Uncertainty bounds for interim calibration cycle [Fig. 18 of Annett et al., 2012].

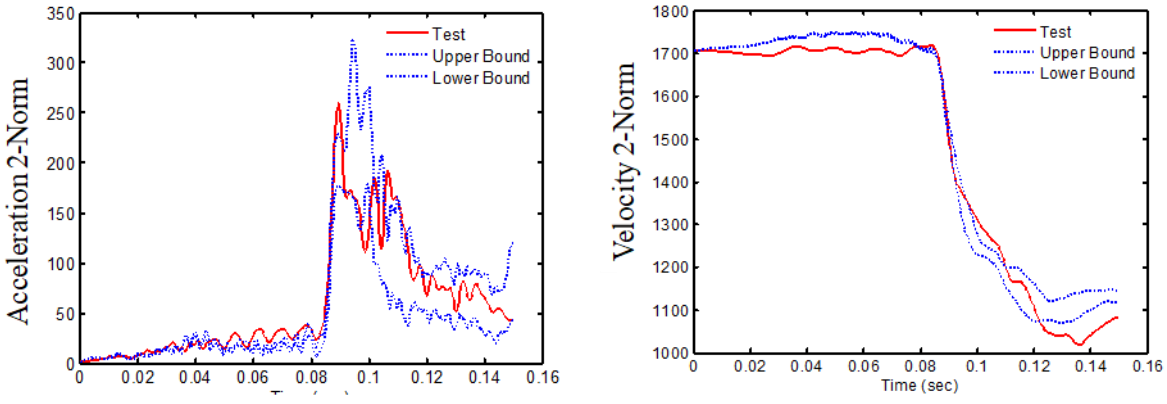

Figure 8.35. Uncertainty bounds for final calibration cycle [Fig. 20 of Annett et al., 2012].

Table 8.2. Calibrated Parameters.

No.	Parameter Description	Nominal	Upper Bound	Lower Bound	Calibrated
1	Belly thickness (in.)	0.09	0.12	0.08	0.089
2	Keel beam thickness (in.)	0.12	0.15	0.10	0.12
3	Seat box thickness (in.)	0.1	0.12	0.08	0.11
4	Seat box bulkhead thickness (in.)	0.05	0.07	0.03	0.065
5	Yield stress (psi)	40,000	45,000	35,000	35,210

As a final check, a model using the five calibrated parameters was executed, and comparisons were made with the test data and the baseline, or original, model. The vertical acceleration at the pilot floor is plotted in Figure 8.36. The overall pulse duration remains about 0.050 seconds. The calibrated model shows a higher acceleration peak magnitude (60 g) than the original model (47 g), and matches the test peak magnitude better (63 g). The passenger floor vertical accelerations are plotted in Figure 8.37. The analytical waveform shapes and duration agree well with the test, but the peak magnitude of the original model was less than the test acceleration by 15 g. The increase in keel beam stiffness has caused an over-correction in peak magnitude, from 30 to 70 g. By treating the keel beam as one continuous property, the pilot-copilot region was calibrated properly, but the model behaves too conservatively when examining the passenger region. Hence during calibration, the keel beam area should have been split into separate segments to adjust the areas independently.

Important Findings and Significance

LS-DYNA model calibration was performed based on two new calibration metrics: (1) a 2-norm velocity bound metric, and (2) orthogonality of test and analysis impact shapes. Results with metric (1) were used to assess the probability of reconciling test with analysis after uncertainty propagation studies. Calibration parameters were selected or removed based on results of metric (1). Of consequence to this study are several important considerations when conducting severe crash tests for the purpose of validating analytical models. First, the sensor suite must cover all critical components, and should be mounted on relatively compliant components, or items of

high mass, to avoid high-frequency saturation of the acceleration output. Second, the accelerometers should be calibrated to ensure their velocity integration is accurate. Third, multiple validation metrics should be applied between test and analysis that comprehensively identify modeling deficiencies, evaluate parameter importance, and propose required model changes. Finally, when dealing with very complex structures, a building-block approach to model calibration can help break up the problem into more manageable subsystems. The objective of certification-by-analysis cannot be achieved practically without methodologies established similar to those discussed herein.

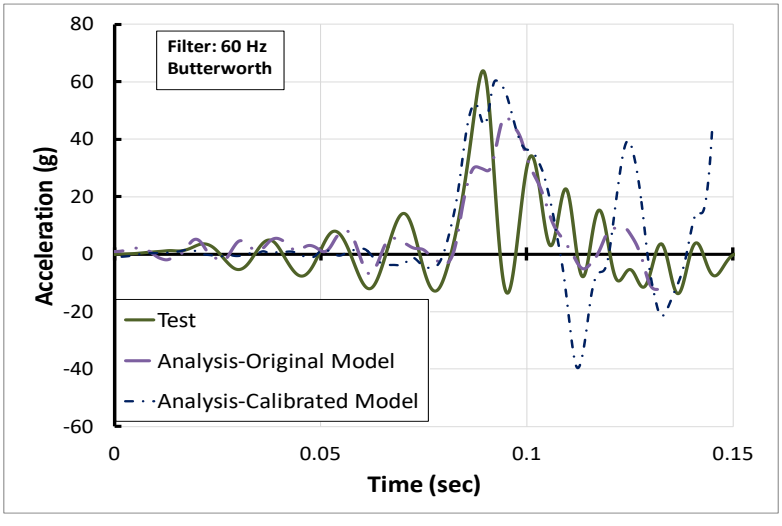

Figure 8.36. Pilot floor vertical acceleration, crash test without DEA [Fig. 23 of Annett et al., 2012].

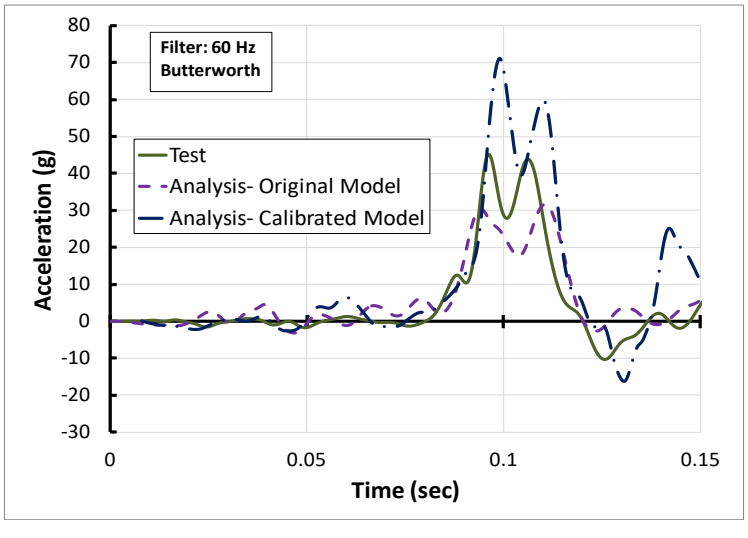

Figure 8.37. Passenger floor vertical acceleration, crash test without DEA [Fig. 24 Annett et al., 2012].

DEVELOPMENT AND EVALUATION OF TWO COMPOSITE ENERGY ABSORBERS

The NASA Rotary Wing Crashworthiness Program [Jackson et al. (2009)] initiated the Transport Rotorcraft Airframe Crash Testbed (TRACT) research program by obtaining two CH-46E helicopters. Full-scale crash tests were conducted to assess dynamic responses of transport-category rotorcraft under combined forward and vertical velocities. The first crash test, TRACT1 [Annett et al. (2014)], was performed at NASA Langley's LandIR facility, and enabled the study of critical interactions between the airframe, seat, and occupant during a controlled crash environment. The CH-46E fuselage is categorized as a medium-lift rotorcraft with a length and width of 45 and 7 feet, respectively, and a capacity for 5 crew and 25 troops. TRACT1 was conducted in August 2013 under combined conditions of 25 ft/s vertical and 33 ft/s forward velocity onto soil, which is characterized as a sand/clay mixture. The primary objectives for TRACT1 were to assess improvements in occupant loads and flail envelope with the use of crashworthy features such as pre-tensioning active restraints and energy-absorbing seats, and to develop novel techniques for photogrammetric data acquisition to measure occupant and airframe kinematics.

The TRACT1 airframe was tested in a baseline configuration with no changes to the structural design, including the discrete aluminum shear panels in the subfloor. A final objective of TRACT1 was to generate crash test data in a baseline configuration for comparison with data obtained from a similar TRACT2 crash test. The crash test of the second CH-46E airframe (TRACT2) was conducted on October 1, 2014, and was performed for the same nominal impact velocity conditions and the same impact surface [Annett (2015)]. The difference is that the TRACT2 airframe was retrofitted with three different composite energy-absorbing subfloor concepts: a corrugated web design [Kindervater et al. (2011) and Billac et al. (2014)] fabricated of graphite fabric; a conical-shaped design, designated the "conusoid," fabricated of four layers of hybrid carbon-Kevlar fabric [Littell (2014, 2017)]; and, a sinusoidal-shaped foam sandwich design, designated the "sinusoid," fabricated of the same hybrid fabric face sheets with a foam core [Littell et al. (2015), and Jackson et al. (2015 and Sept. 2015)]. Since the TRACT2 airframe contained similar seat, occupant, and restraint experiments, one of the major goals of the test was to evaluate the performance of novel composite energy-absorbing subfloor designs for improved crashworthiness.

Following the TRACT1 test, a research effort was initiated at NASA Langley to develop two composite energy absorbers for retrofit into the TRACT2 test article. The design goals were to achieve between 25 to 40 g sustained crush accelerations, to minimize peak crush loads, and to generate relatively long crush-stroke limits under dynamic loading conditions, typical of those experienced during the TRACT1 full-scale crash test [Annett et al. (2014)]. The development of the composite energy-absorbing concepts will be highlighted, based on the building-block approach discussed in Kindervater et al. (2011) and shown in Figure 8.38.

Description of the Energy Absorbers

The first design is a novel conical sinusoid, or "conusoidal" composite energy absorber, designated the "conusoid." This energy absorber was conceived and patented by Dr. Justin D. Littell [Littell (2017)]. The geometry of the conusoid is based on alternating right-side-up and up-side-down half-cones placed in a repeating pattern. The conusoid combines a simple cone design, which has been extensively studied in literature [Price and Hull (1987), Feraboli et al. (2007), Gupta and Velmurugan (1999), and Fleming and Vizzini (1993)], with sinusoidal beam

geometry to create a structure that utilizes the advantages of both configurations. An isometric view of the conusoid is shown in Figure 8.39(a). Variations in geometry, materials, and laminate stacking sequences were evaluated during development of the conusoid, and the final design consisted of four layers of a hybrid carbon-Kevlar plain-weave fabric oriented at +45/–45/ –45/+45 degrees with respect to the vertical direction. A photograph of a typical conusoid component is shown in Figure 8.39(b). The component is 12 inches long and 7.5 inches tall, with an overall width of 1.5 inches. Additional information on the development and fabrication of the conusoid energy absorber can be found in Littell (2014).

The second energy absorber, designated the "sinusoid," consisted of hybrid carbon-Kevlar plain-weave fabric face sheets, two layers for each face sheet oriented at ±45 degrees with respect to the vertical direction, and a closed-cell ELFOAM® P200 polyisocyanurate (2.0 lb/ft^3) foam core. Sine wave energy absorbers have been studied extensively because they offer desirable features under compressive loading [Cronkhite and Berry (1982), Farley (1986), Hanagud et al. (1989), Carden and Kellas (1993), and Feraboli (2008)]. Energy absorption values from sine wave concepts can be similar to values obtained from crush tubes. In addition, sine wave concepts tend to deform in a stable manner through plastic hinge formation and crushing, rather than global buckling. Often, the actual shape of the energy absorber is not truly a sine wave, but a series of alternating half circles. In fact, the sinusoid concept described herein is actually a series of half circles, however the designation of "sinusoid" will continue to be used.

The overall thickness of a sinusoid component was 1.5 inches with a length of 12 inches and a height of 7.5 inches. Design parameters were assessed through component testing including different materials for the face sheets and different laminate stacking sequences. Variations in sinusoid geometry were not evaluated since an existing mold was used in construction. A photograph of a sinusoid foam sandwich specimen is shown in Figure 8.40. Note that in preparation for the component drop test, 0.5-inch-thick polycarbonate plates were attached to both the top and bottom surfaces of the specimen.

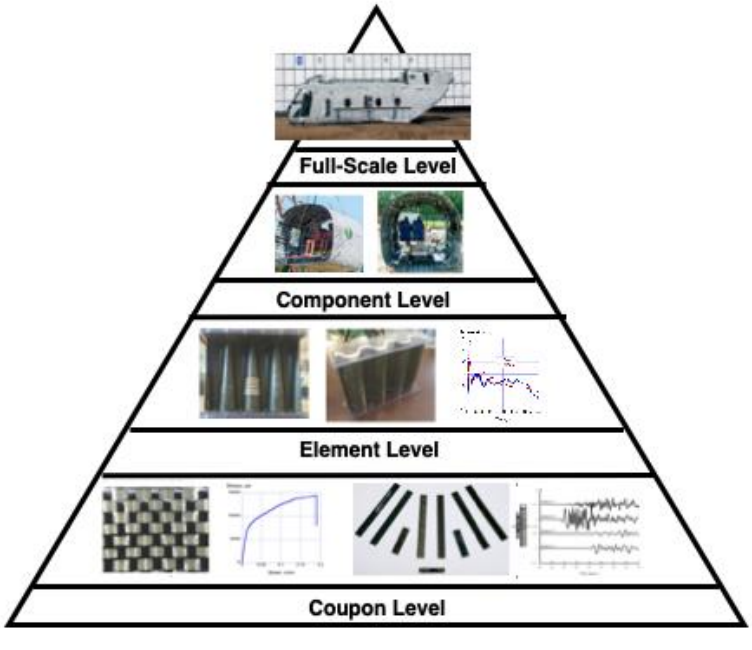

Figure 8.38. Building-block approach for developing crashworthy composite structures [Fig. 5 of Kindervater, 2011; recreated by NASA using NASA photos and data].

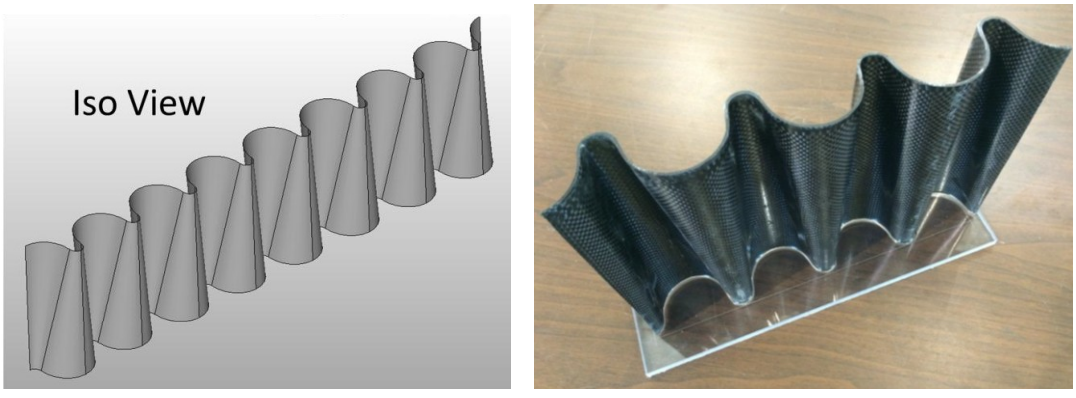

(a) Schematic drawing. (b) Photograph of component.

Figure 8.39. Isometric view and photograph of a conusoid component [Fig. 3 of Jackson et al., 2015].

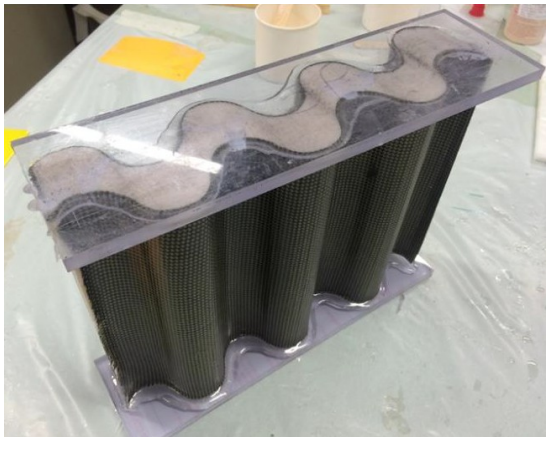

Figure 8.40. Pre-test photograph of a sinusoid foam sandwich component [Fig. 4 of Jackson et al., 2015].

Coupon Level

Properties were obtained for the hybrid carbon-Kevlar plain-weave fabric from standard material characterization tests, such as tensile testing of fabric coupons oriented at 0, 90, and ±45 degrees to obtain longitudinal stiffness and strength, transverse stiffness and strength, and shear stiffness and strength, respectively. These properties were then input as parameters to Mat 58, a continuum damage mechanics based material property in LS-DYNA used to represent composite materials and fabrics [Feraboli (2008) and Matzenmiller et al. (1995)]. Once verified through comparison with coupon test data, these properties were unchanged for all subsequent simulations of the energy absorbers. It should be noted that Mat 58 includes certain parameters, such as the SLIM parameters and ERODS, which cannot be determined based on experimental data. For these parameters, estimates were input based on past experience of the analysts. A close-up photograph is shown in Figure 8.41 of the fabric material. Details of the material property characterization testing and simulation effort can be found in Jackson et al. (2017).

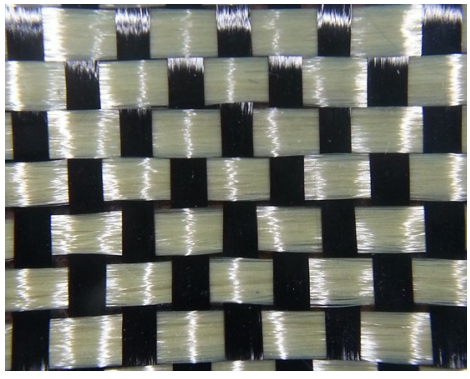

Figure 8.41. Hybrid graphite-Kevlar® plain-weave fabric [Fig. 2 of Jackson et al., 2017].

Element/Component Level

Conusoid energy absorbers were dynamically crushed in a 14-foot drop tower with an instrumented 110-pound falling mass. The impact condition for all of the dynamically crushed specimens was approximately 22 ft/s. The drop mass was instrumented with a 500-g damped accelerometer and data were acquired using a National Instruments DAS sampling at 25 kHz. All post-processed acceleration data were filtered using a low-pass 4-pole Butterworth filter with a 500-Hz cutoff frequency. A high-speed camera filming at 1 kHz captured the deformation time history, depicted in Figure 8.42. The identified failure mechanism is folding of the conusoid walls, which is a desirable failure mode that produces a stable and constant crush response within the design level of 25 to 40 g.

A depiction of the FEM representing the conusoid energy absorber is shown in Figure 8.43. The model contained 185,940 nodes; 44,294 Belytschko-Tsay shell elements; 116,100 solid elements representing the rigid drop mass, 1 initial velocity card assigned to nodes forming the rigid drop mass, and 1 body load card defining gravity. The nominal shell element edge length is 0.032 inches. The shell elements representing the hybrid carbon-Kevlar fabric layers were assigned Mat 58, which is a material model used in LS-DYNA for representing composite laminates and fabrics [Matzenmiller et al. (1995) and Schweizerhof et al. (1998)]. The conusoid model was executed using LS-DYNA SMP version 971 on a Linux-based workstation with 8 processors, and required 11 hours and 49 minutes to execute the simulation for 0.035 seconds.

For the conusoid component, comparisons of predicted and experimental acceleration and displacement time histories of the drop mass are shown in Figures 8.44(a) and (b), respectively. The conusoid model overpredicts the magnitude of the initial peak acceleration, 96 g compared with 61g for the test. However, other than that anomaly, the level of agreement is good. The average acceleration calculated for the test is 28.0 g for a pulse duration of 0.0 to 0.025 seconds, whereas the model average acceleration is 28.4 g for the same duration. The results of the conusoid component test indicate that the configuration of the energy absorber meets all of the design goals, including achieving a sustained acceleration level of between 25 to 40 g. The comparison of vertical displacement time histories also exhibits good agreement, as shown in Figure 8.44(b). The maximum displacement of the test article is 2.9 inches, providing a crush stroke of 38.7 percent. The maximum displacement of the model is 2.53 inches, providing a crush stroke of 33.7 percent.

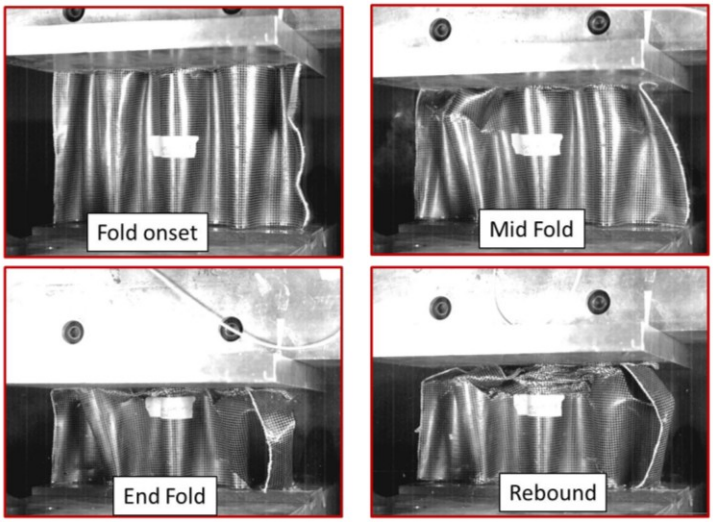

Figure 8.42. High-speed video clips of conusoid deformation [Fig. 5 of Jackson et al., 2015].

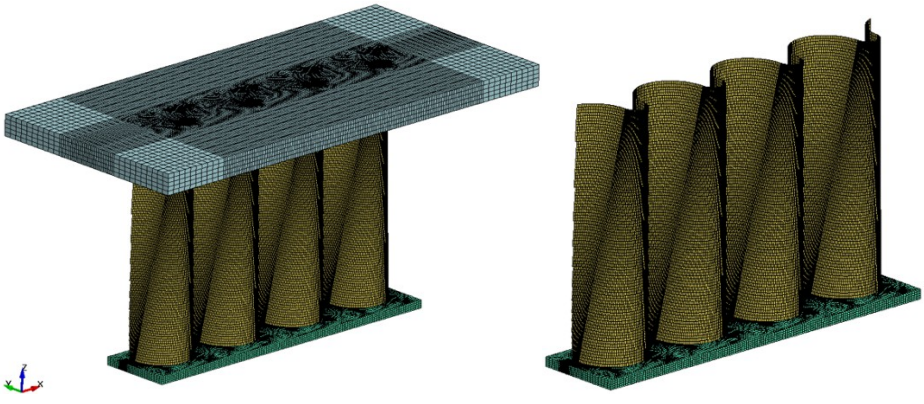

(a) Model with impact mass. (b) Model without impact mass.

Figure 8.43. Depictions of the conusoid component model [Fig. 6 of Jackson et al., 2015].

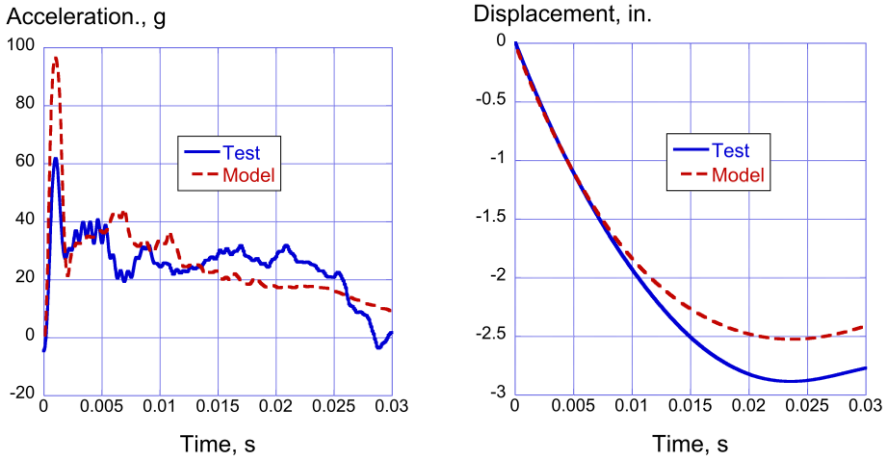

(a) Acceleration responses. (b) Displacement responses.

Figure 8.44. Acceeration and displacement comparisons of the conusoid component drop test [Fig. 7 of Jackson et al., 2015].

The sinusoid foam sandwich energy absorber was initially evaluated through quasi-static and dynamic crush testing of components. A post-test photograph of a typical sinusoid component is shown in Figure 8.45 for a dynamic crush test in which a 113.5-pound mass impacted the sinusoid at 22.08 ft/s. The sinusoid component is approximately 12 inches long, 7.5 inches high, and 1.5 inches wide. A flat 0.5-inch-thick polycarbonate plate was glued to both the top and bottom surfaces of the specimen. As shown in Figure 8.45, the specimen exhibits stable, plastic-like deformation with uniform folding of the face sheets and crushing of the foam core. Crushing initiates along the top edge of the specimen. Note that the sides of the specimen were not covered with face sheets, which allowed splaying of the foam core.

The LS-DYNA FEM representing the sinusoid component drop test is shown in Figure 8.46. The model contained 53,540 nodes; 7,380 Belytschko-Tsay shell elements; 37,515 solid elements; a rigid drop mass; 1 initial velocity card assigned to nodes forming the rigid drop mass; SPCs to fully constrain the bottom nodes of the sinusoid; 1 automatic single surface contact; and 3 material definitions. As with the conusoid, the shell elements were assigned Mat 58, using the properties listed in Jackson et al. (2017). The nominal element edge length in the sinusoid model was 0.2 inches.

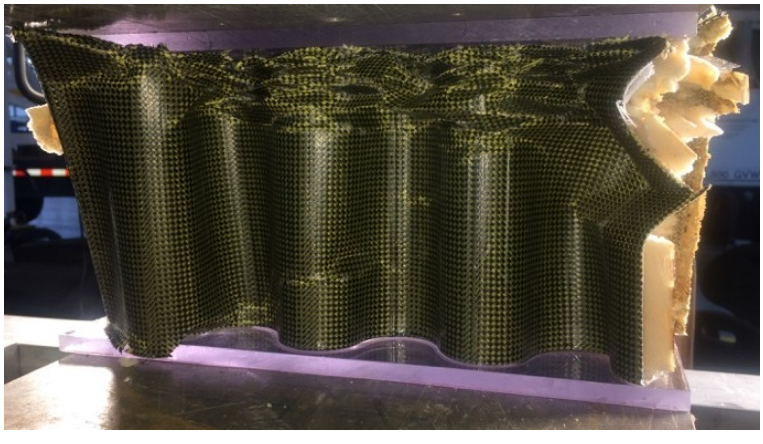

Figure 8.45. Post-test photograph of a typical sinusoid foam sandwich energy absorber [Fig. 9 of Jackson et al., 2015].

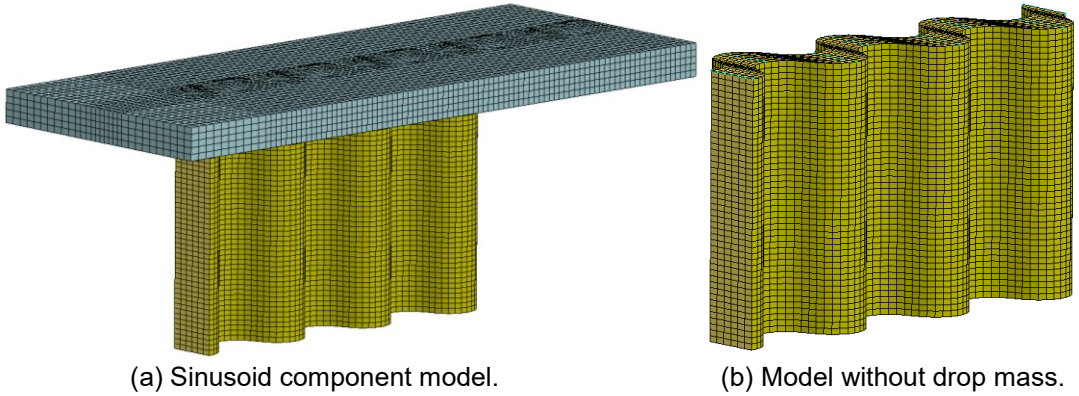

(a) Sinusoid component model. (b) Model without drop mass.

Figure 8.46. Depictions of the FEM of the sinusoid component [Fig. 10 of Jackson et al., 2015].

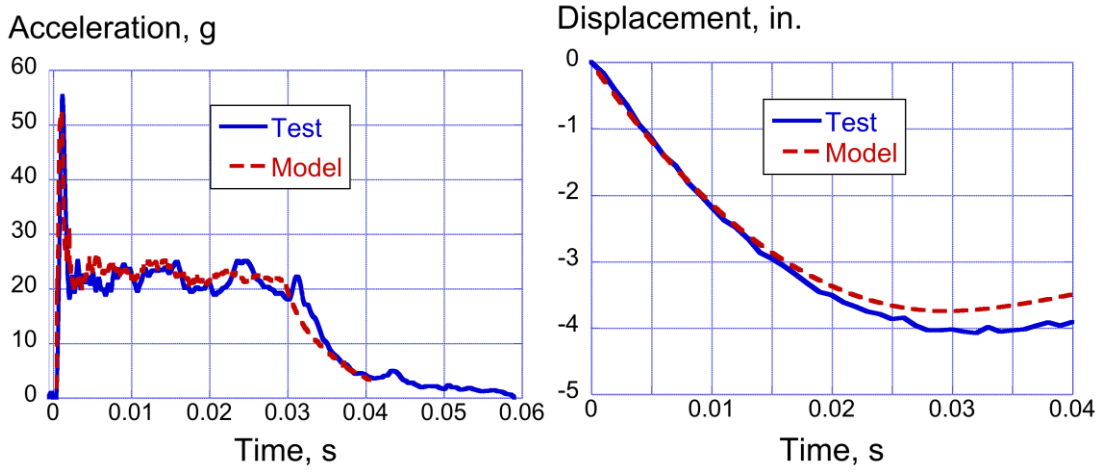

(a) Acceleration responses. (b) Displacement responses.

Figure 8.47. Test-analysis time-history comparisons for the sinusoid component [Fig. 12 of Jackson et al., 2015].

The solid elements representing the foam core were assigned Mat 63, which is a crushable foam material model in LS-DYNA that allows user input of the stress-strain response of the material in tabular format. The sinusoid model was executed using LS-DYNA SMP version 971 on a Linux-based workstation with 8 processors, and required 10 hours and 34 minutes to execute the simulation for 0.04 seconds.

Test-analysis comparisons of time-history responses are plotted in Figure 8.47 for a sinusoid component crush test. These results demonstrate excellent test-analysis agreement. As shown in Figure 8.47(a), the acceleration response of the drop mass achieves an initial peak of 55 g, then drops to approximately 22 g, where it remains constant until the end of the pulse. The model mimics this response, even matching the unloading response near the end of the pulse. The average acceleration calculated for the test is 21.8 g for a pulse duration of 0.0 to 0.03s, whereas the average acceleration of the predicted response is 22.9 g for the same duration. The experimental and analytical displacement responses, shown in Figure 8.47(b), exhibit maximum values of 4 and 3.8 inches, respectively, which represent approximately 50 percent stroke. Note that the average acceleration of the sinusoid component is lower than the design goal (25 to 40 g). However, the lower average acceleration for the sinusoid simply translates into a higher crush stroke than was seen for the conusoid.

Full-Scale Level

The full-scale-level evaluation of the energy absorbers was conducted through a barrel section drop test and a full-scale crash test of a retrofitted TRACT2 helicopter. Following the TRACT1 crash test, a portion of the forward cabin (Fuselage Station (FS) 164 through FS250) was separated from the remainder of the post-test specimen. The resulting barrel section was essentially undamaged during the TRACT1 test and was retrofitted with two of the energy-absorbing concepts planned for TRACT2. The original floor in the barrel section was removed and was replaced with a sheet of 0.5-inch-thick polycarbonate (the reason for this change was to enable viewing of the crushing response of the energy absorbers using high-speed cameras). It was impacted onto concrete at 24.8 ft/s. Unfortunately, this test was compromised by the fact that two steel bolts, which were used to attach the lead ballast to the floor, were left untrimmed.

After drilling through the lead mass and floor, the bolts extended approximately 3.5 to 4 inches into the subfloor crush zone. The extra bolt lengths were not trimmed prior to the test and the bolts impacted the bottom skin of the fuselage section during the test, thus compromising the performance of the energy-absorbing subfloors. Consequently, results of the barrel section drop test are not repeated herein. Additional information can be found in Jackson et al. (2015). The full-scale-level evaluation will focus on the second crash test of the CH-46 helicopter TRACT2.

A second CH-46E helicopter was prepared for crash testing and loaded in a similar manner as the TRACT1 test article [Annett et al. (2014)]. In addition, the TRACT2 aircraft was retrofitted with three different composite energy-absorbing subfloor concepts [Annett (2015)]. The shear panel at FS220 was replaced with a corrugated web energy absorber developed by the German Aerospace Center (DLR) and the Australian Cooperative Research Centre for Advanced Composite Structures (CRC-ACS) and fabricated of graphite fabric material [Kindervater et al. (2011) and Billac et al. (2014)]. The shear panel at FS254 was replaced with the sinusoid foam sandwich energy absorber [Littell et al. (2015) and Jackson et al. (Sept. 2015)] and the shear panel at FS268 was replaced with the conusoid energy absorber [Littell (2014 and 2017)]. Unlike the barrel section, the original floor in the CH-46E was not replaced with polycarbonate material. However, for viewing of the subfloor response during the crash test, rectangular-shaped windows were cut into the floor panels at discrete locations and polycarbonate was used to fill these openings. A photograph showing the retrofit of the sinusoid and conusoid energy absorbers into the TRACT2 subfloor is shown in Figure 8.48. The energy absorbers were 63 inches wide, 9.2 inches tall, 1.5 inches deep, and weighed approximately 13 pounds each. In comparison, the aluminum shear panels that were removed weighed 22 pounds each.

On October 1, 2014, the TRACT2 full-scale crash test was conducted at the NASA Langley LandIR facility. Pre- and post-test photographs are shown in Figure 8.49. Nine organizations, including NASA, took part in the TRACT2 activity, contributing 18 onboard experiments related to occupant seating and restraints, composite crashworthiness, and emergency locator transponder survivability as described in Bark (2015 and May 2015), Desjardins and Labun (2015), and Little et al. (2015). The TRACT2 test article was instrumented with over 360 data channels, including 13 ATDs, 12 on-board high-speed cameras, 10 on-board GoPro cameras, and 12 external high-speed cameras. Data were recovered from over 95 percent of the channels, with only one onboard high-speed camera and two GoPro cameras failing to operate. Measured impact conditions were 33.65 ft/s forward velocity and 25.36 ft/s vertical velocity. The airframe attitude at impact was 2.6 degrees pitch (nose up) and 3.5 degrees roll (left side down). The total weight of the test article was 10,534 pounds.

The impact surface was a sand/clay mixture. Soil characterization testing [Thomas et al. (2008), Fasanella et al. (2008 and 2009), and Heymsfiel et al. (2012)] was performed both prior to and after the crash test to determine soil density, moisture content, bearing strength, and California Bearing Ratio (CBR). The measured moisture content of the soil was high, and it ranged from 9.7 to 16 percent depending on location. Based on post-test measurements, the airframe skidded along the soil surface approximately 47 inches in the forward direction following initial contact.

During the impact, the outer belly skin buckled between FS220 and FS286 and tore as it plowed through the soil. The bottom skin skidded approximately 47 inches along the surface of the soil, leaving an 8- to 9-inch-deep divot (maximum depth). As the outer belly skin failed, the floor continued to move forward, which produced shearing in the subfloor beams. The outer skin was

torn in several places, while the composite energy-absorbing subfloor beams rotated globally under shear loading without significant crushing, as shown in Figure 8.50. The severe outer skin deformation and failure is attributed to wet soil conditions, measured to have a variable moisture content. The test was performed 2 days after a rain storm. Even though the soil was covered, water was able to penetrate a seam in the tarp. The moist soil produced a higher than anticipated coefficient of friction. For example, TRACT1 was tested under the same impact conditions onto the same soil and had a slide out of approximately 90 inches [Annett et al. (2014)].

Following the impact test, the composite subfloors were removed from the test article. Photographs of the sinusiod and the conusiod foam sandwich energy absorbers are shown in Figures 8.51(a) and (b), respectively. Note that both photographs show the energy absorbers as they would be positioned facing rearward. The rearward side of both energy absorbers was painted and marked for camera viewing. The conusoid exhibited fracturing on the left and right sides where the energy absorber attached to the fuselage frames. No evidence of crushing or plastic deformation was observed. The sinusoid displayed areas of crush initiation, especially on the bottom left side, as highlighted in the inset photograph of Figure 8.51(a). Note that a 600-pound mass was attached to the floor on the left side that straddled the sinusoid energy absorber at FS254. However, the amount of crushing was measured to be less than 0.5 inches.

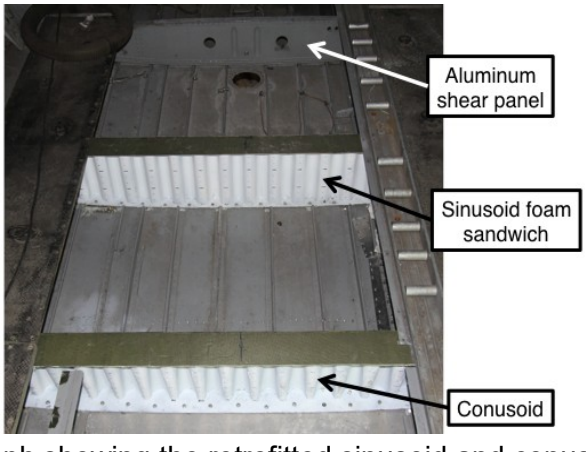

Figure 8.48. Photograph showing the retrofitted sinusoid and conusoid energy absorbers [Fig. 28 of Jackson et al., 2015].

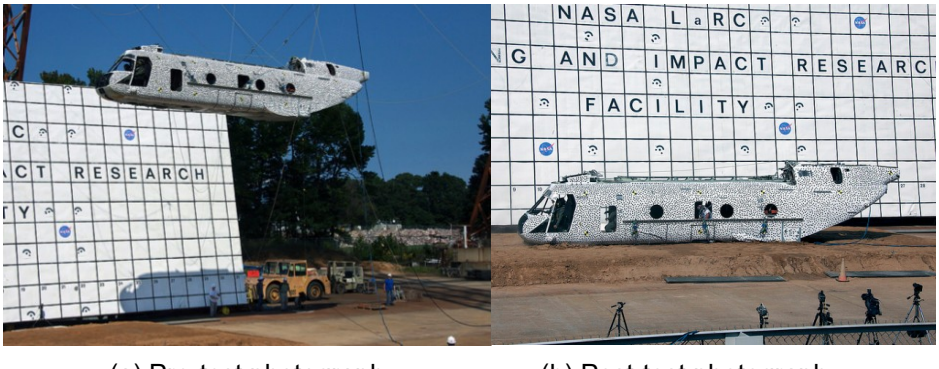

(a) Pre-test photograph. (b) Post-test photograph.

Figure 8.49. Pre- and post-test photographs of TRACT2 [Fig. 30 of Jackson et al., 2015].

Figure 8.50. Post-test photograph of the outer belly skin deformation between FS220 and FS286 [Fig. 32 of Jackson et al., 2015].

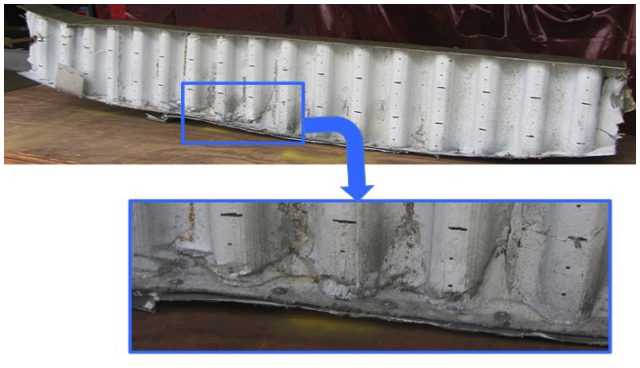

(a) Sinusoid energy absorber, rear view looking forward. Inset shows regions of crush initiation.

(b) Post-test photograph of the conusoid energy absorber, rear view looking forward.

Figure 8.51. Post-test photographs of two composite energy absorbers [Fig. 33 of Jackson et al., 2015].

Development of a FEM of the TRACT2 helicopter was completed and predictions of structural impact responses were generated. The airframe model is shown in Figure 8.52. The model consists of 218,251 nodes; 13,178 beam elements; 102,413 Belytschko-Tsay shell elements; 119,632 solid elements; 473 parts; 27 material properties; 34 element masses; 19 constrained nodal rigid bodies; 1 initial velocity card; and 1 body load representing gravity. The composite shell elements forming the conusoid and the face sheets of the sinusoid foam sandwich energy absorbers were represented using Mat 58, with properties listed in Jackson et al. (2017). The foam in the sinusoid sandwich was represented using solid elements assigned Mat 63.

Finite element models of the sinusoid and conusoid energy absorbers that were incorporated into the TRACT2 model are shown in Figure 8.53. These subfloors were located at FS254 and FS286, respectively. Nominal shell element edge length for the conusoid was 0.3 inches, compared with a 0.25-inch element edge length for the sinusoid. A detailed structural model of the DLR-ACS corrugated web subfloor, located at FS220, was not included and was instead modeled as a typical aluminum shear panel.

The soil was represented using solid elements that were assigned Mat 5 (*MAT_SOIL_AND_FOAM) in LS-DYNA. The soil block was 24 inches deep, 148 inches wide, and 600 inches long. A coefficient of friction of 0.5 between the helicopter and the soil was used in an automatic single surface contact definition. Initially, the soil was represented as a single block with one material model assigned, however, based on the soil characterization results, the model was changed to a layered soil configuration. The top 3-inch-deep layer of soil was represented using Mat 5 with input properties obtained from soil tests conducted on gantry unwashed soil, which were performed for the Orion program [Heymsfiel et al. (2012)]. The bottom 21-inch-deep layer was also represented using Mat 5 with input properties of soft sand, whose bearing strength matched in-situ test results conducted prior to and after the TRACT2 crash test. The bottom and side nodes of the soil were constrained from motion using a Single Point Constraint (SPC) definition in LS-DYNA.

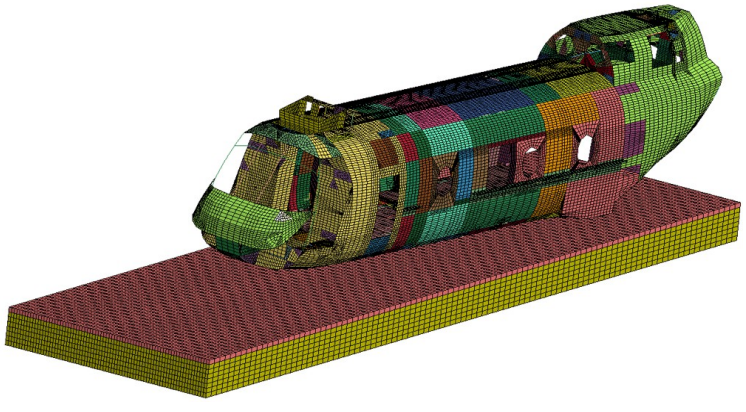

Figure 8.52. Depiction of the TRACT2 FEM [Fig. 34 of Jackson et al., 2015].

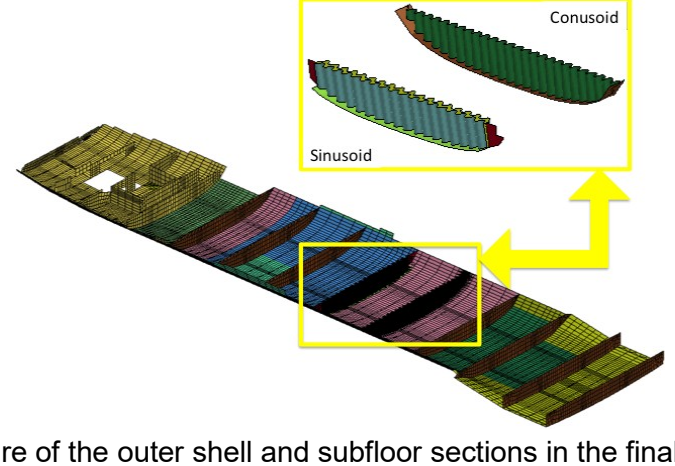

Figure 8.53. Picture of the outer shell and subfloor sections in the final model [Fig. 35 of Jackson et al., 2015].

All nodes forming the helicopter model were assigned initial conditions of 33.65 ft/s forward and 25.36 ft/s vertical velocities, which match the measured test velocities. In addition, the TRACT2 model was oriented to match the measured impact attitude (2.6-degree nose-up pitch, 3.5-degree left-side down roll). Seat/occupant and discrete masses, such as the cargo experiment in the rear of the airframe, were represented using Constrained Nodal Rigid Bodies (CNRBs). In addition, a 600-pound lumped mass was attached to the left-side floor, centered about FS254, and located above the sinusoid energy absorber. The simulation was executed using LS-DYNA Version 971 R6.1.1 SMP (double precision) for 0.1 second, which required 74 hours and 35 minutes of CPU on a Linux-based workstation computer with 8 processors. Nodal output was requested at locations corresponding to accelerometers mounted on the floor in the test article. Test-analysis comparisons were generated at these locations, and the experimental and predicted responses were filtered using a 4-pole Butterworth low-pass filter with a cutoff frequency of 60 Hz.

Selected test-analysis acceleration time histories are shown in Figures 8.54 through 8.58 for FS160 through FS410. In general, these results demonstrate a reasonable level of agreement, especially when considering the fact that the actual deformation and failure behavior of the belly skin between FS220 and FS286 was not captured by the model. In the test, the outer belly skin buckled and tore as it plowed through the soil. It is speculated that shear loading caused the energy-absorbing subfloor beams to rotate globally without crushing, as shown in Figure 8.50. In order to replicate this response, the energy-absorbing subfloor beams in the model would have to be separated from the outer skin and the floor, allowing them the freedom to rotate in a global manner as their top and bottom constraints failed. However, these modifications to the model were not attempted. Instead, the composite subfloor beams in the model behaved in an ideal fashion and exhibited stable crushing.

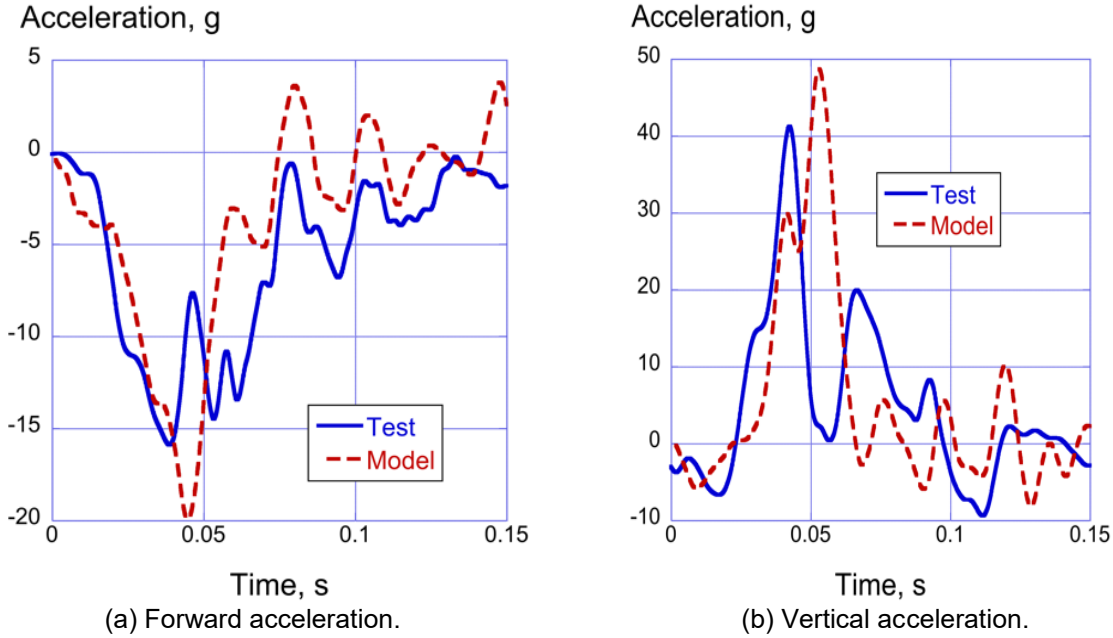

(a) Forward acceleration.

(b) Vertical acceleration.

Figure 8.54. Forward and vertical test and analysis acceleration time histories at right side FS160 [Fig. 38 of Jackson et al., 2015].

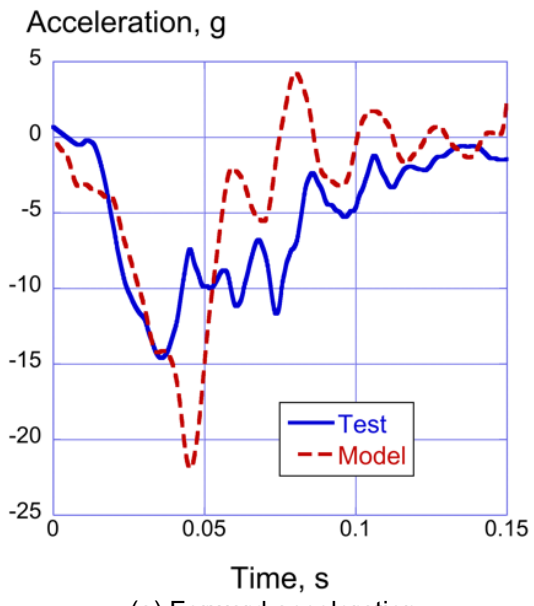

(a) Forward acceleration.

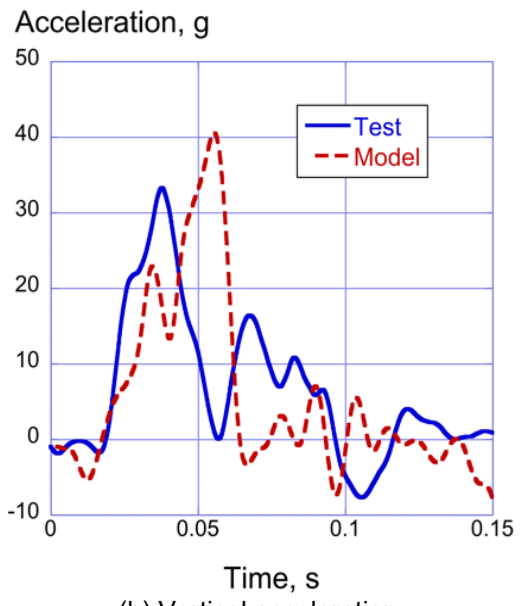

(b) Vertical acceleration.

Figure 8.55. Forward and vertical test and analysis acceleration time histories at right side FS220 [Fig. 39 of Jackson et al., 2015].

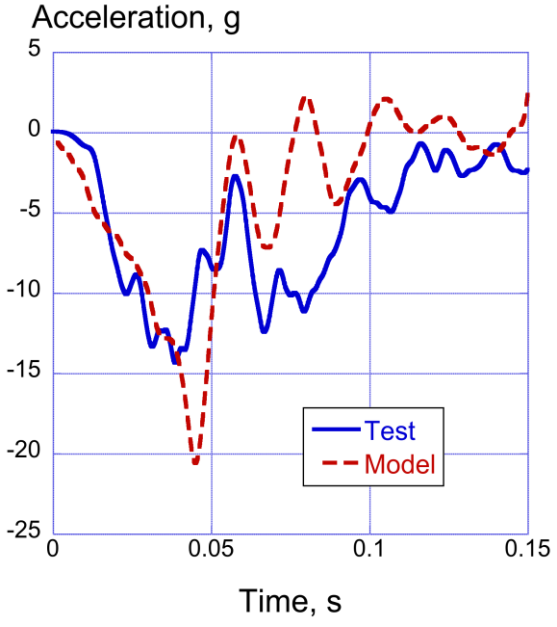

(a) Forward acceleration.

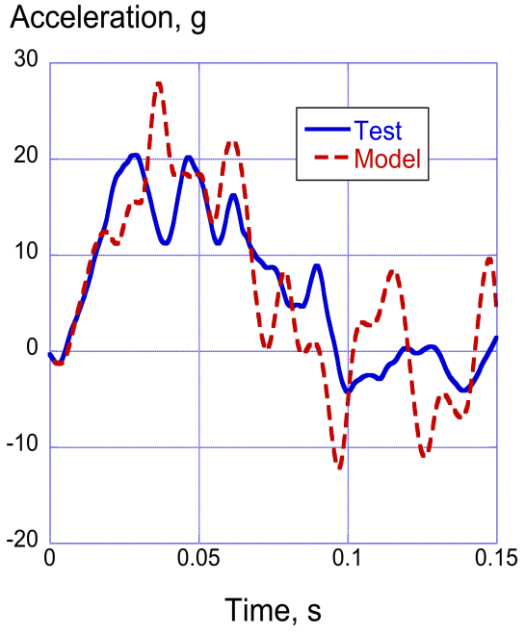

(b) Vertical acceleration.

Figure 8.56. Forward and vertical test and analysis acceleration time histories at left side FS254 [Fig. 40 of Jackson et al., 2015].

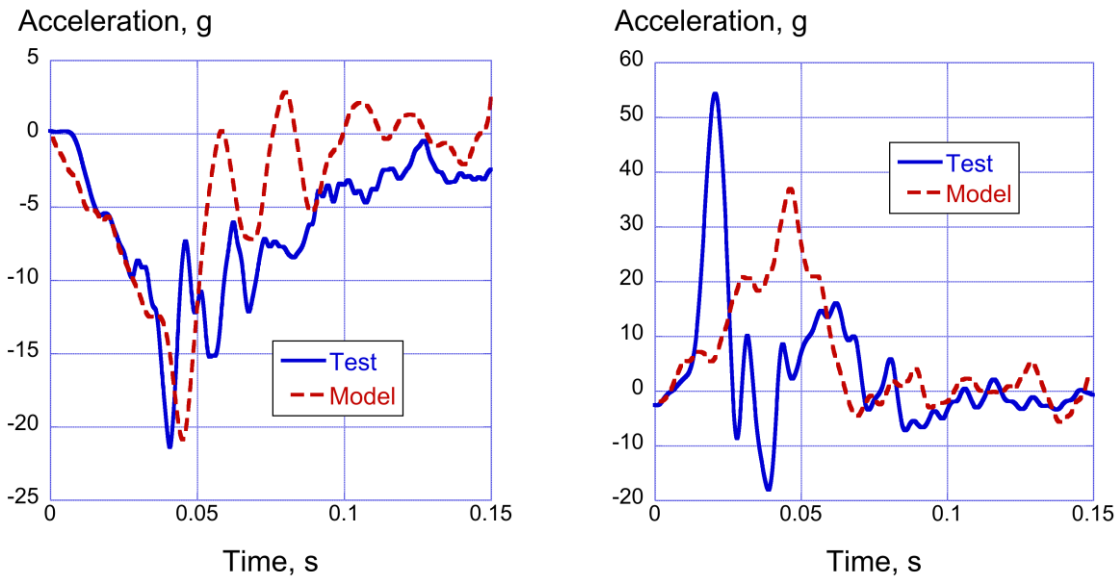

(a) Forward acceleration. (b) Vertical acceleration.

Figure 8.57. Forward and vertical test and analysis acceleration time histories at right side FS350 [Fig. 43 of Jackson et al., 2015].

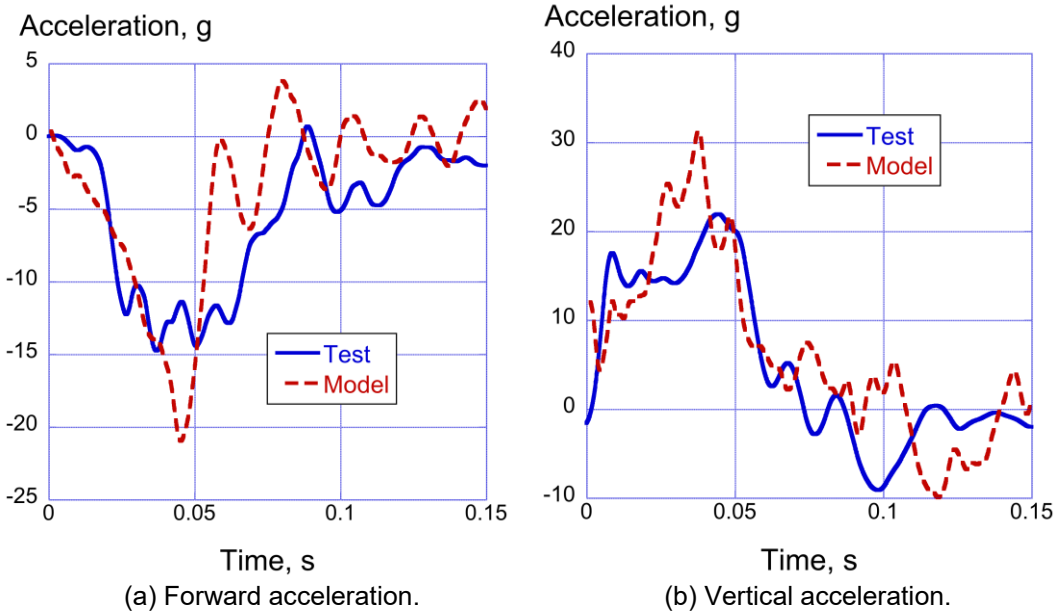

(a) Forward acceleration. (b) Vertical acceleration.

Figure 8.58. Forward and vertical test and analysis acceleration time histories at left side FS410 [Fig. 44 of Jackson et al., 2015].

Important Findings and Significance

Two primary objectives of this project were to assess the capabilities of two novel composite energy absorbers under dynamic impact loading, and to investigate the capabilities of LS-DYNA to predict the experimental behavior. As stated previously, the design goals for the energy absorbers were to achieve between 25 to 40 g average crush accelerations, to minimize peak crush loads, and to generate relatively long crush stroke limits under dynamic loading conditions, typical of those experienced during the TRACT1 [Annett et al. (2014)] full-scale crash test. The results of the element/component level tests proved that the energy absorbers met the goal with average crush accelerations of 28 g for the conusoid and 21.8 g for the sinusoid. The lower average acceleration for the sinusoid translated into a higher crush stroke than was seen for the conusoid. Test-analysis comparisons are listed in Table 8.3 for each level of evaluation—element/component level through full-scale testing. Results are presented as percentage differences of average acceleration and maximum crush displacements, as appropriate. Note that component test-analysis comparisons agreed within 5 percent.

For the TRACT2 test, only average acceleration comparisons were evaluated for both forward (Fwd) and vertical (Vt) acceleration responses generated from floor-mounted accelerometers located between FS160 and FS410, as listed in Table 8.3. Note that for these comparisons, the pulse durations used to determine average accelerations are listed in parentheses in Table 8.3. The test-analysis comparisons range from excellent (4.3 percent agreement for the left-side vertical acceleration response at FS254) to poor (45.1 percent agreement for the left-side vertical acceleration response at FS350). In general, the model did a better job predicting the vertical acceleration responses than the forward acceleration responses.

Table 8.3. Test-Analysis Comparison Metrics.

Test Article Description	Metric	Test	Analysis	% Diff
Conusoid component	Avg. acceleration, g (0.025 s pulse duration)	28.0	28.2	1.43
	Max. crush displacement, in.	2.9	2.53	12.8
Sinusoid component	Avg. acceleration, g (0.03 s pulse duration)	21.8	22.9	5.0
	Max crush displacement, in.	4.0	3.8	5.0
TRACT2, FS160, Rt Fwd	Avg. acceleration, g (0.133 s)	6.3	4.4	30.2
TRACT2, FS160, Rt Vt	Avg. acceleration, g (0.0975 s)	8.7	8.3	4.6
TRACT2, FS220, Rt Fwd	Avg. acceleration, g (0.133 s)	5.9	4.4	25.4
TRACT2, FS220, Rt Vt	Avg. acceleration, g (0.0787 s)	13.0	11.7	9.9
TRACT2, FS254, Lt Fwd	Avg. acceleration, g (0.142 s)	6.0	4.1	31.7
TRACT2, FS254, Lt Vt	Avg. acceleration, g (0.096 s)	10.8	10.3	4.3
TRACT2, FS350, Rt Fwd	Avg. acceleration, g (0.15 s)	7.1	3.9	45.1
TRACT2, FS350, Rt Vt	Avg. acceleration, g (0.0775 s)	8.0	11.6	45.0
TRACT2, FS410, Lt Fwd	Avg. acceleration, g (0.15 s)	5.8	3.8	34.5
TRACT2, FS410, Lt Vt	Avg. acceleration, g (0.0867 s)	10.7	12.6	17.8

BIRD STRIKE SIMULATION

A parameter study of bird strikes on low-noise rotor blades was conducted to determine the geometric optimization constraints for a low-noise rotor blade design [Annett and Pereira (2018)]. The design was targeted for a medium-lift category rotorcraft and intended to reduce overall acoustic sound energy levels. The blade was roughly based on a UH-60 design with a box spar concept, and contained conventional materials such as Ti-6AL-4V, and carbon and glass fiber reinforced plastic. The velocity of impact was based on the nominal rotor speed of 260 rpm.

A bird simulant, weighing 2.2 pounds as specified in 14 CFR §29.631, was used for testing and analysis. The bird simulant finite element model (FEM) was validated through gas gun testing on flat-faced and wedge-faced tubes at NASA Glenn Research Center. Analyses were performed using LS-DYNA with the bird represented using Smooth Particle Hydrodynamics (SPH), as shown in Figure 8.59. Bird strike sensitivity analyses were conducted by varying the bird impact angle on the leading edge, the spanwise location of impact, the spar wall thickness, and the ratio of chord thickness to length (*t/c*). The blade FEM was pre-stressed for centrifugal loading, and then impacted with the bird simulant.

Important Findings and Significance

Based on the preliminary LS-DYNA results, geometric constraints on the bird strike blade in terms of maximum twist angle and minimum spar thickness were defined.

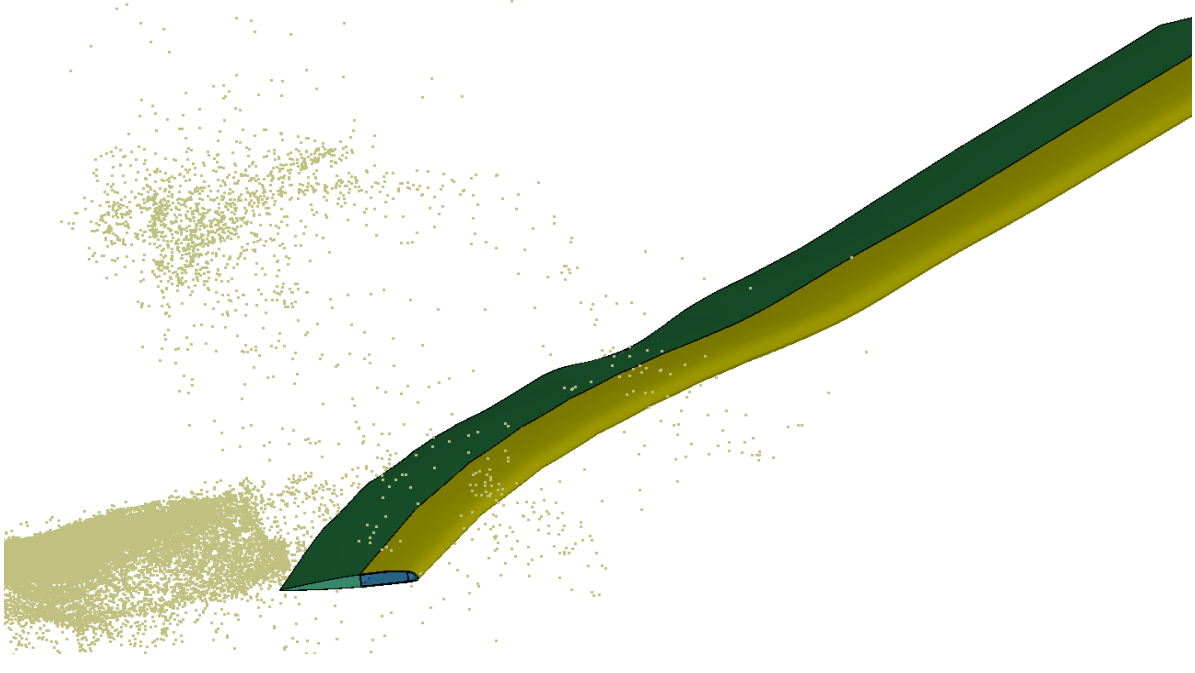

Figure 8.59. Simulation of low-noise blade deflection due to bird strike [Fig. 16 of Annett and Pereira, 2018].

MODELING AND SIMULATION OF THE ATR42-300, A COMMUTER AIRPLANE

In 1998, the U.S. Army Research Laboratory Vehicle Technology Directorate (ARL-VTD) entered into an Inter-Agency Agreement (IAA) with the FAA William J. Hughes Technical Center for the purpose of validating crash simulations of airframe structures. In 2003, the IAA was extended for an additional 5 years, through 2008, and the model validation work entered a new phase with the development of a full-scale FEM of the ATR42-300 aircraft. For this simulation, the model was developed based on hand measurements of geometry, and the final model was executed using the commercial nonlinear explicit transient dynamic finite element code, LS-DYNA. The FAA performed a 30-ft/s vertical drop test of the aircraft to determine the impact responses of the airframe, floor, seat tracks, seats, dummies, and high-wing fuel system. Recently, the FAA has proposed dynamic performance criteria for seats in commuter aircraft that were based on empirical information obtained from prior airplane crash test data, which did not include airplanes representative in size of commuters. Consequently, this drop test was performed to provide impact data to evaluate the seat standards for this category of aircraft. The experimental program, model development, and test-analysis correlations are summarized in the following sections.

Experimental Program

On July 30, 2003, a 30-ft/s vertical drop test of an ATR42 aircraft was conducted using the Dynamic Drop Test Facility located at the FAA Technical Center in Atlantic City, New Jersey [Abramowitz (2006)]. A pre-test photograph of the test article, raised to the drop height of 14 feet, is shown in Figure 8.60. This twin-turboprop high-wing commuter-class aircraft was developed and manufactured through a joint effort by Aérospatiale in France and Aeritalia in Italy. The aircraft has a wingspan of 80 feet, a seating capacity of 42–50 passengers, and a maximum gross takeoff weight of approximately 36,800 pounds. The drop test was performed onto a concrete surface. The purpose of the test was to evaluate the dynamic structural response of the aircraft when subjected to a severe, but survivable, impact. Particular attention was given to the seat and occupant responses to evaluate the FAA's proposed dynamic seat requirements for commuter-class aircraft.

The total weight of the fully loaded and instrumented aircraft was 33,200 pounds. A large portion of the total weight was the 8,700 pounds of water added to the fuel tanks in the wing to represent fuel. In addition, 16 double-occupant aircraft seats weighing 54 pounds each, and 3 single-occupant seats weighing approximately 20 pounds each, were attached to seat tracks on the floor. Seven instrumented ATDs and 16 non-instrumented mannequins, each weighing 170 pounds, were seated in various positions. Ballast weights equaling 135 and 152 pounds were added to some of the empty seats to represent the mass of occupants. The forward and aft storage compartments were filled with 1,450 and 739 pounds of luggage, respectively. In addition to the ballast, two overhead stowage bins were mounted between Frame Station 30 (FS30) and FS34 on the right and left sides of the fuselage. The bins weighed 55 pounds each, 22 pounds empty weight plus 33 pounds (14.97 kg) ballast in each bin. Two cement-filled cylindrical drums were attached to the engine mounts on the wings, each weighing 1,290 pounds, to represent the engines.

A dominant feature of this aircraft is the high wing, which is attached directly to heavy fuselage frames at FS25 and FS27 through four “dog bone” beams. The “dog bone” beams attach to brackets on the fuselage frames at a location approximately 60 inches above the floor. Four upper bracket assemblies are located on the top ends of these two fuselage frames. Prior to the drop test, the longitudinal position of the CG of the aircraft was measured. This measurement closely matches the CG location specified by the airframe manufacturer, as indicated in the Weight and Balance Manual [Anon. (1992)].

A post-test photograph showing an overall exterior view of the aircraft is shown in Figure 8.61. The primary damage mode to the airframe was the failure of the heavy fuselage frames supporting the wing, causing the wing to subsequently displace vertically through the fuselage cabin. The aluminum structure supporting the wing was crushed and fractured. A post-test photograph showing a close-up view of the wing/fuselage region is shown in Figure 8.62(a). Further inspection of the airframe following the test indicated that several of the seats failed, as shown in Figure 8.62(b).

Figure 8.60. Pre-test photograph of the ATR42 aircraft, raised to a drop height of 14 feet [Fig. 1 of Jackson and Fasanella, 2005].

Figure 8.61. Post-test photograph of the ATR42 aircraft showing an overall view [Fig. 4 of Jackson and Fasanella, 2005].

(a) Close-up view (b) Interior view.

Figure 8.62. Additional post-test photographs of the ATR42 aircraft [Fig. 5 of Jackson and Fasanella, 2005].

Model Development

The FEM of the ATR42 aircraft was developed from direct measurements of the airframe geometry, which were input into a preprocessing database file. When completed, the geometry model was discretized into a finite element mesh, element and material properties were assigned, contact and initial velocity conditions were defined, and the model was executed to generate analytical predictions of structural deformation and acceleration and velocity time-history responses. The FEM of the ATR42 aircraft, shown in Figure 8.63, contained 57,643 nodes and 62,979 elements including 60,197 quadrilateral shell elements; 551 triangular shell elements; 526 beam elements; and 1,705 CNRBs that were used to assign concentrated mass to nodes in the model. Additional information on the model development process can be found in Jackson and Fasanella (2004, 2005, and 2008).

An automatic contact definition was specified for the model, which is a generic contact definition in LS-DYNA that prescribes that no node can penetrate through any surface in the model. An impact surface was created to represent the concrete pad beneath the drop tower. This surface was modeled as a 5-inch-thick aluminum plate, encompassing the total length and width of the aircraft, as shown in Figure 8.63. Four main material properties were defined in the model for aluminum Al-2024-T3, aluminum Al-7075-T6, aluminum Al-7050-T7452, and titanium Ti-6Al-4V. The properties were defined using the MAT_PLASTIC_KINEMATIC card in LS-DYNA for a linear elastic-plastic material with input values for density, Poisson's ratio, Young's modulus, yield stress, hardening modulus, and an ultimate failure strain. Most of the sheet metal parts, such as the outer skin, were assigned material properties of Al-2024-T3. The forged metal parts, such as the fuselage frames, floor beams, and seat tracks were assigned material properties of Al-7075-T6, except for the two heavy fuselage frames at FS25 and FS27 that were assigned properties of Al-7050-T7452. The "dog bone" beams used to attach the wing to the fuselage frames at FS25 and FS27 were assigned material properties of titanium. The material property designation and mass of each component were obtained from the aircraft manufacturer's Weight and Balance Manual [Anon. (1992)], and the material property values were estimated based on values found in MIL-HDBK-5H (1998).

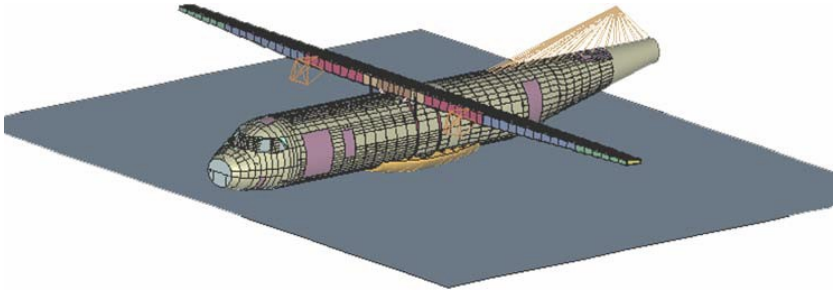

Figure 8.63. Final FEM of the ATR42 aircraft [Fig. 6(d) of Jackson and Fasanella, 2005].

Test-Analysis Comparisons

Comparisons of test article and model deformations are shown in Figure 8.64 from 0.05 to 0.25 seconds in 0.05-second intervals. The pictures of model deformation were obtained from the post-processing file, and the experimental pictures were captured from the high-speed film. In general, the model accurately predicts the structural deformation and failure behavior of the test article, including collapse and failure of the fuselage structure beneath the wing.

The raw experimental acceleration data were plotted versus time, integrated to obtain the velocity time-history responses, and filtered using a low-pass digital filter based on the SAE J211/1 specifications [SAE (1995)]. A variety of cut-off frequencies were applied in an attempt to obtain a well-defined acceleration pulse, while at the same time not distorting the integrated velocity response. A low-pass, cut-off frequency of 33.2 Hz was selected because it generally met these criteria. This filter is equivalent to a Channel Filter Class (CFC) 20 filter [SAE (1995)]. All experimental and analytical acceleration time histories are filtered using this cut-off frequency.

Selected comparisons of time-history responses are shown in Figures 8.65 to 8.71. For additional information, see Jackson and Fasanella (2004, 2005, and 2008). The experimental and analytical acceleration and velocity responses of the left outer floor track at FS20 are shown in Figure 8.65. For the test, the acceleration response exhibits two main peaks, as indicated in Figure 8.65(a). The first acceleration peak (18 g) is smaller in magnitude than the second (28 g). At this location, the predicted acceleration response also exhibits two peaks, however the first peak is higher in magnitude (28 g) than the second (17 g). The filtered experimental and analytical acceleration data were integrated to obtain the velocity responses plotted in Figure 8.65(b). Both curves are closely matched up to 0.06 seconds. After that time, the analytical velocity response crosses zero velocity at 0.075 seconds and exhibits a rebound of about 34 in/s. The experimental response flattens out after 0.06 seconds and does not cross zero until 0.15 seconds. The maximum rebound velocity exhibited by the experimental response is 30 in/s.

The experimental and analytical acceleration and velocity responses of the right outer seat track at FS18 are shown in Figure 8.66. For this location, the peak acceleration values for the test and analysis are of the same magnitude, about 24 g. Also, the predicted velocity response closely matches the experimental response, i.e. both curves cross zero velocity at the same time (.08 seconds) and exhibit approximately the same rebound velocity of 50 in/s.

Time, s	Test article	LS-DYNA simulation
0.05		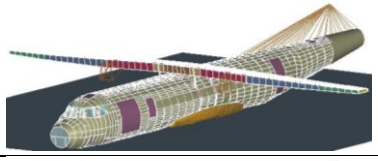
0.10		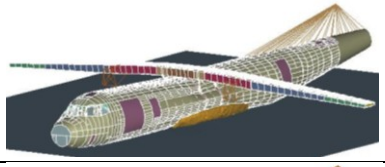
0.15		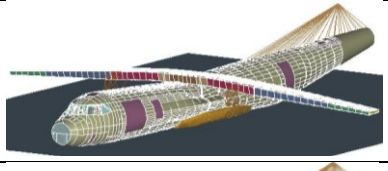
0.20		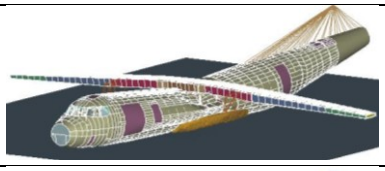
0.25		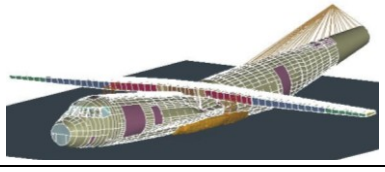

Figure 8.64. Comparison of structural deformation [Fig. 8 of Jackson and Fasanella, 2005].

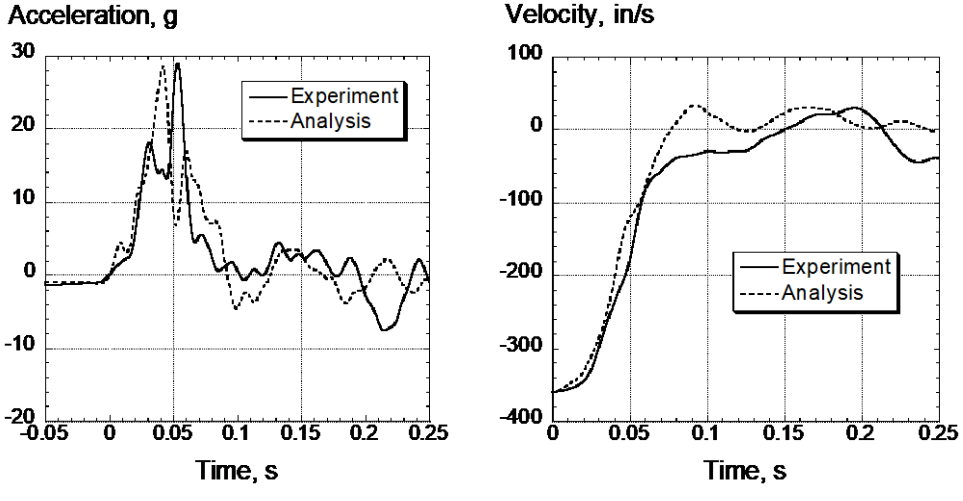

(a) Acceleration response. (b) Velocity response.

Figure 8.65. Experimental and analytical time-history responses for the left outer seat track at FS20 [Fig. 10 of Jackson and Fasanella, 2005].

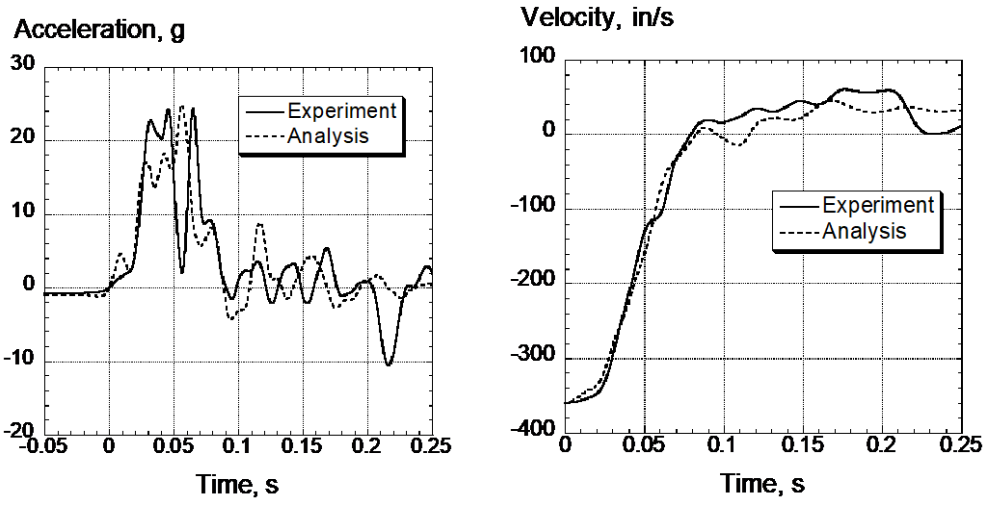

(a) Acceleration responses. (b) Velocity responses.

Figure 8.66. Experimental and analytical time-history responses for the right outer seat track at FS18 [Fig. 11 of Jackson and Fasanella, 2005].

Next, the experimental and analytical acceleration and velocity responses of the right side of the cockpit floor are plotted in Figure 8.67. Again, the experimental acceleration response exhibits two peaks, however in this case the first peak (34 g) is higher in magnitude than the second peak (28 g). The predicted peak acceleration is 26 g. The experimental pulse is shorter in duration than the analytical response by about 0.02 seconds, as indicated in the velocity plot of Figure 8.67(b). However, both curves exhibit the same rebound velocity of 90 in/s.

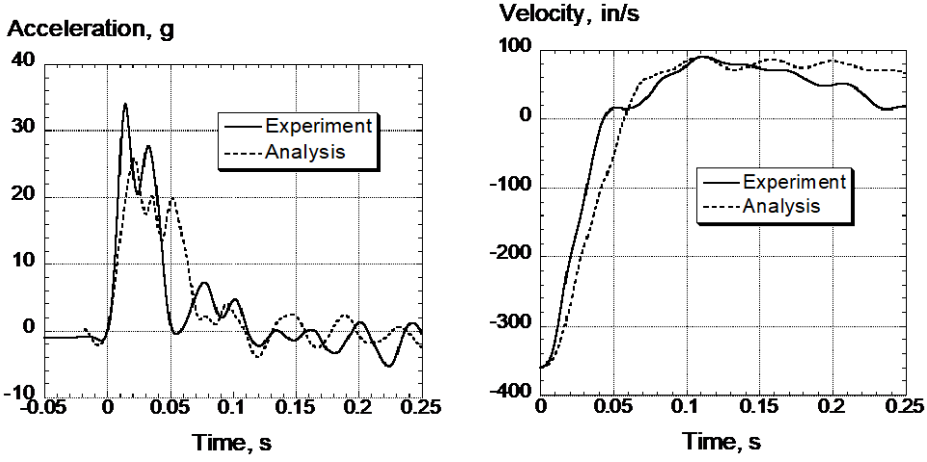

(a) Acceleration responses. (b) Velocity responses.

Figure 8.67. Experimental and analytical time-history responses of the right side of the cockpit floor [Fig. 12 of Jackson and Fasanella, 2005].

The experimental and analytical acceleration and velocity responses of the left inner seat track at FS29 and the right inner seat track at FS35 are plotted in Figures 8.68 and 8.69, respectively. The accelerometer at FS29 is located on the floor slightly to the rear of the fuselage frames supporting the wings, while the accelerometer at FS35 is located on the floor at the very rear of the aircraft. At these two locations, the filtered experimental acceleration responses exhibit high-amplitude, low-frequency responses, making it difficult to discern a well-defined acceleration pulse. In general, the predicted acceleration responses match the peak values and the pulse durations of the experimental acceleration responses at these two locations. However, the comparison of the velocity responses is, perhaps, a better measure of the level of correlation, as shown in Figures 68(b) and 69(b).

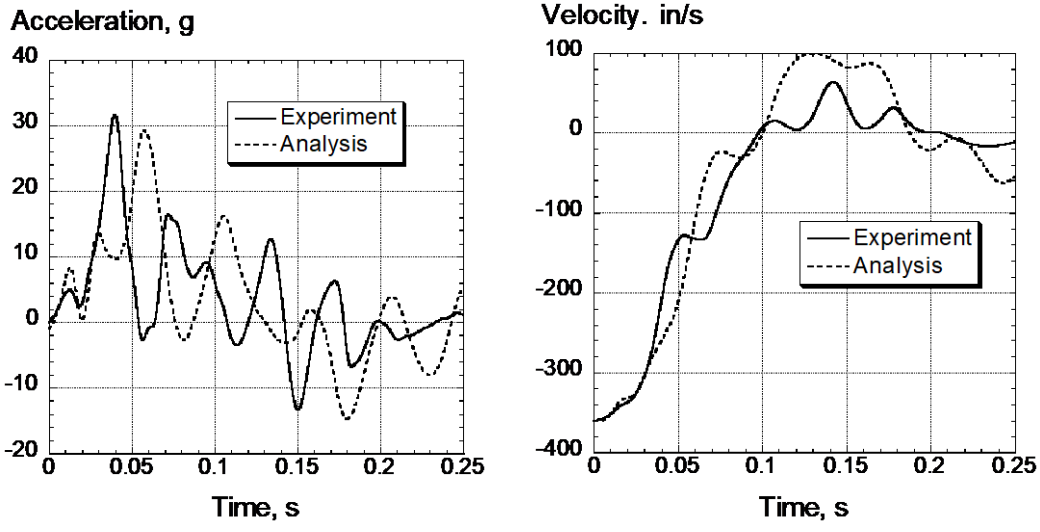

(a) Acceleration responses. (b) Velocity responses.

Figure 8.68. Experimental and analytical time-history responses of the left inner seat track at FS29 [Fig. 13 of Jackson and Fasanella, 2005].

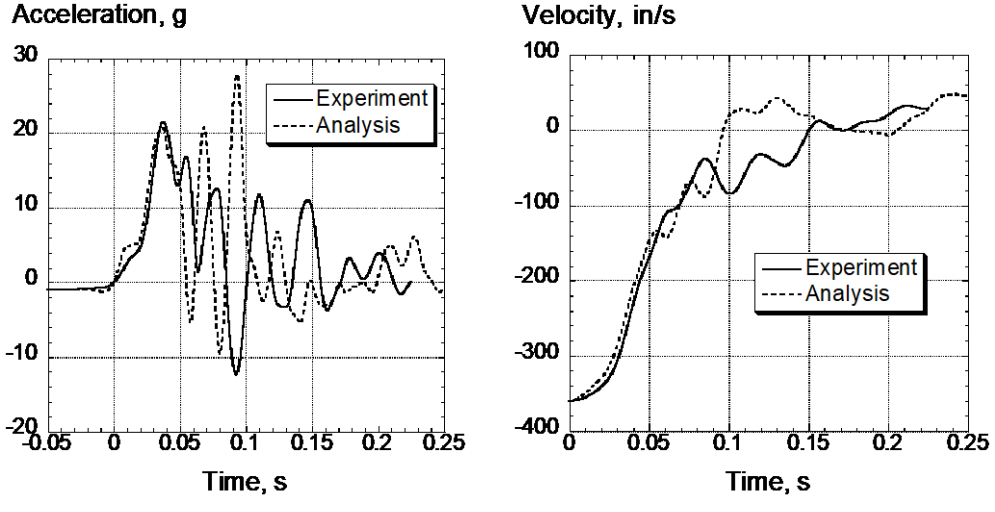

(a) Acceleration responses. (b) Velocity responses.

Figure 8.69. Experimental and analytical time-history responses of the right inner seat track at FS35 [Fig. 14 of Jackson and Fasanella, 2005].

The experimental and predicted acceleration and velocity responses of the center of the tail section at FS47 are plotted in Figure 8.70. Unlike the floor acceleration responses, most of which had pulse durations of 0.1 second or less, this response is 0.2 seconds in duration. Both the experimental and analytical acceleration responses exhibit a single pulse of approximately the same duration and magnitude. The experimental and analytical velocity responses, shown in Figure 8.70(b), show nearly perfect agreement, with both curves crossing zero velocity at nearly the same time (0.16 seconds) and exhibiting a maximum rebound velocity of 147 in/s at 0.21 seconds.

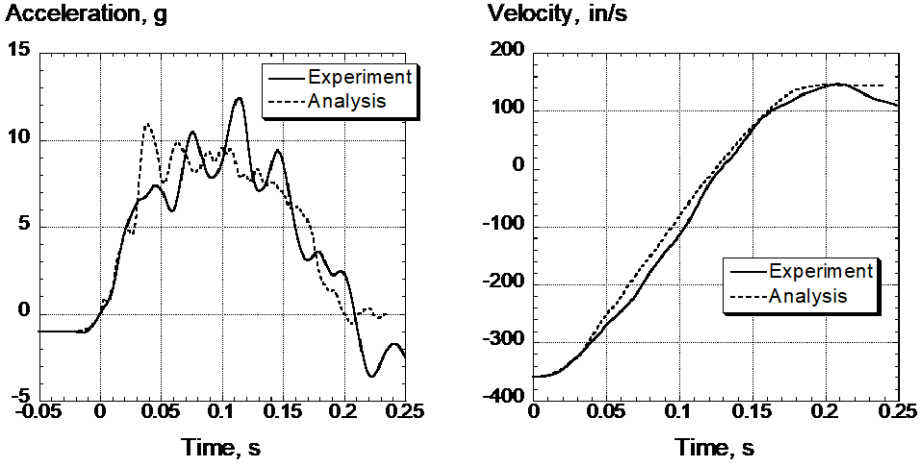

(a) Acceleration responses. (b) Velocity responses.

Figure 8.70. Experimental and analytical time-history responses of the center tail section at FS47 [Fig. 15 of Jackson and Fasanella, 2005].

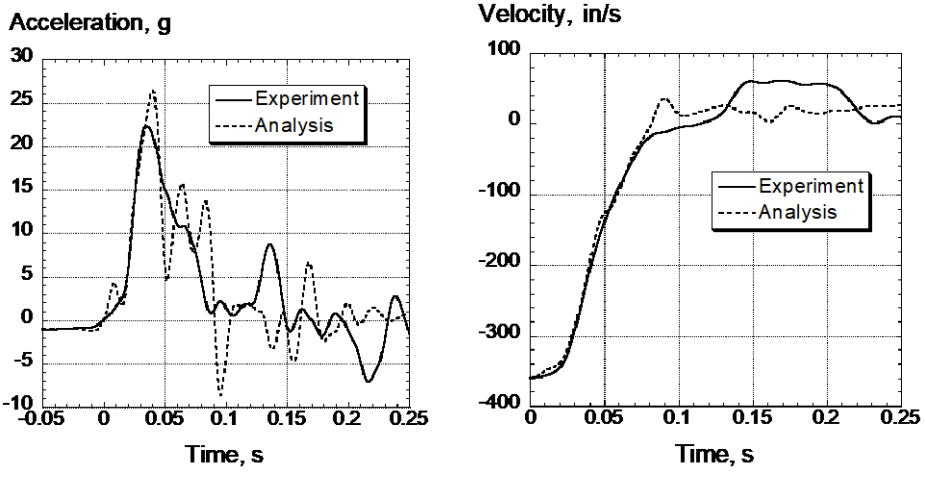

(a) Acceleration responses. (b) Velocity responses.

Figure 8.71. Experimental and analytical time-history responses of the left sidewall at FS18 [Fig. 16 of Jackson and Fasanella, 2005].

The experimental and analytical acceleration and velocity responses of the left sidewall at FS18 are plotted in Figure 8.71. This accelerometer was located on the sidewall approximately 12 inches above the floor and was oriented in the vertical direction. The analytical acceleration response closely matches the magnitude (peak acceleration of 26.5 g for the analysis compared with 22.5 g for the experiment) of the experimental pulse. The velocity responses for the test and analysis, shown in Figure 8.71(b) are close up to 0.075 seconds, after which time the analytical curve crosses zero velocity at 0.08 seconds and exhibits a maximum rebound velocity of 36 in/s. However, the experimental response flattens out and does not cross zero velocity until 0.12 seconds, after which it exhibits a prolonged rebound velocity of 60 in/s, not seen in the analytical curve.

Important Findings and Significance

The level of test-analysis agreement for this experiment was excellent and provides a further step in the ultimate goal of certification-by-analysis. In addition, the test demonstrated the unwise decision to design aircraft with overhead wings.

DROP TESTING AND SIMULATION OF TWO F28 FUSELAGE SECTIONS

Recently, the crashworthy behavior of transport aircraft has become a topic of significant interest by the FAA and NASA. In 2015, the FAA created an Aviation Rulemaking Advisory Committee (ARAC) whose goal is to generate recommendations for establishing whole airframe crashworthiness and ditching requirements for transport aircraft [Federal Register (2015)]. To support this effort, NASA and the FAA signed an interagency research agreement in 2016 that enabled vertical drop tests of two fuselage sections of a Fokker F28 Fellowship aircraft. The drop tests were conducted at the NASA Langley LandIR facility. The portions of the airframe from which the sections were taken are highlighted in the schematic drawing shown in Figure 8.72. This section of the chapter is divided into three parts: Experimental Testing, Model Development, and Test-Analysis Comparisons.

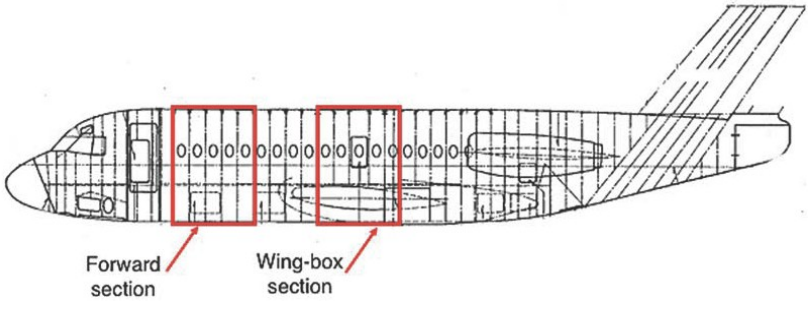

Figure 8.72. Side-view schematic of the F28 highlighting the locations of the two fuselage sections [Fig. 1 of Jackson et al., Feb. 2018].

Experimental Testing

In March 2017 a vertical drop test of a 10-foot-long forward section of a Fokker F28 aircraft was conducted onto soil at the LandIR facility. A pre-test photograph of the fully loaded fuselage section is shown in Figure 8.73(a). Prior to the drop test, the section was configured with two rows of aircraft seats, in a triple-double configuration, as shown in Figure 8.73(b). A total of 10 ATDs were secured in the seats using standard lap belt restraints. The section was also configured with packed luggage in the cargo hold and two hat racks, each with mass loading of 25 pounds per linear foot.

The forward barrel section consists of five windows and six frames between FS5305 and FS7805. The interior paneling and the floor panels were removed. A cargo door is located on the lower right side of the section. The barrel section is approximately 9 feet wide at the floor. Packed luggage (922 pounds) was loaded into the cargo hold of the section and was restrained by netting on both the forward and aft ends. Hat racks were fabricated by attaching c-channel beams to the upper fuselage and adding ballast weight of 116 pounds per side. Floor panels were installed and cut to fit the section length, as needed. The floor was ballasted using a combination of seated ATDs and Data Acquisition Systems (DAS) to achieve a total pre-test weight of 4,465 pounds. Additional information on the forward second drop test can be found in Jackson et al. (Feb. 2018).

The vertical drop test of the F28 forward section was performed by raising the test article approximately 14 feet in the air and releasing it to impact a 2-foot-high soil bed. The measured impact velocity was 346.8 in/s. Prior to the test, one side of the fuselage section was painted white and 1.0-inch-diameter black dots were painted on the white surface in a random pattern. The painted dots were used as targets, which were tracked using 3D full-field photogrammetry [Littell (Oct. 2017)].

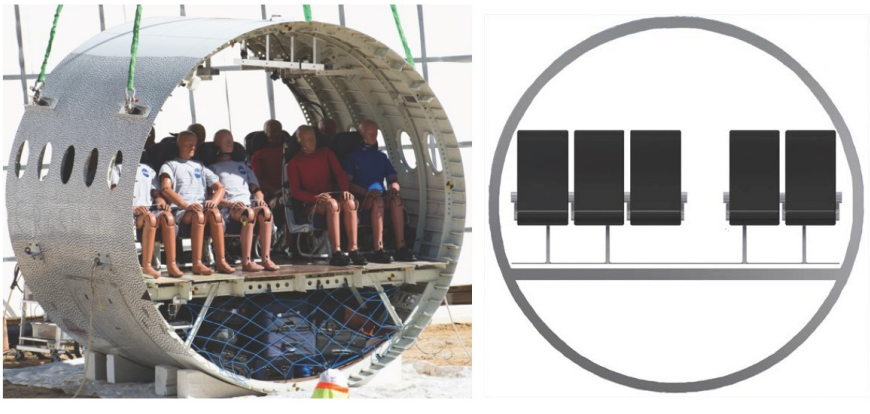

(a) Pre-test photo of the forward section. (b) Schematic depiction of the 3+2 seats.

Figure 8.73. Pre-test photograph of the F28 forward section and a schematic depiction [Fig. 4 of Jackson et al., Feb. 2018].

The F28 wing-box section was cut between FS9805 and FS12405 from a F28 MK1000 full-scale fuselage. All of the interior structure including electronics, lighting, paneling, and hat racks were removed such that only the outer skin, frames, and other structural components of the airframe remained. The floors and seats were removed for storage, and while the original floors were reinstalled for the test, the original seats were discarded. The wings were removed at the wing-box attachment points, and all fluids were drained from the remaining hydraulic lines that were still present in the wing-truss structure and lower cavity below the wing-truss structure.

Two rows of seats were installed in a triple-double configuration, with the triple seats installed on the starboard side of the section and the double seats installed on the port side. Seats were certified to Code of Federal Regulations (CFR) Part 25.562; they were removed from an in-service Boeing 737 aircraft. Seat legs were reconfigured to interface with the seat track dimensions of the F28. For the seats on the double side, the window seat was cut out of a triple configuration to achieve a double configuration. Seat track accelerations were measured by attaching an accelerometer at the base of the seat leg. The rear row of seats was placed between FS10790 and FS11405 while the front seats were centered over FS10305. The seat pitch was 32 inches between rows. All seats were placed in their most upright position and all armrests were placed up, so as not to interfere with the ATD motion.

A combination of ATD sizes, ranging between Hybrid III 5th and 95th percentiles, were installed in the 10 seats onboard the test article. The fully loaded F28 wing-box fuselage section is shown in Figure 8.74. Hat racks were created by adding lead ballast to aluminum c-channel sections, for a total weight of 232 pounds (116 pounds per side). Aluminum c-channels were attached to the existing locations of overhead bin attachment points on the frames and spanned between FS10305 and FS11905. Accelerations were measured at the hat-rack-frame attachment points at FS10305 and FS11405 on the most forward and most aft lead ballast on each side.

Figure 8.74. Photograph of the fully loaded F28 wing-box section [Fig. 6(b) of Jackson et al., Feb. 2018].

After all of the ballast, instrumentation, cameras, and ATDs were installed, the total weight of the test article was 5,180 pounds. The CG was located 4.25 inches forward of FS10790 in the longitudinal direction and 1.4 inches starboard of the geometric center in the lateral direction. The CG vertical height was not measured. The test article was lifted to its release height using soft straps attached to swivel hoist rings that were located at the original wing attachment locations. The fuselage section was pitched downward by utilizing lower wing-attachment holes for the rear lifting locations than in the front. The nominal pitch was calculated to be approximately 4.6 degrees, however the pitch angle at impact was 2.9 degrees. The measured impact velocity was 349.2 in/s.

The test article impacted a mound of soil that was placed over the concrete pad located beneath the LandIR facility. Soil, that was designated Gantry Unwashed Sand (GUS) [Thomas et al. (2008)], was built into a 20- by 20-foot-square mound, with a downward-facing 10-degree slope, such that the rear portion of the test article would contact first, causing a rotational velocity component about the rear impact point. This rotation would cause the forward portion of the test article to impact at a downward pitch angle. The rotation was designed to induce a forward acceleration into the onboard ATDs. For additional information on the F28 forward and wing-box section drop tests, see Littell (Oct. 2017 and 2018), and Jackson et al. (Feb. 2018 and Apr. 2018).

Model Development

A second objective of the NASA/FAA collaborative effort was to assess the capabilities of analytical methods to predict the test responses. Finite element models (FEMs) were developed of the F28 fuselage sections for execution in LS-DYNA, a commercial code for simulating explicit nonlinear transient dynamic problems.

The LS-DYNA model of the F28 forward section, shown in Figure 8.75, was created from a NASA Structural Analysis (NASTRAN) model of the F28 Fellowship aircraft that was provided to NASA by Fokker at the time of original purchase of the airframe hardware. The total weight of the structural model (minus the soil) is 4,310.8 pounds, which includes 922.8 pounds of luggage, 2,044pounds of floor loading, 232 pounds of total hat rack mass, 170 pounds for the DAS box, and 942 pounds for the fuselage empty weight. The measured weight of the fully loaded F28 fuselage section is 4,465 pounds. Thus, the model is approximately 154 pounds too light. The model contained 114,636 shell elements, 48,716 solid elements, 141,080 nodes, 36 parts, 10 materials, 1 contact definition, 1 initial velocity card, and 1 SPC boundary condition that was used to fix the side and bottom nodes of the soil.

Most of the material models were converted directly from the NASTRAN model to represent aluminum components using an elastic-plastic material model in LS-DYNA. The floor panels were constructed of two different materials: aluminum-clad balsa wood, or fiberglass covered Nomex honeycomb. Since no material properties were available for the floor panels, test specimens were obtained, and three-point flexure tests were conducted and simulated to obtain material properties for these parts. The luggage was represented using solid elements that were assigned material properties obtained from a quasi-static crush test of stacked luggage, as described in Jackson and Fasanella (2002). A material model (*MAT_SOIL_AND_FOAM) was assigned to the soil, as reported in Thomas et al. (2008). All nodes forming the bottom and side surfaces of the soil block were fixed (i.e. no translational or rotational motion allowed) using SPCs in the LS-DYNA model.

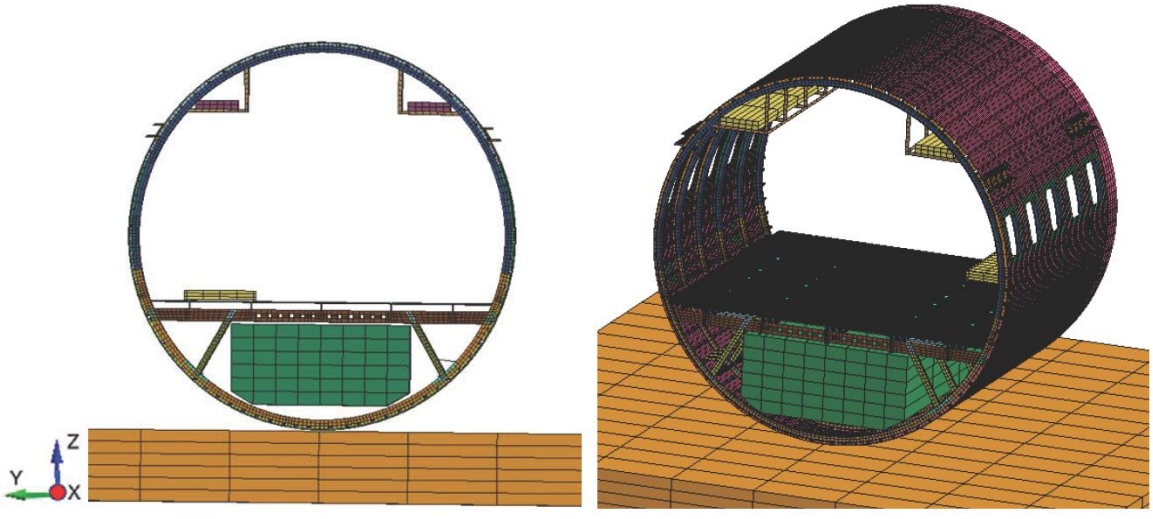

(a) Front view. (b) Three-quarter view.

Figure 8.75. Depictions of the F28 forward section model [Fig. 14 of Jackson et al., Feb. 2018].

The nodes forming the fuselage section were assigned an initial velocity of 346.8 in/s in the downward vertical direction, matching the measured velocity. An automatic contact was defined that prevents any node from penetrating any surface. For these initial simulations, the inertial properties of the seats, occupants, and restraint systems were represented using concentrated masses, placed on the floor at the approximate locations of seat attachment points. The model was executed for an end time of 0.2 seconds and required 35 hours of execution time running LS-DYNA SMP Version 971 double precision, on 8 processors of a workstation computer. Output requests included time-history responses corresponding to accelerometer locations and structural deformations.

Two views of the FEM of the F28 wing-box section are shown in Figure 8.76, a side view and a three-quarter view. The model consists of 78,863 nodes, 7,566 beam elements, 16,636 shell elements, 54,436 solid elements, 794 parts, 75 material cards, 16 concentrated masses, 1 contact definition, 1 initial velocity card, and 1 SPC boundary condition that was used to fix the side and bottom nodes of the soil. As shown in Figure 8.76(a), the soil is canted by 10 degrees with respect to the global x-axis, and the section is pitched down by 2.9 degrees at impact. Because of the pitch attitude, local coordinate systems were defined at each concentrated mass on the floor. Initially, concentrated masses were used to represent the inertial properties of the seats and occupants, and they were located in the model at the approximate seat attachment locations on the floor. Nodal output was requested in the local coordinate system, which moves with the model as it deforms.

One obvious difference between the forward section and the wing-box section models is that a layered soil configuration was used in the wing-box model. In this case, the top six soil elements through the soil depth (which represents 6 inches of soil depth out of a total of 24 inches) were assigned properties of hard soil, whereas the bottom 18 soil elements were assigned properties of soft soil. These properties were input using *MAT_SOIL_AND FOAM or Mat 5 in LS-DYNA. The soil models have been previously reported in Thomas et al. (2008), Fasanella et al. (2008 and 2009), and Heymsfiel et al. (2012). Another difference between the forward section and the wing-box section models is the large number of beam elements in the wing-box model that were

used to define the detailed under-floor structure. Note that the forward section model was modified such that all beam elements were replaced with shell elements.

The structural wing-box model weighed 5,127.4 pounds, which is only 52.6 pounds lighter than the measured weight of the test article (5,180 pounds). The total weight of the model included 2,044 pounds of concentrated masses on the floor representing the seats, occupants, and restraint systems; 209.4 pounds for the DAS box; 232 pounds for the hat rack masses; and, 2,642 pounds for the empty section weight. All nodes in the wing-box section structural model were assigned an initial velocity in the global z-direction of 349.2 in/s, matching the test condition. The model was executed for an end time of 0.2 seconds and required 54 hours and 45 minutes of execution time running LS-DYNA SMP Version 971 double precision, on eight processors of a workstation computer. Output requests included time-history responses corresponding to accelerometer locations and structural deformations.

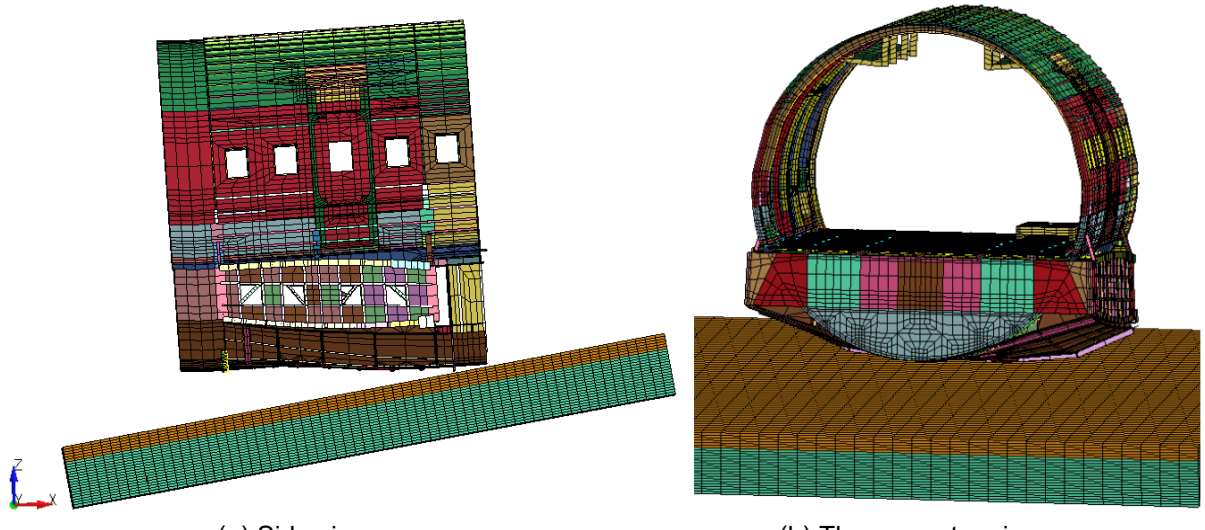

(a) Side view. (b) Three-quarter view.

Figure 8.76. Two views of the F28 wing-box section model [Fig. 16 of Jackson et al., Feb. 2018].

Test-Analysis Comparisons

The vertical acceleration and velocity time-history responses of the test data are compared with analytical predictions for the F28 forward section. Limited time-history comparisons are shown for simulations of the F28 forward section drop test in which the inertial properties of the seats, dummies, and restraint systems were represented using concentrated masses. Later, time-history comparisons were generated for simulations in which the seats, restraints, and dummies were modeled using finite elements; however, these results are not shown, and the reader is referred to Jackson et al. (Feb. 2018 and Apr. 2018). In addition, soil and airframe deformations are compared.

The test/analysis comparisons of vertical acceleration and velocity responses are shown in Figures 8.77(a) and (b), respectively, for the port window location at FS5805. At this location, the model exhibits four acceleration peaks; the first two peaks are higher in magnitude than the test, however the overall pulse durations are similar. It is also interesting to note that, even after

filtering using an SAE CFC 60 filter, the test signal contains more high-frequency content than the analysis. This finding is likely due to the damping effect of adding concentrated masses in the model. The velocity responses at this location, shown in Figure 8.77(b), indicate that both the test and predicted curves agree well during the initial portion of the pulse, up to approximately 0.015 seconds. After this time, the predicted response removes velocity more quickly than the test and crosses zero velocity slightly before the test response.

The test/analysis comparisons of vertical acceleration and velocity responses are shown in Figures 8.78(a) and (b), respectively, for the port aisle location at FS5805. The test and model acceleration time histories both indicate an initial negative peak of 25 g. Subsequently, the model exhibits two peaks of 50 and 30 g, but generally matches the test response following the first large peak. The velocity responses agree well, crossing zero velocity at approximately the same time and exhibiting similar rebound responses.

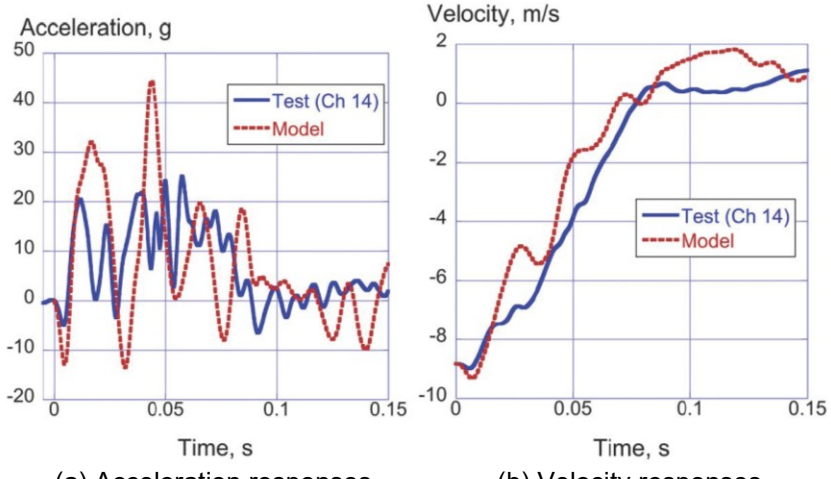

(a) Acceleration responses. (b) Velocity responses.

Figure 8.77. Vertical acceleration and velocity comparisons at the port window at FS5805 for the F28 forward section [Fig. 28 of Jackson et al., Feb. 2018].

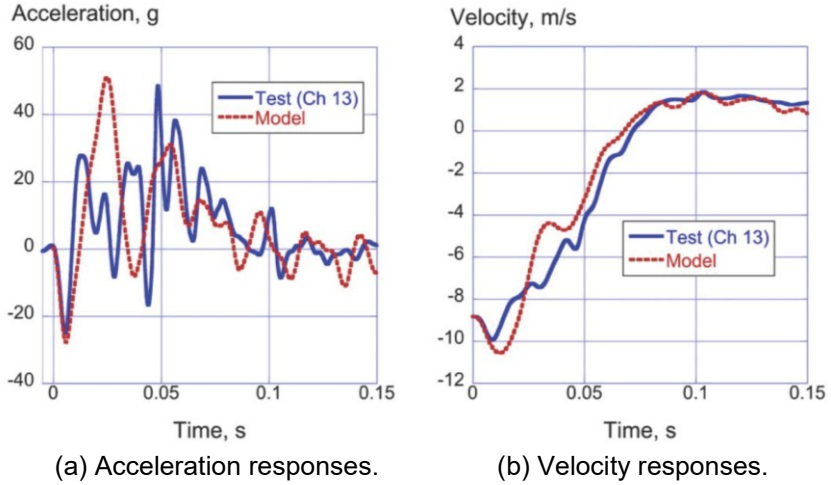

(a) Acceleration responses. (b) Velocity responses.

Figure 8.78. Vertical acceleration and velocity comparisons at the port aisle at FS5805 for the F28 forward section [Fig. 29 of Jackson et al., Feb. 2018].

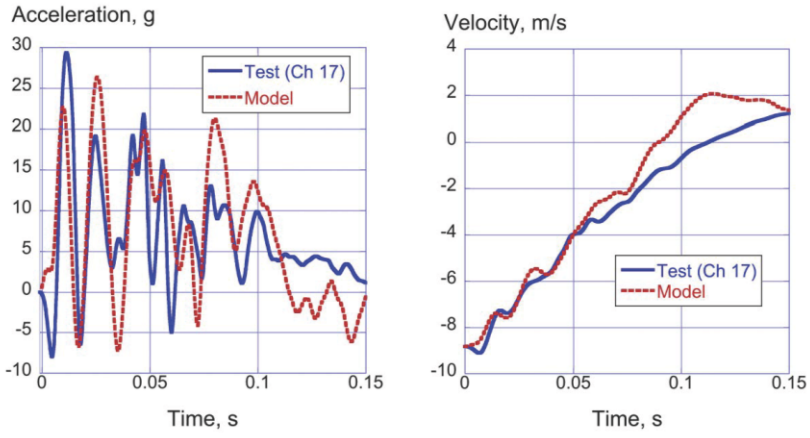

(a) Acceleration responses. (b) Velocity responses.

Figure 8.79. Vertical acceleration and velocity comparisons at the starboard window at FS5805 [Fig. 30 of Jackson et al., Feb. 2018].

The test/analysis comparisons of vertical acceleration and velocity responses are shown in Figures 8.79(a) and (b), respectively, for the starboard window location at FS5805. The test and model acceleration time histories agree very well, especially during the early part of the pulse. The simulation matches the magnitude and phase of the test oscillations, up to 0.075 seconds. After 0.075 seconds, the model overpredicts the magnitude of the test acceleration curve. The velocity responses agree very well, again up to 0.075 seconds. After this time, the two curves deviate and the model curve crosses zero velocity earlier than the test.

As a means of performing a more rigorous test/analysis comparison, the average acceleration was calculated for the experimental and analytical responses. The average acceleration was obtained by calculating the area under the acceleration curve from time zero to the end time of the pulse duration, and then dividing the area by the pulse duration. The pulse duration was determined as the time of maximum rebound. For the test responses, a pulse duration of 0.13 seconds was determined by averaging all of the individual pulse durations for each data channel. For the model, an average pulse duration of 0.128 seconds was calculated in a similar manner. These pulse duration values were used to determine average accelerations, which are listed in Table 8.4. Percentage differences between test and model data were calculated. All of the percentage differences are under 15 percent, indicating a good level of test/analysis agreement. Note that 5 of 7 data points are at or under 10 percent.

A post-test photograph of the F28 forward section is shown in Figure 8.80(a), in which the section has been completely unloaded, including removal of the hat racks, floor panels, and luggage. Discrete failure points at the floor level, as well as plastic deformation of the bottom centerline of the section, are evident. A picture of the model is shown at 0.038 seconds in Figure 8.80(b) without the luggage, hat racks, floor panels, and the soil impact surface. The model exhibits multiple failures of the floor support structure, especially in the central region of the floor. These failures are caused by flexure of the floor supports and pressure from the luggage. As the simulation progresses, these failures become more widespread. The test article exhibits plastic deformation and failures at the bottom centerline region, as shown in Figure 8.80(a). Floor-level failures include one complete separation of the seat tracks, and failures of the side-to-side floor support structure.

Table 8.4. Test-Analysis Comparisons.

Location	Average Acceleration, g		Difference (%)
	Test	Model	
Port window at FS5805	7.4	8.1	9.5
Port aisle at FS5805	8.05	8.24	2.4
Starboard window at FS5805	7.5	8.5	13.3
Port window at FS6805	7.6	8.2	7.9
Port aisle at FS6805	9.2	8.1	11.9
Starboard aisle at FS6805	7.84	7.65	2.4
Starboard window at FS6805	7.7	8.47	10.0

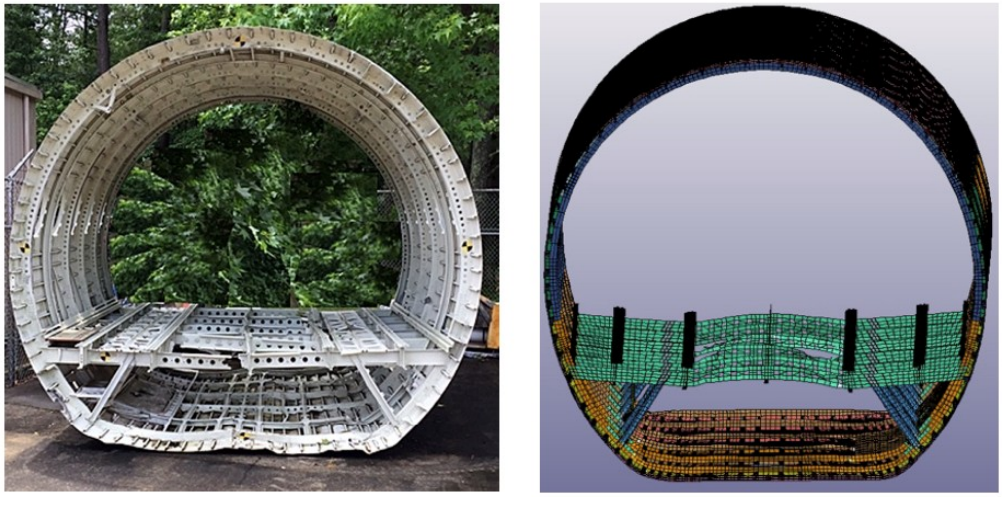

(a) Post-test photo. (b) Model depiction at t = 0.038 seconds.

Figure 8.80. Post-test photo and model depiction of the F28 section at 0.038 seconds [Fig. 35 of Jackson et al., Feb. 2018].

A photograph showing the crater created in the soil by the drop test of the F28 forward section is shown in Figure 8.81(a). The crater measured approximately 9 feet long by 7 feet, 4 inches wide. Depth measurements ranged from 0.25 to 1.75 inches. A fringe plot of z-displacement of the soil model is shown in Figure 8.81(b). Since the soil was represented using properties of hard soil, the maximum predicted soil depth was 0.14 inch, which is considerably less than the measured values. One explanation for the poor level of agreement may be that the soil mesh was fairly crude. In the F28 wing-box section simulation, a much finer soil mesh was used.

The experimental and analytical acceleration responses obtained for the F28 wing-box section were both filtered using an SAE CFC 60 low-pass filter [SAE (1995)]. Selected traces are shown. The predicted acceleration traces were output based on local coordinate systems that were defined at each concentrated mass on the seat tracks. The local coordinates can translate and rotate as the model deforms under impact loading. Thus, since these coordinate systems are not inertial systems, the data obtained using these coordinates cannot be integrated to obtain velocities or average accelerations. Therefore, no velocity comparisons are shown. Instead, plots

of test-analysis forward acceleration responses are included, as well as the vertical acceleration responses. It is important to note that, in this section of the chapter, the term “vertical” refers to acceleration responses that are normal, or perpendicular, to the floor of the fuselage section. Likewise, the term “forward” refers to acceleration responses that are parallel to the floor of the fuselage section.

The test-analysis comparisons of vertical acceleration responses are shown in Figure 8.82 for the port window location at FS10305 for the F28 wing-box section. Note that the forward acceleration data at this location (Channel 17) was over-ranged. The predicted vertical acceleration response matches the magnitude and shape of the test response, even though the peak acceleration of the test response is slightly underpredicted by 3 to 4 g.

The test/analysis comparisons of vertical and forward acceleration responses are shown in Figures 8.83(a) and (b), respectively, for the port aisle location at FS10305. Once again, the predicted vertical acceleration response matches the shape of the test response, however the magnitude is slightly underpredicted. Both acceleration responses exhibit two peaks just after 0.05 seconds, but the predicted response is on the order of 3 g lower in magnitude. As shown in Figure 8.83(b), the model does a reasonably good job of predicting the magnitude and shape of the forward acceleration test response, with the exception of a sharp peak in the model response at 0.065 seconds, which is not seen in the test response.

The test/analysis comparisons of vertical and forward acceleration responses are shown in Figures 8.84(a) and (b), respectively, for the starboard aisle location at FS10305. The predicted acceleration response matches the overall shape of the test acceleration response, but underpredicts the magnitude more dramatically. For example, the test response exhibits a peak of 26.7 g at 0.056 seconds. In comparison, the predicted peak acceleration is 16.9 g at 0.062 seconds. The comparison of forward acceleration responses is good, however, once again, the model exhibits a sharp peak at 0.065 seconds that is not seen in the test response.

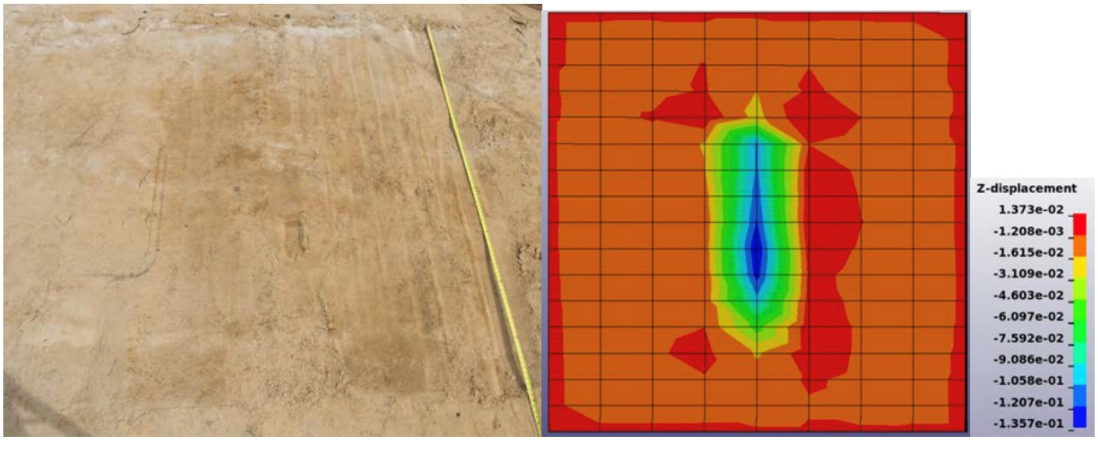

(a) Photograph of crater. (b) Fringe plot of z-displacement of soil.

Figure 8.81. Crater in soil created by the F28 forward section drop test and model deformation [Fig. 39 of Jackson et al., Feb. 2018].

Front- and rear-view photographs of the post-test F28 wing-box section are shown in Figures 8.85(a) and (b), respectively. By examining the front view, it is difficult to observe any regions of structural damage. However, the rear view shows damage that occurred in the lower cavity. This damage is highlighted in Figure 8.86, which shows buckling and tearing of a metal beam and failure of a lower frame. Deformation, yielding, and failure of the beams located in the lower cavity of the model are depicted in Figure 8.87 near the end time of the simulation. Note that the beams are shown in a prismatic format. This picture shows twisting of the beam cross-sections and buckling of the diagonal beams under compressive loading.

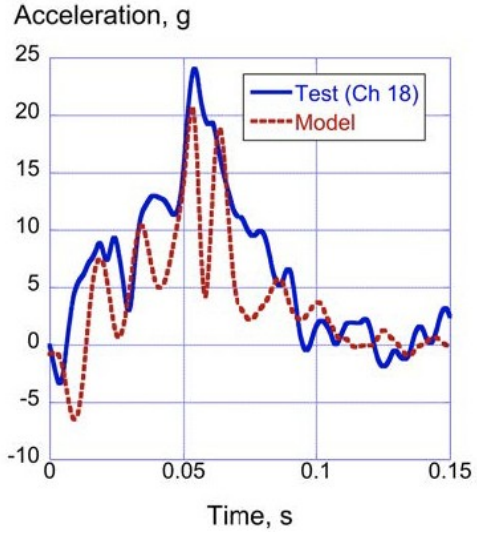

Figure 8.82. Vertical acceleration comparison at the port window at FS10305 for the F28 wing-box section [Fig. 43 of Jackson et al., Feb. 2018].

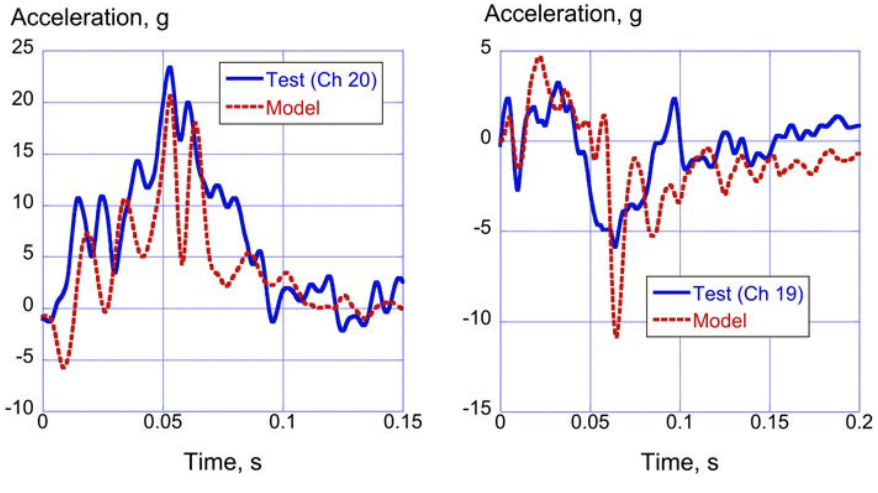

(a) Vertical acceleration responses. (b) Forward acceleration responses.

Figure 8.83. Vertical and forward acceleration comparisons at the port aisle at FS10305 (F28 wing-box section) [Fig. 44 of Jackson et al., Feb. 2018].

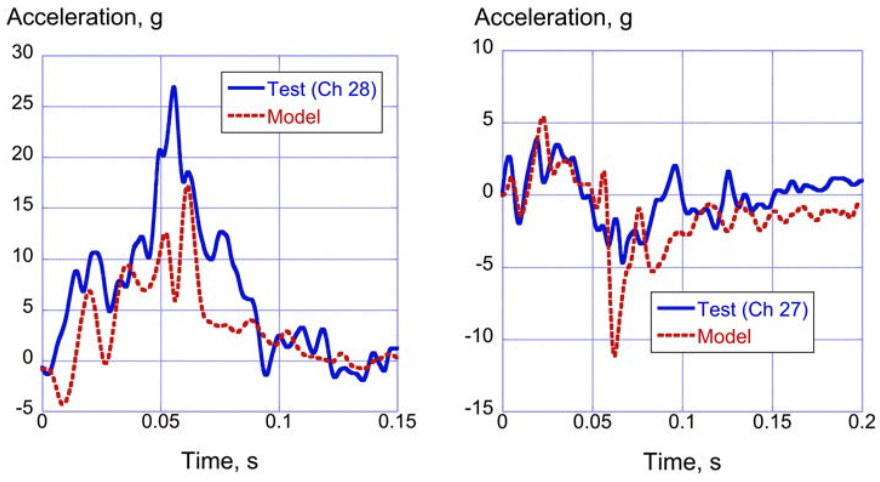

(a) Vertical acceleration responses. (b) Forward acceleration responses.

Figure 8.84. Vertical and forward acceleration comparisons at the starboard aisle at FS10305 (F28 wing-box section) [Fig. 45 of Jackson et al., Feb. 2018].

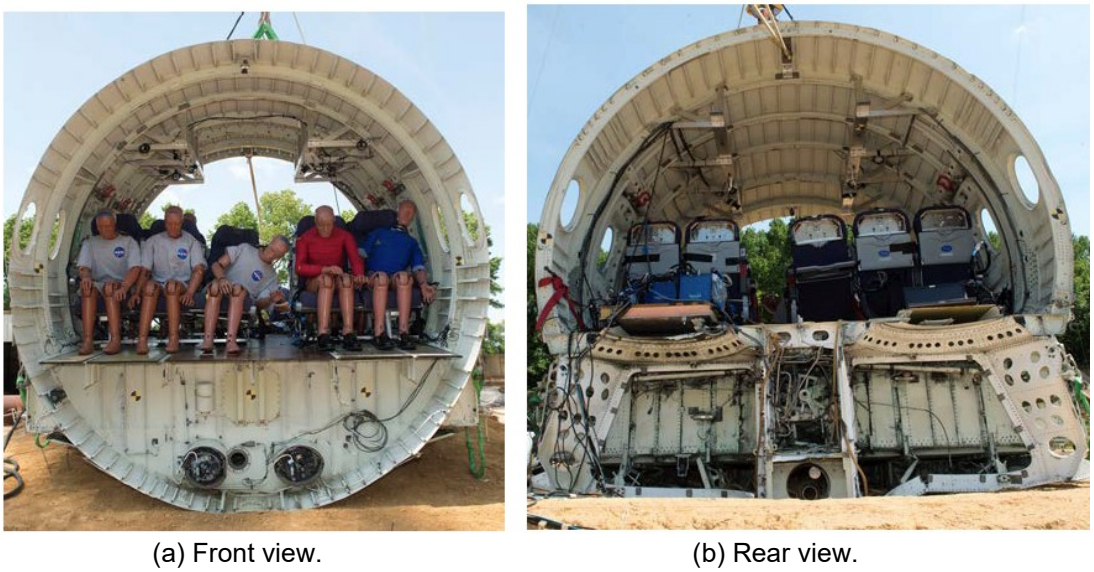

(a) Front view. (b) Rear view.

Figure 8.85. Two post-test photographs of the F28 wing-box section [Fig. 51 of Jackson et al., Feb. 2018].

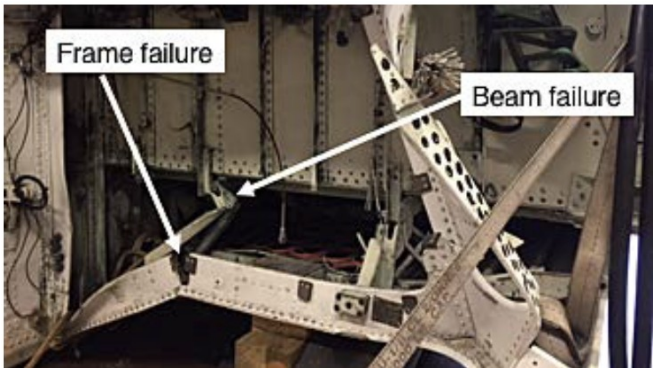

Figure 8.86. Close-up photograph showing damage to the F28 wing-box section [Fig. 52 of Jackson et al., Feb. 2018].

The crater made in the GUS soil following impact of the F28 wing-box section is shown in Figure 8.88. A maximum soil depth of 8 inches was measured at the initial impact location. Soil depths decrease with the distance away from the initial impact location. The two parallel lines evident in Figure 8.88 were created by two fore-aft beam supports, located on the bottom of the section. These beams tended to dig into the soil, leaving the visible marks shown in Figure 8.88.

A fringe plot of vertical (z) displacement is shown in Figure 8.88(b). This plot is taken near the end time of the simulation and shows a large amount of soil displacement (7.96 inches) at the point of section slap down. This behavior is not seen in the test, however the overall shape of the soil deformation pattern matches the test response, shown in Figure 8.88(a), well.

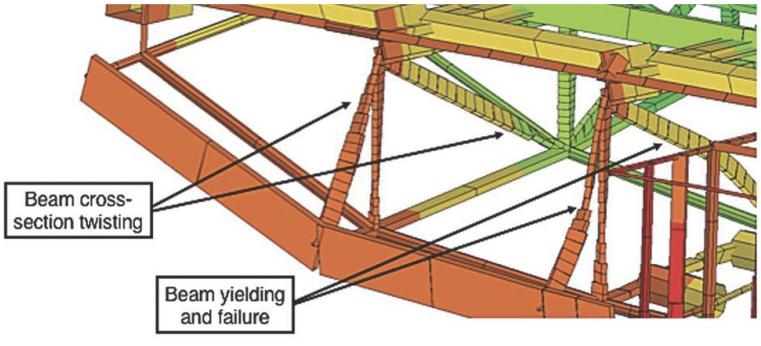

Figure 8.87. Predicted beam element deformation, yielding, and failure in the lower cavity [Fig. 53 of Jackson et al., Feb. 2018].

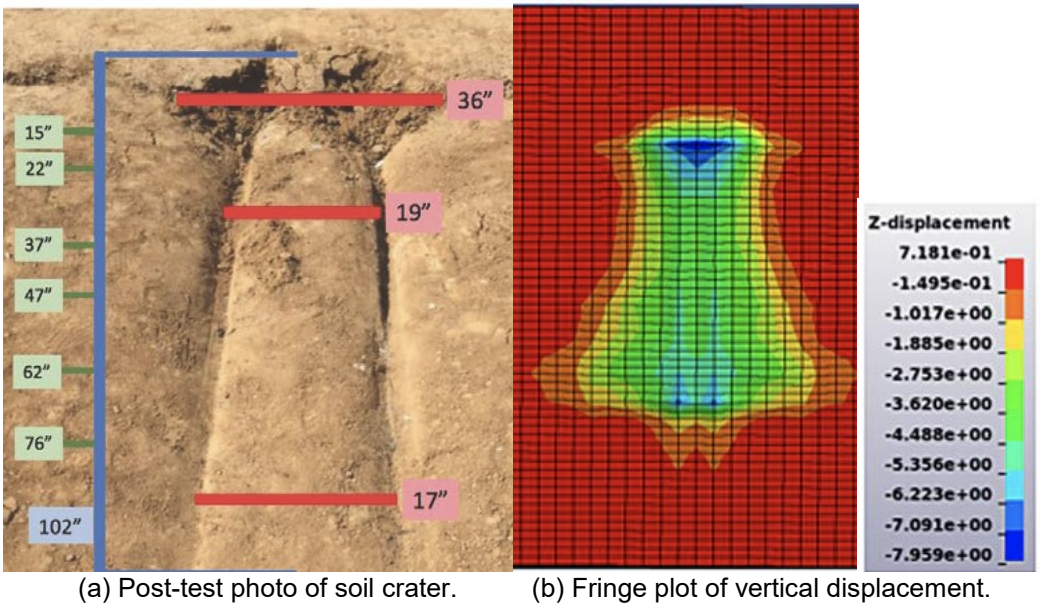

(a) Post-test photo of soil crater. (b) Fringe plot of vertical displacement.

Figure 8.88. Photograph of soil crater following the wing-box section drop test [Figs. 56 and 57 of Jackson et al., Feb. 2018].

Important Findings and Significance

The level of test-analysis agreement for the F28 section drop tests was excellent and provides an additional step towards the ultimate goal of certification-by-analysis.

SURVIVABLE AFFORDABLE REPAIRABLE AIRFRAME PROGRAM (SARAP)

In 2008, the Survivable Affordable Repairable Airframe Program (SARAP) Virtual Prototype and Validation (VPV) program was initiated between Sikorsky Aircraft Corporation and the U.S. Army Aviation Applied Technical Directorate (AATD). The objective of the program was to validate technology advances in design processes, structural efficiency, crashworthiness, materials and manufacturing processes, and reparability of rotorcraft airframe structures. The comprehensive SARAP VPV program included identification, review, and evaluation of various design, analysis, material, and manufacturing technologies [Carstensen et al. (2008)]. As part of this program, a prototype Technology Validation Article (TVA) was constructed, which was representative of the center section of a UH-60 Black Hawk helicopter, as shown in Figure 8.89. Following detailed design, manufacturing, and assembly, a full-scale vertical impact test of the TVA was performed at the LandIR facility at NASA Langley Research Center in August 2008. A post-test photograph of the TVA is shown in Figure 8.89. The purpose of the test was to evaluate the performance of a "tilting roof" concept that was intended to dissipate the kinetic energy of high-mass items, such as the rotor transmission, during a crash event [Carstensen et al. (2008)]. The tilting roof concept required controlled failures of the roof structure with energy absorption obtained through crushing of aluminum tubes.

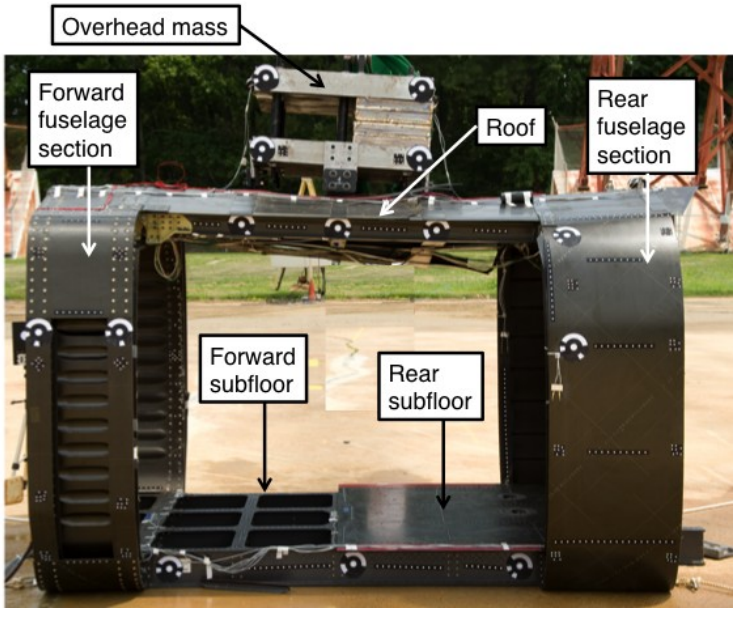

Figure 8.89. Post-test photograph of the SARAP TVA following the 2008 vertical drop test [Fig. 1 of Jackson et al., 2014b].

Post-test inspection of the TVA indicated that damage was primarily limited to the roof area, with little or no damage found in the subfloor, or the forward framed fuselage section. In 2010, NASA Langley obtained the residual SARAP hardware for testing under the NASA Subsonic Rotary Wing Aeronautics Program in crashworthiness research. In May 2011, NASA and Sikorsky signed a Space Act Agreement allowing cooperation between the two organizations to pursue common research interests, including composite material and airframe structural testing under dynamic loading, development of accurate and robust material models to predict aircraft structural response using LS-DYNA, and validation of analytical models through test-analysis correlation [Jackson et al. (2014b), Jackson et al. (June 2014), and Fasanella et al. (June 2014)].

The objective of the joint research program was to assess the capability of LS-DYNA in predicting damage initiation and progressive failure of composite airframe structures subjected to crash loading. Finite element models were developed to represent each of the test articles and simulations were conducted using LS-DYNA. Specifically, two composite material models were evaluated: MAT_ENHANCED_COMPOSITE_DAMAGE (Mat 54), a progressive failure model that uses the Chang-Chang failure criterion to simulate ply-by-ply failure and property degradation, and MAT_LAMINATED_COMPOSITE_FABRIC (Mat 58), a continuum damage mechanics model for representing unidirectional tape and fabric composite materials. Sikorsky provided the material property values for Mat 54, whereas properties for Mat 58 were determined by assessing literature data, by comparing with similar Mat 54 values, and by using a trial and error process in which laminated coupons were simulated under both tensile and compressive loading.

The SARAP residual hardware arrived at NASA in excellent shape. Care was taken to determine the most appropriate use for each portion of the residual hardware to optimize the data generated. Specimens were chosen such that the hardware could be tested from the coupon level all the way to full-scale impact testing. The final layout provided six different types of specimens, with a potential for a future seventh specimen. A depiction of the SARAP residual hardware utilization is shown in Figure 8.90.

The SARAP TVA was manufactured of graphite unidirectional tape composite with a thermoplastic resin system that was cured using both autoclave and in situ techniques. However, the framed fuselage sections on either end of the TVA were constructed primarily of a plain-weave graphite fabric material with a thermoset resin system. Since the TVA had been previously subjected to a fairly severe vertical impact test condition (252 in/s), it was necessary to evaluate the structural integrity of the test specimens extracted from the post-test TVA. Nondestructive Evaluation (NDE) methods were used to assess the smaller coupons and components. Results of these inspections showed that some areas of possible damage were identified for the larger components (I-beams, T-sections, and cruciform sections). However, no specific identifiable flaws were found. Consequently, these specimens were included in the experimental program.

One of the specimens that was tested originally was the I-beam specimen, which was 4.56 inches tall and 6.2 inches wide, with the lower end potted into a rigid foundation such that the main axis of the I-beam was oriented vertically. Corner notches with a 45-degree chamfer angle were cut into the upper ends of the web to initiate specimen crushing and to reduce peak accelerations upon initial contact with the drop mass. A vertical test was conducted by releasing a 204.8-pound drop mass from a height of 4 feet using a 14-foot vertical drop tower, which impacted the upper

end of the I-beam with a measured velocity of 189.6 in/s. Instrumentation included two accelerometers on the drop mass, and a stochastic speckle pattern was painted on the I-beam web for collecting full-field strain photogrammetric data. A labeled schematic and photograph of an I-beam specimen are shown in Figure 8.91.

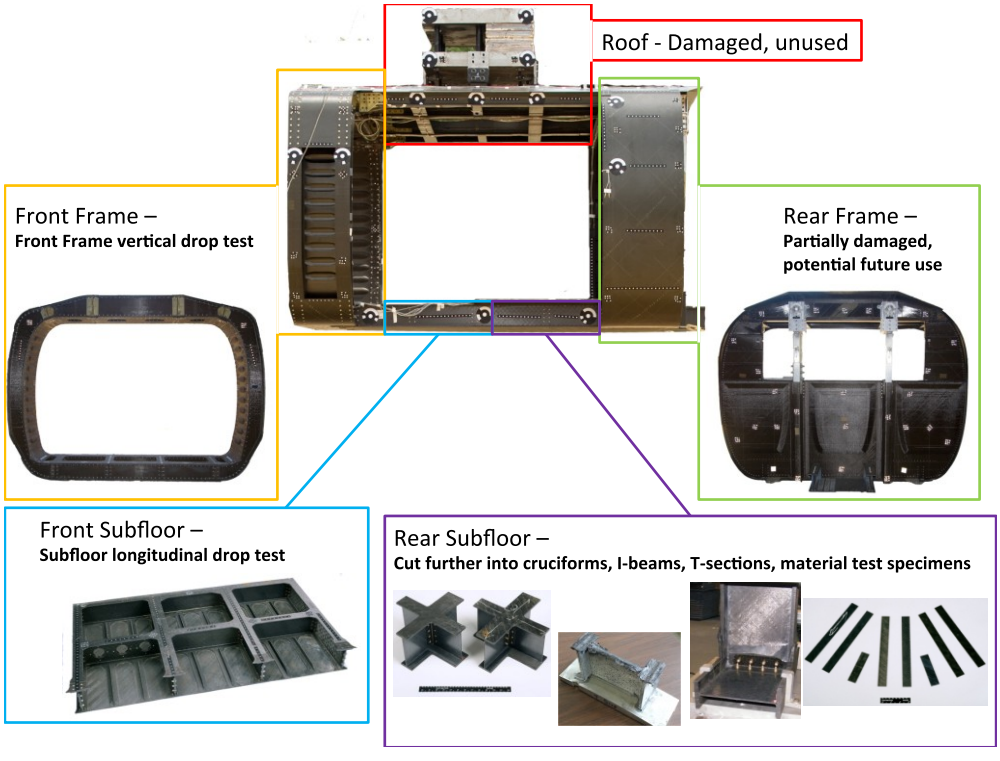

Figure 8.90. SARAP residual hardware utilization [Fig. 2 of Jackson et al., 2014b].

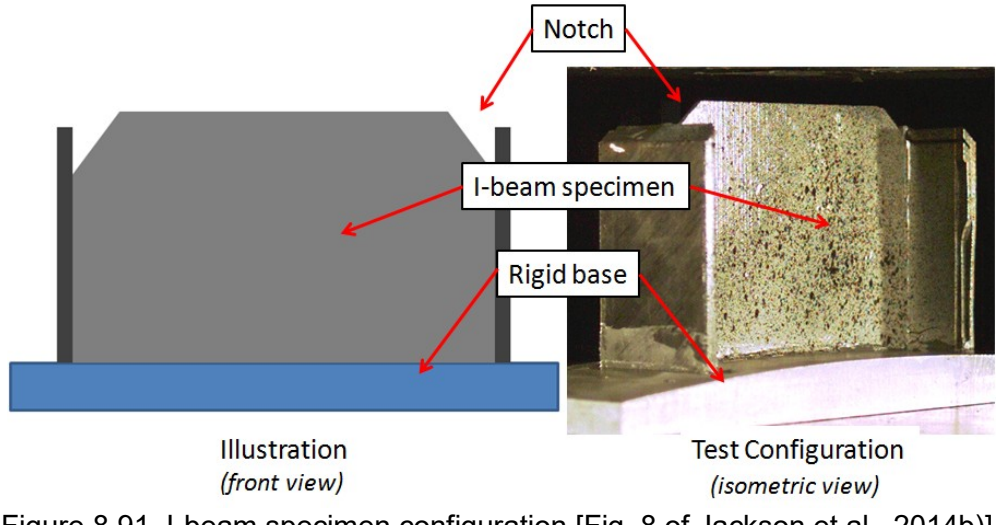

Figure 8.91. I-beam specimen configuration [Fig. 8 of Jackson et al., 2014b)].

An image sequence of structural deformation is shown from the front face of the specimen in Figure 8.92. The upper left image in Figure 8.92 shows the specimen 1 ms before impact. The upper right image shows the specimen 1 ms after impact. At this time, the drop mass has begun crushing the upper edge of the web section, and has just contacted the outer flanges, which were approximately 1/16th of an inch shorter than the web. At 5 ms after impact, the top portion of the I-beam web is crushing with many of the composite layers delaminating and subsequently bending locally at the top of the web. The side flanges have begun to crush, but are not exhibiting significant amounts of delamination. At 10 ms after impact, material crushing and delamination from both the web and flanges can be seen. This time also corresponds to the approximate time of maximum displacement of the impact mass.

Photogrammetric data were collected and sampled at 15 kHz. Compressive strains at two distinct times during the crushing sequence are shown in Figure 8.93. The compressive strain at 1 ms after impact, which occurs on the upward side of the acceleration curve, is shown in Figure 8.93(a). The stress wave can be seen in the specimen by noting that, near the top where the drop mass is touching the specimen, strains are between –0.8 and –1.0 percent. The corners appear to have slightly larger strains, which could potentially be due to an uneven surface at the free edge of the specimen. However, the fixed end of the specimen exhibits between 0.0 and –0.2 percent strain, indicating that the stress wave has not travelled through the specimen and the strain is not fully developed at the fixed end.

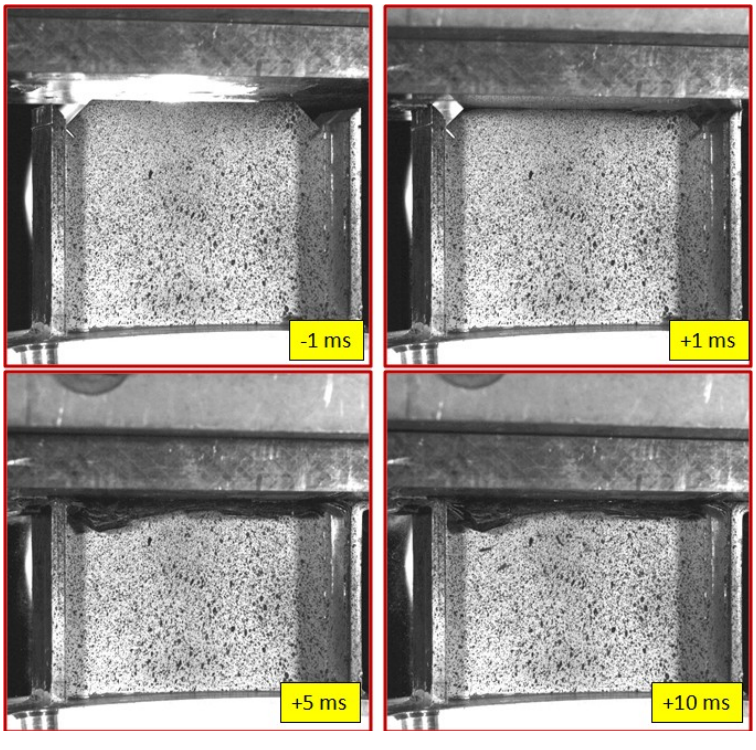

Figure 8.92. Image sequence of the I-beam 4-foot drop test [Fig. 9 of Jackson et al., 2014b].

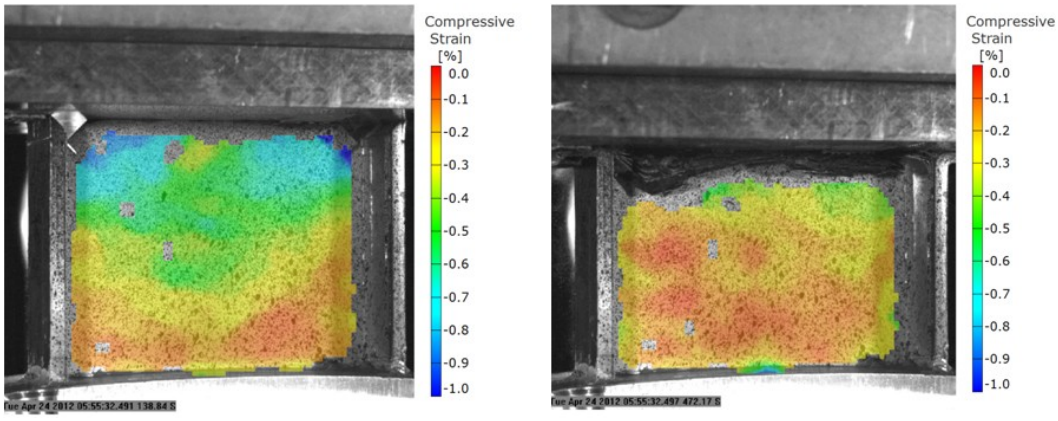

(a) Time = 1 ms. (b) Time = 7.2 ms.

Figure 8.93. Compressive strain at 1 ms and 7.2 ms after impact of the I-beam [Fig. 12 of Jackson et al., 2014b].

Figure 8.93(b) shows the compressive strain at 7.2 ms after impact, or, more specifically, the time of maximum acceleration. Layer delaminations and bending interfere with viewing the uppermost edge of the crush front, so strains cannot be resolved up to the edge. However, by comparison of the two images, much of the middle region of the specimen that once exhibited –0.5 percent strain (in green) is now closer to 0.0 percent strain (in orange). The entire visible portion of the strain data on the specimen is exhibiting this low 0.0 percent value. These results indicate that the strain has become localized in the crush front. This finding is confirmed by examining the videos and pictures post-test. Visual inspections show that the majority of the specimen away from the crush front has stayed intact. Almost all of the damage has occurred at the crush front, and it is best characterized by layer delamination and bending with large amounts of material crushing.

A photograph of the specimen post-test is shown in Figure 8.94. The photogrammetric measurements are confirmed when looking at the failure patterns. The impact surface shows signs of ply delamination, material crushing, and localized bending, while the bottom of the specimen, which is fixed into the rigid base, exhibits no failure.

Finite element models were developed to represent each of the component test articles and simulations were conducted using LS-DYNA. Within LS-DYNA, two composite material models were evaluated: MAT_ENHANCED_COMPOSITE_DAMAGE (Mat 54), a progressive failure model that uses the Chang-Chang failure criterion to simulate ply-by-ply failure and property degradation, and MAT_LAMINATED_COMPOSITE_FABRIC (Mat 58), a continuum damage mechanics model for representing unidirectional tape and fabric composite materials.

An FEM, depicted in Figure 8.95, was developed to simulate dynamic crushing of the I-beam specimens. The model consisted of 24,300 nodes, 3,050 Belytschko-Tsay (ELFORM=Type 2) quadrilateral shell elements representing the I-beam with a nominal element edge length of 0.125 inches, and 16,400 solid elements representing the drop mass. Either Mat 54 or Mat 58 were assigned to the shell elements representing the I-beam, whereas Mat 20 (MAT_RIGID) was assigned to the drop mass. The density of the rigid material was adjusted to ensure that the weight of the drop mass matched that of the test (204.8 pounds). Seven different parts were used including one part for the drop mass, and six parts representing different regions of the I-beam.

Several different PART_COMPOSITE cards were created to represent the upper edges of the I-beam flanges that incorporated ply drop-offs to mimic the reduced thicknesses produced by chamfering. I-beam models were executed using LS-DYNA SMP Version 971 R6.0.0 with double precision and required 5 hours and 51 minutes of CPU on four Linux-based processors for an end time of 0.02 seconds. Finally, the nodes forming the drop mass were assigned an initial velocity to match the test condition of 189.6 in/s. Output from the model included acceleration-, velocity-, and displacement-time histories of a central node on the drop mass, as well as pictures of model deformation.

Poor results were obtained using the Mat 54 material model. Essentially, the model failed in a brittle fashion, exhibiting very little energy absorption. Numerous parameter studies were conducted in an attempt to obtain stable crushing of the model. However, all models provided similar results. Predicted acceleration responses consisted of a series of spikes representing repeated contact and release of the drop mass onto the I-beam. These short-duration spikes occur early in the pulse. Only 50 in/s of velocity is removed during the simulation through failure of the I-beam. The vertical displacement of the drop mass is not alleviated and it continues to displace linearly without abatement. The model fails catastrophically with no sign of stable crushing. The model loses the bottom nodal constraints, as elements are failed and removed.

In contrast, the Mat 58 predicted responses show good agreement with the overall shapes, magnitudes, and pulse durations of the experimental curves, as shown in Figure 8.96. The experimental and predicted acceleration responses were filtered using a 1,000-Hz Butterworth low-pass filter. The displacement results, shown in Figure 8.96(c), include the Mat 58 predicted response, the responses based on double integration of the acceleration data and photogrammetry. The maximum crush displacement predicted by the model (0.85 in.) falls between the experimental results (0.82 to 0.86 inches). A sequence of model deformation is shown in Figure 8.97 for four time steps. These depictions show that the I-beam model exhibits stable crushing from the top edge, matching the deformation patterns of the test article, depicted in Figure 8.92. No global buckling is evident, though some folding of the webs is observed.

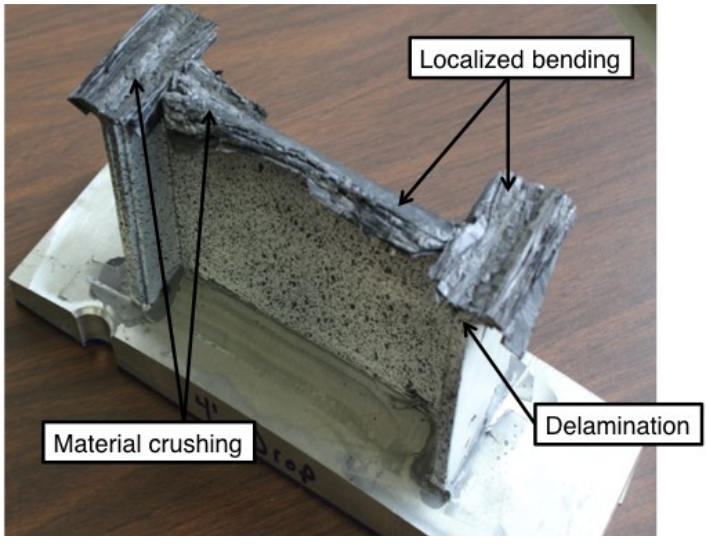

Figure 8.94. Post-test photograph of the I-beam tested at a 4-foot drop height [Fig. 13 of Jackson et al., 2014b].

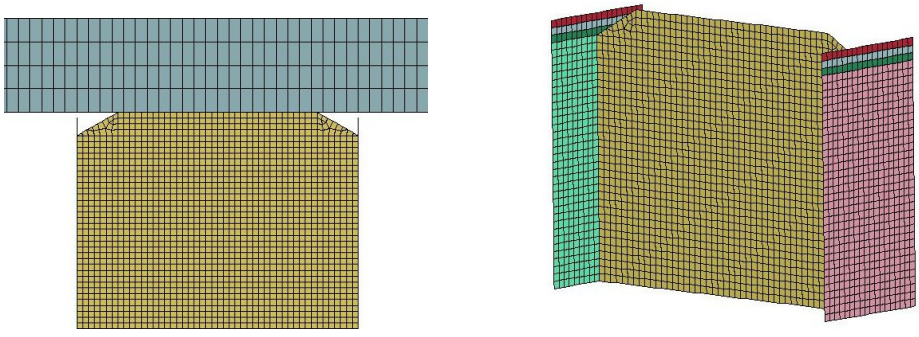

(a) Front view with drop mass. (b) Three-quarter view without drop mass.

Figure 8.95. LS-DYNA model of the I-beam component [Fig. 83 of Jackson et al., 2014b].

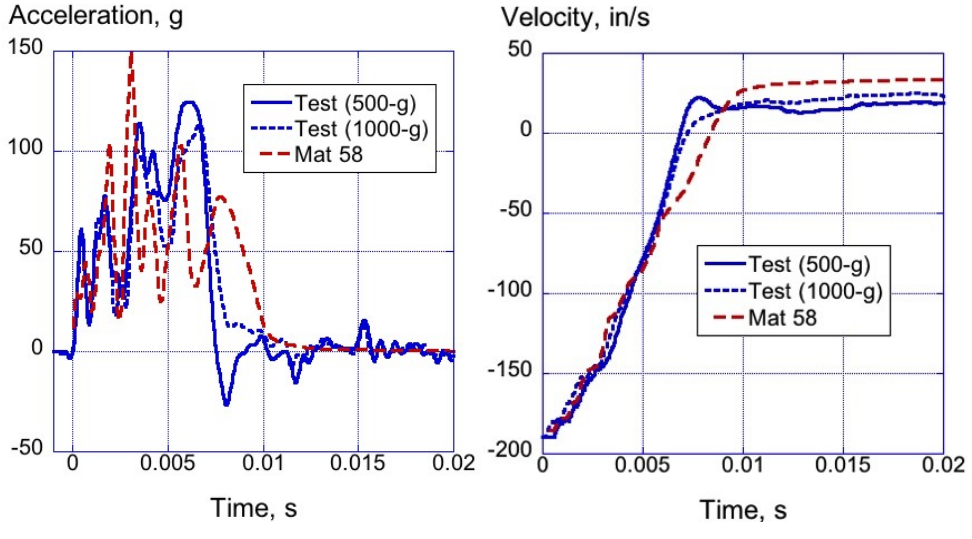

(a) Acceleration responses. (b) Velocity responses.

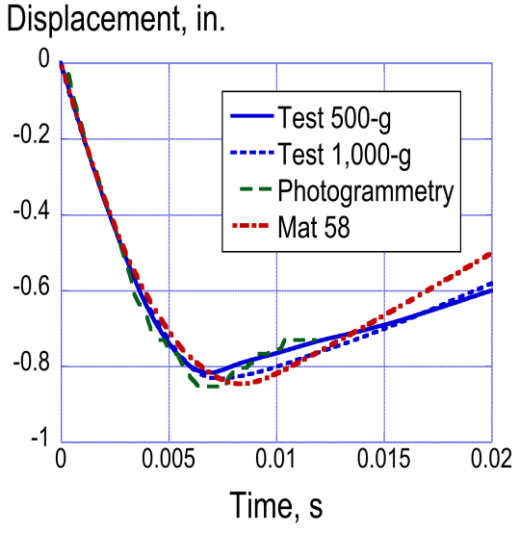

(c) Displacement responses.

Figure 8.96. Experimental and Mat 58 analytical results for the I-beam 4-foot drop test [Fig. 86 of Jackson et al., 2014b].

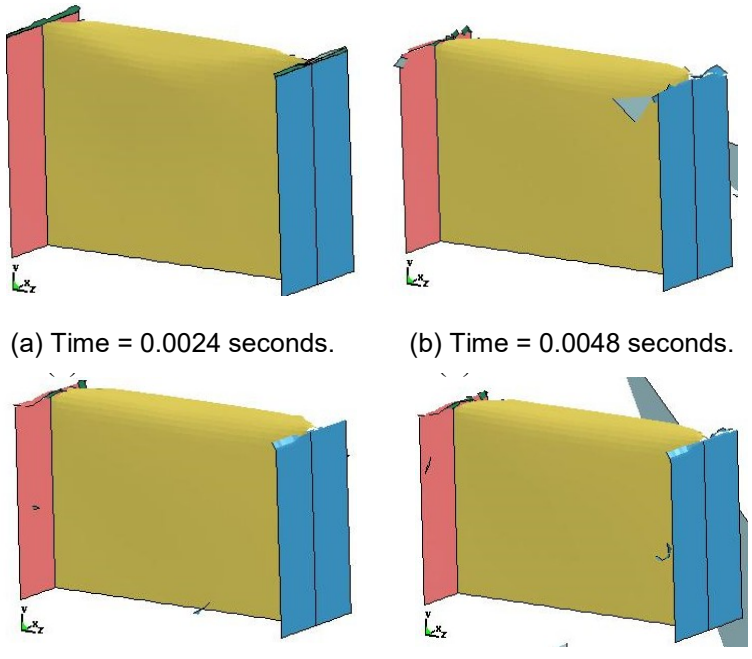

(a) Time = 0.0024 seconds. (b) Time = 0.0048 seconds.

(a) Time = 0.0072 seconds. (b) Time = 0.01 seconds.

Figure 8.97. Time sequence of I-beam model deformation for Mat 58 [Fig. 87 of Jackson et al., 2014b].

Many additional specimens such as T-sections, cruciform sections, a large subfloor section, and a forward framed fuselage section were tested under impact loads and simulated using LS-DYNA with both Mat 54 and Mat 58. Test-analysis comparisons were generated for each test article [Jackson et al. (2014b), Jackson et al. (June 2014), and Fasanella et al. (2014)].

Important Findings and Significance

A variety of composite failure modes were evident during testing including brittle fracture, crushing of the material, ply delamination, layer splitting, and localized bending. The I-beam specimen exhibited uniform crushing of the material from the top edge that was aided by the presence of a crush initiator. The ability to accurately model so many different structural deformation and composite failure modes is a major challenge for the current generation of nonlinear, explicit transient dynamic finite element codes.

Tests of the SARAP components were simulated using LS-DYNA shell-based FEMs. The shell elements were assigned either Mat 54 or Mat 58 material models to represent the behavior of the composite structure. In general, poor levels of correlation were seen when the Mat 54 model was used. The Mat 54 models tended to fail catastrophically in a brittle fashion, absorbing little kinetic energy.

Unlike Mat 54, Mat 58 incorporates parameters such as SLIMs and ERODS, which allow the analyst to incorporate some degree of plastic-like behavior into the model. For each of the component simulations, a parametric study was performed to evaluate the influence of ERODS. Results indicate that setting ERODS correctly is important in capturing the observed behavior. The ERODS parameter allows failed elements to carry small stresses, yet remain in the model.

As seen when using Mat 54, once elements are removed from the simulation, holes are created in the model, resulting in stress concentrations. The model can quickly unzip and collapse. In general, the capability of LS-DYNA to accurately predict all of the composite failure modes is inconsistent. Material crushing of the I-beam components was successfully simulated, however debonding and delamination were not predicted. Current composite material models such as Mat 54 and Mat 58 are not capable of predicting delamination based on either fracture mechanics or energy-based approaches. However, if the location of a potential delamination or debond is known, the model could be modified to account for this failure mode using either tiebreak contact definitions or spot weld connections [Fleming (2000) and Fleming et al. (2008)].

FULL-SPECTRUM CRASHWORTHINESS

Crashworthiness requirements for military rotorcraft are defined by MIL-STD-1290A (AV) (1988), which was cancelled in the mid-1990s but reinstated, without revision, in 2006. The Aircraft Crash Survival Design Guide (ACSDG) (1989) provided the basis for MIL-STD-1290. The ACSDG describes every aspect of a crashworthy design and defines a set of crash scenarios that can be survivable if an aircraft is properly designed. This guidance significantly influenced the design of the AH-64 and UH-60 aircraft in the 1970s. Their performance in crash conditions has shown a great improvement over previous generation helicopters [Safe (2009)].

Over the years, there has been repeated discussion about the need to revise crashworthiness design criteria and crashworthiness qualification methodology. Over time, more mishap data becomes available; tactics, techniques and procedures change; new technologies are developed; and modeling and simulation capability improves. In addition, limitations of existing guidance become more evident. The ACSDG was first published in 1967 with revisions made in 1969, 1971, 1980, and lastly in 1989. MIL-STD-1290 was first published in 1974 and then revised in 1988. Aeronautical Design Standard (ADS) 36 was put together in 1987 and applied only to the Army Light Helicopter development program and has since been cancelled. As the Department of Defense (DoD) moves forward with the development of future systems such as Unmanned Aerial Systems (UASs) and the Joint Multi-Role (JMR), and upgrades of current fleet helicopters, questions have arisen regarding the adequacy of existing specifications and guidelines. The impact of future operations and environments and advanced design configurations on crashworthy design are not fully understood.

Adequate guidelines do not exist to ensure crashworthiness of new-generation rotary wing aircraft in these broad ranges of gross weights. Evidence also suggests that military helicopters are flying lower and faster than anticipated in the ACSDG, and that most crashes do not occur at structural design gross weight on prepared surfaces [Safe (2009)]. Furthermore, past crashworthiness design guidance applied primarily to UH-60- and AH-64-sized and light fixed-wing aircraft. Work has been done to correlate helicopter size and mission to reasonable crash criteria, but it does not address very large rotorcraft and multiple impact surfaces [Simula (1990)]. Many questions exist regarding the appropriate criteria to apply to very large new-generation rotorcraft such as the JMR and larger UASs with expensive payloads, or any other rotorcraft not addressed by previous guidance and requirements such as MIL-STD-1290A (1988).

Even with the current fleet of helicopters, technology could be applied to improve crashworthiness over a range of crash impact surfaces (hard, soft soil, and water), operating weights, and pitch/roll attitudes. All attributes are tradable in a new aircraft design. There is difficulty in comparing crashworthiness qualities from one aircraft design to another. A comparative metric, along with adequate tools, needs to be developed to apply a systems approach to crashworthiness at minimum cost and weight. Despite differences in aircraft, the basic criteria that need to be met to ensure post-crash survival of human occupants remain the same and are typically understood by the acronym CREEP [Shanahan (2004)]:

(1) Container—The structure must provide for a survivable space for the occupant. The survivable space must be free of intrusion, and the occupant must be able to survive inside the container and be able to egress after the crash.

(2) Restraint—proper restraint prevents flailing, distributes loads over the body.

(3) Environment—proper equipment is in place to ensure that occupants are able to survive in the environment that they are operating in. This feature includes taking into account flail envelopes, and eliminating sharp edges and impaling hazards.

(4) Energy Absorption—crash energy is dissipated in a controlled manner.

(5) Post Crash Factors—occupants are able to egress and survive until rescued. Fires are mitigated; emergency locator transmitters provide accurate data to allow for a rescue in the shortest time practical.

The Full Spectrum Crashworthiness (FSC) document addresses the evolution of crash survival design criteria, their influence on rotary wing aircraft crashworthiness, and the application of new and evolving technology to current and next-generation DoD helicopters [Bolukbasi et al. (2011), Pellettiere et al. (2011), and Crocco (2012)]. Emphasis is placed on the need for a total system approach in design for crashworthiness, the need to consider crashworthiness early in the design phase of new aviation development efforts, and the need to consider the crash performance of the aircraft/rotorcraft throughout its life span. Consequently, effective crashworthy designs must consider all likely sources of injury, eliminate or mitigate as many as practicable for likely crash scenarios, and do so at an acceptable cost and weight.

Important Findings and Significance

The FSC criteria establishes a new standard for implementation, starting in the initial stages of system design, for a wide range of rotorcraft classes, types, configurations, and operating conditions that continue over the life cycle of the rotorcraft system. These criteria will identify the key components that contribute to a system's crashworthiness and will provide a quantitative measure of crashworthy performance that is relevant to user needs and future operating environments.

RECOMMENDATIONS FOR FUTURE ROTORCRAFT CRASHWORTHINESS RESEARCH

Recommendations are provided, such that the progress made to date in improved rotorcraft crashworthiness can be continued into the future [Jackson (2018)]. Note that this list represents the author's opinion and does not represent official government policies. The 10 recommendations are categorized by facilities and equipment for conducting crash testing, updated crash certification requirements, the application of crash modeling and simulation techniques, and rotorcraft structural design for improved crash performance.

Facilities and Equipment for Conducting Aircraft Crash Testing

(1) The U.S. Government should take a lead role in maintaining state-of-the-art facilities for aircraft/rotorcraft crash testing and in upgrading equipment used to support crash testing as technology continues to advance. This recommendation is especially focused on the Landing and Impact Research (LandIR) facility at NASA Langley, which has been, and continues to be, threatened with closure and demolition over the past several years.

(2) Anthropomorphic Test Device (ATD) manufacturers are urged to develop an ATD for vertical impact loading. While the market for these ATDs would be relatively small in comparison with the automotive industry, the need exists and it is important. Today, aircraft seats are being certified using ATDs that were designed and calibrated specifically for automotive crashes. Note that the U.S. Army has invested in development of Warrior Injury Assessment MANikin (WIAMAN), which is an ATD designed for under-body blast [Baker et al. (2016)]. This ATD has been specifically developed to overcome some of the deficiencies of existing ATDs, including providing accurate vertical loading along the spine.

Updated Aircraft Crash Certification Requirements

(3) It is recommended that the Army, Navy, Marine Corps, and the FAA, with help from the National Transportation Safety Board (NTSB), perform routine decadal accident surveys on both military and civilian aircraft/rotorcraft mishaps. Accident studies conducted in the 1970s were used in development of MIL-STD-1290A (AV) crash requirements. Army- and Navy-sponsored accident studies were performed in 2009 at the request of the U.S. Congress. The long time span between accident studies is unacceptable. Information gained through decadal accident surveys would be used to assess the general level of crash performance of aircraft, to highlight specific issues that might need to be addressed, and to provide evidence that crash certification requirements are acceptable or need to be adjusted.

(4) It is recommended that whole-aircraft crash certification requirements be developed for civilian aircraft (general aviation to transport aircraft) and rotorcraft. An Aviation Rulemaking Advisory Committee (ARAC) was established to provide recommendations to the FAA regarding the incorporation of airframe-level crashworthiness and ditching standards into Title 14 CFR Part 25 for transport aircraft. The ARAC should complete its work and provide recommendations in 2018 [Federal Register (2015)].

(5) It is recommended that the necessary steps be taken to build confidence in crash certification-by-analysis. Analysis is not envisioned to replace full-scale crash testing, but rather to limit the number of tests that may be necessary for certification.

Crash Modeling and Simulation Techniques

(6) It is recommended that accepted metrics for test-analysis correlation be developed and utilized. These metrics should be established industry-wide as a standard. Many methods exist that could be selected, ranging from Sprague and Geers (2003) to International Standards Organization 16250 (2013) to Correlation of Analysis (CORA) [Thunert (2012)]. Perhaps, the recommended practice developed by the Society of Automotive Engineering (SAE) for seat certification-by-analysis could be leveraged [SAE (2015)]. This document describes the use of modeling and simulation approaches for seat certification and provides guidelines for calibrating analytical or virtual ATD models. As a suggestion, a technical committee or subcommittee of the Vertical Flight Society (VFS), SAE, or the American Institute of Aeronautics and Astronautics (AIAA) could be formed to review existing methods and make a recommendation, similar to the approach reported in Schwer (2007).

(7) It is recommended that accurate ATD models be developed, such that the model reliably and accurately predicts the response of ATDs subjected to impact loading in the vertical, or combined forward and vertical, directions. Currently, ATD test responses obtained during a crash test are compared with ATD model predictions to determine the likelihood of major injuries. In the near future, the impact responses could be used to assess soft-tissue injuries using human occupant models such as the one developed by the Global Human Body Model Consortium (GHBMC) [Schwartz (2015), and Combest and Wang (2016)] or the Total Human Model for Safety (THUMS) [Iwamoto et al. (2007)].

Structural Design for Improved Aircraft Crashworthiness

(8) Development of an energy-absorbing subfloor concept optimized for multi-terrain impact is recommended. This recommendation is especially challenging. The difficulty of this task lies in the fact that the dynamic responses of airframe structures subjected to impact onto rigid surfaces, soft soil, and water, are very different. For a single structure to produce an acceptable crash response for all of these surface conditions will be extremely difficult.

(9) Designers should continue to apply the systems approach to crash safety. The systems approach works, without adding weight to the design. Designers are urged to continue to use composite materials in structural design for improved efficiency.

(10) Finally, in the future, novel aircraft/rotorcraft configurations will be developed, and the crash behavior and certification requirements of these new designs may require rethinking. The aviation community is urged to ensure that crash safety is considered, especially during early stages of design.

CONCLUSIONS

This chapter documents the results of a research program in rotorcraft crashworthiness conducted at NASA Langley over the past 10 years (2009–2018). Under a Space Act Agreement (SAA), NASA performed several drop tests of a redesigned skid gear for the HX-2 Wasp kit-built helicopter. This test program offered an opportunity to evaluate dummy models within LS-DYNA. This research project led to Yvonne Fuchs winning the Robert L. Lichten Award from the Vertical Flight Society. Two full-scale crash tests of an MD-500 helicopter were performed. The first test was performed to evaluate a novel Deployable Energy Absorber (DEA), while the second test was conducted without the DEA as a baseline. The DEA crushed on impact and limited the acceleration levels transferred to the occupants to extremely low levels. A system-integrated finite element model (FEM) was developed for execution in LS-DYNA that included the skid gear, airframe, DEA, seats, restraints, Anthropomorphic Test Devices (ATDs), and overhead ballast. Predictions of floor-level acceleration responses compared well with test data, however predicted occupant responses did not match the ATD responses.

As a result of the MD-500 test and analysis program, two follow-on projects were conducted. First, a series of vertical drop tests were conducted on ATD occupants (Hybrid III with a straight spine, Hybrid III with a curved spine, Hybrid II with a straight spine, and the Test Device for Human Occupant Restraint (THOR) 50th-percentile ATD). The fully instrumented ATDs were seated in a rigid platform that was attached to the rails of a 14-foot drop tower. The seated ATD was raised to the drop height and released to impact a layered paper honeycomb wedge, which tailored the acceleration pulse. In addition to the test program, ATD models were obtained and executed. Results of the test-analysis effort showed that the commercial dummy models provided excellent comparisons with test data, whereas the LSTC downloadable model did not. Also, the THOR model provided excellent prediction of the THOR test response.

A second follow-on project was focused on MD-500 model calibration. Essentially, the system-integrated model of the MD-500 with the DEA was intended to be validated through test-analysis comparison. The model, which was developed for the purposes of predicting acceleration responses from the first crash test, was inadequate when evaluating the more severe conditions seen in the second crash test. A newly developed model calibration approach that includes uncertainty estimation, parameter sensitivity, impact shape orthogonality, and numerical optimization was used to calibrate model results for the second full-scale crash test. This combination of heuristic and quantitative methods was used to identify modeling deficiencies, evaluate parameter importance, and propose required model changes. At the conclusion of the study, guidelines were recommended for future test-analysis comparison studies.

The development and evaluation of two composite energy absorbers, designated the conusoid and the sinusoid, were highlighted. The development process was based on a building-block approach that had been previously documented. The first stage of development involved coupon testing to generate material response data. Next element/component level testing and evaluation was performed. This evaluation involved conducting vertical drop tests of conusoid and sinusoid energy-absorbing components to determine if they achieved the design goals, which they did. Finally, the conusoid and sinusoid energy absorbers were retrofitted into a CH-46E Sea Knight helicopter and a full-scale crash test was conducted. Unfortunately, based on soil anomalies during the crash test, a true assessment of conusoid and sinusoid energy absorption behavior as retrofit concepts could not be performed.

This paper includes a summary of bird strike simulation work, which was performed cooperatively with NASA Glenn Research Center. In addition, NASA was a participant in the Full Spectrum Crashworthiness (FSC) project, which led to the development of new crash guidelines for a range of military helicopters. NASA and Sikorsky conducted a joint research effort to study the impact responses and progressive failure of composite structures removed from residual hardware of the Survivable Affordable Reparable Airframe Program (SARAP). One goal of this effort was to assess the ability of LS-DYNA to predict composite failure modes under transient dynamic loading. Finally, two cooperative research efforts with the FAA Technical Center were accomplished: (1) modeling and simulation of a vertical drop test of an ATR42 aircraft, and (2) vertical drop testing and simulation of two sections of the F28.

REFERENCES

Abramowitz, A. et al. (2006). "Vertical Drop Test of an ATR 42-300 Airplane." DOT/FAA/AR-05/56.

Aircraft Crash Survival Design Guide (ACSDG), (1989). Volumes 1-5, USAAVSCOM TR 89-D-22.

Anderson, M. C. et al. (1998). "Statistical Analysis of Modeling Uncertainty and Predictive Accuracy for Nonlinear Finite Element Models." Proceedings of the 69th Shock and Vibration Symposium, Minneapolis/St. Paul, MN.

Annett, M. S., and Polanco, M. A. (2010). "System-Integrated Finite Element Analysis of a Full-ScaleHelicopter Crash Test with Deployable Energy Absorbers." Proceedings of the American Helicopter Society 66th Annual Forum, Phoenix, AZ.

Annett, M. S. (2010). "LS-DYNA Analysis of a Full-Scale Helicopter Crash Test." 11th LS-DYNA, Users Conference, Dearborn, MI.

Annett, M. S. et al. (2010). "Final Report: Evaluation of Thoracic Injury in Helicopter Crashes Through Testing and Simulation." Office of the Secretary of Defense in fulfillment of Interagency Agreement IA1-983.

Annett, M. S. (2011). "Comparison of Test and Finite Element Analysis for Two Full-Scale Helicopter Crash Tests." Proceedings of the 52nd AIAA/ASME/ASCE/AHS/ASC Structures, Structural Dynamics, and Materials Conference, Denver, CO.

Annett, M. S. et al. (Nov. 2012). "Development, Calibration, and Validation of a System-Integrated Rotorcraft Finite Element Model for Impact Scenarios." NASA/TM–2012-217785.

Annett, M. S. et al. (2012). "Calibration of Airframe and Occupant Models for Two Full-Scale Rotorcraft Crash Tests." Proceedings of the AHS 68th Annual Forum, Ft. Worth, TX.

Annett, M. S. et al. (2014). "Evaluation of the First Transport Rotorcraft Airframe Crash Testbed (TRACT1) Full-Scale Crash Test," NASA/TM–2014-218543.

Annett, M. S. (2015). "Evaluation of the Second Transport Rotorcraft Airframe Crash Testbed (TRACT 2) Full Scale Crash Test." Proceedings of the American Helicopter Society Annual Forum 71, Virginia Beach, VA.

Annett, M. S., and Pereira, M. (2018). “Preliminary Assessment of Bird Strike on Low Noise Rotor Blade Sections.” Proceedings of the 74th American Helicopter Society Annual Forum, Phoenix, AZ.

Anon. (1992). “Weight and Balance Manual,” Avions de Transport Regional, Service Bulletin No. ATR42-34-0114.

Baker, W. et al. (2016). “Development of a Finite Element Model of the WIAMAN Lower Extremity to Investigate Under-Body Blast Loads,” Proceedings of the 14th International LS-DYNA Users Conference, Dearborn, MI.

Bark, L. W. (2015). “Performance Evaluation of Crash-Recording Technologies in a Full-Scale CH-46 Airframe Crash Test,” Proceedings of the 71st Annual Forum of the American Helicopter Society, Virginia Beach, VA.

Bark, L. W. (May 2015). “Testing Mobile Aircrew Restraint Systems in a Full-Scale CH-46 Airframe Crash Test – Exploring the Limits,” Proceedings of the 71st Annual Forum of the American Helicopter Society, Virginia Beach, VA.

Billac, T. et al. (2014). “Validation of Numerical Methods for Multi-terrain Impact Simulations of a Crashworthy Composite Helicopter Subfloor,” Proceedings of the American Helicopter Society 70th Annual Forum, Montreal, Canada.

Bolukbasi, A. et al. (2011). “Full Spectrum Crashworthiness Criteria for Rotorcraft,” RDECOM TR12-D-12.

Buhrman, J. R. (1991). “Vertical Impact Tests of Humans and Anthropomorphic Manikins,” AL-TR-1991-0129.

Burrows, L. T. (1992). “Development and Use of Computational Techniques in Army Aviation R & D Programs for Crash Resistant Helicopter Technology,” Computational Methods for Crashworthiness, NASA Conference Publication 3223, A. Noor, ed., pp. 95-104.

Carden, H. D., and Kellas, S. (1993). “Composite Energy-Absorbing Structure for Aircraft Subfloors,” Proceedings of the DOD/NASA/FAA Conference, SC.

Carstensen, T. A. et al. (2008). “Development and Validation of a Virtual Prototype Airframe Design as Part of the Survivable Affordable Repairable Airframe Program,” Proceedings of the 64th American Helicopter Society Forum, Montreal, Canada.

Crocco, J. (2012). “A Systems Approach to Crashworthiness,” Proceedings of the American Helicopter Society 68th Annual Forum, Fort Worth, TX.

Cronkhite, J. D., and Berry, V. L. (1982). “Crashworthy Airframe Design Concepts, Fabrication and Testing,” NASA Contractor Report 3603, NASA Contract NAS1-14890.

Code of Federal Regulations (1989). Federal Aviation Regulations for Aviation Maintenance Technicians FAR AMT, Part 27 Airworthiness Standard: Normal Category Rotorcraft, 27.562 Emergency Landing Dynamics.

Combest, J., and Wang, J-T. (2016). “Status of the Global Human Body Models Consortium (GHBMC),” Proceedings of the SAE Government and Industry Meeting, Washington D.C.

Desjardins, S. P., and Labun, L. C. (2015). “Selectable Profile Energy Absorber System for Rotorcraft Troop Seats,” Proceedings of the 71st Annual Forum of the American Helicopter Society, Virginia Beach, VA.

Farley, G. L. (1986). "Crash Energy Absorbing Composite Sub-Floor Structure," AIAA Paper 86-0944, Proceedings of the 27th AIAA/ASME/ASCE/and AHS Structures, Structural Dynamics, and Materials Conference, San Antonio, TX.

Fasanella, E. L., and Jackson, K. E. (2002). "Impact Testing and Simulation of a Crashworthy Composite Fuselage Section with Energy-Absorbing Seats and Dummies," Proceedings of the 58th AHS Annual Forum, Montreal, Canada.

Fasanella, E. L. et al. (2014). "Simulating the Response of a Composite Honeycomb Energy Absorber: Part 2. Full-Scale Impact Testing," *Journal of Aerospace Engineering,* vol. 27, no. 3, pp. 437-441. ISSN 0893-1321.

Fasanella, E. L. et al. (2008). "Soft Soil Impact Testing and Simulation of Aerospace Structures," Proceedings of the 10th LS-DYNA Users Conference, Dearborn, MI.

Fasanella, E. L. et al. (2009). "Developing Soil Models for Dynamic Impact Simulations," Proceedings of the American Helicopter Society 65th Annual Forum, Grapevine, TX.

Fasanella, E. L. et al. (June 2014). "Simulating the Impact Response of Full-Scale Composite Airframe Structures," Proceedings of the 13th LS-DYNA Users Conference, Dearborn, MI.

Federal Aviation Regulation (1989). "Emergency Landing Dynamic Conditions," 14 CFR §29.562, Transport Aircraft.

Federal Register (2015). Federal Aviation Administration, Aviation Rulemaking Advisory Committee, Transport Airplane and Engine Issues, vol. 80.

Feraboli, P. et al. (2007). "Design and certification of a composite thin-walled structure for energy absorption," *International Journal of Vehicle Design*, vol. 44, nos. 3/4.

Feraboli, P. (2008). "Development of a Corrugated Test Specimen for Composite Materials Energy Absorption," *Journal of Composite Materials*, vol. 42, no. 3, pp. 229-256.

First Technology Safety Systems (2008). "FTSS LS-DYNA Model of the Hybrid III 50th Percentile Male Dummy User's Manual," Version 7.0.

Fleming, D. C., and Vizzini, A. J. (1993). "Tapered Geometries for Improved Crashworthiness under Side Loads." *Journal of the American Helicopter Society*, vol. 38.

Fleming, D. C. et al. (2008). "Finite Element Simulation of Delamination with Application to Crashworthy Design." *Journal of the American Helicopter Society*, vol. 53, no. 3, pp. 267-281.

Fleming, D. C. (2000). "Modeling Delamination Growth in Composites using MSC.Dytran." Proceedings of the 2nd Worldwide Automotive Conference, Dearborn, MI.

Fuchs, Y. T., and Jackson, K. E. (2008). "Vertical Drop Testing and Analysis of the WASP Helicopter Skid Gear." Proceedings of the 64th American Helicopter Society (AHS) Annual Forum, Montreal, Canada.

Fuchs, Y. T., and Jackson, K. E. (2011). "Vertical Drop Testing and Analysis of the WASP Helicopter Skid Gear." *Journal of the American Helicopter Society*, vol. 56, no. 1, pp. 012005-1 –012005-10.

Gowdy Van et al. (1999). "A Lumbar Spine Modification to the Hybrid III ATD for Aircraft Seat Tests." SAE 1999-01-1609.

Guha, S. (2014). “LSTC_NCAC Hybrid III 50th Dummy – Positioning and Post-Processing.” Livermore Software Technology Company (LSTC), MI.

Gupta, N. K., and Velmurugan, R. (1999). “Axial Compression of Empty and Foam Filled Composite Conical Shells.” *Journal of Composite Materials*, vol. 33.

Hallquist, J. O. (Aug. 2006). “LS-DYNA Keyword User’s Manual,” Volume I, Version 971, Livermore Software Technology Company, Livermore, CA.

Hallquist, J. O. (2006). “LS-DYNA Keyword User’s Manual,” Volume II Material Models, Version 971, Livermore Software Technology Company, Livermore, CA.

Hallquist, J. O. (Mar. 2006). “LS-DYNA Theory Manual,” Livermore Software Technology Company, Livermore, CA.

Halton, J. H. (1960). “On the Efficiency of Certain Quasi-Random Sequences of Points in Evaluating Multi-Dimensional Integrals,” *Numerische Mathematik*, vol. 2, pp. 84-90.

Hanagud, S. et al. (1989). “Energy Absorption Behavior of Graphite Epoxy Composite Sine Webs,” *Journal of Composite Materials*, vol. 23, no. 5, pp. 448-459.

Heymsfiel, E. et al. (2012). “Assessment of Soil Modeling Capability for Orion Contingency Land Landing,” *Journal of Aerospace Engineering*, vol. 25, no. 1, pp. 125-131.

Homma, T., and Saltelli, A. (1996). “Importance Measures in Global Sensitivity Analysis of Nonlinear Models,” *Reliability Engineering and System Safety*, vol. 52, pp. 1-17.

Horta, L. G. et al. (2010). “A Computational Approach for Model Update of a LS-DYNA Energy Absorbing Cell,” *Journal of the American Helicopter Society,* vol. 55, no. 3, pp. 032011-1–032011-8.

Horta, L. G. et al. (2011). “Multi-Dimensional Calibration of Impact Models,” *Aeronautics and Astronautics*, *Edited by Max Mulder, ISBN 978-953-307-473-3, 622 pages, Publisher InTech, Chapters published September 12, 2011 under CC BY-NC-SA 3.0 license* edited by Max Mulder, ISBN 978-953-307-473-3, Chapter 15, pp. 441-457.

Horta, L. G. et al. (2003). “Evaluation of Singular Value Decomposition Approach for Impact Dynamic Data Correlation,” NASA/TM–2003-212657.

Hu, D. Y. et. al. (2009). “Full-Scale Vertical Drop Test and Numerical Simulation of a Crashworthy Helicopter Seat/Occupant System,” *International Journal of Crashworthiness*, vol. 14, no. 6, pp. 565-583.

Hurley, T. R., and Vandenburg, J. M., eds. (2002). “Small Airplane Crashworthiness Design Guide,” AGATE Report Number AGATE-WP3.4-034043-036, Simula Technical Report TR-98099.

International Standards Organization Technical Report. (2013). “Road Vehicles – Objective Rating Metrics for Dynamic Systems,” ISO/TR 16250.

Iwamoto, M. et al. (2007). “Development of Advanced Human Models in THUMS,” Proceedings of the 6th European LS-DYNA Users Conference, pp. 47-56.

Jackson, K. E. et al. (2002). “Occupant Responses in a Full-Scale Crash Test of a Sikorsky ACAP Helicopter,” NASA/TM–2002-211733.

Jackson, K. E., and Fuchs, Y. T. (2007). "Vertical Drop Testing and Analysis of the WASP Helicopter Skid Gear," NASA/TM–2007-214907.

Jackson, K. E., and Fuchs, Y. T. (2008). "Comparison of ALE and SPH Simulations of Vertical Drop Tests of a Composite Fuselage Section into Water," Proceedings of the 10th International LS-DYNA Users Conference, Dearborn, MI, pp. 15-1 through 15-20.

Jackson, K. E. et al. (2009). "Overview of the NASA Subsonic Rotary Wing Aeronautics Research Program in Rotorcraft Crashworthiness," *Journal of Aerospace Engineering*, vol. 22, no. 3, pp. 229-239.

Jackson, K. E. (2010). "Predicting the Dynamic Crushing Response of a Composite Honeycomb Energy Absorber using a Solid-Element-Based Finite Element Model," Proceedings of the 11th International LS-DYNA Users Conference, Dearborn, MI.

Jackson, K. E. et al. (2010). "Evaluation of an Externally Deployable Energy Absorber for Crash Applications," Proceedings of the International Crashworthiness Conference, Leesburg, VA.

Jackson, K. E. et al. (2011). "Experimental and Analytical Evaluation of a Composite Honeycomb Deployable Energy Absorber," NASA/TM–2011-217301.

Jackson, K. E. et al. (2012). "Material Model Evaluation of a Composite Honeycomb Energy Absorber," Proceedings of the 12th International LS-DYNA Users Conference, Dearborn, MI.

Jackson, K. E. et al. (2014a). "Simulating the Response of a Composite Honeycomb Energy Absorber: Part 1. Dynamic Crushing of DEA Components and Multi-Terrain Impacts," *Journal of Aerospace Engineering*, vol. 27, no. 3, pp. 424-436. ISSN 0893-1321.

Jackson, K. E. et al. (2014b). "Impact Testing and Simulation of Composite Airframe Structures," NASA/TM–2014-218169.

Jackson, K. E. et al. (June 2014). "Simulating the Impact Response of Composite Airframe Components," Proceedings of the 13th LS-DYNA Users Conference, Dearborn, MI.

Jackson, K. E. et al. (2015). "Multi-Level Experimental and Analytical Evaluation of Two Composite Energy Absorbers," NASA/TM–2015-218772.

Jackson, K. E. et al. (Sept. 2015). "Impact Testing and Simulation of a Sinusoid Foam Sandwich Energy Absorber," Proceedings of the American Society of Composites 30th Technical Conference, East Lansing, MI.

Jackson, K. E. et al. (2017). "Development of a Continuum Damage Mechanics Material Model of a Graphite-Kevlar® Hybrid Fabric for Simulating the Impact Response of Energy Absorbing Subfloor Concepts," Proceedings of the 73rd Annual AHS Forum, Ft. Worth, TX.

Jackson, K. E. (2018). "Advances in Rotorcraft Crashworthiness – Trends Leading to Improved Survivability," *AHS Journal*, vol. 63, no. 2, pp. 1-25.

Jackson, K. E. et al. (Feb. 2018). "Finite Element Simulations of Two Vertical Drop Tests of F-28 Fuselage Sections." NASA TM 218-219807.

Jackson, K. E. et al. (April 2018). "Vertical Drop Test and Simulation of a Fokker F-28 Fuselage Section," Proceedings of the ASCE 2018 Earth and Space Conference, Cleveland, OH.

Jackson, K. E., and Fasanella, E. L. (2002). "Crash Simulation of Vertical Drop Tests of Two Boeing 737 Fuselage Sections," DOT/FAA/AR-02/62.

Jackson, K. E., and Fasanella, E. L. (2004). "Development of a LS-DYNA Model of an ATR42-300 Aircraft for Crash Simulation" Proceedings of the Eighth International LS-DYNA Users Conference, Dearborn, MI, pp. 11-1 through 11-14.

Jackson K. E., and Fasanella, E. L. (2005). "Crash Simulation of a Vertical Drop Test of a Commuter-Class Aircraft," *International Journal of Crashworthiness*, vol. 10, no. 2, pp. 173-182.

Jackson, K. E., and Fasanella, E. L. (2008). "Development and Validation of a Finite Element Simulation of a Vertical Drop Test of an ATR 42 Regional Transport Airplane," DOT/FAA/ AR-08/19.

Jones, L. E., and Carden, H. D. (1995). "Overview of Structural Behavior and Occupant Responses from a Crash Test of a Composite Airplane," NASA/TM-1995-111954.

Kellas, S. (2006). "Deployable Rigid System for Crash Energy Management," US Patent Nos. 6,755,453 on June 29, 2004; 6,976,729 on Dec. 20, 2005; and 7,040,658 on May 9, 2006.

Kellas, S., and Jackson, K. E. (2010). "Deployable System for Crash-Load Attenuation," *Journal of the American Helicopter Society*, vol. 55, no. 4, pp. 042001-1 through 042001-14.

Kellas, S. et al. (2010). "Full-Scale Crash Test of a MD-500 Helicopter with Deployable Energy Absorbers," Proceedings of the 66th AHS Forum, Phoenix, AZ.

Kellas, S., and Jackson, K. E. (Oct. 2010). "Multi-Terrain Vertical Drop Tests of a Composite Fuselage Section," *Journal of the American Helicopter Society*, vol. 55, no. 4, pp. 042002-1 through 042002-7.

Kindervater, C. et al. (2011). "Validation of Crashworthiness Simulation and Design Methods by Testing of a Scaled Composite Helicopter Frame Section," Proceedings of the American Helicopter Society 67th Annual Forum, Virginia Beach, VA.

Lawrence, C. et. al. (2008). "The Use of a Vehicle Acceleration Exposure Limit Model and a Finite Element Crash Test Dummy Model to Evaluate the Risk of Injuries During Orion Crew Module Landings, NASA/TM–2008-215198.

Littell, J. D. (June 2010). "Large Field Photogrammetry Techniques for Aircraft and Spacecraft Impact Testing," Proceedings of the Society for Experimental Mechanics (SEM), Indianapolis, IN.

Littell, J. D. et al. (2010). "Crash Test of an MD-500 Helicopter with a Deployable Energy Absorber Concept," Proceedings of the International Crashworthiness Conference, Leesburg, VA.

Littell, J. D. (2011). "Full-Scale Crash Test of an MD-500 Helicopter," American Helicopter Society 67th Annual Forum, Virginia Beach, VA.

Littell, J. D. (June 2011). "A Comparative Analysis of Two Full-Scale MD-500 Helicopter Crash Tests," Proceedings of the SEM 2011 Annual Conference, Uncasville, CT.

Littell, J. D., and Annett, M.S. (2013). "The Evaluation of a Test Device for Human Occupant Restraint (THOR) Under Vertical Loading Conditions: Part 1 – Experimental Setup and Results," Proceedings of the 69th American Helicopter Society Annual Forum, Phoenix, AZ.

Littell, J. D., and Annett, M. S. (2018). "The Evaluation of Anthropomorphic Test Device Response under Vertical Loading," Proceedings of the 74th Annual Forum of the American Helicopter Society International, Phoenix, AZ.

Littell, J. D. (2014). "The Development of a Conical Composite Energy Absorber for use in the Attenuation of Crash/Impact Loads," Proceedings of the American Society for Composites 29th Technical Conference, University of California San Diego, La Jolla, CA.

Littell, J. (2017). "Energy absorbing beam member," U.S. Patent #9,616,988, Issued April 11, 2017.

Littell, J. D. et al. (2015). "The Development of Two Composite Energy Absorbers for Use in a Transport Rotorcraft Airframe Crash Testbed (TRACT2) Full-Scale Crash Test," Proceedings of the AHS 71st Annual Forum, Virginia, Beach, VA.

Littell, J. D. (Oct. 2017). "Full Scale Drop Test of a Fokker F28 Forward Fuselage Section onto Soil," Aerospace Structural Impact Dynamics International Conference, Wichita, KS.

Littell, J. D. (2018). "Full-Scale Drop Test of a Fokker F28 Wing-Box Fuselage Section," Proceedings of the ASCE 2018 Earth and Space Conference, Cleveland, OH.

Little, E. J. et al. (2015). "Laboratory and Field Evaluations of Up-Scaled Textile Energy Absorbers for Crashworthy Cargo Restraints," Proceedings of the 71st Annual Forum of the American Helicopter Society, Virginia Beach, VA.

Matzenmiller, A. et al. (1995). "A Constitutive Model for Anisotropic Damage in Fiber Composites," *Mechanics of Materials,* vol. 20, pp. 125-152.

Military Handbook 5H, (1998). U.S. Department of Defense, Dec. 1, 1998.

Military Standard (1988). MIL-STD-1290A (AV), Light Fixed and Rotary-Wing Aircraft Crash Resistance, Department of Defense, Washington, DC.

Mullershon, H., and Liebsher, M. (2008). "Statistics and Non-Linear Sensitivity Analysis with LS-OPT and DSPEX," Proceedings of the 10th International LS-DYNA Users Conference, Dearborn, MI, pp. 4-1, 4-13.

Mullur, A., and Messac, A. (2005). "Extended Radial Basis Functions: More Flexible and Effective Metamodeling," *AIAA Journal*, vol., 43, no. 6.

Mullur, A., and Messac, A. (2006). "Metamodeling Using Extended Radial Basis Functions: A Comparative Approach," *Engineering with Computers,* vol. 21, pp.203-217.

Pellettiere, J. et al. (2011). "Rotorcraft Full Spectrum Crashworthiness and Occupant Injury Requirements," Proceedings of the 67th Annual Forum of the American Helicopter Society, Virginia Beach, VA.

Perry, C., et al. (2000). "Evaluation of Proposed Seat Cushions to Vertical Impact," Proceedings of the 38th Annual SAFE Symposium.

Polanco, M. (2010). "Use of LS-DYNA to Assess Impact Response of a Shell-Based Kevlar/Epoxy Composite Honeycomb," Proceedings of the 11th LS-DYNA Users Conf., Dearborn, MI.

Polanco, M. et al. (2009). "Evaluation of Material Models within LS-DYNA® for a Kevlar/Epoxy Composite Honeycomb," Proceedings of the 65th AHS Forum, Grapevine, TX.

Polanco, M. A., and Littell, J. D. (2011). "Vertical Drop Testing and Simulation of Anthropomorphic Test Devices," Proceedings of the 67th Annual Forum of the American Helicopter Society, Virginia Beach, VA.

Price, J. N., and Hull, D. (1987). "Axial Crushing of Glass Fibre-Polyester Composite Cones," *Composites Science and Technology*, vol. 28.

Putnam ,J. B. et al. (2013). "Validation of the Finite Element THOR-NT Crash Test Dummy for Injury Prediction during Simulated Vertical Loading," Proceedings of the AHS 69th Annual Forum, Phoenix, AZ.

Putnam, J. B. et al. (2015). "Finite Element Model of the THOR-NT Dummy under Vertical Impact Loading for Aerospace Injury Prediction: Model Evaluation and Sensitivity Analysis," *Journal of the American Helicopter Society*, vol. 60, 022004-1 through 022004-10.

Rapaport, M. et. al. (1997). "Establishing a Spinal Injury Criterion for Military Seats," Naval Air Warfare Center, A831644.

Regis, R. G., and Shoemaker, C. A. (2005). "Constrained Global Optimization of Expensive Black Box Functions Using Radial Basis Functions," *Journal of Global Optimization*, vol. 31, pp. 153-171.

Roberts, J. et al. (2007). "Computational and Experimental Models of the Human Torso for Non-Penetrating Ballistic Impact", *Journal of Biomechanics*, vol. 40, no. 1, pp. 125-136.

Roberts, J. et al. (2005). "Modeling the Effect of Non-Penetrating Bullet Impact as a Means of Detecting Behind Armor Blunt Trauma*," Trauma*, vol. 58, pp. 1241-1251.

Safe Inc., (2009). "Rotorcraft Crash Mishap Analysis." Ft. Eustis, VA: Aviation Applied Technology Directorate.

Salzar, R. S. et. al. (2009). "Ejection Injury in the Spine in Small Aviators: Sled Tests of Manikins versus Post-Mortem Specimens," *Aviation, Space, and the Environmental Medicine*, vol. 80. no. 7, pp. 621-629.

Schwartz, D. (2015). "Development of a Computationally Efficient Full Human Body Finite Element Model," Master's Thesis, Biomedical Engineering Department, Wake Forest University, Winston-Salem, NC.

Schweizerhof, K. et al. (1998). "Crashworthiness Analysis with Enhanced Composite Material Models in LS-DYNA® – Merits and Limits," Proceedings of the 5th International LS-DYNA® Users Conference, Dearborn, MI.

Schwer, L. E. (2007). "Validation Metrics for Response Histories: Perspectives and Case Studies," *Engineering with Computers*, vol. 23, pp. 295-309.

Shanahan, D. (2004). "Basic Principles on Crashworthiness."

Shaw, G. et al. (2002). "Comparative Evaluation of the THOR Advanced Frontal Crash Test Dummy." *International Journal of Crashworthiness*, vol. 7, no. 3, pp. 239-254.

Simula, Inc, (1990). "Development of Categorized Crashworthiness Design Criteria for U.S. Army Aircraft." USAAVSCOM.

Sobol, I. M. et al. (2007). “Estimating Approximation Error When Fixing Unessential Factors in Global Sensitivity Analysis.” *Reliability Engineering and System Safety*, vol. 92, pp. 957-960.

Society of Automotive Engineers (SAE) (1995). “Recommended Practice: Instrumentation for Impact Test – Part 1, Electronic Instrumentation,” SAE J211/1.

Society of Automotive Engineers (SAE) (2015). “Aerospace Recommended Practice (ARP) 5765A Analytical Methods for Aircraft Seat Design and Evaluation.”

Space Act Agreement (SAA) (2006). “Crash Safety Evaluation Between NASA Langley Research Center and HeloWerks, Inc.” SAA1-807.

Sprague, M. A., and Geers, T. L. (2003). “Spectral Elements and Field Separation for an Acoustic Fluid Subject to Cavitation.” *Journal of Computational Physics*, vol. 184, pp. 149-162.

Sudret, B. (2008). “Global Sensitivity Analysis Using Polynomial Chaos Expansion.” *Reliability Engineering and System Safety*, vol. 93, pp. 964-979.

Tho, C. H., et al. (2003). “Efficient Helicopter Skid Landing Gear Dynamic Drop Simulation.” Proceedings of the American Helicopter Society 59th Annual Forum, Phoenix, AZ.

Thomas, M. A. et al. (2008). “Constitutive Soil Properties for Unwashed Sand and Kennedy Space Center.” NASA/CR–2008-215334.

Thunert, C. (2012). CORA Release 3.6, User’s Manual.

CHAPTER 9. ICING

Richard E. Kreeger[1]

INTRODUCTION

This chapter addresses the current state of the art in rotorcraft icing research, in particular, the progress made from roughly 2008 to 2018. Since the last decadal survey on rotorcraft technology [Yamauchi and Young, 2009], NASA has made progress in rotorcraft icing computational tool development, validation experiments in the NASA Glenn Icing Research Tunnel (IRT), experimental method development, ice shedding and adhesion prediction, and ice protection systems (IPSs) for rotorcraft.

Background

During an in-flight encounter with icing conditions, ice can build up on unprotected aircraft, rotorcraft, and engine components. IPSs are necessary to mitigate this threat, otherwise the vehicle will be unsafe or unavailable for the mission. Future vehicles may have new capabilities and new requirements that cannot be met by current IPSs. NASA seeks to develop and maintain a capability to evaluate new technologies, to simulate the next generation of IPSs, and to demonstrate compliance with regulatory requirements.

Each class of future vehicle has its challenges. Three classes of vehicles—roughly categorized as large civil transports, next-generation rotorcraft, and highly efficient turbofan engines—are of the greatest interest to NASA Aeronautics Research Mission Directorate (ARMD). Some consideration must also be given to the categories of unmanned air vehicles, on-demand mobility vehicles, business jets, general aviation, aviation instruments, manned and unmanned spacecraft, ground test facilities, and wind energy. Each of these classes of vehicles has its own set of constraints and requirements, although some may overlap. There may also be different constraints and requirements for near-term improvements to the current generation of vehicles as opposed to developing new capabilities for future versions over the long term. Other government agencies and industry may also be interested in the icing of surfaces on consumer goods, ships, power lines, and heating/cooling systems.

NASA's mission is to provide U.S. industry with the tools, methods, and databases needed to develop and certify vehicles for safe flight in icing conditions defined by Federal Aviation Administration (FAA) regulations. NASA is not in the business of developing IPSs since NASA does not need to procure large numbers of such systems. NASA does, however, have the mission of simulating the performance of IPSs to the highest level of fidelity necessary for design and certification, particularly for the civil aviation market. This simulation includes both ground-based test facilities and computational tools.

[1] NASA Glenn Research Center, 21000 Brookpark Road, Cleveland, OH 44135.

It is important that NASA's facilities be well-calibrated and capable of covering the entire envelope envisioned for current and future vehicles. NASA's computational tools must be robust and validated enough to support the next generation of vehicles. NASA wants to provide these capabilities at a reasonable cost to a broad community of industry, academia, and government users.

NASA conducts periodic assessments and workshops to guide research objectives, and to receive feedback from industry, academia, and government on NASA's research plan in emerging areas, solidify existing partnerships, and identify potential future collaborations.

The community confirmed the need for additional research in icing at the NASA Glenn Research Center (GRC) Icing Hazards Workshop held January 28–29, 2015. NASA presented its ongoing research and plans in icephobics research at the first NASA Workshop on Low Ice Adhesion Materials on August 10, 2017. This symposium, held near NASA GRC, presented NASA's plans for icephobics research and allowed key stakeholders and potential partners to present their recent work. The symposium was very successful, and the proceedings will be published as an upcoming NASA Conference Proceedings (CP).

There have been many contacts from industry and academia expressing interest in tool development and icephobic materials research, and these continue. Likewise, the Department of Defense (DoD) is conducting its research (Army, Air Force, and Navy) in the area. The FAA is also a major stakeholder in the icing community.

ROTORCRAFT ICING COMPUTATIONAL TOOL DEVELOPMENT

The simulation of rotorcraft flow fields is a challenging multidisciplinary problem. Successful aerodynamic simulation of a rotor/fuselage system requires the modeling of unsteady three-dimensional (3D) flows that include transonic shocks, dynamic stall with boundary layer separation, vortical wakes, blade/wake and wake/wake interactions, rigid body motion, blade deformations, and the loss of performance caused by ice accretion. The accurate simulation of these physical elements is required for the accurate prediction of aeromechanics performance for rotorcraft. This problem has been addressed in the engineering design environment using simplified codes, called comprehensive codes, in which many facets of the rotorcraft problem—aerodynamics, structural dynamics, trim, etc.—are combined using simplified analyses. For example, aerodynamics are modeled using lifting line theory and/or airfoil table lookups, and structural dynamics are modeled using nonlinear beam theory.

Stand-alone ice accretion prediction tools, as well as ice accretion fully integrated with aerodynamics, currently exist for two-dimensional (2D) airfoils and 3D aircraft configurations. Ice accretion predictions are typically 2D and based on the classical Messinger model. The analysis consists of four critical steps—flow field calculation, water droplet impingement calculation, heat transfer prediction, and ice accumulation normal to the surface.

The success of any ice accretion and growth calculation depends on an accurate estimate of the transition location, which determines the surface heat transfer coefficient. The ice accretion is also influenced by the assumptions and empiricism within the mass balance and thermodynamic

analyses. Many analyses, including the NASA LEWICE solver, employ the classical Messinger model. Extensions to the classical Messinger model have been proposed.

For 3D calculations, most ice accretion models were developed in a strip-theory fashion, although this neglects certain key aspects of flow physics and assumes that the entire problem is quasi-steady. The complex geometries are intensive to the grid while changing over time, and there are a variety of time and size scales that must be resolved. Current approaches, while useful, separate the ice accretion problem from the aerodynamic analysis. There is, at best, loose coupling between the two. The interdisciplinary nature of rotary wing aeromechanics requires a simultaneous treatment of aerodynamics, aeroelasticity, and flight dynamics.

The CFD analysis of a clean rotorcraft configuration is well within the range of current technology. Fully time-accurate simulations of ice accretion on rotorcraft blades are not currently feasible, however. The complexity of the problem demands high-fidelity tools based on first principles, and a tightly coupled, physics-based approach is not currently available.

NASA's objective is a robust, validated coupling of a rotor performance code with an ice accretion code [Kreeger et al., 2015b], as illustrated in Figure 9.1. Three independent approaches were explored: Cartesian methods, unstructured grid methods, and hybrid methods. In parallel, the Georgia Institute of Technology led an effort [Kim et al., 2013, 2014a, 2014b, 2015, 2016; Sankar et al., 2013] (conducted as part of the Vertical Lift Research Center of Excellence (VLRCOE)) to systematically assess the differences between the industry-standard ice accretion analyses such as the LEWICE software program and the ice accretion models based on the extended Messinger model.

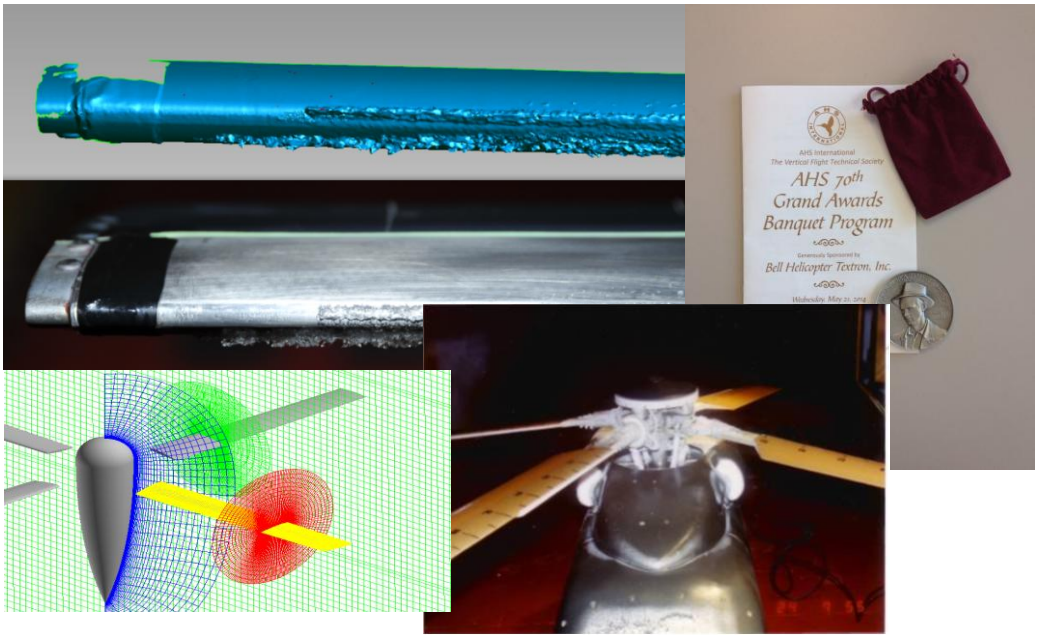

Figure 9.1. Rotorcraft icing computational tool development (photo courtesy of NASA Glenn).

Cartesian Methods

NASA entered into a 2-year contract ("Coupled CFD/CSD/Icing Analysis for Rotorcraft in Forward Flight") with the Boeing Company to develop improved coupling techniques for icing computational fluid dynamics (CFD). The project resulted in a process by which OVERFLOW (the OVERset grid FLOW solver), RCAS (Rotorcraft Comprehensive Analysis System), and LEWICE could be loosely coupled to assess ice accumulation and rotor performance degradation for helicopters in forward flight. The system has been tested and evaluated using an existing wind tunnel or flight data. The result is a computational approach for performing high fidelity simulations with ice accretion of rotorcraft blades.

The icing analysis process that was developed involves the loose coupling of OVERFLOW-RCAS for rotor performance prediction with LEWICE3D post-processor for thermal analysis and ice accretion. This method uses 3D analysis for rotor performance and degradation and 2D analysis for ice accretion. The automated process allows for rapid analysis in a parametric study or for the analysis of an airfoil subject to the many conditions existing on a rotor. For validation, predictions of performance and ice shapes were compared with experimental data for rotors in hover [Narducci and Kreeger, 2010] and in forward flight [Narducci et al., 2011].

Later, Georgia Tech coupled advanced tools for modeling ice accretion based on LEWICE and an extended Messinger model to the HELIOS code [Sankar et al., 2016]. Tools for deicing and ice shedding, using the ice shape computed from the OVERFLOW flow field, are integrated into the HELIOS infrastructure through a set of python-based interfaces. The integrated icing analysis tools are then applied to rotorcraft icing problems. A series of progressively challenging simulations have been carried out. The numerical results were then validated against a set of existing test data for ice shapes and associated measurements.

Unstructured Methods

A novel multi-physics CFD approach [Sarofeen et al., 2010a, 2010b, 2012; Kinzel et al., 2010a, 2010b, 2011] for simulating ice accretion on aircraft was developed through a NASA Research Announcement (NRA), "High Resolution CFD Analysis of Rotorcraft Rotor Icing." A 2-year cooperative agreement with the Pennsylvania State University sought to develop improved coupling techniques for icing CFD. Penn State partnered with Bell Helicopter Textron, Inc. This effort explored both one- and two-way coupling for simulating ice accretion. This project applied a zonal approach to the unstructured flow solver, extended the existing NASA LEWICE ice accretion formulation to the rotorcraft environment, and coupled this module with the outer CFD flow solution. Progress in solution-method development included the development of an Eulerian droplet solver using OpenFOAM software and the beginnings of a film-flow or runback model. The solver incorporates droplet impingement, shear forces moving the film, and body forces. Initial validation was at the model or component level by comparison with existing test data. Various Eulerian approaches were also examined.

Initial results show promise in the development of a generalized, unstructured finite-volume flow solver, and initial validation cases at the component level compared reasonably well with LEWICE and experiments for simple geometries. The work resulted in progress toward an

advanced software tool for performing high-fidelity CFD simulations with ice accretion of rotorcraft blades. Significant work is still required to fully demonstrate this alternate method.

Hybrid Methods

An integrated toolset capable of modeling ice accretion and the overall effects of rotor performance was developed and demonstrated [Bain et al., 2009, 2011a; Nucci et al., 2010a, 2010b; Rajmohan et al., 2010] by a NASA partnership led by Georgia Tech and Sikorsky ("Development of Methodologies for Coupling Ice Accretion Models with Rotary Wing Aeromechanics"). This 2-year cooperative agreement developed improved coupling techniques for icing CFD. Key computational parameters were explored. Preliminary results for cases of practical interest were encouraging.

The hybrid method approach resulted in an integrated toolset capable of modeling ice accretion and the overall effects of rotor performance. This loosely coupled suite of tools (LEWICE, GT-Hybrid, and DYMORE) has been applied to a representative rotor for detailed study. The entire process (clean rotor grid generation, clean rotor analysis, ice accretion simulations, and iced rotor analysis) is automated and modular. The Chimera Grid Tools (CGT) software developed at NASA, as well as commercial and in-house grid generators, can be used to develop the necessary structured grids.

The project uses a 3D Navier–Stokes analysis and a multi-body dynamics tool, coupled with the GT-Hybrid unstructured Cartesian grid-based flow solver, to represent the ice shapes. A time-marching scheme will eventually be developed to model the growth of ice and the resulting changes to the air loads that will enable a computational modeling approach for the simulation of fully 3D ice growth on a rotor in forward flight. Initial validation was by comparison with existing test data. Several different Navier–Stokes flow solvers have been used in this framework, including OVERFLOW, TURNS, and GT-Hybrid. GT-Hybrid is the preferred tool for these forward-flight calculations.

Computational Models

As part of a mutual research effort under the VLRCOE, Penn State, together with NASA, developed a correlation [Han and Palacios, 2016a, 2016b] between icing conditions and surface roughness based on 74 experimental cases. This new correlation was compared to two other existing roughness prediction equations. Ten icing conditions were reproduced at the Adverse Environment Rotor Test Stand (AERTS) facility at Penn State to provide an experimental database for the development of the model. The AERTS at Penn State is a research test facility capable of simulating impact ice accretion and measuring ice adhesion strength [Han et al., 2011; Palacios et al., 2010; Brouwers et al., 2010]. Surface roughness was measured, and heat transfer coefficients were determined from a transient heat transfer measurement technique using an infrared (IR) camera. Icing-physics-based correlations for ice roughness and surface convective heat transfer were developed.

The model prediction results were compared to LEWICE, a widely used ice prediction tool, and showed favorable comparison for both roughness distribution and heat transfer estimation. A novel heat transfer scaling parameter relating Stanton and Reynolds numbers was developed

specifically for the comparison of heat transfer in turbulent regimes for wind tunnel models tested at different Reynolds numbers. The scaling parameter was able to eliminate the effect of Reynolds number on measured heat transfer magnitude in turbulent regimes. The developed models have been coupled to LEWICE to obtain an improved numerical ice accretion tool. Compared to LEWICE, the new prediction model achieved evident improvements in predicting natural ice accretion experiments on rotating airfoils.

VALIDATION EXPERIMENTS IN THE ICING RESEARCH TUNNEL

Simulating aircraft icing, whether experimentally or computationally, involves two separate elements: ice accretion and iced aerodynamic performance. Both have their own challenges when compared to traditional clean aircraft. With ice accretion, for example, there is a need to update the particle collection efficiency and subsequent ice growth, which occur at longer time scales when compared with the aerodynamic flow field. With iced aerodynamics, there is a need to address complex geometries with multiple ice roughness scales that are typically not encountered in most aerodynamic simulation scenarios. All of these issues require collaborative research involving both computational and experimental components [Kreeger and Broeren, 2018].

Heated Tail Rotor Experiments

In order to validate predictive tools, it is necessary to obtain quality experimental data of ice accretion and shedding under various icing conditions. Full-scale helicopter icing testing and a flight testing campaign would have been problematic, so NASA, through its partnership with the National Rotorcraft Technology Center (NRTC) and the Vertical Lift Consortium (VLC), collaborated to test a rotor model in the NASA Glenn Icing Research Tunnel (IRT). NASA was part of the NRTC/VLC High Fidelity Icing Analysis and Validation Team, which won the 2014 Howard Hughes Award from the American Helicopter Society.

A 15-day-test entry of a subscale rotor [Wright and Aubert, 2014] was conducted in the IRT. Figure 9.2 shows a heated tail rotor tested in the IRT. A rotating model configuration was necessary to evaluate the effects of higher speeds, centrifugal effects, and constantly changing local velocity around the azimuth. This was the first rotating model tested in the IRT in 20 years. The test investigated ice accretion and associated increase in power requirement, self-shedding, element on-times versus runback refreeze, spanwise versus chordwise shedding, evaporative anti-ice versus running wet, induced shedding and ice shard breakdown, and conditions from FAA Appendix O. Other notable IRT firsts from this test included the first production use of new 3D scanner capability, first electro-thermal deicing of a rotating scale model, first capture of a rotor shed event with a high-speed camera, and the first super-cooled large droplet icing on a rotor blade in the IRT. This data is being used to validate the latest generation of icing analysis tools for rotorcraft [Narducci et al., 2015]. The data included rotor ice shapes (tracing, photograph, scanner), rotor performance (main balance, instrumented blades), deice/anti-ice performance (temperature), and shed ice trajectory (wall panels, high-speed video).

Figure 9.2. Heated tail rotor model in the IRT (Fig. 2 of Kreeger et al. [2016b]).

Oscillating Airfoil Experiments

Another validation effort sponsored by the VLC was a 10-day-test entry of an oscillating rotorcraft airfoil that was completed in the IRT at NASA GRC [Reinert et al., 2011]. The model was a pressure-instrumented, thermally instrumented helicopter airfoil section with a 15-inch chord. The test was conducted in collaboration with Sikorsky, Boeing, Bell Helicopter, and Georgia Tech.

The main objective of this test was to obtain ice accretion and detailed aerodynamic measurements for 2D clean and iced oscillating airfoils undergoing both steady and transient behavior [Narducci and Reinert, 2011]. This test provides a valuable source of data for the validation of rotorcraft icing CFD codes [Lorber et al., 2013], including digital video recorder (DVR) data, digital photos, ESCORT data, dynamic data (binary), and digitized ice shapes.

EXPERIMENTAL METHOD DEVELOPMENT

Ice shapes that accrete on helicopter blades are inherently complex and highly 3D, making traditional methods of measuring and digitizing ice shapes insufficient for the next generation of icing tools. Current methods to measure ice accretion shapes are either destructive or primarily 2D, leaving room for improvement with nondestructive, 3D capability. Mold-based methods are capable of capturing the relevant 3D features of an ice shape but require special model

considerations such as removable leading edges or parts. They also require moving and handling of the ice shape. There is a cost for materials, and the time required to make a mold can have a significant impact on a test schedule. On the other hand, template-based tracing methods, while much quicker and cheaper, can only capture the ice shape along with a fairly limited number of 2D cuts.

There are three uses for digitized ice shapes: data analysis and archiving, production of models for aerodynamic testing, and development of meshes for CFD. The data analysis and archiving task must be accomplished first, and application to the helicopter problem introduces a number of unique challenges.

A scaling method is a procedure to determine the scaled test conditions to produce the same result as exposing a reference model to the desired cloud conditions. Because of test-section blockage limitations, many components cannot be tested full-size in an icing wind tunnel. Furthermore, facilities that simulate natural icing can provide only limited ranges of airspeed, cloud drop size, and liquid water content. When the full-scale model is too large for a given facility, model-size scaling is applied, and when the desired test conditions are outside the facility operating capability, test-condition scaling is required.

Development of 3D Scanning Techniques

NASA developed a robust and affordable means of recording and archiving fully 3D descriptions of experimental ice accretion geometry for rotorcraft [Kreeger and Tsao, 2014] and demonstrated the ability to capture aerodynamically relevant features of ice shapes accurately.

In order to obtain the ice accretion data for tool validation, it was necessary to develop a robust and affordable means of recording and archiving fully 3D descriptions of experimental ice accretion geometry. The chosen approach was to apply a commercial laser scanning system that had been validated for use in the icing tunnel. The scanner was able to digitize initial roughness shapes, which could not be captured at all by simple 2D techniques, such as hand tracing. Thus, NASA was able to demonstrate the system and procedures using fixed airfoils and was ready to apply it to a rotorcraft application. The first operational use for rotorcraft was demonstrated in August 2013. This capability has since been transitioned to the IRT facility, where it is now available to external customers. Three-dimensional ice shape measurements are shown in Figure 9.3.

The system and procedures were initially developed and demonstrated using fixed airfoils. These early efforts demonstrated the ability to accurately and affordably capture the aerodynamically relevant features of ice shapes [Lee et al., 2014; Hayat, 2013]. NASA has tried to scan ice shapes before; advancements in commercial laser scanning—in particular, the accurate, portable, and reliable commercial arm and scanner combination (able to operate at IRT temperatures) and the robust algorithms of the scanner software—now make it possible.

Another approach to analyzing and characterizing complex ice shapes was developed and successfully implemented using a novel self-organizing map approach [McClain and Kreeger, 2013; McClain et al., 2015].

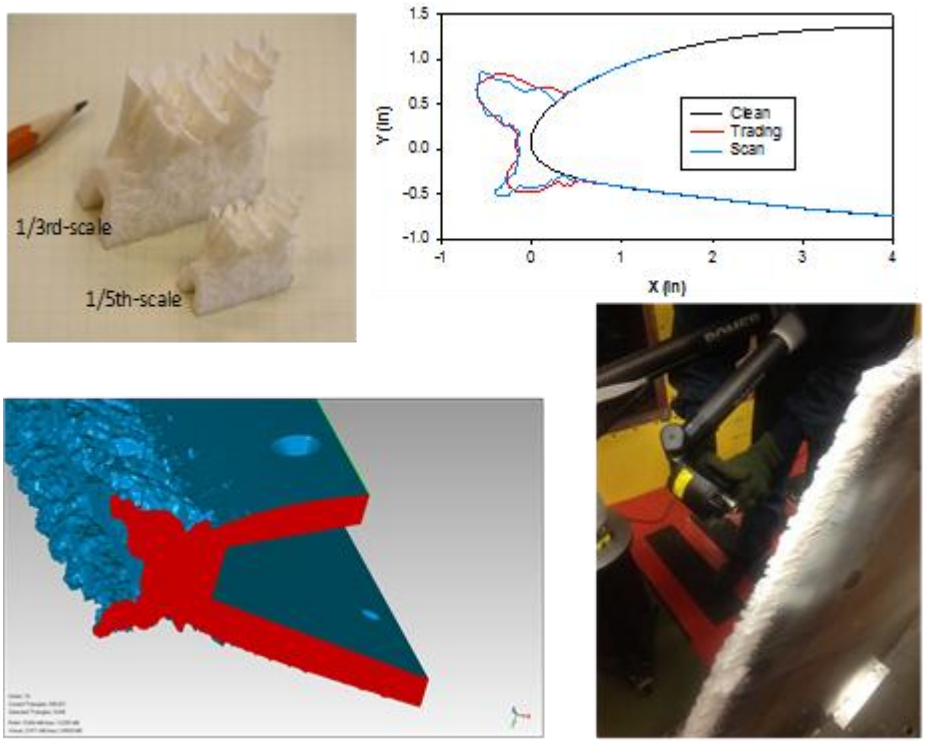

Figure 9.3. Three-dimensional ice shape measurements (photo courtesy of NASA Glenn).

Scaling Techniques for Rotorcraft

A series of icing scaling tests were undertaken with increasing flow and model configuration complexities in the NASA Glenn IRT to evaluate potential scaling methods [Tsao and Kreeger, 2009, 2011]. Unlike the fixed-wing case, there was no single scaling method systematically developed and evaluated for rotorcraft icing applications. The development of an applicable method began, logically, with the current recommended scaling methods for unprotected surfaces on fixed wings. It was particularly crucial to ascertain whether the fixed-wing methods would apply at non-zero angle of attack.

Icing tests were conducted in the NASA Glenn IRT, and evidence from ice-shape comparison suggests that the current recommended scaling methods for fixed-wing icing could be used for some generic rotor blade icing applications without any modification, at least for some angles of attack. However, the data is very limited. Prior to these tests, there was no icing scaling data from the IRT for any airfoil models at a non-zero angle of attack.

It was possible to divide the rotor into several radial regions according to rotation speed. The determination of the local ice shape came from tests performed at various speeds to represent each radial location. Near the tip, speeds would be too high for any icing facility; lower speeds were found by matching a similarity parameter (the Weber number). Matching any of the Weber numbers to simulate a high speed with a lower speed necessitates the use of a larger chord. Therefore, this approach has practical limits for different icing tunnels. Also, film flow and ice shedding due to aerodynamic and centrifugal forces can have a significant effect on ice shape for rotating blades.

Ice Adhesion Measurement

In order to develop effective ice-resistant coatings for aircraft, it is necessary to have a consistent, reliable method for quantifying the adhesion strength of impact ice. It is also necessary to characterize the behavior of candidate materials subjected to realistic environments such as rain, sand, and ultraviolet exposure.

A review of the literature on the measurement of the adhesion of ice [Work and Lian, 2018] comprised over 110 articles presenting adhesion testing on ice. Test methods included the push test, centrifugal adhesion test (CAT), and shear, tension, cantilevered beam, vibrating beam, tensioned beam, torsioned beam, and laser spallation tests. The ice adhesion strength values available in the literature vary widely because of different test methods, material surface roughness, residual stress, stress concentrations/test geometry, and type of ice. Some of the methods evaluated are shown in Table 9.1.

Table 9.1. Adhesion Test Methods (excerpt from Table 3 of Work and Lian [2018]).

Test Method	Advantages	Disadvantages	Average Scatter (%)
CAT	Throughput	SRC, sample variability, SP, edge effects, vibration	Al: 14.7 St:
Push – non-impact ice (with mold)	Throughput, repeatable geometry, SRC, SP, low noise	In-situ impossible, aerodynamics	Al: 18.7 St: 10.8
Push – impact ice (without mold)	Throughput, in-situ possible, SRC, SP, low noise	Sample variability, contact variability, aerodynamics	Al: 26.4 St: 15.9
Rotational Shear	Low stress concentration, SRC, SP, low noise	Difficult geometry, not in-situ	Al: St:
0° Cone & Similar	Well-understood stress distribution, SRC, SP, low noise	Thermal expansion, not in-situ	Al: 9.2 St: 16.9
Lap Shear	Low stress concentration, SRC, sample preserving, low noise, flexible methodology	Not in-situ, edge effects for impact ice	Al: 27.5 St: 31.7
Beam Tests (all)	SRC, Simple geometry, flexible test method, SP, in-situ possible for some	Substrate stiffness limiting, edge effects for impact ice	Al: 33.9 St:
Blister	Mode 1, low-cost equipment, simple geometry, SP, in-situ	SRC, no stress-strain curve, edge effects for impact ice	Al: St:

The Icing Branch Fundamental Adhesion and Shedding Test Laboratory (FAST Lab) at NASA GRC initially included a tensile tester, an optical microscope, an infrared camera, a centrifuge, and a cold chamber. Additional capabilities include a scanning electron microscope, a goniometer, and an optical profilometer. In 2017, the facility was moved to a larger, dedicated space and renamed the Revolutionary Icing Materials Evaluation (RIME) Laboratory. The facility also includes storage, 3D printing, and capabilities for examining impact ice grain structure.

A new experimental method based on a modified lap joint test [Work et al., 2018] was developed and used to characterize a statistically significant number of ice adhesion samples. The modified lap joint test is shown in Figure 9.4. Stainless steel coupons were used to acquire impact ice samples of a baseline material in the IRT. A stainless steel adhesion test coupon and mounting structure are shown in Figure 9.5. Some samples were instrumented with strain gages to quantify the residual strain at the interface. Finite Element Analysis (FEA) was used to estimate thermal strains in the samples. New mounts were designed that reduce loading strains while locking the samples in place with a repeatable load using internal springs. The newly designed mounts induced much smaller strain in the samples (~7x lower) while improving testing efficiency by ~50 percent in the IRT and preventing any samples from spontaneously dismounting. The samples were then tested in the RIME Lab where the adhesion strength was measured.

Rigorous mechanical characterization of impact ice under controlled conditions will help to evaluate future IPSs and provide valuable data for predictive physics-based models. Strain rate, frozen stresses, time sensitivity, and coupon geometry are four newly identified parameters that have not been controlled under most previous methods. Many experimental methods are available to measure adhesion, and deeper examination is needed in order to compare diverse measurements reasonably. There is still a need for a standardized method, but it is necessary to improve ice adhesion testing in order to minimize the influence of unintended mechanical and thermal stresses. Research to characterize the adhesion of impact ice to relevant aircraft materials will continue in order to develop revolutionary predictive tools and enable rational multi-scale material design.

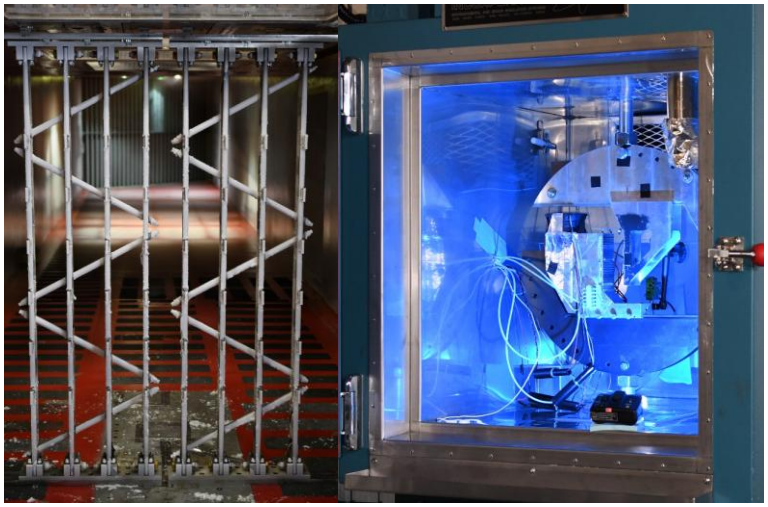

Figure 9.4. Modified lap joint method (photo courtesy of NASA Glenn).

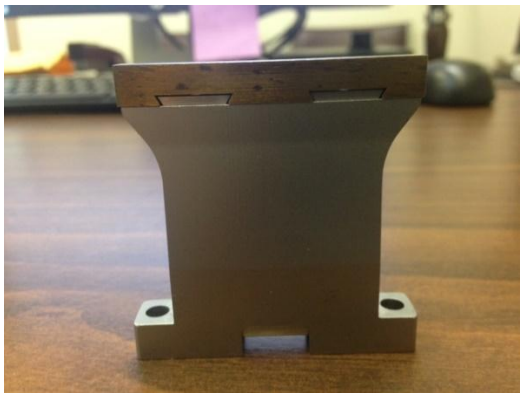

Figure 9.5. Adhesion test coupon (photo courtesy of NASA Glenn).

ICE ADHESION AND SHEDDING PREDICTION

Shedding is an important consideration for rotorcraft. Ice that accretes on the rotor blades can shed and may impact various components or create large dynamic imbalance. The relationship between ice accretion, adhesion, and shedding is complex and poorly understood (few published results, substantial scatter, etc.). Temperature, substrate properties, and formation mechanisms are all known to affect adhesion, but the current generation of empirical codes only account for temperature.

Shedding Prediction

Current methods to predict ice shedding events are sound [Bain et al., 2010, 2011b; Aubert and Wright, 2011] but depend on properties of ice to adhere to the rotor blade and, to a smaller extent, the cohesion strength of ice. Current ice adhesion models (and there are many) are empirically based and exhibit a high degree of scattering. Also, they consider only temperature and substrate as parameters. Research at Georgia Tech, in collaboration with NASA and Penn State, developed improved physics-based models for ice shedding [Gupta et al., 2018] integrated with Navier–Stokes ice accretion tools [Gupta et al., 2019], although further research is necessary.

NASA also undertook an in-house effort to develop an effective method of modeling post-shedding ice trajectories [Kreeger et al., 2016b]. A method to conduct image processing was developed and applied to video data in order to characterize the shed ice by particle size distribution and trajectory. High-frame-rate data of multiple shed events captured in the IRT were analyzed and compared to a new analytical model. The method can define a risk envelope for evaluating the potential damage in the event of a shed. The model predicted shed ice velocity and position reasonably well, however additional data is needed to improve the drag term. The shed ice trajectory tool is shown in Figure 9.6.

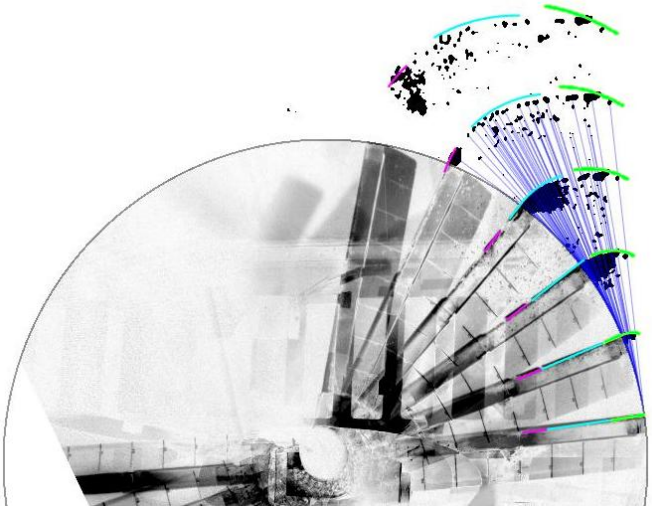

Figure 9.6. Shed ice trajectory tool (Fig. 6 of Kreeger et al. [2016b]).

Ice Adhesion Modeling

A number of technology development programs undertaken to develop new coatings and materials have recently sought to improve ice mitigation properties for aircraft applications [Ma et al., 2018; Zhang et al., 2018]. The ice adhesion strength of impact ice to erosion-resistant materials was experimentally measured and compared to that of metallic materials commonly used in helicopter rotor blade leading edges [Soltis et al., 2015]. In addition, the effects of environmental and material surface properties to ice adhesion strength were determined [Kreeger et al., 2015a] using the Penn State AERTS facility.

With the continuing search for new coatings and materials, it will be beneficial to design chemical and surface properties for both ice mitigation and erosion resistance [Kreeger et al., 2016a]. Improved adhesion models can help in the design and certification of new IPSs. Coatings with controlled surface morphology can help with developing a validated macro-scale model [Knuth et al., 2015] that can then be integrated with the atomistic simulations to guide the development of future materials to improve the performance of IPSs.

Research at the Iowa State University, “Ice Adhesion Characterization of Icephobic Materials for Aircraft Icing Mitigation,” seeks to improve the performance of future IPSs through a combined experimental and numerical effort [Dawood et al., 2018]. Some preliminary efforts were made to establish fundamental correlations between the thermodynamic and aerodynamic effects and ice accretion on airfoil surfaces, and to provide an experimental in-situ characterization of the adhesion and cohesion of impact ice over various icephobic materials.

ICE PROTECTION SYSTEMS (IPSs) FOR ROTORCRAFT

A variety of different methods are used to protect aircraft from the hazard of in-flight icing. These methods can be grouped into three general categories: thermal, mechanical, and chemical (usually freezing point depressant) systems. Thermal systems use heat energy to make critical aircraft surfaces warm enough to prevent ice buildup. Mechanical systems use kinetic energy to break up and debond ice that has adhered to the surface of the aircraft. Chemical systems distribute a fluid along critical aircraft surfaces where ice might accrete. This fluid prevents the supercooled water from freezing to the surface. Mechanical IPSs are also sometimes categorized as deicing systems. Deicing systems allow some ice to build up on the aircraft surface before removing or expelling it. Thermal and fluid chemical systems are typically known as anti-icing systems because they are designed to prevent any ice buildup whatsoever or, at least, prevent any ice buildup on critical aircraft surfaces. In the latter instances, water is prevented from freezing until it runs off the critical surface to an area on the aircraft where some amount of ice buildup can be safely tolerated. Electro-thermal systems can be used for either deicing or anti-icing.

An IPS, regardless of the type, has a number of requirements that must be taken into account, whether making a new design or an incremental improvement. Sometimes, these requirements can be conflicting. An IPS must be capable of removing ice for varying icing conditions, as described in the Federal Aviation Regulations (FAR) Part 25/29 Appendix C envelope. An IPS has to be resistant to corrosion and erosion (sand, rain). It must provide an acceptable aerodynamic penalty when actuated and a negligible penalty when it is not. It must be capable of operating reliably after many repeated actuations. Power consumption and distribution can also be a major design constraint for an IPS. A system must operate over a broad temperature range. It must be durable and able to withstand ultraviolet exposure, solvents, handling, etc. Other factors include system complexity, reliability, repairability, cost, and weight.

Passive and active approaches have been used for reducing ice adhesion in various systems such as aircraft, ships, power lines, wind turbines, and offshore oil platforms. Ice adhesion is sensitive to a wide range of variables, including temperature, surface roughness, ice type, purity, crystal structures, strain rate, and method of loading. Although different methods have been used to quantify ice adhesion strength, there is a clear lack of a standardized method for testing the adhesive strength of ice, which challenges efforts to understand ice adhesion and the development of low-adhesion materials.

There are technical barriers for each of the three main categories of IPSs: mechanical (complexity, durability, weight); electro-thermal (reliability, power, weight); and passive (ice adhesion, hydrophobicity, rain, and sand erosion). Hybrid systems are an area of particular interest. NASA is not currently developing icephobic coatings in-house, but instead uses programs like LEARN and SBIR for technology development. However, it is NASA’s mission to enable advancements in this area by providing new tools, methods, and databases for the benefit of all.

The design of a rotor deicing system requires determination of the amount and location of ice and then designing a way to reliably get the right amount of heat to the right location. For current hybrid and electro-thermal blade IPSs, it is necessary to identify the external geometric

parameters to be used in design optimization tools for system-level analysis. NASA identified the critical geometric design constraints to enable the design of low-noise rotor blades.

NASA was involved in a recent study that illustrated some of the particular issues with regard to a rotary wing unmanned aerial vehicle [Sehgal and Ernst, 2016]. The MQ-8 Fire Scout is a Vertical Takeoff and Landing (VTOL) unmanned aircraft system (UAS) operated by the U.S. Navy in both sea- and land-based environments. In its current configuration, the standard operating procedure is for the air vehicle to avoid operations in known and forecasted icing conditions. The engineering study investigated various system trades to enable operator notification well in advance of flying into an impending icing environment.

Researchers at Penn State, in conjunction with NASA through the VLRCOE, conducted a novel proof-of-concept study to investigate rotor noise during ice accretion [Cheng et al., 2014]. This research sought to determine if different rotor noise source mechanisms (for example, thickness noise, steady loading noise, and broadband noise) could be used to detect the formation and location of accreted ice. The concept proved especially relevant at the early stage of ice accretion when the initial roughness effectively changes the surface roughness of the lifting surface.

A recent NASA LEARN Program successfully demonstrated a novel IPS concept applicable to helicopter rotor blades [Szefi et al., 2014; Palacios et al., 2014; Invercon, 2011].

Under the current funding paradigm, NASA's Small Business Innovative Research (SBIR) program is another area undertaking near-term IPS development. A significant portion of the effort in this part of the industry looks at so-called icephobic coatings, either as a passive system or as a "passive+active hybrid" IPS.

NanoSonic, Inc. has recently worked with NASA to molecularly engineer its material with tailored compositions to impart both low ice adhesion and passive ice accretion temperature reduction while maintaining aerospace durability [Berg et al., 2017]. NASA awarded four Phase I SBIRs in 2016 to advance icephobic materials for aviation applications, intending to implement hybrid IPSs. One of these progressed to Phase II.

SUMMARY

NASA demonstrated the coupling of rotor performance codes with an ice accretion code, completed subscale rotor testing in the Icing Research Tunnel (IRT), developed methods to measure/document 3D ice accretion shapes in the IRT, and initiated research into icephobic coatings. A critical review of the different adhesion measurement techniques that are available highlighted the lack of a standard technique and recommendations for best design practices and test protocols. NASA established an adhesion measurement laboratory and is developing an in-situ technique for characterizing ice shed performance in the IRT.

NASA's icing researchers continue to work closely with industry and university partners to best leverage Revolutionary Vertical Lift Technology (RVLT) investment (NRAs, VLC/NRTC partnerships, and VLRCOE collaboration). This is exemplified through 50 years of Army-NASA Collaboration (1965–2015).

State-of-the-art analysis tools have improved significantly and are capable of generating accurate results, but a best-practice approach that guarantees accurate results at all edges of the icing envelope remains elusive. The analysis tools allow for grid density, solution time-step, heat transfer coefficient models, discretization schemes, etc., to be varied. However, not all experimental cases can be adequately reproduced by computational tools. As the tools continue to be exercised and validated, a best-practice will eventually be established. A new 3D ice growth approach is needed for certain conditions. Models of skin friction and flow separation over realistic ice roughness and calibrated turbulence models are needed to improve the prediction of aerodynamic performance due to ice. Current methods to predict ice shedding events are sound but can be improved with a more extensive database of ice adhesion and cohesion properties.

The following elements should be considered for potential inclusion in a strategic research plan: adhesion and shedding, altitude scaling, runback and refreeze modeling and validation, ice adhesion studies, ice cracking and breakup modeling, and the impact of residual and intercycle ice on aerodynamics.

Future RVLT activities are likely to include small Unmanned Aerial Systems (sUAS) and vehicles in the emerging market of Urban Air Mobility (UAM). Many organizations including NASA are proposing new vehicles and operational models to accommodate the increasing demand for point-to-point, on-demand, air-taxi services in urban areas. In order for on-demand mobility to be successful in urban areas that are often affected by inclement weather, the aircraft must be certified to operate in fog, low visibility, high wind gusts/shear, and icing conditions, including freezing drizzle and freezing rain. Taken together, these hazards require a systems-level approach for integration with the airframe, propulsion system, and control/avionics system.

New, very-low-power ice-protection systems including icephobic coatings may be required for these aircraft, but they do not currently exist in operational form. Since they address the safety of flight concerns for U.S. and international aircraft manufacturers and operators, emerging icing mitigation technologies often have significant market appeal. New FAA icing certification requirements and new emerging airframe designs ensure that the need for research in these technologies will continue well into the future.

Any coating development must also consider erosion resistance caused by sand or rain. Whether the goal is to improve IPS performance by reducing adhesion, or improve predictions of ice shedding from aircraft surfaces, a multi-scale physics-based model of ice adhesion is required. Enhanced test methods, as well as new models and new coatings/materials, are recommended for future research efforts.

REFERENCES

Aubert, R., and Wright, J., "Challenges in Predicting Rotor Blade Ice Protection Coverage Extent using Alternate Flow Solver and Lewice3D," SAE Paper 2011-38-0014, SAE/AIAA/AHS International Conference on Aircraft and Engine Icing and Ground Deicing, Chicago, IL, June 13-17, 2011.

Bain, J., Sankar, L., Egolf, T. A., Flemming, R., and Kreeger, R., "Progress Towards Modeling the Effects of Ice Accretion on Rotorcraft Performance in Hover and Forward Flight," presented at the 35th European Rotorcraft Forum, Hamburg, Germany, Sept. 22-25, 2009.

Bain, J., Cajigas, J., Sankar, L., Flemming, R., and Aubert, R., "Prediction of Rotor Blade Ice Shedding Using Empirical Methods," presented at the AIAA Atmospheric and Space Environments Conference, Toronto, Canada, Aug. 2-5, 2010.

Bain, J., Deresz, R., Sankar, L., Egolf, A., Flemming, R., and Kreeger, R., "Effects of Icing on Rotary Wing Loads and Surface Heat Transfer," presented at the AIAA Aerospace Sciences Meeting, Orlando, FL, Jan. 2011a.

Bain, J., Sankar, L., Aubert, R., and Flemming, R. J., "A Methodology for the Prediction of Rotor Blade Ice Formation and Shedding," SAE Paper 2011-38-0090, SAE/AIAA/AHS International Conference on Aircraft and Engine Icing and Ground Deicing, Chicago, IL, June 13-17, 2011b.

Berg, M., Lalli, J., Claus, R., and Kreeger, R., "Metal Rubber Sensor Technology to Enable In-Flight Icing Measurement," presented at the SPIE Smart Structures/NDE 2017, Portland, OR, March 25-29, 2017.

Brouwers, E., Palacios, J., Smith, E., and Peterson, A., "The Experimental Investigation of a Rotor Hover Icing Model with Shedding," presented at the AHS 66th Annual Forum, Phoenix, AZ, May 11-13, 2010.

Cheng, B., Han, Y., Brentner, K., and Palacios, J., "Quantification of Rotor Surface Roughness Due to Ice Accretion Via Noise Measurement," presented at the 70th American Helicopter Society Annual Forum, Montreal, Quebec, CA, May 20-22, 2014.

Dawood, B., Giuffre, C., and Bastawros, A., "Fracture Mechanics Based Approach for Ice Adhesion Characterization," presented at the 2018 AIAA Atmospheric and Space Environments Conference, June, 2018.

Gupta, A., Halloran, E., Sankar, L., Palacios, J., and Kreeger, R., "Development and Validation of Physics-Based Models for Ice Shedding," presented at the 44th European Rotorcraft Forum, Delft, the Netherlands, Sept. 2018.

Gupta, A., Sankar, L., and Kreeger, R., "A Fully-Integrated Navier–Stokes Ice Accretion Methodology," presented at the Vertical Flight Society Forum 75, Philadelphia, PA, May 2019.

Han, Y., Palacios, J., and Smith, E., "An Experimental Correlation Between Rotor Test and Wind Tunnel Ice Shapes on NACA 0012 Airfoils," presented at the SAE/AIAA International Conference on Aircraft and Engine Icing and Ground De-Icing, Chicago, IL, June 13-17, 2011.

Han, Y., and Palacios, J., "Heat Transfer Evaluation on Ice Roughened Cylinders in Transition Regime," presented at the 8th AIAA Atmospheric and Space Environments Conference, Washington, D.C., June 13-17, 2016a.

Han, Y., and Palacios, J., "Surface Roughness and Heat Transfer Prediction for Development of an Improved Aircraft Ice Accretion Modeling Tool," presented at the 8th AIAA Atmospheric and Space Environments Conference, Washington, D.C., June 13-17, 2016b.

Hayat, C., *Desktop Engineering*, "Metrology Meets Meteorology," July 2013. https://www.digitalengineering247.com/article/wp-content/uploads/2017/09/ Level5_de0713_rev.pdf

Invercon LLC, "Pneumatic Actuator System for a Rotating Blade," request for patent: EFS ID: 9369871, Application No. 13020333, Feb. 2011

Kim, J., Garza, D., Sankar, L., and Kreeger, R., "Ice Accretion Modeling Using an Eulerian Approach for Droplet Impingement," AIAA Paper 2013-0246, presented at the 51st AIAA Aerospace Sciences Meeting, Grapevine, TX, Jan. 7-10, 2013.

Kim, J., Sankar, L., and Kreeger, R., "Assessment of Classical and Extended Messinger Models for Rotorcraft Icing Phenomena," presented at the 40th European Rotorcraft Forum, Southampton, England, Sept. 2-5, 2014a.

Kim, J., Sankar, L., and Kreeger, R., "Numerical Simulations of Ice Accretion Based on a Physics-Based Methodology," presented at the 3rd Asian Australian Rotorcraft Forum, Melbourne, Australia, Dec. 18-19, 2014b.

Kim, J., Sankar, L., Palacios, J., and Kreeger, R., "Numerical and Experimental Study of Rotorcraft Icing Phenomena," presented at the 41st European Rotorcraft Forum, Munich, Germany, Sept. 1-4, 2015.

Kim, J., Sankar, L., Marone, S., and Kreeger, R., "An Assessment of Empirical Models for Rotorcraft Ice Accretion," presented at the American Helicopter Society Technical Meeting on Aeromechanics Design for Vertical Lift, Jan., 2016.

Kinzel, M., Noack, R., Sarofeen, C., Boger, D., and Miller, S., "An OpenFOAM Implementation of ice Accretion for Rotorcraft," presented at the 5th OpenFOAM Workshop, Chalmers, Gothenburg, Sweden, June 21-24, 2010a.

Kinzel, M., Noack, R., Sarofeen, C., Morris, P., and Kreeger, R., "A Finite-Volume Approach to Modeling Ice Accretion," AIAA Paper 2010-4230, presented at the 28th AIAA Applied Aerodynamics Conference, Chicago, IL, Jun 28-July, 2010b.

Kinzel, M., Sarofeen, C., Noack, R., and Kreeger, R., "A CFD Approach for Predicting 3D Ice Accretion on Aircraft," presented at the SAE/AIAA International Conference on Aircraft and Engine Icing and Ground De-Icing, Chicago, IL, June 13-17, 2011.

Knuth, T., Palacios, J., Wolfe, D., Kreeger, R., Smith, J., Wohl, C., and Palmieri, F., "Ice Adhesion Strength Modeling Based on Surface Morphology Variations," presented at the SAE 2015 International Conference on Icing of Aircraft, Engines and Structures, Prague, the Czech Republic, June 22-25, 2015.

Kreeger, R., and Tsao, J., "Ice Shapes on a Tail Rotor," presented at the AIAA 6th Atmospheric and Space Environments Conference, Atlanta, GA, June 16-20, 2014.

Kreeger, R., Knuth, T., and Palacios, J., "Development of Materials and Simulation Models for Ice Mitigation," presented at the Adhesion Society 2015 Annual Meeting, Savannah, GA, Feb. 20-25, 2015a.

Kreeger, R., Sankar, L., Kunz, R., and Narducci, R., "Progress in Rotorcraft Icing Computational Tool Development," SAE paper 2015-01-2088, presented at the SAE 2015 International Conference on Icing of Aircraft, Engines and Structures, Prague, the Czech Republic, June 22-25, 2015b.

Kreeger, R., Vargas, M., Tran, A., Wang, Y., Palacios, J., and Hadley, K., "Multiscale Materials Design for Inflight Icing Mitigation," oral presentation at the Adhesion Society Annual Meeting, San Antonio, TX, Feb. 2016a.

Kreeger, R., Work, A., Douglass, R., Gazella, M., Koster, Z., and Turk, J., "Analysis and Prediction of Ice Shedding for a Full-Scale Heated Tail Rotor," presented at the 8th AIAA Atmospheric and Space Environments Conference, Washington, D.C., June 2016b.

Kreeger, R., and Broeren, A., "Collaborative Experiments and Computations in Aircraft Icing," presented at the AIAA Applied Aerodynamics Conference, 2018.

Lee, S., Broeren, A., Kreeger, R., Potapczuk, M., and Utt, L., "Implementation and Validation of 3-D Ice Accretion Measurement Methodology," presented at the AIAA 6th Atmospheric and Space Environments Conference, Atlanta, GA, June 16-20, 2014.

Lorber, et al. "Oscillating Iced Airfoil Pressure Measurement and Computation," presented at the AHS 69th Annual Forum, Fort Worth, TX, May 21-23, 2013.

Ma, L., Zhang, Z., Gao, L., Liu, Y., and Hu, H., "An Experimental Study on the Durability of Icephobic SLIPS Pertinent to Aircraft Anti-/De-Icing," presented at the 2018 AIAA Atmospheric and Space Environments Conference, June 2018.

McClain, S., and Kreeger, R., "Assessment of Ice Shape Roughness Using a Self-Organizing Map Approach," AIAA Paper 2013-2546, presented at the 5th AIAA Atmospheric and Space Environments Conference, San Diego, CA, June 24-27, 2013.

McClain, S., Kreeger, R., et al., "A Reevaluation of Appendix C Ice Roughness Using Laser Scanning," presented at the SAE 2015 International Conference on Icing of Aircraft, Engines and Structures, Prague, the Czech Republic, June 22-25, 2015.

Narducci, R., and Kreeger, R., "Analysis of a Hovering Rotor in Icing Conditions," presented at the American Helicopter Society 66th Annual Forum, Phoenix, AZ, May 11-13, 2010.

Narducci, R., and Reinert, T., "Calculations of Ice Shapes on Oscillating Airfoils," SAE 2011-38-0015 SAE/AIAA/AHS International Conference on Aircraft and Engine Icing and Ground Deicing, Chicago, IL, June 13-17, 2011.

Narducci, R., Orr, S., and Kreeger, R., "Application of a High-Fidelity Analysis Method to a Model-Scale Rotor in Forward Flight," presented at the American Helicopter Society 67th Annual Forum, Virginia Beach, VA, May 3-5, 2011.

Narducci, R., Wright, J., and Aubert, R., "Rotor Performance of a Full-Scale Heated Tail Rotor," presented at the American Helicopter Society 71st Annual Forum, Virginia Beach, VA, May 5-7, 2015.

Nucci, M., Bain, J., Sankar, L., Egolf, T. A., Flemming, R., and Kreeger, E., "A Methodology for Modeling Effects of Icing on Rotary Wing Aerodynamics," presented at the 36th European Rotorcraft Forum, Paris, France, Sept. 7-9, 2010a.

Nucci, M., Bain, J., Sankar, L., Kreeger, R., Egolf, T. A., and Flemming, R., "Assessment of the Effects of Computational Parameters on Physics-Based Models of Ice Accretion," AIAA-2010-1277, presented at the 48th AIAA Aerospace Sciences Meeting, Orlando, FL, Jan. 4-7, 2010b.

Palacios, J., Brouwers, E., Han, Y., and Smith, E., "Icing Environment Rotor Test Stand Calibration Procedures and Ice Shape Correlation," Journal of the American Helicopter Society, June, 2010.

Palacios, J., Wolfe, D., Bailey, M., and Szefi, J., "Rotor Ice Testing of a Centrifugally Powered Pneumatic Deicing System for Helicopter Rotor Blades," presented at the 70th American Helicopter Society Annual Forum, Montreal, Quebec, CA, May 20-22, 2014.

Rajmohan, N., Bain, J., Nucci, M., Sankar, L., Flemming, R., Egolf, T. A., and Kreeger, R., "Icing Studies for the UH-60A Rotor in Forward Flight," presented at the AHS Aeromechanics Specialists' Conference, Jan. 20-22, 2010.

Reinert, T., Flemming, R., Narducci, R., and Aubert, R., "Oscillating Airfoil Icing Tests in the NASA Glenn Research Center Icing Research Tunnel," SAE 2011-38-0016, SAE/AIAA/AHS International Conference on Aircraft and Engine Icing and Ground Deicing, Chicago, IL, June 13-17, 2011.

Sankar, L., Kunz, R., Kreeger, R., et. al., "Numerical Simulation of Airfoil Ice Accretion Phenomena," presented at the 2nd AHS Asian/Australian Rotorcraft Forum, Tianjin, China, Sept. 8-11, 2013.

Sankar, L., Kim, J., Bain, J., Wissink, A., and Kreeger, R., "Integrated Tools for Rotorcraft Icing Analysis," presented at the AHS 72nd Annual Forum, W. Palm Beach, FL, May 16-19, 2016.

Sarofeen, C., Kinzel, M., and Noack, R., "Rotorcraft Aerodynamics and Icing," Mid-Atlantic OpenFOAM Users Group Meeting, March 27, 2010a.

Sarofeen, C., Kinzel, M., Noack, R., Morris, P., and Kreeger, R., "A Numerical Investigation of Droplet/Particle Impingement on Dynamic Airfoils and Rotor Blades," AIAA Paper 2010-4229, presented at the 28th AIAA Applied Aerodynamics Conference, Chicago, IL, Jun 28-July 1, 2010b.

Sarofeen, C., Noack, R., and Kreeger, R., "A Non-Cut Cell Immersed Boundary Method for Use in Icing Simulations," AIAA Paper 2012-1204, presented at the 50th AIAA Aerospace Sciences Meeting, Nashville, TN, Jan 9-12, 2012.

Sehgal, A., and Ernst, R., "MQ-8 Fire Scout Icing Solution Challenges," presented at the American Helicopter Society 72nd Annual Forum, West Palm Beach, FL, May 16-19, 2016.

Soltis, J., Palacios, J., Eden, T., and Wolfe, D., "Ice Adhesion Mechanisms of Erosion-Resistant Coatings," *AIAA Journal*, vol. 53, no. 3, March 2015.

Szefi, J., Cormier, B., and Ionno, L., “Full-scale Experimental Validation of Dynamic, Centrifugally Powered Pneumatic Actuators for Active Rotor Blade Surfaces,” presented at the 70th American Helicopter Society Annual Forum, Montreal, Quebec, CA, May 20-22, 2014.

Tsao, J., and Kreeger, R., “Evaluation of Scaling Methods for Rotorcraft Icing,” presented at the American Helicopter Society 65th Annual Forum, Grapevine, TX, May 27-29, 2009.

Tsao, J., and Kreeger, R., “Further Evaluation of Scaling Methods for Rotorcraft Icing,” presented at the SAE/AIAA International Conference on Aircraft and Engine Icing and Ground De-Icing, Chicago, IL, June 13-17, 2011.

Work, A., and Lian, Y., “A Critical Review of the Measurement of Ice Adhesion to Solid Substrates,” Progress in Aerospace Sciences 98, March 1-26, 2018.

Work, A., Kreeger, R., Gyekenyesi, A., Vargas, M., and Drabiak, D., “The Adhesion Strength of Impact Ice Measured Using a Modified Lap Joint Test,” presented at the AIAA Atmospheric and Space Environments Conference, Atlanta, GA, June 25-29, 2018.

Wright, J., and Aubert, R., “Icing Wind Tunnel Test of a Full Scale Heated Tail Rotor Model,” American Helicopter Society 70th Annual Forum, Montreal, Quebec, CA, May 20-22, 2014.

Yamauchi, G., and Young, L., “A Status of NASA Rotorcraft Research,” NASA/TP-2009-215369, Sept. 2009.

Zhang, Z., Ma, L., Liu, Y., and Hu, H., “An Experimental Study on the Droplet Erosion Durability of a Hydro-/Ice-phobic Surface Coating,” presented at the 2018 AIAA Atmospheric and Space Environments Conference, June 2018.

CHAPTER 10. STRUCTURES AND MATERIALS

Lee W. Kohlman and Gloria K. Yamauchi[1]

INTRODUCTION

This chapter focuses on advancements made through NASA rotary wing/vertical takeoff and landing (VTOL) research efforts from 2007 to 2018 in the area of materials and structures. Several topics are included in the scope of the materials and structures research ranging from engine components and coatings, to primary airframe structures, cabin noise mitigation, sensing, and actuation. These research areas contribute to the themes of improved efficiency (increased range and payload), reliability, and safety.

There are several approaches for improving efficiency, resulting in increased range and payload and reduced fuel burn. Increasing the temperature of the engine core reduces fuel burn by improving the performance of the engine. Higher engine core temperatures require improvements in engine component operating temperatures. Thermal and environment barrier coatings (typically ceramic based) are used on turbine blades and combustion liners to protect lower-temperature-capable metal structures and materials susceptible to environmental attack including oxidation, corrosion and physical erosion. The other approach to achieving higher core temperatures is to use ceramic and ceramic composite materials directly in the engine hot section. As with ceramic barrier coatings, several challenges exist with ceramic structures, including component design and fabrication methods, physical durability, and environmental degradation.

Payload and range can also be improved by using composite materials for primary structure. Lighter-weight and damage-tolerant structures can be fabricated using composite materials. Carbon fiber/epoxy composites are the main type of composite materials used in aircraft primary structure. Carbon fiber structures can be fabricated from laminates of unidirectional plies, filament winding and fiber placement using carbon fiber tows, and laminates consisting of woven or braided fabrics. Since the final material properties of carbon fiber/epoxy composites are determined by the processing conditions used to fabricate the final part, characterization and prediction of performance are key. As such, an understanding of failure modes and processes is needed.

Safety and acceptability are other considerations important to current and future vertical lift vehicles. One major challenge is interior noise. NASA explored several approaches to reduce the transmission of noise and vibration to the cabin's interior. Approaches included considering panels of various construction including honeycomb core or foam core, and double layer panels with a foam barrier layer.

[1] NASA Ames Research Center, Moffett Field, CA 94035-1000.

An additional area studied was the utility of smart materials—materials that offer a unique coupling of stress and strain with electromagnetic and/or thermal excitation. One example is piezoelectric materials. Mechanical excitation of a piezoelectric material produces an electric potential that can be measured and used in sensing applications. When an electric potential is applied to the material, mechanical excitation is produced that can be used for actuation.

The following sections summarize the research in the aforementioned topics supported by NASA rotary wing research investments.

Erosion-Resistant Thermal Barrier Coatings

Miller [2009] provided a historical review of thermal barrier coatings, focusing on NASA's contributions from 1942–1990. Entering the 2000s, the focus has been on ultra-efficient engine technology.

The use of thermal and environmental barrier coatings (TEBCs) on engine hot section components is key to achieving higher efficiency, reduced emissions, and longer component life. TEBCs protect the underlying structure from high temperatures by having low thermal conductivity and therefore maintaining a high thermal gradient. Additionally, the TEBCs form a protective barrier to environmental attack such as oxidation, corrosion, and erosion. TEBCs can be formed by electron beam physical vapor deposition (EBPVD), plasma spray (PS), or slurry coating [Ali and Bhatt, 2009].

A TEBC is generally made up of two or more layers. The bond-coat layer acts as an interface between the substrate and the coating. This layer prevents sintering of the upper layers and the substrate and reduces permeation of moisture to the substrate [Ali and Bhatt, 2009]. The upper layer or layers consist of low-thermal-conductivity ceramic materials that may or may not take advantage of multi-component defect clustering. Multi-component defect clustering relies on a mixture of several different materials to form a highly irregular lattice structure for the purpose of phonon scattering, thus reducing thermal conductivity [Zhu et al., 2010b, 2012].

Understanding the erosion and impact characteristics of TEBCs to predict the lifespan of coated components is important [Zhu et al., 2009, 2010a]. Figure 10.1 shows the three typical stages of erosion for thermal barrier coatings.

A new test capability was modeled and developed to test the erosion and impact characteristics of TEBC test specimens. The experimental system was then tested and compared with modeling results [Kuczmarski et al., 2011].

Development of new coatings requires first modeling, and then testing, the coating properties. Modeling focuses on the residual stresses introduced by and within the coating. High residual stresses can result in premature failure of the component and/or loss of the coating. Testing was performed to compare model results with measured values [Ali and Bhatt, 2009].

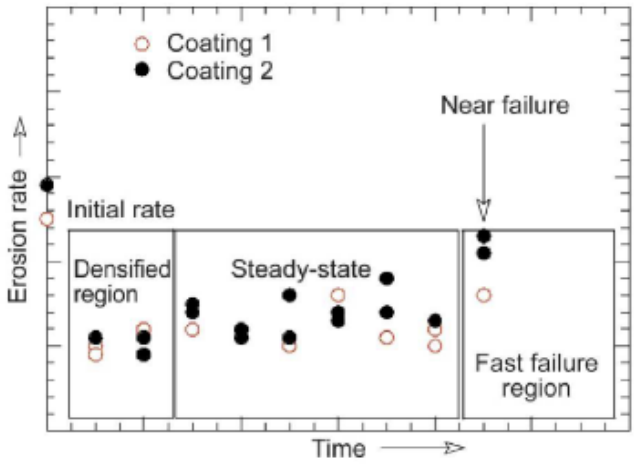

Figure 10.1. Typical erosion rate regimes of thermal barrier coatings. Coating erosion can be characterized by an initial fast erosion, a slower "steady-state" erosion stage, and a third faster erosion stage near failure (Fig. 5 of Zhu et al. [2010a]).

Miller et al. [2011] used FLUENT, a computational fluid dynamics (CFD) analysis validated by laboratory experiments, to design a new erosion rig. The new design had an unattached stationary duct and a pivoting burner rig; the burner would pivot in front of the unattached duct in the heating position and turn away from the duct in the cooling position. The authors determined that the design was feasible for conducting erosion burner-rig exposure of advanced coatings.

Swar et al. [2012] combined experimental and computational efforts to investigate the erosion of TEBC blade surfaces by alumina article ingestion in a single-stage turbine. Their experimental evidence from coupon testing showed that erosion rates increased with increased particle impingement angle, impact velocity, and temperature. For the three-dimensional (3D) simulation, Pointwise V16 meshing software was used to generate the grids used by the ANSYS CFX 12 flow solver. A commercial turbine and a NASA-designed automotive turbine were modeled; computed results showed similar erosion patterns.

Ceramic Materials and Composites

Ceramic materials and ceramic composites offer the potential to dramatically improve engine performance, including increased efficiency, operating temperature, and overall pressure ratio. Improved engine performance results in higher horsepower, better range, increased payload, and reduced operation and support costs.

One of the main concerns for ceramics and ceramic composites in the engine environment is oxidation. In the case of carbon fiber/silicon carbide composite, C/SiC, microcracks in the silicon carbide matrix can allow oxygen at high temperature to oxidize the carbon fibers, resulting in mass loss and eventual component failure. Stressed and unstressed tests were conducted to determine the effect of microcrack opening on oxidation rate [Halbig et al., 2008]. The studies provided insight on potential approaches to prevent oxidation of the fibers within the composite. Figure 10.2 summarizes the results from the stressed oxidation of C/SiC coupons.

Test temperature (°C)	Time to failure	Strain to failure (%)	Residual strength MPa
69 MPa			
1500	65 min	0.930	
1400	86 min	0.757	
1250	142 min	0.750	
1000	124 min	0.324	
750	91 min	0.209	
550	25+h	0.472†	248
350	25+h	1.08†	382
172 MPa			
1500	17 min	1.000	
1400	28 min	0.910	
1250	36 min	0.944	
1000	22 min	0.359	
750	22 min	0.363	
550	25 h	0.450	
350	25+h	1.08†	403

UTS of two as-received C/SiC tensile coupons at room temperature: 351 and 404 MPa. †Strain to failure during residual strength tensile tests.

Figure 10.2. Times to failure and strains to failure for the stressed oxidation of C/SiC coupons in air at a stress of 69 and 172 MPa (Table 1 of Halbig et al. [2008]).

Silicon nitride is well suited for use in small turbine engine components that are projected to significantly raise efficiency and performance in next-generation turbo-shaft engines [Singh et al., 2009]. However, because silicon nitride is less responsive to machining and typical manufacturing, joining techniques are required that enable integrating geometrically simpler parts into complex components. Singh et al. [2009, 2011, 2012] successfully demonstrated the self-joining of St. Gobain Si_3N_4 (NT-154) using a ductile Cu-Al-Si-Ti active braze (Cu-ABA). The shear strength of the Si_3N_4/Si_3N_4 joint was considered very promising.

Asthana and Singh [2009] evaluated two Palladium (Pd)-based brazes to determine their suitability for joining SiN4 and a copper (Cu)-clad-Molybdenum (Mo). The authors concluded that the soft and ductile Pd-Cobalt (Co) braze may be suitable for moderately high temperatures where high thermal conductivity is needed. The less ductile Pd-Ni brazes were unacceptable for joining because of extensive cracking caused by ineffective residual stress relief.

In Halbig et al. [2013], two Ag-Cu-Ti–braze alloys, Ticusil and Cusil-ABA, reinforced with 5, 10, and 15 wt% SiC particulates, were used to join chemical vapor deposited (CVD) silicon carbide to itself in order to control braze thermal expansion to mitigate residual stresses and to enhance the joint strength. The coefficient of thermal expansion of the braze was predicted to decrease by nearly 45–60 percent by including about 45 vol% SiC.

Supported by Small Business Innovation Research (SBIR) funds, Boyle et al. [2015] developed design concepts for a cooled ceramic vane for use in the first stage of the High Pressure Turbine (HPT). Honeywell International Inc. was subcontracted to provide technical guidance for this work to ensure relevance to the gas turbine industry needs. The contracted work was divided into three categories: analysis of the cycle benefits arising from the higher temperature capability of Ceramic Matrix Composite (CMC) compared to conventional metallic vane materials; a series of structural analyses for variations in the internal configuration of a first-stage vane for the HPT of a CF6-class commercial airline engine; and analysis for radial-cooled turbine vanes (one being a NASA-designed vane) for use in turboshaft engine applications.

Durability and Damage Tolerance

Polymer matrix composite materials have the potential to reduce the weight of many rotorcraft components. Understanding the ways in which these materials fail, therefore, is very important.

In Krueger [2011a], benchmark examples for static delamination propagation and cyclic delamination onset and growth were developed for validating a commercial finite-element analysis. The examples were based on a finite-element model of an End-Notched Flexure (ENF) specimen (see Fig. 10.3) and allowed the assessment of growth delamination prediction capabilities in commercial finite-element codes based on the virtual crack closure technique (VCCT). The approach was demonstrated for the commercial code ABAQUS®. The procedure for benchmarking highlighted issues related to input parameters of the particular implementation. Though the results were encouraging, the author concluded that further assessment for mixed-mode delamination was required. Additional details of the study, including an appendix on the inputs used for ABAQUS®, are provided in Krueger [2011b].

The author continued creating benchmark examples, this time focusing on the simulation of mixed-mode I/II fracture using Mixed-Mode Bending (MMB) specimens [Krueger 2012a, 2012c] (see Fig. 10.4). The MMB specimens, with different mixed-mode ratios (20 percent, 50 percent, and 80 percent mode II) and different initial delamination lengths, were simulated. The load and displacements were monitored for each delamination length that was modeled, and the mixed-mode I/II strain energy release rate was calculated for a fixed applied displacement. The benchmark cases were then created, and the approach demonstrated in ABAQUS® with promising results, although further work on mixed-mode delamination fatigue onset and growth was deemed necessary. Krueger [2012b] summarized the development of benchmark cases based on the Double Cantilever Beam (DCB), used in his 2011 and 2012 studies.

Iarve et al. [2011] used a mesh-independent cracking (MIC) framework to predict the evolution and delamination of transverse matrix cracks. A regularized extended finite-element method, MIC allowed cracks to be inserted in directions that are independent of the mesh orientation. The authors applied their methodology to a range of problems including a simple evolution of delamination from existing transverse cracks to strength prediction of complex laminates (without any a priori knowledge). Predictions agreed well with experimental data and/or conventional numerical solutions.

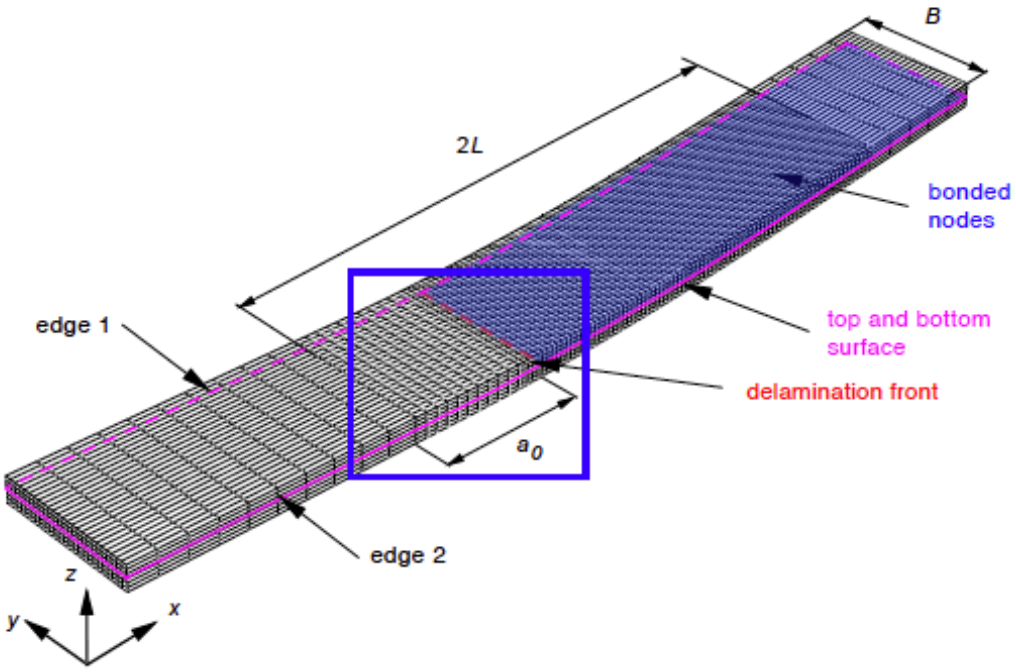

a. *Deformed three-dimensional FE-model with initial delamination front before growth.*

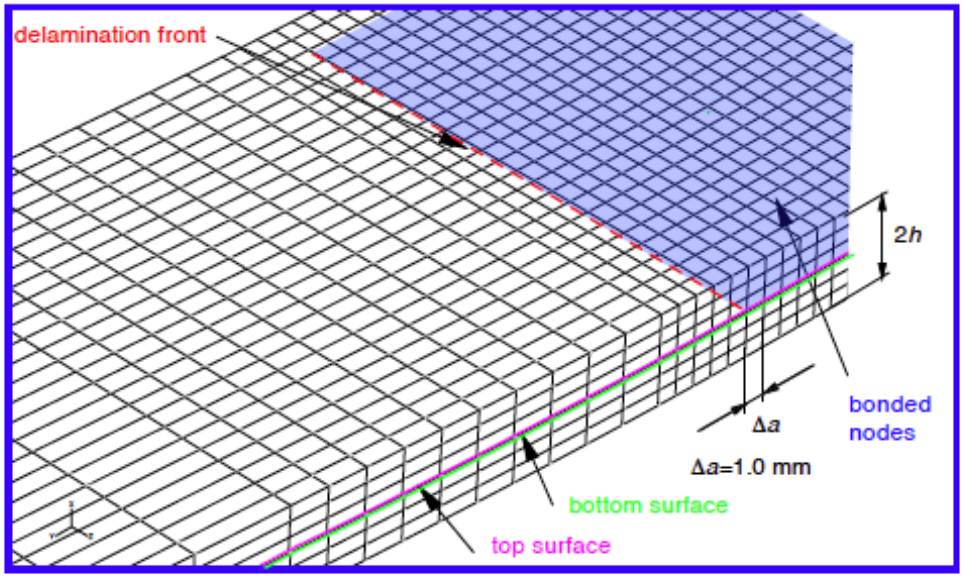

b. *Detail of three-dimensional FE-model around delamination front.*

Figure 10.3. Full 3D finite-element model of an ENF specimen (Fig. 6 of Krueger [2011b]).

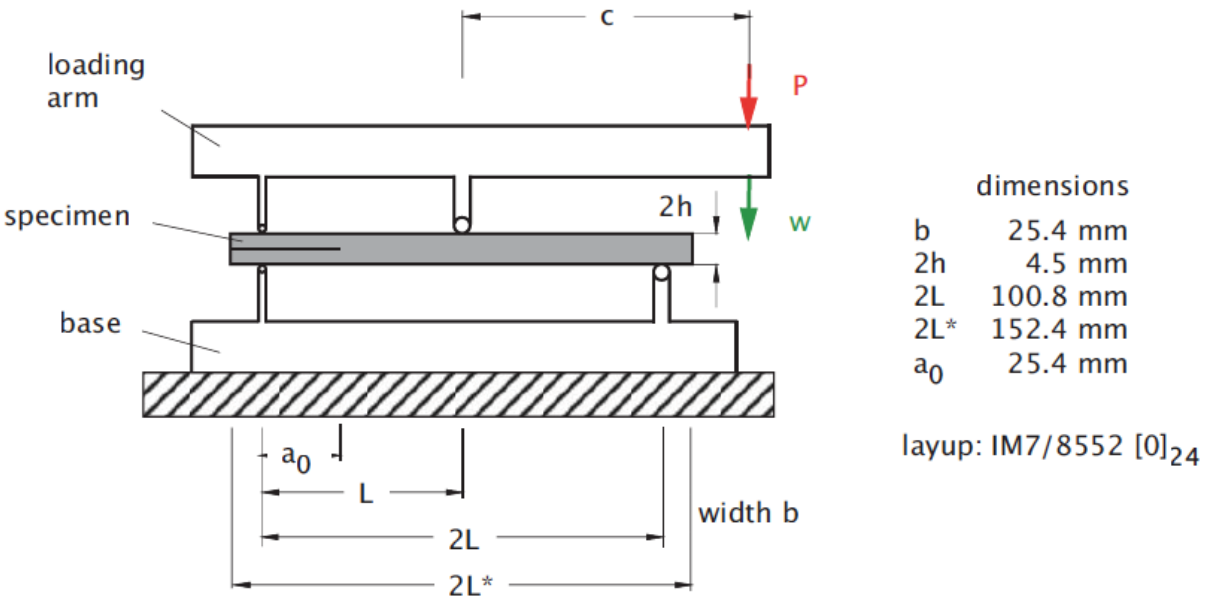

Figure 10.4. MMB specimen (Fig. 1 of Krueger [2012b]; dimensions from J. G. Ratcliffe, personal communication to Krueger).

Murri [2012, 2013] tested IM7/8552 graphite/epoxy DCB specimens, from two different sources, in static and fatigue to determine delamination characterization data. Figure 10.5 shows a DCB specimen in the loading fixture. The fracture toughness and strain energy release rate of the specimens were measured for the onset of delamination and growth under cyclic loading. The data were used in finite-element modeling; in addition, the fatigue test data were used to evaluate a proposed ASTM (formerly known as the American Society for Testing and Materials) standard for determining expressions for the linear range (Paris Law) of delamination growth under mode I loading. By normalizing the delamination growth results using individually fit compliance calibration constants from fatigue data, the author was able to show very good alignment of the specimens from the two different sources (Fig. 10.6). Good agreement between the Paris Law expressions for the two specimens was also achieved.

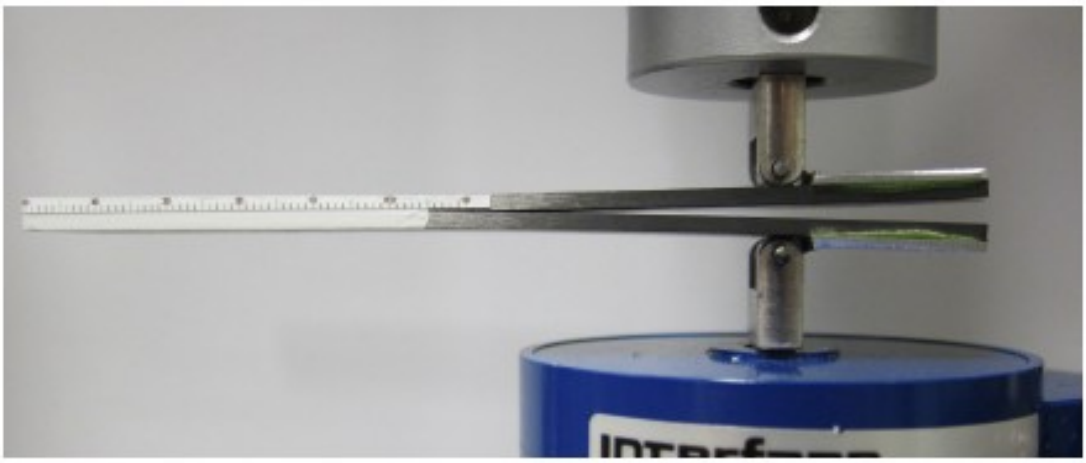

Figure 10.5. DCB specimen and loading fixture (Fig. 3 of Murri [2013]).

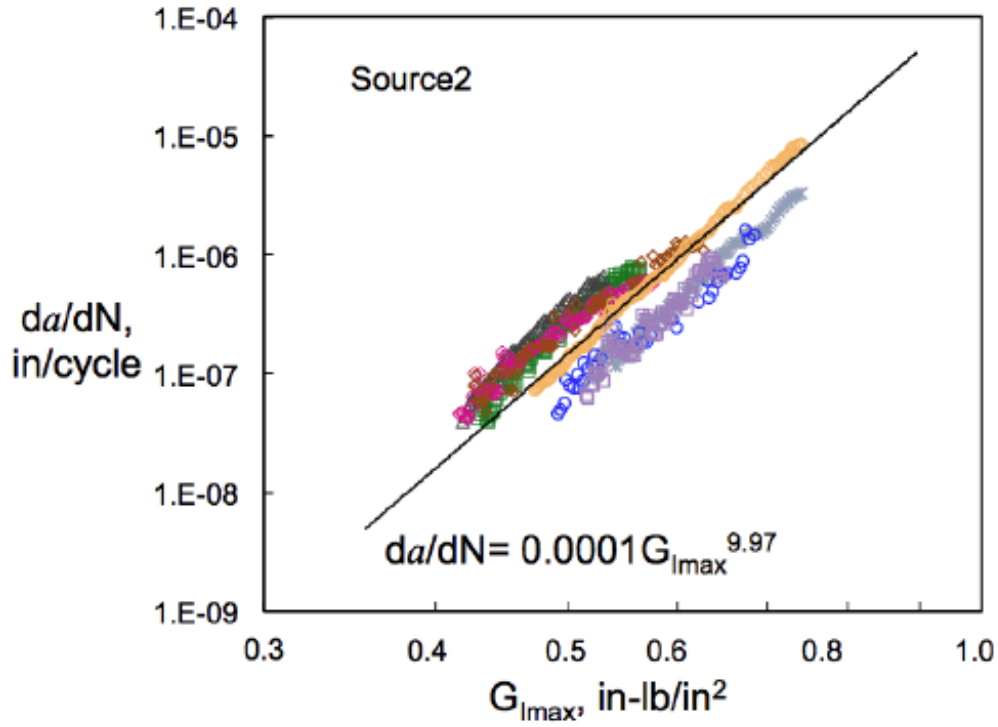

a) Delamination growth results using individually fit compliance calibration constants from fatigue data (Fig. 27 of Murri [2013]).

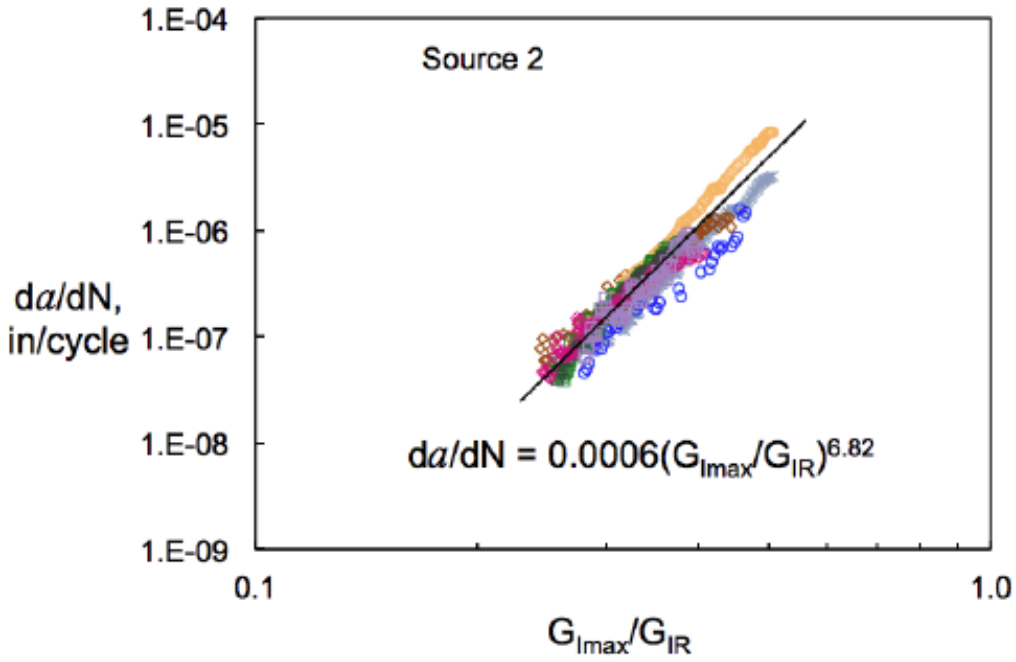

b) Normalized delamination growth results for Source 2 using individually fit compliance calibration constants from fatigue data (Fig. 29 of Murri [2013]).

Figure 10.6. Source 2 delamination growth results.

After a material is damaged, a process that automatically repairs or heals the structure is needed. As described in O'Brien and White [2008], the micro-encapsulation technique involves a polymer-based healing agent encapsulated in thin-walled spheres and embedded into a base polymer along with a catalyst phase. When a crack in the material grows, the spheres fracture and release the agent that then reacts with the catalyst, thereby healing the material. The authors tested composite, skin/stringer flange debond specimens; the specimens were constructed from prepreg containing interleaf layers with a healing agent contained within thin-walled spheres. The tests indicated that self-healing was possible in fiber-reinforced composite material assuming enough time and contact with pressure on the crack surfaces. Also, the amount of healing may be limited to the volume of healing agent available compared to the volume of the crack.

Ballistic impact testing was used on filament wound tubes manufactured with nanosilica additive to evaluate damage resistance and tolerance. The nanosilica increased the modulus and fracture toughness of the matrix material. Tubes with the nanosilica additive had smaller impact damage and higher residual shear strength [Vashisth et al., 2018]. Additional testing found that the impact damage area was decreased by as much as 50 percent, and the residual shear strength (torsion loading of the tubes) was increased by 38 percent [Vashisth et al., 2017].

The mode of failure of a sandwich structure depends on the configuration of the sandwich system and the loading scenario. One of the failure modes is facesheet/core debonding. Ratcliffe [2010] focused on developing a standardized facesheet/core peel debonding test procedure. By measuring the critical strain energy release rate associated with the debonding process, the author was able to characterize facesheet/core peel in a sandwich structure. He used a single cantilever beam (SCB) specimen to begin development of a standardization test procedure. Figure 10.7 depicts SCB versus DCB test specimens. The study resulted in the development of a practical SCB specimen sizing method, appropriate for including into a standardized testing protocol.

Crashworthiness—the ability of a structure to protect occupants during a crash—continues to be a design driver in both the aerospace and automotive industries. Composite structures have excellent specific strength, stiffness, and energy absorption, and as a result, composite structures are replacing metallic structures. Composites are also difficult to model because of their fiber/matrix combinations and the associated failure mechanisms. Nageswara et al. [2010] presented a material model able to simulate the crushing response of composite structures with different fiber architectures. The authors developed a DyCrash module for the LS-DYNA analysis to simulate the crushing response of various textile composites, including Kevlar.

Song et al. [2011] developed continuum damage mechanics (CDM) models to analyze progressive failure in open-hole laminates. They coupled CDM with a cohesive zone model for delamination to predict the failure of the much-studied configuration of a quasi-isotropic, open-hole-tension specimen. The authors studied the pull-out and delamination failure modes. In general, their numerical models predicted the proper failure mechanism and trends in the failure load. For specimens showing delamination failure, the failure loads were overpredicted, while for the specimens showing pull-out failure, the failure loads were underpredicted.

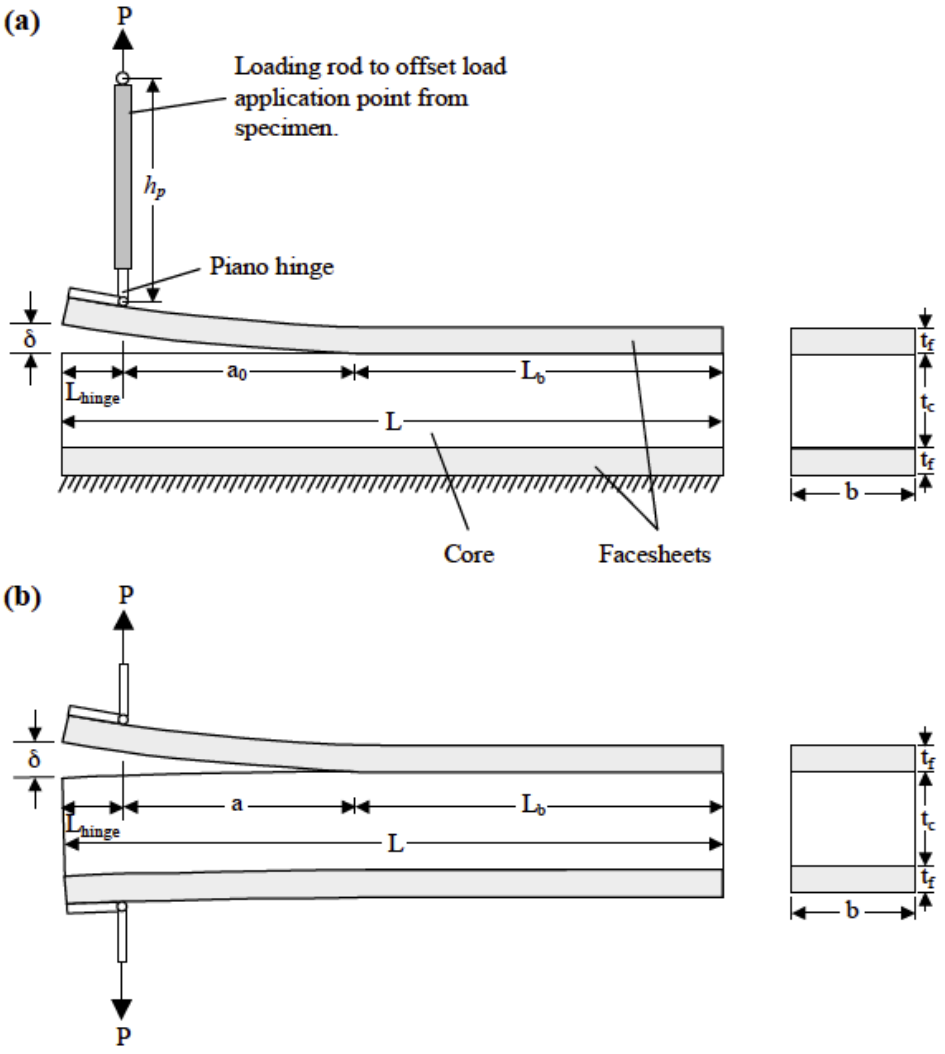

Figure 10.7. Classes of facesheet/core debond tests: (a) SCB-based specimen, and (b) DCB-based specimen (Fig. 1 of Ratcliffe [2010]).

Cabin Noise Reduction

Noise in the cabin of rotorcraft is a major concern for civilian applications. There are several approaches to mitigating cabin noise, including limiting noise at the source and limiting transmission from the source to the cabin.

Hong et al. [2010] considered polyimide foam as a lining in double-panel applications for aircraft sidewalls. Panels consisting of 2-mm-thick aluminum sheets separated by 12.7 cm (5.0 in.) with a layer of 7.6-cm (3.0-in.) polyimide foam in the center were fabricated. Initial tests determined that the flow resistivity of the foam was too high, and a process of systematic compression of the foam was used to reduce the flow resistivity [Silcox et al., 2013]. Overall, the test and modeling prediction showed good agreement [Silcox et al., 2013; and Hong et al., 2010].

Honeycomb core panels are a common element of aircraft structures because of the light weight and high stiffness of this type of construction. Grosveld et al. [2006] and Grosveld [2007] modeled and tested honeycomb core panels in an attempt to increase the acoustic transmission loss of these type of panels. The authors developed finite-element models of panels with areas where the core was removed from the radiating face sheet, thereby creating recessed areas. Compared to the baseline panel, the modified panel had a transmission loss improvement of 3–11 dB for a frequency range from 170–1,000 Hz and a 5.1-percent increase in mass and twice the deflection when excited by a static force. Good agreement between finite-element results and test measurements were achieved.

Foam core panels are another type of structure used in aircraft [Cabell et al., 2012]. Foam core panels also offer high stiffness with reduced weight. Different foams can be used in many applications to improve acoustic transmission loss. Foam core sandwich beams were modeled and fabricated, one with a light, compliant core, another with a higher-density stiff core, and a third with a periodically varying combination of the lighter and the denser foam core materials. Figure 10.8 shows averaged frequency responses for the three beams, normalized relative to their maximum values. Flexural excitation of the beams resulted in deflections that were in good agreement with finite-element predictions.

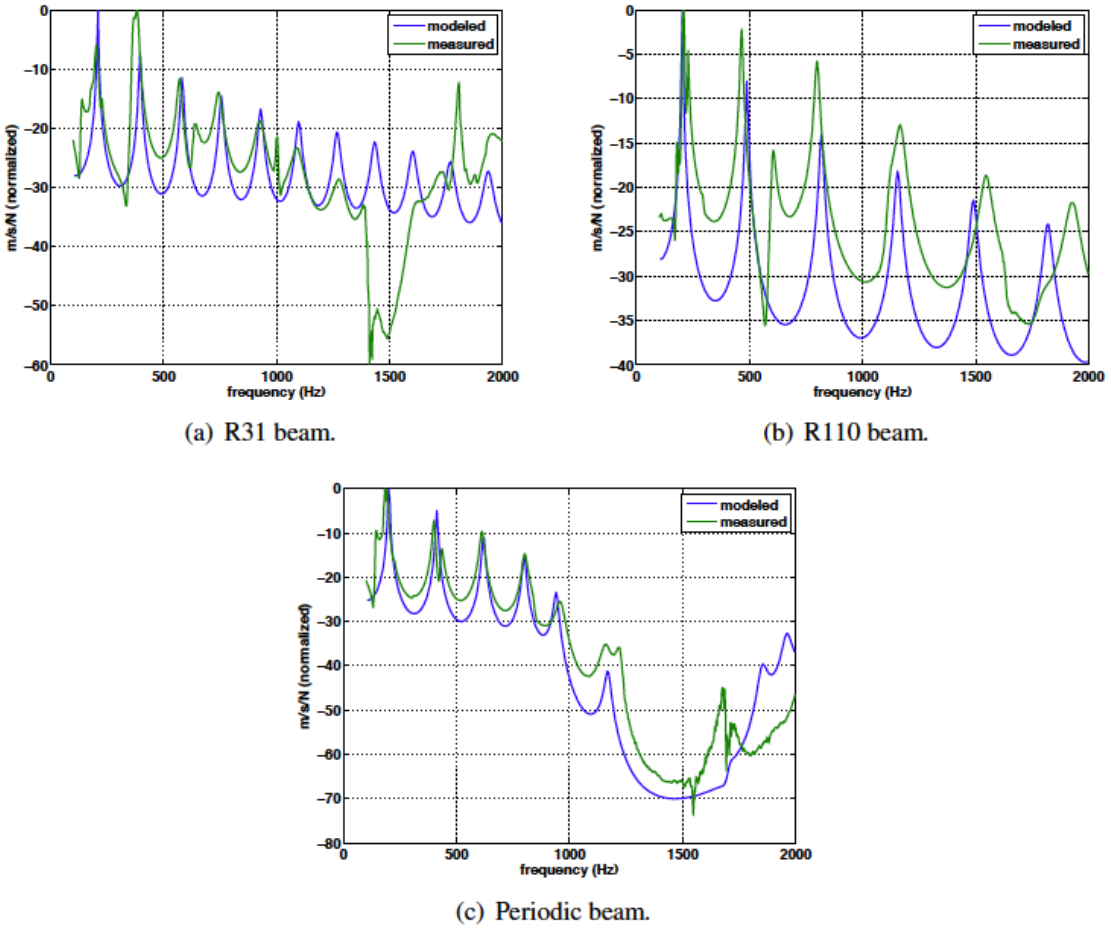

Figure 10.8. Averaged frequency responses between an input force and the response of the opposite end of the beam (Fig. 9 of Cabell et al. [2012]).

Smart Materials

Smart materials can be used in a variety of roles from sensing to actuation in rotorcraft systems. Two types of materials were investigated—applications of piezoelectrics and a magnetostrictive alloy.

Piezoelectric materials are capable of converting mechanical work into electrical excitation, and vice versa. This allows these materials to be used as a sensor, or in damping and energy harvesting applications, converting mechanical work into electrical signals, or as an actuator, producing mechanical work from an applied electric field. Research has focused on packaging, design, optimization, and testing of novel sensors and actuators. Bryant [2007] discusses a variety of packaging concepts. Additional work focused on vibration control using shunted piezoelectric patches [Beck et al., 2008, 2010]. Another application that was investigated was the use of macro-fiber composite (MFC) actuators for structural health monitoring. This application uses the piezo-actuator to create guided waves that interact with damage or structural defects [Collet et al., 2010].

Magnetostrictive materials exhibit a coupling between magnetic and mechanical states. Like piezoelectrics, they can be used for either actuation or sensing. One particular material was investigated—Galfenol (Fe81.6, Ga18.4). The frequency-dependent, effective material properties were calculated from the strain and magnetic flux density response to controlled dynamic stress [Scheidler et al., 2016a, 2016b]. Figure 10.9 shows the custom magnetic circuit developed for this work.

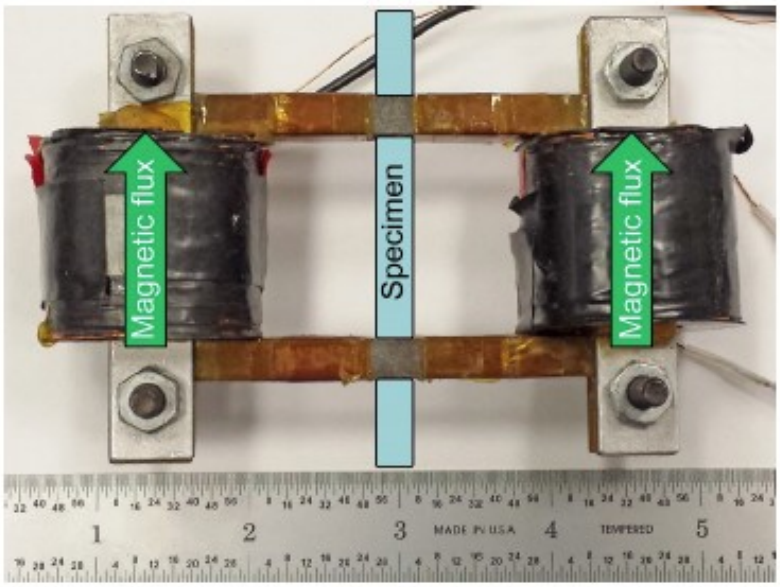

Figure 10.9. Magnetic circuit used to generate uniform magnetic state in the gauge region of a Galfenol specimen, while allowing for independent mechanical excitation (Fig. 1 of Scheidler et al. [2016]).

CONCLUDING REMARKS

The materials and structures work performed and/or supported by NASA rotary wing/VTOL research between 2007 and 2018 was intended to address key research topics relevant to future vertical lift vehicles. The goal of the work was to improve efficiency, payload, range, safety, and durability and focused on engine core technologies and vehicle structures. These efforts resulted in many conference papers, journal articles, presentations, and NASA reports. All work was considered precompetitive and for the benefit of the U.S. aeronautics industry.

REFERENCES

Ali, A-A., and Bhatt, R T., "Thermal Residual Stress in Environmental Barrier Coated Silicon Nitride-Modeled," The American Ceramic Society 33rd International Conference and Exposition on Advanced Ceramics and Composites; Symposium 2: Advanced Ceramic Coatings for Structural, Environmental, and Functional Applications Session: Environmental Barrier Coatings, Daytona Beach, FL, Jan. 18-23, 2009.

Asthana R., and Singh, M., "Evaluation of Pd-Based Brazes to Join Silicon Nitride to Copper-clad-Molybdenum," *Ceramics International,* vol. 35, 2009, pp. 3511-3515.

Beck, B., Cunefare, K.A., and Collet, M., "Experimental Assessment of Negative Impedance Shunts for Vibration Suppression on a Beam," SPIE Smart Structures and Materials + Nondestructive Evaluation and Health Monitoring, San Diego, CA, March 9-13, 2008. Also, Proc. SPIE 6928, Active and Passive Smart Structures and Integrated Systems 2008, 69281X (18 April 2008). DOI: 10.1117/12.775881

Beck, B. S., Cunefare, K. A., Collet, M., and Ruzzene, M. Collet, "Periodic Piezoelectric Sensor-Actuator Array for Vibration Suppression on a Beam," SPIE Smart Structures and Materials + Nondestructive Evaluation and Health Monitoring, San Diego CA, March 2010. Also, Proc. SPIE 7643, Active and Passive Smart Structures and Integrated Systems 2010, 76430P (9 April 2010). DOI: 10.1117/12.847750

Boyle, R. J., Parikh, A. H., and Nagpal, V. K., "Design Concepts for Cooled Ceramic Composite Turbine Vane," NASA/CR–2015-218390, Feb. 2015.

Bryant, R. G., "Overview of NASA Langley's Piezoelectric Ceramic Packaging Technology and Applications," 10th Japan International SAMPE Symposium and Exhibition (JISSE-10), Tokyo, Japan, Nov. 27-30, 2007.

Cabell, R. H., Cano, R. J., Schiller, N. H., and Roberts, G. D. "Modeled and Measured Dynamics of a Composite Beam with Periodically Varying Foam Core," NASA/TM–2012-217565, April 2012.

Collet, M., Ruzzene, M., Cunefare, K A., and Xu, B. "Modeling and Characterization of Macro-Fiber Composite Transducers for Lamb Wave Excitation," Proceedings of the Non-Destructive Evaluation/Smart Materials and Structures Conference, San Diego CA, March 2010.

Grosveld, F. W., Palumbo, D. L., Klos, J., and Castle, W. D., "Finite Element Development of Honeycomb Panel Configurations with Improved Transmission Loss," Inter-Noise 2006 Congress, Honolulu, HI, Dec. 3-6, 2006.

Grosveld, F. W., "Finite Element Development and Specifications of a Patched, Recessed Nomex Core Honeycomb Panel for Increased Sound Transmission Loss," NASA/CR–2007-214898, Sept. 2007.

Halbig, M. C., McGuffin-Cawley, J. D., Eckel, A. J., and Brewer, D. N., "Oxidation Kinetics and Stress Effects for the Oxidation of Continuous Carbon Fibers Within a Microcracked C/SiC Ceramic Matrix Composite," *Journal of the American Ceramic Society*, Feb. 2008, vol. 91, no. 2, pp. 519-526.

Halbig, M. C., Coddington, B. P., Asthana, R., and Singh, M., "Characterization of Silicon Carbide Joints Fabricated Using SiC Particulate-Reinforced Ag–Cu–Ti Alloys," *Ceramics International*, vol. 39, 2013, pp. 4151-4162.

Hong, K., Bolton, J., Cano, R., Weiser, E., Jensen, B., Silcox, R., Howerton, B., Maxon, J., Wang, T., and Lorenzi, T. "Validation of a Polyimide Foam Model for Use in Transmission Loss Applications," NOISE-CON 2010 Conference, Baltimore, MD, April 19-21, 2010.

Iarve, E., Gurvich, M., Mollenhauer, D., Rose, C. A., and Davila, C. G., "Mesh-Independent Matrix Cracking and Delamination Modeling in Laminated Composites," *International Journal of Numerical Methods in Engineering*, vol. 88, no. 8, 2011, pp. 749-773. DOI: 10.1002/nme.3195

Krueger, R., "Development of Benchmark Examples for Static Delamination Propagation and Fatigue Growth Predictions, 67th Annual Forum of the American Helicopter Society, Virginia Beach, VA, May 3-5, 2011a.

Krueger, R., "Development and Application of Benchmark Examples for Mode II Static Delamination Propagation and Fatigue Growth Predictions," NASA/CR–2011-217305, Nov. 2011b. Also NIA report no. 2011-02, 2011.

Krueger, R., "Development and Application of Benchmark Examples for Mixed-Mode I/II Quasi-Static Delamination Propagation Predictions," NASA/CR–2012-217562, April 2012a. Also NIA report no. 2012-01, 2012.

Krueger, R., "Development of Benchmark Examples for Quasi-Static Delamination Propagation and Fatigue Growth Predictions," Simulia Community Conference, Providence, RI, May 14-17, 2012b.

Krueger, R., "Development and Application of Benchmark Examples for Mixed-Mode I/II Quasi-Static Delamination Propagation Predictions," American Society for Composites 27th Technical Conference, Arlington, TX, Oct. 1-3, 2012c.

Kuczmarski, M., Miller, R., and Zhu, D., "CFD-Guided Development of Rigs for Studying Erosion and Large Particle Damage of Thermal Barrier Coatings," Modelling and Simulation in Engineering, vol. 2011, Article ID 837921, 2011, dx.doi.org/10.1155/2011/837921

Miller, R., "History of Thermal Barrier Coatings For Gas Turbine Engines. Emphasizing NASA's Role From 1942 to 1990," NASA/TM–2009-215459, March 2009.

Miller, R., Kuczmarski, M., and Zhu, D., "Burner Rig with an Unattached Duct for Evaluating the Erosion Resistance of Thermal Barrier Coatings," NASA/TM–2011-217008, June 2011.

Murri, G. B., "Evaluation of Delamination Onset and Growth Characterization Methods Under Mode I Fatigue Loading," ASC 27th Technical Conference/15th US-Japan Conference on Composites/ASTM D30 Meeting, Arlington, TX, Oct 1-3. 2012.

Murri, G. B., "Evaluation of Delamination Onset and Growth Characterization Methods Under Mode I Fatigue Loading," NASA/TM–2013-217966, Feb. 2013.

Nageswara R., Janapala, N. R., Chang, F-K, Goldberg, R. K., Roberts, G. D., and Jackson, K. E., "Crashworthiness of Composite Structures with Various Fiber Architectures," 11th International LS-DYNA® Users Conference, Detroit, MI, 2010.

O'Brien, K., and White, S. R., "Assessment of Composite Delamination Self-Healing Via Micro-Encapsulation," 23rd American Society for Composites Technical Conference, Memphis, TN, Sept. 9-10, 2008.

Ratcliffe, J. G., "Sizing Single Cantilever Beam Specimens for Characterizing Facesheet/Core Peel Debonding in Sandwich Structure," NASA/TP–2010-216169, Jan. 2010.

Scheidler, J. J., Asnani, V. M., and Dapino, M. J., "Dynamic Characterization of Galfenol (Fe81.6Ga18.4)," NASA/TP–2016-218754, June 2016a.

Scheidler, J. J., Asnani, V. M., and Dapino, M. J., "Frequency-Dependent, Dynamic Sensing Properties of Polycrystalline Galfenol (Fe81.6Ga18.4*)*," *Journal of Applied Physics*, vol. 119, 244902 (2016b).

Silcox, R. J., Cano, R. J., Howerton, B., Bolton, J. S., and Kim, N. N., "Development of Polyimide Foam for Aircraft Sidewall Applications," AIAA paper 2013-0213, 51st AIAA Aerospace Sciences Meeting including the New Horizons Forum and Aerospace Exposition, Jan. 7-10, 2013, Grapevine, TX. DOI: 10.2514/6.2013-213

Singh, M., Asthana, R., and M. Halbig, M., "Integration Technologies for Silicon Nitride Based Ceramic Systems for Advanced Rotorcraft Applications," 65th AHS Forum, Grapevine, TX, May 27-29, 2009.

Singh, M., Asthana, R., Varela, F. M., and Martínez-Fernández, J., "Microstructural and Mechanical Evaluation of a Cu-Based Active Braze Alloy to Join Silicon Nitride Ceramics," *Journal of the European Ceramic Society*, vol. 31, 2011, pp. 1309–1316.

Singh, M., Martinez Fernandez, J., Asthana, R., and Ramirez Rico, J., "Interfacial Characterization of Silicon Nitride/Silicon Nitride Joints Brazed Using Cu-Base Active Metal Interlayers," *Ceramics International*, vol. 38, no. 4, pp. 2793-2802, May 2012. doi.org/10.1016/j.ceramint.2011.11.050

Song, K., Li, Y., and Rose, C. A., "Continuum Damage Mechanics Models for the Analysis of Progressive Failure in Open-Hole Tension Laminates," AIAA paper 2011-1861, 52nd AIAA Structures, Structural Dynamics and Materials Conference, Denver, CO, April 2011.

Swar, R., Hamed, A., Shin, D., Woggon, N., and Miller, R., "Deterioration of Thermal Barrier Coated Turbine Blades by Erosion," *International Journal of Rotating Machinery*, vol. 2012, Article ID 601837. DOI:10.1155/2012/601837

Vashisth, A., Bakis, C. E., Ruggeri, C. R., Henry, T. C., and Roberts, G. D., "Effects of Nanosilica Filler on the Ballistic Impact Tolerance of Carbon/Epoxy Tubes Loaded in Torsion," AHS International 73rd Annual Forum, Fort Worth, TX, May 9-11, 2017.

Vashisth, A., Bakis, C., Riggero, C., Henry, T., and Roberts, G., "Ballistic Impact Response of Carbon/Epoxy Tubes with Variable Nanosilica Content," *Journal of Composite Materials*, vol. 52, no. 12, May 2018. DOI: 10.1177/0021998317728461

Zhu, D., Miller, R., and Kuczmarski, M., "Development of Life Prediction of Erosion Resistant Turbine Low Conductivity Thermal Barrier Coatings," 65th Annual Forum of the American Helicopter Society, Grapevine, TX, May 27-29, 2009.

Zhu, D., Miller, R., and Kuczmarski, M., "Development of Life Prediction of Erosion Resistant Turbine Low Conductivity Thermal Barrier Coatings," NASA/TM–2010-215669, Feb. 2010a.

Zhu, D., Miller, R. A., and Kuczmarski, M. A., "Design and Performance Optimizations of Advanced Erosion-Resistant Low Conductivity Thermal Barrier Coatings for Rotorcraft Engines," 66th Annual Forum of the American Helicopter Society, Phoenix, AZ, May 10-12, 2010b.

Zhu, D., Miller, R. A., and Kuczmarski, M. A., "Design and Performance Optimizations of Advanced Erosion-Resistant Low Conductivity Thermal Barrier Coatings for Rotorcraft Engines," NASA/TM–2012-217138, May 2012.

CHAPTER 11. CONCEPTUAL DESIGN AND SYSTEM ANALYSIS

Gloria K. Yamauchi and Christopher Silva[1]

INTRODUCTION

Since 2009, the importance of integrated, multidisciplinary tools for rotorcraft, and vertical takeoff and landing (VTOL) aircraft in general, has greatly increased because of new military aircraft competitions (e.g., Joint Multi-Role) and, in the civil world, the emergence of small Unmanned Aerial Systems (sUAS) and the potential of the Urban Air Mobility (UAM) market. In particular, the need for conceptual design and systems analysis tools that can quickly produce trade studies continues to be in demand as of this writing. As both a test of the capabilities of tools and as a means to assess and guide technology development, concept aircraft have also been developed and shared with the community.

Johnson and Sinsay [2009a, 2009b] provide a vision for rotorcraft conceptual design environment tools aimed at government laboratories. The authors stress the requirement to increase the fidelity of analyses early in the design cycle. An information manager, or framework, is proposed to organize information that describes the aircraft, and enable movement of that information to and from analyses. The resulting collaborative design environment, with a unified rotorcraft description, would permit access to analyses of varying fidelity. Though the vision of the authors has not come to complete fruition in 2019, NASA has made substantial progress toward an integrated conceptual design tool chain.

Until about 2012, NASA focus was still on traditional rotorcraft configurations and propulsion systems that supported the NextGen Concept of Operations. Within NASA rotorcraft, a significant effort focusing on Large Civil Tiltrotors (LCTRs) concluded with a major contracted study exploring tiltrotor fleet operations. The LCTR, designed with much lower tip speed to reduce noise, served as a technology "collector" for NASA that focused research on enabling technologies (see Johnson et al. [2005]). For example, the benefits of a 50-percent reduction in main rotor (or prop rotor) speed motivated a long-term NASA research effort in variable speed power turbines (VSPTs) and multi-speed drive systems (see Chapter 7, Engines, and Chapter 6, Drive Systems) that culminated in high–technology readiness level (TRL) technology that is now being transitioned to industry.

By 2015, NASA rotorcraft research began to transition from focusing on traditional rotorcraft to more general VTOL aircraft research. VTOL configurations of sUAS with four or more rotors began saturating the commercial market. Fast on the heels of the sUAS market came the UAM market and another explosion of new (and larger) VTOL aircraft configurations using electric propulsion. In general, NASA rotary wing analyses can be applied to both sUAS and UAM VTOL aircraft (with further development in some discipline tools), but validation data is currently unavailable except at the component level. The new UAM aircraft present a host of interesting challenges in every technical discipline, from acoustics to propulsion to safety.

[1] NASA Ames Research Center, Moffett Field, CA 94035-1000.

This chapter begins by describing the NASA Design and Analysis of Rotorcraft (NDARC) sizing code and the NDARC trade studies of traditional rotorcraft configurations. Next, a section is dedicated to a number of studies on tiltrotors and the LCTR, and smaller variant, the LCTR2. A Technical Challenge (TC) during 2016–2018 is then described. The TC combined tools into a framework in order to develop low-emission and quiet concept vehicles and perform trade studies. Research during 2015–2017 on sUAS is next described, followed by a section on UAM concept vehicles and UAM systems. Concept vehicles and systems directed at public service are provided in the final section of this chapter.

NASA DESIGN AND ANALYSIS FOR ROTORCRAFT (NDARC)

Fortunately, the timely introduction of the NDARC sizing analysis has provided a means of analyzing a wide range of conventional and unconventional aircraft since 2009. NDARC was on the verge of release when Yamauchi and Young [2009] was published. As described in Johnson [2009, 2010a, 2010b], the principal tasks of NDARC are to design (or size) a rotorcraft to satisfy specified design conditions and missions. NDARC is then used to analyze the performance of the aircraft for a set of off-design missions and point operating conditions. Aircraft components, including fuselage, rotors, wings, tails, and propulsion are modeled; attributes such as performance, drag, and weight can be calculated for each component. NDARC is flexible enough to model almost any aircraft, with or without rotors. The software, written in Fortran, includes low-fidelity models, typical of the conceptual design environment. Although a stand-alone code, NDARC typically uses rotor performance maps generated by a rotorcraft comprehensive analysis, such as CAMRAD II [Johnson, 1994]. For most NASA conceptual design efforts, NDARC is supplemented by CAMRAD II rotor performance calculations, which generate the parameters for a surrogate model used in NDARC.

To date, NASA, the U.S. Army, and the U.S. Navy have adopted NDARC as the primary tool for rotorcraft sizing and conceptual design. The Army and Navy users are applying NDARC to requirements development, assessment of proposed new aircraft, and assessment of technology payoff. Figure 11.1 shows the growth in the number and type of NDARC user organizations. Software usage agreements are often with organizations with multiple users, so the number of NDARC users is larger than the number of software usage agreements.

Initially, NDARC was applied to analyze extensions of conventional rotorcraft (CRC) configurations with conventional propulsion systems. Later developments in NDARC included more nontraditional features, as shown in Figure 11.2. The American Helicopter Society (AHS) (now the Vertical Flight Society) biennial aeromechanics specialists' meetings, historically held in San Francisco, California, are shown, as each event was often the opportunity to showcase some new features or applications of NDARC to a broader audience. The conceptual design process was continually improved with each configuration analyzed. Examples of NDARC applications are provided next.

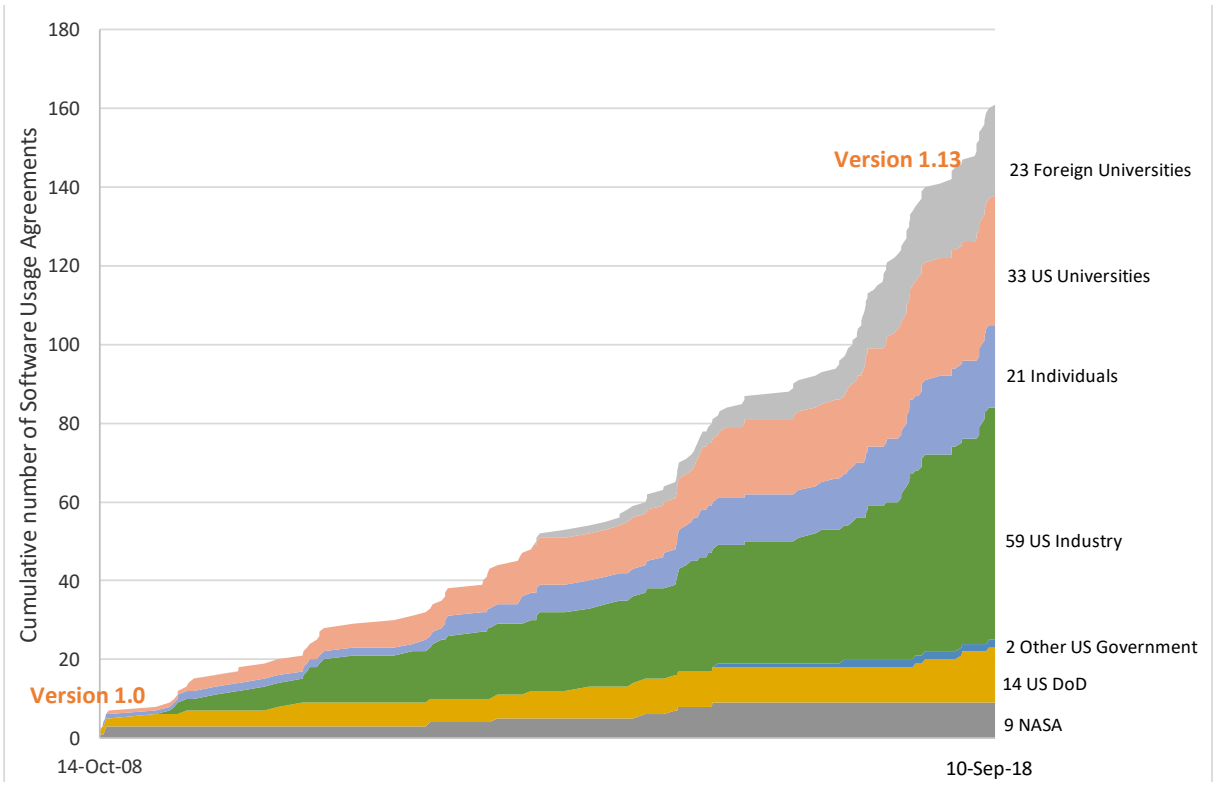

Figure 11.1. NDARC user-base growth from 2008 to 2018.

In one of the early practical applications of NDARC, Silva et al. [2010] exercised CAMRAD II and NDARC to design a winged, single-main-rotor compound helicopter. The design was driven by primarily Joint Services Mission requirements. The authors explored the benefits of trading rotor speed, wing-rotor lift share, and trim strategies for an example set of sizing conditions and missions.

Kottapalli and Harris [2010] used NDARC to model a C-130 Hercules and then transformed the NDARC model to represent a twin-rotor winged compound. Johnson et al. [2012] examined lift-offset rotorcraft designed for short-haul missions, civil and military, and provided two models for estimating rotor blade and hub weights. A large, civil compound helicopter design was developed by Russell and Johnson [2012]. In this study, the goal was to determine missions that were better suited for a compound rather than a tiltrotor or conventional helicopter. The compound included a single-main-rotor, tail rotor, and two cross-linked tractor props mounted on the wing. The compound design (named the CH90) was found to have higher cost than the tiltrotor and the conventional helicopter. Russell and Johnson [2013b] expanded on their 2012 paper by broadening the design space for the compound to include three other designs: 1) SH90–CH90 with swiveling tail rotor, 2) SW90–SH90 with smaller wing, and 3) TC90–tandem rotor configuration with two wing-mounted propellers. For the targeted civil mission, the TC90 provided the best performance. Johnson et al. [2016] explored a coaxial compound for urban military missions that included medevac, cargo delivery, attack, and utility operations. Figure 11.3 illustrates the TC90 concept.

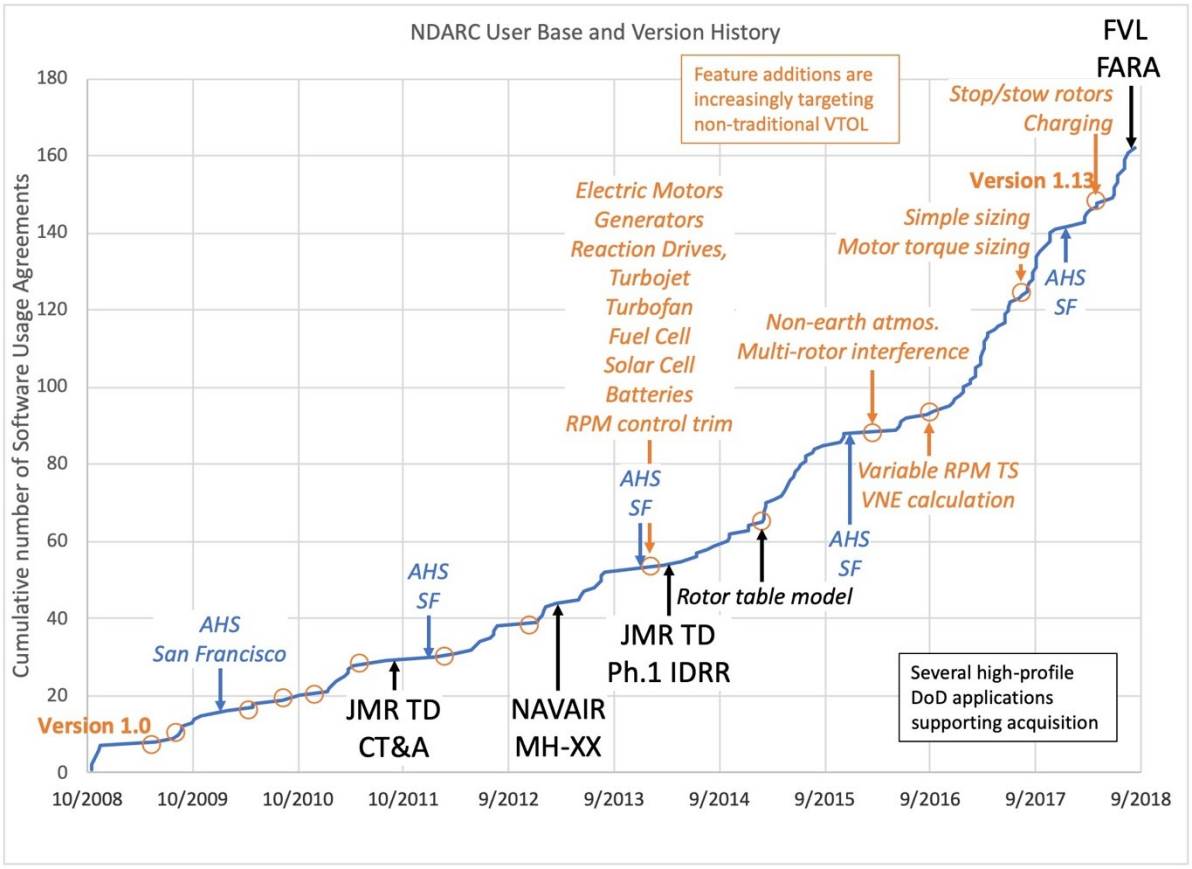

Figure 11.2. Features and events overlaid on NDARC's history. Early uses were primarily military while recent developments shifted to nontraditional VTOL.

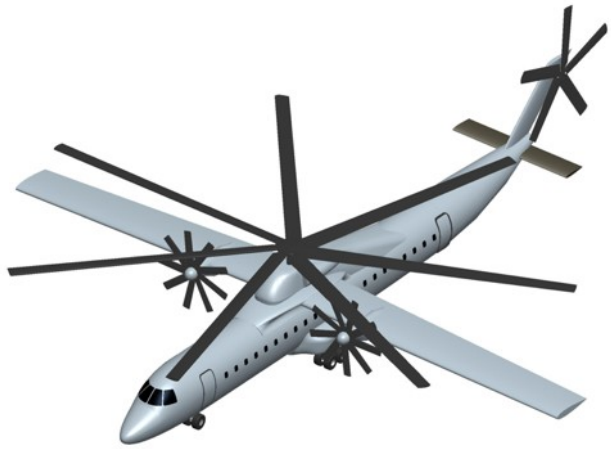

Figure 11.3. TC90 concept aircraft (Fig. 2 of Russell and Johnson [2013b]).

With increasing attention given to green aviation in the past decade [Russell et al., 2015], two major enhancements to NDARC were incorporated: climate impact metrics and nontraditional propulsion. Russell and Johnson [2013a] explored using climate metrics, average temperature response (ATR), and European Union Emissions Trading Scheme (EU ETS) as drivers for rotorcraft design. Using an LCTR design as a baseline configuration, the authors generated several designs for minimum empty weight, fuel burn, and environmental impact. Different assumptions for the ATR model resulted in very different final designs. Russell and Bassett [2015] compared approaches used by NASA and ONERA (the French Aerospace Lab) when designing environmentally friendly rotorcraft. This study stemmed from a task initiated in 2011 under the U.S.-French Project Agreement on rotorcraft studies to collaborate on design methodologies for environmentally friendly rotorcraft. ONERA employed the Concepts of Rotorcraft Enhanced Assessment Through Integrated Optimization Network (CREATION) analysis while NDARC and the comprehensive analysis CAMRAD II were used for the NASA designs. Comparisons were made between the baseline helicopter designs generated by the two tools. Designs were then generated with the aim of reducing environmental impact. The authors concluded that rotorcraft that typically fly at high altitudes, such as tiltrotors, should fly lower and slower to reduce the impact of NOx emissions, with the possible consequence of higher fuel burn and carbon dioxide (CO_2) emissions. Johnson [2014, 2015] implemented a major enhancement to NDARC by including a wide variety of propulsion models, including electric motors and generators, rotor reaction drives, turbojet and turbofan engines, fuel cells and solar cells, batteries, and fuel (energy) used without weight change. NDARC Version 1.10 was released in March 2016 and included environmental impact metrics and the expanded models for propulsion. NDARC was now ready to design environment-friendly aircraft.

CIVIL TILTROTORS (CTRs)

The heavy-lift rotorcraft systems investigation by Johnson et al. [2005] generated specific attention on the LCTR. Acree [2010] analyzed the rotor performance and aeroelastic stability of the LCTR. With a low-mounted wing, hingeless rotors, and a very low cruise tip speed, the LCTR strayed significantly from then-current tiltrotor technology. The author studied the effect of new blade airfoil designs and optimized twist, taper, and precone on performance in hover and cruise. A new airfoil was also designed for the wing, and a composite structure was developed to meet wing load requirements for certification.

Harris [2017] followed up on the LCTR design of Johnson et al. [2005] by investigating the feasibility of a large tiltrotor aircraft capable of cruising at 425 to 450 knots at altitude and having V/STOL capability at Denver (i.e. 5,000 feet) with an outside air temperature (OAT) of 95°F. The author concluded that research aimed at a 120-passenger VTOL civil transport capable of cruising efficiently at 425 knots and at 25,000 feet pressure altitude was worth pursuing and offered a number of recommendations regarding design choices.

The second-generation design of the NASA Large Civil Tiltrotor, the LCTR2 [Acree et al., 2008], was designed for 90 passengers compared to its 120-passenger LCTR predecessor [Johnson, et al. 2005]. Like the LCTR, the LCTR2 served as a technology “collector” that focused and advanced research in multiple disciplines, especially new propulsion architectures.

A key attribute of the LCTR2 is a relatively large reduction in proprotor tip speed in cruise, which yields significantly higher cruise efficiency by matching blade loading to operating condition. Figure 11.4 shows a 3-view of the LCTR2.

The work on heavy-lift rotor systems by Johnson et al. [2005] was relevant not only for civil applications but also for the military's Joint Heavy Lift (JHL) activities during the same time period. Yeo et al. [2010] used CAMRAD II and their internal design code, RC, to explore rotor blade sizing for the baseline design of the military's High Efficiency Tiltrotor (HETR). The overall aircraft performance of the HETR approximated several potential JHL configurations. The LCTR2 was also included in the study of blade sizing. The authors concluded that although rotor solidity is an important parameter for hover and cruise performance, turn performance is a more critical design condition for determining the blade area for the HETR and LCTR2.

The following sections include propulsion architectures for the LCTR/LCTR2, LCTR2 aerodynamics and performance, and a system study of civil tiltrotor (CTR) fleet operations.

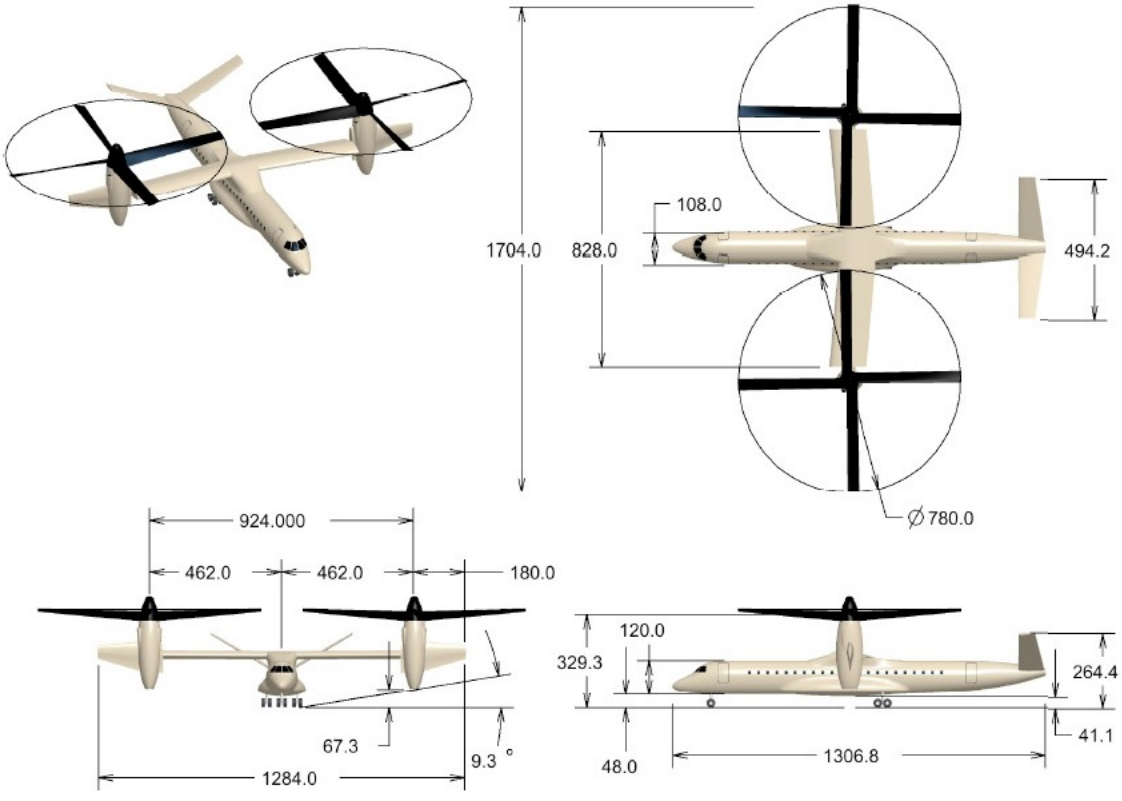

Figure 11.4. LCTR2 geometry (Fig. 1 of Acree et al. [2008]).

Propulsion Architectures for the LCTR/LCTR2

Operating turboshaft engines at reduced rotational speed in cruise is a technical challenge, especially as speeds drop below those reached by past tiltrotors. Veres [2009] developed a turboshaft engine concept for the LCTR. After defining the major components of the propulsion system, Veres [2009] performed a study of two compressor designs that would meet the LCTR design requirements. Following this work, Veres and Thurman [2010] developed several conceptual designs for a compressor appropriate for the smaller LCTR2. In addition to the Numerical Propulsion System Simulation (NPSS) (pressure ratio, mass flow definition) and Weight Analysis of Turbine Engines (WATE) (shaft sizing) codes, Veres and Thurman [2010] used three mean-line compressor design codes (COMDES, TCDES, and QUIK) and a flow analysis code (T-AXI) to arrive at a two-spool, axial-centrifugal compressor that met the requirements for the LCTR2.

NASA funded a multi-year study with Boeing (with subcontractor Rolls-Royce) to identify and evaluate propulsion system concepts to achieve approximately 50 percent rotor tip speed variation for the LCTR2 and to investigate the most advantageous speed variation strategies and technologies for the integrated engine and drive system. The study comprised multiple tasks:

1. NASA NNA06BC41C Task Order 10, "Engine/Gearbox Assessment for 50 percent Variable Rotor Tip Speed."
2. NASA NNA09DA56C Task Order 2, "Option 1 & 3 Dual Speed Gearbox Evaluation for 50 Percent Variable Rotor Speed."
3. NASA NNA09DA56C Task Order 4, "Engine/Gearbox Assessment for 50 Percent Variable Rotor Speed—Extended Tasks."
4. NASA NNA09DA56C Task Order 5, "50 Percent Engine-gearbox Design Study."

An initial analysis began with Snyder et al. [2010]. Several engine and gearbox technology levels were assumed, ranging from commercial off-the-shelf (COTS) to 2025 and 2035 entry-in-service (EIS) technology. The assumptions precluded definitive conclusions regarding the benefit of the engine versus the gearbox to achieve the speed reduction in the early stage of the study. Figure 11.5 presents block diagrams for the fixed- and variable-speed transmission concepts of the LCTR2.

For the first task (Engine/Gearbox Assessment for 50 Percent Variable Rotor Tip Speed, Task 10), Robuck et al. [2011] expanded upon the work of Snyder et al. [2010] by providing additional details of the analysis methodology, conceptual propulsion and drive configurations, and additional vehicle sizing data for the 2035 EIS engine. The 2035 EIS engine performance was optimized near 100 percent engine speed for a fixed-geometry variable speed power turbine (FG-VSPT). In a follow-on paper, Robuck et al. [2013a] use the FG-VSPT as the baseline engine to study cruise tip speed, mission ranges, and cost.

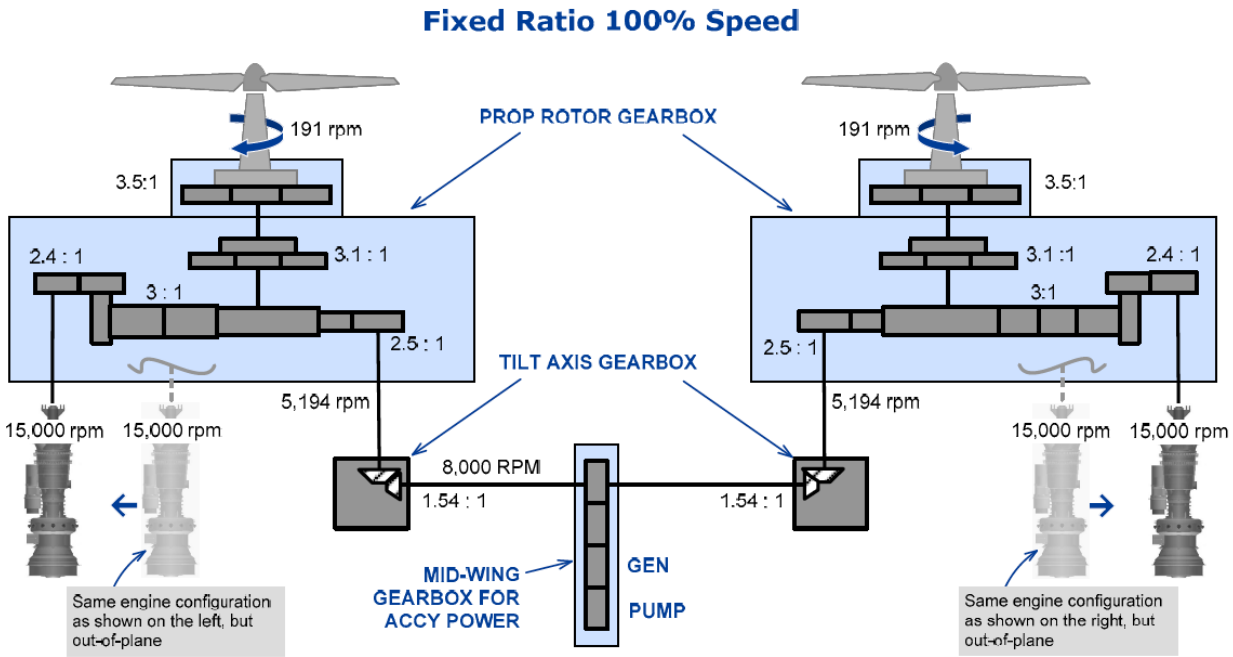

a) Reference drive system of the LCTR2 (Fig. 8 of Snyder et al. [2010]).

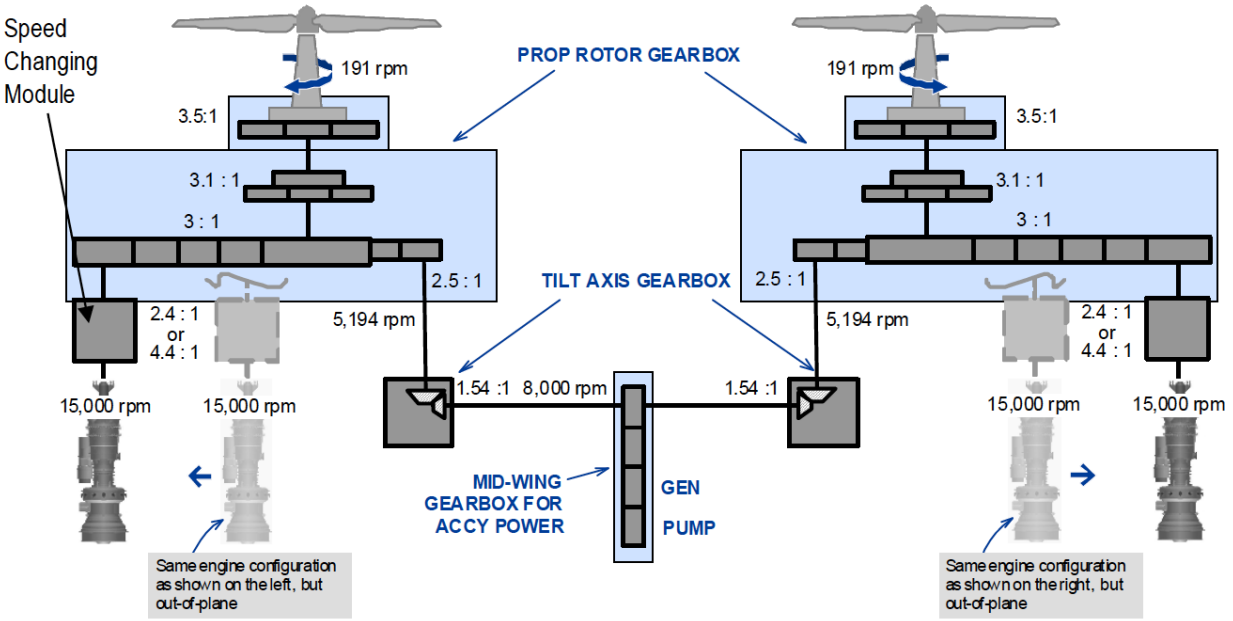

b) Drive system block diagram with speed changing modules (Fig. 10 of Snyder et al. [2010]).

Figure 11.5. Drive system block diagram for the LCTR2.

Combinations of engine rpm reduction and two-speed drive systems were evaluated. Three levels of engine and drive system advanced technology (2015, 2025, and 2035) were assessed; propulsion and drive system configurations that resulted in minimum vehicle gross weight were identified. Design variables included engine speed reduction, drive system speed reduction, technology, and rotor cruise propulsion efficiency. The LCTR2 was resized for over 30 combinations of operating cruise rpm and technology level, quantifying LCTR2 gross weight, size, and mission fuel. An extensive report [Robuck et al., 2013b] provides a summary of results for all four tasks of this multi-year study.

After Snyder et al. [2010], NASA continued internal studies in parallel with Boeing. Snyder [2011, 2013] further defined turbine gas engine requirements for the LCTR2. The One Engine Inoperative (OEI) condition, being the most stringent condition, defined engine power requirements for the four-engine LCTR2. Snyder used both NDARC and NPSS to analyze a range of missions. The effect of different LCTR2 propulsion concepts on sizing and missions was explored in Acree and Snyder [2012]. An advanced, single-speed engine with an advanced conventional engine (ACE) power turbine layout and a variable speed power turbine (VSPT) engine were studied. The lighter ACE required a multi-speed (shifting) gearbox, while the VSPT used a lighter, fixed-ratio gearbox. Trade-offs between rotor and engine efficiency and weight were explored using NDARC, supported by results from CAMRAD II and NPSS. The trade studies revealed that the two propulsion configurations had very similar performance and weight results. In Snyder and Acree [2012], the work of Acree and Snyder [2012] was expanded to include more engine configurations in the trade study. Five VSPT engine concepts were included in the study. Surprisingly, a two-stage FG-VSPT with a fixed-ratio gearbox was the best among these propulsion concepts for most parameters, except for its 3- to 5-percent-higher fuel burn.

Howard [2012] assessed the feasibility of a VSPT concept for the LCTR2 from a rotordynamic perspective. A VSPT would enable high-efficiency propulsion at the high forward velocities anticipated for the LCTR2. The author analyzed critical speed placement in the operating speed envelope, stability analysis up to the maximum anticipated operating speed, and potential unbalance response amplitudes. Figure 11.6 shows a critical speed map for the LCTR2. Howard [2012] concluded that a VSPT is feasible, but not without challenges.

Snyder [2014] summarized the results of the NASA LCTR2 propulsion studies. The design methodology realized significant benefits in performance, weight, and fuel burn by a combination of assumed advanced technologies in turbomachinery, combustors, and materials. Note that the goal of significantly reducing rotor rpm using either the gearbox or engine generated a core research effort summarized in Chapter 6, Drive Systems, and Chapter 7, Engines, herein.

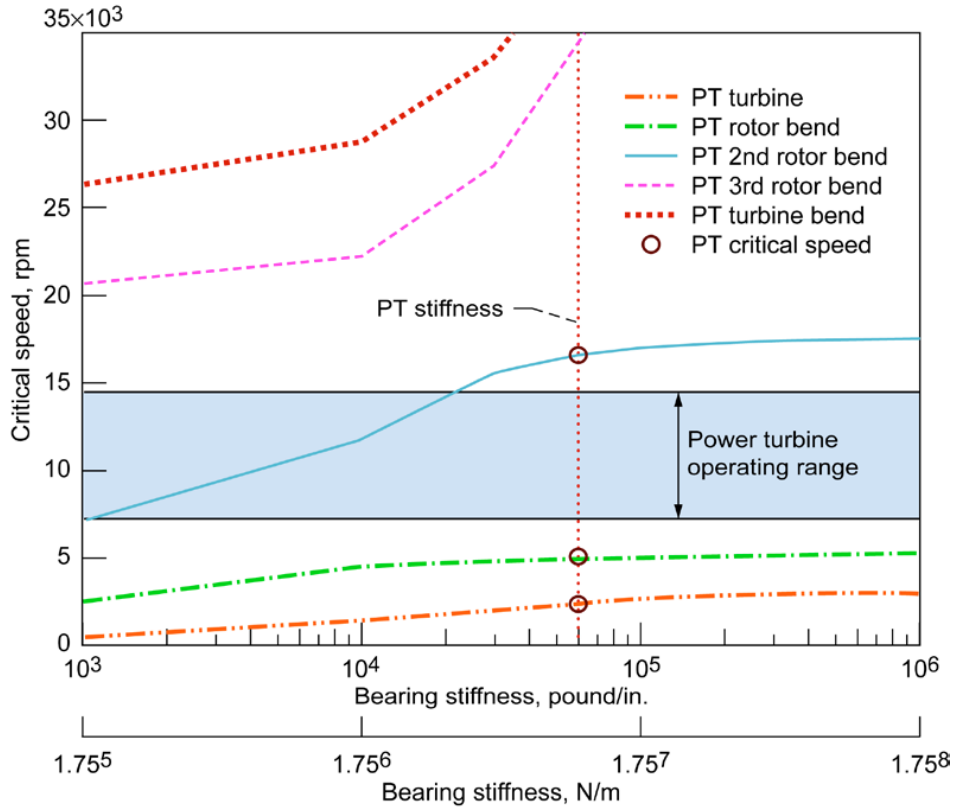

Figure 11.6. Critical speed map for the LCTR2 power turbine rotor (Fig. 4 of Howard [2012]).

Operational Concepts for a Fleet of Civil Tiltrotors

In late 2008, NASA began funding a 3-year study focusing on a fleet of civil tiltrotors (CTRs) and their impact on the Next Generation Airspace Transportation System (NextGen airspace). The contractor team and their main responsibilities included: Science Applications International Corporation (SAIC)—overall lead and vehicle concept of operations (CONOPS) definition; Bell Helicopter, Textron—vehicle conceptual design, pilot-in-the-simulation, and rotorcraft/disaster-relief modeling; Sensis Corporation—regional and National Airspace System (NAS) modeling and simulation; and Optimal Synthesis, Inc.—terminal area procedures and modeling. In the first reporting of this study, Young et al. [2010] describes the parameters and scope of the study. The fleet comprised CTR sizes able to carry 10, 30, 90, and 120 passengers. Figure 11.7 describes the characteristics of the CTR fleet.

The airspace simulation tools, ACES and AvTerminal, were the primary analysis tools used for evaluating fleet impact on the airspace in the northeast corridor. The base of aircraft data (BADA)—the aircraft performance model developed by EUROCONTROL—was required to translate the CTR performance data into input recognized by ACES and AvTerminal. In 2011, Young et al. [2011] built upon the work of Young et al. [2010] by expanding the CTR fleet service from just the northeast corridor to include the Atlanta regional network and a Las Vegas regional network. The Joint Planning and Development Office (JPDO) projections for demand

and capacity for 2025 were used to assess the fleet impact on the three airspace regions. The authors found that *"The NAS-wide average delay decreased from ~22 minutes for the conventional fixed-wing fleet baseline to 7–8 minutes with the combined introduction of the CTR fleet throughout all three primary regional networks."* Chung et al. [2011] provides a detailed description of results and underlying assumptions.

Taking the next step, Chung et al. [2012] focused on the dependence of non-interference operations (NIO) and runway-independent operations (RIO) of the CTR fleet on conventional air traffic flow and runways. A shuttle service between Boston Logan International Airport (BOS) and Newark Liberty International Airport (EWR) served as the test route for examining NIO and RIO. A safety analysis emphasizing CTR thrust-vectoring failure modes was also included using a number of case studies. Chung et al. [2012] concluded that advances that can predict CTR performance and environmental impact with more fidelity are needed in NAS performance analysis tools.

Number of Passengers		10	30	90 (1)	120
Weights:					
Design Gross Weight, DGW	lb	16800	46460		147647
Maximum Gross Weight, MGW (Full Fuel & Payload)	lb	16192	46430		147647
Empty Weight + Trapped Fluids	lb	11022	32160		98737
Payload	lb	2200	6600	19800	26400
Operating Load	lb	470	670	870	1070
Number of Crew	ND	2	3	4	5
Fuel System Capacity	lb	2500	7000		21441
Geometry:					
MR Radius	ft	13.0	19.0		36.1
Number of Blades per Rotor	ND	3	4	6	6
Wing Span	ft	33.8	45.8		100.4
Length Fuselage	ft	n/a	61.6		111.9
Engine/Xmsn:					
Number of Engines	ND	2	2	4	4
Engine Takeoff Power Rating (SLS - uninstalled)	eshp	3000.0	9000.0		9372.0
MCP Xmsn rating @ mast (100%rpm)	hp	n/a	4412.0		13063.0
Aero/Performance Related:					
Main Rotor Tip Speed (100% rpm)	fps	775	700	665	650
Main Rotor Tip Speed, A/P mode (70%rpm)	fps	651	588	466	455
Flat Plate Drag (alpha=0) (3)	sq ft	11.0	23.4		56.3
Design Cruise Altitude	ft	25000	25000	27500	27500
Design Cruise Speed (2)	ktas	n/a	n/a	340	345
Range (5k/ISA+20 deg C takeoff)					
@ max payload, max fuel & Vlrc	nm	821	804		1331
@ max payload, max fuel & Vmcp	nm	750	671		1179 (4)

(1) Characteristics based on linear interpolation between 30 and 120-pax designs
(2) 90 and 120-pax design cruise speeds based on Vmcp
(3) Drag does not include nacelle cooling drag which is inherently built into engine residual thrust.
(4) Vmcp = 345 kts for sizing and mission cruise not exactly the same; Vmcp for mission legs > 345 ktas

Figure 11.7. CTR fleet—final design characteristics (Table 2 of Young et al. [2010]).

In a companion study under this contract, Gibson et al. [2012a, 2012b] evaluated the effectiveness of CTR executing hurricane-Katrina-like post-disaster relief operations. Two rotorcraft fleet mixes were evaluated: 1) CTR-10, -30, and -120 passengers, and 2) light, medium, and heavy CRC. Missions included evacuation (ambulatory and nonambulatory), search and rescue, and cargo transport. The study determined that the higher speed and range of tiltrotors, compared to CRC, can improve the overall effectiveness of hurricane post-disaster operations. Also, augmenting a fleet of CRC by 10 percent with tiltrotors can significantly reduce overall mission response time.

Chung et al. [2012] documented the findings of the 3-year study and provides an extensive list of recommendations and suggestions for future research.

Civil Tiltrotor Aerodynamics

The LCTR2 also served to flesh out the conceptual design process for rotor aerodynamics. Acree [2010] demonstrated a process for integrating aeromechanics analysis (that is, CAMRAD II software) and vehicle sizing (NDARC). By optimizing LCTR2 cruise tip speed with rotor/wing interference, an integrated (though largely manual) design process was demonstrated and valuable lessons learned were generated. Continuing his aerodynamic exploration of the LCTR2, Acree [2014] analyzed an aerodynamically idealized rotor, wing, and airframe, and then repeated the analysis with more realistic assumptions. NDARC, CAMRAD II, and a vortex lattice code were used for the study. Acree [2014] concluded that increasing maximum rotor lift was likely more effective for improving vehicle efficiency compared to higher rotor or wing efficiency. The author also discusses the benefits and limitations of practical layouts for the airframe. An interesting analysis of the aerodynamic damping of a tiltrotor wing with extensions is provided in the appendix of Acree [2014]. Figure 11.8 shows a variation of the LCTR2 wing—one with swept extensions.

Figure 11.8. LCTR2 with 25-ft swept extensions (Fig. 5 of Acree [2014]).

Using a hybrid–computational fluid dynamics (CFD) analysis, RotCFD, Young et al. [2013] explored the LCTR2 wake interactions around terminal areas. The RotCFD analysis [Rajagopalan et al., 2012; Guntupalli et al., 2016] was developed primarily through NASA Small Business Innovation Research (SBIR) funding and NASA contracts. Rotor outwash, wake interactions with buildings, and pressure loading on buildings were included in the study. To gain more understanding of the in-ground-effect aircraft performance and flow field, Young [2015b] then used RotCFD to simulate approximately 1/48th-scale tiltrotor models that were tested with a ground plane and a generic building in a wind tunnel. In Young [2018b], the author offers a variety of nontraditional tiltrotor configurations for consideration. An LCTR2-variant with under-wing-mounted pusher-props is one of the concepts offered (see Fig. 11.9).

a) Hover b) Transition c) Cruise

Figure 11.9. Pusher-proprotor tiltrotor (Fig. 1 of Young [2018b]).

CONCEPTUAL DESIGN TOOL CHAIN DEVELOPMENT

The vehicle design experience with the LCTR and LCTR2 highlighted the growing need for a conceptual design tool chain with modular components operating within an optimization framework. The process of designing a rotorcraft in the U.S. has remained a largely serial process, such that competing design objectives are not evaluated in a formal, streamlined fashion. Instead, the outcome of separate optimization processes representing different disciplines (e.g., rotor aerodynamics, propulsion, etc.) are exchanged and discussed by subject-matter experts from the design team, and an iterative cycle between design groups ensues until certain objectives—usually empty weight and speed—are met. In the past few decades, the U.S. rotorcraft original equipment manufacturers (OEMs) have introduced “new” aircraft that are usually growth versions of existing aircraft and/or represent upgraded control systems and avionics. Hence, the motivation for automating the design process has been limited, since test and field data from legacy aircraft and designer experience are used to project the capabilities of new designs. As with all extrapolations, future configurations generated from the current design process will not stray far from the existing fleet. The established OEMs use a combination of commercial, government, and proprietary analysis tools. For new VTOL aircraft manufacturers, especially those engaged with nontraditional configurations, in-house discipline tools appropriate for rotary wing vehicles are rarely available. A mismatch exists between publicly available analyses and requirements for new and unconventional VTOL concepts.

Conceptual design is the first phase of the design process and requires rapid evaluation by multiple discipline tools of consistent fidelity. NDARC is a state-of-the-art sizing code but it still requires supporting discipline tools such as aerodynamics, acoustics, propulsion, handling qualities, and rotor structures to capture the critical interdisciplinary aspect of rotary wing vehicle design. The majority of these discipline tools do not exist at the level of fidelity required for conceptual design; that is, simplified analyses that provide results in seconds rather than hours and days. Higher-fidelity tools in each of the aforementioned areas exist and are used to verify that the simplified analyses accurately represent the system, provide surrogate models, and analyze final optimized conceptual designs.

In late 2015, with the rapid growth in new VTOL configurations stemming from the sUAS market and the overall emphasis on green aviation, the NASA Revolutionary Vertical Lift Technology (RVLT) Project launched an internal 3-year TC to demonstrate a multidisciplinary design analysis optimization (MDAO) process for vertical lift vehicles. Specifically, the TC addressed the following technical barrier: *A conceptual design optimization process for VTOL aircraft, of any size and configuration, which is multidisciplinary, internally consistent, rigorously integrated, and streamlined, does not exist.*

The 3-year TC had the objective to develop and demonstrate a streamlined, integrated, multidisciplinary optimization process of consistent fidelity for conceptual design of VTOL aircraft. The exit criteria for the TC were: 1) integrate new discipline tools in a design optimization framework, and 2) develop low-noise, low-emission VTOL conceptual designs generated using the new MDAO process. The outcome of the 3-year effort, concluded in September 2018, was evaluated on the basis of fidelity, metric scope, objective function, tool efficiency, and design goals.

The process developed by September 2018 is shown in Figure 11.10. Different optimization loops are possible, depending on the objective of the optimization. A combination of NASA and commercial software products comprise the tool chain. The design and optimization process and tool chain are described next.

A basic aircraft configuration (single main rotor (SMR), tiltrotor, tandem, fixed-wing without props, etc.) is prepared with discrete values of parameterized inputs in order for the sizing tool, NDARC, to start the conceptual design process. Once a closed design is achieved, the design is evaluated by other tools and metrics are computed. The metrics are then passed to an optimization driver. Note that evaluating the performance of the design is always required and standard tools are already in place to compute the metrics of power, weight, fuel (energy), and emissions. These metrics must be included in the Objective Function.

In order to establish a measure of relative improvement because of design optimization, a set of baseline aircraft were considered, designed to a set of reference missions and requirements. These reference missions and requirements span a set of VTOL aircraft capabilities representative of rotorcraft missions that are performed today and that are envisioned for the near future. In order to ensure that the design missions and conditions are consistent between baseline and optimized aircraft, baseline aircraft were also designed with the same conceptual sizing tool, NDARC.

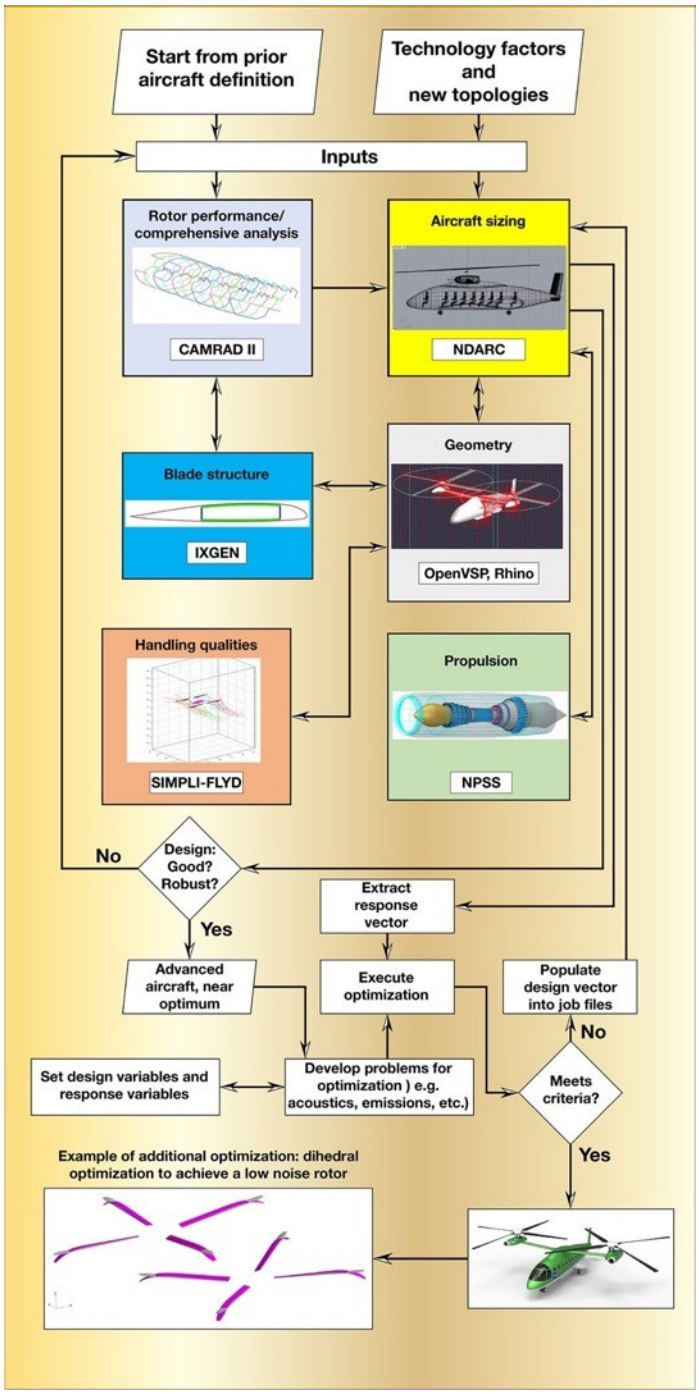

Figure 11.10. Conceptual design process for VTOL aircraft—at completion of TC, September 2018.

The optimization process includes computing the Objective Function, exercising optimization algorithms, and adjusting design parameters. The Objective Function is evaluated first and tolerances checked. The process either stops (outputting a final design that meets the exit criteria) OR the process continues through the optimization process. OpenMDAO includes several optimization algorithms (gradient-free and gradient-based). Eventually, the design parameters are adjusted and a new design solution is sought by invoking NDARC. NDARC contains surrogate models, but if, for example, the rotor design parameters deviate significantly from the surrogate rotor performance models in NDARC, a comprehensive rotorcraft analysis (in this case, CAMRAD II) is used to generate new rotor performance maps for NDARC.

Four primary research tasks were required to enable the process depicted in Figure 11.10 and the TC goals:

1. Developed conceptual design-level tools or surrogates for:
   a. emissions
   b. handling qualities
   c. acoustics
   d. structural integrity
2. Developed appropriate metrics for handling qualities, acoustics, and emissions.
3. Integrated tools within OpenMDAO using a modular approach.
4. Demonstrated process by generating designs of low-noise, low-emission VTOL aircraft.

The following sections describe the four tasks in more detail.

Task 1: Developed Conceptual Design-Level Tools or Surrogates

The emissions metrics explored by Russell and Johnson [2013a] were implemented in the release of NDARC 1.10 in March 2016. Emissions trading scheme (ETS) metrics, average temperature response (ATR) metrics, and emissions species weights were incorporated in the NDARC release. Emissions modeled included direct greenhouse gas carbon dioxide, nitrogen oxides, water vapor, aerosols of soot and sulphate, and aviation-induced cloudiness.

Lawrence et al. [2016a, 2016b, 2018] describe a new design-level tool for handling qualities of multi-rotor vehicles. The Simplified Flight Dynamics for Conceptual Design (SIMPLI-FLYD) tool, co-funded by the U.S. Army and RVLT, was developed and interfaced with NDARC. SIMPLI-FLYD has a dependency on the commercially available (U.S. Government-sponsored development by U.S. Army) CONDUIT software for evaluation of handling qualities metrics and optimization of control system parameters.

Boyd [2017] developed a rotor acoustic calculation tool chain comprising CAMRAD II and ANOPP2 (a suite of noise prediction codes developed by NASA [Lopes and Burley, 2016]), which was subsequently used to optimize rotor blade planforms for low noise. The optimization was performed using code developed by Boyd called AeroAcoustic Rotor Noise (AARON), which couples CAMRAD II and ANOPP2. Figure 11.11 summarizes the result of the rotor design optimization using A-weighted Sound Exposure Level (SEL).

Parameter	Optimized Value	Individual effect	Combined effect
Tip dihedral	-39.4 deg	38.9%	
Tip sweep	-41.9 deg	12.1%	
Tip chord	0.48c	19.1%	
Radius	1.336R	13.5%	
Tip dihedral	-38 deg		59.5%
Tip sweep	-44.5 deg		
Tip chord	0.62c		
Radius	1.049R		

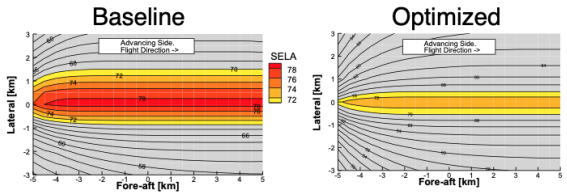

AS350 level flight acoustic footprint prediction.

Figure 11.11. Results of optimization tool chain (CAMRAD II-AARON-ANOPP2) to evaluate the effects of design parameters on noise metrics for the AS350 helicopter.

An analysis for structural integrity has not yet been incorporated into the tool chain. IXGEN, a commercial software that can compute rotor blade and wing structural load and equivalent beam properties based on material properties, was exercised independent of the broader tool chain. Another commercial software, PBWEIGHT, is currently being developed for computing vehicle component structural properties as a Phase III SBIR. Future enhancement of the tool chain will aim to incorporate structural analyses similar to IXGEN and PBWEIGHT.

Task 2: Developed Appropriate Metrics for Handling Qualities, Acoustics, and Emissions

Metrics used for environmental impact included the ETS—which is only a measure of carbon dioxide emission, and ATR, which is a measure of long-time contribution to global temperature. ATR is dominated by carbon dioxide emissions except in cases where aviation-induced cloudiness (AIC, “contrails”) is possible, where the AIC effect dominates.

SIMPLI-FLYD used handling qualities specifications based on rotorcraft (e.g., ADS-33) and fixed-wing (e.g., MIL-STD-1797) established specifications. Design margins for primary control axes were also considered.

The Federal Aviation Administration (FAA) has established limits for certifying helicopters for noise. These limits are a function of helicopter gross weight and three flight conditions (approach, takeoff, and level flyover). The noise measurements are acquired using three microphones at specific locations relative to the flight path of the subject vehicle. Simulations for the concept vehicles for the three FAA flight conditions were executed, and the acoustics at the three corresponding microphone locations were computed. ANOPP2 was used to compute metrics consistent with the FAA guidelines.

Task 3: Integrated Tools Within OpenMDAO Using a Modular Approach

Realization of an integrated and streamlined tool chain, as depicted in Figure 11.10, required development of a new software package. RCOTOOLS [Meyn, 2018] is python-based software that facilitates incorporating NDARC, CAMRAD II, and NPSS into the OpenMDAO (version 1) framework. NDARC and CAMRAD II in particular use file-based inputs and outputs so RCOTOOLS provides software wrappers to update input files with new design variable values, run the codes, and then extract specific values from the output files. The wrappers were written to be easy to use, flexible, and are supported by helpful utilities. RCOTOOLS 1.0 was officially released on May 2018 and can be requested from NASA through the Ames software release process. Figure 11.12 illustrates the RCOTOOLS work flow.

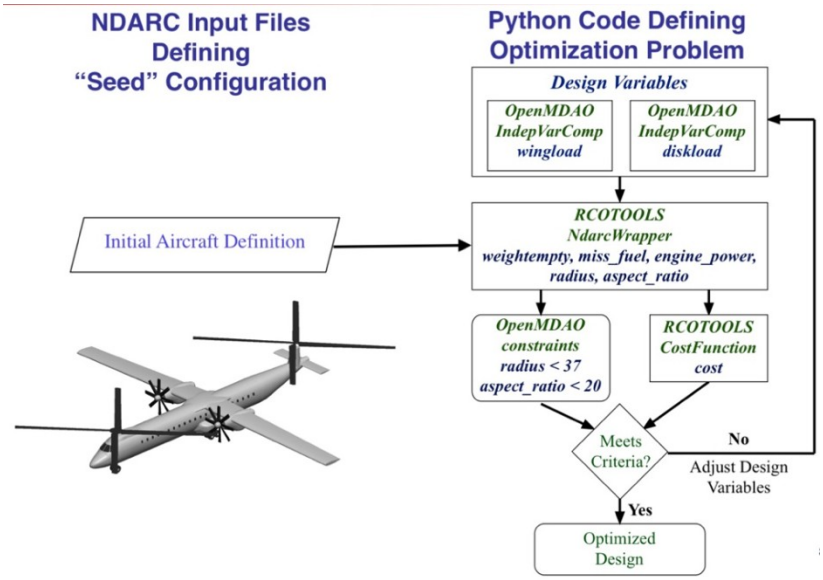

Figure 11.12. Illustration of simple NDARC-OpenMDAO optimization process.

Task 4: Demonstrated Process by Generating Designs of Low-Noise, Low-Emission VTOL Aircraft

Silva et al. [2018a] exercised the major parts of the tool chain shown in Figure 11.10 to successfully design low-emission vehicles in three size classes (A, B, and C). A baseline vehicle representing a currently fielded aircraft was also designed for each size class. For the design activity, missions were developed for three size classes: (A) 6-person aircraft with 400-nautical-mile range, (B) 24-passenger aircraft with 500-nautical-mile range, and (C) 76-passenger aircraft with 1,300-nautical-mile range. Technologies for the baseline aircraft represent helicopters in production in 2015; the advanced technology aircraft take advantage of airframe technologies at a Technology Readiness Level (TRL) of 5 or above by 2020, except for the electric and fuel cell propulsion designs, which were allowed to explore much lower TRLs in the electric systems and ranges as low as 100 nautical miles in order to achieve size parity with the conventional propulsion systems.

The following, taken from Silva et al. [2018a], captures specific observations for the Class A, B, and C weight classes.

Class A

- The lack of efficient small (<1,000 shp) turboshaft development is a limiter for achieving goal of >50% emissions reduction.
- The coaxial helicopter is better than a Single Main Rotor (SMR) helicopter.
- Do you fly high or do you fly low? What should emission objective be?
  - ETS says fly high if wing-borne to burn less fuel.
  - ATR says fly not-too-high to avoid making contrails.
- Tiltrotor does not get light enough to take advantage of cruise efficiency.
  - Drop the wing extension (weight) because small payload and range.
  - Dropping pressurization (weight) and flying low has same emissions.
  - Wing extensions and pressurization require several interrelated inputs to NDARC.
- Batteries fall short (specific energy); U.S. electric grid emissions high.
- Fuel cells cannot make it (specific power); emissions can be very low even if we are getting hydrogen from methane source.

Class B

- The recent focus on engine technologies at this size pays off.
  - Even the advanced tech SMR gets 43% reduction in emissions.
- Tiltrotor might as well fly high (but below AIC).
  - The wing extension is worth it for payload and range.
  - Cruise fuel burn with payload and range favors pressurization.
- Side-by-side looks promising.
  - Low installed power from low disk loading.
  - Light-weight despite the cross-bars due to small engines and fuel.
  - Cruise efficiency 50% better than helicopters.
  - Low flyaway and operating costs, in addition to low emissions.

Class C

- The reduced emissions for the Class C vehicle are relative to a baseline aircraft, which is already fairly efficient, therefore, the reductions are not as significant as for the Class A and B low-emission aircraft.
- The emission reduction is enabled by the long-distance cruise of 1,300 nm, which allows the cruise efficiency of the High Efficiency Commercial Tiltrotor (HECTR) to reduce the fuel load substantially, which in turn reduces vehicle weight and thus the installed power.

Figure 11.13 illustrates the family of low-emission vehicle designs explored for this TC. The total number of distinct vehicles studied and optimized is greater than the seven distinct types and sizes shown; turboshaft, hydrogen-fuel-cell, and battery-powered aircraft were examined for some of these vehicle types. Also, an advanced technology SMR helicopter was designed for Class B, and an advanced technology tiltrotor was designed for Class C. A total of 20 vehicle models were produced: 8 vehicles for Class A, 9 vehicles for class B, and 3 vehicles for Class C.

The final tool chain demonstration supporting this TC was to design a VTOL aircraft with at least 50 percent lower emission and 70–80 percent lower noise than the corresponding baseline vehicle. An interesting observation is that the implementation of a higher technology engine and choice of vehicle type (discrete design variables) accounted for nearly all of the improvement in the objective function, and continuous design variables such as tip speed and disk loading accounted for much smaller improvement. Future algorithm and process work should include the ability to leverage both topological/type variation and gradient-based optimization to help ensure that the results are not limited to local optima. In 2016, the plan was to develop an acoustic module appropriate for conceptual design vehicle optimization—the module or surrogate was not developed by the completion of this TC. The CAMRAD II-AARON-ANOPP2 tool chain, however, proved to be fairly efficient and was therefore used for the final demonstration. The low-emission Class B SBS vehicle was used for the demonstration. The rotor blade geometry was optimized for low-noise using the CAMRAD II-AARON-ANOPP2 tool chain. The blade tip dihedral was optimized to arrive at a low-noise blade geometry. The new rotor geometry replaced the rotor geometry of the low-emission SBS and was “flown” for the three FAA noise certification flight conditions. The results are summarized in Figure 11.14, along with the results for the baseline vehicle (with non-optimized rotor). The low-emission, low-noise SBS vehicle produces 60 percent less emission and is 9.6 dB (~50 percent) quieter than the baseline vehicle.

The MDAO process developed for this TC prompted updates to established codes (NDARC, OVERFLOW) and development of new code interfaces (RCOTOOLS, AARON). Since 2016, the NASA conceptual design capability for VTOL aircraft has progressed significantly. An assessment and optimization of the environmental impact of a new vehicle can now be made with a much more integrated approach.

Continued tool development is especially needed in the following areas: broadband noise, rotor/propeller blade structural analysis, fuselage structural analysis, creating and/or computing airfoil performance tables (needed as input to lifting-line analyses), and non-gradient-based optimization methods.

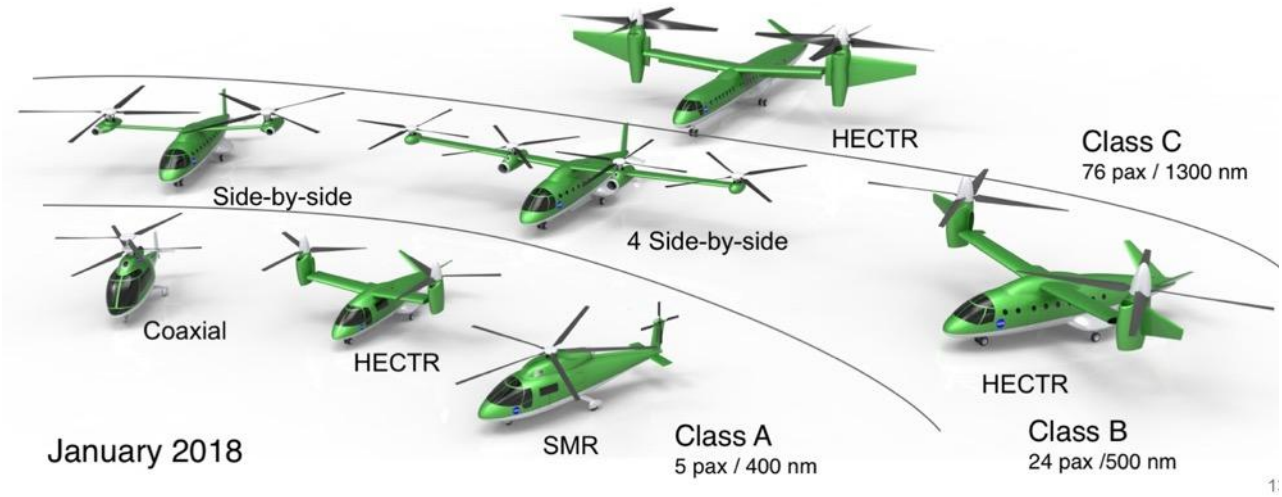

Figure 11.13. Low-emission VTOL aircraft designs.

Vehicle	Average EPNdB
Baseline SMR[2]	100.8
Baseline with optimized rotor	89.0
SBS LE[3]	106.8
SBS LE[3] with optimized rotor	**91.2**

1 average of three microphones located per FAA noise certification for helicopters
2 SMR: single main rotor
3 SBS LE: side-by-side, low emission

Blades with -40 deg tip dihedral are 9.6 EPNdB lower than baseline blades

Figure 11.14. Comparison of predicted noise metrics[1] for FAA descent condition required for noise certification.

The tools and processes developed for this TC have been documented in various technical papers, and much of the software and aircraft descriptions have been made available for researchers and practitioners inside and outside the U.S. Government. The NDARC aircraft models developed for this TC are publicly released and available to registered users of NDARC on the NDARC website, maintained by the NASA Ames Research Center Aeromechanics branch (https://rotorcraft.arc.nasa.gov/ndarc).

OpenMDAO is open-source software available to the public (http://openmdao.org), and under active development by NASA's Transformational Tools and Technologies (TTT) and RVLT Projects. ALPINE is under active development by the U.S. Army and is publicly released, with the software hosted on the NDARC website. AIDEN is under active development by the U.S. Army and NAVAIR, and is scheduled for public release in late 2018; the software will be hosted on the NDARC website. ANOPP2 (rotorcraft aspects), NDARC, and RCOTOOLS are under active development by the NASA RVLT Project; these software tools are available to the U.S. public for no cost, subject to terms of software usage agreements, and requests for distribution are instigated through the software.nasa.gov portal. AARON and SIMPLI-FLYD are under continued active development by NASA in the RVLT Project, and are not yet available to other researchers. SIMPLI-FLYD is being rewritten and enhanced under the new acronym FlightCODE (flight dynamics and control for conceptual design). Similar to SIMPLI-FLYD, FlightCODE currently requires the user to have access to the commercial software MATLAB (available from The Mathworks, Inc.) and CONDUIT (available from USRA-NASA Academic Mission Services (NAMS)).

IXGEN was developed as a Phase I, II, and III SBIR by the U.S. Army, and is available with government purpose rights within the U.S. Government (contact M4 Engineering, Inc. for commercial availability). PBWeight was developed as a Phase I and II SBIR by NASA, and is presently being developed by a Phase III SBIR funded by RVLT and the U.S. Army; the software is also available with government purpose rights. PBWeight is being commercialized as M4 Structures Studio by the contractor, M4 Engineering, Inc.

Though not part of the tool chain shown in Figure 11.10, NASA also supported development of industry sizing analyses. Through NASA SBIR funding, Empirical Systems Aeronautics, Inc. (ESAero) overhauled their internal sizing code known as PANTHER—see Danis et al. [2018]. PANTHER was used to perform trade studies of hybrid-electric rotorcraft based on the XV-15 tiltrotor. PANTHER calculations were compared to NDARC results for baseline vehicle designs provided by NASA, and PANTHER developers benefitted from access to NDARC methodology for edgewise and axial rotor performance, as documented in the NDARC theory manual.

Lessons Learned From the TC

The goal of the TC was to include key discipline modules in the conceptual design process in one tool chain so that different aspects of the vehicle characteristics could be optimized. After 3 years, however, what emerged were segments of the tool chain that were significantly streamlined and other segments that remained either incomplete or largely manual in nature. The idea of a streamlined, efficient tool chain that can produce a conceptual design in a few days did not account for the varying pace of tool development. Reliance on partners (NASA and non-NASA) to develop conceptual-design-level tools assumed schedule risk from the outset. An

important observation is that initial setup of a design that employs higher-fidelity analyses requires the assistance of subject matter experts with significant depth in their field. The timeliness goal of reducing time to an initial optimized aircraft design is constrained by this requirement to coordinate with experts and properly populate the detailed initial models. For instance, acoustics and rotor dynamics/performance models for aircraft that are not single-main-rotor helicopters or tiltrotors require some iteration between people and careful thought to the parameterization approach, and without a validation data set, there is significant uncertainty as to the realism of results. The optimization techniques within OpenMDAO are currently not appropriate for multi-modal and topologically varying problems. OpenMDAO is a very useful framework for integrating disparate codes, however, other optimization approaches will be needed than those currently available in OpenMDAO. For example, Khurana and Silva [2018] exercised NDARC, RCOTOOLS, and particle swarm optimization (PSO) algorithm to study emissions from a high-efficiency tiltrotor design. The authors found that a gradient-based method was too constraining for a multi-modal solution space, but the PSO approach produced significant improvement in the design of a low-emission tiltrotor.

In addition to continued development of the tool chain modules, future endeavors must include validation of the process against experimental results and higher-fidelity analyses.

SMALL UAS (sUAS) RESEARCH

While research supporting the LCTR began winding down by 2012, the rapid growth of the small Unmanned Aerial Vehicle (sUAV) market was already in progress. The UAS market spawned new research in UAS Traffic Management (UTM), noise, and autonomy, and created regulatory challenges for the FAA and other governing bodies. By 2015, NASA began applying discipline tools to new and nontraditional VTOL configurations. Initially, small UASs were the focus of both experimental and analytical efforts. A large body of research was produced by the NASA Design Environment for Vertical Lift Vehicles (DELIVER) Project.

DELIVER was one of the original subprojects under the Convergent Aeronautics Systems (CAS) Project of the Transformative Aeronautics Concepts Program of the NASA Aeronautics Research Mission Directorate (ARMD). Like all CAS subprojects, DELIVER was allotted a relatively small workforce and tasked with exploring a novel research topic in a finite time period. DELIVER, executed over a 3-year window from October 2015 to September 2017, focused on applying NASA design and computational tools to a range of new VTOL aircraft that were entering (almost daily) the sUAS and UAM markets.

Theodore [2018] summarizes the many accomplishments of DELIVER, which in just 3 years, explored the impact of acoustics, autonomy, and electric/hybrid-electric propulsion in the vehicle conceptual design process. Most importantly, DELIVER produced valuable data from sUAS wind tunnel and flight tests that continue to be used to validate NASA tools of varying fidelity.

The remainder of this section summarizes some of the DELIVER research, specifically, those topics that overlap with the UAM research that was already underway within the RVLT Project. The following DELIVER topics are addressed: Performance of Multi-Rotor Vehicles, Acoustics,

and High-Fidelity Simulation. Electric and hybrid-electric propulsion trade studies for larger-sized vehicles were also included in the DELIVER portfolio—these studies are discussed in the section on Urban Air Mobility. For a comprehensive review of DELIVER, Theodore [2018] should be consulted.

Performance of Multi-Rotor Vehicles

Small UASs offer interesting aerodynamic, and consequently acoustic, challenges as the aircraft operate at low Reynolds number compared to full-scale helicopters and tiltrotors. In addition, the UASs are typically multi-rotor configurations with fixed-pitch rotors/props. The UAS is operated by controlling the speed of the electric motors, with each motor directly driving one rotor. The availability of inexpensive COTS UASs of myriad configurations provided opportunities to test complete vehicles in wind tunnels under controlled conditions and with custom instrumentation. In addition to defining the geometry of the vehicles, measured vehicle performance over a range of speeds and vehicle angles-of-attack is required data for validating both comprehensive analyses and high-fidelity CFD.

In 2016, Russell et al. [2016] tested five multicopter sUAS in the U.S. Army 7- by 10-Foot Wind Tunnel at NASA Ames Research Center. The data set for each vehicle included forces, moments, and electrical power as a function of rotor rpm, airspeed, and vehicle attitude. Isolated rotor and bare airframe data were also collected. Figure 11.15 shows the five sUAS vehicles and an isolated propeller installed in the wind tunnel.

Russell and Sekula [2017] used this benchmark data set to develop a CAMRAD II model of an isolated rotor from the SUI Endurance quadrotor, one of the vehicles tested in the U. S. Army 7- by 10-Foot Wind Tunnel in 2016. Like most COTS sUAS vehicles, the airfoil geometries, let alone the airfoil performance, of the rotors are not available. After the 2016 test, therefore, NASA laser-scanned the props of each vehicle to obtain blade airfoil shape at each cross section and overall blade twist distribution. Two flow solvers were used by Russell and Sekula [2017] to generate airfoil performance tables of varying fidelity that were used as input to CAMRAD II. Comparing CAMRAD II predictions with the hover performance data acquired in 2016, Russell and Sekula [2017] assessed the rotor modeling fidelity needed to obtain good hover performance predictions. The authors provided several key conclusions from their parametric studies, including the importance of modeling blade elasticity for rotor injection-molding using plastics or resin. After establishing a CAMRAD II aerodynamic model for the SUI Endurance model, Russell then focused on developing an NDARC model for the Endurance vehicle. NDARC was developed and validated using full-scale aircraft knowledge and data, so the development of a model for a 6-pound Endurance was a good test of NDARC's applicability to sUAS. New scaling laws were developed to replace the full-scale models in NDARC for specific vehicle components. Using a variety of information that included data from the 2016 forward flight and hover tests, CAMRAD II predictions, and vehicle component measurements of the Endurance, Russell et al. [2018a] concluded that NDARC can be used to model and re-size quadrotor sUAS vehicles. The authors conclude that NDARC should be able to model sUAS vehicles of similar scale with more than four rotors.

Figure 2. 3D Robotics SOLO.

Figure 5. Drone America DAx8.

Figure 3. DJI Phantom 3 Advanced.

Figure 6. SUI Endurance.

Figure 4. 3D Robotics Iris+.

Figure 7. Isolated rotor – SUI Endurance.

Figure 11.15. sUAS tested for the DELIVER subproject (Figs 2–7 of Russell et al. [2016]).

The benchmark data set acquired in the U.S. Army 7- by 10-Foot Wind Tunnel, complementary isolated rotor hover data, and the blade geometry data, are all documented in a single report in Russell et al. [2018b].

The final flights of the Greased Lightening (GL-10) vehicle were made possible by the DELIVER subproject. GL-10 is a 50-percent scale model of a NASA VTOL design that features a tiltwing and tilt-tail with distributed electric propulsion. With a maximum takeoff weight of 62 pounds and a wingspan of 124.8 inches, the GL-10 is the largest vehicle tested by the DELIVER subproject. McSwain et al. [2017] provides a complete description of the aircraft and the data acquired from the June 2017 flight test (Fig. 11.16) campaign that included 22 flights. The measured maximum lift-to-drag ratio was more than 60 percent lower than originally predicted by low-fidelity conceptual design tools, highlighting the importance using higher-fidelity analyses for predicting performance of configurations as complex as the GL-10.

Figure 11.16. GL-10 aircraft with test crew (Fig. 20 of McSwain et al. [2017]).

Acoustics

As applications for sUAS grew rapidly, the noise from these vehicles has become an issue. These sUAS vehicles are typically operated at very low altitudes, close to the surrounding population. The rotors turn at very high rpm, so the noise they produce is at higher frequencies than typical rotorcraft. The noise could therefore be more annoying to humans, because of the response of the human ear. The dominant sUAS configuration is a quadcopter, though variations in the number of rotors is common. The rotors are typically of fixed, rigid geometry (no collective or cyclic pitch) and vehicle control is produced by rpm variation between the different rotors, each driven by an electric motor.

Zawodny et al. [2018] summarize the acoustic research accomplished under the DELIVER Project. The research was aimed at defining an appropriate metric that quantifies annoyance because of noise; this metric could then be used in the conceptual design process. A combination of flight testing, component testing, and psychoacoustic testing revealed that an annoyance metric for sUAS could not be easily defined. The findings from the research, however, provided a natural segue to the larger UAM class of multi-rotor vehicles undertaken by the RVLT Project.

Christian et al. [2015] describes the process for developing a flyover auralization of a COTS quadcopter. OVERFLOW was used to compute the blade airloads of a two-bladed isolated rotor. The same rotor, with two different blade sets, was tested in the anechoic facility at NASA Langley Research Center where acoustic measurements were acquired. The computed blade airloads were used as input to the PSU-WOPWOP acoustic solver. A favorable comparison between the computed and measured noise from the rotor provided confidence to proceed to the next step that involved combining the computed results of four isolated rotors. The simulated quadrotor noise was then propagated to produce a flyover auralization of the quadrotor. Continuing this work in Christian and Lawrence [2016], the authors explored various aerodynamic effects on quadrotor noise. They developed a computer simulation of quadcopter flight dynamics that includes effects not typically found in controller models for such vehicles. Using spectrograms of simulated quadrotor auralizations, a systematic evaluation of rotor drag, fuselage drag, and wind turbulence was performed. Also, simulated manufacturing differences in supposed identical electric motors was noticeable in the spectrograms. The simulation process can be used to isolate the important effects relative to annoyance.

Acoustic measurements of four different sUAS—one fixed-wing and three multi-copters—are reported in Cabell et al. [2016]. The multi-copters include a quadrotor, a tricopter, and a hexcopter (shown in Figure 11.17). The fixed-wing UAS had a gas engine while the three multi-copters used electric motors (one per rotor). Flyover acoustic measurements were acquired for all four sUAS; hover acoustics were also acquired for the multi-copters. Spectrograms showed the unsteady nature of the noise, especially for the smallest (quadcopter) vehicle.

Figure 11.17. Tested vehicles, left to right: Y6, Edge 540, Phantom 2, and Hex Flyer (Fig. 1 of Cabell et al. [2016]).

Christian and Cabell [2017] brought together the previously described auralization simulation work and sUAS (several configurations) flyover acoustic data to conduct a human-subject psychoacoustic test to measure annoyance. These tests, conducted in the Exterior Effects Room at NASA Langley Research Center, were the first-ever subjective response tests to the noise of sUAS using human test subjects. In addition to the recorded sUAS flyover noise, the test subjects were exposed to recorded sounds from different ground vehicles. Although the results reported in Christian and Cabell [2017] are for the recorded sounds only, the test subjects were also exposed to computer-generated auralizations. Initial analysis of the data (see Fig. 11.18) shows that for the same SEL, the sUAS sounds scored consistently higher on the annoyance scale compared to the selected ground vehicles, possibly because of the loitering sensation imparted by the sUAS.

Zawodny et al. [2016] explored the hovering acoustics of two isolated rotors, slightly different in diameter but very different in planform. Each rotor was paired with a different electric motor; the operating limits (speed) of the two motors differed by 30–40 percent in terms of rpm. The smaller rotor's noise was calculated using OVERFLOW2 and PSU-WOPWOP (OF2-PSU). The larger and slower-turning propeller was simulated using a simple blade-element analysis within the Propeller Analysis System (within ANOPP), which also calculated the noise. In addition to tonal noise, a noticeable amount of mid- and high-frequency broadband noise was identified from the experimental data. The study concluded that both the rotor and motor must be included to adequately characterize the vehicle's noise. In addition, decomposing the broadband noise contributions will require further study.

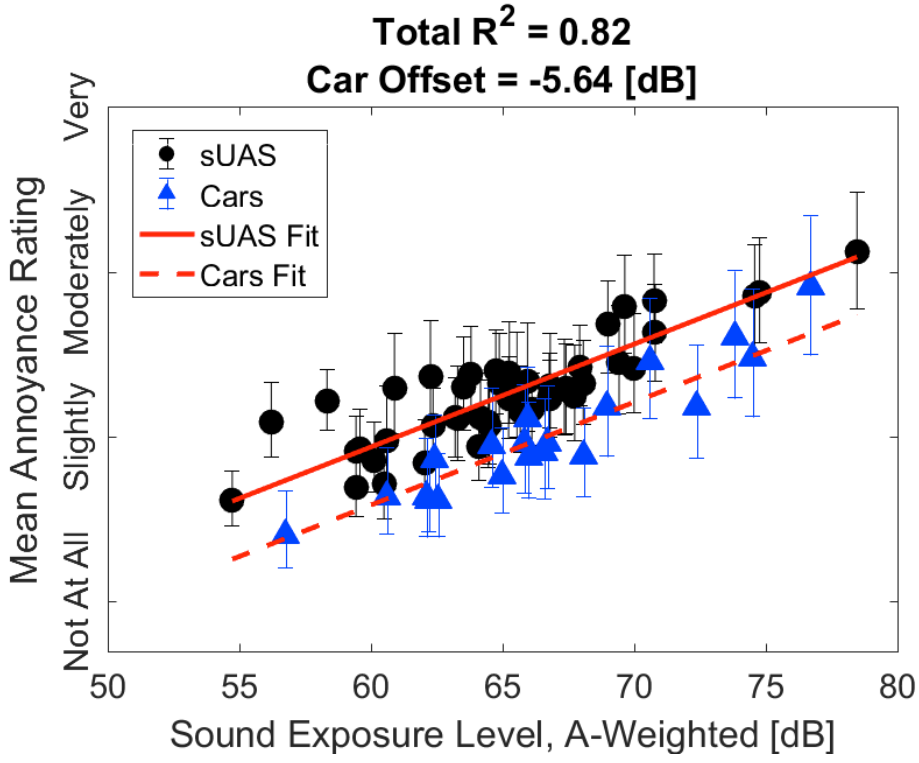

Figure 11.18. Regression results for the augmented linear model for SEL_A (Fig. 10 of Christian and Cabell [2017]).

Zawodny and Boyd [2017] examined the hover acoustic characteristics of a small, isolated rotor-airframe UAS configuration, both experimentally and computationally. Each configuration was comprised of a two-bladed rotor along with a simple representation of a typical mounting arm (see Fig. 11.19). The experiments were conducted in the Structural Acoustic Loads and Transmission (SALT) anechoic chamber facility at NASA Langley Research Center, while the computational results were generated using a coupling of OVERFLOW2 and PSU-WOPWOP. In general, good agreement was shown between the experimental results and the computations. The authors found that having the mounting arm in close proximity to the rotor resulted in significant increases in the tonal noise content of the acoustic signature, while the computational results indicated that the presences of these surfaces can generate noise levels comparable to that of the rotor itself (Fig. 11.20).

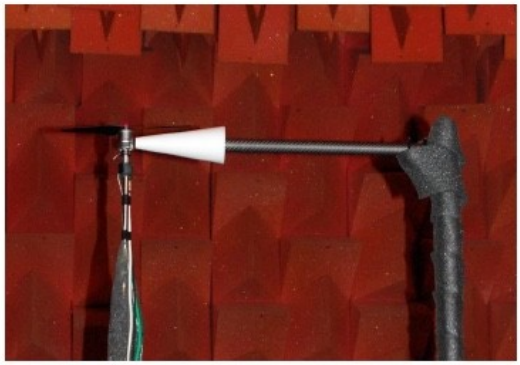

(a) Conical airframe in experimental setup

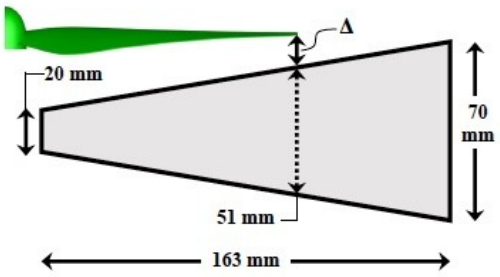

(b) Geometry of conical airframe

Figure 11.19. Image and geometric details of tested conical airframe. (Note: Image (b) drawn to scale for case of ΔR = –0.1.) (Fig. 3 of Zawodny and Boyd [2017].)

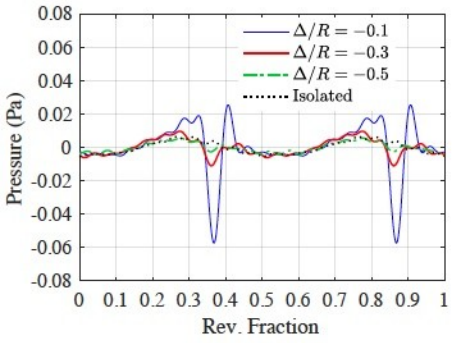

(a) M5 Prediction Time Histories

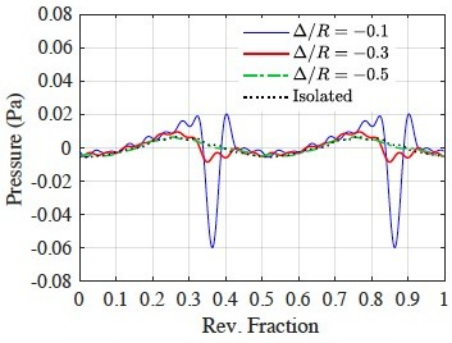

(b) M5 Measurement Time Histories

Figure 11.20. Mean rotor revolution acoustic pressure time history comparisons between (a) OVERFLOW2-PSUWOPWOP predictions and (b) experimental measurements for cases of varying airframe proximity to rotor plane. (Cases: rotor speed = 5400 rpm, ratio of airframe cross-section width to rotor chord at 75% span = 1.08.) (Fig. 15 of Zawodny and Boyd [2017].)

High-Fidelity Simulations

As mentioned in the previous section, high-fidelity simulations of isolated rotors using OVERFLOW provided airloads to predict rotor noise. In parallel, OVERFLOW was also used for coaxial rotor simulations, for the primary goal of understanding the flow behavior. Multi-coaxial rotor configurations were becoming increasingly common in emerging UAM vehicles so they warranted a closer look from a high-fidelity simulation perspective. Using XV-15 rotor geometry, Yoon et al. [2016a] explored the effect of rotor spacing between the upper and lower rotors of a counter-rotating coaxial rotor system in hover using OVERFLOW. Isolated rotor simulations were also performed. A tandem coaxial rotor configuration was then studied by placing two isolated coaxial rotor systems (opposite rotation) in the same horizontal plane. The lateral spacing between the rotors was then varied. Finally, a simple fuselage was added to the tandem rotor configuration. This building-block approach highlighted the magnitude of aerodynamic interactions between the rotors and the fuselage. Note that the upper and lower rotors in all the simulations were not torque balanced. In a follow-on effort, Yoon et al. [2016b] simulated four isolated full-scale XV-15 rotors in hover. The lateral separation distance between the front rotors (and rear rotors) was varied. A fuselage and rotor support structures were then added to the four rotors to represent a generic quadrotor to obtain estimates of download.

Yoon et al. [2017a] continued exploring aerodynamic interactions in hover with the full-scale three-bladed XV-15 rotor, but unlike the work of 2016, Yoon et al. [2017a] balanced the torque of the upper and lower rotors iteratively. The authors then modeled a scaled version of the XV-15 rotor in order to compare with existing experimental measurements of a coaxial rotor system in hover. Having correlated well with the measured performance of the isolated rotor, Yoon et al. [2017a] also showed good comparisons of rotor spacing effects on the ratio of the upper and lower rotor thrust. The authors then simulated a quad-coaxial rotor vehicle with and without balancing the torque between each upper and lower rotor pair and quantified the download on the fuselage.

Yoon et al. [2017b] next simulated two sUAS quadrotors that were tested in flight. First, OVERFLOW calculations of isolated rotor performance were compared with the test data acquired by Zawodny et al. [2016]. Thrust and performance of each of the isolated rotors (one rotor from each vehicle) were well predicted by OVERFLOW. Next, the two quadrotors were simulated: one in hover and one in forward flight (without trimming the vehicle). Vehicle performance was evaluated for two configurations of the hovering quadrotor—rotors above the support arms and rotors mounted below the support arms. Mounting the rotors below the support arms degraded the performance of the rotors. The forward flight simulation revealed that rear rotor performance was negatively affected by operating in the wakes of the front rotors. OVERFLOW was not coupled with a comprehensive analysis for these simulations, so the quadrotor in forward flight was not trimmed.

Ventura-Diaz et al. [2018a] used OVERFLOW to simulate the same two quadrotors as Yoon et al. [2017b] and the Elytron 4S, a joined-wing configuration with a tiltwing and embedded lift fan in the nose of the aircraft. Figure 11.21 shows the simulation of the quadrotor. The Elytron 2S [Grima et al. 2016] is a one-seater precursor to the 4S. The authors explored the effects of wind turbulence on the quadrotor hover performance; also, cameras and landing gear were added below the fuselage causing a reduction in the interaction between the rotors that, in turn, was

interpreted as a reduction in vehicle noise. In a companion paper, Ventura-Diaz et al. [2018b] focused on simulating test conditions from the 2017 test of the Elytron 4S in the U.S. Army 7- by 10-Foot Wind Tunnel at NASA Ames Research Center, performed in 2017. OVERFLOW results were not compared with wind tunnel data but rather the CFD results were used to highlight the complex flow in and around the aircraft. Koning et al. [2018] used the hybrid CFD analysis RotCFD [Guntupalli et al., 2016] to analyze and characterize the performance of the Elytron 4S. Simulation results showed promising comparison with the experimental data.

Except for the Elytron 4S, the CFD work under the DELIVER subproject focused on sUAS. The work provided valuable experience (especially gridding) in simulating complex multi-rotor configurations, in particular, highlighting the interaction of the rotor wakes with each other and with fuselage components. A logical next step was to transition the sUAS simulation experience to the larger passenger-carrying UAM multi-rotor vehicles, where OVERFLOW must be coupled with a comprehensive analysis to achieve vehicle trim and accurate acoustic predictions.

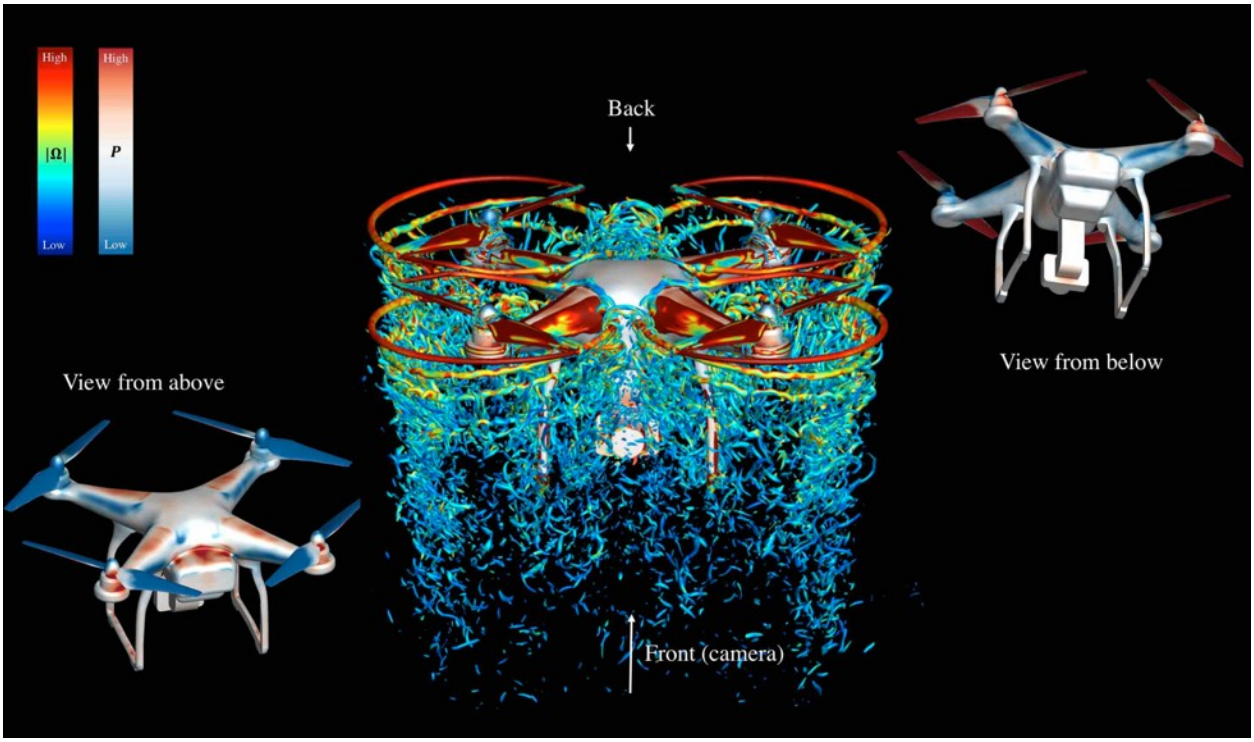

Figure 11.21. Oblique view of the complete DJI Phantom 3 in hover. Q-criterion vorticity iso-surfaces colored with the vorticity magnitude. Pressure is shown at the body surface: red is high pressure, blue is low pressure (Fig. 13 of Ventura-Diaz [2018a]).

URBAN AIR MOBILITY (UAM)

With increasing emphasis on the environment-friendly modes of transportation, entrepreneurs were quick to take the next step from small UASs to manned electrified aircraft. Though the ideas of personal air vehicles and flying cars are not new, the concept of an air taxi service using quiet, green vehicles in urban settings sparked another explosive growth in aircraft configurations, fueled by the popularity of the automotive ride-share business model and the ever-growing frustration with congested roads. In October 2016, ride-share giant Uber created the Uber Elevate Program and published a white paper (https://www.businessinsider.com/uber-elevate-flying-car-plan-white-paper-2016-10) describing their air taxi business concept. The white paper added fuel to the entrepreneurial fire, invigorating the field of Urban Air Mobility (UAM). Workshops on electric propulsion and transformative vertical flight, and panel discussions on aircraft certification processes have been included in the technical conferences of the major aviation societies in recent years. Uber has held Uber Elevate Summits in 2017 (https://www.uber.com/us/en/elevate/summit/2017) and 2018 (https://www.uber.com/us/en/elevate/summit/2018) inviting stakeholders (local government, suppliers, manufacturers, and operators) into a single forum to discuss opportunities and challenges of the UAM vision. The traditional helicopter manufacturers, both in the U.S. and overseas, have joined the dozens of other new companies that have emerged to capitalize on the hoped-for financial bonanza of the UAM market.

In many cases, the attractiveness of minimal moving parts of small UASs translated to the much larger configurations proposed, and being built, for UAM. Unfortunately, UAM configurations designed without regard to rotor aeromechanics ultimately face challenges with aeroelasticity, detrimental aerodynamic interactions, structural loads, and noise. In addition, the flight control system/layout for the numerous vehicle configurations does not follow any universal control strategy. An instructive lesson learned is offered in Dugan [2014], where the author revisits 12 controller designs submitted to the 1961 Tri-Service VTOL transport. The author describes the different designs and the lessons learned from nonintuitive or ambiguous layouts for thrust control. These lessons are relevant in the emerging development of UAM vehicles, where both fixed-wing and VTOL pilots will be at the controls of vehicles that are hybrids of airplanes and helicopters.

The main characteristic common to all of the VTOL UAM vehicles is an electric or hybrid-electric propulsion system. Attempts to scale up propulsion architectures from small UAS configurations to passenger-carrying UAM concepts invited new challenges in thermal management, power quality, and safety issues related to direct-drive, electric power trains.

UAM concept vehicles, propulsion studies, and system studies are discussed next.

UAM Concept Vehicles

In parallel to the environmentally friendly designs developed by Silva et al. [2018a], Johnson et al. [2018] developed concept vehicles for UAM missions. This key publication established a family of vehicles that helped focus subsequent NASA research activities in different disciplines. The NASA concept vehicles were intended to capture the large design space (payload, range,

aircraft type, and propulsion system) represented by the growing number of UAM configurations being developed by industry. The three NASA UAM concepts included a single-passenger (250-pound payload), 50-nautical-mile-range quadrotor with electric propulsion; a 6-passenger (1,200-pound payload), 4x50 = 200-nautical-mile-range SBS helicopter with hybrid propulsion; and a 15-passenger (3,000-pound payload), 8x50 = 400-nautical-mile-range tiltwing with turbo-electric propulsion. Safety considerations, in particular aircraft failure modes, were considered in the design. For example, instead of direct-drive rotors with fixed pitch, the NASA quadrotor was designed with rotor collective control and cross-shafting between rotor pairs, ensuring a controlled landing in the event of a one-engine-inoperative (OEI) or one-motor-inoperative (OMI) scenario.

In response to the proposed mission and payload requirements defined by Patterson et al. [2018], Silva et al. [2018b] developed a new set of NASA UAM concept vehicles, building on the work of Johnson et al. [2018]. The single-passenger quadrotor of Johnson et al. [2018] was scaled up to a six-passenger aircraft and the SBS was slightly modified. Silva et al. [2018b] also introduced a new lift+cruise configuration that was representative of technology in industry. As expected, these UAM designs are serving as foci for other discipline research in the areas of handling qualities, propulsion hazards analyses and failure mode, effects, and criticality analysis (FMECA) studies, acoustics, and high-fidelity CFD. In addition, the conceptual design tool chain continues to be exercised and improved by trade studies of these UAM concept vehicles. Figure 11.22 shows the original versions of the vehicles; these versions will continue to evolve and serve as baselines for future studies.

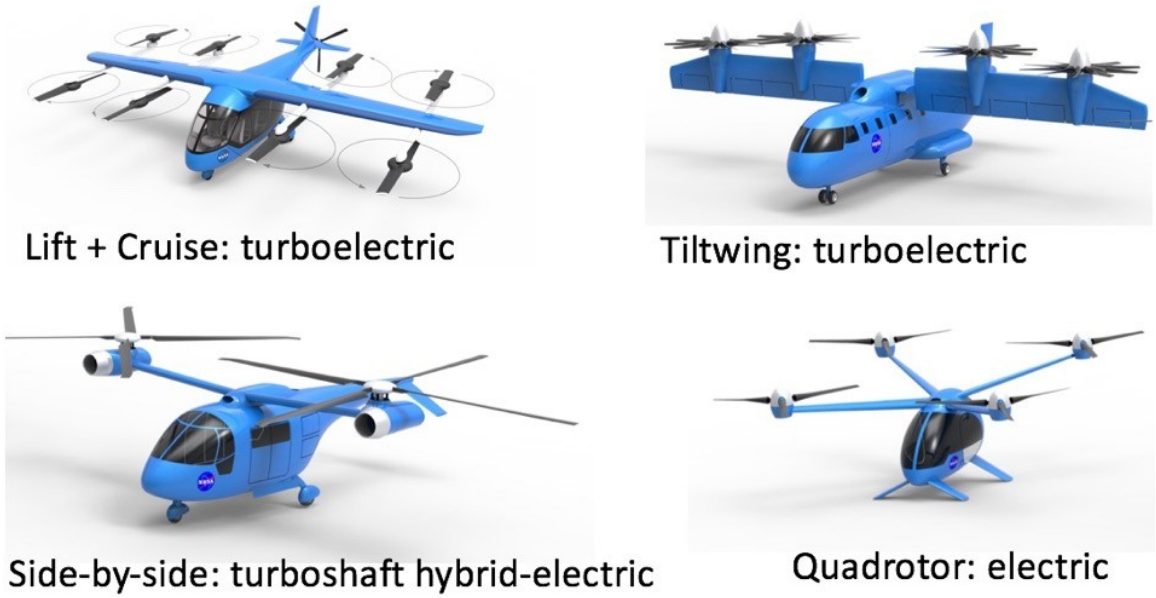

Figure 11.22. NASA UAM concept vehicles.

Electric/Hybrid-Electric Propulsion Studies

Datta and Johnson [2012, 2014] provide conceptual designs of an electric powerplant, for an ultra-light Robinson R22 helicopter. Three designs—fuel cell, battery, and hybrid fuel cell/battery—were evaluated for three mission profiles. The pros and cons of each design are discussed. In the context of the ultra-light R22, the high-torque, low-rpm rotor operation was identified as a barrier to all three propulsion designs.

Snyder [2015] evaluated three representative helicopters to explore electric propulsion and overall vehicle and mission requirements. These vehicle sizes ranged from 1 to 3 occupants to 13 occupants plus cargo. Aircraft characteristics are shown in Figure 11.23.

Like other studies, Snyder [2015] assumed 15- and 30-year advanced technology availability in electric motors, batteries, and diesel/gas turbine engines to perform trade studies of vehicle size, thermal management, and mission performance. NDARC was used to study the effect of sizing and performance for the different technology assumptions for different missions. Hydrocarbon-fueled range extenders were also considered to overcome battery energy-density limitations. Using the same analysis process, Snyder [2016] next studied three electric designs limited to two or three occupants: an SMR helicopter, a tiltrotor, and a distributed electric propulsion (DEP) VTOL (based on the NASA GL-10 configuration). The mission was limited to 1 hour and 100–200 miles. Hydrocarbon-fueled propulsion, all-electric propulsion, and electric with hydrocarbon-fueled range extenders were explored for each aircraft to investigate the interdependency of aircraft performance and propulsion systems using NDARC.

Vehicle class (approximate example) → Parameter ↓	Light utility (Sikorsky S-300C)	Multi-mission (Bell 206L4)	Medium utility (Airbus Helicopters EC175)
Design gross weight (DGW), lb. (kg)	2,050 (932)	4,550 (2,068)	16,000 (7,273)
Empty weight, lb. (kg)	1,100 (500)	2,447 (1,112)	10,100 (4,591)
Nominal fuel weight, lb. (kg), % DGW *	160 (73), 8%	737 (335), 16%	2,143 (974), 13%
Sea level maximum power, hp (kW)	190 (142)	750 (560)	2 x 1,600 (2 x 1,193)
Engine type	Reciprocating (Otto cycle)	Gas turbine	Gas turbine
Engine weight (each), lb. (kg), % DGW	267 (121), 13%	255 (116), 5.6%	430 (195), 5.4%
Engine power / weight, hp/lb. (kW/kg)	0.71 (1.2)	2.94 (4.8)	3.72 (6.1)
Engine volume (each), ft^3, (l)	14.1 (401)	13.0 (369)	14.2 (402)
Sea level PSFC, lb./hp-h (kg/kw-h)	0.500 (0.305)	0.689 (0.420)	0.454 (0.277)
Power / DGW, hp/lb. (kW/kg)	0.09 (0.15)	0.165 (0.27)	0.20 (0.33)
Cruise velocity, knots (km/h) *	95 (176)	120 (222)	130 (241)
Range, nmi (km) *	200 (370)	220 (407)	340 (630)
# crew (C) + passengers (P)	1 C + 1 or 2 P	1 C + 5 P	3C + 10P + 1000 lb. (450 kg)

* *from mission analyses*

Figure 11.23. Table shows vehicle design characteristic used in study (Table 1 of Snyder [2015]).

Focusing on the baseline multi-rotor vehicle, Snyder [2017a, 2017b] explored cryogenic components for the vehicle. NDARC was used to evaluate different electric hybridization schemes for the propulsion system. Battery and diesel technology 15 years in the future was assumed for the study. Hybrid propulsion, using various diesel engines plus a generator to replace some of the batteries, was explored. Conventional air cooling and Liquid Natural Gas (LNG) cryogenic cooling for some of the propulsion components was also included. The hybrid systems resulted in significant improvements in maximum range and number of missions that could be completed before refueling or recharging.

Hartwig et al. [2018] developed a combined thermal-fluid-electrical-mechanical model for hybrid electric vehicle studies using Simulink©. The model can simulate a mission profile for a conventional diesel or a cryogenic-fueled VTOL (or fixed-wing) aircraft. The authors used the NASA GL-10 aircraft [McSwain et al., 2017] as a reference vehicle to validate parts of their model. Using the Simulink model, they then replaced the diesel fuel tanks with LNG fuel tanks, upgraded the electric motor generator to a natural-gas-cooled generator, cooled the motor and generator by immersion in the LNG tank, and cooled the power electronics from the LNG vapor. The authors concluded that an LNG system may be viable for a future cryo-cooled, turbo-electric aircraft.

Using the results from Hartwig et al. [2018], Snyder and Kohlman [2018] replaced the all-battery power system of the notional multi-rotor UAM studied in Snyder [2016, 2017a, 2017b] with an advanced diesel hybrid using either conventional diesel fuel or LNG fuel. The findings from Snyder [2016] were then reevaluated in terms of volume and thermal management using the cryogenic properties of LNG. A power-system study revealed increased power requirements and volume, so the vehicle and mission models were updated. The updated results confirm the significant benefits in range and number of UAM missions for the notional vehicle with cryo-cooling but the benefits were reduced by 12–15 percent compared to the results reported in Snyder [2016].

UAM System Studies

During 2012–2014, the NASA Aeronautics Research Institute (NARI) funded a two-phase study of using electric VTOL aircraft for urban transportation. Phase one of the study, described in Sinsay et al. [2012] and Melton et al. [2014], was aimed at a notional urban transportation system supplemented by a fleet of electric VTOL aircraft. The study investigated VTOL vehicle design, using NDARC, as well as developing a notional network of stations and schedules based on the existing rail system of the San Francisco Bay Area. Other analyses used by the authors included BaySim (a passenger movement model developed for this study) and FACET (an air traffic management (ATM) simulation system used nationally). The VTOL aircraft, referred to as Hoppers, included 6- and 15-passenger conventional helicopters and a 30-passenger tandem rotor aircraft. Several electric propulsion options were analyzed; assumed battery technology available by 2030 coupled with short-distance missions produced feasible aircraft. Key findings from this study were: 1) system and aircraft designed for less than 100 miles per flight leg could be used to serve tens of thousands of daily commuters in a metropolitan area; 2) feasible aircraft designs are

possible using conventional turboshaft-engine propulsion and today's technology; 3) helicopter configurations using electric propulsion should be possible in 10–15 years, with larger vehicles possible in 20–30 years; and 4) aircraft supporting a metro-regional aerial transportation system will likely be required to fly below 5,000 feet to minimize conflict with commercial air traffic.

The second phase of this study, described in Alonso et al. [2017], expanded upon the work of Melton et al. [2014] in several areas. The BaySim software was extended to include population data of the Bay Area, alternate network topologies, an optimization algorithm, and integration of ATM information to simulate dynamic routing. Regarding the Hopper vehicles, power and energy trade-offs of the different propulsion systems (electric, hybrid-electric, fuel-cell) were explored in more detail compared to the phase-one study. Preliminary CFD models of Hopper aircraft in a terminal setting were simulated to assess station design. The two phases of this study combined to provide an integration of vehicle and transportation system designs to afford a holistic view of a mass transit system using electrified VTOL aircraft.

Patterson et al. [2018] studied UAM mission requirements and defined a UAM mission, shown in Figure 11.24, for future studies. In addition, a target payload of 1,200 pounds, or up to six passengers with varying weights of luggage, was proposed.

Kohlman and Patterson [2018] developed a transportation system-level model of a UAM network over the Dallas-Fort Worth (DFW) International Airport for 2025. The model can assess many parameters, including the number of vehicles required to meet demand, the number of vehicles in the air at any given time, and the length of time a vehicle may need to loiter before a landing area becomes available. The studies focused on the effect of different energy storage systems on the UAM vehicles in the transportation system. All-electric and hybrid-electric propulsion systems were explored. Different energy conversion modes for the hybrid-electric systems were included in the study. The authors determined that using LNG as a fuel in the hybrid, solid oxide fuel cell (SOFC) battery turbine system can result in a lower-cost solution with fewer infrastructure issues than a battery-only propulsion system.

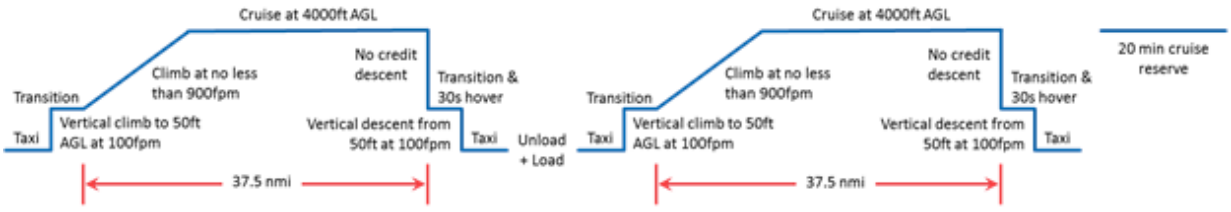

Figure 11.24. UAM mission profile (Fig. 11 of Patterson et al. [2018]).

CONCEPTS FOR PUBLIC SERVICE

The vertical takeoff, vertical landing, and hovering capability of rotorcraft present many opportunities to apply these aircraft toward public service. This section describes ideas for improving rescue efficiency through novel equipment, new VTOL concepts and systems aimed at emergency response, and a multi-modal package delivery system.

Vertical rescue lifts from helicopters are the focus of Young [2007], where a vectored rescue hoist is explored. The author discusses the benefits of a maneuverable hoist/sling that is suspended beneath a helicopter. A robotic hoist can be maneuvered closer to a building or between obstacles while the helicopter remains in a (relatively) stationary hover. The aeromechanic challenges of a vectored rescue hoist are discussed.

In 2011, NASA sponsored a student design competition for an amphibious tiltrotor aimed at civilian rescue operations. The aircraft requirements included vertical takeoff and landing from water (lakes and oceans) and land, a range of 800 nautical miles, a cruise speed of 300 knots, a 50-passenger capacity, and/or use for firefighting. Creaven et al. [2011], representing a team of 10 undergraduate students from Virginia Tech, provided the winning design of a dual-fuselage tiltrotor. The students identified interesting challenges unique to operations very close to water, including ingesting water into the engines.

Using public service as the primary vehicle function, Young [2015b, 2017, 2018a] offers several vehicle design concepts and example missions for sUAS vehicles.

Young [2015b] explored the design space of multi-rotor vehicles, ≤ 25-kg takeoff gross weight, dividing the vehicle into three classes: distributed, modular, and heterogeneous. The author offers a large menu of configuration concepts in each vehicle class (see Figs. 3, 4, and 6, Young [2015b]). These vehicle classes are applied to three emergency response scenarios: search and rescue aerial survey, aerial telecom/data relay, and emergency equipment aerial lift.

Aimed at the small-package-delivery drone market, Young [2017] proposed a multi-modal concept vehicle that mitigates some of the safety concerns related to aerial drones landing close to residences or other destinations with a concentration of people. The multi-modal vehicle would instead fly to a designated landing area and transit the remaining distance to the drop-off location by converting to a ground vehicle. Some of the pertinent design parameters include: two (counterrotating) propellers, 90-km/h cruise speed, 40-km flight range, 2-km ground distance, 2.5-kg payload, 2.2-m maximum vehicle height, and 1-m maximum vehicle dimension. The author compared estimated delivery time, number of delivery packages, and energy expended by a delivery truck versus the multi-modal vehicle concept.

Next, Young [2018a] posits a system of smart, UAS VTOL aircraft that can be mobilized for disaster relief and emergency services. The Smart Precise Rotorcraft InTerconnected Emergency Services (SPRITES) concept vehicle, shown in Figure 11.25—heterogeneous vehicle class—serves as the main configuration for this study. The paper includes a discussion of public acceptance of autonomous vehicles, areas requiring development to interface SPRITES with traditional airspace, and descriptions of different mission scenarios for the SPRITES vehicles

and how they might operate in a networked operation (rather than individually). Excursions on the SPRITES vehicle configuration are explored, motivated by aerodynamic interaction considerations and specific mission requirements.

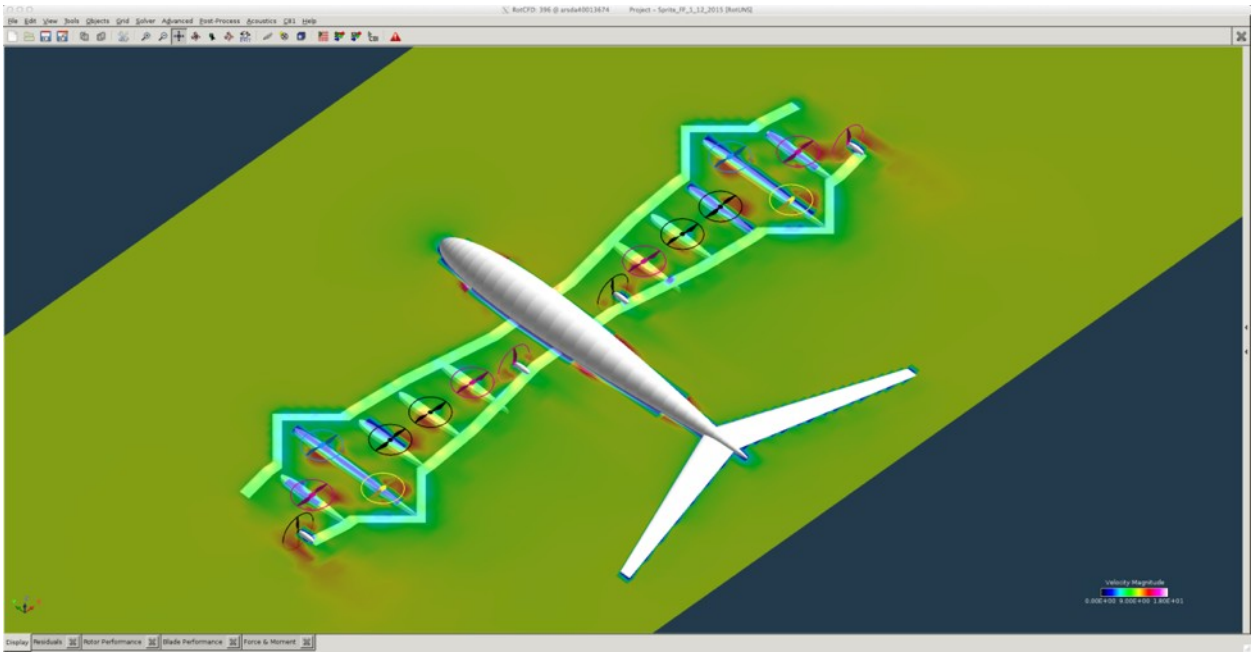

Figure 11.25. SPRITES configuration (Fig. 1(b) of Young [2018a]).

REFERENCES

Acree, C. W., Yeo, H., and Sinsay, J. D., "Performance Optimization of the NASA Large Civil Tiltrotor," International Powered Lift Conference, London, UK, July 2008; also NASA/ TM–2008-215359, June 2008.

Acree, C. W., "Integration of Rotor Aerodynamic Optimization with the Conceptual Design of a Large Civil Tiltrotor," American Helicopter Society Aeromechanics Specialists' Conference, San Francisco, CA, Jan. 20-22, 2010.

Acree, C. W., "Impact of Aerodynamics and Structures Technology on Heavy Lift Tiltrotors," *Journal of the American Helicopter Society*, vol. 55, no. 1, Jan. 2010, DOI:10.4050/JAHS.55.012002

Acree, Jr., C. W., and Snyder, C. A., "Influence of Alternative Engine Concepts on LCTR2 Sizing and Mission Profile," American Helicopter Society Future Vertical Lift Aircraft Design Conference, San Francisco, CA, Jan. 2012.

Acree, Jr., C. W., "Aerodynamic Limits on Large Civil Tiltrotor Sizing and Efficiency," Fifth Decennial American Helicopter Society Aeromechanics Specialists' Conference, San Francisco, CA, Jan. 2014.

Alonso, J. J., Arneson, H. M., Melton, J. E., Vegh, J. M., Walker, C., and Young, L. A., "System-of-Systems Considerations in the Notional Development of a Metropolitan Aerial Transportation System: Implications as to the Identification of Enabling Technologies and Reference Designs for Extreme Short Haul VTOL Vehicles with Electric Propulsion," NASA/TM–2017-218356, Sept. 2017.

Boyd, D. D. Jr., Greenwood, E., Watts, M. E., and Lopes, L. V., "Examination of a Rotorcraft Noise Prediction Method and Comparison to Flight Test Data," NASA/TM–2017-219370, Jan. 2017.

Cabell, R., McSwain, R., and Grosveld, F., "Measured Noise for Small Unmanned Aerial Vehicles," Noise-Con 2016, Providence, RI, June 13-15, 2016.

Christian, A., Boyd, D. D., Zawodny, N. S., and Rizzi, S. A., "Auralization of Tonal Rotor Noise Components of a Quadcopter Flyover," Internoise 2015, San Francisco, CA, Aug. 9-12, 2015.

Christian, A., and Lawrence, J., "Initial Development of a Quadcopter Simulation Environment for Auralization," American Helicopter Society 72nd Annual Forum, West Palm Beach, FL, May 17-19, 2016.

Christian, A., and Cabell, R. A., "Initial Investigation into the Psychoacoustic Properties of Small Unmanned Aerial System," Noise, 23rd AIAA/CEAS Aeroacoustics Conference, AIAA AVIATION Forum, Denver, CO, June 5-9, 2017.

Chung, W. W., Linse, D., Paris, A., Salvano, D., Trept, T., Wood, T., Gao, H., Miller, D., Wright, K., Young, R., and Cheng, V., "Modeling High-Speed Civil Tiltrotor Transports in the Next Generation Airspace," NASA/CR–2011-215960, Oct. 2011.

Chung, W. W., Salvano, D., Rinehart, D., Young, R., Cheng, V., and Lindsey, J., "An Assessment of Civil Tiltrotor Concept of Operations in the Next Generation Air Transportation System," NASA/CR–2012-215999, Jan. 2012.

Creaven, M. P., Tenney, J., Smith, J., Steinert, A., Paetzell, R., Hom, M., Diner, J., Berg, R., Carra, A., and Tomlin, B., "Vertical Takeoff Rescue Amphibious Firefighting Tiltrotor Design Report," Paper AIAA-2011-6998, AIAA Centennial of Naval Aviation Forum "100 Years of Achievement and Progress," Virginia Beach, VA, Sept. 21-22, 2011.

Danis, R. A., Green, M. W., Freeman, J. L., and Hall, D. W., "Examining the Conceptual Design Process for Future Hybrid-Electric Rotorcraft," NASA/CR–2018-219897, May 2018.

Datta, A., and Johnson, W., "Requirements for a Hydrogen Powered All-Electric Manned Helicopter," 14th AIAA/ISSMO Multidisciplinary Analysis and Optimization Conference, Indianapolis, IN, Sept. 17-19, 2012.

Datta, A. and Johnson, W., "Powerplant Design and Performance Analysis of a Manned All-Electric Helicopter," *Journal of Propulsion and Power,* vol. 30, no. 2, March-April 2014, DOI: 10.2514/1.B34843

Dugan, D. C., "Thrust Control of VTOL Aircraft – Part Deux," Fifth Decennial American Helicopter Society Aeromechanics Specialists' Conference, San Francisco, CA, Jan. 22-24, 2014.

Gibson, T., Jagielski, M., and Barber, J., "Disaster Response Effectiveness of a Fleet of Civil Tiltrotor Aircraft Operating in the Next Generation Air Transportation System," NASA/CR–2012-216000, Jan. 2012a.

Gibson, T., Jagielski, M., Barber, J., Chung, W., and Young, L., "Employment of Conceptual Tiltrotor Aircraft in Disaster Response," 68th Annual Forum and Technology Display of the American Helicopter Society, Ft. Worth, TX, May 1-3, 2012b.

Grima, A., Theodore, C., Garrow, O., Lawrence, B., and Persson, L., "Aerodynamic Analysis of the Elytron 2S Experimental Tiltwing Aircraft," SAE International Powered Lift Conference (IPLC), Hartford, CT, Sept. 27-29, 2016.

Guntupalli, K., Novak, L. A., and Rajagopalan, R. G., "RotCFD: An Integrated Design Environment for Rotorcraft," American Helicopter Society Specialists' Conference on Aeromechanics Design for Vertical Lift, San Francisco, CA, Jan. 20-22, 2016.

Harris, F. D., "Tiltrotor Conceptual Design," NASA/CR–2017-219474, March 2017.

Hartwig, J., Niezgoda, B., and Kohlman, L., "A Combined Thermal-Fluid-Electrical-Mechanical Simulink Model for Hybrid Electric Vehicle Studies," 56th AIAA Aerospace Sciences Meeting, Kissimmee, FL, Jan. 8-12, 2018.

Howard, S. A., "Rotordynamic Feasibility of a Conceptual Variable-Speed Power Turbine Propulsion System for Large Civil Tilt-Rotor Applications," NASA/TM–2012-217134, July 2012.

Johnson, W., "Technology Drivers in the Development of CAMRAD II," American Helicopter Society Aeromechanics Specialists' Meeting, San Francisco, CA, Jan. 1994.

Johnson, W., Yamauchi, G., and Watts, M. E., "NASA Heavy Lift Rotorcraft Systems Investigation," NASA/TP–2005-213467, Dec. 2005.

Johnson, W. "NDARC, NASA Design and Analysis of Rotorcraft," NASA/TP–2009-215402, Dec. 2009.

Johnson, W., and Sinsay, J. D., "Rotorcraft Conceptual Design Environment," The 3rd International Basic Research Conference on Rotorcraft Technology, Nanjing, China, October 14-16, 2009a.

Johnson, W., and Sinsay, J. D., "Rotorcraft Conceptual Design Environment," 2nd International Forum on Rotorcraft Multidisciplinary Technology, Seoul, Korea, Oct. 19-20, 2009b.

Johnson, W., "NDARC—NASA Design and Analysis of Rotorcraft: Theoretical Basis and Architecture," American Helicopter Society Aeromechanics Specialists' Conference, San Francisco, CA, Jan. 20-22, 2010a.

Johnson, W., "NDARC—NASA Design and Analysis of Rotorcraft: Validation and Demonstration," American Helicopter Society Aeromechanics Specialists' Conference, San Francisco, CA, Jan. 20-22, 2010b.

Johnson, W., Moodie, A., and Yeo, H., "Design and Performance of Lift-Offset Rotorcraft for Short-Haul Missions," American Helicopter Society Future Vertical Lift Aircraft Design Conference, San Francisco, CA, Jan. 2012.

Johnson, W., "Propulsion System Models for Rotorcraft Conceptual Design," Fifth Decennial American Helicopter Society Aeromechanics Specialists' Conference, San Francisco, CA, Jan. 2014.

Johnson, W., "NDARC. NASA Design and Analysis of Rotorcraft," NASA/TP–2015-218751, April 2015.

Johnson, W., Elmore, J. F., Keen, E. B., Gallaher, A. T., and Nunez, G. F., "Coaxial Compound Helicopter for Confined Urban Operations," American Helicopter Society Specialists' Conference on Aeromechanics Design for Vertical Lift, San Francisco, CA, Jan. 20-22, 2016.

Johnson, W., Silva, C., and Solis, E., "Concept Vehicles for VTOL Air Taxi Operations," American Helicopter Society Technical Conference on Aeromechanics Design for Transformative Vertical Flight, San Francisco, CA, Jan. 16-19, 2018.

Khurana, M., and Silva, C., "Optimization of a High Efficiency Civil Tiltrotor platform for Low Emission Flight," American Helicopter Society Technical Conference on Aeromechanics Design for Transformative Vertical Flight, San Francisco, CA, Jan. 16-19, 2018.

Kohlman, L. W., and Patterson, M. D., "System-Level Urban Air Mobility Transportation Modeling and Determination of Energy-Related Constraints,' Paper AIAA-2018-3677, 2018 AIAA Aviation Forum, 2018 Aviation Technology, Integration, and Operations Conference, Atlanta, GA, June 25-29, 2018, DOI: 10.2514/6.2018-3677

Koning, W. J. F., Russell, C., Solis, E., and Theodore, C., "Mid-Fidelity Computational Fluid Dynamics Analysis of the Elytron 4S UAV Concept," NASA/TM–2018-219788, Nov. 2018.

Kottapalli, A., and Harris, F., "Converting a C-130 Hercules into a Compound Helicopter: A Conceptual Design Study," American Helicopter Society Aeromechanics Specialists' Conference, San Francisco, CA, Jan. 20-22, 2010.

Lawrence, B., Berger, T., Theodore, C. R., Tischler, M. B., Tobias, E. L., Elmore, J., and Gallaher, A., "Integrating Flight Dynamics and Control Analysis and Simulation in Rotorcraft Conceptual Design," 72nd American Helicopter Society Annual Forum, West Palm Beach, FL, May 17-19, 2016a.

Lawrence, B., Theodore, C. R., Johnson, W., and Berger, T., "Handling Qualities Optimization for Rotorcraft Conceptual Design," Rotorcraft Virtual Engineering Conference, Liverpool, UK, Nov. 8-10th, 2016b.

Lawrence, B., Theodore, C. R., Johnson, W., and Berger, T., "A Handling Qualities Analysis Tool for Rotorcraft Conceptual Designs," *The Aeronautical Journal*, vol. 122, no. 1252, June 2018, pp 960–987, DOI: 10.1017/aer.2018.43

Lopes, L. V., and Burley, C. L., "ANOPP2 User's Manual: Version 1.2," NASA/TM–2016-219342, Oct. 2016.

McSwain, R. G., Glaab, L. J., and Theodore, C. R., "Greased Lightning (GL-10) Performance Flight Research—Flight Data Report," NASA/TM–2017-219794, Nov. 2017.

Melton, J., Kontinos, D., Grabbe, S., Sinsay, J., Alonso J. J., and Tracey, B., "Combined Electric Aircraft and Airspace Management Design for Metro-Regional Public Transportation," NASA/TM–2014-216626, Oct. 2014.

Meyn, L., "Rotorcraft Optimization Tools: Incorporating Rotorcraft Design Codes into Multi-Disciplinary Design, Analysis, and Optimization," American Helicopter Society Technical Conference on Aeromechanics Design for Transformative Vertical Flight, San Francisco, CA, Jan. 16-19, 2018.

Patterson, M., Antcliff, K., and Kohlman, L., "An Exploration of Urban Air Mobility Mission Requirements," American Helicopter Society 74th Annual Forum, Phoenix, AZ, May 14-17, 2018.

Rajagopalan, R. G., Baskaran, V., Hollingsworth, A., Lestari, A., Garrick, D., Solis, E., and Haggerty, B., "RotCFD a Tool for Aerodynamic Interference of Rotors: Validation and Capabilities," Future Vertical Lift Aircraft Design Conference, San Francisco, CA, Jan. 18-20, 2012.

Robuck, M., Wilkerson, J., Zhang, Y., Snyder, C. A., and Vonderwell, D., "Design Study of Propulsion and Drive Systems for the Large Civil TiltRotor (LCTR2) Rotorcraft," 67th Annual Forum and Technology Display of the American Helicopter Society, Virginia Beach, VA, May 3-5, 2011.

Robuck, M., Wilkerson, J., Snyder, C. A., Zhang, Y., and Maciolek, B., "Study and Sub-System Optimization of Propulsion and Drive Systems for the Large Civil TiltRotor (LCTR2) Rotorcraft," 69th Annual Forum and Technology Display of the American Helicopter Society, Phoenix, AZ, May 21-23, 2013a. See also NASA/TM–2013-218103, Dec. 2013.

Robuck, M., Wilkerson, J., Maciolek, R., and Vonderwell, D., "The Effect of Rotor Cruise Tip Speed, Engine Technology, and Engine/Drive System RPM on the NASA Large Civil Tiltrotor (LCTR2) Size and Performance," NASA/CR–2013-216593, Sept. 2013b.

Russell, C., and Johnson, W., "Conceptual Design and Mission Selection for a Large Civil Compound Helicopter, American Helicopter Society Future Vertical Lift Aircraft Design Conference, San Francisco, CA, Jan. 2012.

Russell, C., and Johnson, W., "Application of Climate Impact Metrics to Rotorcraft Design," Paper AIAA-2013-1087, 51st AIAA Aerospace Sciences Meeting including the New Horizons Forum and Aerospace Exposition, Grapevine, TX, Jan. 7-10, 2013a, DOI: 10.2514/6.2013-1087

Russell, C., and Johnson, W., "Exploration of Configuration Options for a Large Civil Compound Helicopter," 69th Annual Forum and Technology Display of the American Helicopter Society, Phoenix, AZ, May 21-23, 2013b.

Russell, C. R., and Basset, P.-M., "Conceptual Design of Environmentally Friendly Rotorcraft A Comparison of NASA and ONERA Approaches," 71st Annual Forum and Technology Display of the American Helicopter Society, Virginia, Beach, VA, May 2015.

Russell, C. R., Young, L. A., Yamauchi, G. K., Johnson, W., Boyd, D. D., Gorton, S. A., Snyder, C. A., and Kohlman, L. W., "Greener Helicopters, *Encyclopedia of Aerospace Engineering*, eds R. Blockley and W. Shyy, John Wiley: Chichester. DOI: 10.1002/9780470686652.eae1009, Published 12/29/2015.

Russell, C., Jung, J., Willink, G., and Glasner, B., "Wind Tunnel and Hover Performance Test Results for Multicopter UAS Vehicles," AHS 72nd Annual Forum, West Palm Beach, FL, May 17-19, 2016.

Russell, C., and Sekula, M., "Comprehensive Analysis Modeling of Small-Scale UAV Rotors," 73rd Annual Forum and Technology Display of the American Helicopter Society, Fort Worth, TX, May 9-11, 2017.

Russell, C., Theodore, C., and Sekula, M., "Incorporating Test Data for Small UAS at the Conceptual Design Level," AHS International Technical Conference on Aeromechanics Design for Transformative Vertical Flight, San Francisco, CA, Jan. 16-19, 2018a.

Russell, C., Willink, G., Theodore, C., Jung, J., and Glasner, B., "Wind Tunnel and Hover Performance Test Results for Multicopter UAS Vehicles," NASA/TM–2018-219758, Feb. 2018b.

Silva, C., Yeo, H., and Johnson, W., "Design of a Slowed-Rotor Compound Helicopter for Future Joint Service Missions," American Helicopter Society Aeromechanics Specialists' Conference, San Francisco, CA, Jan. 20-22, 2010.

Silva, C., Johnson, W., and Solis, E., "Multidisciplinary Conceptual Design for Reduced-Emission Rotorcraft," American Helicopter Society Technical Conference on Aeromechanics Design for Transformative Vertical Flight, San Francisco, CA, Jan. 16-19, 2018a.

Silva, C., Johnson, W., Antcliff, K. R., and Patterson, M. D., "VTOL Urban Air Mobility Concept Vehicles for Technology Development," Paper AIAA-2018-3487, AIAA Aviation Forum, 2018 Aviation Technology, Integration, and Operations Conference, Atlanta, GA, June 25-29, 2018b, DOI: 10.2514/6.2018-3847

Sinsay, J. D., Tracey, B., Alonso, J. J., Kontinos, D. A., Melton, J. E., and Grabbe, S., "Air Vehicle Design and Technology Considerations for an Electric VTOL Metro-Regional Public Transportation System," Paper AIAA-2012-5404, 12th AIAA Aviation Technology, Integration, and Operations (ATIO) Conference and 14th AIAA/ISSM, Indianapolis, IN, Sept. 17-19, 2012.

Snyder, C. A., Robuck, M., Wilkerson, J., and Nordstrom, C., "Summary of the Large Civil TiltRotor (LCTR2) Engine Gearbox Study," International Power Lift Conference, Philadelphia, PA, Oct. 5-7, 2010. See also NASA/TM–2010-216908, Nov. 2010.

Snyder, C. A., "Defining Gas Turbine Engine Performance Requirements for the Large Civil TiltRotor (LCTR2)," 67th Annual Forum and Technology Display of the American Helicopter Society, Virginia Beach, VA, May 3-5, 2011. See also NASA/TM–2013-218101, Dec. 2013.

Snyder, C., and Acree, Jr., C. W., "Preliminary Assessment of Variable Speed Power Turbine Technology on Tiltrotor Size and Performance," 68th Annual Forum and Technology Display of the American Helicopter Society, Ft. Worth, TX, May 1-3, 2012.

Snyder, C. A., "Exploring Advanced Technology Gas Turbine Engine Design and Performance for the Large Civil Tiltrotor (LCTR)," AIAA Propulsion and Energy Forum, Paper-AIAA-3442, 50th AIAA/ASME/SAE/ASEE Joint Propulsion Conference, Cleveland, OH, July 2014, DOI: 10.2514/6.2014-3442

Snyder, C., "Exploring Propulsion Systems Requirements for More and All-Electric Helicopters," International Society of Air Breathing Engines (ISABE), Phoenix, AZ, Oct. 25-30, 2015.

Snyder, C., "Range and Endurance Tradeoffs on Personal Rotorcraft Design," AHS 72nd Annual Forum, West Palm Beach, FL, May 17-19, 2016.

Snyder, C. A., "Personal Rotorcraft Design and Performance with Electric Hybridization," AHS International 73rd Annual Forum, Ft. Worth, TX, May 9-11, 2017a.

Snyder, C. A., "Assessment of Urban Aerial Taxi with Cryogenic Components under Design Environment for Novel Vertical Lift Vehicles (DELIVER)," AIAA Aviation Forum and Exposition 2017, Denver, CO, June 5-9, 2017b.

Snyder, C. A., and Kohlman, L. W., "Using Liquid Natural Gas Fuel to Cryogenically Cooling and Enhance a Hybrid Electric Aircraft Power System," 74th Annual Forum of the American Helicopter Society, Phoenix, AZ, May 14–17, 2018.

Theodore, C., "Summary of the NASA Design Environment for Novel Vertical Lift Vehicles Project," AHS International Technical Conference on Aeromechanics Design for Transformative Vertical Flight, San Francisco, CA, Jan. 16-19, 2018.

Ventura-Diaz, P., Yoon, S., and Theodore, C., "High-Fidelity Computational Aerodynamics of Multi-Rotor Unmanned Aerial Vehicles," 56th AIAA Aerospace Sciences Meeting, Kissimmee, FL, Jan. 8-12, 2018a.

Ventura-Diaz, P., Yoon, S., and Theodore, C., "High-Fidelity Computational Aerodynamics of the Elytron 4S UAV," AHS International Technical Conference on Aeromechanics Design for Transformative Vertical Flight, San Francisco, CA, Jan. 16-19, 2018b.

Veres, J., "Compressor Study to Meet the Large Civil Tilt Rotor Engine Requirements," NASA/ TM–2009-215614, 2009.

Veres, J. P., and Thurman, D. "Conceptual Design of a Two Spool Compressor for the NASA Large Civil Tilt Rotor Engine," 66th Annual Forum and Technology Display of the American Helicopter Society, Phoenix, AZ, May 10-12, 2010.

Yamauchi, G. K., and Young, L. A, "A Status of NASA Rotorcraft Research," NASA/TP–2009-215369, Sept. 2009.

Yeo, H., Sinsay, J., and Acree, Jr., C. W., "Selection of Rotor Solidity for Heavy Lift Tiltrotor Design," *Journal of the American Helicopter Society*, vol. 55, no. 1, Jan. 2010, DOI: 10.4050/JAHS.55.012010.

Yoon, S., Lee, H., and Pulliam, T., "Computational Analysis of Multi-Rotor Flows," AIAA 54th Aerospace Sciences Meeting, San Diego, CA, Jan. 4-8, 2016a.

Yoon, S., Lee, H., and Pulliam, T., "Computational Study of Flow Interactions in Coaxial Rotors," AHS Technical Meeting on Aeromechanics Design, San Francisco, CA, Jan. 20-22, 2016b.

Yoon, S., Chan, W. M., and Pulliam, T. H., "Computations of Torque-Balanced Coaxial Rotor Flows," Paper AIAA-2017-0052, 55th AIAA Aerospace Science Meeting, SciTech Forum, Grapevine, TX, Jan. 9-13, 2017a.

Yoon, S., Ventura-Diaz, P., Boyd, D. D., Chan, W. M., and Theodore, C. R., "Computational Aerodynamic Modeling of Small Quadcopter Vehicles," 73rd Annual Forum of the American Helicopter Society International, Ft. Worth, TX, May 9-11, 2017b.

Young, L. A., "Enhanced Rescue Lift Capability, 63rd Annual Forum and Technology Display of the American Helicopter Society, Virginia Beach, VA, May 1-3, 2007.

Young, L., Chung, W., Paris, A., Salvano, D., Young, R., Gao, H., Wright, K., Miller, D., and Cheng, V., "A Study of Civil Tiltrotor Aircraft in NextGen Airspace," Paper AIAA-2010-9106, 10th AIAA Aviation Technology, Integration, and Operations (ATIO) Conference, Fort Worth, TX, Sept. 13-15, 2010, DOI: 10.2514/6.2010-9106

Young, L., Chung, W., Paris, A., Salvano, D., Young, R., Gao, H., Wright, K., and Cheng, V., "Civil Tiltrotor Aircraft Operations," Paper AIAA-2011-6898, 11th AIAA Aviation Technology, Integration, and Operations (ATIO) Conference, Virginia Beach, VA, Sept. 20-22, 2011, DOI: 10.2514/6.2011-6898

Young, L., Yamauchi, G., and Rajagopalan, R., "Simulated Rotor Wake Interactions Resulting from Civil Tiltrotor Aircraft Operations Near Vertiport Terminals," Paper AIAA-2013-0801, 51st AIAA Aerospace Sciences Meeting including the New Horizons Forum and Aerospace Exposition Jan. 7-10, 2013, Grapevine, TX, DOI: 10.2514/6.2013-801

Young, L. A., "Conceptual Design Aspects of Three General Sub-Classes of Multi-Rotor Configurations: Distributed, Modular, and Heterogeneous," Sixth American Helicopter Society International Specialists Meeting on Unmanned Rotorcraft Systems, Scottsdale, AZ, Jan. 20-22, 2015a.

Young, L., "Simulated Tiltrotor Aircraft Operation in Close Proximity to a Building in Wind and Ground-Effect Conditions," Paper AIAA-2015-2700, AIAA Aviation Forum, 15th AIAA Aviation Technology, Integration, and Operations Conference, Dallas, TX, June 2015b, DOI: 10.2514/6.2015-2700

Young, L. A., "A Multi-Modality Mobility Concept for a Small Package Delivery UAV," 7th American Helicopter Society Technical Meeting on VTOL Unmanned Aircraft Systems, Mesa, AZ, Jan. 24-26, 2017.

Young, L., "Smart Precise Rotorcraft InTerconnected Emergency Services (SPRITES)," Paper AIAA-2018-2010, AIAA SciTech Forum, 2018 AIAA Aerospace Sciences Meeting, Kissimmee, FL, Jan. 2018a, DOI: 10.2514/6.2018-2010

Young, L. A., "What is a Tiltrotor? A Fundamental Reexamination of the Tiltrotor Aircraft Design Space," American Helicopter Society Technical Conference on Aeromechanics Design for Transformative Vertical Flight, San Francisco, CA, Jan. 16-19, 2018b.

Zawodny, N., Boyd, D., and Burley, C., "Acoustic Characterization and Prediction of Representative, Small-Scale Rotary-Wing Unmanned Aircraft System Components," AHS 72nd Annual Forum, West Palm Beach, FL, May 17-19, 2016.

Zawodny, N. and Boyd Jr., D. D., "Investigation of Rotor-Airframe Interaction Noise Associated with Small-Scale Rotary-Wing Unmanned Aircraft Systems," 73rd Annual Forum of the American Helicopter Society International, Ft. Worth, TX, May 9-11, 2017.

Zawodny, N., Christian, A., and Cabell, R., "A Summary of NASA Research Exploring the Acoustics of Small Unmanned Aerial Systems," AHS International Technical Conference on Aeromechanics Design for Transformative Vertical Flight, San Francisco, CA, Jan. 16-19, 2018.

CHAPTER 12. MARS HELICOPTER

Winnie Kuang,[1] Athena Chan,[2] and Larry A. Young[3]

INTRODUCTION

In 1997, rotary wing researchers at NASA Ames Research Center considered whether designing and building a Mars helicopter was possible; initial calculations suggested the answer was "yes." The idea was further developed and the concept of a vertical take-off and landing (VTOL) aircraft as an aerial scout for Mars exploration was documented by Young et al. [2000], the first such publication by NASA. The authors proposed two concepts: a tiltrotor and a coaxial helicopter. The coaxial helicopter had the advantage of simplicity and packaging. This seminal paper spawned related work within NASA and universities and, more importantly, provided NASA plausible options for augmenting ground rovers on planetary bodies that had some semblance of an atmosphere.

As described in Young et al. [2000] and Balaram et al. [2018], aerial exploration of Mars could greatly expand the mission capabilities of ground vehicles by quickly scouting safe routes for rovers. Aerial vehicles can also access and explore areas not reachable by rovers such as caves, gullies, and other hazardous terrains. Exploratory data collection and aerial mapping are also potential tasks for a Mars VTOL. The primary challenge for operating an aerial vehicle on Mars is the thin carbon dioxide Martian atmosphere with approximately 1 percent of the density of Earth's atmosphere. In addition, the gravity on Mars is approximately 38 percent of the Earth's gravity and there are large swings in temperature. These challenges, however, were overcome by detailed analysis and a series of tests to characterize the flight dynamics and control of the vehicle.

In 2013, the Jet Propulsion Laboratory (JPL) began the Mars Helicopter (MH) technology development project and reached out to the Revolutionary Vertical Lift Technology (RVLT) Project for assistance in aeromechanic analysis of their coaxial helicopter. In May 2018, NASA made the decision to include the MH as part of the Mars 2020 mission; the helicopter was integrated with the Mars 2020 Rover in August 2019 and is set to launch in July 2020. Nearly two decades after the publication of Young et al. [2000], the idea of a helicopter on Mars is poised to become a reality with the impending deployment of a coaxial helicopter technology demonstrator on Mars in February 2021 in the Jezero Crater. Figure 12.1 shows the MH, and Table 12.1, from Grip et al. [2019], lists the key properties of the vehicle.

[1] Science and Technology Corporation, 21 Enterprise Parkway, Suite 150, Hampton, VA 23666.
[2] Pennsylvania Space Grant Consortium, Temple University, 1801 N. Broad Street, Philadelphia, PA 19122.
[3] NASA Ames Research Center, Moffett Field, CA 94035-1000.

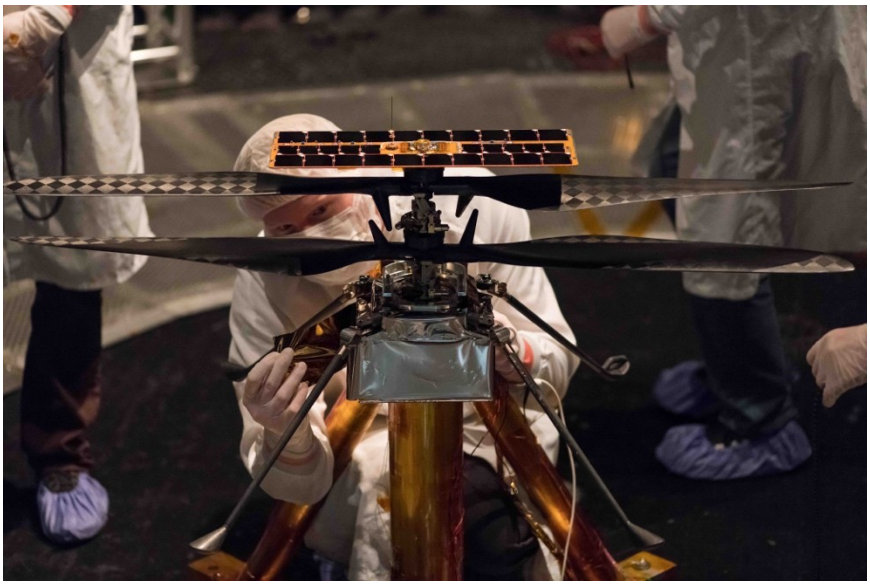

a) Mars Helicopter inside the JPL Space Simulator. Image credit: NASA/JPL-Caltech.

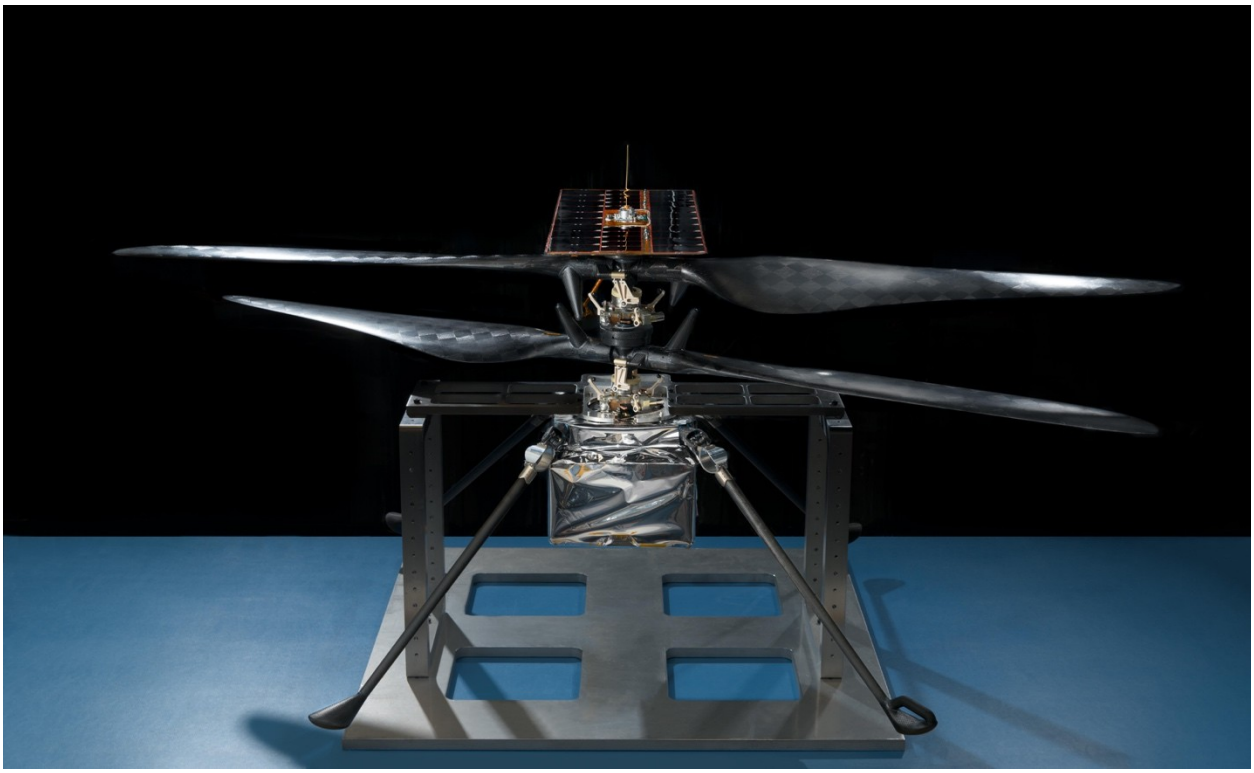

b) The aluminum base plate, side posts, and crossbeam around the helicopter protect the helicopter's landing legs and the attachment points that will hold it to the belly of the Mars 2020 rover. Caption and image credit: NASA/JPL-Caltech.

Figure 12.1. Mars Helicopter.

Table 12.1. Key Properties of the Mars Helicopter (Table 2 of Grip et al. [2019]).

Total mass*	1.8 kg
Rotor diameter	1.21 m
Rotor spacing	0.1 m
Ground clearance* (lower rotor)	0.3 m
Landing gear footprint*	0.6×0.6 m
Thrust-to-weight ratio* (density dependent)	130 % to 160 %
Endurance	$\geq$ 1.5 min
Rotor speed	$\leq$ 2,800 RPM
Collective control (both rotors)	–4.5° to 17.5°
Cyclic control (both rotors)	±10°

*Approximate value.

The MH is designed to operate over a period of 30 sols and must survive temperatures of –100 degrees C or lower at night [Balaram et al., 2018]. In general, daily flights will last up to 90 seconds with a range ≤ 300 m at altitudes ranging from 3 to 10 m above the ground. Flights will be scheduled when Martian winds are expected to be less than 5 m/s.

The development of the MH was very fast-paced, and much of the work contributed by the RVLT Project remains undocumented or only briefly addressed in the papers summarized in this chapter. On the cusp of the launch of the Mars 2020 Rover and the MH, we acknowledge the following RVLT researchers for their contributions that enabled the first attempt at aerial extra-terrestrial planetary exploration:

- Brian Allan—high-fidelity modeling and simulation of the MH vehicle components.
- Geoffrey Ament—surrogate rotor model installation and operation in the JPL Space Simulator (SS); supplemental experimental dust kick-up studies using surrogate coaxial rotor system.
- Farid Haddad—surrogate rotor model controls and instrumentation in the JPL SS.
- Wayne Johnson—MH vehicle and rotor performance; vehicle sizing and design tool development.
- Witold Koning—MH airfoil performance calculation.
- Carlos Malpica—MH flight dynamics and control modeling; system identification in hover and forward flight.
- Eduardo Solis—surrogate rotor model test director, model installation, and flow visualization in the JPL SS.
- Alan Wadcock—surrogate rotor flow visualization, velocity measurements, and low-Re pitot-tube velocity measurement development in the JPL SS; supplemental experimental dust kick-up studies using surrogate coaxial rotor system.

- Gina Willink—analysis and design of the surrogate rotor model installation in the JPL SS.
- Larry Young—analysis and CFD simulation of flow recirculation in hover in the JPL SS and other test chambers; development/analysis of concepts for simulated MH forward-flight testing in the JPL SS.

Finally, the strong advocacy of Susan Gorton (RVLT Project Manager) and William Warmbrodt (Chief, Aeromechanics Branch, NASA Ames Research Center) in support of the JPL team and the goals of the MH are also recognized.

This chapter highlights the published work performed by the RVLT Project in support of the MH development, including testing in the JPL SS, flight dynamics modeling, and rotor aerodynamic model development. In parallel with the MH development, a separate activity supported by the Aeromechanics Office at NASA Ames was initiated to test a surrogate Mars rotor for edgewise forward-flight conditions in the NASA Ames/Arizona State University Planetary Aeolian Laboratory (PAL). The purpose of the PAL testing was to further explore the behavior of rotors in a Mars-like atmosphere and produce rotor performance measurements for code validation. Testing in the PAL and aerodynamic analysis of airfoils suitable for Mars' conditions are described at the end of this chapter.

TESTING IN THE JPL SPACE SIMULATOR

Balaram et al. [2018] provides a summary of the modeling tools, simulations, and test campaigns supporting the MH from 2016–2018. Since duplicating the Martian flight conditions on Earth for testing vehicle designs was not feasible, research activities supporting the MH included multidisciplinary analyses augmented and validated by testing in facilities where the pressure (and therefore density) could be controlled. Key tests were performed in the 85-foot-high, 25-foot-diameter Space Simulator (SS) at JPL.

Though the SS is a large facility, testing a hovering rotor in an enclosed space will cause recirculation of the rotor wake—the wake hits the ground, travels along the ground, proceeds to flow upwards along the walls, and is eventually ingested into the rotor. Recirculation causes flow unsteadiness and the "hover" conditions quickly degrade. If the vertical dimension of the enclosed test environment is more than several rotor diameters, an option to mitigate flow recirculation is to operate the rotor so that the direction of thrust is down and the wake convects upward (opposite the direction of the floor). Based on simulations using the RotCFD analysis [Rajagopalan et al., 2012; and Guntupalli et al., 2016] of a hovering rotor in the SS, the MH team decided to test a surrogate rotor system in the SS to assess flow recirculation prior to the initial test of the MH prototype. The surrogate rotor test, described in McCoy et al. [2016], was performed in December 2015, on a very tight schedule, using hardware from NASA Ames. The rotor system comprised two co-rotating rotors in a stacked configuration. Each rotor had two blades and both rotors had a diameter of 40 inches. The rotors were clocked at a fixed 90 degrees relative to each other and were separated vertically by 2.57 inches. The rotor system is shown in Figure 12.2.

As described in McCoy et al. [2016], the rotor system was tested at two locations in the chamber—on the chamber centerline and 2 m off-axis. The rotor was tested in both upright and inverted configurations for 500 < RPM < 2000. Testing was performed at Earth's, rather than Mars', atmospheric conditions. Fluorescent micro-tufts, arranged in a grid pattern on a movable frame, were used to identify regions of recirculation. A sonic anemometer was used to measure velocities on the entrainment side of the rotor. Figure 12.3 shows the installation in the SS.

As shown in Figure 12.4, the fluorescent tufts successfully revealed the ambient flow direction inside the hover chamber, confirming the advantage of testing an inverted rotor compared to testing an upright rotor. An upright rotor (thrust = up, wake = down) was shown to operate with a ring vortex between the plane of the rotor and the chamber floor (Fig. 12.4b).

The sonic anemometer velocity measurements were made on the intake side of the rotor close to the 75-percent radial station for both thrust-up/wake-down and thrust-down/wake-up configurations. The measurements were helpful in documenting the typical expected turbulent gust in the chamber due to recirculation and ensuring that the control authority for the MH prototype was sufficient for free flight inside the SS.

Informed by the 2015 test results and a parallel intensive design effort, the MH prototype was tested in the SS in May 2016 to explore the flight dynamics and controllability of the vehicle [Grip et al., 2017]. The prototype (demonstration vehicle) is shown in Figure 12.5.

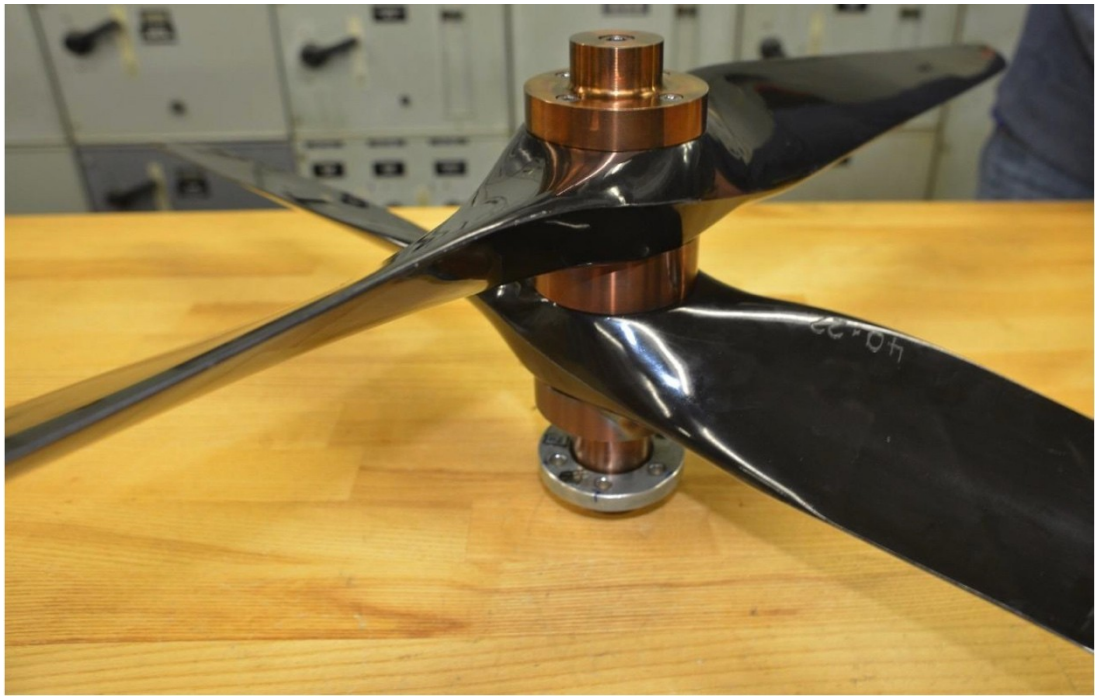

Figure 12.2. "Stacked" rotor system tested in the JPL SS, December 2015
(Fig. 5 of McCoy et al. [2016]).

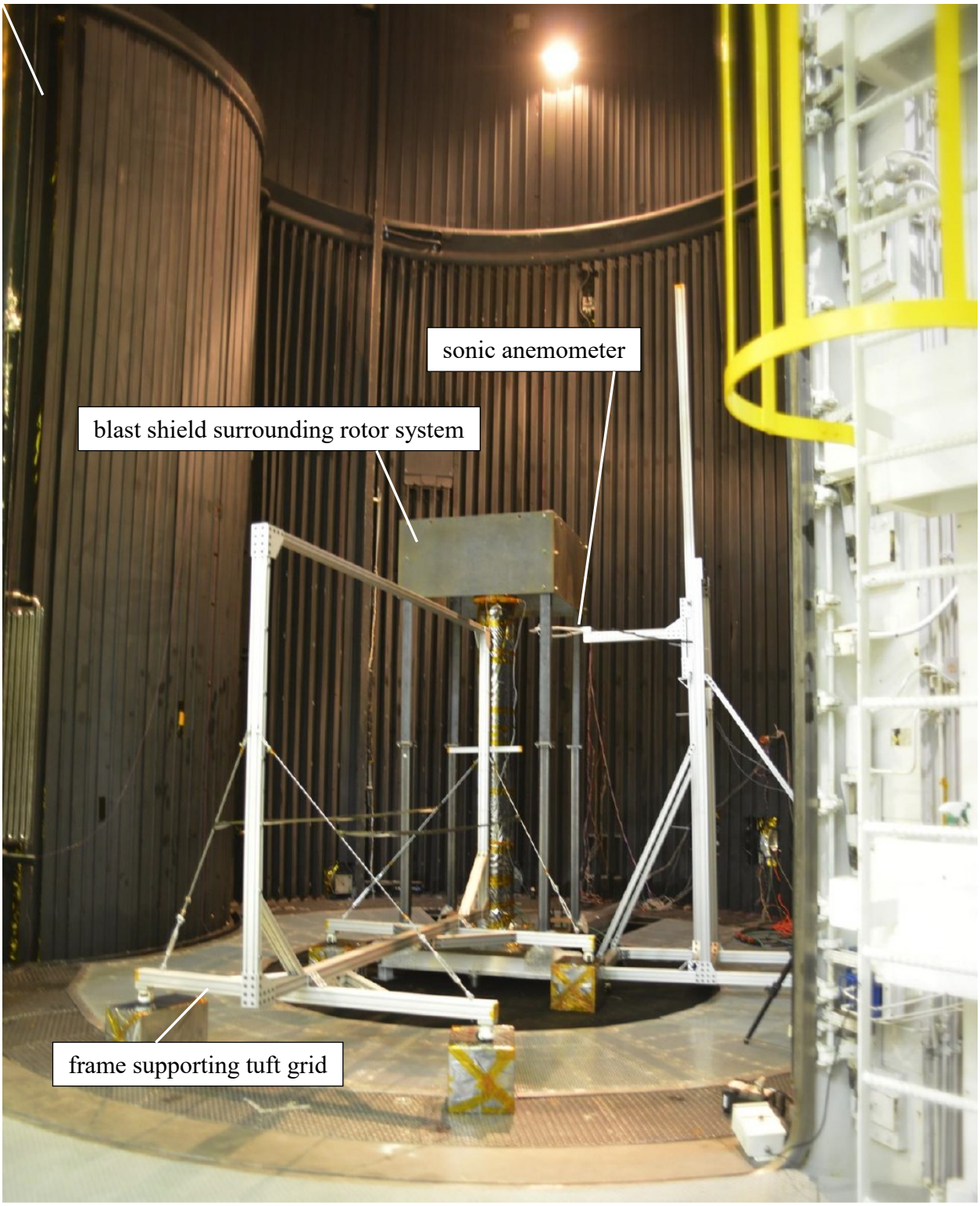

Figure 12.3. Installation for recirculation assessment in the JPL SS, December 2015 (Fig. 14 of McCoy et al. [2016]).

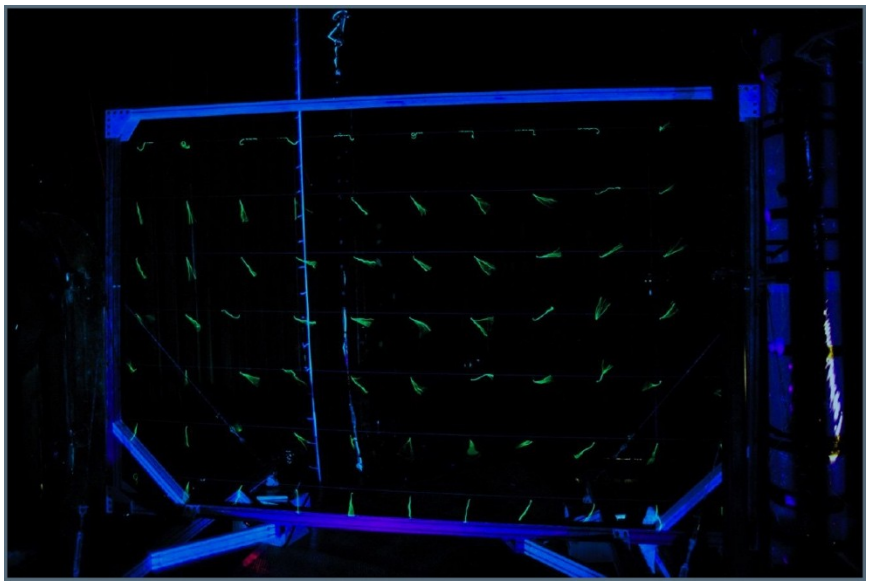

a) Run 1 Point 1 (thrust = down, wake = up), rotor RPM = 500 (Fig. 19 of McCoy et al. [2016]).

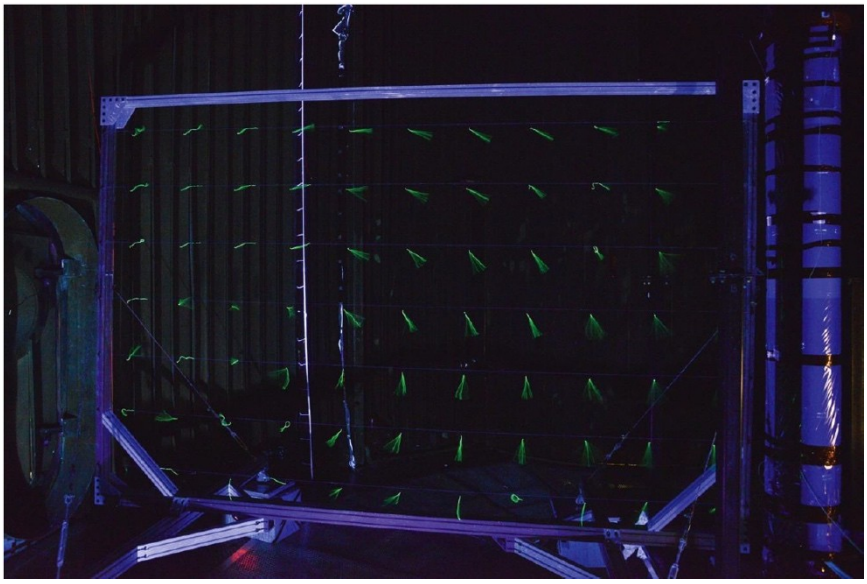

b) Run 4 Point 1 (thrust = up, wake = down), rotor RPM = 500 (Fig. 20 of McCoy et al. [2016]).

Figure 12.4. Tuft grid revealing flow behavior in the JPL SS.

Each of the hingeless rotors shown in Figure 12.5 has a diameter of 1.2 m; the rotors are counter-rotating with a vertical separation of about 17 percent of the rotor radius and are designed to operate at 2800 RPM. Both rotors have collective control but only the lower rotor has cyclic control. Components not required to meet the test objective of controlled flight were not included on the vehicle to minimize weight. Grip et al. [2017] developed the Helicopter Control Analysis Tool (HeliCAT) specifically to model and analyze the flight dynamics of the demonstration vehicle. CAMRAD II [Johnson, 1994, 1998] was used to augment HeliCAT results. System identification of the vehicle was successfully performed for three vehicle mounting

configurations: locked down with vehicle mounted on a force-torque sensor, vehicle mounted on a force-torque sensor at the end of a swinging arm, and vehicle mounted on a gimbal with roll and pitch degrees of freedom. Based on the lessons learned from the 2015 surrogate rotor test, the vehicle was tested in the inverted position, except when mounted on the swing-arm, to minimize recirculation in the SS chamber. The vehicle was also flown (upright) and controlled in free flight. The fully autonomous free flight consisted of takeoff, hover, climb, and landing. Details of the control design are provided in Grip et al. [2018]. The testing conditions were under Martian densities but set at a warmer temperature than what would be expected on Mars. Martian atmospheric density was achieved by pumping down the chamber to 500 mTorr and then filling the chamber with carbon dioxide at a density of 0.0175 kg/m^3 [Balaram et al., 2018].

Two Engineering Development Models (EDMs) were built next. Figure 12.6 shows the EDM of the MH from Balaram, et al. [2018].

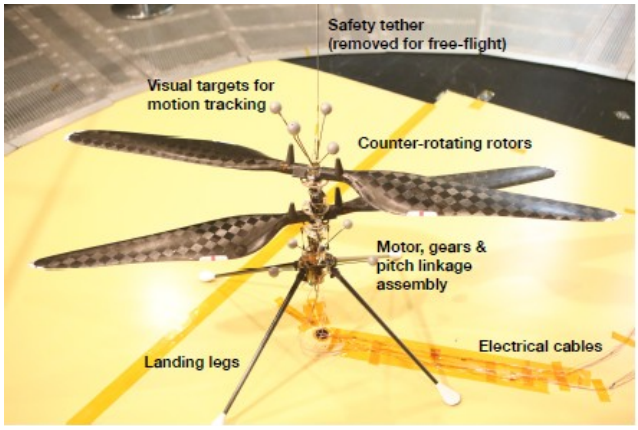

Figure 12.5. Demonstration vehicle (built by AeroVironment, Inc.) used for the controlled-flight demonstration in Martian atmospheric conditions (Fig. 4 of Grip et al. [2017]).

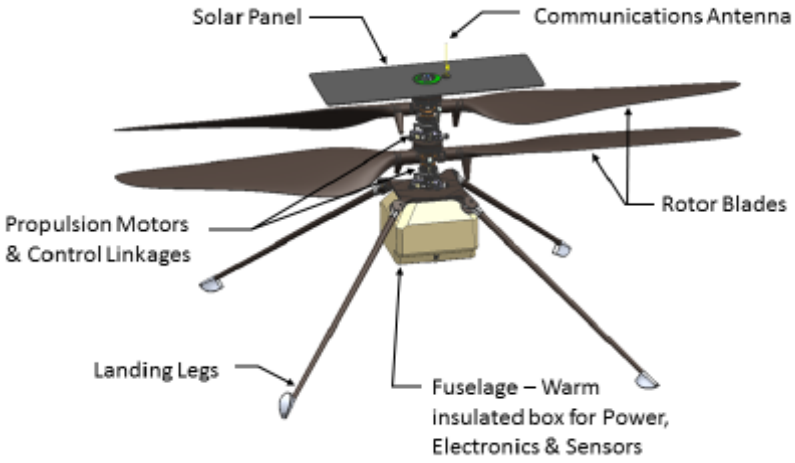

Figure 12.6. EDM design (Fig. 6 of Balaram, et al. [2018]).

Both models were full-scale versions of the flight vehicle, with EDM-1 dedicated to aerodynamic and flight control testing [Grip et al., 2019]. Unlike the demonstration vehicle, both rotors of the EDM vehicles have collective and cyclic control, and instead of a single motor driving both rotors, the EDM vehicles have two direct-drive motors. Successful verification and validation of the EDM-1 flight control system comprised a series of tests [Grip et al., 2019]:

- Simulation of end-to-end flights using HeliCAT.
- System identification in the JPL 25-foot SS.
- Gravity-offloaded flight testing in the JPL 25-foot SS.
- Outdoor testing of the navigation system using a surrogate commercial platform.
- Gravity-offloaded drop testing of the landing gear, performed by AeroVironment, Inc.

Similar to the system identification testing of the demonstration vehicle, the EDM-1 was mounted in the inverted position on a pitch gimbal in the SS. Transition from hover to forward flight was simulated by exposing the EDM-1 to winds of up to 11 m/s generated by 900 small commercial fans within the SS chamber (Fig. 12.7).

For a complete summary of the MH development from 2016–2018, consult Balaram et al. [2018].

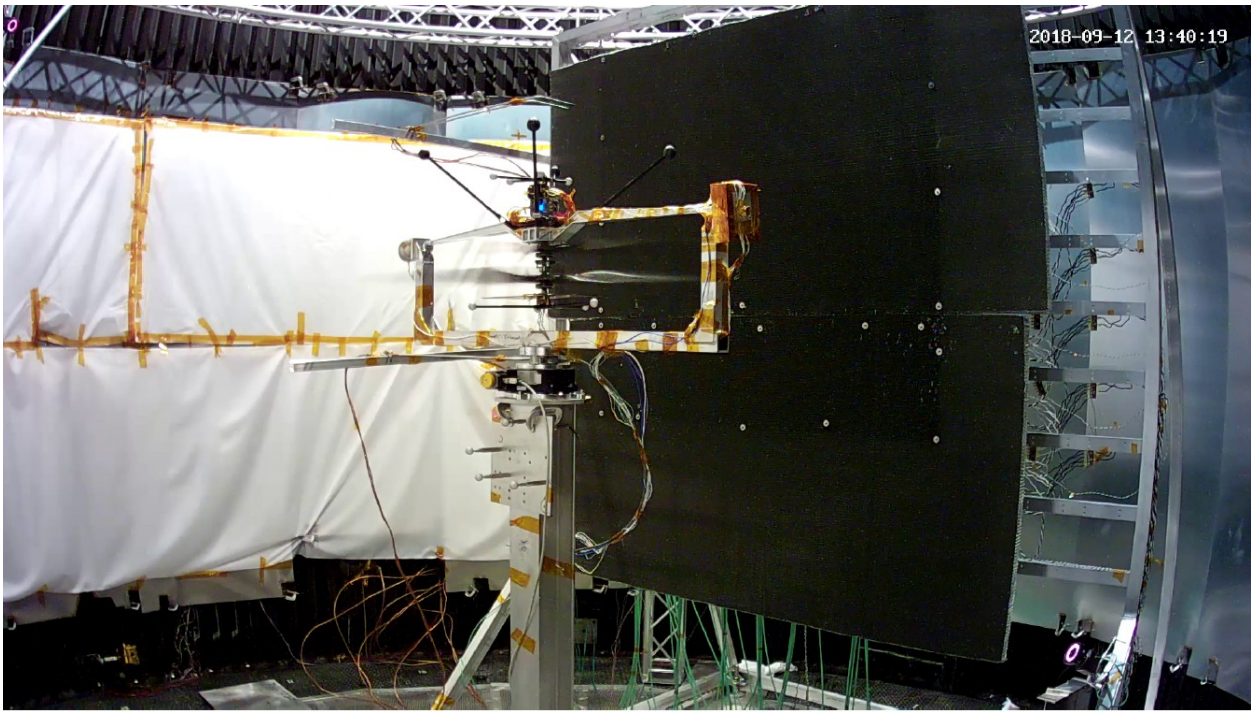

Figure 12.7. EDM-1 during a system identification experiment in front of the wind wall inside the JPL 25-foot SS. The helicopter was mounted upside down on a pitch gimbal and was under closed-loop control to maintain stability. A cyclic frequency sweep was applied to induce pitch variation (Fig. 12 of Grip et al. [2019]).

By 2016, AeroVironment, Inc. had already designed and built a prototype rotor system for the MH. The RVLT Project focused on developing a rotor performance model of the prototype using CAMRAD II, a comprehensive rotorcraft analysis [Johnson, 1994, 1998]. CAMRAD II represents the rotor blade using lifting-line theory and steady two-dimensional (2D) airfoil characteristics. The airfoil characteristics are in the form of lift, drag, and pitching moment coefficients as a function of angle of attack and Mach number, arranged in tabular format known as the c81-format. These airfoil tables can be populated with experimental values, computed values, or a combination thereof. For the MH rotor blade airfoils, no test data exists so the tables were populated with computed values. The low-density Martian atmosphere, coupled with the small-chord of the MH blades, results in very low (~10^3 to ~10^4) Reynolds number and high Mach number flows—a very challenging environment to analyze. Koning et al. [2018a] describes the approach used to develop airfoil tables for the MH rotor by leveraging previous low-Reynolds-number research and a Reynolds-Averaged Navier–Stokes (RANS) solver to compute the airfoil characteristics. C81Gen—an interface tool developed by Sukra Helitek, Inc.—used the RANS solver to compute airfoil characteristics for a range of angle of attack and Mach numbers with the results output in c81 format. In the absence of data, the C81Gen results were compared with OVERFLOW calculations; the agreement was deemed to be "close enough" as shown in Figure 12.8.

The airfoil deck was then used by CAMRAD II to compute the isolated hover performance of the MH; the results are compared to the data acquired in the SS, as shown in Figure 12.9.

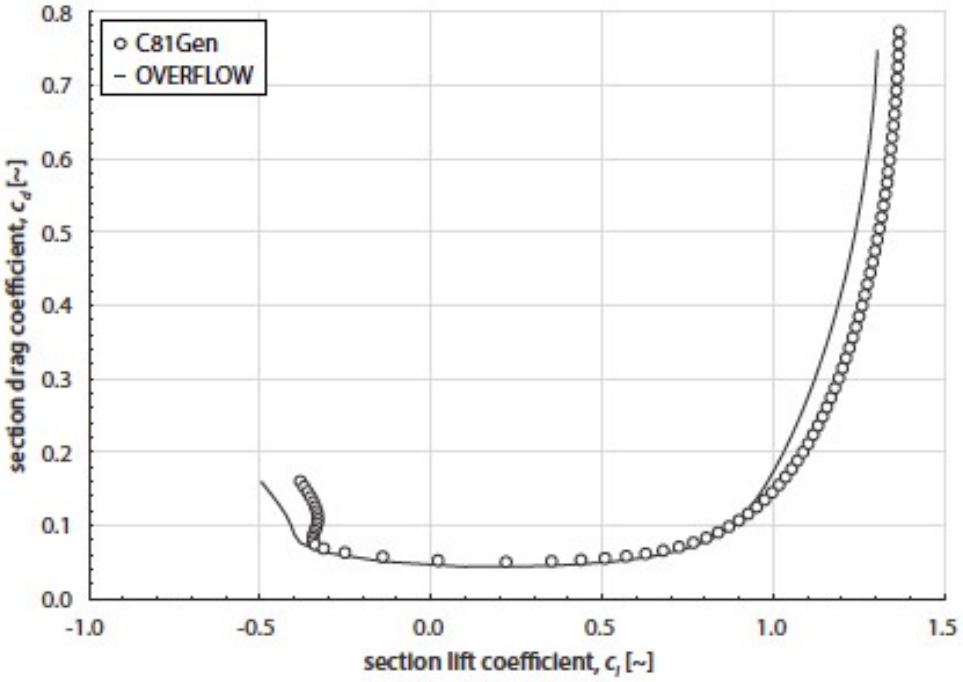

Figure 12.8. The lift-drag curve comparison between C81Gen and OVERFLOW for the clf5605 airfoil at T = 295 K, M = 0.7, and $Re\#$ = 7,600 (Fig. 21 from Koning et al. [2018a]).

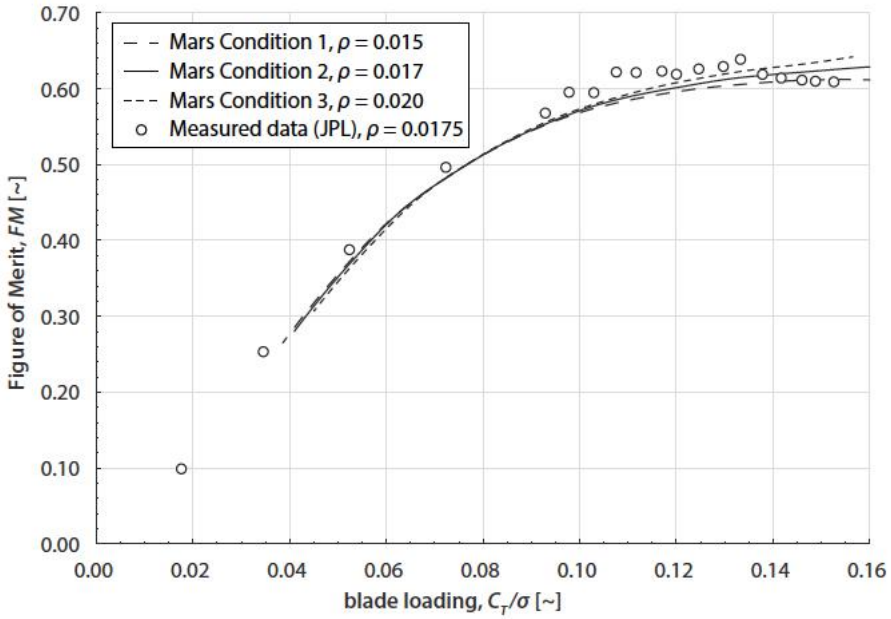

Figure 12.9. Figure of merit versus blade loading for several Martian conditions (Fig. 26 of Koning et al. [2018a]).

SUPPLEMENTAL TESTING AND ANALYSIS IN A MARS ENVIRONMENT

While JPL led the push to satisfy technical requirements for the MH, supplementary testing and analysis were performed by NASA Ames to further understand the aerodynamics of a rotor in Mars' atmospheric conditions.

Testing in the Planetary Aeolian Laboratory (PAL)

The stacked rotor system described in McCoy et al. [2016] was tested in the Martian Surface Wind Tunnel (MARSWIT) of the Planetary Aeolian Laboratory (PAL) at NASA Ames. The test campaign is described in Ament and Koning [2018], Ament et al. [2019], and Perez Perez et al. [2019].

The Planetary Aeolian Laboratory (PAL), shown in Figure 12.10, is a facility used for simulating atmospheric conditions that can range from approximately 1 bar to 5.5 mbar, which is the equivalent of a range of Earth's atmosphere to less than Mars' atmosphere. The facility is 98.5 feet high, and 459,090 cubic feet in volume, and is a near-vacuum. The MARSWIT (Fig. 12.11) is an open-circuit 43-foot-long atmospheric boundary-layer wind tunnel, located inside the PAL near-vacuum chamber. The internal cross section has a height of 3.3 feet and a width of 4 feet. The MARSWIT can be tested in all atmospheric conditions specified within the PAL. For instance, at 5 mbars, the wind speeds reach up to 328 ft/sec, while at 1018 mbar, the wind speeds are up to 34.5 ft/s. The tunnel is used to study the physics of particle entrainment, and to test spacecraft instruments and rotor performance, all under Martian conditions.

The single-rotor and stacked dual-rotor systems are shown in Figure 12.12.

Operationally, testing in the MARSWIT was challenging, though Ament and Koning [2018] were able to successfully test the single- and dual-rotor configurations in forward flight for 1 atm down to Mars' atmospheric pressures. Rotor thrust, torque, and power measurements were collected at constant pressures of 8, 14, and 28 mbar, 30 to 200 mbar while pressure drifted at 1 mbar per minute, and at 1 atm (see Fig. 12.13). Perez Perez et al. [2019] extended the work of Ament et al. [2019] by providing more detail about the test, in particular, the post-processing of the data.

Figure 12.10. The NASA Ames PAL (Fig. 1 of Ament and Koning [2018]).

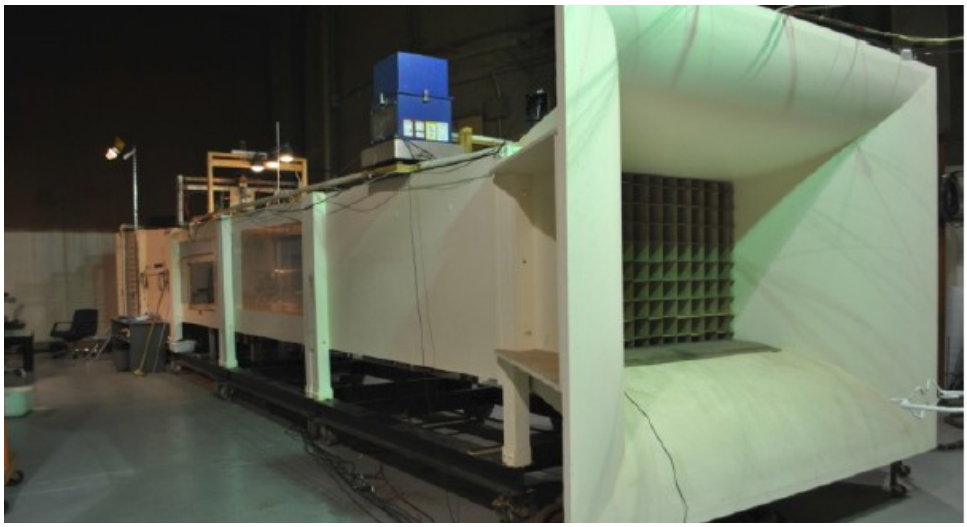

Figure 12.11. The MARSWIT (Fig. 2 of Ament and Koning [2018]).

Figure 12.12. Single-rotor (left) and dual-rotor (right) configurations tested in the MARSWIT test section of the PAL (Fig. 3 of Ament and Koning [2018]).

As described in Koning [2018], the geometry of one of the rotor blades was measured using a three-dimensional (3D) laser scanner. Radial stations at r/R = 0.29, 0.58, and 0.78 were chosen as the critical airfoil locations, and the spanwise twist and chord distribution were extracted from the scanned geometry.

The C81Gen and RotCFD analyses, both developed by Sukra Helitek, were used by Ament and Koning [2018] to simulate the single rotor in free-field hover and in forward flight. Given the geometry of an airfoil, C81Gen computes the lift, drag, and moment coefficient for a desired range of angle of attack and Mach number, and outputs the results in a C81-formatted table. The table is then used by the flow solver RotCFD to compute the aerodynamic loads on the rotor blades. RotCFD results correlated well with experimental 1-atm free-field hover thrust data for both single and dual rotors. For forward flight testing at 1 atm, the single-rotor thrust was well predicted but torque and power were underpredicted by about 30 percent. At 28 mbar in the MARSWIT, the single-rotor thrust and torque were underpredicted by about 35 percent and 20 percent, respectively.

Perez Perez [2018] continued the RotCFD simulation of the single-rotor configuration tested by Ament and Koning [2018] and Ament et al. [2019] and also assessed the effect of the MARSWIT walls. Simulations were performed for 1 atm and 14 mbar. The effect of wind tunnel walls was not the primary source contributing to the large discrepancies between the computed and measured thrust and torque. Other parameters that were varied in the simulation, such as time step, grid density, and increasing the length of the wind tunnel, did not result in meaningful changes in thrust or power. Perez Perez subsequently updated the RotCFD simulations by using airfoil performance tables calculated for fully laminar flow conditions (instead of turbulent flow), resulting in much improved correlation with the test data. The results will be published in 2020.

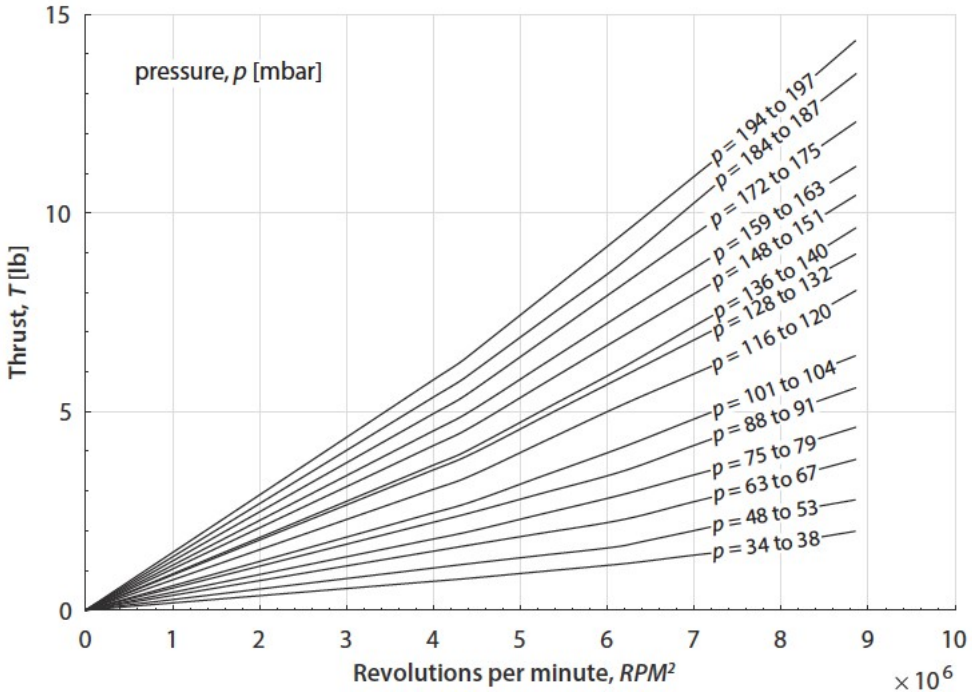

a) Single rotor: thrust vs. RPM^2 as chamber pressure was increased from about 30 to 200 mbar (Fig. 15 of Ament and Koning [2018]).

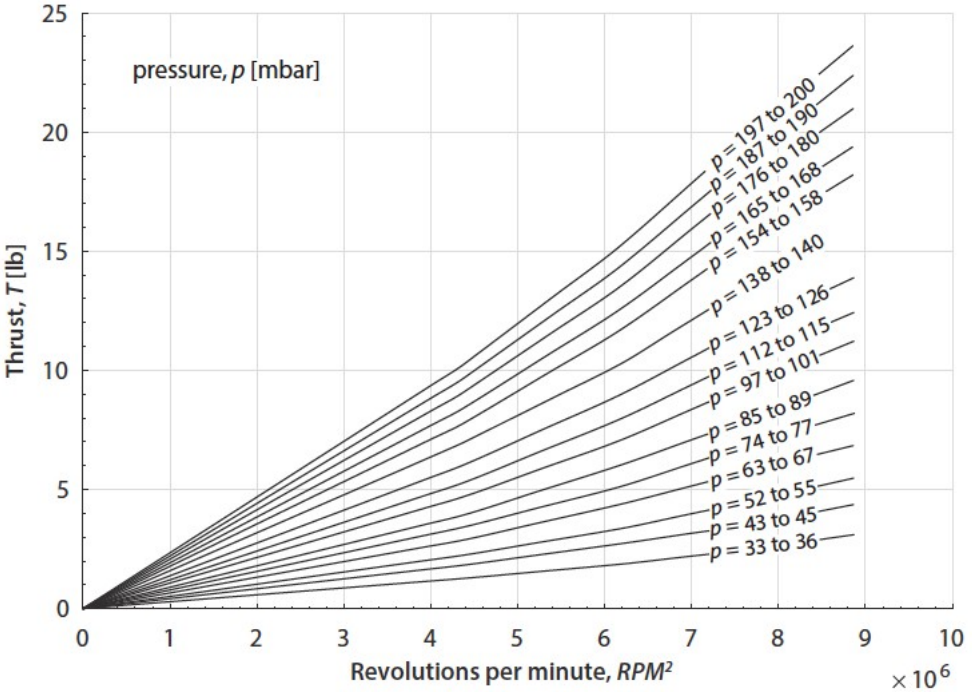

b) Dual rotor: thrust vs. RPM^2 as chamber pressure was increased from about 30 to 200 mbar (Fig. 16 of Ament and Koning [2018]).

Figure 12.13. Rotor thrust behavior for different chamber pressures.

Wagner [2019] used RotCFD to simulate the single rotor and dual stacked rotor in hover for 1 atm and 14 mbar. Like Perez Perez [2018], Wagner explored facility effects by including the PAL walls, test stand, and the blast shields installed for test safety. Overall, facility effects had a minimal impact on the calculated performance. The overall thrust was not affected by the addition of the N242 walls, in both Earth and Martian testing, and for both the single- and dual-rotor configurations. The use of the blast shields and test stand had some effect (a 10-percent change in thrust) for the simulated Mars' conditions.

Rotor Aerodynamic Analysis

The lessons learned from analyzing the challenging low-Reynolds-number flows in Koning et al. [2018a] encouraged further studies, led by Koning, on airfoil designs for applications on Mars. In Koning et al. [2018b], the authors used the same tools (CAMRAD II, OVERFLOW, and C81Gen) to compare calculated hover performance of several airfoil profiles with the MH airfoil. At Reynolds numbers representing conditions on Mars, a cambered plate rotor model was calculated to have 5 percent higher figure of merit and 7 percent greater maximum thrust, over the design thrust range, than the MH rotor, given the same blade twist and chord distribution. Following this work, Koning et al. [2018c] used OVERFLOW to perform time-accurate simulations of the flow field of the airfoils defined at eight radial stations of the MH rotor blade. For each of the eight airfoils, the trailing edge thickness was adjusted to represent a realistic thickness, and the density of the computation mesh was increased compared to earlier works by the authors. Also, two separate rotor models were developed: one for the test condition in the JPL SS and one for a density of 0.017 (kg/m^3) and temperature of –50 degrees C. For both conditions, the rotor model with transition and the model with fully turbulent flow performed similarly over the design thrust range [Koning et al., 2018c].

Armed with more knowledge about low-Reynolds-number flow, Koning [2019] surveyed potential airfoil geometries for the next-generation Mars VTOL aircraft. The author concluded that the cambered-plate airfoil presented a promising avenue for further research, in particular, exploring the effects of nonlinear camber lines and chordwise plate-thickness distributions on the performance of the airfoil. A custom airfoil design algorithm, written by the author, is described. The algorithm performs OVERFLOW grid generation and executes the solver, varies the airfoil geometry within set constraints, and performs post-processing. The optimized airfoil shapes can then be used to generate airfoil tables that are used as input to CAMRAD II or other comprehensive analyses as previously described in Koning et al. [2018a, 2018b, 2018c].

In Koning et al. [2019], the author developed a genetic algorithm to optimize airfoil shapes for use in atmospheric conditions on Mars. The optimization allowed for camber and thickness variations of curved and polygonal thin airfoils with sharp leading edges. Design conditions targeted a future Mars Science Helicopter (MSH); the MSH is expected to have a mass of about 20 kg and have the ability to carry 0.5–2 kg of payload in addition to conducting flights up to 3,000 m. Four different airfoils were studied: cambered plate (CP), arbitrary continuous airfoil (ACA), double-edged plate (DEP), and polygonal airfoil (PAT). The airfoil performance was evaluated at the highest attainable lift-to-drag ratio near a moderate lift coefficient at

compressible Mach numbers, as expected for Martian rotor application. For the two representative flight conditions for Mars rotor operation (Mach = 0.35, Reynolds number = 11,352, and Mach = 0.50, Reynolds number = 16,682), the CP and DEP airfoils showed increases between 16 and 29 percent in airfoil lift-to-drag ratio at fixed lift coefficients compared with the clf5605 MH airfoil studied in Koning et al. [2018a, 2018b, 2018c] (see Fig. 12.14). Compared to the hover figure of merit calculated for the previous rotor models of the MH, the author estimates a 4- to 10-percent improvement if an optimized airfoil were used.

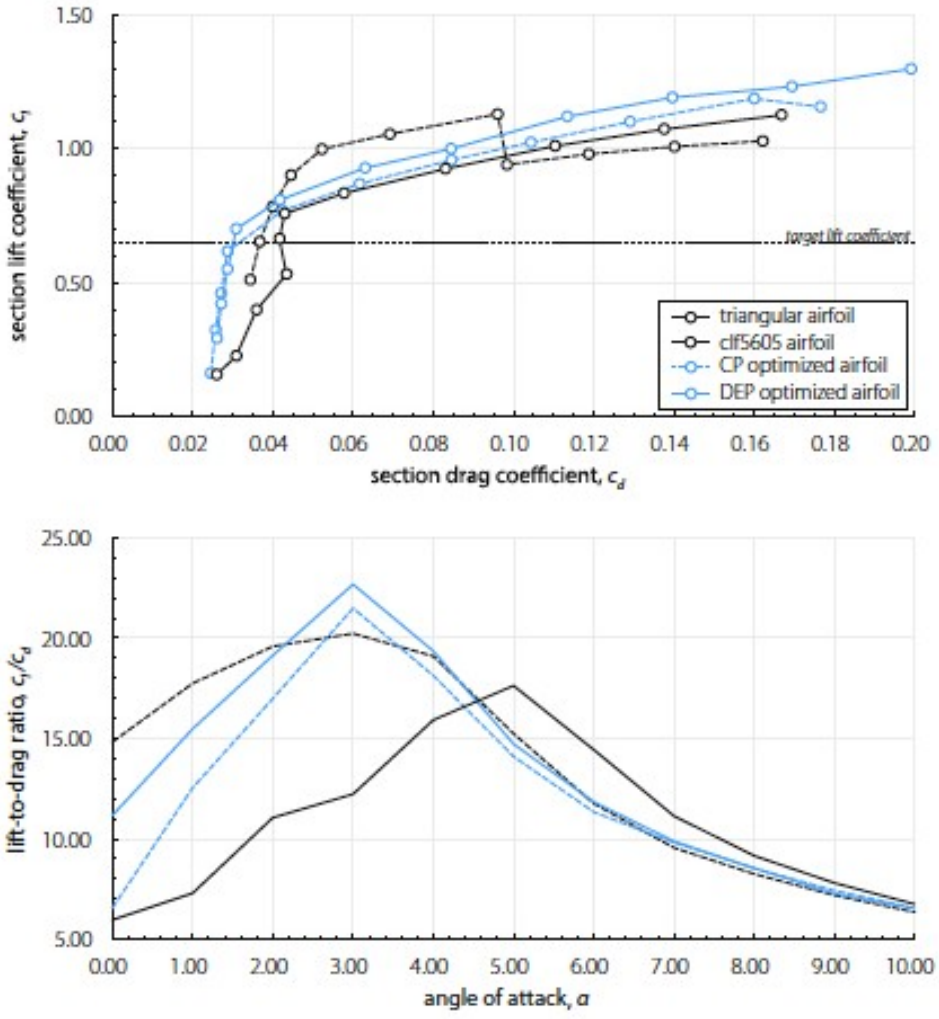

Figure 12.14. CP and DEP optimized airfoils at target section $c_l = 0.65$, versus clf5605 at M = 0.50 (Fig. 23 of Koning et al. [2019]).

REFERENCES

Ament, G. A., and Koning, W. J. F., "Isolated Rotor Forward Flight Testing From One Atmosphere Down to Martian Atmospheric Densities," AHS International Technical Conference on Aeromechanics Design for Transformative Vertical Flight, San Francisco, CA, Jan. 16-19, 2018.

Ament, G. A., Witold, J. F. K., and Perez, B. N. P., "Isolated Rotor Forward Flight Testing at Martian Atmospheric Density Data Report," NASA/CR–2018-219736, May 2019.

Balaram, J., Canham, T., Duncan, C., Golombek, M., Grip, H. F., Johnson, W., Maki, J., Quon, A., Stern, R., and Zhu, D., "Mars Helicopter Technology Demonstrator," Paper No. 2018-0023, AIAA SciTech Forum, 2018 AIAA Atmospheric Flight Mechanics Conference, Kissimmee, FL, Jan. 8-12, 2018, DOI: 10.2514/6.2018-0023

Grip, H. F., Johnson, W., Malpica, C., Scharf, D., Mandi, M., Young, L., Allan, B., Mettlerz, B., and San Martin, M., "Flight Dynamics of a Mars Helicopter," 43rd European Rotorcraft Forum, Milan, Italy, Sept. 12-15, 2017.

Grip, H. F., Scharf, D., Malpica, C., Johnson, W., Mandic, M., Singh, G., and Young, L., "Guidance and Control for NASA's Mars Helicopter," AIAA Paper No. 2018-1849, AIAA SciTech Forum, 2018 AIAA Guidance, Navigation, and Control Conference, Kissimmee, FL, Jan. 8-12, 2018, DOI: 10.2514/6.2018-1849

Grip, H. F., Lam, J. N., Bayard, D., Conway, D. T., Singh, G., Brockers, R., Delaune, J., Matthies, L., Malpica, C., Brown, T., Jain, A., Martin, M. S., and Merewether, G., "Flight Control System for NASA's Mars Helicopter," AIAA Paper No. 2019-1289, AIAA SciTech 2019 Forum, Jan. 6, 2019, DOI: 10.2514/6.2019-1289

Guntupalli, K., Novak, L. A., and Rajagopalan, R. G., "RotCFD: An Integrated Design Environment for Rotorcraft," American Helicopter Society Specialists' Conference on Aeromechanics Design for Vertical Lift, San Francisco, CA, Jan. 20-22, 2016.

Johnson, W., "Technology Drivers in the Development of CAMRAD II," American Helicopter Society Aeromechanics Specialists' Meeting, San Francisco, CA, Jan. 1994.

Johnson, W. "Rotorcraft Aeromechanics Applications of a Comprehensive Analysis." HeliJapan 1998: American Helicopter Society International Meeting on Rotorcraft Technology and Disaster Relief, Gifu, Japan, April 1998.

Koning, W. J. F., Johnson, W., and Allan, B. G., "Generation of Mars Helicopter Rotor Model for Comprehensive Analyses," American Helicopter Society Technical Meeting on Aeromechanics Design for Vertical Lift, San Francisco, CA, Jan. 16–18, 2018a.

Koning, W. J. F., Romander, E. A., and Johnson, W., "Low Reynolds Number Airfoil Evaluation for the Mars Helicopter Rotor," American Helicopter Society International 74th Annual Forum and Technology Display, Phoenix, AZ, May 14-17, 2018b.

Koning, W. J. F., Johnson, W., and Grip, H. F, "Improved Mars Helicopter Aerodynamic Rotor Model for Comprehensive Analyses," 44th European Rotorcraft Forum, Delft, The Netherlands, Sept. 18-21, 2018c.

Koning, W. J. F., “Generation of Performance Model for the Aeolian Wind Tunnel (AWT) Rotor at Reduced Pressure,” NASA/CR-2018–219737, Dec. 2018.

Koning, W. J. F., “Airfoil Selection for Mars Rotor Applications,” NASA/CR–2019-220236, July 2019.

Koning, W. J. F., Romander, E. A., and Johnson, W., “Performance Optimization of Plate Airfoils for Martian Rotor Applications Using a Genetic Algorithm,” 45th European Rotorcraft Forum, Warsaw, Poland, Sept. 17-20, 2019.

McCoy, M., Wadock, A. J., and Young, L. A., “Documentation of the Recirculation in a Closed-Chamber Rotor Test,” American Helicopter Society International Technical Conference on Aeromechanics Design for Transformative Vertical Flight; San Francisco, CA, Aug. 1, 2016.

Perez Perez, B. N., “Rotor CFD Analysis at Terrestrial and Martian Atmospheric Densities,” NASA/CR–2018-219780, 2018.

Perez Perez, B.N., Ament, G.A., and Koning, W.J.F., "Experimental Forward Flight Rotor Performance Testing From Terrestrial to Martian Atmospheric Densities," NASA/CR–2019–220229, 2019.

Rajagopalan, R. G., Baskaran, V., Hollingsworth, A., Lestari, A., Garrick, D., Solis, E., and Haggerty, B., “RotCFD a Tool for Aerodynamic Interference of Rotors: Validation and Capabilities,” Future Vertical Lift Aircraft Design Conference, San Francisco, CA, Jan. 18-20, 2012.

Wagner, L. N., “Simulations of the Mars Helicopter Test Propeller in Hover Configuration at Martian Pressure and Air Density,” NASA/CR–2019-220062, Feb. 2019.

Young, L. A., Chen, R. T. N., and Briggs, G. A., “Design Opportunities and Challenges in the Development of Vertical Lift Planetary Aerial Vehicles,” American Helicopter Society, International Vertical Lift Aircraft Design Specialists’ Meeting, San Francisco, CA, Jan. 19-21, 2000.